ARO 32824.1-EL-CF

ULTRAFAST PHENOMENA

19950203 248

Sponsored by
Optical Society of America

1994 TECHNICAL DIGEST
SERIES VOLUME 7

MAY 2–6, 1994
DANA POINT, CALIFORNIA

REPORT DOCUMENTATION PAGE

Form Approved
OMB No. 0704-0188

Public reporting burden for this collection of information is estimated to average 1 hour per response, including the time for reviewing instructions, searching existing data sources, gathering and maintaining the data needed, and completing and reviewing the collection of information. Send comments regarding this burden estimate or any other aspect of this collection of information, including suggestions for reducing this burden, to Washington Headquarters Services, Directorate for Information Operations and Reports, 1215 Jefferson Davis Highway, Suite 1204, Arlington, VA 22202-4302, and to the Office of Management and Budget, Paperwork Reduction Project (0704-0188), Washington, DC 20503.

1. AGENCY USE ONLY (Leave blank)	2. REPORT DATE	3. REPORT TYPE AND DATES COVERED
	Nov 94	Final 11 Apr 94 - 10 Apr 95

4. TITLE AND SUBTITLE
Organization of 1994 Optical Society of America Ultrafast Phenomena Topical Meeting

5. FUNDING NUMBERS
DAAH04-94-G-0104

6. AUTHOR(S)
David W. Hennage (principal investigator)

7. PERFORMING ORGANIZATION NAME(S) AND ADDRESS(ES)
Optical Society of America
Washington, DC 20036

8. PERFORMING ORGANIZATION REPORT NUMBER

9. SPONSORING/MONITORING AGENCY NAME(S) AND ADDRESS(ES)
U.S. Army Research Office
P.O. Box 12211
Research Triangle Park, NC 27709-2211

10. SPONSORING/MONITORING AGENCY REPORT NUMBER
ARO 32824.1-EL-CF

11. SUPPLEMENTARY NOTES
The views, opinions and/or findings contained in this report are those of the author(s) and should not be construed as an official Department of the Army position, policy, or decision, unless so designated by other documentation.

12a. DISTRIBUTION/AVAILABILITY STATEMENT
Approved for public release; distribution unlimited.

12b. DISTRIBUTION CODE

13. ABSTRACT *(Maximum 200 words)*

Summaries of papers presented at the Ultrafast Phenomena Topical Meeting, May 2-6 1994, Dana Point, California

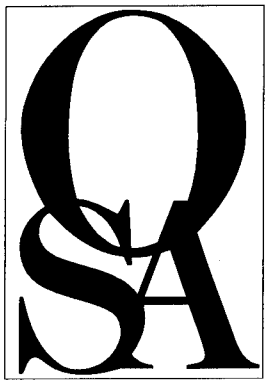
DTIC
ELECTE
FEB 09 1995
B

14. SUBJECT TERMS
Solid State Lasers, Solutions, Light Pulses, Electric Fields Spectroscopy, Solvents, Ultrafast Phenomena, Biology

15. NUMBER OF PAGES

16. PRICE CODE

17. SECURITY CLASSIFICATION OF REPORT	18. SECURITY CLASSIFICATION OF THIS PAGE	19. SECURITY CLASSIFICATION OF ABSTRACT	20. LIMITATION OF ABSTRACT
UNCLASSIFIED	UNCLASSIFIED	UNCLASSIFIED	UL



Ultrafast Phenomena

Summaries of papers presented at the Ultrafast Phenomena Topical Meeting

May 2–6, 1994
Dana Point, California

1994 Technical Digest Series
Volume 7

CONFERENCE EDITION

Sponsored by
Optical Society of America

Optical Society of America
2010 Massachusetts Avenue NW
Washington DC 20036–1023

Articles in this publication may be cited in other publications. In order to facilitate access to the original publication source, the following form for the citation is suggested:

Name of author(s), title of paper, in Ultrafast Phenomena, Vol. 7, 1994 OSA Technical Digest Series (Optical Society of America, Washington, DC, 1994), pp. xx-xx.

ISBN Number

Conference Edition	1-55752-338-X
Postconference Edition	1-55752-339-8
1994 Technical Digest Series	1-55752-321-5

Library of Congress Catalog Card Number

Conference Edition	93-65350
Postconference Edition	93-65351

Copyright © 1994, Optical Society of America

Individual readers of this digest and libraries acting for them are permitted to make fair use of the material in it as defined by Sections 107 and 108 of the U.S. Copyright Law, such as to copy an article for use in teaching or research, without payment of fee, provided that such copies are not sold. Copying for sale or copying for use that exceeds fair use as defined by the Copyright Law is subject to payment of copying fees. The code 1-55752-321-5/94/$6.00 gives the per-article copying fee for each copy of the article made beyond the free copying permitted under Sections 107 and 108 of the U.S. Copyright Law. The fee should be paid through the Copyright Clearance Center, Inc., 21 Congress Street, Salem, MA 01970.

Permission is granted to quote excerpts from articles in this digest in scientific works with the customary acknowledgment of the source, including the author's name and the name of the digest, page, year, and name of the Society. Reproduction of figures and tables is likewise permitted in other articles and books provided that the same information is printed with them and notification is given to the Optical Society of America. Republication or systematic or multiple reproduction or of any material in this digest, including contents and abstracts, is permitted only under license from the Optical Society of America; in addition, the Optical Society may require that permission also be obtained from one of the authors. Electrocopying or electrostorage of any material in this digest is strictly prohibited. Address inquiries and notices to Director of Publications, Optical Society of America, 2010 Massachusetts Ave., NW, Washington, DC 20036. In the case of articles whose employees of the U.S. Government or its contractors or grantees, the Optical Society of America recognizes the right of the U.S. Government to retain a nonexclusive, royalty-free license to use the author's copyrighted article for U.S. Government purposes.

Printed in the U.S.A.

Contents

Schedule of Events v
MA Femtosecond Solid-State Lasers 1
MB Reaction and Dynamics in Solution 17
MC Ultrashort Light Pulses 29
MD Poster Session 1 43
ME Nonlinear Spectroscopy and Solvent Dynamics 135
MF Panel Discussion: Real World Ultrafast Sources 151
MG Panel Discussion: Real World Ultrafast Applications 153
TuA Ultrafast Dynamics in Solids 155
TuB Biology 169
TuC Surfaces 189
TuD Poster Session 2 203
TuE Quantum-Confined Systems 279
WA High Spatial and Temporal Resolution 296
WB Dispersion 317
WC Poster Session 3 331
WD Panel Discussion: Coherent Control? 425
WE Panel Discussion: New Frontiers in Ultrafast 427
ThA High Intensity 429
ThB Gas Phase Clusters 445
ThC High Field Atomic Physics 459
ThD Poster Session 4 471
ThE Reactions in Solution 559
FA Dynamics in Solution 573
FB Biological Spectroscopy and Medical Applications 589
Key to Authors and Presiders 607

For
:I ☑
☐
:d ☐
ion
ion/
Availability Codes
Dist | Avail and/or Special
A-1

TECHNICAL PROGRAM COMMITTEE

Gerard Mourou, *University of Michigan, Chair*
Ahmed H. Zewail, *California Institute of Technology, Chair*
Paul F. Barbara, *University of Minnesota, Program Chair*
Wayne H. Knox, *AT&T Bell Laboratories, Program Chair*
John E. Bowers, *University of California, Santa Barbara*
Philip H. Bucksbaum, *University of Michigan*
Paul B. Corkum, *National Research Council of Canada*
Irl N. Duling, *U.S. Naval Research Laboratory*
Roger N. Falcone, *University of California, Berkeley*
James G. Fujimoto, *Massachusetts Institute of Technology*
Edwin J. Heilweil, *National Institute of Standards and Technology*
Daniele Hulin, *Laboratoire d'Optique Appliquee, France*
Anthony M. Johnson, *AT&T Bell Laboratories*
James D. Kafka, *Spectra Physics, Inc.*
Takayoshi Kobayashi, *University of Tokyo, Japan*
Heinrich Kurz, *Institute of Semiconductor Electronics, Germany*
R. J. Dwayne Miller, *University of Rochester*
Margaret M. Murnane, *Washington State University*
Anne B. Myers, *University of Rochester*
Keith A. Nelson, *Massachusetts Institute of Technology*
Martin C. Nuss, *AT&T Bell Laboratories*
Sanford Ruhman, *Hebrew University, Israel*
Wilson Sibbett, *University of St. Andrews, U.K.*
John D. Simon, *University of California, San Diego*
Jurgen Troe, *Institut fur Physikalische Chemie de Universitat, Germany*
Douwe A. Wiersma, *University of Groningen, The Netherlands*
Keitaro Yoshihara, *Institute for Molecular Science, Japan*
Wolfgang Zinth, *University of Munich, Germany*

ADVISORY COMMITTEE

D. H. Auston, *Columbia University*
K. B. Eisenthal, *Columbia University*
Graham Fleming, *University of Chicago*
Charles B. Harris, *University of California, Berkeley*
Eric Ippen, *Massachusetts Institute of Technology*
Robin Hochstrasser, *University of Pennsylvania*
W. Kaiser, *Technical University of Munich, Germany*
J. L. Martin, *ENSTA, France*
Arnold Migus, *ENSTA, France*
Gerard Mourou, *University of Michigan*
C. V. Shank, *Lawrence Berkeley Laboratories*
Anthony Siegman, *Stanford University*
Tatsuo Yajima, *The University of Tokyo, Japan*
Keitaro Yoshihara, *Institute for Molecular Science, Japan*
Ahmed Zewail, *California Institute of Technology*

SCHEDULE OF EVENTS

Sunday, May 1, 1994

5:30pm		Postdeadline papers due at Conference Registration Desk
7:00pm–8:30pm		Conference Registration and Informal Reception

Monday, May 2, 1994

7:00am–6:00pm		Conference Registration/Slide Preview Desk Open
8:15am–8:30am		Welcome
8:30am–10:00am	MA	FEMTOSECOND SOLID-STATE LASERS
10:00am–10:30am		Coffee Break and Exhibits
10:30am–12:00m	MB	REACTIONS AND DYNAMICS IN SOLUTION
12:00m–1:30pm		Lunch (on your own)
1:30:pm–3:00pm	MC	ULTRASHORT LIGHT PULSES
3:00pm–4:30pm	MD	POSTER SESSION 1 AND EXHIBITS (Refreshments served)
4:30pm–6:00pm	ME	NONLINEAR SPECTROSCOPY AND SOLVENT DYNAMICS
6:00pm–9:00pm		Dinner (on your own)
9:00pm–10:00pm	MF	PANEL DISCUSSION: REAL WORLD ULTRAFAST SOURCES
10:00pm–11:00pm	MG	PANEL DISCUSSION: REAL WORLD ULTRAFAST APPLICATIONS

Tuesday, May 3, 1994

7:30am–6:00pm		Conference Registration/Slide Preview Desk Open
8:30am–9:30am	TuA	ULTRAFAST DYNAMICS IN SOLIDS
9:30am–10:00am		Coffee Break and Exhibits
10:00am–12:00m	TuB	BIOLOGY
12:00m–1:30pm		Lunch (on your own)
1:30pm–3:00pm	TuC	SURFACES
3:00pm–4:30pm	TuD	POSTER SESSION 2 AND EXHIBITS (Refreshments served)
4:30pm–6:00pm	TuE	QUANTUM-CONFINED SYSTEMS

Wednesday, May 4, 1994

8:00am–12:00m		Conference Registration/Slide Preview Desk Open
8:30am–10:15am	WA	HIGH SPATIAL AND TEMPORAL RESOLUTION
10:15am–10:45am		Coffee Break and Exhibits
10:45am–12:00m	WB	DISPERSION
12:00m–4:00pm		No activities planned
4:00pm–5:30pm	WC	POSTER SESSION 3
5:30pm–7:00pm		Conference Reception
7:00pm–9:00pm		Dinner (on your own)
9:00pm–10:00pm	WD	PANEL DISCUSSION: COHERENT CONTROL?
10:00pm–11:00pm	WE	PANEL DISCUSSION: NEW FRONTIERS IN ULTRAFAST

Thursday, May 5, 1994

8:00am–6:00pm		Conference Registration/Slide Preview Desk Open
8:30am–10:00am	ThA	HIGH INTENSITY
10:00am–10:30am		Coffee Break
10:30am–12:00m	ThB	GAS PHASE CLUSTERS
12:00m–1:30pm		Lunch (on your own)
1:30pm–3:00pm	ThC	HIGH FIELD ATOMIC PHYSICS
3:00pm–4:30pm	ThD	POSTER SESSION 4 (Refreshments served)
4:30pm–6:00pm	ThE	REACTIONS IN SOLUTION
6:00pm–9:00pm		Dinner (on your own)
9:00pm–10:00pm		POSTDEADLINE PAPER SESSION

Friday, May 6, 1994

8:00am–10:30am		Conference Registration/Side Preview Desk Open
8:30am–10:00am	FA	DYNAMICS IN SOLUTION
10:00am–10:30am		Coffee Break
10:30am–12:15pm	FB	BIOLOGICAL SPECTROSCOPY AND MEDICAL APPLICATIONS
12:15pm–12:30pm		Closing Remarks

Monday, May 2, 1994

Femtosecond Solid-State Lasers

MA 8:30am–10:00am
Dana Point Ballroom

A.J. Schmidt, *Presider*
Quantumelektronik, Germany

Ultrafast Solid State Lasers: Status and Prospects

F. Krausz, Ch. Spielmann, P. F. Curley†, T. Brabec, S. M. J. Kelly, A. Stingl,
R. Szipöcs††, E. Wintner, and A. J. Schmidt

Abteilung Quantenelektronik und Lasertechnik
Technische Universität Wien
Gußhausstrasse 27-29 A–1040 Wien, Austria
Phone: +43-1-58801-3879, Fax: +43-1-504-2477
E-mail: krausz@ps1.iaee.tuwien.ac.at

Until recently the passively mode-locked dye laser has been the only reliable, widely used source of femtosecond optical pulses. Dramatic advances in all-optical modulation techniques and the appearance of novel broad-band solid state gain media over the last few years opened up a new era in femtosecond pulse technology [1]. More than two decades after the first demonstration of a picosecond mode-locked laser, we have recently witnessed the emergence and evolution of a new generation of ultrashort-pulse lasers based exclusively on solid state components [2]. Intensive research efforts resulted in a good understanding of the basic physical processes dominating pulse formation in these novel sources [3], giving rise to a rapid progress of femtosecond solid state laser technology. This research culminated in the generation of sub-20 fs optical pulses directly from Ti:sapphire laser oscillators [4].

In this paper the major theoretical aspects and technological issues of the development of ultrafast solid state lasers will be discussed. Particular emphasis will be placed on recent advances in Ti:sapphire lasers as well as the development of a "prismless" femtosecond oscillator that uses specific dielectric mirrors as the source of negative group delay dispersion [5]. This novel technology offers the possibility of generating optical pulses from extremely compact systems with unprecedented duration, stability, and reproducability. Kilohertz amplification of the output of these novel femtosecond sources operating in the 10fs region will open up new prospects for nonlinear optics and ultrafast spectroscopy of condensed matter.

References

1. E. P. Ippen, "Principles of passive mode locking," *Appl. Phys. B*, March 1994

2. F. Krausz, M. E. Fermann, T. Brabec, P. F. Curley, M. Hofer, M. H. Ober, Ch. Spielmann, E. Wintner, and A. J. Schmidt, *IEEE J. Quantum Electron.* **QE-28**, 2097 (1992)

3. T. Brabec, Ch. Spielmann, F. Krausz, *Opt. Lett.* **16**, 1961 (1991), *Opt. Lett.* **17**, 748, 1292 (1992); H. A. Haus, J. G. Fujimoto, and E. P. Ippen, *IEEE J. Quantum Electron.* **QE-28**, 2086 (1992); H. A. Haus, J. D. Moores, and L. E. Nelson, *Opt. Lett.* **18**, 51 (1993); T. Brabec and S. M. J. Kelly, *Opt. Lett.* **18**, 2002 (1993)

4. Ch. Spielmann, P. F. Curley, T. Brabec, E. Wintner, and F. Krausz, *Electron. Lett.* **28**, 1532 (1992); C. P. Huang, M. T. Asaki, S. Backus, M. M. Murnane, H. C. Kapteyn, and H. Nathel, *Opt. Lett.* **17**, 1289 (1992); B. Proctor and F. Wise, *Opt. Lett.* **17**, 1295 (1992); B. E. Lemoff and C. P. J. Barty, *Opt. Lett.* **17**, 1367 (1992)

5. A. Stingl, Ch. Spielmann, F. Krausz, and R. Szipöcs, *Opt. Lett.* **19**, Febr. 1 (1994)

† Present address: Laboratoire D'Optique Appliquee
Ecole Polytechnique-ENSTA
Batterie De L'Yvette, 91120-Palaiseau, France

†† Permanent address: Optical Coating Laboratory
Research Institute for Solid State Physics
H-1525 Budapest, POB 49, Hungary

Intracavity Pulse-Duration Measurements in a sub-10 fs Ti:sapphire Laser Oscillator

J. Zhou, G. Taft, C. Shi, Henry C. Kapteyn and Margaret M. Murnane
Department of Physics, Washington State University, Pullman, WA 99164-2814
Phone: (509) 335-6389 FAX: (509) 335-7816
Milan Kokta
Union Carbide Crystal Products, Washougal, WA 98671

Recent advances in ultrashort-pulse Ti:sapphire laser technology[1-6] have made it possible to routinely generate optical pulses of ~10 fs duration using stable, reliable, and easy-to-use lasers. The Kerr-lens modulation mechanism for mode-locking in these lasers has been identified,[7] and the effect of high-order dispersion on the pulse duration has also been demonstrated.[1-4] However, a comprehensive theory covering the operation of these lasers has not been developed, and the ultimate limit of the obtainable pulse-duration is still unclear. We have made measurements demonstrating that sub 10-fs pulses can be produced from a mode-locked laser. We have also compared spectral measurements from the laser with calculations of the dispersion of the laser, and have concluded that even in the case of an 8-9 fs pulse, the primary limitation on even shorter pulse duration is dispersion, and not non-linear effects. Thus, there remains the prospect of generating even shorter-duration pulses from a Ti:sapphire laser. We have also made measurements of the time-duration and chirp of the optical pulse at various points within the laser cavity. These measurements are also consistent with linear dispersion.

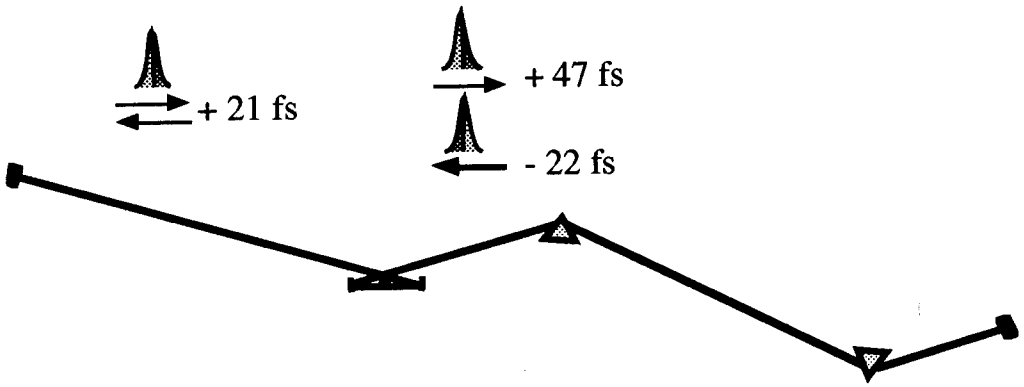


Figure 1: The basic configuration of a self-mode locked Ti:sapphire laser, including pulse duration measurements illustrating the evolution of pulse duration as the pulse travels through the cavity.

In this work, we have used a laser with a 2 mm long crystal. By placing a pellicle beamsplitter at near Brewster angle within the laser cavity, we can pick-off a small amount of light at various positions within the cavity. Using an autocorrelator with a pellicle beamsplitter, we can virtually eliminate the effects of extracavity dispersion on the pulse, and directly measure the pulse duration in the laser. Preliminary data is shown in Figure 1. The pulse is negatively chirped as it travels away from the prism pair, and is shortest near the center of the crystal. It is positively chirped in the other direction of propagation through the crystal. The fact that the pulse duration of the laser is shortest inside the crystal and not at an end, indicates that optimization of the Kerr-lensing in the cavity is not simple to predict.

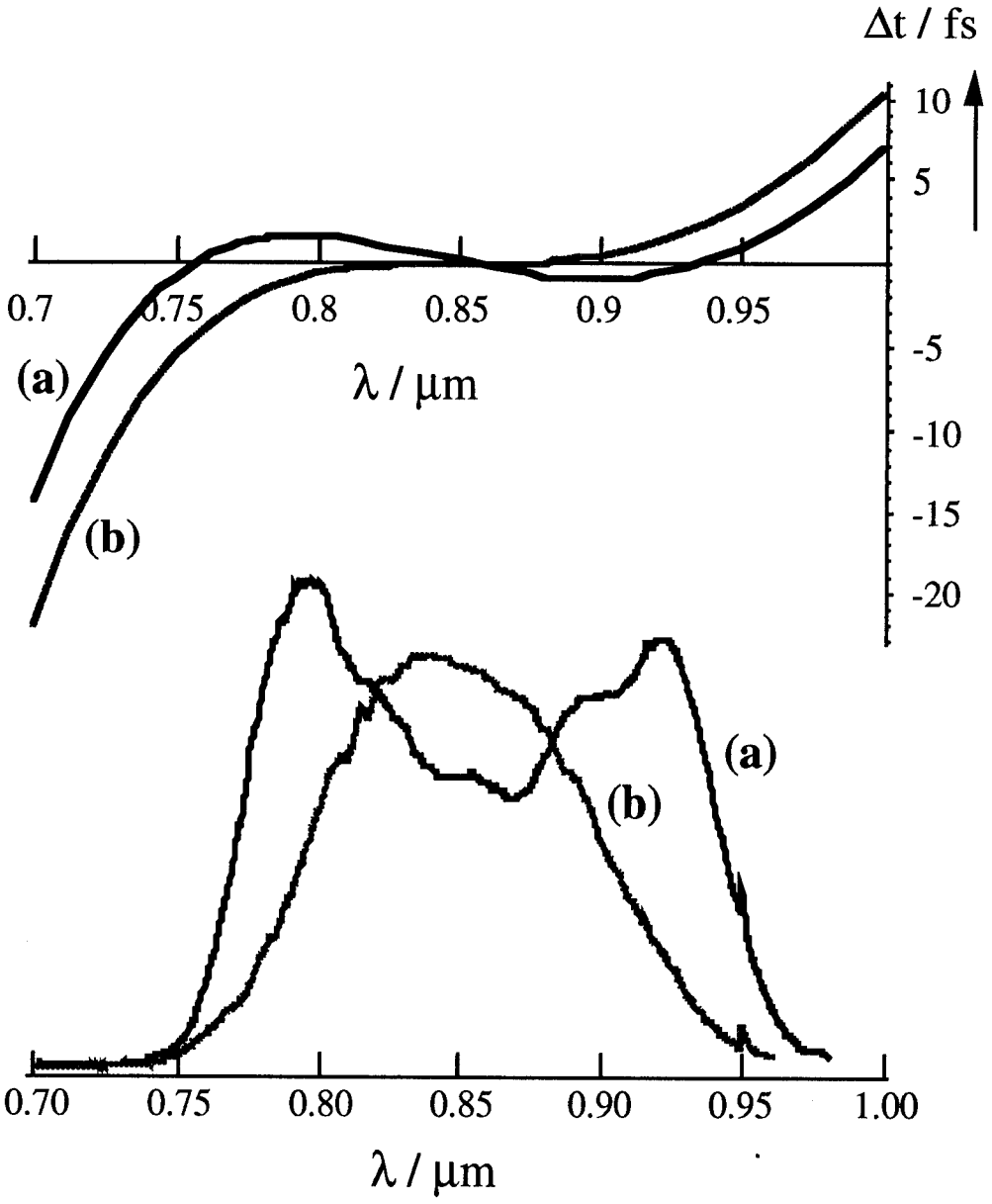


Figure 2: Calculated dispersion and experimental spectral measurements of the output of the laser of figure 1, for two different prism insertions. The top curves are calculated cavity round-trip time as a function of wavelength. The bottom curves are corresponding pulse spectra.

Other data illustrates that imperfect dispersion compensation still limits the pulse duration which can be generated using these lasers. The top curves in figure 2 shows a calculation of the variation in total round trip time for light inside the laser cavity, for two slightly different configurations. For curve (a), one prism was moved by ~300 μm to insert more glass compared with curve (b). The spectrum (bottom curves) corresponding to curve (b) has a Gaussian shape, with a width of 110 nm. The peak of the spectrum corresponds to near the zero-dispersion point. On the other hand, the spectrum

corresponding to curve (a) is more complex, with a width of 170 nm, and shows spectral splitting corresponding to the shape of the dispersion curve.

Figure 3 shows the shortest pulse-duration obtained to date. It was obtained by extracting the beam as it exits the prism pair before reaching the crystal. The pulses are negatively-chirped at this point in the cavity, so that by adding a small amount of fused silica in the beam path, the chirp can be compensated. The spectrum corresponding to this measurement has a shape intermediate between the two curves of figure 2.

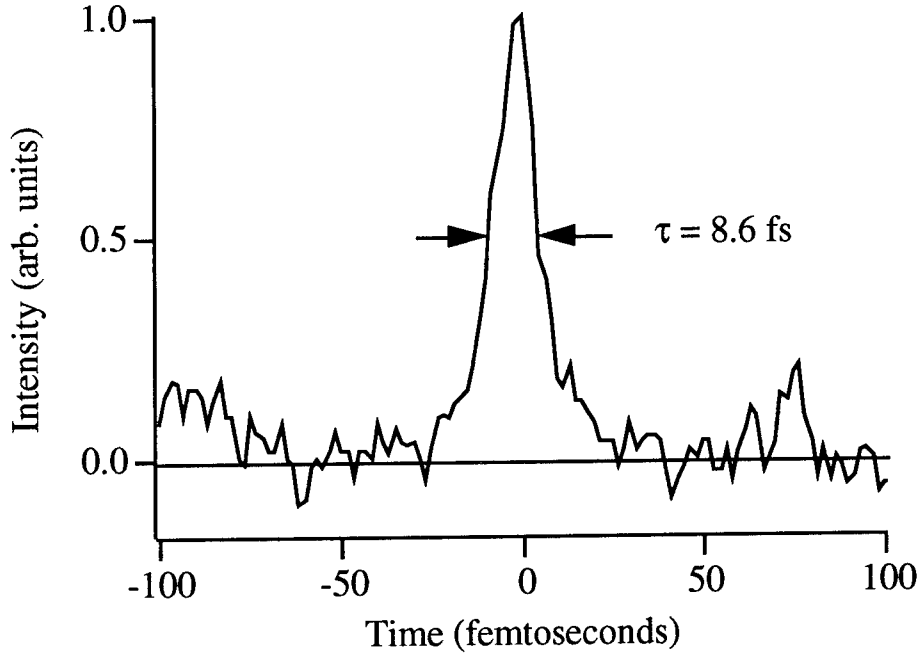


Figure 3: Autocorrelation trace of shortest-obtained pulse. The autocorrelation FWHM is 13.5 fs, corresponding to a pulse duration of 8.6 fs assuming a sech^2 pulse shape, or 9.3 fs assuming a Gaussian pulse shape.

In conclusion, we have demonstrated that it is possible to generate sub-10 fs pulses from a Ti:sapphire laser. Imperfect dispersion compensation still seems to be the primary limitation on pulse duration; thus, further advances are possible.

1.C. P. Huang, H. C. Kapteyn, J. W. McIntosh, M. M. Murnane, Opt. Lett. **17**, 139 (1992).
2.C. P. Huang, M. T. Asaki, S. Backus, M. M. Murnane, H. C. Kapteyn, H. Nathel, Opt. Lett. **17**, 1289 (1992).
3.C. P. Huang, M. Asaki, S. Backus, H. Nathel, M. M. Murnane, H. C. Kapteyn, at the*Ultrafast Phenomena VIII* Paper 160 (Antibes, France, 1992).
4.M. T. Asaki, C. P. Huang, D. Garvey, J. Zhou, H. C. Kapteyn, M. M. Murnane, Opt. Lett. **18**, 977 (1993).
5.P. Curley, C. Spielmann, T. Brabec, F. Krausz, E. Wintner, A. Schmidt, Opt. Lett. **18**, 54 (1993).
6.B. Proctor, F. Wise, Opt. Lett. **17**, 1295 (1992).
7.L. Spinelli, B. Couillaud, N. Goldblatt, D. K. Negus, at the*CLEO/QELS '91* (Baltimore, MD, 1991).

All-Solid-State Diode-Pumped C.W. Femtosecond Cr:LiSrAlF$_6$ Laser

R. Mellish, P. M. W. French and J. R. Taylor

Femtosecond Optics Group, Physics Department, Imperial College,

London SW7 2BZ, U.K.

Tel. : 071-225-8861 Fax. : 071-589 9463 Telex: 929484 IMPCOL G

P. J. Delfyett and L. T. Florez

Bell Communications Research, Red Bank, NJ 07701, USA

The widespread application of ultrafast technology will require the development of compact, versatile lasers. We aim to develop an all-solid-state diode-pumped tunable femtosecond laser system employing Cr:LiSAF as the gain medium in both amplifier and oscillator to yield ultrashort pulse energies up to a few μJ for only a few watts of diode pump power. The diode-pumping at ~670 nm of a c.w. Cr:LiSAF laser has been demonstrated [e.g. 1]. Here we report on picosecond and femtosecond pulse generation from the first c.w. mode-locked, diode-pumped tunable solid-state lasers based on Cr:LiSrAlF$_6$ (Cr:LiSAF).

Our preliminary experiments yielded 33 fs pulses from an argon-ion laser-pumped Cr:LiSAF laser using a saturable absorber dye to initiate KLM and achieve self-starting [2]. With an intracavity MQW saturable absorber replacing the dye jet stream, we generated transform-limited pulses of ~90 fs duration [3] for only 500 mW absorbed pump power. On progressing to diode-pumping, we set up a simple astigmatically-compensated cavity with an end-pumped Cr:LiSAF rod. The InGaAlP laser diodes used typically provided ~500 mW cw pump power at ~ 670 nm. The laser threshold was 70 mW and the laser tuned from 799 to 880 nm with up to 100 mW of of true c.w. output power.

Active mode-locking was demonstrated using an acousto-optic modulator which yielded full duty-cycle cw mode-locked pulses of ~300 ps duration [4]. We then demonstrated an all-

solid-state passively mode-locked laser using RPM [e.g. 5] with the MQW absorber of reference [3]. Stable, self-starting, cw mode-locked pulse trains at 250 MHz were observed which were as short as ~60 ps duration, as measured using a sampling streak camera [5]. When a standard four prism sequence was incorporated into the cavity to optimise GVD, trains of pulses as short as 600 fs were measured using an SHG autocorrelator.

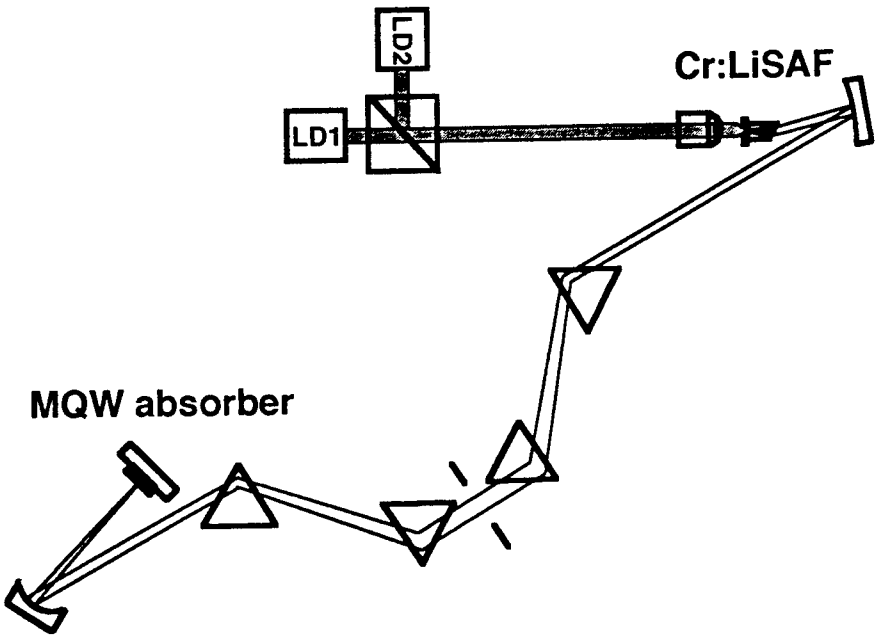


Figure 1 *Cavity configuration of Cr:LiSAF laser passively mode-locked with an intracavity MQW absorber*

We have now demonstrated self-starting, c.w. passive mode-locking with an intracavity MQW absorber, using the cavity configuration shown in figure 1, and have generated transform-limited pulses of 220 fs. Figure 2 shows the autocorrelation trace and spectrum of these pulses for which the time-bandwidth product was 0.33. The MQW absorber limited the tuning range to ~ 5 nm.

In conclusion, we have demonstrated the first picosecond/femtosecond all-solid-state diode-pumped tunable mode-locked lasers. Using Cr:LiSAF pumped by InGaAlP laser diodes, we have demonstrated both active mode-locking and RPM and have generated pulses as short as 220 fs by passive mode-locking with an intracavity MQW saturable absorber.

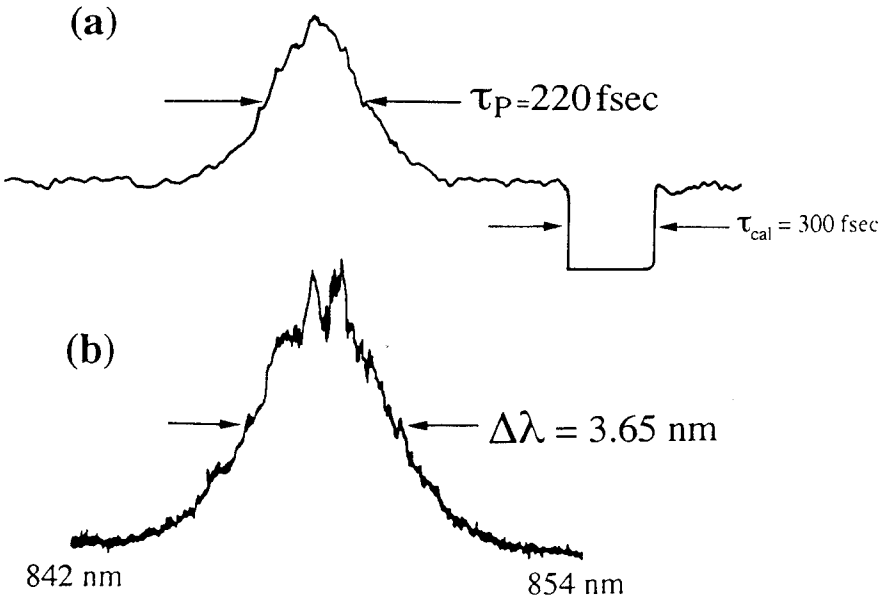


Figure 2 *Autocorrelation trace (a) and spectral profile (b) of pulses generated by Cr:LiSAF laser passively mode-locked with an intracavity MQW absorber*

References

1) G. J. Dixon, Q. Zhang and B. H. T. Chai, *Sixth Interdisciplinary Laser Science Conf.*, (American Physical Society, 1990) paper B3-1

2) N. H. Rizvi, P. M. W. French and J. R. Taylor, Opt.Lett. **17**, 1605 (1992)

3) N. H. Rizvi, P. M. W. French, J. R. Taylor, P. J. Delfyett and L. T. Florez *Opt. Lett.* **18**, 983-985 (1993)

4) P. M. W. French, R. Mellish, J. R. Taylor, P. J. Delfyett and L. T. Florez *Electron. Lett.* **29**, 1263 (1993)5)

5) U. Keller, W. H. Knox and G. W. t'Hooft, *IEEE J. Quant. Electron.* **QE-28**, 2123-2133 (1992)

A self-modelocked $Ti:Al_2O_3$ laser pumped by a frequency-doubled Nd:YLF minilaser.

K. Lamb, D.E Spence, J. Hong, C. Yelland and W. Sibbett
J.F Allen Physics Research Laboratories
Department of Physics and Astronomy
University of St. Andrews
St. Andrews
Fife KY16 9SS
Scotland, U.K.
Tel: +44 334 76161
Fax: +44 334 63104

Recent advances in high power laser diode technology has led to vigorous research activity in the development of diode-laser-pumped, solid-state lasers. These so-called minilasers are especially useful because of their compactness and excellent beam quality, and in particular, a frequency-doubled Nd:YLF system is well-suited to the pumping of a $Ti:Al_2O_3$ crystal. Argon-ion lasers having powers ranging from 1-20W, have generally been used as pump sources for $Ti:Al_2O_3$ lasers. However these large-frame systems tend to have relatively noisy outputs, and are prone to having 50Hz and 300Hz intensity ripple. An efficient diode-laser-based pump source for self-modelocked $Ti:Al_2O_3$ lasers is therefore more desirable. It is expected that such a system will exhibit less phase noise due to the superior characteristics of the power supply units that are used. This is especially relevant to applications in optical sampling and to synchronous streak camera measurements which both require sources of low noise, ultrashort laser pulses.

To date, pulsed operation of $Ti:Al_2O_3$ lasers has been reported using frequency-doubled, modelocked and Q-switched Nd:YLF[1,2], and frequency-doubled Q-switched Nd:YAG lasers[3]. More recently, commercial frequency-doubled, cw diode-laser pumped Nd:YAG lasers have achieved average powers suitable for pumping a $Ti:Al_2O_3$ laser, which had been specifically designed for low threshold operation at around 200mW[4]. Unfortunately the relatively high oscillation threshold for continous-wave operation of $Ti:Al_2O_3$ at around 1W, has made such diode-based minilaser pumping rather difficult.

In this paper we present, for the first time to our knowledge, an all-solid-state, self-modelocked Ti:sapphire laser. The basic configuration of our regeneratively-initiated, self-modelocked $Ti:Al_2O_3$ laser is similar to the argon-ion pumped system that has been described in detail elsewhere[5]. In the present case the gain medium was a 10mm long, Brewster-angled $Ti:Al_2O_3$ rod having a pump absorption coefficient of 1.9 cm^{-1} and a figure of merit in excess of 250. It was incorporated in a resonator having optics that were dielectrically coated for the 700-850nm spectral region. The output coupling was 2%, and two SF14 prisms were included for intracavity dispersion compensation. For initiation and stabilization of the self-

modelocking process, a regeneratively-driven acousto-optic modulator was located near the high reflectivity cavity end mirror.

The pump source for the Ti:Al_2O_3 laser was a diode-pumped, intracavity-frequency-doubled, cw Nd:YLF laser. This laser produced a single longitudinal mode output at powers up to 1W at 523nm, in a TEM_{00} beam. Pump powers of approximately 600mW resulted in 20mW of average output power being produced by the self-modelocked Ti:Al_2O_3 laser. In the arrangement shown in figure 1, the Ti:Al_2O_3 laser generated 110fs pulses at a repetition rate of approximately 86MHz, and a wavelength of 806nm. This system has also been operated in a more compact configuration producing femtosecond pulses at repetition rates up to ~140MHz, limited by the maximum operating frequency of our regeneratively-driven acousto-optic modulator.It was observed that the pump power threshold for cw laser oscillation was approximately 400mW, with a threshold for self-modelocking at 500mW.

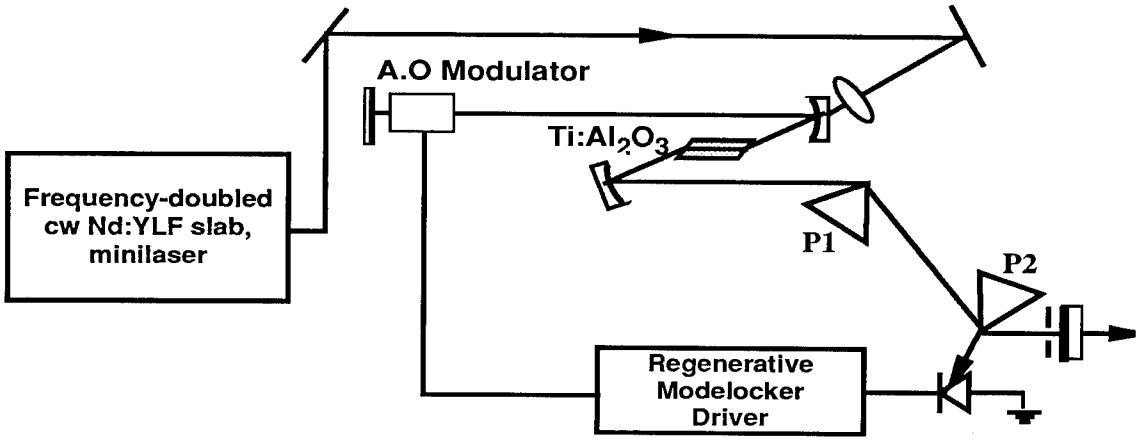


Figure 1: Schematic diagram of the all-solid-state, self-modelocked Ti:Al_2O_3 laser cavity.

It can be seen from the intensity (Fig.2a) and interferometric (Fig.3) autocorrelation data that the pulse duration was 110fs and the spectral data implies a pulse bandwidth of 9.2nm. This corresponds to a duration-bandwidth product of ~0.46, which indicates that the pulses are not quite transform-limited under these self-modelocking conditions.

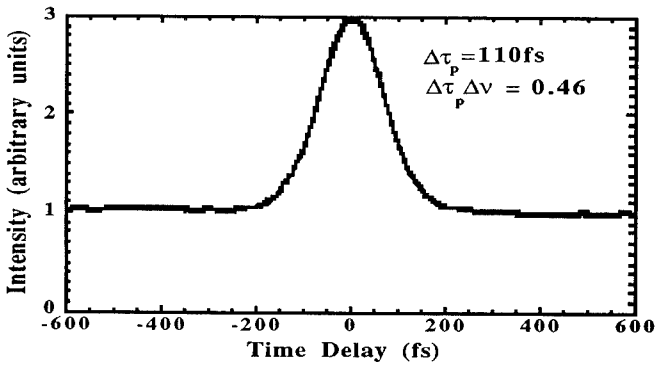


Figure 2a: Intensity autocorrelation of the laser output.

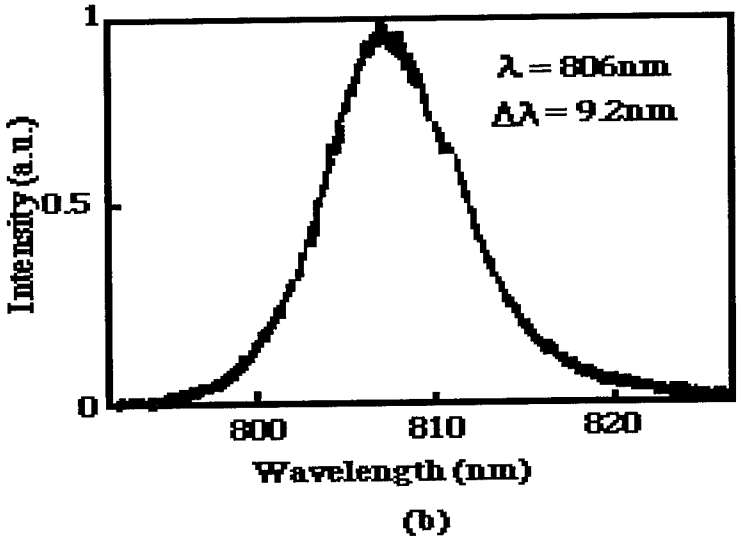


Figure 2b: Spectral data for the laser output.

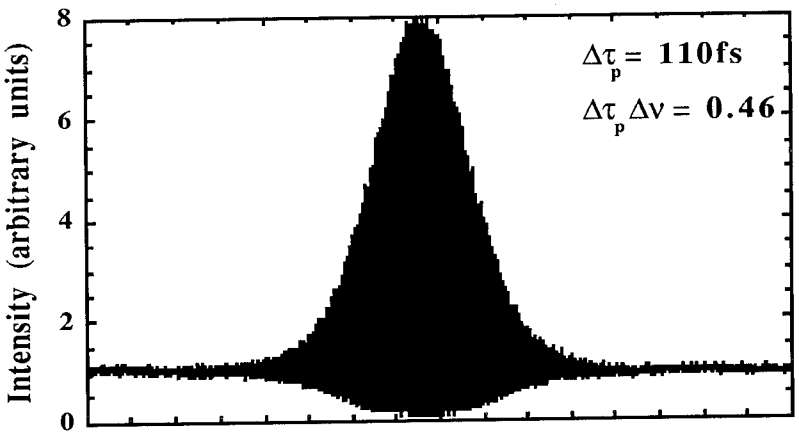


Figure 3: Interferometric autocorrelation trace for the all-solid-state, self-modelocked Ti:Al_2O_3 laser.

The operation of this all-solid-state, self-modelocked Ti:Al_2O_3 laser at higher pump power levels will be discussed together with additional features such as its phase noise characteristics. Its suitability for use in conjuction with a synchronously-operating streak camera will also be highlighted in this presentation.

1. G.T Maker and A.I Ferguson, Opt. Lett. **15**, 375 (1990).
2. G.P.A Malcolm and A.I Ferguson, Opt. Commun. **82**, 299 (1991).
3. T.R Steele, D.C Gerstenberger, A. Drobshoff and R.W Wallace, Opt. Lett. **16** 399 (1991).
4. J. Harrison, A. Finch, D.M Rines, G.A Rines and P.F Moulton, Opt. Lett. **16** 581 (1991).
5. D.E Spence, J.M Evans, W.E Sleat and W. Sibbett, Opt. Lett. **16** 1762 (1991).

Sub-100fs homogeneously and inhomogeneously broadened Nd:glass lasers

F. X. Kärtner, D. Kopf and U. Keller

Ultrafast Laser Physics Laboratory, Institute of Quantum Electronics,
Swiss Federal Institute of Technology, ETH Hönggerberg, HPT,
CH-8093 Zürich, Switzerland,Tel.: [011] 41 1 633 2736

Previously, we have introduced a spectral filtering technique and applied it to a passively modelocked Nd:glass laser using an antiresonant Fabry-Perot saturable absorber (A-FPSA) [1]. Pulses as short as 130 fs are achieved in a standard dispersion compensated delta - cavity design with a 4mm Nd:glass plate inserted at Brewster's angle. The Nd:glass laser system is interesting from the point of view of an all solid state laser technology because it can be diode pumped. To further investigate the modelocking dynamics in Nd:glass lasers, we performed the following experiments: First we demonstrated a regeneratively, actively mode-locked phosphate Nd:glass laser (LG760, Schott), resulting in stable pulses with 310 fs pulsewidth, secondly a passively modelocked phosphate Nd:glass (LG700) laser with 105 fs and thirdly a passively modelocked silicate Nd:glass (LG680) laser with 92 fs. The passive modelocking experiments used an A-FPSA to both start and sustain stable mode locking without self-Q-switching. The different Nd:glass hosts were chosen because the phosphate Nd:glass can be considered as a quasihomogeneous laser material whereas the silicate Nd:glass is strongly inhomogeneous. Despite the completely different cw-behaviour of the lasers when the homogeneous or the inhomogeneous gain material is used, the modelocking performance is comparable and leads to almost the same pulsewidth in contrast to previously obtained results based on additive pulse mode locking [2]. Calculations as well as the experimental results show that KLM does not contribute to the modelocking performance.

1) Regeneratively, actively modelocked Nd:glass laser: Fig. 1 shows the fluorescence spectrum of the quasihomogeneously broadened phosphate Nd:glass material.

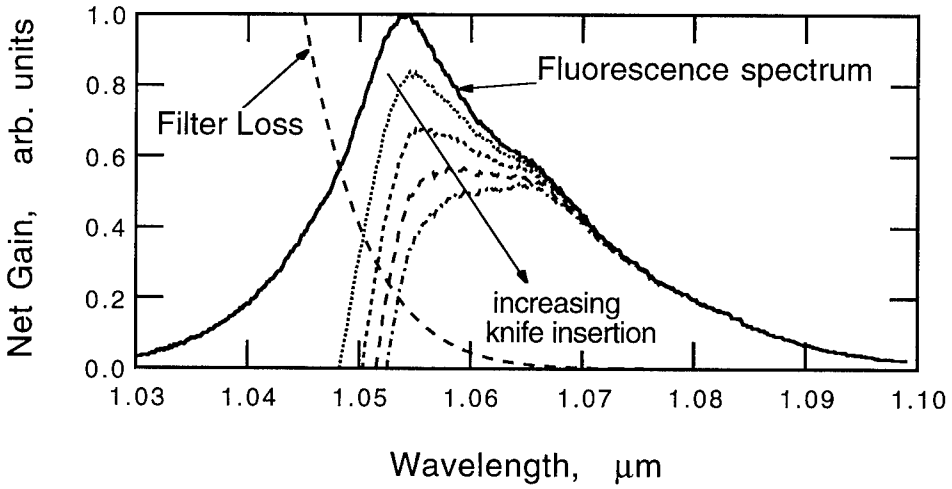


Figure 1: Measured fluorescence spectrum of the Nd:glass LG760 and calculated net gain profile due to intracavity filtering.

The FWHM bandwidth of the laser material is about 20nm. Using this gain material in an

actively, regeneratively mode-locked laser produces 5 ps pulses which exhibit strong sidelobes in the autocorrelation. However, by properly introducing a knife edge into the beam acting as a long-pass wavelength filter, the laser generates pulses as short as 310fs. This can be understood by looking at the net gain profile, i.e. saturated gain plus wavelength dependent loss, as shown in Fig. 1. The insertion of the knife edge opens up a broad and flat window in the net gain which allows for pulses as short as 310fs even with only active modelocking. From soliton perturbation theory one can show that in the case of a large enough ratio between group velocity dispersion and gain dispersion, the active modelocker can reduce the pulse width until a solitary wave is formed. This demonstrates that the action of the filter in the modelocking process is to flatten the net gain profile.

2) Passive modelocking of quasihomogeneous Nd:glass lasers: Femtosecond pulse generation by passive modelocking with the A-FPSA is possible due to the fast response of the semiconductor absorber [3] based on carrier thermalization which is in the range of 160 - 210 fs. In the case of the quasihomogeneous laser material LG700 and under usual conditions, i.e. output coupling of the laser of several percent, no intracavity filter, and weak focusing onto the saturable absorber, the laser only generates picosecond pulses with moderate stability. As soon as the knife edge is at the proper position a very stable train of pulses as short as 125 fs is produced. This observation again can be explained by the reshaping of the net gain profile, which also causes the observed spectral jump of 10 nm to longer wavelength, see Fig. 1. This assumes that the saturable absorber is still fast enough to achieve stable mode-locking. Further reduction of the gain filtering or increasing the saturable absorber action should also lead to femtosecond pulses even in the absence of the additional filter. Therefore, we reduce the output coupling from 1% to 0.4%, while keeping the intracavity power constant by reducing the pump power. Doing so results in a reduced saturated gain and therefore less filter action due to the finite gain bandwidth while maintaining the same self-phase modulation and saturable absorber action. This results in stable pulsing with approximately the same duration as before but without the need of a knife edge, i.e. additional filtering. In addition decreasing the spotsize on the A-FPSA by a factor of 2 while keeping the intensity in the gain medium constant decreases the saturation power in the sample by a factor of 4 and increases the saturable absorber action. This results in very stable sech-shaped pulses as short as 105 fs directly out of the Nd:glass laser

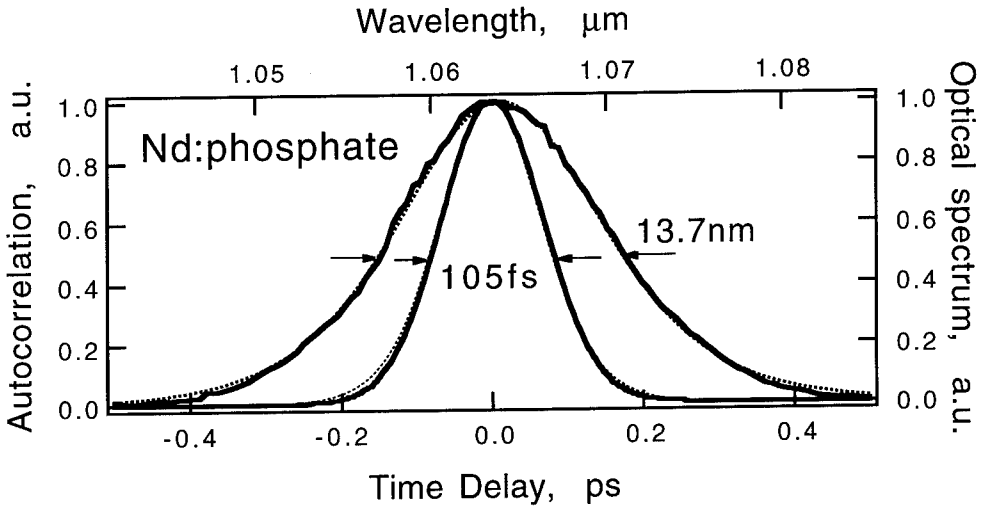


Figure 2: Measured autocorrelation signal and spectrum of the phosphate Nd:glass laser and the corresponding fits (dashed lines) assuming a sech-shaped pulse (average output power 33mW, repetition rate 180MHz, 0.4% output coupler).

as shown in Fig. 2. The pulses are almost transform-limited with a time bandwidth product of 0.38.This demonstrates that the fast saturable absorber action comes from the A-FPSA

and not from KLM. Pulses as short as 90 fs were also observed at the same power level with poor stability.

3) Passive mode locking of inhomogeneously broadened Nd:glass lasers: Silicate laser glasses are strongly inhomogeneous laser materials which shows up in the cw operation, where the output spectrum is spread over a typical range of 10 nm (LG680). In this inhomogeneous case there is no need for an intracavity filter to obtain femtosecond pulses. The fluorescence linewidth is 30nm. The common theories of passive modelocking [4] are not applicable to the case of inhomogeneous gain media. However, due to the operation in the negative dispersion regime, the dominant pulse shaping mechanism is solitary wave formation in the cavity due to the interplay between GVD and SPM, which again results in perfectly sech-shaped pulses and spectra. Because of the low total losses, the effects of gain, its associated filtering, loss, and the saturable absorber are on the level of 1% per roundtrip, whereas the changes in the pulse due to GVD and SPM are on the order of 10% per roundtrip. Therefore, the gain filtering and the saturable absorber are not dominant in the pulse shaping. However, the saturable absorber keeps the pulse stable against growth of cw radiation. Fig. 3 shows the autocorrelation of the pulse and the spectrum. We obtained pulses as short as 92 fs with the low output coupling of 0.4%.

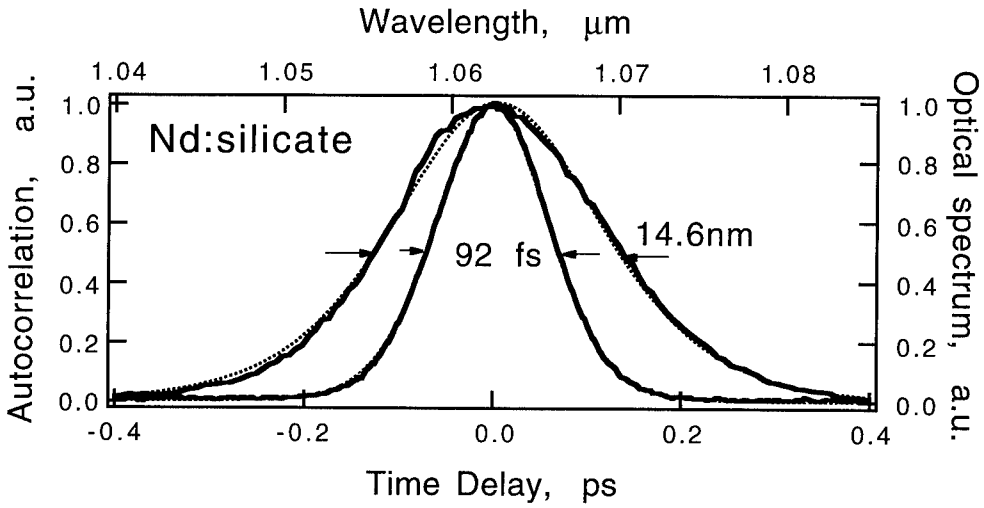


Figure 3: Measured autocorrelation signal and spectrum of the silicate Nd:glass laser and the corresponding fits (dashed lines) assuming a sech-shaped pulse (average output power 40 mW, repetition rate 180 MHz, 0.4% output coupler).

In conclusion the results are qualitatively in full agreement with the theory of fast saturable absorber mode locking in the presence of GVD and SPM [4]. Quantitatively, there are deviations due to the bitemporal behavior of the saturable absorber and due to the fact that the pulsewidth achieved is already equal to or even below the recovery time of the fast saturable absorber part and the spectrum extends already beyond the parabolic gain approximation. The A-FPSA is the first saturable absorber which allows for the exploitation of almost the full gain bandwidth of both homogeneously as well as inhomogeneous Nd:glass lasers for sub-100fs pulse generation.

References:

[1] U. Keller, T. H. Chiu and J. F. Ferguson, *Optics Lett.* **18**, 1077 (1993).
[2] J. Zehetner, Ch. Spielmann and F. Krausz, *Optics Lett.* **17**, 871 (1992).
[3] L. Brovelli, U. Keller and T. H. Chiu, submitted to *Ultrafast phenomena* (1994).
[4] H. Haus, J. G. Fujimoto and E. P. Ippen, *J. Opt. Soc. Am. B* **8**, 2068 (1991).

Monday, May 2, 1994

Reaction and Dynamics in Solution

MB 10:30am–12:00m
Dana Point Ballroom

Charles Harris, *Presider*
University of California, Berkeley

Electronic Relaxation Dynamics in Solution

Peter J. Rossky, Benjamin J. Schwartz, and Wen Shyan Sheu
Department of Chemistry and Biochemistry
The University of Texas at Austin
Austin, Texas 78712-1167
U. S. A.
(512) 471-3555

Due to the significance of local electric fields and rapid solvent response for the ultrafast processes involved in chemical reactions, explicit molecular descriptions of the solvent and solute have an essential role in understanding the underlying microscopic dynamics. Recent progress in laser technology is enabling direct experimental observation of the fundamental events. At the same time, significant advances have been made in theoretical methods. The present contribution focusses on the direct connection now accessible between the two at the spectroscopic level, and the molecularly detailed pictures that are emerging. Here, we outline selected theoretical results for two experimentally investigated systems, namely aqueous halide ions and the hydrated electron.

The detailed computer simulations considered here employ a classical model for water[1] but explicitly treat the quantum electronic character of the solute, with a pseudopotential for the electron-solvent interaction[2]. From a simulated sequence of solvent configurations and the respective eigenstate manifolds, the vertical excitation energies and the corresponding dipole transition matrix elements provide direct access to steady state and transient spectra. Our algorithm for non-adiabatic dynamics[3] prescribes a semiclassical simulation of the electronic and solvent nuclear dynamics via a sequence of time steps composed of time propagation of the wavefunction, a statistical branching among adiabatic electronic eigenstates, and a time propagation of the nuclear coordinates subject to an appropriate total force.

We first consider studies of photoexcited aqueous halides.[4-6] These ions exhibit strong, broad UV absorption spectra in solution (charge-transfer-to-solvent (CTTS) states) but not in the gas phase, and solvated electrons can result from photoexcitation[7-9]. However, due to the limited tools available, the theoretical description of these states predated our studies by about thiry years[8,9]. Femtosecond spectroscopic data have also recently been reported[10,11]. Long et al.[11] have carried out transient multiphoton absorption experiments on an aqueous iodide ion and concluded that the relaxation proceeded via an initial CTTS state. Using a pseudopotential model for the halide, the properties of the solute ground and excited electronic states have been analyzed[4]. The CTTS spectra are comprised of several overlapping subbands: the principal excited state band consists of six states where a single electron is excited from the p-like valence orbital to an orbital of mixed s and d character. Above, this lies a band of three states with the single excitation of predominantly p to p type character. The former would be strongly one photon allowed and the latter would exhibit relatively strong two photon absorption

Direct dynamical simulation of the halide following two photon excitation[5,6] shows that, although direct, nonadiabatic, electron transfer to a preexisting solvent cavity can occur, the predominant excited state relaxation channel observed exhibits direct electronic relaxation, as shown in Fig. 1 for a typical trajectory. Within 20 fs, the initially excited p-like excited electron crosses into the principal CTTS band and reaches the lowest excited state via a series of transitions after about 450 fs. Within another 50 fs, one observes the onset of a gradual electronic detachment, leading after about an additional 1 ps to a contact halogen atom-hydrated electron pair.

This sequence of events has an identifiable spectroscopic signature both in absorption and emission. As shown in Fig. 2, the (experimentally unresolved) red absorption spectra of the initially excited p-like electron (3 fs) decays very rapidly to that characteristic of the states of the principal CTTS band (103 fs) which lies somewhat to the blue of the hydrated electron and is narrower as well. With detachment, the spectrum red shifts and broadens so that the electron-atom

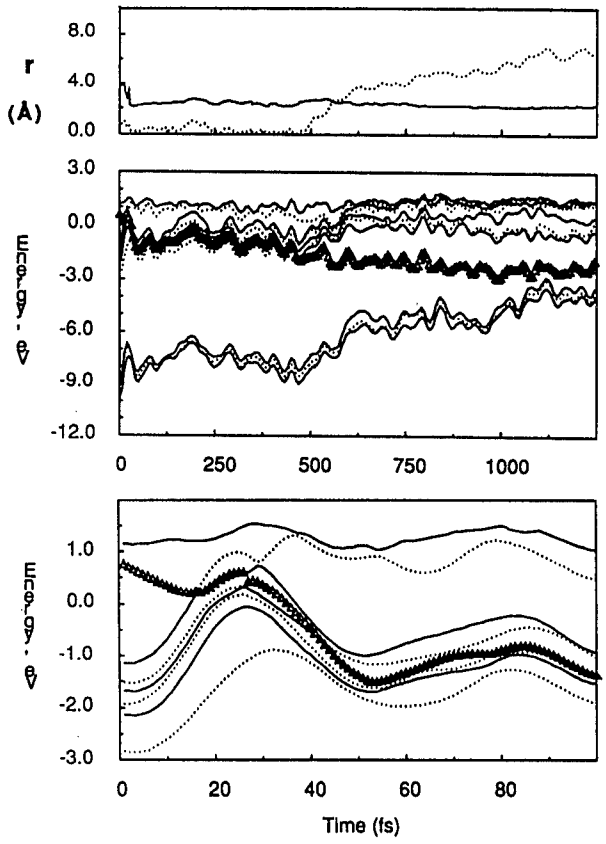


Figure 1. Simulated dynamics of two photon excited aqueous halide. Top: electronic radius of gyration (solid), separation of electronic center of mass from nucleus (dotted). Center: adiabatic one electron eigenstates; occupied state indicated by bold symbols. Bottom: short time behavior of excited eigenstates.

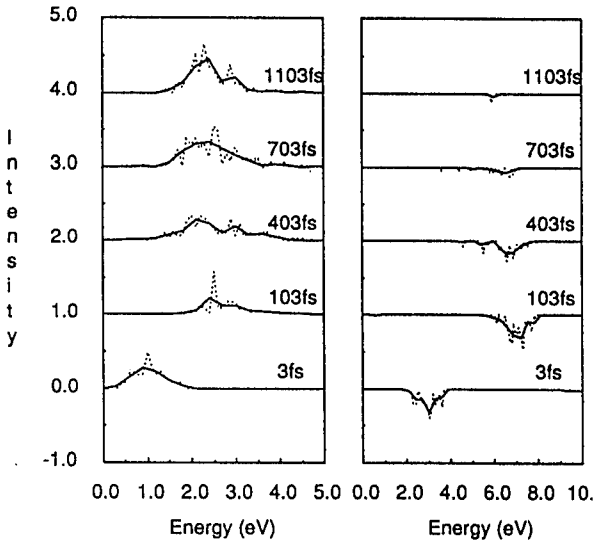


Figure 2. Simulated transient absorption (left) and emission (right) spectra for relaxation of two photon excited aqueous halide. (Calculated energies shown are expected to lie about 0.7 eV above observed values).

pair is characterized by a spectrum that is rather similar to that of an isolated hydrated electron. The emission spectra (not yet observed experimentally) are much more distinct in that the CTTS emission occurs in the UV and completely disappears with the separation into *ground* states of the halogen and electron.

The hydrated electron is ubiquitous in aqueous photochemistry[12]. However, a deeper understanding of the process of energetic relaxation and electron localization has been the subject of much recent progress in the period since the original ultrafast experiments in water[10,13] demonstrated spectroscopically a stepwise solvation process. Simulation of the relaxation of an initially energetic excess electron in water[14] has led to results that are consistent with contributions from intermediate excited states. However, if the spectral properties were characterized simply by static excited and ground state spectra, a simple two-state kinetic model, as used to interpret these experiments[10,13,15], would explain the observed spectral dynamics, but this has been the subject of some controversy.[13,15,16]

More recent hole-burning experiments have examined the transient spectroscopy of photoexcited equilibrium hydrated electrons.[17] These experiments employ a three pulse sequence: a UV pulse to generate electrons, a near infrared pump pulse to promotes the electrons to their first excited state, and a third, probe, pulse. The experiments[17] detect complicated spectral transients, in contrast to a simple two state model. The bluest probe wavelengths reveal a net transient bleach,

at red probe wavelengths, a net transient absorption is seen, and, in between, just to the red of the pump laser, an initial bleach which overshoots into a longer lived transient absorption is observed.

Quantum dynamical simulations corresponding precisely to these experiments[18] yield calculated transient spectra in near quantitative agreement with experiment (see Fig. 3), indicating the simulation correctly captures the essential physics of the hydrated electron. In particular, the computed spectra manifest each of the observed blue spectral bleach, red transient absorption, and biphasic temporal behavior in the intermediate spectral region. Further, the time scales for spectral evolution correspond well to those observed. By evaluating the spectra that would result in the absence of various dynamical factors, we find that the complex spectral dynamics are the result of both excited state absorption and ground state bleach evolution, with the latter making the larger contribution. Slower spectral changes on the picosecond time scale are the result of electrons which still remain in the excited state; ground state cooling after the transition is not found to play a critical role, in contrast to earlier speculation[17b].

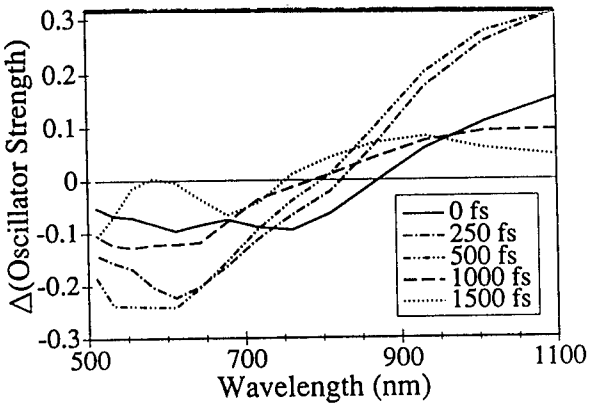


Figure 3: Calculated transient spectroscopy of the hydrated electron. The wavelength scale reflects an energetic shift equal to the difference between theory and experiment for ground state absorption.

As the work presented here demonstrates, via the use of a combination of measured ultrafast spectroscopy and simulated results, substantially greater microscopic insight into chemical dynamics can be obtained then is accessible by either technique alone.

References

1. K. Watanabe and M. L. Klein, Chem. Phys. **131**,157 (1989).
2. J. Schnitker and P.J. Rossky, J. Chem. Phys. **86**, 3462 (1987).
3. F. Webster, P. J. Rossky, and R. A. Friesner, Comput. Phys. Commun. **63**, 494 (1991).
4. W.-S. Sheu and P. J. Rossky, J. Am. Chem. Soc. **115**, 7729 (1993).
5. W.-S. Sheu and P. J. Rossky, Chem. Phys. Lett. **302**, 186 (1993).
6. W.-S. Sheu and P. J. Rossky, Chem. Phys. Lett. **213**, 233 (1993).
7. J. Jortner, M. Ottolenghi, and G. Stein, J. Phys. Chem. **68**, 247 (1964).
8. T. R. Griffiths and M. C. R. Symons, Trans. Faraday Soc. **56**, 1125 (1960).
9. J. Jortner, and A. Treinin, Trans. Faraday Soc. **56**, 1503 (1961).
10. Summaries of a number of recent measurements are provided in : H. Lu, F. H. Long, and K. B. Eisenthal, J. Opt. Soc. Am. B **7**, 1511 (1990); Y. Gauduel, S. Pommeret, A. Migus, N. Yamada, and A. Antonetti, *ibid.* **7**, 1528 (1990).
11. F. H. Long, H. Lu, X. Shi, and K. B. Eisenthal, Chem. Phys. Lett. **169**, 165 (1990); F. H. Long *et al.* (to be published).
12. see, for example, J. C. Mialocq, J. Chim. Phys. **85**, 31 (1988).
13. A. Migus, Y. Gauduel, J. L. Martin, and A. Antonetti, Phys. Rev. Lett. **58**, 1559 (1987).
14. F. J. Webster, J. Schnitker, M. S. Friedrichs, R. A. Friesner, and P. J. Rossky, Phys. Rev. Lett. **66**, 3172 (1991).
15. F. H. Long, H. Lu, and K. B. Eisenthal, Phys. Rev. Lett. **64**, 1469 (1990).
16. S. Pommeret, A. Antonetti, Y. Gauduel, J. Am. Chem. Soc. **113**, 9105 (1991); F.H. Long, H. Lu, H., X. Shi, K. B. Eisenthal, Chem. Phys. Lett. , **185**, 47 (1991).
17. (a) J. C. Alfano, P. K. Walhout, Y. Kimura, P. F. Barbara, J. Chem. Phys. **98,** 5996 (1993); (b) Y. Kimura, J. C. Alfano, P. K. Walhout, and P. F. Barbara, J. Phys. Chem. (in press).
18. B. J. Schwartz and P. J. Rossky, J. Phys. Chem. (submitted for publication).

Ultrafast Optical and Vibrational Studies of some Simple Chemical Reactions in Solutions

Robin M. Hochstrasser

Department of Chemistry
University of Pennsylvania
Philadelphia, PA 19104-6323

The dynamics of a few known gas reactions are different in solvents; evidenced by rates, solvent sensitivity, state distributions, phase propagation and transition state properties.

Transient Resonance Impulsive Stimulated Raman Scattering study of nascent diiodide ions; experiment and simulation.

Uri Banin[a] , Ronnie Kosloff[b] & Sanford Ruhman[c]
Department of Physical Chemistry, the Hebrew University, Givat Ram, Jerusalem 91904 Israel
Tel; a) 972-2-586-322, b) 972-2-585-485, c) 972-2-585-326

A novel coherent spectroscopy is applied to measure ultrafast vibrational relaxation. Its performance is quantitatively evaluated through computer simulations. Transient Resonant Impulsive Stimulated Raman Scattering (TRISRS), is used to record vibrational relaxation in rapidly evolving nascent I_2^-, following photodissociation of I_3^- in solution. The TRISRS experiment involves a sequence of three pulses. A primary UV photolyzing pulse at 308 nm initiates triiodide dissociation. At a certain delay with respect to the photolysis a secondary intense 'push' pulse at 616 nm sets in motion ground state coherent vibration. Its decay is followed via periodic transmission modulations of a continuously delayed tunable probing pulse[1]. In essence these modulations record a Raman Free Induction Decay (FID) whose duration defines the minimum time that a dynamic variable must be followed in order to reconstruct its power spectrum. Master equation simulations of vibrational relaxation, coupled to quantum wave-packet representation of the light-matter interaction[2], are combined to provide a quantitative analysis of the experimental results.

The experimental results are summarized in figures 1 and 2. The first shows a detail of TRISRS bleaches at push delays of 2, 2.67 and 4 psec. Notice that the zero of time in figure 1 and 2 is defined as the center of the push pulse interaction. A marked evolution, both in the frequency and dephasing rate of the observed modulations is manifest. The modulations are fit to an exponentially decaying sinusoid. The modulation frequency is 102, 105 and 112 cm^{-1}, and the dephasing times .5, .9 and 1.2 psec at the three delays respectively. In addition, 112 cm^{-1} is the frequency of TRISRS signals recorded at all subsequent pushing delays. Changing the probing pulse wavelength results in a phase shift of observed modulations, as shown in figure 2, where TRISRS modulations are depicted for probing at 680 and 840 nm, at a common 4 psec push delay.

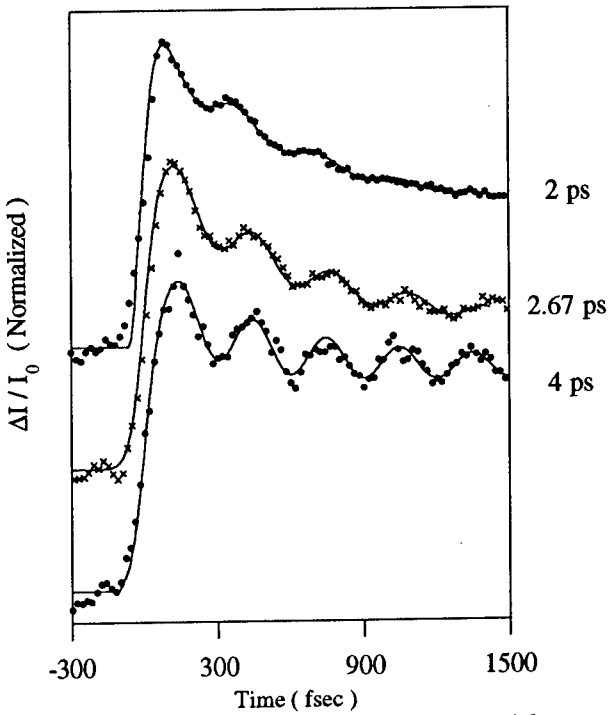


Figure 1: TRISRS data recorded at three push delays. The convoluted fits are shown as solid lines.

Qualitative interpretation of these trends involves extraction of a vibrational energy content of the fragment ions from the frequency of spectral oscillations, and dephasing parameters from the dynamics of their dissipation. At early push delays the nascent I_2^- is vibrationally excited, and the coherence built up in the high lying levels, oscillates at a reduced

frequency due to the substantial anharmonicity of the potential. At these high levels of excitation efficient mechanisms of vibrational dephasing are manifest. As the delay increases vibrational energy relaxes rapidly, leading to an increase in the modulation frequency for coherences near the bottom of the potential, and the efficiency of vibronic dephasing is reduced. No further evolution is observed after a push delay of 4 psec, corroborating the conclusion that I_2^- relaxation is very rapid, derived earlier from transient absorption results[3], and from I_2^- dissociation-recombination experiments[4]. Probe pulses are most sensitive to the evolving coherent hole as it traverses the point in coordinate space where the probe is at resonance. Different probe frequencies are therefore sensitive to different stages of the periodical evolution, giving rise to the observed phase shift in the spectral modulations (c.f. figure 2).

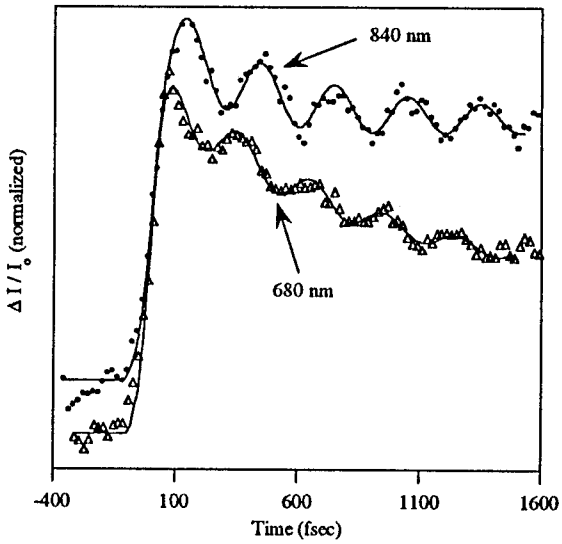


Figure 2: TRISRS signals at 840 and 680 nm probe wavelength for a similar push delay of 4 psec

In order to put analysis of the data on a quantitative footing, transient vibrational distributions are generated using a Master equation model, previously introduced to describe I_2^- relaxation following recombination[4]. Integrating the Master equation begins with 40 vibrational quanta, and energy relaxes exponentially with a rate constant of $0.43/\tau$. A grid based wave packet propagation technique is used, in conjunction with a model for I_2^- potentials, in order to represent the light matter interactions. Push-probe transient transmission scans are then simulated for the various incoherent vibrational distributions obtained from the rate equations. First, push-probe cycles starting with a single vibronic level v are simulated. Then spectral modulations from the different v's are combined, according to their probability in a certain transient distribution, in order to produce the TRISRS signals. No homogeneous mechanisms of vibrational dephasing are included in these simulations, and dissipation is represented only through the incoherent evolution of vibrational populations through the Master equation model.

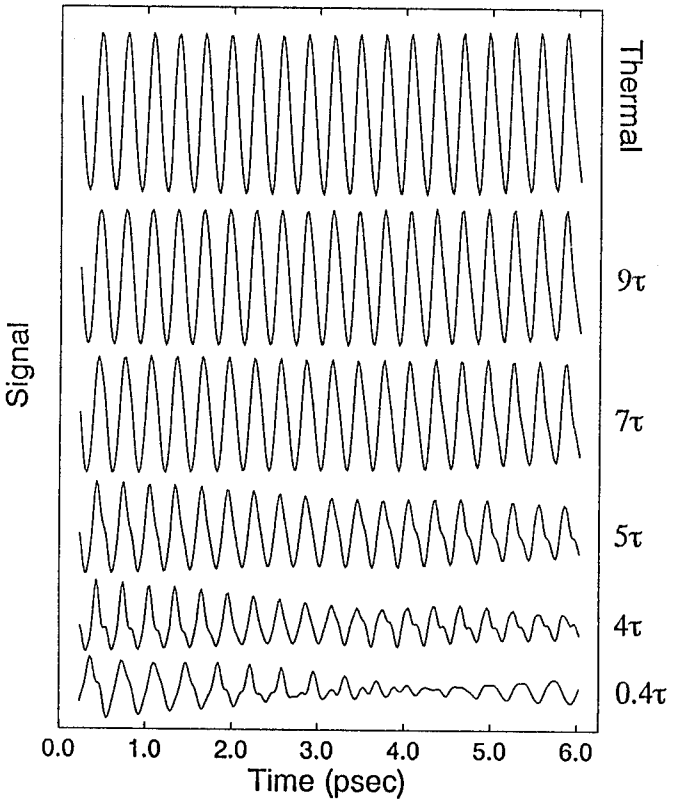


Figure 3: Simulated TRISRS signals at different delays for a probe pulse of 840 nm

The calculation clearly

demonstrates that the push interaction at 620 nm is capable of instilling vibrational coherence in all chemically excited vibronic levels. In addition, the frequency of simulated spectral modulations after pushing the individual eigenlevels closely follows the vibronic Bohr frequency for the initially populated v's. Thus, as previously assumed, this aspect earmarks the levels populated at the instant of the push interaction. The simulations do however exhibit a nonuniform sensitivity to initial populations in different vibronic levels, with preference for detecting low lying levels. Simulated TRISRS signals for an 840 nm probe, are depicted in figure 3, along with the delay in reduced units of τ. At early delays, for high vibrational energies, the signals are complex and relatively low in amplitude. At later times the response resembles a single sinusoid, and grows in amplitude. In order to extract a frequency for the modulations, the signals in figure 3 have been Fourier transformed. Results are depicted in an overlay in figure 4. The fundamental peak in the transforms evolves more or less linearly up to a delay of 3τ, and then saturates at the asymptotic frequency of 112 cm^{-1}, despite the fact that substantial relaxation is still proceeding. The quantitative measure by which the simulations and experiments can be compared is the frequency of spectral modulations, and the dependence of this frequency upon the delay time. Such comparison that enables to extract τ, will be discussed.

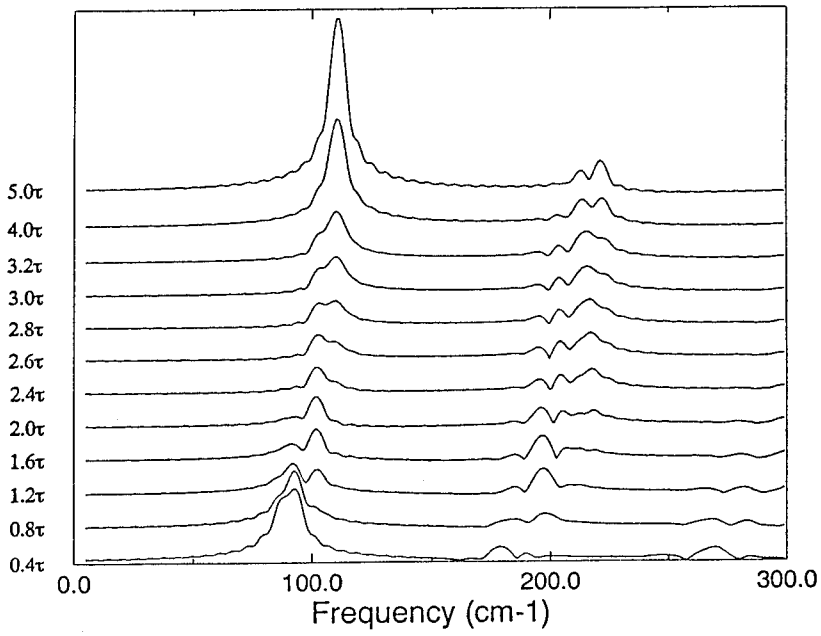


Figure 4: Fourier transforms of TRISRS signals at 840 nm, demonstrating the change in central modulation frequency

In conclusion, the viability of the TRISRS scheme for following vibrational relaxation has been demonstrated experimentally, and via detailed computer simulation. The two main requirements for its utility, i.e. that the frequency of spectral modulations in probe transmission earmark the initially populated vibronic levels, and that a single push pulse can induce coherence in a wide range of v's, have both been quantitatively verified by simulations. These show a strong preference, under the present experimental conditions, for detecting low lying vibronic levels. This stresses the complimentary nature of TRISRS and transient absorption, which are able to recover either the early or the later stages of vibrational relaxation for highly excited initial populations respectively. Further improvements to include all aspects of dissipation, including dephasing, will be discussed.

[1] U. Banin and S. Ruhman, *J. Chem. Phys.*, **99**, 9318 (1993).

[2] B.Hartke, R.Kosloff & S.Ruhman, *Chem. Phys. Lett.* **158**, 238 (1988).

[3] U. Banin, and S. Ruhman, *J. Chem. Phys.*, **98**, 4391 (1993).

[4] J. C.Alfano, Y. Kimura, and P.F.Barbara, *Chem. Phys.*, **175**, 147 (1993)

DIRECT TRANSIENT ABSORPTION SPECTROSCOPY OF THE SOLVATED ELECTRON IN WATER AND ALCOHOLS

P. F. Barbara, P. K. Walhout, Y. Kimura, and J. C. Alfano
Department of Chemistry, University of Minnesota, Minneapolis, MN 55455

In this paper, we report the results of the first direct IR-pump/variable-wavelength-probe time-resolved transient absorption spectroscopy on the solvated electron in room-temperature alcohols. We also describe extensive new results on the solvated electron in water. The experiments employ a three laser pulse sequence, where an ultraviolet (UV) synthesis pulse (390 nm, 25-30 μJ, 2 kHz) generates excess electrons by two photon photodetatchment of I^-. After a delay of ~4 ns, the resultant equilibrated electrons are promoted to the electronically excited p-state by an IR-pump pulse (780 nm, 3–25 μJ, 2 kHz), with the resulting spectral dynamics interrogated by a variable-wavelength (500 – 1000 nm) probe pulse.

The absorption transients of the solvated electron in ethanol are displayed in Fig. 1. Transients obtained probing on the blue edge of the ground state absorption band (600 – 740 nm) show a fast, instrument-limited reduction in optical density (bleach) followed by a bleach recovery that occurs on two timescales, having both a fast, ~0.5 ps component and a slower 5–10 ps component. Transients probing on the red edge of the ground state absorption band (950 nm) show a transient *increase* in optical density, which decays on a 20 ps timescale. Finally, transients probing in the intermediate spectral region (860 nm) show complicated non-monotonic behavior, where the recovery of the initial bleach "overshoots" to yield a transient increased absorption, which decays on a 5 – 10 ps timescale.

The initial bleach at blue wavelengths and increased absorption at red wavelengths result from promotion of the ground state electron into the excited p-state, which has been demonstrated in water to have an absorption band peaking near 1100 –1300 nm. The excited p-state undergoes a radiationless decay, yielding a partially desolvated s-state which has an absorption spectrum intermediate between that of the equilibrated, fully solvated s-state and the excited p-state. Ground state solvation with the concomitant blue-shifting of the transient absorption band then occurs on the characteristic ~10 ps timescale previously observed in other transient solvation experiments in ethanol.

Experiments have been performed in methanol, ethanol, propanol, and butanol. All solvents display a fast ~0.5 ps component due to electronic relaxation and a slower 5–25 ps component resulting from ground-state solvation. Additionally, a permanent bleach caused by reaction of the p-state electron with solvent is observed.

This interpretation of subpicosecond electronic relaxation of the p-state followed by ground state solvation in alcohols is consistent with recent IR-pump/variable wavelength probe time-resolved experiments investigating the relaxation of excess electron in water, see fig. 2. These experiments were analyzed using a model that considered the effects of both electronic relaxation and ground state solvation and cooling. The aqueous solvated electron was found to have an excited state lifetime of 310±80 fs.

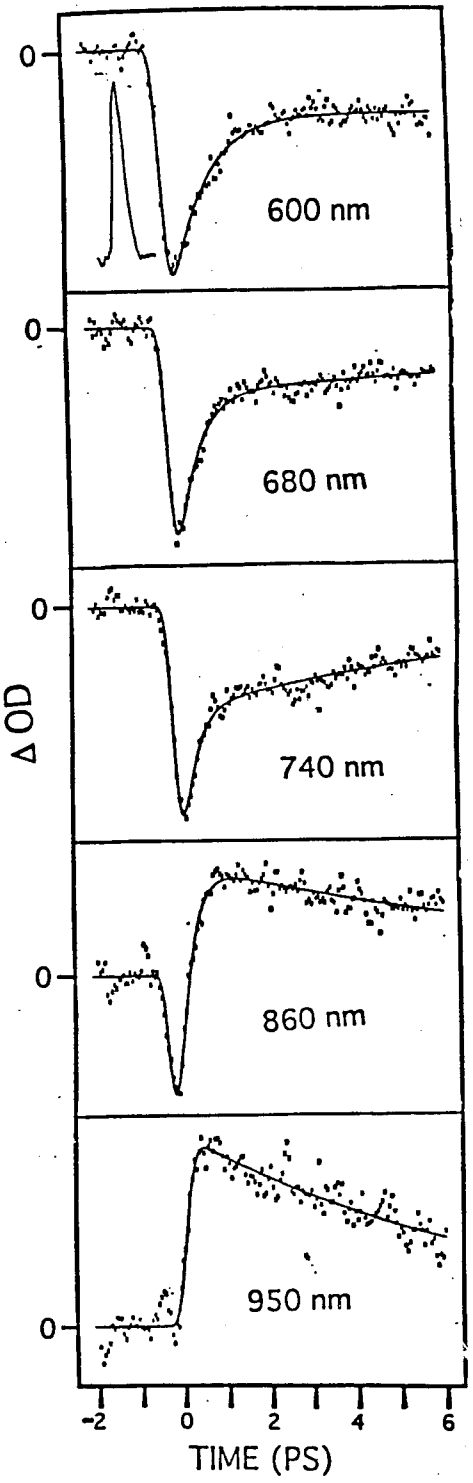


Fig. 1. Pump-probe transient of the solvated electron in 250 mM TBAI solutions in ethanol at a variety of probe wavelengths. The instrumental response function is 0.3 ps FWHM and is shown in the top spectrum. Maximum DOD values were about 0.005, which corresponds to a change in transmittance of 1%.

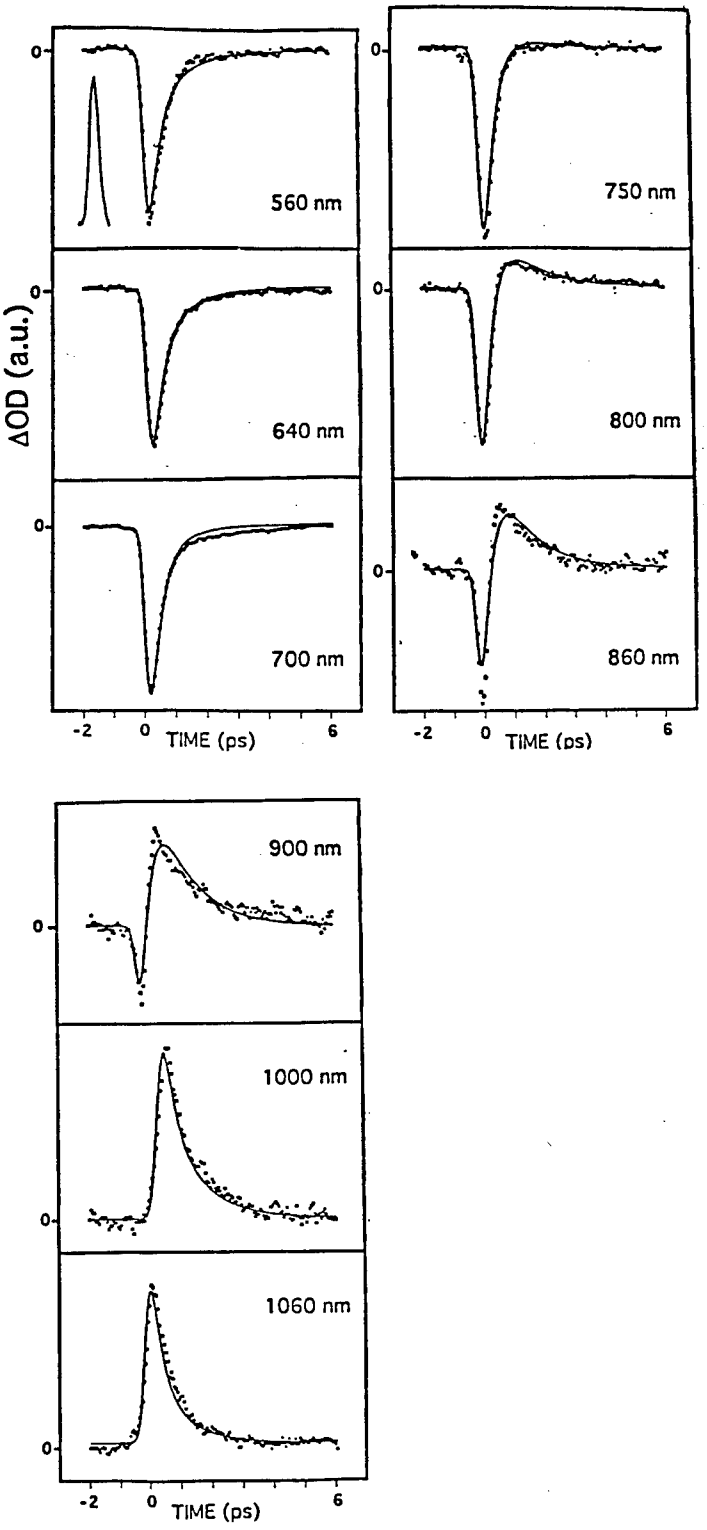


Fig. 2. Pump-probe transient of the solvated electron in 50 mM KI solutions in water at a variety of probe wavelengths.

The displacement of the solvent coordinate along the slowly responding modes cannot result from diffusive solvent motion in the excited state. If diffusive solvent motion were responsible for the excitation of the solvent coordinate, then during the excited-state lifetime of the electron the solvent would have to significantly reorient in order to solvate the excited state and desolvate the ground state. Since the ground state is solvated in ~5–25 ps, solvation in the excited state occurs on a similar timescale. However, a 0.5 ps excited state lifetime is not nearly long enough for the solvent to reorient in order to solvate the excited state. Thus diffusional motion in the excited p-state on the timescale of the diffusional longitudinal relaxation cannot account for the observed spectral dynamics since the excited state lifetime is not long enough to permit discernable displacement of the slow solvent degrees of freedom. During this nonradiative decay process, 1.7 eV of electronic energy is deposited into solvent accepting modes. Radiationless transition theory predicts that in this system the dominant accepting modes are the high-frequency OH stretching vibrations. Non-adiabatic molecular dynamics simulations also suggest that high-frequency hydrogenic motions are the primary accepting modes in this system.[1] The energy deposited into high frequency hydrogenic motions, such as OH stretches, can rapidly flow into the lower frequency hydrogen bonds, a process that has been shown to occur on a picosecond timescale.

It is important to distinguish our proposed mechanism involving specific energy deposition from a more statistical mechanism involving local statistical heating of the solvent followed by linear response-like motion of the solvent in the ground state. Given the relatively small magnitude of the resulting temperature jump, there clearly is not enough time for that to occur.

The ground-state solvation is related to recent investigations involving relaxation of charged or dipolar species in solution. The fastest component, referred to as the inertial component, typically occurs on a <50 fs timescale and results from free-streaming rotational motion of the solvent. The slow component of solvation occurs on a 10–100 ps timescale in room-temperature alcohols and results from diffusive-like solvent motion. This diffusional solvation had been related to microscopic thermally activated crossings over local barriers in the solvent-solvent potential. The slow component seen in the absorption transients of electrons in alcohols likely results from slow diffusional solvation, with the fast inertial solvation occurring within the time-response of our apparatus.

Acknowledgements

We acknowledge the support of the NSF. We wish to thank Chuck Jonah, Dave Bartels, Peter Rossky, and Ken Eisenthal for useful discussions. We thank Peter Rossky for unpublished results.

References

1. F. J. Webster, J. Schnitker, M. S. Friedrichs, R. A. Friesner, and P. J. Rossky, Phys. Rev. Letters 66, 3172(1991); T. Murphrey and P. J. Rossky, J. Chem. Phys. 99, 515(1993); E. Neria, A. Nitzan, R. N. Barnett, and U. Landman, Phys. Rev. Letters 67, 1011(1991).

Ultrashort Light Pulses

MC 1:30pm–3:00pm
Dana Point Ballroom

Charles V. Shank, *Presider*
Lawrence Berkeley Laboratories

Applications of the Chronocyclic Representation of Ultrashort Pulses

J. Paye
DLPP/EME/IE,
Commissariat à l'Energie Atomique,
Centre d'Etudes de Limeil-Valenton,
94195 Villeneuve-Saint-Georges Cedex,
France.
Tel. 33 - 1 - 45 95 66 06.

The chronocylic representation[1] is a way to display an ultrashort light pulse in a time-frequency space. It uses the Wigner distribution function applied to the complex electric field of the pulse. It thus contains both the amplitude and phase information but is a two-dimensional real function, although it can take negative values. Its mathematical properties make it as close as possible to a representation of the energy distribution of the pulse as a function of both time and frequency.

So far, the chronocyclic representation was used to describe ultrashort pulses in a more intuitive way than using the complex electric field. In particular, chirp properties and effects of the uncertainty relation appear clearly in this representation. It was also proven that the chronocylic representation of any pulse (or equivalently its amplitude and phase) could be measured by spectrally-resolved cross-correlation with a perfectly known reference pulse.[1] Later, the measurement of the chronocyclic representation of a pulse was obtained (without reference pulse) by spectrally-resolved autocorrelation.[2]

In this presentation, the chronocyclic representation will be applied to the analysis of linear optical devices commonly used in femtosecond optics, such as dispersive elements, Fabry-Perot étalons, stretchers and compressors etc. By defining a spectrally-resolved temporal response function, this approach can provide a better understanding of the action of these linear devices.

If the complex electric of an ultrashort light pulse is written as $\tilde{\mathcal{E}}(\omega)$ in the spectral domain, its chronocyclic intensity is defined as the following function of time and frequency:

$$W(\tilde{\mathcal{E}};t,\omega)=\frac{1}{2\pi}\int_{-\infty}^{+\infty}\tilde{\mathcal{E}}\left(\omega+\frac{\omega'}{2}\right)\tilde{\mathcal{E}}^{*}\left(\omega-\frac{\omega'}{2}\right)\exp[-i\omega' t]d\omega' \tag{1}$$

All linear devices can be described by a response function defined in the temporal domain. If the input complex electric field is $\mathcal{E}(t)$ in the temporal domain, the output electric field $\mathcal{E}'(t)$ can be written as:

$$\mathcal{E}'(t)=\int_{-\infty}^{+\infty}\chi(\tau)\mathcal{E}(t-\tau)d\tau \tag{2}$$

$\chi(t)$ is the temporal response function. Causality imposes that:

$$\chi(t)=0 \quad \text{if} \quad t<0 \tag{3}$$

The Fourier transform of Eq. (2) reads:

$$\tilde{\mathcal{E}}'(\omega)=\tilde{\chi}(\omega)\tilde{\mathcal{E}}(\omega) \tag{4}$$

Using a well-known property of the Wigner function, the chronocylic intensity of the output pulse can be written as:

$$W(\tilde{\mathcal{E}}';t,\omega)=W(\tilde{\chi}\tilde{\mathcal{E}};t,\omega)=\int_{-\infty}^{+\infty}W(\tilde{\chi};\tau,\omega)W(\tilde{\mathcal{E}};t-\tau,\omega)d\tau \tag{5}$$

This equation shows that the linear response of a system can be expressed in chronocyclic representation. The chronocyclic intensity of the output pulse is the temporal convolution of the chronocyclic intensity of the input pulse with the chronocyclic representation of the response function. In other words, each spectral slice of the chronocyclic representation of the input pulse is transformed by a linear system with a response function defined as the corresponding spectral slice of the chronocyclic representation of the complex response function. In chronocyclic representation, a separate temporal response function can be defined for each frequency. The chronocyclic representation of the response function is indeed a spectrally-resolved temporal response function.

Let us apply these concepts to a few simple examples. The first one is the propagation in a dispersive medium. The response function of this linear system is simply:

$$\tilde{\chi}(\omega) = \exp[ik(\omega)z] \tag{6}$$

where z is the coordinate in the direction of propagation and $k(\omega)$ is the wave vector. If the wave vector can be expanded in the vicinity of ω_0 to second order according to:

$$k(\omega) = k_0 + k_0'(\omega - \omega_0) + \frac{1}{2}k_0''(\omega - \omega_0)^2 \tag{7}$$

then the chronocyclic response function is:

$$W(\tilde{\chi};t,\omega) = \delta(t - k_0'z - k_0''(\omega - \omega_0)z) \tag{8}$$

where δ is the Dirac function. This is interpreted obviously in the following way: each frequency component of the input pulse is delayed by the dispersive medium, but this delay depends linearly on the frequency itself.

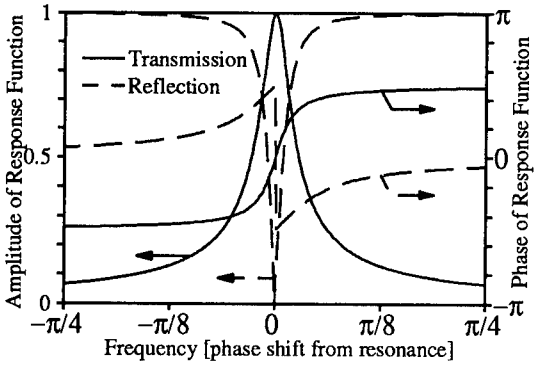


Figure 1. Response function of a Fabry-Perot Etalon both in transmission (solid line) and in reflection (dotted line). The amplitude (left-hand scale) and the phase (right-hand scale) are represented.

A more interesting example is the action of a Fabry-Perot étalon on an ultrashort pulse. The étalon is made of two identical absorptionless mirrors with a reflectivity coefficient R=95 %, the optical path length between the two mirrors is a. It is a well-known result that the response function of this device used in transmission is:

$$\tilde{\chi}_t(\omega) = \frac{(1-R)\exp(i\omega a/c)}{1 - R\exp(i2\omega a/c)} \tag{9}$$

where $2\omega a/c$ is the round-trip phase shift. This complex response function is plotted in Fig. 1 (solid line), both in amplitude and phase.

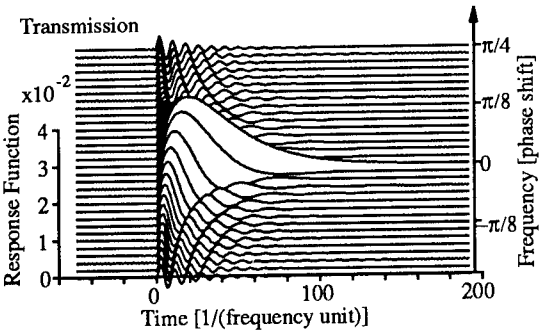


Figure 2. Chronocyclic representation of the response function of a Fabry-Perot étalon used in tranmission.

From the complex response function in Fig. 1, it is difficult to have an intuitive feeling of the action of such a device on an ultrashort light pulse, apart from amplitude filtering. The chronocyclic representation of this response function is plotted in Fig. 2. As expected, it is zero at negative times, according to causality requirements. It also shows immediately that the response of the étalon is much longer at resonance than off-resonance. A pulse with a chronocyclic intensity concentrated near resonance is lengthened by such a device much more than when its frequency is moved away from resonance. This is clear, since at resonance the spectrum of the pulse is narrowed by the étalon much more than off-resonance, therefore its duration must be increased. This example shows how the effects of the time-frequency uncertainty relation appear naturally in chronocyclic representation.

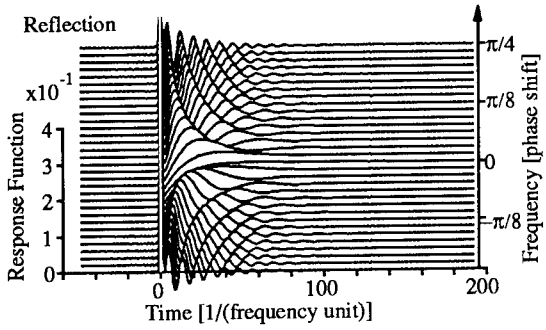


Figure 3. Chronocyclic representation of the response function of a Fabry-Perot étalon used in reflection. Each curve exhibits a Dirac δ-function at zero time.

If the étalon is used in reflection, its response function is:

$$\tilde{\chi}_r(\omega) = \sqrt{R}\,\frac{1-\exp(i2\omega a/c)}{1-R\exp(i2\omega a/c)} \qquad (10)$$

which is also plotted in Fig. 1 (dotted line). The chronocyclic representation of this response function is plotted in Fig. 3. Here again, the action of the device appears very clearly. For all frequencies, the response function exhibits a delta function at $t = 0$. It is the signature of the direct reflection on the input mirror of the étalon. Around resonance, the reflection response function shows more features, mainly negative which correspond to the partial cancellation of the direct reflection by waves trapped in the device exiting through the input mirror at later times.

In conclusion, it is possible to define a spectrally-resolved response function for any linear device by applying the chronocyclic representation to the complex response function. Simple examples show that it is possible to analyze with this method, in a very simple way, the action on ultrashort pulse of commonly used linear devices. In this presentation, this approach will be used to describe intuitively the consequences of causality and of the time-frequency uncertainty, in such systems as Gires-Tournois interferometers, pulse stretchers and compressors, pulse shapers, etc.

[1] J. Paye, IEEE J. Quant. Electron. 28, 2262 (1992).
[2] J. Paye, M. Ramaswamy, J. G. Fujimoto and E. P. Ippen, Opt. Lett. 18, 1946 (1993).

Measurement of the Intensity and Phase of Ultrashort Pulses from a Ti:Sapphire Laser Using Second-Harmonic-Generation Frequency-Resolved Optical Gating

K. W. DeLong and Rick Trebino
Sandia National Laboratories, Livermore, CA 94551

James Hunter and William E. White
Lawrence Livermore National Laboratories, Livermore, CA 94550

Daniel J. Kane
Southwest Sciences, Inc., Santa Fe, NM 87501

Recently, we developed a simple and general technique, which we call Frequency-Resolved Optical Gating (FROG), that succeeds in measuring the full intensity and phase evolution of an individual, arbitrary ultrashort pulse.[1-3] In brief, FROG involves measuring the pulse spectrogram, i.e., the spectrum of the signal pulse in an auto- or cross-correlation using any instantaneous nonlinearity, yielding signal intensity vs. delay and frequency. This trace can then be shown to fully and uniquely characterize the pulse—the pulse extraction problem is equivalent to two-dimensional phase retrieval, a solved problem from image science.

In previous work, we have demonstrated FROG on a single-shot basis in the visible and ultraviolet using a polarization-gate (PG) beam geometry, where a newly improved version of our phase-retrieval algorithm operates reliably and quickly and without ambiguity, even in the presence of significant amounts of noise.[4] In this work with lower-intensity pulses, however, we utilize (multi-shot) self-diffraction (SD) and second-harmonic-generation (SHG) FROG arrangements, for which all previously published algorithms[3,5] are unreliable. As a result, we have made significant improvements to these algorithms for these arrangements, including the use of least-squares optimization, generalized projections, Weiner-filtering, and a variety of other techniques. We report significantly improved performance, especially for SHG FROG.

We have also performed an in-depth study, using SHG FROG, of the operation of a Kerr-lens-mode-locked Ti:Sapphire oscillator. We have fully characterized the output train of ~100-fsec, ~2.5-nJ pulses for a wide range of operating parameters, obtaining the pulse intensity and phase evolutions as a function of the lasing wavelength and the amount of glass in the cavity. For most stable operating modes, we typically find little higher-order phase distortion. For operation with much glass, we find almost pure cubic chirp. When some linear chirp is present, we typically also find that chirp of the opposite sign occurs in the wings of the pulse.

Figure 1 shows a typical SHG FROG trace for the pulse train from the Ti:Sapphire laser oscillator. Recall that, using SHG FROG, the trace is necessarily symmetrical in delay and, as a result, has ambiguity in the direction of time. Thus, unlike PG FROG, which directly yields a frequency-vs.-time plot of the pulse, SHG FROG traces require running the algorithm in order to obtain usable information regarding the pulse. Fortunately, the SHG FROG algorithm is fairly robust (although not as robust as our PG FROG algorithm), and the intensity and phase derived for the above FROG trace are shown in Fig. 2. Figure 3 shows a careful comparison of the derived pulse fields with independently taken pulse autocorrelations and spectra, indicating excellent agreement between autocorrelations and spectra calculated for the derived pulses and these experimental measurements. Note that the intensity is smooth and that a small amount of residual quadratic phase (linear

chirp) is present, although it is not possible to determine whether it is positive or negative due to the time-direction ambiguity. Note also that, in the wings of the pulse, the sign of chirp has the opposite sign. This is a common feature of these Ti:Sapphire laser pulses. It is reasonable in view of the self-phase modulation and compression occurring in the laser.

While the laser generally produced pulses similar to that shown above, it was also possible to obtain more complex pulses when much intracavity glass was inserted in the beam. Figure 4 shows a FROG trace with considerable structure. This structure is indicative of spectral cubic chirp. We have recovered this pulse's intensity and phase evolution from its FROG trace (see Fig. 5). It is shows the intensity structure and phase jumps representative of cubic phase vs. frequency.[5] Figure 6 shows the spectrum and phase in the frequency domain, where the cubic phase dependence vs. frequency is more evident.

In conclusion, while FROG has already been shown to be effective for measuring ultrashort pulses of energy greater than about 1 μJ, we believe that, with this work, we are close to achieving with FROG a very simple and general diagnostic for low-energy ultrashort pulses, as well. In addition, our study of the Ti:Sapphire oscillator should shed light on the dynamics of the mode-locking process in this laser.

References

1. D. J. Kane and R. Trebino, IEEE J. Quant. Electron. **29**, 571 (1993).
2. D. J. Kane and R. Trebino, Opt. Lett. **18**, 823 (1993).
3. R. Trebino and D. J. Kane, J. Opt. Soc. Amer. A **10**, 1101 (1993).
4. K. DeLong and R. Trebino, "Improved Ultrashort-Pulse Retrieval Algorithm for Frequency-Resolved Optical Gating," J. Opt. Soc. Amer. A *in press* (1994).
5. J. Paye, M. Ramaswamy, J. Fujimoto, E. Ippen, Opt. Lett. **18**, 1946 (1993).
6. K. W. DeLong, R. Trebino, and D. J. Kane, "A Catalog of Frequency-Resolved-Optical-Gating Traces for Common Ultrashort Pulses," J. Opt. Soc. Amer. B, *in press* (1994).

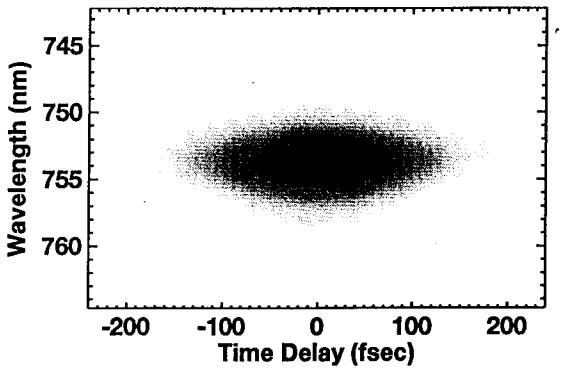


Figure 1. SHG FROG trace for a train of pulses from a Ti:Sapphire laser exhibiting near-transform-limited behavior.

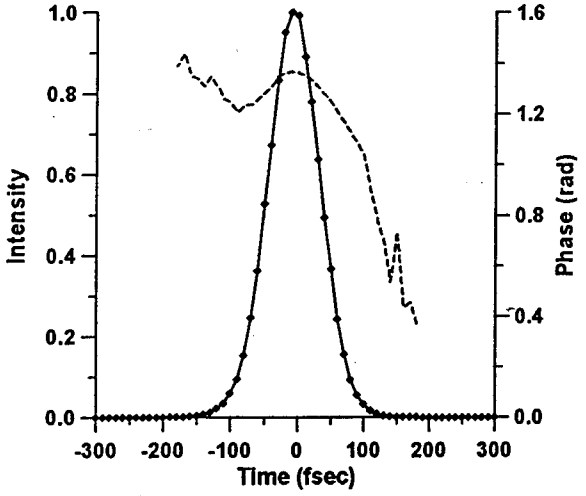


Figure 2. Intensity (solid line) and phase (dashed line) derived for the pulse whose SHG FROG trace is shown in Fig. 1. Note the smooth intensity profile and the small amount of quadratic phase (linear chirp). Note also the opposite sign of chirp in the leading wing of the pulse.

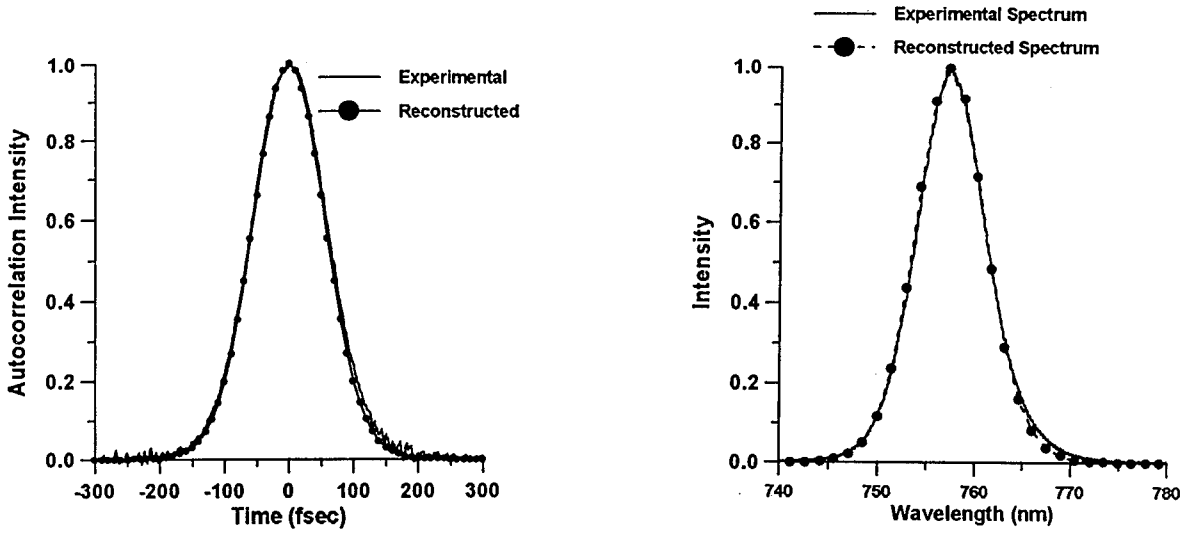


Figure 3. Comparison of the derived and independently measured intensity autocorrelation and spectrum of the pulse in Figs. 1 and 2. Agreement is excellent.

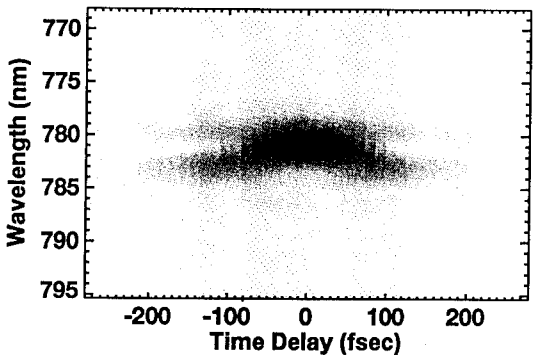


Figure 4. SHG FROG trace for a train of pulses from a Ti:Sapphire laser exhibiting cubic phase vs. frequency. Note the characteristic parabolic group delay vs. frequency (which is symmetrized in this SHG FROG trace due to the time-reversal ambiguity in SHG FROG).

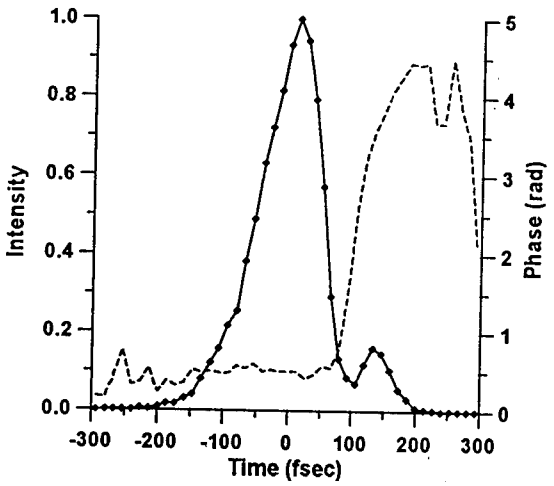


Figure 5. Intensity (solid line) and phase (dashed line) derived for the pulse whose FROG trace is shown in Fig. 4. Note the ~π-phase-shifted satellite pulse, indicative of cubic phase vs. frequency.

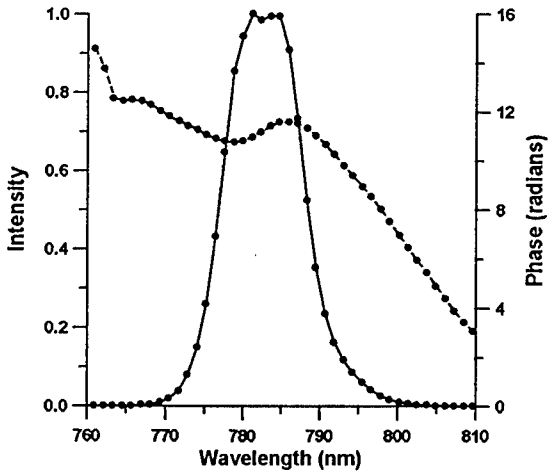


Figure 6. Spectrum (solid line) and phase (dashed line) vs. frequency derived for the pulse whose FROG trace is shown in Fig. 4. Note the smooth intensity and parabolic phase vs. frequency.

Spatio-Temporal Holograpy

Martin C. Nuss, Melissa Li, T. H. Chiu, and Afshin Partovi
AT&T Bell Laboratories, 101 Crawfords Corner Rd., Holmdel, NJ 07733-3030
Tel. (908) 949-5358; Fax: (908) 949-2473

There are quite a few examples of analogies between spatial problems and their corresponding temporal counterparts in optics. One example is the space-time duality between diffraction and dispersion, which has recently resulted in the concept of a "time lens" [1,2]. Another one is the similarity between holographic and photon-echo optical memories [3].

Here, we present yet another variety of such a time-space duality. Our experiment makes use of the fundamental equivalence of time and space in Fourier-transform holography with its two incarnations, conventional (spatial) holography and temporal (sometimes also called "spectral") holography [4,5]. But unlike in the previous examples of time-space dualities, time and space versions of the information can be present at the same time in the same setup, and hence temporal information can be readily converted into spatial information and vice versa. As a first example, we convert temporal (pulse shape) information from femtosecond pulses into spatial images that can be displayed and recorded in real time with a video camera.

Figure 1 illustrates the principle of our experiment, which contains elements of both spatial and temporal holography setups. A signal pulse $E_S(t)$ carrying the temporal information and a short, featureless reference pulse $E_R(t)$ are spectrally dispersed by a diffraction grating in the input plane, collimated by a lens, and interfere in a holographic medium placed at the spectrum plane to form a temporal hologram. The interference fringes in the hologram contain terms $E_S^* E_R$, $E_S E_R^*$, which describe correlations of the two input signal when transformed back into the time domain [5].

The action of the grating can be described by multiplying the spectrum $E_0(\omega)$ of the input pulse with the complex filter function of the grating [6]:

$$E(x,\omega)=e^{i\beta(\omega-\omega_0)\cdot x/c}\,E_0(\omega),$$

where ω_0 is the center frequency of the pulse, $\beta=\lambda_0/d\cos\theta$ the dispersion parameter of the grating, d the pitch of the grating, θ the diffraction angle and c the speed of light. Transforming back into the time-domain, the diffracted pulse right behind the grating has the form $E(x,t)=E_0(t-\beta\cdot x/c)$, which describes a spatial "image" of the input pulse projected onto the grating with a time-to-space scaling factor β/c and surfing across the grating at a speed $v=c/\beta$. Hence, a conversion of temporal information into spatial information has taken place in the grating plane, where the signal pulse shape is present as a spatial *image*.

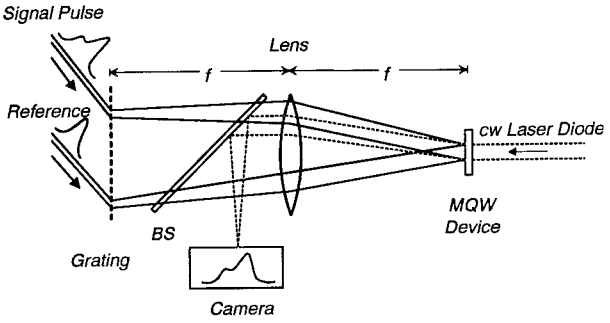


Figure 1
Schematic view of the spatio-temporal holographic setup.

We can show that there is no difference between diffraction at a grating due to the finite bandwidth of the input pulse and Fresnel diffraction of a monochromatic wave at a screen which reproduces the pulse shape (in amplitude and phase) with the scaling factor β/c. Once the hologram is written, it can fundamentally not be distinguished whether the hologram was recorded using temporal information or spatial information as long as the holographic medium is spectrally non-selective. Thus, this offers the opportunity to convert temporal data

into spatial data and vice versa. For example, in the experiment described below, we accomplish time-to-space mapping by writing a temporal hologram with spectrally dispersed pulses, but then interpret the temporal hologram as a spatial hologram by reading it out with a monochromatic plane wave (Figure 1). Conversely, space-to-time mapping can be achieved by writing a spatial hologram using a spatial light modulator and then reading out the hologram with a spectrally dispersed short optical pulse.

In the experiment, we use a 600 lines/mm diffraction grating and a 200 mm focal length Fourier-transform lens. The center wavelength λ_0 of the femtosecond laser is roughly 830 nm and each of the two beams has about 5 mW average power. The angle of incidence is chosen so that the diffracted beam is parallel to the surface-normal of the grating in all our experiments (Figure 1). A multi-quantum-well (MQW) photorefractive device, located at the spectrum plane, serves as a real-time holographic medium. This device has a response time of less than 1 μs at an energy density of 1 μJ/cm^2 and a diffraction efficiency of a few percent [7]. The MQW device is read out with a few mW from a collimated single-mode diode laser at 850 nm. The diffracted light travels back through the setup and is being picked off by a thin beam splitter *BS* and focused onto the detector plane. The correlation peaks in the detector plane are recorded either by a charge-coupled device (CCD) video camera or by a silicon diode array.

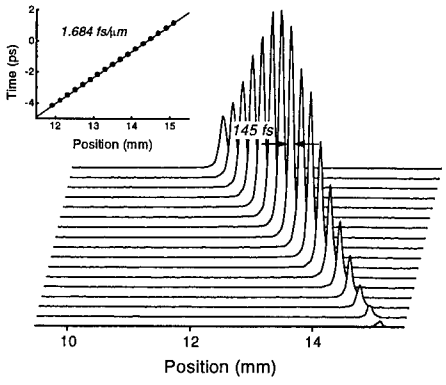


Figure 2
Auto-correlation peaks of 100 fs pulses recorded by an array detector in the camera plane.

Figure 2 shows the correlation peaks observed in the camera plane for different time delays between the signal and reference pulses in the case where both signal and reference are identical 100 fs laser pulses. The time delay between successive traces is 333 fs. As the time delay between the two input pulses is varied, the correlation peaks move on the detector array. We can obtain a calibration of the time-to-space mapping process by plotting the position of the correlation peaks versus the time delay between the two femtosecond input pulses (see inset in Figure 2). This calibration constant is $1.684 \pm 0.03\ fs/\mu m$. The figure also shows that there is a limited range over which the input delay can be changed and still being able to see a correlation peak. This window ΔT results from the finite spectral resolution of the setup and amounts to roughly 7 ps. Using gratings with finer lines or larger beam diameters, this windows can easily be extended to several hundred picoseconds.

When the signal pulse is longer than the input pulse, we obtain the square of the electric-field cross-correlation between signal and reference pulse. To demonstrate this, we let one of the 100 fs pulses propagate through roughly 50 cm of single-mode fiber to stretch out the pulse duration. The power in the fiber is less than 5 mW, so that mainly linear dispersion occurs in the fiber without much self-phase-modulation. Then, the signal pulse emerges from the fiber stretched out and with a linear frequency chirp. The cross-correlation profile recorded in the detector plane is shown in Figure 3. The FWHM is now 200 μm, corresponding to 340 fs. Within a few percent, the same pulse duration is also measured by conventional intensity cross-correlation at the setup.

In conclusion, we have demonstrated conversion of temporal information into spatial information in a temporal holography setup. This is possible because there is no significant difference between recording a temporal hologram, in which temporal frequencies (wavelengths) are recorded, and a spatial hologram, in which spatial frequencies are recorded.

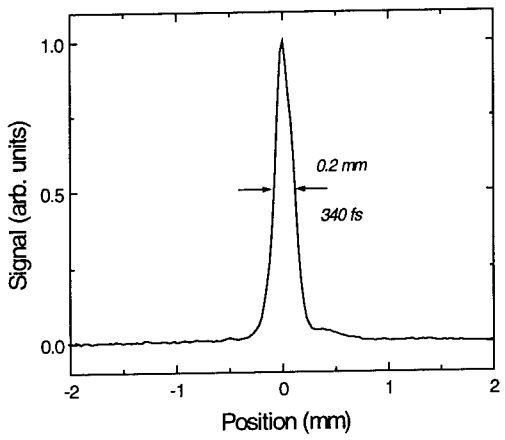


Figure 3
Cross-correlation of two 100 fs pulses, with one of the pulses being broadened by propagation through 50 cm of single-mode fiber.

REFERENCES

[1] B. H. Kolner et al., Opt. Lett. **14**, 630 (1989)
[2] A. A. Godil et al., Appl. Phys. Lett. **62**, 1047 (1993)
[3] M. Mitsunaga, Opt. and Quant. Electr. **24**, 1137 (1992)
[4] Y. T. Mazurenko, Appl. Phys. **B 50**, 101 (1990)
[5] A. M. Weiner et al., IEEE Journ. Quant. Electr. **J-QE 28**, 908 (1992)
[6] O. E. Martinez, Opt. Comm., **59**, 229 (1986)
[7] A. Partovi et al., Appl. Phys. Lett. **62**, 464 (1993)

Programmable femtosecond multiple pulse generation and spectroscopy

Marc M. Wefers and Keith A. Nelson

Department of Chemistry, Massachusetts Institute of Technology, Cambridge, MA 02139. (617)-253-1562

The ability to 'shape' femtosecond pulses into arbitrary ultrafast optical waveforms will profoundly expand the capabilities of optical spectroscopy (1,2). This field extends the context of spectroscopy to emphasize detailed optical control over chemical events. Demonstrations of some of these possibilities have already been reported (3-5). Recently we reported programmable generation of user-specified ultrafast waveforms with emphasis on an expanded range of possible waveforms and increased user-friendliness (6). The present discussion will describe the current developments in our lab pertaining to this rapidly expanding technology.

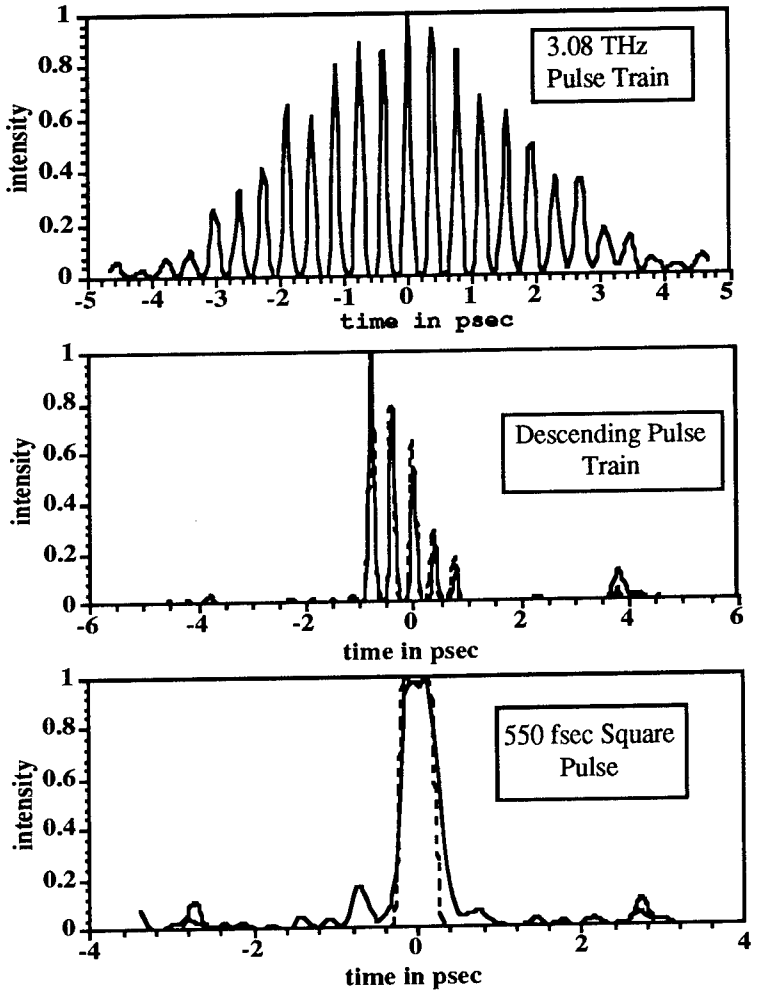
The generation of shaped ultrafast waveforms was pioneered by Weiner and coworkers at Bellcore (7-9). Femtosecond pulses are shaped by filtering the spatially separated frequency components of an incident pulse using a spatially varying mask. Recombining the spectrally filtered frequency components yields a 'shaped' waveform in the time domain. The use of an electronically addressable liquid crystal (LC) spatial light modulator (SLM) as the spatially varying mask made it possible for these shaped waveforms to become programmable (9). The current challenge is to produce high fidelity shaped waveforms with arbitrary temporal profiles and to do so in such a way that the user need only specify the desired waveform and not detailed mask patterns.

Systematic limitations are imposed by the spatial resolution of the LC SLM, which limits the temporal range of the shaped waveform, and by the available bandwidth of the incident pulse which limits the temporal resolution of the shaped pulse. In principle, the number of arbitrary features in the shaped waveform is limited by the number of pixels on the SLM. An important practical consideration is the need to use two masks to impart arbitrary attenuation and retardation to each frequency component, permitting control over both amplitude and phase profiles of the shaped waveform. Other practical issues are the fixed pixel widths of the SLM masks, and the small 'gaps' between adjacent electrodes on the SLM so parts of the mask filter are not properly controlled.

Originally, we used two separate 70-element SLMs in combination with various polarization optics to produce an arbitrary frequency filter (6). More recently we have worked with

Cambridge Research and Instrumentation (CRI) in the development of a device in which two 128-element SLMs with smaller gaps are combined into a single unit. This will increase the fidelity and temporal range of the shaped waveforms, while substantially simplifying the optical alignment.

Examples of ultrashort waveforms generated with 70 element SLMs are shown below. The dotted curves for the descending pulse train and square pulse give the anticpated waveform assuming perfect calibration and alignment.



We have also completed a rigorous theoretical analysis of the pulse shaping operation, including careful description of the effects of diffraction off the two spatially varying masks. Such diffraction effects should be considered in general, but especially for cases in which the masks are not in the focal plane of the imaging system. This is necessarily the case for the device in which two masks are combined into a single unit. Our results describes diffraction as well as other systematic limitations of the masks in such a way that efficient algorithms can be designed to generate the mask pattern needed for generation of a specified waveform.

A significant result of the theoretical analysis is that spectral filtering necessarily alters the transverse spatial profile of the shaped pulse. In particular, there is a small transverse shift that varies linearly with time along the shaped waveform. Thus different pulses within a pulse train are spatially centered on different points along the transverse axis of the beam. This shift depends on the mask width and on the lenses and gratings used to spectrally disperse the input pulse. Proper design of pulse-shaping systems should recognize this temporal-spatial shaping and its impact on spectroscopic experiments.

Current spectroscopic efforts utilizing shaped pulses include the use of phase-locked pulses for fluorescence-detected photon echoes, and verification of a recent prediction (10) that coherent two-photon spectroscopy can be conducted with phase-related pulses in a manne somewhat similar to coherent spectroscopy with one-photon transitions, even thought the two-photon transitions lead to coherent polarizabilities rather than coherent polarizations. Even the simplest experiments using phase-locked pulse pairs are important at this stage since the phase relationship between multiple pulse waveforms produced in this way have yet to be experimentally verified. Other objectives include manipulation of coherent phonon responses in crystals, and the combination of multiple-pulse excitation with single-shot femtosecond data acquisition (11). This will permit high-intensity mutliple excitation pulses to be used on condensed materials without cumulative sample damage, and will permit multiple-pulse spectroscopy data to be recorded even if sample damage occurs in a single laser shot.

1. W. S. Warren, H. Rabitz, M. Dahleh, Science **259**, 1581 (1993)
2. M. M. Wefers, K. A. Nelson, Science **262**, 1381 (1993)
3. E. D. Potter, J. L. Herek, S. Pedersen, Q. Liu, A. H. Zewail, Nature **355**, 66 (1992)
4. N. F. Scherer, R. J. Carlson, A. Mato, M. Du, A. J. Ruggiero, V. Romero-Rochin, J. A. Cina, G. R. Fleming, S. A. Rice, J. Chem. Phys. **95**, 1487 (1991)
5. A. M. Weiner, D. E. Leaird, G. P. Weidderrecht, K. A. Nelson, Science **247**, 1317 (1990)
6. M. M. Wefers, K. A. Nelson, Opt. Lett. **18**, 2032 (1993)
7. J. P. Heritage, A. M. Weiner, R. N. Thurston, Opt. Lett. **10**, 609 (1985)
8. A. M. Weiner, J. P. Heritage, E. M. Kirschner, J. Opt. Soc. Am. B **5**, 1563 (1988)
9. A. M. Weiner, D. E. Leaird, J. S. Patel, J. R. Wullert, Opt. Lett. **15**, 326 (1990)
10. H. Kawashima, K. A. Nelson, submitted to Chem. Phys. Lett.
11. L. Dhar, J.T. Fourkas, and K.A. Nelson, Opt. Lett., in press.

Poster Session 1 and Exhibits

MD 3:00pm–4:30pm
Dana Point Ballroom

Femtosecond Studies of Photoinduced Electron Dynamics at the Liquid-Solid Interface of Semiconductor Nano-particles in Water

J. Z. Zhang, R. H. O'Neil, T. W. Roberti, and J. L. McGowen

Department of Chemistry and Biochemistry, University of California,
Santa Cruz, CA 95064, USA

Abstract. We report direct measurements of the dynamics of photoinduced electrons at the liquid-solid interface of aqueous CdS colloids on the femtosecond time scale. Surface electron trapping was found to occur in < 100 fs, followed by rapid decay of the trapped electrons through primarily electron-hole recombination.

1. Introduction

The liquid-semiconductor interface plays a key role in several fields including photocatalysis, photoelectrochemistry, and solar energy conversion [1]. One of the most crucial issues involved is the dynamics of the electron at this heterogeneous interface, including trapping and electron-hole recombination. Recently, particulate or colloidal semiconductors with diameters of 10 - 100 Å have received considerable attention [1,2] because they exhibit optical and electronic properties different from those of bulk semiconductors due to the quantum size-confinement effect [3], making them potentially useful in the design of new photoelectrochemical systems and photocatalysts. One of the most extensively studied systems is CdS [3,4]. The static absorption and emission properties of colloidal CdS particles have been well characterized [3]. Nanosecond and picosecond flash photolysis as well as picosecond resonance Raman experiments have also been performed to examine the interfacial charge transfer process in colloidal CdS [4]. Recently several femtosecond studies have been reported on the investigation of charge carrier dynamics in nanocrystals [3f,5,6], however, to date only a few femtosecond studies have been performed to examine the electron dynamics in aqueous CdS colloids [7,8] and the assignment of the observed transient absorption is still the subject of controversy [4c,7,8]. In this paper, we report a study of the interfacial electron dynamics in aqueous CdS colloids using femtosecond laser spectroscopy and show new evidence of trapped electrons at the liquid-solid interface based on the sensitive dependence of the decay dynamics on the excitation intensity and the solvent.

2. Experiment

The experiments were performed on aqueous CdS colloids using a pump-probe scheme with a regeneratively amplified, mode-locked femtosecond Ti-Sapphire laser. The details of the experiment and the laser system have been reported elsewhere [8]. The CdS colloids were prepared following the procedure given in Ref. 3c. The femtosecond laser pulses were generated by a laser system based on the design of Salin et al. [9]. Pulses of 40 fs duration with 5 nJ/pulse energy at 100 MHz were obtained from a home-built, mode-locked Ti-Sapphire oscillator [10] and amplified in a Ti-Sapphire regenerative amplifier (Quantronix) using chirped-pulse amplification [11]. The final output pulses, typically 150 fs with a pulse energy of 350 μJ, centered at 780 nm, was doubled in a KDP crystal to generate 30 μJ/pulse of 390 nm light, which was used to excite the CdS colloid. The remaining fundamental was focused into quartz to generate a white light continuum, from which the desired probe wavelength was selected.

3. Results and Discussion

The bandgap for bulk CdS crystal is around 500 nm (2.5 eV) and it shifts to higher energy for

smaller particles of CdS due to quantum size-confinement, causing a blue shift of the absorption spectrum [3]. Since the absorption spectrum is strongly size-dependent, it can be used to infer the particle size. The absorption spectrum of the colloid used in this study has an excitonic peak at 430 nm and absorption onset around 470 nm, indicating a particle size of 30 Å [3]. We chose to excite the colloid at 390 nm and probe at the red-infrared, where the electron is expected to absorb strongly.

The time evolution of the photoinduced electrons probed at 780 nm is shown in Fig. 1 The transient absorption has been assigned to electrons trapped at the liquid-solid interface based on the sensitive power dependence and solvent dependence, as explained in detail elsewhere [8]. The transient spectra feature a very fast rise followed by a fast and a slow decay; it then levels off up to 1 ns. The data fit well to a 100 fs exponential rise and a fast 2.5 ps exponential decay followed by a slower 50 ps exponential decay, plus an offset. The initial rise indicates that the trapped electrons are formed with a time constant of <100 fs. The population reaches a maximum in about 350 fs and then starts to decay. More than 50% of the initially generated population decays in < 10 ps. The very fast rise (<100 fs) suggests that the electrons are either created directly at the surface or generated inside the particle and then migrate to the surface within 100 fs. This observation of extremely fast surface electron trapping is consistent with previous studies [4c,5,7].

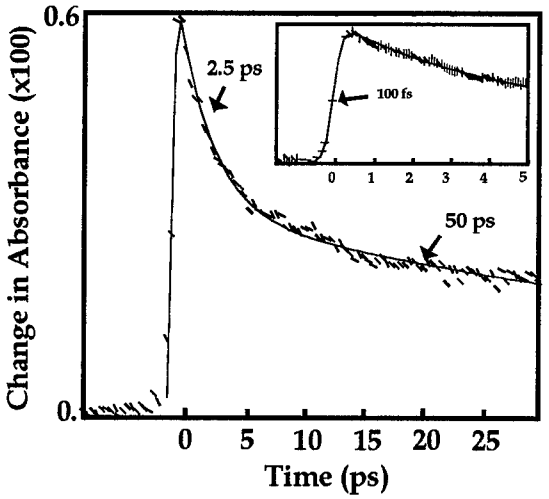


Fig. 1. The time evolution of the photoinduced electrons at the CdS-water interface probed at 780 nm following excitation at 390 nm. The pump fluence is 1.18 photons/Å2. The dotted lines are the experimental data; the solid lines are fits using the function discussed in the text.

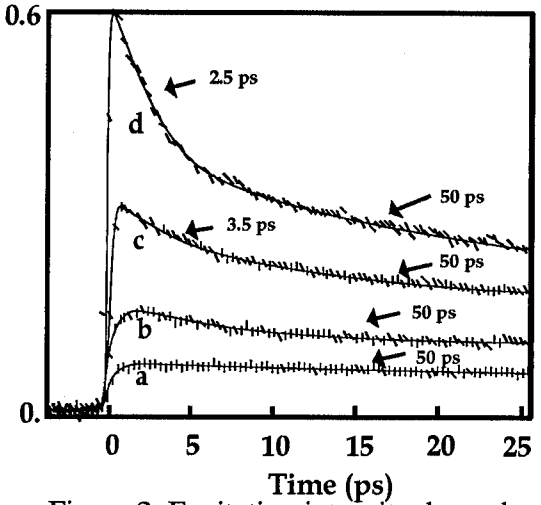


Figure 2. Excitation intensity dependence of the dynamics probed at 780 nm. The photon fluence is as follows (photon/Å2): a. 0.12; b. 0.20; c. 0.59; d. 1.18.

Immediately following the initial fast rise, the population of the trapped electrons begins to decay (Fig. 1). The double exponential decay components (2.5 ps and 50 ps) suggests that the trapped electrons disappear through a non-first-order decay process. The amplitudes for both decays, especially the faster decay, are found to be sensitive to the pump power. The pump power used in recording the spectra in Fig. 1 is 3 μJ/pulse. When the power is varied from 3 μJ/pulse (1.18 photons/Å2, about 10 photons per CdS particle) to 0.3 μJ/pulse (0.118 photons/Å2), the amplitude of the 2-3 ps decay component decreases almost linearly with the pump power and becomes negligible at 0.3 μJ/pulse, while the 50 ps decay component also decreases but is still weakly visible at 0.3 μJ/pulse (Fig. 2). We have attributed both the fast and slow decay components to trapped electron-hole recombination [8]. At low pump power (Fig. 2a and 2b) the decay is dominated by a single exponential with a time constant of 50 ps. The amplitude, but not

the rate, increases with the pump power. We assign this slow decay to geminate electron-hole recombination, analogous to the geminate electron-H_2O^+ recombination observed in neat water [12]. At high pump power (Fig. 2c and 2d) we observed enhancements both in the amplitude and in the rate of the fast decay component. We attribute this fast decay to non-geminate electron-hole recombination [8]. We have also studied the solvent dependence of dynamics and found that both the fast and slow decays are sensitive to species in the liquid that are likely to be adsorbed onto the particle surface, e.g. I^- and OH^-, but are not particularly sensitive to changes of the solvent mixture, e.g. water, water-ethanol (1 to 1, v/v), and water-acetonitrile, at least on the time scale of < 50 ps, substantiating the proposal that the observed decay processes take place at the liquid-solid interface.

In summary, we have performed direct femtosecond measurements of the dynamics of electrons trapped at the liquid-solid interface of aqueous CdS colloids. The average transient time for surface electron trapping is found to be < 100 fs. The majority of the trapped electrons decay within 10 ps through predominantly electron-hole recombination at high excitation intensities. At low intensities the decay dynamics are dominated by a single slow (50 ps) decay process, assigned to geminate electron-hole recombination. One important implication of this study is that the electron needs to be intercepted for photocatalysis on the picosecond or shorter time scale in order to avoid electron-hole recombination and to control or improve the light harvesting efficiency.

References

1. (a) Gratzel, M. *Heterogeneous Photochemical Electron Transfer*, CRC Press: Boca Raton, Florida, 1989; (b) Fox, M. A.; Dulay, M. T. *Chem. Rev.* **1993**, *93*, 341; (c) Kamat, P. V. *Chem. Rev.* **1993**, *93*, 267.
2. (a) Kalyanasundaram, K. *Photochemistry in Microheterogeneous Systems*, Academic Press: New York, 1987; (b) Henglein, A. *Topics in Curr. Chem.* **1988**, *143*, 113.
3. (a) Chestnoy, N.; Harris, T. D.; Hull, R.; Brus, L. E. *J. Phys. Chem.* **1986**, *90*, 3393; (b) Brus, L. E. *J. Chem. Phys.* **1983**, *79*, 5566; (c) Colvin, V. L.; Goldstein, A. N.; Alivisatos, A. P. *J. Am. Chem. Soc.* **1992**, *114*, 5221; (d) Wang, Y. *J. Phys. Chem.* **1991**, *95*, 1119; (e) Lippens, P. E.; Lannoo, M.; *Phys. Rev. B* **1989**, *39*, 10935; (f) Schoenlein, R. W.; Mittleman, D. M.; Shiang, J. J.; Alivisatos, A. P.; Shank, C. V. *Phys. Rev. Lett.* **1993**, 70, 1014.
4. (a) Nosaka, Y.; Miyama, H.; Terauchi, M.; Kobayashi, T. *J. Phys. Chem.* **1988**, *92*, 255; (b) Haase, M.; Weller, H.; Henglein, A. *J. Phys. Chem.* **1988**, *92*, 4706; (c) Kamat, P. V.; Ebbesen, T. W.; Dimitrijevic, N. M.; Nozik, A. J. *Chem. Phys. Lett.* **1989**, *157*, 384; (d) Rossetti, R.; Brus, L. E. *J. Phys. Chem.* **1986**, *90*, 558.
5. Bawendi, M. G.; L. Wilson, W. L.; Rothberg, L.; Carroll, P. J.; Jedju, T. M.; Steigerwald, M. L.; Brus, L. E. *Phys. Rev. Lett.* **1990**, *65*, 1623.
6. Peyghambarian, N.; Fluegel, B.; Hulin, D.; Migus, A.; Joffre, M.; Antonetti, A.; Koch, S. W.; Lindberg, M. *IEEE J. Quant. Elect.* **1989**, *25*, 2516.
7. Kaschke, M.; Ernsting, N. P.; Muller, U.; Weller, H. *Chem. Phys. Lett.* **1990**, *168*, 543.
8. (a) J. Z. Zhang, R. H. O'Neil, T. W. Roberti, J. L. McGowen, and J. L. Evans, *Chem. Phys. Lett.* (in press), 1994; (b) J. Z. Zhang, R. H. O'Neil, T. W. Roberti, *J. Chem. Phys.* (submitted), Nov. 1994.
9. Salin, F.; Squier, J.; Vaillancourt, G.; Mourou, G. *Optics Lett.* **1991**, *16*, 1964.
10. Huang, C.-P.; Asaki, M. T.; Backus, S.; Nathel, H.; Murnane, N. M.; Kapteyn, H. C. *Optics Lett.* **1992**, *17*, 1289.
11. Maine, P.; Strickland, D.; Bado, P.; Pessot, M.; Mourou, G. *IEEE. J. Quantum Electro.* 1988, *QE-24*, 398.
12. Long, F. H.; Lu, H.; Shi, X.; Eisenthal, K. B. *Chem. Phys. Lett.* **1991**, *185*, 47.

Femtosecond Time-Resolved Thermomodulation of Small Copper Particles in Glass

Arao Nakamura and Takashi Tokizaki

Department of Applied Physics, Nagoya University,
Chikusa-ku, Nagoya 464-01, Japan
TEL 81-52-781-5111 FAX 81-52-782-2129

In recent years, optical nonlinearity of small metal particles in dielectric has attracted much attention, because of the possibility of the high polarizability and the fast response [1,2]. Enhancement of the local field inside the particle at the surface plasmon resonance causes enhancement of a third-order nonlinear susceptibility $\chi^{(3)}$.

Our recent study has shown that copper particles provides the high susceptibility of the particles ($\chi_m^{(3)} \sim 3\times10^{-6}$ esu) compared to other noble metals because of the contribution from the d band transition [3]. If the relaxation process of nonequilibrium electrons is determined by the electron-phonon interaction as was proved for the thin films [4], the time response is expected to be a cooling time of hot electrons. However, a response time of small particles has not yet been measured in the femtosecond time region.

Femtosecond pump and probe experiments were performed for copper particles with a radius of 40 to 320 A in glass. The wavelength and duration of pumping pulses were 605 nm and 100 fs, respectively, and the pumping laser fluence was changed from 0.2 to 4.0 mJ/cm^2. From spectral and temporal behaviors of thermomodulation spectra we discuss nonlinear response times and cooling mechanisms of nonequilibrium electrons. Small metal particles in glass were prepared by means of a conventional melt and heat-treatment procedure using a $50BaO - 50P_2O_5$ mole percent glass system.

Figure 1(a) shows the linear absorption spectrum of copper particles with a radius of 40 A at 300 K. A surface plasmon peak is observed at 2.2 eV and a large shoulder is due to the transition from the d band. Shown in Fig.1(b) are differential absorption spectra for various delay times. The spectra exhibit a bleaching at the plasmon peak and the absorption increase emerges on the both sides of the peak, which suggests the broadening of the plasmon absorption band.

Figure 2 shows the time evolution of the bleaching signal measured at 2.2 eV

for various laser fluences. The decay behavior depends on the pumping laser fluence and the decay for the fluence of 0.21 mJ/cm ^{2} is $\sim$ 1 ps. This behavior is quite similar to results of the thermomodulation of thin copper films observed by Elsayed-Ali et al.[4]. We now examine the relaxation dynamics of the electron temperature by the usual electron-phonon coupling model. The time evolution of the electron and the lattice effective temperatures, T_e and T_l, respectively, is described by the coupled differential equations:

$$C_e(T_e)\frac{\partial T_e}{\partial t} = \kappa \Delta^2 T_e - G(T_e - T_l) + P(t)$$

$$C_l\frac{\partial T_l}{\partial t} = G(T_e - T_l)$$

where $C_e(T_e)$ is the temperature-dependent electronic heat capacity, C_l is the lattice heat capacity, κ is the thermal conductivity, G is the electron-phonon coupling constant, P(t) is the excitation energy density per unit time and unit volume in a particle.

In Fig. 3 we show the calculated results of the electron temperature as a function of the delay time for the pumping fluences of 0.21, 0.52, 2.1, 4.0 mJ/cm ^{2} used in the experiments. We used the values of C_e and C_l for the bulk Cu crystal and the value of G = 0.8x10 ^{17} W/m ^{3} K, which is slightly smaller than that for the thin film ($\sim$ 1x10 ^{17} W/m ^{3} K). The decay behavior depending on the pumping fluence can be well reproduced by this model.

In summary, the nonlinear time response of small Cu particles can be described by the same model for the hot electron relaxation as the thin films. This indicates that size effects on the electron-phonon interaction and the heat capacities are not noticed for the small particles with radii of more than 40 A.

References

[1] D. Ricard, P. Roussignol and C. Flytzanis, Opt. Lett. 10 (1985) 511.

[2] M. J. Bloemer, J. W. Haus and P. R. Ashley, J. Opt. Soc. Am. B 7 (1990) 790.

[3] K. Uchida et al., J. Opt. Soc. Am. B, in press.

[4] H. E. Elsayed-Ali, T. B. Norris, M. A. Pessot and G. A. Mourou, Phys. Rev. Lett. 58 (1987) 1212.

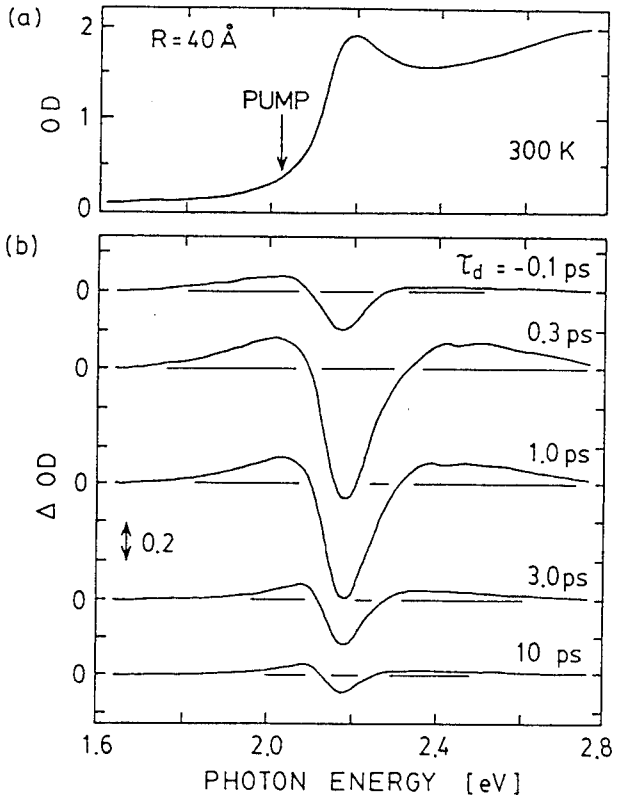


Fig. 1 (a) The linear absorption spectrum of copper particles with a radius of 40 A at 300 K, (b) the differential absorption spectra for various delay times with the pumping laser fluence of 4.0 mJ/cm ^{2} .

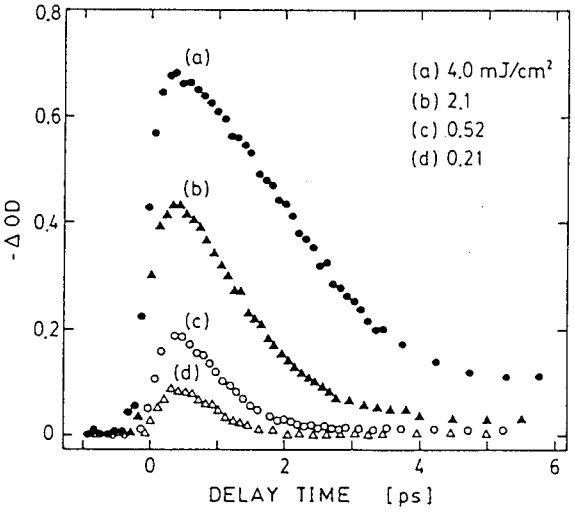


Fig. 2 The time evolution of the bleaching signal measured at 2.2 eV for various laser fluences.

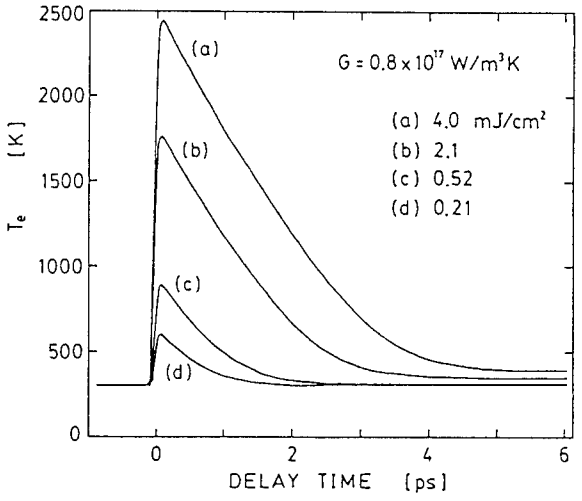


Fig. 3 The calculated results of the electron temperature as a function of the delay time for measured laser fluences.

Impulsive Stimulated Raman Scattering and Coherent Soft Phonons in $LaAlO_3$

Y. Liu, A. Frenkel*, J. F. Whitaker, R. Merlin and C. Uher

University of Michigan
Center for Ultrafast Optical Science
2200 Bonisteel Blvd., Room 1006
Ann Arbor, Michigan 48109-2099
Tel: 313-763-4875

* National Institute of Standards and Technology
Gaithersburg, MD 20899

INTRODUCTION

The generation of coherent phonons and molecular vibrations using pulsed lasers has recently attracted much attention [1-8]. Systems for which such coherent transient modes have been studied include molecular crystals and dyes [1], semiconductors [2], semimetals [3], high-T_c superconductors [4-5] and ferroelectrics [6-7]. As with other stimulated processes, phonon coherences result from nonlinear coupling between photons and the vibrational field. While in most cases the relevant mechanism has been ascribed to stimulated Raman scattering, this has not always been supported by a symmetry analysis of its properties. In addition, there is some controversy surrounding experiments performed under resonant excitation [5,8].

Here, we report on a pump-probe study of phonon coherences in $LaAlO_3$ and compare the results to those of spontaneous Raman scattering [9]. $LaAlO_3$ undergoes an antiferroelectric transition at $T_c \sim 800$ K characterized by the softening of a triply degenerate mode at the R-point which splits into two modes below T_c [10]. Our differential transmission data in the antiferroelectric phase reveal large oscillations associated with the two soft phonons. The dependence of the signal on both the pump and probe polarization and intensity support the identification of the nonlinearity as due to impulsive stimulated Raman scattering (ISRS).

SAMPLE AND EXPERIMENT

Above and below T_c, $LaAlO_3$ crystallizes in the cubic perovskite and rhombohedral (D_{3d}) lattices, respectively. The rhombohedral soft modes transform according to the A_{1g} and E_g representations of D_{3d} [9-10]. It is important to emphasize that the low-temperature structure is invariant under inversion. Accordingly, the Raman active modes are even, and unlike infrared-allowed phonons, they cannot directly couple to photons to yield polaritons.

Data were obtained from a single crystal of $LaAlO_3$ in the range T = 5-100 K. The sample dimensions are 0.5 x 10 x 10 mm^3 with the large surfaces normal to the pseudo-cubic [001] axis. The experiments were performed in the standard pump-probe transmission configuration using 75-fs pulses from a self-mode-locked Ti-sapphire laser at a repetition rate of 76 MHz; the pump and probe polarizations were perpendicular to [001]. Refractive index changes induced by the coherent phonons lead to a modulation of the intensity of the probe pulses, which were detected by a p-i-n diode and plotted versus the pump-probe delay time.

RESULTS

Figure 1(a) shows results at 20 K for various pump polarizations. The spectra exhibit an initial transient peak which is pulse-width limited followed by large oscillations. The initial response is not relevant to this work; it is tentatively attributed to third-order nonlinearities, specifically, to the so-called coherent artifact. The oscillations arise from the modulation of the refractive index by coherent phonons. The most pronounced oscillation, with a period of approximately 1 ps, is due to the soft E_g mode. For $\theta = 41^\circ$ and 51° (θ being the angle between the pump and probe polarization when the latter is along [010]), the traces exhibit beating between this mode and an oscillator with a period of 0.23 ps, which corresponds to the soft A_{1g} phonon. The Fourier transform of the $\theta = 41^\circ$ data is depicted in Fig.1(b). The frequencies of the A_{1g} and E_g modes at 20 K are found to be, respectively, 4.33 and 1.09 THz. This should be compared with conventional Raman results giving 4.30 and 1.18 THz [9].

Figure 2 shows the dependence of the amplitude of the oscillation on the pump polarization angle, for the probe beam polarized along [010]. The 2-θ angular dependence is consistent with Raman selection rules for E_g -symmetry [11]. In general, the ISRS signal can be represented by products involving the pump and probe fields and associated Raman tensors which are derived solely from symmetry considerations [11]. The dashed line in Fig. 2 is a fit to the data using these expressions [11]. From fits such as this, the ratio between Raman tensor components for both E_g and A_{1g} scattering can be uniquely determined.

Our temperature-dependent studies of the coherent phonons show a pronounced softening with increasing temperature concomitant with a strong decrease of the dephasing time. This behavior is consistent with that found in spontaneous Raman experiments [9]. Comparison between the latter and ISRS results will be discussed in the context of the antiferrodistortive phase transition of $LaAlO_3$.

CONCLUSIONS

In summary, we have observed coherent phonons in $LaAlO_3$ and studied their dependence on temperature in the rhombohedral phase. By analyzing its symmetry properties, we have conclusively shown that the mechanism at work is ISRS.

We wish to thank S. Y. Hou and J. M. Phillips for providing $LaAlO_3$ samples. This work was supported by the National Science Foundation through the Center for Ultrafast Optical Science under STC PHY 8920108.

REFERENCES

[1] S. DeSilvestri, J. G. Fujimoto, E. B. Gamble, L. R .Williams and K. A. Nelson, *Chem. Phys. Lett.* 116, 146 (1985).
[2] G. C. Cho, W. Kütt, and H. Kurz, *Phys. Rev. Lett.* 65, 764 (1990).
[3] T. K. Cheng, S. D. Brorson, A. S. Kazeroonian, J. S. Moodera, G. Dresselhaus, M. Dresselhaus, and E. P. Ippen, *Appl. Phys.Lett.* 57, 1004 (1990).
[4] J. M. Chwalek, C. Uher, J. F. Whitaker, and G. A. Mourou, *Appl. Phys.Lett.* 58, 980 (1991).
[5] W. A. Kütt, W. Albrecht, and H. Kurz, *IEEE J. Quantum Electron.* 28, 2434 (1992).
[6] H. J. Bakker, S. Hunsche, and H. Kurtz, *Phys. Rev. Lett.* 69, 2823 (1992).
[7] T. P. Dougherty, G. P. Wiederrecht, and K. A. Nelson, *J. Opt. Soc. Am. B* 9, 2179 (1992).
[8] T. K. Cheng, S. Vidal, M. J. Zeiger, G. Dresselhaus, M. S. Dresselhaus, and E. P. Ippen, *Appl. Phys. Lett.* 59, 1923 (1991).
[9] J. F. Scott, *Phys. Rev.* 183, 823 (1969).
[10] See, *e.g.*, J. D. Axe, G. Shirane, and K. A. Müller, *Phys. Rev.* 183, 820 (1969); J. K. Kjems, G. Shirane, K. A. Müller, and H. J. Scheel, *Phys. Rev. B* 8, 1119 (1973).
[11] Y. Liu, A. Frenkel, J. F. Whitaker, R. Merlin, and C. Uher, unpublished.

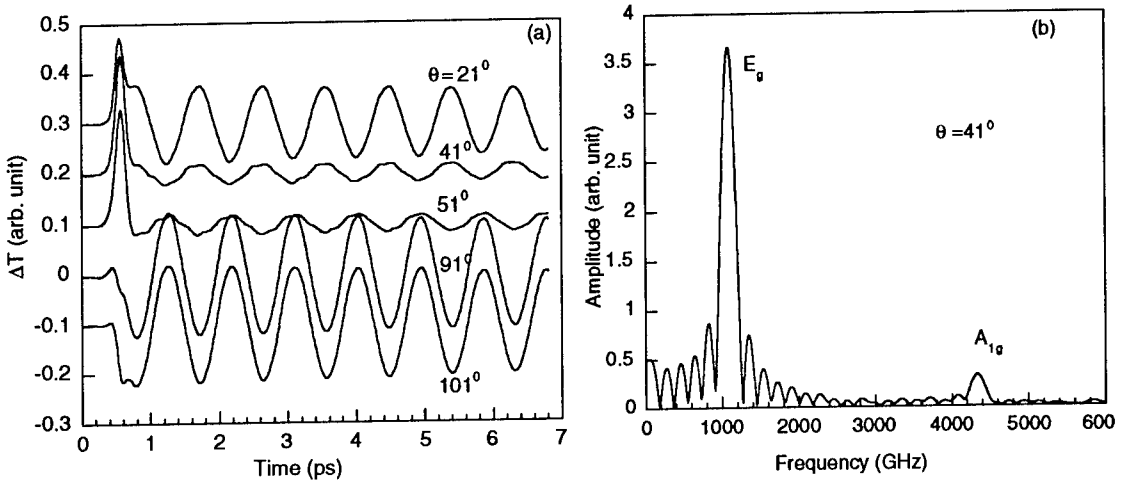


Fig.1 (a) Time-resolved differential transmission at T = 20 K. θ is the angle between the pump and the (fixed) probe polarization, the latter is parallel to [010].
(b) Fourier transform showing E_g and A_{1g} peaks.

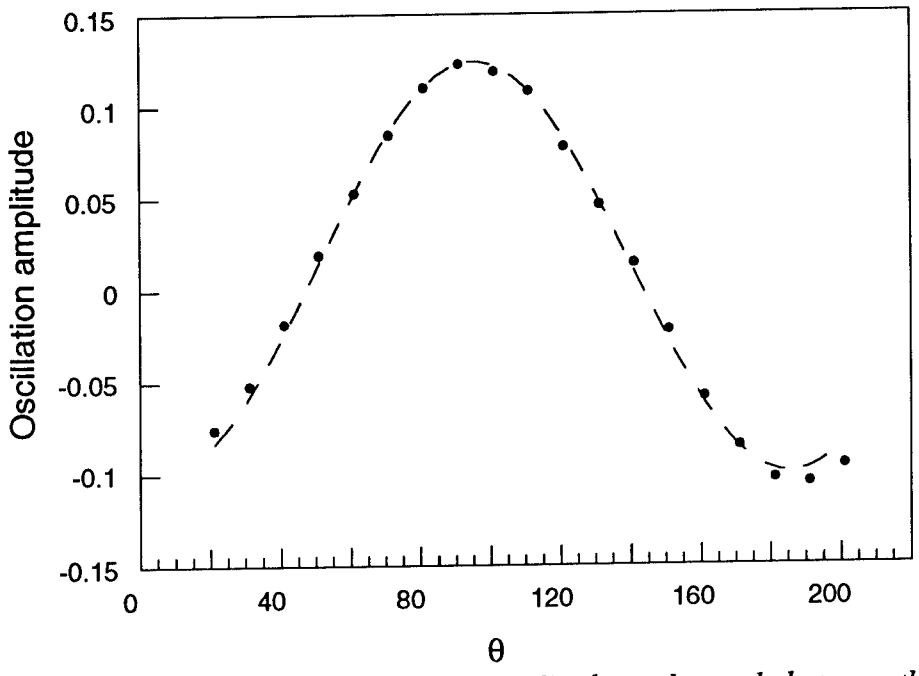


Fig. 2. The dependence of the E_g oscillation amplitude on the angle between the pump polarization and the [010] axis; the probe is along [010]. The dashed line is a two-parameter theoretical fit to the data [11].

Locally ordered structures in molecular liquids revealed with femtosecond Fourier-transform Raman spectroscopy

William T. Lotshaw and P. Randall Staver
G.E. Research, Rm. KWC 627, 1 River Road, Schenectady, NY 12309 (518) 387-5163
Dale McMorrow and Joseph S. Melinger
Naval Research Laboratory, Code 6613, Washington, D.C. 20375 (202) 767-3939

The issue of local order in molecular liquids, and the influence of such order on molecular dynamics and dielectric relaxations in liquids and solutions, is a topic of substantial importance to theoretical representations of the liquid state and interpretations of solvent effects in solute relaxations and chemical reactivity in solutions. In this report we present the results of new studies of intermolecular interactions and dynamics in the liquid state, which interrogate the intermolecular vibrational modes of the local structure of liquids at constant temperature and pressure. Previously [1] we have utilized time and frequency domain analyses of the optical heterodyne detected optical Kerr effect (OHD OKE) to examine the complicated vibrational and Brownian motions of molecules in pure liquids, and identified the intermolecular origin of the low-frequency Raman band in organic liquids (which is typically centered between 10 and 100 cm^{-1}). These bands have been attributed to Raman-active restricted orientational motions, or librations, in non-associated molecular liquids, and exhibit widths in the range of 20 to 100 cm^{-1}.

In this paper we address the question of local order in molecular liquids by investigating the intermolecular dynamics and spectra of a series of dilutions of benzene in carbon tetrachloride (CCl_4) and methylcyclohexane. Benzene is a simple, non-hydrogen-bonding aromatic liquid, and may be considered representative of this class of liquids. Previous work [2] revealed a distinct bimodal structure in the non-diffusive part of the intermolecular Raman spectrum (fig. 3, *vide infra*). Based on symmetry considerations, it was suggested [2] that the low-frequency portion of this bimodal spectrum might be associated with locally ordered structures (dimers or other aggregates) in the bulk liquid. The results of the current study support this interpretation, and provide direct evidence for locally-ordered structures in aromatic liquids.

Experiments were performed using a synchronously pumped continuously tunable Ti:Sapphire laser that generates $\leq$40 fs pulses at average powers $\geq$0.5 W. OHD OKE transients were measured as described elsewhere [1], except that the pure heterodyne signals were isolated for the data analysis [3]. OHD serves to linearize the detected signal in both the pump and probe pulse intensities, permitting application of powerful discrete Fourier-transform (FT) data analysis procedures [1].

Figure 1 (*left*) shows the OHD OKE transient measured for 9.1% benzene in CCl_4. The purely electronic hyperpolarizability dominates the response near $\tau = 0$, with significant contributions from both benzene and CCl_4 present at positive delays. The prominent oscillations are due to the *intra*molecular vibrational Raman modes of CCl_4 at 217 and 314 cm^{-1}. Analysis of this very complex transient is facilitated by the use of Fourier transform methods, which are described in detail elsewhere [1]. The frequency response function of the OKE transient of fig. 1, deconvoluted from effects of the finite-duration excitation and probing pulses, is shown in the right panel of fig. 1. The intramolecular Raman modes noted above, and a broad low-frequency band that is associated with the *inter*molecular dynamics of the liquid are evident.

The data of fig. 1 contain several overlapping contributions that must be separated before a detailed interpretion of the intermolecular dynamics is possible. Since we are interested in the intermolecular vibrational part of the response, the Brownian relaxations due to diffusive reorientation are removed using a tail-matching procedure that has been discussed previously [1]. For the 9.1% benzene solution contributions from both solvents can be significant. A reason for choosing CCl_4 as a solvent is the presence of strong *intra*molecular resonances that serve as an internal standard for removing the

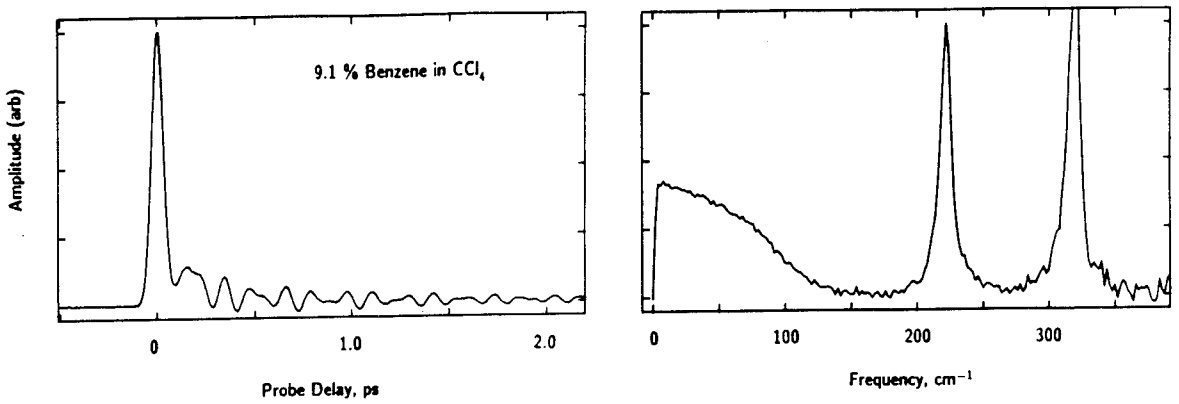


Figure 1. (*upper*) Femtosecond OHD OKE transient measured for a 9.1% solution of benzene in carbon tetrachloride; (*lower*) spectral density representation of the transient data.

CCl_4 contribution from the intermolecular part of the spectrum ($\Delta\omega$ <165 cm^{-1}). This operation relies on the principle of linear superposition in the response function and requires the assumption that the intermolecular vibrational spectrum of CCl_4 is not changed significantly in the 9.1% benzene solution. This assumption is reasonable, and is supported by the unaltered lineshape of the intramolecular resonances on dilution (*cf.*, fig. 2).

The dashed curve of fig. 3 shows the vibrational Raman part of the benzene OHD OKE deduced from the FT analysis. The shape of this spectrum is the focus of this study. Previously we had attributed this lineshape to a bimodal vibrational response in which, based on the symmetry of the isolated molecule, the low frequency part was attributed to dimers or higher aggregates, and the high-frequency part was attributed to nonaggregated molecules. Dilution of benzene is expected to reduce the number density of any aggregate structures, resulting in a decrease in the low-frequency amplitude of the vibrational spectrum. The solid curve of fig. 3 shows the vibrational Raman part of the 9.1% benzene/CCl_4 solution with the CCl_4 contribution subtracted off as described in the previous paragraph (this procedure is illustrated in fig. 2). The decrease in low-frequency amplitude of the lower spectrum supports the dimer/ aggregate interpretation of the neat benzene spectrum.

Figure 4 shows the time domain representation of the spectra in fig. 3. The short time portions (<250 fs) of the two transients are very nearly identical, suggesting that the librational degrees of freedom for benzene are not significantly altered in the predominately CCl_4 environment. Significant deviations occur, however, for delays greater than 250 fs, with the longer time contributions significantly diminished in the 9.1% solution. These longer-time relaxations, which exhibit a 1/e time constant of 450 fs in neat benzene [2], can be identified with the dynamics of dimer/aggregate structures.

The changes we observe in the intermolecular Raman spectrum of benzene occur at frequencies less than ~50 cm^{-1}, and are nearly impossible to address by spontaneous light scattering due to elastic scattering and background problems. The femtosecond OHD OKE methods are ideally suited to the analyses presented here because the attributes of: *i*) background supression and phase sensitive signal detection permit isolation of the spectroscopic signal of interest; *ii*) high sensitivity and signal-to-noise ratio result in the precise characterization of the picosecond Brownian dynamics; and *iii*) a wide dynamic range and order reduction in the nonlinear response function permit a highly accurate discreet FT analysis of the more complicated elements in the measured transients. In addition to the data presented here, a complete dilution series has been performed for methylcyclohexane solvent. Temperature-dependent measurements are in progress, and will be reported at the conference.

1. D. McMorrow and W.T. Lotshaw, Chem. Phys. Lett. 174, 85 (1990); J. Phys. Chem. 95, 2028 (1991).
2. D. McMorrow and W.T. Lotshaw, Chem. Phys. Lett. 201, 369 (1993).
3. T.R. Dickson, PhD Thesis, University of Toronto, 1991.

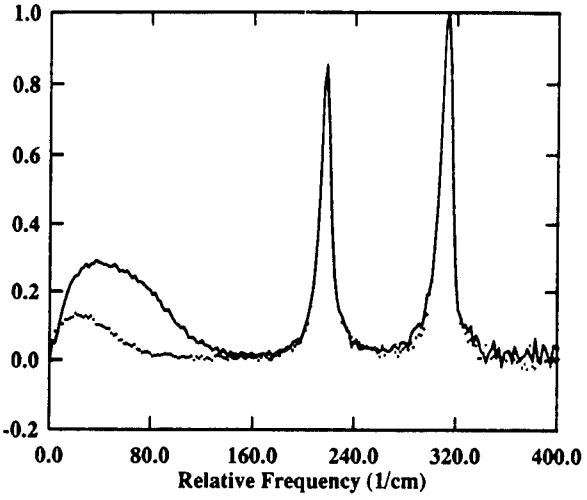


Figure 2. (*solid*) Vibrational part of the intermolecular Raman spectrum for the 9.1% benzene /CCl_4 solution, together with (*dotted*) the spectrum measured for neat CCl_4. This figure illustrates the relative contribution of CCl_4 to the vibrational response of the solution. The two curves in this figure are subtracted to obtain the spectrum of fig. 3.

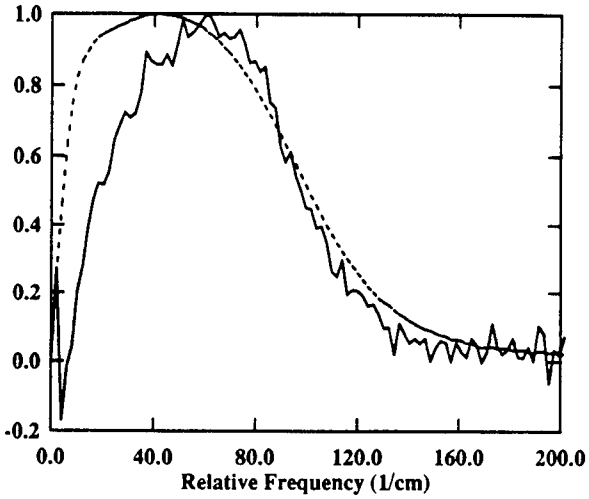


Figure 3. Vibrational part of the intermolecular Raman spectra for neat benzene (*dashed*) and the benzene contribution to the 9.1% solution of benzene in carbon tetrachloride (*solid*) illustrating the rather significant spectral evolution that occurs on dilution.

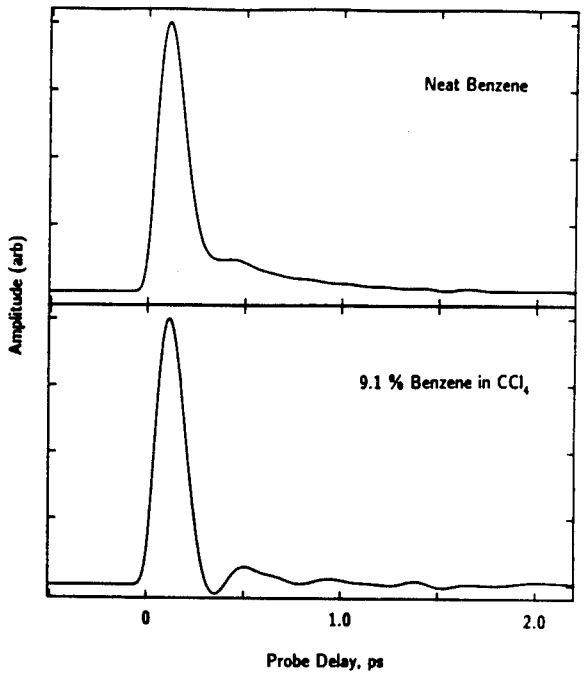


Figure 4. Vibrational part of the intermolecular OHD OKE transient for neat benzene and the 9.1% solution of benzene in carbon tetrachloride.

Contributions of Bound and Unbound Two-Exciton States to the Nonlinear Optical Response of GaAs Quantum Wells

J. Kuhl, E.J. Mayer, and G.O. Smith
Max-Planck-Institut für Festkörperforschung,
Heisenbergstr. 1, D-70569 Stuttgart, Germany
Phone: (49) 711 689 1633, FAX: (49) 711 689 1010

D. Bennhardt, T. Meier, A. Schulze, and P. Thomas
Department of Physics, Philipps University
Renthof 5, D-35032 Marburg, Germany

R. Hey and K. Ploog
Paul-Drude-Institut für Festkörperelektronik
D-10117 Berlin, Germany

The strong influence of exciton/exciton interaction on the nonlinear optical response of the 2D exciton in GaAs quantum wells has been demonstrated in several recent experimental studies. The theoretical model for the microscopic coupling mechanism is still the subject of controversy, however. In ref. [1], we have presented a model including a density dependent coupling between opposite spin excitons which assumes that the interaction results in a renormalization of the matrix elements, dephasing rates and energies of the transition from the single-exciton state to the two-exciton state with respect to the corresponding quantities for the single exciton transitions. In contrast, Wang et al. claim that all experimental observations are explained by a density induced dephasing rate and that biexciton states play no role [2]. Here we present a new 3-pulse degenerate-four-wave-mixing (DFWM) configuration which is able to differentiate between pure local field effects and biexcitonic contributions to the time-integrated signal. Experiments were performed on an almost homogeneously broadened GaAs/$Al_{0.3}Ga_{0.7}As$ single QW (well width 20 nm, photoluminescence line 0.3 meV, homogenous linewidth 0.15 meV) in the backward reflection geometry. The sample was cooled to 10 K and excited by a sequence of three pulses (1.1 ps duration) with equal intensity, wave vectors

$\vec{k}_1, \vec{k}_2, \vec{k}_3$ and delays τ_{12} and τ_{13} between the second and first and the third and first pulse, respectively. The signal was monitored in the direction $\vec{k}_s = \vec{k}_1 + \vec{k}_2 - \vec{k}_3$ which provides no signal for the chosen pulse length if local field and renormalization effects are negligible. The peak intensity of the time-integrated DFWM signal has been calculated by solving the optical Bloch equations for a system of two non-interacting two-level systems (2LS) with opposite circular polarization selection rules (local field effect) and for the renormalized four-level system (4LS) depicted in Fig. 1 which assumes the formation of biexcitons between excitons with opposite spins. The signal strength is proportional to the strength of the local field in the case of the 2LS and to the renormalization for the 4LS. The peak signal intensities expected for pure local field and pure biexction contributions are summarized in the second and third column of Table 1 for eight experimental configurations applying different linear and circularly polarized pulses. The values are normalized to the signal strength predicted for three parallel linearly polarized pulses. Close inspection of the data reveals remarkable differences of the peak amplitude with polarization geometry for the two coupling models.

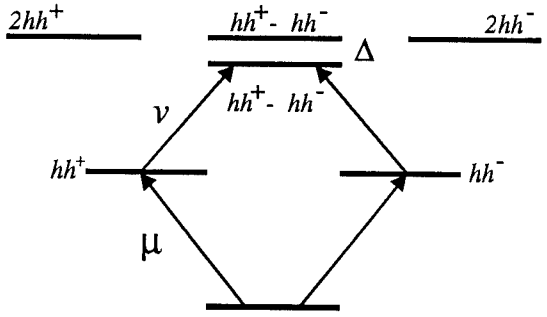


Fig. 1 The renormalized four-level-system including bound and unbound two-exciton states where Δ is the binding energy of the biexciton.

Polar.	Local Field	Bi-exciton	Exp.
∥ ∥ ∥	1	1	2.3
⊥ ∥ ∥	1	0	0.5
∥ ⊥ ∥	1	0	-
∥ ∥ ⊥	1	1	2.3
$\sigma^+\sigma^+\sigma^+$	4	0	1.1
$\sigma^-\sigma^+\sigma^+$	0	1	1.7
$\sigma^+\sigma^-\sigma^+$	0	1	1.5
$\sigma^+\sigma^+\sigma^-$	0	0	0.04

Table 1 Calculated DFWM signal strength for the case of local field and biexciton mechanisms and the measured peak signal intensities for various polarizations.

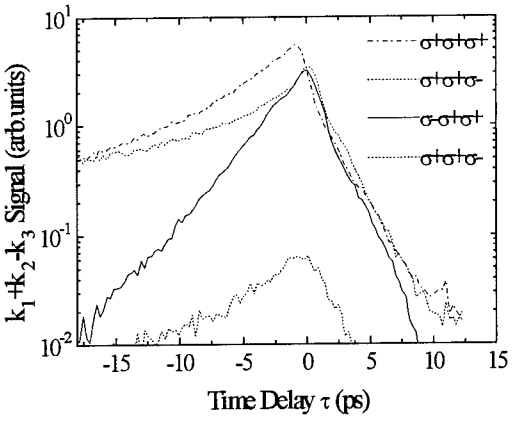


Fig. 2a DFWM signal versus the delay time τ for various circular polarizations.

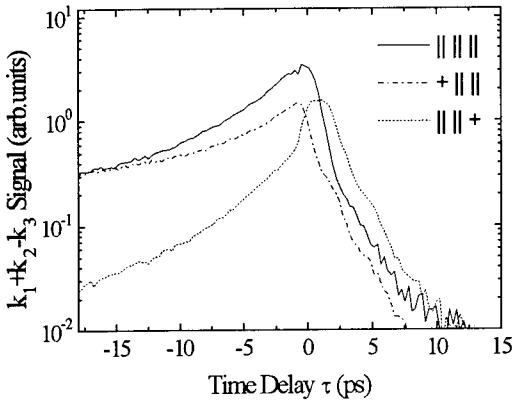


Fig. 2b DFWM signal versus the delay time τ for various linear polarizations.

Fig. 2a and 2b show the time-integrated intensity measured for $\tau = \tau_{12}$ and $\tau_{13} = \tau_{12} + 1.3$ ps for seven combinations of linearly or circularly polarized pulses. In order to eliminate artificial coherent coupling effects between the interacting optical fields appearing during pulse overlap, we have chosen $\tau_{13} = \tau_{12} + 1.3$ ps and have taken the intensity observed for a delay of $\tau = 1.3$ ps. Comparison of the experimental data which are summarized in the fourth column of Table 1 proves that neither pure local field effects nor biexcitons alone provide a satisfying agreement between experiment and theoretical predictions. Thus we have to conclude that both bound and unbound two-exciton states contribute to the nonlinear optical response of the 2D exciton.

[1] K. Bott, O. Heller, D. Bennhardt, S.T. Cundiff, P. Thomas, E.J. Mayer, G.O. Smith, R. Eccleston, and J. Kuhl, Phys. Rev. B **48**, 15 Dec.(1993).

[2] H. Wang, K. Ferrio, D.G. Steel, Y.Z. Hu, R. Binder, and S.W. Koch, Phys. Rev. Lett. 71, 1261(1993).

Femtosecond Coherent Spectroscopy of Excitonic and Free Carrier Polarizations in Bulk GaAs

T. Elsaesser[1,2], A. Leitenstorfer[2], A. Lohner[2], P. Leisching[2], T. Kuhn[3], F. Rossi[4], and W. Stolz[4]

[1] *Max-Born-Institut für Nichtlineare Optik und Kurzzeitspektroskopie, Rudower Chaussee 6, D-12489 Berlin, Germany*
[2] *Physik Department E 11, Technische Universität München, D-85748 Garching, Germany*
[3] *Institut für Theoretische Physik, Universität Stuttgart, D-70550 Stuttgart 80, Germany*
[4] *Fachbereich Physik, Universität Marburg, D-35032 Marburg, Germany*

Femtosecond spectroscopy of coherent optical polarizations gives insight into the dynamics and the coupling of elementary excitations in semiconductors. In this paper, we present spectrally and temporally resolved four-wave-mixing (FWM) studies of undoped and p-doped bulk GaAs, providing new information on the nonlinear polarization close to the bandgap. The experimental results are analyzed by theoretical calculations based on the optical Bloch equations for the FWM geometry including Monte Carlo simulations of the carrier dynamics.

In our experiments, 0.5 μm thick layers of undoped and p-doped GaAs (doping concentration 10^{18} cm^{-3}) clad by AlGaAs barriers are studied in a degenerate FWM geometry using 100 fs pulses from a mode-locked Ti:sapphire laser. The spectrum and the temporal characteristics of the FWM signals diffracted from the transient grating are measured with the help of a frequency-selective detection system and parametric up-conversion in a nonlinear crystal, respectively.

In undoped GaAs, excitonic and free-carrier components both occurring within the bandwidth of the laser pulses are distinguished for the first time [1]. In Figs. 1 (a,b), the spectrally resolved FWM signals are plotted for different excitation densities and time delays T_{12} between the two pulses generating the transient grating. The excitonic part dominates at carrier densities below 10^{16} cm^{-3} and follows a picosecond kinetics governed by many-body effects. The excitonic contribution persists up to an excitation density of 6×10^{16} cm^{-3} which is much higher than the equilibrium Mott density of excitons of several 10^{15} cm^{-3}. At carrier densities above 10^{16} cm^{-3}, non-thermalized free carriers give rise to an additional polarization with a spectrum resonant to the laser pulse. With increasing T_{12}, the spectrum of this contribution shifts towards smaller photon energies while the excitonic enhancement disappears (Fig. 1 b). The free-carrier component shows a femtosecond photon-echo like time behavior [1].

The nonlinear response at the bandgap of the p-type material is governed by excitons which are bound to impurities and - consequently - show a slower dephasing kinetics than free excitons. In the time resolved FWM signal plotted in Fig. 2, a prompt component due to phase space filling and a second delayed contribution related to exciton-exciton interaction [2,3] are clearly distinguished.

The two components of nonlinear polarization and their change with carrier density are quantitatively reproduced by the theoretical calculations. The MC simulations give insight into the momentary carrier distributions and show that the photoexcited carriers

thermalize on a time scale of 200 fs to Fermi distributions with different electron and hole temperature. The broad carrier distributions result in a reduced screening of the attractive electron-hole interaction and - consequently - in an elevated Mott density of excitons. For increasing T_{12}, the diffracted intensity due to many-body effects in the carrier system is reduced, leading to a decrease of the excitonic component of the FWM signal.

[1] A. Lohner, K. Rick, P. Leisching, A. Leitenstorfer, T. Elsaesser, T. Kuhn, F. Rossi, and W. Stolz, Phys. Rev. Lett. **71**, 77 (1993)

[2] S. Weiss, M.-A. Mycek, J.-Y. Bigot, S. Schmitt-Rink, and D.S. Chemla, Phys. Rev. Lett. **69**, 2685 (1992)

[3] D.S. Kim, J. Shah, T.C. Damen, W. Schäfer, F. Jahnke, S. Schmitt-Rink, and K. Köhler, Phys. Rev. Lett. **69**, 2725 (1992)

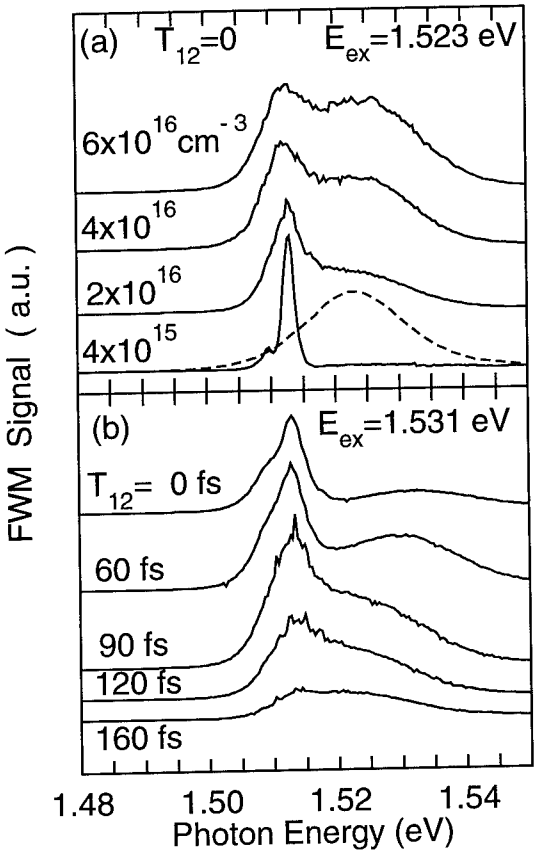


Fig. 1 *Spectrally dispersed FWM signals from undoped GaAs.*
(a) Spectral profiles found for zero delay (T_{12}=0) between the two pulses generating the transient grating in the sample (dashed line : spectrum of the 100 fs pulses centered at E_{ex} = 1.523 eV).
(b) Spectrally resolved FWM signals for different delay times T_{12} (E_{ex}=1.531 eV, excitation density 1.5×10^{16} cm^{-3}).

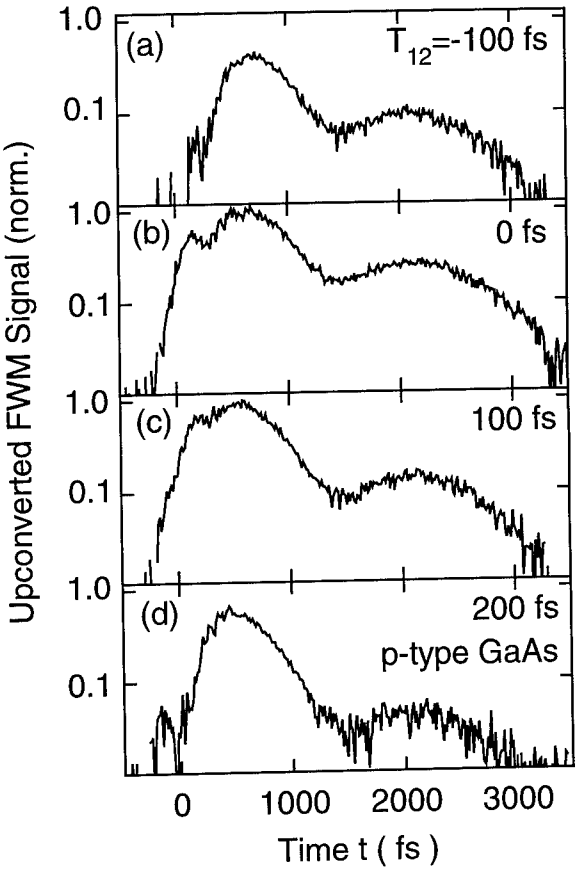


Fig. 2 *Temporal profiles of the FWM signal from p-type GaAs. The diffracted intensity is plotted as a function of the delay time t between the second pulse forming the grating and the (third) up-conversion pulse. Data are shown for different delays T_{12} (excitation density 6×10^{15} cm^{-3}).*

Femtosecond Studies of Charge Separation in the Fluorescent State of DCM

H. Zhang, A.M. Jonkman, P. van der Meulen, and M. Glasbeek
Laboratory for Physical Chemistry, University of Amsterdam,
Nieuwe Achtergracht 127, 1018 WS Amsterdam, The Netherlands
Phone: (31) 20 5256996; Fax: (31) 20 5255698

Solvation dynamics has long been recognized to be of great importance for the understanding of the rate of intramolecular electron transfer (ET) reactions[1,2]. Especially when the ET reaction takes place in the so-called strong adiabatic coupling limit, solvation dynamics may predominantly determine the ET rate constant. Under such conditions one has $\kappa \gg 1$, where the adiabaticity parameter[3], κ, is given by $\kappa = \pi V^2 \langle\tau\rangle / \hbar\lambda_m$, in which V is the electronic coupling between the locally excited (LE) and charge transfer (CT) states involved in the electron transfer process, $\langle\tau\rangle$ is the solvent relaxation time and λ_m is the solvent reorganization energy. Recently, for a number of molecules solvent controlled ET in the photo-excited state has been considered in the strong adiabatic coupling regime[4]. In this report, we present results of a femtosecond pump-probe study of the charge separation reaction in the photo-excited state of a large laser dye molecule, 4-(dicyanomethylene)-2-methyl-6-(*p*-dimethylaminostyryl)-4-H-pyran (DCM). We have performed a subpicosecond study of the solvatochromism of the DCM molecule. A major finding is that following the pulsed excitation of the molecule, the integrated intensity of the spontaneous fluorescence exhibits a transient decay to approximately 50% of its initial value in a few picoseconds. The results are consistent with strongly mixed LE and the CT excited states for DCM (i.e., the adiabatic coupling limit applies) so that the solvation dynamics constitutes the rate determining step in the ET process.

In our experiments we have applied the fluorescent up-conversion technique. Pulses from a femtosecond Tsunami Ti:sapphire laser (80 MHz) were led through a BBO frequency doubling crystal to produce pulses in the wavelength region 360-440 nm. Typically, pulses with a duration of about 80 fs and an energy of about 1 nJ/pulse were used for photoexcitation of DCM, dissolved in methanol ($\sim 10^{-4}$ M). The emission of the sample at ambient temperature was focused onto a 0.5 mm thick BBO crystal, together with the gating beam, i.e., the fundamental ($\lambda \sim$ 800 nm, $\sim$150 mW) from the Ti:sapphire laser. The sum frequency signal of the fluorescence and the gating laser beam was focused on the entrance slit of a monochromator. Photodetection was by means of a photomultiplier connected to a photon-counting system. The gating pulses were scanned in steps using a variable delay line (minimum step-length $\sim$ 0.7 fs). The time resolution in our experiment is approximately 150 fs.

Fig. 1 shows fluorescent decays observed for DCM dissolved in methanol at a few detection wavelengths. After deconvolution of the experimental decay signals using the instrumental response function also presented in Fig.1, the signal intensity, $I(\lambda,t)$, could in all cases be fitted to a sum function of three exponential functions. The three characteristic time constants were found to be near 300 fs (typical of the initial fluorescent intensity increase following the laser pulse), 3 ps (related to the solvation process) and 1300 ps (which corresponds to the population decay time of the emissive state of DCM), respectively. In reconstructing the time-resolved spectra we followed the procedure outlined in Ref. 5. All of the time-resolved spectra were fitted to a log-normal shape function[5], the time-dependence of which characterizes the (sub)picosecond photodynamics of the system. In Fig. 2 we plot the time-dependent Stokes shift C(t), where $C(t)=(\nu(t)-\nu(0))/(\nu(\infty)-\nu(0))$ and $\nu(t)$ corresponds to the frequency of the maximum of the fluorescence band, of DCM

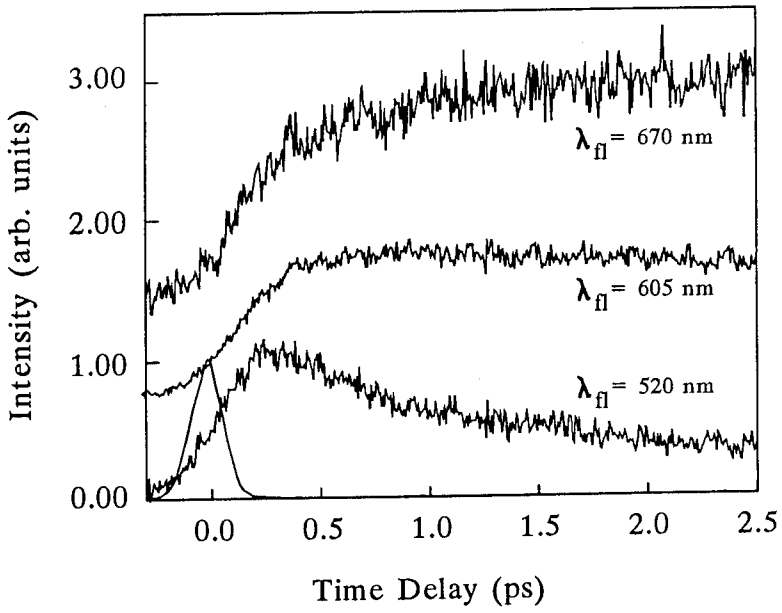


Fig.1 Normalized fluorescence decays of DCM in methanol observed at 320, 350, and 370 nm, corresponding to fluorescence emitted at 520, 605 and 670 nm, respectively. The instrument response function is also shown.

in methanol. The data points of C(t) fit a biexponential function with decay time constants of 1 ps and 10 ps (in a intensity ratio of 7:3), respectively. These time constants appear to be equal to the solvent relaxation times for methanol[6]. It is concluded that the time dependence of the Stokes shift for DCM in methanol is fully determined by the solvation dynamics.

Interesting new results were obtained when examining the integrated intensity of the spontaneous fluorescence spectra of DCM in methanol as a function of time. Fig. 2 also presents the evolution with time of the integrated fluorescence intensity of DCM in

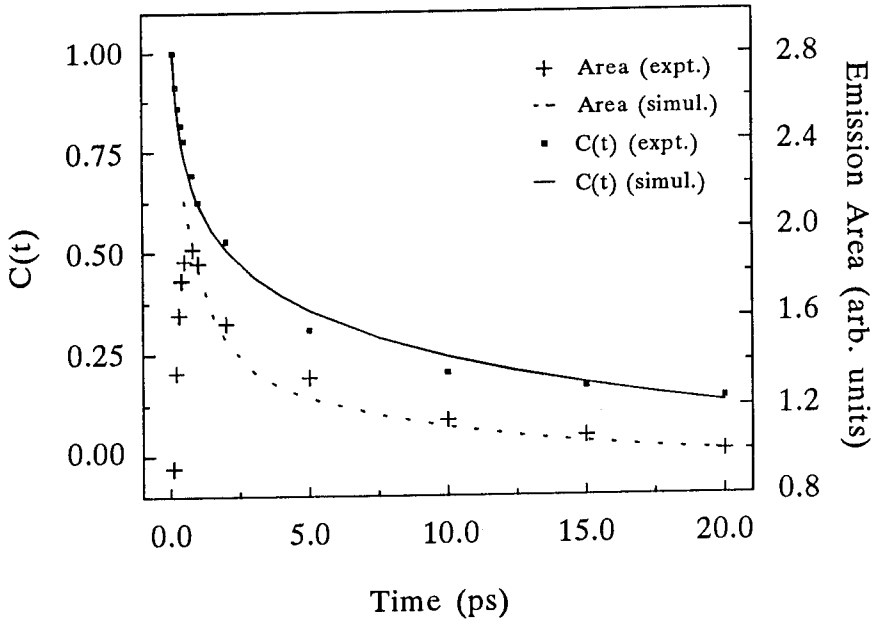


Fig.2 Experimental and computer simulated time-dependent Stokes shift, C(t), and integrated fluorescence intensity, I(t), of DCM in methanol.

methanol. Firstly, it is noted that the initial rapid increase of the fluorescence occurs with a time constant of about 300 fs. We consider this time as characteristic of an intramolecu lar vibrational relaxation process which takes place immediately after the pulsed optical excitation of the molecule and which leads to the population of the vibrationless lowest excited state of DCM. Secondly, *the integrated intensity shows a rapid decrease to about 50 % of its maximum value on the (picosecond) time scale of the solvation process.* Recently, time-resolved Stokes shift measurements of DCM in a few alcoholic solvents have also been studied using stimulated emission as a probe[8]. However, in the latter work the integrated intensity was not considered explicitly. As is well-known, the radiative decay rate of an emissive state changes as ν^3, and since solvation gives rise to a decrease of $\nu(t)$ of the emissive state, one expects that the integrated intensity of the emission from CT will decrease as well. However, it is readily verified that on this basis the picosecond integrated intensity decay component of Fig. 2 should be less than 20%.

We believe that the temporal behavior of the integrated intensity is relevant for understanding the time-dependence of the charge separation process itself. As has been discussed in a few recent papers[4,7], in the limit of strong adiabatic coupling of the LE and CT states solvation will appreciably affect the electronic structure, and concomitantly, the radiative character of the excited state will also be changed as time progresses. In an attempt to quantitatively simulate the dynamical effects of solvation, we have followed the computational procedure outlined in Refs.4 and 7 for the calculation of the time evolution of the emission spectrum. Assuming linear coupling of the electronic states with the surrounding dielectric medium with λ_m =1000 cm^{-1}, V =750 cm^{-1}, a ratio of the electronic transition dipole moments of the LE and CT states of approximately 3, and numerically solving the generalized Smoluchowsky equation for the excited state population density distribution $\rho(t)$, we simulate time dependences for the function, C(t), and the integrated intensity for the spontaneous emission, as represented by the plotted curves in Fig.2. From the satisfactory agreement between the simulated and the experimental results, it is concluded that *the intramolecular ET process for DCM in polar solvents is appropriately discussed within the strong adiabatic coupling model in the inverted regime.* It also follows that the solvation dynamics provides the rate determining step in the charge transfer process.

References

1. R.A. Marcus and N. Sutin, Biochim.Bioph.Acta **811**, 265 (1985).
2. J.Ulstrup, *Charge Transfer Processes in Condensed Media*, Springer-Verlag, Berlin, 1979.
3. I. Rips and J.Jortner, J.Chem.Phys., **87**, 6513 (1987).
4. K. Tominaga, G.C. Walker, W. Jarzeba, and P.F. Barbara, J.Phys.Chem., **95**, 1075 (1991); T.J. Kang, W. Jarzeba, and P.F. Barbara, Chem.Phys., **19**, 81 (1990).
5. M. Maroncelli and G.R. Fleming, J.Chem.Phys., **86**, 6221 (1987).
6. W. Jarzeba, G.C. Walker, A.E. Johnson, and P.F. Barbara, Chem.Phys., **152**, 57 (1991).
7. K. Tominaga, G.C. Walker, T.J. Kang, P.F. Barbara, and T. Fonseca, J.Phys.Chem., **95**, 1085 (1991).
8. D.C. Easter and A.P. Baronavski, Chem.Phys.Letters **201**, 153 (1993).

Operation Parameters of Antiresonant Fabry-Perot Saturable Absorbers for Passively Mode-Locked Solid-State Lasers

L. R. Brovelli and U. Keller
Swiss Federal Institute of Technology, Institute of Quantum Electronics
ETH Hönggerberg HPT, CH-8093 Zurich, Switzerland
Telephone: ++41-1-633 27 36
T. H. Chiu
AT&T Bell Laboratories, Holmdel, NJ 07733, U.S.A.

The semiconductor A-FPSA (antiresonant Fabry-Perot saturable absorber) (Fig. 1) has passively mode-locked successfully many different solid-state lasers such as Nd-YLF [1, 2], Nd:YAG [2], Nd:fiber [3] and Nd:glass [4, 5] lasers with ps- to sub-100-fs pulses. So far, the A-FPSA is the only intracavity saturable absorber in an all-solid-state ultrafast laser technology for which the modelocking is always self-starting and stable against Q-switching. The main reason is that the operation parameters, such as saturation intensity, losses, and impulse response of the A-FPSA can be custom designed and adapted to the requirements of solid-state lasers. Knowledge of these parameters therefore is of central importance for the optimization of the mode-locking performance.

We discuss the operation parameters of the A-FPSA, based on detailed measurements on the low-temperature grown InGaAs/GaAs material (Fig. 1), and discuss their influence on mode-locking. The dominant mechanism in the A-FPSA is the nonlinear reflectivity change due to bandfilling. Nonlinear phase shifts due to free carriers, Kerr-effect etc. do not result in any significant change in reflectivity of the A-FPSA because the Fabry-Perot is operated at antiresonance. However, these phase effects form a lens and can lead to self-focusing of the cavity mode in the gain medium which results in higher gain. As we will discuss, these effects are typically much smaller than the amplitude effects.

For use in a passively mode-locked solid state laser, the most important parameters are the recovery time and the effective saturation energy. To reach saturation intensities inside the absorber we performed all the measurements on AR-coated samples grown at different temperatures (Fig. 2a). The impulse response has been determined with a standard noncollinear pump-probe experiment, with perpendicular polarization of pump and probe, using 120-fs-pulses from a Ti-Sapphire laser (Fig. 2b). The first, fast decay with a time constant in the order of 200 fs is due to intraband thermalization, and the subsequent slower time constant (Fig. 3a) is associated with carrier recombination.

Picosecond and mode-locking build-up regime:

In this regime, only the slower part of the impulse response of the samples is significant. The saturation fluence $E_{sat} = h\nu/\sigma$ and the non-saturable background losses $\Delta R_{ns} \equiv 1 - R(E \to \infty)$ (Fig. 3c) have been determined from the measured reflectivity as a function of incident pulse energy density on the AR-coated samples using a theoretical fit based on a travelling-wave rate equation model (Fig. 3b). For this measurement we chose to increase the pulse duration to ≈ 1.4 ps in order to determine the saturation fluence of the thermalized carrier distribution. The cw saturation intensity $I_{sat} = E_{sat}/\tau_c$ follows then directly from the carrier lifetime τ_c. Because the measurements are performed on AR-coated samples the effective saturation fluence of the A-FPSA is increased by a factor of $1/\xi$:

$$E_{sat}^{eff} = \frac{1}{\xi} E_{sat} \quad \text{with} \quad \xi = \frac{1 - R_t}{\left(1 + \sqrt{R_t R_b}\, e^{-2\alpha d}\right)^2 - 4\sqrt{R_t R_b}\, e^{-2\alpha d} \sin^2\left(nkd + \frac{\varphi_t}{2} + \frac{\varphi_b}{2}\right)}$$

where R_t, φ_t, R_b, and φ_b are the reflectivities and phases of the top and bottom mirror, respectively, and d, n, and α the thickness, refractive index, and amplitude absorption coefficient of the absorber. Thus, it is possible to choose the proper saturation fluence by varying R_t , d, or the absorption edge. We typically used a 98% top reflector which yields a ξ of 0.007, causing an increase of the saturation fluence by a factor of 140.

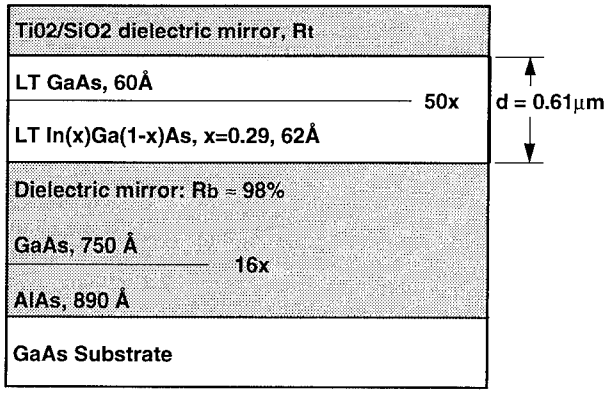


Fig. 1: Structure of an A-FPSA.

The measured I_{sat} determines the initial mode-locking driving force given by

$$\frac{\partial(\Delta R)}{\partial I} \sim \frac{1}{I_{sat}} \sim \tau_c$$

where ΔR is the change in reflectivity due to absorption bleaching for cw intensities. This was experimentally confirmed with a ps Nd:YLF laser, for which we obtained shorter mode-locking build-up times for longer carrier lifetimes τ_c [6] (Fig. 3d). For our typical laser parameters the above defined mode-locking driving force is $\approx 10^{-6}$ W^{-1}. In comparison, the KLM driving force is typically more than 10 times smaller because the laser is operated close to the middle of the stability regime. An upper limit for the carrier lifetime is given by the onset of Q-switching. Therefore, it is a great advantage to be able to optimize for each type of laser the carrier lifetime for efficient self-starting and good stability without affecting the intracavity losses.

Even though the non-saturable background losses ΔR_{ns} (Fig. 3c) increase with lower MBE growth temperature, its effect on intracavity losses is strongly reduced for an A-FPSA with a high top reflector.

The measurements at different wavelengths (i.e. 1000, 1020, 1040, 1060 nm) showed as expected a higher saturation fluence for shorter wavelengths (i.e. 137, 97, 50, 45 μJ/cm^2 for the sample with a growth temperature of 315°C and similar for the others) which results in smaller nonlinearities at shorter wavelengths. Especially for the low-temperature grown materials ΔR_{ns} shows a strong wavelength dependence, which is under further investigation.

The total nonlinear reflectivity change between cw and pulsed operation of the A-FPSA was calculated to be ≈ 0.2 % for both a Nd:YLF laser [1] and a Nd:glass laser [5]. In both cases we are still in the linear saturation regime.

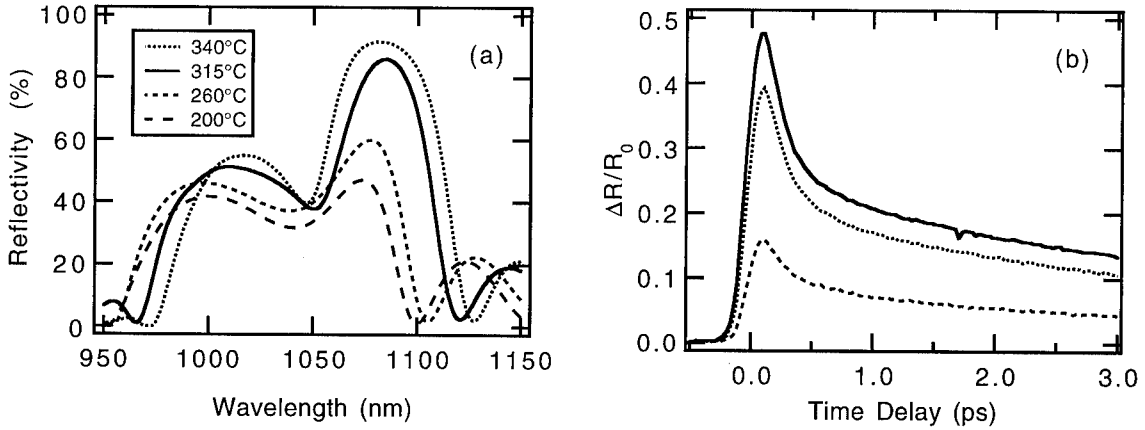


Fig. 2: (a) Reflectivity of AR-coated samples and (b) bitemporal impulse response of the 260°C-sample .

Femtosecond regime:

The A-FPSA also can be used to produce femtosecond pulses [4, 5] because the Fabry-Perot is operated at antiresonance and the impulse response has a fast thermalization component (Fig. 4) which decreases with higher excitation pulse energy and therefore higher carrier density as expected. The antiresonance reduces bandwidth limitations because the free spectral range of the A-FPSA (Fig. 1) is typically ≥ 140 nm. In addition, antiresonance provides a constant group delay over the high reflectivity band (i.e. 2 fs ± 0.5 fs within 100 nm) as our calculations have shown.

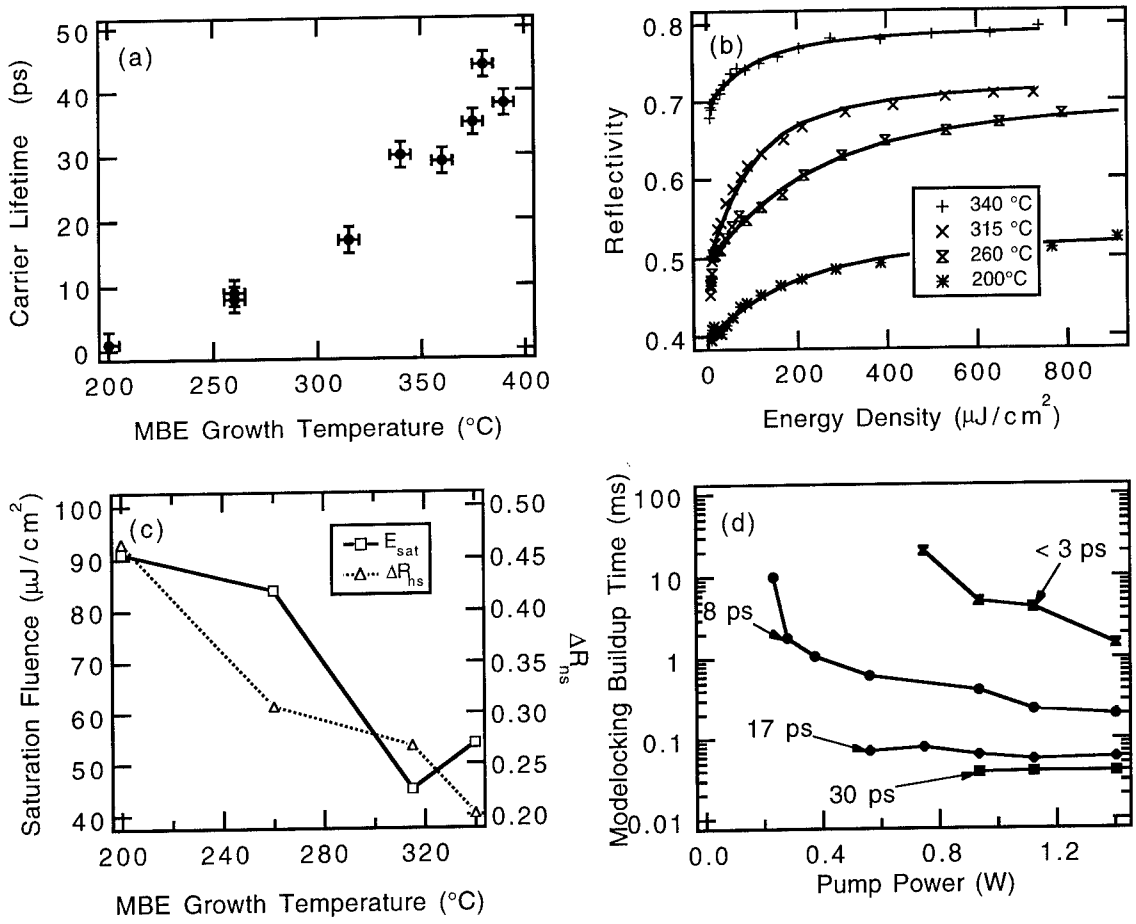


Fig. 3: (a) Carrier lifetime vs. growth temperature, (b) nonlinear reflectivity vs. energy density at λ=1060nm of AR-coated samples, (c) saturation fluence vs. growth temperature of AR-coated samples, and (d) mode-locking build-up time vs. pump power for A-FPSA's with different growth temperatures.

Stable sub-100-fs pulses have been demonstrated from a self-starting passively mode-locked Nd-glass laser, where the fast time component is necessary to sustain stable ≈ 100 fs pulse duration [5]. Also in this case KLM is negligible because the laser is operated in the middle of the stability regime. The decrease of thermalization time with increasing growth temperature (Fig. 4) agrees with the observation of shorter pulses when samples grown at higher temperatures are used as absorbers (i.e. 140 fs for a 340°C-sample and 160 fs for a 314°C-sample where all other parameters have been left constant [4]).

In conclusion, our calculations and measurements show that the A-FPSA is well suited for the generation of self-starting ps- as well as fs-pulses from solid-state lasers. The great flexibility in the design of the essential parameters allows for adaption of the absorber to a wide range of laser materials.

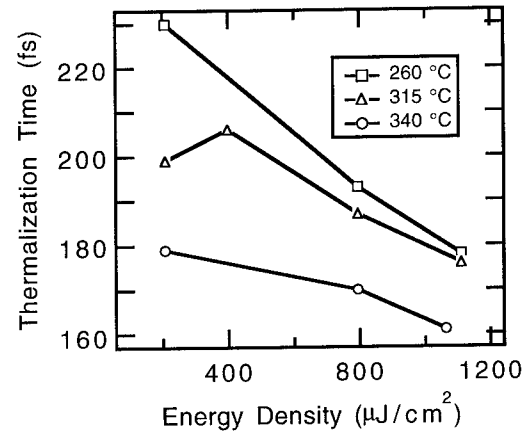


Fig. 4: Thermalization time vs. energy density at λ=1060nm.

References

1. U. Keller, D. A. B. Miller, G. D. Boyd, T. H. Chiu, J. F. Ferguson, M. T. Asom, *Optics Lett.* **17**, 505 (1992)
2. K. J. Weingarten, U. Keller, T. H. Chiu, J. F. Ferguson, *Optics Lett.* **18**, 640 (1993)
3. M. H. Ober, M. Hofer, U. Keller, T. H. Chiu, *Optics Lett.* **18**, 1532 (1993)
4. U. Keller, T. H. Chiu, J. F. Ferguson, *Optics Lett.* **18**, 1077 (1993)
5. F. X. Kärtner, D. Kopf, U. Keller, submitted to Ultrafast Phenomena 1994
6. U. Keller, T. H. Chiu, J. F. Ferguson, *Optics Lett.* **18**, 217 (1993)

Microscopic study of ferroelectrics with ultrashort phonon polaritons

H.J. Bakker, S. Hunsche, and H. Kurz

Institut für Halbleitertechnik, RWTH Aachen, Sommerfeldstr. 24, 52074 Aachen, Germany
Tel. +49-241-807895; Fax. +49-241-86165

We investigate the low-frequency dielectric response of the ferroelectrics $LiTaO_3$ and $LiNbO_3$ via the impulsive excitation and phase-sensitive detection of THz phonon polaritons. The low-frequency dielectric response of these crystals is dominated by a ferroelectric mode of A_1 symmetry. This mode leads to a strong absorption at 6 THz (200 cm^{-1}) in $LiTaO_3$ and to a strong absorption at 7.5 THz (250 cm^{-1}) in $LiNbO_3$ at room temperature The strength and frequency of this mode strongly change when the temperature is increased towards the ferroelectric phase-transition temperature (890 K for $LiTaO_3$ and 1480 K for $LiNbO_3$).

The polaritons are excited via difference-frequency mixing of ultrashort laser pulses (τ_p = 60 fs, λ = 625 nm, E = 5 μJ). These laser pulses are split into three. Two of the three pulses serve as excitation pulses and are focussed into the sample under a chosen angle to a common focus with a diameter of 200 μm. This angle defines the wavevector of the polariton. The polariton frequency that corresponds with this wavevector is obtained out of the broad bandwidth of the laser pulses. The polaritons are phase-sensitively detected with the third pulse via the electro-optic effect. By varying the wavevector and measuring the corresponding polariton frequency, the polariton dispersion is obtained. At most wavevectors only one polariton frequency is generated.

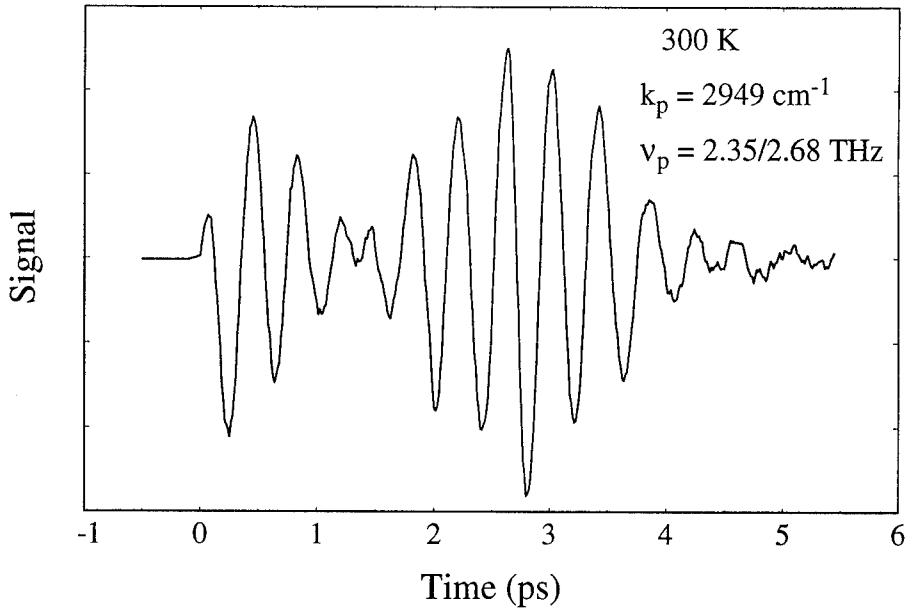


Figure 1: Time-resolved measurement of phonon polaritons in $LiNbO_3$. The signal is presented as a function of the delay between the probe and the two pump pulses.

However, at specific wavevectors, two polaritons of different frequency are generated, leading to a beating phenomenon (Fig. 1). This beating strongly indicates the presence of a weak resonance at 2.4 THz. This resonance leads to an avoided crossing in the polariton dispersion and makes it possible to excite two polaritons of different frequency at one particular wavevector. The frequency difference is determined by the absorption strength of the resonance. We found that there are four avoided crossings in the polariton dispersion of $LiNbO_3$ due to four weak resonances at 1.3 THz, 2.4 THz, 3.4, and 4.1 THz (Fig. 2). For $LiTaO_3$, we also found an avoided crossing at 1 THz. None of these resonances has been found in previous infrared reflectivity and Raman-scattering studies. Hence, the coherent excitation of phonon polaritons using ultrashort pulses appears to be a much more sensitive probe for weak resonances than these conventional techniques.

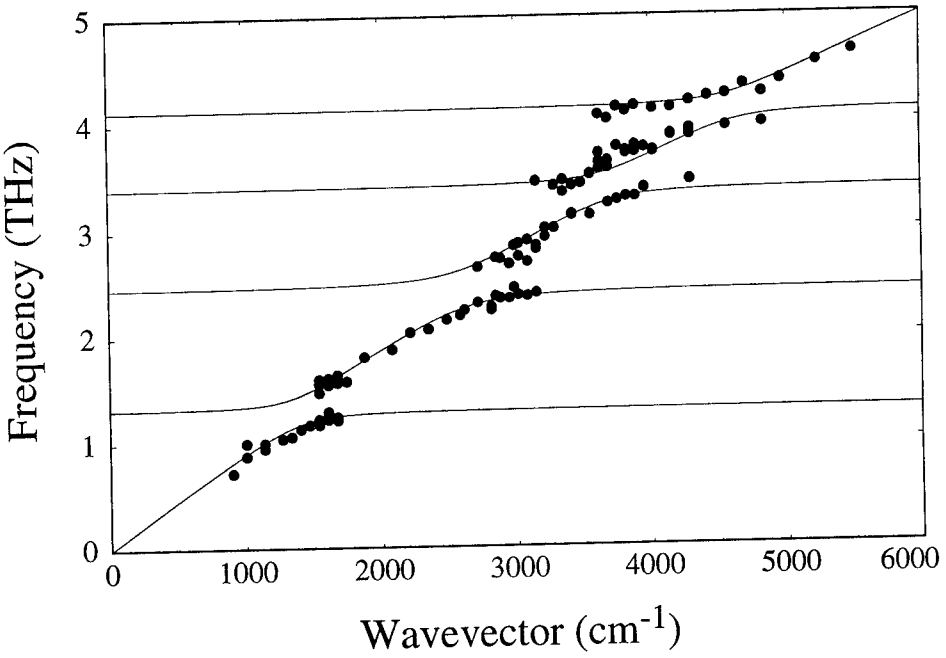


Figure 2: Phonon-polariton dispersion of $LiNbO_3$ at 300 K. The measurements are represented by points. The solid curves are calculated assuming resonances at 1.3, 2.4, 3.4 and 4.1 and 7.5 THz. are calculated

The occurence of these resonances can be explained from the extreme anharmonic character of the ferroelectric mode. It has been found that the dielectric properties of $LiTaO_3$ and $LiNbO_3$ can be described best with a potential for the vibrational states of the ferroelectric mode that contains three minima in one unit cell [1]. The measured frequencies and absorption strengths of the resonances provide detailed information on the shape of the triple-well potential and thereby on the microscopic origin of the ferroelectricity. The resonances at low frequencies turn out to be due to transitions between high-energy vibrational levels that are delocalized over two of the three wells of the potential. The calculated frequencies and absorption strengths of the vibrational transitions agree well with the experimental values that are derived from the measured polariton dispersion. The resonances at 1.3 THz in $LiNbO_3$ and at 1 THz in $LiTaO_3$ are tunneling resonances since their energy is below the top of the barrier that separates two of the three wells of the potential. The triple-well potential also provides a microscopic description of the ferroelectric phase transition.

According to this description, the absorption strength of the resonances at 6 THz in $LiTaO_3$ and at 7.5 THz in $LiNbO_3$ decreases with increasing temperature. The model also predicts that with increasing temperature in both crystals several strong resonances near 3.5 THz will arise that result from transitions between delocalized levels in the triple-well potential. In addition, the model predicts that at temperatures close to the ferroelectric phase-transition temperature a strong resonance near frequency zero (central mode) will be present. This central mode is responsible for the divergence of the static dielectric constant at the phase-transition temperature.

The dispersion and damping of the polaritons are strongly affected by these changes in the absorption [2]. We find that for $LiTaO_3$ the damping time constant at all polariton frequencies

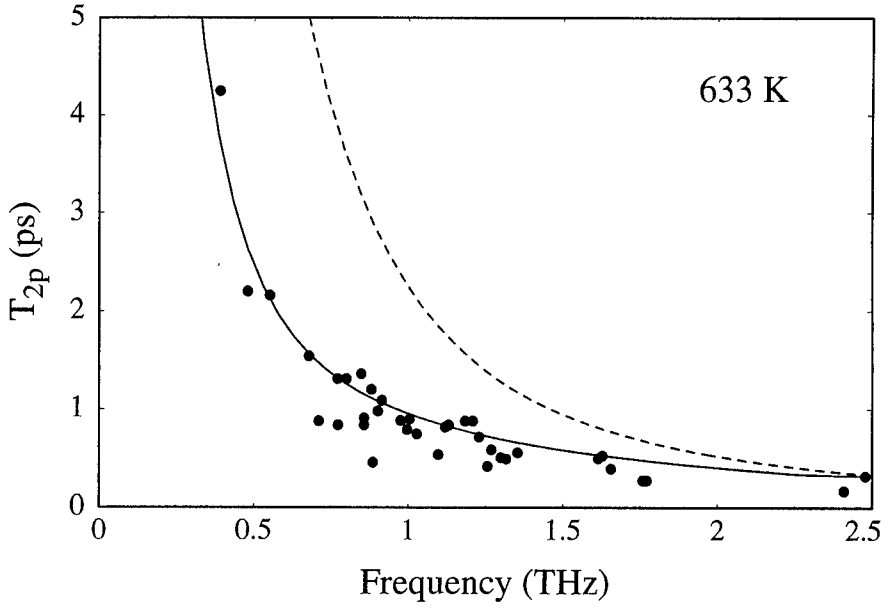


Figure 3: Measured and calculated polariton damping-time constants T_{2p} at 633 K in $LiTaO_3$. The measurements are represented by points. The solid curve represents a calculation of T_{2p} incorporating both the response of the vibrational transitions in the potential and the central mode. The dashed curve represents a calculation of T_{2p} without considering the central mode.

becomes smaller with increasing temperature. Fig. 3 shows that at 633 K the central mode plays an essential role in $LiTaO_3$ in the damping of low-frequency polaritons.

In conclusion, we showed that the low-frequency dielectric response of $LiTaO_3$ and $LiNbO_3$ can be investigated in detail by measuring the polariton dispersion and damping. These results demonstrate the power of time-resolved optical techniques in obtaining microscopic dynamical information.

References

[1] M.E. Lines, Phys. Rev. B **2**, 698 (1970)

[2] H.J. Bakker, S. Hunsche and H. Kurz, Phys. Rev. B **48**, 9331 (1993)

Carrier transport in 1.5 μm quantum well laser structures

S. Marcinkevičius, U. Olin, K. Fröjdh, J. Wallin+ and G. Landgren+

Department of Physics II, Royal Institute of Technology, and Institute of Optical Research, S-100 44 Stockholm, Sweden, tel. +46 8 791 1325

+ KTH Semiconductor Laboratory, Electrum 229, S-164 40 Kista, Sweden, tel. +46 8 752 1288

Carrier transport time is one of the main factors limiting the high-speed performance of the quantum well lasers [1]. Thus, investigations of the transport mechanisms are essential for the improvement of the laser characteristics. In this paper we examine the carrier transport in the 1.5 μm InGaAs/InP graded-index separate-confinement heterostructure (GRINSCH) laser by means of time-resolved photoluminescence (PL). Such measurements produce a direct picture of the carrier motion and allow to draw conclusions about the transport mechanisms.

The laser structure, grown by MOVPE, is schematically shown in Fig. 1. The active layer of the structure consists of eight 3.5 nm thick InGaAs quantum wells separated by 8 nm thick InGaAsP barriers. All the layers of the structure are lattice matched to InP. The PL was measured with the up-conversion technique using a Ti:sapphire laser for excitation (wavelength 770 nm, pulse

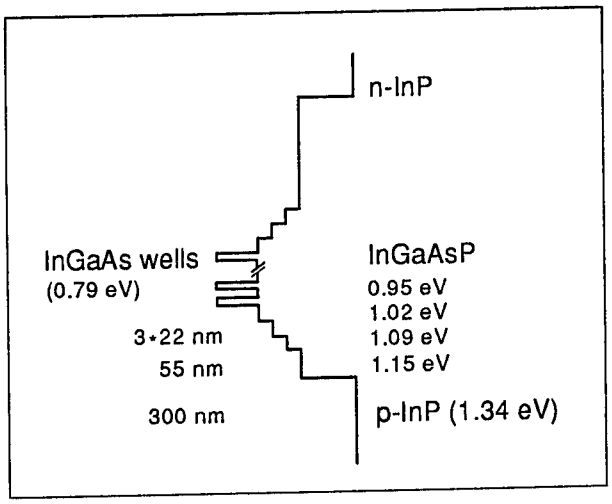


Fig. 1. Schematic diagram of the studied laser diode structure.

duration 100 fs, repetition frequency 80 MHz). The temporal resolution of the measurements, estimated from the cross-correlation signal between the laser pulse and the light scattered from the sample surface, was 130 fs. To simulate the operating conditions of the laser diode, high average excitation intensities (20 to 200 mW) were used. These excitation intensities correspond to the excited carrier densities of 10^{18} to 10^{19} cm^{-3}. The measurements were performed at room temperature.

Characteristic PL spectra at various time delays after the exciting pulse are shown in Fig 2. The carriers are excited mainly in the *p*-InP barrier. Already after 2 ps most of them have

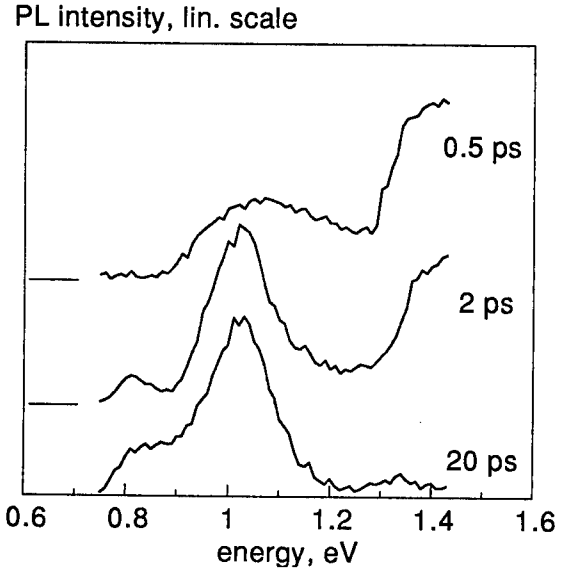


Fig. 1. PL spectra at several time delays

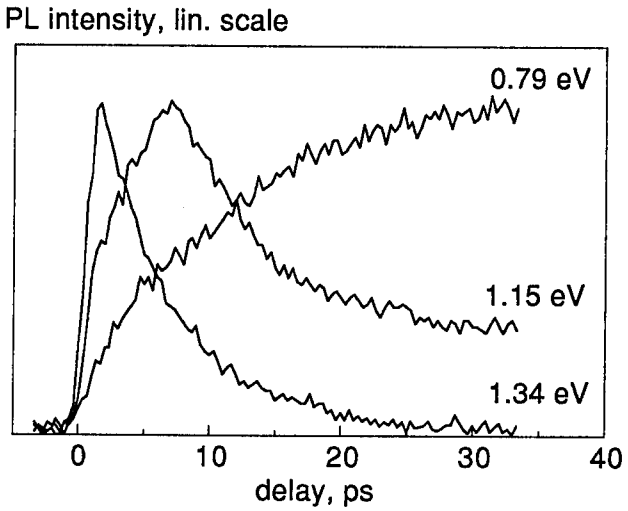


Fig. 2. Temporal dependencies of the PL at various band gap energies of the structure

energies,

transferred into the GRIN layers. At longer time delays, carriers fill the quantum well states and part of the GRIN reservoir. The temporal dependencies of the PL at energies, corresponding to the band gaps of several different layers, are presented in Fig. 3. A fast decay of the barrier PL corresponds to the rise-time in the first step of the GRIN structure. The PL rise-times, measured

at the energies of the subsequent steps, continuously increase up to 22 ps, the rise-time of the quantum well PL.

The temporal dependencies of the PL signal at different wavelengths allow to follow the carrier motion from the barrier towards the quantum wells. Since the excited carrier density is larger than the doping level of the structure layers, ambipolar diffusion is the most viable transport process. However, contrary to the ordinary diffusion, the PL rise-times increase linearly with the layer distance from the barrier. This suggests that the carriers move by the step driven diffusion [2], where within each step of the structure the transport proceeds by diffusion, but the presence of steps prevents carrier motion in the backward direction. The ambipolar diffusion coefficient, estimated from the relation [2] $D \approx 0.2l^2/t$ (where t is the time during which the carrier packet moves along the step of the length l), is equal to 3.1 $cm^2V^{-1}s^{-1}$ and is in good agreement with the value of 2.9 $cm^2V^{-1}s^{-1}$ reported for InGaAsP optical amplifiers [3]. This supports the model that the step-driven diffusion is the main carrier transport mechanism in the investigated GRINSCH laser structure.

---

1. R. Nagarajan, M. Ishikawa, T Fukushima, R.S. Geels and J.E. Bowers, IEEE J. Quantum Electron. **28**, 1990 (1992).

2. B. Deveaud, J. Shah, T.C. Damen, B. Lambert and A. Regreny, Phys. Rev. Lett. **58**, 2582 (1987).

3. S. Weiss, J.M. Wiesenfeld, D.S. Chemla, G. Raybon, G. Sucha, M. Wegener, G. Eisenstein, C.A. Burrus, A.G. Dentai, U. Koren, B.I. Miller, H. Temkin, R.A. Logan and T. Tanbun-Ek, Appl. Phys. Lett. **60**, 9 (1992).

Coherent Optical Polarization of Large Coherence Length Frenkel Excitons in Pseudoisocyanine J Aggregates

Shunsuke Kobayashi and Fumio Sasaki
Electrotechnical Laboratory, 1-1-4 Umezono, Tsukuba, Ibaraki 305, Japan
Telephone:(81)-298-58-5449, Telefax:(81)-298-58-5459

Recently the collective optical response in mesoscopic structures has attracted much attention because such structures are expected to show large nonlinear optical (NLO) properties and ultrafast optical response. These features are essential for the materials of the photonics application.

One dimensional molecular aggregates called J aggregates show a sharp exciton absorption and a superradiant emission as a result of collective excitation [1]. We have reported that the J aggregates of pseudoisocyanine (PIC) show an extraordinary large NLO susceptibility and also fast switching-off time (1.3 ps) at 77 K [2]. Furthermore PIC J aggregates show a novel excitation density dependent NLO response which could be useful as an optical logic element [3]. These unique NLO properties are attributed to the one-dimensional Frenkel excitons with the large coherence length which is extended over thousand molecules at 77 K [2]. It is interesting to clear the detailed mechanism of the dynamics of the large coherence length excitons.

In this report we present results of experiment in which the coherent interaction between Frenkel excitons of PIC J aggregates and a radiation field measuring a perturbed free induction decay (FID) by using a standard pump-probe method with low density (1 to 10 $\mu J/cm^2$) 200 fs pulse. The pump field produces any substantial changes in the probe field through materials polarization. Important information on the many body interactions such as exciton-exciton interaction are contained in the temporal line shape of optical response under ultrashort pulse excitation [4,5].

Samples were made by dissolving PIC bromide to a concentration of 4 mM in a 1:1 mixture of water and ethyleneglycol (WEG). Details of the aggregate forming procedure were reported previously [2]. The pulses are the amplified output of a hybrid mode-locked dye laser with 1 kHz repetition. The pump and probe pulses are obtained through the generation of a white light continuum in a water cell. The pump pulse is selected with an interference

filter of 8 nm band width centered at 570 nm (Fig.1) and is 200 fs duration.

Figure 1 shows the oscillatory structures at the J band in the differential transmission spectra ($\Delta T/T$) of the probe pulse at the very early time when the probe pulse proceeds the pump pulse. The oscillatory structure is assigned to the perturbed FID [4] and has been reported in dye solutions [4] and semiconductors [5] but there has been no report about Frenkel excitons. When PIC J aggregates were excited with relatively high density ultrashort pulse (a few mJ/cm^2) such oscillatory structures were disappeared [6]. Passing through zero delay dispersion-type $\Delta T/T$ spectra characteristics for the one-dimensional Frenkel exciton [7] are observed. The dispersion-type $\Delta T/T$ decays with fast (1.3 ps) and slow (20 ps) decay component [6,8]. The fast decay was attributed to the scattering of large coherence length excitons by phonons [8] and the slow decay was the population decay of excitons (T_1).

The amplitude of the oscillatory structures are increased with time (Fig.2). The rise-up of the signal indicates the dephasing time (T_2) of polarization [4] and one can estimate T_2 between 300 fs and 600 fs depending on the models applied. The dephasing of the polarization comes from the inhomogeneity of the J band. The fluctuation of the exciton energy level causes the FID [4]. The dephasing time estimated from the width of the J band (30 cm^{-1} in WEG at 77 K) is 300 fs which is consistent with the value obtained from the FID signals. The measured dephasing time of PIC J aggregates is one order of magnitude longer than that of the dye solutions [4] and is comparable to that of the excitons in semiconductors [5]. This longer dephasing time produces the large NLO susceptibility of J aggregates. When J aggregates were excited with high density the phase coherence was lost by multiple exciton transitions and no FID signal was observed.

The origin of the broadening of the J band was discussed by Fidder et al [9] with diagonal disorder (monomer energy level fluctuation) and off-diagonal disorder (transfer energy fluctuation). The Fidder's model was based on the dipole-dipole interaction between neighbor monomer and can not directly applied to the present results because the FID signals in this case are observed at the exciton band and are caused by exciton-exciton interactions. To explain the observed T_2 we need the model based on the fluctuation of the exciton energy level and the exciton-exciton interaction between them. In the present experiment we observe only the time integrated FID signal. To clear the detailed mechanisms of dephasing of large coherence length Frenkel excitons the time resolved FID signal measurements are also necessary.

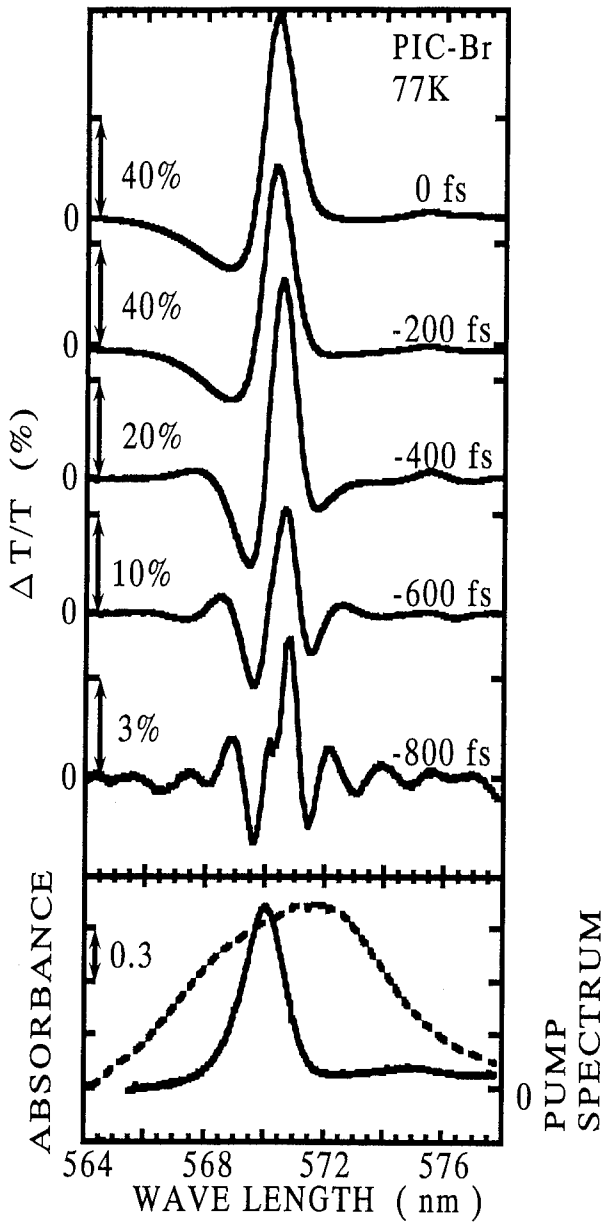


Fig.1. Differential transmission spectra for various negative time delays (upper) together with absorption spectrum and pump spectrum (lower) for PIC J aggregates in WEG at 77 K.

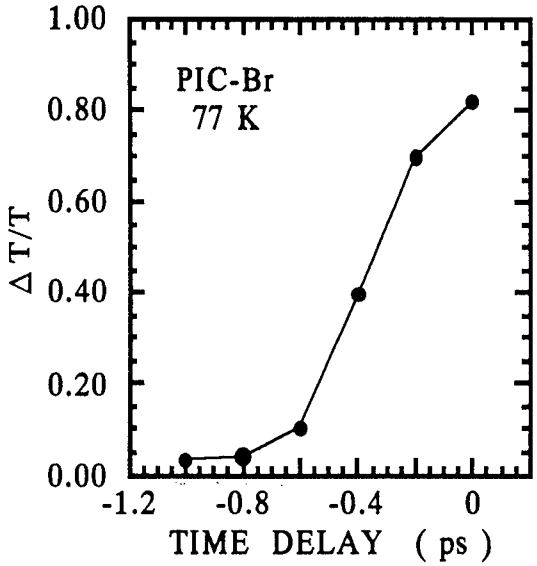


Fig.2. Rise-up of differential transmission peaks at 570 nm.

References.

[1] S.de Boer and D.A.Wiersma, Chem.Phys.Lett. 165, 45 (1990).
[2] S.Kobayashi and F.Sasaki, Nonlinear Optics 4, 305 (1993).
[3] F.Sasaki and S.Kobayashi, Appl. Phys. Lett. 63, 2887 (1993).
[4] C.H.Brito Cruz, J.P.Gordon, P.C.Becker, R.L.Fork and C.V.Shank, IEEE J. Quantum Electron. QE-24, 261 (1988).
[5] S.Weiss, M.-A.Mycek, J.-Y.Bigot, S.Schmitt-Rink and D.S.Chemla, Phys.Rev.Lett. 69, 2685 (1992) and references there in.
[6] K.Minoshima, M.Taiji, K.Misawa and T.Kobayashi, Chem.Phys.Letter, [in press]
[7] F.C.Spano and S.Mukamel, Phys.Rev. A40, 5783 (1989); H.Ishihara and K.Cho, Phys.Rev. B42, 1724 (1990).
[8] S.Kobayashi and F.Sasaki, J.Luminescence, [in press]
[9] H.Fidder,J.Knoester and D.A.Wiersma, J.Chem.Phys. 95, 7880 (1991).

Investigation of the Energy Transfer and Electronic Excitation Transport in Photosystem II Reaction Center Using Time-resolved Fluorescence Spectroscopy

Shuicai Wang[a], Tong Ye[a], Yan Cui[a], Yaodong Chen[a], Jianmin Hou[b], Kunyun Yang[b], Zhenbao Yu[b],Chongqin Tang[b], Tingyun Kuang[b],and Xun Hou[a]

[a]State Key Lab of Transient Optics Technology, Xi'an Institute of Optics and Precision Mechanics, Academia Sinica, P.O.Box 80(25), Xi'an, 710068, P.R. China
[b]Laboratory of Photosynthesis Research, Beijing Institute of Botany, Academia Sinica, Jian Guo Men Wai 141, Beijing 100044, P.R.China

The energy transfer(ET) and electronic excitation transport(EET) are two important ultrafast primary processes in PS II reaction centers. All kinds of ultrafast laser spectroscopy techniques are used in the dynamic study on PS II reaction center[1]. Although many results have been obtained, much debate still exists on the structure and function of the reaction center, the physical mechanism and rates of the ET and EET[2]. In this paper we report some experimental results on the ultrafast dynamic study on the ET and EET in the PS II reaction center. The PS II reaction center, D1/D2/cyt-b559 complex, is isolated and purified from the spinach, which contains 4 or 5 Chla molecules, 2 pheoa molecules, 1 β-carotene molecule.

We investigate the ET and EET by the means of the time-resolved fluorescence spectroscopy in the time-scale from subpicosecond to nanosecond. Two measurement systems have been established, one for the ps time resolution measurement and the other for the subps.

In ps measurement system(Fig1), a mode-locking argon ion lasers with 200 ps pulse width and 82MHz repetition rate is used. The fluorescence from the sample is detected and analyzed by the photomultiplier, the Boxcar Averager and Processor. After deconvolution of the instrument response function, the time resolution of system is 100 picosecond. Four lifetime components are obtained by the multi-exponential curve fitting, for the 488 nm excitation, they are 350 ps, 1.5 ns, 6.0 ns, and 38 ns, and for the 514.5 nm, <100 ps, 1.5 ns, 6.0 ns, 3[illegible] nensional graphs of the time-resolved spectra are given in the Fig.2. The different fast component between two excitations is based on the different energy transfer path.

In the femtosecond measurement set up(Fig.3), the fluorescence upconversion technique[3] is used. The system includes: a mode-locking femtosecond Ti:sapphire lasers with 100 fs pulse width and 82MHz repetition rate, the upconversion crystal 0.5 mm BBO, a monochrometer and a photocounting system. The time-resolution of the system is about 300 fs. The fast fluorescence components and the initial rise time of the fluorescence for the D1/D2/cyt-b559 are measured.

The measurement results are analyzed and discussed. A novel dynamic model is expected to obtained by the wide time range investigation of the time-resolved fluorescence spectra.

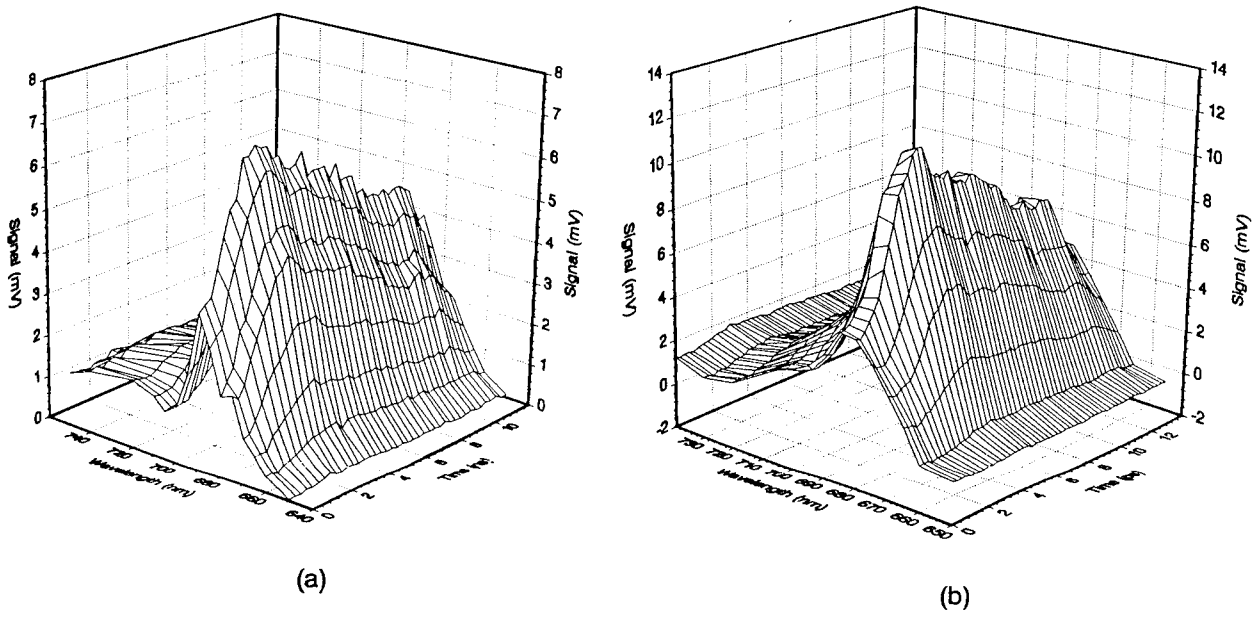


Fig.2 The 3-dimensional graphs of the time-resolved fluorescence spectra of D1/D2/cyt-b559: (a)excited by the 488nmlight; (b)execited by the 514.5nm light

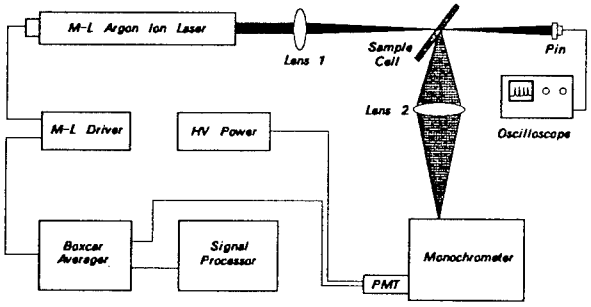


Fig.1 Setup of the ps time-resolved fluorescence spectra measurement

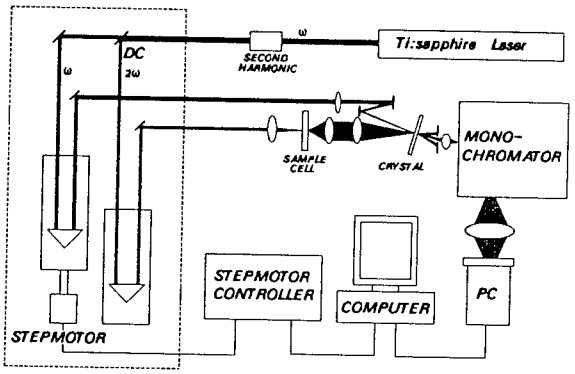


Fig.3 Setup of the subps time-resolved fluorescence spectra measurement

Reference

1. T. Ye, Y. Cui, S. Wang, X. Hou, *Acta Photonica Sinica*, **22**, Z1 ,55

2. M. R. Wasielewski, D. G. Johnson, M. Seibert, Govindjee, *Proc. Natl. Acad. Sci. USA*; 1989, **86**, 524; G. Hastings, J. R. Durrant, J. Barbaer. G. Porter, and D. R. Klug, *Biochemistry*, 1992, **31**, 7638

3. J. Shah, *IEEE J. of Quantum Electronics*, 1988, **24**,276; M. A. Kahlow, Wlodzimierz, T. P. DuBruil, and P. L. Barbara, *Rev. Sci. Instrum.*, 1988, **59**, 1098

Influence of Inhomogeneous Broadening on Quantum Beats

J. Erland, K.-H. Pantke, V. Mizeikis,
Fysisk Institut, Odense Universitet, DK-5230 Odense M,
Denmark, Tel. +45-66158600

V.G. Lyssenko, and J.M. Hvam,
Mikroelektronik Centret, The Technical University of Denmark,
DK-2800 Lyngby, Denmark, Tel. +45-45934610

Current issues in the study of light-matter interactions are coherence and quantum interference. With ultrafast nonlinear spectroscopy such as transient four-wave mixing (TFWM) the imposed coherence on the optical excitations in e.g. GaAs multiple quantum wells has been studied. In this contribution, we study the influence of inhomogeneous broadening on quantum beats observed by spectrally resolved TFWM. In artificially grown semiconductor structures as e.g. quantum wells, inhomogeneities due to interface-disorder has, up till now, been inevitable. In the experiments, the light-hole exciton (lhx) and the heavy-hole exciton (hhx) in a 100 Å GaAs multiple quantum well are excited simultaneously with 150 fs pulses from a self mode-locked Ti:sapphire laser. The spectral profile is shown in the inset of Fig. 1.

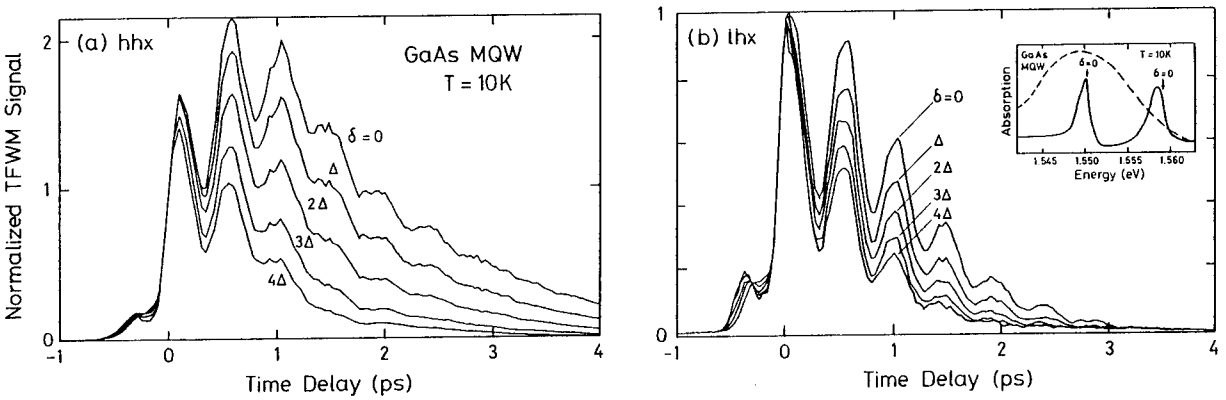


Fig. 1. Experiment with spectrally resolved TFWM at hhx (a) and at lhx (b) in a GaAs multiple quantum well. Each curve is for different detunings, in steps of Δ = 0.21 meV, and all curves are normalized at zero delay, τ = 0. The inset shows the absorption spectrum together with the spectral profile of the laser used in the experiments. In the inset, the arrows indicate zero detuning from the nonlinear resonances.

The inset also shows the absorption spectrum. For this particular sample the FWHM of the hhx and lhx is: Γ_{hhx} = 1.5 meV and Γ_{lhx} = 2.1 meV. The TFWM signal is dispersed in a spectrometer with a resolution of 0.1 meV. For different spectral components above the hhx-resonance and above the lhx-resonance, the normalized TFWM signal, as a function of the

delay τ between the incident pulses, is shown in Fig. 1 (a) and (b), respectively. The normalization is done at $\tau = 0$. The sample temperature was kept at 10 K and the average power per beam was 0.8 mW focussed into a 50 μm spot on the sample. The TFWM signal is modulated with $T_{beat} = 460$ fs corresponding to a hhx-lhx splitting of 8.9 meV, see inset of Fig. 1. The phase of the beats is constant through the resonances showing the quantum beat nature of the modulation.[1] For the hhx-resonance, the modulation decays faster than the signal does. In the lhx-resonance, the modulation persists as long as the signal does, because of the shorter dephasing time of the lhx-resonance compared to the hhx-resonance. In both resonances a clear dependence on detuning δ is observed, as the signals decay faster for increasing detuning. This dependence is stronger for the hhx-resonance than for the lhx-resonance. Additionally, we observe a shift of the maximum of the TFWM signal in the center of the hhx away from zero delay to $\tau_{max} \approx 0.8$ ps.

In a previous publication[2], the third-order polarization $P^{(3)}_{QB,homo}(\tau,\omega)$ for a homogeneously broadened three-level system, assuming δ-pulses and neglecting terms from pulse-overlap, has been calculated. The model is based on the atomic optical Bloch equations and assumes exciton-levels rather than exciton-bands and neglects exciton-exciton interaction[3] and self-interaction terms[4]. For the purpose of describing the influence of inhomogeneous broadening on quantum beats the model is, however, useful as demonstrated below. Assuming equal dipole matrix elements of the transitions with frequencies ω_{10} and ω_{20} and distinctly different dampings of the two levels involved in the beating, e.g. $\gamma_{20} >> \gamma_{10}$, a simple expression for the intensity of the TFWM signal detected near one resonance is obtained,

$$I_{TFWM} \propto \frac{e^{-2\gamma_{10}\tau}\left[1 + e^{-\gamma_{20}\tau}\cos(\omega_{21}\tau)\right]}{(\omega_{10}-\omega)^2 + \gamma_{10}^2} \qquad (1)$$

where $\omega_{21} = \omega_{20}-\omega_{10}$. Thus, the average signal decays with the slowest damping rate, whereas the decay of the beat modulation decays with the fastest damping rate. Eq. (1) is consistent with the experimental results presented in Fig. 1.

We introduce a correlated distribution of ω_{10} and ω_{20} to describe the inhomogeneous broadening in a three-level system[5]

$$g_N(\omega_{10},\omega_{20},\lambda) = \frac{4\cdot\ln(2)}{\pi\tilde{\omega}_{10}\tilde{\omega}_{20}}\exp\left[-4\cdot\ln(2)\cdot\left\{\left(\frac{\omega_{10}-\omega_{10}^0}{\tilde{\omega}_{10}}\right)^2 - 2\lambda\frac{(\omega_{10}-\omega_{10}^0)\cdot(\omega_{20}-\omega_{20}^0)}{\tilde{\omega}_{10}\tilde{\omega}_{20}} + \left(\frac{\omega_{20}-\omega_{20}^0}{\tilde{\omega}_{20}}\right)^2\right\}\right] \qquad (2)$$

where λ is the correlation parameter and ω^0_{i0} is the center frequency of the inhomogeneously broadened line. $\lambda=0$ means no correlation. In the case $\lambda=1$ (full correlation) the broadenings of the different resonances follow each other. In Eq. (2), $\tilde{\omega}_{i0} = \Gamma_{i0}\hbar^{-1}(1-\lambda^2)^{1/2}$, where Γ_{i0} indicates the linewidth obtained in a linear experiment. It is seen, that the correlation makes the effective linewidth smaller, when λ increases from 0 towards 1. From Eq. (2), we can calculate the third-order polarization from an inhomogeneously broadened three-level system

$$P^{(3)}_{QB,inh}(\tau,\omega) \propto \iint g_N(\omega_{10},\omega_{20},\lambda)\, P^{(3)}_{QB,homo}(\tau,\omega_{10},\omega_{20},\omega)\, d\omega_{10} d\omega_{20} \qquad (3)$$

Fig. 2 shows a calculation of the TFWM signal from the absolute square of Eq. (3) for energies above the energetically lowest resonance in the quantum beat as illustrated in the inset of Fig. 2. For an inhomogeneous broadening Γ of 7 times the homogeneous broadening γ of the lower resonance the dependence on detuning δ is evident. For large detuning the

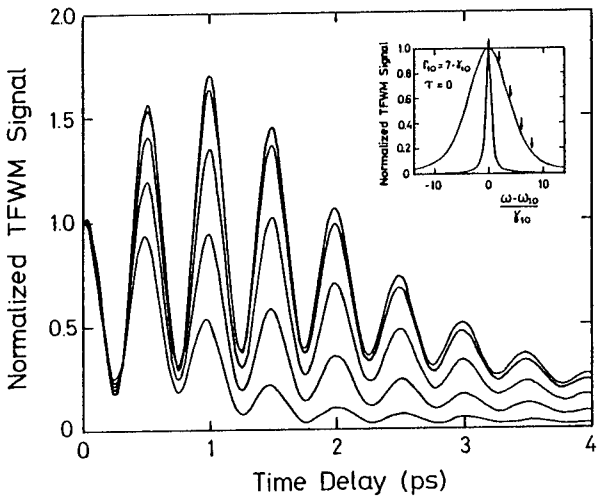


Fig. 2. Calculated TFWM-signal as function of delay τ and detuning δ *above* the energetically lowest resonance. The inset shows the calculated homogeneous and inhomogeneous lines with arrows indicating the energies of the calculated and normalized τ-dependent curves. The parameters are T_{beat} = 0.5 ps, T_2^{20} = 3 ps, T_2^{10} = 7 ps, $\lambda \approx 1$ and $\Gamma_{10} = \Gamma_{20} = 7\gamma_{10}$. The dipole matrix elements are chosen equal for the two resonances.

quantum beat signal decays faster than on resonance. This dependence is related to the ratio $\beta=\Gamma/\gamma$. From the data presented in Fig. 1, we estimate $\beta_{hhx} \approx 7.5$ and $\beta_{lhx} \approx 4.7$. For this calculation we have chosen almost full correlation ($\lambda \approx 1$), which gives maximum number of beats in the signal. For small correlation ($\lambda \approx 0$) the modulation of the signal only persists on a time scale given by Γ^{-1}. We can therefore conclude, that the inhomogeneous broadenings of the hhx and the lhx are highly correlated.

We stress that, for a *purely* homogeneously ($\beta=0$) broadened system all normalized spectral components are indistinguishable i.e. without any dependence on detuning. With this technique we are therefore able to determine simultaneously the homogeneous linewidth γ and the inhomogeneous linewidth Γ, even for $\beta < 1$, as will be presented.

References

1. V.G. Lyssenko, J. Erland, I. Balslev, K.-H. Pantke, B.S. Razbirin, and J.M. Hvam, "Nature of nonlinear four-wave mixing beats in semiconductors", *Phys. Rev. B* **46**, 5720 (1993).
2. J. Erland and I. Balslev, "Theory of quantum beat and polarization interference in four-wave mixing", *Phys. Rev. A* **48**, 1765 (1993).
3. K. Bott, O. Heller, D. Bennhardt, S.T. Cundiff, P. Thomas, E.J. Mayer, G.O. Smith, R. Eccleston, J.Kuhl, and K. Ploog, "Influence of exciton-exciton interactions on the coherent optical response in GaAs Quantum Wells", *Phys. Rev. B* **48**, xx (1993).
4. M. Wegener, D.S. Chemla, S. Schmitt-Rink, and W. Schäfer, "Line shape of time-resolved four-wave mixing", *Phys. Rev. A* **42**, 5675 (1990).
5. S.T. Cundiff, "The effect of correlation between inhomogeneously broadened transitions on quantum beats in transient four-wave mixing", submitted.

Time-Domain Interferometric Measurement of Photonic Band Structure in a One-Dimensional Quasicrystal

Toshiaki Hattori, Noriaki Tsurumachi, Sakae Kawato, and Hiroki Nakatsuka

Institute of Applied Physics, University of Tsukuba, Tsukuba, Ibaraki 305, Japan

Although ultrashort optical pulses are used for the time-domain study of transmission of pulses through dispersive media, interferometric measurements using white light with an ultrashort correlation time can very often be much more powerful and useful [1,2]. Here, we present an application of Fourier-transform interferometry to the study of photonic band structure in a one-dimensional quasiperiodic structure. Photonic band formation in periodical dielectric structures and localization of light in random structures have been a subject of great interest in recent years [3]. Studies on photonic quasiperiodical structures will extend this new area of research furthermore. Our sample of one-dimensional quasiperiodic system was a photonic Fibonacci lattice, which was proposed by Kohmoto *et al.* [4]. Fractal behavior of wave functions and the energy spectrum in it has been theoretically predicted.

The Fibonacci lattice sample was a multilayer dielectric film of SiO_2 and TiO_2 deposited on a glass substrate. The sequence of the layers is based on the Fibonacci sequence, which is defined by $S_{j+1} = \{S_{j-1},S_j\}$, $S_0 = \{A\}$, and $S_1 = \{B\}$. The sequence of the sample used in the present study was S_9. The number of the layers in S_9 is 55, which is Fibonacci number F_9. Layer A corresponds to that of SiO_2, and B to TiO_2. The optical thickness of each layer was 644 nm/4, *i.e.*, $4n_Ad_A = 4n_Bd_B = 644$ nm, where n_A and n_B are the refractive indices of SiO_2 and TiO_2, and d_A and d_B are the physical thicknesses of layers A and B. These layers were deposited on a glass substrate by vacuum deposition.

The time-of-flight profile of the light transmitted through the sample was obtained by using a Michelson-type interferometer with white light of 6 fs correlation time. The experimental schematic was as shown in Fig. 1. The light source for the interferometer was a halogen lamp, and the light was focused to a 100-μm pinhole and collimated by a lens. The light was divided into two arms by a cube beam splitter, reflected by corner-cube prisms, combined by the same beam splitter, and detected by a photomultiplier tube. The path length of one arm was modulated at 20 kHz by a piezo-electric actuator attached to the corner-cube prism. The amplitude of the path-length modulation was about 250 nm. The path length of the other arm could be scanned by a stepping-motor-driven translation stage. One step of the stepping motor nominally corresponded to a path length of 44 nm. The output of the photomultiplier tube was fed into a lock-in amplifier, and the signal at the frequency of the path-length modulation was measured. A beam of light at 632.8 nm from a He-Ne laser was passed in the interferometer parallel to the white-light beam, and the interferogram of it was simultaneously monitored for the calibration of the path length.

Two interferograms were obtained in this setup. One was the autocorrelation of the white light. The other was the cross-correlation of the light before and after transmission through the Fibonacci lattice. The cross-correlation was obtained by inserting the Fibonacci lattice on a glass substrate into one arm of the interferometer, and a glass substrate of the same thickness without a Fibonacci lattice on it into the other arm. Thus the change of the optical path length due to the substrate was compensated for. The autocorrelation and the cross-correlation obtained in this interferometric measurement are shown in Fig. 2, along with the simulated wave form of the cross-correlation. The agreement between the experimental and the simulated cross-correlation data is fairly good. The cross-correlation can be regarded as the wave shape of the optical pulse after the transmission through the Fibonacci lattice which originally had a wave shape of the autocorrelation. The temporal width of the autocorrelation, which was about 6 fs, determines the time resolution of this

time-domain measurement. Thus ultrahigh time resolution was achieved without ultrashort pulses.

The amplitude and the phase of the light transmitted through the sample was obtained by a Fourier-transform analysis of the interferograms. The complex transmission coefficient, $t(\omega)$, of the Fibonacci lattice can be obtained by $t(\omega) = \mathcal{F}\{C_C(t)\}/\mathcal{F}\{C_A(t)\} = |t(\omega)|\exp[i\phi(\omega)]$. Here, $C_A(\tau)$ and $C_C(\tau)$ are the autocorrelation and the cross-correlation, with τ being the delay time, and $\mathcal{F}\{\ \}$ denotes the Fourier transform of the function in the bracket. The transmissivity of light through the sample is the squared magnitude, $|t(\omega)|^2$, and the spectrum of the phase of the light is given by $\phi(\omega)$.

The transmission spectrum of the sample is shown in Fig. 3. Figure 3(a) is the calculated transmission spectrum of the Fibonacci lattice on a glass substrate. Figure 3(b) is the transmission spectrum of our sample obtained with a monochromator. Comparing Figs. 3(a) and 3(b) with each other, we see that correspondence of peaks and dips between the calculated one and the measured one is fairly good. There are two wide gaps around 570 THz and below 380 THz, where the transmissivity is almost zero. The region between the gaps is divided into three by two transmission dips. Each of these three is divided into three again by two shallower dips. In Fibonacci lattices with increasing generations, the trifurcation is repeated, resulting in a self-similar structure of the transmission spectrum. This trifurcation structure is clearly seen in the experimentally observed spectrum. Imperfect agreement of the experimental spectrum with the calculated one is probably due to small fluctuations in the thickness of each layer and due to dispersion of light in the materials. The transmission spectrum obtained by the Fourier-transform analysis of the interferograms is shown in Fig. 3(c). The remarkable agreement of it with the spectrum obtained by a conventional method using a monochromator demonstrates the accuracy of the present Fourier-transform technique.

In Fig. 4, the spectrum of the phase of the transmitted light obtained by the Fourier transformation is shown, along with the theoretical curve. These spectrum can be regarded as the dispersion relation of photons in the finite-length Fibonacci lattice, since the phase, ϕ, is related to the wave vector, k, and the sample thickness, L, by $\phi = kL$. In the shown curve, shift of the phase by a multiple of 2π is arbitrary. At the frequency regions of the two largest band gaps the phase is not plotted since the transmitted light was too weak there to obtain a value of the phase with enough accuracy. The obtained phase spectrum shows very good agreement with the calculated one, and clearly shows the self-similar structure of the band structure typical of Fibonacci lattices. Besides the positions of the largest gaps, smaller gaps are also clearly observed at the right positions, and the overall shape of the spectrum agrees very well with the calculated phase spectrum. Thus we could actually observe the photonic band structure in a one-dimensional quasiperiodic lattice experimentally.

The Fourier-transform interferometric technique presented here can be applicable to various time- and frequency-domain studies of coherent propagation of light in dispersive media. The technique can also be utilized to the simultaneous measurement of the real and the imaginary parts of the refractive index of optical materials.

In summary, a photonic Fibonacci lattice was made by depositing two dielectric materials on a glass substrate, and the photonic band structure of it was experimentally observed by a Fourier-transform technique using a Michelson-type interferometer. The obtained phase spectrum clearly shows the self-similar structure of the band structure typical of Fibonacci lattices.

[1] K.Naganuma, K.Mogi, and H.Yamada, Opt.Lett. **15**, 393 (1990).
[2] H.Nakatsuka, A.Wakamiya, K.M.Abedin, and T.Hattori, Opt.Lett. **18**, 832 (1993).

[3] C.M.Soukoulis, ed., *Photonic Band Gaps and Localization*, (Plenum, New York, 1993).
[4] M. Kohmoto, B. Sutherland , and K. Iguchi, Phys.Rev.Lett. **58**, 2436 (1987).

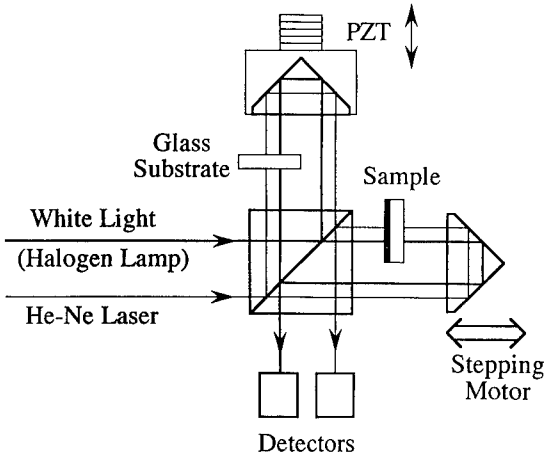


Fig. 1. The experimental schematic for the time-domain interferometric measurement of the amplitude and the phase of the light transmitted through a photonic Fibonacci lattice.

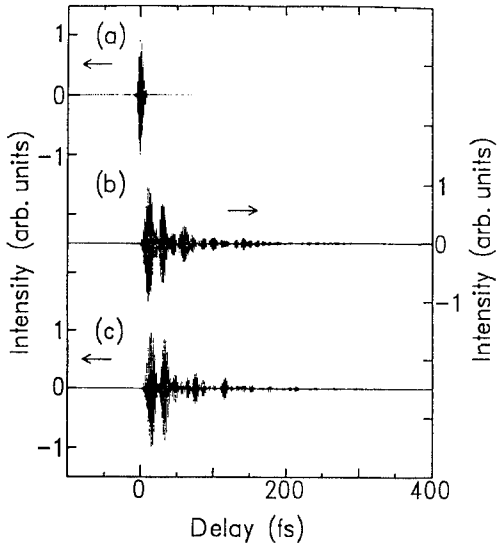


Fig. 2. The interferograms obtained by the Michelson-type interferometer. (a) The autocorrelation. (b) The cross-correlation. (c) The simulated wave form for the cross-correlation.

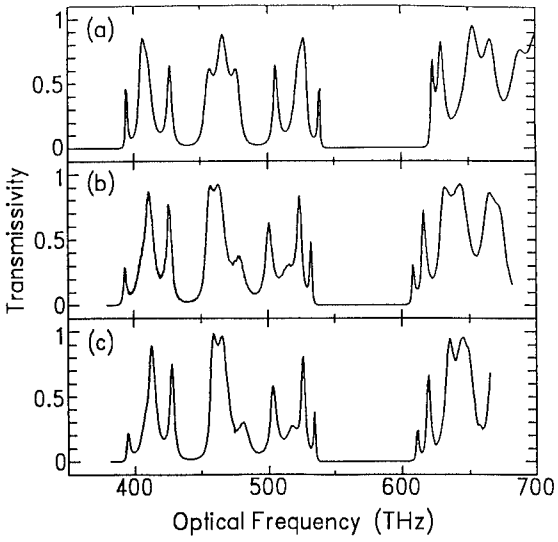


Fig. 3. The transmission spectrum of the sample obtained by (a) calculation based on an ideal Fibonacci lattice, (b) using a monochromator, and (c) Fourier transformation of the interferograms.

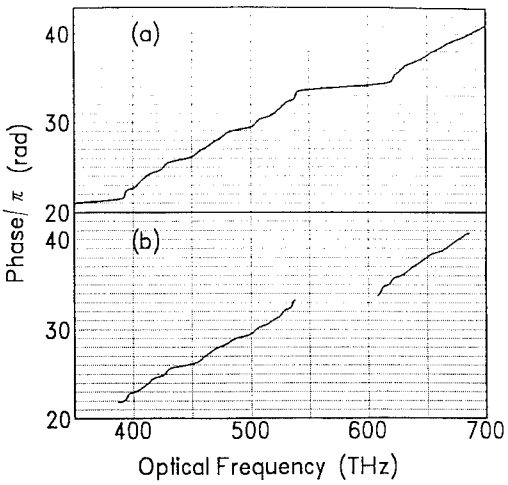


Fig. 4. The phase change of the light transmitted through the S9 Fibonacci lattice obtained by (a) theoretical calculation, and (b) the Fourier-transform interferometry.

Time-Resolved Optoelectronic Measurements of Nitrogen-Implanted GaAs Crystals

S. Hong*, Y. Jin, G. Wagoner, and X.-C. Zhang

Physics Department
Rensselaer Polytechnic Institute
Troy, NY 12180-3590 USA
Tel: (518) 276-3079
Fax: (518) 276-6680
E-mail: zhangx2@rpi.edu

and

L. Kingsley

Pulse Power Center
Army Research Laboratory
Ft Monmouth, NJ 07703
Tel: (908) 544-2895
Fax: (908) 542-3348
E-mail: kingsley@monmouth-etdl1.army.mil

Understanding the effects of electrochemical passivation on the electronic properties of semiconductor surface states is crucial to semiconductor device fabrication. Previous results indicated that the static electric field across the surface of a semiconductor is substantially modified by hydrogen plasma passivation. As an example, after 30 minutes of passivation, the surface field from n(p)-type GaAs samples has been shown to increase by up to a factor of 2(10). Herein, we report the results of our recent measurements of the transient optoelectronic properties of nitrogen-ion implanted GaAs, where the nitrogen ions served as isoelectronic centers and surface implantation densities ranged from $1x10^8$ cm^{-2} to $5x10^{15}$ cm^{-2}. Optically induced THz electromagnetic radiation and time-resolved photoreflectance ($\Delta R/R$) measurements were made and the results of these two different optoelectronic techniques was compared. Both measurements show strong dependence on implantation density and either technique is a good diagnostic of surface implantation density.

GaAs substrates were cleaved from a single semi-insulating GaAs wafer. The measured resistivity and steady state mobility were over 10^7 Ω·cm and 4,000 $cm^2 \cdot V^{-1} \cdot s^{-1}$, respectively. The substrates were then implanted with nitrogen ions. One GaAs substrate remained unimplanted and served as a reference sample. The implantation was performed on a Varian 350R Medium-Energy & Medium-Current ion implanter. The beam current ranged from 0.18 μA to 100 μA, increasing proportionally with dose level. The typical sample temperature was kept below 80 °C and no annealing was performed after ion-implantation. The energy of the incident nitrogen ions was set at 180 keV. Nitrogen ion surface densities ranged from

---

* Present Address: Institute of Semiconductors, Chinese Academy of Sciences, Beijing, China.

$1x10^{8}$ cm^{-2} to $5x10^{15}$ cm^{-2}, with incremental steps alternating between a factor of 2 and 5 successively. The mean value of the damage depth in the samples was approximately 0.6 μm which is comparable to the optical absorption length (α^{-1} = 0.7 μm at λ = 810 nm).

The optical source was a mode-locked Ti:sapphire laser, operating at a central wavelength of 810 nm. During the measurement of optically-induced THz radiation emitted from the wafers, the waist of the normally-incident, unfocused optical beam was approximately 4 mm. Further, the wafers were subjected to an external magnetic field of roughly 0.3 Tesla, which was perpendicular to the direction of optical propagation and was applied via pair of permanent magnets. The forward THz radiation was detected by an ultrafast photoconducting antenna. In the time-resolved photoreflectance experiment (pump / probe), the laser beam was focused to spot size of approximately 100 μm. Both experiments were performed at room temperature.

Because the unimplanted GaAs wafer was slightly n-type, the direction of its surface depletion field was outward. However, since nitrogen ions are an isoelectronic element for GaAs, after implantation, the field direction reversed. The THz radiation waveforms emitted from a GaAs wafer prior to, and after implantation at $5x10^{11}$ cm^{-2} are shown in Fig. 1. The observed polarity flip is associated with a reversal in the direction of the surface depletion field. Fig. 2 displays THz radiation waveforms from several ion-implanted samples with implantation surface densities ranging from $5x10^{11}$ cm^{-2} to $5x10^{14}$ cm^{-2}.

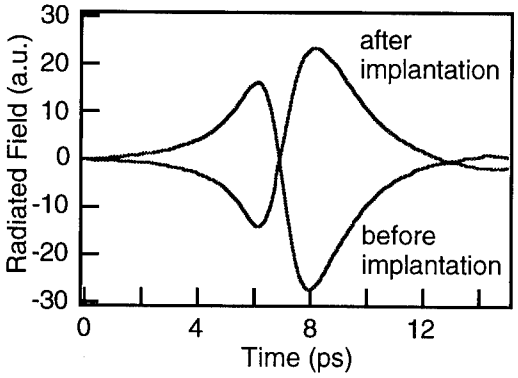


Fig. 1

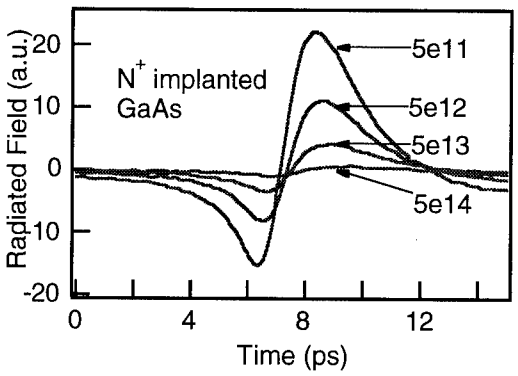


Fig. 2

Fig. 3 plots the amplitude of THz radiation versus ion dose level. THz signal decreases as surface implantation density increases.

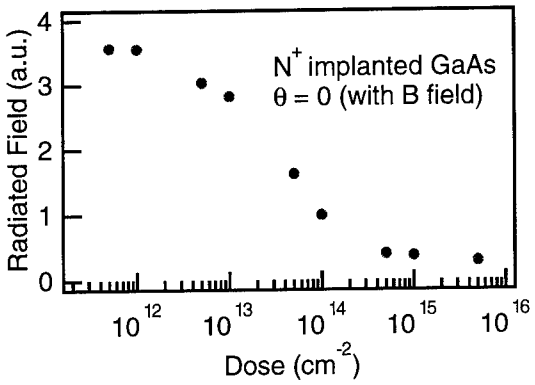


Fig. 3

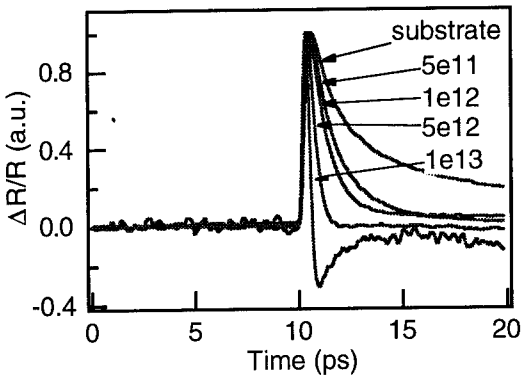


Fig. 4

Fig. 4 shows normalized temporal waveforms of modulated photoreflectance signals, ($\Delta R/R$) from both implanted and unimplanted samples. Corresponding with increased implantation density, is a significant decrease in the $\Delta R/R$ waveform decay time. For samples with ion dose levels greater than $1x10^{13}$ cm^{-2}, decay times as short as 0.35 ps have been observed.

Fig. 5 plots the peak values of the photoreflectance signal versus implant density. From samples with implant densities greater than 10^{14} cm^{-2}, we observe a sign change in the peak value of the photoreflectance signal.

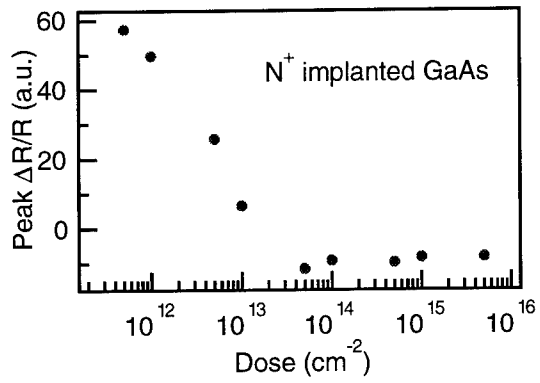


Fig. 5

In summary, we report the measurement and comparison of optically induced THz radiation and time-resolved photoreflectance from nitrogen-ion implanted GaAs samples.

This research was supported by NSF.

Highly efficient second harmonic generation of ultra-intense Nd:glass laser pulses

G. Korn, C.Y. Chien, J.S. Coe, J. Squier and G. Mourou

Center for Ultrafast Optical Science, University of Michigan

2200 Bonisteel, IST Bldg., Room 1006, Ann Arbor, MI 48109-2099

Tel: (313) 763-4875 Fax: (313) 763-4876

R. S. Craxton

Laboratory for Laser Energetics, University of Rochester

250 East River Road, Rochester, NY 14623-1299

Tel: (716) 275-5101 Fax: (716) 275-5960

J.C. Kieffer

INRS-Energie et Matériaux

1650 Montée Ste-Julie, Varennes, Québec, Canada J3X 1S2

Tel: (514) 449-8123 Fax: (514) 449-8102

The technique of chirped pulse amplification (CPA) [1] has been successfully used to generate peak laser powers well beyond the terawatt region [2-4]. These subpicosecond laser pulses when focused can produce intensities exceeding 10^{18} W/cm^2, thus giving access to new regimes of laser-matter interaction. Second harmonic generation (SHG) in nonlinear crystals is important because it extends the available wavelength range and significantly improves the contrast ratio. This is an important issue for high density laser-

plasma experiments in which the fs-laser radiation should interact with the solid rather than with a pre-formed plasma.

We have investigated both Type I and Type II second harmonic generation (SHG) in KDP crystals using our terawatt Nd:glass laser system [2]. In these experiments the laser system delivered energies up to 1.5 J with a pulse duration of 400 fs (FWHM) and a beam diameter (at half maximum) of 2.6 cm. The energy conversion efficiencies of SHG for both Type I and Type II have been studied as functions of the laser intensity, angular mismatch and polarization tuning. With input intensities up to several hundreds of GW/cm^2 on the crystal, more than an order of magnitude higher than previously reported, we have found conversion efficiencies as high as 70%-85% with no obvious damage to the crystals.

Conversion efficiencies of SHG using a 4-mm Type I crystal are shown in Fig.1 together with numerical simulations of the code MIXER [5] . Overall efficiencies of order 80% have been obtained for intensities in the range 200-500 GW/cm^2 . The shift between the theoretical curve and the experimental data points at the lower intensities might be explained by an slightly overestimated intensity in the fundamental wave. At the higher intensities where predicted sensitivity to phase mismatch is greater, the data lie above the calculated curve for 200 μrad detuning, suggesting that nonlinear mismatch induced by the high laser intensities is not a significant concern.

We have also investigated the predelay scheme suggested by Wang [6] using a Type II, 4-mm KD*P predelay crystal followed by a 5-mm, Type II KDP doubling crystal. This shows a 70% conversion efficiency at 80 GW/cm^2. The intensity and polarization dependence of the predelay scheme generally matches the computer predictions very well. The computer simulations also show a strong green pulsewidth shortening (from 400 fs to 67 fs) at 90 GW/cm^2 with 0.5% side-lobe intensity contrast. First single-shot autocorrelation measurements of the green pulses show some pulse shortening, but less than predicted. The shortest pulses obtained to date have a width of 170 fs (assuming a sech^2 pulse shape). The pulsewidth measurements need further investigation.

The green pulses generated with the Type I crystal have been focused with an off-axis parabola to intensities up to $4x10^{18}W/cm^2$ on solid aluminum and tantalum targets. The keV x-ray spectra show that plasmas with electron densities of $3x10^{23}cm^{-3}$ have been produced, indicating the interaction of high contrast green pulses with the solid. This is necessary for the creation of ultrashort high brightness x-ray bursts [7], [8].

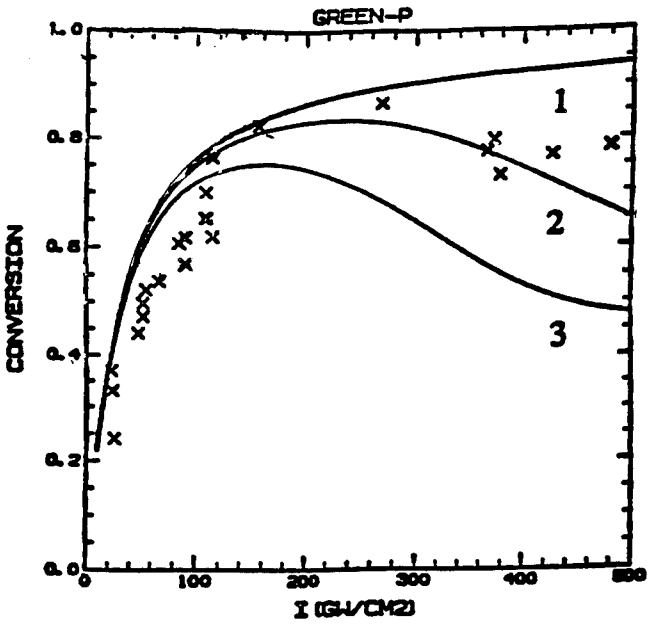


Fig.1
Conversion efficiency as a function of the input intensity. Solid lines: theory for a 0, 200, 400 μrad mismatch (curves 1, 2, 3 respectively)

References:

[1] P. Maine, D. Strickland, P. Bado, M. Pessot, and G. Mourou, IEEE J. Quantum Electron. **24** , 398 (1988).
[2] F.G. Patterson, R. Gonzales, and M.D. Perry, Opt. Lett. **16**, 1107 (1991).
[3] Y. Beaudoin, C.Y. Chien, J.S. Coe, J.L. Tapié, and G. Mourou, Opt. Lett. **17**, 865 (1992).
[4] C. Rouyer, É. Mazataud, I. Allais, A. Pierre, S. Seznec, C. Sauteret, G. Mourou, and A. Migus, Opt. Lett. **18**, 214 (1993).
[5] R.S. Craxton, IEEE J. Quantum Electron. **QE-17**, 1771 (1981).
[6] Y. Wang and R. Dragila, Phys. Rev. A **41**, 5645 (1990).
[7] J. C.Kieffer, M. Chaker, J.P. Matte, H. Pepin, C. Y. Cote, Y. Beaudoin, C.Y. Chien, S. Coe, and G. Mourou, Phys. Fluids **5** , 2676 (1993).
[8] M.M. Murnane, H.C. Kapteyne, and R.W. Falcone, Phys. Rev. Lett. **62**, 155 (1989).

Acknolwledgments:

This work was supported by the National Science Foundation trough the Center for Ultrafast Optical Science under STC PHY 8920108 and by the U.S. Department of Energy Office of Inertial Confinement Fusion under Cooperative Agreement No. DE-FC03-92SF19460, the University of Rochester, and the NEW YORK State Energy Research and Development Authority. The Support of DOE does not constitute an endorsement by DOE of the views expressed in this article.

Femtosecond Switching of the Solid-State Phase Transition in VO_2

Michael F. Becker, A. Bruce Buckman, and Rodger M. Walser

The University of Texas at Austin
Laboratory for Smart Materials and Devices
Electrical and Computer Engineering Department
Austin, Texas 78712 U. S. A. (512) 471-6995

Thierry Lépine, Patrick Georges, and Alain Brun

Institut d'Optique Théorique et Appliquée
Unité de Recherche Associée au C. N. R. S. No. 14
Université Paris-Sud, B.P. 147
91403 Orsay, FRANCE

We have measured the transient change in the optical parameters of VO_2 thin films for laser excitation through the first-order phase transition near 68° C. Femtosecond laser excitation at 780 nm from an amplified, passively modelocked Ti:sapphire laser was used in a pulse-probe configuration to excite the VO_2 film through the semiconducting to metallic phase transition. The transient reflection and transmission were measured on a femtosecond and picosecond time range by a delayed probe pulse also at 780 nm. We have transformed the raw measurements of dynamic reflection and transmission to complex refractive index using a thin film model.

The motivation for these experiments derives from the widespread use of VO_2 films in various smart systems that require fast switching speeds. Examples include agile mirrors for infrared lasers,[1,2] elements in active microwave networks,[3] optical data storage media,[4,5] and flash protection devices. The speed of switching and the values of parameters such as n and k are needed for the design of these VO_2 film devices.

The first attempt to measure the switching speed of the optically induced VO_2 phase transition was made by Roach and Balberg[6] using 20 ns ruby laser pulses at 694 nm as the excitation source and a cw HeNe laser as the probe. They found the transition to be faster than their experimental resolution with 20 ns pulses. Subsequently, Becker[7] and Walser[8] conducted the first pump-probe measurements on the VO_2 phase transition using 30 ps pulses from a mode-locked Nd:YAG laser, exciting and probing at 1064 nm. Again, the transition was abrupt and proved to be faster than the experimental resolution. In the experiments reported here, we extend the VO_2 phase transition measurement resolution down to the femtosecond time scale.

We have recently demonstrated the capability to deposit VO_2 films using a sputtering process with a maximum process temperature of only 290° C.[9,10] In summary, the process involved sputtering vanadium in an oxygen-hydrogen-argon plasma at a temperature <250°C, followed by annealing in a static nitrogen atmosphere at a temperature ≥ 290° C. The films were verified to be polycrystalline, stoichiometric VO_2 by TEM/TED and x-ray analyses. The electrical resistivity and optical transmission and reflection spectra were identical to those for conventionally processed VO_2 films. During the transient optical experiments, the film was held just below the phase transition onset temperature, between 39 and 41° C, by an electrically heated and insulated substrate holder with an embedded thermistor. The films used in our experiments were deposited on a glass

microscope slides and were 31 nm thick. The film thickness was determined by fitting the measured transmission and reflection of the semiconducting state versus wavelength from 500 to 2000 nm to that calculated by a thin-film model using reported values for the complex permittivity of a VO_2 thin film.[11]

The optical setup used to conduct the pulse-probe measurements was a relatively conventional pump-probe configuration. The laser source was a cw passively modelocked Ti:sapphire laser at 780 nm wavelength with a regenerative amplifier operating at 20 Hz and a grating pulse compressor.[12] The pulsewidth was measured by zero-background sum frequency generation in the sample plane and was in the range of 450 to 550 fs FWHM (assuming a sech pulse amplitude profile). The slower behavior of reflection and transmission for nanosecond and longer times was measured using a cw HeNe laser at 633 nm and a fast photodiode. The femtosecond probe beam and the cw HeNe beam diameters at the sample plane were adjusted to be less that one-third of the pump beam diameter. The pump beam fluence was adjusted to be just sufficient to excite the complete phase transition, 3.7 mJ/cm^2 at the sample plane. Data for transmission and reflection were first corrected for the probe pulse behavior with the pump beam blocked and then fit at large negative time delay to the transmission and reflection measured by the spectrometer at 780 nm.

Conversion of the data to a refractive index format was done using a thin-film model for the VO_2 film and substrate. A coherent reflection was assumed from the film-substrate interface, and an incoherent reflection was assumed for the substrate rear interface. A numerical solver routine was used to obtain a best fit value of n and k for each delay time given the measured values of transmission and reflection. The same thin-film model had been used earlier to obtain the film thickness based on the transmission and reflection spectra of the semiconducting state. The data for complex refractive index, $\tilde{n} = n - jk$, are shown in Fig. 1.

From Fig. 1 one sees that the complex refractive index reached or exceeded its high temperature (metallic) value within 5 ps. The real part of the refractive index, n, decreased just over halfway to the metallic value by the end of the 500 fs excitation pulse. It then decreased more slowly to equal steady-state metallic value by 5 ps. On the other hand, the imaginary part of the part of the refractive index, k, reached 100% of the metallic value by the end of the excitation laser pulse and overshot by 36% at 7 ps. After smaller fluctuations, both n and k had reached their final values by 300 ps. If the laser energy was not in excess of that required for the phase transition, decay back to the semiconducting state was observed on a nanosecond time scale consistent with heat conduction to the substrate. The observed transient change at 300 ps was equal to the change caused by an increase in the temperature through the phase transition. This was determined by heating the sample through the phase transition while monitoring the nanosecond and static optical parameters with the cw HeNe laser. Our results can be easily generalized to the near IR and visible spectral regions. One can reasonably expect the VO_2 film to switch in 5 ps between the semiconducting and metallic transmission and reflection spectra for the visible and near IR. Whether the same applies to the IR and microwave spectral regions depends on whether the VO_2 film truly has reached the high-temperature metallic phase in 5 ps. Such questions of alternative states and the fraction of transition to the metallic state raise questions regarding the physics of the transition dynamics. We plan to address some of these aspects in future publicationsFig. 1. Complex index of refraction for a VO_2 film versus time derived from the measured data in Fig. 4 for two time scales: (a.) -50 to 400 ps and (b.) -5 to 15 ps.

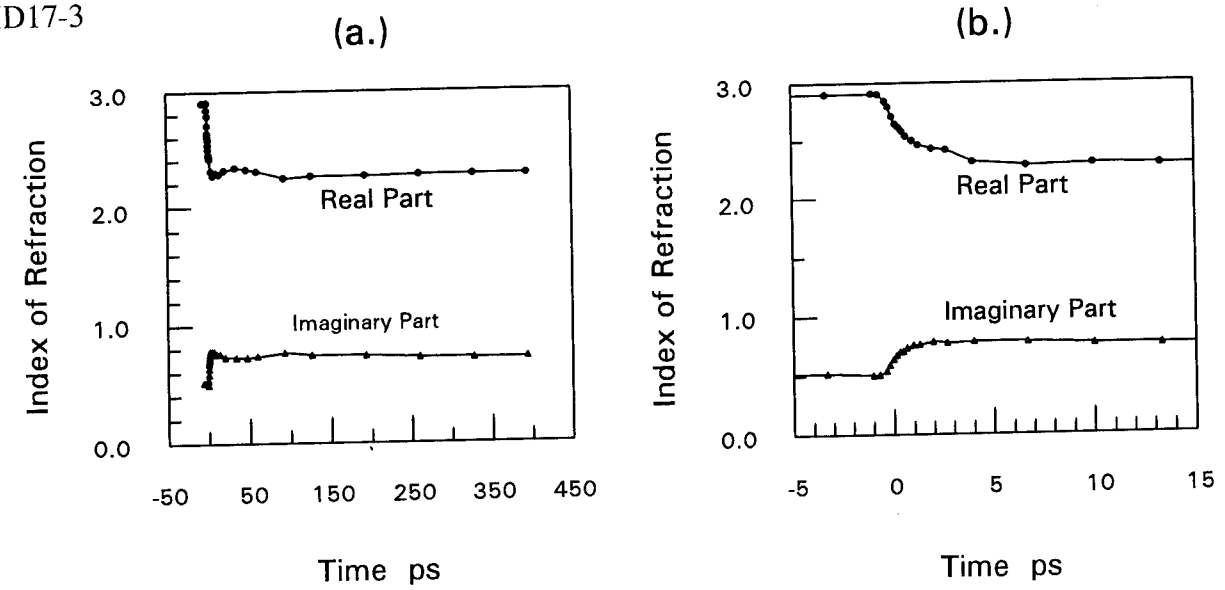


Fig. 1. Complex index of refraction for a VO_2 film versus time derived from the measured data in Fig. 4 for two time scales: (a.) -50 to 400 ps and (b.) -5 to 15 ps.

M. F. Becker acknowledges partial support from the University Research Institute at The University of Texas and from the University of Paris 11, Faculty of Physics. The VO_2 samples were fabricated under the sponsorship of the Energy Research in Applications Program of the Texas Higher Education Coordinating Board.

[1] J. S. Chivian, W. E. Case, and D. H. Rester, "A 10.6 μm scan laser with programmable VO_2 mirror," IEEE J. Quant. Elect. **QE-15**, 1326-1328, 1979.

[2] J. S. Chivian, M. W. Scott, W. E. Case, and N. J. Krausutsky, "An improved scan laser with a VO_2 programmable mirror," IEEE J. Quant. Elect. **QE-21**, 383-390, 1985.

[3] J. C. C. Fan, H. R. Fetterman, F. J. Bachner, P. M. Zavraky, and C. D. Parker, "Thin-film VO_2 submillimeter-wave modulators and polarizers," Appl. Phys. Lett. **31**, 11-13, 1977.

[4] A. W. Smith, "Optical storage in VO_2 films," Appl. Phys. Lett. **23**, 437-438, 1973.

[5] M. Fukuma, S. Zembutsu, and S. Miyazawa, "Preparation of VO_2 thin film and its direct optical bit recording characteristics," Appl. Opt. **22**, 265-268, 1983.

[6] W. R. Roach and I. Balberg, "Optical induction and detection of fast phase transition in VO_2," Solid State Comm. **9**, 551-555, 1971.

[7] M. F. Becker, R. M. Walser, and R. W. Gunn, "Fast laser excitations in VO_2 at the semiconducting-metallic phase transition, in *Picosecond Phenomena*, Shank, Ippen and Shapiro eds., 236-239, Springer-Verlag, New York, 1978.

[8] R. M. Walser and M. F. Becker, "Fast laser kinetic studies of the semiconductor-metal phase transition in VO_2 thin films," in *Laser-Solid Interactions and Laser Processing-1978 MRS Conference*, Ferris, Leamy, and Poate eds., 117-122, American Institute of Physics, New York, 1979.

[9] R. M. Walser, H. C. Joung, M. F. Becker, R. W. Bene, and A. B. Buckman, "Process compatible thermochromic films for smart thermal control materials," *SPIE Symposium on Smart Structures and Materials '93*, Albuquerque, N.M., February 1993.

[10] R. M. Walser, H. C. Joung, M. F. Becker, and A. P. Valanju, "Low-temperature vanadium dioxide thin film process," submitted to Appl. Phys. Lett., 1994.

[11] H. W. Verleur, A. S. Barker, Jr., and C. N. Berglund, "Optical Properties of VO_2 between 0.25 and 5 ev," Phys. Rev. **172**, 788-798, 1968.

[12] D. Strickland and G. Mourou, "Compression of amplified chirped optical pulses," Opt. Comm. **56**, 219-221, 1985.

Ultrafast Dynamics as reflected in MPI-photoelectron spectra: Aniline, Azulene, Phenanthrene and Carbon disulfide

N. Thantu, B. Kim and P. M. Weber
Department of Chemistry, Brown University, Providence, RI 02912; (401) 863-3767

Very short lived resonances can cause unobservably small yields of resonant multiphoton ionization (MPI) processes, and severely alter the photofragmentation pattern of the resulting ions.[1] These effects, which are frequently observed when using high lying electronic states of medium size or large molecules, are usually interpreted as a consequence of fast intramolecular processes such as internal conversion (IC), intersystem crossing (ISC), Intramolecular Vibrational redistribution (IVR) or Photodissociation. In the present paper we investigate the interplay of such dynamical phenomena with the laser pulse characteristics. To illustrate the range of possible effects we investigated the photoionization of aniline ($C_6H_5NH_2$), phenanthrene ($C_{14}H_{10}$), azulene($C_{10}H_8$) and carbon disulfide (CS_2).

The spectroscopic technique chosen for our experiments is two-photon ionization coupled with photoelectron spectroscopy. The molecules are seeded in helium carrier gas and expanded in a molecular beam.[2] Molecules are ionized by two UV laser photons originating in a mode-locked, cavity dumped dye laser system. The photoelectron spectra are recorded with a microchannel plate coupled to standard time resolved single particle counting electronics, and converted to an energy scale using the methodology developed by Baer et al.[3,4]

Aniline: The photoelectron spectrum of aniline (Figure 1) is obtained by ionizing the molecule with two photons of a single laser pulse tuned to the S_1 origin at 293.8 nm. The laser bandwidth of the 7 ps pulse is sufficiently large to span the entire width of the resonant absorption feature, which is about 10^{-3} cm^{-1}. The laser pulse therefore prepares a molecular state that closely resembles the S_1 zero-order Born-Oppenheimer state. As expected, the photoelectron spectrum shows a vibrational structure that reflects ionization out of the pure S_1 electronic state.

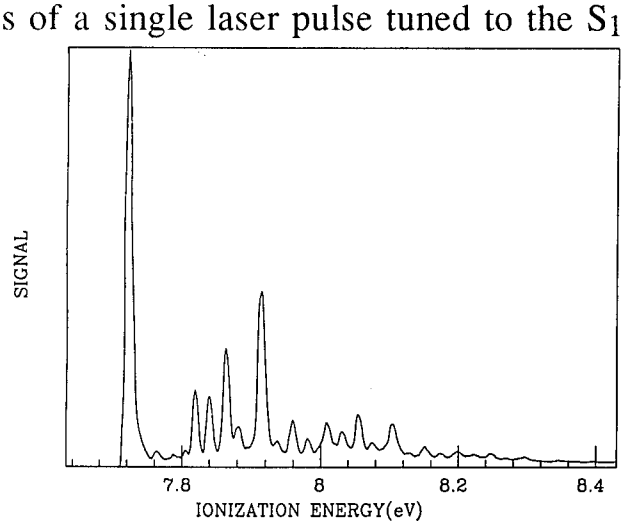


Figure 1

Phenanthrene: Phenanthrene exhibits a short lived resonance at 282.7 nm that is assigned to the S_2 electronic state. The two-photon ionization photoelectron spectrum obtained using this state as an intermediate resonance is displayed in figure 2. In addition to the signal at 7.9 eV that corresponds to ionization out of the S_2 origin the spectrum reveals an additional feature at 8.65 eV that can be traced to ionization out of the lower lying S_1 state. The appearance of the broad peak is explained as follows: the molecular absorption width exceeds with 13 cm^{-1} the bandwidth of the transform limited laser pulse, which in this case amounts to 2.5 cm^{-1}. The laser therefore does not coherently couple all the eigenstates that make up the zero order S_2 state. The intermediate resonant state that is prepared by the laser is thus an unspecified molecular state composed of both S_2 and the lower S_1 electronic state. The photoelectron spectrum reflects the relative contents of these two electronic states, weighted by their respective ionization cross section.

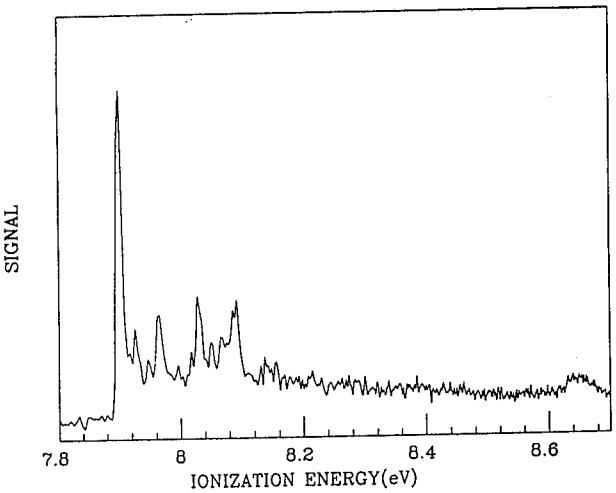


Figure 2

Azulene: The photoelectron spectrum of azulene, ionized via its S_3 electronic state, is reproduced in figure 3. The S_3 state has a spectral width of 140 cm^{-1}, which indicates a lifetime of about 35 fs. The absorption width of azulene greatly exceeds the bandwidth of the picosecond dye laser. Following the argument advanced above the laser should now prepare a state that contains very little character of the bright S_3 electronic state, and a rather large fraction of the lower electronic state that couples to the S_3 state. The photoelectron spectrum of figure 3 is consistent with this picture: the signal at 7.42 eV corresponding to ionization out of S_3 is exceedingly small. The spectrum is dominated by a broad peak at 8.12 eV that is identified as ionization out of the S_2 electronic manifold.

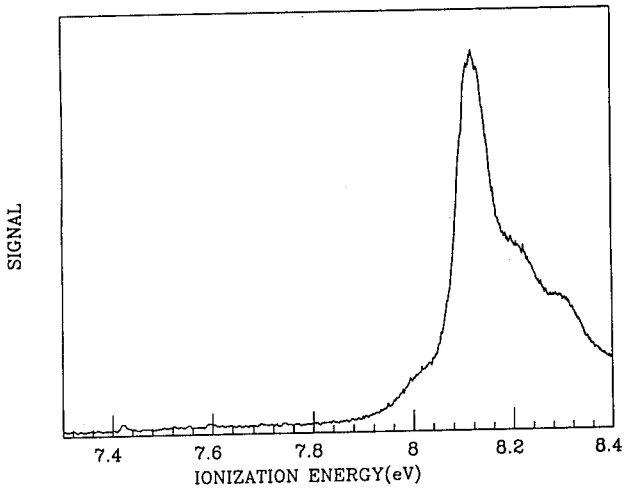


Figure 3

Carbon Disulfide: While the previous examples illustrate the effect of rapid internal conversion processes on the two-photon ionization, the next case involves vibrational predissociation. CS_2 is excited by a 199.8 nm photon to the S_3 electronic state which is known to dissociate on a picosecond timescale.[5] Ionization can be induced by either a second photon of the same laser pulse, or by another pulse derived from a second dye laser. The photoelectron spectrum displayed in figure 4, obtained in the latter fashion, shows extensive vibrational structure of the molecular ion. Based on the symmetry of the intermediate resonance and the molecular ion one should expect vibrational activity only in the symmetric stretch and bend vibrations. However, a detailed analysis of the two-photon ionization spectrum reveals significant progressions of antisymmetric stretch vibrations. We interpret these vibrational bands as arising from antisymmetric stretch states of the S_3 manifold that are populated by intramolecular vibrational redistribution. The vibrational density of states at the investigated region is with 0.5 cm too low to support fast IVR. However, the lacking density of states can be contributed by the dissociation continuum. The two-photon ionization spectrum therefore appears to catch the molecule in the process of dissociation. We note that the coordinate that receives population as a consequence of the vibrational relaxation process, the antisymmetric stretch vibration, is closely related to the reaction coordinate leading from CS_2 to CS + S.

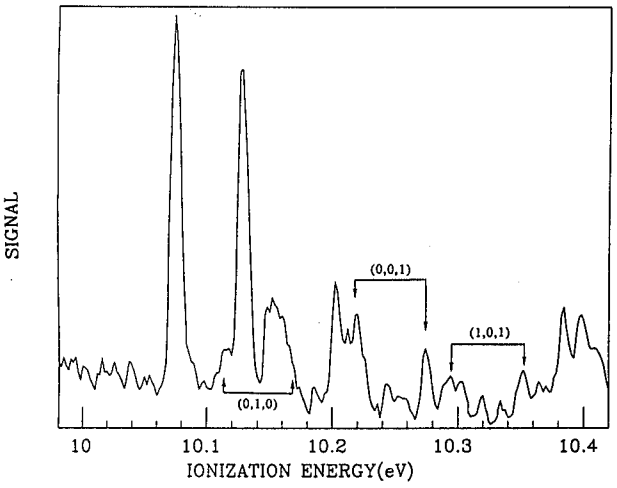


Figure 4

Conclusions

Two-photon ionization photoelectron spectroscopy is a powerful technique to study intramolecular redistribution and dissociation phenomena. The absence of dark states in photoionization paired with a time resolution typical of pump-probe experiments allows unambiguous determinations of all states participating in the molecular dynamical processes. We demonstrate the utility of the technique on a range of molecules chosen to illustrate a variety of molecular relaxation phenomena.

References:

1. D. H. Parker; in "Ultrasensitive Laser Spectroscopy"; *ed.* D. S. Kliger, Acad. Press (1983).
2. B. Kim, N. Thantu and P. M. Weber, *J. Chem. Phys.*, **97**, 5384 (1992).
3. T. Baer, W. B. Peatman and E. W. Schlag, Chem. Phys. Lett. **4**, 243 (1969).
4. P. M. Weber, J. Stanks, N. Thantu and R. Hellmer, *Journal of Vacuum Science and Technology*, **A10**, 408 (1992).
5. I. M. Walker and J. W. Hepburn, *J. Chem. Phys.*, **87**,3263 (1987).

Phase-matching optima for high-order multiwave mixing and harmonic generation beyond perturbation limit

P. L. Shkolnikov, A. E. Kaplan, and A. Lago

Department of Electrical and Computer Engineering
The Johns Hopkins University, Baltimore, MD 21218
Tel. (410)516-7220

High-order optical harmonics generation (HHG) has recently attracted much attention as a possible source of short-wavelength coherent radiation [1]; harmonics of the order up to the 135th and wavelengths as short as 7.6 nm have been observed [2,3]. Conversion efficiency of HHG, however, remains too low for applications, largely due to poor phase matching. Phase-matching optimization could substantially increase the output. The actual experimental conditions, however, are, most likely, very far from optimal. Indeed, reported HHG experiments are conducted in almost dispersionless (gases) or positively dispersive (plasma) media, whereas phase-matching optimization of HHG, at least according to perturbation theory, requires strong negative dispersion, if beam are focused. To avoid this obstacle, another multiphoton process, high-order difference frequency mixing (HDM)

$$\omega = m\omega_1 - l\omega_2 \tag{1}$$

where m, l are integers, $m >> 1$, $m > l$, $\omega_1 > \omega_2$, was suggested for large-scale frequency upconversion in ionized gases [4]. It was shown that the phase matching for a given combination m, l is optimal if

$$b\Delta k/2 \approx -(m-l), \tag{2}$$

where b is the confocal parameter of both beams, Δk is the phase mismatch due to the medium dispersion. For HDM in plasma, Δk is large negative, which may allow one to attain optimal phase matching. This conclusion, however, relied on the perturbation theory; it is unclear whether Eq. (2) would hold beyond perturbation approximation. Unfortunately, the exact dependence of the induced nonlinear polarization on strong pumping fields remains unknown as of now. Moreover, to the best of our knowledge, no model calculations of the dipole moment induced by strong biharmonic pumping, have been published yet. In the present paper we theoretically demonstrate, however, that the optimal phase-matching conditions for both HHG and HDM *does not depend*, to a large extent, on a particular form of this dipole moment, as long as some quite general assumptions are valid. As a result, we expect the conditions for phase-matching optimization, Eq. (2), to remain largely intact in strong pumping fields.

We begin with a particular model suggested in Ref. [5] for phase matching in HHG of a strong field, by stating explicitly the underlying assumptions of the model and by extending it to include other multiwave mixings, Eq. (1) with $l \neq 0$. We consider pumping with lowest-order Gaussian beams propagating along z-axis and focused at $z = 0$ with the same confocal parameters, b (typical situation for most of the experiments), so that the incident field can be written as:

$$E = \tilde{E}_1(r,u)\cos(\omega_1 t + \phi_1) + \tilde{E}_2(r,u)\cos(\omega_2 t + \phi_2) \tag{3}$$
$$\tilde{E}_{1,2}(r,u) = E_{1,2}(1+u^2)^{-1/2}\exp[-k_{1,2}r^2/b(1+u^2)],$$
$$\phi_{1,2} = -k_{1,2}z + \tan^{-1}u - k_{1,2}r^2 u/b(1+u^2),$$

$u = 2z/b$, $r = (x^2+y^2)^{1/2}$, and $k_{1,2}$ are the wavevectors of the pumping beams. Generalizing the model [5], we assume that the Fourier component of the induced nonlinear polarization responsible for high-order difference-frequency mixing, Eq. (1), of strong fields is:

$$P_{m,l} = A_0\, p(\tilde{E}_1, \tilde{E}_2)\exp(i\phi),\ p^* = p, \tag{5}$$

$$\phi = -k'z - (m-l)\tan^{-1}u + uk'r^2/(1+u^2), \quad k' = mk_1 - lk_2,$$

where A_0 contains the nonlinear susceptibility and other factors which do not depend on r,u and, therefore, are irrelevant here. The space-dependent amplitude p is real; in other words, we assume that the *space–dependent* phase of the induced dipole moment is the same, ϕ, for both weak and strong fields (compare with [4]). In contrast to Ref. [5], however, we do not presume any particular expression for the amplitude p; in fact, our conclusions do not depend on such an expression. Instead, it is enough for the amplitude p, Eq. (5), to be a positive, monotonous, rapidly increasing function of E_1, E_2 and, therefore, a rapidly decreasing function of r,u. Consequently, we will neglect contributions to the generated field from the points of a medium that are sufficiently far from the focal point. Then the electric field $\mathcal{E}(r',z')$ generated in a homogeneous medium and observed at a point (r',z') in the far-field area $u' = 2z'/b \gg 1$, $u' \gg u$, can be written as (see e. g. [5]):

$$\mathcal{E}(r',u',M) \sim \int exp(-iMu)\,[F_1(u) + i\,F_2(u)]\,du, \quad M = b\Delta k/2 + (m-l), \tag{6}$$

$$F_1(u) \approx \int dr\, r\, J_0\left(2kr'r/bu'\right) p(r,u)/u', \qquad F_2(u) \approx \int dr\, 2kr^3\, J_0\left(2kr'r/bu'\right) p(r,u)/bu'^2,$$

where J_0 is the ordinary Bessel function of the zeroth order, $\Delta k = k - k'$, $k' = mk_1 - lk_2$, and k is the wavevector of the generated field. It can be shown that for any positive, monotonously decreasing function $\tilde{f}(r)$, $\int_0^{r_0} \tilde{f}(r)\,J_0(ar)dr > 0$ for $a > 0$, $r_0 > 0$. Therefore, $F_{1,2}(u) > 0$ for any u. Now, since $cos(0) \geq cos(Mu)$ for any u and $M \neq 0$, both the real and the imaginary part of $\mathcal{E}$, and, therefore, the generated field amplitude $|\mathcal{E}|$, are maximal if $M = 0$, which corresponds to the optimal phase matching of HDM in perturbation theory, Eq. (2).

Now, the question is under what conditions the assumption, Eq. (4), together with the assumed monotonous behavior of p, can be justified. First of all, Eq. (4) is valid if the induced nonlinear polarization $P(x,y,z,t)$ is a (continuous) function of the incident field:

$$P(x,y,z,t) = f[E(x,y,z,t)] \tag{7}$$

In other words, we presume here spatial and temporal locality of the induced polarization, as well as non-depletion of the pumping. One may expect Eq. (13) to hold for the pumping pulses being much longer that the relaxation times of the nonlinear media; pumping frequencies being far from any resonances; and the generated field being so weak that the induced polarization is largely determined by the pumping field. In the simpler case of the q-th harmonic generation ($l = 0$, $m = q$) with a monochromatic pumping field, $f = f(E)$ is periodical in time with the period $2\pi/\omega$, so that $P_{q\omega} = \frac{\omega}{\pi}\int_{-\pi/\omega}^{\pi/\omega} dt\, f\{\tilde{E}_1 \exp[i(\omega t + \phi)]\} \exp(iq\omega) = p\,\exp(-iq\phi), \quad p = p^*$. With two pumping frequencies, ω_1 and ω_2, there is no common "time scale", and the time shift cannot be applied. Instead, we use a well known mathematical result: any continuous on some finite interval function can be approximated on this interval, to any required accuracy, by a weighed sum of orthonormal polynomials. Then it could be shown that $P_{m,l} = p\,\exp[-i(m\phi_1 - l\phi_2)]$, $p = p^* = A_{ml}(E_1, E_2)$.

In real experiments, however, one can hardly expect Eq. (7) to be strictly correct. Consequently, any deviation from Eq. (7) would be reflected in p being a complex, and not real, function with an intensity-dependent (and, therefore, coordinate-dependent) phase $\Psi(|E_1|^2, |E_2|^2)$. Nevertheless, if this phase is a *slow–varying* function of the intensity, one may neglect it in Eq. (8). Then, if also $|p|$ decreases with $|E_1|$ rapidly and monotonously, Eq. (12) can still hold. Due to the present lack of calculations of the single-atom response to strong biharmonic pumping, we may try to verify these assumptions only for HHG. The three models of HHG [6,7,8] that have been most successfully compared with experimental data, seem to show slow variation of the phase Ψ for the most intensity domains. Indeed, the intensity-dependent phase of the dipole moment of the 51st harmonic, calculated in Ref. [3] according to the model [7], changes only by $\sim\pi/3$ if the pumping amplitude changes by 15%

(that is, within the interval of interest, $|u| = 0$–0.6), whereas the change of the geometrical phase qu is $0.6q$ on the same interval, which for large q is much larger than $\pi/3$. Although published results of a numerical model developed in LLNL/Saclay (see e. g.. [8]) do not include Ψ explicitly, in all the theoretical considerations this phase is assumed to be constant (see e. g. [9]), or at least not to interfere strongly with phase matching [5]. Finally, the non-perturbative two-level model of HHG [6] predicts the intensity-dependent phase which is almost constant between the intensity-induced resonances, and experiences a jump by π at such resonances; obviously, such behavior allows one to neglect this phase in Eq. (6).

As to $|p|$, in Ref. [3], as well as in the simplified quantum-mechanical model published recently [10], it behaves in a desirable manner up to the cutoff intensity. On the other hand, in the both LLNL/Saclay [8] and the two-level [6] models, $|p|$ experiences sharp resonance-like jumps, so that within some intervals of the incident intensity it may even be a decreasing function. Such intervals, however, are relatively small, so that for most values of the pumping intensity, and on average, the amplitude of the dipole moment *is* a monotonous and rapidly increasing function of the pumping intensity, in accordance with experimental dependence of the output on the incident field. Moreover, in all the experiments on HHG and HDM, the pumping field is in a form of a pulse, so that its intensity at any given point changes in time. Obviously, for most of the pulse duration, we should expect p to be smaller at the points in space where the pumping intensity is lower. To the best of our knowledge, no calculations of the amplitude and phase of the induced dipole moment in HDM have been published yet. If our general assumptions hold also for this process, the optimal phase-matching conditions, Eq. (2), calculated in Ref. [5] within the perturbation-theory limit, would present a quite accurate approximation for nonperturbative HDM as well.

In conclusion, we have demonstrated that optimal phase-matching conditions for high-order harmonic generation and high-order difference-frequency mixing of weak fields remain largely intact beyond the perturbation limit under quite broad assumptions regarding nonlinear polarization. It allows one to use safely perturbative phase-matching conditions for both HHG and HDM in strong fields.

This work is supported by AFOSR; A. Lago (on sabbatical leave from UFSC, Brazil) is supported by CNPq of Brazil.

References

1 A. McPherson *et al* , JOSA B 4, 595 (1987); M. Ferray *et al* , J. Phys. B 21, L31 (1988).

2 A. L'Huillier and Ph. Balcou, Phys. Rev. Lett. 70, 774 (1993).

3 J. J. Macklin, J. D. Kmetec, and C. L. Gordon III, Phys. Rev. Lett. 70, 766 (1993).

4 P. L. Shkolnikov, A. E. Kaplan, and A. Lago, Opt. Lett. 18, 1700 (1993).

5 A. L'Huillier *et al* , in *Atoms in Intense Laser Field* , Ed. M. Gavrila (Acad. Press, Inc., Boston, 1992), p.139.

6 A. E. Kaplan and P. L. Shkolnikov, to appear in Phys. Rev. A.

7 W. Becker, S. Long, and J. K. McIver, Phys. Rev. A 41, 4112 (1990).

8 A. L'Huillier *et al* , Phys. Rev. A 46, 2778 (1992).

9 A. L'Huillier, Ph. Balcou, and L. A. Lompre, Phys. Rev. Lett. 68, 166 (1992).

10 A. L'Huillier *et al* , Phys. Rev. A 48, R3433 (1993).

FEMTOSECOND EXCITON DYNAMICS IN POLYANILINE AND POLYANILINE -POLYMETHYL MATHACRYLATE

Wei-Zhu Lin , Hui Wang , Tian-Shu Lai , and Dong Mo

(Department of Physics, Zhongshan University , Guangzhou, 510275, China)

Yang-Meng Ou and Ke-Cheng Gong

(Department of Chemistry, Technology University of South China , Guangzhou , 510641)

Polyaniline (PAn) and derivatives have been again the subject of great interest owning to the larger nonlinearity , easy fabrication and its excellent stability under ambient condition in comparison with other families of conducting polymer. Photoinduced absorption and bleaching in PAn have been observed and attributed to the existence of localized molecular excitons and polaron pairs.[1,2] For nonlinear optical device applications , the dynamics of the nonlinearity response is the important aspect of the polymer properties which in PAn and derivatives , however, has not been investigated intensively. In this paper we report femtosecond absorption saturation studies on exciton dynamics in PAn and polyaniline-polymethyl mathacrylate (PAn-PMMA) blend films for the first time. Time-resolved absorption traces show significant different excitonic dynamics in these two polymers . In PAn a initial ultrafast absorption saturation recovery is observed . In PAn-PMMA pump-probe trace shows an efficient two-photon absorption . We present a brief discussion on these ultrafast phenomena and predict their potential applications in optics.

Time-resolved absorption saturation measurements are performed using a typical pump-probe setup and a femtosecond pulse train which is generated from a colliding pulse mode-locked dye laser (CPM) and has a repetition rate of 110 MHz , pulse width of ~ 50 fs, average power of 20 mW, and at 630 nm (~ 2 eV). The PAn sample studied is an emeraldine base (EB) form of PAn . The absorption spectrum of it shows two absorption band centered at ~ 3.8 and ~ 2.0 eV. The absorption band at 3.6 eV arises from benzenoid $\pi - \pi^*$ transition and defines the optical band gap of the material . The broad absorption band at $\sim 2eV$ is assigned to the formation of exciton centered on the quinoid-ring. The pump beam separated from the pulse train is used to excite the molecular excitons of the samples and the dynamics of the exciton deformation is measured by the probe beam delayed with respect to the pump beam.

Fig.1 shows the time-resolved absorption saturation trace of PAn at ~ 2 eV and room temperature. The trace exhibits a rapid decay near zero delay followed by a slow recovery . The coherent coupling artifact, which arises from the parallel polarized pump and probe beam and presents one half of the total signal at zero delay , has been removed from the trace in Fig.1 . With a model of a sum of exponential decay the time constant of the rapid decay is deduced to be $\sim 100fs$. The slow recovery includes a picosecond ($\sim 30ps$) component and a long- lived (nonoseconds) component. This two step (fast and slow) absorption recovery process may describe the relaxation dynamics of the excitons in PAn . The slow process has been observed by Epstein et al. in a picosecond pump-probe experiment in PAn and has been attributed to the excitons decay either through geminate recombination or dissociation into positive and negative carriers [2]. Our measurements suggest that exciton initial relaxation in PAn happens within ~ 100 fs . One possible mechanism responsible for this initial exciton relaxation is the self-trapping because the photoexcited excitons can relax very rapidly into a self-trapped state in gap . Since the self-trapping exciton is regarded as fused polaron (a neutral bipolaron) , the mechanism of self-trapping is expected to be similar to the polaron formation . The induced absorption spectrum of PAn has indicated the generation of photoexcited polarons which induces absorption peaks similar to that observed in the absorption spectrum of protonated PAn (ES form).[2,3] On the basis of multi-phonon transition and one dimension system approximation , Yu et al. have calculated the formation time of a neutral bipolaron to be 100-200 fs and the bipolaron deformation time to be few nonoseconds for the polymers with nondegenerate ground state [4] . The measured two step relaxation process also reflect the polaron formation and deformation dynamics in PAn.

In visible region , PAn has larger optical nonlinearity but lower transmission which limits the application of this material in optics. PAn-PMMA film , however, has been tested as a qualified optical film with higher transmission ($T < 20$ % depending on the fraction of PAn) and a comparable nonlinearity with that of PAn . The absorption spectrum of PAn-PMMA shows a band gap absorption at $\sim 4.9eV$ and a broad shoulder about 2.8 eV which is assigned to exciton generation in this blend film . The pump-probe photon energy is now below the exciton resonant energy , no absorption saturation is expected to observed. The pump-probe trace of PAn-PMMA at 2 eV shown in Fig.2 displays a negative instantaneous response at zero delay consistent with two-photon absorption . As a kind of photoinduced

absorption , the observed two-photon absorption may be attributed to the chain distortion of the polymer under photoexcitation . This distortion is characterized by the appearance of new absorption processes below the band gap. The rapid induced absorption response has been observed in polydiacetylene (PDA) with an exciting photon energy resonant with the exciton and a probe energy below the resonance.[5] . It seems from Fig.2 that chain distortion in PAn-PMMA occurs in a shorter time. The precise nature of the photoinduced chain distortion is necessary to characterized in further studies.

In conclusion, we have studied the dynamics of third-order nonlinear optical response in PAn and PAn-PMMA polymers with femtosecond absorption saturation measurements . In PAn a rapid initial exciton relaxation process with time constant of $\sim 100fs$ is measured . In contrast, in PAn-PMMA blend film an efficient two-photon absorption is observed . The significant different behavior of optical nonlinearity in these two materials reflects the difference in the nonlinearity mechanism . The ultrafast response of the nonlinearities in PAn and PAn-PMMA make the material candidate for applications in high speed optical devices.

References:

[1] N.S. Sariciftci, L. Smilowitz, Y. Cao, and A.J. Heeger,*J.Chem.Phys.* 98, 2684 (1993).

[2] A.J. Epstein, J. M. Ginder, M.G. Roe, T.L. Gustafson, M. Angelofoulos, and A. G. Macdiarmid, *Mat. Res. Soc. Symp. Proc.*, 109, 313 (1988).

[3] Yong-Yao Lin, Dong Mo, Ke-Cheng Gong, and Gui-Ping Zhang, *Atca Physica Sinica (Overseas Edition)*, 2, 816, (1993).

[4] Zhi-Gang Yu, Qing-Feng Huang, and Xin Sun, *Acta Physica Sinica*, 42, 1822 (1993).

[5] J. M. Huxley, P. Mataloni, R.W.Schoenlein, J.G. Fujimoto, E.P. Ippen and G.M. Carter, *Appl. Phys. Lett.*, 56, 1600 (1990).

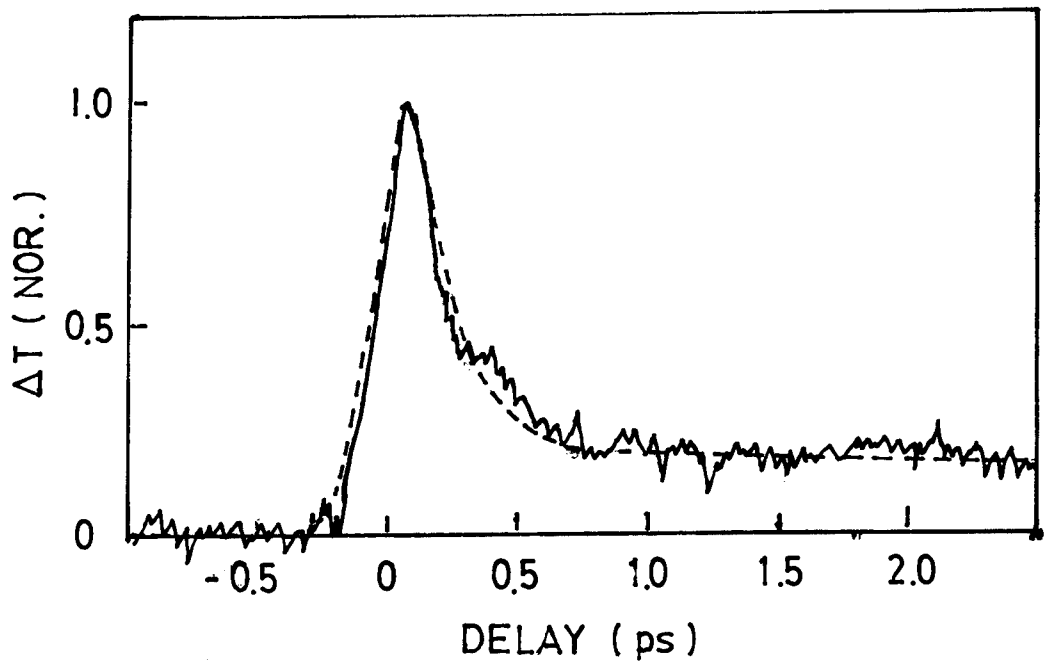


Fig.1 Time-resolved absorption saturation trace of PAn at 2eV. and 300 K. The dashed curve is a theoritical fit.

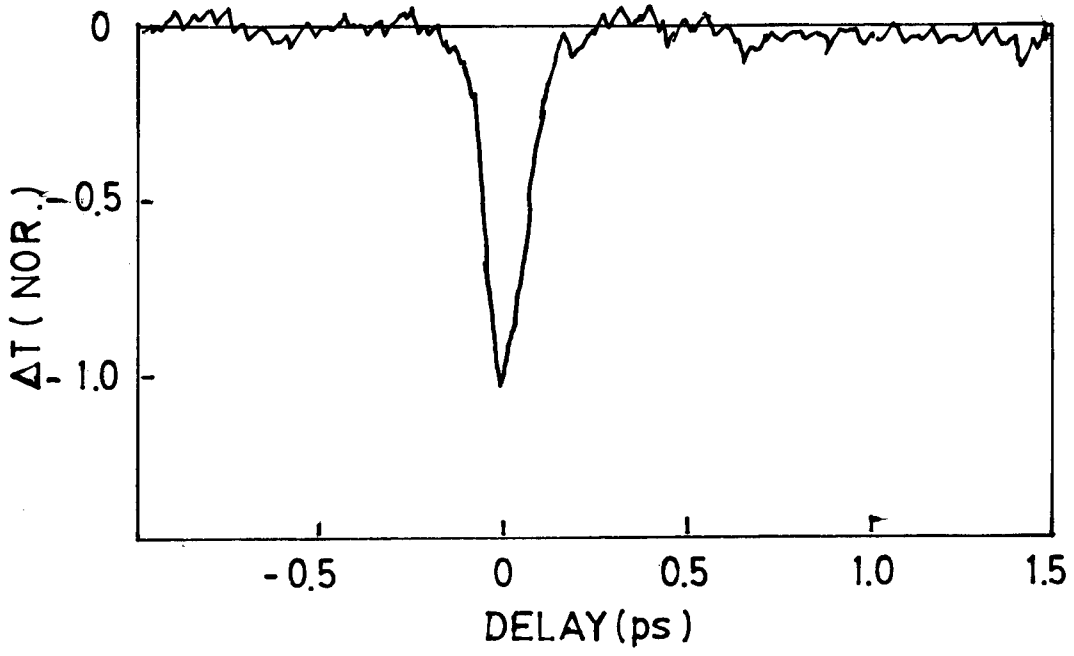


Fig.2 Two photon absorption curve of PAn-PAAM at 2eV and room temperature.

Calculation of photogenerated carrier escape rates from single GaAs / $Al_xGa_{1-x}As$ quantum wells.

D.J. Moss and T.Ido
Hitachi Central Research Laboratory, 1-280 Higashi-Koigakubo
Kokubunji-shi, Tokyo 185, Japan Fax: +81-423-27-7673

There has been intense interest in the past few years in photogenerated carrier escape mechanisms from quantum wells[1]. This process is not only fundamental to understanding carrier dynamics in quantum confined systems, but has direct relevance to speed and intensity saturation limits for quantum well waveguide photodetectors and electroabsorption modulators[2], reverse biased laser structures[3], and optical SEED devices[4]. Only recently[1], however, have escape times for both electrons and holes from single quantum wells been simultaneously and unambiguously measured with sub-picosecond resolution, and the results appeared to contradict simple existing theories for escape rates based on thermionic emission[5] and tunneling. In this paper, we directly compare the results of our theory for photogenerated carrier escape rates as a function of applied field from single GaAs/AlGaAs quantum wells, with the experimental results from [1]; that is, for wells with x=0.2 and x=0.4 barriers at room temperature. We include thermionic emission (and for electrons include the effects of indirect conduction band minima in the well), thermally assisted, and direct tunneling. Our expressions for thermionic emission reduce, in the limit of large well width, to those[5] which assume a 3D density of states. We assume that carriers in the well are in thermal equilibrium with each other and with the lattice, so "thermally assisted tunneling" refers here to tunneling from thermally occupied upper sub-bands - the 2D equivalent of Fowler-Nordheim tunneling. We also assume parabolic bands for holes within the quantum well, accounting for light / heavy hole mixing by using effective in-plane masses taken from the literature. Tunneling lifetimes are calculated using a standard[6] transfer matrix approach to obtain the linewidths and energy levels of the quasi-bound states as a function of applied field. Under these assumptions the thermionic emission rate for electrons is

$$\left[\frac{1}{\tau^{TE}}\right]_{El} = \frac{1}{\bar{N}d}\sqrt{\frac{kT}{2\pi m^*_\Gamma}}\left(1+\alpha_L e^{+\Delta E_b^L\,\vartheta(-\Delta E_b^L)/kT}\right)e^{-\Delta E_b^\Gamma/kT} \tag{1}$$

where $\alpha_L = \frac{4}{\sqrt{3}}\frac{m_t^*}{m_\Gamma^*}\sqrt{2\frac{m_\ell^*}{m_t^*}+1}$, m_ℓ^* and m_t^* are the longitudinal and transverse effective masses, respectively, of the L valley minima, $\Delta E_b^{\Gamma,L} = E_\Gamma^{Barrier} - E_{\Gamma,L}^{Well} - \frac{eFd}{2}$ are the effective barrier heights for states at the Γ and L points, respectively, and $\vartheta(x)$ is the Heaviside function. The thermally assisted tunneling time from sub-band i is

$$\frac{1}{\tau_i^{NET}} = \frac{1}{\tau_i^{2D}}\frac{2\sqrt{\pi}}{\bar{N}d}\sqrt{\frac{\hbar^2}{2m_\Gamma^* kT}}\,e^{-\Delta E_i/kT} \tag{2}$$

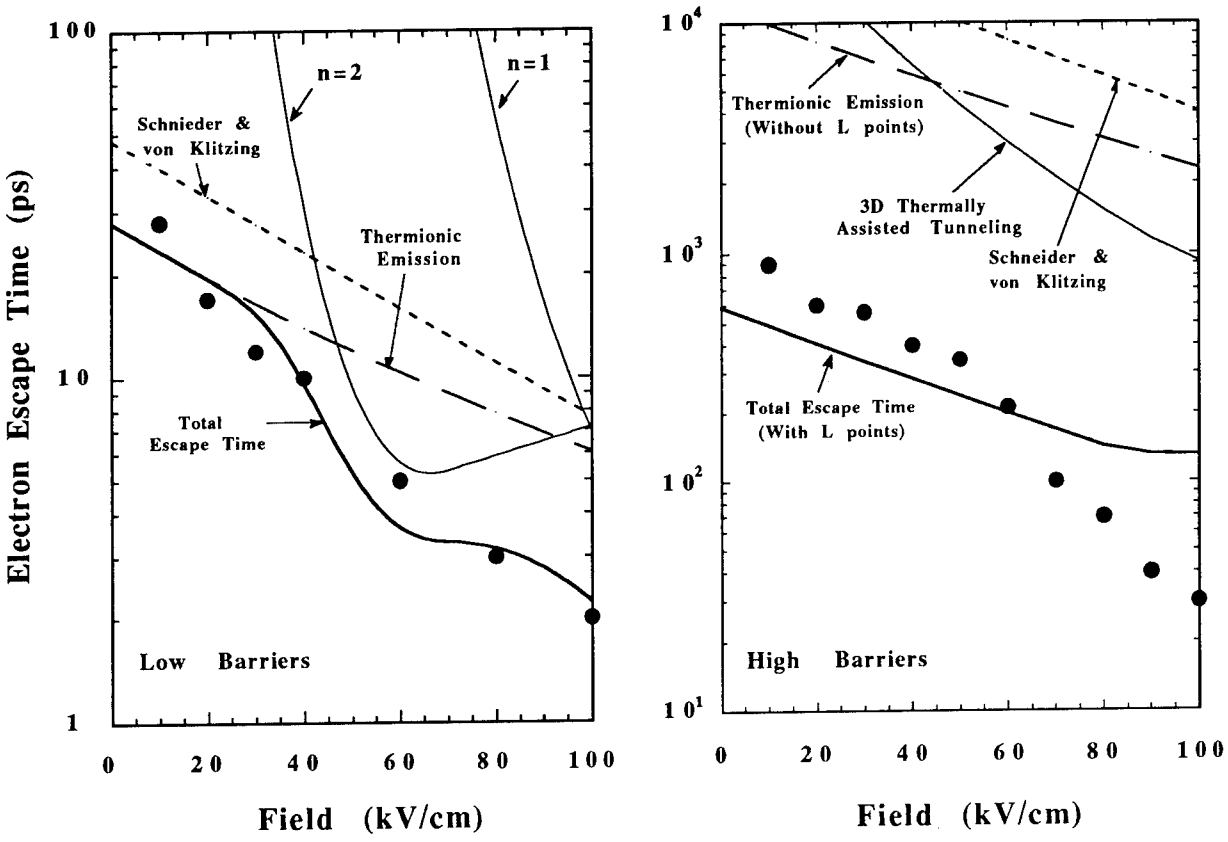


Figure 1 Electron escape times as a function of applied field from wells with a) low (x=0.2) barriers (left) and b) high (x=0.4) barriers (right). The solid circles are experimental data from Ref[1]. The light solid lines in a) are thermally assisted tunneling times from the n=1 and n=2 levels and the results labelled Schneider and von Klitzing are from Ref[5].

where $\Delta E_i = E_i - E_\Gamma^{Well}$ is the quantum energy of the i^{th} sub-band, and τ_i^{2D} is the quasi-bound state lifetime obtained from the scattering linewidth[6]. In Eqs (1,2), $\overline{N}$ is a factor related to the quasi-Fermi level

$$\overline{N} = \frac{2}{\sqrt{\pi}}\left\{\pi\frac{\overline{d}}{d}\sum_i e^{-\Delta E_i/kT} + \int_B^\infty x^{1/2}e^{-x}dx - \sqrt{\Delta E_b^\Gamma/kT}\,e^{-\Delta E_b^\Gamma/kT} + \frac{\sqrt{\pi}}{2}\left(\frac{m_L^*}{m_\Gamma^*}\right)^{3/2} e^{-(E_L^{Well}-E_\Gamma^{Well})/kT}\right\}$$

where $m_L^* = 4^{2/3} m_t^{*2/3} m_\ell^{*1/3}$ is the effective density of states mass at the L point. For wells with low (x=0.2) barriers where effects of the L points are not significant, Eq.(1) reduces to

$$\frac{1}{\tau_{TE}} = \frac{1}{\overline{N}}\frac{1}{\tau_0^{TE}} \qquad (3)$$

where,

$$\tau_0^{TE} = d\sqrt{\frac{2\pi m^*}{kT}}\; e^{-\Delta E_b(F)/kT}$$

is the result for thermionic emission from [5] obtained by using a 3-D density of states. It is straightforward to show that for large well width, $\overline{N}$ approaches unity, so our expression thermionic emission from a quantum well approaches the 3D result from [5]. For 100A wide wells at room temperature, $\overline{N}$ is roughly one half (for barrier heights in the range of $0.2 < x < 0.4$). We found that the effects of the X indirect conduction band minima were not significant. The corresponding equations for holes are much more complicated and are not reproduced here.

Figure 1 shows the results for electrons for wells with both low (a) and high (b) barriers, and it is clear that we achieve excellent results, supporting the assumptions made here, particularly that of thermal equilibrium. For wells with low barriers, electron escape at low fields (<40kV/cm) occurs via thermionic emission; at moderate fields (< 100kV/cm) via thermally assisted tunneling from the n=2 level; and at even higher fields via direct tunneling from the n=1 level. The agreement between theory and experiment is improved by accounting for the 2D density of states. For wells with high barriers, electron escape largely occurs by thermionic emission via the indirect "L" (or (111)) conduction band minima, and including this contribution improves agreement with experiment over a factor of 20 over previous estimates[1]. At high fields (>70kV/cm) our results are slightly higher than experiment, and we believe this could be due to our underestimation of bulk-like Fowler-Nordheim tunneling present in the samples with asymmetric barriers. For holes, both thermionic emission and thermally assisted tunneling depend very strongly on the in-plane effective masses. Our results for holes (not shown) do not agree with experiment as well, and we attribute this primarily to our assumption of equal in-plane masses for all hole sub-bands (but different for light and heavy holes). A full k.p calculation of the hole sub-bands would improve the results.

In conclusion, we have carried out theoretical calculations of photogenerated carrier escape times for single GaAs/AlGaAs quantum wells and compared the redults directly with recent experiments. Agreement for electrons is extremely good, when thermionic emission, thermally assisted tunneling, the contribution of the L point conduction band minima, and the 2D density of states are all included.

References:

1. J.A.Cavailles, D.A.B.Miller, J.E.Cunningham, P.Li Kam Wa, and A.Miller, IEEE Journal of Quantum Electronics, **28** 2486 (1992).
2. T.H.Wood, J.Z.Pastalan, C.A.Burrus Jr., B.C.Johnson, J.L.de Miguel, U.Koren, and M.G.Young, Applied Physics Letters **57** 1081 (1990).
3. D.Moss, D.Halliday, S.Charbonneau, G.Aers, D.Landheer, R.Barber F.Chatenoud, and D.Conn, SPIE proceedings, Quantum Well and Superlattice Physics IV, Somerset NJ, **1675** 418 (1992);
4. D.A.B.Miller,Opt. and Quantum Electronics **22** S61-S98 (1990).
5. H.Schneider and K. von Klitzing, Physical Review B **38**, 6160 (1988).
6. P.J.Stevens, M.Whitehead, G.Parry, and K.Woodbridge, IEEE Journal of Quantum Electronics, **24** 2007 (1988).

SOLVENT INFLUENCE ON BARRIER CROSSING IN THE S_1-STATE OF CIS- AND TRANS- "STIFF"-STILBENE

R.Mohrschladt,J.Schroeder,J.Troe,P.Vöhringer,M.Votsmeier

Institute of Physical Chemistry, University of Göttingen
Tammannstr. 6, 37077 Göttingen, Germany
Phone:-49-(0)551-393127/FAX:-49-(0)551-393144

Diffusion-controlled chemical rearrangements in the liquid phase are in general well described by the Kramers-Smoluchowski model for barrier crossing processes under the influence of frictional forces.
The photoisomerization of trans-stilbene has been a subject of considerable interest in this respect as it is one of the few systems, which show a fractional power dependence of the reaction rate on viscosity [1,2].

Apart from the reactive motion around the double-bond the t-stilbene molecule has as an additional degree of freedom the rotation of the phenyl groups, whereas the bridged t-stilbene derivative trans-1-[1-indanyliden]-indan (trans-"stiff"-stilbene) is restricted to a basically one dimensional potential energy surface.
Early measurements of the fluorescence yields of t-"stiff"-stilben indicated that the molecule shows no deviation from the viscosity dependence predicted by the Kramers-Smoluchowski equation [1]. This observation has stimulated a lot of effort to extend Kramers' one-dimensional model to include the multidimensional nature of molecular dynamics and to elucidate the influence of multidimensionality on the solvent-friction dependence of diffusive barrier crossing rates [4].

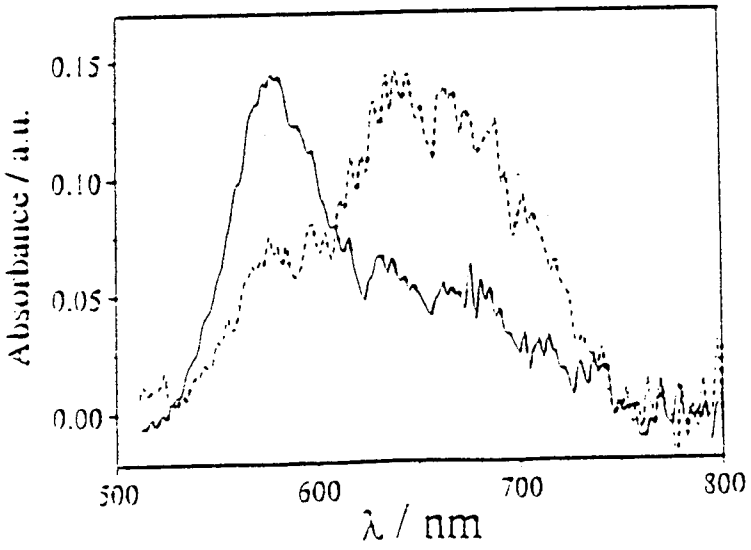


Fig. 1: Transient spectra of trans-(solid) and cis-(dashed)-"stiff"-stilbene 5 ps after excitation

In this work we investigate the S_1-lifetime of trans- and, for the first time, cis-"stiff"-stilbene with 0.5 ps excitation-pulses at 308 nm, recording the transient absorption in the wavelength-range between 450nm and 750 nm. Fig. 1 shows the transient absorption spectrum of cis- and trans-"stiff"-stilben in octane solution 5 ps after excitation.
The broad absorption of trans-"stiff"-stilbene centers at 560 nm, while that for the cis-configuration has a maximum at 660 nm. Time resolved measurements were performed for both species at the respective wavelengths of maximum absorption. In Table 1 the absorption decay rates for cis- and trans-"stiff"-stilbene are compared. In contrast to the stilbene system, where the decay of the cis species is by two orders of magnitude faster than that of the trans-species , one observes a reversal of this order in the "stiff"-stilbene system: In all tested solvents the trans-isomer has a shorter lifetime than the cis species.

table 1: S_1 decay rates for cis- and trans-"stiff"-stilbene in 10^{12} s^{-1}

solvent	cis-"stiff"-stilbene	trans-"stiff"-stilbene
n-pentane	0.1	0.29
n-octane	0.075	0.15
n-dodecane	0.047	0.07
n-hexadecane	0.036	0.05

Cis-stilbene dynamics are dominated by sterical hinderance between the two phenyl-groups which leads to a torsion of these groups out off the plane formed by the double bond. This causes a weakening of electronic resonance and consequently a reduction of the effective barrier height for photoisomerization. One could imagine that the short S_1-lifetime of trans-"stiff"-stilbene is caused by a similar effect: a lowering of the barriers of cis- as well as trans-"stiff"-stilbene are be caused by sterical hinderance between the bridge-hydrogen-atoms and the neighbouring phenylrings.

In comparison to the isomerization of t-stilbene this effect of molecular overcrowding should result in a very low activation energy for the rotation around the t-"stiff"-stilbene double bond. Measuring fluorescence quantum yields Saltiel et al. have found an activation energy of 8.4 kJ/mol in methylcyclohexane including the temperature dependence of solvent viscosity [3]. In order to get an estimate of the intrinsic activation energy we have studied the transient absorption decay in methylcylohexane in the pressure-range up to 7000 bar. These experiments have been carried out for both absorption maxima at 560 and 660 nm. From the measured viscosity dependence of the rate coefficient at 300 K and the temperature dependent data from ref.[3] we calculated a very small activation energy of 1.5 kJ/mol for the barrier crossing process in t-"stiff-stilbene, i.e. approximately 0.5 k_BT at room temperature. For t-stilbene an activation energy of 14 kJ/mol has been determined. This low barrier to photoisomerization of t-"stiff"-stilbene reflects the fact, that in contrast to t-stilbene the dynamics are dominated by sterical hinderance. In this respect its potential energy surface in the region controlling the barrier crossing process is comparable to those of cis-stilbene and tetraphenylethylene .

Fig. 2 shows the viscosity dependence of the t-"stiff"-stilbene photoisomerization rates in different alkane solvents. The viscosity dependence to a great extent resembles the behaviour observed earlier for cis-stilbene [5]. Systematic deviations from an inverse viscosity dependence are observed. In both cases these can be explained by the dependence of microscopic friction on the size of solvent molecules.

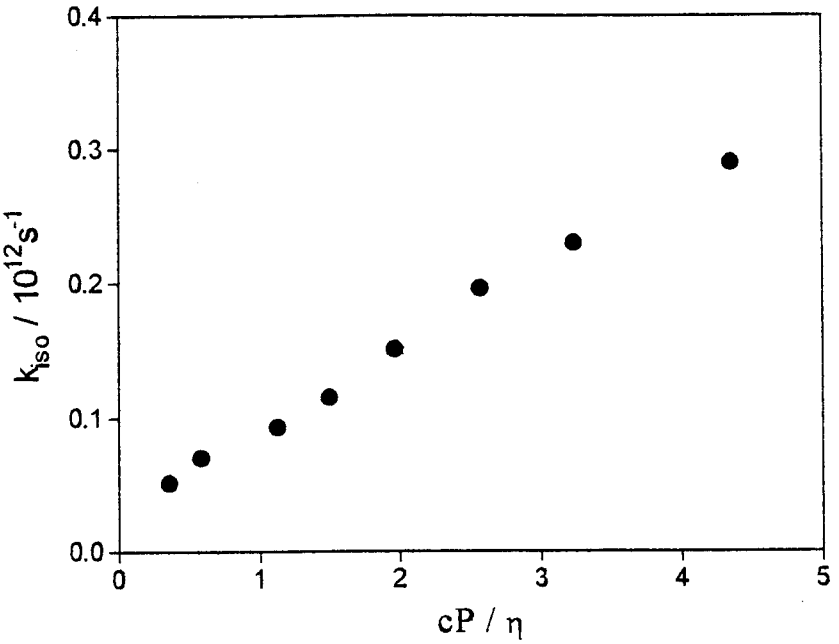


Fig.2: Viscosity dependence of trans-"stiff"-stilbene S_1 decay rate

In summary, one can notice that there exist more fundamental differences between the potential surfaces of t-stilbene and its bridged derivative t-"stiff"-stilbene than just dimensionality with respect to the reaction path. This gives rise to the question whether t-"stiff"-stilbene is an appropriate model compound for testing the influence of multidimensionality effects on t-stilbene diffusional barrier crossing.

References

[1] G. Rothenberger, D.K. Negus, and R.M. Hochstrasser
J. Chem. Phys. **79**, 5360 (1983)

[2] S.K. Kim S.H. Courtney and G.R. Fleming
Chem. Phys. Let. 159, **543** (1989)

[3] J. Saltiel, J.T. D'Agostino[4]
J. Am. Chem. Soc. **94**, 6445 (1972)

[4] N. Agmon, R. Kosloff
J. Phys. Chem. **91**, 1988 (1987)

[5] L. Nikowa, D.Schwarzer, J. Troe, J.Schroeder
J. Chem. Phys. **97**, 4827 (1992)

Group−delay dispersion measurement of laser mirrors by spectrally resolved white light interferometry

A. P. Kovács, R. Szipőcs[1], K. Osvay, Z. Bor

Dept. of Optics and Quantum Electronics, JATE University, H−6720 Szeged, Dóm tér 9, Hungary, Tel./Fax: +36 62 322 529
[1] Optical Coating Laboratory, Research Institute for Solid State Physics, H−1525 Budapest, P.O. Box 49, Hungary

It is known, that the temporal shape of a femtosecond pulse is altered while propagating through dispersive optical components and mirrors. Specially designed chirped dielectric high reflectors [1−3] have been proven to be efficient tools for controlling the intracavity group velocity dispersion in femtosecond lasers. In designing high performance femtosecond laser systems, the direct measurement of the frequency dependent group delay of mirrors is essential. Recently, a number of works have been devoted to the problem of measurement of the group−delay dispersion [4−9]. In [4,5] white light time−of−flight interferometer has been used. In [6,7] a phase locked Michelson interferometer was used to measure the phase response. Knox [8] measured the total group delay in an operating Ti:sapphire femtosecond laser by analyzing the pulse train with a digital frequency counter. Schwider [9] used superposition−fringes interferometry to determine the phase changes upon reflection from a dielectric multilayer. Spectrally resolved white light interferometry has been used for refractive index measurements of dye solutions [10]. In this paper a spectrally resolved white light Michelson interferometer is used to measure the group delay of mirrors.

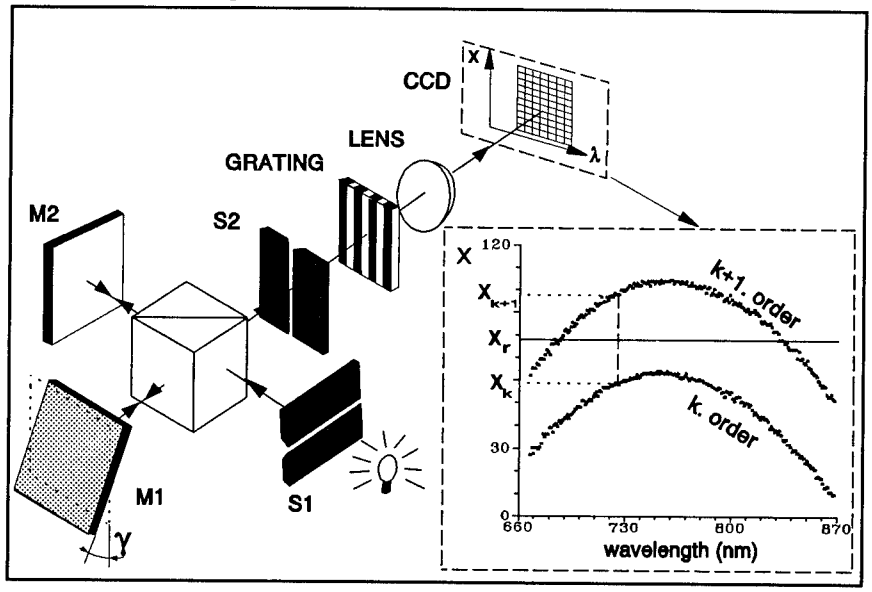


Fig. 1 *Spectrally resolved white light interferometer. The interference fringes formed in plane S2 are spectrally dispersed with a grating and imaged onto the 2D CCD camera. The shape of the fringes carries information about the phase response of mirror M2.*

Fig. 1 shows the experimental setup. Slit S1 is used to increase the spatial coherence of the white−light source (halogen lamp). After that the light is divided by a high quality beam splitter cube. In the reference arm of the interferometer a gold mirror M1 having negligible phase dispersion [4] is used. In the other arm the dielectric mirror M2 under study is placed. The reference mirror M1 is slightly turned around a horizontal axis with an angle γ while mirror M2 is vertical in this way so horizontal interference fringes are formed on the exit plane of the interferometer. Slit S2 is used to cut out a vertical stripe from this fringe pattern. This stripe is spectrally dispersed in the

horizontal direction by a grating and is imaged onto a 2D CCD camera. Due to the phase response (φ_M) of mirror M2 the optical path difference between the two beams of the Michelson interferometer in the plane of the slit (S2) is given by

$$\Delta = x\sin(2\gamma) + \frac{\lambda}{2\pi}\varphi_M,$$

where x is a vertical coordinate in the plane of S2. Fig. 2 and 3 show the spectrally dispersed interference fringes with a gold mirror and dielectric mirror respectively. The curve determined by the minima as a function of the wavelength is linear for the gold mirror (see Fig. 2).

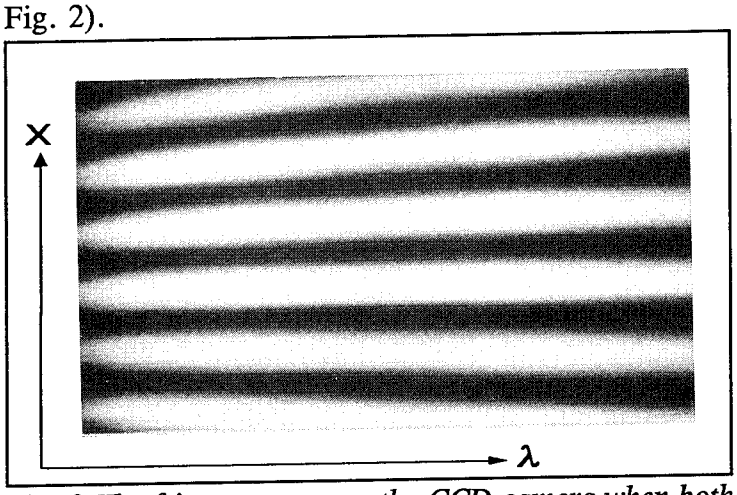


Fig. 2 *The fringe pattern on the CCD camera when both mirrors are gold mirrors.*

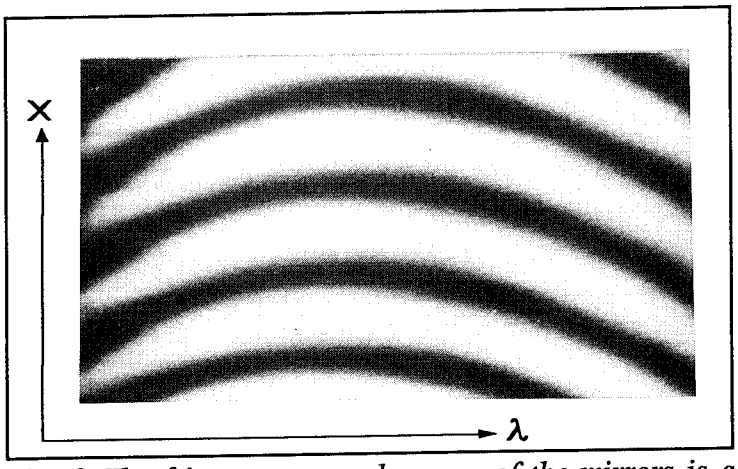


Fig. 3 *The fringe pattern when one of the mirrors is a dielectric mirror (having phase dispersion).*

It can be shown that the phase response of the mirror M2 can be determined with an accuracy of an additive constant (ψ) as

$$\varphi_M = 2\pi\frac{x_r - x_k}{x_{k+1} - x_k},$$

where x_k and x_{k+1} are the x−coordinate of the minima of the k^{th} and $k+1^{th}$ order interference fringe at a given wavelength and x_r is an arbitrary chosen reference coordinate independent of the wavelength (see inset of Fig. 1). (The values of x can also be measured in units of channel number.) The additive constant ψ disappears when calculating the group−delay dispersion (GDD=$d^2\varphi/d\omega^2$) and its higher order derivatives. The sensitivity of the interferometer can be increased by using multiple reflection from mirror M2 from an additional gold mirror (not shown in Fig. 1). In our case we used 4 reflections. The geometry of the interferometer allowed to make 16−fold reflection as well.

The setup has been successfully used for fast, accurate group−delay dispersion measurement of dispersive dielectric high reflectors on a bandwidth of 150 nm with a spectral resolution of 1 nm (see Fig. 1). The mirror was designed for dispersion control in a Kerr−lens modelocked Ti:sapphire laser. With five reflections on the dispersive mirrors (upon one round trip) the laser is supposed to generate pulses in the sub−10 fs regime [1]. The accuracy of the measurement will be increased considerably with a more sophisticated analysis of the

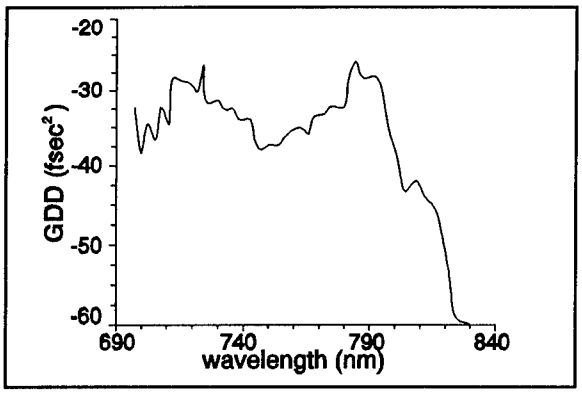


Fig. 4 *The measured group−delay dispersion of a laser mirror as a function of the wavelength.*

interference fringes, when the full interference pattern will be analyzed instead of the minima only.

This work has been supported by the U.S.−Hungarian Science and Technology Joint Fund and the OTKA Foundation.

REFERENCES:

[1] R. Szipőcs, K. Ferencz, Ch. Spielmann, F. Krausz, to be appear in Opt. Lett. in February 1994)
[2] J. Kuhl and J. Heppner, IEEE J. Quantum Electron. **QE−22**, 182 (1986).
[3] K. Ferencz, R. Szipőcs, Opt. Eng. **32**, 2525 (1993).
[4] W. H. Knox, N. M. Pearson, K. D. Li and C. A. Hirlimann, Opt. Lett. **13**, 574 (1988).
[5] Zs. Bor, Z. Gogolak, G. Szabo, Opt. Lett. **14**, 862 (1989).
[6] M. Beck, I. A. Wamsley and J. D. Kafka, IEEE J.Quantum Electron. **QE−27**, 2074 (1991).
[7] M. Beck, I. A. Wamsley, Opt. Lett. **15**, 492 (1990).
[8] W. H. Knox, Opt. Lett. **17**, 514 (1992).
[9] J. Schwider, Appl. Opt. **31**, 6107 (1992).
[10] C. Sainz, J. E. Calatroni and G. Tribillon, Meas. Sci. Technol. **1**, 356 (1990).

Passive Modelocking of a Flashlamp Pumped Ti:Al_2O_3 Laser

B. Bouma[1], A. Gouveia-Neto[1], J. Russell[2], R. Sierra[2], J. A. Izatt[1], U. Keller[3], J. G. Fujimoto[1]

[1]Department of Electrical Engineering and Computer Science, Research Laboratory of Electronics, Massachusetts Institute of Technology, Cambridge, MA 02139 (617) 253-8528; [2]Candela Laser Corporation, Wayland, MA 01778; [3]Institute of Quantum Electronics, Swiss Federal Institute of Technology, ETH Hönggerberg, HPT, CH-8093 Zürich, Switzerland.

Nearly all modelocked Ti:Al_2O_3 lasers to date have been cw modelocked systems with relatively low pulse energies. Short pulse energies in the range of microjoules to millijoules can be generated using regenerative and multipass amplifier systems[1]. While these techniques achieve excellent performance, they are relatively costly and complex. In this paper we demonstrate a high performance, all solid-state, modelocked flashlamp pumped Ti:Al_2O_3 laser. The flashlamp pumped Ti:Al_2O_3 laser is a simple, economical, high peak power laser source which can be an attractive alternative technology to conventional oscillator-amplifier approaches. In addition, the development of new techniques for modelocking flashlamp pumped lasers can be generalized to a broad class of new solid state laser materials currently being developed.

Modelocking transient flashlamp pumped systems is extremely challenging because unlike cw lasers, the pulse energy grows rapidly in time. Relatively few investigations of modelocking have been performed in flashlamp pumped Ti:Al_2O_3. Modelocking with saturable absorber dyes[2] and intracavity second harmonic generation[3] have been demonstrated resulting in long pulse durations of $\sim$ 100 ps.

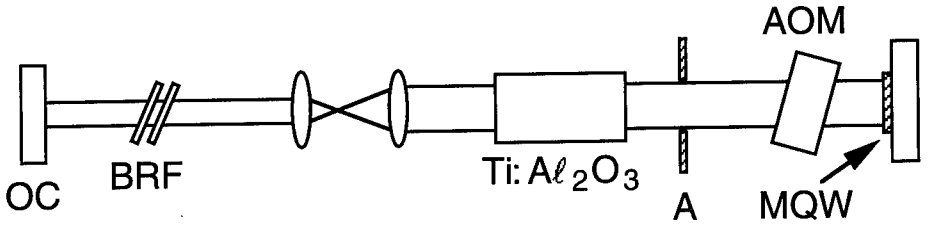


Fig. 1. Schematic of the flashlamp pumped modelocked oscillator. OC: output coupler, BRF: birefringent filter, T: telescope, LH: flashlamp pumped laser head, A: aperture, AOM: acousto-optic modulator, MQW: multiple quantum well.

To address the problem of modelocking in flashlamp pumped lasers, we used a combination of active and passive modelocking with an antiresonant Fabry-Perot saturable absorber (AFPSA) to achieve optimum pulse shortening during the rapid pulse build-up time. The laser cavity, shown schematically in Figure 1, incorporates a 15 cm long, 8 mm diameter, Ti:Al_2O_3 laser rod pumped by two close-coupled flashlamps which are driven with 15 μs electrical pulses of up to 12 kV. Operating multimode with a simple planer resonator (not shown), pulse energies as high as 1 J can be generated at 10 Hz repetition rate. The high small signal gain of up to 5 per pass permits a wide range of cavity designs to be implemented. An intracavity telescope consisting of two

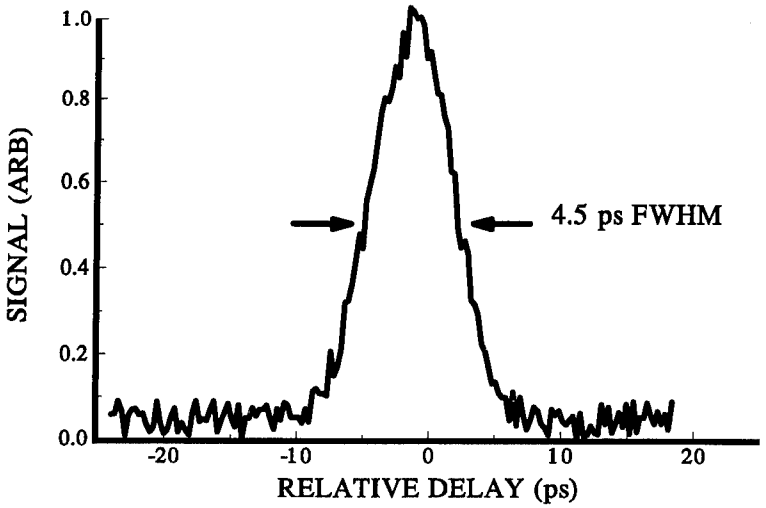


Fig. 2. Slow scan autocorrelation of average modelocked pulse duration in second relaxation spike. The pulse duration is 4.5 ps assuming a sech^2 pulse.

anti-reflection coated lenses was used to achieve the mode control necessary for stable saturable absorber modelocking and to scale the spot sizes to control energy extraction and saturable absorption. A 14% transmission output coupler (OC) was used.

Short pulse formation during the rapid pulse build-up time is achieved using a hybrid modelocking technique. Active modelocking rapidly shortens pulses which are long compared to the modulation period while fast saturable absorber modelocking provides a pulse shortening velocity that increases inversely as the pulse duration. In this experiment we used a Brewster cut fused silica acousto-optic modulator driven at a resonance frequency of $\sim$ 52 MHz. Sub-nanosecond pulses are generated within the first few oscillations at the onset of lasing. When this device was used as the only modelocking element, the minimum pulse duration that could be generated was 100 ps.

To further reduce the pulse duration, we employed an antiresonant semiconductor Fabry-Perot saturable absorber (AFPSA)[4]. The saturable absorber was a low temperature (LT) ($\sim$ 300°C) molecular-beam-epitaxy grown AlGaAs-GaAs multiple quantum well (MQW) structure with 38 periods of 10 nm thick GaAs quantum wells and $Al_{0.3}Ga_{0.7}As$ barriers. The LT MQW structure was grown on top of an $Al_{0.3}Ga_{0.7}As/AlAs$ dielectric mirror stack grown on a GaAs substrate at normal growth temperature. The excitonic resonance occurs at $\sim$ 840 nm. An antiresonant Fabry-Perot is formed by the front surface of the LT MQW (nominal reflectivity of 10%) and the high reflecting mirror stack. As described previously, this antiresonant design allows the effective cross section of the absorber to be decreased. In addition, the LT growth temperature allows the recovery time of the absorber to be controlled. Thus, in principle the saturable absorber characteristics may be explicitly designed to achieve optimum modelocked performance[4]. The overall small signal reflectivity of the AFPSA was nominally 60% at 825 nm. Pump probe measurements showed a differential reflectivity of $\sim$ 15% at a pump fluence of $\sim$ 200 $\mu J/cm^2$.

Because of the high gain and long pump pulse duration associated with flashlamp pumping, the laser output consists of relaxation oscillation spikes. At our typical operating pump energy of $\sim$ 120 J or 1.2 times threshold, the output consists of two

relaxation oscillation spikes separated by $\sim$ 2 μs containing $\sim$ 15 and 25 pulses respectively. The pulse formation dynamics can be studied using fast ($<$ 1 ns response time) photodiodes to simultaneously monitor the intensity of the pulse train and its second harmonic generated in phase matched $LiIO_3$. This measurement shows that the AFPSA can produce an extremely rapid pulse shortening, approximately a factor of 20 between pulses in the first and second relaxation oscillations.

A standard (multiple shot) non-collinear autocorrelation was performed using a photodiode to detect the second harmonic. The average modelocked autocorrelation within the second relaxation spike was 6.9 ps FWHM, corresponding to a pulse duration of 4.5 ps (assuming a $sech^2$ pulse). The wavelength was 824 nm and the time integrated spectral bandwidth was 0.8 nm giving a time-bandwidth product of 1.6. The entire pulse train contains 800 μJ of energy, corresponding to $\sim$ 20 μJ per modelocked pulse. Using an intracavity two-plate birefringent filter the laser can be tuned from 820 nm to 835 nm with a maximum pulse duration of 7.5 ps.

The pulse energy, duration, and limited tunability demonstrated with this laser are superior to previous flashlamp pumped $Ti:Al_2O_3$ systems; however, performance can be significantly improved. Pulse energy may be increased by scaling the mode size in the resonator and single pulses can be extracted using cavity dumping. Using these techniques, we believe that it should be possible to generate picosecond pulse durations in the millijoule energy range. The tuning range of the laser could also be increased by using a broadband AFPSA design[5]. It should also be noted that the hybrid modelocking concepts demonstrated can also be extended to other nonlinearities that are inherently broad bandwidth, such as Kerr rotation of elliptical polarization, self-focusing, and carrier induced index changes.

In conclusion, we have demonstrated a new all solid state technique for modelocking flashlamp pumped lasers. The combined pulse shaping mechanisms of active and passive modelocking used in conjunction with the high gain and high energy storage supplied by flashlamp pumping makes possible the development of a simple, cost effective source of high peak power optical pulses.

A. Gouviea-Neto was visiting from the Departamento de Física, Universidade Federal de Alagoas, Maceió, Brasil. The LT MQW samples were grown by M. T. Asom of AT&T Bell Laboratories. We gratefully acknowledge helpful scientific discussions with E.P. Ippen and H.A. Haus. This research was supported in part by JSEP grant DAAL03-92-C-0001, AFOSR grant F49620-91-C-0091, and ONR MFEL grant N00014-91-C-0084.

References

[1] J. Squier, F. Salin, G. Mourou, and D. Harter, Opt. Lett. **16**, 324 (1991).

[2] S. Oda, Y. Segawa, and N. Kodama, Jap. Journ. Appl. Phys. **28** 1977 (1989).

[3] K. Hamai, K. A. Stankov, H. Jelinkova, I. Prochazka, and M. Koselja, *Inst. Phys. Conf. Ser. No. 126*, Section I, Paper presented at International Symposium on Ultrafast Processes in Spectroscopy, Bayreuth, 1991, p. 59.

[4] U. Keller and T. H. Chiu, IEEE J. Quant. Electron. **28**, 1710 (1992).

[5] G. R. Jacobovitz-Veselka, U. Keller, and M. T. Asom, Opt. Lett. **17**, 1791 (1992).

Ultrafast Relaxation Dynamics of Photoexcitations in Nanometer-Size Amorphous Selenium Clusters

V.P.Mikhailov, K.V.Yumashev, P.V.Prokoshin, S.P.Jmako

International Laser Center, Belarus State University, 7 Kurchatov Str., Minsk 220064, Belarus, Phone/Fax 0172-785726

V.S.Gurin, M.V.Artemyev

Physico-Chemical Problems Research Institute, Belarus State University, 14 Leningradskaya Str., Minsk 220080, Belarus, Phone 0172-265608

The search for new materials with a large nonlinear optical susceptibility and the simple synthesis of selenium clusters of various crystal structure has caused the investigation of nonlinear optical properties of nanometer-size selenium clusters. Samples of PVA films with a-Se clusters on quartz glass were investigated by picosecond pump-probe laser spectroscopy equipment with two photodiode matrices as detectors. Laser pulses with wavelength of 540 nm, duration of 15 ps and repetition frequency of 1 Hz served as pump beam .White continuum was used as probe beam.

Figure 1 shows differential absorption spectra ΔD of a-Se clusters in PVA film obtained at the various delay time between pump and probe pulses and the energy of pump pulse of 80 mJ/cm^2 . Excitation of a-Se particles results in appearance of induced absorption around E=2.1 eV (Fig.1 shows decay of absorption). Development of induced absorption finished practically after pump pulse action within the resolution time of our picosecond device (15 ps). The decay time of induced absorption is significantly greater than pump pulse duration. Position of maximum in spectra of induced absorption at the energy scale depends on delay time between pump and probe pulses.

In Fig. 2 the kinetics of induced absorption ΔD vs time delay in a-Se clusters are shown for six different energies of photons of probe pulses. From this figure can be made conclusions that the decay time of induced absorption depends on energy of

photons and the relaxation of induced absorption at various energies of photons has the exponential character.

Spectral behaviour of decay time τ is presented in Fig. 3. Values of t are independent of photon energy in the range of 2.1 - 2.2 eV and equal to ~ 550 ps. Below 2.1 eV values of t decrease down to 260 ps at 1.75 eV.

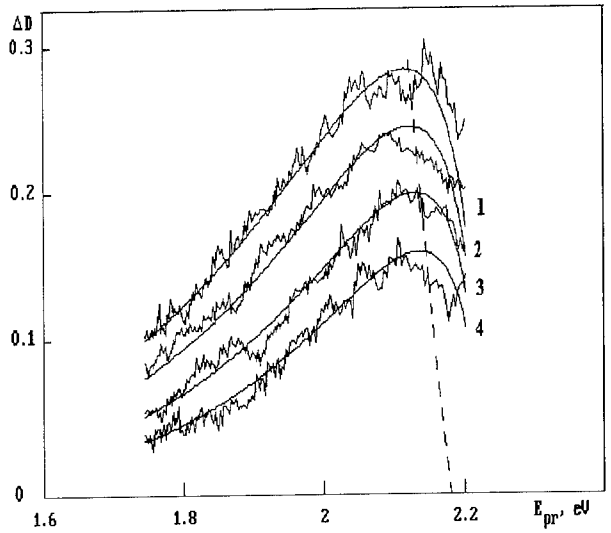


Fig.1. Differential absorption spectra $\Delta D=-\lg(T/T_0)$ of a-Se particles in PVA film at the various delay time t between pump and probe pulses of 15 ps duration. The energy of photons of pump pulse is 2.3 eV and pulse energy is 80 mJ/cm^2 . T_0 and T are the transmittance of sample before and after pumping. t_d (ps) = 78 (1), 196 (2), 286 (3), 376 (4). Solid lines are the best theoretical fit of experimental curves.

We assume the effect of induced absorption in nanometer-size a-Se clusters can be explained due to realization of the two- photon transition with formation of biexcitons, i.e. two bounded electron-hole pairs. Pump pulse creates the excitons with life time of around few hundreds of picoseconds and observation of probe pulse absorption through that period is conditioned by exciton-biexciton optical transition.

The solid lines in Fig. 1 drawn through the experimental points show the best fit of data using Boltzman energy distribution of excited states.

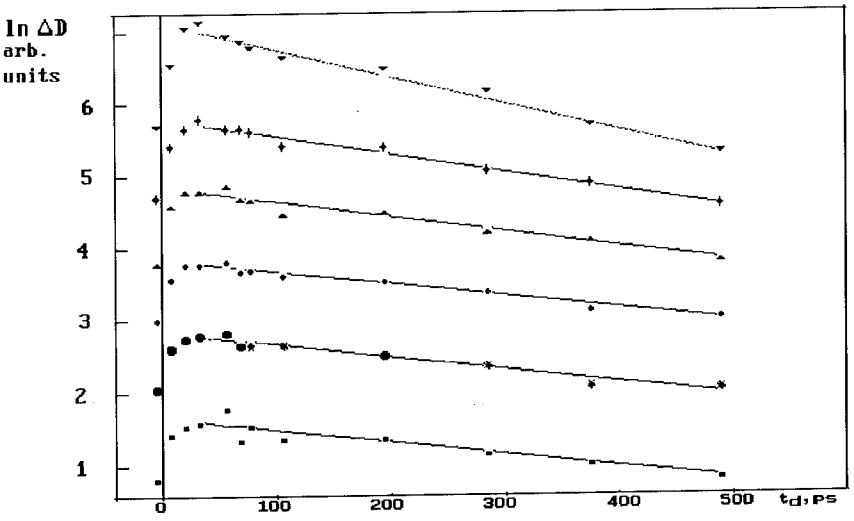


Fig.2. The kinetics of induced absorption ΔD vs t_d in a-Se particles at the different energy of photons of probe pulses E_{pr} (eV) = 1.75 (1), 2.0 (2), 2.05 (3), 2.1 (4), 2.125 (5), 2.2 (6). All curves are shifted arbitrarily along ordinate.

The exponential form of low energetic side in induced absorption spectra (Fig.2) reflects the Boltzman distribution tails of thermalized excitons.

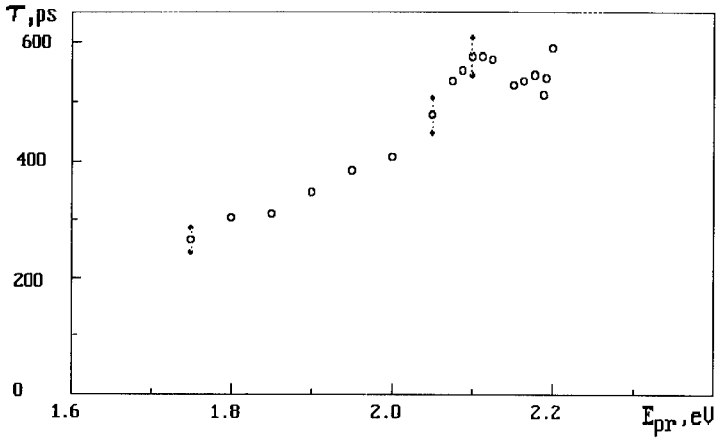


Fig.3. Decay time t of induced absorption in a-Se particles vs the hoton energy E_{pr} of probe pulses.

Quasithermal distribution of excitons with some temperature T_x appears at the time less than 15 ps. Shift of maximum in induced absorption spectra reflects the evolution of the effective exciton temperature in semiconductor. During the first 450 ps after the pump pulse action T_x reduces from 5900 to 3300 K exponentially with time constant 1085 $\pm$ 245 ps and the total number of excitons N_x decreases more than three times. Therefore, reduction of total number of excitons takes place before reaching the thermal equilibrium. Such variation of N_x can be conditioned by surface recombination of excitons in nanometer size clusters of a-Se. Thus the time behaviour of induced absorption is determined by the recombination and cooling of excitons.

Picosecond Optical Time Domain Reflectometer for Optoelectronic IC Device Characterisation

Y. Beaulieu[+], R. Normandin[*], P. van der Meer[*],

F. Chatenoud[*], A. Delage[*] and B.K. Garside[+]

[*] Optoelectronic Devices

Institute for Microstructural Sciences

National Research Council

Ottawa, Ontario

[+] Opto-Electronics Inc.

unit 9, 2538 Speers Rd.

Oakville, Ontario

Introduction

Several years ago Stegeman and Normandin predicted, and subsequently demonstrated [1], the nonlinear mixing of oppositely propagating guided waves. The resultant second harmonic field was coupled to radiation modes and propagated in a direction perpendicular to the waveguide surface, in the case of equal fundamental frequencies. Its application to picosecond signal processing [2], the creation of all optical transient digitizers [3] and spectrometers [4] demonstrated the potential usefulness of this approach. Finally, the nonlinear cross section for uniform GaAs optical waveguides was calculated and published [5], and recently this GaAs prediction was verified [6] by Vakhsoori et al. In their geometry, the oppositely propagating beam was supplied by the reflection from the exit surface. Their use of picosecond pulses also demonstrated the potential for optical correlation in a geometry similar to references 2 and 3. However, the use of simple GaAs films results in low conversion efficiencies, due to difficult input coupling and absorption and phase cancellation effects at the harmonic wavelength.

Destructive interference effects can be reduced by creating a multilayer waveguide. By using the $Ga_{1-x}Al_xAs$ alloy, $\lambda/2$ layers of high conversion efficiency (low Al content) can alternate with transparent $\lambda/2$ layers of low conversion efficiency (high Al content). The in-phase and out-of-phase contributions have different intensities and the second harmonic generation efficiency can be enhanced by many orders of magnitude.

Theoretical considerations

When two optical pulses interact in a nonlinear waveguide, the second harmonic polarisation source field will reflect their convolution. For input pulses of picosecond duration the harmonic output is much too rapid for direct observation by a commercial photodetector. However, if the signal from each element of the waveguide surface is integrated over the signal overlap time, the output corresponds to the square of the convolution of the two waveforms with a time compression of 2. By using a detector array that integrates the total light output at each position of the waveguide, it is therefore possible to obtain directly the temporal convolution of the two input pulses.

Experimental Aspects

The instrumental set-up is shown schematically in Fig. 1. Light from a short pulse laser is first split in two beams which will propagate along different optical paths: a reference path, consisting of a variable optical delay, and a signal path, which is used to probe a discrete or integrated optoelectronic device in transmission (T) or reflection (R) mode. For demonstration purposes, the pulses are generated by a Nd-YAG laser (100 ps at 1.06 μm) and compressed to 5 ps FWHM with a standard fiber and grating pair set-up. Light from the two paths is then fed into opposite faces of a SHG waveguide. By properly adjusting the optical delay in the reference path, pulses from both paths will meet in the SHG waveguide, thereby producing light spots that can be directly observed from above the nonlinear waveguide. This SHG waveguide consisted of 6 repetitions of $\lambda/2$ layers of $Ga_{1-x}Al_xAs$, where the Al content alternates between 70 and 90%, grown on a buffer layer deposited on a GaAs substrate.

Results

In our proof-of-concept experiment, we used a piece of bulk GaAs (about 0.65 mm thick) as a sample, observed in transmission mode. In Fig. 2, a picture of the SHG waveguide (3.02 mm wide) and the two input fibers is shown. On the waveguide surface, two spots can be identified: the intense spot corresponds to the pulse transmitted through the sample, while the second spot corresponds to the pulse reflected once inside the sample. The output intensity across the sample can easily be obtained from the grey-scale picture. In Fig. 3, the distribution of the light output intensity across the sample is represented by dots, while the

least-square fit (using Gaussian broadening) is represented by a line. Compared to Fig. 2, the effective signal-to-noise ratio has been increased by mathematically binning the pixels perpendicular to the trace. The separation between the two peaks can be accurately obtained from the fit (about 37 pixels). Knowing the index of refraction of the SHG waveguide and of GaAs, this separation is calculated to be 0.65 mm, in good agreement with the measured thickness. The two spots are very easily resolved in this case, since the resolution is about 0.15 mm in the sample with our 5 ps pulses.

Conclusion

We have demonstrated a stable OTDR for optical ranging without the use of interferometric techniques or the need of Fourier transforms. The set-up has no moving parts and is fiber compatible. Efficiencies are sufficient for real time CCD monitoring. The 0.15 mm interfeature resolution and the 50 μm position uncertainty are presently limited by the laser pulse FWHM of about 5 ps.

References

1. R. Normandin and G.I. Stegeman, "Nondegenerate Four-Wave Mixing in Integrated optics", Optics Lett., 4, 58-60 (1979)
2. R. Normandin and G.I. Stegeman, "Picosecond Signal Processing with Planar, Nonlinear Integrated optics" Appl. Phys. Lett., 36, 253-257 (1980)
3. R. Normandin and G.I. Stegeman, "A Picosecond Transient Digitizer Based on Nonlinear integrated optics" Appl. Phys. Lett., 40, 759-761 (1982)
4. in "Integrated Optical Circuits and Components", Edited by L.D. Hutcheson, Dekker Inc., New York, (1987) USA Chap. 9 by G.I. Stegeman et al, and many references therein.
5. P.J. Vella, R. Normandin and G.I. Stegeman, "Enhanced Second Harmonic Generation by Counter Propagating Guided Optical Waves" Appl. Phys. Lett., 38, 759-761 (1981)
6. D. Vakhshoori and S. Wang, "Demonstration of an AlGaAs/GaAs Integrable Optical Correlator Using Surface-emitting Second-harmonic Generation "Appl. Phys. Lett., 53, 347-49 (1988)

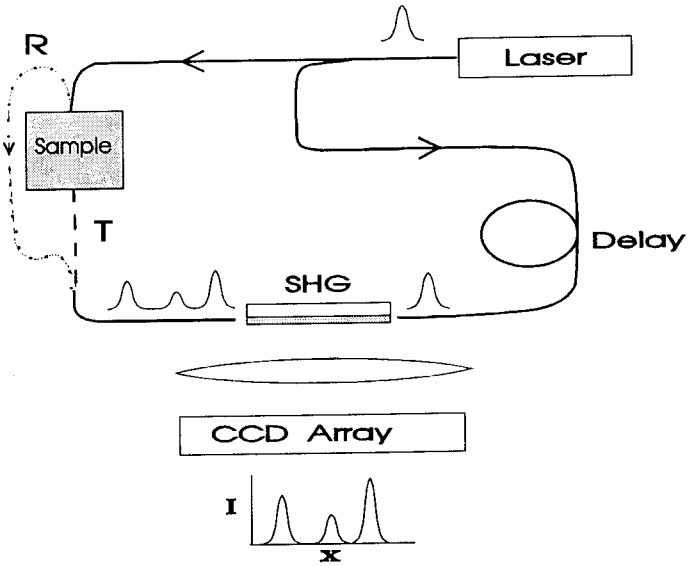


Fig. 1. Instrumental set-up used for optical time domain reflectometry. The signal path is used to probed a sample in transmission (T) or reflection (R) mode.

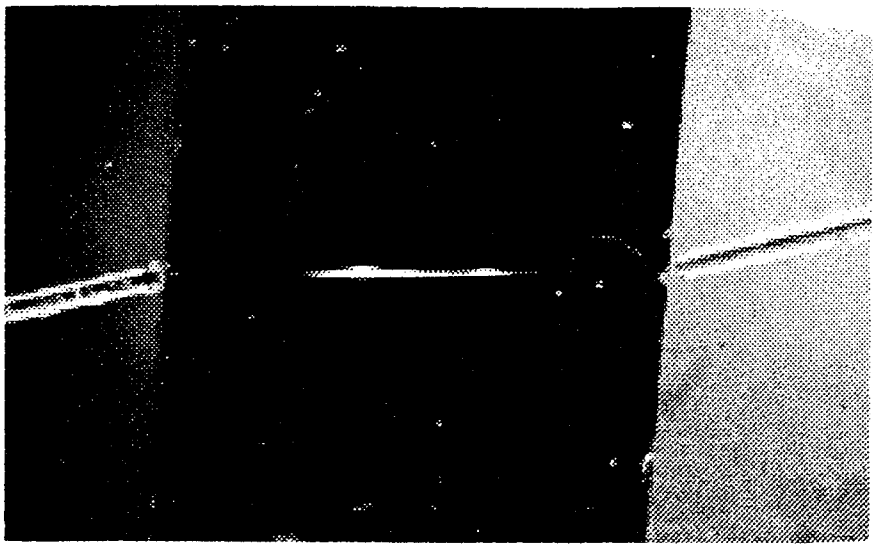


Fig. 2. Data from a CCD camera showing two input fibers and a SHG waveguide, when probing a 0.65 mm thick GaAs substrate. The second harmonic light can be observed on the surface of the waveguide.

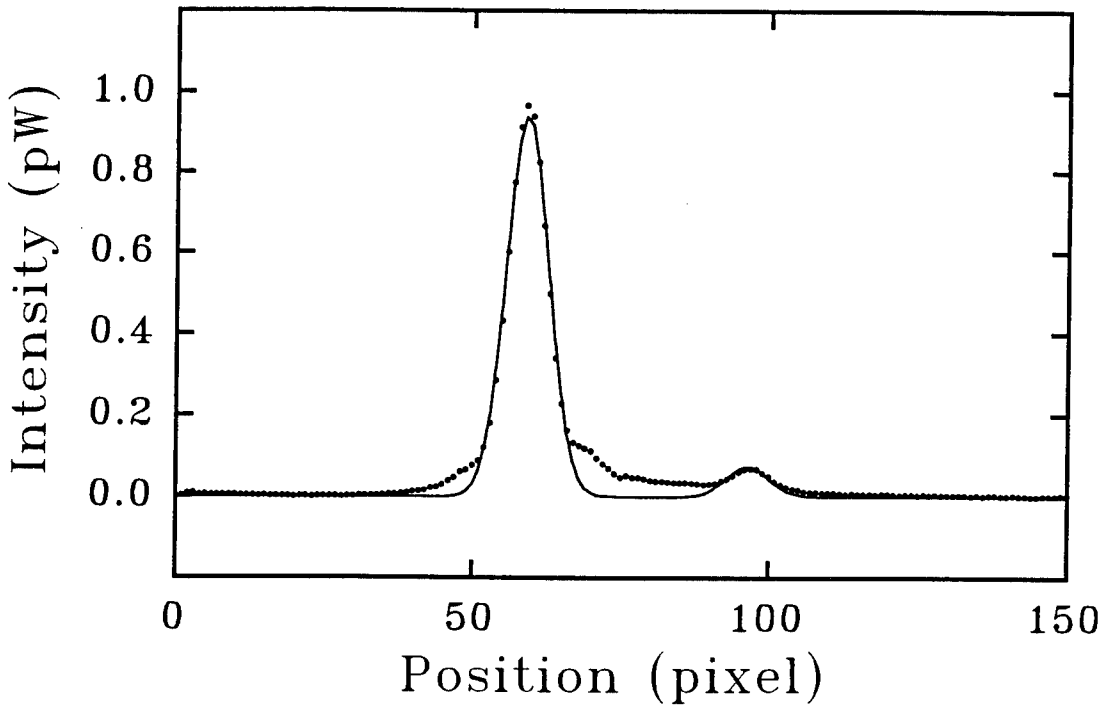


Fig. 3. Second harmonic light intensity across the nonlinear waveguide surface when probing a 0.65 mm thick GaAs substrate. The actual data is represented by dots, while the least-square fit is represented by a line. The length of the nonlinear guide is 3.02 mm or 151 pixels.

Phase Delay in Grating-Pair Pulse Compressors

K.A. Stankov
Laser Laboratorium, Hans-Adolf-Krebs-Weg 1
D-37077 Göttingen, FRG
Phone: (551) 503545, Fax:(551) 503599

Compressors based on a pair of identical parallel gratings are widely used for stretching, compressing and shaping ultrashort light pulses. The basic parameters of a light pulse compressor are the group delay τ_g, and the group-delay dispersion, D_g, which are calculated from the phase delay $\phi(\omega)$ in accordance with: $\tau_g=\partial\phi(\omega)/\partial\omega$, and $D_g=\partial^2\phi(\omega)/\partial\omega^2$, respectively. The expression for the phase delay was first derived more than two decades ago by Treacy /1/. However, it has been always confusing due to an additional phase term whose physical interpretation is not clear /2-4/. According to Treacy, the phase delay between two identical parallel gratings (for the simplified geometry of normal incidence transmission gratings as presented in Fig.1) is given by:

$$\phi(\omega)=(\omega/c).(G/\cos\alpha) - (2\pi/d).G.\tan\alpha \qquad (1)$$

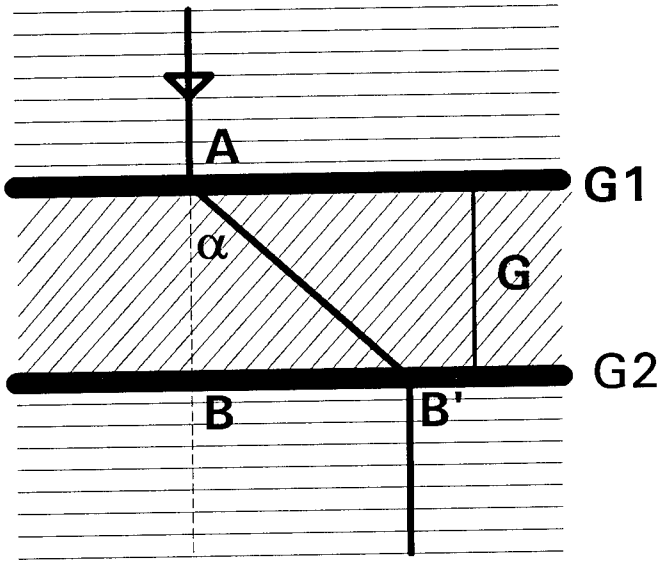


FIG.1. A simplified arrangement for a grating compressor. The parallel thin straight lines represent the phase fronts.

Here G denotes the perpendicular distance between the two gratings, d is the grating constant, α is the angle of diffraction, and c is the speed of light.

The first term in (1) is associated with the phase delay accumulated along the direction of propagation of light wave between the two gratings, from point A to point B'. The second term is attributed to the phase jumps at each groove along the second grating. The total phase shift due to the individual phase jumps is calculated over a distance BB'=G.tanα. The introduction of the second term in (1) by Treacy is more intuitive than rigorous. Also, its sign is adjusted in such a way that a correct expression for the group delay is obtained. A number of papers have addressed the difficulties in interpreting this phase term /2-5/. The difficulties arise from the fact that by diffraction, the wavefronts of the wave emerging from the grating are a *superposition* of the wavefronts of the incident wave /2/. Therefore, it is impossible to relate explicitly the phases of the two plane waves on the opposite sides of the grating, before and after diffraction as was implicitly assumed by Treacy. Diffraction of a plane wave by a grating results in a phase discontinuity:. In the example given in Fig.1, on one side of the grating the phase is constant, on the other side it varies periodically by 2π along the grating with a spatial period d. Therefore, the assumption for explicit relation of the phases on both sides of the grating /1/ leads to an incorrect

result and an additional "heuristic" term $-(2\pi/d)G.\tan\alpha$ is then needed /2/. There is no doubt that an additional phase term should be present in order to obtain a correct value for the group delay. Neglecting this additional phase term may lead to incorrect results /5/. Nevertheless, the question of its simple interpretation remains open.

It is the purpose of this paper to present a new approach in analysing the phase delay in grating compressors, which not only avoids the introduction of the questionable phase term, but also leads to a simpler and more accurate expression for the phase delay which contains ad additional frequency-independent phase term..

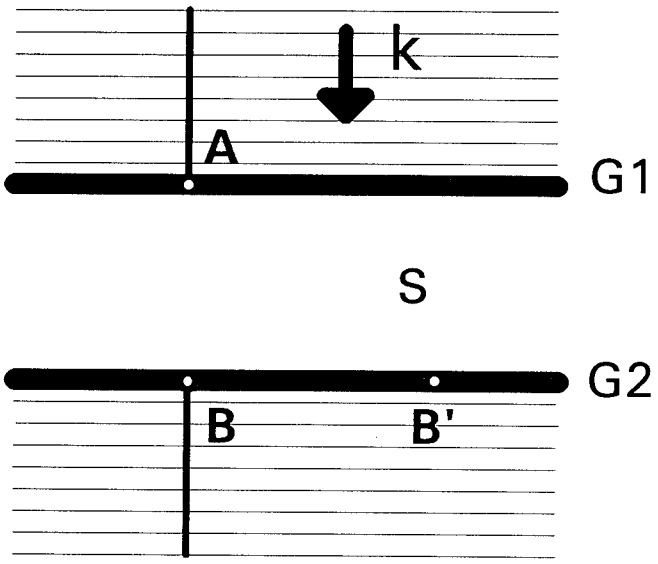


Fig.2.

Let us consider the situation shown in Fig. 2, where an infinite monochromatic plane wave falls normally to a transmitting infinite slab S confined between the planes G1 and G2. The plane wave exits as an infinite plane wave in exactly the same direction which implies that the slab has either zero or compensated angular dispersion. Let us consider for an instant that the modification of the plane wave within the slab is unknown (the slab is considered as a black box) and we are interested only in the phase delay for the transition through the slab. Since we are dealing with infinite plane waves, the phase delay problem is reduced to finding the delay *in the slab* between any pair of points A and B from a straight line parallel to the direction of the wave normal. There is no reason to chose another direction in order to calculate the phase delay, say AB' as was done in the Treacy's paper.

Next, let us consider the situation presented in Fig.3, where G1, G2 are parallel identical gratings which are ruled in a direction perpendicular to the drawing. The incident plane wave is transformed into another plane wave which propagates at an angle α with respect to the grating normal. The angle in the m-th order (m=0,±1,±2, ...) is determined by the grating constant d and the angular frequency ω in agreement with the grating equation:

$$d.\sin\alpha = m2\pi c/\omega \qquad (2)$$

In calculating the phase delay between points A and B (Fig.3) we apply the textbook definition for a phase delay between two arbitrary points in a space filled with an infinite plane wave. The phase delay is given by the scalar product of the wave vector **k** in the space between the gratings and **AB,** along which the phase delay is evaluated: $\phi(\omega) = \mathbf{k.AB}=(\omega/c).AB.\cos\alpha$, where AB is the distance between the two points. For the situation depicted in Fig.3, the phase delay will be expressed by the distance between the gratings G = AB and the angle of diffraction α which is also the angle the angle between the wave vector **k** and **AB** :

$$\phi(\omega) = \mathbf{k.AB}=(\omega/c).G.\cos\alpha \qquad (3)$$

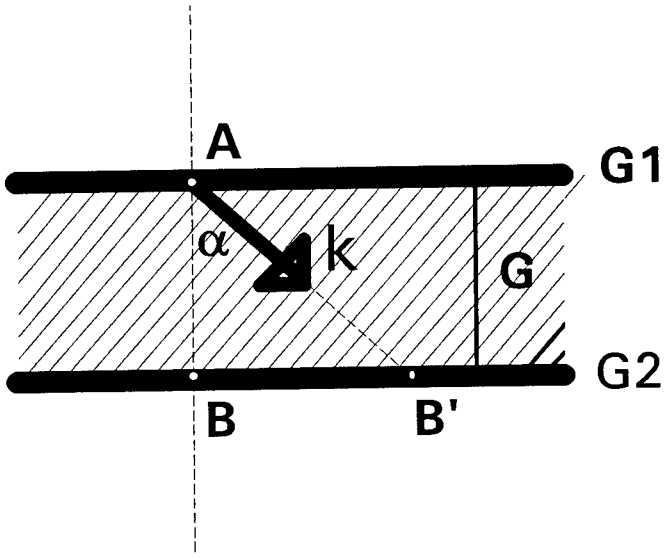


Fig.3

Equation (3) is the new expression for the phase delay experienced by a plane wave after passing the two gratings. It is very tempting to choose the direction for the phase delay along the wave normal (AB') as was done by Treacy. From the discussion of Fig.2, it follows that we have no reason to do this.
Expression (3) is identical to (1) as can be seen from the following algebraic transformations:

$$\phi(\omega)=(\omega/c)G.\cos\alpha =$$
$$(\omega/c)G.\cos^2\alpha/\cos\alpha=$$
$$(\omega/c)G.(1-\sin^2\alpha)/\cos\alpha=$$
$$(\omega/c)G/\cos\alpha-2\pi(G/d).\tan\alpha$$

To obtain the last expression, we have substituted $\sin\alpha=2\pi c/\omega d$ by applying the grating equation (2) for m=1.
For an arbitrary angle of incidence $\gamma\neq 0$ the expression is easily generalized to:

$$\phi(\omega)=(\omega/c)(G/\cos\gamma)\cos(\gamma-\alpha) \qquad (4)$$

Expression (4) is identical (within a frequency-independent term) to that of Treacy's one. Moreover, it can be shown that the frequency-independent term must also be present in Treacy's expression. From the discussions concerning Fig.2 it is evident that the way of calculating the phase delay is very general and it is applicable to any parallel structures with compensated angular dispersion. Martinez et al /6/ applied the same approach in the case of slab structures and prism-pair pulse compressors.
In conclusion, a simpler form for the expression of the phase delay in a grating compressor is found. The derivation avoids the necessity of an additional "heuristic" phase term and has a simple physical interpretation. The approach is very general and provides a unified description of arbitrary structures with compensated angular dispersion, including both grating and prism compressors. The new expression was succesfully applied in analysing recently proposed "modeless" laser cavity /7/.

References:

1. E.B. Treacy, IEEE J.Quant.Electr. QE-5 (1969) pp. 454 - 458.
2. M. Couture and M. Piche, Appl. Phys. B 45 (1988) pp. 93 - 95.
3. Brorson and H. Haus, J.Opt. Soc.Am. B 5 (1988) pp. 247,
4. A. E.Siegman, Appl. Phys. B 42 (1987) pp. 165 - 166.
5. K. A. Stankov, , Appl. Phys. B 40 (1986) pp. 103 - 105.
6. O.E.Martinez, J.P.Gordon and R.L.Fork, J.Opt.Soc.Am. A (1984) pp. 1003 - 1006
7. K. A. Stankov, **Modeless laser cavity,** Paper CThL5, Conference on Lasers and Electro-Optics, CLEO'93, May 2 - 7, 1993, Baltimore, USA

A 3-D NUMERICAL CODE FOR THE PROPAGATION OF SHORT OPTICAL PULSES IN NONLINEAR MEDIA

M.A. Franco, B.S. Prade, J-Y. Vinet, A. Mysyrowicz
Laboratoire d'Optique Appliquée
Centre National de la Recherche Scientifique URA 1406
ENSTA - Ecole Polytechnique - 91120 Palaiseau, FRANCE

Analytical solutions of the propagation of optical pulses in nonlinear media are limited to very simple situations. Simulation codes are therefore indispensable to extend the field of applications.

We have developed a numerical code able to calculate the propagation of short ultra-intense pulses through transparent nonlinear media. The method is similar to the well-known split-step algorithm used for optical fibers, except for the fact that the fully three-dimensional character of the problem is considered.[1] In a first step, diffraction and dispersion effects are calculated for each spectral component of the pulse over an arbitrarily small propagation distance by matrix multiplication of the corresponding propagator; in a second step the temporal shape of the pulse is reconstructed and the nonlinear effects are calculated in the time domain over the same distance. This method is well adapted to a propagation through various successive media, and can encompass the group velocity dispersion to all orders in a natural way. The code has been developed for (a) axi-symmetric cases by the use of the Hankel transform method and (b) for a spatially asymmetric two-dimensional problem by the use of Fourier transforms. The Hankel transform method yields a reduction of computation time by typically two orders of magnitude when compared to the fully 3-D case.

The field of applications of the code includes the description of the propagation of intense short optical pulses through air and glass . Various

initial conditions can be introduced such as chirped pulses or sequences of pulses which are coupled by nonlinear effects inside the medium. Also the effect of different transverse intensity profiles of the beam can be modeled enabling the study of self-focusing and self-guiding.

Our algorithm has been validated by comparison of the results with limiting cases of known analytical solutions. It has been applied to interpret the interference pattern observed in the spectrum of very intense femtosecond pulses from an amplified Ti:saphire laser after propagation through air and various optical glasses.[2]

One interesting application of the code is the modelling of a simple focusing system for femtosecond oscillator-amplifier systems delivering Terawatt powers. By a proper choice of the geometry of a transparent optical material, it should be possible to obtain a non-linear lens without increasing the pulse duration.

references:

1) R. A. Fisher, W. K. Bischel J. Appl. Phys.46, 4921 (1975)

2) E. Nibbereing et al to be published

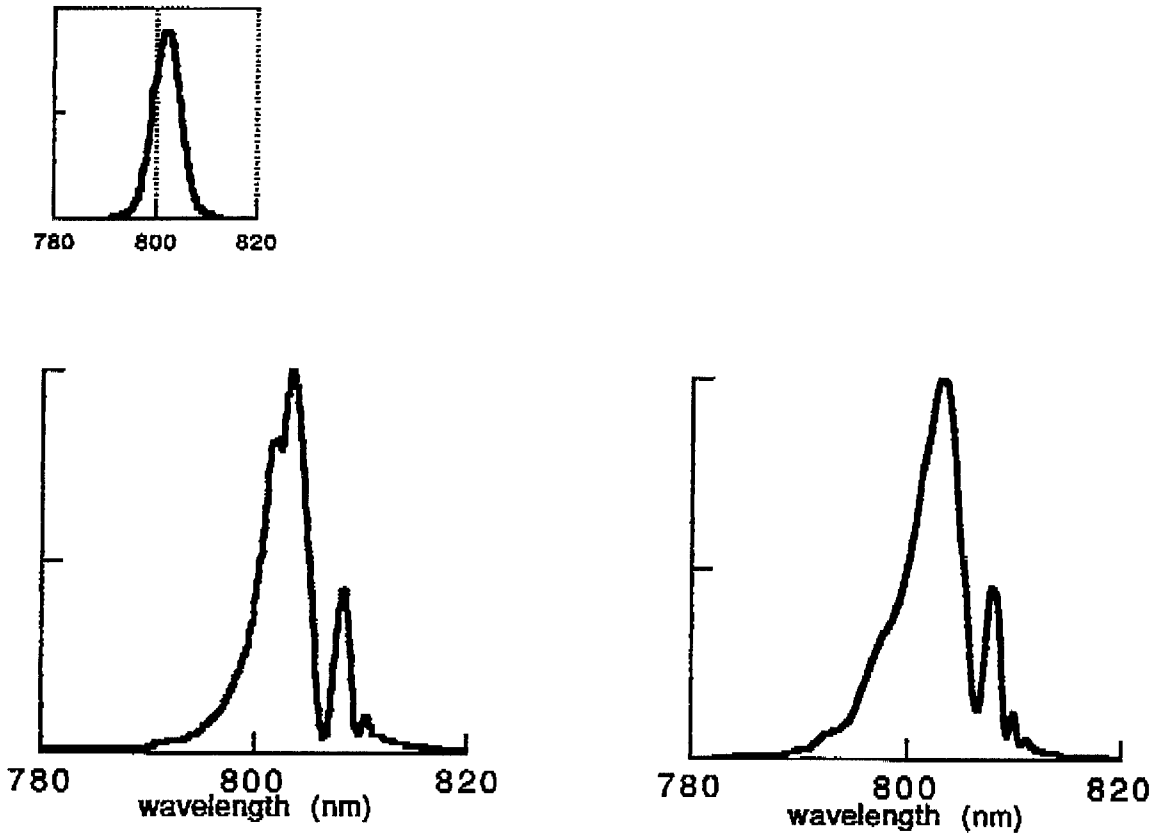


Figure caption:

Left : spectrum of a 150fs (FWHM) optical pulse from a Ti:sapphire laser after a propagation through 1cm of BK7 glass (input energy: 26 mJ; beam diameter of gaussian profile: 2cm). The inset shows the input spectrum.

Right : calculated spectrum of the same pulse using the 3D numerical code. The observed spectral structures are sensitive to the 3^{d} and 4th order phase distortion of the input spectrum.

Upper satellite conduction band population dynamics in GaAs measured by femtosecond UV pump - IR probe absorption spectroscopy

Michael A. Cavicchia and R. R. Alfano

Institute for Ultrafast Spectroscopy and Lasers, Center for Advanced Technology for Photonic Materials and Applications, Physics Department,
The City College and The Graduate School of the City University of New York,
Convent Avenue @ 138th Street, New York, New York 10031
phone: (212) 650-5531, fax: (212) 650-5530
e-mail: cav@scisun.sci.ccny.cuny.edu, alfano@scisun.sci.ccny.cuny.edu

Over the past twenty years hot electron dynamics have been studied in the central (i.e., k=0), Γ, and satellite (i.e., k≠0), L and X_6, *lower* conduction band valleys in bulk GaAs and quantum wells using ultrafast laser spectroscopy.[1-4] A Monte Carlo calculation has shown that the satellite, X_7, *upper* conduction band valley plays an important role in the high-field transport properties of GaAs.[5] We will present for the first time an experimental study of the intervalley relaxation dynamics of a hot electron population in the satellite, X_7, *upper* conduction band valley in GaAs using time-resolved UV pump-IR probe absorption spectroscopy.

An intense, 500-fs UV (293 nm) pump pulse is used to photoexcite electrons from the valence bands to the central, Γ, lower conduction band valley. The photoexcited electrons obtain sufficient kinetic energy to undergo intervalley scattering to both the X_6 and X_7, satellite conduction band valleys (see Fig. 1). Subsequent energy relaxation occurs and the electrons are redistributed among the conduction band valleys by inter- and intravalley scattering among and within the X_6, X_7, L, and Γ valleys (see Fig. 2). A weak, 500-fs, IR (4.7 μm) probe pulse is used to monitor the temporal behavior of the induced IR absorption due to the free electron populations in the conduction band valleys.

Fig. 3 shows the transient change in IR absorption, ΔO.D., as a function of pump-probe

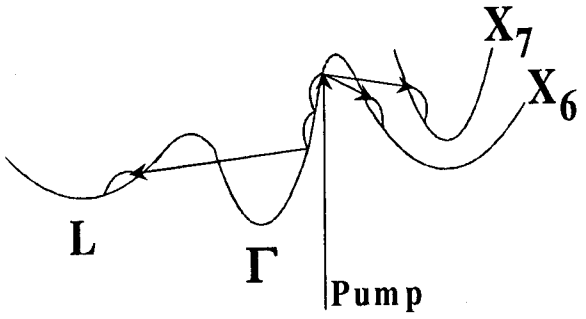


Fig. 1 The initial relaxation channels involving the lower X_6, Γ, and L valleys and the upper X_7 valley, subsequent to UV photoexcitation.

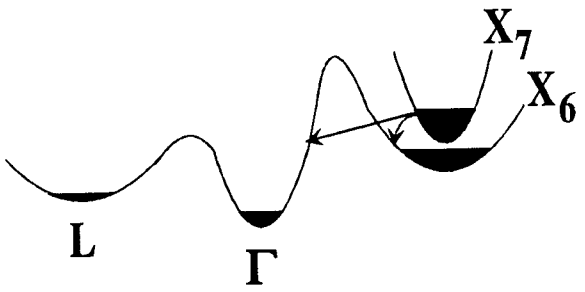


Fig. 2 The X_7 valley population is depleted by intervalley scattering to the X_6 and central Γ valleys.

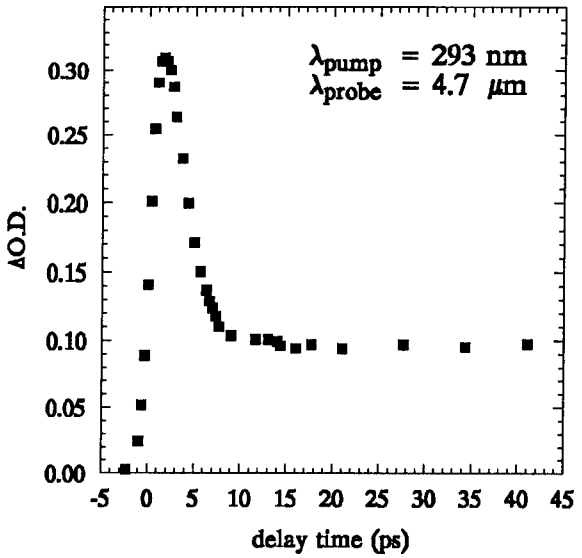


Fig. 3 Transient induced IR absorption where λ_{pump} = 293-nm and λ_{probe} = 4.7-μm.

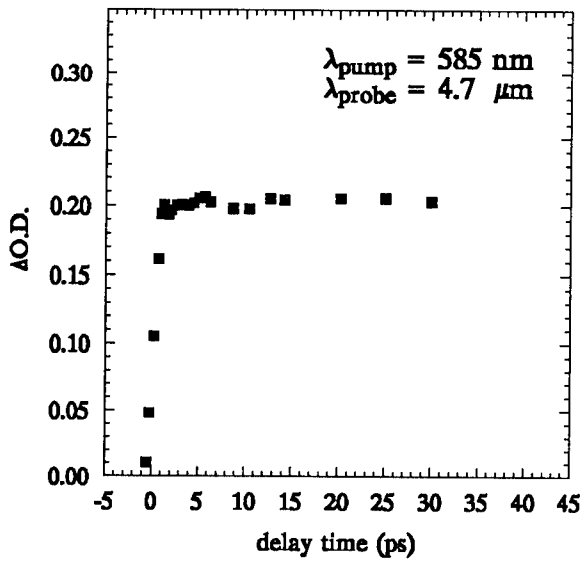


Fig. 4 Transient induced IR absorption where λ_{pump} = 585-nm and λ_{probe} = 4.7-μm.

delay time for λ_{pump} = 293-nm and λ_{probe} = 4.7-μm. The temporal behavior is characterized by a rapid rise in absorption, followed by a fast decay component (~ 4 ps), and finally a slow decay component which is flat during the experimental time range of 100-ps. Measurements of the induced IR absorption spectra have shown that probe photons with a wavelength of 4.7-μm are not energetic enough to cause electron transitions from the X_6 valley to the X_7 valley.[6,7] Intervalence band absorption is negligible for our experimental conditions.[6,7] Therefore, it is assumed only free carrier absorption (FCA) contributes to the induced absorption. The peak observed in Fig. 3 at early delay times is not seen when λ_{pump} = 585-nm and λ_{probe} = 4.7-μm. This result is shown in Fig. 4 and is characterized by a rapid rise in absorption and only a slow decay component which is flat during the experimental time range of 100-ps.

For λ_{pump} = 293-nm, there are electron populations in both the X_6 and X_7 valleys. From lineshape fits to the induced spectra it has been shown for our experimental conditions that essentially all of the photoexcited electrons are in the X valleys and have thermalized at a delay time of 2-ps.[6] As the electrons in the X valleys cool, the X_7 valley is depopulated by intervalley scattering, $X_7 \rightarrow X_6$ and $X_7 \rightarrow \Gamma$. The minimum energy of the X_7 valley barely overlaps the maximum energy of the L valley so $X_7 \rightarrow$ L intervalley is negligble.[8] On the other hand, for λ_{pump} = 585-nm, the photoexcited electrons do not obtain sufficient kinetic energy to undergo intervalley scattering to the X_7 valley. Thus, for this experimtental condition, there is no electron population in the X_7 valley and there is no depopulation of the X_7 valley. Therefore, we attribute the observed 4-ps decay in Fig. 3 to depopulation of the satellite, X_7, upper valley.

In the classical Drude model, the FCA at a particular wavelength is related to the carrier density, N, the carrier effective mass, m*, and the carrier mobility, μ, by $\Delta O.D. \propto N/(m^*\mu)$. Therefore, electrons residing in different valleys, with different effective masses and mobilities, will have different FCA cross-sections. To obtain the contribution of the X_7 valley electrons to the total FCA, the flat region of Fig. 4 is normalized to the flat region of Fig. 3 and then Fig. 4 is subtracted from Fig. 3. The resulting points are shown in Fig. 5 and on an expanded time scale in

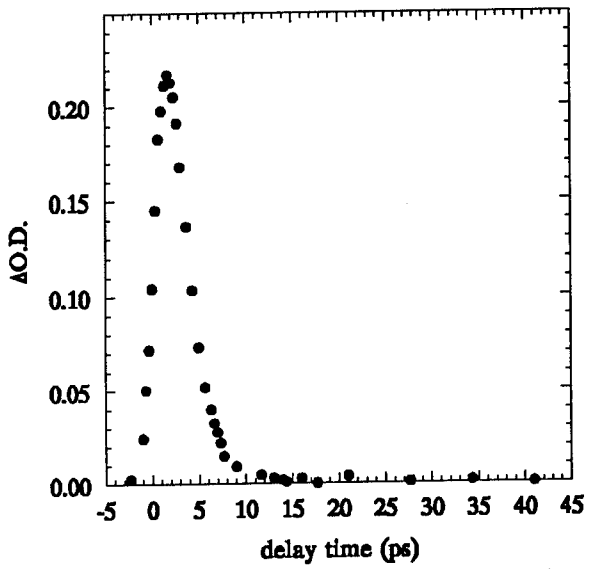


Fig. 5 The X_7 valley electron population contribution to the induced FCA. The peak is at 1.7-ps and the decay time is 3.4-ps.

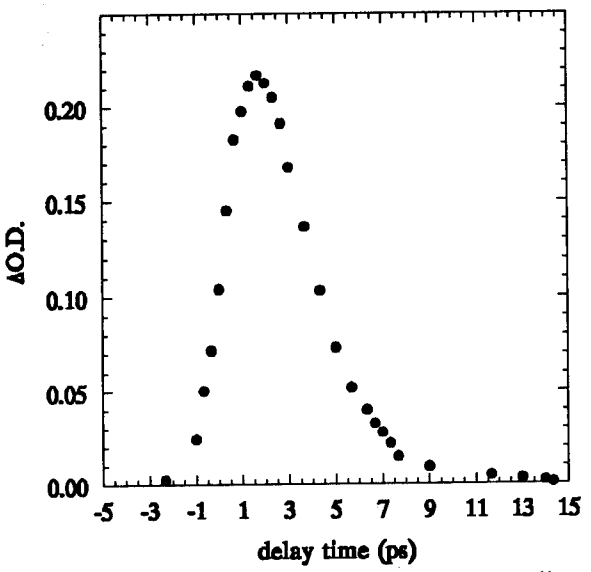


Fig. 6 The temporal profile of the X_7 valley electron population contribution to the induced FCA on an expanded time scale.

Fig. 6. This curve is proportional to the temporal evolution of the X_7 valley electron population. The X_7 valley electron population peaks at 1.7-ps and has a decay time of 3.4-ps. For λ_{pump} = 293-nm, the electrons are excited to an excess energy of 1.58-eV and it is estimated an electron will undergo intervalley scattering back and forth between the X_7 valley and the X_6 and Γ valleys 19 times before its energy falls below the X_7 valley minimum. Consequently, an upper limit for the intervalley scattering time for an electron in the X_7 valley to either the X_6 or the Γ valley, $X_7 \rightarrow X_6,\Gamma$, is determined to be 180-fs.

In conclusion, a femtosecond time-resolved UV pump - IR probe absorption measurement has provided a **direct** observation of the intervalley relaxation dynamics of the satellite, X_7, *upper* conduction band band valley for the first time and has allowed a determination of an upper limit for the $X_7 \rightarrow X_6$, Γ intervalley scattering time.

References

1. M. C. Nuss, D. H. Auston, and F. Capasso, Phys. Rev. Lett. **58**, 2355 (1987).
2. R. W. Schoenlein, W. Z. Lin, S. D. Brorson, E. P. Ippen, and J. G. Fujimoto, Appl. Phys. Lett. **51**, 1442 (1987).
3. J. L. Oudar, A. Migus, D. Hulin, G. Grillon, J. Etchepare, and A. Antonetti, Phys. Rev. Lett. **53**, 384 (1984).
4. W. H. Knox, C. Hirlimann, D. A. B. Miller, J. Shah, D. S. Chemla, and C. V. Shank, Phys. Rev. Lett. **56**, 1191 (1986).
5. T. González Sánchez, J. E. Velázquez Pérez, P. M. Gutiérrez Conde, and D. Pardo Collantes, Semicond. Sci. Technol. **6**, 862 (1991).
6. M. A. Cavicchia and R. R. Alfano, Phys. Rev. B **48**, 5696 (1993).
7. W. B. Wang, N. Ockman, M. A. Cavicchia, and R. R. Alfano, Appl. Phys. Lett. **57**, 395 (1990).
8. J. R. Chelikowsky and M. L. Cohen, Phys. Rev. B **14**, 556 (1976).

Coherence Transfer in Photoinitiated Solution Phase Reactions

Nick Pugliano, Arpad Z. Szarka, Dipak K. Palit, and Robin M. Hochstrasser
Department of Chemistry, 231 S. 34th St., University of Pennsylvania
Philadelphia, Pennsylvania 19104
(215) 898-8247

Introduction

The use of ultrashort laser pulses to photoinitiate chemical reactions in solution has lead to the observance of vibrational coherence transfer from reactant states into the product manifold. By resolving the wavepacket contributions in the transient response, the solvent influence on the reaction pathway may be probed. As a result, information regarding product state distributions and the existing offdiagonal density matrix elements becomes accessible. For many photochemical processes the initiation pulse must be in the ultraviolet spectral region. Therefore, a femtosecond pump/probe spectrometer, capable of delivering 70 fs; 5 μj 310 nm pulses, has been constructed for this purpose. It has enabled the study of the solvent sensitivity of wavepacket dynamics in two photochemical reactions; the photodissociation of HgI_2[1] and the photoisomerization of cis-stilbene. These experimental results, and an improvement in the time resolution of the femtosecond spectrometer will be summarized below.

The experimental setup used to generate the present results utilizes a 20 Hz, Nd:YAG amplified CPM dye laser pulse, which is recompressed and imaged into an optical fiber. The resulting white light continuum produced is used to seed a three stage Nd:YAG pumped amplifier. This produces a pulse centered at 620 nm which is compressed to a width of 35 fs with a grating pair. A portion of the 620 nm light is frequency doubled to a create a 310 nm pump pulse having a width of ca. 70 fs. The remaining 620 nm light is directed into a variable delay line and is used to create a second white light continuum with which the sample is probed. The results described below were acquired with this experimental arrangement. Recently, a prism pair has been added to the compression of the 620 nm pulse to obtain better time resolution. The combination of the grating pair/prism pair has further compressed the 620 nm pulse to 19 fs. Cross correlating this 19 fs visible pulse with the UV pulse generated in 50 μm of BBO yields a 40 fs $sech^2$ pulse at 310 nm.

Wavelength Dependence of Vibrational Dynamics in HgI_2

The results described in Ref. 1 were presented in two solvents; ethanol and DMSO. HgI_2 is photolyzed with the UV pump to produce HgI and atomic iodine. The spectroscopic data along with a bleaching experiment and a nanosecond time resolved absorption spectrum, verify that the photoproduct is in fact HgI.[1] All of the data presented within uses ethanol as the solvent and illustrates the wavelength dependence of the wavepacket dynamics[2] and the vibrational cooling which subsequently follows the dephasing of the coherence. In Figure 1, two time resolved transients are shown at the indicated probe wavelengths of 660 nm and 520 nm. Both data sets exhibit a rapidly damped oscillatory component indicating that the HgI fragment is born in a superposition of its vibrational states. The data were fit to the following model,

$$A\exp(-t/\tau_A) + B\exp(-t/\tau_B)\cos(2\pi c\nu_B t + \phi) + C\exp(-t/\tau_C)\cos(2\pi c\nu_C t). \quad (1)$$

The first term in Eqn. 1 describes the population decay of the vibrational distribution probed at the specified wavelength. The most prominent oscillation is described with the second term, and the bump on the rising edge of the signal is interpreted as a zero phase oscillation resulting from probing the dissociating HgI_2 through a two photon absorption. The contribution from this zero phase beat is extremely small in the 660 nm transient although its amplitude increases as the wavelength of the second photon is tuned to the blue. This indicates that the excited state absorption cross section from the dissociating surface of HgI_2 becomes larger as the energy of the second photon increases. In Figure 2 the same experiments show the hot vibrational population decaying into an absorption plateau which represents the vibrationally equilibrated HgI radical. In fitting the oscillations, which are excluded from the fits in Figure 2, the values for τ_A are fixed. The relevant parameters describing the vibrational dynamics for the transients probed at 660/520 are ν_B=89.5/92.2 cm^{-1}, ν_C= Not Determined/129 cm^{-1}, τ_A= 2.8/16 ps and τ_B = 330 fs is approximately the same for both data sets.

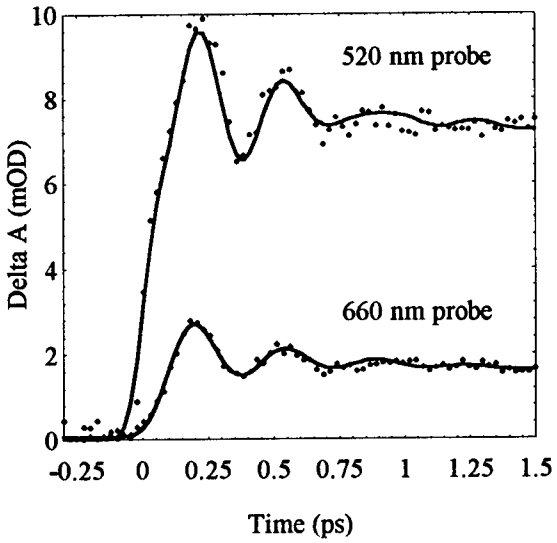


Figure 1. Wavelength dependence of the vibrational coherence in the solvated HgI.

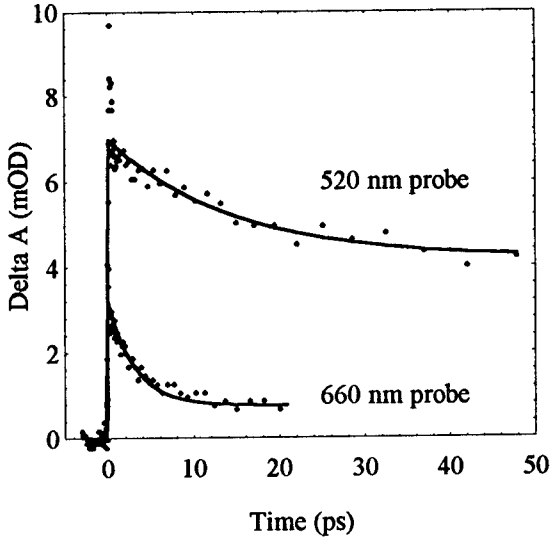


Figure 2. Wavelength dependence of vibrational relaxation in solvated HgI.

It is clear from the values of τ_A that the rate of vibrational relaxation rate is slower for the results probed at bluer wavelengths. This is most likely because the portion of the HgI vibrational distribution probed at 520 nm is energetically lower on the ground state of the diatomic. This is also corroborated by the increase in vibrational frequency at 520 nm. The value of ν_C is slightly lower than the frequency for the symmetric stretching vibration of HgI_2 in ethanol of 149 cm^{-1}. This feature is assigned as this mode in the dissociating parent, and its decay of 340 ± 100 fs characterizes the lifetime of the transition state. Furthermore, the increase in signal size at long time delays, upon tuning to the blue verifies the earlier work[1] which showed that the vibrationally equilibrated HgI spectrum increased from 660 nm to 400 nm. A full picture of the solvated electronic states will become possible as more wavelength dependent studies are completed. Finally, wavelength dependent anisotropy experiments are also being conducted to unravel the rotational contributions to the product state distribution, and to evaluate the symmetry of the state to which the HgI is probed.

Excited State Wavepacket Dynamics of cis-Stilbene

The isomerization of stilbene has long been considered a prototype for one dimensional barrier crossing processes. Essentially no information is available for this system which relate the vibrational dynamics evolving on the femtosecond timescale to the isomerization coordinate in solutions. Such information is needed to connect the knowledge of the initial dynamics obtained from Raman scattering[3] to the longer timescale generation of vibrationally excited products.[4] By examining vibrational coherences in the excited state conformers, it will be possible to further characterize the excited state potential surface. When exciting cis, oscillations were observed in absorption as a function of wavelength (690, 650, and 600 nm) and solvent (methanol and hexane). The coherent responses of the excited state were distinctly solvent sensitive and differed from recent observations of gaseous stilbene.[5] A representative transient is shown in Figure 3 for a methanol solution. The data were fit to Eqn. 1 with C being fixed at zero. This yielded a frequency of 124 cm^{-1} for the oscillation and a dephasing time constant of 100 fs. As the wavelength is tuned to the red, a relative phase shift toward π is observed. These results show critical features of the reactive excited state surface and characterize the spatial extent of this region.

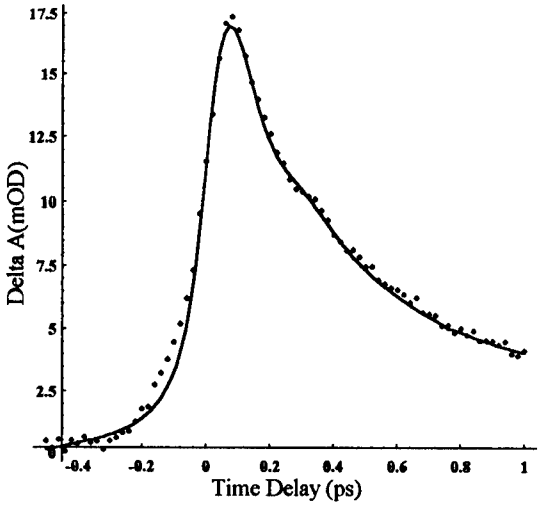


Figure 3. A representative excited state cis-stilbene transient in methanol.

Currently the shorter pulses described above are being used to further examine the vibrational dynamics of HgI_2 and stilbene. These results along with a complete analysis of the earlier data will be presented at the meeting.

[1] N. Pugliano, D. K. Palit, A. Z. Szarka, and R. M. Hochstrasser, J. Chem. Phys. **99**, 7273 (1993).
[2] M. Greubele, G. Roberts, and A. H. Zewail, Phil. Trans. R. Soc. London, Ser A **332**, 223 (1990).
[3] A. B. Myers and R. A. Mathies, J. Chem. Phys. **81**, 1552 (1984).; A. B. Myers, M. O. Trulson, R. A. Mathies, J. Chem. Phys. **83**, 5000 (1985).
[4] R. J. Sension, A. Z. Szarka, and R. M. Hochstrasser, J. Chem. Phys. **97**, 5339, (1992).; D. L. Phillips, J. Rodier, and A. B. Myers, Chem. Phys. **175**, 1 (1993).
[5] S. Pedersen, L. Banares, and A. H. Zewail, J. Chem. Phys. **97**, 8801 (1992).

Monday, May 2, 1994

Nonlinear Spectroscopy and Solvent Dynamics

ME 4:30pm–6:00pm
Dana Point Ballroom

Michael D. Fayer, *Presider*
Stanford University

Homogeneous and Inhomogeneous Dephasing in Liquids Probed by Multi-Dimensional Femtosecond Spectroscopy

Y. Tanimura[1,2] and S. Mukamel[1]

[1]Department of Chemistry, University of Rochester,
Rochester, NY14627
T EL (716)275-3080, FAX (716)473-6889
[2]Institute for Molecular Science, Myodaij, Okazaki 444, Japan

The interpretation of vibrational lineshapes in liquids has been the subject of numerous experimental and theoretical studies. Dephasing processes are crucial for the interpretation of optical processes in condensed phases. These processes are traditionally classified as either homogeneous or inhomogeneous. When different molecules have different transition frequencies because of varying local environments or initial states, the spectral lineshape is said to be inhomogeneously broadened. This broadening carries no dynamical information. Homogeneous broadening arises from an interaction with a bath with a very fast time scale, causing rapid fluctuations in the local environment. Since nuclear motions in liquids cover a broad range of time scales, it is not clear whether spectral lineshapes can be classified as either homogeneous or inhomogeneous. Even when such classification is possible by virtue of separation of timescales, it is not easy to firmly establish it experimentally.

Impulsive stimulated Raman scattering performed using multiple pulses (Fig. 1) has the capacity to distinguish between various microscopic models of nuclear dephasing. We have calculated the nuclear response function to an arbitrary number of pulses, using a harmonic model for nuclear motions with a nonlinear coupling to the radiation field through the nonlinear dependence of the electronic polarizability on nuclear coordinates. Using electronically off-resonant optical fields, this multidimensional spectroscopy is shown to provide direct information

regarding the nature of the spectral density obtained from optical birefringence measurements. Our theory also interpolates continuously to the resonant limit where electronically excited state dynamics is being probed. The interplay of electronic and vibrational dephasing can be thus clearly demonstrated.

We illustrate how the 5'th order ($\chi^{(5)}$) off-resonant signal is affected by the nature of homogeneous and inhomegeneous distribution of nuclear oscillators. We also show that the 7'th order off-resonate signal does not show a conventional echo signal, but it has a maximum at $T_1=T_2$. This is because the model does not reduce to the simple two-level model for nuclear motions.

Y. Tanimura and S. Mukamel, J. Chem. Phys. **99**, 9496 (1993); J. Phys. Soc. Jpn. **63**, 66 (1994).

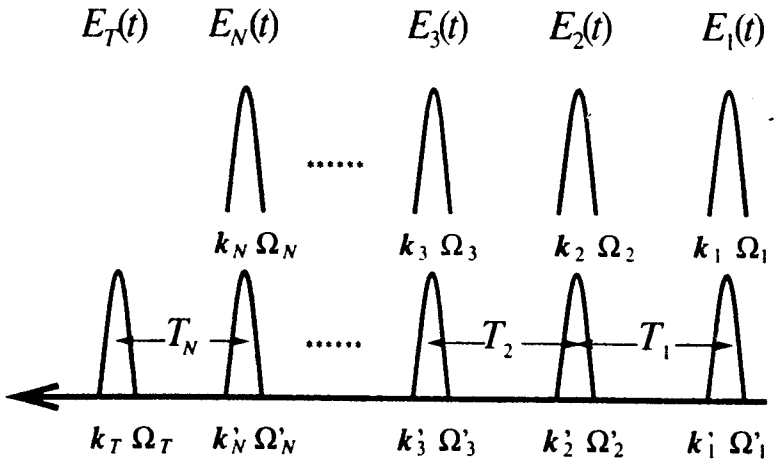


FIG. 1. Pulse configuration for a $2N+1$th order experiment. The system first interacts with N pairs of pulses, which have the same time profile $E_j(t)$, but different wave vectors $\mathbf{k}_j$ and $\mathbf{k}'_j$ and frequencies Ω_j and Ω'_j for the jth pair of pulses, respectively. The last pulse ($\mathbf{k}_T$, Ω_T) is the probe that generates the signal.

Femtosecond Photon Echo Study of Solution Dynamics Using a Cavity-Dumped Ti:sapphire Laser

Wim P. de Boeij, Maxim S. Pshenichnikov, Koos Duppen and Douwe A. Wiersma

Ultrafast Laser and Spectroscopy Laboratory
Department of Chemistry, Material Science Centre,
University of Groningen,
Nijenborgh 4, 9747 AG Groningen, The Netherlands
Telephone: -31-50634324 Telefax: -31-50634441
Internet: wiersma@chem.rug.nl

It has long been recognized that a better grasp of solution dynamics is essential to our understanding of chemical reactions in the liquid phase. A prime example of reaction dynamics is the so-called "cage" effect, where products of a fragmentation reaction cannot escape from one another because of collisions with solvent molecules. A more profound understanding of this phenomenon and other solvent dynamics, like solvation, remains a formidable challenge and is at the heart of physical chemistry.

Only recently the ultrafast dynamics of solute-solvent interaction has become accessible by direct time-domain nonlinear optical experiments[1]. However, the technology required to perform these experiments - based on compression of the amplified CPM laser - has been acquired only by a few laboratories, not the least due to the high cost of the necessary laser equipment.

With our recent success in the construction of a cavity-dumped Ti:sapphire laser[2], which produces 13 fs pulses at a 200 kHz repetition rate with pulse energies exceeding 60 nJ, this situation will change, as now a relatively cheap ultrafast laser can be made that is suitable to generate fs photon echoes in the condensed phase. The interferometric autocorrelation of the laser output is shown in Fig. 1, while the corresponding spectrum is given in Fig. 2a. By injection of the cavity-dumped 13 fs pulse in a single-mode fiber a continuum is generated, depicted in Fig. 2b, that extends from 500 nm to over 1 μm. Compression to pulses of less than 10 fs has also been demonstrated.

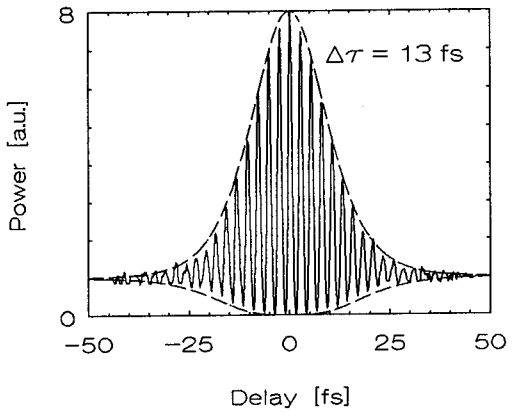


Fig.1. Interferometric autocorrelation of cavity-dumped pulses. The pulse duration is 13 fs, assuming sech^2(t) intensity profile. The dashed lines represent the calculated envelop for interferometric fringes.

The question may be raised why the direct 80 MHz output of a mode-locked Ti:sapphire laser is not used for the aforementioned experiments, as pulses of such a laser can

be made as short as 11 fs. For some optical coherence experiments, like the accumulated photon echo, this option is indeed available. However, in ***single-shot*** four-wave mixing experiments like the (stimulated) photon echo it is essential that every excitation cycle probes a relaxed state of the system. For solutions this can be realized by flowing the sample; nevertheless, the flow-speed cannot be made so high that with a modelocked laser every pulse from the train excites a fresh spot. In order to prevent thermal accumulation effects use of a cavity-dumped laser is therefore essential. Nonlinear optical experiments with a cavity-dumped Ti:sapphire laser will also greatly benefit from the fact that the pulse energy is increased by an order of magnitude. Also we note that chirped four-wave mixing experiments with a Ti:sapphire laser are only possible by cavity-dumping of the laser.

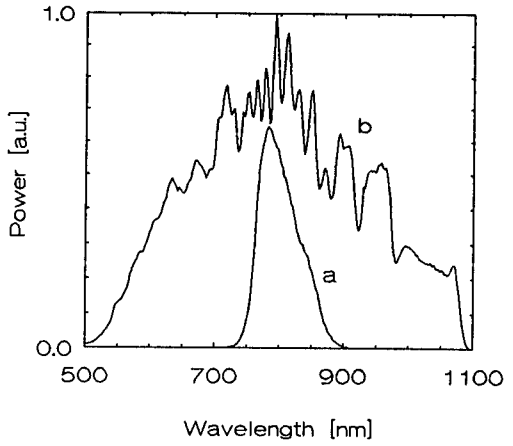


Fig.2. Spectra of pulses from cavity-dumped Ti:sapphire laser (a) and after their passage through fiber (b).

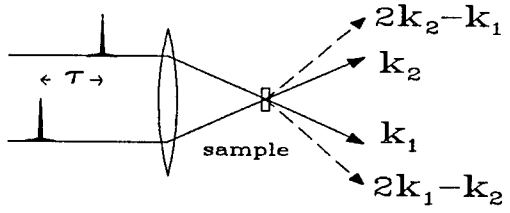


Fig.3. Schematics of experiments. The signals in both $2k_2$-k_1 and $2k_1$-k_2 phase matching directions are detected simultaneously.

We have performed a series of four-wave mixing experiments using 13 fs pulses and chirped pulse excitation. In this study several IR dyes (IR140, DNTTCI, DDCI-4, HITCI) in the solvents ethylene glycol (EG), methanol and dimethylsulphoxide (DMSO) were examined; here we present our results on the dye solution HITCI/EG. In a recent pump-probe study[3] the dephasing dynamics of this system was investigated, using the Bloch model for analysis. The optical absorption spectrum of the dye is given in Fig. 3, while the schematics of the four-wave mixing setup is shown in Fig 4. Figures 5a and 5b present the two-pulse photon echo and chirped four-wave mixing signals, respectively, detected in conjugate phase-matched directions ($2k_1$-k_2; $2k_2$-k_1). Simultaneous detection of the signals in these directions allows an accurate determination of the zero delay point, which is important in the analysis. The photon echo is found to decay with a time constant of 14 ± 2 fs, which in the Bloch model corresponds to a dephasing time constant T_2 of 56 ± 8 fs, and which is about a factor of two longer than reported in Ref. 3.

From previous photon echo experiments by the Shank group[1] and ourselves[4], it has become clear that solution dynamics cannot be modeled by use of the optical Bloch equations, but that a stochastic modulation model must be employed. Recently the so-called multi-mode Brownian oscillator (MBO) model was shown to provide an excellent description of the solvent dynamics in the case of resorufin in DMSO[4,5].

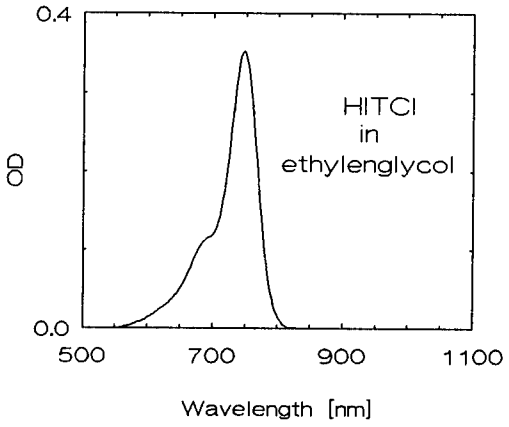


Fig.4. Absorption spectrum of HITCI in ethylenglycol.

The important parameters in the MBO model are Δ, representing the amplitude of the stochastically fluctuating force and Λ, its inverse correlation time. In the aprotic solvent DMSO only one Brownian oscillator was needed to capture the important solvent motions. Stimulated photon echo experiments on other dye solutions, however, show that generally a larger number of Brownian oscillators are needed to capture all relevant solvent motions.

Our results on HITCI in EG show, not surprisingly, that at least two Brownian oscillators are needed to simulate the optical dynamics of HITCI in this protic solvent. This can be immediately concluded by comparing Figs. 5a and 5b. The fact that the chirped four-wave mixing[5] signal is distinctly asymmetric and peaking near zero-delay time is clear evidence for the existence of a solvent motion whose correlation time is slow compared to the echo decay time. By simulating both the photon echo and chirped four-wave mixing response a reasonable fit could be made to both sets of data and to the optical spectrum by using two Brownian oscillators: one representing a nearly static situation (inhomogeneous broadening) $\Delta >> \Lambda$, the other showing intermediate dynamics $\Delta \approx \Lambda$. The nearly "static" oscillator is assigned to solvent motion correlated with the breaking of hydrogen bonds in the solvent, the other oscillator, most likely, reflects dynamics in the first solvation shell.

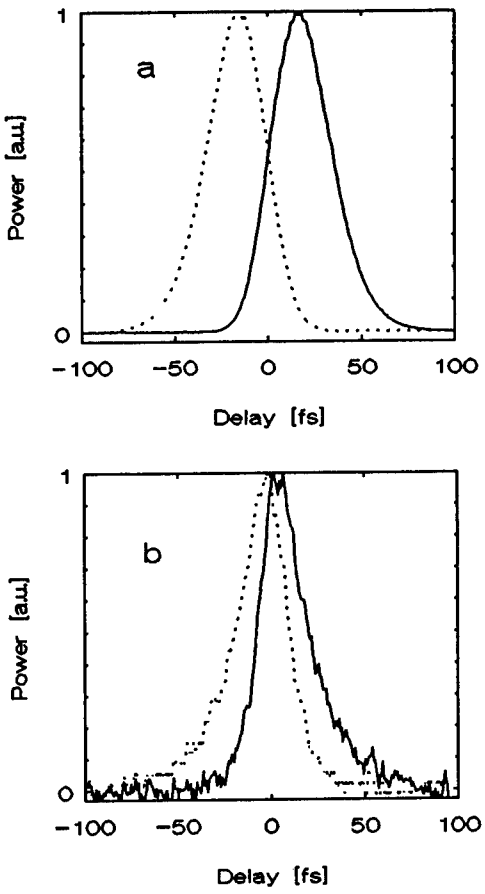


Fig.5. Two-pulse photon echo (a) and chirped four wave mixing (b) signals detected in both $2k_2$-k_1 (solid line) and $2k_1$-k_2 (dotted line) directions.

References

1. P.C.Becker, H.L.Fragnito, J.-Y.Bigot, C.H.Brito-Cruz, R.L.Fork and C.V.Shank, Phys. Rev. Lett. **63**, 505 (1989); J.-Y.Bigot, M.T.Portella, R.W.Schoenlein, C.J.Bardeen, A.Migus and C.V. Shank, Phys. Rev. Lett. **66**, 1138 (1991).
2. M.S.Pshenichnikov, W.P. de Boeij and D.A.Wiersma, Opt. Lett., submitted for publication.
3. P.Cong, H.P.Deuel and J.D.Simon, Chem. Phys. Lett. **212**, 367 (1993).
4. E.T.J.Nibbering, D.A.Wiersma and K.Duppen, Phys. Rev. Lett. **66**, 2464 (1991); ibid. **68**, 514 (1992).
5. K.Duppen, F. de Haan, E.T.J.Nibbering and D.A.Wiersma, Phys.Rev. **A47**, 5120 (1993). E.T.J.Nibbering , D.A.Wiersma and K. Duppen, Chem. Phys., to be published.

Mechanical relaxation and solvation dynamics in nonpolar solutions

John T. Fourkas, Andrea Benigno, Jangseok Ma,
David Vanden Bout and Mark Berg

Department of Chemistry and Biochemistry,
University of Texas, Austin, Texas 78712, USA
(512) 471-4999
(512) 471-8696 (FAX)

We have used transient hole burning measurements to make the first measurements of solvation dynamics in a completely nonpolar system: dimethyl-*s*-tetrazine (DMST) in *n*-butylbenzene.[1,2] A new model for solvation based on the mechanical response of a viscoelastic solvent explains the main experimental features and predicts new features on the femtosecond timescale. Although the mechanical solvation mechanism is most prominent in nonpolar systems, it should play a role in all solvation[3,4] and electronic dephasing[5-8] processes.

Experimentally, the solvation dynamics are found to consist of two distinct components distinguished by their different temperature dependences. Although both components are subpicosecond at room temperature, as the temperature is lowered, one component remains subpicosecond, while the other slows dramatically.

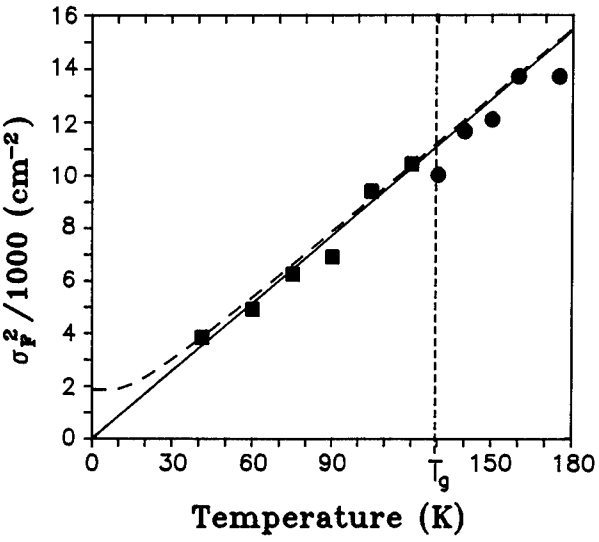


Fig. 1. Phonon-induced broadening of the DMST electronic transition in the solid glass (■). Fits to the full (dashed) or high-temperature (solid) theories of phonon-induced broadening are extrapolated above the glass transition (T_G) into the liquid phase. The transient hole burning widths at 1.5 ps (•), reflecting the ultrafast solvation component, match the extrapolation of the solid-state phonon mechanism.

The fast component is caused by the liquid-phase analog of solid-state phonons, as demonstrated in Fig. 1. The low-temperature side of the figure shows the amount of phonon-induced broadening of the electronic transition in the glassy phase as measured by permanent hole burning. A fit to standard solid-state theories is extrapolated into the liquid phase at high temperatures. In the liquid phase, the broadening of the transient hole burning at 1.5 ps reflects the magnitude of the fast solvation component. The extrapolated solid-state results exactly matches the amount of subpicosecond solvation in the liquid.

Following the phonon-induced solvation, there is a second relaxation related to reorganization of the solvent structure. Through a combination of transient hole burning and time-resolved fluorescence, this structural relaxation has been followed over 4

orders-of-magnitude change in relaxation time. In Fig. 2, the structural solvation time is compared to the shear relaxation time of the solvent. The shear relaxation time is derived from viscosity and ultrasound data and is entirely independent of our solvation measurements. The structural solvation and shear relaxation times are almost exactly equal over the entire observable range.

We have explained these results by proposing a new mechanism for solvation. The solvent is treated as a viscoelastic continuum which responds mechanically to changes in solute size and shape on changing electronic state. Example calculations based on this model are shown in Fig. 3. Two relaxation components are seen. One component is subpicosecond and nearly temperature independent and is caused by the creation of propagating waves (phonons). The time of the second relaxation is determined by the shear relaxation time (structural). It slows markedly at low temperatures, but merges with the phonon component at high temperatures.

This model not only accounts for the observed experimental features, it also predicts oscillation in the phonon-induced solvation. The timescale is slow enough to be readily accessible to current femtosecond techniques.

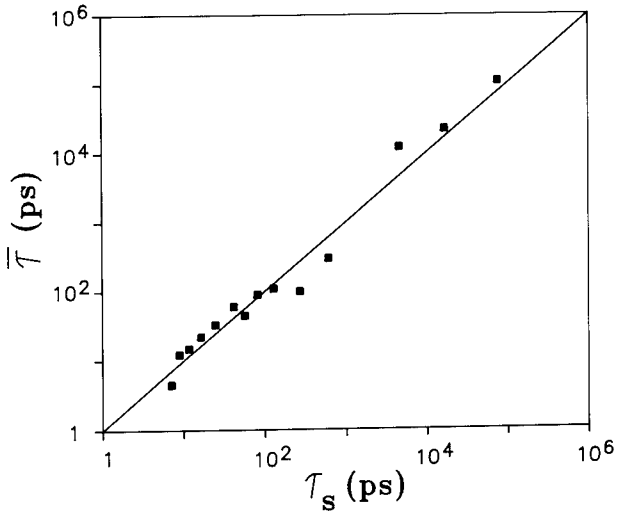


Fig. 2. Comparison of the structural solvation time τ and the shear relaxation time τ_S. The times are measured independently. The line indicates strict equality.

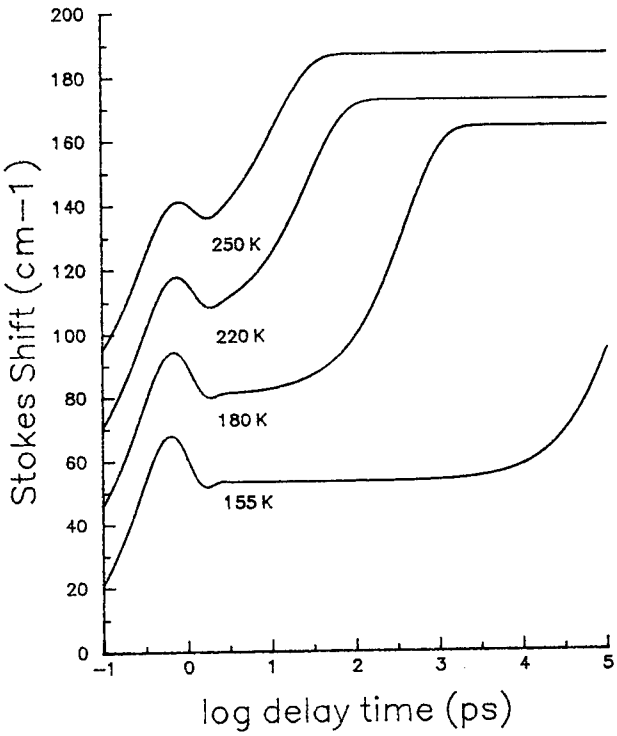


Fig. 3. Calculations of the time-resolved Stokes' shift based on a mechanical solvation model. Note the logarithmic time scale. Each temperature is shifted vertically 25 cm^{-1} for clarity. A temperature-independent, subpicosecond relaxation due to phonon creation is followed by a second relaxation determined by the shear relaxation rate.

1. J.T. Fourkas and M. Berg, J. Chem. Phys. **98**, 7773 (1993).
2. J.T. Fourkas, A. Benigno, and M. Berg, J. Chem. Phys. **99**, 8552 (1993).
3. P.F. Barbara and W. Jarzeba, Adv. Photo. Chem. **15**, 1 (1990).
4. M. Maroncelli, J. Mol. Liq., in press.
5. P.C. Becker, H.L. Fragnito, J.Y. Bigot, C.H. Brito Cruz, R.L. Fork and C.V. Shank, Phys. Rev. Lett. **63**, 505 (1989).
6. J.-Y. Bigot, M. Portella, R.W. Schoenlein, C.J. Bardeen, A. Migus and C.V. Shank, Phys. Rev. Lett. **66**, 1138 (1991).
7. C.J. Bardeen and C.V. Shank, Chem. Phys. Lett. **203**, 535 (1993).
8. E.T.J. Nibbering, D.A. Wiersma and K. Duppen, Phys. Rev. Lett. **66**, 2464 (1991).

Determination of 2-Pulse Photon Echos from Solvent Spectral Densities

D.C. Arnett, P. Vöhringer, R.A. Westervelt, M.J. Feldstein and N. F. Scherer

Department of Chemistry
University of Pennsylvania, Philadelphia, PA 19104-6323

The dynamic nature of a liquid or fluid medium causes structural changes to occur on timescales corresponding to the Fourier transform of the far-infrared or Raleigh-wing spectrum of the material.[1,2] Experiments that are performed on such short timescales are capable of directly capturing the solvent effect on or response to chemical processes.[3] For example, successful comparison of the solvent spectral density obtained from optical Kerr effect measurements and the time correlation function for solvation, obtained from fluorescence Stokes-shift measurements, has already been made.[3]

Two, three and four-pulse experiments can be treated as four-wave mixing (FWM) processes, where the pump and probe pulses combine in the sample to create a nonlinear polarization that, in turn, radiates an electric field. The nonlinear response function description of third-order polarization, $P^{(3)}(t_1,t_2,t_3)$, spectroscopy[4,5] shows that different FWM measurements of the time evolution of a solute-solvent system contain complementary information about the time correlation function of solvent fluctuations. In particular, chromophore optical dephasing is determined by the correlation function of the chromophore electronic frequency modulation and the magnitude of the coupling of the chromophore transition dipole to the bath. Photon echo methods, or more generally degenerate four wave mixing (DFWM), have been applied to the study of optical (i.e. electronic) dephasing of molecules in solution by several groups.[6-11]

We describe the results of experimental measurements and numerical calculation of the DFWM response, i.e. 2-pulse photon echo, of the cyanine dye HITCI in acetonitrile. Analogous measurements have been performed in DMSO and alcohol solutions.[12] The experiments involve the simultaneous measurement of the echo signal in the $k_3=2k_1-k_2$ and $k_3'=2k_2-k_1$ phase matched directions. This approach facilitates accurate determination of the temporal shift of the two echo signals. Solvent spectral densities, obtained from impulsive optical Kerr effect (OKE) measurements, are used to generate the lineshape function used in the nonlinear response function formalism to simulate the echo signal. Steady state solvent stokes shift parameters have been measured[13] and were used to fix the coupling strength of the oscillator and bath to their high temperature limiting values for each of the different solvents.

The short pulse source is a home-built Kerr lens modelocked Ti:Sapphire laser[14] producing 18-22 fs duration gaussian pulses with 45-50nm spectral bandwidth. The beam is split into pump and probe beams that are focused into a flowing dye jet (150μm thick) of the chromophore in various polar solvents. The echo signals in the two k-vector directions have reflection symmetry about the zero delay time. The simultaneous measurement of both diffracted beams allows an accuracy of $\approx$2fs in determining the temporal shift between the two signal maxima. The temporal shift is measured by taking the difference $\tau_{shift}(k_3) - \tau_{shift}(k_{3'})$. This temporal shift is an important constraint in fitting the echo signals.

Figure 1 shows the spectral density of acetonitrile obtained as the imaginary part[15] of the deconvoluted Fourier transform of our measured impulsive optical Kerr effect (OKE) response. Deconvolution is with respect to the pump-probe intensity autocorrelation function. The line through the data is obtained using two Ohmic functions of the form

$$C(\omega) = N\omega^{\alpha}\exp\left(\frac{\omega}{\omega_0}\right), \tag{1}$$

where α and ω_0 are fitting parameters.

In the nonlinear response function framework of $P^{(3)}$ spectroscopy any FWM optical signal can be expressed as a convolution of the correct molecular response function with a proper sequence of excitation fields. The molecular response function, $R(t,\tau)$, contains the temporal response of the system for pulses separated in time by τ and optical lineshape function g(t). We assume a well-separated pulse limit in the calculations. A general form for the lineshape function has been reported[6] that allows incorporation of solvent dynamics through a spectral density function, $C(\omega)$. The real part of the lineshape function is given by[6]

$$g(t) = \frac{1}{2\pi}\int_{-\infty}^{\infty} d\omega \frac{1-\cos(\omega t)}{\omega^2} C(\omega). \tag{2}$$

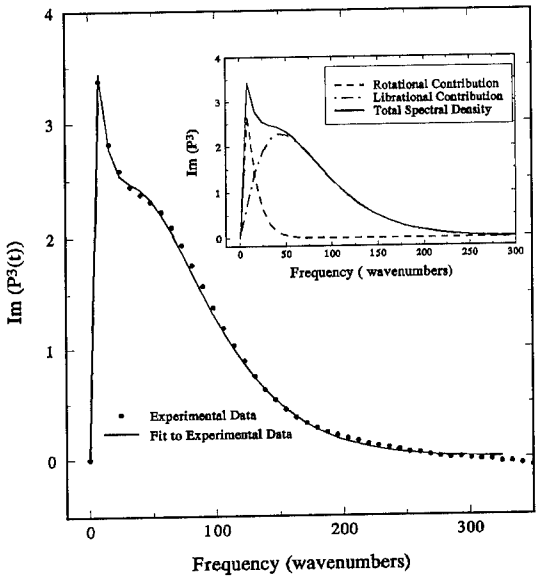
The spectral density is given by eq.(1) above.

Two-pulse photon echo calculations were performed by importing measured stokes shift magnitudes (λ) and coupling strengths ($\Delta^2 = 2\lambda k_B T/\hbar$ for $\hbar\omega << k_B T$) for HITCI in various solvents.[13] The solvent spectral density is used to fix the spectrum of solvent fluctuations that contribute to the 2-pulse photon echo signals. The calculated echo signal shown in Figure 2 is in good agreement with the experimental signal. A thermal grating contribution to the signal causes a discrepancy at early times. The fit of the time shift is primarily dictated by the spectral density while the echo width is dictated by the magnitude of the solute-solvent coupling.

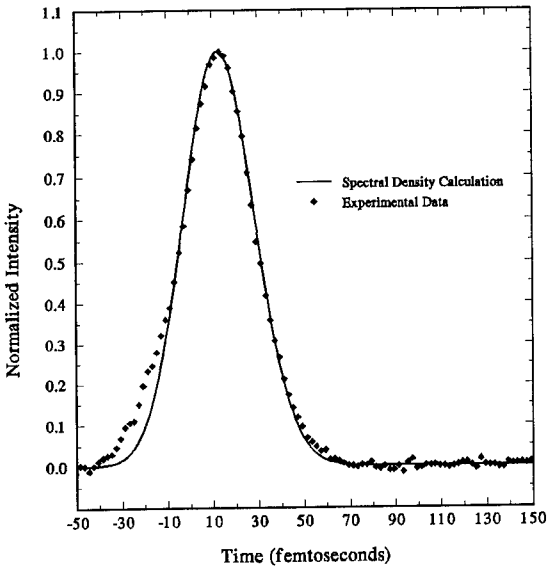
The observed 2-pulse photon echo signals of this symmetric cationic cyanine dye is similar to the two-pulse echo signals observed in oxazine dyes.[11] The echo shape is also similar to calculated photon echo signals calculated using the nonlinear response function formalism.[16] Furthermore, the timescale for and nonexponential decay of the echo signals is in agreement with recent semiclassical photon echo simulations.[17]

The principal result of this study is that the 2-pulse PE signal can be "predicted" from the neat solvent spectral density and steady-state Stokes-shift data. To emphasize, there are no free adjustable parameters other than those required to fit the spectral density. The calculated two-pulse echo signals obtained using the measured spectrum of solvent fluctuations are in close agreement with the measured 2-pulse photon echos. This suggests that the solvent spectral density obtained from impulsive OKE measurements accounts for the solvent fluctuations that determine the evolution of optical coherence of HITCI in acetonitrile. Apparently, no frequency-dependent couplings are required.

Deconvoluted Spectral Density of Acetonitrile



2-Pulse Photon Echos of HITCI in MeCN



References

1. P.A. Lund, O.F. Nielsen and E. Praestgaard, Chem. Phys., **28**, 167 (1978).
2. I. Ohime and M. Sasai, Prog. of Theor. Phys. Suppl., **103**, 61 (1991).
3. M. Cho, S.J. Rosenthal, N.F. Scherer, L.D. Ziegler and G.R. Fleming, J. Chem. Phys., **96**, 5033 (1992).
4. S. Mukamel and R.F. Loring, J. Opt. Soc. Am. **B3**, 595 (1986);Y.J. Yan and S. Mukamel, Phys. Rev. A, **41**, 6485 (1990); J. Chem. Phys., **94**, 179 (1991).
6. W.B. Bosma, Y. Yan and S. Mukamel, Phys. Rev. A, **42**, 6920 (1990).
7. A.M. Weiner, S. Fe Silvestri and E.P. Ippen, J. Opt. Soc. Am **B2**, 654 (1985).
8. P.C. Becker, H.L. Fragnito, J.Y. Bigot, C.H. Brito Cruz, R.L. Fork and C.V. Shank, Phys. Rev. Lett., **63**, 505 (1989).
9. J.-Y. Bigot, M.T. Portella, R.W. Schoenlein, C.J. Bardeen, A. Migus and C.V. Shank, Phys. Rev. Lett. **66**, 1138 (1991).
10. E.J. Nibbering, D.A. Wiersma and K. Duppen, Phys. Rev. Lett. **66**, 2464 (1991).
11. T. Joo and A.C. Albrecht, Chem. Phys., **176**, 233 (1993).
12. P. Vöhringer, D.C. Arnett, R.A. Westervelt, M.J. Feldstein and N. F. Scherer, J. Chem. Phys., submitted (1994).
13. P. Vöhringer, R. Westervelt, D. Arnett, M. Feldstein and N. F. Scherer, J. Chem. Phys., submitted (1993).
14. M.T. Asaki, C.P. Huang, D. Garvey, J. Zhou, H.C. Kapteyn and M.M. Murnane, Optics Letters, **18**, 977 (1993); F. Krausz, Ch. Spielmann, T. Brabec, E. Wintner and A.J. Schmidt, Optics Letters, **17**, 204 (1992).
15. D. McMorrow, W.T. Lotshaw, J. Phys. Chem., **95**, 10395 (1991).
16. M. Cho and G.R. Fleming, J. Chem. Phys., **98**, 2848 (1993).
17. N.E. Shemetulskis and R.F. Loring, J. Chem. Phys., **89**, 1217 (1992); A.M. Walsh and R.F. Loring, Chem. Phys. Lett., **160**, 299 (1990).

Development of Femtosecond Resonance Raman Gain Spectroscopy and Observation of Vibrational Spectrum of Excitons with 1 ps Lifetime in Polydiacetylene

Takayoshi Kobayashi[1], Masayuki Yoshizawa[2], and Yasuhiro Hattori[3]

[1]Department of Physics, Faculty of Science, University of Tokyo, Hongo 7-3-1, Bunkyo-ku, Tokyo 113, Japan
Phone +(81)-3-3812-2111 ext 4227
FAX +(81)-3-3818-7812
[2]Department of Physics, Faculty of Science, Tohoku University, Aramaki, Aoba-ku, Sendai-shi 980, Japan
Phone +(81)-22-222-1800 ext 3274
FAX +(81)-22-225-1891
[3]New Chemistry R&D Laboratories, Sumitomo Electric Industries, Shimaya 1-1-3, Konohana-ku, Osaka-shi 554, Japan

In the present paper we have developed a Raman gain spectroscopy with femtosecond resolution. The advantage of the method is as follows. (1) The method is not suffered from disturbance by fluorescence. (2) The interference of signal with nonresonant background does not appear. This is extremely advantageous to the time-resolved CARS spectroscopy. We have applied this new method to the excitons in polydiacetylene (PDA) with only 1.5 ps lifetime. This offers the vibrational spectrum with the highest time resolution.

Conjugated polymers have attracted much attention because of their unique properties as model compounds of one-dimensional electronic systems. Conjugated polymers have localized excited states with geometrical relaxation. We have investigated self-trapped exciton (STE) in polydiacetylene (PDA) using femtosecond spectroscopy [1-6]. The formation process of STE from free-exciton (FE) has been observed as a spectral change of photoinduced absorption with a time constant of about 150 fs [4]. Transient fluorescence from FE in PDA observed by probe saturation spectroscopy (PSS) has a peak at 1.9 eV and decays with the formation of the STE [6].

Time-resolved resonance Raman spectroscopy has been recognized as a powerful method for studying structures of transient species and electronic excited states. Terai et al. have calculated phonon modes of localized excited states in $(CH)_x$ and predicted that solitons and polarons can be distinguished by Raman spectroscopy [7]. However, only a few time-resolved Raman experiments have been performed in conjugated polymers because of the difficulty due to very short lifetime of the excited states [8,9]. However, the observed signals are due to the depletion of the ground state. New phonon modes of excited states in conjugated polymers have not been observed by transient Raman spectroscopy.

The femtosecond Raman gain spectroscopy was performed using three pulses of femtosecond durations as shown in Fig. 1. The 1.97-eV femtosecond pulse was generated by a colliding-pulse mode-locked dye laser and amplified by a four-stage dye amplifier [1]. The duration and energy of the amplified pulse were 100 fs and 200μJ, respectively. The amplified pulse was split into three beams. The first beam (pump-1) generated excited states in PDA. A part of white continuum generated from the second one was amplified by a two-stage dye amplifier. The amplified pulse has the center photon energy of 1.78 eV and the duration of 200 fs and was used for the pump pulse of the Raman gain spectroscopy (pump-2). The probe pulse was white continuum generated from the last beam. Using this technique the time dependence and spectra of

photoinduced absorption, bleaching, stimulated emission, and Raman gain were observed at the same time. The Raman gain signal was distinguished using the time dependence and sharp structure. Polarizations of the three beams were parallel to oriented polymer chains of PDA-3BCMU deposited on a KCl crystal [5]. All the experiment was done at room temperature.

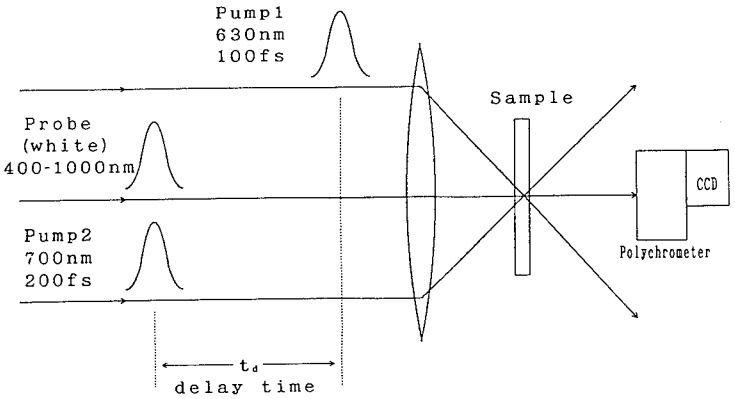


Fig.1 Time-resolved Raman gain spectroscopy.

Figure 2 shows Raman gain spectra obtained using the 1.78-eV pulse at several delay times after the 1.97-eV photoexcitation. At -0.5 ps, two Raman gain peaks are observed at 1440 and 2060 cm^{-1}. They are assigned to the stretching vibrations of the C=C and C≡C bonds in the acetylene-like structure of the ground state. The spectrum at 0.0 ps has broad signal below the 1440 cm^{-1} Raman peak down to 1000 cm^{-1}. At delay time longer than 0.2 ps the Raman signal has a clear peak at 1200 cm^{-1}. The spectral change of the Raman signal around 1200 cm^{-1} is reproducible and is observed also in PDA-C_4UC_4. The width of the 2060 cm^{-1} Raman signal becomes slightly broader after the photoexcitation, but no new Raman peak is observed around 2000 cm^{-1}.

Figure 3 shows the transient Raman gain change at 1200 and 1440 cm^{-1}. The negative change at 1440 cm^{-1} is explained by the depletion of the ground state due to the formation of STE. The time dependence is consistent with the decay kinetics of the STE. The signal appears slightly slower than the 1.97-eV pump pulse and decays within several picoseconds. The solid curve is the best

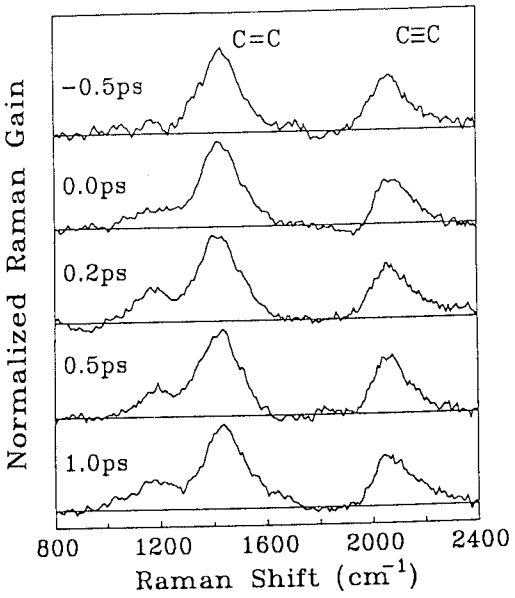


Fig. 2. Normalized resonance Raman gain spectra at several delay times after the 1.97-eV photoexcitation.

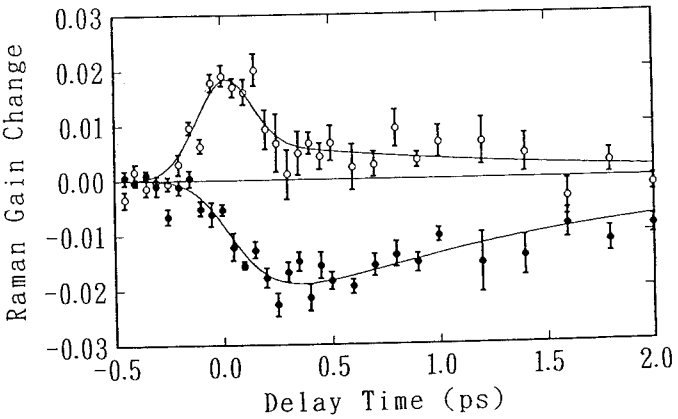


Fig. 3. Transient Raman gain changes at 1200 cm^{-1} (open circles) and 1440 cm^{-1} (closed circles) after the 1.97-eV photoexcitation. The solid curves are the best fitted curves with time constants of 150 fs and 1.5 ps. The resolution time is 300 fs.

fitted curve using time constants of 150 fs and 1.5 ps. The change at 2060 cm^{-1} is also negative and has similar time dependence with the 1440-cm^{-1} signal. The time dependence of the Raman signal at 1200 cm^{-1} has two components. The long-life component decays within several picoseconds and is assigned to the STE. The short-life component has time constant shorter than the present resolution time of 300 fs and is probably due to the nonthermal STE, because the 1.78-eV pulse can be resonant with the transition between the nonthermal STE and the ground state.

The theoretical calculation has predicted that the localized excitations in *trans*-$(CH)_x$ have several Raman active phonon modes [7]. The expected signal is the reduction of the stretching vibration modes and new Raman lines at lower frequencies than the stretching modes. The Raman signal observed in PDA is similar to this feature. However, the phonon modes of the STE in PDA have not been investigated. Here, the observed Raman frequency is compared with stretching modes of center bonds in unsaturated hydrocarbons with four carbon atoms, i.e. repeat units of PDA [10]. The formation of the STE in PDA is expected to be the geometrical relaxation from the acetylene-like structure $(=CR-C\equiv C-CR=)_x$ to the butatriene-like structure $(-CR=C=C=CR-)_x$. The C=C bond in *trans*-butene-2 ($CH_3-CH=CH-CH_3$) has a stretching mode with 1675 cm^{-1}, while the frequency of the C-C bond in *trans*-1,3-butadiene ($CH_2=CH-CH=CH_2$) is 1202 cm^{-1}. Therefore, the 1200 cm^{-1} Raman peak can be assigned to the C-C bond in the butatriene-like structure. However, Raman signal due to the C=C bond in the butatriene-like structure cannot be observed in this study. It can be explained by close frequencies of the stretching modes of the center C=C bond in butatriene ($CH_2=C=C=CH_2$) and the C≡C bond in dimetylacetylene ($CH_3-C\equiv C-CH_3$), 2079 and 2235 cm^{-1}, respectively. The expected new Raman signal near the 2060 cm^{-1} peak cannot be resolved in this study because of the broad pump spectrum.

In conclusion, we developed a new timr resolved Raman spectroscopy and the new Raman peak due to self-trapped exciton in PDA has been observed at 1200 cm^{-1} for the first time by the femtosecond time-resolved Raman gain spectroscopy. The observed Raman signals indicate the butatriene-like structure due to the formation of the STE after the geometrical relaxation from the acetylene-like structure in the FE state.

References

[1] M. Yoshizawa, M. Taiji, and T. Kobayashi, IEEE J. Quantum Electron. QE-25, 2532 (1989).
[2] T. Kobayashi, M. Yoshizawa, M. Hasegawa, and M. Taiji, J. Opt. Soc. Am. B7, 1558 (1990).
[3] M. Yoshizawa, A. Yasuda, and T. Kobayashi, Appl. Phys. B53, 296 (1991).
[4] M. Yoshizawa, K. Nishiyama, M. Fujihira, and T. Kobayashi, Chem. Phys. Lett. 270, 461 (1993).
[5] M. Yoshizawa, Y. Hattori, and T. Kobayashi, Phys. Rev. B47, 3882 (1993).
[6] A. Yasuda, M. Yoshizawa, and T. Kobayashi, Chem. Phys. Lett. 209, 281 (1993).
[7] A. Terai, Y. Ono, and Y. Wada, J. Phys. Soc. Jpn. 58, 3798 (1989).
[8] L. X. Zheng, R. E. Benner, Z. V. Vardeny, and G. L. Baker, Synth. Metals 49, 313 (1992).
[9] G. Lanzani, L. X. Zheng, G. Figari, R. E. Benner, and Z. V. Vardeny, Phys. Rev. Lett. 68, 3104 (1992).
[10] L. M. Sverdlov, M. A. Kovner, and E. P. Krainov, *Vibrational Spectra of Polyatomic Molecules*, (John Wiley & Sons, New York, Toronto, 1970), pp.282-323.

Panel Discussion: Real World Ultrafast Sources

MF 9:00pm–10:00pm
Dana Point Ballroom

Wayne H. Knox, *Presider*
AT&T Bell Laboratories

Real World Ultrafast Sources

Panel Speakers

Ursula Keller, *Institute of Quantum Electronics, Switzerland*

Martin Fermann, *IRMA America*

Wilson Sibbett, *University of St. Andrews, U.K.*

Paul M.W. French, *Imperial College, U.K.*

Peter Delfyett, *University of Central Florida, CREOL*

Panel Discussion: Real World Ultrafast Applications

MG 10:00pm–11:00pm
Dana Point Ballroom

Martin C. Nuss, *Presider*
AT&T Bell Laboratories

Real World Ultrafast Applications

Panel Speakers

Willes H. Weber, *Ford Motor Company*

Kevin Smith, *BT Laboratories, U.K.*

Jay Wiesenfeld, *AT&T Bell Laboratories*

Steve Williamson, *University of Michigan*

Andy Weiner, *Purdue University*

Mark Rodwell, *University of California, Santa Barbara*

Robert Alfano, *City College of New York*

Ultrafast Dynamics in Solids

TuA 8:30am–9:30am
Dana Point Ballroom

Presider to be announced

Direct observation of ultrafast ionic screening

T. K. Cheng[a], M. S. Dresselhaus[a,b], E. P. Ippen[a]
[a]Department of Electrical Engineering and Computer Science
[b]Department of Physics
Massachusetts Institute of Technology, Cambridge, MA 02139

Recently, it has been shown that coherent optical phonons can be excited in semimetals[1,2], semiconductors[2-4] and superconductors[5]. In all cases, pulses of laser light, which are short compared to the optical phonon period, are used to impulsively generate the coherent lattice vibrations. While the experimental methods for phonon excitation are similar, the physical mechanisms responsible for phonon generation appear to differ among the various materials types. For semimetals and narrow-gap semiconductors, the reflectivity modulation observed with the pump-probe technique have been particularly large (on the order of 10% in some materials) and have suggested significant modulation of the material's electronic structure. In these cases, we have determined that the coherent phonon excitation is caused by a mechanism we call Displacive Excitation of Coherent Phonons (DECP) [2,6].

The DECP mechanism uses the pump pulse to promote electrons in the solid from bonding orbitals to anti-bonding orbitals, thereby changing the ionic potential's coordinate of minimum energy. Because the lattice cannot respond adiabatically to this rapid displacement of the ionic *equilibrium* coordinate, the lattice is set into *cosinusoidal* oscillation about the new equilibrium. We note that the DECP mechanism is different from previously studied Impulsive Stimulated Raman Scattering (ISRS) type mechanisms, where the pump pulse is used to drive the lattice directly through a second-order process.

With the DECP mechanism, the generated coherent phonon can be large enough to modulate significantly the energy bands of a solid through a deformation potential coupling [7]. Energy band modulation is manifested through transient reflectivity modulations as large as 12% in semiconducting Ti_2O_3 at the A_{1g} optical phonon frequency (~ 7 THz). In experiments involving high excitation intensities, it is observed that the optical phonon is screened by the photoexcited carriers, resulting in an initial down-shift of the optical phonon frequency relative to the value found through spontaneous Raman scattering. Subsequently, as the system relaxes back to the pre-pump state, the phonon frequency correspondingly relaxes.

In this paper we report transient reflectivity measurements on single crystal Sb as a function of pump intensity (at the pulse energies: 300, 150, 75, and 30 pJ/pulse). The purpose is to study systematically the phenomenon of the time-evolving phonon frequency in Sb's DECP response. Our pump-probe experiment [8] uses a dispersion compensated CPM laser which generates pulses at a center photon energy of 2 eV, with pulse duration of 50 fs, at a repetition rate of 80 MHz, and at an average output power of 50 mW. The pump and probe are focused onto the sample with a 40x objective with a relative intensity ratio of 8:1.

Figure 1 shows the intensity dependence of Sb's transient reflectivity response. The transient reflectivity response of each trace in the figure has been normalized to unity to allow easy examination of the data at each power level. The reflectivity modulation amplitude $\Delta R/R$ scales linearly with pulse excitation energy and is 3.1% (as measured by the initial rise near t=0) for the maximum pulse energy of 300 pJ/pulse. Subsequent to pump excitation at t=0, the sample reflectivity changes

sharply, followed by a decay back to equilibrium. Superimposed on this relaxation are large oscillations which are the signatures of the coherent optical phonon. In Figure 2 we have plotted the time evolution of the coherent phonon frequency for two pulse intensity levels. The values for ν_{ph} in figure 2 were generated by piece-wise frequency matching 0.5 ps blocks of the raw data in figure 1. This fitting method gives values for ν_{ph} that are accurate to within 2% for the signal-to-noise levels in our data.

Figure 2 shows that the phonon frequency initially down-shifts away from the Raman frequency (A_{1g} frequency = 4.5 THz, from spontaneous Raman scattering on Sb [9]) near zero time delay. This frequency shift increases as a function of pump excitation power. In each case, the coherent phonon frequency relaxes back towards the Raman frequency as the solid returns to equilibrium.

The transient shifts in the phonon frequency are directly related to the time evolving curvatures of the ionic potential in the crystal. One possible mechanism for this evolving ionic potential is a plasma induced effect caused by the pump pulse absorption. The plasma screens the bare-ion potential of the solid yielding a "dressed" phonon with a modified phonon frequency, analogous to the case of acoustic phonons in metals [10]. However, unlike a metal, the plasma induced by the pump is highly non-equilibrium and will evolve as a function of time. By monitoring the phonon frequency, we directly measure the relaxation of the carrier-ion screening process.

In most femtosecond studies of carrier dynamics, the induced optical changes are the result of carrier distributional changes that evolve with energy and momentum loss to the lattice. In the present experiment, the induced optical changes are dominated by the lattice and we measure changes in the phonon frequency as affected by the ions' interaction with the excited carriers. In the most direct way possible, we observe electron-phonon interactions as experienced from the point of view of the lattice itself.

References

[1]T.K. Cheng, S.D. Brorson, A.S. Kazeroonian, J.S. Moodera, G. Dresselhaus, M.S. Dresselhaus, E.P. Ippen, Appl. Phys. Lett. **57**, 1004 (1990).
[2]T.K. Cheng, J. Vidal, H.J. Zeiger, E.P. Ippen, G. Dresselhaus and M. S. Dresselhaus, Appl. Phys. Lett. **59**, 1923 (1991).
[3]G. C. Cho, W. Kutt and H. Kurz, Phys. Rev. Lett. **65**, 764 (1990).
[4]W.A. Kutt, W. Albrecht and H. Kurz, J. Quant. Elect. **28**, 2434 (1992).
[5]J.M. Chwalek, C. Uher, J.F. Whitaker, G.A. Mourou and J.A. Agostinelli, Appl. Phys. Lett. **58**, 980 (1991).
[6]H.J. Zeiger, J. Vidal, T.K. Cheng, E.P. Ippen, G. Dresselhaus and M.S. Dresselhaus, Phys. Rev. **B45**, 768 (1992).
[7]T.K. Cheng, J. Vidal, H.J. Zeiger, E.P. Ippen, G. Dresselhaus and M.S. Dresselhaus, Appl. Phys. Lett. **62**, 1901 (1993).
[8]See, for example, E. P. Ippen and C. V. Shank, in *Ultrashort Light Pulses*, edited by S. L. Shapiro, (Springer-Verlag, Berlin, 1984), Chap. 3, p. 83.
[9]R. N. Zitter, in *The Physics of Semimetals and Narrow Gap Semiconductors* (D. L. Carter and R. T. Bates eds.), Pergamon Press, New York (1971) p. 285.
[10]For "dressed" acoustic phonons in metals, see D. Pines, *Elementary Excitations in Solids*, (Addison-Wesley, NY, 1963) p241.

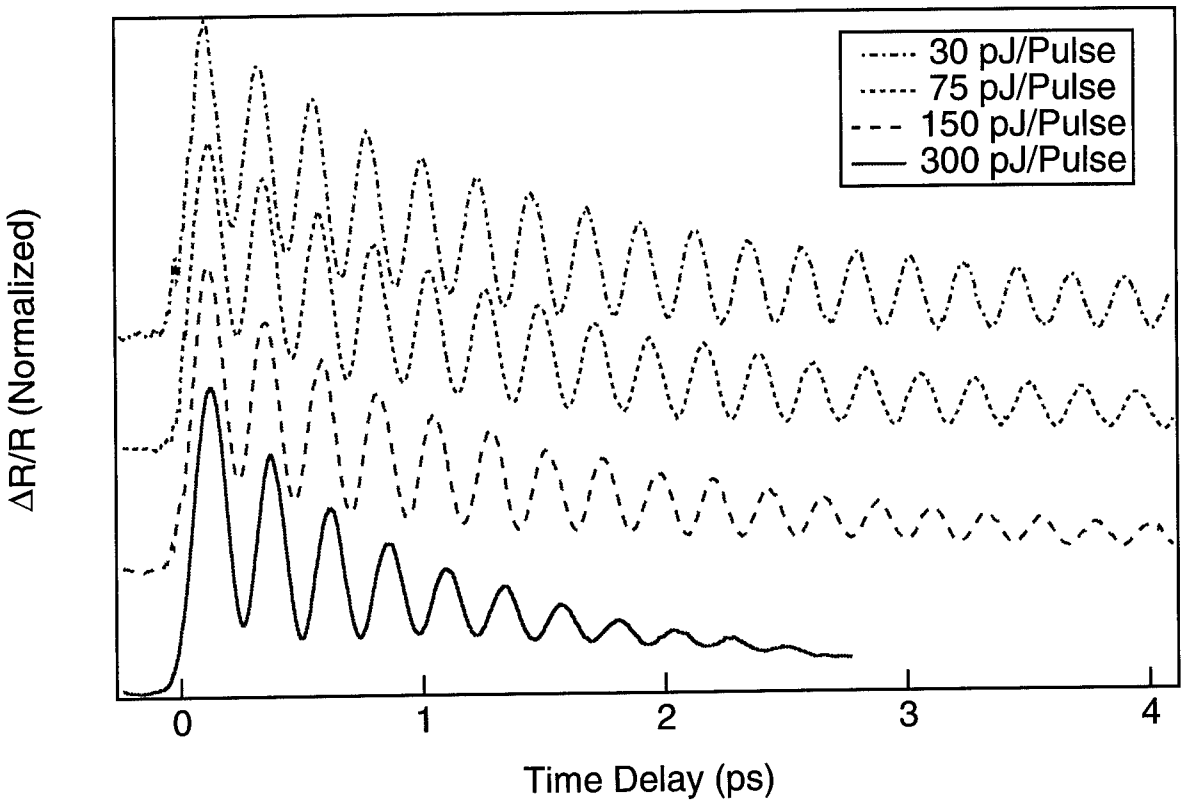


Figure 1: Power dependence of transient reflectivity for Sb.

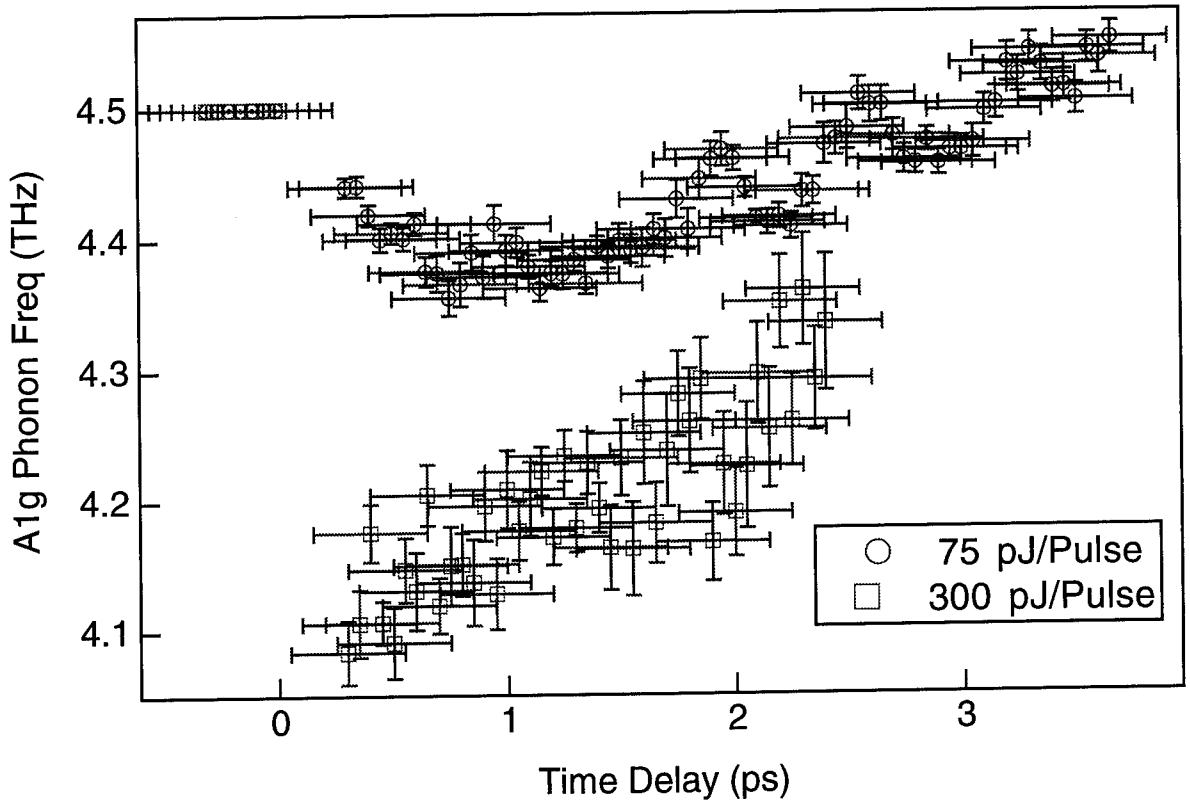


Figure 2: Power dependence of transient phonon frequency shifts for Sb.

Optical breakdown in wide-band-gap material as function of pulse duration

D. Du, X. Liu, G. Korn, J. Squier, and G. Mourou

Center for Ultrafast Optical Science,

The University of Michigan,

2200 Bonisteel Blvd., Room 1006

Ann Arbor, MI 48109-2099

TEL: (313) 763-4875 FAX: (313) 763-4876

The phenomena of optical breakdown of normally transparent optical materials such as fused silica has been studied for three decades[1]-[3]. Through the nonlinear photon-matter interaction (electron avalanche process or multiphoton ionization), a plasma is generated at the focal spot and laser energy is deposited to material, which heats the material that can lead to the irreversible damage to the material. The breakdown threshold is pulse-width dependent, and an empirical scaling law of breakdown threshold exists: $F_{th} \sim \tau^{1/2}$, for pulse duration greater than 10 ps.

We systematically studied the pulse-width dependence of laser-induced optical breakdown threshold in SiO_2 and MgF_2, with laser pulse width from 150 fs to 7 ns, using a chirped-pulse amplication (CPA) laser system[4]. A CPA system has the advantage to produce variable pulse duration continuously. A Ti:sapphire-based CPA laser system was used in the experiments. The experimental setup is shown in Fig. 1. The sample thickness of SiO_2 is 150μm, and 500μm for MgF_2. Fig. 2 shows the experimental result. The empirical scaling law of breakdown threshold as a function of pulse width failed when pulse width became less than 10 ps. We observed, for the first time, that the fluence breakdown threshold increased when pulse width decreased below ten picoseconds in SiO_2 and MgF_2. This surprising result can be explained on the basis of avalanche ionization theory. The impact ionization coefficient α is given by[5]

$$\alpha(E) = \frac{eE}{U_i} \exp\left(-\frac{E_i}{E(1+E/E_p)+E_{kT}}\right),$$

Where E_{kT}, E_p, and E_i are threshold fields for electrons to overcome the decelerating effects of thermal, phonon, and ionization scattering, respectively. Breakdown is reached when $\alpha v_d \tau \sim 30$. Where v_d is the electron drifting speed. When $E > \sqrt{E_p E_i}$ is satisfied, $\alpha \sim E$, the breakdown threshold $F_{\text{th}} \propto E^2 \tau_p \sim 1/\tau_p$, i.e., the fluence threshold will increase for ultrashort laser pulses.

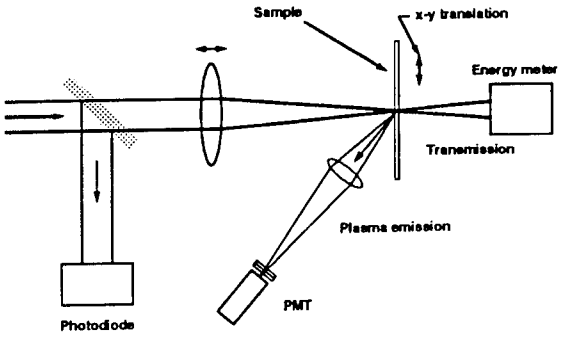


Figure 1: Experimental setup

Calculation of the impact ionization coefficient α gives good agreement between theory and experiment as shown in Fig. 3. The correction factor of 1.7 could be attributed to systematic errors such as spot size measurement and/or the uncertainty of v_d. It leads to the conclusion that avalanche ionization is the dominant mechanism in laser-induced breakdown in SiO_2 down to 150 fs.

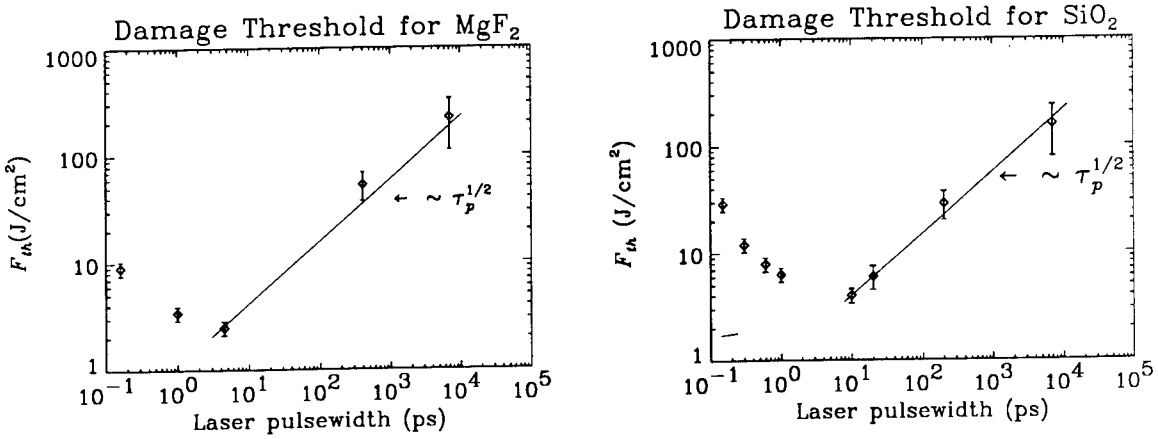


Figure 2: Breakdown threshold as a function of pulse-width

In conclusion, we have observed the increase of breakdown threshold when the laser pulse width becomes less than a few picosecond. The scaling of breakdown threshold changes from $F_{\text{th}} \sim \tau_p^{1/2}$ to $F_{\text{th}} \sim 1/\tau_p$ at short pulse limit. Optical breakdown

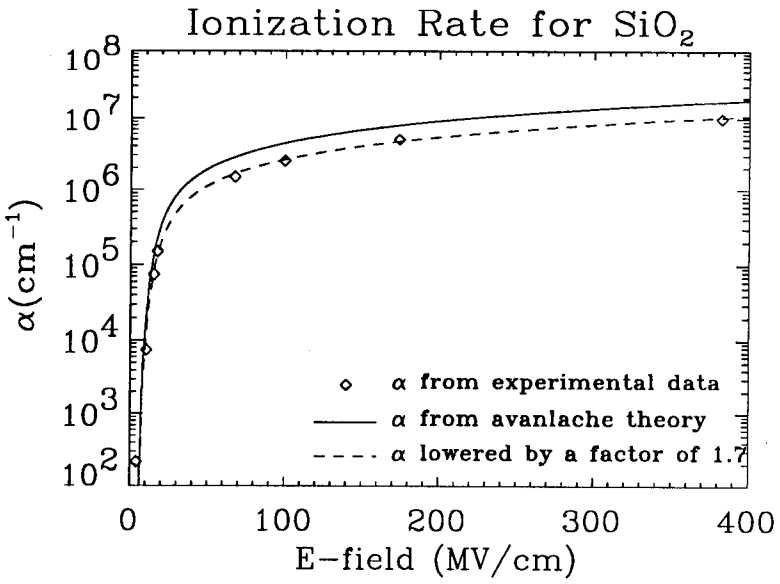


Figure 3: Impact ionization rate per unit distance α determined from experiment and theory as a function of electric field

remains an electron avalanche dominant process for pulse-width down to 150fs. Photoionization is responsible for the initial electron generation. Due to the assistance of photoionization, breakdown with short pulses is deterministic, whereas for nanosecond pulses, the breakdown is statistical. The short laser-material interaction time and the deterministic aspect of the breakdown with femtosecond pulses could have important applications. The plasma generated by ultrashort pulses during breakdown remained localized at threshold, which could provide precise control of the interaction region for material processing and medical laser applications when ultrashort laser pulses are used.

References

[1] Proceedings of the Boulder Damage Symposium: Laser Induced Damage in Optical Materials

[2] N. Bloembergen, IEEE J. Quantum Electron. QE-**10**, 375 (1974)

[3] S. C. Jones, P. Braunlich, R. T. Casper, Xiao-An Shen, and P. Kelly, Opt. Eng. **28**, 1039-1067 (1989)

[4] D. Strickland and G. Mourou, Opt. Commun. **56**, 219 (1985)

[5] K. K. Thornber, J. Appl. Phys. **52**, 279 (1981)

Ultrafast Time-Resolved Dynamics of Hot Electron Distributions in Silicon

J. A. Prybyla and J. R. Goldman
AT&T Bell Laboratories
600 Mountain Avenue, Murray Hill, NJ 07974
908-582-5053

While ultrafast optical techniques have been applied extensively to the study of hot electron dynamics in GaAs, there have been very few such studies of Si because conventional optical pump-probe schemes are difficult to interpret for indirect gap materials. This is unfortunate since understanding hot electron behavior in Si is key to understanding and predicting the properties of next-generation Si devices. Here we report the first direct subpicosecond (150 fsec) time-resolved measurement of the energy relaxation of optically excited electrons in Si. This is accomplished in a laser pump-probe format by analyzing the *photoelectron* spectrum generated by an ultrashort uv probe pulse. By this method, we obtain *directly* the time–evolution of the photo-excited electron distribution function (bulk and interface) in Si with 150 fsec resolution. These measurements would not be possible by either reflectivity/transmission or luminescence schemes.

We also report a new effect in two-photon photoemission unique to ultrashort laser pulses resulting in a sensitive new monitor of electron dynamics. We show that at high enough probe intensities excited conduction band (cb) electrons from the pump pulse can 'block' the dominant two-photon photoemission from the valence band, leading to a depletion, D(E), in the probe-induced photoemission at certain energies. A simple model shows this depletion to be proportional to the *fractional* occupation of intermediate (cb or surface) states.

The experiments were carried out using a 2 eV photon energy pump pulse followed by a 4 eV probe on a UHV-clean Si(100) sample. The cross-correlation of the 2 eV pump with the 4 eV probe was 150 fsec. The ultrafast time–resolved photoemission results are shown in Figures 1 and 2. Spectral assignment is identical to that of reference 1 for longer laser pulses. In Figure 1, we show the photoemission spectra N(E) (electron energy distribution) for delay times of 120 and 180 fsec. Conduction band electrons fit a *thermal* distribution by 120 fsec;

this gives an upper bound on the electron-electron scattering time of <120 fsec under the conditions of our experiment (10^{18}carrier/cm^3). At this delay, a best-fit Boltzmann distribution gives a temperature of T~1600K. By 180 fsec, the distribution has cooled to ~800K. This cooling rate is extremely fast (~10x faster than a metal) but is broadly consistent with previously calculated electron-phonon scattering rates using a pseudopotentials approach [2]. We are presently in the process of quantitatively extracting the *energy* dependence of the scattering rates from our experiment through use of Monte Carlo modeling.

After 200 fsec, the cooling rate is much slower, as seen in the depletion D(E) spectra of Figure 2. Again, D(E) gives the fractional occupation of the cb or surface states at E_{cb}, and is obtained by taking the difference between the probe and pump-probe photoemission spectra normalized by the probe. This slower cooling rate at longer delay times is consistent with the scattering rate decreasing as electrons move toward lower energy. The D(E) spectra at 700 fsec delay shows a broad distribution of excited electrons extending from gap states to above the cb minimum (cbm). In going from 0.7 psec to 1 psec (Figs. 2(a)-(c)), there is an increase in electron occupation (D(E)) in the cbm region, E_{cb}=0. This indicates that the cb electrons had not yet equilibrated to the (bulk) lattice for these <1 psec delays. By 1 psec, the cb electrons have clearly reached equilibrium with the bulk lattice since beyond this delay relaxation *into* the cbm region is over. Beyond 1 psec, excited electrons are left only to recombine with holes in the valence band.

One highlight of our long delay-time data is the prominent shoulder feature which grows in by 1 psec on the high energy side of the cbm. We show that this represents the first direct *spectral* observation of transient cb electron accumulation at the surface due to the formation of a space charge layer (SCL) induced by the optical pumping. Beyond 1 psec, we find the surface recombination dynamics to then be dominated by the presence of this SCL. More detailed discussion and results of our modelling will be presented [3].

In summary, we have obtained the first microscopic picture of the subpicosecond electron dynamics of photo-excited *silicon*, including bulk and (high energy) surface states. We have

measured an electron-electron thermalization time of <120 fsec, an extremely fast *initial* electron cooling rate, followed by an electron-phonon thermalization time of ~1 psec, and overall a strong energy dependence to the electron scattering rate. At longer delays, the spectra give direct evidence for transient cb electron accumulation at the surface. We are presently combining our results with Monte Carlo simulations in order to quantitatively extract the energy-dependent scattering rates.[3] We show this combination of ultrafast time-resolved photoemission with Monte Carlo simulations to be a powerful approach for extracting scattering rates in materials.

*Present Address: J.R. Goldman, Harvard University, Division of Applied Physics.

References

1. M. W. Rowe, H. Liu, G. P. Williams, Jr., and R. T. Williams, Phys. Rev. B, **47**, 2623 (1993).
2. M.V. Fischetti and J.M. Higman, Monte Carlo Device Simulation: Full Band and Beyond, ed. Karl Hess, p.123, (Kluuer Academic Publishers, 1991).
3. J.R. Goldman and J.A. Prybyla,to be published.

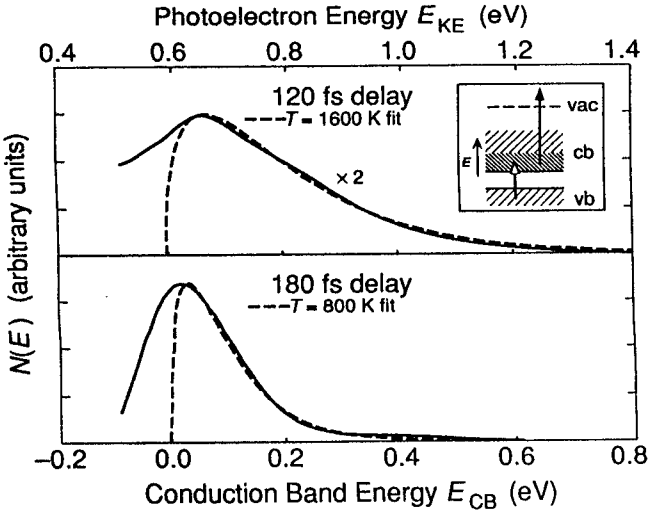


Figure 1.

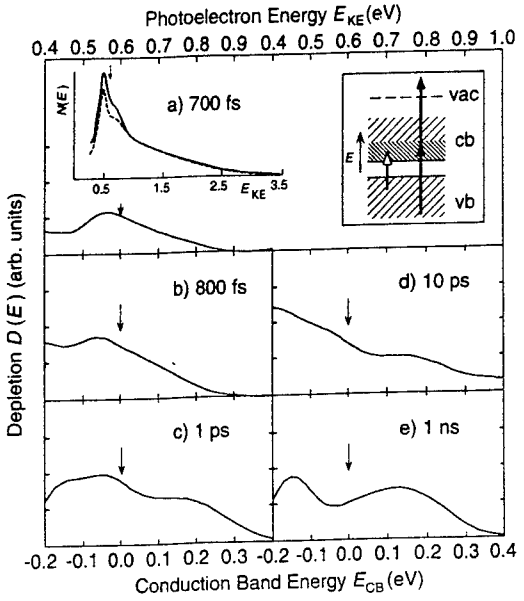


Figure 2.

Figure 1. Time-resolved photoemission N(E) vs. photoelectron energy. The cbm is at E_{cb}=0. The data are fit to thermal distributions (dashed lines).

Figure 2. Time-resolved photoemission D(E) vs. photoelectron energy. The arrow marks the cbm at $E_{cb} = 0$. Gap surface states are present below this energy. The inset to (a) shows the probe-only (solid) and pump-probe (dashed) spectra at 700 fsec delay.

Femtosecond ellipsometric study of nonequilibrium carrier dynamics in $Si_{1-x}Ge_x$

X.F.Hu and M.C.Downer
Physics Department, University of Texas at Austin, Austin, TX78712, 512/471-7251

In III-V semiconductors, comparison of femtosecond time scale optical measurements[1] with microscopic carrier dynamic theory[2] has become direct and quantitative. In Column IV semiconductors, on the other hand, quantitative experiment-theory comparison has been achieved only on a picosecond time scale.[3] This paper presents a systematic study of the fs.-time-resolved ellipsometric response of epitaxial $Si_{1-x}Ge_x$ ($0 \le x \le 1$) alloys as a first step in measuring and modelling subpicosecond bulk carrier dynamics. Pump and probe beams were derived from either an unamplified CPM laser[4] (620 nm wavelength) or an unamplified KLM laser(800nm + 400nm second harmonic). The time-dependent optical response is related to free carrier density $N_{eh}(t)$, reduced effective mass $\mu^*(t)$ via a time-varying Drude-Lorentz dielectric function:

$$\varepsilon(t) = \varepsilon_1(t) + i\varepsilon_2(t) = \left[\varepsilon_{10}(t) - \frac{4\pi N_{eh}(t)e^2}{\mu^*(t)(\omega^2 + \gamma^2)} \right] + i\left[\varepsilon_{20}(t) + \frac{4\pi N_{eh}(t)e^2\gamma}{\mu^*(t)\omega(\omega^2 + \gamma^2)} \right]$$

where $\varepsilon_{20}(t)$ and $\varepsilon_{10}(t)$ describe interband absorption and polarizability, respectively. For visible wavelength probes ($\omega >> \gamma$), the free carrier absorption term in the imaginary part and γ^2 term in the denominator are negligible. Since pump and probe frequencies lie above the band gap, the pump-induced changes $\Delta\varepsilon_1(t)$ and $\Delta\varepsilon_2(t)$ both contribute to observed changes in optical properties. Therefore, we have developed a femtosecond ellipsometric technique, described elsewhere,[4] which measures both $\Delta\varepsilon_1(t)$ and $\Delta\varepsilon_2(t)$ of epitaxial films on opaque substrates in reflectance mode, thus providing a complete basis for modeling femtosecond carrier dynamics in terms of the above equation. Our alloy films were grown by molecular beam epitaxy (MBE) on Si(100) or Ge(100) substrates to thicknesses 1 um < d < 8 um, and were thus optically thick and relaxed in the optically probed depth. Native oxides were independently diagnosed and properly taken into account by a three-layer dielectric model when analyzing the data. Results were extensively cross-checked on different samples to rule out artifacts derived from surface oxides or contaminants, preparation methods, or strain.

Data on ten distinct alloy compositions spanning the range ($0 \le x \le 1$) have been acquired. Fig.1 shows the measured $\Delta\varepsilon_1(t)$ and $\Delta\varepsilon_2(t)$ data for a representative selection of alloy compositions and pump-probe wavelengths: 620 nm pump and probe, approximate pump fluence 10^{-4} J/cm^2 (fig.1(a)-1(d)); 400 nm pump, 800 nm probe, several time smaller pump fluence (fig.1(e)-1(h)). In all cases, the real part $\Delta\varepsilon_1(t)$ behaves qualitatively according to the conventional Drude response of a diffusing electron-hole plasma (second term in first bracket of above equation). Specifically, $\Delta\varepsilon_1(t)$ decreases with pulse width limited fall time as the pump injects free carriers $N_{eh}(t)$; $\Delta\varepsilon_1(t)$ then recovers as surface N_{eh} decreases primarily because of ambipolar diffusion into the bulk. Indeed, closer inspection shows that the maximum magnitude and recovery rate of $\Delta\varepsilon_1(t)$ both increase with increasing pump absorption coefficient α_{pump}, which in turn increases both the initial carrier density N_{eh} and initial vertical carrier density gradient dN_{eh}/dz which governs diffusion rate. These trends are evident, first of all, from a vertical (column) comparison of the 620 nm data, which shows $|\Delta\varepsilon_1(t)|_{max}$ and the recovery rate both increasing monotonically as Ge content (and therefore α_{pump} (620nm)) increases. α_{pump} is about the same for cases e thru g (λ_{pump}=400 nm), yielding similar $|\Delta\varepsilon_1(t)|_{max}$ and recovery rates. They are evident, secondly, from a horizontal comparison, which shows comparatively faster recovery rates for the 400 nm pump in cases where it creates a stronger initial density gradient. The imaginary part $\Delta\varepsilon_2(t)$, on the other

hand, shows a more interesting and complicated dependence on alloy composition and pump-probe wavelength configuration. For all Si-like alloys(e.g. Bottom 2 rows of fig.1), $\Delta\varepsilon_2(t)$ is positive, signifying induced absorption, and shows a remarkable similarity in the shape of its temporal development despite very different magnitudes, which approximately track α_{pump} (a similarly shaped response also occurs for pure Ge with 620 nm pump-probe(fig.1a)). In these cases the photon energy $h\nu_{probe}$ is on an indirect transition, and therefore insensitive to transient interband absorption saturation effects. For Ge-like alloys(including pure Ge), on the other hand, $\Delta\varepsilon_2(t)$ is sometimes negative and shows complicated temporal behavior which depends strongly on alloy composition and pump-probe configuration. In all these cases, $h\nu_{probe}$ is on a direct transition, and therefore sensitive to transient interband absorption saturation effects.

Fig.2 presents modelling results for Ge at 620 nm pump-probe, derived from a kinetic model of carrier generation and transport developed by van Driel et al.[3], which is based on the Boltzmann equation with phonon generation and lattice heating determined by a microscopic model of carrier-phonon interactions. Ge serves as a quantitative example, since the microscopic parameters (deformation potentials, Auger coefficients, heat capacities, etc.) are best known. Fig.2(a) shows the calculated time dependence of $N_{eh}(t)$, $T_e(t)$, $T_h(t)$, and $T_L(t)$ at the Ge surface for our experimental conditions. For the first approximation, the calculated Drude contribution, which involves only $N_{eh}(t)$, is shown by the dashed curves in Fig.2(b). Note $\Delta\varepsilon_1(t)$ is approximately explained, but calculated $\Delta\varepsilon_2(t) \approx 0$ in this approximation. The observed $\Delta\varepsilon_1(t)$ and $\Delta\varepsilon_2(t)$ are well explained by introducing band gap renormalization (BGR) by hot carriers. The dielectric functions $\Delta\varepsilon_{1,2}(t)$ are directly related to the exchange-correlation energy ΔE_g, which equals the downward shift of the band gap when free carriers of density $N_{eh}(t)$ and temperature $T_{e\text{-}h}(t)$ are generated. Zimmermann[5] has derived a universal analytic formula for ΔE_g, which shows that ΔE_g increases approximately as $N^{1/4}$, but decreases with increasing carrier temperature. The revised $\Delta\varepsilon_{1,2}(t)$ from BGR is shown by the open circles in Fig.3(b). This model clearly captures the basic observed dynamics of $\Delta\varepsilon_2(t)$. Carrier injection produces the initial increase; a diffusion-dominated decrease in $N_{eh}(t)$ causes a temporal decrease; carrier cooling then causes the delayed increase. The solid curves in Fig2(b) (reproduced as dashed curves in Fig.1(a)) show further revised $\Delta\varepsilon_{1,2}(t)$ which agree better with the data as a result of including phenomenologically a time-varying carrier reduced effective mass $\mu^*(t)$, shown in the inset, plus a correction for lattice heating. Preliminary calculations show that a similar model explains the dielectric responses of all of the Si-like materials.

To further test this Zimmermann BGR model, we investigated the dependence of dielectric response on pump intensity. Fig.3(a) shows $\Delta\varepsilon_{1,2}(t)$ for three pump intensities as an example. Fig.3(b) shows the log-relations between the peak $\Delta\varepsilon_{1,2}(t)$ and the pump intensity. Because the carrier density N_{eh} varies linearly with pump intensity, i.e. $I \sim N_{eh}$, Fig.3(b) actually shows $\log(\Delta\varepsilon_{1,2}(t))$ vs. $\log(N_{eh})$. The slope for $\Delta\varepsilon_2^{max}$ relative to N_{eh} is ~ 1/4, which agrees very well with Zimmermann BGR theory. The slope for $\Delta\varepsilon_1^{max}$ relative to N_{eh} is about 1.3, which agrees well with Drude model assuming linear absorption. The $Si_{1-x}Ge_x$ samples were provided by T.E. Haynes(Oak Riadge National Laboratory).

1 Shoenlein et al., APL 51, 1442 (1987).
2. Stanton et al., PRL 65, 231 (1990).
3.A. Othonos et al., Sol. State Commun. 82, 325(1992); A. Othonos et al., Phys. Rev. B 43, 6682(1991); H. M. van Driel, ibid. 35, 8166(1986).
4. H.R. Choo, X.F. Hu, M.C. Downer, and V.P. Kesan, APL 63, 1507(1993).
5. R. Zimmermann, Phys. Status Solidi B 146, 371 (1988).

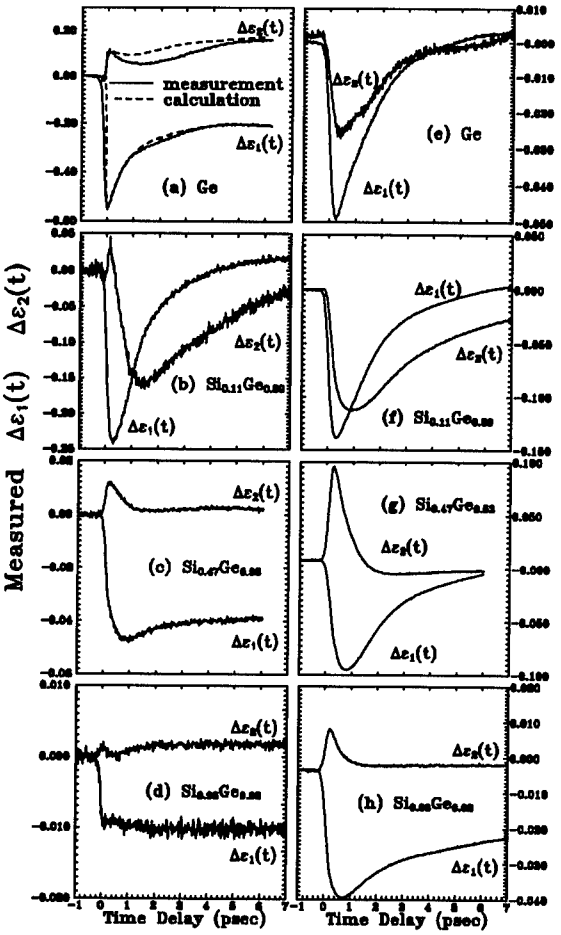


Figure 1: Femtosecond time-resolved changes in the real and imaginary parts of the dielectric function.

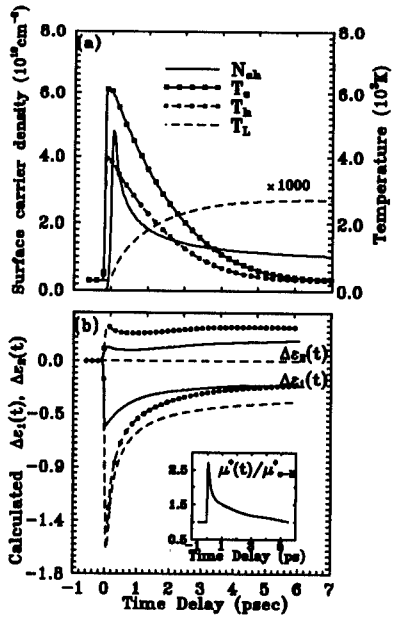
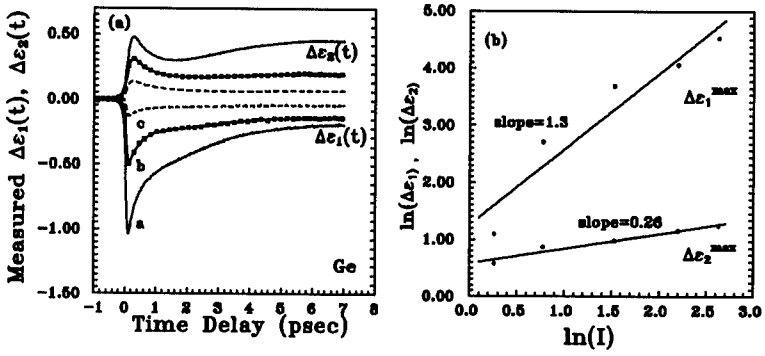


Figure 2: Carrier dynamics calculations for Ge. (a) Calculated evolution of free carrier density N_{eh} and electron temperature T_e, hole temperature T_h, and lattice temperature T_l. (b) Calculated changes in dielectric function using simple Drude model (dashed curves), Drude+band-gap renormalization (open circles), Drude+BGR+intervalley scattering and lattice heating (solid curve).

Figure3: Dependence of dielectric response on pump intensity. (a) $\Delta\varepsilon_{1,2}$ for three pump intensities at 620nm with $I_a > I_b > I_c$. (b) log relation between peak $\Delta\varepsilon_{1,2}$ and pump intensity.



Biology

TuB 10:00am–12:00m
Dana Point Ballroom

Robin M. Hochstrasser, *Presider*
University of Pennsylvania

Direct Observation of Vibrational Dephasing in Functional Proteins

J.L. Martin, M.H. Vos, J.C. Lambry, J. Breton, M.R. Jones, C.N. Hunter

Ecole Polytechnique/ENSTA
Laboratoire d'Optique Appliquee
CNRS URA 1406 - Insrerm U 275
Betterie de L'Yvette
91120 Palaiseau, France

Summary not available at time of printing.

Femtosecond Vibrationally Coherent Photochemistry in the Primary Event in Vision

Q. Wang[a,b], R.W. Schoenlein[a], L.A. Peteanu[b], S.J. Rosenthal[a,b], R.A. Mathies[b] and C.V. Shank[a,b]

[a]Lawrence Berkeley Laboratory, MS 70-193A
Berkeley, CA 94720 (510) 486-6558
[b]Department of Chemistry, University of California, Berkeley

Understanding the role of vibrational coherence in photochemical reactions is a fundamental problem in photochemistry and biology.[1,2,3] Vibrational coherence may play a significant role in reactions which occur on a time scale shorter than the relevant nuclear vibrational periods. One of the fastest chemical reactions is the first step in vision,[4,5,6] the 11-*cis* → all-*trans* isomerization of the retinal chromophore in rhodopsin (Fig. 1). We have demonstrated that this reaction is essentially complete in only 200 fs.[4,5,6] This time is comparable to or shorter than the period of torsional vibrational modes that are expected to make up the reaction coordinate, suggesting that this reaction has approached the adiabatic limit. We report here the observation of vibrational coherence in the photoproduct of the isomerization reaction in rhodopsin. The presence of vibrational coherence in the photoproduct indicates that the ultrafast isomerization of rhodopsin is mediated by nonstationary vibrational states which couple from the excited state of the reactant to the ground state of the photoproduct in a non-adiabatic process.

Femtosecond pump-probe measurements are performed on a flowing jet of the bovine visual pigment rhodopsin using 35 fs pump pulses at 500 nm, the absorption maximum of the reactant (Figure 1). Transient changes in absorption are measured from 450 to 640 nm using 10 fs blue probe pulses and 10 fs red probe pulses. Kinetic information at specific wavelengths is obtained by filtering the probe pulses after the sample.

Figure 2A presents differential transmission measurements at 500, 530, 550, 580 and 610 nm. Measurements near 500 nm ($\Delta T/T>0$) indicate the bleaching of the ground-state reactant while measurements near the photoproduct (bathorhodopsin) absorption maximum at 550 nm ($\Delta T/T<0$) indicate the formation of photoproduct within 200 fs.[4,5] Measurements at 500, 530, 580 and 610 nm show clear evidence of vibrational coherence with a period of ~500 fs, which persists for several picoseconds. Figure 2B shows the Fourier transform power spectra calculated from each pump-probe measurement. These spectra indicate vibrational coherence at ~60 cm^{-1} (550 fs) at all probe wavelengths.

Several important details of the oscillations and the Fourier transforms indicate that the oscillations are the result of coherent vibrational motion of the ground-state photoproduct, rather than non-stationary motion on the excited-state surface,[3] or impulsive excitation of the ground state reactant.[7] Figure 3 presents a phase analysis of the Fourier transform of the ~60 cm^{-1} oscillation. The phase of the oscillations exhibit a strong wavelength dependence, with the oscillations in the blue (500 and 530 nm) having a phase of -90 degrees, and the oscillations in the red (580 and 610 nm) having a phase of +90 degrees. The 180-degree phase change occurs near 550 nm, the photoproduct absorption maximum. In addition, the amplitude of the ~60 cm^{-1} oscillation (Fig. 2A) is small at the edges of the photoproduct absorption (500 and 610 nm), and

the oscillations are largest when the probe wavelength is on the steep sides of the absorption band (530 and 580 nm, Fig. 1). Furthermore, at the photoproduct absorption maximum (550 nm), the ~60 cm^{-1} oscillation is diminished, and there is evidence of higher frequency oscillations.

These observations are consistent with the behavior of a vibrationally coherent population (wavepacket) with an absorption maximum near 550 nm as shown schematically in Fig. 1. The vibrational motion will result in a strong modulation of the absorption where the derivative of the absorption is largest and a weaker modulation of the absorption in the wings and near the peak of the absorption band. Furthermore, the modulation on the red side of the absorption maximum will be 180 degrees out of phase with the modulation of the blue side of the absorption maximum. Thus, the phase and amplitude relations between the ~60 cm^{-1} oscillations at different wavelengths strongly suggest that these oscillations are from vibrationally coherent photoproduct, rather than from hot ground-state reactant or excited-state species. Such a low-frequency mode is most likely a torsional mode, and the coherence of this mode is maintained for more than 1 ps. Since the formation time of the photoproduct is only 200 fs (~1/3 of the vibrational period) it is possible that this mode has a large projection along the reaction coordinate.

The observation of vibrational coherence in the rhodopsin photoproduct indicates that this ultrafast isomerization proceeds directly from the excited-state potential surface of the reactant, through a nearly barrierless curve-crossing, to the ground-state potential surface of the photoproduct. This highly efficient, nonadiabatic transition can be described as a Landau-Zener tunneling process (indicated by the dashed lines in Figure 1) which expresses the quantum yield of a reaction in terms of the speed along the reaction coordinate. Thus, the high quantum yield of rhodopsin isomerization (0.67) may be largely determined by the ultrafast speed of the reaction. Our measurements further indicate that the speed of the reaction is mediated by non-stationary states which give rise to vibrational coherence in the photoproduct. Such vibrational coherence may play an important role in a variety of highly efficient photochemically active systems.

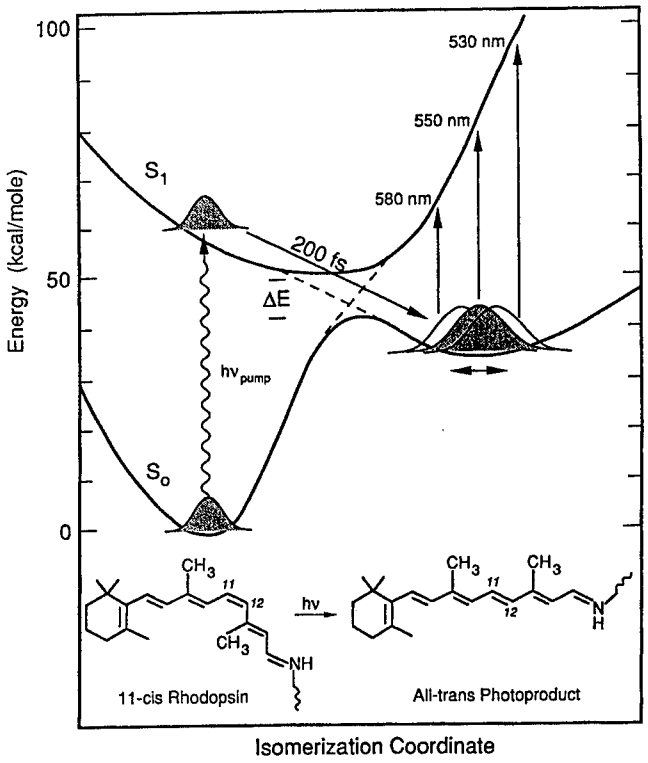


Figure 1. Schematic ground-state and excited-state potential energy surfaces for the 11-*cis* → all-*trans* isomerization in rhodopsin. The coherent vibrational motion of the initial ground-state photoproduct is indicated.

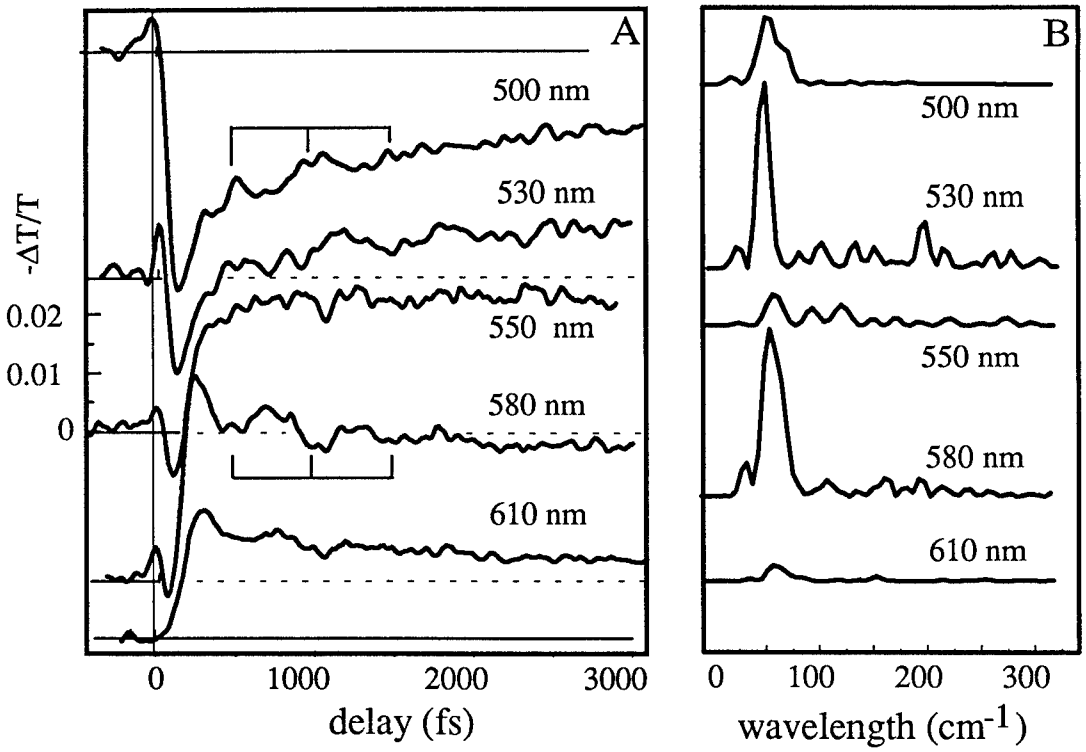


Figure 2. (A) Light-induced differential transmittance (ΔT/T) of rhodopsin as a function of delay between the 35 fs pump and 10 fs probe pulses at 500, 530, 550, 580 and 610 nm. (B) Fourier power spectra of the oscillatory part of the measured response.

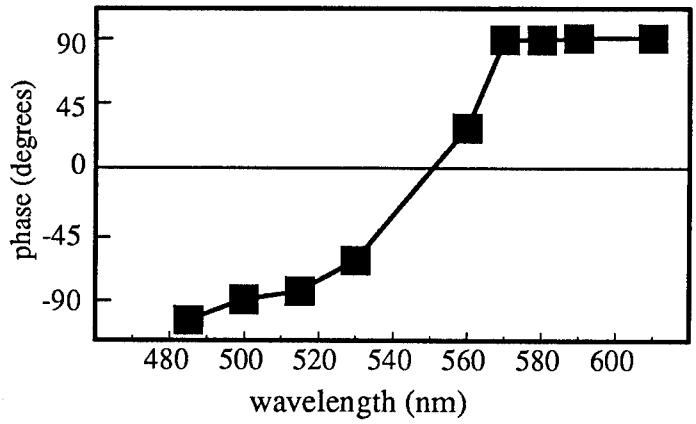


Figure 3. Phase of the ~60 cm^{-1} oscillatory part of the pump-probe signal as a function of probe wavelength. A phase difference of 180 degrees between the red edge and the blue edge of the photoproduct absorption spectrum is observed.

1. K. Wynne, C. Galli and R.M. Hochstrasser, Ultrafast Phenomena, 217 (1992)
2. U. Banin and S. Ruhman, *J. Chem. Phys,* **98**, 4391, (1993)
3. M.H. Vos, F. Rappaport, J.C. Lambry, J. Breton and J.L. Martin, *Nature*, **363**, 320, (1993)
4. R.W. Schoenlein, L.A. Peteanu, R.A. Mathies and C.V. Shank, *Science*, **254**, 412, (1991)
5. L.A. Peteanu, R.W. Schoenlein, Q. Wang, R.A. Mathies and C.V. Shank, *Proc. Natl. Acad. Sci. USA.*, **90**, 11762 (1993)
6. R.W. Schoenlein, L.A. Peteanu, Q.W. Wang, R.A. Mathies, and C.V. Shank, *J. Phys. Chem.* **97**, 12087 (1993)
7. S.L. Dexheimer, Q. Wang, L.A. Peteanu, W.T. Pollard, R.A. Mathies, and C.V. Shank, *Chem. Phys. Lett.*, **188**, 61 (1992).

Femtosecond energy transfer and coherent oscillations in BChl *c* light-harvesting antennae of chlorosomes from the green photosynthetic bacterium *Chloroflexus aurantiacus*

S. Savikhin[1], Y. Zhu[2], S. Lin[2], R. E. Blankenship[2], and W. S. Struve[1]

[1]Ames Laboratory-USDOE and Department of Chemistry, Iowa State University, Ames, IA 50011 (515-294-4276) and [2]Department of Chemistry and Biochemistry and Center for Early Events in Photosynthesis, Arizona State University, Tempe, AZ 85287-1604 (602-965-1439)

Chlorosomes are the principal light-harvesting bodies in green photosynthetic bacteria. These 100x30x12 nm ellipsoidal bodies contain ~10^4 bacteriochlorophyll (BChl) *c* chromophores, as well as a BChl *a* pigment-protein complex that forms an interfacial baseplate between the chlorosome and the cytoplasmic membrane. The BChl *c* pigments in chlorosomes are organized into large oligomers, whose electronic and vibrational spectroscopy is remarkably similar to that of BChl *c* aggregates that form spontaneously from BChl *c* monomers in solution. This unique self-aggregating property has attracted wide attention because of its potential applications in artificial photosynthesis. The BChl *c* and BChl *a* antennae of chlorosomes from the green bacterium *Chloroflexus aurantiacus* exhibit broad Q_y ($S_1 \leftarrow S_0$) electronic absorption bands centered at ~740 and ~790 nm, respectively. Downhill BChl *c* $\rightarrow$ BChl *a* energy transfer occurs with ~10 ps kinetics in isolated chlorosomes [1,2]. In this work, we have focussed on the femtosecond internal energy transfer events within the BChl *c* antenna. It is currently believed [3] that this 740 nm antenna comprises several distinct BChl *c* spectral forms (*c*727, *c*744, *c*766 etc.) Equilibration among chlorophyll and bacteriochlorophyll spectral forms requires several hundred fs in most pigment-protein antenna complexes that have been studied to date [4].

EXPERIMENTAL

The self-mode-locked Ti:sapphire laser (9 mm rod) was built after the design by Huang et al. [5]. An intracavity single-plate birefringent filter was used for one-color pump-probe experiments, producing ~80 fs pulses with 8-10 nm output bandwidth. The birefringent filter was omitted in two-color experiments, yielding pulses with < 40 fs duration and 20-40 nm bandwidth. These were split and passed through interference filters to yield ~7 nm bandwidth pulses centered at the selected pump and probe wavelengths. In most experiments, GVD in the pump-probe optics was precompensated using extracavity SF-10 prisms. The laser cross-correlation was typically 120 fs fwhm in one-color experiments, and 160-220 fs fwhm in two-color experiments.

RESULTS

The chlorosome absorption difference signal at times later than ~ 50 fs is dominated by photobleaching and stimulated emission (PB/SE) for probe wavelengths $\geq$ 730 nm, and by

excited state absorption (ESA) for probe wavelengths ≤ 725 nm. Two-color experiments were performed for many combinations of pump and probe wavelengths between 740 and 790 nm, in order to search for PB/SE risetime features signalling equilibration between BChl *c* spectral forms. Figure 1(a) shows a typical PB/SE profile that was obtained by exciting and probing chorosomes at the BChl *c* absorption wavelengths 730 and 750 nm, respectively. Like all profiles obtained in this wavelength range, it exhibits *no* rise behavior; its decay components exhibit lifetimes of 101 fs, 1.33 ps, and 10.6 ps. However, rise behavior is obtained when the pump and probe wavelengths are < 800 nm and > 800 nm, respectively, as shown in Fig. 1(b). In this case, the 790→820 nm two-color profile exhibits PB/SE rise components of 103 fs, 2.08 ps, and 9.93 ps. These risetimes approximately mirror the decay components that are found at shorter pump/probe wavelengths, cf. Fig. 1(a). In a dynamical scenario consistent with our results, much of the excitation deposited within the BChl *c* antenna equilibrates rapidly (within ~ 100 fs) among BChl pigments with peak absorption wavelengths ranging from ~730 to ~800 nm. Subsequent transfers to lower-energy BChl *a* pigments in the baseplate require ~10 ps. However, other experiments (not shown) indicate that some of the BChl *c* spectral equilibration occurs on slower time scales than 100 fs.

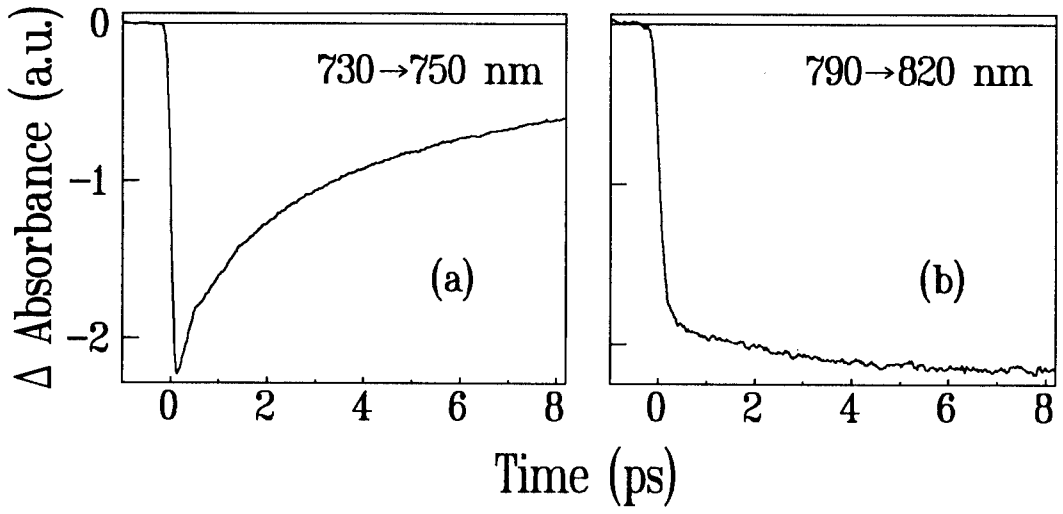


Figure 1. Two-color absorption difference profiles of chlorosomes for (a) 730→ 750 nm and (b) 790→820 nm pump-probe experiments. In (a) both wavelengths are in the BChl *c* region, while in (b) the pump and probe wavelengths are in the BChl *c* and *a* regions, respectively. Negative-going ΔA signals correspond to photobleaching and/or stimulated emission.

Many of the one- and two-color profiles for pump/probe wavelengths in the BChl *c* region exhibit coherent oscillations, which are damped within 2 ps (Fig. 2). No analogous oscillations are observed for probe wavelengths in the BChl *a* region, nor are they observed in FMO trimers (the BChl *a* pigment-protein complex from the green bacterium *Chlorobium tepidum* [4c]). These oscillations differ in several respects from the vibrational coherences observed in bacterial reaction center mutants [6]: the apparent phase of the intermediate-frequency oscillations varies with wavelength in *one-color*

experiments, and their Fourier-transform spectra are more complex. These features may stem from the fact that ESA, PB, and SE all contribute to the pump-probe signal in the BChl *c* antenna, whereas SE strongly dominates the signal in the reaction centers.

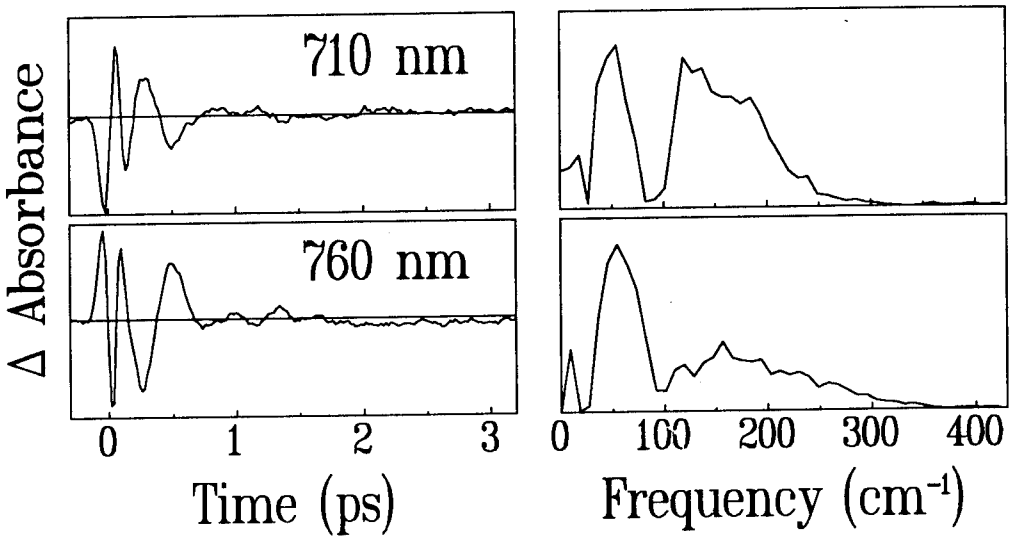


Figure 2. Oscillating parts of one-color BChl c antenna absorption difference signals at 710 and 740 nm (left) and their Fourier-transform spectra (right). The total absorption difference signals at 710 and 740 nm are dominated by ESA and PB/SE, respectively.

REFERENCES

1. Holzwarth, A. R., Müller, M. G., and Griebenow, K., J. Photochem. Photobiol. B5, 457-465 (1990)

2. Miller, M., Gillbro, T., and Cox, R. P., in Current Research in Photosynthesis (ed. M. Baltscheffsky), Vol. II, pp. 4.181-4.184, Kluwer Academic Publishers, Dordrecht.

3. Matsuura, K., Hirota, M. Shimada, K., and Mimuro, M., Photochem. Photobiol. 57, 92-97 (1993).

4. (a) Du, M., Xie, X., Jia, C., Mets, L., and Fleming, G. R., Chem. Phys. Letts. 201, 535-542 (1993); (b) Du, M., Xie, X., Mets, L., and Fleming, G. R., Photochem. Photobiol. 57, 17S (1993); (c) Savikhin, S., Zhou, W., Blankenship, R. E., and Struve, W. S., Biophys. J. in press (1994).

5. Huang, C. P., Asaki, M. T., Backus, S., Nathel, H., Murnane, M. M., and Kapteyn, H. C., Opt. Letts. 17, 1289-1292.

6. Vos, M. H., Rappaport, F., Lambry, J.-C., Breton, J., and Martin, J.-L., Nature 363, 320-325 (1993).

Ultrafast Protein Relaxation: Time-Resolved Infrared Studies of Protein Dynamics Triggered by CO Photodissociation from CO Myoglobin

R. Brian Dyer and Timothy P. Causgrove

Division of Chemical Science and Technology, (CST-4, Mail Stop J567), Los Alamos National Laboratory, Los Alamos, NM 87545, USA
Tel.: (505) 667-4194

A critical feature of the biological function of heme proteins is the direct coupling of protein motion to the process of binding exogenous ligands to the heme. In carbonmonoxymyoglobin (MbCO), a substantial, specific conformational relaxation is associated with the transition from the ligated to the unligated form of the protein. The analogous tertiary structural changes of the monomer heme subunits of hemoglobin ultimately lead to the R→T quaternary structural transition, the allosteric control mechanism of O_2 binding efficiency [1]. We have studied these processes on the earliest timescales, using picosecond, time-resolved infrared (TRIR) spectroscopy. It has long been known that infrared spectra in the amide region are sensitive to protein secondary conformation [2]. Recent advances in equipment and techniques have permitted researchers to quantitatively predict secondary structures from infrared spectra [3,4], particularly in the amide I region [4]. Therefore, it is now possible to study protein motion in time-resolved experiments on dynamics and function. The ligation reactions of small molecules such as CO with the heme site of Mb exemplify the mechanisms available to O_2. CO is an ideal candidate for initial time-resolved IR experiments in the amide I region because it is easily photolyzed, exhibits little geminate recombination [5], and the structure of both MbCO and unligated Mb have been studied by crystallographic methods [6]. TRIR has already been applied to the stretching vibrations of the bound and free CO ligand [7,8]; dynamics of the protein, however, have yet to be probed by TRIR spectroscopy of the protein vibrations. Here we report results on the motions of the protein in response to ligation reactions, probed in the amide I region centered about 1650 cm^{-1}.

Ultrafast TRIR measurements were obtained by means of a pump-probe experiment as previously described [9]. The IR probe pulse was generated by using a two step nonlinear mixing process. In the first step, the difference frequency between the 1064 nm pulse from the regenerative amplifier and the amplified dye pulse was generated in a KTP crystal, producing a pulse at 1.3 μm; this pulse was then differenced again with the 1064 nm pulse in $AgGaS_2$. Tuning the dye laser yields IR pulses (~4 ps, 100 nJ) tunable from 1200 to 2100 cm^{-1}.

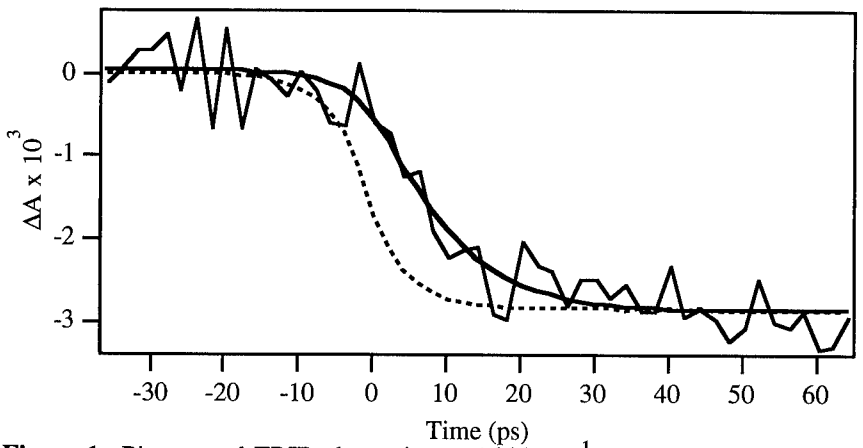


Figure 1. Picosecond TRIR absorption at 1666 cm^{-1}, together with the measured instrument response function (dashed line) and the best fit to the data of a convolution of this function with an exponential function (τ = 8.1 ps).

Picosecond TRIR measurements of photodissociation of CO indicate that the time-resolved bleaching of the Fe-CO absorption at 1943 cm^{-1} is indistinguishable from the instrument response, determined using a Si wafer. This is consistent with UV-Vis [10] and TRIR [8] measurements which indicate that CO photodissociation occurs in less than 150

fs. The protein response immediately following the photolysis of CO was probed at 1666 cm^{-1} (Figure 1). The convolution of the 6 ps $sech^2$ instrument response function with an 8 ps exponential function is also plotted in Figure 1. Positive transients (absorptions) were observed at 1680 cm^{-1}, but the signal-to-noise was insufficient to permit fitting the data to extract dynamics.

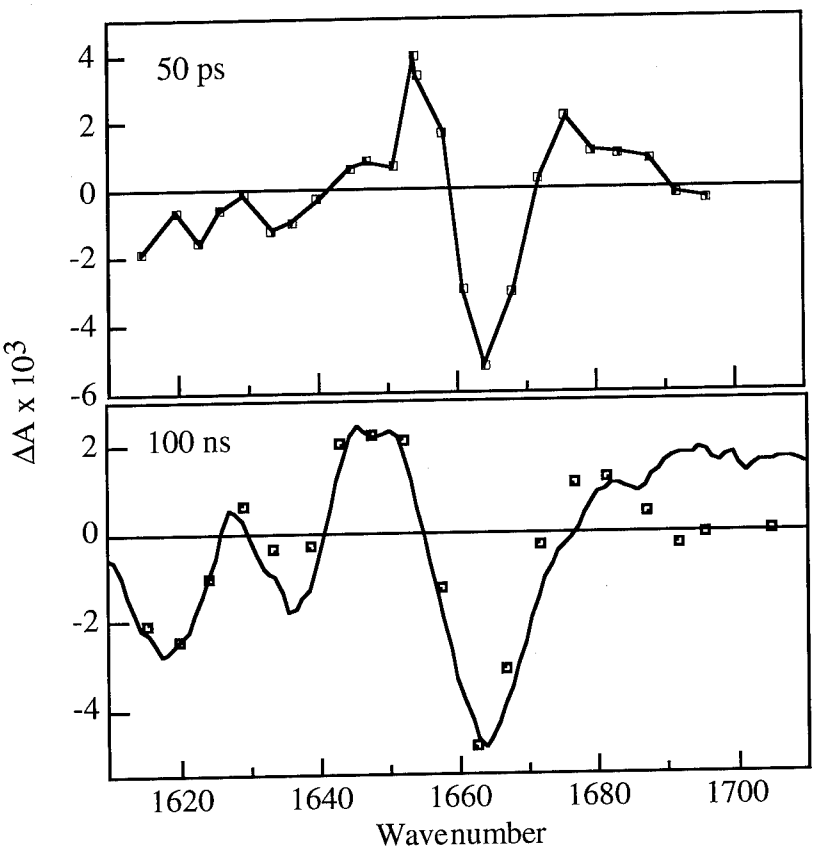


Figure 2. TRIR spectra of photodissociated MbCO. Top Panel: 50 ps spectrum. Bottom Panel: 100 ns spectrum (squares) and static FTIR difference (Mb - MbCO) spectrum (line).

A transient spectrum in the amide I region was generated by fixing the pump/probe delay at 50 ps and scanning the IR wavelength and determining the change in absorbance at each point. The 50 ps spectrum is shown in the top panel of Figure 2. The 100 ns spectrum (squares) together with the static FTIR difference spectrum (Mb - MbCO) are plotted in the lower panel for comparison. The 100 ns spectrum is identical within experimental error to the static FTIR difference spectrum; hence we conclude that the protein relaxation to the deoxyMb conformation is complete on this timescale. While many of the features of the static and 100 ns spectra are developed on the 50 ps timescale, there are distinct differences that suggest that the protein relaxation is not complete on this timescale.

Picosecond TRIR experiments give information on the initial stages of protein motion, and provide a connection between molecular dynamics simulations and actual protein motion. The results for Mb at 1666 cm^{-1} suggest that at least part of the conformational change occurs in 8 ps. These dynamics can be compared to resonance Raman results [11], which showed that the Fe-N(his) stretching frequency reaches its equilibrium deoxy value within the 30 ps pulsewidth of the resonance Raman probe pulse. Transient grating spectroscopy [12] suggests that a global change in the protein structure is occurring in less than 30 ps. In contrast, relaxation of the circular dichroism spectrum probed at 355 nm of photodissociated MbCO to the equilibrium deoxy spectrum requires 300 ps [13]. The differences among these measurements may be due to the differences in what is being probed. In our TRIR measurements at 1666 cm^{-1} we are probing a specific part of the protein backbone structure. Measurements at other frequencies may reveal different dynamics.

Recently, development of Fourier self-deconvolution and second derivative spectra [3,14] and criteria for the subtraction of water and water vapor bands have allowed tables of amide I band assignments to be made for proteins in H_2O and D_2O solution [3]. The most straightforward assignment is that for α-helix, which shows only a single narrow band at 1653-1656 cm^{-1}. The Mb difference spectra (Fig. 2) have an isosbestic point near this frequency, consistent with the finding that the helix structures of Mb are quite similar between the CO and deoxy forms, but

only shift relative to each other [6]. The bleach at 1664 cm^{-1} in the difference spectrum is in the region assigned to turn structures; bands at 1676 cm^{-1} (a transient absorption in Fig. 2) have been assigned to either turn or extended chain conformations. The other main absorption at 1645 cm^{-1} is in the area assigned to unordered structure. Bands at lower frequency have been assigned to general β-type structures [4]. Specific structural assignments to the spectral features in Fig. 2 will require pH-dependent studies, selective isotopic labeling or site-directed mutagenesis. It is clear, however, that the major IR difference features are due to changes in the polypeptide backbone conformation. We conclude that these changes correspond to the global relaxation of the proximal helices of the protein. This relaxation is almost complete on the 50 ps timescale, with at least some motions having an 8 ps time constant. The changes in secondary conformation measurable in the amide I band are complete by 100 ns.

In conclusion, we have demonstrated that TRIR in the amide I region gives structural information regarding protein conformational changes in real time. Assignment of many of the amide I peaks to specific amide or side chain structures will require much additional effort. It is clear, however, that enormous potential exists for elucidating structural relaxation dynamics and energetics with a high degree of structural specificity using this approach.

References

1. Perutz, M. F., Fermi, G., Luisi, B., Shannan, B. , & Liddington, R. C. *Acc. Chem. Res.* **1987**, *20*, 309-321.
2. Elliott, A.; Ambrose, E. J. *Nature* **1950**, *165*, 921-922.
3. Dong, A.; Huang, P.; Caughey, W. S. *Biochemistry* **1990**, *29*, 3303-3308.
4. Dousseau, F.; Pézolet, M. *Biochemistry* **1990**, *29*, 8771-8779.
5. Henry, E. R.; Sommer, J. H.; Hofrichter, J.; Eaton, W. A. *J. Molec. Biol.* **1983**, *166*, 443-451; Gibson, Q. H.; Olson, J. S.; McKinnie, R. E.; Rohlfs, R. J. *J. Biol. Chem.* **1986**, *261*, 10228-10239.
6. Kuriyan, J.; Wilz, S.; Karplus, M.; Petsko, G. A. *J. Mol. Biol.* **1986**, *192*, 133-154; Takano, T. *J. Mol. Biol.* **1977**, *110*, 569-584.
7. Anfinrud, P. A.; Han, C.; Hochstrasser, R. M. *Proc. Natl. Acad. Sci. USA* **1989**, *86*, 8387-8391.
8. Jedju, T. M.; Rothberg, L.; Labrie, A. *Opt. Lett.* **1988**, *13*, 961-963.
9. Stoutland, P. O.; Dyer, R. B.; Woodruff, W. H. *Science* **1992**, *257*, 1913-1917.
10. Petrich, J. W.; Poyart, C.; Martin, J. L. *Biochemistry* **1988**, *27*, 4049-4060; Petrich, J. W.; Martin, J. L. *Chem. Phys.* **1989**, *131*, 31-47.
11. Findsen, E. W.; Friedman, J. M.; Ondrias, M. R.; Simon, S. R. *Science* **1985**, *229*, 661-665.
12. Richard, L.; Genberg, L.; Deak, J.; Chiu, H.-L.; Miller, R. J. D. *Biochemistry* **1992**, *31*, 10703-10715.
13. Xie, X.; Simon, J. D. *Biochemistry* **1991**, *30*, 3682-3692.
14. Surewicz, W. K.; Mantsch, H. H. *Biochim. Biophys. Acta* **1988**, *952*, 115-130.

Femtosecond Coherence Spectroscopy of Heme Proteins

L. Zhu, P. Li, J.T. Sage and P. M. Champion

Department of Physics, Northeastern University, Boston, MA 02115
617-373-2902

Heme proteins such as cytochrome c and myoglobin contain a heme prosthetic group, which exhibits a strong $\pi-\pi^*$ transition in the deep blue (~400-430nm) known as the Soret band. A great deal of information concerning this important class of biomolecules has been obtained using the technique of Soret band enhanced resonance Raman scattering[1]. Here we explore the analogous technique of femtosecond transmission coherence spectroscopy, using pump and probe frequencies in resonance with the Soret band[2].

When the laser pulses are shorter than the vibrational periods of the resonant heme chromophore, the electric fields and frequencies contained within the pump and probe pulses lead to a third order polarization of the medium that is modulated by the coherences involving the resonance Raman active ground vibrational states of the heme. The oscillation and decay of these coherences can be probed by suitably delaying the arrival of the probe fields. In resonance, there are several time-ordered histories that can contribute to the observed signal, and these have been described in detail elsewhere[3]. We note that the rapid ($\lesssim$50fs) electronic population dephasing of the resonant Soret state damps all oscillatory signals except those originating from the ground state vibrational coherences. Signals from excited electronic states appear only as population decay terms, without oscillation, because phase coherence is lost during the rapid non-radiative transitions from the Soret state that lead to the creation of these states. Since the oscillatory part of the third order polarization signal probes the ground state vibronic manifold of the heme chromophore, these experiments are time domain analogs of resonance Raman scattering.

The experimental arrangement consists of a self mode-locked Ti:Sapphire laser (Coherent, Inc.) pumped by an argon ion laser, which produces 85fs laser pulses centered between 800-900nm. These pulses are doubled and compressed using a thin BBO crystal and SF10 prisms. The blue pulses (Fig. 1) are fit best with a simple Gaussian time profile (solid line), which leads to a pulsewidth of 57fs. The sech^2 function leads to a pulsewidth of 50fs, but the residuals demonstrate a deterioration in the quality of the fit (dashed line). The pump-probe pulse train is focused in a near parallel configuration into a thin quartz sample cell containing the biological solution. The recollimated probe beam is separated from the pump beam by spatial filtering and polarization selection. The signal from the spectrally filtered probe pulse is then detected so that only the change in the probe beam intensity, induced by the pump beam excitation, is ultimately recorded.

In Fig. 2 we display some results on cytochrome c. The autocorrelation trace is shown in the expanded data by the dashed line. The insert (a) shows the full data trace and coherent coupling signal, while (b) allows a comparison of the resonance Raman spectrum (lower trace) to the oscillatory components of the time domain signal derived using a linear predictive singular value decomposition (LPSVD) algorithm[4].

In other experiments (Fig. 3), we have demonstrated the fluorescence rejection capability of femtosecond coherence spectroscopy. In one example, metMb was mixed with a buffer saturated with the dye coumarin 460. Frequency domain spectroscopy does not yield any vibrationally specific information, due to the broad band spontaneous dye fluorescence (upper insert). However, the impulsive stimulated scattering signals of the dye contaminated solution and a pure metMb sample in buffer are identical. This result demonstrates the potential utility of the time domain spectroscopy compared to the traditional frequency domain spontaneous resonance Raman spectroscopy. A crucial element in the development of this technique will involve improvement of the "fidelity" between the time domain signals and the frequency domain spectra. Good agreement is observed for the relatively simple metMb spectrum (lower insert). However, as the number of frequencies increases in complex biomolecular systems, the ability to extract the frequencies, linewidths and phases accurately and unambiguously may become a significant problem (cf. Fig. 2b).

As discussed previously[2], the ultrafast experiments offer the opportunity to detect lower frequency modes than normally observed using spontaneous resonance Raman spectroscopy. In Fig. 4, we present a set of experiments on deoxyMb using 75fs pulses with varying monochromator settings. Generally, we find that the signal enhancement is greatest in the wings of the pulse (dashed line) rather than in the wings of the resonance (solid line). Moreover, we observe a mode near 100 cm^{-1} (b) that is enhanced separately from the well-known Fe-His mode at 220 cm^{-1} (e). We have suggested that this mode may be coupled to a blue-shifted charge transfer transition underlying the Soret band, since earlier Raman excitation profile studies[5] demonstrated unusual blue-shifted activity of another low frequency mode at 150 cm^{-1}.

An additional feature at 50 cm^{-1}, which is evident in both the LPSVD and discrete Fourier transform analysis of the time domain data, is near the frequency expected for heme doming motion. As a result, we have suggested[2] that the modes observed at 100 cm^{-1} and 150 cm^{-1} may be overtones of a heme doming mode strongly coupled to an underlying blue-shifted charge transfer band. Further systematic studies of the ultrafast oscillatory signals of deoxyMb as a function of the pump (λ_o) and probe (λ_m) wavelengths as well as the sample temperature are in progress.

REFERENCES

1. *Biological Applications of Raman Spectroscopy* Vol. III, T. Spiro (Ed.), Wiley (1988).

2. L. Zhu, P. Li, J.T. Sage and P.M. Champion, Phys. Rev. Lett. **72**, 301 (1994).

3. Y. Yan and K. Nelson, J. Chem. Phys. **87**, 6240 (1987); S. Mukamel, Annu. Rev. Phys. Chem. **41**, 647 (1990); W. T. Pollard et al., J. Phys. Chem. **96**, 6147 (1992); L.D. Ziegler et al., J. Chem. Phys. (to be published).

4. F.W. Wise et al., IEEE J. Quant. Elect. **QE-23**, 1116 (1987).

5. O. Bangcharoenpaurpong, K.T. Schomacker and P.M. Champion, J. Am. Chem. Soc. **106**, 5688 (1984).

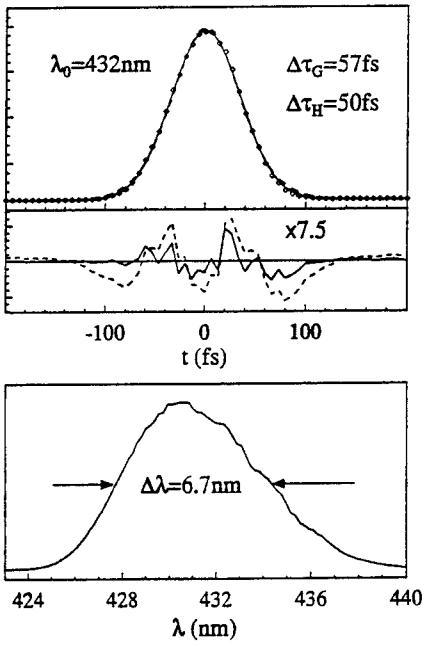


Fig. 1

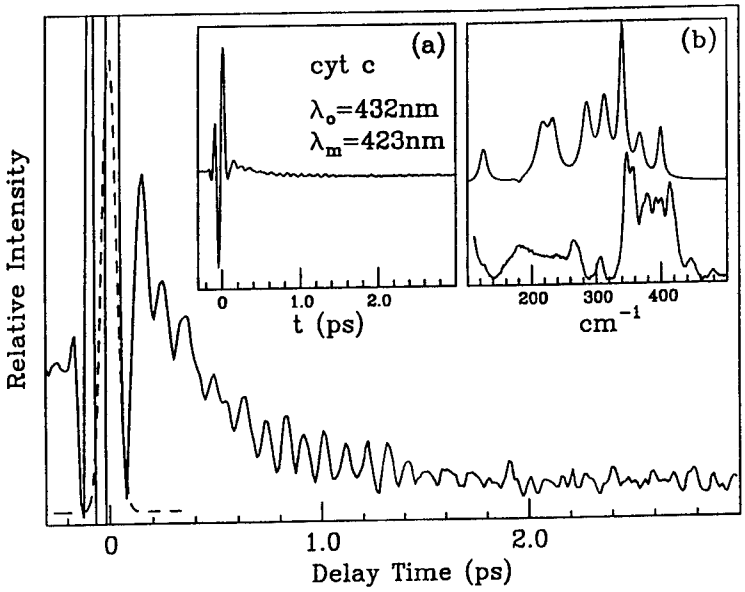
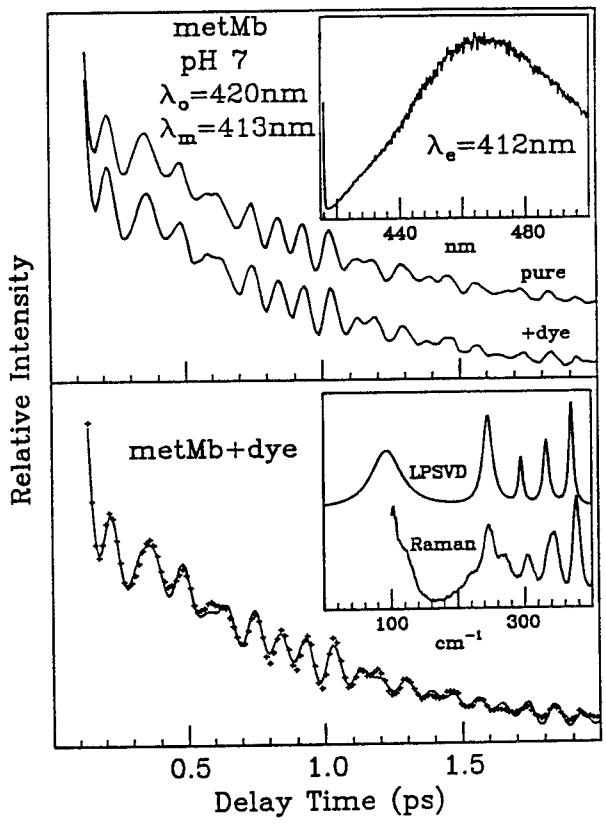
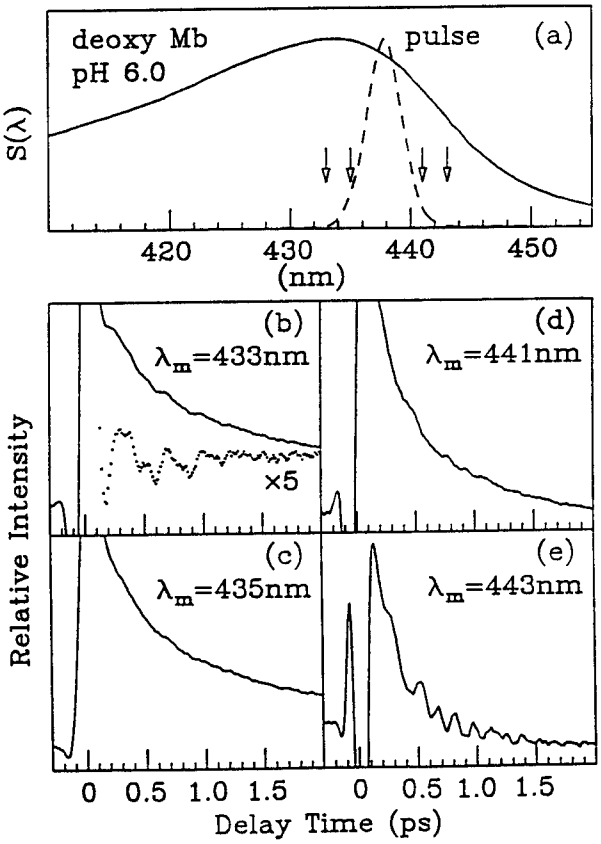


Fig. 2

Fig. 3

Fig. 4





Coherent Nuclear Motions and Exciton State Dynamics in Photosynthetic Light-Harvesting Pigments.

M. Chachisvilis, T. Pullerits, M.R. Jones*, C.N. Hunter* and V. Sundström

Department of Physical Chemistry, University of Umeå, S-90187 Umeå, Sweden
* Krebbs Institute for Biomolecular Research, University of Sheffield, Sheffield S10 2UH, U.K.

Introduction

The light-harvesting (LH) pigment-proteins of photosynthetic purple bacteria have been extensively studied with picosecond [1] and now recently with femtosecond [2] pulses. These investigations have helped to make these pigments to the probably best studied and characterized LH systems. Several bacteria, including the presently studied species *Rhodobacter sphaeroides*, contain two types of LH pigments, a core LH1 antenna surrounding the photochemical reaction centers and a more peripheral LH2 antenna. Both these LH pigments are believed to be organized in small minimum units of 2-4 polypeptides holding about the same number of chromophores, which aggregate to form the network of the intact antenna. Energy transfer between minimum units is believed to occur in a non-coherent hopping fashion. Interaction within a unit is probably quite strong and spectral evidence suggest that it should be characterized as strong exciton interaction leading to the formation of delocalized exciton states. In this report we will mainly be concerned with the ultrafast dynamics within such a minimum unit.

Results and Discussion

Coherent nuclear motions in LH-proteins

Coherent nuclear motions (wave packets) have previously been observed in small molecules both in the isolated state [3] and in the condensed phase [4], in large dye molecules in solution [5] and recently in modified (non-functional) photosynthetic reaction centers [6]. From the frequency and damping characteristics of these coherent motions information can be obtained about the nature and interactions of vibrations coupled to the optical transition. Using the ~40 fs tunable pulses from a mode-locked Ti:Sa laser we have for the first time observed coherent nuclear motions in two intact photosynthetic light-harvesting pigments. The coherent oscillations are most clearly observed at 4 K, but are also distinguishable at higher temperatures, up to room temperature (see Fig. 1). In the LH1 protein the dominating vibration has a period of approx. 250 fs corresponding to a ~100 cm^{-1} vibrational frequency. The Fourier spectrum of the time domain measurements in addition reveals vibrations of lower amplitude at higher frequencies, ~200 and ~300 cm^{-1}. Frequencies below 60 cm^{-1} have been cut from the spectrum shown in Fig. 1B, because at the moment the appearance of these very low frequencies is very sensitive to the quality of the fit to the exponential decay. The oscillations observed in the red part of the spectrum are primarily a result of the stimulated emission detected excited state wave packet, while oscillations at shorter wavelengths probably also have contributions from both the excited- and ground state wave packets, detected via excited state absorption and ground state bleaching, respectively. Similar observations were made for the LH2 protein, but somewhat different frequencies and spectral behaviour were observed.

Theoretically, we treat our pump-probe experiment as a sequence of two linear experiments where the pump pulse creates a wave packet on the excited state vibronic potential surface and a corresponding "hole" on the ground state potential surface. The evolution of the system is monitored by the response (absorption from the ground and excited state, stimulated emission from excited state) to the probe pulse. In order to find the initial nonstationary state created by the pump pulse we apply the harmonic Franck-Condon approximation where the probability distribution of coordinate and corresponding momentum on the excited potential surface are determined from the initial stationary ground state distribution, nuclear overlap integral and energy conservation rule. The dynamics on the potential surfaces are described by the

Langevin equation where a Gaussian random force and a Markovian friction are related by the fluctuation-dissipation relation of the second kind. In each timestep we keep trace of the excitation transfer which leads to the loss of coherence of the excited state but gives a rise to a new possible wave packet on the ground state surface. The response to the probe pulse is averaged over a large number of random trajectories. In accord with the experiment the calculations show that the damping of the oscillations is not significantly enhanced with the temperature. At the same time the rise of temperature makes it impossible to create a coherent wavepacket if kT>>hν.

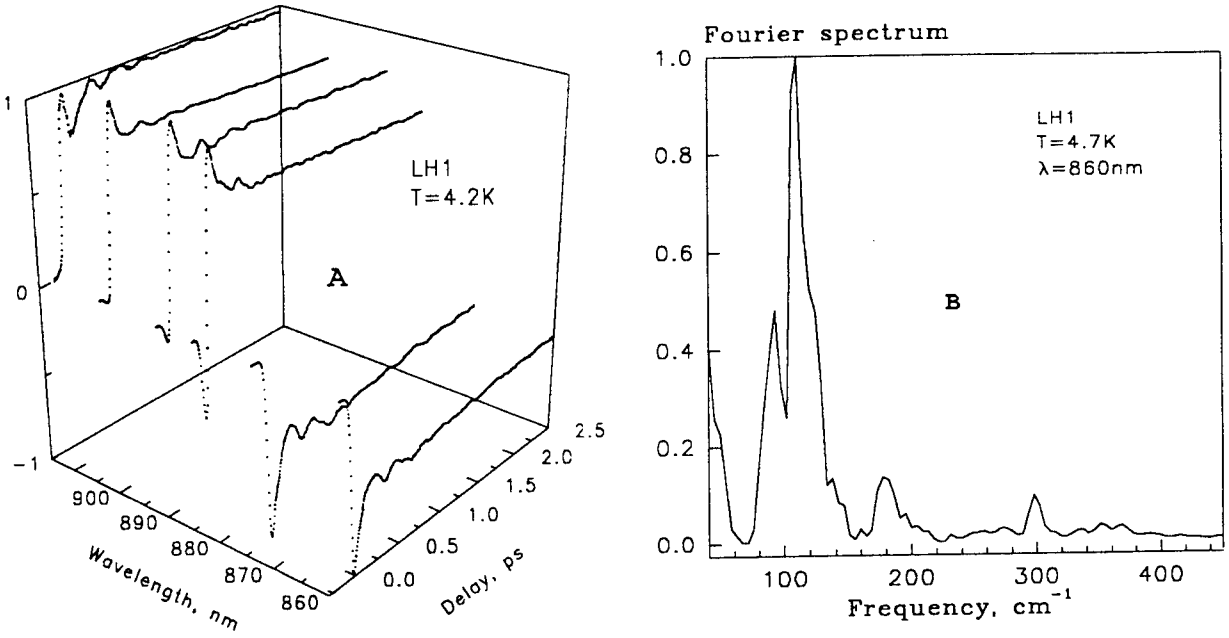


*Fig. 1. **A.** Transient absorption kinetics of Rb. sphaeroides LH1 measured at several wavelengths at 4 K. **B.** Example of Fourier spectrum of a time domain measurement. The oscillations observed in the kinetics (**A**) is seen to correspond to a major frequency of ~100 cm^{-1} and lower intensity vibrations at ~200 and ~300 cm^{-1}.*

Exciton state dynamics in LH-proteins.

Steady state optical spectroscopy and theoretical calculations suggest that strong dipole-dipole interaction, leading to the formation of exciton states, may exist in photosynthetic light-harvesting pigments in general and in LH1 and LH2 of purple bacteria in particular. Theoretical estimates have suggested very fast (10-100 fs) relaxation from upper to lower exciton states ((-)→(+) in Fig 2B). Experimental transient absorption spectra of the presently studied LH1 and LH2 pigments of purple bacteria display intense excited state absorption to the blue of the ground state absorption bleaching, reminiscent of the predicted exciton state absorption spectra. Some measurements of picosecond kinetics in LH systems (phycocyanin of blue-green bacteria) have been interpreted as exciton state relaxation although the observed lifetimes were as long as ~10 ps. Non-photochemical hole burning measurements on LH pigments similar to those studied here demonstrated the presence of ~100 fs relaxation processes that were interpreted as inter exciton state relaxation [7]. Thus, there exist substantial spectral evidence that exciton states are present in photosynthetic LH pigments, but in our view, up to now there has not been any direct measurements of the dynamics associated with the the relaxation processes between these exciton states.

Using ~40 fs infrared pulses to excite and probe the transient absorption kinetics in the

blue wing of the absorption spectrum of the 850 nm absorption band of LH2 we observe a very fast highly polarized relaxation at wavelengths which coincide with the expected upper exciton state of a B850 aggregate (835-845 nm, at 4 K). The kinetics displayed in Fig 2A exhibits an induced absorption which relaxes with a time constant of ≤20 fs to a bleaching signal which in turn relaxes with a 100-200 fs time constant. We interprete the absorption immediately following excitation by the 40 fs pulse as excited state absorption from the upper (-) exciton state which relaxes very rapidly (≤20 fs) to the lower (+) exciton state (see Fig 2B). The slower 100-200 fs relaxation time represents energy transfer to the (+)-state of other B850 units which absorb light at a slightly different energy due to different interactions with other pigment molecules and the environment (inhomogeneous spectral broadening of the B850 absorption band). This energy transfer is temperature and wavelength dependent.

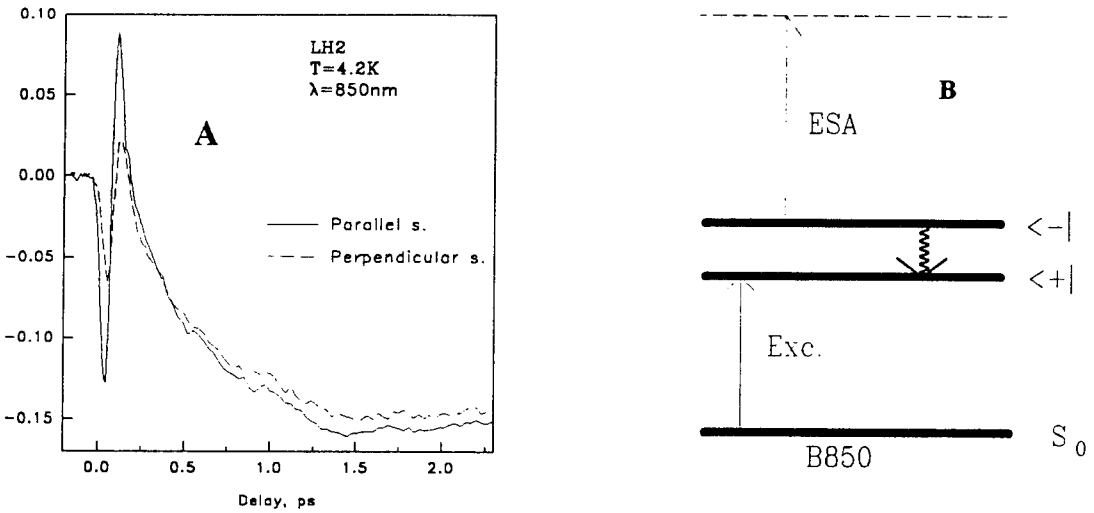


Fig.2. ***A.*** *Transient absorption kinetics of Rb. sphaeroides LH2 measured at 850 nm with a 40 fs pulse. The very fast initial decay of induced absorption corresponds to ≤20 fs time constant and is interpreted as the decay from the upper (-) to the lower (+) exciton state of B850.* ***B.*** *Schematic energy level diagram of an exciton coupled B850 unit.*

In order to find the possible antenna configurations which would give rise to the observed magnitude of ESA and polarization we have applied the 0-th order exciton theory for the singly and doubly excited states in an aggregate containing N chromophores. The corresponding wavefunctions are expanded in the basis of localized singly or doubly (a pair of chromophores) excited states. The frequency, polarization and strength of all possible transitions is calcualted from eigenvalues and eigenvectors of the appropriate Hamiltonians.

References

1. F.G. Zhang, R. van Grondelle and V. Sundström. Biophys. J. 61(1992)911
2. S. Hess, F. Feldshtein, A. Babin, I. Nurgaleev, T. Pullerits, A. Sergeev and V. Sundström, Chem. Phys. Lett. in press
3. A.H. Zewail, J. Phys. Chem. 97(1993)12427
4. N.F. Scherer, L.D. Ziegler and G.R. Fleming, J. Chem. Phys. 96(1992)5544
5. H.L. Fragnito, J-Y. Bigot, P.C. Becker and C.V. Shank, Chem. Phys. Lett., 160(1989)101
6. M.H. Vos, F. Rappaport, J-C. Lambry, J. Breton and J-L. Martin, Nature 363(1993)320
7. N.R.S. Reddy, R. Picorel and G.J. Small, J. Phys. Chem., 96(1992)6458

DIRECT OBSERVATION OF THE ACCESSORY BACTERIOCHLOROPHYLL IN THE PRIMARY ELECTRON TRANSFER IN BACTERIAL REACTION CENTERS

W. Zinth, S. Schmidt, T. Arlt, H. Huber, T. Nägele, M. Meyer, H. Scheer

Institut für Medizinische Optik der Universität München, Barbarastraße 16/IV, 80797 München, Fed. Rep. Germany, Tel. 49-(0)89 185031/32, Fax. 49-(0)89 183969

Early femtosecond experiments on bacterial reaction centers (RC) performed nearly one decade ago did not exhibit transient absorption features related to the reduction of the accessory bacteriochlorophyll (B) located between the primary electron donor (the special pair P) and the electron accepting bacteriopheophytin H. The absence of such a component led to the conclusion that B is not a real electron carrying intermediate. However in later experiments |1-3| we found a subpicosecond component which had relatively weak amplitudes. The spectral dependence of this component and additional experiments on mutated and modified RC suggested that B is a real electron carrier. This interpretation was not generally accepted in the literature. One main objection came from the fact that the subpicosecond kinetic component was only observed in "congested" spectral region where other intermediates caused strong absorption changes. It is the purpose of this contribution to present new experimental results proving unambiguously that the accessory bacteriochlorophyll is a real electron carrier.

The new aspect of the experiments is the extension of the spectral range up to probing wavelengths of 1040 nm. In this range (around 1.000 nm) bacteriochlorophyll anions in vitro have a pronounced absorption band |4|. In addition there is no absorption from ground state B, H, H^- and special pair bands.

A first set of experiments treats unmodified RC from *Rb. sphaeroides R 26.1* in the spectral range of 920 nm to 1.040 nm. At the shorter wavelengths 920 - 980 nm there is strong stimulated emission decaying with an average time constant of about 3 ps. When probing at the longer wavelengths the strong 3 ps component becomes weaker and practically vanishes at $\lambda >$ 1.020 nm. From 980 nm on, one finds a strong contribution of a 0.9 ps component which is strongest around 1.020 nm (see Fig. 1). Here the amplitude of the 0.9 ps component is stronger than all other amplitudes. Analysing the data within the stepwise reaction model yields the correct spectrum of intermediate P^+B^- (with a peak at 1.020 nm) as well as the correct

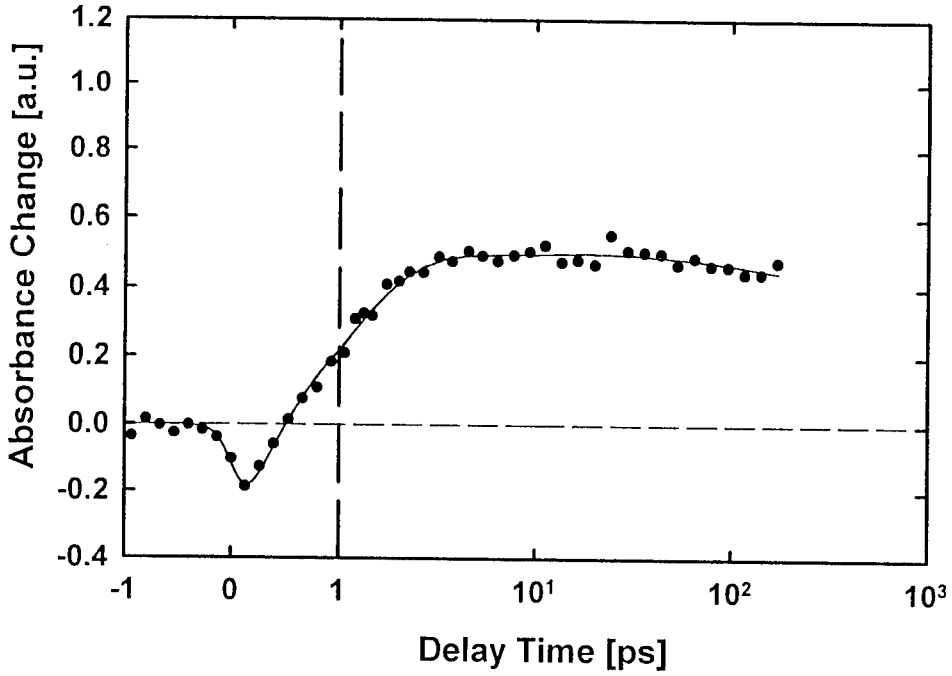


Fig. 1: Transient absorption changes for native RC at 1.020 nm. The large initial absorption transient has a time constant of 0.9 ps. It is related with the absorption increase due to the formation of a bacteriochlorophyll anion

orientation of the transition dipole moment of B^-. In the frame of a superexchange model with direct electron transfer to H there would be no explanation for the strong 0.9 ps kinetic component observed in the 1.000 nm range.

A second set of experiments treated modified RC where the bacteriopheophytins are replaced by pheophytins by a special procedure which leaves the rest of the RC unchanged. This replacement should increase the energy of the radical pair P^+H^-. In vitro data of the redox potential of pheophytin suggest an energy rise of 0.2 eV which brings P^+H^- close to the state P*. In this case one should expect (for a stepwise electron transfer via B), a long-lasting population of the radical pair state P^+B^-. As expected the modification causes severe changes of the reaction dynamics. Of special interest is the signal trace at 1.020 nm (see Fig. 2) which shows a long-lasting increased absorption which can only be assigned to the bacteriochlorophyll anion B^-.

In conclusion: The new experimental data prove that the accessory bacteriochlorophyll B is a real electron carrier in the primary reaction of native bacterial reaction centers.

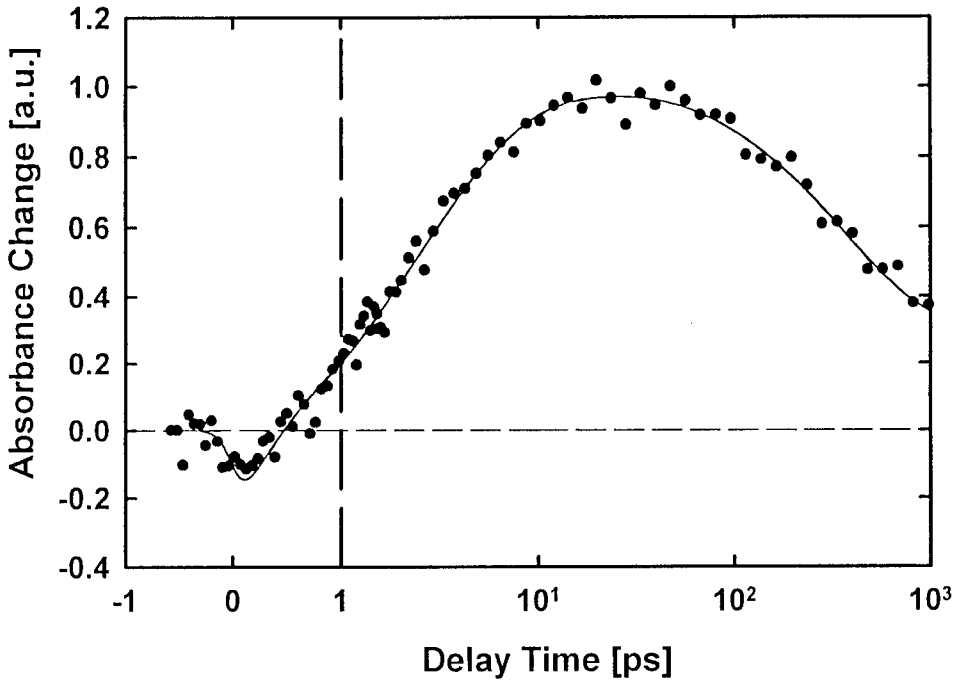


Fig. 2: Transient absorption changes for modified RC containing pheophytin instead of bacteriopheophytin. The induced absorption at the early times is similar to that found in native RC (Fig. 1). A further increase of ΔA with ~ 3 ps and a late decrease with a 370 ps time constant reflect a long-lasting formation of a bacteriochlorophyll anion in equilibrium with the pheophytin anion.

References:

1. W. Holzapfel, U. Finkele, W. Kaiser, D. Oesterhelt, H. Scheer, H.U. Stilz, W. Zinth
Chem. Phys. Lett. 160 (1989)1-5

2. W. Holzapfel, U. Finkele, W. Kaiser, D. Oesterhelt, H. Scheer, H.U. Stilz, W. Zinth
Proc. National Acad. Science USA , 87 (1990) 5168-5172

3. U. Finkele, C. Lauterwasser, A. Struck, H. Scheer, W. Zinth
Proc. Natl. Acad. USA, 89 (1992) 9514-9518

4. J. Fajer, D.C. Brune, M.S. Davis, A. Forman & L.D.Spaulding
Proc. National. Acad. Science. USA, 72 (1975) 4956-4960

Surfaces

TuC 1:30pm–3:00pm
Dana Point Ballroom

Harry W. K. Tom, *Presider*
University of California, Riverside

Nonlinear Vibrational Spectroscopy of Liquids and Liquid: Air Interfaces with Ultrashort Laser Pulses

A. Laubereau and K. Wolfrum

Physics Department E11
Technical University Munich
D-85748 Garching, Fed. Rep. Germany

Novel aspects of the vibrational dynamics of bulk and surface molecules are investigated by "magic" 3-colour femtosecond CARS and picosecond sum-frequency spectroscopy in the infrared.

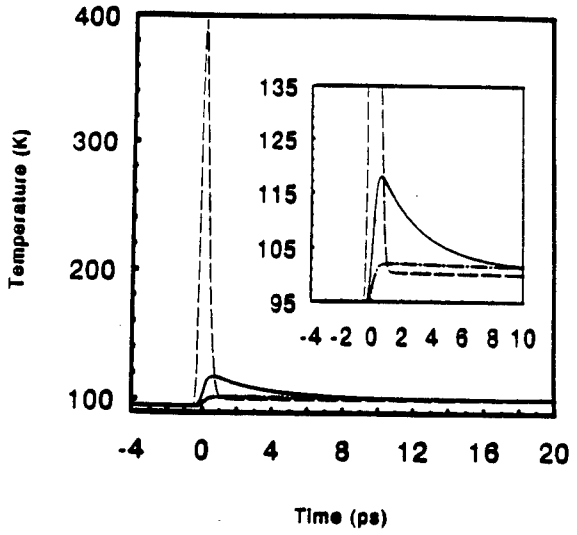
Adsorbate Infrared Spectral Response Following Femtosecond Metal Substrate Heating

A. G. Yodh[1], *J. P. Culver*[1], *M. Li*[2],
L. G. Jahn[1,2], *and R. M. Hochstrasser*[2].

Department of Physics[1], Department of Chemistry[2] and
Laboratory for Research on the Structure of Matter,
University of Pennsylvania, Philadelphia,
Pennsylvania, USA 19104. (215)898-6354

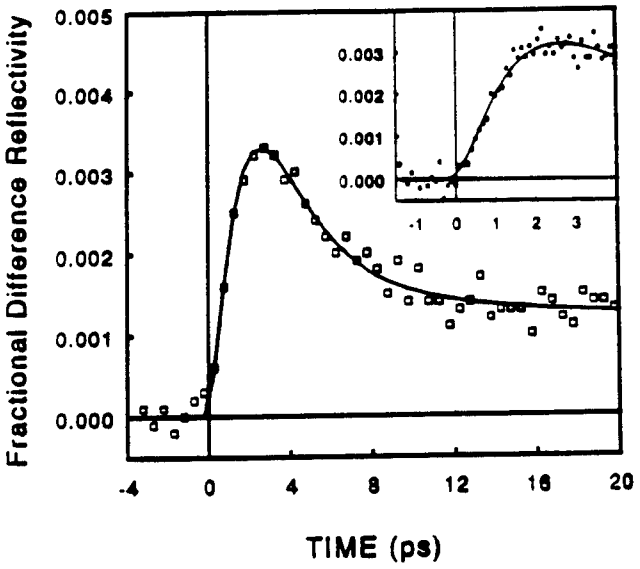
Ultrafast laser heating pulses create unique environments for surface chemistry on metal surfaces. Recent femtosecond experiments have shown, for example, that nonequilibrium substrate conditions can play a central role in laser induced desorption[1]. In these experiments extremely high electronic temperatures (4000 °K) are produced which modify adsorbates in a manner which is impossible to achieve via a conventional thermal process. Here we report the results of probing the internal vibrations of CO adsorbate molecules as a function of time following the impulsive excitation of electrons in the underlying Cu(111) substrate by 300 fs visible light pulses[2]. We find that a low frequency CO mode couples to substrate electrons and phonons, and that the representative coupling rates can be separately determined[2,3]. Importantly, with increased excitation of the substrate, our measurements provide indication of stronger, temperature dependent couplings between the adsorbate vibrations and the substrate reservoirs[4].

Our experiment uses a gated upconversion technique in order to follow the time evolution of the CO internal stretch vibration ($\omega_o = 2073.5\ cm^{-1}$, $\Gamma_o = 4.5\ cm^{-1}$) as a function of time after the heating of the substrate. The metal substrate excitation is described by electron and lattice temperatures, T_e and T_l, having distinctly different temporal profiles (Fig. 1).



1) Calculations of electron and phonon reservoir temperature as a function of time: electronic (dashed line), phonon (dotted dashed line): Adsorbate temperature (solid line) calculated using the best fit values of $\gamma_e = 167(24)\ GHz$ and $\gamma_l = 145(56)\ GHz$. Inset: same with expanded scale.

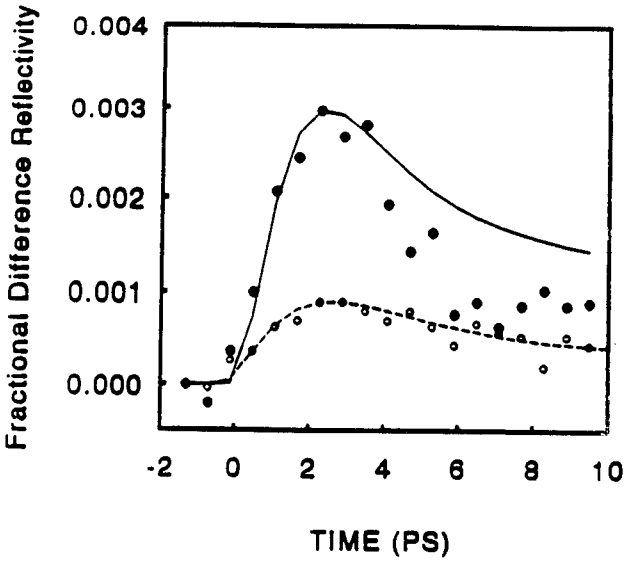
Although the stretch mode is nominally populated through interaction with these substrate reservoirs, the dominant spectral change is a result of a temperature dependent shift of the oscillator complex frequency. The stretch mode is anharmonically coupled to the frustrated translation mode of the CO complex. As the frustrated translation mode is heated by the excited substrate, the stretch motion absorption broadens and shifts to lower frequency. By measuring the adsorption at 2075 cm^{-1}, the time evolution of the low frequency mode population can be discerned (Fig. 2).



2)Transient fractional difference reflectivity with the probe laser tuned to the high frequency side of the unperturbed CO stretch Lorentzian absorption. The fluence absorbed by the substrate was $F_{abs} = 0.9\ mJ/cm^2$: Data (open squares), a best fit (solid line) using the model and values described in the text. Inset: rise of the signal.

The change in temperature of the low frequency mode can be predicted using a rate equation with independent couplings to the electron (γ_e) and to the phonon (γ_l) reservoirs. Temperature dependent FTIR spectra and exchange theory are used to predict the corresponding changes in the stretch mode complex frequency. By calculating the time evolution of the spectra, the rate equation and exchange model predictions can be compared with the data. A best fit gives the coupling rates of $\gamma_e = 167(24)\ GHz$ and $\gamma_e = 145(56)\ GHz$. Couplings to both reservoirs are revealed to be necessary and as a result of differences in their respective temporal profiles, their relative contributions can be distinguished .

With three times greater excitation of the substrate (Fig. 3) we see deviations from this model. Preliminary analysis indicates that the deviations maybe indicative of temperature dependent adsorbate-substrate coupling rates. As the molecule approaches excitation levels near the desorption threshold there are several mechanisms by which energy may be more quickly exchanged with the substrate. These new mechanisms, which include other anharmonic couplings between the adsorbate-like modes, temperature dependencies of γ_e or γ_l, and combined electron-lattice effects, have been discussed in recent molecular dynamics calculations for CO on Cu(100)[4]. We will describe our observations of the temperature-dependent low frequency mode coupling rates, and discuss their relevance to ultrafast laser induced surface reactions.



3)Transient fractional difference reflectivity at higher average fluence absorbed; $F_{abs} = 0.25\ mJ/cm^2$ (solid circles), $F_{abs} = 0.12\ mJ/cm^2$ (open circles). The lines represent fits for the relevant fluences using the best fit values of γ_e and γ_l from the $F_{abs} = 0.9\ mJ/cm^2$ data . The data clearly indicate that the model is breaking down.

References

[1] F. Budde, T. F. Heinz, M.M.T. Loy, J. A. Misewich, F. deRougemont and H. Zacharias, Phys. Rev. Lett. **66**, 3024 (1991). J. A. Prybyla, H. W. K. Tom, and G. D. Aumiller, Phys. Rev. Lett. **68**, 503 (1992). F. J. Kao, D. G. Bush, D. Cohen, D. G. Dacosta and W. Ho, Phys. Rev. Lett. **71**, 2094 (1993).

[2] J. P. Culver, M. Li, L. G. Jahn, R.M. Hochstrasser, and A.G. Yodh, Chem. Phys. Lett. **214**, 1 (1993).

[3] T. A. Germer, J. C. Stephenson, E. J. Heilweil and R. R. Cavanagh, J. Chem. Phys. **98**, 9986 (1993). T. A. Germer, J. C. Stephenson, E. J. Heilweil and R. R. Cavanagh, Phys. Rev. Lett. **71** 3327 (1993).

[4] J. C. Tully, M. Gomez and M. Head-Gordon, J. Vac. Sci. Technol. **A11**, 1914 (1993).

Ultrafast Isomerization Dynamics at Interfaces by Time-Resolved Second Harmonic Generation

E. Borguet, X. Shi and K. B. Eisenthal
Department of Chemistry, Columbia University,
New York NY 10027, USA

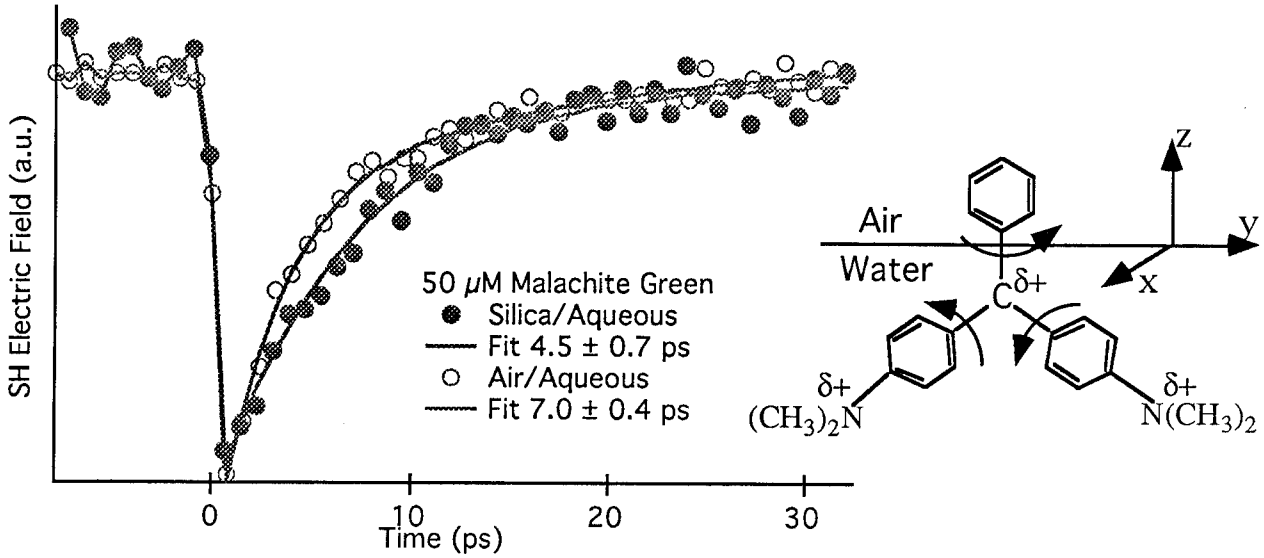
Ultrafast studies of molecular relaxation in the bulk have been of great value in revealing the dynamics of fundamental chemical and physical events. However, our knowledge of these processes at interfaces is still in its infancy. The present contribution focuses on the interfacial nature of one of the simplest chemical reactions; molecular isomerization. The interface is a unique environment, of interest in its own right, providing a further test of our understanding of elementary molecular processes. Time resolved second harmonic generation, by avoiding the complications of bulk contributions, enables surface species to be probed directly and on an ultrafast timescale[1,2]. Our results on the barrierless isomerization of an organic dye indicate novel and unanticipated behavior: a very large change in relaxation rates, differing by an order of magnitude from those in the bulk and surprisingly similar rates at very different interfaces, namely the air/liquid, liquid/liquid and liquid/solid interfaces.

As a prototype system we have explored the isomerization of Malachite Green at a number of aqueous interfaces; silica/aqueous, hexadecane/aqueous, octane/aqueous and air/aqueous. In the bulk the ultrafast relaxation dynamics of triphenylmethane dyes, such as Malachite Green, are sensitive to the nature of the molecular environment[3]. The fluorescence quantum yield and excited state relaxation rate show a strong dependence on solvent viscosity. The rate limiting step is believed to involve the rotation of the three aromatic groups about the bond between each one and the central carbon atom. The solvent drag forces opposing these rotations are manifested by the slowing down of the isomerization as the macroscopic bulk solvent viscosity increases.

An amplified CPM laser provides 130 fs pulses, at 625 nm at a repetition rate of 10 Hz. The intense laser light is focused at the interface and the second harmonic radiation is separated from the reflected fundamental using filters and a monochromator. Polarizers enable distinct components of the surface nonlinear susceptibility to be probed. Incident photon flux is kept below $1 mJ/cm^2$ to prevent saturation of the molecular response and the detection system. The system is an ideal candidate for TRSHG because the S_0 to S_1 transition of Malachite Green is centered close to the laser fundamental at 620 nm and S_0 to S_n transitions are resonant with the second harmonic.

The dynamics of distinct nonlinear susceptibility elements were examined. Both χ_{zxx} and χ_{xzx}, which depend differently on molecular orientation, show similar behavior. The dynamics of the SHG response were found to be independent of the pump polarization (s or p). The polarization of the radiated second harmonic fields are similar, spanning a range of 10^o for the interfaces

studied. This result indicates that the molecular orientations are similar at the various interfaces. The same time dependent decays observed for different susceptibility elements reveal that molecular rotation is not significant on the timescale investigated. The relaxation dynamics are characterized by a single exponential decay* (4.5±0.7 ps at the air/aqueous interface, 4.3±0.3 ps at the octane/aqueous interface, 4.5±0.3 ps at the hexadecane/aqueous interface and 7.0±0.3 ps at the silica/aqueous interface). These rates are significantly slower than the dominant component of decay (0.7 ps) reported in several investigations of Malachite Green in bulk water[4,5].



We will now analyze these results in terms of the following considerations. First, the generally accepted model for the photoisomerization of triphenylmethane dyes in bulk solution involves the intramolecular rotations (twisting) of the three aromatic groups about their respective bonds with the central carbon atom. This change in the twist angle of each of the aromatics from their ground state equilibrium angles is initiated by the change in the charge distribution of the molecule following excitation to the first excited singlet state. The frictional resistance exerted by the solvent against the twisting motions of the aromatic moieties in the bulk isomerization dynamics is seen in the viscosity dependence of the kinetics. We expect that the isomerization at the interface will also be sensitive to the friction experienced along the twisting coordinates.

Let us now consider the molecule of interest, Malachite Green, at the air/aqueous interface. It is known from many studies that the hydrophobic part of a molecule, in this case the phenyl group, would be pointed away from the aqueous phase and the more hydrophilic part, in this case the partially charged dimethylaniline groups would be oriented into the aqueous phase[6]. At the air/aqueous and alkane/aqueous interfaces the phenyl group would project into the air and alkane phases, respectively. The twisting motions about the carbon-phenyl group bond are therefore expected to be very sensitive to the frictional properties of the phase into which the phenyl group is projecting. The air vs. the octane vs. the

hexadecane phase should offer very different frictional resistances to the twisting of phenyl group. Contrary to the expectations, based on these considerations, that the isomerization dynamics would differ markedly, we found that the isomerization dynamics were the same at these interfaces having the values of 4.5±0.7 ps, 4.3±0.3 ps and 4.5±0.3 ps at the air/aqueous, octane/aqueous, and hexadecane/aqueous interfaces, respectively. We thus conclude that the photoisomerization dynamics in the triphenylmethane dye, Malachite Green, do not involve the rotation of the phenyl group. This is contrary to the generally accepted model which assumes that the twisting of all the aromatic moieties determines the rate of isomerization. Our results suggest that it is the nitrogen containing dimethylaniline moieties that determine the isomerization rate. Since these more hydrophilic moieties project into the aqueous phase, at approximately the same orientations, the twisting motions experience the same aqueous friction, and therefore yield the same isomerization dynamics at these various interfaces. It is of interest to note that at the silica/aqueous interface, where the phenyl group as well as the dimethylaniline groups are immersed in the water phase, the isomerization dynamics are slower than at the air/aqueous and alkane/aqueous interfaces. Although the phenyl group and the dimethylaniline groups are immersed in the aqueous phase, the isomerization dynamics are different (slower) than in the bulk aqueous phase. This result has a bearing on the considerable interest and some experimentally based inferences that the structure of water and its viscosity are different near solid/aqueous interfaces[7]. The SH results reported here provide support for these ideas, which have important implications for aqueous interfaces in many physical, chemical and biological systems.

In summary, we have succeeded in measuring the dynamics of photoisomerization at various aqueous interfaces. We have found that the dynamics are not only slower than in the bulk solution but surprisingly are the same at the air/aqueous and alkane/aqueous interfaces, contrary to the current models of isomerization of triphenylmethane dyes. We suggest on the basis of the SH experiments that rotation about the central carbon-phenyl bond is not important in the structure change dynamics. The twisting motions of the dimethylaniline groups control the photoisomerization dynamics. The isomerization dynamics at the silica/aqueous interface are consistent with the idea that the friction and therefore the structure of water in the neighborhood of the solid (silica)/aqueous interface differs from that of bulk water.

---

[1]E.V. Sitzmann and K.B. Eisenthal, J. Phys. Chem. **90**, 2831 (1989)
[2]A. Castro, E.V. Sitzmann, D. Zhang and K.B. Eisenthal, J. Phys. Chem. **95**, 6752 (1991)
[3]D. Ben-Amotz and C.B. Harris,J. Chem. Phys. **87**, 4856 (1987)
[4]D.J. Erskine, A.J. Taylor and C.L. Tang ,J. Chem. Phys. **80**, 5338 (1984)
[5]A. Migus, A. Antonetti, J. Etchepare, D. Hulin and A. Orszag, J. Opt. Soc. Am. B **2**, 584 (1985)
[6]K.B. Eisenthal, Ann. Rev. Phys. Chem **43**, 627 (1992)
[7]T.S.Filligan, S.B.Zhu, S.Yao, J.Lee and G.W.Robinson, Chem. Phys. Lett. **161**, 444 (1989)

Femtosecond Photoemission Studies of Electron Relaxation at Cu Surfaces

C. A. Schmuttenmaer, M. Aeschlimann, R. J. D. Miller
Center for Photoinduced Charge Transfer
Department of Chemistry
University of Rochester
Rochester, NY 14627-0219, USA
(716)-275-4079

D. Mantell
Xerox Webster Research Center
Webster, NY 14850, USA

J. Cao, Y. Gao
Department of Physics
University of Rochester
Rochester, NY 14627, USA

A number of recent studies have illustrated the importance of photoexcited electrons in surface reactions at metal surfaces. This work focuses on directly determining the relaxation dynamics for photoexcited electrons at Cu(100) surfaces. This particular surface is important as recent observations for photoinduced desorption of CO have found quantum yields as high as 15% for the hot electron reaction channel at high laser fluences.[1] Equal pulse correlation studies employing 3 eV pulses (50-60 fs) with both parallel and crossed polarization and low energy (<100 nJ/cm^2) have been used to characterize the intrinsic electron relaxation dynamics in the absence of excess lattice heating or transient collective effects. This low energy limit corresponds to photoinduced surface chemistry employing conventional low flux CW light sources such as arc lamps. These results are shown in Figure 1. The inset shows the observed photoemission spectrum. The highest energy electrons give a pulse width limited response function which can be used to deduce the slower relaxation dynamics of the lower energy electrons. The slower relaxation dynamics are clearly resolved as a broadening in the FWHM of the two pulse correlation of the photoemitted electron at specific energies. The deconvolved relaxation times for the electron energy distribution are shown in which the solid line through the data is a fit to a calculation based on Fermi liquid theory for electron relaxation scaled by a factor of 2.45. The extent of this agreement for the electron relaxation dynamics at a single crystal surface is similar to the relaxation dynamics observed previously for polycrystalline gold surfaces at higher fluences.[2] At lower energies above E_F, hot electron transport effects become noticeable and can be understood in terms of a ballistic transport model. These results fully characterize the non-radiative relaxation of electrons at low fluence and peak power.

As the excitation intensity is increased for power levels approaching those of previous studies of photoinduced desorption, interesting effects are observed in the photoemitted electron distribution. Above threshold photoemission (ATP) effects are observed at intensities as low as 10^8 W/cm^2 due to surface plasmon enhancement of the local field in the surface region. Representative data are shown in Figure 2, in which the energy distribution is clearly shifted to higher energies from the low fluence spectrum by multiple photon processes above the work function. At certain points along a deliberately roughened surface, discrete steps in the photoemission spectrum were observed, separated by the photon energy, which is the classic signature of ATP effects. Space charge effects were absent in these studies (<1 emitted electron/pulse), but the enhanced electron emission rapidly leads to space charge effects at fluences above 5 GW/cm^2.

These studies at high and low powers give a detailed description of the competing non-radiative electron relaxation channel which is important in understanding the hot electron induced photochemistry observed at these surfaces.

References

1. J. A. Prybyla, H. W. K. Tom, and G. D. Aumiller, *Phys. Rev. Lett.* **1992,** *68*, 503.

2. W. A. Fan, R. Storz, H. W. K. Tom and J. Bokor, *Phys. Rev. B* **1992**, *46*, 13592.

Figures

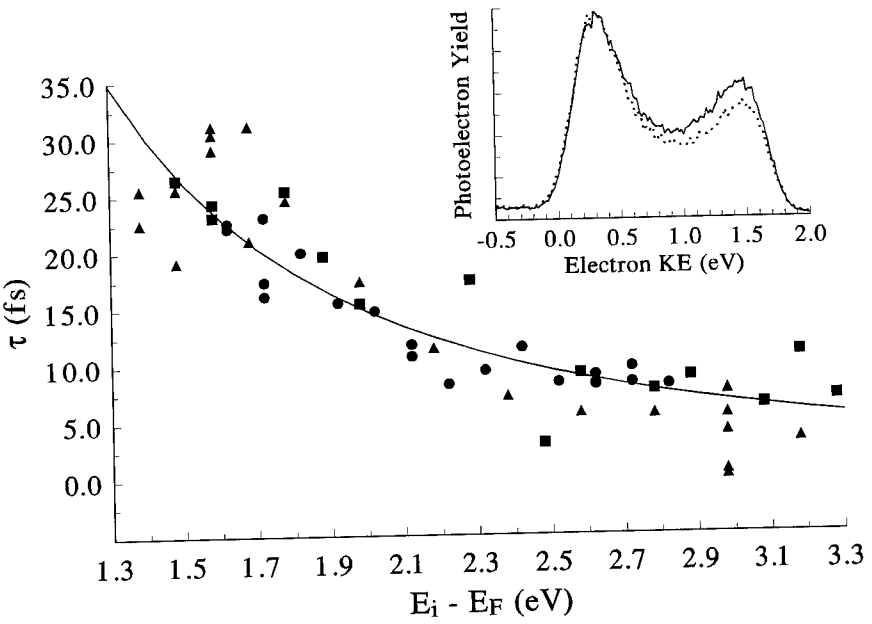


Figure 1. Time resolved photoemission decays for different electron energies above the fermi level, corresponding to three different sets of data. The inset shows the normalized full spectrum for two time delays (solid, t = 0; dotted, t = 60 fs).

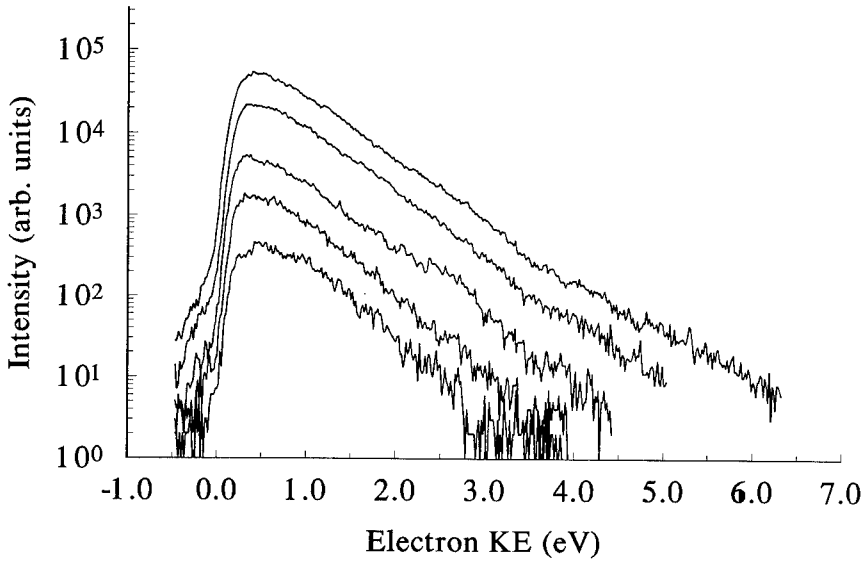


Figure 2. Semilog plot of multiphoton photoemission spectra from Cu(110) at different intensities; I = .17, .28, .41, .68 and 1.0 GW/cm^2 from lower to upper curves, respectively (λ_{ex} = 1.6 eV).

Time Evolution of Excited States in CdSe Nanocrystals, by V. L. Colvin[a], J. J. Shiang[a], W. Hoheisel[a], C. Johnsona, R. W. Schoenlein[b], D. M. Mittleman[b], S. J. Rosenthal[a], C. V. Shank[ab], and A. P. Alivisatos[a]
Lawrence Berkeley Laboratory, 1 Cyclotron Road, Berkeley, CA 94720, (510) 643-7371
[a]Department of Chemistry, University of California, Berkeley
[b]Department of Physics, University of California, Berkeley

Early theoretical work predicted that quantum dots would exhibit discrete, well separated optical excitations, with narrow linewidths, and uncommonly large excited state polarizabilities[1]. This unusual combination could result in some unusual nonlinear properties. Ever since there has been steady progress in the preparation and characterization of nanometer size semiconductor nanocrystals, with CdSe still remaining the prototypical direct band gap material[2]. During the past two years we have undertaken a systematic study of the size dependent photophysics in these materials. Colloidally prepared II-VI nanocrystals embedded in polymers and cooled to low T lend themselves readily to the application of many time and frequency resolved optical characterization techniques[3]. These include absorption, fluorescence, electric field modulation of the absorption and fluorescence, three pulse photon echoes, and resonance Raman scattering. All of these experiments are summarized in the accompanying figure.

The optical absorption and fluorescence spectra of the CdSe nanocrystals at 77 K show pronounced quantum confinement effects. The spectra shift to higher energy from the bulk band gap by as much as 0.75 eV in nanocrystals of 10 Å radius. Further, the density of the electronic excitations is much more sparse in the smaller particles, with level spacings on the order of 0.1 eV in the smallest particles. These shifts are consistent with simple confinement models, indicating that at least one of the carriers is confined. Many other features of our experiments suggest that the simple confinement picture does not suffice to describe the electronic excitations in the CdSe nanocrystals, and that the surface states of the nanocrystals need to be explicitly accounted for.

The electric field modulated absorption and fluorescence data as a function of the size, all scaled to be the same size, are also shown in the accompanying figure. The electro-absorption signals are of order $\Delta A/A \cong 10^{-5}$, and for all but the smallest size of nanocrystal they strongly resemble the second derivative of the unperturbed absorption spectrum[4]. This data is inconsistent with a spherically symmetric electronic excited state in which the electron and hole share a common center. Rather, the broadening of the absorption spectrum that occurs when the external field is applied is consistent with discrete, separated excited states in which one of the carriers is partially surface trapped even at the instant of optical excitation. The electro-fluorescence signal is much larger than the electro-absorption signal, of the order $\Delta F/F \cong 10^{-3}$. The signal drops off substantially in nanocrystals of smaller size, and the lineshape also appears to evolve smoothly with size. The electro-fluorescence data cannot be modeled with any combination of zeroth, first and second derivatives of the unperturbed spectrum. The data can be modeled well under the assumption that the emission arises from a quasi-continuum of surface excitations that are strongly coupled to the ionic lattice of the nanocrystals. In such a model, the external field polarizes the excited state, resulting in both a substantial loss of oscillator strength, as well as a change in the lattice coupling, and hence the emission lineshape. Thus the electric field modulation experiments show that the discrete states prepared by absorption are already mixed

with the surface excitations of the nanocrystals, and that subsequently further coupling to this quasi-continuum of surface states occurs.

The ultrafast three pulse photon echo experiments shown in the accompanying figure support this point of view[5]. In these experiments, quantum beats can be observed at the LO mode frequency of the CdSe nanocrystals when the first and third pulses are delayed with respect to each other. The relative intensity and temporal profile of these beats match the observed frequency, cross section and linewidth measurements from resonance Raman experiments. Both experiments reveal strong coupling to the LO modes, but a drop off in the coupling strength in smaller sizes. Again, the strength of the coupling of the initially prepared optical excitations to the lattice cannot be explained assuming the electron and hole have the same masses as in the bulk material, and are in spherically symmetric wavefunctions with a common center[6]. Rather, some localization of one or the other carrier is required, and polaron effects must be accounted for.

Finally, the dephasing time of the initially prepared excited state has been measured by echo experiments in which the first and second pulse are delayed with respect to each other. The experiments are performed with the third pulse set to suppress the effects of the LO mode coupling. The dephasing times are extremely fast, order 100 fs at 15 K, and are faster in smaller nanocrystals. Temperature dependent studies suggest that these fast dephasing times are due in large measure to two effects: strong coupling of the initially prepared state to the quasi-continuum of surface states, and coupling to low frequency vibrations of the nanocrystals. Recent measurements show that this dephasing time depends in detail on the surface derivatization of the nanocrystals.

Although presently available II-VI nanocrystals show many of the effects predicted by simple quantum confinement models, these real samples also show many effects that are due to the surface. Most notably, the lifetimes of the confined states are very short, resulting in linewidths for the optical excitations that are of the order 10 meV at low temperature. Further work on surface modification is requisite before the full range of quantum confinement effects can be observed in these systems.

References

[1]Schmitt-Rink, S,. Chemla, D. S., and Miller, D. A. B., *Phys. Rev. B* **32**, 6601 (1985).

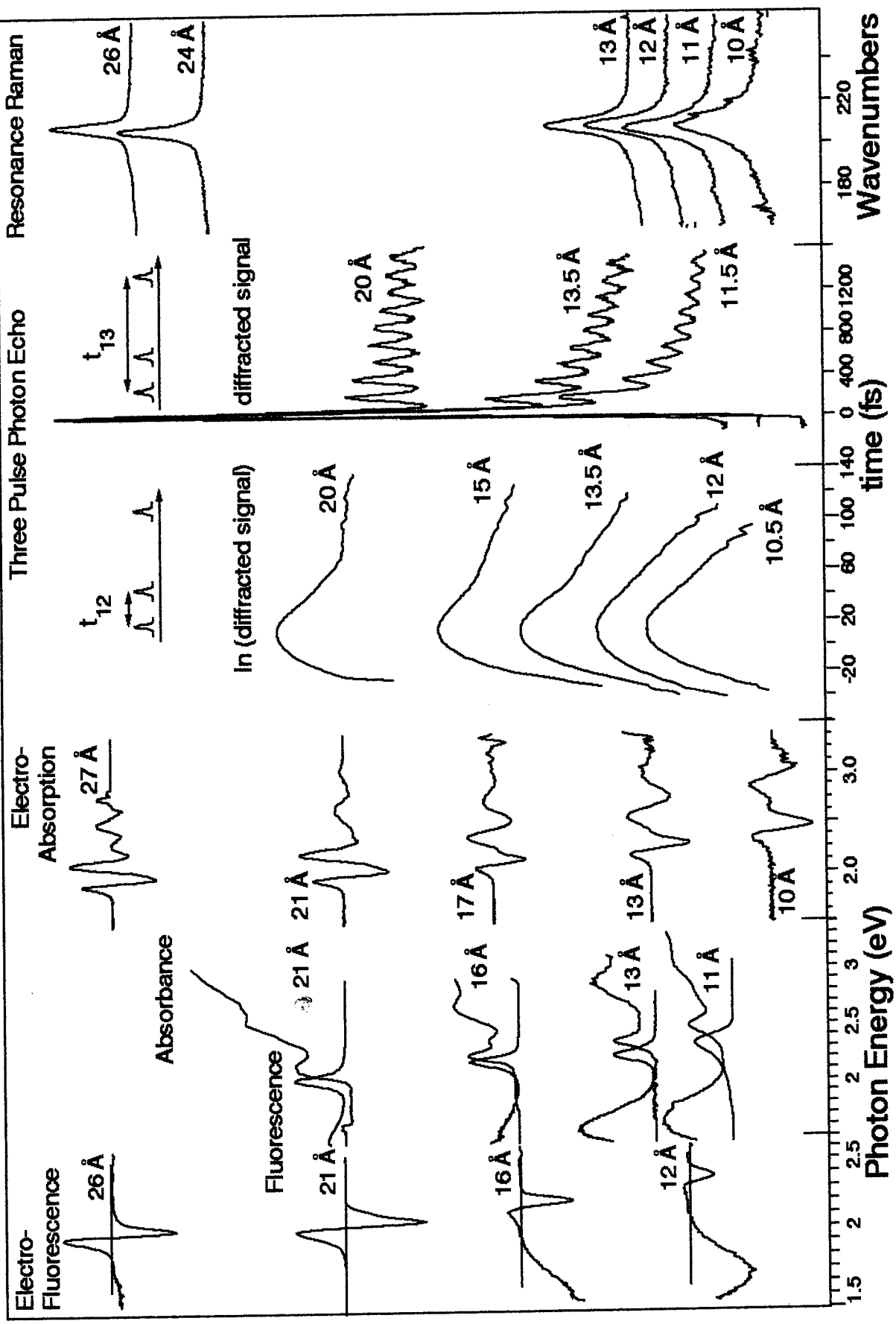
[2]Bawendi, M. G. Steigerwald, M. L., and Brus, L. E., *Adv. Chem. Phys.* **41**, 477 (1990); M. G. Bawendi, P. J. Carroll, W. L. Wilson, and L. E. Brus, *J. Chem. Phys.* **96**, 946 (1992).

[3]Murray, C. B., Norris, D. J., and Bawendi, M. G. *J. Am. Chem. Soc.*, **115**, 8706 (1993); J. B. Katari, V. L. Covin, and A. P. Alivisatos, "X-ray Photoelectron Spectroscopy of CdSe Nanocrystals with Application to the Nanocrystal Surfcae," submitted.

[4]V. L. Colvin and A. P. Alivisatos, *J. Chem. Phys.* **97** 730 (1992); V. L. Colvin, K. Cunningham, and A. P. Alivisatos, *J. Chem. Phys.*, submitted.

[5]Schoenlein, R. W., Mittleman, D. M., Shiang, J. J., Alivisatos, A. P., and Shank, C. V., *Phys. Rev. Lett.* **70**, 1014 (1993).

[6]J. J. Shiang, S. Risbud, and A. P. Alivisatos, *J. Chem.Phys.* **98**, 8432 (1993).


Summary of CdSe Nanocrystal Photophysics Experiments
Electro-Fluorescence
Electro-Absorption
Three Pulse Photon Echo
Resonance Raman
26 Å
27 Å
Absorbance
Fluorescence
21 Å
21 Å
21 Å
16 Å
16 Å
17 Å
13 Å
13 Å
12 Å
11 Å
10 Å
t_{12}
t_{13}
ln (diffracted signal)
20 Å
15 Å
13.5 Å
12 Å
10.5 Å
diffracted signal
26 Å
24 Å
20 Å
13.5 Å
11.5 Å
13 Å
12 Å
11 Å
10 Å
1.5
2
2.5
2
2.5
3
2.0
3.0
Photon Energy (eV)
-20
20
60
100
140
0
400
800
1200
180
220
time (fs)
Wavenumbers

Poster Session 2 and Exhibits

TuD 3:00pm–4:30pm
Dana Point Ballroom

Nonlinear Optical Studies of Microstructured GaAs/AlAs

S.T. Cundiff, E.O. Göbel
Fachbereich Physik und Wissenshaftliches Zentrum für Materialwissenschaft,
Phillips-Universität, Renthof 5, D-35032 Marburg, Germany
+49 6421 28 4221

V.P. Kochereshko, P.S. Ko'pev, N.N. Ledentsov
A.F. Ioffe Physico-Technical Institute
194021 St. Petersburg, Russia

The wealth of new phenomena which has been observed in semiconductor heterostructures displaying quantum confinement in a single dimension (quantum wells) has prompted efforts to fabricate structures which provide higher degrees of confinement [1]. Theoretical predictions of a strong reduction in scattering for structures which display confinement in two dimensions (quantum wires), and consequently a large mobility [2], also encouraged the efforts. Optical techniques have proved particularly suited to studying heterostructures [3]. However, definitive observations of many of the expected low dimensional phenomena have been hindered by fabrication difficulties. Nevertheless there has been some success with etched quantum wires, including the observation of a reduction in exciton-exciton scattering [4] and the observation of transient four-wave-mixing (TFWM) [5], which is particularly interesting because of its sensitivity to scattering processes. Although significant work on semiconductor quantum dots imbedded in a glass matrix has been performed, attempts at fabricating them in a semiconductor have faced similar difficulties as quantum wires.

We have performed time-integrated TFWM on a microstructured GaAs/AlAs sample in which GaAs clusters form due to the thermodynamics of the molecular beam epitaxial growth process. A schematic of the expected cluster geometry is shown as an inset in Figure 1b. The structure consists of a GaAs/AlAs superlattice grown on a non-(100)-oriented faceted surface, the GaAs clusters are introduced into one AlAs layer. The transverse dimensions of the clusters is estimated to be 32-35 Å and to be relatively constant, although the transverse wavefunction associated with the clusters will extend into the neighboring GaAs regions [6] and hence be approximately 100 Å across. The longitudinal dimension is estimated to be on the order of several 100 Å, and to exhibit significant variation. As a consequence these clusters should display behaviors which vary between quantum dots and wires. Further details of the growth are given elsewhere [7]. The clusters exhibit a strong polarized optical resonance in reflectivity, photoluminescence and photoluminescence excitation [8]. The strength of this resonance is in of itself remarkable, however it is consistent with the oscillator strength enhancement expected due to quantum confinement.

The 2-pulse TFWM experiments are performed using 150 fsec pulses in the reflected geometry, where the signal direction is the reflection about the plane of the sample of $2\mathbf{k}_2-\mathbf{k}_1$, where $\mathbf{k}_1$ is the direction of the first pulse, and $\mathbf{k}_2$ that of the second (see inset Fig. 1a). The signal is strongly resonant with a center frequency of 1.69 eV (see Fig. 1b), which corresponds to the resonance observed in the PL/PLE spectra and assigned to the clusters [8]. The signal is also strongly polarized, with the signal corresponding to the electric field of the excitation beams (which are co-polarized with each other) polarized along the axis of the clusters (co-polarized in Fig. 1b) being 4-5 times stronger than when they are cross-polarized with respect to the clusters. Additionally there is no observable signal at the energy corresponding to the superlattice resonance (1.75 eV).

The signal as a function of delay between the pulses is determined by the dephasing time (Fig. 1a). There are clear beats evident in the short time behavior of the signal. The beat frequency corresponds to an energy splitting of 5 meV. No corresponding resonances are evident in the frequency domain data, although the inhomogeneous widths are approximately 13 meV and hence

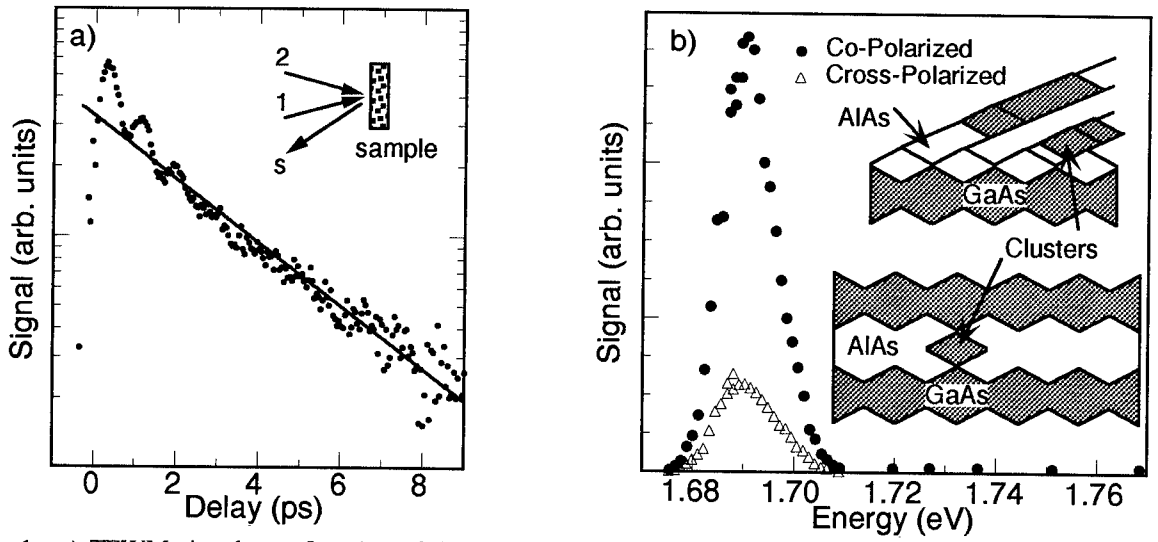


Fig. 1. a) TFWM signal as a function of delay between pulses. Inset shows experimental geometry. b) Signal strength as a function of photon energy for the incident fields co- and cross-polarized with respect to axis of the clusters. Inset is a schematic perspective view (upper) and cross-section (lower) of the clusters in the sample.

obscures the resonances giving rise the beats. Although beating between transverse subbands should occur and has been observed in quantum wires with of larger dimension [5], the transverse subband splitting in this sample should be hundreds of meV and so cannot explain the beats. They may be due to subbands arising from the confinement along the long dimension of the cluster, and would be consistent with clusters that are 400 to 500 Å long.

While in principle it is possible to extract dephasing rates for both the resonances contributing to the beats, this requires an understanding of both whether or not they are quantum beats or polarization interference, and the nature of the correlation between the levels in an inhomogeneously broadened system [9]. Therefore we will fit the long time behavior where the beats are damped out and the signal is monoexponential. Such a fit is shown by the solid line in Fig. 1a and yields a dephasing time of 13±0.5 ps. These data are taken at 5.5 K, at sufficiently low excitation density that the excitation induced contribution to the dephasing is small and spectrally at the center of the resonance. The dephasing rate is dependent on the spectral position within the inhomogeneously broadened line and increases by approximately a factor of 4 between the low and high energy extremes. The observed dephasing time is a factor of 4 longer than that observed in a high quality single quantum well [10]. An increase in the dephasing time would be expected to accompany the reduction in scattering associated with higher degrees of confinement. The possibility of a suppression of scattering merely due to localization must also be considered, however the observed linear temperature dependence (below) suggests that the excitons are not localized. The inhomogeneous broadening and spectral dispersion of the dephasing times is typically associated with well width fluctuations and hence localization in quantum wells, however this is complicated in the quantum clusters considered here due to the facts that (i) a substantial portion of the inhomogeneous broadening is due to length fluctuations, (ii) the longitudinal motion is quantized and (iii) the transverse wavefunction substantially extends into the neighboring GaAs layers.

The dephasing rate is also temperature and density dependent. In Fig. 2a the dephasing rate as a function of temperature is plotted between 4 and 40 K. At low temperature the dependence is linear due to scattering by acoustic phonons, as is seen in GaAs/AlGaAs quantum wells [10] and in etched GaAs/AlGaAs quantum wires [5]. The temperature dependence is a reflection of the exciton-phonon coupling, and in a system such as GaAs/AlAs where the lattice match is very good the phonons are insensitive to the interfaces and hence the temperature dependence should be

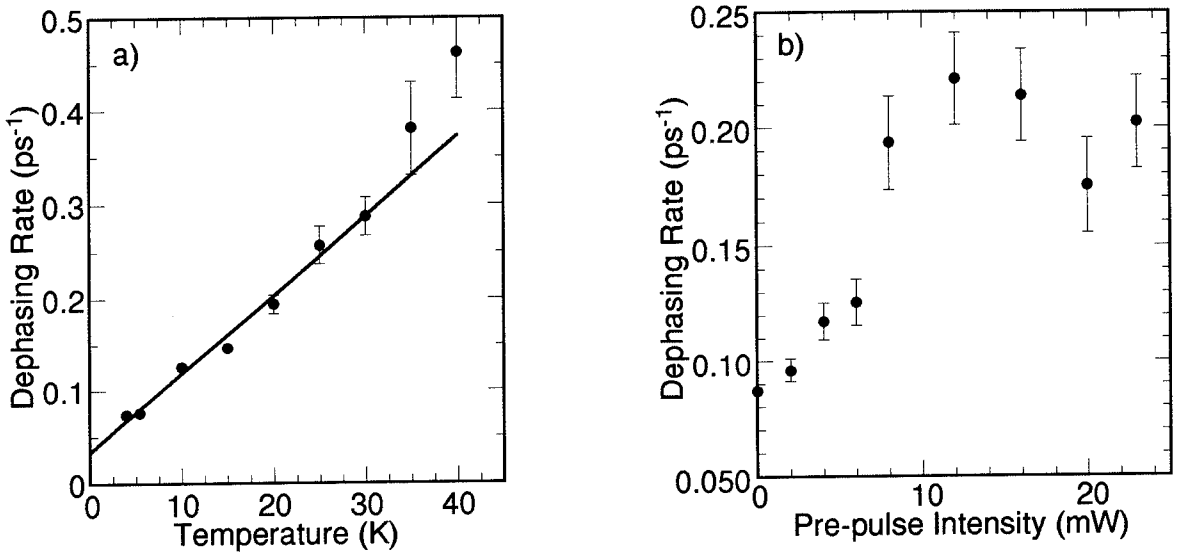


Fig. 2. a) Dephasing rate as a function of temperature, line is linear fit. b) Dependence of dephasing rate on the excitation density induced by a pre-pulse.

relatively independent of the confinement. The linear dependence is associated with delocalized excitons in quantum well samples, suggesting that localization is not playing a strong role in the exciton dynamics in this sample. The faster than linear increase above 30 K is probably due to an LO-phonon contribution.

The density dependence of the dephasing rate was measured by exciting the sample with a prepulse which preceded the TFWM pulses by more than a dephasing time (20 ps). The results in Fig. 2b show a relatively strong density dependence at low density, which flattens out at high density. Unfortunately there is no good way to estimate the excitation density as the absorption coefficient is unknown, therefore we have left the excitation density in terms of incident optical density. Again the linear low density dependence is similar to that seen in other systems [5, 10].

In summary, we have observed TFWM from the resonance that corresponds to confined excitons in a microstructured GaAs/AlAs sample. The strong signal is a result of the large oscillator strength in this resonance, and this alone makes the results very interesting. The fact that some aspects of the TFWM results suggest confinement, while others are not substantially different from those observed for bulk or quantum well excitons, is probably a reflection of the complicated nature of the sample morphology. Further investigations of the optical properties and morphology are in progress.

[1] K. Kash, J. Lumin. **46**, 69 (1990).
[2] H. Sakaki, Jap. J. App. Phys. **19**, L735 (1980).
[3] F. Henneberger, S. Schmitt-Rink, and E.O. Göbel, ed. *Optics of Semiconductor Nanostructures* (Akademie Verlag, Berlin, 1993).
[4] M. Oestereich, W.W. Rühle, H. Lage, D. Heitmann, and K. Ploog, Phys. Rev. Lett. **70**, 1683 (1993).
[5] E.J. Mayer, *et al.*, accepted by Phys. Rev. B (1994).
[6] E.L. Ivchenko and A.A. Kiselev, JETP Lett. **58**, 32 (1993).
[7] Z.I. Alferov, *et al.*, Sov. Phys. Semicond. **26**, 959 (1992).
[8] V.P. Kochereshko, E.L. Ivchenko, A.V. Kavokin, P.S. Kopev, and N.N. Ledentsov, in 3rd Inter. Conf. on Optics of Exciton in Conf. Sys., Montepellier, 1993, supplément au Journal de Physizue II Colloque **C5**
[9] S.T. Cundiff, accepted by Phys. Rev. A (1994).
[10] L. Schultheis, A. Honold, J. Kuhl, K. Köhler, and C.W. Tu., Phys. Rev. B **34**, 9027 (1986).

Collinear Transient Four-Wave-Mixing and Rabi Flopping in Semiconductors

S.T. Cundiff, A. Knorr, J. Feldmann, B. Spill, W. Stolz, S.W. Koch, E.O. Göbel
Fachbereich Physik und Wissenshaftliches Zentrum für Materialwissenschaft,
Phillips-Universität, Renthof 5, D-35032 Marburg, Germany
+49 6421 28 4221

The ready availability of sub-picosecond pulses from mode locked lasers has led to a large number of experiments being performed on the coherent interaction between light and extended electronic states in semiconductors and semiconductor heterostructures [1]. In tandem with these experimental efforts the theoretical understanding of these phenomena has also made significant strides [2]. However, one theoretical prediction which has not been directly experimentally observed is the phenomenon of Rabi-flopping in semiconductors [3]. Rabi-flopping is the oscillation of the excited state population induced by a strong light field. Here we present experimental results based on the nonlinear interaction of two copropagating pulses and show that in the theoretical treatment the observed behavior arises from the occurrence of a Rabi flop.

The experiments are performed by launching two ~200 fsec pulses separated by 700-900 fsec into a semiconductor waveguide. The waveguide consists of a 1.2 μm thick $Al_{0.3}Ga_{0.7}As$ core surrounded by $Al_{0.5}Ga_{0.5}As$ cladding layers and is 400 μm long. A 100 Å single quantum well is inserted slightly off center in the waveguide core and the experiments are performed resonantly with the heavy hole exciton resonance in the quantum well. The sample is held at 10 K in a cold finger cryostat that allows the necessary access for waveguide experiments. After propagation through the sample the pulses are time resolved by cross correlation with a reference pulse in a second harmonic crystal. By chopping both pulses and using a lock-in amplifier to detect the sum frequency only the component which is due to both pulses, and hence their interaction in the sample, is detected. This result is plotted in the upper panel of Fig. 1a for resonant excitation and Fig. 1b for non-resonant excitation, along with the results for propagation of each pulse alone. The negative contribution to the signal during the first pulse in Fig. 1b is due to interference between the pulses and is apparent only because the other contributions to the signal are so weak.

The dynamics of the slowly varying envelope E of the light pulse during its propagation through a semiconductor are described by the reduced wave equation for plane waves

$$\frac{\partial E(\xi,\eta)}{\partial \xi} = \frac{i\mu_0\omega_0^2}{k_0 V}\sum_{\mathbf{q}} P_{\mathbf{q}}(\xi,\eta), \quad \eta = z - \frac{t}{v_g}, \qquad \xi = z \tag{1}$$

where v_g is the pulse group velocity [4, 5]. The interband polarization $P_{\mathbf{q}}$ is determined from the solution of the semiconductor Bloch equations [2]

$$\frac{\partial P_{\mathbf{q}}}{\partial \eta} = -i\left(\Delta_{\mathbf{q}} - \omega_p\right)P_{\mathbf{q}} - i\Omega_{\mathbf{q}}\left(f_{\mathbf{q}}^{e} + f_{\mathbf{q}}^{h} - 1\right) + \left.\frac{\partial P_{\mathbf{q}}}{\partial \eta}\right|_{coll}, \qquad \frac{\partial f_{\mathbf{q}}^{e,h}}{\partial \eta} = \left(iP_{\mathbf{q}}^{*}\Omega_{\mathbf{q}} + c.c\right) + \left.\frac{\partial f_{\mathbf{q}}^{e,h}}{\partial \eta}\right|_{coll} \tag{2}$$

where $\Omega_{\mathbf{q}} = \frac{\Omega}{2} + \frac{1}{\hbar}\sum_{\mathbf{q}'} V_{\mathbf{q}-\mathbf{q}'}P_{\mathbf{q}'}$ is the renormalized Rabi frequency. The $f_{\mathbf{q}}$ denote the distribution functions for electrons or holes and $\Delta_{\mathbf{q}} = \varepsilon_{\mathbf{q}} - \frac{1}{\hbar}\sum_{\mathbf{q}'} V_{\mathbf{q}-\mathbf{q}'}\left(f_{\mathbf{q}'}^{e} + f_{\mathbf{q}'}^{h}\right)$ is the excitation dependent energy dispersion. The Coulomb potential, $V_{\mathbf{q}}$, is treated within a quasi-static screening model.

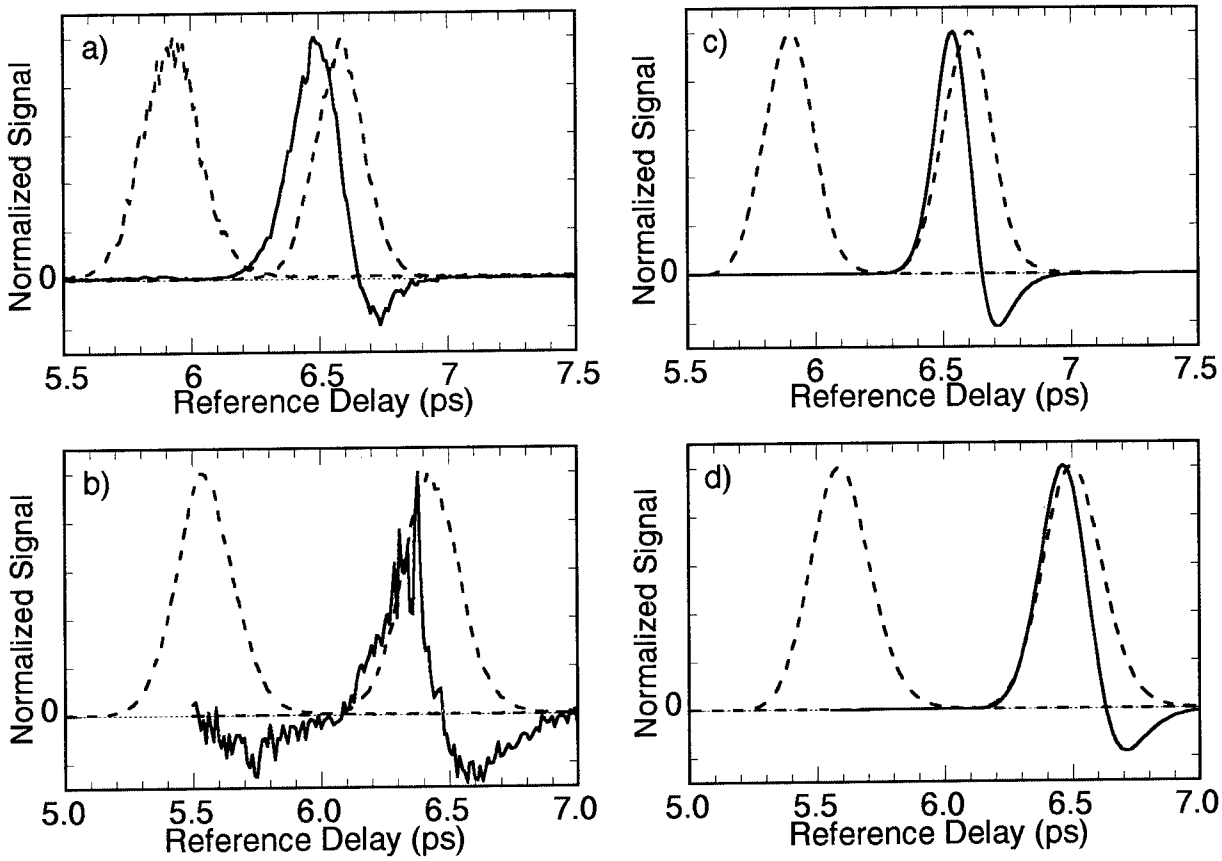


Fig. 1. Experimental results for a) resonant and b) non-resonant excitation and theoretical results for c) resonant and d) non-resonant excitation for two collinear pulses in a semiconductor. In all panels the solid line is the nonlinear interaction between the pulses, and the dashed lines are for propagation of the single pulses. All signals are cross-correlations with a reference pulse.

The bare Rabi frequency $\Omega = \frac{d_{cv} \cdot E}{\hbar}$ is determined by the dipole matrix element d_{cv} and the amplitude of the external electric field $\tilde{E} = E(\eta, \xi) e^{-i\omega_0 t + ik_0 z}$.

The two pulses E_1 and E_2 are copropagating but temporally separated. The measured signal intensity is given by the fields after propagation through the sample

$$I_{sig} = \left|E_1^d + E_2^d\right|^2 - \left|E_1^s\right|^2 - \left|E_2^s\right|^2 = \left|E_2^d\right|^2 - \left|E_2^s\right|^2 + \left(E_2^s \left(E_1^d\right)^* + c.c.\right) \qquad (3)$$

where d designates that both pulses propagate through the sample, and s that only a single pulse does so and for the second step $\left|E_1^d\right| = \left|E_1^s\right|$ due to causality. If the pulses do not temporally overlap we can neglect the cross term.

The full system of coupled Maxwell-Bloch equations must be solved numerically, however it is possible to obtain some insight analytically by applying perturbation theory with respect to the propagation length [5]. Using equations (1) and (2) we derive a propagation equation for the pulse intensity $|\Omega|^2$ and perform a perturbation expansion with respect to the short propagation distance $\delta\xi$. The result shows that the signal is proportional to the difference between the polarizations due to the second pulse with and with out the first pulse.

For a two-level system, i.e. neglecting all Coulomb effects, $V_q \to 0$, we find that $I_{sig} \propto \frac{\partial N_2^s}{\partial \eta} \propto \Omega_2 \, \mathrm{Im}(P_2^s)$ where $N_2^s = \sum_q f_q$ is the total electron-hole density induced by the second pulse. This shows that we directly measure the polarization or density change one pulse induces in the system. In this sense a zero crossing corresponds to one Rabi-flop. The measured effect occurs because the amplitude of the Rabi-flop induced by the second pulse is reduced in the presence of the electron-hole population created by the first pulse due to phase space filling. Dephasing on time-scales less than the pulse width suppresses Rabi-flopping because the trailing edge of the pulse must coherently interact with the population created by the leading edge. Consequently in the limit of very short dephasing times the zero-crossing due to Rabi-flopping is not present.

This simple analysis does not consider propagation effects, which also can result in a signal which displays a zero crossing. This results from propagation effects due to the change in v_g resulting from the bleaching of the absorption by the electron-hole population created by the first pulse. Because the propagation effects are only dependent on the presence of an electron-hole population, which may be incoherent, they are not suppressed by rapid dephasing. They are, however, suppressed for a sufficiently short propagation length. Consequently the experimental conditions must be carefully chosen to isolate the Rabi flopping contribution.

The distinction between the Rabi-flopping contribution and the propagation effects can clearly be seen in the comparison of the experimental results with the theoretical results in Fig. 1. The theoretical results are obtained by a numerical solution of the full coupled Maxwell-Bloch equations which inherently includes all the effects, however by varying the input parameters (primarily dephasing rate and absorption coefficient) the contributions can be separated. In both Fig. 1c and Fig. 1d, which correspond to resonant and non-resonant excitation respectively, the Rabi-flopping contribution is responsible for the signal. Comparison with the corresponding experimental results shows that the resonant cases differ, the experimental result is clearly advanced with respect to the second pulse, while the theoretical one is not. A large propagation induced contribution is consistent with the experimental observations of large absorption (αL ~ 1.5) and strong differential transmission ($\Delta T/T$ ~ 130%) in a non-collinear experiment at this energy. For the non-resonant case, where the experimental absorption is much smaller (αL ~ 0.3) and differential transmission negligible ($\Delta T/T$ < 1%), the theory and experiment are both coincident with the second pulse, demonstrating that in this signal is due to Rabi-flopping.

In summary, we have presented experimental results on the nonlinear interaction of two collinear pulses in a semiconductor. In the experimental data a zero crossing is observed. In the theoretical treatment a zero crossing can arise from Rabi flopping. Further experimental and theoretical studies are in progress to confirm the origin of the experimental observation.

[1] F. Henneberger, S. Schmitt-Rink, and E.O. Göbel, ed. *Optics of Semiconductor Nanostructures* (Akademie Verlag, Berlin, 1993).

[2] H. Haug and S.W. Koch, *Quantum Theory of the Optical and Electronic Properties of Semiconductors* (World Scientific, Singapore, 1993) 2nd ed.

[3] R. Binder, S.W. Koch, M. Lindberg, N. Peyghambarian, and W. Schäfer, Phys. Rev. Lett. **65**, 899 (1990).

[4] W. Schäfer and K. Henneberger, Phys. Stat. Sol. b **159**, 59 (1990).

[5] A. Knorr, R. Binder, M. Lindberg, and S.W. Koch, Phys. Rev. A **46**, 7179 (1992).

Direct Determination of the S_2 Lifetime of β-carotene by Femtosecond Time-Resolved Fluorescence Spectroscopy

Hideki Kandori,*,+ Hiroyuki Sasabe,+ and Mamoru Mimuro$

+Frontier Research Program, The Institute of Physical and Chemical Research (RIKEN), Wako, Saitama 351-01, Japan

$National Institute for Basic Biology, Okazaki 444, Japan

*Correspondence to Dr. Hideki Kandori, Department of Biophysics, Faculty of Science, Kyoto University, Sakyo-ku, Kyoto 606-01, Japan

(TEL) 81-75-753-4211 (FAX) 81-75-753-4210

Femtosecond time-resolved fluorescence spectroscopy (up-conversion) was applied to directly determine the S_2 lifetime of β-carotene at room temperature. Upon excitation of β-carotene in *n*-hexane with a 425 nm femtosecond pulse, the fluorescence lifetime was estimated to be 195 ± 10 fs throughout the whole emission wavelength. Absence of dynamic Stokes shift suggests that the intramolecular relaxation processes occur within 50 fs, followed by the internal conversion from S_2- to S_1-state in 195 fs.

Carotenoids have important physiological function in photosynthesis. They work as light harvesting pigments due to a large oscillator strength in the visible region and an efficient singlet energy transfer to chlorophyll's. Further they work as a quencher of triplet state and of singlet molecular oxygen due to a low-lying triplet state. Carotenoids are, in general, polyenes belonging to C_{2h} point group [1]. In their electronic states, two energetically low-lying singlet states are expected; one is closely related to the 2Ag state which is dipole forbidden from the ground state by parity, and the other is related to the 1Bu state which is optically allowed. The Bu-based state is responsible for a strong visible absorption of carotenoids, while the Ag-based state is in a lower energy level (S_1-state) than the Bu-based state (S_2-state).

According to the above assignment, we can expect the following relaxation processes of carotenoids; optical excitation to the S_2-state induces an internal conversion to the S_1-state, followed by relaxation to the ground state. Singlet energy transfer to chlorophyll is a competitive relaxation process from the both states, it is very important to estimate the accurate excited-state dynamics. The S_1-lifetime was estimated by the ground state recovery, which was in a range of ~10 ps for β-carotene [2]. An estimation of the S_2 lifetime was carried out by the subpicosecond transient absorption on β-carotene [2b]. In their study, complicated kinetics including two relaxation processes were analyzed, which eventually provided the S_2 lifetime to be 200 or 250 fs in ethanol or CS_2, respectively, and the S1 lifetime, 9.5 or 11 ps, respectively. However, a direct measurement of the S_2 lifetime is necessary to characterize the excited-state dynamics.

In order to measure the femtosecond fluorescence, a conventional time-correlated single photon counting apparatus or a streak camera system is not sufficient in the time-resolution. Thus, we adopted fluorescence up-conversion technique to determine directly the S_2 lifetime of β-carotene. In our system, combination of the sum frequency generation and single-photon counting detection ensured a high sensitivity for the fluorescence in fs time regime. The second harmonic (425 nm) of the mode-locked Ti:Sapphire laser was used to excite a sample, and fluorescence and a fundamental gate pulse (850 nm) were focused onto a phase-matched thin BBO crystal to generate ultraviolet sum-frequency light. The polarization angle between the excitation and gate pulses was normally set to be 54.7^{o}, while parallel and parpendicular polarizations were applied to obtain the time-resolved anisotropy change. The present instrumental response function, obtained by the cross-correlation measurement between the excitation and gate pulses, had a Gaussian shape of 200 fs (FWHM, Fig. 2, broken line).

β-carotene was purchased from Wako chemicals and its all-*trans* form was selectively isolated by high-performance liquid chromatography. β-carotene dissolved in *n*-hexane was kept under N_2-saturated condition during measurements. We measured the steady-state fluorescence spectrum (Fig. 1). Since molecular structure of β-carotene is highly symmetric, fluorescence predominantly came from the S_2 state. Based on the spectrum, we chose 6 wavelengths (Table 1) and applied the fs up-conversion. For the experiment, β-carotene/*n*-hexane solution was put in a 1-mm cell in a concentration of 2.5×10^{-5} M. The excitation energy was 80 mW with a 0.1 mm diameter, thus about 0.6 % of the molecule were excited with the laser beam. A fresh sample was prepared for each measurement, and no spectral change of the sample absorption was found after measurements.

Upon excitation of β-carotene in *n*-hexane with a 425 nm fs pulse, the fluorescence was observed only in fs regime at all probing wavelengths. Typical kinetics at 513 nm were shown in Fig. 2, where the deconvolution gave a lifetime of 195 ± 5 fs. It is noted that the fluorescence appeared without any delay and decayed to almost zero within 1 ps. The kinetic feature was essentially wavelength-independent; at 6 probing wavelengths, the estimated S_2 lifetimes of β-carotene in *n*-hexane were in a range of 190 to 200 fs (Table 1) at room temperature. Fluorescence anisotropy was also measured at 539 nm (Fig. 3). It gave a high value, $r = 0.39 \pm 0.02$, throughout the emission time, indicating that fluorescence directly originated from the S_2 state. The estimated fluorescence quntum yield was 1.7×10^{-4}.

The 425 nm excitation yields the 0-2 vibrational transition of the S_2 state with ~2500 cm^{-1} excess energy. In this case, we may expect the dynamic Stokes shift due to intramolecular vibrational relaxation processes, as often mentioned by ultrafast spectroscopic techniques. However the observed kinetics gave a unique lifetime for the whole emission wavelengths (Table 1). The failure to observe the dynamic Stokes shift suggests that the intramolecular relaxation in the S_2 state occurs faster than the present time-resolution, and we estimated it shorter than 50 fs. Time-resolved

spectroscopy with ~10 fs time-resolution could indicate such dynamic Stokes shift, probably as well as the oscillatory signal due to a coherent C-C stretching in the time domain.

In conclusion, an up-conversion technique gave a highly accurate S_2 lifetime of β-carotene in n-hexane, and at the same time, suggests the intramolecular relaxation time of shorter than 50 fs. This leads to better understanding of the excited-state dynamics of carotenoids than those by other previous reports.

[1] B.S. Hudson et al., *Excited States* 6, 1 (1982).

[2] (a) M.R. Wasielewski and L.D. Kispert, *Chem. Phys. Lett.* 128, 238 (1986). (b) A.P. Shreve et al., *ibid.* 178, 89 (1991). (c) H.A. Frank et al., *ibid.* 207, 88 (1993).

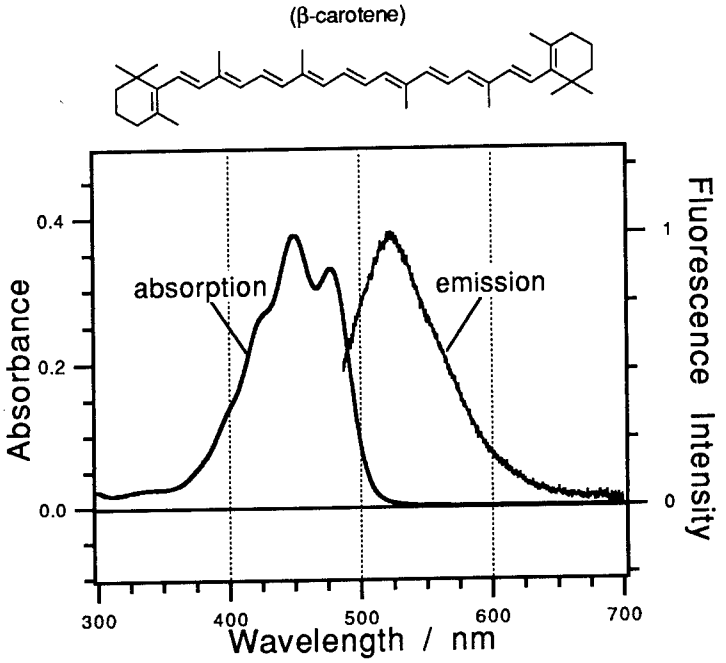


Fig. 1 Absorption and corrected fluorescence spectra of β-carotene in *n*-hexane.

Table 1.

S_2 lifetime obtained by the femtosecond fluorescence measurement

wavelength	lifetime
488 nm	195 ± 10 fs
513 nm	195 ± 5 fs
539 nm	195 ± 5 fs
595 nm	200 ± 10 fs
624 nm	190 ± 30 fs

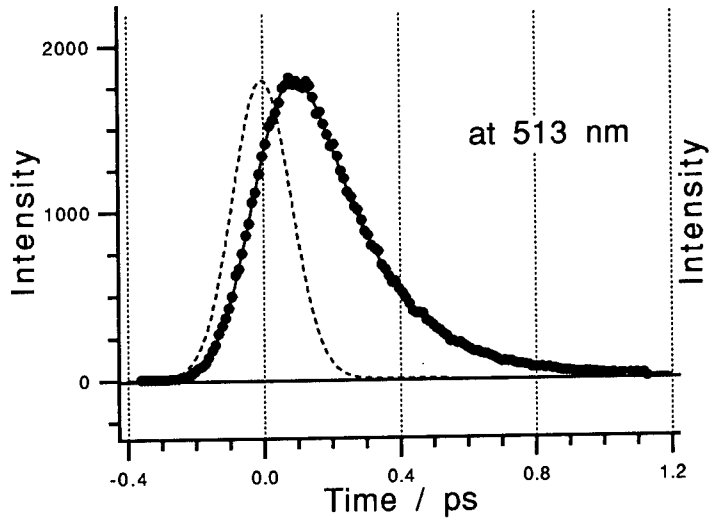


Fig. 2 Typical fluorescence decay kinetics of β-carotene in *n*-hexane.

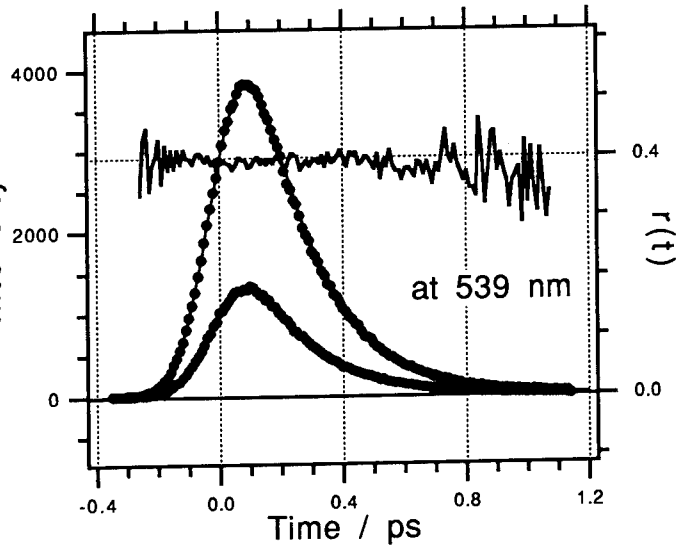


Fig. 3 Anisotropic fluorescence decays and anisotropy change of β-carotene in *n*-hexane.

ULTRASHORT HIGH-ENERGY PULSES FROM LONG-STRIPE ACTIVELY-MODE-LOCKED LASER DIODES IN EXTERNAL CAVITY

N. STELMAKH, A. AZOUZ, J-M. LOURTIOZ
Institut d'Electronique Fondamentale, URA 22 du CNRS, Bât. 220, Université Paris-Sud, 91405 Orsay Cedex, FRANCE, (Phone 33 1 69 41 62 99, Fax 33 1 60 19 25 93)

P. GAVRILOVIC
Microelectronics Center, Polaroid Corporation, 21 Osborn Street, Cambridge, Massachusetts 02139 , USA (Phone 617 577 42 37 , Fax 617 494 8230)

Short-pulse mode-locked laser diodes could become an interesting alternative to more conventional sub-picosecond lasers for time-resolved spectroscopy and optical testing of materials. Pulsewidth limits have been substantially lowered down to ~ 200 fs in recent experiments [1,2] and still better performances are expected when considering the very large amplification bandwidth of laser diodes. However, practical applications also require high output energies (or peak-powers) and much effort has to be made in this direction. Up to now, pulse energy delivered by sub-picosecond laser diodes has been typically in the range of a few picojoules. In this paper, we report on a one-order-of-magnitude improvement of pulse energy with the use of long-stripe (1-2 mm) quantum well AlGaAs lasers in an active mode-locking scheme. The overall pulse performances attained with 2 mm long lasers ($\Delta t \approx$ 460 fs, E ≈ 50 pJ) are believed to be the best reported to date without using additional amplifier sections.

Fig.1 shows the experimental set-up. Single-transverse-mode high-power AlGaAs laser diodes at 0.83 μm are used with a standard ≈ 1% AR coating on one facet. Active mode-locking in external cavity is achieved by applying a strong RF signal at 630 MHz (a few watts) superimposed onto the dc bias. The 24 cm long external cavity simply consists of a microscope objective and an end-reflector (R=98%). A four-pass grating compressor [3] equipped with an holographic grating serves to compress the laser pulses, the compressor dispersion being continuously adjustable from - 20 to +20 ps/nm. Laser pulses are measured with a $LiIO_3$ autocorrelator. The time-resolved spectroscopic image of the laser emission is obtained with a streak camera which also allows us to verify the absence of satellite pulses in one period.

Fig.2 shows the autocorrelation trace of mode-locked pulses obtained with 1mm long lasers. As seen, more than 90% of the emitted energy is concentrated in one peak. For an average output power of 5 mW, the pulse energy is thus estimated to be ≈ 8 pJ. The width of the autocorrelation trace is ≈ 500 fs, which corresponds to a laser pulsewidth of ≈ 330 fs after compression. The spectral width is separately measured to be 11 nm, which should a priori lead to ≈ 100 fs pulses in the Fourier-transform limit.

Fig.3 shows the results obtained with 2 mm long lasers. As confirmed by streak camera measurements, the total energy is now concentrated in a single peak. The average laser power is increased up to 30 mW, which corresponds to a pulse energy of ≈ 50 pJ. The

laser pulsewidth estimated from the autocorrelation trace is ≈460 fs, while a value of ≈ 150 fs could be expected in the Fourier transform limit for a measured spectral width of ≈ 8 nm.

Results reported in Figs 2 et 3 were reproduced for a large number of devices. Although mode-locking was more easily achieved with 2 mm long lasers, many similar behaviours were observed for the two laser lengths. Optimal compression of the mode-locked pulses was achieved for anomalous dispersions of the compressor (≈ -1 ps/nm), which corresponds to previous observations in the case of passive mode-locking [1,2]. However, the absence of any laser self-pulsing after several hours of operation as well as the high RF power level needed for mode locking rule out the eventual existence of strong saturable absorber in the laser medium. Long-stripe laser diodes thus appear to be good candidates for the generation of high-energy femtosecond pulses by active mode-locking.

(1) P.J. Delfyett et al., IEEE J. Quantum Electron., QE-28, pp. 2203-2219, (1992)
(2) N.Stelmakh et al., Electron. Lett. 29, pp. 160-161, (1993)
(3) O.E. Martinez, IEEE J. Quantum Electron., QE-23, pp. 59-64, (1987)

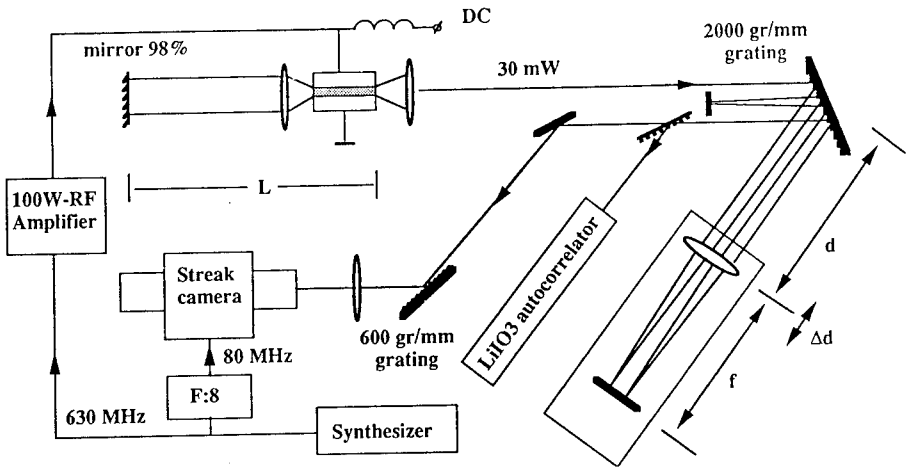


Fig.1: Experimental set-up

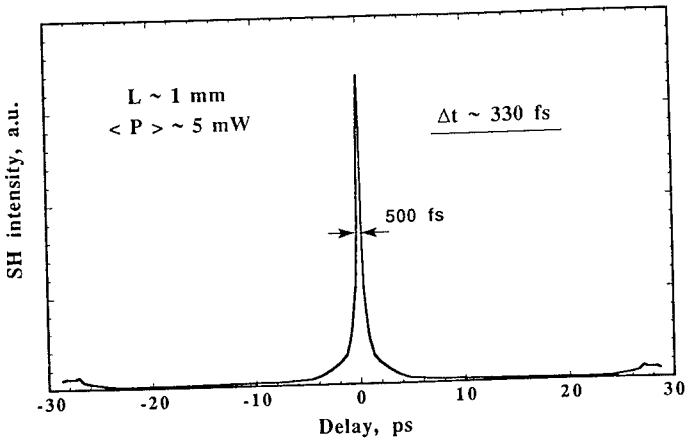


Fig.2: Autocorrelation trace of 1mm long laser pulses

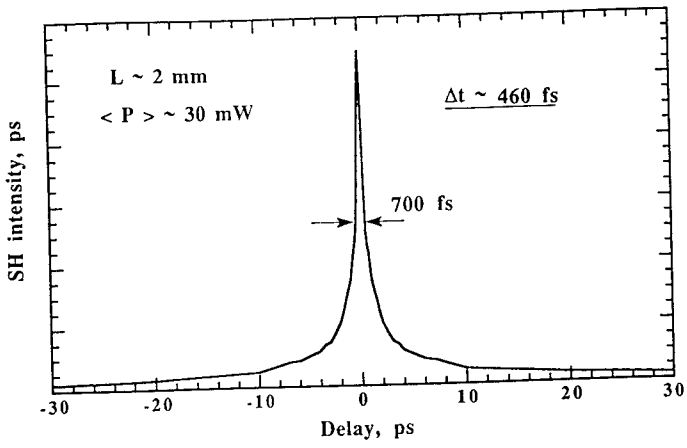


Fig.3: Autocorrelation trace of 2mm long laser pulses

Intensity and phase measurements of femtosecond pulses from a chirped pulse amplifier

Bern Kohler, Vladislav V. Yakovlev, and Kent R. Wilson
Department of Chemistry 0339, University of California, San Diego
La Jolla, CA 92093-0339 USA

Jeff Squier
Center for Ultrafast Optical Science, University of Michigan
2200 Bonisteel, IST Bldg, Rm 1006, Ann Arbor, MI 48109-2099 USA

Kenneth W. DeLong and Rick Trebino
Combustion Research Facility, Sandia National Labs
Livermore, CA 94551 USA

Chirped pulse amplification (CPA) with a Ti:sapphire regenerative amplifier has produced femtosecond pulses with millijoule energies at kHz repetition rates [1]. The performance of these laser systems has been limited primarily by the inability to compensate the spectral pulse phase to all orders in the compressor after the pulse has been stretched and amplified by making typically twenty roundtrips in a regenerative amplifier. Several authors have used dispersive ray tracing calculations to modify the design of the pulse stretcher and / or compressor in order to reduce the residual phase distortions which cause pulse broadening in a CPA system [2]. In order to further shorten the pulses from CPA systems, it would be extremely useful to measure directly the actual intensity and phase of the amplified pulses under different conditions. This information would then provide a means for checking the dispersive ray tracing models of the stretcher / compressor as well as providing information on precisely what sort of phase compensation is needed.

Here we report measurements we have made of the total electric field of the amplified pulses from a Ti:sapphire CPA laser system using frequency-resolved optical gating (FROG). This recently developed technique measures a two-dimensional spectrogram which can be uniquely inverted to determine the intensity and phase of an ultrashort pulse [3]. FROG traces were recorded using both second-order [4] and third-order optical nonlinearity [3] to provide the gating. Due to the lower pulse energy requirement, the second-harmonic FROG technique was used to characterize the pulses from a self-modelocked Ti:sapphire oscillator (Clark Instruments Model NINJA-4) before amplification. The intensity and phase of the unamplified pulse are shown in the time domain in figure 1 (FWHM of I(t) = 70 fs). This pulse is very nearly transform-limited and exhibits a modest amount of quadratic temporal phase which arises primarily from material dispersion due to optics placed between the oscillator and our FROG measurement setup.

Pulses from the oscillator are stretched by two 1200 l/mm gratings in a pulse stretcher described in reference 1. After 19 roundtrips in the regenerative amplifier the stretched pulse is cavity dumped and compressed by two 1200 l/mm gratings in a parallel configuration.

For characterizing the amplified pulses polarization-gated FROG (PG-FROG) was used [3]. This technique requires a third-order optical nonlinearity and was easily performed using less than 10 microjoules of amplified light. Figure 2 shows the intensity and phase of an amplified pulse which was recorded following the pulse compressor. A series of asymmetrical sub-peaks are observed in the intensity envelope which clearly indicate the presence of residual cubic spectral phase. Fitting a polynomial to the measured spectral phase of the pulse yields a value of -6.9×10^4 fs^3 for the cubic term. Changing the compressor grating separation by a small amount about the distance which yields the shortest pulses changes the observed pulse intensity and phase in a

predictable way. The magnitude of the spectral cubic phase changes slightly but retains the same algebraic sign (negative in our amplifier) while the quadratic spectral phase changes sign depending on whether the grating separation is too large or too small. Although the pulse stretcher and pulse compressor have phase contributions which are equal and opposite to all orders (in the absence of aberrations), dispersion suffered in the regenerative amplifier and the Faraday rotator introduce additional distortion. By making the grating angle of incidence different in the pulse compressor than in the pulse stretcher it is possible to compensate the phase through third order [1]. Using the measured amount of cubic spectral phase the optimum grating angle in the compressor can be readily computed. Thus, precise measurements of the pulse shapes are expected to be useful in optimizing CPA performance.

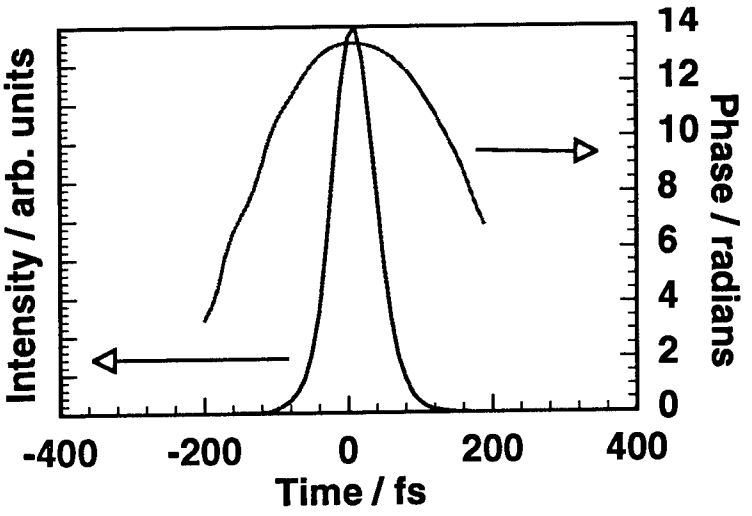


Figure 1. Temporal intensity and phase of oscillator pulse.

We used measurements of the intensity and phase of two amplified pulses which differed only by one cavity roundtrip to study the dispersion of the regenerative amplifier. The difference in the Taylor series coefficients of the pulse phase provides a direct measurement of the phase accumulated by the injected pulse after one roundtrip. Systematic analysis of this data provides information about linear dispersion and gain narrowing suffered in the amplifier resonator and can be used to further improve the design of the stretcher/compressor.

Finally, the FROG technique will be invaluable for characterizing shaped ultrashort pulses. In a preliminary experiment, a simple amplitude mask was placed in the focal plane of the pulse stretcher to block the central frequency components of the stretched pulse. The temporal intensity and phase of the measured pulse after amplification and passage through the grating pulse compressor are shown in figure 3. A liquid crystal display could be placed in the pulse stretcher and used either to reduce residual distortions to provide a shorter pulse or to intentionally introduce phase and amplitude modulation to produce shaped, amplified femtosecond waveforms.

In conclusion we have made detailed measurements of the full amplitude and phase of femtosecond optical pulses from a chirped pulse amplifier. We believe that complete pulse characterization measurements such as these may well be required to bring the amplified pulse duration of a CPA laser system down closer to the values currently obtainable from oscillators. Furthermore, we expect techniques such as FROG to have a significant impact on experiments which require shaped, ultrashort pulses.

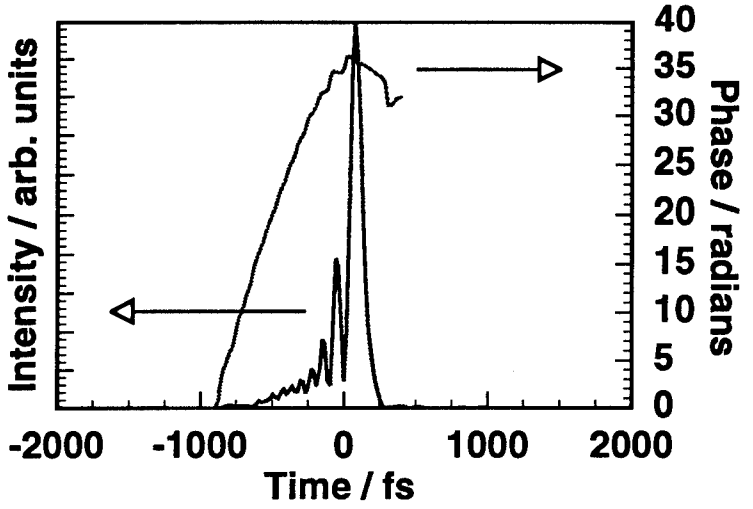


Figure 2. Temporal intensity and phase of amplified pulse, exhibiting residual cubic phase.

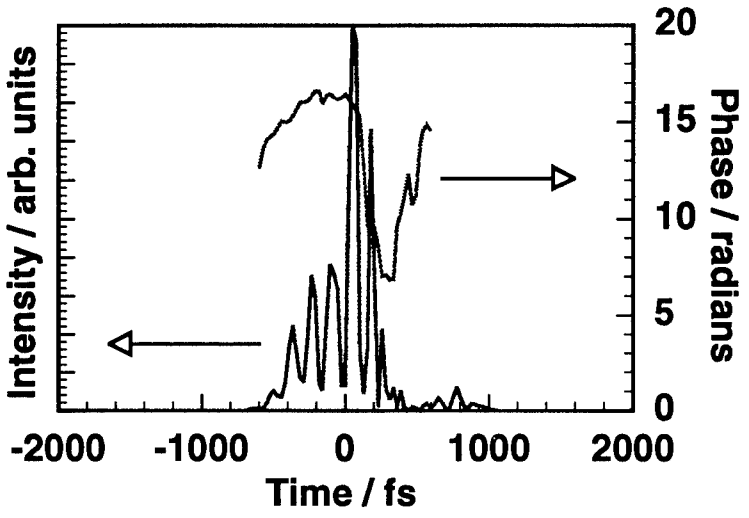


Figure 3. Temporal intensity and phase of a shaped, amplifed pulse.

References

1. J. B. Rudd, G. Korn, S. Kane, J. Squier, G. Mourou, P. Bado, Opt. Lett. **18**, 2035 (1993).
2. W. E. White, F. G. Patterson, R. L. Combs, D. F. Price, and R. L. Shepherd, Opt. Lett. **18**, 1343 (1993); B. E. Lemoff and C. P. J. Barty, Opt. Lett. 18, 1651 (1993).
3. D. J. Kane and R. Trebino, Opt. Lett. **18**, 823 (1993); R. Trebino and D. J. Kane, J. Opt. Soc. Amer. A **10**, 1101 (1993).
4 J. Paye. M. Ramaswamy, J. G. Fujimoto, and E. P. Ippen, Opt. Lett. **18**, 1946 (1993); K. W. DeLong and R. Trebino, in preparation.

TUNABLE FEMTOSECOND PULSES IN THE VISIBLE BY OPTICAL PARAMETRIC AMPLIFICATION

J. Watson, T. Lépine, P. Georges and A. Brun

Institut d'Optique Théorique et Appliquée
Unité de recherche associée au CNRS N°14
Bâtiment 503, B.P. 147, 91403 Orsay Cedex, FRANCE
Phone number: (33-1) 69 41 68 96 Fax number: (33-1) 69 41 31 92

For femtosecond time resolved spectroscopy experiments, it is often interesting to change the wavelength of the pump and the probe. Generally, the production of tunable femtosecond pulses is obtained through spectral continuum generation in order to produce a white light. However, there are some limitations in energy and the spatial profile is altered by self focusing. Optical parametric generation is a non linear process which plays an important role in the development of easily and widely tunable coherent sources [1-3].

In this paper we present a femtosecond Optical Parametric Amplifier (OPA) tunable throughout the visible spectrum based on the highly nonlinear BBO crystal. Pulses as short as 260 fs at 630 nm with an energy of 1 μJ have been produced in a double-pass OPA pumped by the second harmonic of an amplified titanium sapphire laser working at 780 nm.

We have compared our results with theoretical calculations giving the tuning curve (wavelength of signal and idler versus orientation of the crystal) of the BBO optical parametric amplifier. Another important parameter is the Group Velocity mismatch (GV mismatch) between the pump at 390 nm and the signal in the visible domain as a function of signal wavelength (see figure 1). One has to note that this GV mismatch is always greater than 50 fs per mm of BBO crystal. After two passes in a 6 mm BBO crystal, one would expect this large amount of GV mismatch to severely limit the efficiency of the system. We also determined the expected walk-off angle between the different beams as a function of signal wavelength.

Our double-pass OPA is presented in figure 2. As the pump laser we use a self mode-locked Ti:Sapphire oscillator amplified in a regenerative amplifier by using the chirped pulse amplification technic producing 150 fs, 2 mJ pulses at 780 nm at a 20 Hz repetition rate. We first

frequency doubled the amplified pulses in a 4 mm LBO (type I) crystal and obtained pump pulses at 390 nm with an energy of 150 μJ. Using these blue pulses to pump the OPA allowed us to tune over the entire visible range. We then pumped a 6 mm BBO (type I) crystal to create parametric fluorescence. We separated the 390 nm from the fluorescence and introduced a delay line in one arm to compensate for GV mismatch between the two beams. We finally recombined the beams in the same BBO crystal in order to parametrically amplify the on-axis fluorescence.

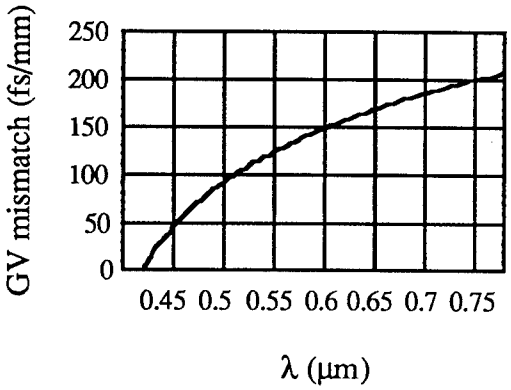


Figure 1. Calculated GV mismatch (fs/mm) between the pump and the signal versus signal wavelength.

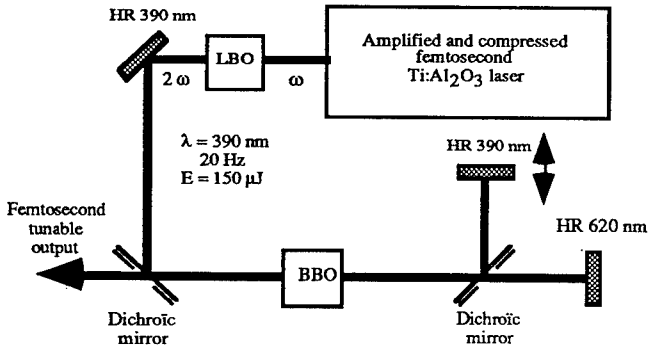


Figure 2. Experimental set-up.

With a pump energy of 150 μJ at 390 nm, we obtained 1 μJ pulses around 630 nm with a pulsewidth of 260 fs. A typical spectrum is shown in figure 3. Figure 4 gives an autocorrelation. The relatively low efficiency of our OPA is due to the high GV mismatch between the blue pump and the signal compared to results obtained by Banfi et al [2]. In their case, they have a pump at 620 nm and a signal in the near infrared where the GV mismatch is lower (around 20 fs/mm).

We also show that to maximize the efficiency of the system, one must precompensate for the Group Velocity Dispersion (GVD) in the crystals by adding negative dispersion to the

amplified pulses at 780 nm. This is done with the grating compressor following the regenerative amplifier of the Ti:Sapphire laser. In this way, the pump pulse at 780 nm has negative GVD and a duration around 7 ps, leading to a signal pulse with the highest energy and the lowest duration.

Our measurements of the wavelength dependence on crystal orientation for the OPA corresponded very well to the theoretical tuning curve. As regards the GV mismatch, the desire to pump in the blue to extend the tuning range over the visible spectrum has magnified the difficulty of reaching a high efficiency. Precompensating for the GV mismatch by adding a delay line between the passes of the OPA has allowed us to offset this difficulty to some degree.

In conclusion, crystal length of our OPA seems to be a critical parameter : if too short, there is not enough gain, if too long, GV mismatch and GVD can severely limit the efficiency. In the near future, we plan to add another stage to the amplifier to boost the energy of the output pulses. Further results of these experiments will be presented at the conference.

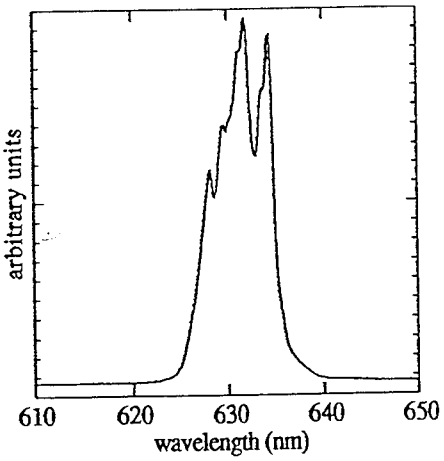


Figure 3. Typical spectrum of the OPA pulses.

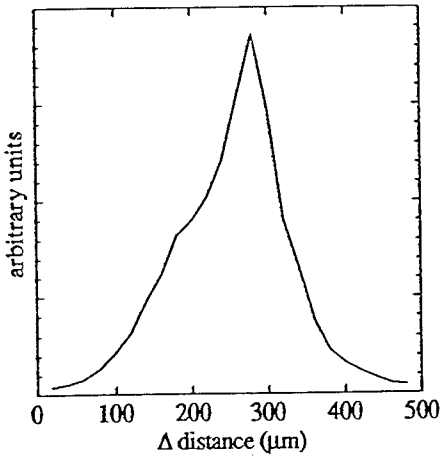


Figure 4. Autocorrelation of OPA pulses around 630 nm. Pulsewidth is approximately 260 fs.

REFERENCES

[1] W. Joosen et al., *Parametric generation in β-barium borate of intense femtosecond pulses near 800 nm*, J.Opt.Soc.Am.B **8**, p.2087 (1991).

[2] G. P. Banfi et al., *Femtosecond traveling-wave parametric generation with lithium triborate*, Opt. Lett. 18, p. 1633 (1993).

[3] J.Y. Huang et al., *High-power, widely-tunable, picosecond coherent source from optical parametric amplification in barium borate*, Appl.Phys.Lett. **57**, p. 1961 (1990).

Femtosecond Optical Spectroscopy of Partially Deoxygenated Y-Ba-Cu-O Thin Films

L. Shi, T. Gong, W. Xiong, X. Weng, Roman Sobolewski, and P. M. Fauchet
LABORATORY FOR LASER ENERGETICS
and DEPARTMENT OF ELECTRICAL ENGINEERING
University of Rochester
250 East River Road, Rochester, NY 14623-1299
Tel. (716) 275-1920, Fax (716) 275-5960
(email: lshi@lle.rochester.edu)

Very recent spectroscopic data of $YBa_2Cu_3O_{7-\delta}$ (YBCO) films suggest that oxygen doping dramatically changes the electronic structure of the CuO_2 plane.[1,2] The femtosecond 2-eV-pump/white-light-continuum-probe experiments performed at room temperature on YBCO thin films with various oxygen contents showed that in fully oxygenated YBCO samples (T_c ~90 K) the transient optical reflectivity ($\Delta R/R$) signal remains positive for all probe energies from 1.91 eV to 2.25 eV, whereas the response of oxygen-poor films (T_c ~0 K) is negative down to 1.46 eV.[3] The lack of sign reversal for $\Delta R/R$ in either type of YBCO suggests that the results for the oxygen-rich samples could be interpreted as intraband free-carrier absorption, while the response in the oxygen-poor YBCO resulted from the saturation of interband absorption across the charge-transfer gap.

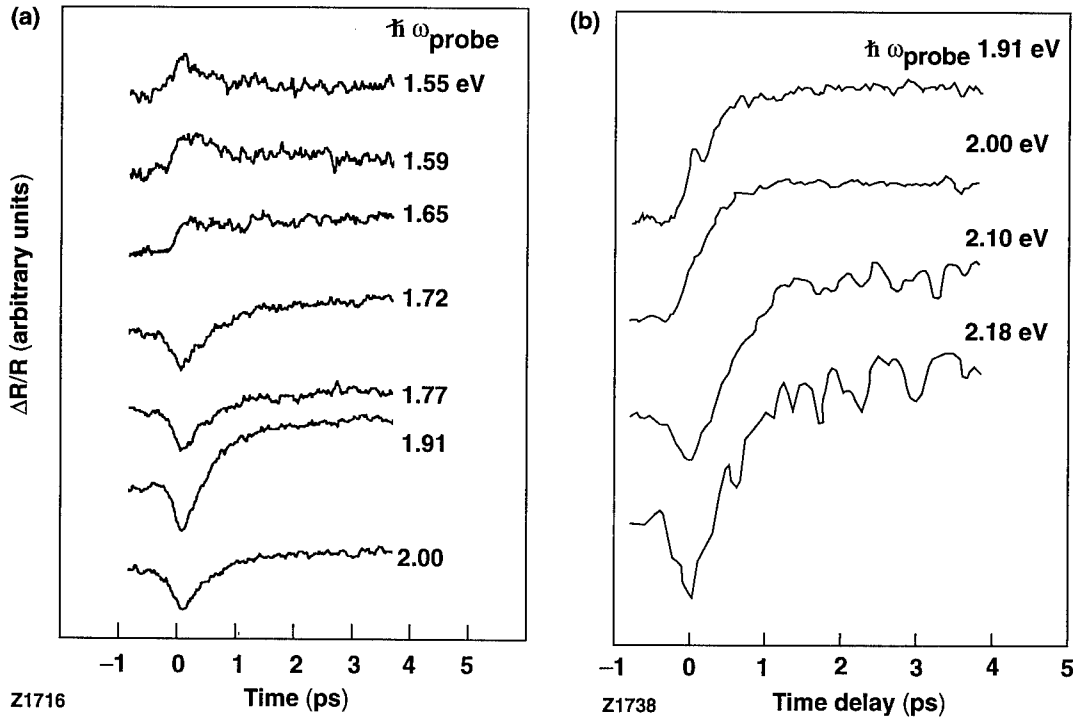


Fig. 1 Temporal $\Delta R/R$ waveforms measured on (a) 55-K and (b) 60-K YBCO films for a 2-eV pump and various probing photon energies. The pump intensity is ~ 20 $\mu J/cm^2$ and the measurement temperature is 300 K.

In this communication we present white-light-probing experiments performed on YBCO films with a critical temperature T_c between 50 K and 60 K. Partially oxygen depleted YBCO is especially interesting, since it has been proposed that its energy band diagram can be simplified to a d-band and p-band system.[1] In the presence of d-to-p-band transitions near the Fermi level E_F, the dominant contribution to the femtosecond optical response arises from the Fermi smearing effect.[4] The sign reversal of $\Delta R/R$ can thus be used to determine the position of E_F in these materials.[5] By

varying the oxygen doping δ, a quantitative relationship between T_c and δ can be determined. Furthermore, the nonequilibrium carrier dynamics can yield coupling strength of the electron-phonon intercation. This information is important for understanding the electronic structure of the doped CuO_2 plane and the physical mechanisms leading to high temperature superconductivity.

Figure 1 shows ΔR/R waveforms for a 55-K sample and a 60-K sample. In both cases, the signal changes from negative to positive as the probing photon energy is scanned from 2.18 eV to 1.55 eV. In the framework of the thermomodulation model, the sign change of ΔR/R at t~0$^+$ ps suggests that E_F is 1.7 eV and 2 eV above the Cu d^9/d^{10} band for the 55-K and 60-K samples, respectively. The large difference (~300 meV) that we observe in the position of E_F is not completely understood, but could be associted with local variations of the oxygen content, routinely observed in partially oxygen depeleted YBCO. Nevertheless, we can conclude from our white-light study that E_F is shifted downward when the oxygen content is decreased (in the hole picture). Furthermore, the thermomodulation model provides a satisfactory qualitative explanation for the ΔR/R data in samples with different oxygen contents. However, a more detailed electronic structure of the CuO_2 plane should be taken into account for an accurate quantitative description.

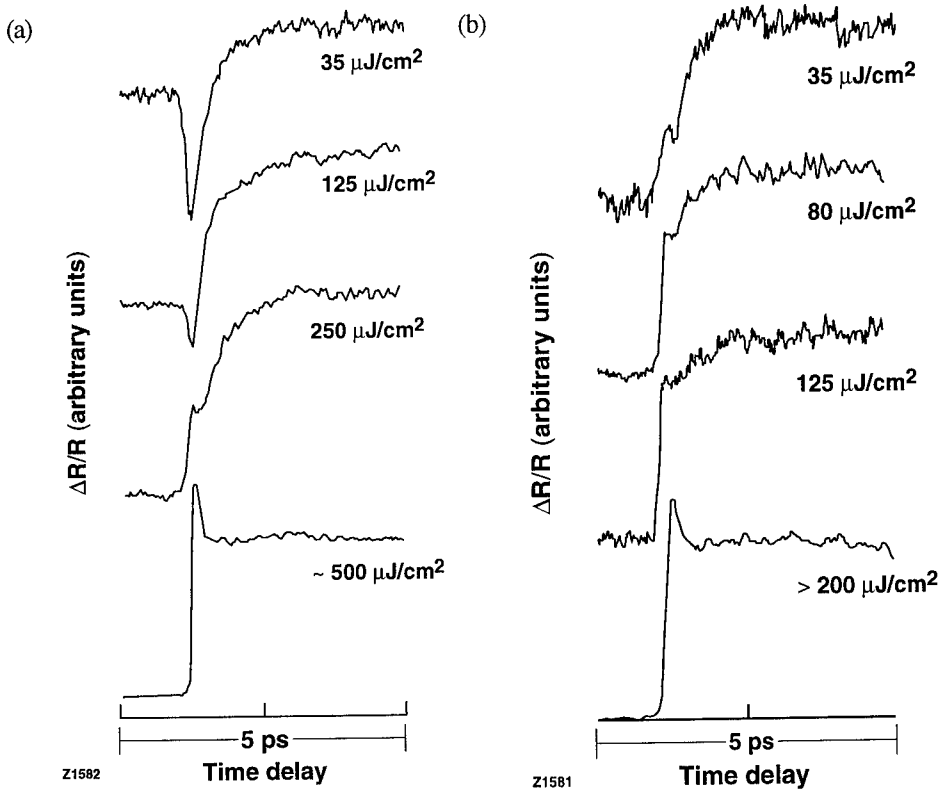


Fig. 2
Intensity dependence of the transient reflectivity waveforms measured on a 60-K YBCO film at two different regions (a) and (b).

In order to shed more light of the uniformity of oxygen doping in partially depleted YBCO films, we compare two different regions of the same 60-K sample. According to our pump-probe measurements, region (a) corresponded to $E_F < 2$ eV, while in region (b) $E_F > 2$ eV. In these two regions we have measured the intensity dependence of the optical response at 2-eV pump/2-eV probe. Figures 2(a) and 2(b) display the measured ΔR/R waveforms at various pumping intensities. In region (a), a gradual change of sign at t~0$^+$ is observed: The signal initially displays a large negative spike at t~0$^+$, which becomes less pronounced with increasing pump intensity and eventually turns into a positive peak. At the highest pump intensity, the data resemble that of a fully oxygenated sample.[2] This clearly suggests that E_F, initially below 2 eV, is up-shifted upon the increase of the pump intensities. On the other hand, if we start with E_F above the energy of the

probe beam [Fig. 2(b)], the signal is always positive: $\Delta R/R$ at $t\sim0^+$ quickly evolves from a step-like response to a spike at very high pump intensities. Thus, in this case, the increase of the pump intensity also leads to the up-shift of E_F. It is important to point out that the intensity dependence is fully reversible, i.e., reducing the pump intensity restores the initial waveform. Hence, the possibility of any stoichiometric changes in the film, such as oxygen displacement, can be excluded.

To quantitatively study the intensity dependence, the amplitudes of $\Delta R/R$ at $t\sim0^+$ ps, corresponding to regions (a) and (b), are plotted in Fig. 3. The $\Delta R/R$ changes at $t\sim0^+$ ps can be evaluated by calculating the change of the state occupancies with the initial Fermi level E_{F0} as an adjustible parameter. By taking into account the temperature dependence of the chemical potential, we obtain the theoretical fits given by the solid lines. We find that $E_{F0} = 1.96$ eV and 2.03 eV, respectively. The good fit strongly suggests that the thermomodulation model is indeed valid for partially oxygen-depleted YBCO. It also shows that the intensity dependence of $\Delta R/R$ can be explained by the up-shifting of the Fermi level with respect to the 2-eV-probe photon energy.

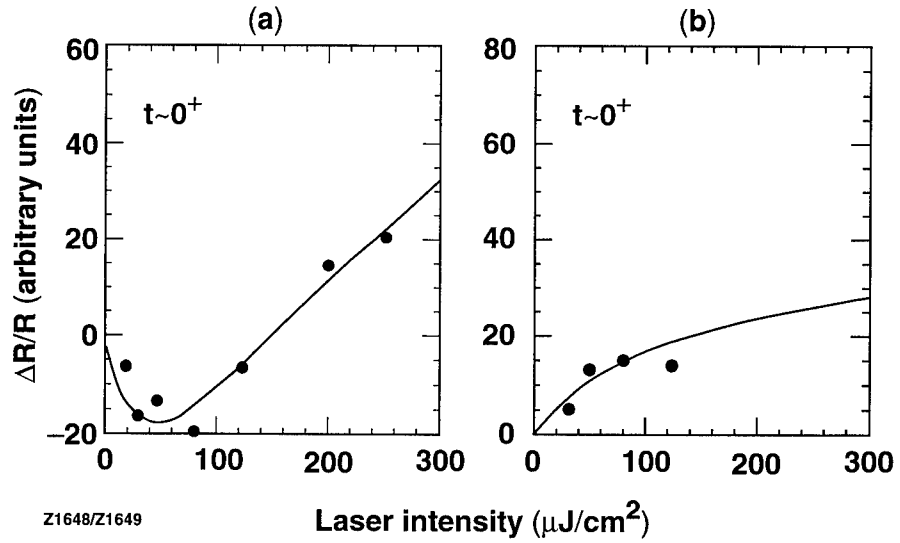


Fig. 3 Magnitudes of the $\Delta R/R$ signals at $t\sim0^+$ ps from regions (a) and (b) plotted as a function of the pump intensity. The solid lines represent theoretical fittings.

In conclusion, we have performed femtosecond reflectivity measurements in partially oxygen depleted YBCO thin films at room temperature. The validation of the thermomodulation model was discussed by examining the optical responses of 55-K and 60-K YBCO films. In addition, we have demonstrated that the change in reflectivity strongly depends on the intensity of the pump laser near the Fermi energy. We observe an up-shift in the Fermi level upon increase of the pump intensity, which can be directly attributed to the nonequilibrium hole heating.

This work was supported by Army Research Office grant DAAH04-93-G-0211.

1. S. Uchida, Jpn. J. Appl. Phys. **32**, 3784 (1993).
2. S. L. Cooper, D. Reznik, A. Kotz, M. A. Karlow, R. Liu, M. V. Klein, W. C. Lee, J. Giapintzakis, and D. M. Ginsberg, Phys. Rev. B**47**, 8233 (1993).
3. T. Gong, L. X. Zheng, W. Xiong, W. Kula, Y. Kostoulas, R. Sobolewski, and P. M. Fauchet, Phys. Rev. B**47**, 14495 (1993).
4. S. D. Brorson, A. S. Kazeroonian, D. W. Face, T. K. Cheng, G. L. Doll, M. S. Dresselhaus, G. Dresselhaus, E. P. Ippen, T. Venkatesan, X. D. Wu, A. Inam, Solid State Commun. **74**,1305 (1990).
5. G. L. Eesley, Phys. Rev. Lett. **51**, 2140 (1983).

Femtosecond Transient Grating Studies of Electron Transfer in Porphyrin and Chlorophyll Donor-Acceptor Molecules

Gary P. Wiederrecht, Walter A. Svec, and Michael R. Wasielewski
Chemistry Division
Argonne National Laboratory, Argonne, IL 60439
(708) 252-6963

I. Introduction

Transient grating experiments have been utilized to study a variety of condensed phase phenomena. Most of these studies are performed on transparent media, resulting in non-resonant probing of the material response of the system. Such experiments include the study of orientational dynamics in liquids, acoustic and optical phonon dynamics as they relate to phase transitions in solid state media, optical Kerr effects, intramolecular vibrations, etc. In its simplest form, the technique requires two beams to be temporally and spatially overlapped in the sample. An interference pattern is created, which modulates the real part of the index of refraction through the third order susceptibility ($\chi^{(3)}$). A phase grating results, through which a variably delayed probe beam incident on the sample may diffract and provide temporal information about the material response.

Resonant transient grating experiments are also frequently utilized to perform studies on a variety of photophysical and photochemical processes. They include electron transport in semiconductors, energy transfer, and simple chemical reactions. An absorption (amplitude) grating modulates the imaginary part of the susceptibility tensor. Such chemical systems are generally carefully chosen to avoid interference from non-resonant phase gratings or multiple absorptions. Interference between the phase and amplitude gratings can complicate the time-dependent results and obscure the phenomena of interest. However, the exploitation of the polarization selective nature of transient grating experiments that was first done by Etchepare et al. and further enhanced by Deeg and Fayer has resulted in a leap in the ability to probe the desired phenomena of interest (1,2). It was shown that the different elements of the nonlinear susceptibility tensor possess different polarization characteristics and can be individually probed through prudent choices for the input and detection polarizations. Etchepare et al. first showed how to eliminate the nuclear and optical Kerr effect in CS_2 (1). Deeg and Fayer were the first to utilize this technique with an absorption contribution to the diffracted signal and to show that the anisotropy of the excited state grating can be utilized to provide valuable information about the relation between the excitation transition dipole and the probed transition dipole (2).

II. Experimental

In addition to the polarization characteristics of the transient grating technique, it is also a background free experiment, enabling higher sensitivity than with pump-probe experiments. The greater sensitivity enables one to utilize lower excitation intensities and

avoid higher order effects that sometimes plague pump-probe experiments. In our experiments, we utilize a femtosecond dye laser system that has been described in detail previously (3). The output is 75 fsec pulses amplified at 1 kHz at 585 nm up to 20 uJ. The white light that is utilized for the variably delayed probe is generated through focussing into a rotating quartz block and the scattered light is detected with a PMT.

III. Results

The goal of this report is to lay the groundwork for transient grating studies of electron transfer in artificial photosynthetic systems. Such systems include simple donor-acceptor molecules where the donor, typically a chlorophyll or porphyrin, is rigidly attached to an easily reduced species such as napthoquinone or benzoquinone. Over the last few years, we have made significant progress in the synthesis of acceptor molecules which have well defined absorption bands upon reduction which are well removed from the excited and cationic states of porphyrins and chlorophylls. They also possess large molar extinction coefficients (100,000 M^{-1} cm^{-1}) that dominate the spectra and also have well defined polarization characteristics. These traits are ideal for polarization sensitive transient grating experiments which will enable accurate determination of the angle of the transition dipole between the initial excitation and the acceptor probe, dynamic solvation effects on the charge separated species, and any time dependent rotation of the chromophores relative to each other (i.e. twisted intramolecular charge transfer states), etc.

An example of the type of molecule that we utilize for these experiments is shown in Figure 1. It consists of a free base porphyrin (HP) donor and a pyromellitic diimide (PI) acceptor directly bonded to the porphyrin ring. When PI is reduced, a large absorption band at 710 nm results. Utilizing a polarization sensitive transient grating experiment to diffract at 710 nm can give us information about the time dependent orientation of PI relative to the porphyrin by probing the anisotropy of the absorption grating. For such, an experiment to be succesful, electron transfer must occur on a time scale that is faster than the rotational diffusion of the molecule or all polarization information is lost. Here, electron transfer occurs in 16 ps in benzonitrile and the rotational diffusion time of the molecule is approximately 200 ps. Figure 2 shows the results of the transient grating experiment both with no polarization selectivity and with polarization selection for elimination of contributions from the fully charge separated species. In the latter case, the time dependent change in the anisotropy of the absorption grating is probed. The technique is also utilized to probe solvent interactions with the charge separated species. In addition to studying charge transfer compounds, results

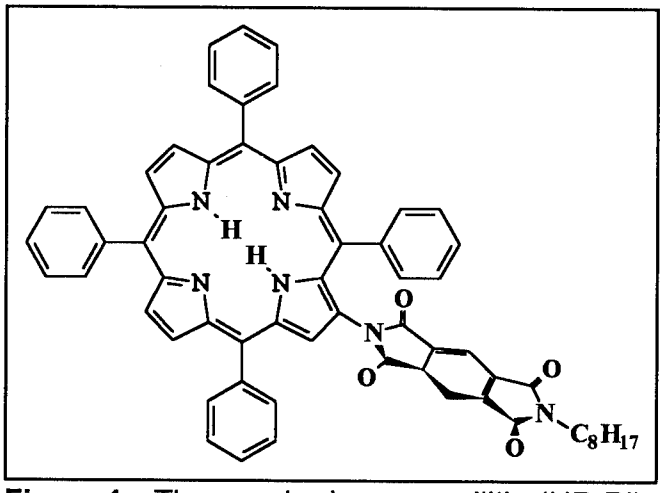


Figure 1: The porphyrin-pyromellitic (HP-PI) molecule.

from probing the excited states of chlorophyll a and bacteriochlorophyll are also presented.

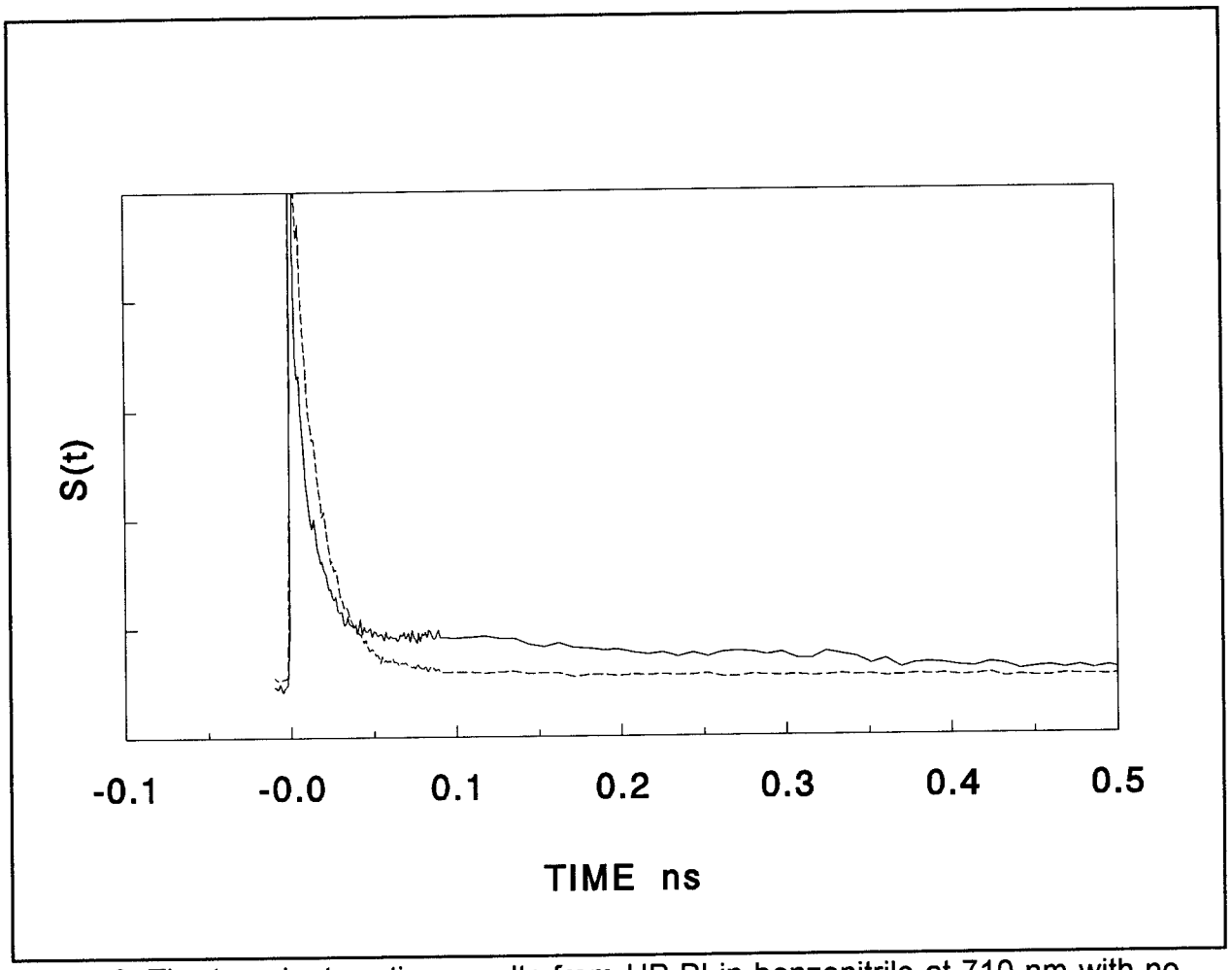


Figure 2: The transient grating results from HP-PI in benzonitrile at 710 nm with no (—) polarization selectivity and with the reduced PI species elimiinated (- - -) from the detected signal.

iV. References

1. J. Etchepare, G. Grillon, J.P. Chambaret, G. Hamoniaux, and A. Orszag, Opt. Commun. **63**, 329 (1987).
2. F.W. Deeg and M.D. Fayer, J. Chem. Phys. **91**, 2269 (1989).
3. G.P. Wiederrecht, S. Watanabe, and M.R. Wasielewski, Chem. Phys. 176, 601 (1993).

Production of programmable amplified, shaped pulses in femtosecond lasers

Dan Pinkos, Jeff Squier
Center for Ultrafast Optical Science
University of Michigan
2200 Bonisteel, Rm 1006, IST Bldg
Ann Arbor, MI 48109-2099
Phone: 313-763-4875 FAX:313-763-4876

B. Kohler, V.V. Yakovlev, K.R. Wilson
Department of Chemistry
University of California, San Diego
9500 Gilman Drive
LaJolla, Ca 92093-0339

D. Schumacher, P. Bucksbaum
Department of Physics
University of Michigan
Ann Arbor, MI 48109

A heretofore unexploited capability of femtosecond chirped pulse amplification systems is the production of shaped pulses. This can be accomplished by phase and amplitude modulation of the pulses prior to amplification by a series of strategically located liquid crystal modulators. The system is suitable for kilohertz amplifiers which produce pulses with peak powers on the order of 10 GW, or 10-Hz amplifiers which can produce TW peak powers. Such a laser source is capable of addressing a variety of challenging scientific problems in a number of fields including chemistry, atomic and plasma physics.

The first demonstration of programmable phase control of femtosecond pulses using liquid crystal arrays was by Weiner et al [1]. More recently, Wefers and Nelson demonstrated independent programmable amplitude and phase control using similar techniques [2]. We have designed two liquid crystal modulators which provide independent amplitude and phase control and can work within the diffractive stretcher system of the laser. To our knowledge, this system has enabled us to produce, for the first time, amplified, shaped femtosecond pulses with a 10-Hz amplifier.

In contrast to previous works, our modulators have been designed to work at the conjugates of a stretcher system which provides the stretched seed pulse for a TW laser. In addition, the amplitude and phase control are accomplished in a single pass at the same transform plane, whereas multiple transform planes are required in other configurations. Previous work has incorporated liquid crystal modulators which have an interpixel spacing ranging from 2-30 μm. This area is essentially a "dead" space. This dead space degrades the temporal fidelity of the pulse. We have designed unique modulators which have virtually no dead space in order to avoid this problem.

The pulse shaper incorporates all reflective optics to eliminate chromatic aberrations. The input to the pulse shaping apparatus is split, so that the output can be cross-correlated with the original pulse, and thus characterized. Figure 1 shows the experimental and calculated cross-correlation traces. An odd pulse has been created by introducing a phase delay of π radians to only half of the frequency components of the pulse. At present the model does not include diffractive effects or effects due to aberrations. Future versions will include such considerations. However, we still obtain excellent agreement for these shaped pulses.

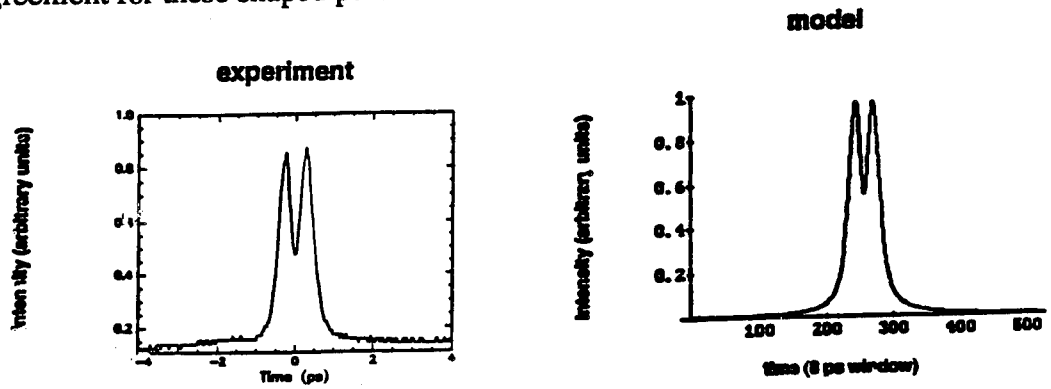


Figure 1. Experimental and modeled cross-correlations of odd pulse.

In figure 2 a square pulse has been produced. This is a demonstration of combined amplitude and phase shaping. The spectrum of the input pulse is reshaped into a sinc function using the amplitude mask. The individual lobes of the sinc function are alternatively delayed by 0 to π with the phase mask.

Finally, figure 3 shows the single shot autocorrelation trace of an amplified picket fence. More detailed characterization of these pulses is necessary using more sophisticated autocorrelation techniques which make it possible to accurately determine the amplitude and phase of not only the amplified pulse, but the seed pulse as well. Spectrally resolved autocorrelation techniques, and frequency resolved optical gates are currently being investigated for this purpose [3,4].

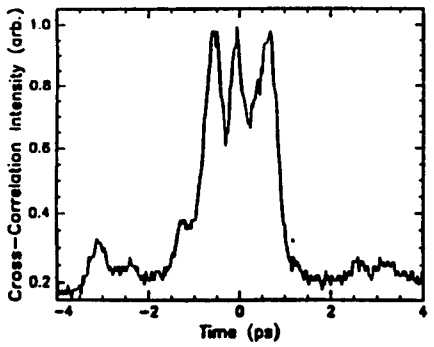


Figure 2. Measured square pulses.

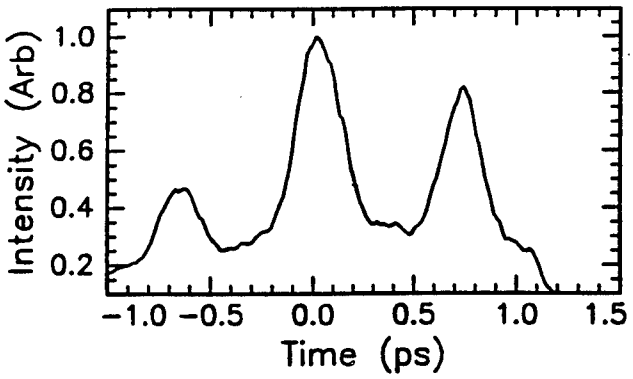


Figure 3. Single shot autocorrelation of an amplified picket fence.

In conclusion, we have demonstrated a programmable pulse shaper for use with amplified pulses. The potential applications of a programmable amplitude and phase modulator system are multi-fold. For instance, it may provide a method of higher order dispersion compensation. Amplitude reshaping effects which are a result of the amplification process may also be compensated. Used in combination, the production of clean, ultrashort pulses (<30 fs) could be made fairly routine under a variety of operating conditions. Other applications include the production of specifically tailored light fields to drive matter to a desired state or target.

This work was partially supported by the National Science Foundation through the Center for Ultrafast Optical Science under STC PHY 8920108.

References

1. A.M. Weiner, D.E.Leaird, J.S. Patel, J.R. Wullert, Opt. Lett. **15**, 326 (1990).

2. Marc M. Wefers and Keith A. Nelson, Opt. Lett. **18**, 2032 (1993).

3. J. Paye, M. Ramaswamy, J. Fujimoto, E. Ippen, Opt. Lett. **18**, 1946 (1993).

4. D.J. Kane, R. Trebino, Opt. Lett. **18**, 823 (1993); R. Trebino, D.J. Kane, J. Opt. Soc. Am. A **10**, 1101 (1993).

Picosecond Time-Resolved Vibrational Spectrum of Batho-Rhodopsin at Room Temperature: Concentration Effect

A. Popp, L. Ujj, G.H. Atkinson

Department of Chemistry, University of Arizona, Tucson AZ 85721, Tel. (602) 621-6293

Abstract

The first vibrational spectrum of batho-rhodopsin (Batho), an intermediate formed during the initial 50 ps of the visual process of rhodopsin (Rh) at room temperature, has been measured by picosecond time-resolved coherent anti-Stokes scattering (PTR/CARS). The Batho spectrum is obtained through a third-order susceptibility ($\chi^{(3)}$) analysis of the measured PTR/CARS data in which the resonant and non-resonant contributions to the signal are separated. The PTR/CARS spectrum of Batho reveals structural changes during the Rh photo-reaction which have not previously been recognized.

1. Introduction

The visual pigment Rh is responsible for the conversion of light into nerve impulses resulting in vision[1]. After excitation by a photon, a cascade of Rh photo-intermediates are formed which trigger, through G-protein coupling, a sequence of events in the rod cells of vertebrate retina. These events eventually result in nerve excitation. The sequence of the early steps following the absorption of a photon by Rh are currently under discussion[2][3][4]. It is well accepted, however, that the photo-intermediates such as Rh*(90) and/or photo-rhodopsin do not exist 200 ps after excitation and the only meta-stable intermediate Batho is present on the nanosecond time-scale.

2. Experimental and Analysis

The vibrational degrees of freedom of bovine-Rh[5] and Batho were examined by PTR/CARS. The experimental setup and analysis procedures are described in detail elsewhere[6][7]. The PTR/CARS signal (I_a) is proportional to the absolute square of the $\chi(\omega_a,\omega_1,\omega_1,-\omega_s)^{(3)}$ signal. Laser wavelengths (ω_1=568nm, ω_s=623±5nm, $\tau_1=\tau_s$=8ps) were selected to resonantly enhance only the retinal chromophore. To obtain the CARS spectrum of Rh alone, the PTR/CARS spectrum of Rh in water must be divided by the PTR/CARS spectrum of water measured under identical conditions. This removes instrumental responses. The water signal (I_a^{Water}) is proportional to the absolute square of the non-resonant susceptibility $\chi^{(3)}_{NR}$. If the sample contains two types of retinal chromophores (e.g., Rh and Batho 200 ps after Rh excitation), then the ratio of $\chi^{(3)}$ of the sample and $\chi^{(3)}_{NR}$ can be written as:

$$\left|\frac{\chi^{(3)}}{\chi^{(3)}_{NR}}\right|^2 \propto \frac{I_a}{I_a^{Water}} = \mu^2\left|1+\eta\frac{\chi^{(3)}(Rh)}{\chi^{(3)}_{NR}}+(1-\eta)e^{i\theta}\sum_{j=1}^{N}\frac{A_j}{-\delta_j-i}\right|^2,\ \delta_j=\frac{\Omega_j-(\omega_1-\omega_s)}{\Gamma_j} \qquad (1)$$

where Ω_j is the jth vibrational frequency of Batho having a bandwidth Γ_j (HWHM) and $e^{i\theta}A_j$ is the complex amplitude of the jth oscillator strength. The μ^2 term can be considered as a scaling factor and η is the concentration ratio between the two chromophores. The ratio $\chi^{(3)}(Rh)/\chi^{(3)}_{NR}$ can be derived from probe only measurements and η from picosecond transient absorption measurements under the same experimental conditions [8]. To avoid high power effects, the intensity of the excitation beam at 568 nm was chosen so that < 0.25 of the rhodopsin molecules in the sample volume are excited. The intensities of the probe beams are an order of magnitude smaller than the excitation beam to minimize photophysical perturbations.

3. Results and Discussion

The PTR/CARS spectra in the C=C stretching region of Rh at different concentrations is presented in Fig. 1. All spectra are fitted with the same parameters shown in Table 1, columns 4 and 5 (only the concentration of Rh was changed). The wavenumber displacements measured for the major PTR/CARS band origins as well as bandwidths and phase factor obtained from the $\chi^{(3)}$ fits to these spectra, and the positions of the intensity maxima of the corresponding resonance Raman (RR) bands appearing in this region, are presented in Table 1.

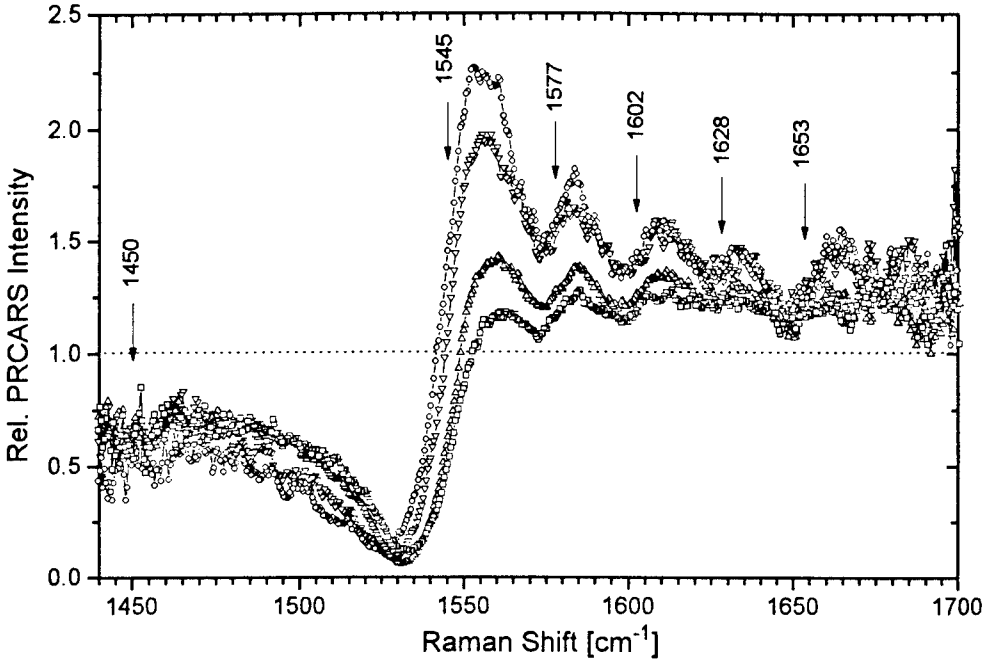


Fig. 1: PTR/CARS spectra of Rh at different concentrations from 1440 cm^{-1} - 1700 cm^{-1}. The positions of the bands are marked by arrows. The concentration of Rh in the sample decreases from OD_{498}= 3.2 to 0.9 from the upper to the lower trace.

Tab. 1: Band origin positions (Ω) and bandwidths (Γ) obtained by fitting the C=C stretch region of the PTR/CARS spectra of Rh at room temperature (Fig. 1) to a $\chi^{(3)}$ relationship given in Equ. 1. The phase factor (θ) in Equ. 1 is 0.5. Intensity maxima positions measured by RR spectroscopy as well as probing wavelengths also are presented to facilitate comparisons.

Resonance Raman (RR)			PTR/CARS	
600nm [9]	590nm [10]	488nm [11]	568nm/623nm	
Bandmaxima [cm^{-1}]			Ω [cm^{-1}]	Γ [cm^{-1}]
1450	1440	1435	(1450)	(24)
1545	1545	1546	1545	14
1580	1595	1580	1577	7
1605		1607	1602	8
-	1633	1635	1628	6
1660	1655	1658	1653	7

The PTR/CARS data from Rh are in good agreement with the previous published RR data[9]-[11]. Differences between the RR and PTR/CARS data might be due to different experimental conditions or congested Raman spectra. The 1450 cm^{-1} band in the PTR/CARS data is on the edge of the measured spectral region where data are noisy, but this band must be introduced to obtain a reasonable $\chi^{(3)}$ fit.

In Fig. 2 the PTR/CARS spectrum in the C=C stretching region of a mixture of Batho and Rh recorded 200 ps after excitation is presented. To accurately fit these PTR/CARS data, the relative contribution from Rh (i.e., probe only PTR/CARS data) must be quantitatively known. The result

from three different Rh contributions are presented in Fig. 2.

A quantitative $\chi^{(3)}$ analysis of PTR/CARS data from the Rh/Batho mixture (using Equ. 1) shows that major changes occur in both the C=C stretching region near 1542 cm^{-1} and in the Schiff'base region near 1651 cm^{-1}. By comparing the results presented in Figs. 1 and 2, it is evident that these spectral changes are not related to Rh concentration differences.

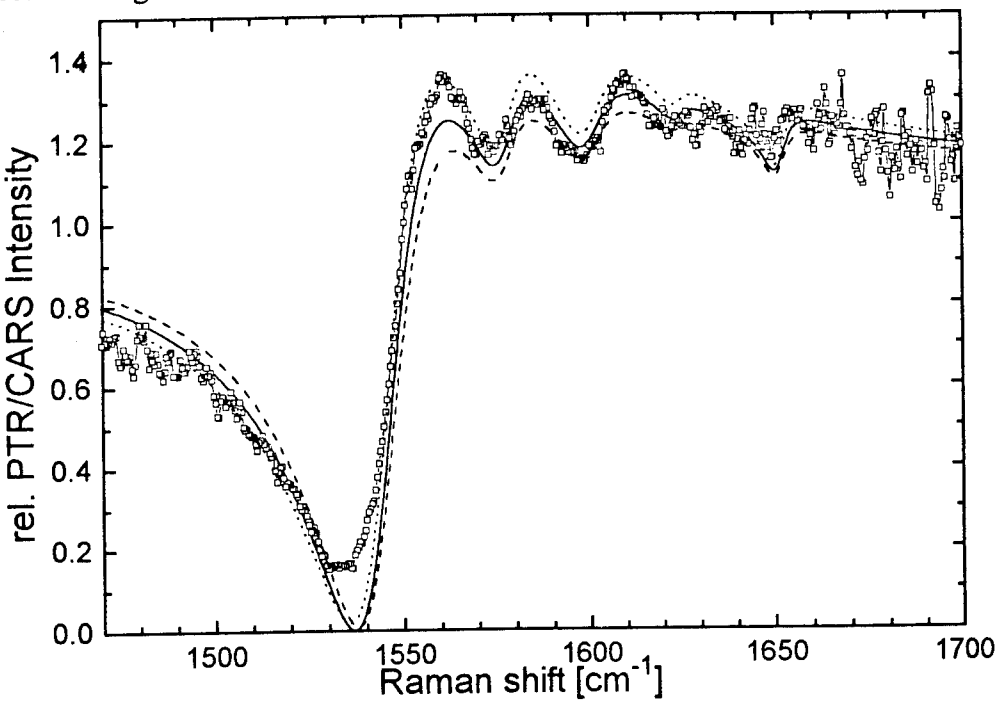


Fig. 2: PTR/CARS spectrum of excited Rhodopsin after 200 ps from 1480 cm^{-1} - 1700 cm^{-1} (□). Rh spectra for different excitation levels (η = 0.9 ···, η = 0.8 —, η = 0.7 ---) are shown to illustrate the spectral contribution of Batho.

This first time-resolved vibrational spectrum of Batho at room temperature shows the same major structure as that found in previously published RR-spectra of Batho at low temperature (≤ 120 K) [10][12][13]. Nevertheless, significant differences can be observed, i.e. the Schiff'base vibration frequency at room temperature is significant lower than at low temperature and the C=C stretch vibration of Batho at ambient temperature is only decreased by 3 cm^{-1} compared to Rh instead of 9 cm^{-1} observed in the low temperature measurements. These differences underline the importance of room temperature measurements of the vibrational degrees of freedom of the early rhodopsin photointermediates to elucidate the molecular processes of vision.

4. References

1. (a) R. Birge *Annu.Rev.Phys.Chem.*(1990) **41** 683-733. (b) P. Hargrave *Curr.Opin.Struct.Biol.*(1991) **1** 575-581.
2. Y. Shichida *Photochem. Photobiol.* (1990) **52** 1179-1185.
3. R.W. Schoenlein, L.A. Peteanu, R.A. Mathies, C.V. Shank *Science* (1991) **254** 412-415.
4. M. Yan, D. Manor, G. Weng, H. Cao, L. Rothberg, T.M. Jedju, R.R. Alfano, R.H. Callender *Proc. Natl. Acad. Sci. USA* (1991) **88** 9809-9812.
5. J.S. Horwitz, J.W. Lewis, M.A. Powers, D.S. Kliger *Photochem. Photobiol.* (1983) **34** 375-384.
6. L. Ujj, B.L. Volodin, A. Popp, J.K. Delaney, G.H. Atkinson *Chem. Phys.* (1994) accepted.
7. L. Ujj, A. Popp, G.H. Atkinson *Chem. Phys.* (1994) submitted.
8. G.H. Atkinson, T.L. Brack, D. Blanchard, G. Rumbles *Chem. Phys.* (1989) **131** 1-15.
9. R. Mathies, A.R. Oseroff, L. Stryer *Proc. Natl. Acad. Sci. USA* (1976) **73** 1-5.
10. M.A. Marcus, A. Lewis *Photochem. Photobiol.* (1979) **29** 699-702.
11. I. Palings, J.A. Pardoen, E. van den Berg, C. Winkel, J. Lugtenburg, R. Mathies Biochemistry (1987) **26** 2544-2556.
12. H. Deng, R.C. Callender *Biochemistry* (1987) **26** 7418-7426.
13. G. Eyring, R. Mathies *Proc. Natl. Acad. Sci. USA* (1979) **76** 33-37.

Distinguishing between Energy and Electron Transfer Processes in Photosystem Two Reaction Centres.

David R. Klug‡, Thomas Rech‡, D. Melissa Joseph§‡, James R. Durrant§‡ , Robert S. Knox§‡†, James Barber§ and George Porter‡.

‡Molecular Dynamics and §AFRC Photosynthesis Research Groups, Centre for Photomolecular Sciences, Department of Biochemistry, Imperial College, SW7 2AY, U.K, and †Department of Physics and Astronomy, University of Rochester, NY 14227-0171, U.S.A..

The photosystem two (PS2) reaction centre (RC) undertakes both electron and energy transfer processes as part of its function. Distinguishing between these two processes is an essential pre-requisite for meaningful studies of the primary photochemistry of this complex. In the reaction centre (RC) of purple bacteria, the energy transfer processes are relatively simple, and result in the unidirectional transfer of excitation energy to the special pair in approx. 100fs. In contrast, in the PS2 RC of higher plants, extensive forward and backward energy transfer is expected due to the relatively small energy separation between the S1 states of the RC chlorins.

We have previously reported the observation of a 100fs equilibration of excitation energy between P680, the primary electron donor, and some accessory chlorins in isolated PS2 RC's [1]. In addition there have been several reports of much slower energy transfer processes in PS2 RC's with lifetimes of 10 -100 ps [2-5]. Uncertainty regarding how these slower energy transfer processes affect the observed lifetime of charge separation has complicated the current controversy over whether the charge separation occurs in 3 ps or 21 ps [1-7].

The results reported here employ photoselective excitation of either P680 or the accessory chlorins (694 nm or 665 nm excitation respectvely) in order to identify energy transfer processes between these pigments. In addition we employ a home built multi-channel diode array detector (MCD) of great sensitivity and dynamic range. The MCD comprises the following. The output from two linear 128 element diode arrays is digitised to 14 bit precision at a total frequency of 1.6MHz to give a frame rate of 6.5kHz for each array. One array detects the intensity of the probe beam while the other records intensity fluctuations via a reference arm of the spectrometer. The outputs are averaged and preprocessed in a home built controller/digital signal processor along with the output from a single diode which detects intensity fluctuations in the excitation beam, before being output to a PC. The dynamic range of the multichannel detector is 10^7 at 1Hz bandwidth when used in conjunction with our 6.5kHz laser system. Multichannel data were globally analysed simultaneously at 128 wavelengths using a marquardt least squares algorithm.

Analyses of data collected over a wide range of probe wavelengths between 450 nm and 860 nm have determined that, following photoselective excitation of P680, formation $P680^+Ph^-$ in PS2 RC's proceeds primarily with a 21±1 ps lifetime (6,7). Following photoselective exciation of the accessory chlorins, the observed lifetime of radical pair formation increases to 27±3 ps. Figure 1 compares spectra of the amplitude of these 21 ps and 27 ps components between 640nm and 730nm. The positive maxima at 680nm in both spectra

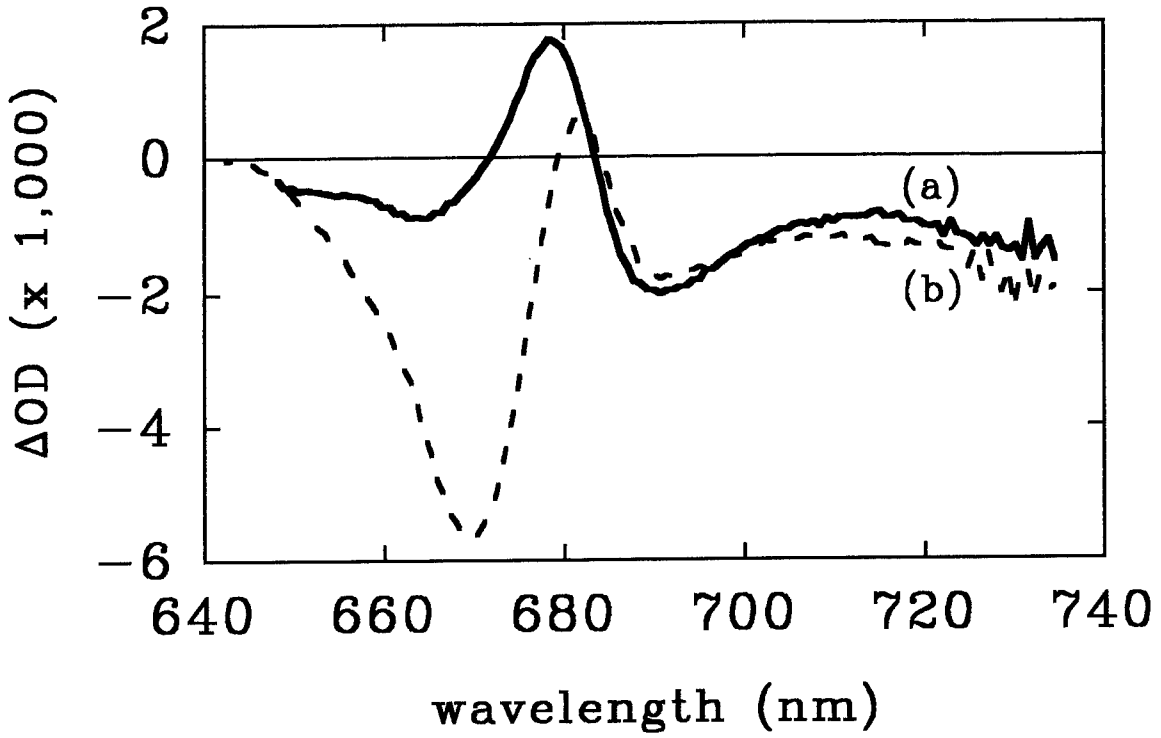


Figure 1. Spectra of the amplitudes of (a) (solid line) a 21±1 ps component observed using photoselective excitation of P680, and (b) (dashed line) a 27±3 ps component observed using photoselective excitation of 670nm absorbing chlorins. Isolated PS2 RC's were studied at 295K as previously [6].

are assigned to bleaching of the pheophytin Q_y-absorption band due to charge separation, while the negative features circa 670nm and to the red of 682nm are attributed primarily to loss of stimulated emission and/or appearance of radical pair absorption. The difference between these spectra circa 670 nm indicates that the 27 ps component is accompanied by a much greater loss of population from the 670 nm absorbing chlorophylls than the 21 ps component. This observation, and the observed difference in the lifetime of radical pair formation, can only rationalised if, in addititon to the sub-picosecond energy transfer processes reported previously [1], there is at least one other chlorin which transfers excitation energy to P680 much more slowly.

A kinetic model which is consistent with these observations is shown in figure 2. The model includes four states: the excited singlet state of P680, the radical pair $P680^+Ph^-$ and singlet excited states of two pools of accessory chlorins $C670_I$ and $C670_{II}$. Excitation energy is rapidly transfered between P680 and the $C670_I$ chlorin pool. However, energy transfer from the $C670_{II}$ chlorin pool to P680 is relatively slow, which prevents equilibration of excitation energy between these pigments prior to RP formation, and results in a slower rate of RP formation. Photoselective excitation of the C670 pigments will excite both the $C670_I$ and $C670_{II}$ chlorin pools, and will therefore result in a slower <u>average</u> time constant of RP formation than that which is observed when P680 is directly excited. This kinetic model is the simplest one which can take account of the observations reported here. It should however not be considered a complete kinetic model for the primary photochemistry of

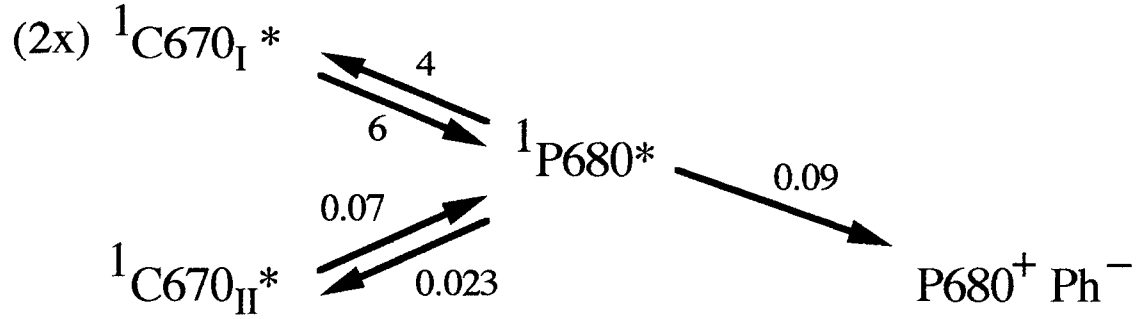


Figure 3. Kinetic model of isolated PS2 RC's including energy transfer between two pools of 670 nm absorbing chlorins (C670) and P680, and charge separation. The numbers refer to the rates (in ps^{-1}) of the respective energy and electron transfer processes.

isolated PS2 RC's, as we know that other processes occur in this complex with lifetimes of 1 -3 ps [2-7], which are not included in this model.

The results presented here are in agreement with those of many other groups that some energy transfer processes are observed with lifetimes of 15 - 30 ps between some accessory pigments and P680 in PS2 RC's [2-5]. These slow energy transfer processes are effectively avoided by photoselective excitation of P680 as reverse energy transfer is slower than the forward electron transfer. However, our results crucially differ from those of other groups as we find that following photoselective excitation of P680, a 21 ps transient absorption component is still observed which is strongly associated with radical pair formation. Thus both slow energy transfer processes, and charge separation not limited by these slow energy transfer processes, can be observed in PS2 RC with similar but distinguishable lifetimes. Distinguishing between these energy and electron transfer processes has been achieved by a combination of photoselective exciation of different pigments, collection of detailed and precise spectral data using the MCD, and collection of data over a wide range of probe wavelengths. We conclude that if P680 is photoselected in PS2 RC's, formation of $P680^+Ph^-$ is observed with a 21 ps lifetime, apparently not limited by any slow energy transfer steps.

References.

1) Durrant, J. R., Hastings, Joseph, D.M., Barber, J., Porter, G., and Klug, D. R. (1992) *Proc. Natl. Acad. Sci. USA 89*, 11632-11636.
2) Wasielewski, M. R., Johnson, D. G., Govindjee, Preston, C. and Seibert, M. (1989) *Photosynth. Res. 22*, 89-99.
3) Tang, D., Jankowiak, R., Seibert, M., Yocum, C.F. and Small, G.J. (1990) *J. Phys. Chem. 94*, 6519-6522.
4) Roeloffs, T. A., Kwa, S.L.S., van Grondelle, R., Dekker, J.P. and Holzwarth, A. R. (1993) *Biochim. Biophys. Acta 1143*, 147-157.
5) Schelvis, J.P.M., van Noort, P.I., Aartsma, T.J. and van Gorkom, H.J. (1994) *Biochim. Biophys. Acta* , in press.
6) Durrant, J. R., Hastings, G., Hong, Q., Barber, J., Porter, G., and Klug, D. R (1993) *Biochemistry 32*, 8259-8267.
7) Hastings, G., Durrant, J. R., Hong, Q., Barber, J., Porter, G., and Klug, D. R. (1992) *Biochemistry 31*, 7638-7647.

Paper Withdrawn

All Solid State Laser System for the Generation of Tunable Femtosecond Pulses down to 175 nm

F. Seifert, J.Ringling, F. Noack, V. Petrov, and O. Kittelmann

Max-Born-Institut für Nichtlineare Optik und Kurzzeitspektroskopie
Rudower Chaussee 6
D-12474 Berlin
Germany

Phone: +49-30-63921272

Ultrashort optical pulses tunable in the vacuum ultraviolet (VUV) spectral region are of great interest for spectroscopic investigations of various ultrafast processes, e.g. photodissociation of molecules and clusters. We report on the generation of femtosecond pulses in the wavelength range from 175 to 182 nm by phase matched sum frequency mixing of femtosecond ultraviolet and near infrared optical pulses in lithium triborate (LBO). Due to its superior transparency range down to 160 nm and its high nonlinear coefficients only this crystal can be used for nonlinear conversion processes in the wavelength range below 189 nm. Unfortunately phase matching is possible only for two widely separated wavelength, e.g. $\lambda_{UV} < 205$ nm and $\lambda_{IR} > 1.7\mu m$ to obtain a wavelength at 185 nm or below (Ref.1). To ensure the synchronism both the ultraviolet (UV) and infrared (IR) pulses have to be derived from a single ultrashort pulse source. Up to now the shortest wavelength generated by sum frequency mixing in nonlinear crystals was 187.7 nm using nanosecond pulses (Ref.2).

We employed a commercial femtosecond Ti:Sapphire regenerative amplifier system operating at 1kHz repetition rate (Spectra-Physics "Tsunami", Quantronix 4810/20 RGA). The experimental setup is shown in Fig.1. The amplified pulses of the Ti:Sapphire laser (150 fs, 300 μJ) are split into two equal parts to pump an optical parametric generator/amplifier and to generate the fourth harmonic, respectively. The latter is performed by subsequent sum frequency mixing in three ß-barium borate (BBO) crystals. This method has been demonstrated to be suitable for the generation of tunable femtosecond optical pulses down to 189 nm at microjoule levels (Ref.3). We measured a pulse duration of 170fs of the fourth harmonic by a cross correlation technique. The bandwidth of 0.4 nm indicates nearly Fourier limited pulses.

Sub-100fs infrared pulses are provided by an optical parametric generator/amplifier scheme. A 5 mm long LBO crystal (z-cut, noncritical type II phase matching) is employed to generate spectrally clean seed pulses for further parametric amplification. At room temperature and a pump wavelength of 805 nm we observed a signal wavelength of 1465 nm corresponding to idler pulses at 1800 nm. The amplification of the signal in a 4 mm long BBO crystal (cut at $\theta=20°$, type I phase matching) leads to nearly bandwidth limited 50fs signal pulses of about 1μJ energy and sub-100 fs idler pulses at the same energy level (Ref.4). The polarization directions of both signal and idler pulses are parallel to the generated 4th harmonic of the Ti:sapphire laser which is important

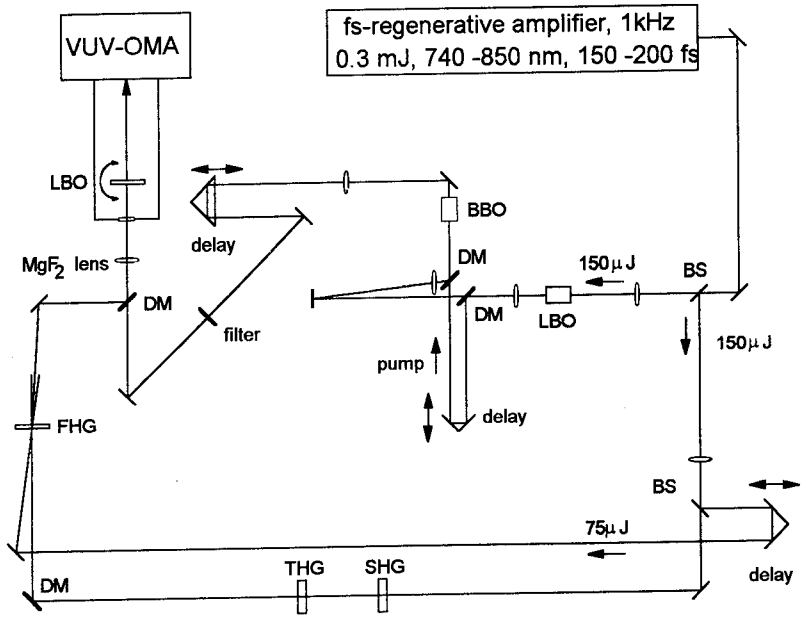


Fig.1:
Experimental setup
BS - beam splitter
DM - dichroic mirror

for the final sum frequency mixing in LBO (angle tuned type I phase matching, θ=90°, φ=73°). We combined the IR-beam and the fourth harmonic at a dichroic mirror and focused them (by a f=15cm MgF_2 lens) into a 1mm long LBO crystal properly housed in a vacuum chamber to avoid the strong absorption of the VUV beam by air. Tuning the Ti:Sapphire system from 777 nm to 810 nm we achieved angle tuned (φ=70° ...≈90°) phase matched sum frequency mixing of the fourth harmonic (194.2 nm - 202.4 nm) and the idler pulse at ≈1800 nm as calculated from the dispersion data of LBO (Ref.2). The corresponding spectra of the VUV pulses tunable from 175.5 nm to 182.2 nm are shown in Fig.2. We determined the spectral width of the sum frequency signal in the second diffraction order of the spectrometer to be 0.4 nm at 182.2 nm which corresponds to a pulse duration of 130 fs assuming a time-bandwidth product of 0.5. From a detailed analysis of the nonlinear conversion process taking into account the different group velocities of the three interacting pulses we estimated the pulse width of the VUV signal to be <200 fs.

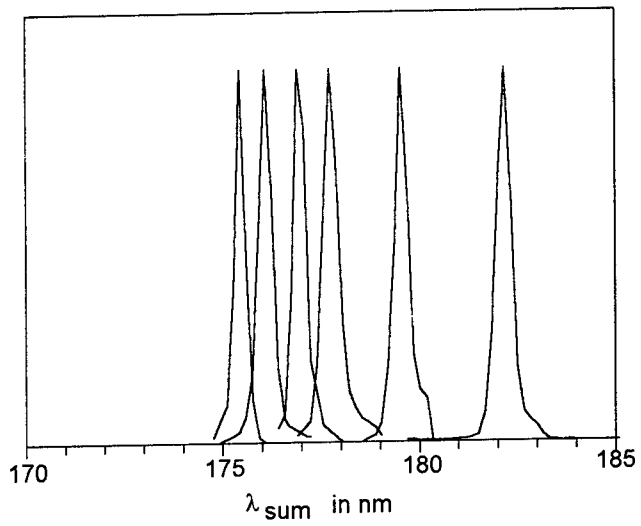


Fig.2:
Normalized spectra of the generated femtosecond VUV pulses tunable from 175.5 to 182.2 nm

Although the Ti:Sapphire system might be tuned to 850 nm (corresponding to VUV mixing wavelength of about 190 nm) the tuning range was limited to 183 nm at the long wavelength side because of the reflective properties of the last dichroic mirror (in fact a mirror for an ArF-excimer laser centered at 193 nm). The short wavelength edge of the tuning range was determined by the phase matching properties of LBO. At an IR wavelength of 1800 nm we calculated the shortest possible VUV wavelength to be 174 nm. Tuning the optical parametric generator to 1900 nm which can be done by heating the LBO seeder to about 180°C at 760 nm pump wavelength one expects phase matching down to 172.5 nm. Since the efficiency of the fourth harmonic generation drops down below 190 nm a further decrease of the sum frequency wavelength is not realistic. Thus our scheme allows a possible tuning range of 172.5 nm - 190 nm overlapping with the lower end of the fourth harmonic tuning range.

In summary we reported the effective generation of up to now the shortest wavelength by means of sum frequency mixing in LBO. The experiments have shown the possibility of femtosecond pulse generation in the VUV (175.5 nm - 182.2 nm) using only solid state materials for both the laser system and the nonlinear optical media.

References:

1. A. Borsutzky, R. Brünger, and R. Wallenstein, Appl. Phys B 52 (1991) 380
2. B. Wu, F. Xie, and Ch. Chen, Opt. Comm. 88 (1992) 451
3. J.Ringling, O.Kittelmann, F.Noack, G.Korn, and J.Squier, Opt. Lett. 18 (1993) 2053
4. F.Seifert, V.Petrov, and F. Noack, submitted to Appl. Phys. Lett.

COHERENT EVOLUTION FOLLOWING PHOTOLYSIS OF $Mn_2(CO)_{10}$

Amir Waldman & Sanford Ruhman
the Department of Physical Chemistry, and the Farkas center for light-induced processes, the Hebrew University Jerusalem 91904, Israel, Tel; 972-2-585-326

In this letter we report a study of $Mn_2(CO)_{10}$ photodissociation using photoselective transient transmission on a 100 fsec timescale. Absorption in the UV is known to induce both metal-metal bond fission, as well as decarbonylation, leading to $Mn(CO)_5$ and $Mn_2(CO)_9$ as primary photoproducts[1]. The overall quantum efficiency for decomposition is ~0.4, three quarters of which involves the metallic bond breaking. Flash photolysis studies have associated the $Mn(CO)_5$ and $Mn_2(CO)_9$ with transient absorption bands centered at 800 and 500 nm respectively[2]. The former has been studied extensively through ultrafast spectroscopy. Rapid initial features in the near IR spectral region have been associated either with metallic bond cleavage through a metastable excited state, or to recombination following an ultrafast initial dissociation[3,4].

In this study we concentrate our attention on probe frequencies within the band associated with the $Mn_2(CO)_9$ fragment, and in the UV. Figure 1 depicts transient transmission scans at three wavelengths, following photolysis at t=0 with a 60 fsec pulse at 308 nm. The scans have been normalized to a common height, and offset in order to facilitate observation. Immediately following the pump interaction absorption is manifest throughout the tested spectral region. For the initial ~ 300 fsec of delay a rapid red shifting in the visible absorption band is observed as a continued rise in the absorption at 520 nm, and a rapid fall off in absorption at 460 nm. Following this red shift, optical density falls off at both visible probing frequencies, giving way to a slower decay which is superimposed with two observable undulations, which show up at identical delays both at 520 and 460 nm.

The UV probing is conducted at precisely the same wavelength as the pumping. The scan at this wavelength shows that instead of inducing a bleach, the pump increases the optical density, indicating that both the excited state absorption of the parent, and absorption of the products is higher, at this wavelength, than the ground state absorbance of $Mn_2(CO)_{10}$. The UV scan exhibits a strong increase of absorption concomitant with the red shift in the visible band, and later, a decay with similar modulations showing up at virtually identical times with those observed in the visible.

In order to understand the underlying dynamics, transmission scans were conducted both with parallel and perpendicular relative polarizations of the pump and probe. From these experiments an anisotropy of the differential transmission r(t) is calculated. The anisotropy for the measurements at 460 nm in ethanol solution evolves in three phases, as shown in figure 2. The initial spans 0.5 psec of delay, overlapping the stage of red shifting, and during this stage the value of r(t) actually rises. Further decay of anisotropy takes place in a biexponential fashion, with an initial decay time of 0.6 psec, giving way at ~2.5 psec to an exponential decay with a 7.5 psec characteristic timescale.

Solvent effects on the observed trends were looked for by conducting these experiments in a series of molecular solvents, such as isobutanol, ethanol and hexane. Figure 3 depicts transmission scans at 460 nm for all three solvents. The scans are virtually superposable, indicating

that none of the processes giving rise to the modulations of transmission during the first few picoseconds of delay are solvent induced, including the late undulations of transmission which show up at all probe frequencies. At later delays the absorption at both visible frequencies relaxes to an asymptotic level at a delay of 3-5 psec. Their decay at longer times is not strictly identical, but no drastic or rapid changes take place following 5 psec as shown in figure 4.

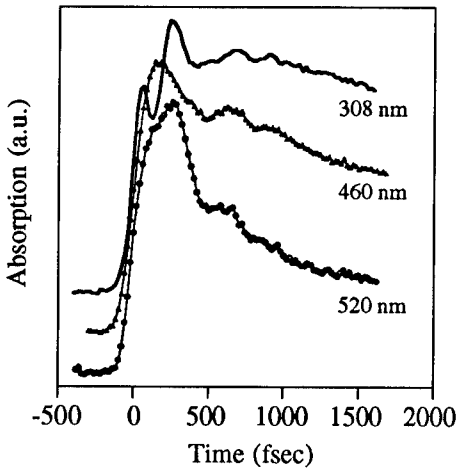


Fig 1: Transient transmission scans in ethanol.

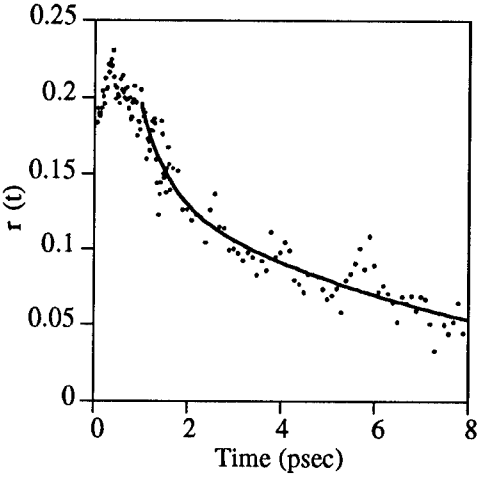


Fig 2: Absorption anisotropy at 460 nm.

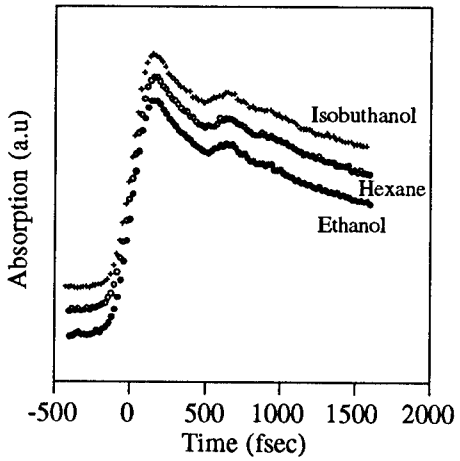


Fig 3: Transmission scans in different solvents, probed at 460 nm.

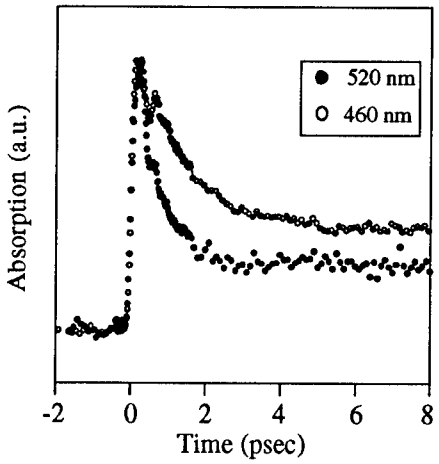


Fig 4: Transient transmission at longer time delays.

Our interpretation focuses on the process of decarbonylation, since none of the modulations observed here show up in the near IR region. We rationalize our observation by concentrating attention on one excited metal center, considering the other $Mn(CO)_5$ subgroup to be a ligand with σ and π donating nature[1]. UV excitation in the σ–σ^* band, initially effects the metal-metal binding, but later the locally excited state, focussing on either of the metal centers, is populated through curve crossing. The rapid red shift is interpreted to represent the stage of CO bond

fission, but must of course include the electronic relaxation to the locally excited state. This interpretation is in accord with the anisotropy measurements, which indicate that a rapid change in the electronic state of the system is taking place.

The shifting to the red is also consistent with the limited *d* orbital scheme. In the pentacarbonyl center degeneracy between the xz yz and xy orbitals is removed, with a stabilization of the xy orbital. Similarly the e_g orbitals are also split to lower the z^2 orbital. Thus the locally excited state involves excitation of an electron from the xz/yz orbitals into the empty z^2 orbital. This selectively labializes the axial CO, due to its σ acceptor nature. The scission of the metal carbonyl bond however, leaves the limited *d* system intact in an excited state. The departure of the CO will however lower the energy of the *d* (z^2) orbital, yet increase that of the almost full xz/yz system, from which the carbonyl no longer accepts electron density. Therefore further excitation will involve a lower transition energy and red shift the excited state absorption of the decarbonylated species.

The later modulations in O.D. are probably due to Berry pseudorotation and motion of a carbonyl from the intact metal center into a bridging position[5], which should involve coherent nuclear motion along the metal metal coordinate. All this takes place while the $Mn_2(CO)_9$ product is excited electronically. This should be followed by a stage of internal conversion, which could have impact both on the absorption, and on the value of absorption anisotropy, which is electronic state dependent. Accordingly, we attribute the rapid phase of anisotropy decay, and the solvent independent reduction of absorbance in the $Mn_2(CO)_9$ band, to relaxation of this fragment to its ground state. Intramolecular mechanisms for the evolution in transmission have been selected all the way to this point in view of the total absence in solvent dependence for the first 2 psec of spectral change. The later anisotropy decay of the transient transmission at 460 nm must be attributed finally to reorientation in the solvent. This point has not yet been verified by measuring the anisotropy in solvents other than ethanol.

In conclusion we have monitored the process of $Mn_2(CO)_{10}$ photolysis with UV photons through transient transmission in the 500 nm product band. The evolution of absorbance and its anisotropy lead us to believe we are observing the emergence of $Mn_2(CO)_9$ through the loss of CO, followed by coherent nuclear motion leading to carbonyl bridging between the metal atoms. Later solvent independent relaxations are related to internal conversion of the nanocarbonylic fragment. We wish to draw attention to the possibility of electronically excited fragments in other metal carbonyl photolysis reactions.

---

[1] T. J. Meyer and J. V. Caspar, *Chem. Rev.*, **85**, 187 (1985).

[2] L. J. Rothberg, N. J. Cooper, K. S. Peters, and V. Vaida, *J. Am. Chem. Soc.*, **104**, 3536 (1982).

[3] a) A. G. Joly, and K. A. Nelson, *Chem. Phys.*, **152**, 69 (1991). b) A. G. Joly, and K. A. Nelson, in *Advances in Laser Science*, **IV** (AIP New York) 333.

[4] a) J. Z. Zhang, and C. B. Harris, *J. Chem. Phys.*, **95**, 4024 (1991). b) B.J. Schwartz, J.C. King, J. Z. Zhang, and C. B. Harris, *Chen. Phys. Lett.*, **203**, 503 (1993).

[5] C. Daniel and A. Veillard, *Nouv. J. Chim.*, **10**, 83 (1986).

Local Order and Ultrafast Molecular Dynamics of Liquids: Subpicosecond Transient Grating Optical Kerr Effect Experiments.

Abhijit Sengupta and M. D. Fayer
Department of Chemistry, Stanford University, Stanford, CA 94305.
Tel. (415)723-4446

Advances in theoretical and experimental methods are making possible in depth studies of the structure and dynamics of disordered condensed systems. The very concept of order and disorder is no longer an absolute one rather as the time domain and scattering measurements suggest it depends on the distance and time scale of an observation. In this paper, we explore the extent of local order, the time scale of its persistence, and its influences on molecular dynamics in several systems in their isotropic liquid phase. The results of subpicosecond transient grating optical Kerr effect (TG-OKE)[1] are presented.

Anisotropic interactions in liquids create short range local orientation correlation. Local structures have been observed recently in CCl_4 [2], benzene[3,4] and naphthalene[3] in the liquid phase using neutron scattering and Raman measurements. The TG-OKE results give insight to the influence of local structure on ultrafast dynamics of liquids. Local orientational relaxation does not necessarily couple to the low frequency hydrodynamic modes and does not obey the Debye Stokes Einstein (DSE) equation[5]. The subpicosecond pulses excite the librational modes in liquids through stimulated Raman scattering. In a crystal, stimulated Raman scattering excites optical phonons. Because of the well defined lattice structure, damping of the optical phonons returns the molecules to their original positions, leaving no residual anisotropy. In a liquid, damping of the optically excited librations can result in orientational displacements from the initial configurations. This leaves a longer lived residual anisotropy that will decay by some form of orientational relaxation. The orientational relaxation becomes nonhydrodynamic if the local liquid structure is preserved during the relaxation.

Post librational dynamics in neat 2-ethylnaphthalene (2EN) shows a triexponential decay of residual anisotropy. The slowest dynamics are composed of a biexponential decay that obeys the DSE equation (hydrodynamic rotational diffusion like many small molecule simple liquids). However, there is an additional fast relaxation ($\tau_f = 3.5$ps) process that displays no temperature dependence over a temperature range of 2° to 40°C. This behavior is described in terms of relaxation of local structures in the liquid rather than orientational diffusion. Dilution of 2EN in carbon tetrachloride eliminates the local structures in the liquid, and a hydrodynamic biexponential decay is observed at all but the highest (5M) concentration. (Neat 2EN is 6.35M.) We propose that τ_f is the time for local structure relaxation. In liquid naphthalene (as in benzene), pairs of molecules are known to form a somewhat crooked "T" shaped structure[3]. It is reasonable to assume that 2EN forms similar structures. Dilute 2EN in CCl_4 will not have these structures, and τ_f is not observed in the dilution experiments.

Study of phase transitions gives a different perspective for understanding the physics of more complex long range order in terms of the correlation between the spontaneous fluctuations of the system. Critical phenomena in many different systems are associated with a complex temperature dependent long range order. One such thermodynamic criticality occurs near the nematic isotropic phase transition of liquid crystals. The nematic-isotropic phase transition is a

very interesting phenomenon where criticality is superimposed on a weak first order transition. The characteristic order parameter of this critical transition is a measure of orientational correlation. Many pretransitional phenomena in liquid crystals have their origins in this local orientational order. Fast timescale orientational dynamics of the liquid crystals 5-cyanobiphenyl (5CB) and N-(methoxybenzylidene)butylaniline (MBBA) in their isotropic phases will be discussed. The dynamics of the orientationally correlated domain and intradomain molecular dynamics are studied using the TG-OKE technique. The slow dynamics (>1 ns) in the isotropic phase of liquid crystals is associated with the domain randomization. The dynamics are determined by a critical length ξ and follow Landau deGennes (LdG) theory close to the phase transition[6]. When ξ falls below $3\xi_0$ ($\xi_0 \equiv$ a characteristic molecular length), both 5CB and MBBA begin to make a transition from an ordered liquid to a simple liquid, and deviation from LdG theory are observed. The intradomain orientational dynamics occur over a wide range of times from psec to nsec. Although the bulk sheer viscosity changes considerably over the wide temperature range of the experiments, the signal decay is independent of temperature. The dynamics within the domains do not change because the dynamics are controlled by the local domain structures. The time dependence of the intradomain dynamics in both MBBA and 5CB is a power law decay with an identical power law exponent of 0.63. These identical features of the two systems suggest a universality of the fast time scale dynamical behavior in the isotropic phase of liquid crystals.

Local structure can also emerge near the point of dynamic criticality. In glass forming liquids, a dynamic critical transition occurs at T_c ($T_c > T_g$) and the density correlations at short time spontaneously arrest below T_c.[7] Thus local structure causes a bifurcation of the relaxation processes below T_c. The side group dynamics in polymer glass forming liquids contribute to the fast temperature independent β relaxation. The side group dynamics in two very different polymers poly(2-vinylnaphthalene) (P2VN) and poly(methylphenylsiloxane) (PMPS) are studied. The TG-OKE experiments are able to observe solely the side group dynamics in P2VN and PMPS. The side group dynamics of P2VN and PMPS in solution indicates that the short range order, existing at the fast time scales, is created by the restricted geometry of the backbones in polymer. P2VN (T_g=424 K) has a nonpolar backbone and is not very flexible primarily due to steric interactions between the adjacent bulky naphthyl groups. On the other hand, PMPS (T_g=228 K) is a very flexible polymer with polar siloxane backbone.

Solid P2VN undergoes a single 140 fsec exponential decay. This is attributed to the librational damping. In solution, P2VN exhibits a psec time scale biexponential orientational decay ($\tau_1 = 0.95$ps and $\tau_2 = 9.5$ps) in addition to the ultrafast librational damping. A particularly interesting observation is that the orientational relaxation of P2VN in CCl_4 does not show a temperature dependence between -3°C and 55°C, even though the viscosity of CCl_4 and the sheer viscosity of the bulk polymer solution changes considerably over this temperature range. This is in contrast to 2-ethylnaphthalene in CCl_4 which displays a normal (hydrodynamic) temperature dependence.

In the solid, the observation of a single 140 fsec decay with no residual long lived anisotropy suggests that the conformations of the naphthyl side groups are rigidly defined and little or no conformational freedom exists. The lack of temperature dependence for the longer lived decays in solution demonstrates that the dynamics are dominated by local structural environments rather than bulk properties of the solution.

The TG-OKE experiments on PMPS were conducted over a broad temperature range,

25 °C to 143 °C. Over this broad temperature range, the ratio of the viscosity to the temperature, η/T, changes by a factor of 40. However, the orientational dynamics of the phenyl side groups are independent of temperature throughout the entire temperature range. Experimental results on poly(dimethylsiloxane) (PDMS) are also presented. Comparison of the PMPS and PDMS data demonstrate that the observed temperature independent orientational dynamics of PMPS arise from motions of the phenyl side groups. Comparison to the TG-OKE results on PMPS in solution show that interchain interactions in the melt influence the phenyl side group dynamics. The viscosity data of PMPS melt obey a Vogel-Fulcher-Tammann (VFT) equation. The observed VFT temperature dependence of the viscosity is a characteristic feature of small molecule liquids in the regime where the relaxation processes are bifurcated into α and β relaxations. In the PMPS melts, following the ultrafast librational dynamics, we observe an exponential decay (τ = 1.95 ps) at short time that merges (~10 ps) into a power law decay. In solution there is also a fast exponential (τ=~0.7 ps) that merges into a power law by 5 ps. The power law exponent of the melt and solution decays are 0.82 and 0.87 respectively. Relaxations under a distribution of local inhomogeneities or nonergodic constrained release dynamics can give such power laws. The temperature independent nature of the dynamics and the local character of the dynamics are distinctive features of β relaxation in glass forming liquids.

References

(1) F. W. Deeg, and M. D. Fayer, J. Chem. Phys. 91, 2269 (1989)
(2) M. Misawa, J. Chem. Phys. 91, 5648 (1989)
(3) M. Misawa, and T. Fukunaga, J. Chem. Phys. 93, 3495 (1990).
(4) J. P. Pinan-Lucarre, J. Loisel, L. Berreby, E. Dayan, and E. Dervil, J. Raman Spectroscopy 23, 67 (1992).
(5) DSE: B. J. Berne, and R. Pecora, *Dynamic Light Scattering* (Wiley, New York, 1976).
(6) (a) P. G. deGennes, The Physics of Liquid Crystals (Clarendon, Oxford, 1974).
(b) S. Chandrasekhar, Liquid Crystals, 2nd ed. (Cambridge, New York, 1992).
(7) (a) E. Leutheusser, Phys. Rev. A **29**, 2765 (1984). (b) D. Bengtzelius, Phys. Rev. A **34**, 5059 (1986). (c) W. Gotze, and L. Sjogren, J. Phys.: Condens. Matter **1,** 4183 (1989); ibid. **1**, 4203(1989).

Nonequilibrium Dynamics of Holes in p-Type Germanium Studied by Femtosecond Infrared Spectroscopy

M. Woerner[1,2], T. Elsaesser[1,2], C. Ludwig[1], M. T. Portella[1], W. Frey[1], and W. Kaiser[1]

[1]Physik Department E 11, Technische Universität München, James-Franck-Str., D-85748 Garching, Germany

[2]Max-Born-Institut für Nichtlineare Optik und Kurzzeitspektroskopie, Rudower Chaussee 6, D-12489 Berlin, Germany

The ultrafast thermalization of nonequilibrium carriers in semiconductors, i.e. the relaxation to a Fermi-like distribution, has mainly been investigated by femtosecond absorption and luminescence studies of photoexcited electron-hole plasma. In this paper, we present the first time resolved observation of thermalization in a single component plasma, providing specific insight into the subpicosecond dynamics of holes in p-type germanium.

In our experiments, holes are promoted to the split-off band by excitation with femtosecond pulses around 3 μm (E_{ex}=430 meV). The subsequent redistribution dynamics is monitored in temporally and spectrally resolved measurements of inter-valence band absorption from the heavy hole to the split-off band. We investigate a Ga-doped germanium crystal with an impurity concentration of 3×10^{17} cm^{-3}. Femtosecond pump and probe pulses of 250 fs duration that are independently tunable in the wavelength range from 2.5 to 5 μm, are generated by parametric difference frequency mixing [1].

In Fig. 1 (a), the stationary absorption spectrum due to transitions between the heavy hole (HH) and the split-off (SO) band is plotted versus photon energy for lattice temperatures of T_L = 10K and 80K. In Figs. 1 (b-d), the transient increase of intervalence band absorption is presented for three photon energies E_{pr} of the probe pulses. At the different E_{pr}, the enhanced absorption rises with a common delay time of approximately 700 fs (solid lines: calculated response, dashed line in Fig. b: time integrated cross-correlation function of pump and probe) and decays subsequently on a slower picosecond time scale by carrier cooling [2]. The present data and additional measurements at other spectral positions demonstrate that spectral hole burning does not occur on the subpicosecond time scale.

The absence of a bleaching signal around delay zero shows that within our time resolution of 100 fs (i) holes excited to the SO band are scattered out of the optically coupled states and (ii) HH states depleted by the pump pulse are essentially repopulated by equilibration among unexcited holes. The holes in the SO band scatter back to the HH band mainly by emission of optical phonons via the deformation potential within the first 100 fs. These nonequilibrium carriers populating high-lying states loose energy by emission of optical phonons

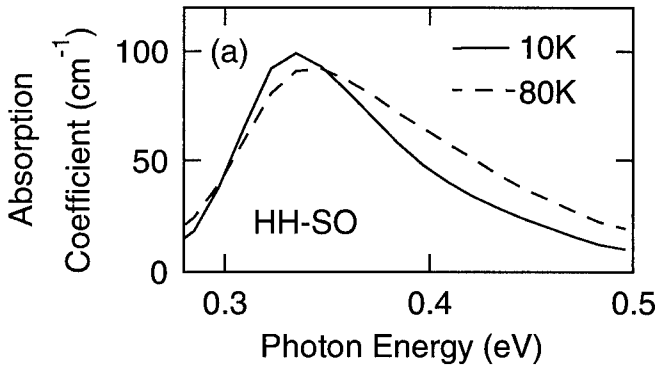
and - more important - by heating the cold plasma of unexcited holes via inelastic carrier-carrier collisions, resulting in an equilibration of the hole distribution. The concomitant rise of occupation probability of HH states leads to the observed increase of absorption with rise times around 700 fs, i.e. the thermalization of photoexcited holes is directly monitored in our experiments.

The rates of energy loss by inelastic carrier-carrier scattering and by emission of optical phonons are derived from a theoretical simulation including a dynamically screened Coulomb interaction [3]. We estimate thermalization times of 0.5 ps, in good agreement with the experimental results.

[1] C. Ludwig, W. Frey, M. Woerner, and T. Elsaesser, Opt. Commun. **102**, 447 (1993)

[2] M. Woerner, T. Elsaesser, and W. Kaiser, Phys. Rev **B 45**, 8378 (1992)

[3] J.F. Young, N.L. Henry, and P.J. Kelly, Solid State Electron. **32**, 1567 (1989)



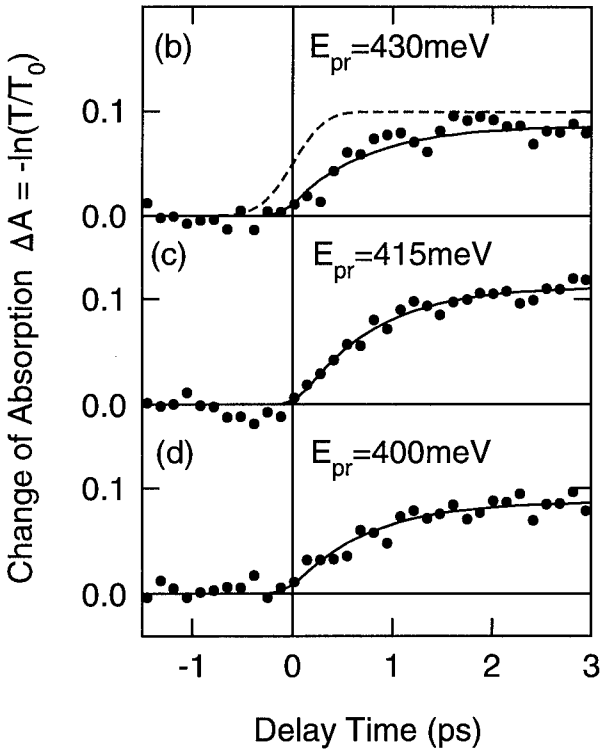


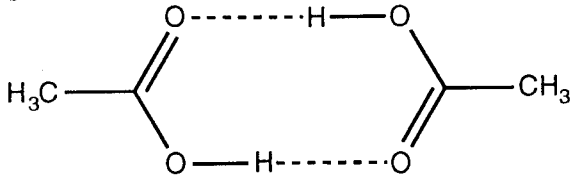
Fig. 1 *(a) Intervalence band absorption of p-type germanium at lattice temperatures of 10 and 80 K. (b-d) Transient increase of intervalence band absorption of p-type Ge after femtosecond excitation at $E_{ex} = 430\ meV$ (2.9 μm, $T_L = 10\ K$). The change of absorption $\Delta A = -\ln(T/T_0)$ is plotted versus the delay time between pump and probe pulses for three different probe frequencies E_{pr} (T_0, T : transmission before and after excitation). The dashed line in (b) gives the time-integrated cross-correlation of pump and probe.*

Femtosecond Dynamics in Hydrogen-Bonding Solvents: Temperature-Dependence of the Inertial and Diffusive Relaxation of Liquid Acetic Acid

Yong Joon Chang and Edward W. Castner, Jr.
Brookhaven National Laboratory
Chemistry Department
Building 555A
Upton, NY 11973-5000
Tel. (516) 282-4362

Femtosecond nonlinear optical spectroscopy has proven to be a powerful tool with which to probe both the inertial and diffusive dynamics of molecular liquids.[1] Only very recently have these techniques been applied to the study of dynamics in complex, strongly-interacting Hydrogen-bonding (H-bonding) liquids.[2] We present here new results on the study of neat liquid acetic acid, CH_3CO_2H. The measurements of the inertial and diffusive dynamics were made using the optical-heterodyne-detected, optical-Kerr-effect (OHD-OKE) technique, which is an electronically non-resonant polarization spectroscopy providing a signal linear in the third-order nonlinear-optical response.[1a] Our measurements have been made as a function of sample temperature, with data taken at 19 and 108 °C. The melting and boiling points of acetic acid are *ca.* 16.2 and 117 °C, respectively, so our measurements have probed the extremes of the liquid phase. One of the most important uses for such ultrafast solvent relaxation data is to predict the rate of solvent-limited chemical reactions in solution, particularly adiabatic electron-transfer reactions.

Because of a two-fold H-bond, acetic acid forms a cyclic dimer of C_2 symmetry in the crystalline, liquid, and gas phases, as shown below.



Unlike other complex H-bonding liquids such as the amides[2a] or water[2b,2c], which may form linear chains and tetrahedrally coordinated networks, liquid acetic acid is only observed as a monomer or dimer. Turi and Dannenberg[3] used high level *ab initio* and semi-empirical molecular-orbital calculations to explain this observation as resulting from the increased stability of 3.1 kcal/mole, of the doubly H-bonded configuration relative to the singly H-bonded dimer. Thus, the acetic acid liquid is a simpler system in which to study the dynamics of H-bonding liquid interactions.

Our raw transient birefringence data for acetic acid are shown in Figure 1, for temperatures near the melting and boiling points. The rising edge of the transient tracks the non-resonant electronic hyperpolarizability response, while the fall from the peak of the transient immediately indicates the inertial nuclear dynamics. On a longer time scale (not shown), the diffusive relaxational regime dominates. After many molecular collisions, on a 0.5-1.0 picosecond time scale, the transient becomes a multi-exponential decay, with the longest time constant being 22 picosecond at room temperature. This molecular relaxation process is a measure of the diffusive rotational correlation function of the molecule. The dynamics occurring in the inertial regime, before the dephasing resulting from molecular collisions has occurred, is best studied in the frequency domain representation of our data.

By doing a Fourier-transform deconvolution on the birefringence transients shown in Figure 1,[1a] we obtain a frequency domain representation of the nonlinear-optical susceptibility, shown in Figure 2A, which we call $Im[R_{OHD\text{-}OKE}(\nu)]$. Lineshape analysis resolves this low-frequency spectrum into three intermolecular vibrational bands. The low-frequency Raman work of Faurskov-Nielsen and Lund shows that the three intermolecular vibrational (or librational) frequencies of liquid acetic acid have peaks at 55, 115, and 165 cm^{-1} in the $R(\nu)$ representation of their data. They have assigned these bands to a symmetric stretch, an out-of-plane bend, and a librational motion, respectively.[4] The $R(\nu)$ representation of the Raman spectrum, $I_{Raman}(\nu)$ is commonly used in low-frequency Raman and Rayleigh-wing spectroscopy to enable observation of the intermolecular dynamics from underneath the large, Lorentzian peaks arising from the diffusive rotational relaxation. This nonlinear-optical susceptibility is related to the low-frequency Raman spectrum by a Boltzman factor, i.e.,

$$Im[R_{OHD\text{-}OKE}(\nu)] \propto I_{Raman}(\nu)[1-\exp(-h\nu/kT)], \quad (1)$$

and the $R(\nu)$ representation is thus connected to our frequency domain representation by:

$$R(\nu) = \nu \cdot I_{Raman}(\nu)[1-\exp(-h\nu/kT)]. \quad (2)$$

The inter-relationships between the three spectral representations are presented graphically in Figure 2. Precisely because we can analyze the rotational correlation function directly from our measured transients, we are then able to analyze the inertial intermolecular dynamics in the frequency domain, without resorting to the $R(\nu)$ representation that distorts the low-frequency spectrum.

Figure 1

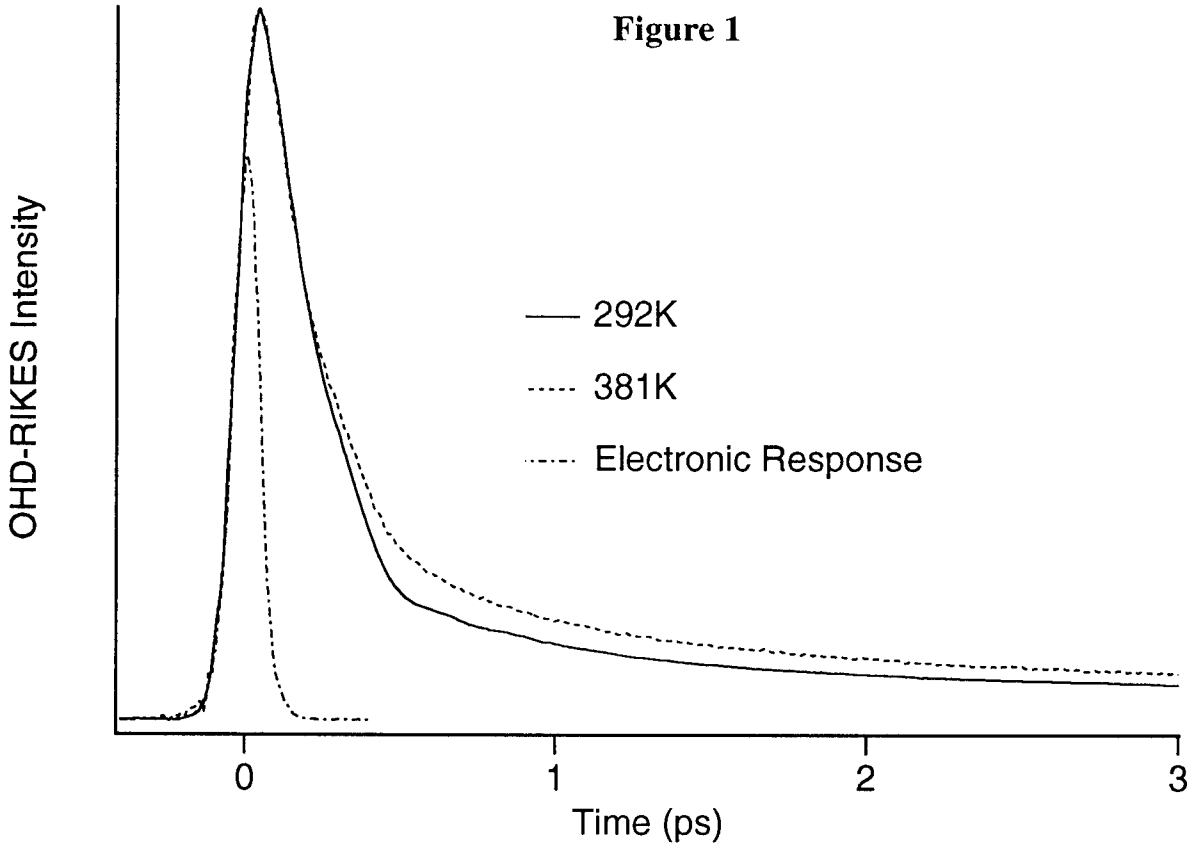
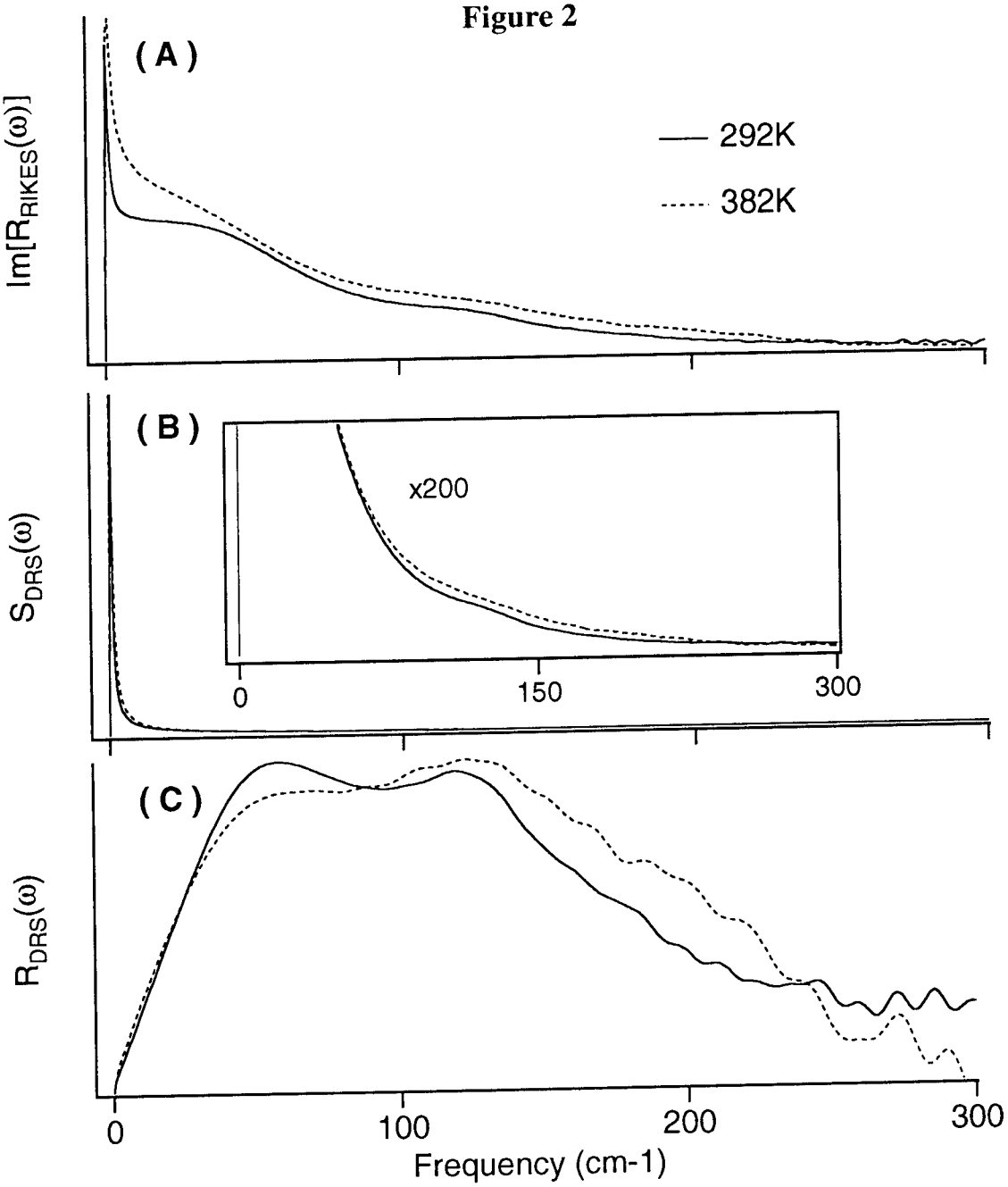


Figure 2



REFERENCES

1. (a) D. McMorrow and W. T. Lotshaw, J. Phys. Chem.**95**, 10395 (1991); (b) Y.-X. Yan, L.-T. Cheng, and K. A. Nelson, *Advances in Nonlinear Spectroscopy*, eds. R. J. H. Clark and R. E. Hester (Wiley, Chichester, 1988), p. 299.
2. K. Wynne, C. Galli and R. M. Hochstrasser, Chem. Phys. Lett. 193, 17 (1992); Y.J. Chang and E. W. Castner, Jr., J. Chem. Phys. **99**, 7289 (1993); *ibid*, **99**, 113 (1993); S. Palese, L. Schilling, R. J. D. Miller, and W. T. Lotshaw, J. Phys. Chem., *in press*.
3. L. Turi and J. J. Dannenberg, J. Phys. Chem. **97**, 12197 (1993).
4. O. Faurskov Nielsen and P.-A. Lund, J. Chem. Phys. **78**, 652 (1983).

Optical Dephasing Dynamics in Room-temperature Liquids

Peijun Cong, Yi Jing Yan, Hans Deuel, and John D. Simon

Department of Chemistry, Institute for Nonlinear Science

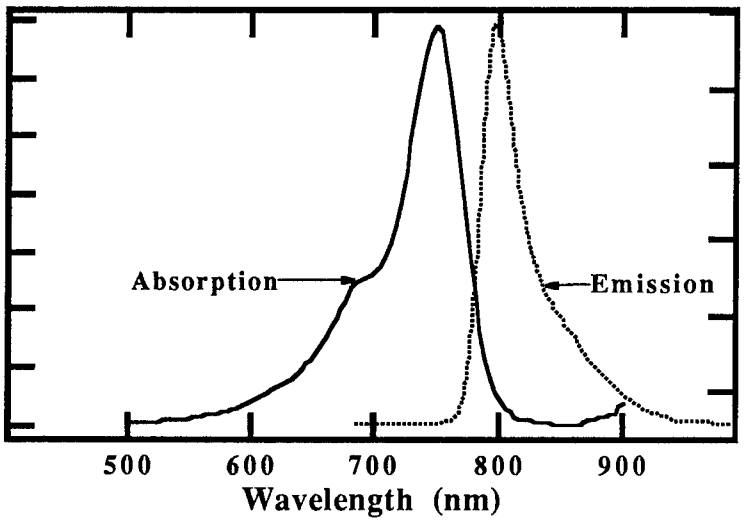
University of California at San Diego

9500 Gilman Drive, La Jolla, California 92093-0341, U.S.A.

Tel.: (619) 534-6699

The dynamic aspects of electronic relaxation of molecules in solution are central to the understanding of a wide range of condensed phase photophysical and photochemical processes. While the population relaxation rate of electronically excited species can be measured by a number of spectroscopic methods, the evolution of the phase coherence in liquids has been difficult to characterize due to its ultrafast nature. With advances in the technology of generating ultrashort laser pulses, the relaxation of electronic coherence can finally be studied in real time. In the past decade, femtosecond photon echo measurements have provided information on the electronic dephasing dynamics of molecules in room-temperature solution [1-3]. A prerequisite for using this method to address such dynamics is that the laser pulses must be much shorter than the time scale of the dephasing process. It has been demonstrated by Shank and co-workers [2] and Wiersma and co-workers [3] that ~ 10 fs pulses are needed to resolve the electronic dephasing dynamics of dye molecules in room-temperature solution. In this paper, a new approach to study the ultrafast dephasing dynamics in liquids is presented: degenerate femtosecond pump-probe spectroscopy that utilizes variable laser pulse-widths and tunable wavelengths [4]. In particular, the dephasing dynamics of an infrared dye, HITCI (absorption and emission spectra are shown in Figure 1), is examined in detail. A comprehensive theoretical treatment based on a multimode Brownian oscillator model of solvation [5] is developed and quantitative agreement between theory and experiment is obtained.

FIGURE 1:



The experimental setup for transient absorption has been described elsewhere [4, 6]. We concentrate on the experimental results here. The signal observed around zero time delay in a degenerate four-wave-mixing (4WM) experiment is composed of both population bleaching

kinetics and coherent coupling between the pump and probe laser beams. Fixing the central wavelength of the laser, the relative contribution of the coherent coupling term increases with increasing laser pulsewidth. This dependence is shown in Figure 2 and has been explained in ref. [4]. In Figure 3, the results of wavelength tuning experiments at constant pulse width are

FIGURE 2:

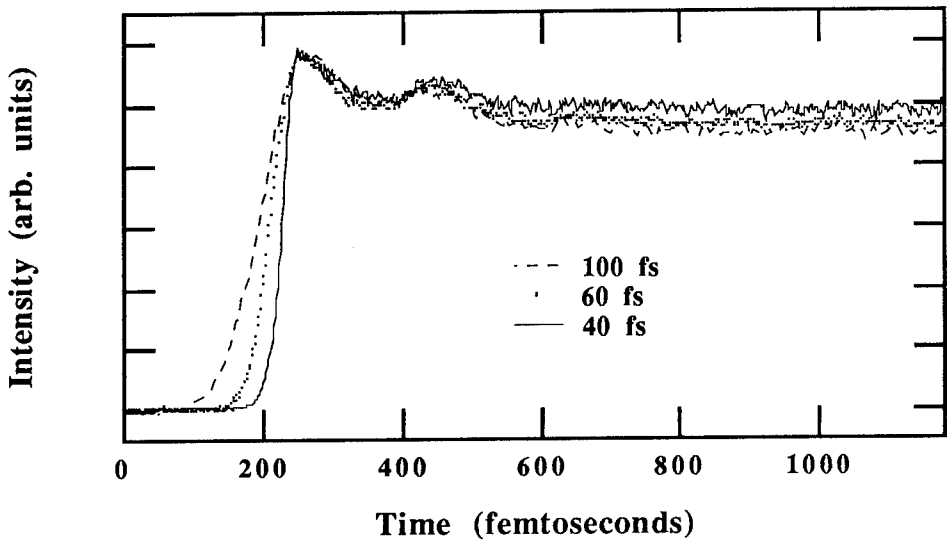
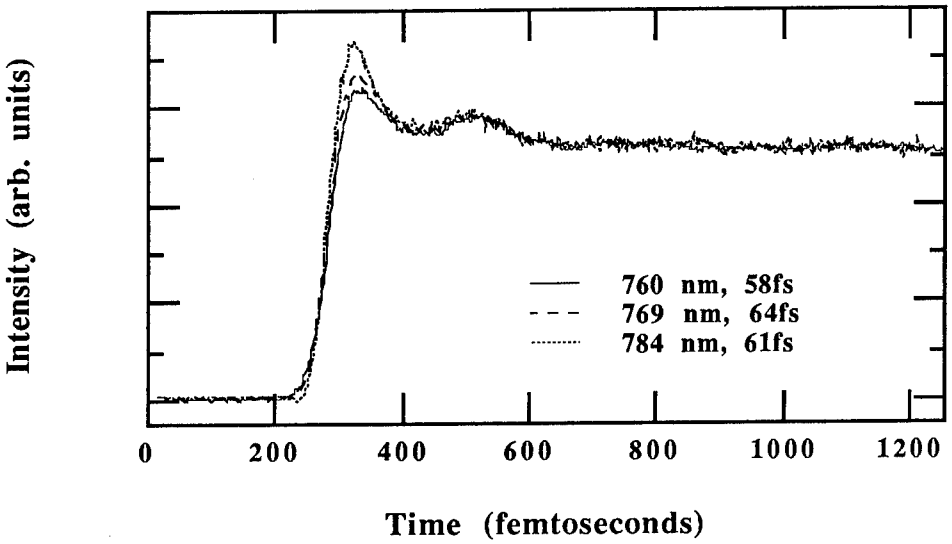


FIGURE 3:

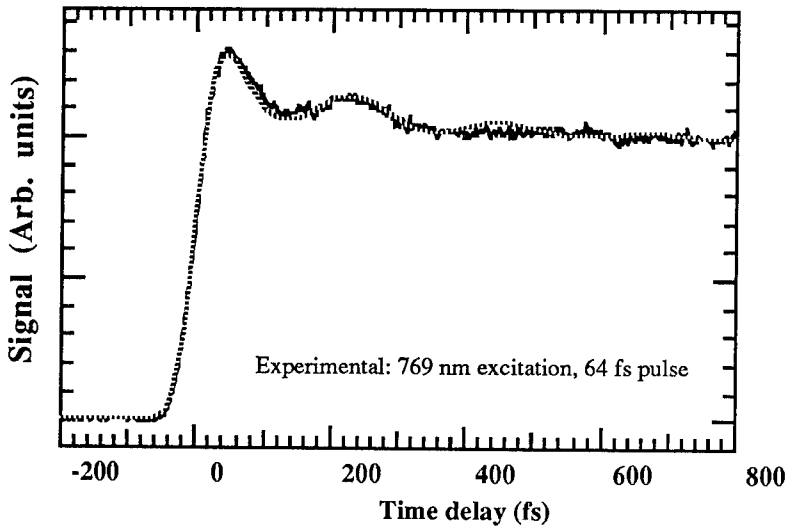


presented. Clearly, the coherent spike amplitude increases when the central frequency of the laser is tuned away from the resonance wavelength (750 nm, for HITCI in ethylene glycol, see Figure 1). It is rather straightforward to understand this phenonmenon. The population term is proportional to $1/\Delta\omega^2$, ($\Delta\omega = |\omega(\text{laser}) - \omega(\text{mol})|$), and the coherent contribution decays as $1/\Delta\omega$. The larger the detuning, the more dominant the coherent term becomes near zero time delay (see ref. [4] and [6] for more details). Therefore, in addition to the laser pulsewidth, the laser wavelength also affects the relative contribution of coherence and population dynamics to the overall absorption signal. This provides a second experimental parameter whose evolution in a degenerate 4WM experiment depends on the material dephasing time. A quantum beat pattern is also present in both curves. These clearly overdamped oscillations are caused by the coherent

excitation and propagation of vibrational states of the dye molecule accompanying the electronic transition.

Electronic dephasing dynamics can be described by a variety of theoretical models, ranging from the Bloch equation approach [4, 7], to non-Markovian descriptions such as the Kubo model [2,3] and multi-mode Brownian oscillator model [5]. We have recently developed a comprehensive theoretical model [6] that is based on a multi-mode Brownian oscillator description of solvation [6]. Unlike earlier work, the pump and probe laser pulsewidths and wavelengths are explicitly treated in our theoretical analysis. The experimental data shown in Figure 3 can be quantitatively described by this multi-mode Brownian oscillator model. The fit requires a spectral fluctuation of 150 wavenumbers, a solvent correlation time of 300 fs, an intramolecular vibrational frequency of ~ 150 wavenumbers, and an inhomogeneous linewidth of 550 wavenumbers. A comparison between theory and experiment is shown in Figure 4. This result clearly demonstrates the inhomogeneous nature of the absorption spectrum and the non-Markovian aspects of the dynamics.

FIGURE 4:



In conclusion, we have shown that degenerate 4WM spectroscopy can be used to elucidate quantitative information about electronic dephasing of molecules in room-temperature solutions. It is important to note that molecular information can be obtained from this approach when combined with comprehensive theoretical modeling.

References:

1. K. A. Nelson and E. P. Ippen, *Adv. Chem. Phys.* 75 (1989) 1, and references therein.
2. E. T. J. Nibbering, D. A. Wiersma, and K. Duppen, *Phys. Rev. Lett.* 68 (1991) 2464.
3. J.-Y. Bigot, M. T. Portella, R. W. Schoenlein, C. J. Bardeen, A. Migus, and C. V. Shank, Phys. Rev. Lett. 66 (1991) 1138.
4. P. Cong, H. P. Deuel, and J. D. Simon, *Chem. Phys. Lett.* 212, 367 (1993).
5. Y.-J. Yan and S. Mukamel, *J. Chem. Phys.* 89 (1988) 5160.
6. P. Cong, Y. J. Yan, H. P. Deuel, and J. D. Simon, *J. Chem. Phys.* in press.
7. M. W. Balk and G. R. Fleming, *J. Chem. Phys.* 83 (1985) 4300.

Femtosecond Time-Resolution in Scanning Tunneling Microscopy

G. Gerber, F. Sattler, S. Vogler
Fakultät für Physik, Universität Freiburg, D-79104 Freiburg, Germany
phone 011-49-761-2035727 ; fax 011-49-761-2035873
J.Y.Grand, P. Leiderer, R. Möller
Fakultät für Physik, Universität Konstanz, D-78434 Konstanz, Germany

Scanning tunneling microscopy (STM) allows to study surfaces with extremely high spatial resolution down to nanometer dimensions. This has changed the field of surface science. However, the time resolution of the STM is limited to the microsecond range due to the tunneling current measurement.

Femtosecond laser pump-probe techniques provide a time-resolution limited by the temporal pulse duration of the ultrashort laser pulses. However, the spatial resolution is limited to the diffraction limit of the laser beam, which is for visible light of the order of a few micrometer. So, the ultimate solution to study ultrafast dynamical processes on surfaces is the combination of these two extremely powerful techniques. This contribution reports our first results obtained employing 40fs light pulses of an amplified home-built Ti:Sapphire laser to the tip-surface gap of a STM. The femtosecond time-resolution is achieved by scanning the time delay between the identical pump and probe pulses and integrating the photoelectron current. Au and WSe_2 surfaces are chosen to demonstrate the feasibility of the new experimental technique. A measurement of the interferometric autocorrelation of the 40fs laser pulses making use of the nonlinear response of the tip – Au surface interaction nicely shows the phase stability of the femtosecond light pulses. By illuminating the tunneling gap between the tip and the Au surface with 40fs laser pulses photoelectrons from the Au-surface are detected. The interaction of the femtosecond pump pulse with the Au-surface induces an excitation which shows a relaxation on a 200fs time scale. By scanning the time delay between the pump and probe laser pulses this relaxation time is evident from the cross-correlation of the tip-Au surface response. Such cross-correlation measurements of the tip-sample response allow us to study dynamical phenomena on surfaces in real time and in real space simultaneously with femtosecond and nanometer resolution.

Direct Measurement of the Nuclear and Solvent Contributions to the Electron-Transfer Dynamics in Mixed Valence Metal Dimers

P. J. Reid[1], *C. Silva*[1], *Y. Dong*[2], *J. T. Hupp*[2], *and P. F. Barbara*[1]

[1]Department of Chemistry, University of Minnesota, Minneapolis, MN 55455, USA
[2]Department of Chemistry, Northwestern University, Evanston, IL 60208, USA

The electron-transfer in mixed valence metal dimers is investigated with sufficient time resolution (20 fs) to unravel coherent and incoherent electronic, vibrational, and solvent motion for the first time. These compounds represent an ideal class of reactions on which to develop condensed-phase electron-transfer (ET) theories.[1, 2] An example in these reactions is the ruthenium-ruthenium mixed valence compound (RuRu):

$$(NH_3)_5\text{-Ru(III)-NC-Ru(II)-(CN)}_5^- \underset{\text{b-ET}}{\overset{h\nu}{\rightleftharpoons}} (NH_3)_5\text{-Ru(II)-NC-Ru(III)-(CN)}_5^-$$

Photoexcitation initiates the migration of an electron between metal centers with internal conversion from the excited state to the ground state corresponding to the back-electron transfer. We have constructed a 20-fs absorption spectrometer based on a Ti:Sapphire oscillator which is capable of measuring the ultrafast reaction dynamics.[3]

This work represents the first direct measurement of the electron-transfer time of RuRu in water allowing for the investigation of both nuclear and solvent motion in the reaction dynamics.

The transient pump-probe signal for RuRu in H_2O is shown in Figure 1A. The largest component of the response is the symmetric, coherence coupling signal centered at zero time. Closer evaluation of the transient (Figure 1B) reveals the presence of the ground-state bleach that evolves into an absorption with the decay of this feature completing the dynamics. Kinetic analysis of this transient reveals that the coherence coupling signal follows the instrument response. The ground-state bleach recovers with a time-constant of 85 ± 10 fs. The ground-state absorption corresponding to excess energy in vibrational and/or solvent degrees of freedom decays in 880 ± 160 fs.

The coherent nuclear response of RuRu is observed in residual difference between the fit and the transient (Figure 1B). Figure 2 presents the Fourier transform of the residual. The frequencies determined from this analysis agree with those observed in the post-resonance Raman spectrum demonstrating that this response originates from the solute. This observation combined with the absence of an excited-state absorption in this spectral region indicates that the oscillatory response is due to a displaced ground-state population created by impulsive-stimulated Raman scattering (ISRS).[4] The residual was also modeled with three components with frequencies at 170, 280 and 480 cm^{-1} and separate dephasing times. An average vibrational dephasing time of ~300 fs was determined in agreement with the Raman linewidths.[5]

Excitation perpendicular to the probe polarization results in a dramatic reduction in the amplitude of the coherence coupling signal relative to ground-state bleach and absorption due to anisotropy differences between these features (Figure 1C).[6] The kinetics observed for perpendicular excitation were in agreement with the parallel data demonstrating that we have accurately measured the electron-transfer dynamics.

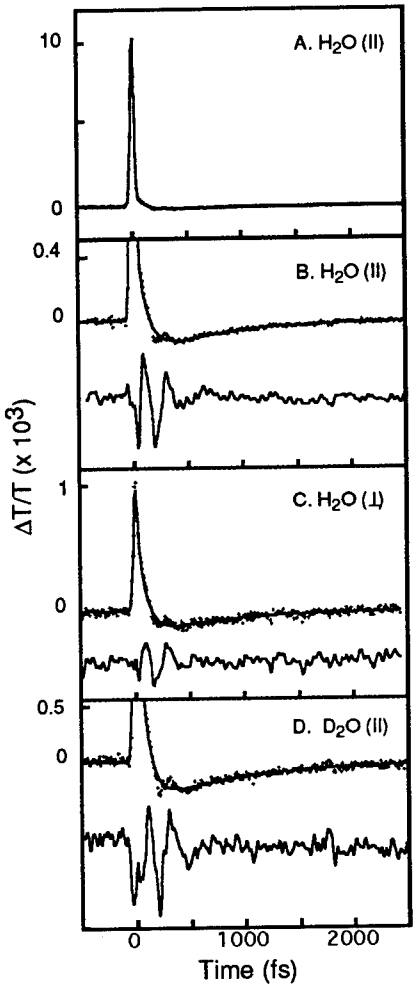


Figure 1. A. Transient absorption of RuRu in H_2O. B. Expansion of A with residual difference between the data and fit at the bottom. C. Transient for perpendicular pump polarization. D. RuRu in D_2O.

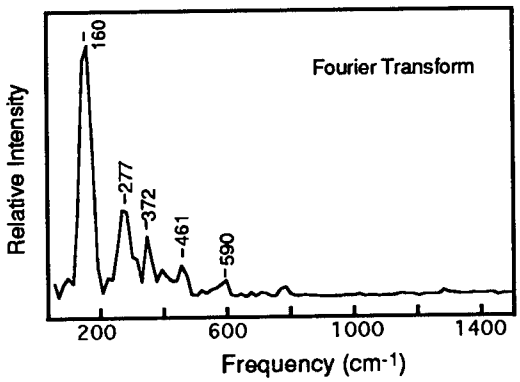


Figure 2. Fourier transform of residual in Fig. 1B.

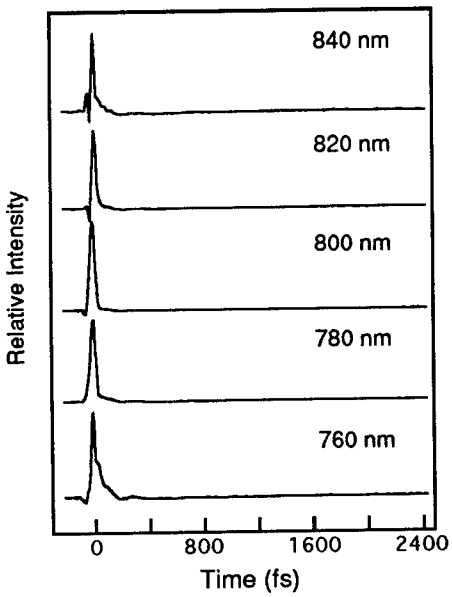


Figure 3. Dynamic absorption spectra of RuRu in H_2O.

Figure 1D presents the pump-probe transient obtained for RuRu in D_2O. Although the transient appears similar to that obtained in H_2O, anlaysis of the ground-state dynamics reveals that the time-constant for bleach recovery increases to 122 ± 20 fsec. The ground-state absorption decays in 800 ± 240 fsec similar to the H_2O dynamics. To ascertain the role of hydrogen solvent/ligand exchange on the kinetics in D_2O, the dynamics at pH 2.2 were also investigated. At this lower pH, the exchange half-life is 8 hours providing ample time to measure the kinetics in the absence of this process.[7] The kinetics determined from this study were in agreement with the pH 7 results demonstrating that the rate reduction in D_2O is due to the solvent.

The data presented here provide a detailed picture of RuRu electron-transfer dynamics:

Rapid electronic dephasing. The symmetric shape of the coherence coupling signal and the observation that the signal follows the instrument response indicates that electronic dephasing is rapid. Also, the amplitude of this signal relative to the ground-state bleach was insensitive to a 2-fold increase in pulse width unlike the behavior observed in other systems in which the electronic dephasing and pulse width are comparable.[8] This observation establishes that the electronic

dephasing time is ≤20 fs.[9] Analysis of the ground-state electronic absorption band has demonstrated that the solvent contribution to the reorganization energy is 3700 cm^{-1} consistent with large coupling between the solvent and the electronic transition.[10] This interaction results in rapid electronic dephasing providing for an electronically incoherent back-electron transfer.

Electron-transfer is faster than vibrational dephasing. Decay of the oscillatory nuclear response demonstrates that ground-state vibrational dephasing occurs in ~300 fsec. If we project a similar dephasing time in the excited state, the electron transfer would occur before vibrational dephasing. This is in agreement with measurements of ground-state vibrational energy deposition in excess of that expected if vibrational relaxation of the excited state were complete.[11] However, the electron-transfer times measured here are similar to estimates from previous absorption experiments in which coherent excitation of vibrational modes was not possible. [10, 12] Therefore, the rapidity of the back-electron transfer is most likely the result of strong electronic coupling and not due to the existence of vibrational coherence.

Solvent hydrogenic motions are coupled to the back-electron transfer. The back-electron transfer rate reduction between H_2O and D_2O demonstrates that solvent hydrogenic motions are involved in the reaction dynamics. Molecular dynamics simulations on similar systems have suggested that librational motions of the first solvent shell participate in the electron transfer.[13] This study provides direct experimental evidence for this hypothesis. Also, the observation of specific solvent vibrational motions participating in the reaction dynamics illustrates the limitation of dielectric continuum based electron-transfer theories to model the quantum aspects of solvation.

Mixed valence metal dimers are ideal for the development of electron-transfer theories. In Figure 3, we present the dynamic absorption spectra of RuRu obtained throughout the probe spectral profile. The spectral trends are as expected with the coherence term largest at the pump-probe frequency, a larger absorption signal on the red-edge of the ground-state absorption band and an oscillatory response which is phase shifted between 840 and 760 nm consistent with ISRS. The results presented here in combination with the previous static and transient absorption and resonance Raman data establishes a unique opportunity to develop and test theoretical descriptions of electron transfer. Accurate modeling of these data is currently underway to develop a complete picture of RuRu reaction dynamics.

Acknowledgment. This research was supported by the NSF and DOE-BES.

References

1. N. S. Hush, Prog. Inorg. Chem. **8**, 391 (1967).
2. C. Creutz, Prog. Inorg. Chem. **30**, 1 (1983).
3. M. T. Asaki, C. P. Huang, D. Garvey, J. P. Zhou, H. C. Kapteyn, and M. M. Murnane, Optics Lett. **18**, 997 (1993)
4. K. A. Nelson, in *Raman Spectroscopy: Sixty Years on Vibrational Spectra and Structure*, edited by H. D. Bist, J. R. Durig, and J. F. Sullivan (Elsevier Science Publishers B. V., Amsterdam, 1989).
5. S. K. Doorn, R. L. Blackbourn, C. S. Johnson, and J. T. Hupp, Electrochimica Acta. **36**, 1775 (1991).
6. Z. Vardeny and J. Tauc, Optics Comm. **39**, 396 (1981).
7. D. A. House, Coord. Chem. Rev. **114**, 249 (1992).
8. P. Cong, H. P. Deuel, and J. D. Simon, Chem. Phys. Lett. 212, 367 (1993).
9. M. W. Balk and G. R. Fleming, J. Chem. Phys. 83, 4300 (1986).
10. K .Tominaga, D. A. V. Kliner, A. E. Johnson, N. E. Levinger and P. F. Barbara, J. Chem. Phys. **98**, 1228 (1993).
11. S. K. Doorn, R. B. Dyer, P. O. Stoutland, and W. H. Woodruff, J. Am. Chem. Soc. **115**, 6398 (1993).
12. D.A. V. Kliner, K. Tominaga, G. C. Walker, and P. F. Barbara, J. Am. Chem. Soc. **114**, 8323 (1992).
13. J. S. Bader and D. Chandler, Chem. Phys. Lett. **157**, 501, (1989).

Infrared Pulse Generation using a Subpicosecond OPO

J. D. Kafka, M. L. Watts and J. W. Pieterse
Spectra-Physics Lasers, Inc.
1330 Terra Bella Ave., Mountain View, Ca 94043

For many ultrafast experiments it is desirable to have synchronized subpicosecond pulses at multiple wavelengths. Recently, synchronously pumped parametric oscillators (SPPO) have been used to satisfy this requirement as well as produce ultrafast pulses at wavelengths beyond 1 μm. In this paper, we demonstrate the synchronism inherent in an SPPO by measuring a 100 fsec cross-correlation between the pump and signal pulses. We then use the synchronization between the signal and *idler* to generate pulses at longer wavelengths by difference frequency mixing in lithium niobate and silver gallium sulfide.

Our pump source consists of a mode-locked Ti:sapphire laser that produces 2 W at 770 nm when pumped by 12 W from an Argon ion laser (Fig. 1). The SPPO contains a temperature tuned 90° phase matched LBO crystal in a linear cavity [1]. This system has generated pulses as short as 40 fsec or average powers as high as 450 mW. The cavity length and

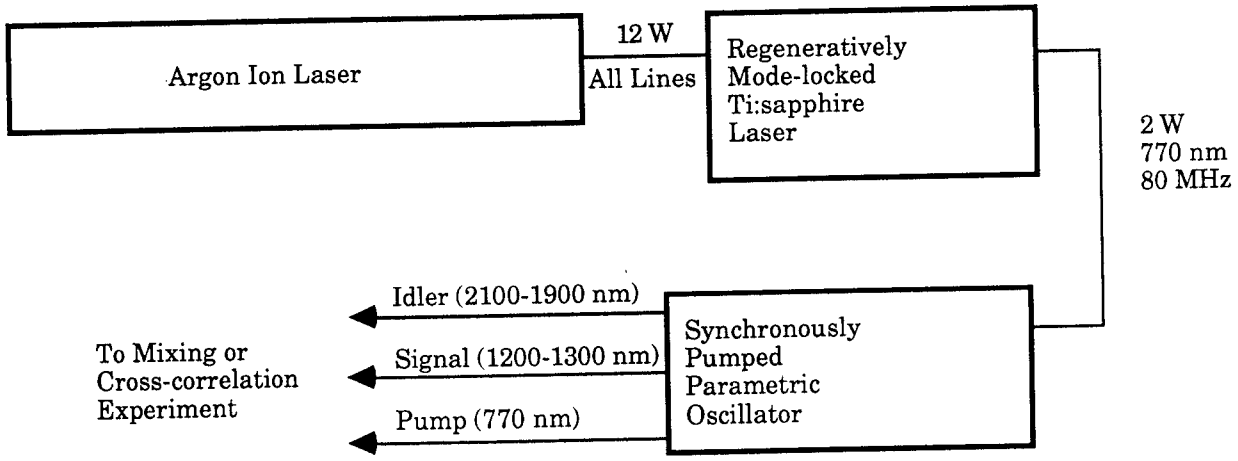
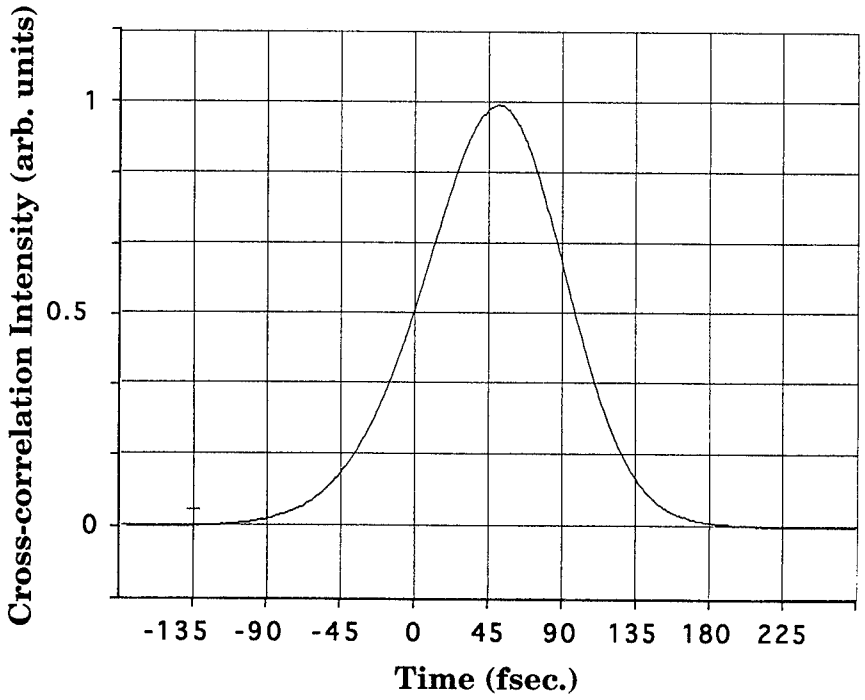


Fig. 1 The experimental configuration for the cross-correlation and for difference frequency generation.

crystal temperature are controlled by a microprocessor and we have demonstrated automated tuning over 80 nm. We have obtained pulses from 1.1 to 2.4 μm with two sets of optics. For wavelengths shorter than 1.3 μm, we use intracavity prisms for dispersion compensation.

We have measured the cross-correlation between the pump and signal pulses using a BBO crystal. The duration of the pump pulse at 770 nm is 72 fsec after passing through a pair of prisms. The duration of the signal pulse at a wavelength of 1.32 μm is 65 fsec directly from the SPPO. The best cross-correlation is shown in Fig. 2 and is an average of 32 traces over a period of several seconds. The cross-correlation has a FWHM of less than 100 fsec and thus the jitter between the pump and signal pulses is less than 20 fsec. We have also measured the cross-correlation between the signal and idler pulses and typically obtain a FWHM of 180 fsec.

Fig. 2 The cross-correlation between the 72 fsec pump pulse and the 65 fsec signal pulse. The FWHM is less than 100 fsec.



The signal and idler pulses from an SPPO are ideal for difference frequency mixing since a small change in the signal wavelength corresponds to a large shift in the difference wavelength. We use a 4 mm thick lithium niobate crystal cut at $\theta = 47°$. At 3.4 μm we observe 100 μW of average power. As we tune the signal wavelength from 1.18 to 1.30 μm the idler wavelength tunes from 2.2 to 1.9 μm. The difference frequency signal

is measured with a PbSe detector and the tuning range is calculated to be 2.6 to 4.3 μm. Lithium niobate is convenient for this tuning range since only an 8° change in phase matching angle is needed.

To generate longer wavelengths, we switch to a $AgGaS_2$ crystal which is 2 mm thick and cut at $\theta = 50°$. At 3.4 μm the power increases to 400 μW as measured with both the PbSe detector and a power meter. As we tune the signal wavelength from 1.18 to 1.34 μm we generate the tuning curve displayed in Figure 3. The powers have been measured using the PbSe detector and take into account the wavelength dependence of the detector sensitivity.

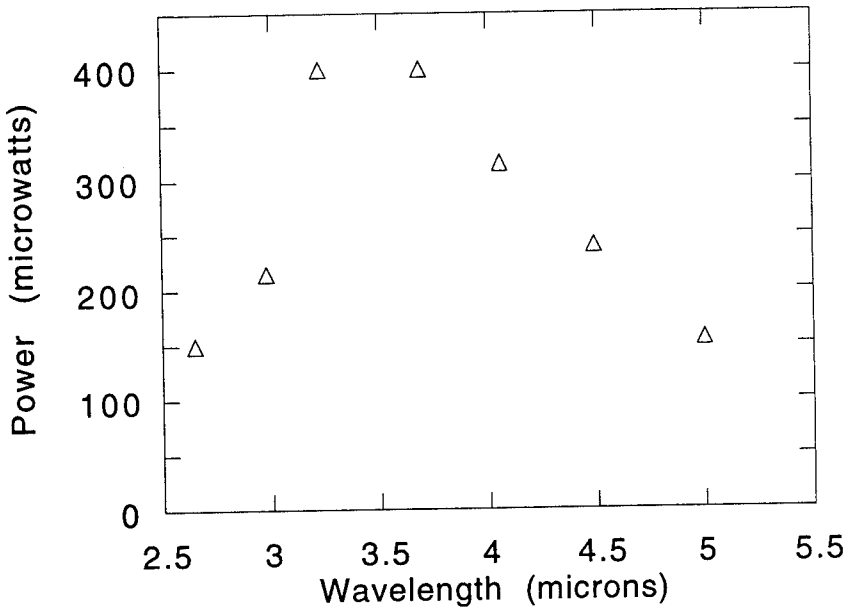


Fig. 3 The average power as a function of wavelength generated by difference frequency mixing in a 2 mm thick $AgGaS_2$ crystal.

In conclusion, we have demonstrated the generation of subpicosecond infrared pulses with a tuning range of 2.7 μm using a single set of optics. The combination of a Ti:sapphire pumped SPPO with a mixing crystal produces synchronized ultrafast pulses at 0.7, 1, 2 and 3 to 5 μm simultaneously.

References

1. J. D. Kafka, M. L. Watts and J. W. Pieterse, in *Conference on Lasers and Electro-Optics,* (Optical Society of America, Washington, DC, 1993), Postdeadline Paper CPD32.

Terahertz spectroscopy of silicon micromachined three-dimensional photonic bandgap crystal

E. Özbay, E. Michel, G. Tuttle, R. Biswas, K. M. Ho,
Microelectronics Research Center and DOE Ames Laboratory, Iowa State University, Ames, IA 50011
(515)-294-1814

J. Bostak and D.M. Bloom
Edward L. Ginzton Laboratory, Stanford University, Stanford, CA 94305
(415)-723-0294

In analogy to electrons in a crystal, the propagation of electromagnetic (EM) waves in a three-dimensional dielectric structure can be forbidden for a certain range of frequencies. These three-dimensional structures that are called photonic band gap crystals, have recently received both theoretical and experimental attention[1-3]. The early research in the field has concentrated on possible optical frequency range applications that take advantage of reduced spontaneous emission, such as thresholdless semiconductor lasers and single-mode light-emitting diodes. The proposed applications were later extended to the millimeter and sub-millimeter wave regime, like efficient antennas, sources, waveguides and other components that take advantage of the unique properties of photonic bandgap materials[4]. But, the difficulties associated with the fabrication of smaller scale structures along with the unfeasible three-dimensional structure designs, have restricted the experimental demonstration of the basic photonic band gap crystals to microwave frequencies (12-15 GHz).

We have recently designed a new three-dimensional structure that may alleviate some of the problems associated with earlier photonic band gap designs[5]. The new structure exhibits a sizable and robust photonic band gap over a range of structural parameters. We have shown the feasibility of structures with 100 GHz photonic band gap frequencies by using semiconductor micromachining techniques[6]. In this paper, we demonstrate the scalability of the new structure to a band gap frequency of 500 GHz, which was measured by terahertz spectroscopy techniques. Such a performance offers a readily available structure for the demonstration of the proposed millimeter and sub-millimeter wave applications.

The new structure, shown in Fig. 1, is constructed of layers of dielectric rods. The stacking sequence repeats every four layers, corresponding to a single unit cell in the stacking direction. In order to build the 500 GHz crystal , we have used fabrication techniques similar to the one used to build 100 GHz crystals[6]. Fabrication consisted of defining stripes that were parallel to (111) planes and subsequently etching the wafers in an KOH etch solution. The well-known anisotropic etching properties of aqueous KOH etch solutions resulted in parallel rods with rectangular cross sections, similar to one of the single layers described in Fig.1. The fabricated stripes were 2.0 cm long and 50 microns wide, separated by 185 micron wide gaps. A total of 86 parallel stripes were fabricated on each wafer, resulting in a square 2.0 cm x 2.0 cm pattern. The individual etched wafers were then stacked to form the photonic crystal using a holder with pins that align to the guide holes that were etched through the wafers. The (110) silicon wafers used in this work were each two inches in diameter and 100 ± 5 μm thick. Relatively high-resistivity wafers (>100 Ω-cm) were chosen in order to minimize absorption losses in the silicon. During the course of fabrication, we gave extra caution to the handling of the thin silicon wafers that were susceptible to breakage. A layer of oxide that was used to protect the back surface of the silicon wafer during the KOH etch, was intentionally kept after the etch. This gave a robust support to the relatively long stripes, preventing individual stripes from bending and bonding to the adjacent stripes.

The testing was performed by using a terahertz free-space spectroscopy setup shown in Fig.2. EM pulses were generated and detected by an all-electronic approach designed and built around nonlinear transmission line technology along with magnetic dipole (slot) antennas. Two phaselocked microwave synthesizers with an offset frequency of 7 Hz, were used to drive the generator and detector circuits. A spectrum analyzer was used to directly compute the Fourier spectra of the detected signals. The dynamic range of the system was around 30 dB for frequencies up to 550 GHz. We have carried out the free-space spectroscopic measurements of the photonic crystal by placing the structure on the beampath of the radiated signal. By comparing the detected signals with and without the crystal in place, we obtained the phase and magnitude transmission properties of the structure as a function of frequency. Since the pulses were periodic, the frequency domain information was limited to the harmonics of the input signal frequency (6.4 GHz). The setup used high resistivity silicon lenses to collimate and focus the radiation generated and detected by the antennas. The resulting test beam was highly collimated where 95% of the output radiation remained within a 10° radiation cone.

We used a structure that consisted of 16 stacked silicon wafers (corresponding to 4 unit cells) for transmission measurements. The characteristics along the stacking direction were obtained by placing the structure on the beam path, so that the transient radiation propagated in a plane perpendicular to the top surface of the structure. Figure 3 shows the transmission characteristics of the propagation along the stacking direction. The lower edge of the photonic gap is at 370 GHz, while the upper edge is at 520 GHz. This is very close to the calculated bandgap edges of 378 GHz and 518 GHz. The average measured attenuation within the bandgap was around 30 dB which was limited by the dynamic range of the experimental setup. Our calculations for the bandgap frequencies predicted the attenuation to be as low as 65 dB.

As explained above, the difficulties associated with the unfeasible three-dimensional structure designs have restricted the experimental demonstration of the basic photonic band gap crystals to microwave frequencies. Our new structures built around the new fabrication technique bring a viable solution to this problem. We expect the new design and the fabrication technique to be used to demonstrate most of the suggested applications at the millimeter and sub-millimeter wave regime. To the best of our knowledge, our new photonic band gap crystal has the highest reported bandgap frequency.

References

1. K. M. Ho, C. T. Chan, and C. M. Soukoulis, Phys. Rev. Lett. **65**, 3152 (1990).
2. E. Yablonovitch, T. J. Gmitter, and K. M. Leung, Phys. Rev. Lett. **67**, 2295 (1991).
3. For a recent review, see the articles in *Photonic Bandgaps and Localization*, C. M. Soukoulis, Ed. (Plenum, New York, 1993).
4. See the articles in the J. Opt. Soc. Am. B 10 (1993), a special feature edited by C.M. Bowden, J.P. Dowling, and H.O. Everitt.
5. K. M. Ho, C. T. Chan, C. M. Soukolis, R. Biswas, and M. Sigalas, to be published in Solid State Communications.
6. E. Ozbay, E. Michel, G. Tuttle, M. Sigalas, R. Biswas, and K. M. Ho, to be published.

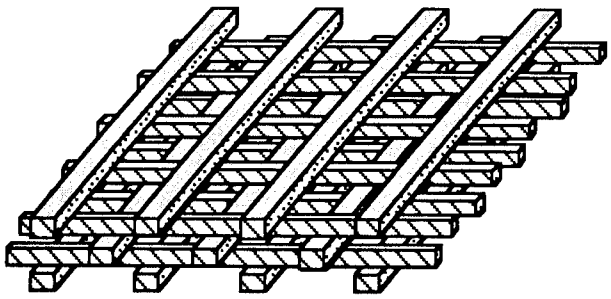


Figure 1. This figure schematically illustrates the design of the three-dimensional photonic bandgap crystal. The structure is built by an orderly stacking of dielectric rods and repeats every four layers in the stacking direction.

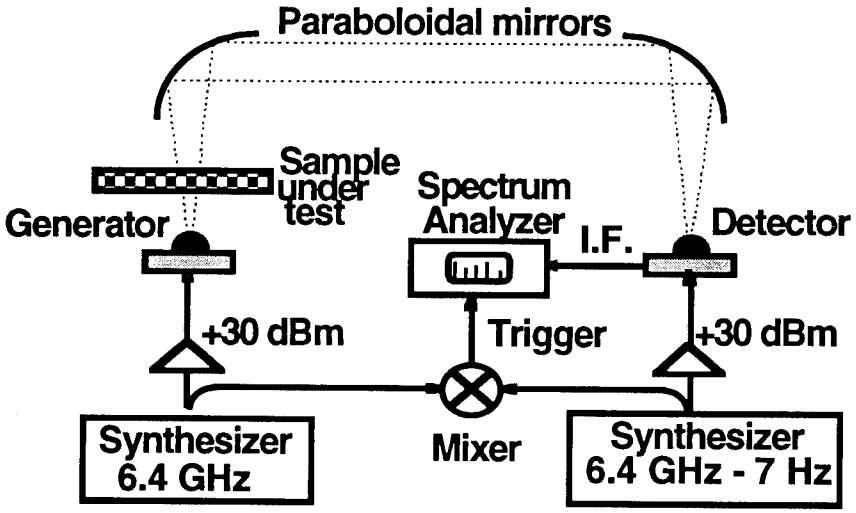


Figure 2. Diagram of the all-electronic THz free-space spectroscopy system.

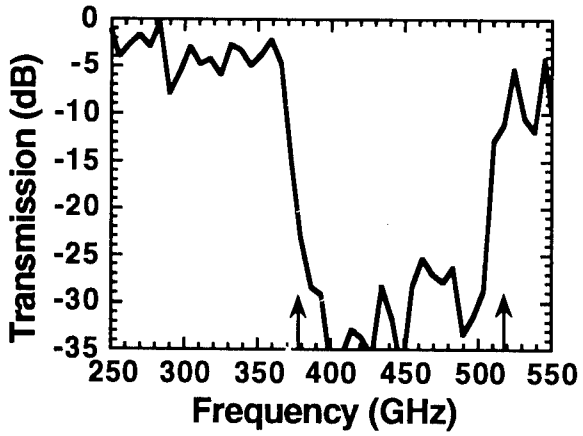


Figure 3. EM wave transmission through the micromachined crystal in which the wavevector of the incident radiation is normal to the wafer surfaces. The arrows indicate calculated band edge frequencies.

Chirped pulse amplification of ultrashort pulses using neodymium- and erbium-doped fiber amplifiers

L.-M. Yang, M. L. Stock and G. Mourou
Center for Ultrafast Optical Science
University of Michigan
2200 Bonisteel Blvd, 1006 IST, Ann Arbor, MI 48109-2099
(313) 763-4875
FAX: (313) 763-4876

A. Galvanauskas, M. E. Fermann and D. J. Harter
IMRA America, Inc.
1044 Woodridge
Ann Arbor, MI 48105

As an important step toward the realization of compact, optical fiber-based, femtosecond pulse systems of the highest possible energies, we demonstrate chirped pulse amplification (CPA) of ultrashort pulses using rare-earth doped fiber amplifiers for the first time. The technique of CPA [1] is well established to produce the highest energy ultrashort pulses in bulk systems. Rare-earth doped fibers are attractive as amplifiers due to the broad bandwidth available in glass hosts. This property has already been exploited in rare-earth doped fiber lasers which have produced pulses as short as 42 fs with Nd-doped fiber [2] and 77 fs with Er-doped fiber [3]. Thus, these fibers can support sub-100 fs pulses. Here, Nd-doped fiber is used to amplify 1.06 μm seed pulses and Er-doped fiber is used to amplify 1.55μm seed pulses in initial experiments toward reaching the saturation energy of several micro-Joules [4] attainable in rare-earth doped fiber amplifiers.

The technique of CPA involves temporally stretching a short pulse through a dispersive delay prior to amplification. This allows for the avoidance of gain saturation and nonlinear effects such as self-phase modulation, cross-phase modulation and Raman scattering, all easily obtainable within optical fiber by high-peak power ultrashort pulses. The amplified pulse is then recompressed by passing it through a dispersive delay opposite in effect to the stretcher. In the absence of gain narrowing and higher-order mismatches in the dispersive delay lines, the original pulse-width can be obtained.

A block diagram of the experimental arrangement used in both demonstrations is shown in Fig. 1. In the case of the Nd-doped fiber amplifier, the seed pulse is from a MIRA Ti:sapphire oscillator operating at 1.064 μm generating bandwidth limited 100 fs pulses at a repetition rate of 77 MHz. The operating wavelength was tuned to match the center wavelength of the amplifier. This pulse is stretched to 500 ps in 500 m of communication type SMF-28 fiber. At the same time, by the process of self-phase modulation, the spectrum is increased from 13 nm to 25 nm. The stretched pulse is injected into the fiber amplifier which consists of a 60 cm Nd-doped fiber of dopant concentration approximately 0.05 wt%. The average launched power into the amplifier is 7.5 mW. The amplifier is pumped with a launched average power of 250 mW at 532 nm resulting in an average output power of 45 mW, or a 7.7 dB single-pass gain. Finally, pulses are compressed by a grating pair. An autocorrelation trace of the compressed amplified pulse shows a 220 fs duration assuming a sech^2 fit as shown in Fig. 2(a). The amplified pulse experienced gain narrowing giving an amplified and compressed spectrum of 14 nm, shown in Fig. 2(b). The chirped output pulse and the pedestal component observed in the

autocorrelation are due to high order dispersion from the fiber stretcher [5] which remains uncompensated in the compressor stage.
The experimental set-up for the Er-doped fiber amplifier as reported by Stock et al [6] is similar to that of the Nd-doped fiber amplifier system and is described below. The seed pulses are from an environmentally stable Kerr-type modelocked erbium fiber laser [7]. This source generates band-width limited 250 fs pulses at a repetition rate of 33 MHz with an energy content of up to 100 pJ at a wavelength of 1.567 μm. The oscillator pulses were stretched to a width of 50 ps in a length of 450 m of standard communications type Corning SMF-28 fiber prior to amplification. The amplifier consists of a length of 40 m of low-NA erbium doped fiber. The second spectral peak of the Er-doped fiber amplifier is approximately 12 nm shorter than the oscillator center wavelength. Both the oscillator and the amplifier are pumped with a launched power of 200 mW at a wavelength of 980 nm via a variable coupler, where 40 mW are directed to the oscillator and the rest is directed to the amplifier. With a pulse energy of about 30 pJ (average power approximately 900 μW) launched into the amplifier a single-pass gain of 18 dB was achieved, resulting in an output energy of 1.7 nJ (average power approximately 50 mW). After the fiber amplifier a grating pair was employed for pulse recompression. Due to loss on the gratings, after compression the output energy was about 1.4 nJ. The amplified pulses had a typical FWHM pulse width of 440 fs (assuming a sech^2 shape) and were approximately bandwidth limited as shown in Fig. 3(a). The corresponding pulse spectrum of 6 nm (again experiencing gain narrowing) is shown in Fig. 3(b). As noted in the Nd-doped amplifier experiment, higher-order dispersion from the stretching stage is uncompensated.
Improvements to be implemented in further designs include the following. Replacing the fiber stretcher with a grating stretcher would allow the compensation of higher order dispersion and improve the output pulse compressibility and quality. Using a mixed material amplifier scheme as has already been demonstrated in bulk systems [8] would eliminate the problem of gain narrowing which was observed in both experiments, allowing for sub-100 fs pulse amplification. A pulse selector in conjunction with a multi-stage amplifier set-up would allow full energy extraction. One recent design proposal for erbium-doped fiber amplifiers would make it possible to reach the 100 μJ level [9].
In summary we have demonstrated CPA of ultrashort pulses using both a Nd-doped fiber amplifier and an Er-doped fiber amplifier for the first time. The technique shows the potential of CPA for compact 1.06 μm and 1.55 μm laser systems. With proposed improvements, the CPA technique will be able to reach the micro-Joule saturation energy possible with current rare-earth doped fiber amplifiers in a compact system with sub-100 fs pulses.

The erbium-doped amplifier work was carried out at IMRA, America. MLS, L-MY and GM acknowledge support from the National Science Foundation through the Center for Ultrafast Optical Science under STC PHY 8920108. MEF acknowledges financial support from the Alexander von Humboldt Stiftung.

References

[1] Donna Strickland and Gerard Mourou, Opt. Commun. 56 (1985) 219
[2] M. H. Ober, M. Hofer and M. E. Fermann, Opt. Lett. 18 (1993) 367
[3] K. Tamura, E. P. Ippen, H. A. Haus and L. E. Nelson, Opt. Lett. 18 (1993) 1080
[4] G. P. Agrawal, IEEE Phot. Tech. Lett. 2 (1990) 381
[5] W. J. Tomlinson and W.H. Knox, J. Opt. Soc. Am. B 4 (1987) 1404
[6] M. L. Stock, A. Galvanauskas, M. E. Fermann, G. Mourou and D. J. Harter, Nonlinear Guided Wave Phenomena Topical Meeting, Cambridge (1993) paper PD5
[7] M. E. Fermann, L.-M. Yang, M. L. Stock and M. J. Andrejco, to be publ. in Opt. Lett.

[8] C. Rouyer, E. Mazataud, I. Allais, A. Pierre, S. Seznac, C. Sauteret, G. Mourou and A. Migus, Opt. Lett. 18 (1993) 214
[9] Johan Nilsson and Bozena Jaskorzynska, Opt. Lett. 18 (1993) 2099

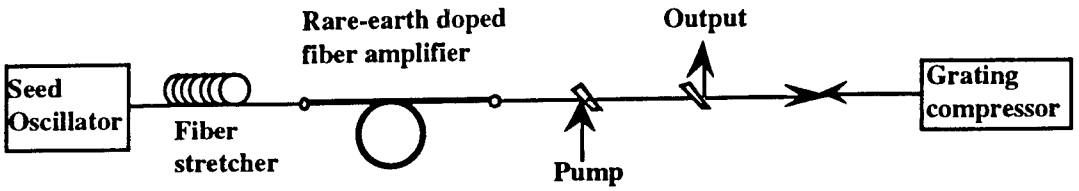


Fig. 1 Schematic of a CPA fiber amplifier system

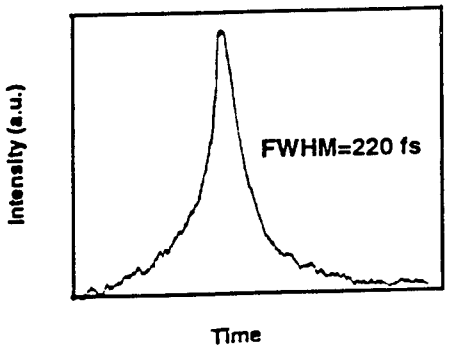


Fig. 2(a)

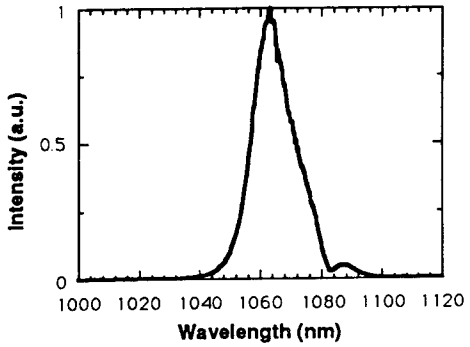


Fig. 2(b)

Fig. 2(a) Autocorrelation trace and (b)spectrum of the shortest recompressed pulse The FWHM pulse duration is 220 fs and the FWHM spectral width is 14 nm.

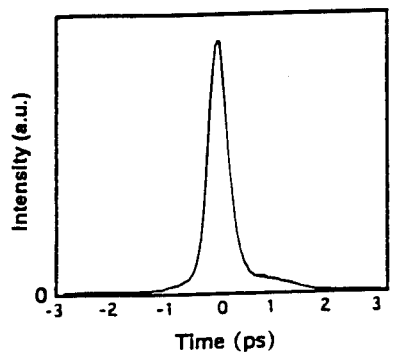


Fig. 3(a)

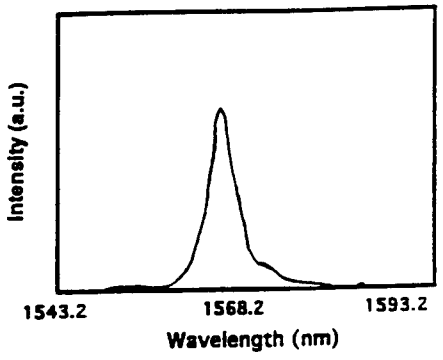


Fig. 3(b)

Fig. 3(a) Autocorrelation trace and (b)spectrum of the shortest recompressed pulse The FWHM pulse duration is 440 fs and the FWHM spectral width is 6 nm.

Excitation-Induced Phase Shifts of Heavy and Light Hole Quantum Beats in Multiple Quantum Wells

W. Sha, A. E. Paul, S. Patkar and Arthur L. Smirl
Center for Laser Science & Engineering, University of Iowa,
144 Iowa Advanced Technology Laboratories, Iowa City, IA 52242, USA.
Tel: (319) 335-3460 Fax: (319) 335-3462

In recent years, transient four-wave mixing (FWM) techniques have been used to investigate the dephasing times of non-equilibrium carriers in semiconductor heterostructures by monitoring the decay of the macroscopic polarization. Initially, this decay was measured by temporally-integrating the scattered FWM signal as a function of time delay between two (or more) pump pulses. More recently, the macroscopic polarization decay has been measured by time-resolving the FWM signal by cross correlating it with an ultrashort laser pulse via frequency up-conversion in a nonlinear crystal. When excitons with slightly different energies are excited, oscillations (or beats) have been observed both in the time-integrated FWM signal and in the time-resolved FWM signal. Such beats have been observed, for example, between light- and heavy-hole excitons and between excitons in wells of different widths. Both the spectral behavior[1] of the time-integrated FWM signal and the temporal behavior[2] of the time-resolved signal have been shown to allow the distinction between the polarization interference associated with two independent oscillators and the quantum beats associated with two coupled oscillators which share a common level. In addition, it has been demonstrated[3] that the quantum beats produced by incident pulses with parallel polarizations are exactly out of phase (by π) with the beats produced by orthogonally polarized pulses. In each case[1-3], the period and phase of the beats and the polarization of FWM signal were explained by using a six-level model, which excluded many-body effects, to describe the J=1/2 conduction and J=3/2 valence states. Within the last few months, however, it has been shown that a complete description of the polarization selection rules for the FWM signal requires excitation-induced dephasing[4] or disorder-induced coupling of the σ^+ and σ^- excitonic transitions[5].

Here, we report an excitation-dependent shift in the phase of the periodic oscillations observed in the time-resolved FWM signal from GaAs/AlGaAs multiple quantum wells (MQWs). The phase is observed to shift dramatically as the incident fluence on the sample is varied or as the central frequency of the incident pulses is tuned relative to the excitonic line centers. We demonstrate that these oscillations are quantum beats, as opposed to polarization interferences, and we demonstrate that the phases of the beats are determined by many-body effects, such as local field corrections and excitation-induced dephasing. While the role of many body effects in describing the formation and decay of the macroscopic polarization and in determining the polarization of the FWM signal is now established, to our knowledge, this is the first demonstration that many body effects are necessary for an accurate description of the quantum beats.

In our experiments, we generate the coherent polarization by using a conventional two-beam mixing (or pump-probe) geometry and monitor its decay by time resolving the FWM signal. Specifically, a ~100 fs pulse produced by a mode-locked Ti:Sapphire laser, which can be tuned across the excitonic resonances of the MQW, is split into three parts. Two parts (pulses with wavevectors $\mathbf{k}_1$ and $\mathbf{k}_2$) are spatially overlapped in the MQW with a small angle (of ~10^0) between the two beams and with a variable time delay τ_{12} between the two pulses. The third part is delayed by a time τ_{13} and is cross correlated with the FWM signal traveling in the direction $2\mathbf{k}_2-\mathbf{k}_1$ by mixing in a second harmonic crystal. The up-converted signal is then measured as a function of τ_{13} for various pump fluences and for various detunings of the central frequency relative to the excitonic line centers. From these measurements, we extract the decay of the polarization and the period and phase of the beats. In this presentation, we focus on the results from a MQW sample composed of 50 periods of 10 nm-wide GaAs wells separated by 7.5 nm-wide $Al_{0.3}Ga_{0.7}As$ barriers. The sample is cooled to ~80 K to allow temporal resolution of the beats, yet ensure that the broadening is homogeneous.

Representative measurements of the up-converted signal are presented in Fig. 1 for

several incident fluences and for s-polarized pump pulses. The decay times and the phases of the quantum beats extracted from these time-resolved FWM signals are summarized in Fig. 2. The relative extracted phases are also indicated schematically by the arrows in Fig. 1. Notice that the decay time for the FWM signal initially decreases with increasing excitonic density then saturates at higher densities, behavior that is consistent with density-induced dephasing processes when excitonic screening is taken into account[4]. By comparison, the phase of the quantum beats increases with increasing density at the lower fluences, but saturates at the higher densities. The similar saturation behavior for the phase suggests that it too may be determined by many body effects. A variation of the quantum beat phase as the central frequency of the incident pulses is tuned relative to the heavy-hole excitonic line center is also observed and is illustrated in Fig. 3.

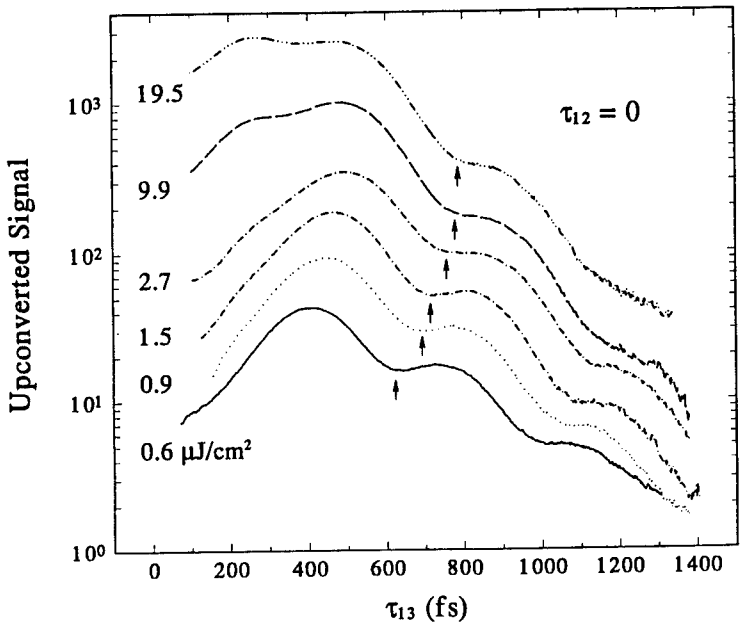


FIG. 1 The upconverted FWM signal as a function of time relative to the first incident pulse for several fluences and for a sample temperature of 80 K. The curves are offset for convenience in viewing, and the arrows indicate positions of a constant phase for the beats, as extracted from these curves and as plotted in Fig. 2.

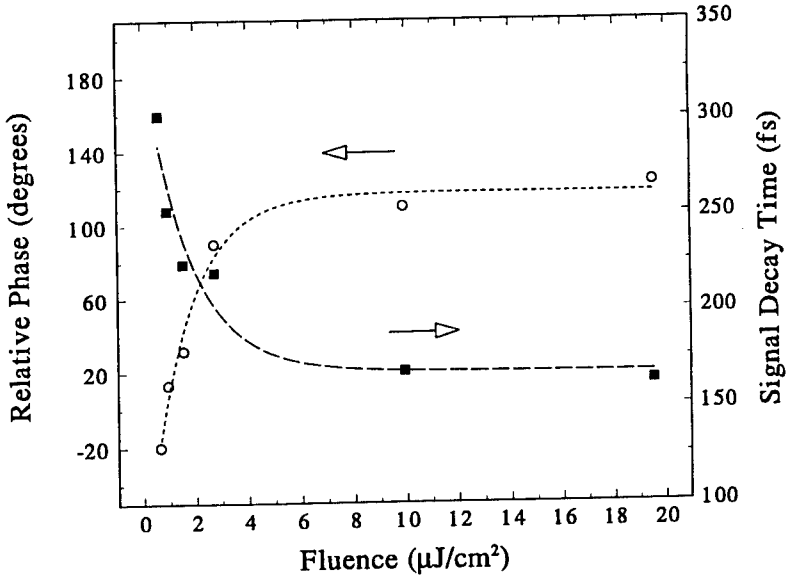


FIG. 2 The quantum beat phases (in degrees) and the decay times (in femto-seconds) extracted from Fig. 1 plotted as a function of total incident fluence.

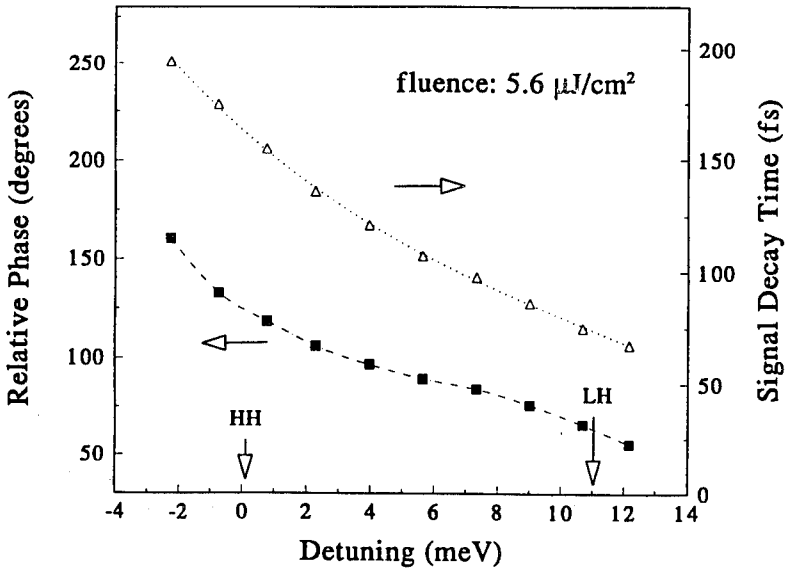


FIG. 3 The quantum beat phases (in degrees) and the decay times (in femtoseconds) extracted from a similar set of time-resolved FWM signals obtained by tuning the central frequency of the exciting radiation from the heavy-hole exciton toward the light-hole exciton.

We compare our results to two phenomenological models. Both describe the J=1/2 conduction and J=3/2 valence bands in terms of a six level model. One, however, excludes many body effects, while the other includes a local field correction and exicitation-induced dephasing. The model without many body effects predicts no shift of the quantum beat phase with either excitation level or detuning (except for finite pulse effects, which are small compared to those measured). By contrast, the many-body model predicts large phase shifts and saturation behavior similar to that measured. In addition, the many-body model predicts that the beat frequency will be shifted slightly from that predicted by the light-hole and heavy-hole splitting and that the phase will be chirped (i.e. change in time). Both of these features agree qualitatively with our measurements. A detailed comparison of the calculated and measured features will be presented.

References

1. V.G. Lyssenko, J. Erland, I. Balslev, K.-H. Pantke, B.S. Razbirin, and J.M. Hvam, Phys. Rev. B **48**, 5720 (1993).
2. M. Koch, J. Feldmann, G. von Plessen, E. O. Gobel, P. Thomas, and K. Kohler, Phys. Rev. Lett. **69**, 3631 (1992).
3. S. Schmitt-Rink, D. Bennhardt, V. Heukeroth, P. Thomas, P. Haring, G. Maidorn, H. Bakker, K. Leo, D.-S. Kim, J. Shah, and K. Kohler, Phys. Rev. B **46**, 10460 (1992).
4. H. Wang, K. Ferrio, D. Steel, Y.Z. Hu, R. Binder, and S. W. Koch, Phys. Rev. Lett. **71**, 1261 (1993).
5. R. Eccleston, J. Kuhl, D. Bennhardt, and P. Thomas, Solid State Comm. **86**, 93 (1993).

Resonance Transient Population Grating Spectroscopy of Ultrafast Solvation Dynamics

B.D Fainberg, S.Y. Goldberg and D.Huppert

Beverly and Raymond Sackler Faculty of Exact Sciences, School of Chemistry,

Tel Aviv University, Ramat Aviv, Tel Aviv 69978, Israel

Tel: 972-3-6408903

Solvation dynamics has been extensively studied in the past decade using time resolved luminescence (TRL) techniques [1]. Large polar molecules embedded in polar liquids exhibit a broad and featureless electronic optical spectra. For such molecules, there is a hierarchy of relaxation times of the vibronic transition under consideration [2]: $\sigma_2^{-1/2} < T' << \tau_c$. Here $\sigma_2^{-1/2}$ plays the role of the reversible dephasing time of a vibronic transition, σ_2 is the second central moment of a spectrum corresponding to the vibronic transition, τ_c is the vibrational relaxation time, and $T'=(\tau_c\sigma_2^{-1})^{1/3}$. The experimental conditions of our transient degenerate four-wave mixing experiment have been chosen to provide similar information to the ones given by time-resolved luminescence studies. TRL experiments investigate the hot luminescence processes occurring after the completion of the electronic transition phase relaxation (with a characteristic decay time T') and during the vibrational and solute-solvent relaxation in the excited electronic state.

We have used relatively long pulses with durations $t_p >> T'$ ($t_p \approx 140$ fs, $T' \approx 20$ fs [2]) to avoid the polarization grating contribution to the signal that is destroyed during the time T'. For carrying out specific calculations we considered that the intramolecular relaxation took place within t_p. The following topics have been considered:

1. "Condon" RTPGS

The principles of the "Condon" RTPGS is illustrated in the insertion to Fig.1. Two pump pulses with wave vectors $\mathbf{k}_1$, $\mathbf{k}_2$ and frequency ω, create a hole in the initial thermal distribution relative to the generalized solvation coordinate in the ground electronic state. Apparently, such formations have a space modulation $\sim\exp[-i(\mathbf{k}_1-\mathbf{k}_2)\mathbf{r}]$. These distributions tend to the equilibrium of the corresponding potentials over time, and are also broadened during their movements. The changes are measured by the probe pulse ω, $\mathbf{k}_3$ delayed by a time τ relative to the pump pulses. We have shown that the signal intensity $J_S(\tau)$ can be expressed by the correlation function of the solvation dynamics $S(\tau)$. We plot in Fig.1 the calculated $J_S(\tau)$ (curve a) corresponding to $S(\tau)$ (curve b). One can see that the dependence of $S(\tau)$ and $J_S(\tau)$ reflects the fine details of $S(\tau)$. We have used LDS 750 as a probe molecule and the solvents used were monools and diols. Fig.2 shows the time resolved signal of LDS 750 in 1,3-propanediol measured by RTPGS. The experimental signal can be fitted by a short Gaussian component ~100 fs followed by several exponential components. The fact that we observe more than one relaxation time is in agreement with the dielectric relaxation properties of alcohols. The RTPGS data between ~50 ps and 200 ps match quite nicely to the solvation dynamics measured by TRL measurements. The experimental (Fig.2) and the theoretical behavior of

the signal are similar. Thus, the RTPGS can be used for the study of ultrafast solvation dynamics.

2. Transient polarization "non-Condon" spectroscopy

We have developed the principles of a new method for the investigation of Herzberg-Teller (HT) effects (mixing different electronic molecular states by vibrations) by transient polarization four-photon spectroscopy. The method is based on the following. The signal behavior in transient resonance four-photon spectroscopy does not depend on the polarization of the excitation pulses if one assumes that the electronic waves functions do not depend on the nuclear coordinates ("Condon" approximation). In contrast, when electronic wave functions and, consequently, the dipole moment of the electronic transition depend on the nuclear coordinates (due to the HT interactions), then in general, the signal depends on the polarization. Thus, we propose to conduct transient four-photon resonance experiments by two methods: (a) RTPGS with parallel polarizations of all pulses, and (b) induced resonance optical Kerr effect (OKE). The comparison of both signals provides pertinent information on the contribution of HT interactions. We have obtained expressions for the "non-Condon" signal and conducted OKE measurements of LDS 750 in monools and diols.

3. A new model for the description of solvation dynamics: the non-Markovian oscillator (NMO)

The theory of RTPGS and the transient polarization spectroscopy of solvation dynamics connects a four-photon signal with the solvation correlation function S(t). Its calculation is an independent problem. We propose a new model (NMO) for the description of solvation dynamics. Fig.3 shows the correlation function S(t) for the NMO model (3a) and the corresponding RTPGS signal $J_S(\tau)$ (3b). We also used the NMO model for the description of a number of experimental and computer simulations of solvation correlation functions. Using a model comprised of two NMOs, we have described the experimental correlation function of Reference [1b] and computer simulations data given in references [3,4]. The fit (solid line) to the latter data (circles) is shown in Fig.4. The NMO model allows to diminish essentially the number of fitting parameters in comparison with a model consisting of a multimode Brownian oscillator [3].

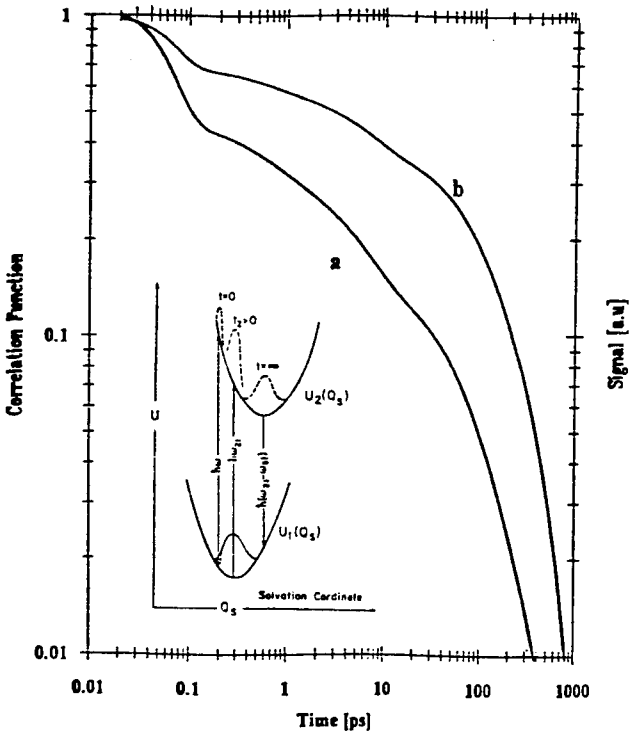


Fig. 1

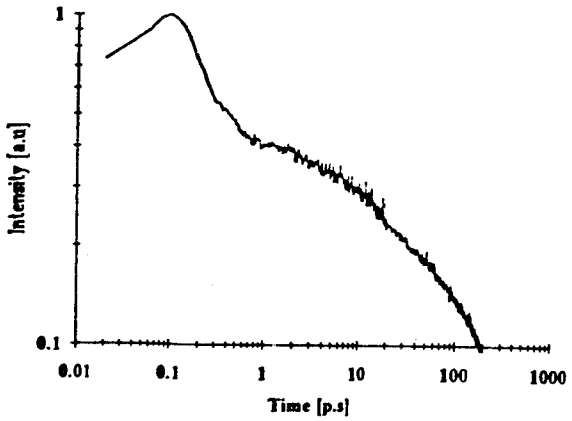


Fig. 2

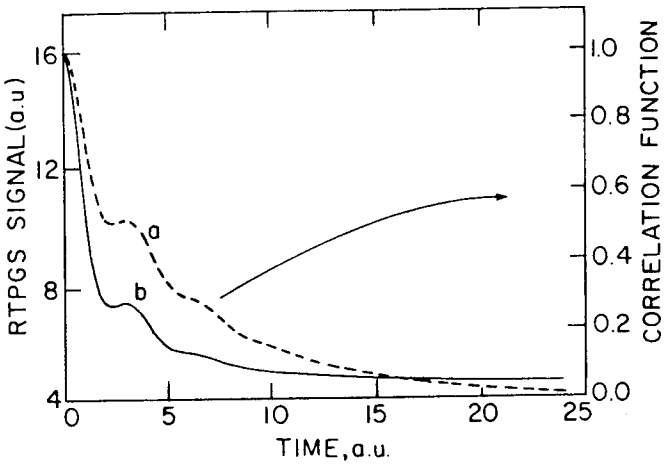


Fig.3.

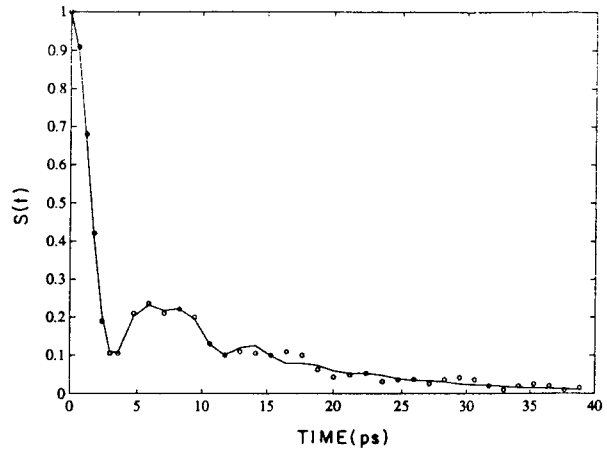


Fig.4.

References

1. a) P.F.Barbara, and W.Jarzeba. Adv. Photochem., 15 (1990) 1; b) S.J. Rosensthal, X. Xie, M. Du, and G.R. Fleming. J. Chem. Phys. 95 (1991) 4715.
2. B.D. Fainberg. Opt. Spectrosc. 68 (1990) 305; Chem. Phys. 148 (1990) 33; Phys. Rev. A 48 (1993) 849.
3. L.E. Fried, N. Bernstein, and S. Mukamel. Phys. Rev. Lett. 68 (1992) 1842.
4. E. Neria, A. Nitzan. J. Chem. Phys. 96 (1992) 5433.

The role of solvent and vibrations on proton tunneling in clusters

JACK A. SYAGE

The Aerospace Corporation, P. O. Box 92957/M5-754, Los Angeles, CA 90009 (310-336-1583)

Clusters are an important medium for studying properties of the bulk on an atomic or molecular level and for understanding departures from bulk-phase behavior as the system size approaches the single-molecule gas-phase limit. In this paper we investigate the role of solvent vibrations on proton tunneling by comparing emerging theories of tunneling in clusters to recent time-resolved measurements. Our ultimate goal is to develop a theory that is applicable to both the cluster and bulk-phase limits.

These discussions focus on excited-state proton transfer reactions (ESPT) of the form

$$ROH^* \cdots B_n \underset{k}{\longrightarrow} [RO^{*-} \cdots H^+B_n]_{ur} \underset{k_s}{\longrightarrow} [RO^{*-} \cdots H^+B_n]_r$$

where ROH is an aromatic acid (e.g., 1- and 2-naphthol, and phenol), B is a base-type solvent molecule, and n is the number of solvent molecules in the cluster. We assume a two-step process involving initial proton transfer followed by solvent reorganization from an unrelaxed ur to a relaxed r configuration. In a typical experiment, a molecular beam of clusters is photoexcited by a pump pulse and the evolution of reactant and product is monitored by a variably-delayed probe pulse using multiphoton ionization. Measurements are conducted by mass spectrometry or photoelectron spectroscopy.[1–3] The following observations summarize our understanding of ESPT in clusters:

(1) A distinct minimum cluster size is evident for ESPT, which is explained by a free energy $\Delta G_{0,n}$ that decreases in discrete steps for small values of n.[1–6] The reaction threshold for $PhOH(NH_3)_n$ occurs at $n = 5$ as observed in Fig. 1.[1,3] The onset occurs at $n = 3$ for 1-$NpOH(NH_3)_n$, as measured by Zewail *et al.*[4] and Kelley and Bernstein *et al.*,[5] and is due to the greater acidity of 1-NpOH relative to PhOH. In both cases, the reaction rate is fairly constant with increasing n.

(2) The measured rates of ESPT are relatively slow and increase with energy suggesting a barrier process.[1–5] The potential energy diagram in Fig. 1 indicates that the proton transfer state derives from a high-lying charge-transfer state of phenol that is stabilized by solvent molecules. A barrier arises from a surface crossing.

(3) A tunneling mechanism is evident by a strong proton/deuteron isotope effect for 1-NpOH[5] and PhOH[1] in $(NH_3)_n$. In phenol/ammonia at 2500 cm^{-1} vibrational energy the ESPT lifetimes for $n = 5$ and 6 range from 1–2.5 ns for deutero clusters versus about 60 ps for the protio clusters.[2] The observation of ESPT from the vibrationless levels of 1-$NpOH(NH_3)_n$ also supports a tunneling mechanism.[4,5]

(4) The proton is strongly coupled to product and solvent vibrational modes as evidenced by a large structural change that occurs after proton transfer. In time-resolved experiments using mass spectrometry and photoelectron spectroscopy, we measured a reorganization time of 300 ps and a reorganization energy of about 0.5 eV.[3]

Concerning proton tunneling models for clusters, Hineman *et al.* (HBKB)[5] considered a bound-to-continuum proton transition while we adopted a solvent-activated model[7] involving a bound-to-bound proton transition.[2] Recently, we extended the solvent-activated model to include coupling of the reaction coordinate to a manifold of product vibrations. The HBKB model, by assuming

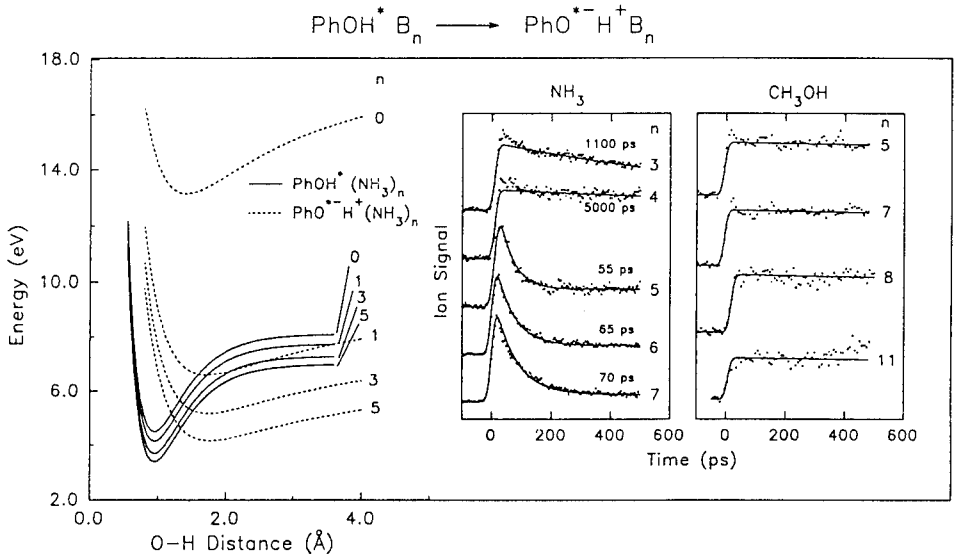


Figure 1. Approximate $PhOH(NH_3)_n$ cluster potential energy curves for the reactive PhO–H coordinate. Insert shows observed lifetime of the reactant $PhOH^*B_n$ (as measured by $PhOH^+B_n$ detection) in solvent clusters $(NH_3)_n$ and $(CH_3OH)_n$ at 2500 cm^{-1} internal energy.

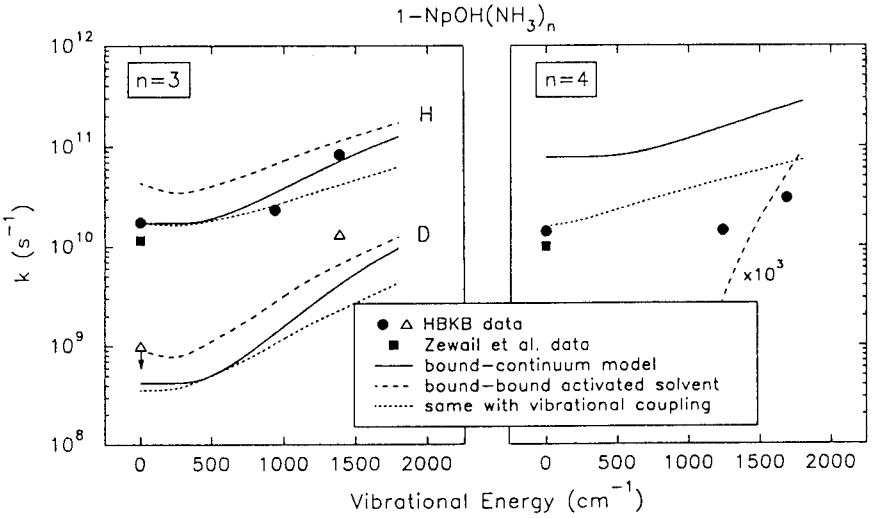


Figure 2. Calculated energy dependence of k by the three models of tunneling and comparison to measurements for 1-$NpOH(NH_3)_n$ and 1-$NpOD(ND_3)_n$. See Ref. 2 for details,

a continuum of product states, does not predict a rate dependence on ΔG_0, other than that due to changes in the O–H barrier. The activated solvent model predicts a steep dependence of k on ΔG_0 and an exaggerated inverted region. The inverted region becomes less severe when vibrational coupling is included. Our treatment of the manifold of product accepting states is based on a Franck-Condon treatment common to radiationless transition and resembles a structured quasicontinuum.[2]

Calculated results are compared to experiment in Figs. 2 and 3. The HBKB model agrees well with the vibrational energy dependence of k for 1-$NpOH(NH_3)_n$ and 1-$NpOD(ND_3)_n$. However, it is unsuccessful in predicting the relative rate for $n = 3$ versus $n = 4$,[2,5] due to the use of a product continuum, which assumes that k is independent of ΔG_0. The bound-bound tunneling models, on the other hand, predict a strong dependence of k on ΔG_0. For $n = 3$ in Fig. 2, the solvent-activated bound-bound tunneling model predicts a decrease in $k(E)$ for small E followed by an increase at larger E. The downturn is a peculiarity of the classical solvent model when the solvent barrier is

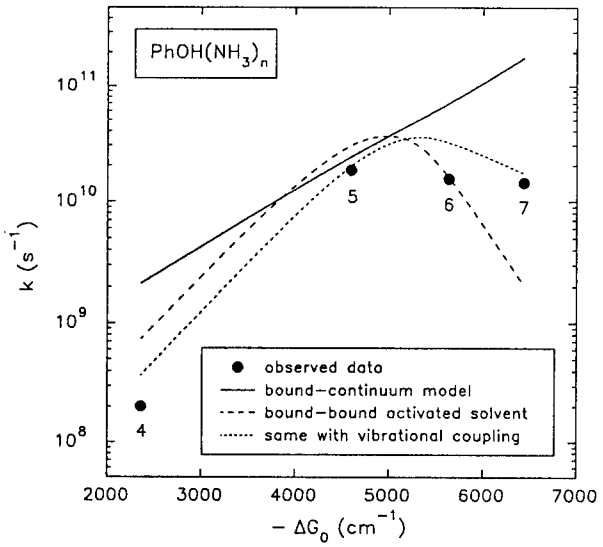


Figure 3. Calculated dependence of k on cluster size n and ΔG_0 by the three models of tunneling and comparison to measurements for $PhOH(NH_3)_n$. See Ref. 2 for details

at a minimum. For $n = 4$, ΔG_0 decreases by about 0.3 eV as determined from stepwise solvation energies reported elsewhere.[1,3] Hence, ΔG_0 enters the inverted region where the activated-solvent model predicts very slow rates and a highly exaggerated $k(E)$ energy dependence. Including the coupling of product vibrations to the O–H coordinate overcomes this problem as illustrated in Fig. 2. A moderate and smoothly varying $k(E)$ energy dependence is obtained.

An important feature to note is that the bound-bound models are in better agreement with the absolute value of k for $n = 4$ better than is the bound-continuum model. This is seen more clearly in Fig. 3 where the calculated results are compared to the measured cluster size dependent rate constants for $PhOH(NH_3)_n$ (Fig. 2). As noted earlier, k is relatively insensitive to n and ΔG_0 for 1-$NpOH(NH_3)_n$ and $PhOH(NH_3)_n$, an observations that at first seemed baffling. The HBKB bound-continuum model predicts an exponentially increasing k with ΔG_0 due to a decrease in the barrier height and width along the O–H coordinate. The activated-solvent models have an additional dependence on ΔG_0 that appears in the solvent activation energy. However, in the absence of product vibrational coupling, the dependence is exaggerated (Fig. 3). With vibrational coupling added to the model, the effect is moderated and more realistic.

1. J. A. Syage and J. Steadman, *J. Chem. Phys.* **95,** 2497 (1991). J. Steadman and J. A. Syage, *J. Am. Chem. Soc.* **113,** 6786 (1991).

2. J. A. Syage *J. Phys. Chem.* **97,** 12523 (1993). J. A. Syage, *Faraday Discuss. Chem. Soc.,* in press (1994). J. A. Syage, *Proc. SPIE - Int. Soc. Opt. Eng.* **2124,** in press (1994).

3. J. A. Syage, in *Ultrafast Spectroscopy in Chemical Systems,* edited by J. D. Simon (Kluwer Academic Publishers, New York, 1993), p. 289. J. A. Syage, in *Femtosecond Chemistry,* edited by J. Manz and L. Wöste (VCH Publishers, New York, 1994).

4. J. J. Breen, L. W. Peng, D. M. Willberg, A. Heikal, P. Cong, and A. H. Zewail, *J. Chem. Phys.* **92,** 805 (1990).

5. M. F. Hineman, G. A. Bruker, D. F. Kelley, and E. R. Bernstein, *J. Chem. Phys.* **97,** 3341 (1992).

6. O. Cheshnovsky, and S. Leutwyler, *J. Chem. Phys.* **88,** 4127 (1988). C. Jouvet, C. Lardeux-Dedonder, M. Richard-Viard, D. Solgadi, and A. Tramer, *J. Phys. Chem.* **94,** 5041 (1990).

7. D. C. Borgis and J. T. Hynes, *Chem. Phys.* **170** 315 (1993). P. F. Barbara, G. C. Walker, and T. P. Smith, *Science,* **256,** 975 (1992).

Paper Withdrawn

Picosecond Photon Echo Studies of Mixed Molecular Solids at High Pressure

Eric L. Chronister
Department of Chemistry, University of California, Riverside
Riverside, California 92521
Phone: (909) 787-3288 FAX: (909) 787-4713

High pressure photon echo results are presented for pentacene doped naphthalene, pentacene doped (triclinic and monoclinic) p-terphenyl, and rhodamine doped PMMA. Figure 1 illustrates typical photon echo intensity decays in a high pressure diamond anvil cell at variable low temperatures. The effect of pressure and temperature on the homogeneous dephasing is used to characterize the interactions between the impurity molecule and the host crystal, as well as provide a unique probe of local polymorphic phase changes.

Narrowing of the homogeneous linewidth is observed at high pressure, and temperature dependent photon echo measurements of electronic dephasing yield an Arrhenius behavior, as shown in Figure 2. Pressure induced changes in the activation energy indicate that the longer dephasing times of pentacene in monoclinic p-terphenyl at high pressure are due to an increase in the pseudolocal phonon frequency (i.e. a decrease in the thermal occupation), as shown in Figure 2. In contrast, pressure dependent photon echo measurements on pentacene in the triclinic form of p-terphenyl show that the pseudolocal phonon frequency *decreases* at higher pressure. The, pressure dependent changes in electronic dephasing in the triclinic host crystal occur due to changes in the pseudolocal phonon *lifetime* at high pressure. Both the mode softening in the triclinic crystal and the pressure induced frequency increase in the monoclinic phase are summarized in Figure 3. The triclinic to monoclinic phase transition is near 6 kbar at low temperature and is most likely the origin of the observed pseudolocal mode softening.

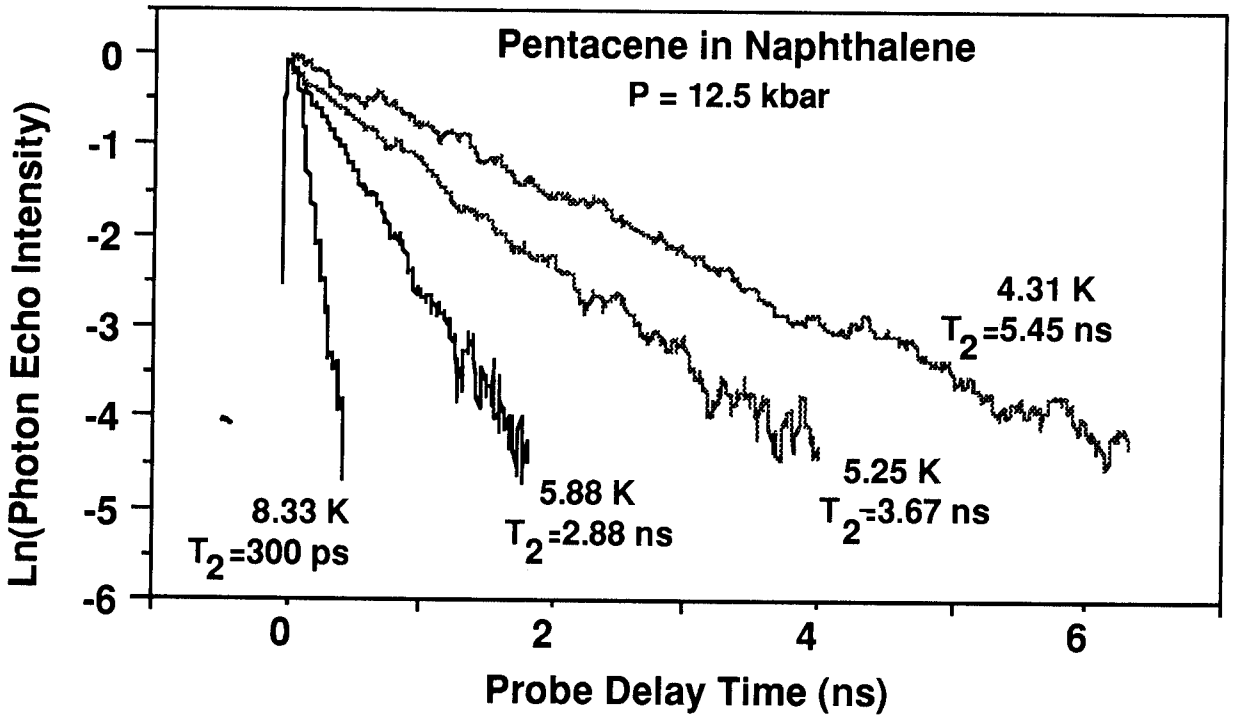


Figure 1. Photon echo decays at several temperature in a high pressure diamond anvil cell

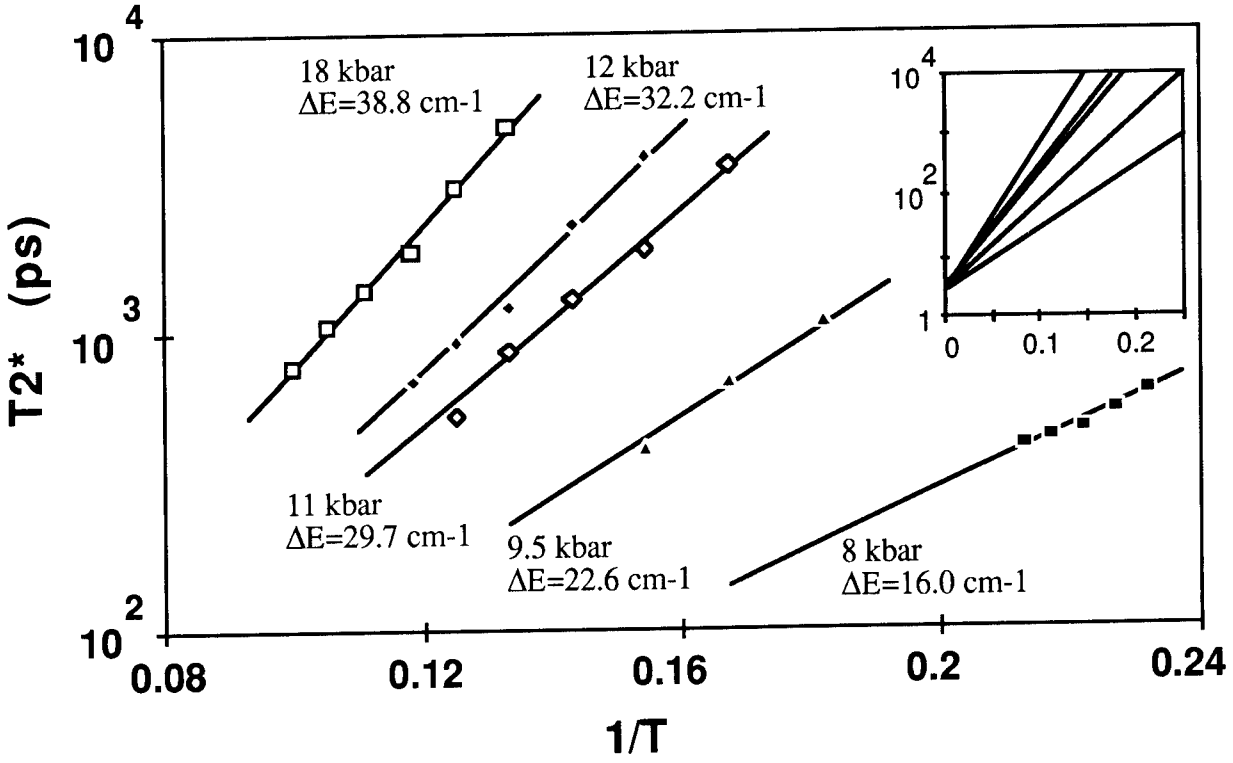


Figure 2. T_2^* results from photon echo measurements of pentacene in monoclinic p-terphenyl

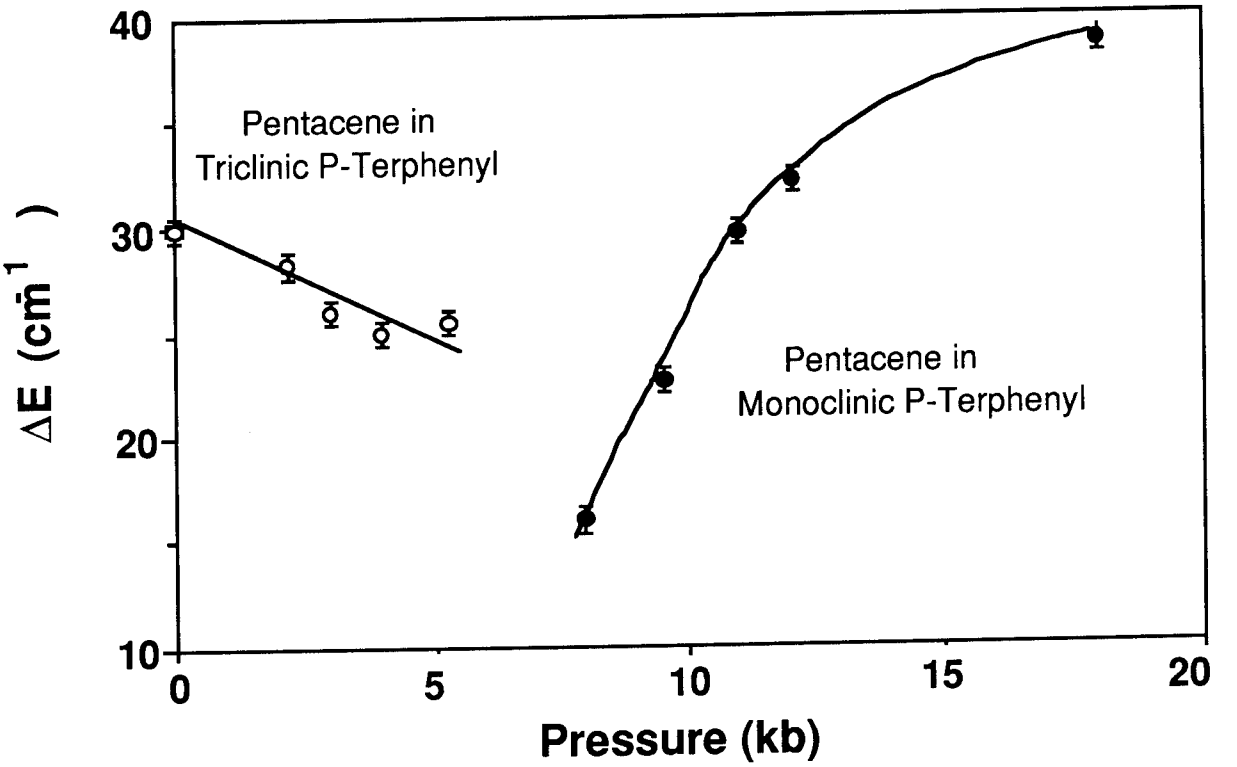


Figure 3. Pseudolocal phonon energy (ΔE) vs. pressure.

Quantum-Confined Systems

TuE 4:30pm–6:15pm
Dana Point Ballroom

Jagdeep Shah, *Presider*
AT&T Bell Laboratories

Trends in Ultrafast Physics of Quantum Confined Systems

Daniel S. Chemla
Department of Physics, University of California at Berkeley
Materials Sciences Divisions, Lawrence Berkeley Laboratory

In the last decade, quantum confined semiconductor structures (QCSS) have attracted much attention because of their novel properties and their potential for electronic and photonic applications [1]. Quantum size effects appear in a semiconductor structure when one of its dimensions is in the range 10Å <L<500Å. In these materials the typical values of group and phase velocities of elementary excitations are such that the corresponding times are in the range 10fs<t<500fs. Therefore reduced dimensionality also implies ultrafast dynamics. In this talk we review the most significant results obtained in the investigation of ultrafast processes in QCSS. We also describe recent experiments that reveal some open questions in ultrafast physics of QCSS, which we discuss. The present summary gives a flavor of the topics covered by the lecture.

Electrical and optical properties of QCSS are governed by quantum statistics and Coulomb correlation. In particular, quantum confinement modifies the electronic density of states and enhances excitonic effects. Conventional effective mass approximation models of semiconductors taking into account these two aspects of QCSS physics were able to interpret the first experimental studies of ultrafast processes in QCSS. This includes exciton ionization by LO-phonon collision, underlying Fermi statistics of dense exciton gases [1] and relaxation of non-thermal populations of electrons and holes (e-h) [2]. This approach was applied to elucidate the ultrafast physics of optoelectronic devices, such as gain compression in QW lasers, saturation and carrier sweep out in modulators and charge accumulation in resonant tunneling diodes.

Quickly, however, experimental observations demanded more elaborate theories. For example, it was found that relaxation of non-thermal e-h distributions in the presence of a Fermi-sea of electrons could be completed in a time shorter than the inverse plasma frequency [2]. In pump probe

experiments the spectral hole was found to be red shifted with respect to the pump spectrum [2]. Excitation in the transparency domain resulted in an excitonic AC-Stark effect whose features departed significantly from that observed in atomic systems [3]. In coherent wave mixing experiments, signals were observed at negative time delay, Δt, in clear contradiction with independent level models of optical transitions [4]. The recognition that Coulomb correlation is responsible for these novel effects leads to description of semiconductor-light interaction in which the internal Coulomb interaction is treated on the same footing as the applied electromagnetic field [5]. This approach, which generalizes the Bloch theory of optical transitions in atomic systems, is now referred to as the Semiconductor Bloch Equations (SBE) [6]. It has been successful in explaining some of the aforementioned observations. An intuitive, and yet physically sound, way to explain the main point of the SBE is that the effective mass parameters, conduction-valence band energy differences, interband transition amplitude, effective masses etc, all experience an electromagnetic field induced renormalization. In the case of excitation by ultrashort pulses this renormalization is, of course transient. Within this formalism the excitonic AC Stark effect was explained as a Bose condensation of virtual excitons, stimulated by the applied EM field. Several unusual features, such as shifts without saturation, were observed [7] and explained by SBE theories [8]. It was recognized that even for real excitation, in the initial phase of the interaction the off diagonal terms of the density matrix are as important as the diagonal ones. Hence, polarization wave scattering plays a very important role on the ultrashort time scale. Furthermore, since each photocarrier generated by ultrashort pulse is spread over a large portion of k-space, polarization wave scattering has nontrivial dynamics [9]. This scattering adds to the usual "Boltzmann one" accelerating the relaxation. A number of unusual effects directly related to polarization wave scattering were observed. For example it was found that the coherent emission from quantum wells consisted of two contributions, the one due to Coulomb mediated polarization wave being significantly time delayed with respect to the instantaneous response due to Pauli exclusion [10].

More recently, careful pump and probe experiments demonstrated that the photo-generated carriers behaved as non-equilibrium Fermi-sea causing the shift of the spectral hole [11]. This was interpreted as a non-equilibrium Fermi-edge singularity [12]. Three pulse photon echo on zero dimensional

microcrystalites [13] revealed the importance of the electron-phonon interaction and was able to separate LO-phonon scattering from other sources of polarization dephasing. The unusual temperature dependence of this remaining relaxation hinted at a strong contribution from acoustic phonons as supported by subsequent theory [14]. Spectroscopic experiments were extended to measurement of the phase in coherent wave mixing in QW [15]. The general features of these very delicate investigations were accounted for by SBE models. The theory, however, failed to explain important aspects of the observations which could be traced to the Lorenztian treatment of dephasing and statistical description of screening [16]. This points out the need for a non-Markovian theory of both the electron-electron and the electron-phonon interaction. Finally excitation of modulation doped heterostructures in the transparency domain demonstrated the distinct nonlinear response of Fermi-edge singularities as compared to excitons [17], challenging theorists to develop novel approaches [18]

The most recent studies clearly show that as the experimental methods become more refined, they reveal the importance of memory effects. The combination of extremely short time scale of the measurements with extremely small size of QCSS limits the number of elementary interactions to a few processes. This therefore calls for a rigorous description of kinetic processes in QCSS, departing from the mean-field and statistical approaches that have been successful to describe bulk materials. Although the framework of these theoretical developments is now available [19], they have not yet been applied to complicated experiments.

This work was supported by the Director, Office of Energy Research, Office of Basic Energy Sciences, Division of Materials Sciences of the US Department of Energy, under contract No. DE-AC03-76SF00098.

References

[1] S. Schmitt-Rink, D.S. Chemla, D.A.B. Miller, Adv. Phys., **38**, 89 (1989),
[2] W.H. Knox , "Optical Studies of Femtosecond Carrier Thermalization in GaAs", in "Hot Carriers in Semiconductor Nanostructures", Ed. J. Shah, Academic Press, NY (1992) and reference therein.
[3] A. Mysyrowicz, D. Hulin, A. Antonetti, A. Migus, W.T. Masselink, H. Morkoc, Phys. Rev. Lett. **56**, 2748 (1986); A. Von Lehmen, D.S. Chemla, J.E. Zucker, J. Heritage, Opt. Lett. **11**, 609, (1986).
[4] K. Leo, M. Wegener, J. Shah, D.S. Chemla, E.O. Gobel, T.C. Damen, S. Schmitt-Rink, W. Schafer, Phys. Rev. Lett. **65**, 1340 (1990); M. Wegener, D.S. Chemla, S. Schmitt-Rink, W. Schafer Phys. Rev **A42**, 5675 (1990)
[5] S. Schmitt-Rink, D.S. Chemla, Phys. Rev. Lett. 57, 2752 (1986); S. Schmitt-Rink, D.S. Chemla, H. Haug, Phys. Rev. **B37**, 941 (1998)
[6] W. Schäfer, "Manybody Effetcs in Nonlinear Optics of Semiconductor Structures" in "Optics of Semiconducror Nanostructures" ed. F. Henneberger, S. Schmitt-Rink E.O. Göbel, Akademie Verlag, Berlin (1993) and references therein
[7] W.H. Knox, D.S. Chemla, D.A.B. Miller, J.B. Stark, S. Schmitt-Rink, Phys. Rev. Lett. **62**, 1189, (1989), M. Joffre, D. Hulin, A. Antonetti, J. Phys. Paris, **C5**, 537 (1987)
[8] C. Ell, J.F. Muller, K. El-Sayed, H. Haug, Phys. Rev. Lett. **62**, 304, (1989), W. Schafer, Festkorperprobleme/ Advances in Solid State Physics, **28**, 63 (1988)
[9] A.V. Kuznetsov, Phys. Rev. **B44**, 8721 (1991-II) and 13381 (1991-II)
[10] S. Weiss, M-A Mycek, J-Y. Bigot, S. Schmitt-Rink, D.S. Chemla Phys. Rev. Lett. **69**, 2685 (1992), D-S. Kim, J. Shah, T.C. Damen, W. Schaffer, F. Jahnke, S. Schmitt-Rink, K. Kohler, Phys. Rev. Lett. **69,** 2725 (1992)
[11] J.-P. Foing, D. Hulin, M. Joffre, M.K. Kackson, J.-L. Oudar, C. Tanguy, M. Combescot, Phys. Rev. Lett. **68**, 110 (1992)
[12] C. Tanguy, M. Combescot, Phys. Rev. Lett. **68**, 1935 (1992)
[13] R.W. Schoenlein, D.M. Mittleman, J.J. Shiang, A.P. Alivisatos and C.V. Shank, Phys. Rev. Lett. **70**, 1014 (1993)
[14] T. Takagahara, Phys. Rev. Lett. **71**, 3577 (1993)
[15] J.-Y. Bigot, M.-A. Mycek, S. Weiss, R. G. Ulbrich, D.S. Chemla, Phys. Rev. Lett. **70**, 3307 (1993)
[16] D.S. Chemla, J.-Y. Bigot, M.-A. Mycek, S. Weiss, and W. Schäfer submitted to Phys. Rev.,.
[17] I.E. Brener, W.H. Knox, W. Schäfer , to be published
[18] I.E. Perakis and D.S. Chemla submitted to Phys. Rev. Lett.
[19] M. Hartman and W. Schäfer, Phys. Stat. Sol. b173, 165 (1992), D.B. Tan Thoai and H. Haug. Z. Phys. B91, 199 (1993)

Time-Resolved Studies of Bloch Oscillations in Semiconductor Superlattices

P.Leisching, T.Dekorsy, C.Waschke, W. Beck, H. Roskos, K.Leo[1], H.Kurz, K.Köhler[2]

Institute of Semiconductor Electronics, RWTH Aachen, 52056 Aachen, Germany

[1]Institute of Applied Photophysics, TU Dresden, 01062 Dresden, Germany

[2]Fraunhofer-Institute of Applied Solid State Physics, 79108 Freiburg, Germany

The atomic-layer precision achieved in the MBE growth of GaAs/AlGaAs semiconductor superlattices (SLS) has allowed to observe a variety of interesting novel coherent phenomena on a pico- and subpicosecond time scale upon resonant excitation with femtosecond laser pulses.

Since the discovery and exploration of coherent motion of wavepackets in quantum well structures, the evidence for the existence of Bloch oscillations (BO) moved in the center of interest. BO have been predicted in 1970 by Esaki and Tsu for SLS [1] as the periodic motion of Bloch electrons in a homogeneous electric field F. This has been shown to be equivalent to the beating of coherently excited Wannier-Stark states of the SLS [2]. The first observation of BO succeeded by femtosecond degenerate four-wave mixing (DFWM) experiments [3]. More recently, further evidence was obtained with THz-emission experiments [4].

Here, we report on a comparative study of BO in a series of GaAs/AlGaAs superlattices for temperatures up to 200 K by time-resolved optical and THz experiments performed with Kerr-lens modelocked Ti:sapphire laser pulses.

In the first part, the results of time-integrated and time-resolved DFWM-experiments are presented. In time-integrated experiments, several oscillations are visible if the excitation energy is peaked slightly below the spatially direct heavy hole (0hh) excitonic Wannier-Stark transition. The oscillation frequency can be tuned by an external electric bias up to the frequency resolution limit of the experimental setup at 5 THz. In samples with 50 meV miniband width, BO are observed up to 200 K.

In time-resolved DFWM experiments, free-carrier-induced effects can be clearly separated from the coherent motion of excitonic wavepackets. In Fig. 1, the results of a time-resolved DFWM ex-

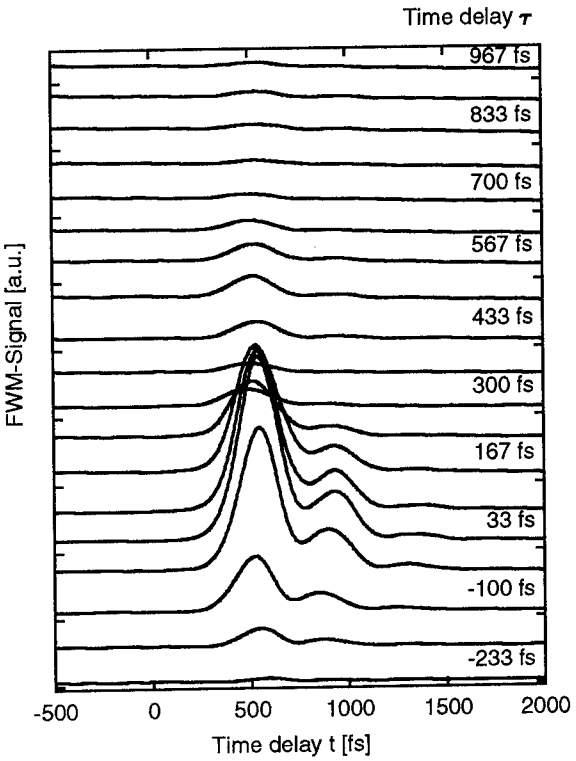


Figure 1: Time resolved DFWM signal for different delays τ at an excitation density of $3*10^9 cm^{-2}$ carriers per period.

periment is summarized. The temporal evolution of the DFWM signal set up by two co-polarized input pulses is mapped out by a third pulse gating the DFWM signal via upconversion. The data are plotted for different delay times τ between the two input pulses at an excitation density of $3*10^9 cm^{-2}$ per period. Due to the excitonic nature of the excited Wannier-Stark states the signal is delayed in time by approximately the phase relaxation time as in earlier experiments in single quantum wells [5]. The delayed signal exhibits BO with a period of 400 fs. Further details give clear evidence for coherent polarization-wave behavior. At an excitation density close to $10^{10} cm^{-2}$ (not shown), a new "prompt" feature appears with a rise time comparable to the duration of the exciting pulses. It can be attributed to free-carrier-induced nonlinear polarization phenomena. The BO-induced DFWM signal appears with the same time-delay as for the lower density. It is weaker due to the interaction between exciton wavepackets and free carriers.

The final proof whether the excitonic wavepacket undergoes BO as predicted by the semiclassical theory is possible by time-resolved transmittive electro-optic sampling (TEOS) and THz experiments. The amplitude and phase of the THz pulse emitted from the wavepacket is temporally resolved by an optically gated subpicosecond photocon-

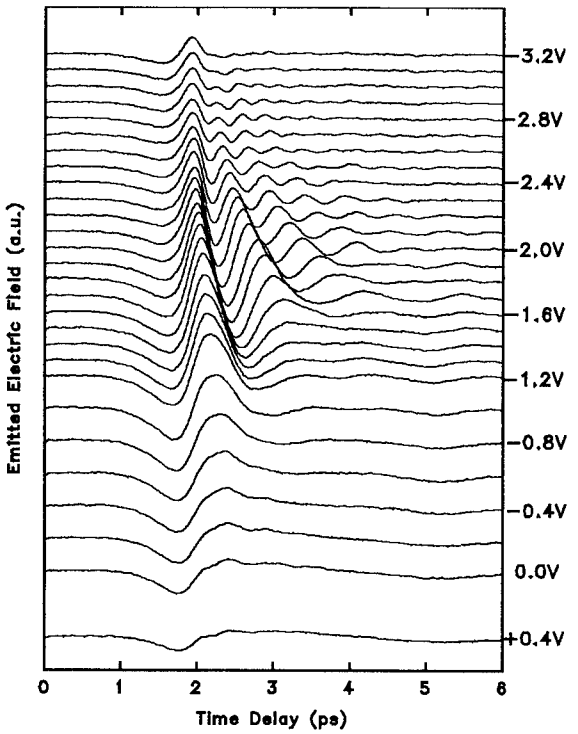


Figure 2: Measured coherent electromagnetic transients at a lattice temperature of 10K.

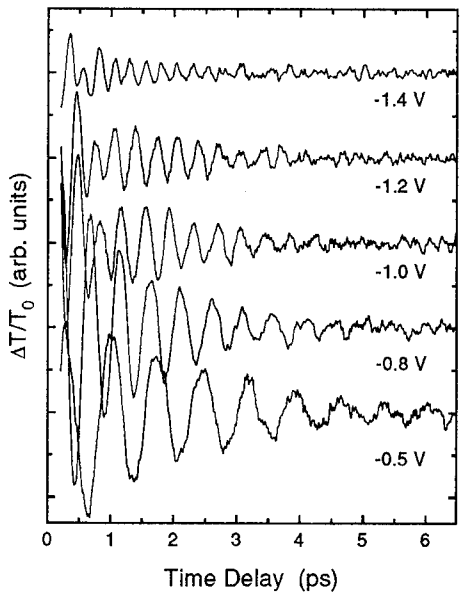


Figure 3: Oscillatory traces of TEOS signals for different voltages applied.

ductive dipole antenna. In Fig. 2, the emitted field transients are plotted at different electrical bias levels. At a reverse bias of -1.6 V, a strong BO-related signal emerges, whose period decreases linearily with increasing applied voltage. Up to six BO are visible at 10 K. The initial part of the transients at high bias voltage is attributed to instan-

taneous polarization associated with the generation process of spatially separated electron-hole pairs.

Complementary results are obtained by an alternative time-resolved technique, electro-optic sampling (TEOS). The experimental measurement of the amplitude and phase of the excitonic wavepacket oscillations launched are of central importance for the fundamental understanding of BO. These data can easily be obtained by electro-optic sampling of the temporal evolution of the dipole moment associated with BO. The oscillating dipole moment induces birefringence resulting in an anisotropic phase retardation of the probe pulse, which can be detected in a pump-probe geometry with femtosecond time-resolution. Such measurements provide details on the amplitude and phase of the total oscillating polarization over a wide range of excitation parameters. As an example, Fig. 3 depicts the periodic modulation of the polarization of the probe pulse transmitted through a SLS biased at different levels. Up to 10 periods of the BO are clearly detected over a time interval much longer than in the case of the DFWM experiments. The frequency shift with bias voltage is clearly visible. The decrease of the amplitude at high reverse bias results from the increasing localization of the Wannier-Stark states leading to a reduction of the dipole moment associated with BO.

Of particular interest is the question, wether the phase of the dipole moment of the coherent wavepacket can be reversed by tuning the wavelength of the excitation. Such a phase reversal is expected for selective excitation of the upper and lower branches of the Wannier-Stark ladder, respectively.

In summary, these comparative studies provide a large body of essential information on Bloch oscillations of wavepackets photo-injected into GaAs/ AlGaAs superlattices. Among many other results, evidence for the interaction between wavepackets and free carriers in continuum states is found. The instantaneous polarization associated with the generation of electron-hole pairs is detected. The dependence of the dipole moment of the Bloch oscillations on the bias field has been measured.

This work has been supported by the Deutsche Forschungsgemeinschaft, the VW foundation and the A. v. Krupp foundation.

[1] L. Esaki, and R. Tsu, IBM J. Res. Dev. **61**, 61 (1970).

[2] G. Bastard and R. Ferreira, in *Spectroscopy of Semiconductor Microstructures*, NATO ASI Series (Plenum, New York, 1989), p. 333.

[3] J. Feldmann, K. Leo, J. Shah, D. A. B. Miller, J. E. Cunningham, S. Schmitt-Rink, T. Meier, G. von Plessen, A. Schulze, and P. Thomas, Phys. Rev. B **46**, 7252 (1992); K. Leo, P. Haring Bolivar, F. Brüggemann, R. Schwedler, and K. Köhler, Solid State Commun. **84**, 943 (1992).

[4] C. Waschke, H. G. Roskos, R. Schwedler, K. Leo, H. Kurz, and K. Köhler, Phys. Rev. Lett. **70**, 3319 (1993).

[5] D.-S. Kim, J. Shah, T. C. Damen, W. Schäfer, F. Jahnke, S. Schmitt-Rink, and K. Köhler, Phys. Rev. Lett **69**, 2685 (1992).

Interplay between Inhomogeneous Broadening and Coulomb Interaction in the Dynamics of Excitonic Wave Packets

M. Koch[1], F. Jahnke[2], T. Meier[1], J. Feldmann[1], W. Schäfer[2], P. Thomas[1], S.W. Koch[1], E.O. Göbel[1], and H. Nickel[3]

[1] *Fachbereich Physik and Wiss. Zentrum f. Materialwissenschaften, Renthof 5, 35032 Marburg, Germany.*

[2] *Optical Sciences Center, University of Arizona, Tucson, Arizona 85721, USA*

[3] *Deutsche Bundespost, Telekom, Fernmeldetechnisches Zentralamt, 64295 Darmstadt, Germany*

Phone: 49–6421–284111 Fax: 49–6421–287036

A proper description of subpicosecond four-wave-mixing (FWM) experiments for excitonic transitions in semiconductor heterostructures must consider the fact that the spectrally broad laser pulses excite not only the $1s$ bound exciton state but also energetically higher bound exciton states and the lower-lying part of the unbound continuum states. In this paper, we report results of transient and time-resolved FWM-experiments in which such 'excitonic wave packets' play a crucial role. In addition, a theoretical treatment of the problem based on the solution of the semiconductor Bloch equations is presented. We show that the time-dependent nonlinear response is determined by an interplay between inhomogeneous broadening and Coulomb interaction.

Recent experiments have shown that the simultaneous excitation of bound and unbound excitonic transitions leads to pronounced modulations of the time-integrated FWM-signal as a function of the time delay τ between the two exciting laser pulses.[1] These experiments have been performed on high-quality, strained InGaAs/GaAs quantum well samples. Due to the inherent strain the $n = 1$ light-hole excitonic transition is considerably blue-shifted and thus allows the sole excitation of the bound and unbound states of the $n = 1$ heavy-hole exciton.[1] A typical result for the transient FWM-signal (measured time-integrated with a slow photodetector) is shown in Fig.1. The observed characteristic temporal modulations can be understood *qualitatively* in terms of the simple excitation scheme shown in Fig.1.[1] The pronounced minimum after the fast initial decay and the subsequent recovery of the signal is due to interference between the $1s$ exciton transition and the continuum transitions. The weak periodic modulations for larger time delays are ascribed to the $1s$-$2s$ beating. As will be shown in this paper, a *quantitative* description,

in particular of the time-resolved FWM-signal, must include inhomogeneous broadening and Coulomb interaction.

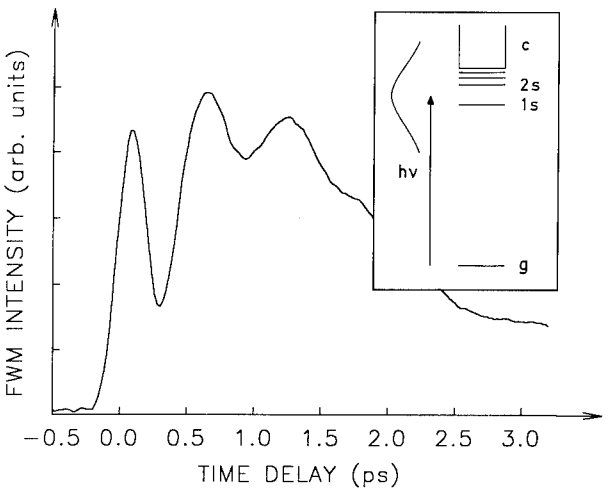
Fig.2a summarizes the experimental results. The time-integrated FWM-signal and the linear absorption spectrum are shown in the insets of Fig.2a. The vertical arrow in the linear spectrum indicates the central photon energy of the laser pulses. The exciton binding energy can be estimated from the linear spectrum and is approximately $7.5meV$, i.e., much smaller than the spectral width of the laser pulses of $21meV$. The main part of Fig.2a shows the time-resolved FWM-signals for various time delays τ. For each time delay τ, an unmodulated, echo-like signal is observed. In particular, the temporal width of this echo-like nonlinear signal increases with increasing time delay, which cannot be explained on the basis of a simple multi-level system.

A quantitative theoretical analysis of the experimentally observed time-integrated and time-resolved FWM-transients must be based on the semiconductor Bloch equations. Numerical solutions of these equations show that the temporal evolution and the strength of the FWM-signal are dominated by Coulomb interactions.[2,3] In particular, the time-resolved FWM-signal consists of a prompt and a delayed, interaction-induced part, which basically reflect, respectively, the electric field term and the polarization term of the renormalized Rabi-frequency.[2,3] Numerical calculations show that a quantitative reproduction of the experimentally observed pronounced modulations of the time-integrated signal and of the unmodulated, broad temporal evolution of the time-resolved signal (see Fig.2a) only occurs when inhomogeneous broadening and excitation induced screening of the Coulomb potential are taken into account. The results of such numerical calculations are summarized in Fig.2b. The agreement between these numerical results and the experimental data shown in Fig.2a is excellent.[4] The beating observed for the time-integrated signal due to interference effects between several bound and unbound excitonic states and the feature-less, echo-like behavior of the time-resolved signal and its changing temporal width are all well reproduced.

The screening of the Coulomb-interaction has two important consequences for the FWM-signals. First, it weakens the delayed interaction-induced part of the time-resolved FWM-transient and partly explains its feature-less appearance. Secondly, the temporal position of the second maximum of the time-integrated signal, which is basically given by the inverse of the exciton binding energy, increases with increasing excitation density.

The fact that the exciton Rydberg energy determines the temporal positions of the beating can be exploited to determine exciton binding energies in semiconductor systems, where inhomogeneous broadening makes a proper determination from linear optical spectra impossible.[5]

FIG. 1: Typical FWM-transient for time-integrated detection together with the excitonic level-system.



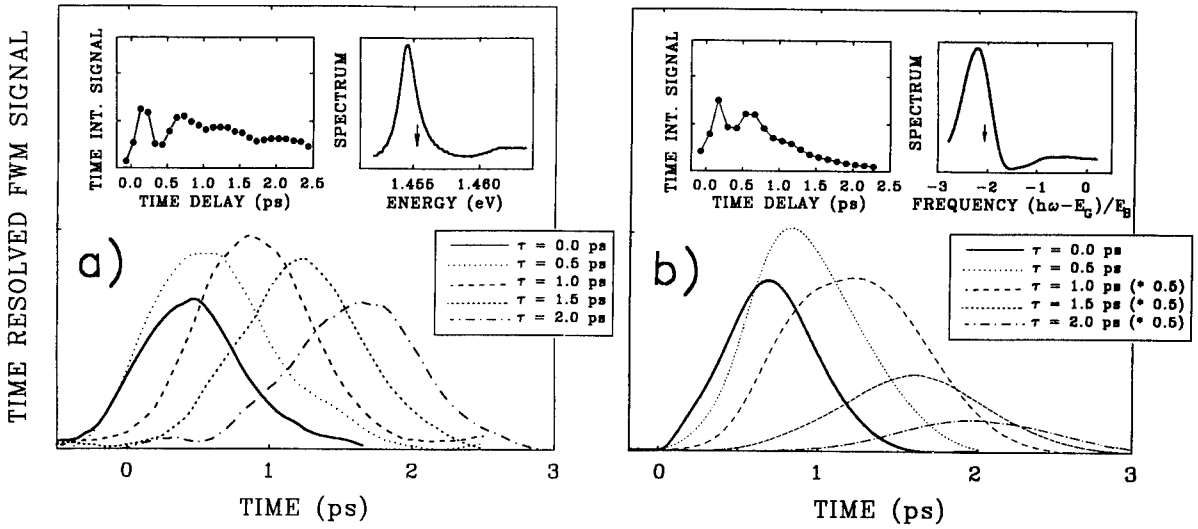


FIG. 2: Comparison of experimental (a) and theoretical (b) results. The figures show the time-resolved FWM-signals for various time-delays τ and the respective insets show the corresponding time-integrated FWM-signals and the linear spectra.

REFERENCES:

1.) J. Feldmann, T. Meier, G. von Plessen, M. Koch, E.O. Göbel, P. Thomas, G. Bacher, C. Hartmann, H. Schweizer, W. Schäfer, and H. Nickel, Phys. Rev. Lett. **70**, 3027 (1993).

2.) M. Lindberg, R. Binder, and S.W. Koch, Phys. Rev. **A45**, 1865 (1992).

3.) W. Schäfer, F. Jahnke, and S. Schmitt-Rink, Phys. Rev. **B47**, 1217 (1993).

4.) A better choice of the dephasing time would certainly lead to a perfect fit.

5.) M. Koch, T. Meier, J. Feldmann, W. Stolz, and E.O. Göbel, to be published.

Coherent Optical Spectroscopy of Electron Scattering in a Two Dimensional Electron Gas in High Magnetic Fields

S. Bar-Ad, I. Bar-Joseph, Y. Levinson and H. Shtrikman
Department of Physics, The Weizmann Institute of Science, Rehovot 76100, Israel
Phone: 972-8-342579 FAX: 972-8-344128

Coherent optical spectroscopy has emerged as an important experimental tool in the study of carrier dynamics in semiconductor quantum wells (QWs). Numerous studies of exciton dynamics have shown that the coherent nonlinear interaction in intrinsic QWs could be described in most cases by a simple two level system model. A more complex behavior is expected in modulation doped (MD) structures, where the interaction between the photo-excited electron-hole pairs and the two-dimensional electron gas (2DEG) is important.

Only a limited number of time resolved optical experiments have been performed on these metal-like systems. Knox *et al.* used differential absorption to study the thermalization in MD QWs.[1] Kim *et al.* have recently conducted a four wave mixing (FWM) experiment in n type MD QWs,[2] and shown that the dephasing of the induced polarization is due to electron-electron (e-e) scattering. In agreement with theory, the scattering rates were proportional to the square of the excess energy above the Fermi level. Such experiments have not been performed in high magnetic fields. The magnetic field significantly changes the electronic wave functions and density of states (DOS), modifying matrix elements, the available phase space for scattering, and thus the scattering rate.

We report the results of FWM measurements in GaAs MD QW in magnetic fields up to B=8T at 4K. We find that the dephasing time at high B, when all the electrons are in the lowest Landau level (LL), is longer than that at B=0, and interpret this as a suppression of the e-e scattering rate in high magnetic field. We discuss e-e scattering, and show that it depends crucially on the inhomogeneous LL broadening. We show that the FWM spectrum at high magnetic field is characterized by a strong enhancement for transitions into the lowest LL. We associate this enhancement with the Fermi edge singularity (FES).

In the experiment we have used a mode-locked, Nd-YAG pumped Styryl 8 dye laser, with a temporal resolution of ~0.7 ps and a spectral width of ~2 meV. The exciting pulses were linearly polarized, either crossed or parallel. We have studied two MD samples, consisting of 30 100 Å GaAs wells between 500 Å $Al_{0.3}Ga_{0.7}As$ barriers, the center 100 Å of which were doped with silicon. The carrier densities in the wells at 4K, $1.8 \cdot 10^{11}$ cm^{-2} and $1.0 \cdot 10^{11}$ cm^{-2}, were deduced from V.d.P. measurements, which also gave mobilities of $4\text{-}5 \cdot 10^4$ cm^2/Vs. The excitation power densities were kept below ~ 10^{10} cm^{-2}, or about 5% of the electron densities in the wells. The absorption spectra of the samples show a gradual change from a continuous two dimensional density of states to discrete LLs as the magnetic field is increased. A new peak appears at the absorption edge each time the Fermi level shifts to a lower LL. The peaks appear at different fields in the two samples, corresponding to the different carrier densities.

The FWM signals from both samples show identical magnetic field dependencies, up to a scaling with the carrier density. Figure 1 compares the FWM signal, which is measured close to the Fermi energy at B=0, to that measured at B=6.5 T, in the high density sample. The high field signal is substantially stronger than that at B=0. Both the rise and the fall times of the two signals are different. The B=0 signal is slightly asymmetric but roughly follows the autocorrelation of the laser pulse, peaking at zero time delay. This indicates a very short dephasing time, comparable with the pulse width. This is in agreement with Ref. [2], where dephasing times of less than 1 ps were measured at the Fermi energy at similar excitation densities. The high field signal rises more slowly, with a rise time which is the pulse autocorrelation width (1 ps), and decays exponentially with a time constant of 1.5 ps. As we tune our laser throughout the spectral width of the lowest LL, the same temporal behavior is measured.

Our measurements imply that the e-e scattering rate τ_{ee}^{-1} in high magnetic fields is lower and is not as sensitive to excess energy as compared with the zero field case. However, we can only set an upper limit for τ_{ee}^{-1}. It is possible that impurity scattering is the limiting process which determines the dephasing time at high magnetic field in our measurements. In fact, the measured dephasing time of 1.5 ps at 7 T is very similar to the Drude scattering time determined from the mobility measurements.

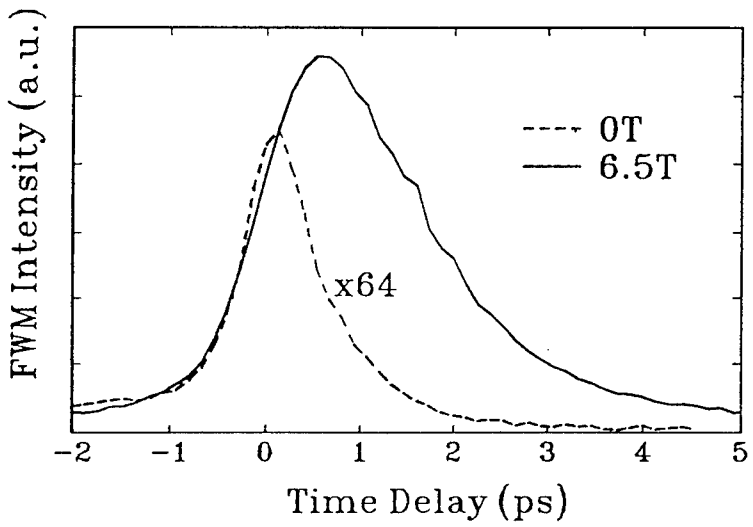


Figure 1: The temporal evolution of the FWM signal close to the Fermi energy at 0 T, and in the first Landau level at 6.5 T (high density sample).

The measured increase of the dephasing time for $B\neq 0$ is expected for samples with substantial inhomogeneous broadening. For the ideal case, where the energy spectrum consists of discrete, unbroadened LLs, it can be shown [3] that the dominant e-e scattering is intra LL (i.e. for electrons which scatter within their initial LLs). The scattering rate for such processes increases with the magnetic field strength (due to the increasing degeneracy). However, this argument is reversed when inhomogeneous broadening is taken into account, due to the requirements for energy and momentum (guiding center) conservation. The calculation of τ_{ee} in this case is rather involved and we present here only simple considerations (valid for a test electron and a scattering electron which are both in the lowest, partially-filled LL) explaining why the scatterting is suppressed. We consider a 2DEG subjected to a smooth random potential U with a correlation length Λ large compared to the Fermi wavelength. At zero magnetic field such a smooth potential slightly changes the DOS and does not affect τ_{ee}^{-1} significantly. However, in strong B severe limitations are imposed on the phase space for e-e scattering. This is because without this potential the DOS of the 2DEG in a magnetic field is singular. For the scattering electrons, whose wavefunctions are localized within one magnetic length a_B, the scattering matrix elements do not vanish, and energy is conserved, only if both electrons are near the Fermi level, and located within a distance of the order of a_B from each other. The excess energy of the test electron is limited by $(\Delta\varepsilon_{max})_B = a_B \nabla U \approx \Gamma a_B / \Lambda$, where Γ is the width of the LL. This energy is small compared to the width of the LL. For larger excess energies the scattering rate is exponentially small.

We now turn to the spectral behavior of the FWM signal. Figure 2a illustrates the evolution of the FWM spectrum as the magnetic field is increased. These spectra were measured with cross polarized exciting pulses at zero time delay with the low density sample. Similar results were obtained at later time delays and with exciting pulses with parallel polarizations. It can be seen that the FWM spectra are dominated by a single peak, which at 3 T shifts to lower energy and significantly increases in intensity. These changes are correlated with the jump of the Fermi level from the second LL to the first LL. The peak signal at 7 T is weaker by about 3 orders of magnitude than that measured in intrinsic samples. This reflects the screening of excitonic effects in the MD samples. Replotting the FWM spectra on a logarithmic scale (Fig. 2b) it is possible to identify the signal from the second LL, which in high magnetic fields is weaker by more than

two orders of magnitude than the signal from the first LL. The peak which dominates the spectra at low fields evolves into the second LL transition, but *decreasing* its strength with increasing magnetic field. This anomalous behavior is opposite to what one finds in intrinsic samples. Also, it is surprising to note the apparent lack of any contribution to the FWM signal from light hole related transitions. The temporal signal which is measured at the second LL shows two components, a fast one which follows the pulse and a slower one, which rises and decays on a time scale comparable to that of the dephasing in the first LL. Experiments are in progress to investigate this anomalous response.

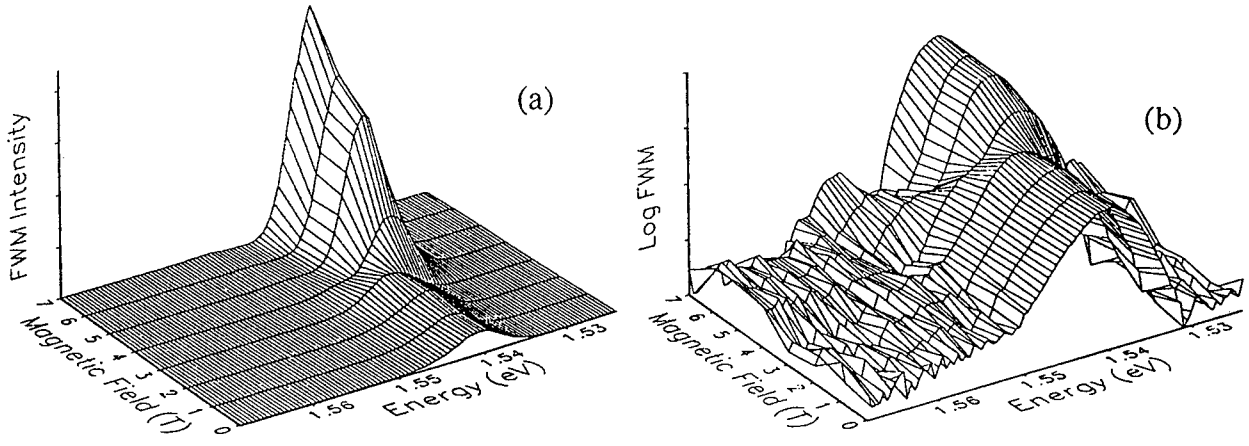


Figure 2: FWM spectra for increasing magnetic field for the low density sample, plotted on (a) linear and (b) logarithmic scales.

It is evident from our results that the proximity of the Fermi level to the excitation energy strongly affects the observed FWM signal in the MD samples. Unlike the measurements in zero magnetic field,[2] where a strong dependence of the FWM intensity on the excess energy corresponded to a decrease of τ, our high magnetic field measurements do not exhibit a strong dependence of τ on excess energy. The strong enhancement at the Fermi level and the absence of spectral peaks above the second LL strongly suggest that the observed signal is related to the FES.[4] The FWM peak intensity decreases exponentialy with temperature, with a decay constant of 17K (~1.4 meV), while no significant changes of τ are observed up to 30K. These temperature and energy scales are characteristic of the FES in absorption and PL measurements.[5] We thus arrive at the conclusion that the measured signal in our FWM experiments is the nonlinear manifestation of the FES.

The FES results from the scattering of conduction electrons by the photo-excited holes. This important process was not considered in our discussion of the dephasing. It is obvious that our results cannot be fully explained in terms of e-e scattering only, and that a better theory is needed, which would take into account e-e scattering, scattering by holes, and the effect of disorder.

References:
[1] W. H. Knox *et al.*, Phys. Rev. Lett. **61**, 1290 (1988).
[2] D. S. Kim *et al.*, Phys. Rev. Lett. **68**, 2838 (1992).
[3] V. F. Gantmakher and Y. B. Levinson, in "*Carrier scattering in metals and semiconductors*", North-Holland (1987).
[4] G. D. Mahan, Phys. Rev. **153**, 882 (1967).
[5] M. S. Skolnick *et al.*, Phys. Rev. Lett. **58**, 2130 (1987); G. Livescu *et al.*, IEEE J. Quant. Electron. **QE 24**, 1677 (1988).

Dynamics of Coherently Excited Semiconductor Microcavities

J.-K. Rhee[1], T. B. Norris[1], Y. Arakawa[2], M. Nishioka[2], and C. Weisbuch[3]

[1] Center for Ultrafast Optical Science, University of Michigan
2200 Bonisteel Blvd., Ann Arbor, MI 48109, U.S.A.
[2] Institute of Industrial Science, University of Tokyo
7-22-1 Roppongi, Minato-ku, Tokyo 153, Japan
[3] Thomson-CSF, Laboratoire Central de Recherches
Domaine de Corbeville F-91404, Orsay CEDEX, France

Recently, cavity quantum electrodynamic (QED) effects in semiconductor microcavities have been of considerable interest since, in the weak-coupling regime they play an important role in selectively increasing spontaneous emission into the lasing mode of vertical-cavity surface-emitting lasers (VCSEL's) [1,2] , enabling low-threshold, high speed, and high efficiency. In a strong-coupling regime, the normal modes of the coupled system are superpositions of the exciton and cavity modes. Hence the impulsively excited system will evolve in time with the energy oscillating between the exciton and cavity modes. This is known as a vacuum-Rabi oscillation (VRO), with a frequency of $\Omega=\bar{d}\cdot\bar{E}/\hbar$, where $\bar{d}$ is the transition dipole moment of atoms and $\bar{E}$ the vacuum-field strength. Of course, VRO are observable only when the cavity lifetime and exciton dephasing time are long enough compared to VRO period. Recently, Weisbuch *et al.* [3] have reported an observation of the normal-mode vacuum Rabi splitting in 2-D-exciton/planar-DBR microcavities. The observed splittings were as large as 6 meV in reflection and transmission spectra, implying 690-fs vacuum Rabi oscillations.

Many research groups have extensively studied VRO in atom-cavity systems in the past ten years [4–6]. However, vacuum Rabi oscillations in semiconductor microcavities are manifested in a different way from those of atom-cavity systems. First, in slab-like microcavities, coupled exciton-cavity systems show 2-D-exciton/polariton behavior as pointed out by Weisbuch *et al.*Secondly, microcavities are usually designed to have a single mode (λ cavity) resonantly tuned to an excitonic transition. In this case, the coupling is enhanced by a factor of a few orders due to stronger confinement of cavity modes, leading to subpicosecond VRO periods, and the cavity lifetime and exciton dephasing time are typically of order 1 ps or less. Thus one may observe femtosecond time-scale responses from microcavities. Therefore, it is important to determine to what extent microcavity systems approach the ideal case of two-level-absorber/single-mode-cavity systems. In this paper, we present an investigation of time-domain vacuum Rabi oscillations in a semiconductor microcavity using femtosecond upconversion and interferometric pump-probe experiments. There are several motivations for performing a time-domain investigation of microcavity QED. First, unlike the spectral domain analysis, we may observe detailed time-domain vacuum Rabi oscillations with oscillation phase information for better understanding of cavity QED dynamics. Secondly, it is interesting to probe the coherence of the coupled-mode polarization.

The sample used in the present work was the same as those used by Weisbuch *et al.* [3]. The sample was grown by metal-organic chemical vapor deposition (MOCVD). The front and back distributed-Bragg- reflectors (DBR's) consisted of 24 and 33 pairs of AlAs/$Al_{0.4}Ga_{0.6}As$-$\lambda/4$ layers to have approximately 98-% reflectivity, with a separation of one optical wavelength, leading to a cavity finesse of about 150. Five 76-Å-$Al_{0.2}Ga_{0.8}As$/GaAs quantum wells were situated in the center of the λ cavity, where the electric-field amplitude of the cavity

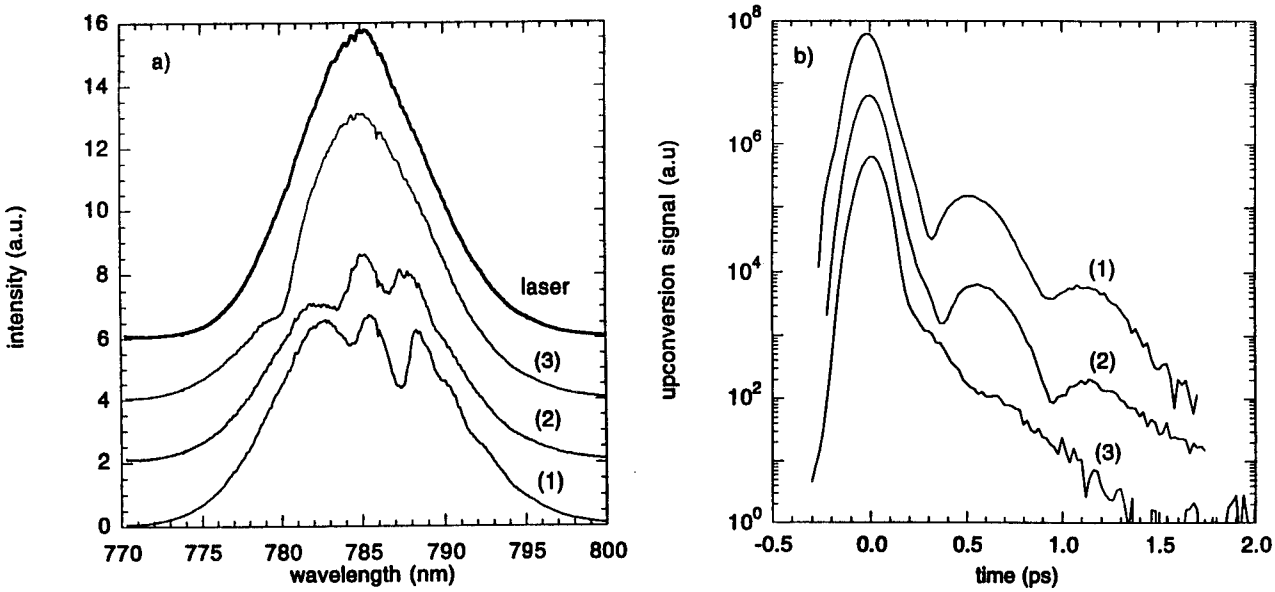


FIG. 1. Reflection spectra of pump lasers (a) and the upconversion experiment signal of the corresponding reflection beams (b) at various positions on the sample: (1) for exciton-cavity resonance case, (2) for 1.2-nm off-resonance case, and (3) for 5-nm off-resonance case. The thick curve in figure (a) shows the laser spectrum.

mode is maximum. Due to a slight spatial growth-rate variation caused by the temperature gradient over the substrate, the cavity resonance wavelength can be tuned in and out of the exciton resonance as one scans across the sample in one direction. The cavity lifetime was estimated to be 140 fs by reflectivity spectrum at an off-resonance position on the sample.

In our experiment, the microcavity sample was impulsively excited with 80-fs laser pulses from a Ti:sapphire oscillator tuned near the exciton and cavity resonance with an incidence angle of about 3°. The sample temperature was kept at 12 K so that the exciton dephasing time was about 1 ps [7]. The optical fluence of the excitation pulse is kept small, so as not to bleach the exciton absorption or excite the driven-field Rabi oscillation. Subsequently, the coupled exciton-photon modes evolve in time with VRO, showing radiation oscillations with the expected vacuum- Rabi frequency. In Fig. 1(a), the reflection spectra at various positions on the sample are shown. Fig. 1(b) presents the corresponding time-resolved emission signals from the sample using a standard upconversion technique. When the exciton and cavity modes are resonantly tuned (case 1), we can observe 600-fs vacuum Rabi oscillations with a 260-fs decay time, following the first peak corresponding to the reflected pump pulse. Note that the signal decay time is about twice the cavity lifetime due to linewidth averaging [5,6]. The initial state of the exciton-cavity system is the superposition of the normal modes corresponding to the photon state. As further evidence of VRO, we observed the same oscillation period at lower optical fluences. When the cavity is slightly detuned (case 2), the VRO period is reduced to 580 fs due to larger normal mode splitting and the first dip of the emission signal is shifted by 60 fs. This shift is because the VRO phase shifts as a function of detuning [4] so that the initial state is a mixture of weak-exciton and strong-cavity modes. When the cavity and the exciton modes are out of resonance (case 3), VRO is weakened but the period is reduced to 370-fs, corresponding to 5-nm normal-mode splitting.

In order to probe the coherence of the the polarization of the coupled exciton-cavity modes, we have developed an interferometric pump-probe technique. The experimental

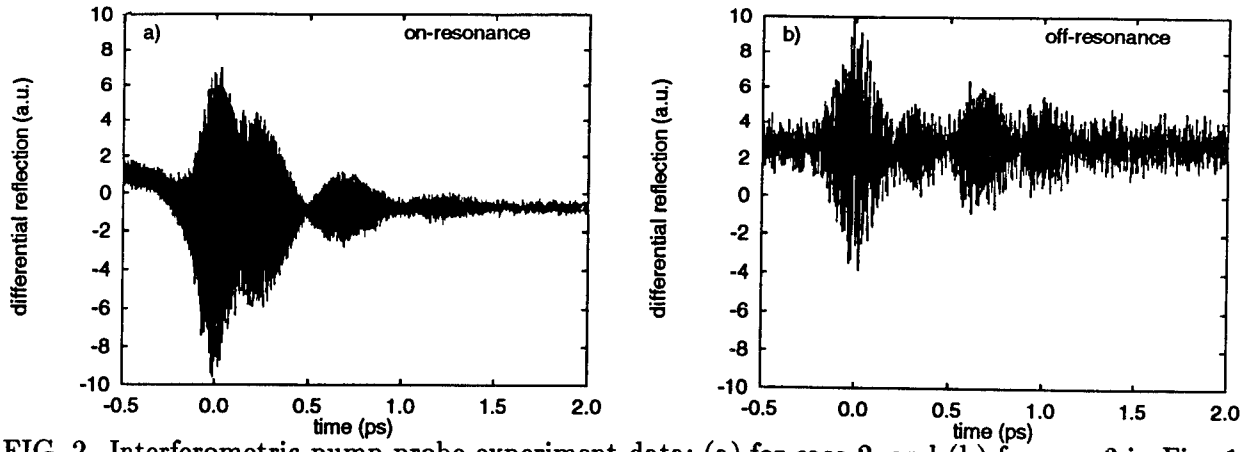


FIG. 2. Interferometric pump-probe experiment data; (a) for case 2, and (b) for case 3 in Fig. 1

setup is the same as conventional reflection pump-probe setups, although the angle between the pump and probe beams is kept small (within 3 degrees). The pump and probe beams are focused on a same spot on the sample with a diameter of 160 μm. Since in general, epitaxially grown crystals have defects due to mole-fraction and growth-rate fluctuations, the relatively large focal spot overlaps defects which serve as scattering centers. When the probe pulse is coincident with the pump or the emission from the sample, the scattered pump beam or the cavity emission in the reflected probe beam direction produces interference fringes on the detector. The fringes are, of course, observable when the resolution or time delay between pump and probe pulses (0.67 fs for our case) is finer than one optical period. Fig. 2 shows the result of the interferometric pump-probe experiment of the microcavity sample with the same experimental conditions, (a) as for case 2, and (b) as for case 3. The slow envelope of the signal represents the VRO. The fine fringes of the signal after timing zero is the result of the coherent emission from the sample. Note that this technique probes the electric field strength of the emission; hence the decay time is twice that observed in the upconversion experiment.

The work at the University of Michigan was supported by the NSF through the Center for Ultrafast Optical Science under STC PHY 8920108.

---

[1] Y. Yamamoto, S. Machida, and G. Björk, Phys. Rev. A **44**, 657 (1991).
[2] T. Baba, T. Hamano, F. Koyama, and K. Iga, IEEE J. Quantum Electron. **28**, 1310 (1992).
[3] C. Weisbuch, M. Nishioka, A. Ishikawa, and Y. Arakawa, Phys. Rev. Lett. **69**, 3314 (1992).
[4] G. S. Agarwal, Phys. Rev. Lett. **53**, 1732 (1984).
[5] M. G. Raizen *et al.*, Phys. Rev. Lett. **63**, 240 (1989).
[6] Y. Zhu *et al.*, Phys. Rev. Lett. **64**, 2499 (1990).
[7] L. Schultheiss, J. Kuhl, A. Honold, and C. Tu, Phys. Rev. Lett. **57**, 1635 (1986).

High Spatial and Temporal Resolution

WA 8:30am–10:15am
Dana Point Ballroom

Wayne H. Knox, *Presider*
AT&T Bell Laboratories

Brave New Nanoworld: Probing the Realm of Ultrafast, Ultrasmall Electronics

D.M. Bloom, A.S. Hou, and F. Ho
Edward L. Ginzton Laboratory, Stanford University, Stanford, CA 94305

Abstract

We have developed a new tool for measuring ultrafast voltages on integrated circuit devices. Our scanning force microscope probing system has 100-picosecond, submicron resolution and the ability to probe though passivating layers.

Introduction

Quite recently, there has been a surge of interest in using scanning probe microscopes for the high-speed characterization of nano-scale devices.[1-5] It has been realized that a probe tip nonlinearity can be used for heterodyning very high-speed signals. Our group has developed such an ultrafast system, based on the scanning force microscope (SFM), that theoretically is sensitive enough to map a voltage profile with subpicosecond time resolution and sub-micron spatial resolution. It is non-invasive, rugged, and does not require vacuum. By using the square-law force interaction between the SFM and sample for mixing and sampling, we are able to measure frequencies far above the mechanical resonant frequency of the SFM cantilever.

Theory of Operation

Fig. 1 shows the concept of an SFM probe system. Fig. 2 is a picture of our latest probe head mounted on an XYZ stage. A scanning force microscope operates by using a CW laser and a position-sensitive detector to sense the deflection of a cantilever to which is attached a sharp tip. We operate an SFM in a non-contact mode, in which a gap of about 10-100 nm is maintained between the tip and the circuit sample. There is a periodic high-speed voltage V_S on the sample that we wish to measure. We apply a pulse-train sampling voltage V_P to the tip. The voltage across the gap between the tip and the sample is $V_P - V_S$. The measured force is a function of the square of this voltage and therefore contains a mixing term at an intermediate frequency (IF) corresponding to the offset frequency between V_P and V_S. This IF is chosen low enough so that the cantilever deflection can follow an equivalent-time representation of V_S.

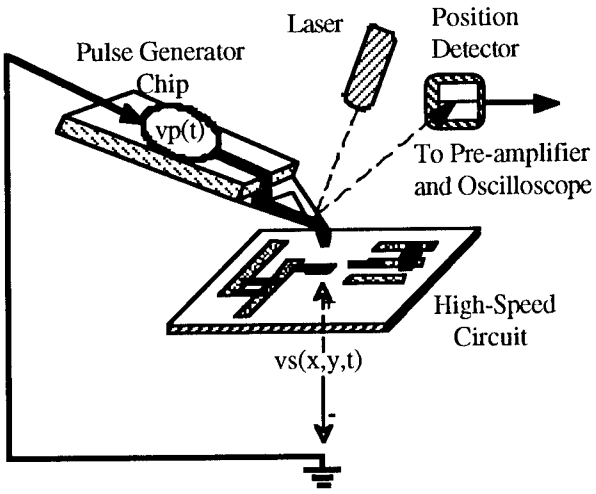


Figure 1. High-speed SFM probe system.

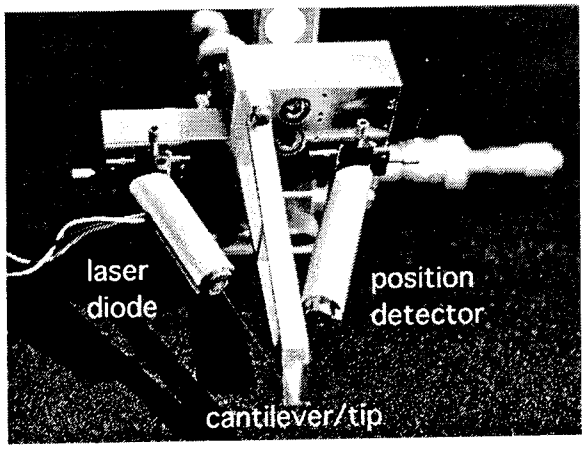


Figure 2. SFM probe head consisting of laser diode, probe arm, and detector..

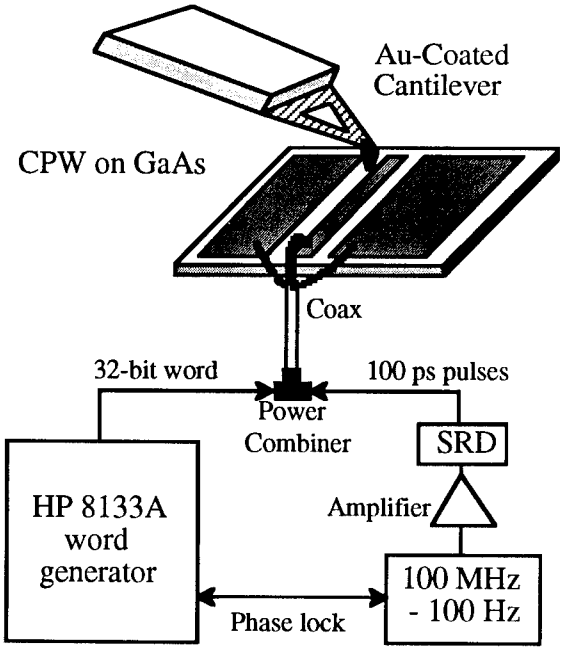


Figure 3. Setup for 3.2 GHz digital data sampling experiments

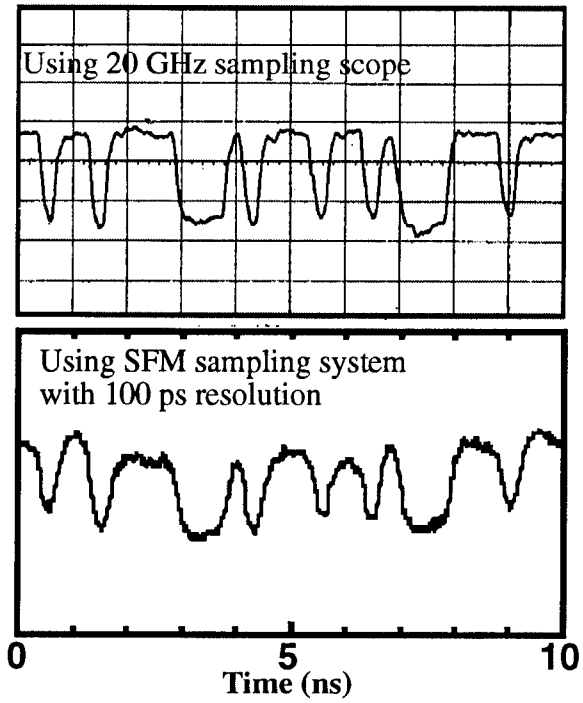


Figure 4. 3.2 GHz digital data as measured directly from word generator (top) and as probed on the CPW circuit. (bottom).

Experiments

To illustrate the operation of the probe, we describe here the results from three experiments. The first experiment demonstrates the concept of high-speed time-domain sampling. The setup is diagrammed in Figure 3. The SFM system is used to sample the output of an HP 8133A word generator. The test word consists of 32 bits, with digital voltage levels of 0 and 3.3 volts. The clock rate is 3.2 GHz, corresponding to about 310 ps for each bit. A step-recovery diode (SRD) comb generator is used to generate a train of 100 ps sampling pulses at the repetition rate of 100 MHz - 100 Hz. The word generator output and the sampling pulses are combined and launched onto the CPW sample. Because there is a 100 Hz frequency offset between the digital data stream and the pulse train, the pulses effectively "walk through" the data, yielding an equivalent-time signal at 100 Hz. Fig. 4 shows that the sampled result agrees very well with the direct output of the HP 8133A as measured with a 20 GHz sampling scope.

In the second experiment, we measured clock signals on a digital-to-analog converter (DAC) circuit. This integrated circuit had been fabricated in a CMOS process on silicon, and was covered with about one micron of passivating glass. The circuit was clocked at 1 MHz. We located two top-layer metal pads on the circuit that carried opposite phases of the clock, positioned our SFM tip over the pads, and measured the two traces shown in Fig. 5. They are exactly 180° out of phase, as expected. What is important to note is that voltages can be sensed through relatively thick passivation, a good example of non-invasive testing.

In a third experiment, we probed various signals on an Intel 80486 microprocessor that had been depassivated. The experiment consisted of two parts. In the first part, we operated the microprocessor with a 20 MHz clock and probed the voltages on two metal lines on the microprocessor that carried opposite phases of the clock; this is shown in Figure 6. The strobe pulses supplied to the tip were 2 ns wide, which meant that the time resolution was 2 ns. Next, we operated the '486 in its self-test mode with a 10 MHz clock. In that mode, the

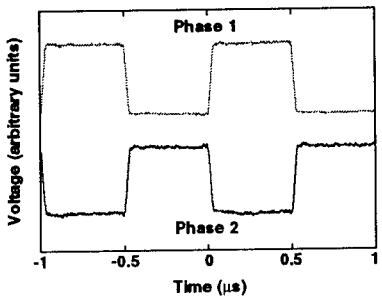


Figure 5. Clock phases measured through passivation on DAC.

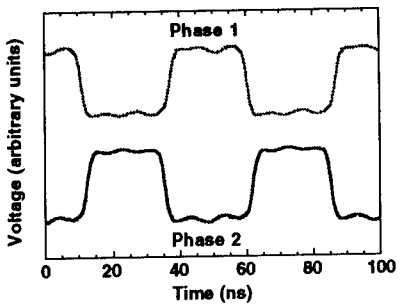


Figure 6. Two clock phases on the 80486 microprocessor.

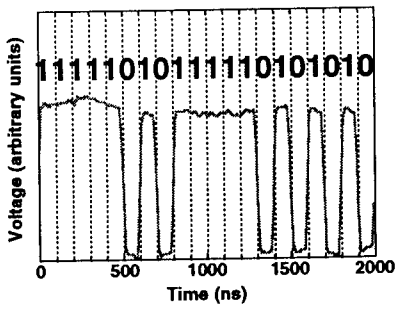


Figure 7. Self-test sequence of the 80486 microprocessor.

microprocessor goes through a pre-defined series of logic states every time it receives a reset signal. By applying a reset every 20 clocks, we obtained a repeating self-test sequence. The resulting signal, measured on the circuit using our probing technique, is shown in Figure 7.

Conclusion

Scanning force microscope probes hold great promise for measuring voltage signals with subpicosecond time resolution and submicron spatial resolution. We are achieving this goal by integrating high-speed circuitry with a microfabricated cantilever and tip.

This work is supported by ONR/DARPA contract N00014-92-J-1769. We are grateful to Bob Rao and Debbie Cook (at Intel Corp.), Pauline Prather, and David Su.

References

[1] A.S. Hou, F. Ho, and D.M. Bloom, "Picosecond electrical sampling using a scanning force microscope", *Electronics Letters,* **28**, (1992) 2302.

[2] D.M. Bloom, "Voltage-contrast scanning probe microscopy",Proceedings of the 4th European Conference on Electron and Optical Beam Testing of Integrated Circuits, Zurich, Switzerland 1-3 Sept. 1993 (To be published in Microelectronic Engineering)

[3] S. Weiss, D.F. Ogletree, D. Botkin, M. Salmeron, and D.S. Chemla, "Ultrafast scanning probe microscope", *Appl. Phys. Lett.*, **63**, (1993) 2567.

[4] K. Takeuchi, and Y. Kasahara, "High-speed optical sampling measurement of electrical waveform using scanning tunneling microscope", *Appl. Phys. Lett.*, **63**, (1993) 3548.

[5] G. Nunes Jr. and M.R. Freeman, "Picosecond resolution in scanning tunneling microscopy," *Science,* **262**, (1993) 1029.

Advances in Ultrafast Scanning Probe Microscopy

S. Weiss, D. Botkin, D.F. Ogletree, M. Salmeron and D.S. Chemla

Department of Physics
University of California at Berkeley
and
Materials Sciences Division, MS 2-300
Lawrence Berkeley Laboratory
Berkeley, CA 94720
Tel: (510) 486 - 5202

Recently, we have proposed a general technique to wed ultrafast laser spectroscopy and Scanning Probe Microscopies (SPM) to obtain simultaneous picosecond time and atomic space resolution.[1] Demonstration of this concept immediately followed: we have implemented this general technique in a specific device, the Ultrafast Scanning Tunnelng Microscope (USTM).[2] Ultrafast time response occurs when the SPM probe has a nonlinear response to a short laser pulse. This nonlinearity can be essential to the nature of the probe-sample interaction or can be artificially introduced to the probe. For instance, the intrinsic nonlinearity of the STM I-V characteristic can be used to obtain ultrafast time resolution.[1,3] The tip nonlinearity mixes the high frequency (short time) responses to produce a DC (correlation) signal. Temporal resolution is defined by the temporal width of the nonlinear tip response and the width of the laser pulses. Spatial resolution should be comparable to the resolution of the normal SPM. In the first demonstration, the nonlinear element was a fast photoconductive switch integrated with the STM tip assembly. Conceptually, the switch acts as a several picoseconds long gate.

In the experiment, the sample was an Au transmission line. A short (100 fs) laser pulse switched a photoconductive switch on the sample, to generate short (650 fs) voltage pulses on the line. A second laser pulse gated the Scanning Tunnelng Microscope (STM) tip. Thus, we could excite the tunneling gap of the STM with a short voltage pulse, and measure its response. We used this instrument to image surfaces with 2 ps time resolution and better than 50 Å spatial resolution. The details of the experimental set-up are described eleswhere.[2]

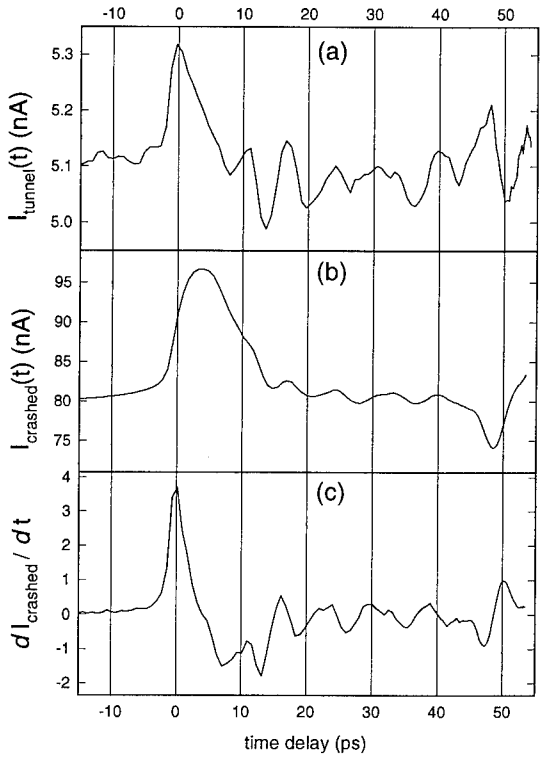


Figure 1. Time resolved current cross-correlation detected on the tip: (a) in tunneling range (5nA and 80mV settings), and (b) when the tip is crashed into the sample. (c) is the time derivative of (b).

A typical signal measured by the STM consists of a small AC component which varies with time delay riding on a large DC background. The background is simply the nominal tuneling current, given by (bias voltage)/(gap resistance). Fig 1a shows a 4.5 ps wide cross-correlation pulse detected by the STM while tunneling at 5 nA with a +80 mV bias on the strip. The 10% to 90% rise

time is 2 ps. The average tunnel current is increased by ~0.25 nA when the transmission line pulse passes beneath the tip at zero time delay. This increase corresponds to a signal/background ratio, DI/I, of 5%. Fig. 1b shows a cross-correlation recorded while the tip was in ohmic contact with the sample.

There are several features in this data. The large signal at a time delay of 47 ps is a reflection from one end of the sample transmission line. This reflection also appeared in our standard sampling measurements. The structure following the main correlation peak is due to ringing in the tip structure, as we will show below. The FWHM of the correlation peak in Fig. 1b is much broader (10 ps) than the pulse on the transmission line. The broadening is, most likely, a result of dispersion of the electrical pulse on the tip. The bipolar correlation peak in Fig. 1a is significantly different from what we would expect for a purely ohmic response; in fact it bears some resemblance to Fig. 1c, which is the numerical derivative of the trace in Fig. 1b. Apparently, a large portion of the tunneling signal comes from a capacitive-like response. However, the tunneling gap height dependence of this capacitive-like response is very different from the one expected for the geometrical capacitance of the junction; as we will show below, the geometrical capacitance of the tip assembly contributes negligibly to the signal. The existance of an intrinsic capacitance associated with the tunneling process has been discussed in the context of Coulomb Blockade (CB) and Single Electron Tunneling (SET).[4] This capacitance is beleived to be very small (on the order of 10^{-18} F). The RC discharge time for such a capacitance at reasonable tunneling gap resistances is on the order of a few ps and can be directly investigated with our USTM.

Fig. 2a displays a series of cross-correlation pulses recorded by the STM while tunneling with a +80 mV bias on the strip for gap resistances from 16 MW to 512 MW. For clarity, the DC background in each curve has been removed. In Fig. 2b, we normalize the peak height of the traces in Fig. 2a to unity in order to show changes in the lineshape of the signal. The figure shows that the fall time of the correlations increases with increasing gap resistance. This increase may be associated with the RC discharge time discussed above.

The spectra of the traces in Fig. 2a are shown in Fig. 2c. These spectra were calculated for data in the range -10 ps to 37 ps. Additionally, the heights of the low frequency peaks have been normalized to 1. The low frequency peak describes the main bipolar correlation peak. The smaller high frequency peaks represent the ringing effect in the correlation traces. This ringing is probably due to an impedance mismatch between the tip and the sample and between the tip and the sampling switch. As the tunneling resistance is reduced, the mismatch is reduced, and the amplitude of the ringing peak is reduced. The fine structure in the ringing has not been identified.

The height of the correlation peak in each trace, as function of the corresponding DC current is shown in Fig. 3. The filled squares represent measurements at 16, 32, 64, 128, 256 and 512 MW gap resistances

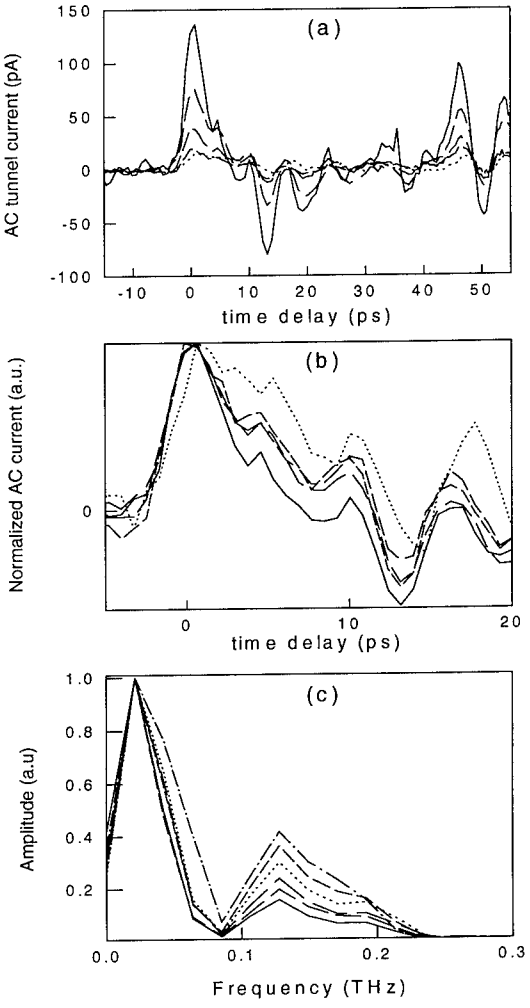


Figure 2. a) The tunnel-current DI(Dt) for different gap resistances. (solid line is 16 MW, long dash - 32 MW, medium dash - 64 MW, short dash - 128 MW, dotted-256 MW, dash-dot - 512 MW). b) Traces in a) with peak heights normalized to unity. c) Spectra of the curves in a).

gap resistances (the point at the top right of the figure corresponds to 16MW). The dashed line is a linear regression to the data. It is clear from the figure that the AC part of the tunneling current has the same gap impedance, and hence distance, dependence as that of the DC current. Moreover, when the tip is withdrawn from the surface by 50 Å, not only does the DC tunnel current vanish (as expected), but the AC part nearly vanishes as well. This means that the observed cross-correlation signal has little or no contribution from stray capacitance in the leads or from radiative coupling.

A detailed study of the nature and the origin of the tunnel-gap capacitance is currently under way. By varying the tip length, the gap conditions (by controlling the oxide layer) and the bias voltage on the transmission line, we will separate the contribution of the stray capacitance of the leads and reflections along the tip from the intrinsic response of the tunneling junction itself. We plan to improve the time resolution of our USTM by microfabricating the entire tip-switch assembly.

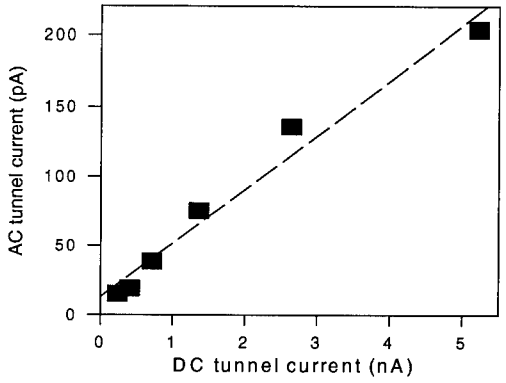


Figure 3. Amplitude of the time resolved signal versus DC background. The dotted line is a linear regression to the data.

One of the most exciting prospects for USPM is the potential to create movies of surface dynamics. We believe that by improving the sensitivity, dynamic range, and time resolution of this technique, we will be able to animate surface dynamics by collecting a series of STM images for increasing values of time delay. This will allow us to study dynamical phenomena in real space with atomic resolution. Such a tool will open a window for the observation of processes and excitations which propagate at velocities of a few Å per fs (or less). It should be possible to spatially resolve in real time phenomena such as vibronic motion on the atomic scale, carrier transport in semiconductor structures, electric field and voltage wavefront propagation at metal semiconductor interfaces. The operation of sub-micron electronic/optoelectronic devices can be directly characterized with such a technique.

USPM is not limited to the STM. As we discussed before,[1] the non-linear nature of the probe-sample interactions in STM, AFM and near field optical microscopy (NSOM) offer many opportunities for resolving ultrafast phenomena on a nanometer scale.

Acknowledgements

The authors would like to thank J. Beeman for tremendous help with tip fabrication. This work was supported by a Laboratory Directed Research and Development grant from the Lawrence Berkeley Laboratory, under the US Department of Energy, contract DE-AC03-76SF00098 and by ONR/DARPA under contract #N000-14.93.105.36

References

[1]S. Weiss, D. Botkin and D.S. Chemla, OSA proceedings on *Ultrafast Electronics & Optoelectronics*, vol.14, San Francisco, January 25 1993, edited by J. Shah and U. Mishra, (OSA, Washington D.C. 1993), pp.162-165.

[2]S. Weiss, D.F. Ogletree, D. Botkin M. Salmeron and D.S. Chemla, Appl. Phys. Lett., **63**, 2567 (1993).

[3]G. Nunes and M.R. Freeman, Science, **262**, 1029 (1993).

[4]For example, K.K Likharev, IBM J. Res. Develop., **32**, 144 (1988).

Real time 2-photon confocal microscopy using a femtosecond, amplified Ti:sapphire system.

Jeff Squier, Ted Norris
Center for Ultrafast Optical Science
University of Michigan
2200 Bonisteel, IST Bldg RM 1006
Ann Arbor, MI 48109-2099
Ph:313-763-4875 FAX:313-763-4876

Christyne Bliton
Meridian Instruments, Inc.
2310 Science Parkway
Okemos, MI 48864

G. J. Brakenhoff
Confocal Microscopy Group
Department of Molecular Cell Biology
University of Amsterdam
Plantage Muidergracht 14
1018 TV Amsterdam

Brian Athey
Department of Anatomy and Cell Biology
University of Michigan Medical School
Ann Arbor, MI 48109-0616

Confocal microscopes improve resolution by creating optical sections with spatial filtering. These optical sections can be reconstructed to produce complete three-dimensional images suitable for studying a variety of important biological problems. However, over the time course of an image scan, confocal microscopes illuminate the full specimen volume with the excitation wavelength (as in standard fluorescence microscopy) which can limit the image quality. The use of a short optical pulse (from an ultra-short pulse laser) allows one to utilize two-photon excitation, which occurs only at the focus of the (high NA) objective, with several advantages following. Background scattered light is lower, and fluorophore

bleaching only occurs at the objective focus instead of throughout the sample volume. Consequently, three-dimensional imaging experiments may be performed at higher excitation powers, greatly improving signal-to-noise, or lower excitation power could be used, and the number of image sets collected over time could be increased. Finally, since the excitation volume is lower with two-photon excitation, caged compounds may be released in a small (diffraction-limited) volume in a specimen. Thus, a new tool may be developed for the researcher: a miniature (micron-cubed) opto-chemical probe that can be used in a very non-invasive way.

2-photon laser scanning fluorescence microscopy was first demonstrated by Denk et al [1]. We have extended this technique to a confocal imaging system which uses a line focus and bilateral scanning technology to provide the fastest image capture available. Thus, we are able to produce real-time 2-photon images, to our knowledge, for the first time.

The laser source is a 450 kHz Ti:sapphire amplifier system [2]. The output of the system can be readily varied in repetition rate and energy. The chirp of the output pulse can also be varied positively or negatively, enabling us to compensate for quadratic and cubic phase errors which might occur as the pulse travels through the microscope. The flexibility of the laser enables us to study the various parameters which produce the most optimal images.

An example of the images produced by this technique are shown in figure 1.The laser pulse width was approximately 120 fs, at a center wavelength of 800 nm. The sample is spathaphyllum pollen, acridine orange label, and 4.7 μm beads, phycoerythrin label. Figure 2 is a graph of the fluorescence intensity as a function of laser input power. The quadratic dependence is characteristic of 2-photon fluorescence. A video tape of the images as they occur, will be presented at the meeting.

One of the interesting capabilities of the Ti:sapphire amplifier system is that it can also produce supercontinuum when operated at a critical peak power in virtually any type of media. The continuum, or white light, can extend from the ultraviolet through the infrared. In addition, this white light remains short -- it is still femtosecond in duration. Thus, this tunable, short pulse light also has interesting implications for the confocal microscope.

This work was partially supported by the NSF through the Center for Ultrafast Optical Science under STC PHY 8920108.

References

1. Denk, Strickler, Webb, Science, **248**, 73 (1990).

2. T. B. Norris, Opt. Lett. **17**, 1009 (1992).

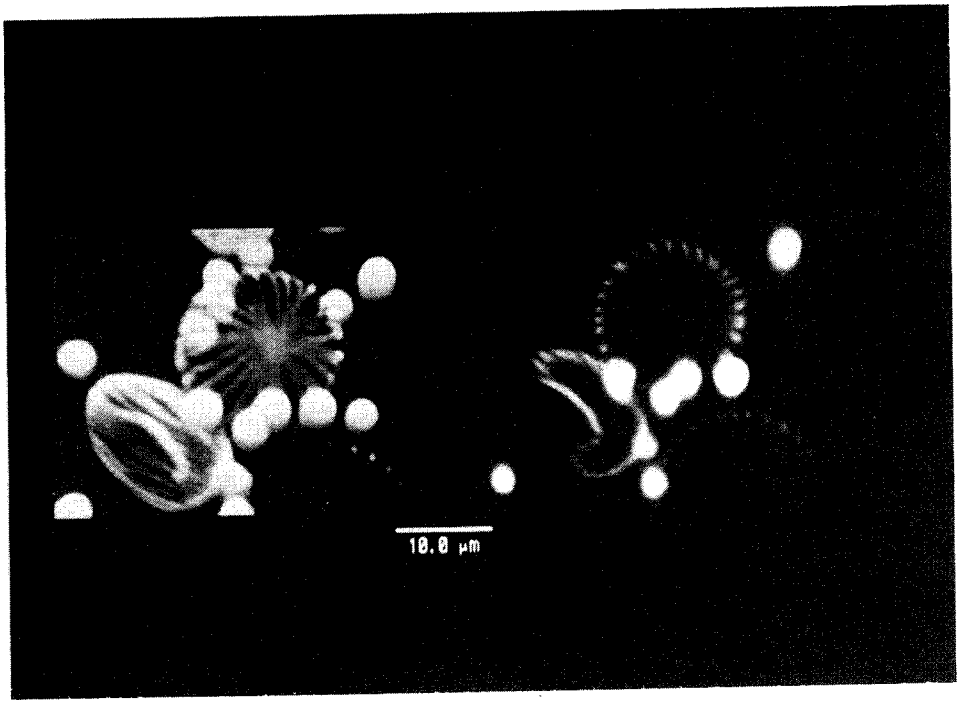


Figure 1. Image on the left is a three-dimensional image of spathaphyllum pollen, acridine orange label, and 4.7 µm beads, phycoerythrin label. The second image is one of the two-dimensional cross-sections which are used to reconstruct the full three-dimensional profile.

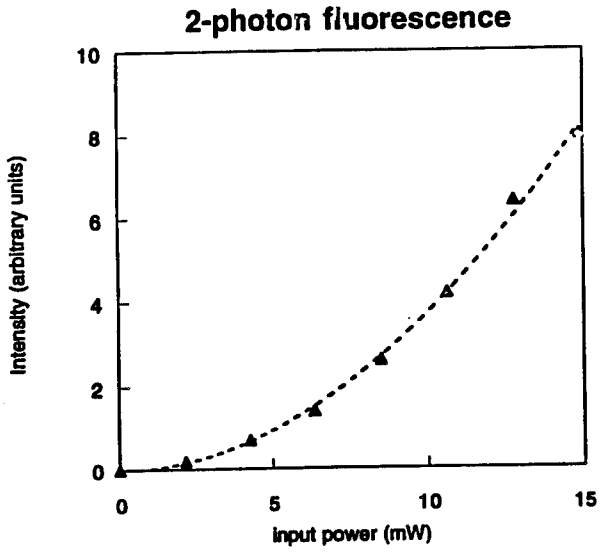


Figure 2. Flourescence intensity measured at the output of the microscope, as a function of input laser power, which was measured at the input to the microscope. The triangles are measured points, the dashed line is a second order polynomial fit to the data, illustrating the clear quadratic dependence of the 2-photon fluorescence.

Integrated atomic force microscope and ultrafast sampling probe

John A. Nees*, Shin ichi Wakana**, Chun-Ying Chen*
*University of Michigan, Ultrafast Science Laboratory
2200 Bonisteel Blvd. 1006/IST Ann Arbor MI 48109-2099 USA
fax/phone (313) 764-9271

**FUJITSU Laboratories Ltd.
1-10 Morinosato Wakamia Atsugi, Kanagawa 243-01, Japan
phone 81-046-248-3896 ext. 4311

The reduction of line dimensions in integrated circuits and the increase in the device speeds has led to the need for high-speed probes with sub-micron spatial resolution. This need is addressed by combining Atomic Force Microscopy (AFM), with its sub-nanometer spatial resolution, and photoconductive sampling, with single picosecond temporal resolution.[1]

Probe fabrication

Formation of this probe is as follows: Low-Temperature-Grown GaAs is grown by molecular-beam epitaxy on an AlGaAs etch-stop layer on a semi-insulating GaAs substrate; The probe's perimeter is defined by front-side etch penetrating through both epi-layers; Electrodes defining a photoconductive switch are placed by photolithography; The sub-micron probe tip is formed by self-terminating lift-off;[2, 3] The substrate is removed by polishing and a back-side etch, freeing the 1.5 μm thick film of LT GaAs and AlGaAs; UV curing cement is used to attach the probe to a glass support; The finished probe is placed on a translation stage for use.

Probe use

The probe is designed to be used in place of conventional AFM probes, in the following way: It is mounted on an AFM scanner; A cw laser is reflected from the back side of the cantilever to a quadrant detector; The tip is lowered to the device under test; Feedback is engaged; An image is generated by monitoring the height-signal as the tip is scanned in the transverse directions; Once an image of the device-under-test is scanned the probe tip is positioned at the desired location and pressed into low-force contact with the signal-line to be interrogated; A sub-picosecond switching beam is directed at the back side of the probe to the photoconductive switch; The optical pulses open the photoconductive switch for a period of about 1 ps (This samples the electronic waveform on the device-under-test by allowing an amount of current proportional to the waveform voltage to pass on to the detection electronics); The optical delay of the switching beam is scanned to perform equivalent time sampling of the repetitive waveform.

The experiment

We have fabricated probes following the above description and used them in separate experiments to acquire high spatial-resolution images and high temporal-resolution waveforms. For image acquisition we followed a procedure identical to that used for commercial AFM probes on the Topometrix Explorer 1000 system.

For high temporal-resolution waveform acquisition we made a probe using LT GaAs which displayed sub-picosecond transient reflectivity. It was mounted as described above. In low-force contact, the probe has a dark conductance of 0.05 nS as measured using a Fluke 27

multimeter. This represents the leakage current flowing through the photoconductive switch and the tip to the device under test. The signal to be measured was generated by a 20 x 20- m photoconductive switch on LT GaAs and carried on a coplanar stripline with 20- m wide strips having 40- m center-to-center spacing. The generating switch and the sampling switch were activated by two beams derived from the same 100-fs Ti:Sapphire laser operating at 800 nm. Delay in the arrival of the two beams was scanned by a computer controlled optical delay line. The laser operated at a repetition rate of 100 MHz and produced 9 mW in the excitation beam and 0.8 mW in the probe beam.

The results

The flexibility and strength of our cantilevers are similar to those observed for commercially available probes. Reflectivity of the AFM signal was lower by a factor of three due to absorption in the GaAs, but atomic force imaging is quite reproducible on the 100-nm scale (10-nm in z). A scanned image of a 2- m test pattern is shown in figure 1.

Using the same type of probe we measured an impulse response of 2.5 ps (see figure 2). Signal-to-noise equal to unity was seen at a signal level on the order of 10 V/ Hz. These preliminary results display an offset equal to 42% of the peak signal. The baseline to signal proportion does not scale with the power in either pump or probe beams. We are exploring the effects of photovoltaic signals generated on the probe and the possible effects of light leaking through the switch. The condition of the probe after measurement is shown in figure 3.

Conclusions

We have demonstrated atomic force imaging using a photoconductive probe with 2.5-ps response-time and 10- V sensitivity. It is clear that the combination of these measurements into a single instrument will allow us to make time resolved measurements on nanometric structures. This will provide a valuable tool for high-speed, high-density device testing.

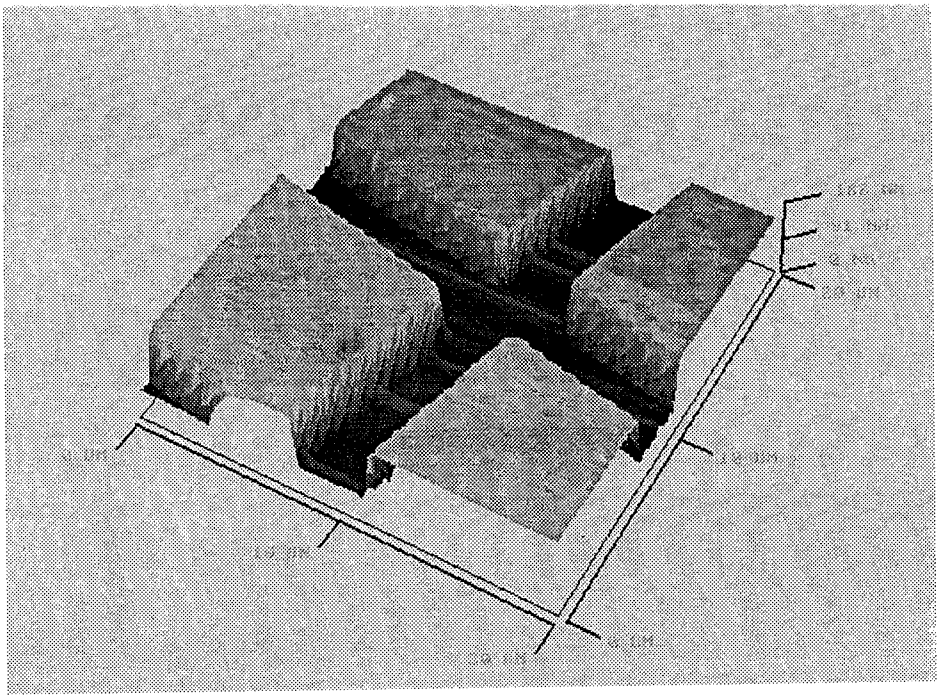


Figure 1.
AFM image acquired by the photoconductive probe

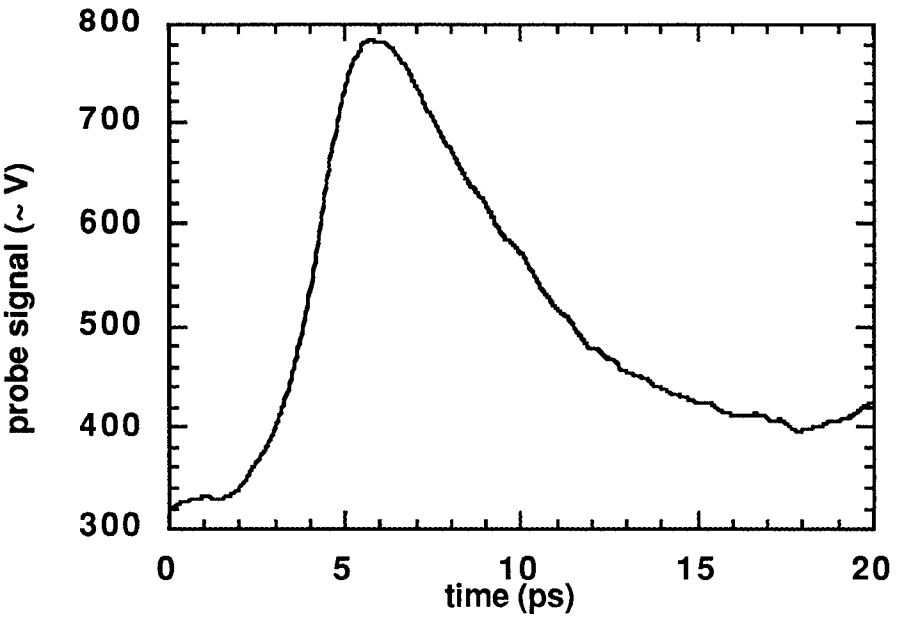


Figure 2.
Waveform acquired 60 m from a 20x20- m photoconductive switch on LT GaAs

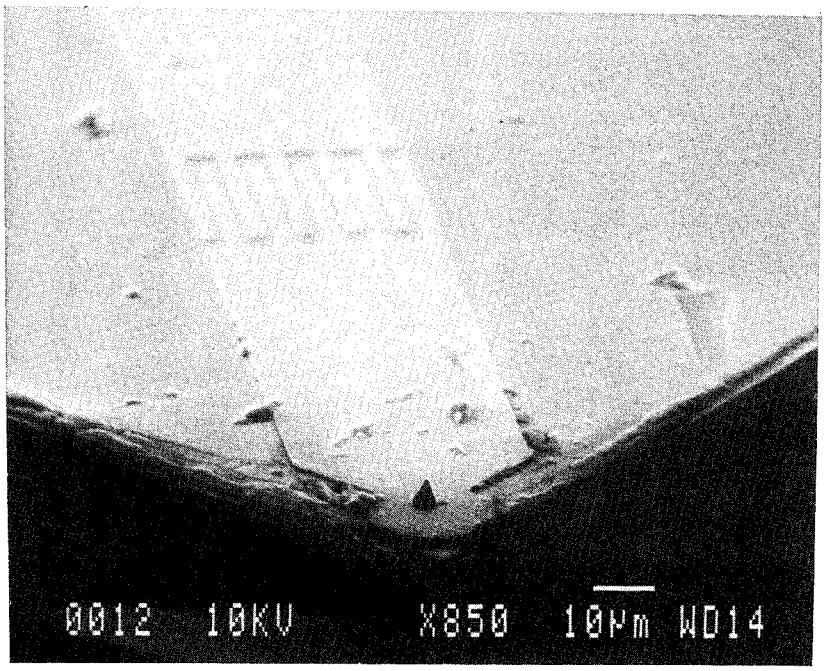


Figure 3.
SEM picture of the probe after it was used to make waveform measurements

References

D. R. Grischkowsky, M. B. Ketchen, C-C Chi, I. N. Duling III, N. J. Halas, and J. M. Halbout, IEEE J. Quantum Electron. **QE-24**, 221 (1988)

J. Kim, S. Williamson, J. Nees, S. Wakana, and J. Whitaker, Appl. Phys. Lett. **62** (18), 3 May 1993.

C.A. Spindt, L. Brodie, L. Humpfrey, and E. R. E. R. Westerberg, J. Appl. Phys. **47**, 5248 (1976).

Time-Resolved Nonlinear Near Field Scanning Optical Microscopy of Semiconductor Microdisks

J. B. Stark, U. Mohideen, E. Betzig and R. E. Slusher

AT&T Bell Laboratories
Murray Hill, NJ 07974

The experiments described here use nonlinear, time-resolved, near field scanning optical microscopy (NSOM[1]) techniques to study the local carrier dynamics and spatial distributions in GaAs microdisks. GaAs quantum wells in the plane of the microdisk provide a gain material for microlasers based on the whispering-gallery modes propagating around the edge of the microdisk[2]. We are exploring the carrier density regime required for lasing. What are the energy relaxation times and spatial diffusion lengths near the microdisk edge? How do these properties vary with surface treatment and carrier densities? These questions can best be answered using the high spatial resolution provided by NSOM and the temporal resolution of short excitation and probe pulses tuned to frequencies near the GaAs bandedge.

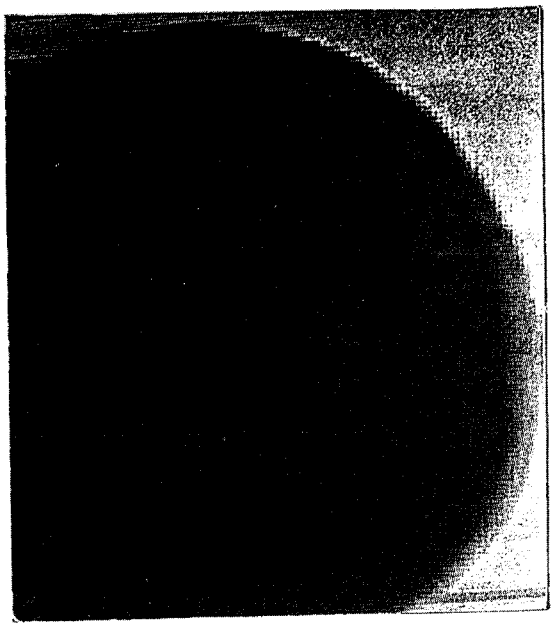
Semiconductor fabrication techniques have advanced to the stage where it is possible to make optical resonators with dimensions of the order of an optical wavelength[3]. In this microcavity limit there is only one low loss mode that interacts with the optically active material in the cavity. In addition to the very low threshold lasers that can be obtained with these microcavities, there are many interesting phenomena associated with microcavities including control of the statistics of the emitted light as well as the spontaneous emission rates, anomalous laser linewidth behavior, and nonequilibrium effects in the active region. All of these phenomena depend on the dynamics and spatial distribution of the carriers in the gain region. Since the lasing whispering-gallery mode in our microdisks propagates within a few tenths of a micron of the disk edge, the carrier dynamics near the edge are crucial for describing the lasing phenomena. There is a severe problem for GaAs/

AlGaAs system since nonradiative surface recombination can reduce the gain by as much as two orders of magnitude if the surface is not passivated. We have recently found an effective method for passivating the surface[4] which results in gains near the bulk value and good stability over long periods of time (months). Using this method we have achieved low threshold lasing at wavelengths near 830nm for GaAs/AlGaAs disks using optical pumping with substrate temperatures near liquid nitrogen temperatures.

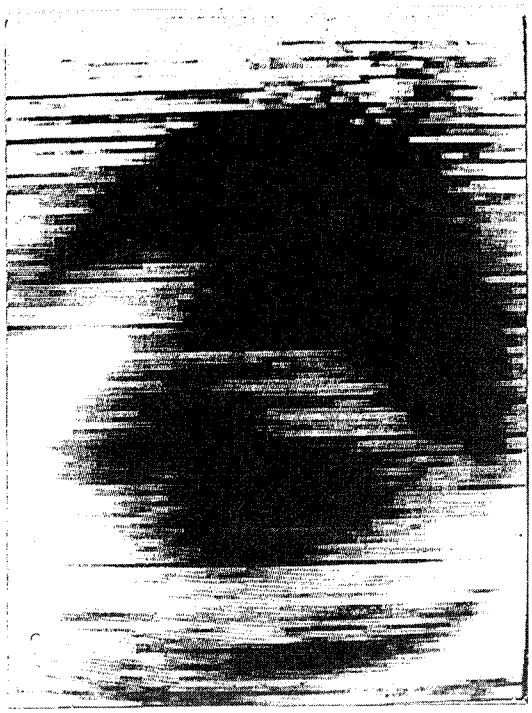
The gain region of the microdisk is a 0.12μm thick layer with eight 100Å GaAs quantum wells with 50Å barriers within a total disk thickness of 0.15μm including a 200Å $Al_{0.28}Ga_{0.72}As$ protective layer on the top and bottom of the disk. A vertical-geometry MOCVD reactor was used to grow the layered structure. Microdisks with diameters between 2 and 10μm are floated off a GaAs substrate by dissolving an AlGaAs layer below the disk and allowed to settle on a sapphire substrate for use in the transmission mode NSOM. The microdisks in these experiments are at room temperature.

The excitation and probe optical pulses are generated by a mode-locked Ti:sapphire laser with output pulse widths below 20fs. The central pulse wavelength of 800nm overlaps the GaAs quantum well bandedge absorption at room temperature. The 40 to 80nm spectral bandwidth of this laser allows us to obtain a complete picture of the carrier dynamics over a broad spectral range near the GaAs bandedge. A grating precompensator disperses the pulses so that after propagating through the NSOM input optical fiber the pulse widths are 40fs. Nonlinear mixing in the input fiber is not a severe problem in these experiments. The peak power densities at the sample with a one milliwatt average input to the NSOM fiber and a loss of 10^{-5} at the NSOM tip are in the range from 1 to 100kW/cm^2, sufficient for nonlinear excitation of the GaAs quantum wells in the spectral region near the bandedge.

Initial experimental images are shown in Figure 1.



(a)



(b)

Figure 1

A NSOM image of a 10μm diameter microdisk is shown in Fig.1(a) obtained while regulating the tip-sample separation by monitoring the shear viscosity of an oscillating tip. A nonlinear transmission image of this disk is shown in Fig.1(b) where the signal is the averaged amplitude of the transmitted pump and probe pulses at the sum of the frequencies used to chop these beams. The pump-probe delay is 100fs. The feedback beam is turned off for the nonlinear image. The tip is positioned less than 100nm above the microdisk surface. The nonlinear signal time constant is a few hundred femtoseconds. We are studying the carrier dynamics as a function of carrier energy, pump power, position on the disk, sample temperature, and the chemical treatment of the disk surfaces. We think these techniques will result in a major advance in our understanding of semiconductor lasers and optical microstructures.

1 E. Betzig and J. K. Trautman, Science 257, 189 (1992).

2 U. Mohideen, W. S. Hobson, S. J. Pearton, F. Ren, and R. E. Slusher, Appl. Phys. Lett., to be published.

3 Y. Yamamoto and R. E. Slusher, Physics Today 46, 66 (1993).

4 W. S. Hobson, U. Mohideen, S. J. Pearton, R. E. Slusher, and F. Ren, Electron. Lett. 23, 345 (1993).

Near-field Time Resolved Fluorescence Spectroscopy on Single Proteins: Application to Photosynthetic Membranes

X. Sunney Xie[1], Robert C. Dunn[1], Gary R. Holtom[1], Laurens Mets[2]
[1]Pacific Northwest Laboratory, Molecular Science Research Center
P.O. Box 999, Richland, WA 99352
[2]University of Chicago, Molecular Genetics and Cell Biology
1101 E. 57th Street, Chicago, IL 60637

Introduction

The spatial resolution of conventional optical measurements is limited by far field diffraction effects. Recently a new optical technique has been demonstrated in which the spatial resolution can be much higher than the diffraction limit. Near-field optical microscopy involves scanning a spot of light, of dimension much smaller than the optical wavelength, in close proximity to the surface of a sample. To form the spot of light, a technique has been developed in which a single mode optical fiber is pulled to an ultrafine tip and coated with aluminum.[1] The tapered fiber tip funnels light through a small aperture (tens of nanometer) whose size determines the near-field spatial resolution. Furthermore, because of the inherently low background signal in these microscopes, emission signals from a single molecule can be detected.[2,3]

Combining the high spatial resolution of the near-field technique with a high time resolution capability promises to be extremely useful for biological applications. In photosynthetic membranes, for example, this will not only allow the study of energy and electron transfer processes in more detail, but also offer the possibility of a spectroscopic mapping of the photosynthetic membrane. The spatial distribution of the light harvesting complex (LHC), Photosystem I (PSI) and Photosystem II (PSII) in the thylakoid membrane is still not well understood. With the near-field technique, however, the distinct spectral properties, such as fluorescence lifetimes, can be used to identify the various complexes within the intact membrane.

We recently demonstrated the near-field fluorescence imaging of allophycocyanin (APC), a photosynthetic antenna protein which contains only six chromophores.[3] Here we report results on imaging single proteins and photosynthetic membranes with spatial resolution beyond the diffraction limit. We have incorporated a time-correlated single photon counting apparatus into the near-field microscope and conducted fluorescence lifetime measurements of LHC II proteins embedded in individual membrane fragments. We believe that this technique offers a unique approach for studying photosynthetic membranes.

Experimental

Typically, the aluminum coated fiber tips with 100nm apertures deliver approximately 10^{10} photons/sec to the far field with 5mW coupled in. The tip is brought in close proximity (approximately 5-10nm) to the sample in order to obtain the high spatial resolution. To maintain this small gap while the sample is scanned in a raster fashion, a feedback mechanism based on shear force is implemented.[4] This results in a simultaneous force mapping of the sample surface with a vertical resolution of 1nm and lateral resolution smaller than the tip diameter. The near-field assembly is supported on an inverted fluorescence microscope and the emission from a transmissive sample is collected with a high numerical aperture oil emersion objective. A combination of a holographic beamsplitter and notch filter are used to separate the residual excitation from the emission. The total emission is detected by a photon counting avalanche photodiode (APD) modified for fast time response[5], which maintains a high quantum efficiency (70% at 650nm) and low dark noise (<30 counts/sec).

For the time-resolved experiments described here, a picosecond pulse train (5ps, 633nm, 9.5MHz repetition rate) with 2mW average power from a synchronously pumped dye laser system was coupled into the fiber. We have shown that at this power level, no broadening of the picosecond pulses occurs while passing through the aluminum coated fiber tips.[6] The fluorescence decay times were measured using the time-correlated single photon counting technique in the reverse counting arrangement. The combination of the particular APD and the

detection electronics results in an instrumental response time of 120ps full-width half maximum (FWHM) with a full-width at one-hundredth maximum of 710ps.

Crosslinked APC trimer (Molecular Probes) was purified, and dispersed on a cleaned glass cover slip by spin coating. Thylakoid membranes from the Chlamydomonas reinhardtii PSI-PSII doubly deficient C2 strain containing only LHC II was chosen for this initial study because of the high fluorescence quantum yield.[7] The thylakoid membrane fragments are dispersed on a freshly cleaved mica substrate such that single layers of the photosynthetic membrane pieces lie down flat on the mica substrate. All the near-field measurements were done on dry sample at room temperature.

Results and Discussion

To demonstrate the sensitivity and resolution of the near-field microscope, Fig. 1 shows a 3μmx3μm near-field fluorescent image of single APC trimers dispersed on a glass cover slip. APC is a water soluble light harvesting protein complex in cyanobacteria. The APC trimer is a disc-like protein with a diameter of 11nm and a thickness of 3nm. Each APC trimer contains six open chain tetra-pyrrole chromophores covalently bound to the protein. These chromophores give rise to strong absorption and emission bands peaked at approximately 650nm and 670nm, respectively. The distinct features seen in Fig. 1 are attributable to single proteins and have a full-width-half-maximum (FWHM) of approximately 100nm. The 100nm spatial resolution, which is well beyond the classical diffraction limit, corresponds to the diameter of the tip used to image the proteins. Using the scan rate and the counts per pixel we estimate the count rate expected for positioning the tip above a feature at 8000 counts/sec. This count rate is more than enough to spread the counts in frequency or time and make spectroscopic measurements on the individual proteins.

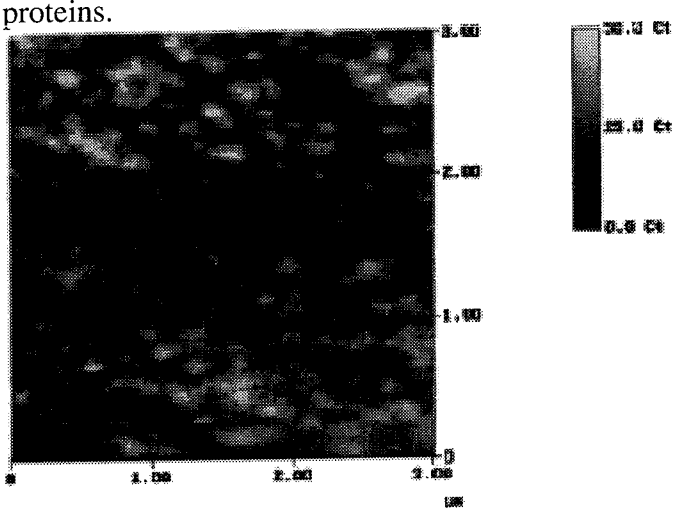


Figure 1. 3μmx3μm near-field fluorescence image of single APC trimers dispersed on a glass cover slip. Each trimeric APC protein contains only six chromophores.

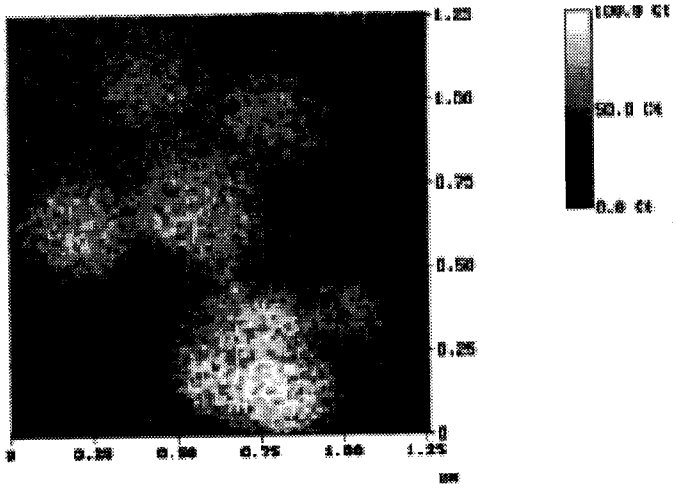


Figure 2. 1.25μmx1.25μm near-field fluorescence image of single fragments of intact photosynthtic membrane containing only light harvesting complexes. The single bilayer membranes lie down flat on the mica surface.

Figure 2 shows a 1.25μmx1.25μm near-field fluorescence image of intact photosynthetic membranes containing only the light harvesting complexes (LHC II) (9nm in diameter with 7 Chl a and 8 Chl b embedded). The emission is from the chlorophyll a of LHC II. The 160 pixel x 160 pixel fluorescence image was accumulated with a collection time of 4 ms per pixel. The simultaneous shear force image (not shown) shows that the emission signals arise from single layers of the photosynthetic membrane, laying flat on the mica surface. The fluorescence image in Fig. 2 lacks specific features and merely reflect the size of the membrane pieces. This is consistent with electron micrograph studies which showed that the LHC II proteins tend to aggregate in the membrane to form a two dimension lattice.

Figure 3 shows the fluorescence decay data taken by positioning the near-field fiber tip at the center of a membrane piece and keeping the tip-sample gap at 10nm. The inset in Fig. 3 shows the instrumental response function which has a FWHM of 120ps. The decay can be fit with a sum of two exponentials with a fast component of 450ps (65%) and the long component of 2.7ns (35%). These lifetimes are in close agreement with previous solution phase measurement of the same sample.[7] This result indicates that the quenching of the fluorescence by the aluminum coating of the fiber probe is not significant at a gap of 10nm. It is important to stress that time resolved fluorescence measurements were conducted on a single intact membrane with nanometric spatial resolution. To date, most of the informative experiments were done with big ensembles of isolated protein complexes in buffer solutions. The heterogeneity of the sample is often problematic, contributing to the complexity of the fluorescence decay kinetics. Isolation of the protein from the membrane also tends to reduce the integrity of the membrane protein. Conducting time-resolved fluorescence measurements with nanometer spatial resolution on intact thylakoid membranes makes it possible to study the energy and electron transfer dynamics on a single protein basis in its native state, free from these complications.

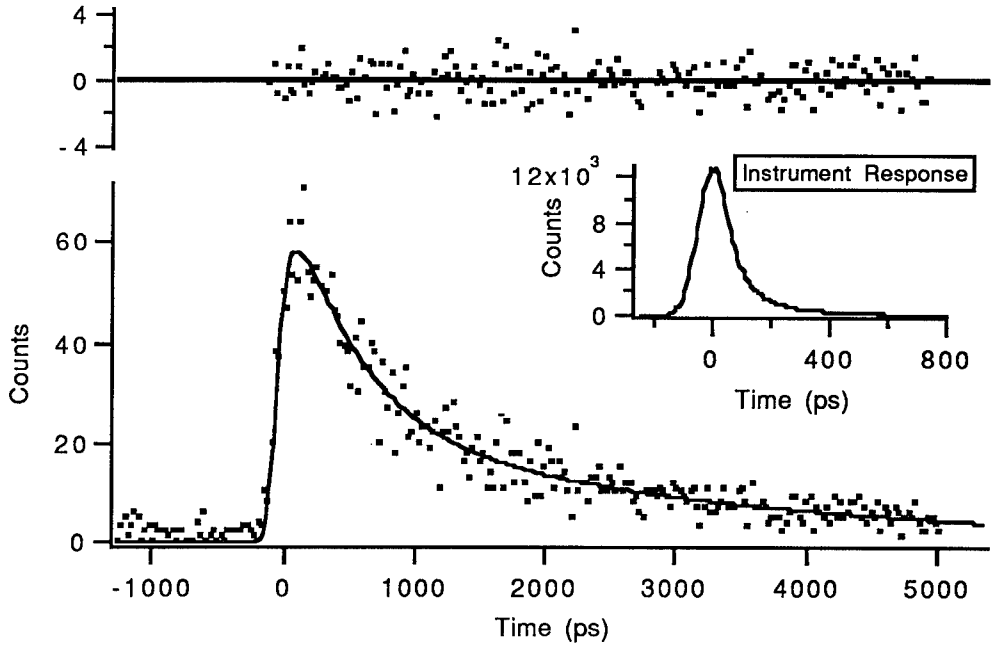


Figure 3. Fluorescence decay of LHC II proteins in an intact membrane taken with the near field microscope. The decay is fit with a sum of exponentials with lifetimes of 450ps (65%) and 2.7ns (35%). The inset shows the instrument response function which has a FWHM of 120ps.

To summarize, we have obtained near-field fluorescence images of single APC trimers as well as intact photosynthetic membranes with 100nm spatial resolution. We have demonstrated the feasibility of time correlated photon counting with near-field optics. Fluorescence lifetime measurements on a single photosynthetic membrane fragment have been made possible. We believe the high time resolution, spatial resolving power, single molecule sensitivity and noninvasive nature make this technique a powerful new approach for the study of photosynthesis, and other biological systems.

Acknowledgments

We thank Vey Allen and Gordon Anderson for their help in the development of the microscope, Aida Pascual for help in preparing the membrane samples. We are grateful to Digital Instruments for their technical support. This work was supported by the Chemical Sciences Division in the Office of Basic Energy Sciences of the U. S. Department of Energy at Pacific Northwest Laboratory under Contract No. DE-AC06-76RLO 1830.

References

1. E. Betzig, J. K. Trautman, T. D. Harris, J. S. Weiner, R. L. Kostelak: Science **251**, 1468 (1991)
2. E. Betzig, R. J. Chichester: Science **262**, 1422 (1993); W. P. Ambrose, P. M. Goodwin, J. C. Martin, R. A. Keller: Phys. Rev. Lett., submitted
3. R. C. Dunn, E. V. Allen, S. A. Joyce, G. A. Anderson, X. S. Xie: Ultramicroscopy, in press
4. E. Betzig, P. L. Finn, J. S. Weiner: Appl. Phys. Lett. **60**, 2484 (1992); R. Toledo-Crow, P. C. Yang, Y. Chen, M. Vaez-Iravani: Appl. Phys. Lett. **60**, 2957 (1992)
5. L. Li, L. M. Davis: Rev. Sci. Instrum. **64**, 1524 (1993)
6. R. C. Dunn, X. S. Xie: Ultramicroscopy, in press
7. D. D. Eads, E. W. Castner, R. S. Alberte, L. Mets, G. R. Fleming: J. Phys. Chem. **93**, 8271 (1989)

Dispersion

WB 10:45am–12:00m
Dana Point Ballroom

Herman A. Haus, *Presider*
Massachusetts Institute of Technology

Interferometric measurements of femtosecond laser cavity dispersion

K. Naganuma

NTT Opto-electronics Laboratories

3-1 Morinosato-wakamiya, Atsugi-shi, Kanagawa, 243-01 JAPAN

telephone: +81 462 40 3239, facsimile: +81 462 40 4303

1. Introduction

Wavelength dispersion measurement method has been drawing much attention as an indispensable tool for femtosecond laser development. For individual optical element, these methods have already been established using interferometers.[1-3]

W. H. Knox developed a method called frequency domain dispersion (FDD)[4] and opened a way for measuring *in-situ* dispersion in live mode-locked lasers. However, arena for FDD is restricted to lasers which manifest spontaneous pulsation without external modulation as well as have an intra-cavity tuning element keeping the cavity length constant. For semiconductor lasers, femtosecond time-of-flight measurements were conducted to detect wavelength-dependent time separation between internally reflected sub-pulses.[5] This is not very practical, because a near-infrared tunable femtosecond light source is not easy to attain.

In this paper, we describe a new interferometric method to measure the laser cavity dispersion. With this method, in principle any laser, irrespective of lasing mode, can be measured for the entire gain band wavelengths.

2. Principle of Cavity FTC

In interferometric dispersion measurements, a white light electric field E_i is crosscorrelated to convoluted field $E_s = E_i \otimes t_s$, where t_s is transfer function of sample. To obtain the convoluted field, ordinary optics needs to be inserted in one of arms of a Michelson interferometer. In contrast, when the sample is a cavity, the convoluted field is automatically generated while the light is circulating inside the cavity, which enables dispersion measurements on the cavity placed outside the interferometer. The path difference of the now empty interferometer should be equal to the sample cavity length to allow E_s to catch up to E_i. If the sample cavity is light emitting, i.e. laser or an optical amplifier, its amplified spontaneous emission (ASE) can be used as the light source. Therefore, the resulting measurement setup is just an imbalanced Michelson interferometer.

A long-range scan of interferometric correlation for a 1.55-μm laser diode is depicted in Fig. 1. Ordinary interferogram, or electric field autocorrelation $S_0(\tau)$ appears near the zero-delay posi-

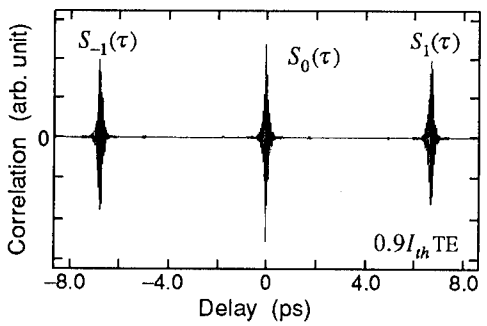


Fig. 1 Typical interferometric correlation for a semiconductor laser diode. In addition to the ordinary interferogram S_0, subfringe S_1 carrying round-trip transfer function information appears. In the opposite time-delay direction, its mirror image S_{-1} comes out with functions of interferometer arms exchanged.

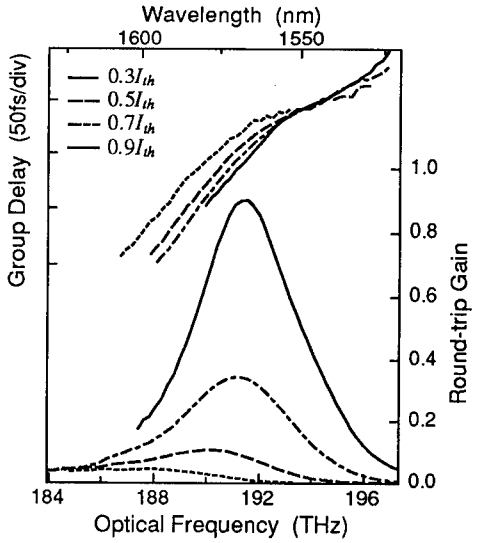


Fig. 2 Measurement results on a 1.55-μm strained-layer quantum well BH laser diode. When the current is raised to I_{th}, the gain approaches unity as expected.

tion. When time delay τ is increased, an interference signal reappears near the cavity round-trip time ($\approx$7 ps). The subfringe $S_1(\tau)$ should contain information about the transfer function of the cavity. To extract this information, we exploit Fourier transform of interference signals which is expressed as $\tilde{S}_0(\omega) = t_{\text{bias}}(\omega)U(\omega)$ and $\tilde{S}_1(\omega) = t_{\text{RT}}(\omega)t_{\text{bias}}(\omega)U(\omega)$. By calculating the quotient, $\tilde{S}_1(\omega)/\tilde{S}_0(\omega)$, pure round-trip transfer function $t_{\text{RT}}(\omega)$ can be separated with the apparatus-specific bias $t_{\text{bias}}(\omega)$ and the ASE spectrum $U(\omega)$ completely eliminated. Then round-trip gain is calculated as $|t_{\text{RT}}(\omega)|^2$, while the group delay spectrum is obtained by $d\arg[t_{\text{RT}}(\omega)]/d\omega$.

In experiment, we used a Michelson interferometer whose path difference is calibrated by a He-Ne laser. ASE from a sample cavity was fed to the interferometer through a signal-mode optical fiber, to reduce beam divergence. The semiconductor sample cavity was temperature-controlled during measurements to prevent cavity length drift. The results for a 1.55-μm strained-layer quantum well BH laser diode are shown in Fig. 2. On the longer wavelength side, group delay decreases for larger injection current due to the α-parameter effect. In the case of this laser, the dispersion at the gain peak wavelength remains almost constant across different injection currents, allowing extrapolation of these below-threshold measurements to lasing state.

3. Dual interferometer scheme

With typical femtosecond lasers where discrete optics are assembled on a chassis, the cavity length fluctuates ceaselessly (ca. $\Delta L \approx 0.5$ μm) because of air flow and ambient vibration, which hindered measurement efforts. To address this problem, we devised a dual interferometer scheme shown in Fig. 3 in which one of the interferometers is dedicated to detecting length change in the test cavity and enabling influence of fluctuations to be nullified.

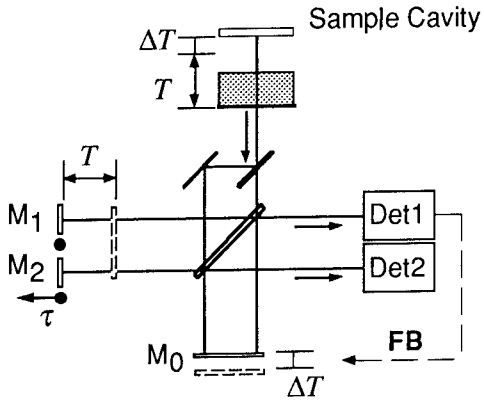


Fig. 3 Dual interferometer scheme. Interferometer #1 which is kept still detects cavity length fluctuations and shifts the time-delay origin accordingly by moving the PZT-attached mirror M_0.

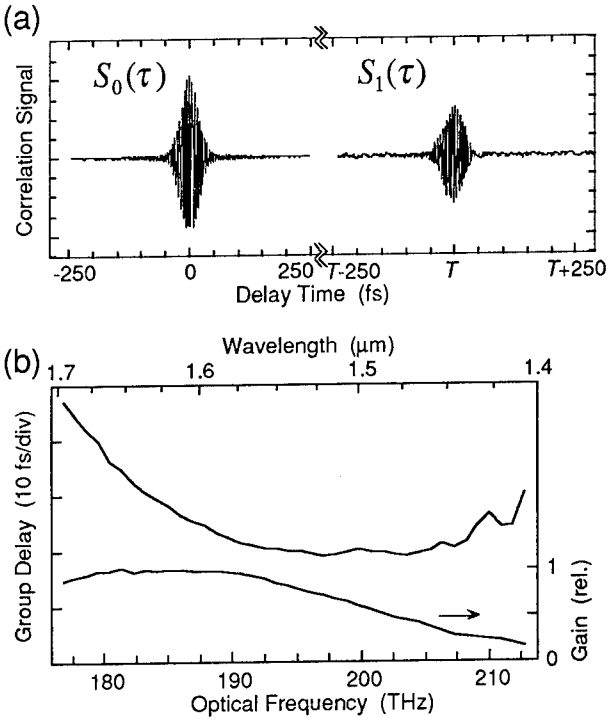


Fig. 4 Measurement results for a femtosecond color-center laser cavity. (a) correlation signals. (b) group delay and power gain spectrum. Tiny dispersion in a femtosecond domain has been clearly detected.

Figure 4 shows measurement results on a NaCl:OH^- color-center laser cavity. The laser was a Burleigh Instruments Model FCL-230 with a 150-cm cavity length ($L/2$), and generated 130-fs pulses under an additive-pulse modelocking (APM) operation. Correlation signals were measured for an ASE light with a power of 48 nW out of the fiber. In Fig. 4(a), the small difference between the interferogram $S_0(\tau)$ and the crosscorrelation $S_1(\tau)$ implies that intracavity dispersion is tiny.

Figure 4(b) shows the obtained spectrum for group delay and power gain. Accuracy for these measurements is estimated to be 0.59 fs for group delay and 3.4% for gain with a 3.7-THz (28-nm) resolution. The group delay spectrum shows that this laser operates in wavelengths where cavity dispersion is very close to zero. For a NaCl:OH^- color-center amplifier, Sucha *et al.*[6] pointed out that negative dispersion of glass partially compensates positive dispersion accompanied by the crystal. Similar circumstances hold true for this laser cavity.

In conclusion, the new interferometric method (Cavity FTC) provides an universal and quick way to detect femtosecond group delay.

References

1. W. H. Knox, N. M. Pearson, K. D. Li, and C. A. Hirlimann, Opt. Lett. **13**, 574 (1988).
2. K. Naganuma, K. Mogi, and H. Yamada, Opt. Lett. **15**, 393 (1990).
3. M. Beck, and I. A. Walmsley, Opt. Lett. **15**, 492 (1990).
4. W. H. Knox, Opt. Lett. **17**, 514 (1992).
5. K. L. Hall, G. Lenz, and E. P. Ippen, IEEE J. Lightwave Technol. **LT-10**, 616 (1992).
6. G. Sucha, S. R. Bolton, and D. S. Chemla, IEEE J. Quantum Electron. **QE-28**, 2163 (1992).

Frequency Domain Study of Cross-coupling in a Two-wavelength Self-modelocked Ti:Sapphire Laser

D. R. Dykaar, W. H. Knox*, and S.B. Darack
AT&T Bell Laboratories Murray Hill, NJ 07974
*Holmdel, NJ 07733

The recent demonstration of self-modelocking in broadband solid state gain media [1] has caused an resurgence of interest in studies of bulk self-focusing interactions. In particular, two-color nonlinear interactions have been the subject of much interest in soliton communications [2], and operation of the Ti:Sapphire laser exhibits some soliton-like features [3]. Recently, the Ti:Sapphire laser has been modelocked at two wavelengths simultaneously using a single laser rod [4-6]. These lasers produce two independently tunable trains of pulses of <100 fs duration. Under certain conditions these pulse trains will precisely synchronize themselves, exhibiting a jitter of < 50 fs. In the present paper we discuss measurements of the frequency-pulling characteristics of a 2-color self-modelocked Ti:Sapphire laser based on the design of Dykaar [6]. These measurements demonstrate the strong nonlinearity of the cross-modelocking process, and may provide insight into two-wavelength soliton interactions.

Figure 1 shows a conceptual picture of our experiment. A single Ti:Sapphire laser rod is placed in a double cavity. In the laser rod, each pulse experiences a self-focusing nonlinearity, which causes it to modelock in a steady-state [1]. If the cavity is carefully aligned, the two pulses interact and feel the combined self-focusing field. Thus, the two pulses will achieve the highest net gain in their respective cavities when they travel together precisely in time and nearly so in space through the focus region. We find that the interaction between the pulses changes their cavity round-trip times. Recently, intracavity dispersion has been studied by monitoring the wavelength dependence of the cavity round-trip time by using a digital frequency counter [7]. We use this technique to perform two experiments. In the first, we change the length of one cavity and monitor the repetition rate of the two cavities. In the second, we show that the repetition rate of the second pulse is changed by the presence of the first pulse. In the actual laser, two argon laser pump beams are used to create two gain regions within a single Ti:Sapphire laser rod. Two cavities are configured with two sets of prisms that can be individually optimized for different wavelengths. As such, the two cavities the two cavities may have different dispersion characteristics.

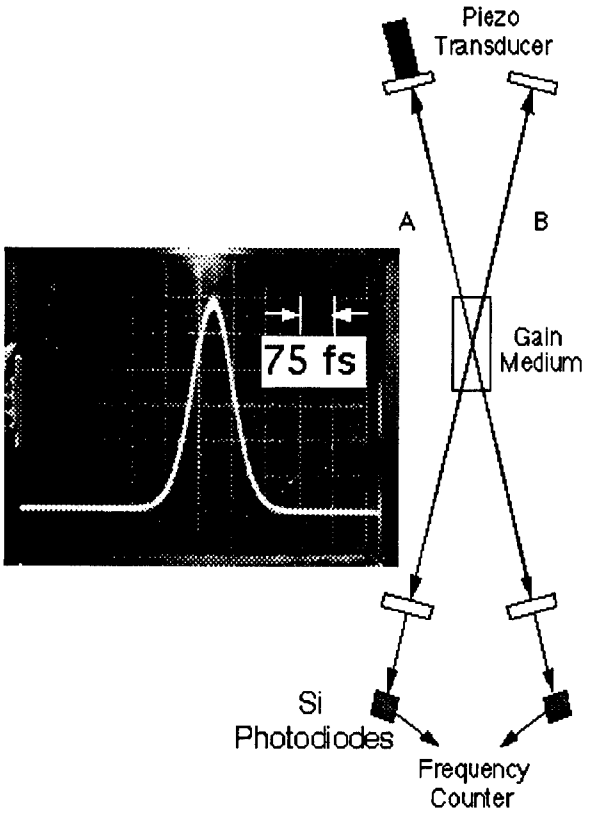


Figure 1. Two self-modelocked Ti:Sapphire lasers are cross-modelocked by sharing the same gain medium. One cavity is perturbed, and the change in the other cavity is measured. Inset shows cross correlation.

Two silicon photodiodes detect the separate pulse trains, and the repetition rates are measured using a digital two channel frequency counter with 11-digit readout and computer (Fig. 1). For a given set of operating conditions, the cavity length can be adjusted so that the two pulse trains lock in precise synchronization, producing the stable cross correlation shown in Fig. 1. In Figure 2(a), we show the two cavity frequencies. As cavity "A" is mechanically shortened using a piezoelectric transducer, cavity "B" remains rigorously locked and its frequency changes in exactly the same manner until a maximum length mismatch is attained. At that point, the two cavities unlock, taking on two different repetition rates corresponding to a weakly-coupled regime. The maximum cavity offset of ± 3 μm for cross-locking corresponds to a time difference of 20 fs, or about 20% of the pulse width. ***Therefore, the nonlinear pulse advance can be as large as 1/5 of the pulsewidth in every round trip.*** Clearly, self-focused modelocking results in very strong pulse shaping effects. We then slowly return the length of cavity "A" to its original length. When detuning becomes < 3 Hz, the cavities once again cross lock. Noise in the locked regimes corresponds to the paired cavity repetition rate (thermal) drift [6, 8].

In the second experiment, the laser is placed in the cross-locked state and then the beam of cavity "B" (Fig. 2(b)) is physically blocked. When cavity "B" is present, the repetition rate of cavity "A" corresponds to that of the coupled cavities. When cavity "B" is blocked, cavity "A" relaxes to its unperturbed repetition rate. After the block is removed, cavity "A" is frequency-pulled,

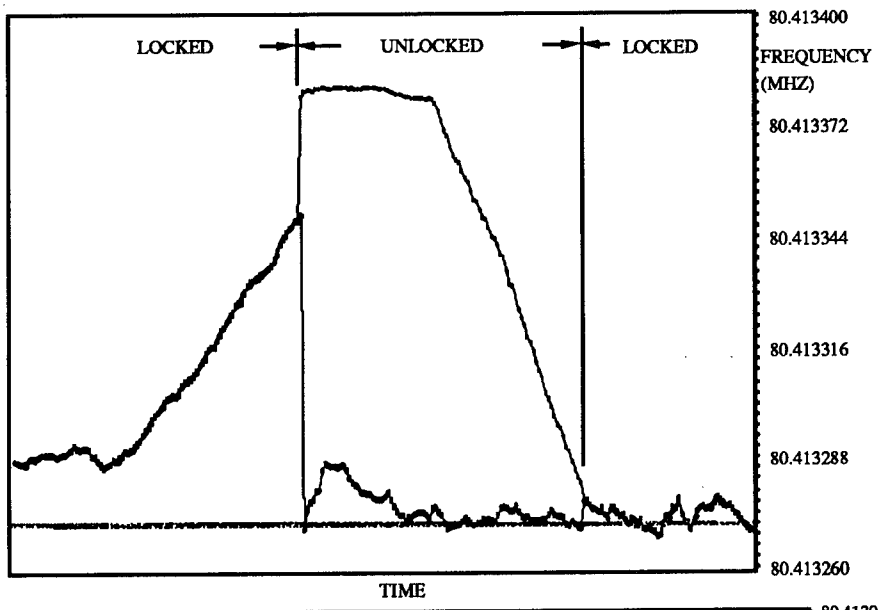


Figure 2(a). Frequency (repetition rate) versus time (~1 minute). Initially, both cavities repetition rates track as one cavity length is changed until the locking limit is reached. Then *both* cavities relax to their unperturbed repetition rates, until the adjustable cavity length is brought back inside the capture range.

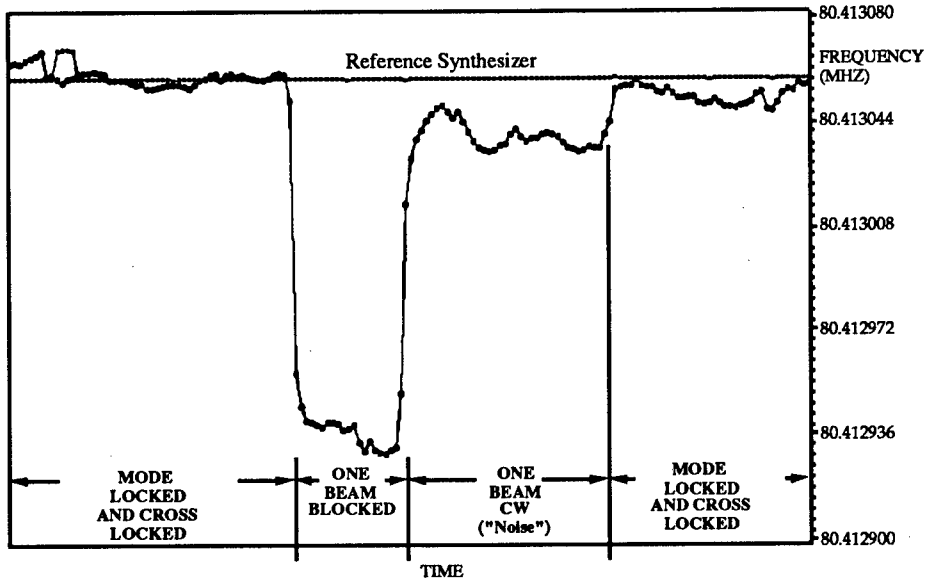


Figure 2(b) Here, one beam is allowed to relax to the unperturbed state by blocking the second beam. Once unblocked, even cw operation is sufficient to pull the repetition rate.

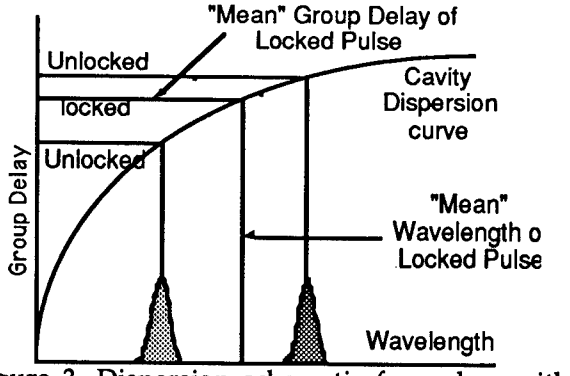


Figure 3. Dispersion schematic for pulses with different wavelength traveling at a common mean group delay.

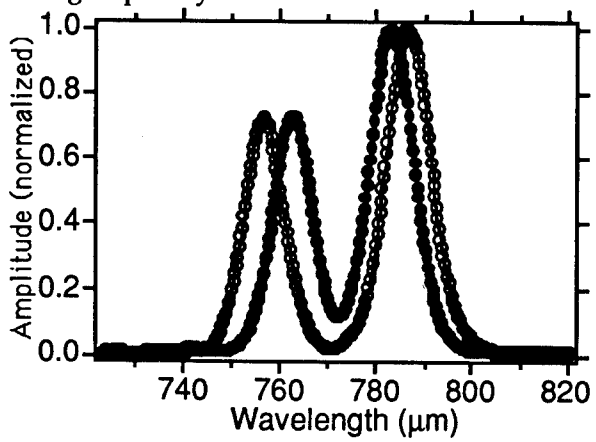


Figure 4. Spectra taken of both beams simultaneously at the cavity detuning maxima, ~6 μm total offset.

despite the fact that cavity "B" re-starts in a state of cw ("noise"). Even in this state there is clear evidence of oscillation at the cavity "B" round trip time as seen via a photodiode on an oscilloscope. When the optical table is tapped, the two beams return to the cross locked state. The time scale in Figs. 2(a) and (b) is ~1 min.

This can be understood in terms of the frequency-dependent group delay described by Knox [7,9]. Consider the cavity group delay to be described by a single generalized curve shown in Fig. 3. In fact, each cavity will have a slightly different dispersion. The two pulses would travel at different round-trip times if they were not interacting, however in the "locked" condition, the group delay becomes a common "mean"
value for both cavities, despite the fact that the wavelength are very different. This is the locked condition that results in a stable cross correlation. A consequence of this condition is that the resulting pulse can now also described by a "mean" wavelength as shown in the Fig. 3. The pulses are traveling together as a *single pulse*, despite having very different spectra and a An additional, and perhaps more complex, consequence of the locked condition is the wavelength pulling shown in Fig. 4. The two cross-locked beams are combined at the entrance slit of a spectrometer, and the spectra are recorded at the +3 and -3 μm cavity detuning points. The spectrum of both pulses beam overlap in the laser rod which occurs only in the wings of the spatial distribution [6]. An additional consequence of the locked condition is the wavelength pulling shown in Fig. 4. The two cross-locked beams are combined at the entrance slit of a spectrometer, and the spectra are recorded at the +3 and -3 μm cavity detuning points. Both wavelengths are seen to be shifted, as would be expected for equal pump intensities (i.e. there is no master or slave cavity in this configuration). In addition, the shift is different for each cavity as the cavities are not identical. This phenomena is not presently understood and warrants further study.

In conclusion we have investigated the mode-locking dynamics of a two-color cross-mode locked laser. We have shown that the frequency-dependent group delay model of mean wavelength and mean group delay can be extended to a pair of cross-locked pulses with disparate spectra and spatial distribution in a nonlinear regenerative system. Further, wavelength pulling is seen to be an additional consequence of the cross-locked condition.

REFERENCES

1. D. E. Spence, P. N. Kean, and W. Sibbett, Optics Letters, **16** 42 (1991).
2. H. A. Haus, J. G. Fujimoto, and E. P. Ippen, IEEE JQE Special Issue on Ultrafast Optics and Electronics, **28** 2086 (1992).
3. F. Ouellette, and M. Piche, JOSA **B5** 1228 (1988).
4. M. R. X. deBarros, and P. C. Becker, Optics Letters, **18** 631 (1993).
5. J. M. Evans, D. E. Spence, D. Burns, and W. Sibbett, Optics Letters, **18** 1074 (1993).
6. D. R. Dykaar, and S. B. Darack, Optics Letters, **18** 634 (1993).
7. W. H. Knox, Optics Letters, **27** 1 (1992).
8. S. B. Darack, D. R. Dykaar, and G. T. Harvey, Optics Letters, 16 1677 (1991).
9. W. H. Knox and J. P. Gordon, JOSA **B10** 2071, (1993).

Ultrashort pulse multiterawatt Ti:sapphire laser system

C. P. J. Barty, B. E. Lemoff, and C. L. Gordon III
Edward L. Ginzton Laboratory, Stanford University, Stanford, California 94305

Introduction

A new class of ultrashort pulse laser systems has been developed as a pump source for diagnostic x-ray generation and XUV laser experiments. This system is presently capable of producing 135 mJ, 35 fs, 800 nm pulses with near diffraction limited beam quality at a 10 Hz repetition rate. To our knowledge, it is the first such system to produce sub-50 fs pulses with multiterawatt peak powers and the first to control femtosecond timescale phase and amplitude distortions during terawatt level amplification. In order to produce these pulses, the system incorporates several unique innovations which alleviate problems inherent to other short pulse amplification schemes.

Chirped pulse amplification (CPA) has become a common technique for circumventing optical damage and nonlinear effects during the amplification of short optical pulses in solid state laser media.[1] Terawatt level pulses with durations ranging from ~1 ps to ~100 fs have been produced by a number of systems. Although much shorter pulse oscillators exist, the implementation of CPA with pulses on the order of 10 fs has not been accomplished. In conventional CPA systems, uncompensatable phase errors in the expansion and recompression process and distortions due to refractive optics produce broadenings which are much greater than 10 fs. In order to alleviate these problems, a novel expander/compressor design has been developed and a lens-free amplification system has been constructed.

High Fidelity Pulse Expansion and Compression

The laser system uses a regeneratively-initiated, self-mode-locked, 20-fs Ti:sapphire oscillator to provide ~5-nJ seed pulses for amplification.[2] In order to avoid self focusing in the amplifier medium and optical damage of dielectric coatings, it is necessary to temporally stretch the oscillator output to several hundred picoseconds before amplification. By doing so, the peak intensity in the amplifier chain is limited to less than 10 GW/cm^2. To accurately expand and recompress 20-fs pulses, a new cylindrical mirror based expander and compressor system is used. This system is capable of temporally stretching a 20-fs pulse by a factor of 15,000 and recompressing it to within 0.1 fs of the original duration.[3] A schematic of the expander is shown in Figure 1. The arrangement avoids chromatic errors due to refractive optics present in conven-

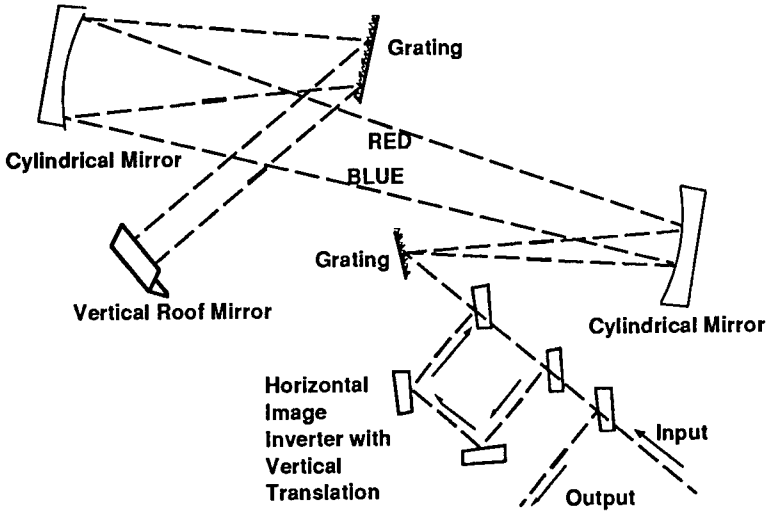


Figure 1. Schematic of mirror-based expansion and compression system

tional designs. Also key is the use of an image inversion mirror arrangement after one pass through the system. This allows spatially uniform temporal expansion of pulses with finite input diameter and divergence. This latter problem is also present in conventional designs. With 20 fs input pulses, the error produced by a system without image inversion is greater than the pulse duration. A detailed ray tracing analysis is used to calculate the correct placement, orientation and separation of the expander and compressor elements and the correct amount of optical material necessary to eliminate 2nd, 3rd and 4th order spectral phase distortions. The model predicts that element placement must be accurate to within 100 microns, grating and mirror angles must be accurate to within 2 arc minutes and that correct material path must be accurate to within 1 cm. Tests without amplification verify these predictions.[3]

High Spatial Quality Amplification

The output energy of the pulses from the expander is approximately 500 pJ. Amplification to 260 mJ is accomplished in a two stage arrangement. The first stage is a regenerative amplifier consisting of one Pockels cell, two polarizers and a 13 mm long Ti:sapphire crystal.[4] The crystal is pumped with ~50 mJ of gaussian spatial profile 532 nm radiation. This allows the gain medium to act as a weak gaussian spatial filter and results in excellent output beam quality. The output energy of the regenerative amplifier is ~9 mJ. The beam diameter is then increased to ~5 mm with an off axis spherical mirror telescope. It should be noted that conventional refractive telescopes cannot be used for this application. Such telescopes lead to curved pulse fronts with center to edge beam delays on the order of 10 fs and thus to increases of focused interaction times of the same order. The 5 mm diameter beam is then amplified in a four pass arrangement consisting of a 13 mm diameter x 13 mm long Ti:sapphire crystal. The crystal is pumped with ~850 mJ of 532 nm radiation. Again the green spatial profile is approximately gaussian. The resulting 260 mJ pulse is spatially expanded to a ~25 mm diameter with a final off axis spherical mirror telescope. 1200 groove/mm, gold coated ruled gratings are used in the expander and compressor. Grating diffraction losses result in a compressor throughput of ~55%.

The focusability of this amplified beam is critical to many proposed experiments. A measurement of the beam quality was made by focusing the compressed output with a 1 m focal length spherical mirror and measuring the beam waist as a function of longitudinal and transverse position. Beam profiles were obtained with a computer controlled scanning slit and photodiode. The top hat equivalent waist of the horizontal and vertical profiles are 1.02 and 1.89 times that of a gaussian with the same far field divergence respectively. We believe that the decreased beam quality in the vertical dimension is due to the spatial multiplexing that occurs in the four pass amplifier. Nonetheless, the compressed pulses should be capable of producing focused intensities of ~1×10^{20} W/cm^2 with f1 optics.

Control of Gain Narrowing

Because linear phase distortion is controlled in this system, the duration of the amplified pulse is determined by its spectral content and thus by the spectral response of the amplifiers. Gain narrowing severely limits this spectral content. To estimate the shortest possible pulse that we may obtain, we operate the amplifiers unseeded but with the same output energy. The spectrum of the resulting amplified spontaneous emission (ASE) is equivalent to that produced by delta function input pulse of no energy. The result would correspond to a pulse of ~30 fs in duration. Since we start with a finite duration input pulse of small energy we expect a significantly longer result. A typical seeded and amplified spectrum corresponds to a pulse of ~45 fs in duration. In order to produce shorter pulses we modify the spectrum of the seed pulse. This is easily accomplished by placing a spatially varying filter of the correct attenuation in the focal plane of the first cylindrical mirror of the pulse expander. By doing so, one may

significantly increase the FWHM of the seed pulse spectrum at the expense of reducing the seed pulse energy. As an example, Figure 2 illustrates the input, filtered and amplified spectra corresponding placement of a circular card at the focal plane of the expander. The card blocks approximately 50% of the vertical extent of the beam and is located at a transverse position corresponding to the peak of the pulse spectrum. Because of the large distance, the diffraction caused by this card is not present at the amplifier. The duration of the transform limit of the amplified spectrum is 34.5 fs which agrees well with single shot autocorrelations of the amplified and compressed pulse. While a simple card illustrates the utility of spectral shaping, a more accurate filter based on transmission gratings which are etched in chromium films is currently under development.

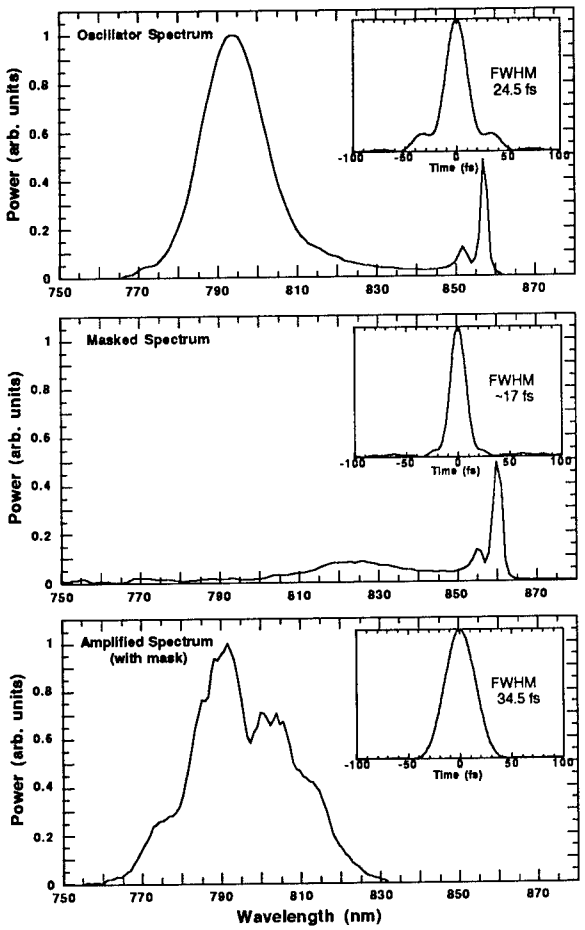


Figure 2. Input, masked, and amplified spectra with transform limited pulse shapes (inset).

Conclusions

Pulses from the present system will be used in laser generated diagnostic x-ray and XUV laser experiments. The ability to control femtosecond distortions during amplification will benefit other applications as well. These include bond-selective chemistry in which moderate energy, <100 fs shaped optical fields are desired and high energy, sub-picoseond infrared generation in which multiple frequency, temporally coincident amplified pulses are necessary. It should also be noted that because this design can accommodate large amounts of optical material in the amplification chain, straightforward scaling to higher energies is possible. Laboratory scale, petawatt (10 J in 10 fs) systems are feasible with currently available optical components.

References

1. D. Strickland and G. Mourou, Opt. Comm. 56, 219(1985)
2. B. E. Lemoff and C. P. J. Barty, Opt. Lett., 17, 1367(1992)
3. B. E. Lemoff and C. P. J. Barty, Opt. Lett., 18, 1651(1993)
4. J. D. Kmetec, J. J. Macklin and J. F. Young, Opt. Lett. 16, 1001(1991)

Ultrashort-Pulse Amplification in Ti:sapphire

Jianping Zhou, Chung-Po Huang, Henry C. Kapteyn and Margaret M. Murnane
Department of Physics, Washington State University, Pullman, WA 99164-2814

The extremely broad gain bandwidth of Ti:sapphire has made this material one of the most promising for the generation of ultrashort optical pulses.[1] Recent advances in ultrashort-pulse Ti: sapphire lasers have made it possible to routinely generate optical pulses of ~10 fs in duration, with nJ energies.[2-5] However, many applications of ultrashort pulses such as ultrafast x-ray generation, short-wavelength lasers, XUV harmonic generation, and multi-photon ionization require higher energies, and therefore it is of great interest to amplify the low energy pulses from the laser to higher energies, while maintaining their ultrashort duration. Recently we have demonstrated the generation of 0.5 mJ, 21 fs pulses, with a near-transform limited bandwidth of 44 nm, from our amplifier system.[6,7] In this paper, we present preliminary results from a second stage of amplification, which demonstrate pulse energies of up to 45 mJ, with spectral bandwidths of 37 nm. This bandwidth corresponds to a pulse duration of less than 30 fs.

Our amplifier uses a chirped-pulse amplification (CPA) scheme,[8] in which the broad-bandwidth pulse from the laser oscillator passes through a diffraction grating set-up to stretch the pulse in time. This pulse is then amplified to high energy, while maintaining a modest intensity within the amplifier crystal. Following amplification, the stretched pulses can be re-compressed by passing it through a grating pair. In designing an amplifier system capable of supporting ultrashort pulses, higher order dispersion must be minimized. We achieved this by minimizing the amount of material through which the beam passes, by using short, highly-doped amplifier crystals, and by using a multipass amplifier design. We also carefully compensate for the residual third order dispersion, (introduced into the amplifier because of the need to compensate for dispersion due to the material in the amplifier), by introducing a prism pair into the amplifier beam path. The prism pair has a third order dispersion of opposite sign to that of the stretcher-compressor pair. This approach works well for the modest stretch factors we use (x 1000), which also reduce high order dispersion. Finally, we use an all-reflective stretcher and compressor to reduce spectral clipping and material in the amplifier.

Figure 1 shows the configuration of our system. The input of our amplification system is from a self modelocked Ti:sapphire oscillator that produces transform-limited 11 fs duration pulses, at a center wavelength of 796 nm, and with a FWHM bandwidth of 62 nm.[5] The initial pulse energy is 5 nJ. The beam passes through the all reflective stretcher which uses a single grating, a single parabolic mirror, and two flat mirrors. The pulses are stretched to approximately 20 ps after the stretcher. The first stage amplifier uses an 8 mm long, highly-doped (0.23%), Brewster-cut Ti:sapphire rod. It is pumped longitudinally with 100 mJ of 532 nm light from a doubled Q-switched Nd:YAG laser. The amplifier rod is at the focus of four 1-meter radius-of-curvature dielectric mirrors, which form an eight-pass figure "8" amplifier. To suppress ASE, the beam focuses through a four-hole array placed near the crystal, and a saturable absorber is used before the final pass through the amplifier. Another saturable absorber is placed between the two amplifier stages to prevent ASE from the second stage from being amplified through the first stage. The second amplifier uses a normal incidence, anti-reflection-coated, 8 mm long crystal. The beam is passed through this amplifier three times without focusing, and is pumped by approximately 400 mJ of green light.

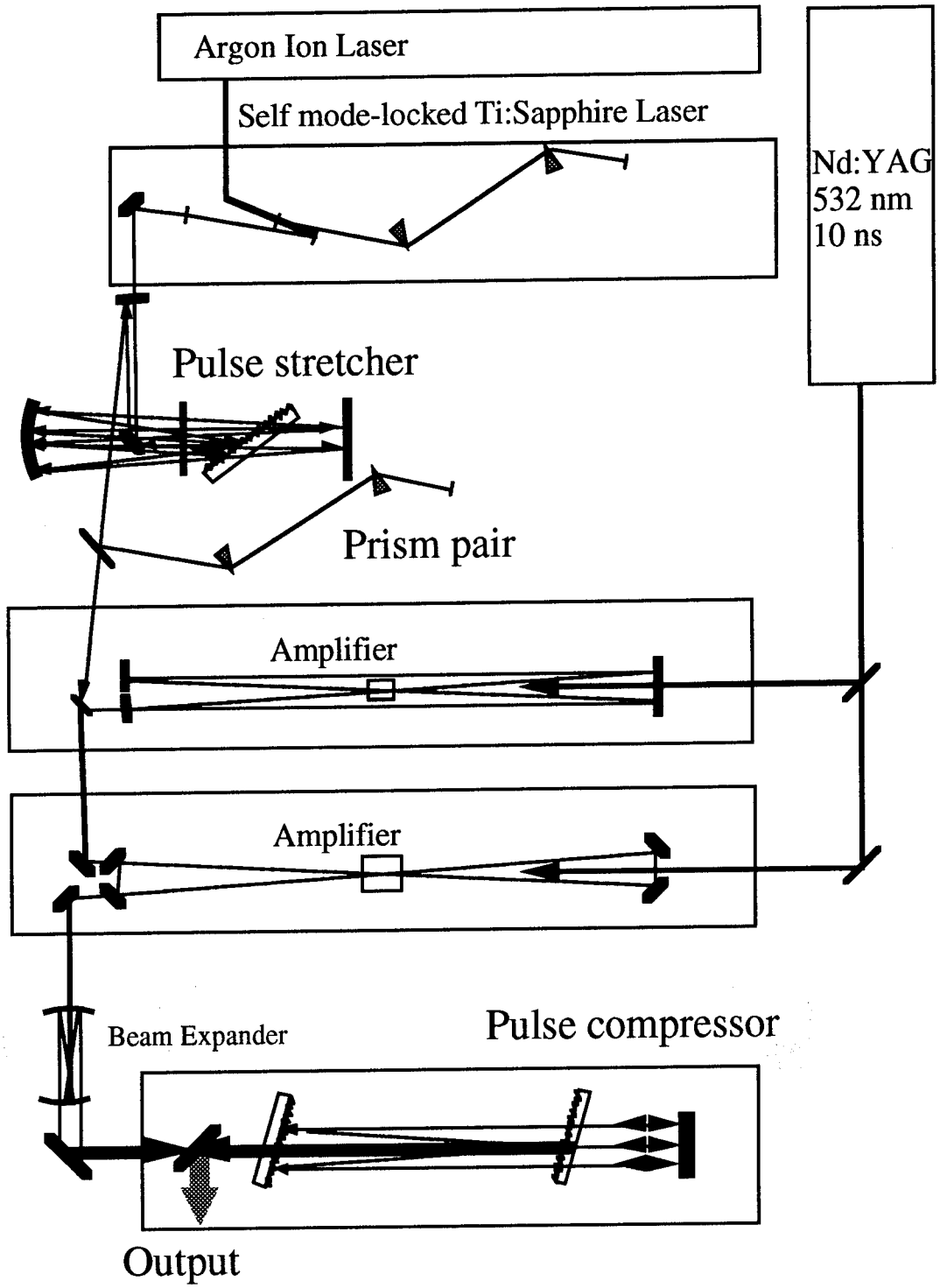


Figure 1: The configuration of the amplifier system, including a self-modelocked Ti:sapphire laser and two multi-pass amplifiers. The combination of SF 18 prism pair and the 300 g/mm grating pair is used to reduce both second and third order dispersion.

In the first stage amplification, the pulse experiences a gain of nearly 10^7, and is amplified to an energy of approximately 2 mJ. We observe strong gain narrowing in this amplifier, and red shifting due to gain saturation. The beam is then passed three times

through the second amplifier stage, to obtain output energies of 45 mJ per pulse, with FWHM bandwidths of 37 nm. A typical spectrum is shown in Figure 2. This bandwidth corresponds to a pulse duration of less than 30 fs. Following the first stage of amplification, we can recompress the output to between 18 and 21 fs.

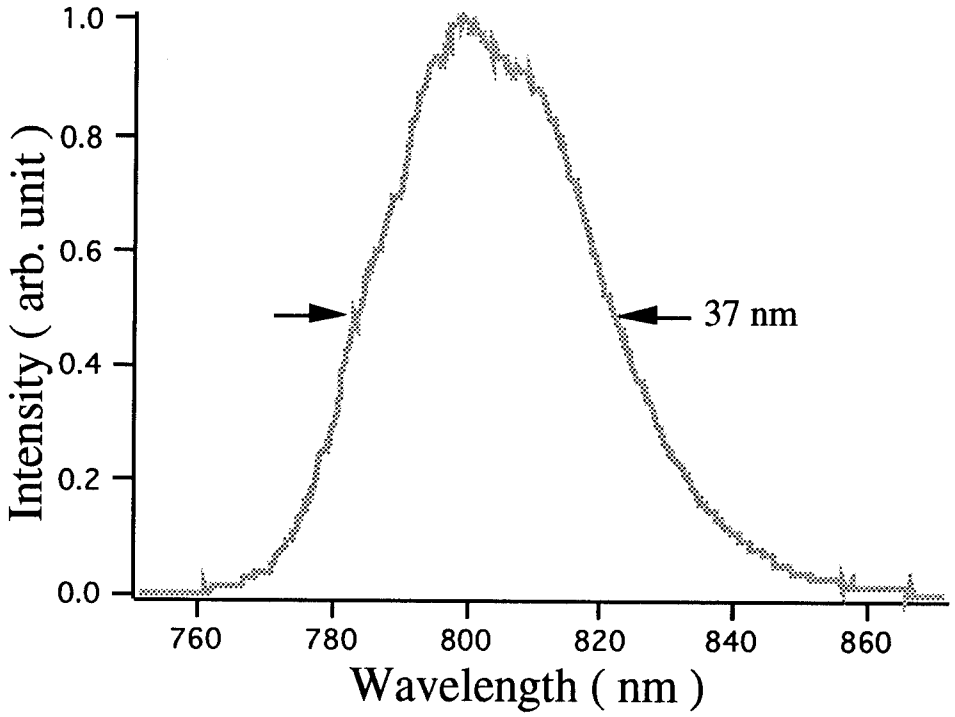


Figure 2.: Typical spectrum of the 45 mJ amplified pulse with FWHM spectrum of 37 nm.

References

1. P. F. Moulton, J. Opt. Soc. Am. B **3**, 125 (1986).
2. C. P. Huang, H. C. Kapteyn, J. W. McIntosh, M. M. Murnane, Opt. Lett. **17**, 139 (1992).
3. C. P. Huang, M. T. Asaki, S. Backus, M. M. Murnane, H. C. Kapteyn, H. Nathel, Opt. Lett. **17**, 1289 (1992).
4. C. P. Huang, M. Asaki, S. Backus, H. Nathel, M. M. Murnane, H. C. Kapteyn, at the *Ultrafast Phenomena VIII* Paper 160 (Antibes, France, 1992).
5. M. T. Asaki, C. P. Huang, D. Garvey, J. Zhou, H. C. Kapteyn, M. M. Murnane, Opt. Lett. **18**, 977 (1993).
6. J. Zhou, D. Garvey, C. P. Huang, M. T. Asaki, H. Nathel, H. C. Kapteyn, M. M. Murnane, SPIE OE LASE **1860**, 2 (1993).
7. J. Zhou, C. P. Huang, C. Shi, M. M. Murnane, H. C. Kapteyn, Opt. Lett., To be published, (1993).
8. M. Pessot, P. Maine, G. Mourou, Opt. Comm. **62**, 419 (1987).

Poster Session 3

WC 4:00pm–5:30pm
Dana Point Ballroom

High-repetition-rate blue-pumped βBaB_2O_4 femtosecond optical parametric oscillator tunable in the visible

G. M. GALE & F. HACHE
Laboratoire d'Optique Quantique du CNRS
Ecole Polytechnique
91128 Palaiseau, FRANCE
☎ (+33 1) 69.33.47.64

L. I. Pavlov
Institute of Electronics
Bulgarian Academy of Sciences
Sofia-1784, BULGARIA

High-repetition-rate femtosecond optical parametric oscillators (OPO) are potentially very useful devices in many areas of science due to their wide tunability, relatively short pulse duration and automatic synchronisation with the pump laser, which can allow, for example, sum and difference frequency generation, further extending the range of tunability of the OPO. To date continuous wave femtosecond OPO's have employed KTP [1-3] or KTA [4], mainly pumped by the fundamental wavelengths of a Ti:sapphire laser. These sources operate in the near- to mid- infrared, although intracavity frequency doubling of a KTP OPO has been described recently [5].

We report here the successful operation of a first version of a BBO OPO pumped by the ***second harmonic*** of a Ti:sapphire laser. This system is simple to align and operate and is very robust due to the high parametric gain of BBO. Even though the effective non-linear coefficient, d_{eff}, of BBO is smaller than that of KTP, the shorter wavelengths involved here and the fact that the signal/idler temporal walk-off is smaller in BBO than in KTP combine to give a much higher gain for the femtosecond BBO OPO. This gain is measured to be 15% per pass at 800 nm in a separate experiment. The present optical parametric oscillator set-up is shown in Fig. 1. An e (pump) ⇨ o (signal) + o (idler) type I geometry is employed with 6.7° external off-axis pumping for spatial walk-off compensation. With 900 mW of pump at 400 nm we obtain a total output signal power of 120 mW using a 3% transmission output coupler. Output is tunable from 575 to 660 nm with the present mirror set. The potential tuning range (for a 400 nm pump) is from 470 nm to 800 nm (idler from 2.7 μm to 800 nm). This tuning range could be extended into the UV by pumping with the third harmonic of the Ti:sapphire.

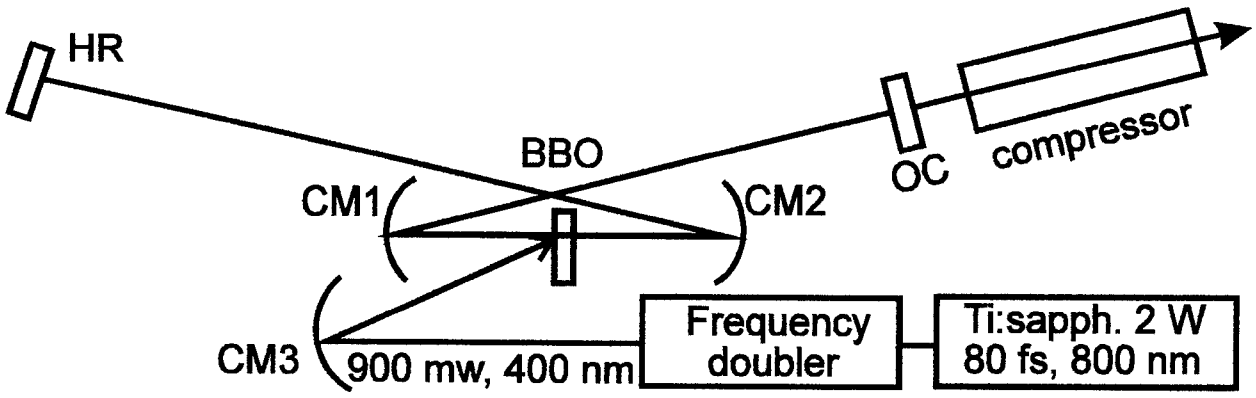


Fig. 1 Femtosecond BBO OPO. HR high reflector. CM curved mirror. OC 3% output coupler.

Without intra-cavity dispersion compensation the output pulses are chirped except in a small wavelength range around 640 nm where pulses with a time bandwidth product of 0.38, very close to the Fourier transform limit, are produced (see fig. 2) and the corresponding pulse width is 59 fs. This effect is attributed to signal chirp compensation [6]. Away from this wavelength region the spectrum assumes the typical near trapezoidal shape of chirped pulses and external compression becomes necessary. For example, at 590 nm the uncompressed pulse duration is about 200 fs and the compressed duration about 70 fs. We expect that the introduction of intra-cavity dispersion compensation, the use of a shorter crystal and pumping near 350 nm will allow the production of even shorter high-power pulses thoughout the whole visible region. We note equally, based on experience of mixing two Ti:sapphire lasers [7], that parametric intra- or extra-cavity difference frequency mixing of these OPO pulses with the Ti:sapphire fundamental, near 800 nm, will permit generation of high-repetition-rate sub-100 fs pulses in the mid infrared and beyond.

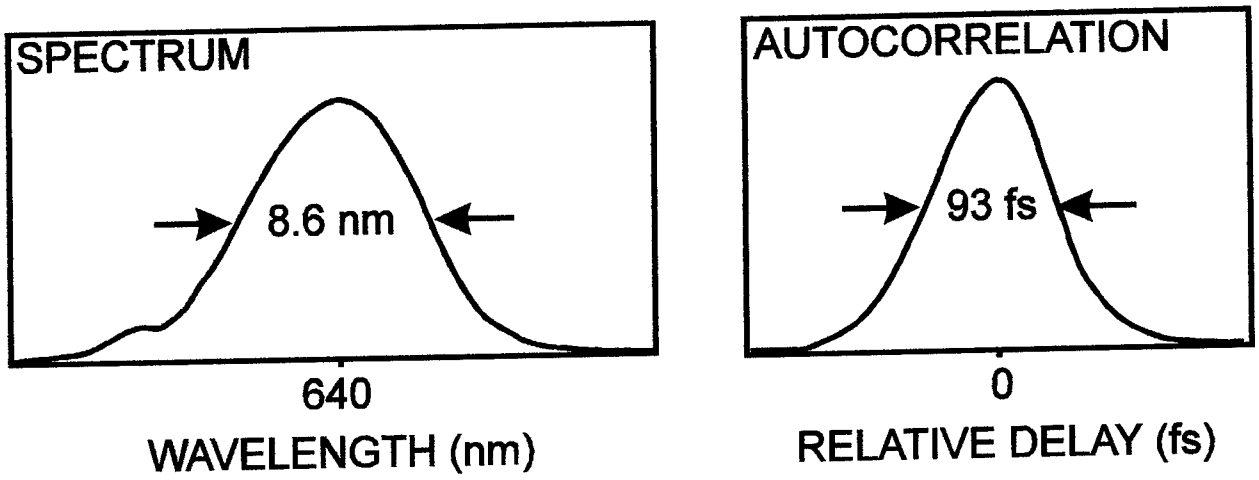


Fig. 2 Spectrum and autocorrelation function of the BBO OPO at 640 nm. Pulse duration is 59 fs assuming a $sech^2$ pulse shape and time-bandwith product is 0.38.

1] E. S. Wachman, D. C. Edelstein and C. L. Tang
Optics Letters **15**, 136 (1990)

2] W. S. Pelouch, P. E. Powers and C. L. Tang
Optics Letters **17**, 1070 (1992)

3] Q. Fu, G. Mak and H. M. van Driel
Optics Letters **17**, 1006 (1992)

4] P. E. Powers, S. Ramakrishna, C. L. Tang and L. K. Cheng
Optics Letters **18**, 1171 (1993)

5] R. J. Ellingson and C. L. Tang
Optics Letters **18**, 438 (1993)

6] R. Laenen, H. Graener and A. Laubereau
Optics Letters **15**, 971 (1990)

7] M. Cavalleri, G. M. Gale, F. Hache, L. I. Pavlov and E. Rousseau
to be published

Relaxation of Highly Vibrationally Excited Cycloheptatriene in Liquids Studied by Picosecond UV Absorption Spectroscopy

S. Linkersdörfer, J. Benzler, K. Luther and J. Troe

Institut für Physikalische Chemie, Universität Göttingen,
Tammannstrasse 6, 37077 Göttingen, Germany
Phone 49-551-393120/21
Fax 49-551-393150

To understand in detail the relaxation of highly vibrationally excited polyatomics in dense fluid media experimental answers on fundamental mechanistic aspects are still urgently needed. It has been demonstrated on the relaxation of azulene that too simple applications of isolated binary collision models do not account for the observed relaxation dynamics in liquid solutions [1] and that e.g. cluster type effects may play a role in media like rare gas liquids [2].

However, much more systematic experimental evidence is necessary to establish how far a gas phase type description of energy transfer rates $\langle\Delta E\rangle \cdot Z$ (with effective collision numbers Z and average amounts of transferred energy $\langle\Delta E\rangle$) is valid and scales e.g. with D^{-1} (the inverse self diffusion coefficient of the fluid [3]) as opposed to the onset of basically different energy transfer mechanisms in higher density fluids.

A very suitable molecule for collisional energy transfer studies from low pressure gas phase to compressed liquids is 1,3,5-cycloheptatriene (CHT), which is photophysically and -chemically well characterized. Excitation in the S_1 band - e.g. at 248 nm - leads to ultrafast internal conversion ($k_{ic} > 10^{12}$ s^{-1} [4]) resulting in an rovibrational energy of about 40000 cm^{-1}, which corresponds to a temperature T > 2000 K. Subsequent collisional deactivation is monitored by observing the transient UV absorption at suitable wavelenghts which shows known - and experimentally calibrated - energy dependence [5]. Conversion of the measured transient absorption curves (see e.g. Figs. 1 and 2) with the energy dependent $\varepsilon(\lambda)=f(E_{int})$ lead to energy vs time profiles of the relaxation process (see Fig. 3). Extensive energy transfer studies on vibrational deactivation in the CHT system at very low gas pressures (in this case the stuctural isomer of CHT toluene is observed) have been conducted by this UV absorption [6] and alternatively by a multiphoton ionisation (KCSI) technique [7].

In the present work, 0.5 ps, 2 mJ - pump pulses at 248 nm were obtained from a hybrid excimer - dye laser system similar to that described in ref. [8]. Somewhat longer probe pulses at 312 nm (2. Stokes) and 224 nm (1. Anti-Stokes) were generated from stimulated Raman scattering by focusing a second 248 nm pulse into a cell with compressed hydrogen. These pulses were used to monitor the transient absorption of solutions of CHT in different alkane, alcohole and halogenated alkane solvents at ambient pressure as well as heptane solutions at pressures between 1 bar and 3000 bar. Typical profiles of absorption vs time delay at the two probe wavelenghts for a solution of CHT in trichlorotrifluoroethane are shown in Fig. 1 and Fig. 2.

The initial spike of the 312 nm signal results from absorption by excited electronic states of solvent molecules generated by multiphoton absorption. These excited states decay with a time constant of less than 1 ps [9]. The remaining part of this signal as well as the transient absorption at 224 nm is due to increased absorption by vibrationally excited CHT molecules.

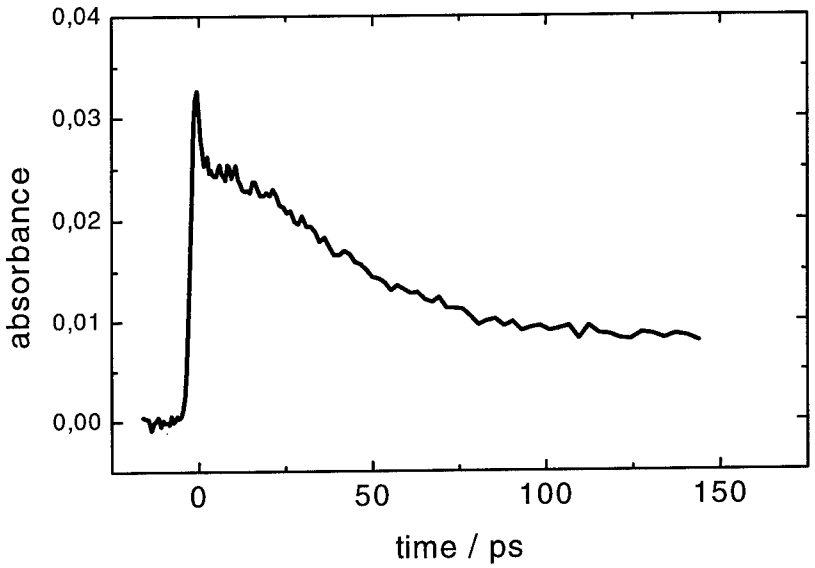


Fig.1: absorption vs time profile of CHT in trichlorotrifluoroethane at 1 bar recorded at 312 nm after excitation at 248 nm

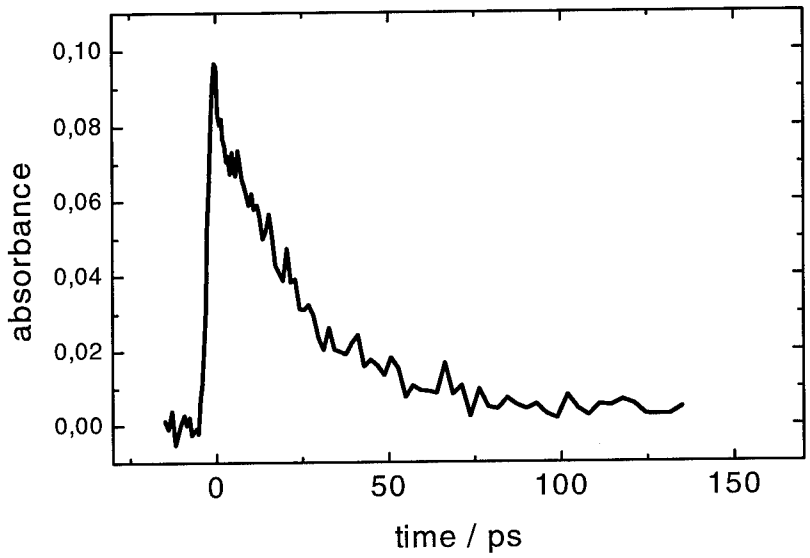


Fig.2: absorption vs time profile of CHT in trichlorotrifluoroethane at 1 bar recorded at 224 nm after excitation at 248 nm

Fig.3 shows the transformation of Figs. 1 and 2 into the time dependent average energy of the relaxing CHT population. As expected, the differences in the shapes of the absorption curves in Figs. 1 and 2 are only due to the different $\varepsilon(E)$ dependences at the probe wavelenghts and both measurements lead to the same $\langle E \rangle(t)$ curve in Fig. 3. Monoexponential fits to the energy vs time profiles for different solvents yielded relaxation time constants between 5 and 16 ps. In heptane, the time constant decreases from 8 ps to 5 ps as the pressure is increased from 1 bar to 3000 bar.

In a computer simulation of the energy relaxation, a model was tested that assumes deactivation of the CHT molecule by binary collisions but takes into account that the initial energy transfer increases the temperature of the surrounding solvent molecules such that the effective energy transfer rate from the vibrationally excited CHT* molecules decreases fast due to a rapidly decreasing energy difference between CHT* and the nearest solvent molecules, as it has been observed in comparative situations in the gas phase as well. The dissipation of energy within the solvent is approximated by macroscopic heat conduction. With the model it is possible to reproduce the time constants of vibrational relaxation in different solvents and at different pressures using solvent parameters like energy transferred per collision, thermal conductivity and heat capacity. The simulated energy profiles also reproduce to a good approximation the form of the experimental energy vs time profiles.

Further experiments in dense gases are underway to establish further the density range and the conditions at which the vibrational relaxation starts to deviate from scaled low pressure gas phase dynamics.

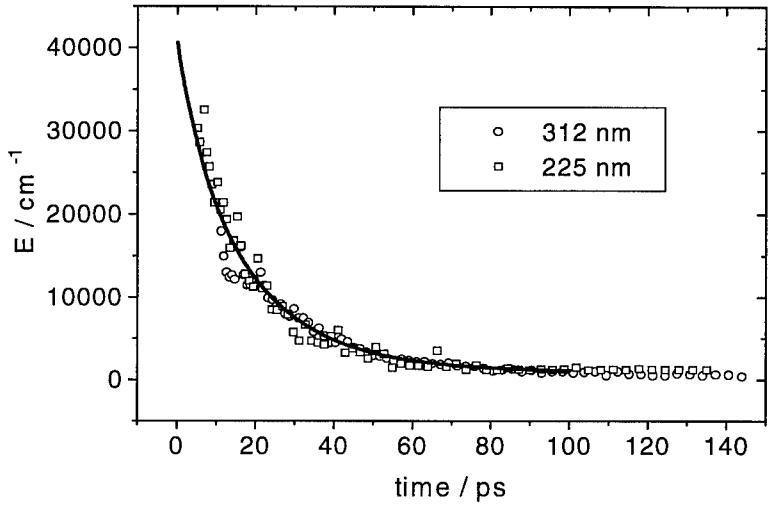


Fig. 3: Energy vs time profile of CHT in trichlorotrifluoroethane at 1 bar after excitation at 248 nm. Circles: from 312 nm absorption profile; squares: from 225 nm absorption profile; solid line: simulation.

References:

[1] U. Sukowski, A. Seilmeier, T. Elsaesser, S.F. Fischer, *J. Chem. Phys.*, **1990**, *93*, 4094

[2] K.E. Schultz, D.J. Russell, C.B. Harris, *J. Chem. Phys.*, **1992**, *97*, 5431

[3] B. Otto, J. Schroeder, J. Troe, *J. Chem. Phys.*, **1984**, *81*, 202

[4] P.M. Borell, H.G. Löhmannsröben, K. Luther, *Chem. Phys. Lett.*, **1987**, *136*, 371

[5] D.C. Astholz, L. Brouwer, J. Troe, *Ber. Bunsenges. Phys. Chem.*, **1981**, *85*, 559

[6] H. Hippler, J. Troe, H.J. Wendelken, *J. Chem. Phys.*, **1983**, *78*, 6709

[7] K. Luther, K. Reihs, *Ber. Bunsenges. Phys. Chem.*, **1988**, *92*, 442

[8] S. Szatmari, F.P. Schäfer, *Optics Comm.*, **1988**, *68*, 196

[9] M.U. Sander, U. Brummund, K. Luther, J. Troe, *J. Phys. Chem.*, **1993**, *97*, 8378

FEMTOSECOND PULSE GENERATION AT 1.3 μm FROM A PRASEODYMIUM FIBRE LASER

M. J. GUY, A. BOSKOVIC, D. U. NOSKE & J. R. TAYLOR

Femtosecond Optics Group, Physics Department, Imperial College,
Prince Consort Road, London SW7 2BZ, England. Tel: (+44 71) 225 8844

Femtosecond pulses have been generated in erbium doped fibre lasers using a number of different cavity designs and mode-locking techniques. These have proven capable of directly generating pulses as short as 98 fs at 1.55 μm[1], the lowest loss "window" in optical fibre used for telecommunications. A second low loss window exists at 1.3 μm and recently considerable interest has been directed towards Praseodymium (Pr^{3+}) doped fluoride fibre as an amplifier providing gain at this wavelength. Pr^{3+} doped into a fluoride glass host exhibits high gain over a range of ~50 nm and this broad bandwidth has the potential to support femtosecond pulses.

One problem with Pr^{3+} doped single mode fibres is that they tend to be highly normally dispersive at 1.3 μm, making it difficult to exploit the soliton-like pulse compression effects that lead to ultrashort pulses in similar erbium-doped silica based systems. The shortest pulse duration from a Pr^{3+} fibre laser reported until now is 1.6 ps with a time-bandwidth product of 0.85 from a "Figure-of-Eight" laser (F8L) cavity configuration whose overall dispersion was normal[2]. We have built a F8L with anomalous overall dispersion which generates almost transform-limited pulses as short as 620 fs. Figure 1 shows the schematic cavity layout.

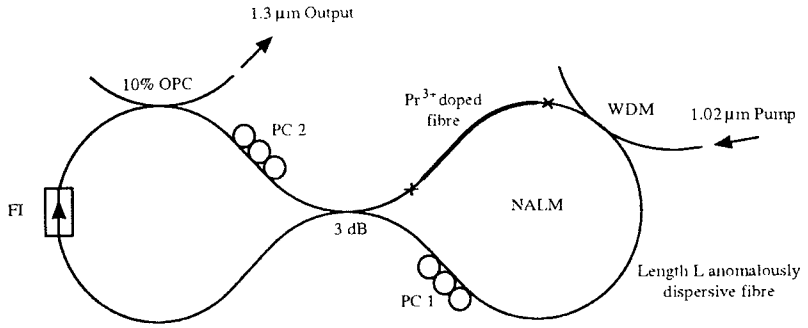


Figure 1. Schematic diagram of Pr^{3+} fluoride fibre F8L cavity. FI: Faraday isolator, PC: Polarisation Controller, OPC: Output Coupler.

The total length of the optimised laser cavity was 166 m, including a 7 m length of Pr^{3+} doped fibre. The dopant concentration was 2000 ppm and the laser was pumped by up to 1 W from a Ti:Sapphire laser tuned to 1.02 μm. The fluoride fibre cannot be fusion-spliced to standard silica fibre because they have different melting points. These connections were therefore made with mechanical splices (denoted by 'x') which had a measured loss of 0.4 dB each. The anomalously dispersive fibre in the NALM had a minimum dispersion at 1.27 μm and an estimated dispersion of ~ +4.5 ps/nm/km at 1.3 μm.

Figure 2 shows the autocorrelation (with spectrum inset) of 620 fs pulses generated by the laser. The time-bandwidth product was calculated to be ~0.50, but it was noticed that the measured pulse duration changed slightly if the polarisation of the input light to the autocorrelator was rotated. It was found that the laser output could be resolved into two orthogonally polarised components with slightly different pulse durations and spectra, as has recently been observed in a similar erbium-based system[3]. The time-bandwidth product calculated using the appropriate spectral component is 0.32, close to the transform limit for $sech^2$ pulses.

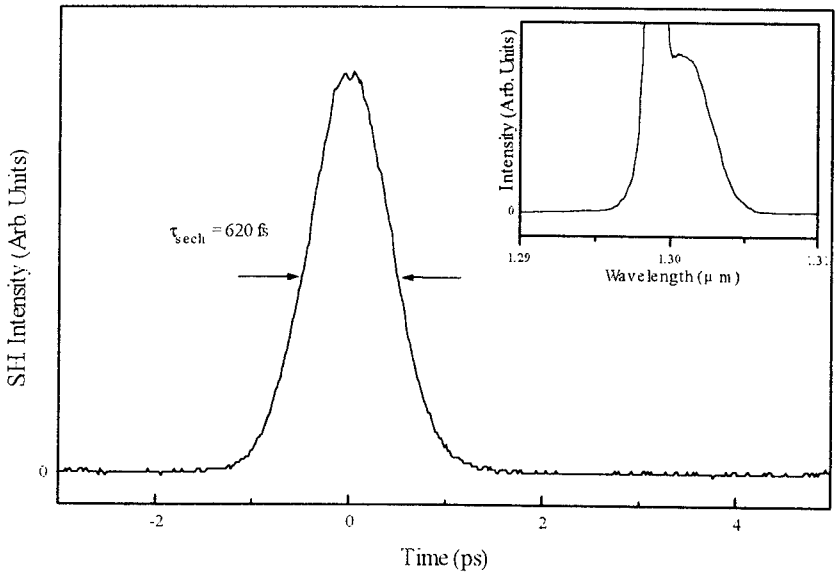


Figure 2. Autocorrelation trace of 620 fs pulses generated from Pr^{3+} laser with spectrum inset.

In general this laser exhibited the well known temporal output of F8Ls consisting of bunches of randomly spaced short pulses periodic at the round trip time of the cavity. It also displayed

some novel modes of mode-locked operation, however, in which the random stream of pulses would self-organise over a period of a few seconds into a well defined pulse train at harmonics of the round trip frequency, as has recently been observed in a ytterbium-erbium doped fibre ring laser[4]. This was observed both at low harmonics (up to 7th, ~5 MHz) and high harmonics of the cavity, with a maximum repetition rate of 437 MHz, corresponding to the 617th harmonic. These different repetition rates were selected by adjustment of the two polarisation controllers and once established exhibited long term stability. In the case of the low harmonic stabilisation the pulses were generally found to have a square envelope and were of the order of 2 ns long, the exact duration being proportional to the pump power. It was also possible to generate subpicosecond pulses in this case. For the higher harmonics, however, the pulses were always in the femtosecond regime.

In addition to the temporal output regimes described above, it was also possible through adjustment of the fibre strainers to generate bursts of femtosecond pulses at repetition rates of up to 200 GHz with the number of pulses present in the burst dependent on the pump power. This effect has also been observed in Yb-Er based systems[5] and is attributed to spectral beating caused by birefringence in the NALM.

In conclusion, we have demonstrated the generation of femtosecond soliton pulses in a Pr^{3+} doped fibre laser for the first time. We have thoroughly characterised this laser and report the novel self-organisation of pulses into continuous pulse trains with well defined repetition rates at both low and high harmonics of the fundamental cavity frequency. The source of this self-organisation is the subject of further research.

References

[1] M. Nakazawa, E. Yoshida and Y. Kimura, Electron. Lett. **29**, 63 (1993)

[2] T. Sugawa, E. Yoshida, Y. Miyajima and M. Nakazawa, Electron. Lett. **29**, 902 (1993)

[3] M. J. Guy and J. R. Taylor, Electron. Lett. **29**, 2044 (1993)

[4] A. B. Grudinin, D. J. Richardson and D. N. Payne, Electron. Lett. **29**, 1860 (1993)

[5] M. J. Guy, D. U. Noske and J. R. Taylor, Opt. Lett. **18**, 1447 (1993)

Femtosecond Blue Continuum Generation and its Application to the Time-Resolved Study of Mn^{2+} Emission in Mn-Doped ZnS Nanocrystals

T. Sosnowski, P.B. Klein[1], T.B. Norris

University of Michigan, Center for Ultrafast Optical Science
2200 Bonisteel Blvd, Ann Arbor MI 48109-2099, (313) 763-4875

[1]and Naval Research Laboratory, Code 6874, Washington DC 20375-5347

R.N. Bhargava

Nanocrystals Technology, P.O. Box 820, Briarcliff Manor, NY 10510 (914) 923-1142

and

D. Gallagher

Philips Laboratories, 345 Scarborough Rd., Briarcliff Manor NY 10510 (914) 945-6048

Recently, the achievement of high quantum efficiency light emission from semiconductor nanocrystals using transition metal doping was reported[1] in the ZnS:Mn system. While this system is of considerable interest both scientifically (physics of low dimensional structures) and technologically (fast, high speed phosphors), the excitation dynamics in doped nanocrystals are still not well understood. In order to probe such a system on the picosecond or sub-picosecond time scale, a tunable ultrafast UV source is required. We have developed such a source by using the frequency-doubled output of a 250kHz Ti:sapphire regenerative amplifier[2] to produce the blue continuum.

The pump pulses were created by chirped-pulse amplification in a CW-argon-pumped, Ti:sapphire regenerative amlifier. The system produced 2 μJ, 85 fsec pulses with a repetition rate of ≥ 250 kHz. The 800nm pump pulses were frequncy-doubled by weakly focusing into a 0.5 mm BBO crystal. Approximately 20% conversion efficiency is achieved, resulting in ≈0.4μJ, 400nm pulses. The 400nm pulses were focused at f/2.2 into a 3mm sapphire crystal to create a continuum. Sapphire was chosen in part because its UV transmittance extends to wavelengths as short as 155nm.

Fig. 1 shows the continuum spectrum generated with the 400nm, 0.4μJ pulses. The spectrum is centered around the 400nm pump with a range of ≤250nm to ≥680nm. The spectrum was measured with a Hammamatsu model 375 photomultiplier with a multialkali photocathode, and with a 0.5m. grating spectrometer using either a 2400gpm holographic grating or a 1200gpm ruled grating. The spectrum is not corrected for the wavelength response of the optical system. The blue portion of the spectrum extends below 250nm. However, at shorter wavelengths the measurements were noise limited due to the lack of an appropriate filter to eliminate scattered light in the spectrometer from the much more intense parts of the spectrum. The threshold pulse energy for blue continuum generation in this configuration was as low as 0.08μJ, which is 4-5 times lower than the threshold for 800nm generation in the identical configuration.

Bulk Zns:Mn has been employed as a phosphor material for many years. The crystal field split $^4T_1$ to $^6A_1$ transition of Mn^{2+} is responsible for the long-lived (1.8msec)

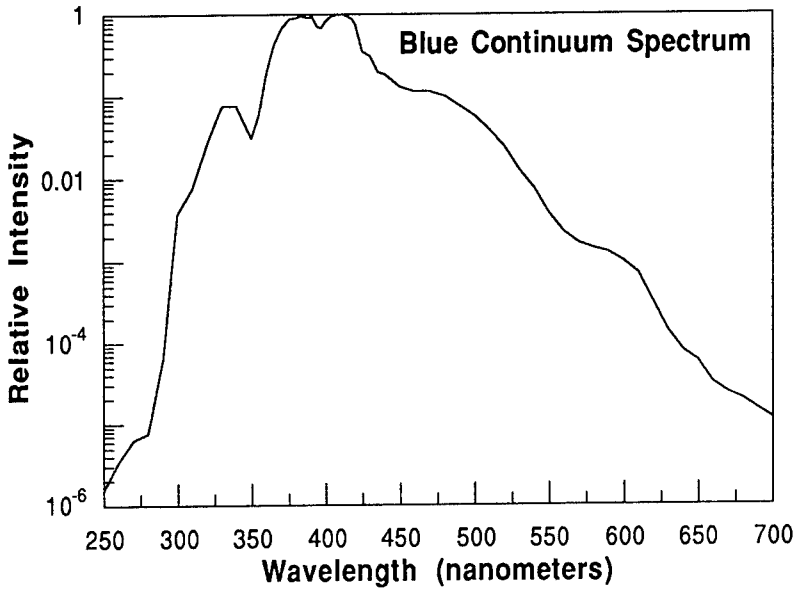


Figure 1.
Spectrum of the blue continuum generation excited by frequency doubling Ti:sapphire.

yellow emission (584nm peak) that is characteristic of the phosphor. Recently, Bhargava et al.[1] have shown that ZnS nanocrystals as small as 30Å can be doped with Mn, and that high radiative efficiencies (≥18%) can still be achieved. This was a dramatic observation, as semiconductor nanocrystals are notoriously inefficient because of enhanced surface recombination resulting from the large surface to volume ratio in these materials[3]. In nanocrystals of this size, the exciton Bohr radius becomes comparable or smaller than that of the nanocrystal, and carrier localization effects resulting from quantum confinement become important. The enhanced efficiency in the nanocrystals was associated with carrier localization at the Mn center. In contrast to the millisecond decay of the Mn^{2+} photoluminescence (PL) signal of the bulk material, Bhargava et al. observed a fast (3.7 nsec) decay in the nanocrystals. The much faster decay and large radiative efficency in the nanocrystals was interpreted in terms of a localization-induced change in the mixing of the 3d wavefunctions of Mn^{2+} with that of the ZnS host. Attempts by Bhargava et al. to observe the energy transfer process between the photoexcited carrier system and the Mn center by monitoring the time-dependent rise of the luminescence signal was limited by the 0.5 nsec response of their system.

In the present work we have extended those measurements to the picosecond regime by exciting the nanocrystal above the ZnS band edge with the blue continuum source described above. As one of the goals of this work will be to selectively excite a specific size nanocrystal (smaller crystals absorb at shorter wavelength due to confinement) from within the distribution that exists within each sample, it is important to excite with a tunable source rather than simply tripling the 800nm fundamental.

The blue continuum was passed through a Schott UG-11 filter, resulting in a broad band excitation centered at 320nm with about 100nm bandpass. The PL emission was imaged onto a streak camera and detected by a CCD array. The PL temporal response in the nsec range for 30Å crystals was observed to exhibit a bi-exponential dependence, with decay

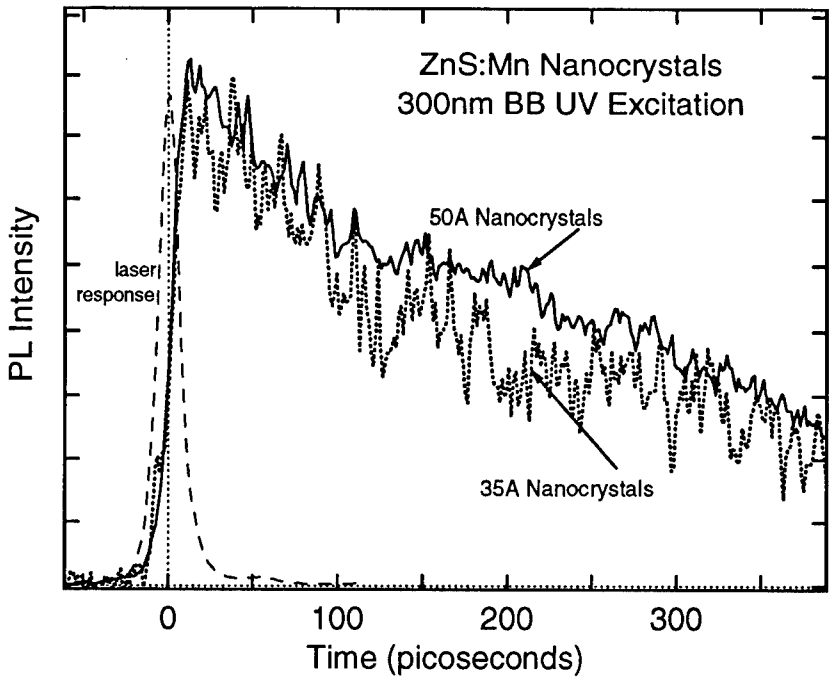


Fig. 2. PL response of 35Å and 55Å ZnS:Mn nanocrystals to a ≈100 fsec UV pulse.

components of 3.3 and 0.4 nsec. The slower decay corresponds to that observed by Bhargava et al., while they were unable to resolve the faster component. The rise of the

PL was system limited. Fig. 2 shows similar data on a shorter time scale for 30Å and 55Å nanocrystals. Again, the PL rise is limited by the system response of ≈17psec, while the decay in in the 300psec range and appears to have more than one component in the 55Å nanocrystals. This may be of some significance, as different crystal sizes are expected to exhibit different decay times.

The fact that the rise in the PL signal is system limited might suggest that the energy transfer process between the photoexcited carriers and the Mn center is shorter than 17psec. However, in carrying out the same experiment in bulk ZnS:Mn powder, we find that the PL rise is still system limited. It is unlikely that the energy transfer process is similar for the bulk and nanocrystal samples, as strong confinement effects are expected for processes that involve the carriers. In fact, the observed high efficiencies suggest a very efficient (fast) carrier trapping by the Mn center. Recently, Heitz et al.[4] have studied the Ni^{2+} center in II-VI compounds and have found that subsequent to carrier capture, an intracenter relaxation to the luminescent state from higher lying excited states occurs via a nonradiative cascade process, with a time constant of a few picoseconds. It is quite likely that we are observing a similar process in the rise of the Mn^{2+} PL. Since this process does not involve the carriers, it would be expected to be similar in both bulk and nanocrystalline samples. In order to investigate the energy transfer process itself, a pump-probe experiment is presently being set up.

REFERENCES

1. R.N. Bhargava, D. Gallagher, X. Hong and A. Nurmikko, Phys. Rev. Lett. **72**, 416 (1994).
2. T.B. Norris, Opt. Lett. **17**, 1009 (1992).
3. L.E. Brus, IEEE J. Quantum Electron. QE-**22**, 1909 (1986).
4. R. Heitz, A. Hoffman and I. Broser, J. Lum. **53**, 359 (1992).

THz Radiation from delta-doped GaAs

D. Birkedal and O. Hansen
Mikroelektronik Centret +45 45 93 46 10
Building 345 East, Technical University of Denmark
DK-2800 Lyngby, Denmark

C. B. Sørensen
Ørsted Laboratory, Niels Bohr Institute
Universitetsparken 5, DK-2100 Copenhagen, Denmark

K. Jarasiunas, S. D. Brorson, and S. R. Keiding
Fysisk Institut, Odense Universitet
Campusvej 55, DK-5230 Odense M, Denmark

The emission of ultrafast THz pulses after femtosecond laser pumping was recently introduced by Zhang and Auston [1] as a sensitive probe of the semiconductor surface region. Photoexcited carriers created near the surface are accelerated by the electric field present due to band-bending. The resulting photo current radiates an electro-magnetic pulse posessing frequency components in the THz-regime. The detailed structure of the THz pulse carries information about the built-in surface fields in the sample.

The presence of a delta-doped layer in the vicinity of the surface creates a very large field at the surface. Electric fields up to 100 kV/cm have recently been inferred from the observation of Franz-Keldysh oscillations in the photoreflectance spectra of delta-doped GaAs [2, 3]. These characteristics of the delta-doped structures make them very interesting as sources of THz-radiation, where both the high field and the high mobility should make the emitted THz amplitude greater than that emitted from bulk GaAs surfaces.

In this work we study the THz-emission from four delta-doped samples having different spacings between the doping layer and the surface. The polarity of the emitted THz pulses is found to be opposite that of pulses emitted from samples having bulk n-type doping. For increasing doped-layer – surface distance, we observe a decrease in the THz pulse amplitude. We find that the amplitude of the THz pulse depends linearely on the spacing between the delta-doped layer and the surface, independent of the magnitude of the associated electric field. By performing photoreflectance measurements (PR) on the same samples we have been able to extract information about the built-in fields on both sides of the doping layer and correlate this information with the behavior of the THz pulses.

The delta-doped GaAs samples used in this work were grown by molecular beam epitaxy on Cr-doped semi-insulating GaAs substrates. The 4 delta-doped samples have the doped layer positioned at a distance, d, of 25 nm, 50 nm, 100 nm, and 200 nm from the surface. The delta-doping was of n-type with Si as dopant. The same Si dose was used for each sample. A 1 μm buffer layer of undoped GaAs with a background p-type concentration of approximately 2×10^{14} cm^{-3}, was grown between the substrate and the delta-doped layer. As reference samples for the THz experiments, we used a semi-insulating liquid-encapsulated Czochralski (LEC) GaAs sample and a uniformly doped n-type MBE grown GaAs layer having a carrier concentration of 5×10^{17} cm^{-3}.

The experimental setup used in the THz experiments is described in Ref. [4]. The laser source was a mode-locked titanium sapphire laser producing $\approx$ 200 fs pulses at 840 nm. The beam was gently focused to a diameter of approximately 1 mm at the sample surface. The pump power was 100 mW, corresponding to a sheet carrier density of 1×10^{12} cm^{-2}. The THz-signal generated from the surface propagates to a receiving dipole antenna defined on ion implanted silicon on sapphire.

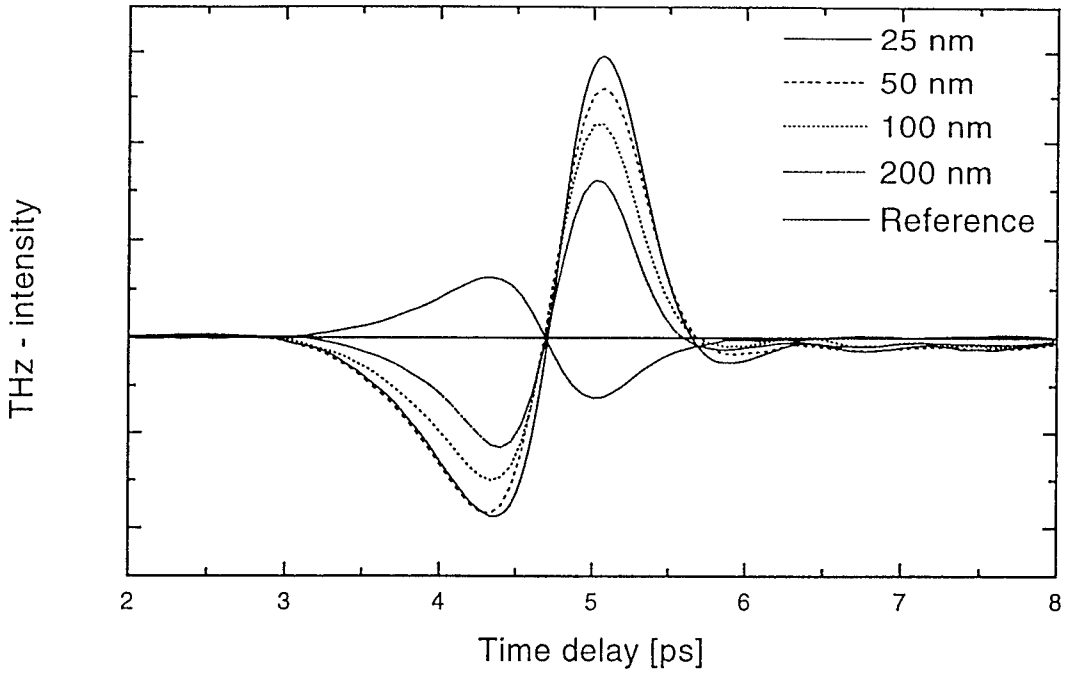


Figure 1: THz-pulse radiated from the 4 delta-doped samples and the GaAs reference sample with the Ti:sapphire laser operating at 830 nm.

The receiver has a bandwidth extending to 2 THz, mainly limited by the dielectric loss in the sapphire substrate.

THz signals radiated from the delta-doped samples upon laser pumping at 840 nm are shown in Fig. 1. The curves are labeled to indicate the type of sample. The THz-signal shows a characteristic damped oscillation with an approximate period of 2.6 ps. Also shown are pulses radiated from the LEC GaAs reference sample. It is observed that the THz-pulses from the delta-doped samples show the opposite polarity of the THz-pulse emitted by the LEC GaAs sample.

We show in Fig. 2 the rms values of the THz-pulses emitted from the four delta-doped samples as a function of the position of the delta-doped layer. The straight line is a fit to the data and is explained in the following way: The source current responsible for the radiated THz-pulse originates from both sides of the delta-doped layer. The PR measurements showed that the field on the surface side of the delta-doped layer is constant and well approximated with $F = -V_s/d$, where V_s is the surface potential equal to 0.6 V. The field on the substrate side of the delta-doped layer is almost constant equal to 9.1 kV/cm within the absorption length. Hence, the surface and substrate side contributions have opposite sign; the total THz signal is the sum of these contributions. The contribution to the THz signal from the surface side of the delta-doped layer is proportional to the depth of the delta-doped layer as discussed earlier in the text. Since the depletion width on the bulk side is much larger than the absorption length, which in turn is larger than the depth of the delta-doped layer, the contribution from the substrate side of the delta doped layer is approximately independent of the delta-layer depth. The two terms cancel out when the depth of the delta-doped layer equals one half of the absorbtion depth as reflected by the extrapolation to zero THz-amplitude in Fig. 2.

The sign of the electric field radiated from the surface, and correspondingly the direction of the photo-current can be determined from the measured pulses by calibrating the response of the detection system with a biased THz-antenna, where the direction of the current is fixed by

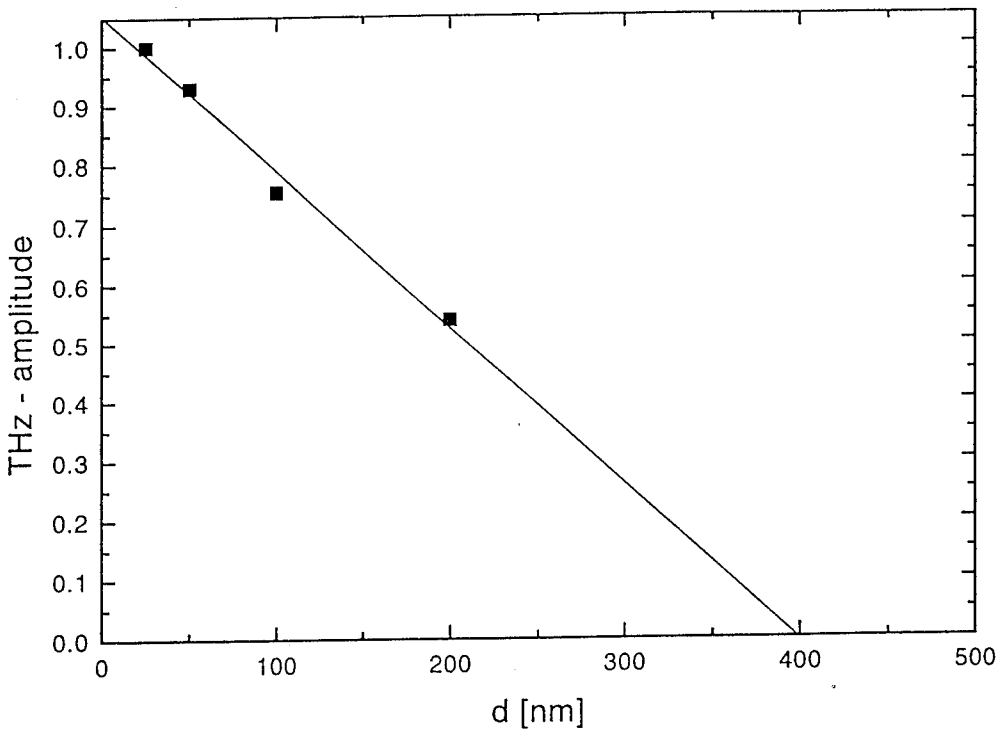


Figure 2: Rms values of the THz-pulses emitted from the delta-doped sample relative to the $d = 25$ nm sample as a function of delta-layer depth. The line represents a linear fit to the data.

the polarity of the applied bias. We find that the observed polarity of the pulses radiated from the delta-doped samples corresponds to a net current directed toward the the substrate. This is consistent with the majority of the THz signal arising from the substrate side of the delta-doped layer providing evidence of the importance of the electric field distribution at the delta-doped region to THz pulse generation.

In summary, we have performed THz-experiments on four delta-doped GaAs samples. The results of the THz-experiments are qualitatively explained in a model where the radiated THz-amplitude is proportional to the width of a region generating a current following fs laser excitation. We observe that the THz-amplitude is independent of the magnitude of the electric field, which is not fully undestood. However, the sign of the electric field is directly reflected in the emitted THz-pulse.

References

[1] X. C. Zhang and D. H. Auston, J. Appl. Phys. **71**, 326 (1992).

[2] D. G. Liu *et al.*, **72**, 1468 (1992).

[3] T. M. Hsu *et al.*, **72**, 1065 (1992).

[4] J. E. Pedersen, I. Balslev, J. M. Hvam, and S. R. Keiding, Appl. Phys. Lett. **62**, 1392 (1992).

Transient reflective polarization spectroscopy of hidden anisotropy in cubic crystals

N.I.Zheludev, A.R.Bungay, S.V.Popov
Department of Physics, University of Southampton,
Highfield, Southampton, S09 5NH, UK.
Tel: +44 703 593566

Yu.P.Svirko
General Physics Institute, 38, Vavilov Street,
Moscow 117333, Russia.

It is often anticipated that the linear optical properties of GaAs as a cubic material are isotropic. More careful consideration, however shows that spatial dispersion terms in the optical response lead to a small linear birefringence in this crystal. The crystal anisotropy becomes more pronounced in the nonlinear optical response where the symmetry of the nonlinear susceptibility tensors differs vastly from being isotropic. Local and non-local nonlinear anisotropy, for example, leads to the dependence of the efficiency of the two-photon absorption process on the crystal orientation and to a variety of nonlinear polarization-affecting phenomena for propagating light. Here we report the first observation of a new fine, but quite pronounced pump-probe polarization sensitive transient effect in reflected light which results directly from the anisotropy of the zinc-blende structure. It has the potential to become a new method for the investigation of cubic crystal anisotropy and nonlocality and is especially suitable for non-transparent materials such as narrow-gap semiconductors and superconductors where the application of transmission methods is not possible.

If a (001) surface of a zinc-blende crystal is stimulated with linearly polarized light propagating along the [001] direction, this affects the polarization state of the probe wave reflected from the surface (see fig.1). If the initial directions of polarization of the pump and the probe are different, this would lead to the domination of the optical Kerr effect for the probe due to the virtual birefringence induced by the pump. However if the pump and the probe are initially identically linearly polarized, only hidden crystal anisotropy could lead to the alteration of the reflected probe polarization since in an isotropic material all polarization changes are forbidden due to the existence of a symmetry plane, containing the wave vector and the polarization direction (In this configuration, the optical Faraday effect is forbidden since it requires a circularly polarised pump [1]). If the following material equation containing local and non-local susceptibilities is adopted:

$$D_i = \varepsilon_{ij}E_j + \gamma_{ijk}\nabla_k E_j + \chi_{ijkl}E_jE_kE_l + \Gamma_{ijklm}E_jE_k\nabla_m E_l + \ldots$$

the alteration of the polarization azimuth $\delta\alpha_r$ of the probe, induced by the linearly polarized incoherent pump is given by the following formula

$$\delta\alpha_r = \frac{|\boldsymbol{E}|^2 \left[Re(\chi_{xxxx} - 2\chi_{xxyy} - \chi_{xyyx}) \sin 4\Phi - 4kn^2\, Im(\Gamma_{xyyyz}) \cos 2\Phi\right]}{2n(1-n^2)(1+n^2)}$$

indicating the involvement of the "cubic anisotropy" term ($\Delta\chi = \chi_{xxxx} - 2\chi_{xxyy} - \chi_{xyyx}$, this combination is equal to zero in any isotropic media) and the "cubic nonlocality" terms (Γ_{xyyyz}). Here Φ is the angle that the initial polarization direction of the probe makes with the [100] axis of the crystal. The "cubic anisotropy" and the "cubic nonlocality" terms have different dependencies on Φ, giving the opportunity to experimentally separate them.

In the configuration shown in fig.1, with a 2ps Ti:Sapphire laser working on the wavelength of 750nm we have clearly observed both the "cubic anisotropy" and "cubic nonlocality" terms of a GaAs crystal optical response. This experiment was performed with a 1μrad-sensitive polarimeter using the technique for suppression of the coherent pump-probe interaction reported elsewhere [1]. At this wavelength GaAs is completely opaque with a penetration depth of about $\ell = 1\mu m$ ($\hbar\omega \approx 1.65eV$, $E_g \approx 1.43eV$). We have studied the reflected probe light polarization rotation as a function of the relative pump-probe delay, pump intensity and crystal orientation, i.e the angle between the initial polarization plane direction and the crystal [100] axis (i.e. angle Φ) by rotating around the [001] direction. It was found that the time-domain dependence of the rotation of the probe polarization azimuth induced by the pump has two components. The time-domain and orientation dependencies of the two components are presented in the insets of the fig.2. The observed rotation is approximately 20 times weaker than the optical Faraday effect, with a circularly polarised pump, observed under similar conditions and reported elsewhere [2].

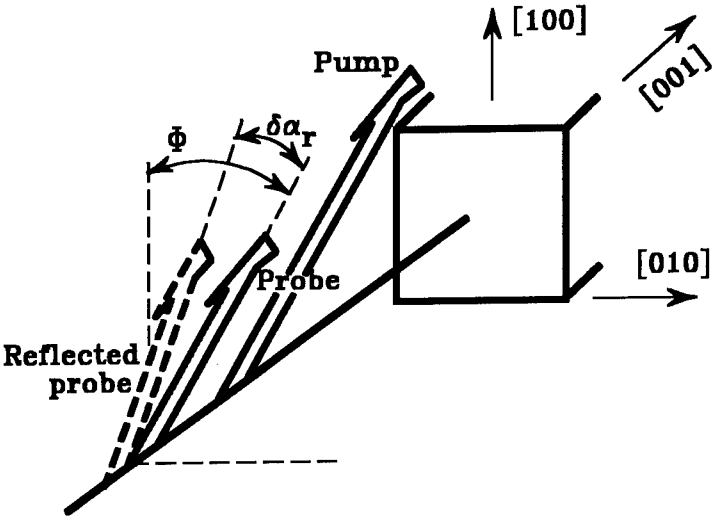


Figure 1. Observation of specular induced anisotropy in zinc-blende crystal

The first component gives rise to the initial sharp peak on fig.2. It appears and disappears immediately with the excitation indicating that it is due to a very fast nonlinearity. When the crystal is rotated around the [001] direction this fast component oscillates as sin4Φ, i.e. exactly as predicted by the above formula for the cubic anisotropy term. This anisotropic nonlinearity may be attributed [3] predominantly to the valence- conductivity band transitions involving the heavily-warped heavy-hole sub-band, i.e the difference in the heavy-hole effective mass for momentum in the [111] and [100] directions. This anisotropy is known to lead to an orientational dependence of GaAs hot luminescence resulting from stimulation

with linearly polarized light [4]. The relaxation time of the nonlinearity here is controlled by the holes fast quasi-momentum relaxation time. A similar effect might be expected in all cubic materials and may be useful for obtaining information on zone structure warping where the anisotropic hot luminescence technique is not efficient.

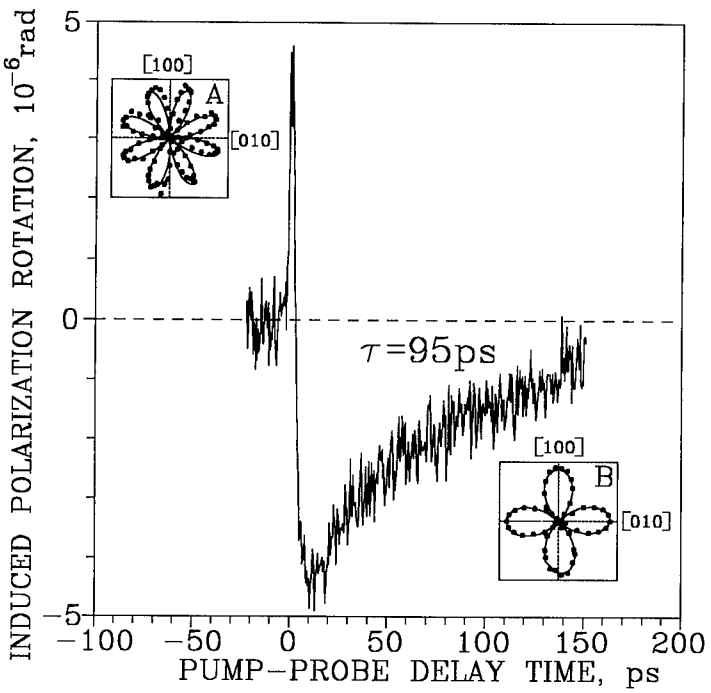


Figure 2. Induced reflected probe polarization rotation as a function of pump-probe delay, pump intensity = 100MW/cm^2.

The second component in the time-delay dependence behaves in the following way. Accumulating the energy of the absorbed pump, the effect reaches its maximum at the end of the pump pulse. It then decays slowly, in an exponential manner within 95ps. Its orientational dependence is dramatically different from the orientational dependence of the first component: with very good accuracy it obeys the cos2Φ rule and may be attributed to the second term in the above formula. We believe that the effect is due to the absence of an inversion centre in zinc-blende crystals which (taking into account the spin-orbit interaction) leads to an effective anisotropic magnetic field, normal to the direction of the electron quasi-momentum and acting on the electron spins [4]. From the point of view of the probe wave the situation is partially analogous to the Zeeman effect in the transverse configuration.

REFERENCES

[1] S.V.Popov, Yu.P.Svirko, N.I.Zheludev. Optics Letters, **19**, 1 (1994)

[2] N.I.Zheludev, R.T.Harley, S.V.Popov, A.R.Bungay, I.R.Shatwell. Submitted to Ultrafast Phenomena, May 1-5, 1994, Dana Point, CA.

[3] M.G.Dubenskaya, T.M.Ilinova, A.V.Trukhov, A.A.Fortigin. Izvestia Akademii Nauk SSSR, Seria Fizicheskaia, **56,** 95 (1992).

[4] F.Meier, B.P.Zakharchenia "Optical Orientation", North-Holland, 1984.

Importance of Femtosecond Solvent Motions on Electron-Transfer Reactions: A Study of Electrolyte Solutions

Hans P. Deuel, Peijun Cong, and John D. Simon
Department of Chemistry, Institute for Nonlinear Science
University of California at San Diego
9500 Gilman Drive, La Jolla, California 92093-0341, U.S.A.
Tel.: (619) 534-6699

Electrolytes can influence chemical reaction dynamics in vastly different ways. In this paper we focus our attention on fast solvent motions in electrolyte solutions and their effect on the rate constants of electron transfer reactions. The experimental methodologies employed in this paper are femtosecond optically-heterodyne-detected Raman-induced-Kerr-effect spectroscopy (OHD RIKES) and transient absoption spectroscopy.

As a particular example, we consider the back electron transfer that occurs upon the photoexcitation of the bimolecular donor-acceptor complex between stilbene and fumaronitrile. This chemical reaction has been studied by a wide variety of reseachers. Excitation of the ground state complex creates a contact ion-pair. This intermediate undergoes competition between back electron transfer and diffusive separation to form free ions. Our group has reported a complete study on the effect of electrolytes on this chemical reaction [1]. Addition of alkali salts accelerates the rate of electron transfer in both acetonitrile and ethyl acetate solutions. On the other hand, molecular salts (tetra-alkyl ammonium perchlorates) have no influence on the reaction dynamics. Added salts can, in principle, influence the reaction process in two ways. First, the reaction exothermicity can be effected due to solution polarity changes. Second, changes in the dynamic time scales of the liquid can lead to changes in the frequency factors for the rate constant.

In our analysis of these experimental results, Marcus electron-transfer theory was invoked. For this particular reaction, the dynamics occur in the Marcus inverted region. In this limit, a decrease in reaction exothermicity causes an increase in the reaction rate constant. Addition of alkali salts to acetonitrile increases the solution polarity. As a result, the ion-pair intermediate is stabilized to a greater extent than the ground state complex in the electrolyte solution. This causes a decrease in reaction exothermicity and an increased rate is expected. This is experimentally observed. However, it is not clear from this observation whether there is a corresponding change in the prefactor, which would reflect changes in solvent dynamic effects on the reaction rate. To address this question, a free energy parameterization of the reaction energetics in salt solutions was developed using the S_0 - S_1 energy gap of 3-aminofluorenone as a polarity probe [2]. This enabled direct determination of the frequency factors associated with the rate constants. Within experimental error, the values obtained for the frequency factors were independent of salt concentration. This was observed for both acetonitrile and ethyl acetate solutions, although the value was different for the two solvent systems. The insensitivity of the kinetic prefactor to added electrolytes is a subject currently under investigation in our laboratory. Understanding this observation requires a detailed understanding of how added salt influences the molecular dynamics of the solution.

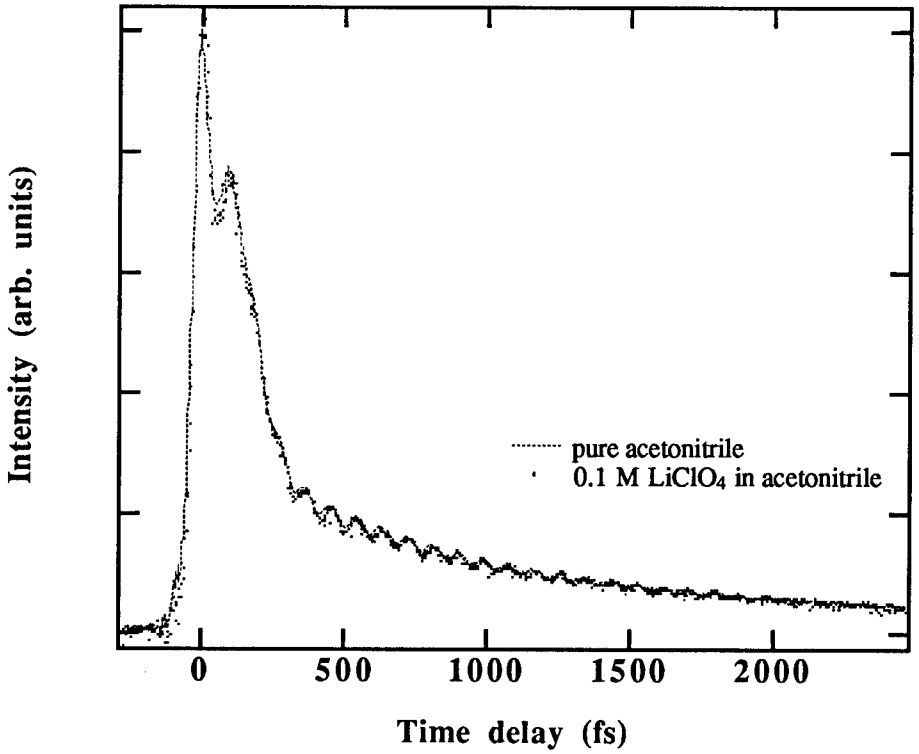
Before addressing what is known about the time-scales of molecular motions in electrolyte solutions, it is important to recall that electron transfer rates and solvation dynamic time scales are strongly correlated. Recent experimental evidence [3a], as well as numerical simulations based on the Hynes model of solvent friction [3b], support the role of the fast solvent motions (librations, tens of fs) in determining reaction rates. In a study of the self-exchange reaction in a variety of metallocenes, Barbara and coworkers concluded that the fast solvent relaxation components revealed by C(t) measurements make important contributions to the magnitude of the prefactor [3a]. Even though C(t) measurements of electrolyte solutions with femtosecond resolution have not been reported in the literature, picosecond C(t) measurements do reveal some interesting features of the effects of electrolytes on solvation dynamics [4, 5]. In

particular, Huppert and coworkers have determined C(t) for salt solutions in both acetonitrile and ethyl acetate [4]. For example, C(t) for a 0.09M $LiClO_4$ acetonitrile solution reveals a long time component (decay constant of 11.75 ns) that is not present in the neat solvent. Similar results were observed for ethyl acetate solutions. For concentration as low as 10 mM, long time decay components appeared in the C(t) function. In THF solutions, the four salts $NaClO_4$, $LiClO_4$, $Mg(ClO_4)_2$ and Bu_4NClO_4 all show the same relaxation time for the concentration range 10 - 400 mM. These workers interpreted these data in terms of a salt-induced relaxation process that could be described by the Debye-Falkenhagen theory, which has been questioned by Chapman and Maroncelli recently [5]. Due to the limits of the time resolution of the photon counting technique, the dynamics on the time scale of a few picoseconds and faster was not resolved.

Comparing these picosecond C(t) measurements with our electron-transfer rate data, one is led to the conclusion that the slow relaxation of the ionic atmosphere does not contribute to the magnitude of the kinetic prefactor. However, the C(t) measurements do not provide any information of the effects of salts on the fast solvation dynamics. Such information is vital if one is to assess whether or not these modes play a role in determining the kinetic frequency prefactor. OHD-RIKES can provide this information. In particular, the OHD-RIKES data contains information on rotational motions as well as translational and librational dynamics. The connection between TDSS C(t) measurements and OHD-RIKES measurements has been demonstrated for the case of acetonitrile by Cho et al. [6], where it was shown that these two techniques are sensitive to the same liquid dynamics occuring on the femtosecond time-scale.

With the goal of exploring the electrolyte effects on fast solvent motions, OHD-RIKES transients were measured for acetonitrile and ethyl acetate with added salts. Figure 1 shows the OHD-RIKES data for a 0.1 M $LiClO_4$ acetonitrile solution. Within our experimental resolution, the transient signal of this electrolyte solution is identical to that observed for the neat liquid. Electrolyte solutions in ethyl acetate are similarly unaffected. Addition of salt does not effect any of the femtosecond dynamic processes that contribute to the Kerr signal. At the concentrations studied, infrared absorption and NMR studies have shown that these salts undergo negligible ion-pairing [7].

FIGURE 1:



The data shown in Figure 1 indicate that the fast relaxational processes in acetonitrile are unaffected upon addition of electrolytes, with identical results in ethyl acetate. It is clear from the picosecond C(t) measurements that electrolytes strongly influence the picosecond and longer solvent motions. If these modes were to dominate the kinetic prefactor in an electron transfer process, the magnitude of the prefactor should be highly sensitive to electrolyte concentration. This is the opposite of what is experimentally observed [1]. The dynamical solvent modes responsible for the electron transfer barrier crossing were shown to be independent of electrolyte concentration. As figure (1) clearly demonstrates, only the ultrafast solvent modes show this independence. These results indicate that it is the ultrafast solvent modes which couple to electron transfer barrier crossing.

References:

1. P. A. Thompson and J. D. Simon, *J. Am. Chem. Soc.* **115**, 5657 (1993).
2. P. A. Thompson and J. D. Simon, *J. Chem. Phys.* **97**, 4792 (1992).
3. (a) M. J. Weaver, G. E. McManis, W. Jarzeva and P. F. Barbara, *J. Phys. Chem.* **94**, 1715 (1990); (b) G. E. McManis, M. J. Weaver. *J. Chem. Phys.* **90**, 912 (1989).
4. (a) D. Huppert, V. Ittah and E. M. Kosower, *Chem. Phys. Lett.* **159**, 267 (1989); (b) V. Ittah and D. Huppert, *Chem. Phys. Lett.* **173**, 496 (1990). (c) E. Bart and D. Huppert, *Chem. Phys. Lett.* **195**, 37 (1992).
5. C. F. Chapman and M. Maroncelli, *J. Phys. Chem.* **95**, 9095 (1991).
6. M. Cho, S. J. Rosenthal, N. F. Scherer, L. D. Ziegler and G. R. Fleming, *J. Chem. Phys.* **96**, 5033 (1992).
7. (a) M. K. Wong, W. J. McKinney, A. J. Popov, *J. Phys. Chem.* **75**, 56 (1971); (b) R. H. Erlich, E. Roach, A. I. Popov, *J. Am. Chem. Soc.* **92**, 4989 (1970); (c) M. S. Greenverg, R. L. Bodner, A. I. Popov, *J. Phys. Chem.* **72**, 2449 (1973).

Quantum Dynamical Evalution of Ultrafast Pump&Probe Laser Pulse Control of Selective, Vibrationally Mediated Transitions in K_2 and Na_3

R. de Vivie-Riedle, J. Manz, B. Reischl
Institut für Physikalische und Theoretische Chemie, FU Berlin, Takustr. 3, D-14195 Berlin, Germany, Tel.: +49 30 838 3338

The concept of pump&probe spectroscopy for femtosecond chemistry [1] maybe extended to a pump&control approach for selective, vibrationally mediated, molecular transitions [2]: The first pump pulse, typically in the domain of 100 fs, induces coherent molecular vibrations either in the electronic ground [3] or excited states [1]. As a consequence, the initial configuration is changed selectively and periodically into the Franck-Condon region for the second control laser pulse which may then induce the transition to the desired product. This general strategy [1,2] is extended here to two novel applications, selective ionizations (K_2), and specific populations of barrier regions or transition states (Na_3). These simulations are carried out by wavepacket propagations on *ab initio* or empirical potential energy surfaces [4], see also [5].

Selective vibrationally mediated ionization of K_2 by pump&control laser pulses is achieved as follows (see Fig. 1:) The first laser pulse induces coherent vibrations not only in the excited but also in the electronic ground state. As a consequence, the wavepacket moves periodically between inner and outer turning point (see first snapshot in Fig. 1). The probability density at the inner turning point populates the Franck-Condon region for the desired coherent three-photon-ionization (TPI) which is induced by the second control pulse, (snapshots 2 and 3 in Fig. 1). The resulting pump&control signal (Fig. 2b) reflects the periodic vibrations of K_2 in the electronic ground state, as induced by the initial pulse, and compares well with corresponding pump&probe TPI spectrum (see Fig. 2a) measured by K. Kobe et al. [6].

Selective vibrationally, or more precisely pseudorotationally mediated populations of the transition states of Na_3 by pump&control are achieved by an analogous strategy: The first pump pulse induces the electronic X $\rightarrow$ B transition. Subsequent pseudorotations drive the system periodically from its equilibrium (i.e. obtuse triangle) to the transition state (i.e. acute triangle) configuration (Fig. 3). Here the second control pulse induces the B $\rightarrow$ X deexcitation and prepares the system at its transition state. This strategy should be a challenge to experimentalists motivated by good agreement of experimental and theoretical absorption spectra (Fig. 4a,b) of the pseudorotating Na_3 (B), using the time-dependent approach, see Fig. 4a,b and compare with Ref. 5. Further details will be published elsewhere.

References:

1. A.H. Zewail, in: Femtosecond Chemisty, Verlag Chemie, Eds. J. Manz and L. Wöste, 1994, chapter 2 (in press)
2. D.J. Tannor, S.A. Rice, Adv. Chem. Phys. 70(I) (1988) 441
3. B. Hartke, R. Kosloff, S. Ruhman, Chem. Phys. Lett. 158 (1989) 238
4. R. de Vivie-Riedle, J. Manz, W. Meyer, B. Reischl (to be published)
5. J. Gaus, K. Kobe, V. Bonačić-Koutecký, H. Kühling, J. Manz, B. Reischl, S. Rutz, E. Schreiber, L. Wöste, J. Phys. Chem. 97 (1993) 12509
6. K. Kobe, Doktorarbeit, FU Berlin, 1993; S. Rohland, Diplomarbeit, FU Berlin, 1993

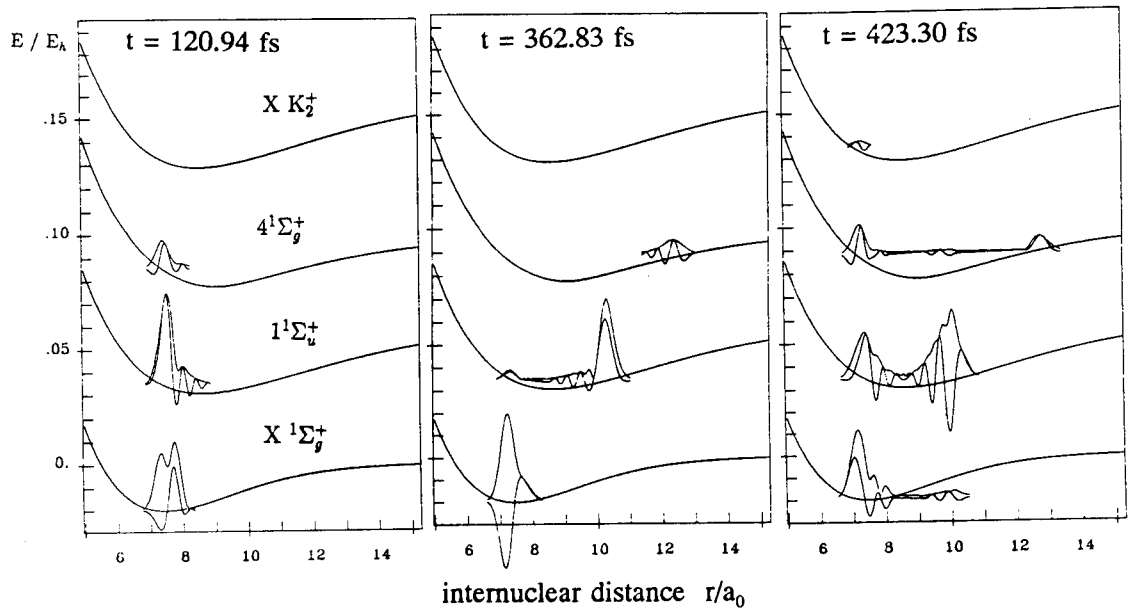


Fig.1: *ab initio* potential curves for the K_2 system. Indicated are three selected snapshosts for a delay time of 300 fs between pump and probe laser pulse.

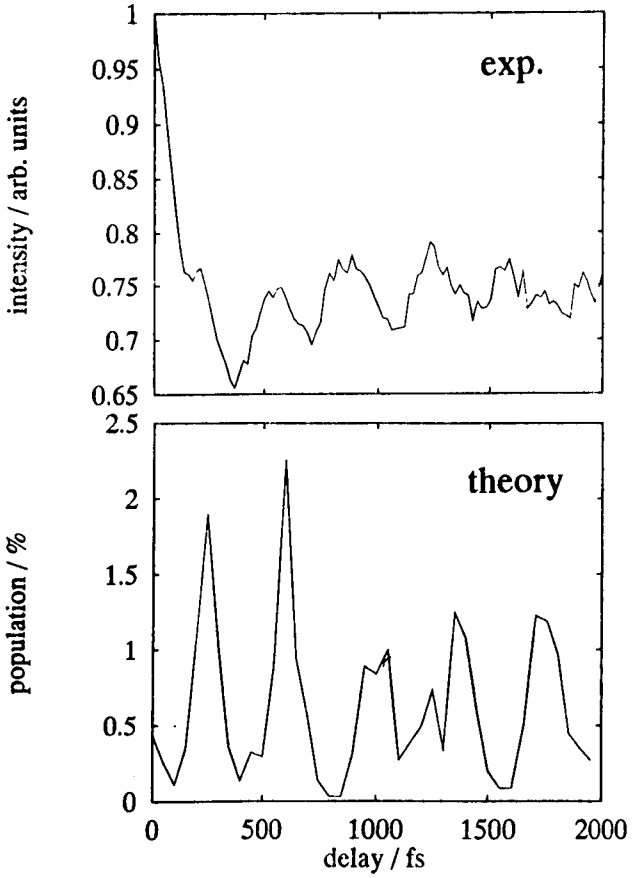


Fig. 2a: Experimental pump&probe spectrum of the K_2 ion signal.
Fig. 2b: Theoretical simulation of the pump&probe spectrum represented as a time-dependent population of the K_2 ion.

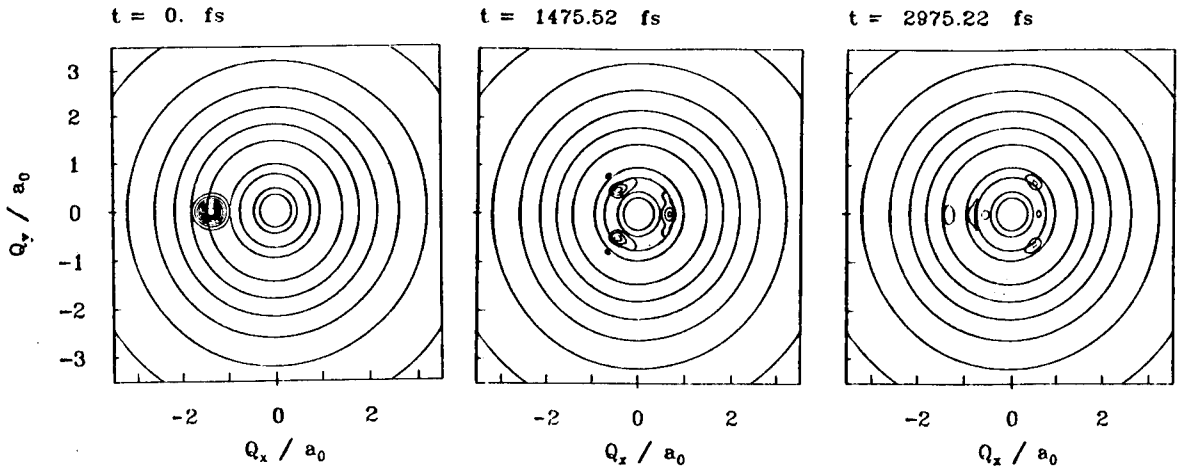


Fig. 3: Molecular dynamics or Na_3 (B), illustrated by selected snapshots. Snapshot 2 represents an acute shaped tringle after a half pseudorotational period while snapshot 3 represents an obtuse shaped triangle after a whole period.

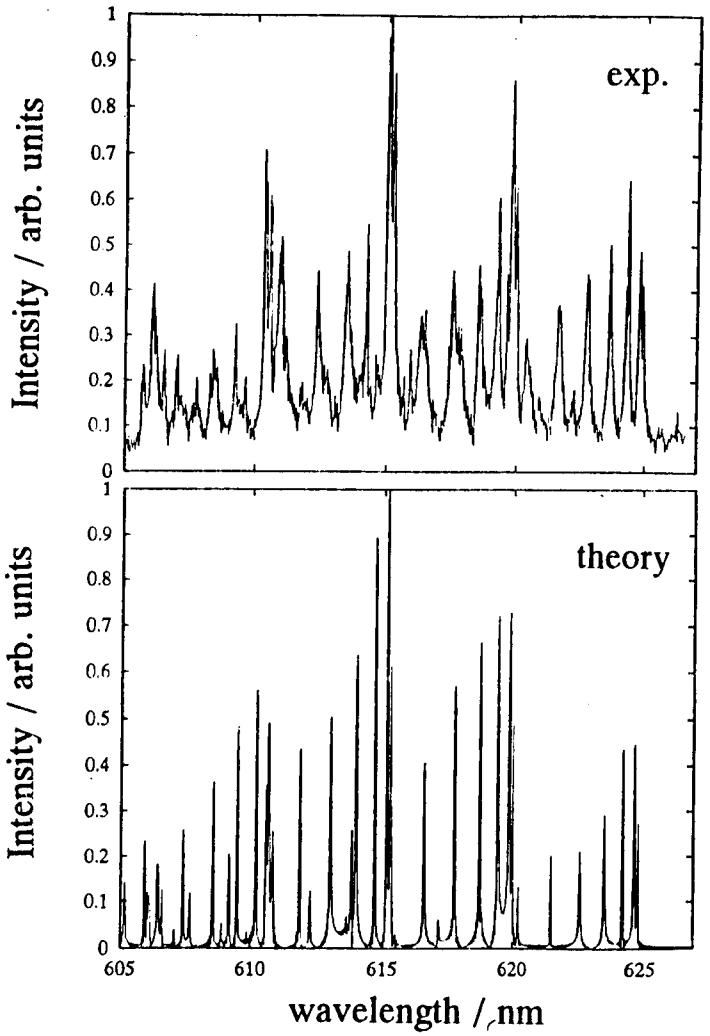


Fig. 4a: Experimental TPI absorption spectrum of Na_3 (B).
Fig. 4b: Theoretical simulation of the Na_3 ($X \rightarrow B$) transition.

Time-resolved thermionic electron emission and nonthermal ion emission from Au excited by intense fs pulses

D. M. Riffe,* X. Y. Wang,† Y.-S. Lee, and M. C. Downer

Physics Department, The University of Texas, Austin TX 78712

Phone: (512) 471-6054

Present Addresses:

**Physics Department, Utah State University, Logan, UT 84322-4415*

Phone: (801) 750-3896

†*Columbia Radiation Laboratory, Columbia University, New York, NY 10027*

Phone: (212) 854-8449

Electron and ion emission have long been used as probes of the interaction of laser pulses with solid-state materials.[1] For excitation by femtosecond pulses most of the focus has been on either the low excitation regime where single or multiphoton electron emission dominates and surface states play an important role or in the very intense regime where significant x-ray generation occurs. Notably absent are emission studies in the transition region across the damage threshold where electron temperatures are ~1 eV, a temperature region where the relaxation dynamics of electrons are important in nanoscale microelectronic devices, ultrafast desorption of adsorbates, and fs-laser plasma physics.[2]

In this paper we present electron- and ion-emission data obtained on polycrystalline Au for incident intensities between 10^{11} and 10^{13} W/cm^2, intensities which span the damage threshold of Au at ~2×10^{12} W/cm^2. Below the threshold the emission is dominated by electrons. For laser intensities above 0.4×10^{12} W/cm^2 the electron emission is predominantly thermionic in nature as shown by earlier single-pulse measurements.[3] Here we extend the earlier single-pulse work to time-resolved (two-pulse correlation) measurements of the electron emission. This extension allows the cooling rate of the nonequilibrium electrons to be quantitatively determined in this high-excitation regime for the first time. The measured electron cooling rate is much faster than that predicted with low-temperature parameterizations of the electron-phonon coupling G, electronic specific heat C_e, and thermal conductivity κ. However, by specifically accounting for the temperature dependencies of κ, G, and C_e we have successfully modeled the measured cooling curves and peak electron temperatures. Above the damage threshold we find that ion emission becomes increasingly important as observed in ps-excitation studies.[4] Surprisingly, we observe a sharp ($\Delta E/E\approx0.3$), nonthermal peak of H^+ ions with average energies up to ~300 eV. We propose that the H^+ ions come from adsorbed H atoms and that they are accelerated by the space-charge fields of the concurrently emitted thermionic electrons.

A polycrystalline gold sample of 5000 Å thickness was prepared by evaporation onto a clean Si wafer in a vacuum chamber of ~10^{-6} Torr. It was then immediately placed in an ultrahigh vacuum chamber which was maintained at a base pressure of $<2\times10^{-10}$ Torr. The experiments were performed with 120 fs, 630 nm laser pulses generated by a CPM dye laser and a 10-Hz, four-stage YAG-pumped dye amplifier. For the time-resolved electron-emission measurements the amplified pulses are split into two nearly equal intensity beams and then recombined to form a colinear p-polarized beam incident at 68° with variable time delay Δt between the two pulses. In the ion-emission experiments single pulses were used. The net yield was determined with a picoammeter while the energy distributions of the emitted particles

were obtained with a time-of-flight detector. The spot size on was typically on the order of 5×10^{-4} cm^2. Other experimental details are as described earlier. [3]

In the electron-emission experiments the total electron yield per laser shot was measured as a function of the delay between two nearly equal-intensity pulses For an intensity of 1.5×10^{12} W/cm^2 (inset of Fig. 1) the yield monotonically decreases to a flat baseline for pulse separations greater than 1.5 ps. Previous quantification of space-charge-limited ultrafast thermionic emission, which has shown for electronic heating on a time scale < ~10 ps that the total yield in this excitation regime is proportional to the peak electron temperature T_{peak} [3], provides a basis for quantitative analysis of the two-pulse data. The measured yield can thus be converted to the peak temperature T_{peak} which arises as a result of the two incident pulses; this representation of the data is displayed as closed circles in Fig. 1 for several intensities. This T_{peak} created by two equal-intensity laser pulses is dependent upon the value of the electron temperature T_e when the second pulse arrives. For exactly overlapping pulses the resulting T_{peak} is obviously a maximum. If the second pulse arrives after the electrons have recooled to near RT then T_{peak} (and the yield) induced by the pair of pulses should be the same as that from a single pulse, as is observed in the inset of Fig. 1 (to within 5% for all data). The data in Fig. 1 thus indicate that electron cooling (from one pulse) takes place within a few ps for these high excitation levels in Au.

We assess the significance of these cooling rates by employing the coupled differential equations of Anisimov, et al. [5] Using RT formulations of G, C_e, and κ results in calculated cooling rates and T_{peak}'s much larger than experimentally determined; see Fig. 2. However, when we include the temperature dependencies of G and C_e, which both have a substantial high-T_e contribution from the thermally excited Au *5d* states, by extending the formalism of Allen [6], and the temperature dependence of κ (through T_e and $T_{lattice}$ dependent scattering rates [7]), the calculated cooling curves agree remarkably well with the measured results in terms of both the absolute temperature and shape of the cooling curves; see the dotted lines in Fig. 1.

As shown in the inset of Fig. 3, the total yield above the damage threshold increases dramatically above extrapolation from the below-threshold region where electron emission prevails. The change in the character of the emission is due to the formation of a solid-density plasma and the subsequent emission of both electrons and ions. Fig. 3 further shows time-of-flight spectra obtained for excitation of the gold target between 6.2 and 10×10^{12} W/cm^2. In addition

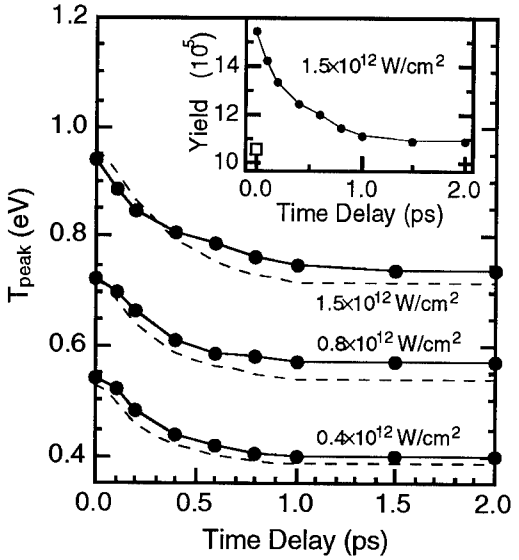


Fig. 1. T_{peak} and yield (inset) vs time delay between two (nearly) equal intensity laser pulses at indicated incident laser intensities. Solid circles—experiment, dashed lines—calculation, open square—single pulse.

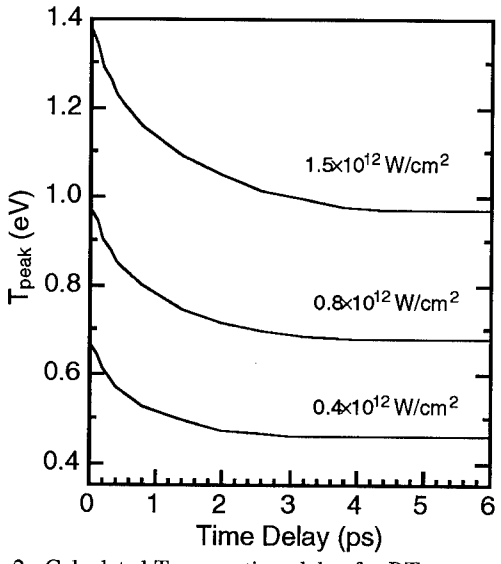


Fig. 2. Calculated T_{peak} vs time delay for RT parameterizations of G, C_e, and κ for experimental conditions in Fig. 1. Note that T_{peak} and the cooling rates are much larger than the corresponding data in Fig. 1

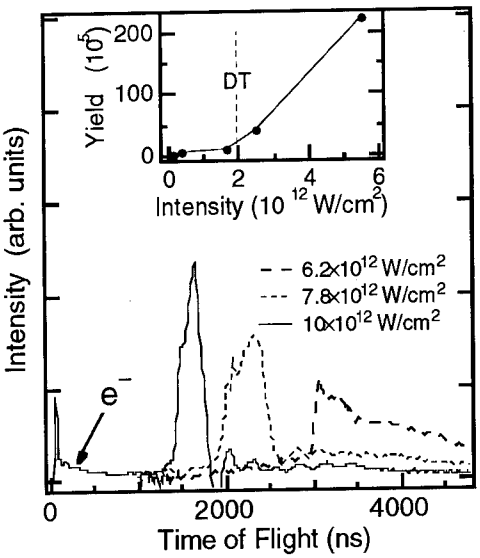


Fig. 3. Time-of-flight data showing electrons at < 1μs and H^+ spectra as a function of laser intensity. Inset: total yield vs laser intensity. DT marks the damage threshold

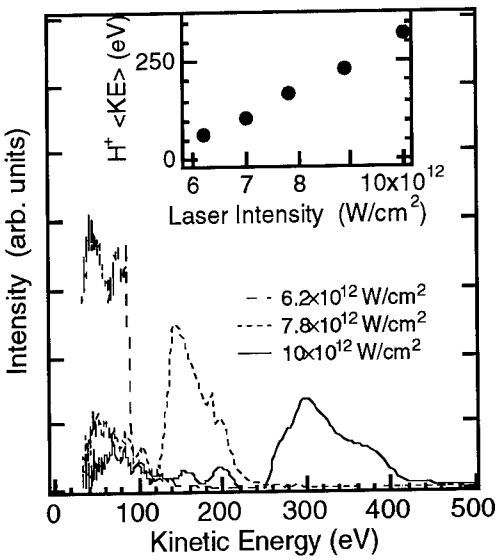


Fig. 4. Energy distributions of H^+ as a function of laser intensity. Inset: Average energy in H^+ peak as a function of laser intensity.

to the thermionic electron distributions seen for times <1 μs, there exists a delayed peak which increases in kinetic energy (decreases in flight time) as the laser intensity is increased. Electrostatic mass spectrometry identifies the ions as H^+, which arise from H adsorbed on the Au surface. The time of flight can thus be converted to kinetic energy; see Fig. 4. The inset in Fig. 4 shows that the average energy is quite linear vs the intensity in this (limited) intensity range.

The sharp distributions and large energies shown in Fig. 4 are surprising given the thermionic nature of electron emission and the peak electron temperatures of only ~10 eV at 10^{13} W/cm^2. However, we propose that it is just these thermionically emitted electrons which provide the force necessary to accelerate the H^+ ions to the observed kinetic energies. In the intensity regime studied here the electron density is so high that the Coulombic (space-charge) fields of the faster electrons (and their image charges) significantly suppress the slower electrons from escaping. Just below the damage threshold the suppression is so great that only one in ~10^5 electrons escape compared to the theoretical yield without space charge.[3] Any surface-adsorbed H atom which is ionized near the surface experiences these same space-charge fields. However, due to its positive charge, it accelerates away from the surface. Preliminary calculations indicate that the force from the thermionic cloud of electrons is indeed sufficient to produce the measured ion energies. The fairly narrow distributions arise because all of the H^+ begin accelerating at nearly the same time from the surface. Possible uses as an injector source in proton-accelerator applications are intriguing. Future extensions of the two-pulse electron-emission technique into the above-damage regime would certainly prove fruitful in elucidating the physics of solid-density plasmas and fs-pulse x-ray generation.

References

[1] See e.g., J.F. Ready, Phys. Rev. **137**, A620 (1965); E. Bernal, J.F. Ready, and L.P. Levine, IEEE J. Quantum Elect. **2**, 480 (1966).
[2] See, e.g., H. Shichijo and K. Hess, Phys. Rev. B **23**, 4197 (1981); M.M. Murnane, et al., Science **251**, 531 (1991); F. Budde, et al., Phys. Rev. Lett. **66**, 3024 (1991).
[3] D.M. Riffe, X.Y. Wang, M.C. Downer, D.L. Fisher, T. Tajima, and J.L. Erskine, J. Opt. Soc. Am. B **10**, 1424 (1993); M.C. Downer, D.M. Riffe, X.Y. Wang, J.L. Erskine, D.L. Fisher, T. Tajima, and R.M. More, *Ultrafast Phenomena VIII*, J. L. Martin, R. Migus, G. A. Mourou, and A.H. Zewail, eds. (Springer Verlag, Berlin, 1993), p. 357.
[4] See, e.g., A.M. Malvezzi, H. Kurz, and N. Bloembergen, Appl. Phys. A **36**, 143 (1985).
[5] S. I. Anisimov, et al., Sov. Phys. JETP **39**, 375 (1974).
[6] P.B. Allen, Phys. Rev. Lett. **59**, 1460 (1987).
[7] A.H. MacDonald, Phys. Rev. Lett **44**, 489 (1980).

Tunable Femtosecond sources and Optical Parametric Generators

François Salin et Frederick Estable

B.M. Industries
CE 2901
91029 EVRY Cedex
FRANCE

Sources of tunable, energetic, femtosecond pulses are of substantial interest to a variety of scientific communities. Previously, femtosecond pulses in the microjoule range were only possible through complex dye amplifier schemes. With the introduction of self-modelocked Ti:sapphire oscillators, tunable sub-100 fs pulses became available although most of the experiments ask for spectral ranges not reachable by Ti:sapphire oscillators alone. In addition to generating short pulses, Ti:Al_2O_3 has also been shown to be an outstanding amplifier for producing ultra-high peak power pulses. Although energies up to 1 J have been produced, the maximum repetition rate of these amplifiers is typically on the order of 10 Hz. This low repetition rate prevents the use of powerful spectroscopy techniques such as heterodyne or phase sensitive detection. We previously demonstrated multi-kHz amplification of femtosecond pulses[1] wich was a first step toward the production of tunable high power pulses tunable over the whole optical spectrum. We present here a femtosecond source producing microjoules pulses tunable from 250 nm to 2 μm.

In order to fully exploit the storage capability of Ti:Al_2O_3 we used chirped pulse amplification (CPA). A femtosecond pulse is first stretched to 500 ps and then amplified. The stretched pulse can be safely amplified since the peak power has been significantly lowered, thereby avoiding any non-linear effects which could result in damage to the amplifier or its components. After amplification the pulse is finally recompressed to its initial duration. Our source uses a MIRA 900 Ti:sapphire oscillator (Coherent Inc.) producing sub-100 fs pulses tunable from 720 nm to 900 nm. The pulses were stretched up to 300 ps and then send to a Ti:sapphire regenerative amplifier (see fig.1). The amplifier was pumped by a B.M. Industries Nd:YLF laser model 621D producing over 10 W of 523 nm pulses at 1 kHz repetition rate. The output of the amplifier was recompressed to 150 fs. The compressed pulse energy was 600 μJ at 7 W pump power. In order to tune the system we must tune both the compressor and the stretcher. Both use gratings and the angles of incidence must be kept equal within a few minutes of arc in order to keep the pulse duration short. Last year we introduced a new design based on single grating strecher and compressor mounted on the same rotation table. Using this set-up we produced high power pulses tunable from 750nm to 850 nm. The tuning curve is given in figure 2. The pulse duration stayed under 170 fs over that range.

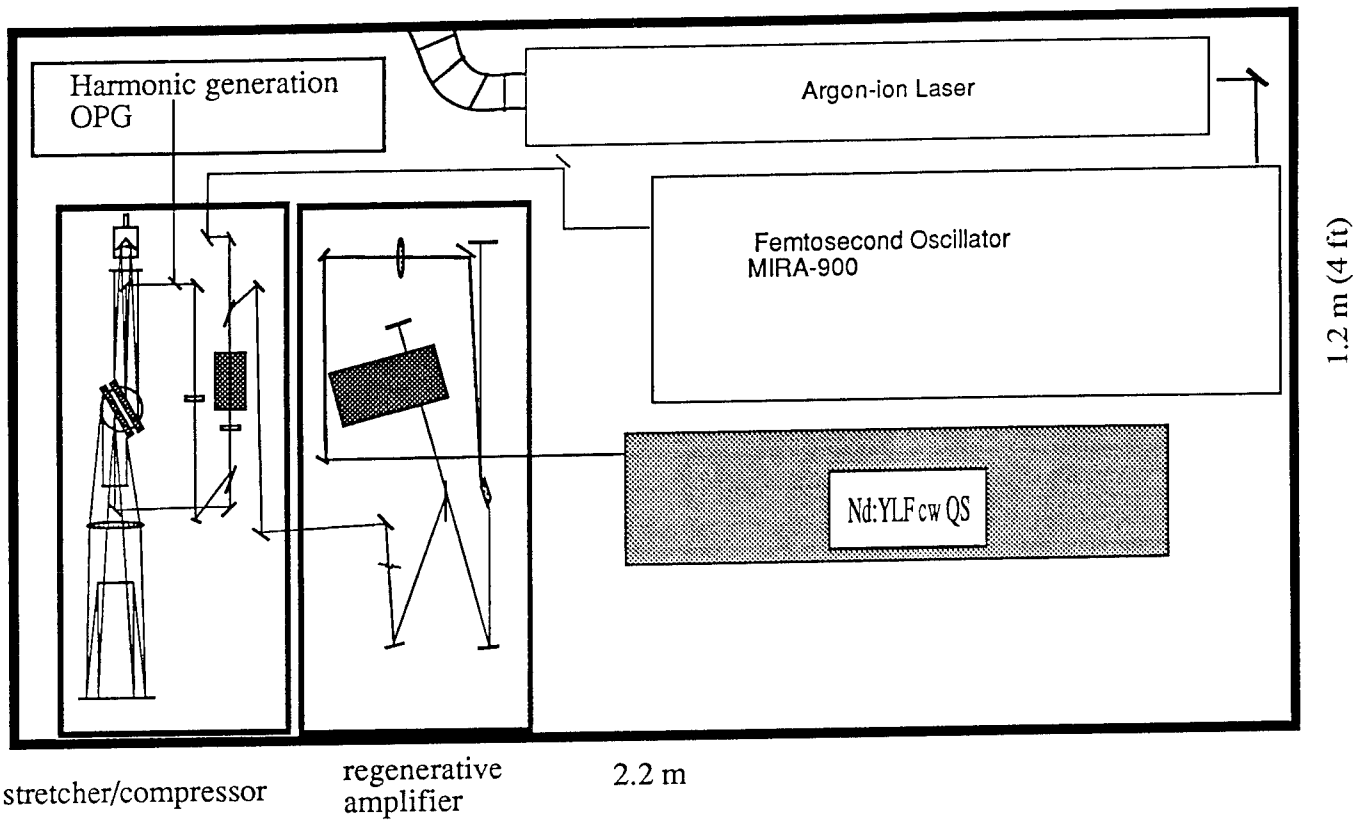


Fig.1

In order to extend the tuning range in the UV we frequency doubled the pulses by using a 1mm BBO crystal. We achieved up to 48 % efficiency at 400 nm. The IR beam was then splitted off and delayed to compensate for the group velocity dispersion in the doubling crystal. After recombination the IR and blue beams were send to a 1mm BBO crystal cut for third harmonic generation around 800 nm. Up to 60 μJ of 267 nm were obtained at 1 kHz repetition rate. Although this source is tunable in the near-IR (750-850 nm), the blue (375-425 nm) and the UV (250-280 nm) there is still large parts of the spectrum missing.

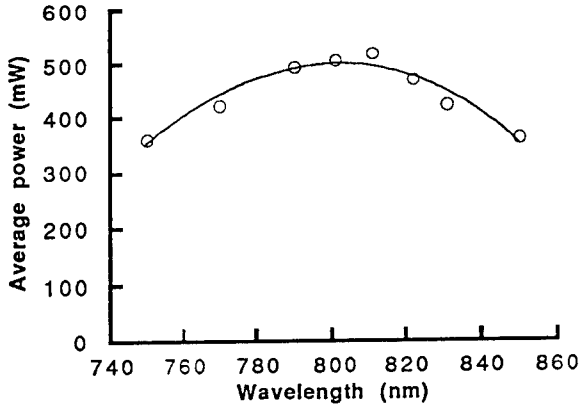


Fig.2

In order to get real tunability over the visble and the 1-4 μm region we developped optical parametric generators pumped by femtosecond pulses. The peak power of femtosecond pulses is in the gigawatt range and parametric gain over 10^7 are easily achieved even with relatively short crystal. Our first OPG uses a BBO crystal in a double pass configuration. The OPG was pumped by the second harmonic output of the femtosecond laser source described above (B.M.I.model Alpha-1000). Up to 300 μJ per pulse at 400 nm and 1 kHz were incident on the OPG. The output of the OPG was a smooth,collimated beam, tunable from 500 nm up to 1.9 μm. A typical tuning curve is given in figure 3. The peak powef in the output of the OPG was high enough to create a highly stable spectral continuum in a 3 mm piece of sapphire. The beam profile was about 2 x diffraction limited and the peak to peak stability about ± 8%. This femtosecond source has several advantages over the usual spectral continuum. It has a much higher spectral density. The pulse spectral width versus wavelength is given in fig.4. The spectral density is 100 times higher than that of a spectral continuum and the output beam can be use without subsequent amplification for most spectroscopical applications. The beam quality is also much better than that of the continuum allowing higher intensity to be reached.

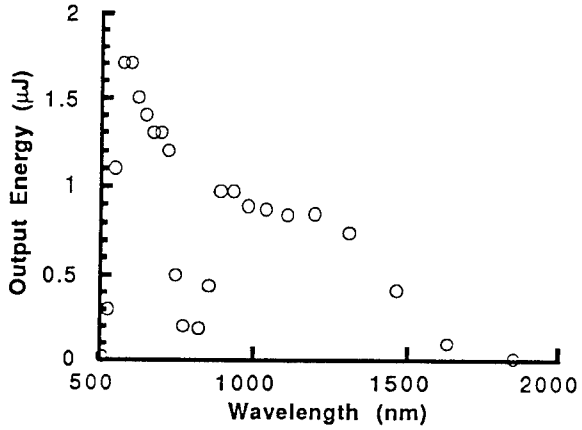


Fig.3

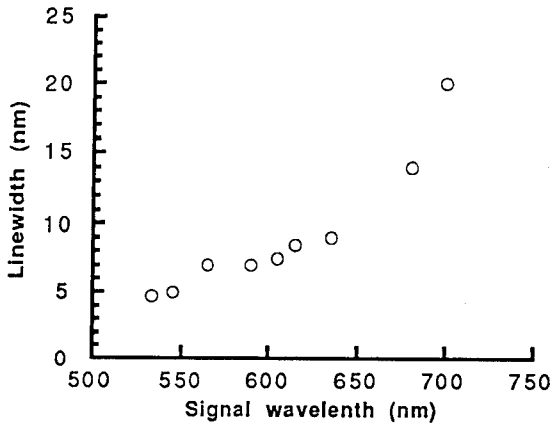


Fig.4

Finally we developped a new OPG/OPA system to boost the energy to 20 μJ. The pump beam was splitted in two parts. The first part pumped the OPG described above while the second beam pumped a second crystal working as an amplifier for the OPG output. The characteristics of the OPA output were the same than that of the OPG exept the energy.

In summary we report on the possibility of building all solid-state tunable femtosecond sources. We demonstrated tunnability from 250 nm to 2μm with over 10 MW peak power over that range. We will discuss extensions of this technique including tunability in the 2-4μm range and in the UV.

1. F. Salin, J. Squier, G. Mourou, G. Vaillancourt, Opt. Lett. **16**, 1964 (1991).

THz Emission by Coherent Lattice Vibrations in Tellurium

T. Dekorsy, H. Auer, C. Waschke, H. J. Bakker, H. G. Roskos, and H. Kurz

Institute of Semiconductor Electronics, RWTH Aachen, 52056 Aachen, Germany
Tel. +49-241-807896; Fax. +49-241-86165

We report on the time-resolved observation of coherent infrared-active phonons excited by fs-laser pulses in single crystal Tellurium. The coherent lattice vibrations are detected in an optical pump-probe experiment in amplitude and phase. The emission of electro-magnetic waves at THz frequencies associated with the coherent lattice vibration is observed. This is the first demonstration of THz emission by coherent phonons for any semiconductor.

Tellurium is a single-element semiconductor with IR-active phonons. The IR activity arises from the large electronic polarizability and the lack of inversion symmetry [1]. In addition to a strong, fully symmetrical Raman-active A_1-mode, three other phonon modes exist: two Raman- and IR-active E-modes and one only IR-active A_2-mode.

In time-resolved pump-probe measurements with fs laser-pulses on high quality, single crystal Te the anisotropic part of the reflectivity, *e. g.* $R_x - R_y$, is detected. The same detection method has been used for coherent LO-phonons in GaAs [2]. The laser source is an unamplified CPM laser at 2 eV photon energy and a pulse-width of 50 fs. The data are recorded with differential lock-in technique detecting the time derivative of the signal. Figure 1 depicts the anisotropic reflectivity changes from a Te crystal with the plane perpendicular to the c-axis (x-y plane). The density of photo-excited carriers is $5\times10^{18}\mathrm{cm}^{-3}$. The salient signature of the reflectivity changes results from a mode beating between the E_{TO}- and E'_{TO}-phonon at 2.77 THz and 4.2 THz, respectively. The Fourier transform is shown in the inset. There is no contribution from the fully symmetrical A_1-phonon at 3.6 THz, which is known to strongly modulate the isotropic reflectivity [3]. The anisotropic reflectivity change is also free of contributions from nonlinear electronic processes. From numerical fits to the data the dephasing times of the coherent modes are accurately determined. The dephasing time of the E_{TO}-mode at 2.77 THz is 10 ps and 5 ps for the E'_{TO}-mode. This surprisingly slow dephasing of the E_{TO}-mode is about 5 times longer than the dephasing time of the A_1-phonon measured under the same excitation conditions. Obviously the coherent E_{TO}-mode does not couple to the carrier plasma simultaneously generated by the pump pulse.

In previous time-resolved coherent-phonon experiments, only Raman-active A_1-phonons could be observed in Te, but not the E-modes [3]. The excitation of the A_1-

mode is explained by the ultrafast displacement of the atoms due to the optically excited non-equilibrium electron-hole plasma [3], while the E-modes are most likely excited by a stimulated Raman process. The modulation by the A_1-mode is fully isotropic, i. e. there exists no dependence on the pump or probe pulse polarization. As a result of this isotropy the A_1-mode does not appear in the anisotropic detection. The reflectivity changes due to the E-modes observed in our experiments are two orders of magnitude smaller than the changes induced by the coherent excitation of the A_1-mode.

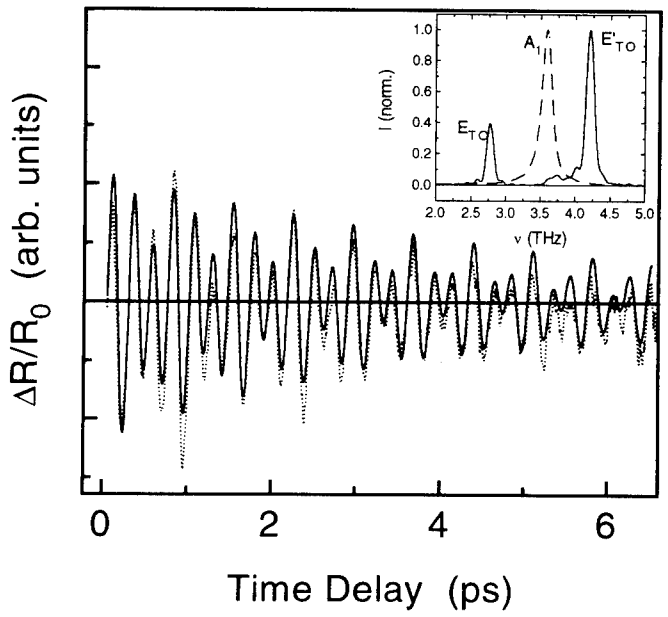


Fig. 1: Time-resolved anisotropic reflectivity changes $\Delta R = R_x - R_y$ from Te (dashed line) and numerical fit to the data (solid line). The inset shows the direct Fourier transform of the anisotropic reflectivity (E_{TO} and E'_{TO}-mode, solid line) and of the isotropic reflectivity (A_1-mode, dashed line, not shown in time domain).

The optical stimulation of coherent IR-active phonons in Te is associated by the emission of THz radiation from the surface irradiated. THz radiation has been observed from coherent electronic states [4] and molecular vibrations in organic crystals [5], but no radiation has been detected from coherent lattice vibrations in semiconductors yet.

In the THz experiment, the same sample is excited with a Ti:Sapphire laser with 1.7 eV photon energy and a pulse width of 150 fs. The THz radiation from the sample is focused on an optically gated dipole antenna, which allows a direct measure of amplitude and phase of the emitted wave.

The THz signal is composed of a strong instantaneous contribution and an oscillating part associated with coherent phonons. In Figure 2 the instantaneous contribution at zero-time delay has been substracted to reveal the oscillatory part. As in the optical experiment, the vibration is traced for at least 6 ps. The Fourier transform shown in the inset gives a sharp peak at 2.8 THz, close to the E_{TO}-frequency observed in the pump-probe experiment. The higher IR-active E'_{TO}-mode at 4.2 THz is above the bandwidth of the detection antenna. The A_1-mode is not expected to emit any radiation.

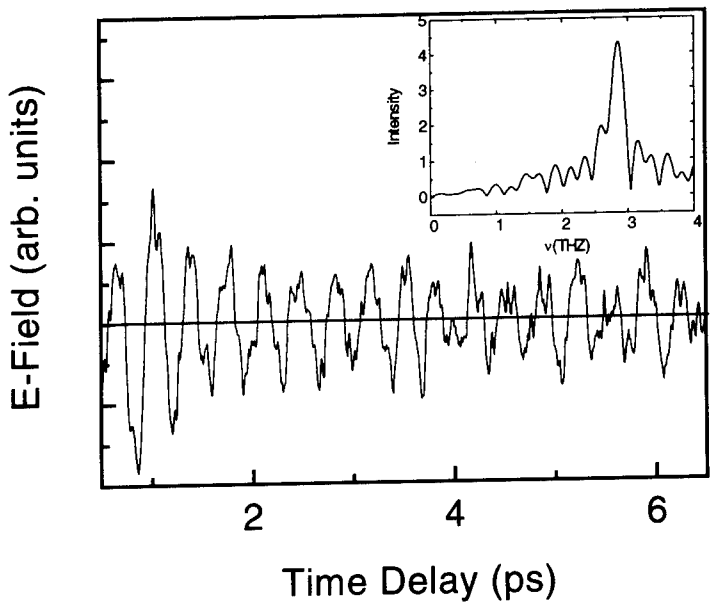


Fig. 2: THz emission from coherent phonons in Te (plane perpendicular to the c-axis). The inset shows the Fourier transform. Time delay zero is arbitrarily.

Complementary experiments are performed at crystal planes parallel to the c-axis. In both, the optical and the THz-emission experiment, coherent vibrations at 3.2 THz are observed, which is close to the E_{LO}-frequency. The dephasing time of this mode is significantly shorter than for the E_{TO}-mode, indicating a coupling of the LO-mode to the simultaneously excited carrier plasma. The change of the frequencies for different crystal orientations is in accordance with Raman measurements of extraordinary phonon-polaritons in Tellurium [6].

These experiments provides the first demonstration of THz emission by coherent phonons in semiconductors and open a new field in the spectroscopy of coherent lattice dynamics.

We thank P. Grosse for supplying the high-quality Tellurium samples.

[1] P. Grosse, Springer Tracts in Modern Physics **48**, Springer (Berlin, Heidelberg, New York 1969).

[2] G. C. Cho, W. Kütt, and H. Kurz, Phys. Rev. Lett. **65**, 764 (1990).

[3] T. K. Cheng et al., Appl. Phys. Lett. **59**, 1923 (1991), and H. J. Zeiger et al., Phys. Rev. B **45**, 768 (1992).

[4] H. G. Roskos et al., Phys. Rev. Lett. **68**, 2216 (1992).

[5] X. -C. Zhang et al., Appl. Phys. Lett. **61**, 3080 (1992).

[6] W. Richter, J. Phys. Chem. Solids **33**, 2123 (1972).

Ultraviolet Picosecond Pulse Amplification in New Solid-state Laser Medium: Ce^{3+}:$LuLiF_4$

Nobuhiko SARUKURA, Zhenlin LIU, and Yusaburo SEGAWA
Photodynamics Research Center, The Institute of Physical and Chemical Research,
Nagamachi Koeji 19-1399, Aoba-ku, Sendai, Miyagi 980, Japan
Telephone: +81 22 228 2012 Facsimile: +81 22 228 2010
Keiichi EDAMATSU, Yoshiro SUZUKI, and Tadashi ITOH
Department of Applied Physics, Tohoku University,
Aoba, Aramaki, Aoba-ku, Sendai, Miyagi 980, Japan
Vadim V. SEMASHKO, Alexander K. NAUMOV, Stella L. KORABLEVA, Ravil Yu. ABDULSABIROV, and Mark A. DUBINSKII
Kazan State University, Lenin Street 18, 420008 Kazan, Russia

Recent progress in tunable solid-state-laser materials in the infrared region has enabled development of completely new ultrashort-pulse laser sources. Such innovations will also be expected in the ultraviolet region. Several Ce^{3+}-doped tunable ultraviolet laser crystals have been developed including $YLiF_4$,[1] LaF_3,[2] $LiCaAlF_6$,[3] $LiSrAlF_6$,[4] and $LuLiF_4$.[5] In spite of their broad gain bandwidth, no short-pulse application of these materials has been reported. In this presentation, we will describe the properties of Ce^{3+}:$LuLiF_4$ and its application to picosecond-pulse amplification.

Ce^{3+}:$LuLiF_4$ has a broad fluorescence spectrum (300 to 345 nm). The absorption spectrum is suitable for excitation by KrF-excimer lasers (248 nm), and the fluorescence lifetime is 40 ± 2 nsec. Small-signal gain and saturation fluence were evaluated using the second harmonic (325 nm) of a nanosecond DCM-dye laser as a probe. The single-pass gain in the small-signal region was over 6-dB/cm with 0.5-J/cm^2 excitation, and it is sufficiently large for the practical use. The saturation fluence was measured to be ~50 mJ/cm^2, which is much higher than that of organic dyes (~ mJ/cm^2). These results indicate its high potentiality as a power amplification medium. The gain spectrum was measured using the second harmonic of a picosecond mode-locked DCM-dye laser as a probe, and a KrF-laser as a pumping source (Fig. 1). The gain spectrum from 323 nm to 335 nm was confirmed, and it is broad enough to amplify tunable femtosecond pulses.

Using this new laser material, an all-solid-state ultraviolet picosecond laser system was designed. The seed picosecond ultraviolet pulses at 325 nm were generated by the sum-frequency of 835-nm picosecond pulses from a Ti:sapphire amplifier and the second harmonic of a Nd:YAG laser. The 10-Hz Q-sw Nd:YAG laser was synchronized to an 82-MHz mode-locked Ti:sapphire laser oscillator, and delivered 50-mJ pulse energy for pumping the amplifier and 10-mJ pulse energy for frequency mixing. 10-nJ, 1.5-psec pulses in the mode-lock pulse train from the oscillator without any single-pulse selection were amplified typically up to 100-μJ level by a double-side-pumped confocal 4-pass Ti:sapphire amplifier.[6] For efficient sum-frequency generation, the peak position of the 532-nm, 7-nsec pulses was adjusted to the largest pulse among the amplified picosecond pulse train by an optical delay (40-nsec). In this way, a single ~1-μJ, 325-nm seed pulse was generated at a 10-Hz repetition rate using a 5-mm thick BBO crystal cut at 35 degrees.

The duration of the ultraviolet pulses was evaluated to be less than 3-psec using a streak camera.

The Ce^{3+}:$LuLiF_4$ amplifier was designed with a side-pumped confocal 4-pass configuration similar to the coaxially pumped confocal multi-pass configuration of Ti:sapphire amplifier.[7] The amplifier consisted of a gain medium located at the beam waist of a confocal lens pair (10-cm focal-length) and two turning prisms for small displacement of each pass (Fig. 3). This configuration allowed the passes to overlap well in a small pumped region. A side pumping scheme is necessary because of its rather high absorption (~3 cm^{-1}) at the pumping wavelength. The 1-cm crystal was cut cylindrically, and a flat window was polished on the side. To reduce the unfavorable color-center formation effects,[7] the pumping laser was operated at a 0.5-Hz repetition rate synchronized to 10-Hz ultraviolet seed pulses. 35-mJ, 10-nsec KrF-laser pulses were weakly focused by a 10-cm focal-length cylindrical lens on the side window with 0.1 J/cm^2 fluence. 14-dB gain was confirmed for the transmitted 325-nm picosecond pulses as shown in Fig. 4. Using the streak camera, the duration of amplified ultraviolet pulses was evaluated to be less than 2.9 psec, and the measurement was limited by the resolution of the apparatus (Fig. 5). This result shows that there was no significant pulse width broadening in the amplifier due to dispersion in the present condition. Further optimization will improve the gain factor, because 20-dB gain was possible for a cw He-Cd laser in a similar configuration. The amplification of much shorter pulse can also be expected with the full use of its bandwidth.

In conclusion, Ce^{3+}:$LuLiF_4$ was proven to be an ultraviolet amplification medium with broad gain bandwidth which is attractive for ultrashort pulse applications. Using this material, direct amplification of ultraviolet pulses in solid-state media was demonstrated for the first time.

References

1. D. J. Ehrlich, P. F. Moulton, and R. M Osgood, Jr., Opt. Lett. 4, 184 (1979).
2. D. J. Ehrlich, P. F. Moulton, and R. M Osgood, Jr., Opt. Lett. 5, 339 (1980).
3. M. A. Dubinskii, V. V. Semashko, A. K. Naumov, R. Y. Abdulsabirov, and S.L. Korableva, Advanced Solid-State Lasers '93, paper ATuA6.
   M. A. Dubinskii, V. V. Semashko, A. K. Naumov, R. Y. Abdulsabirov, and S.L. Korableva, Laser Phys., 3, 216, (1993).
4. M. A. Dubinskii, R. Y. Abdulsabirov, S. L. Korableva, A. K. Naumov, and V. V. Semashko, IQEC '92, Paper FrL2.
   M. A. Dubinskii, V. V. Semashko, A. K. Naumov, R. Y. Abdulsabirov, and S.L. Korableva, J. Mod. Opt., 40, 1, (1993).
5. J.F. Pinto, G.H. Rosenblatt, L. Esterowitz, and G.J. Quarles, LEOS '94 , Paper PDI. 4.
6. N. Sarukura and Y. Ishida, J. Quant. Electron. 28, 2134 (1992).;
   N. Sarukura, Y. Segawa, and K. Yamagishi, Advanced Solid State Lasers '93, paper ATuD3.
7. Ki-Soo Lim and D. S. Hamilton, J. Opt. Soc. Am. B7, 1401 (1989).

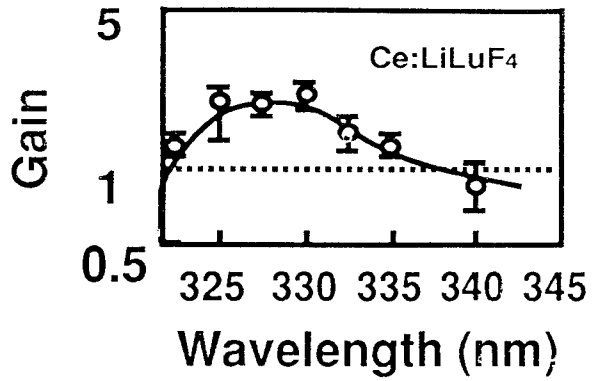


Fig. 1 The gain spectrum of Ce3+:LuLiF4 under the pumping of a KrF laser. The gain bandwidth is broad enough to amplify 10-fsec pulses.

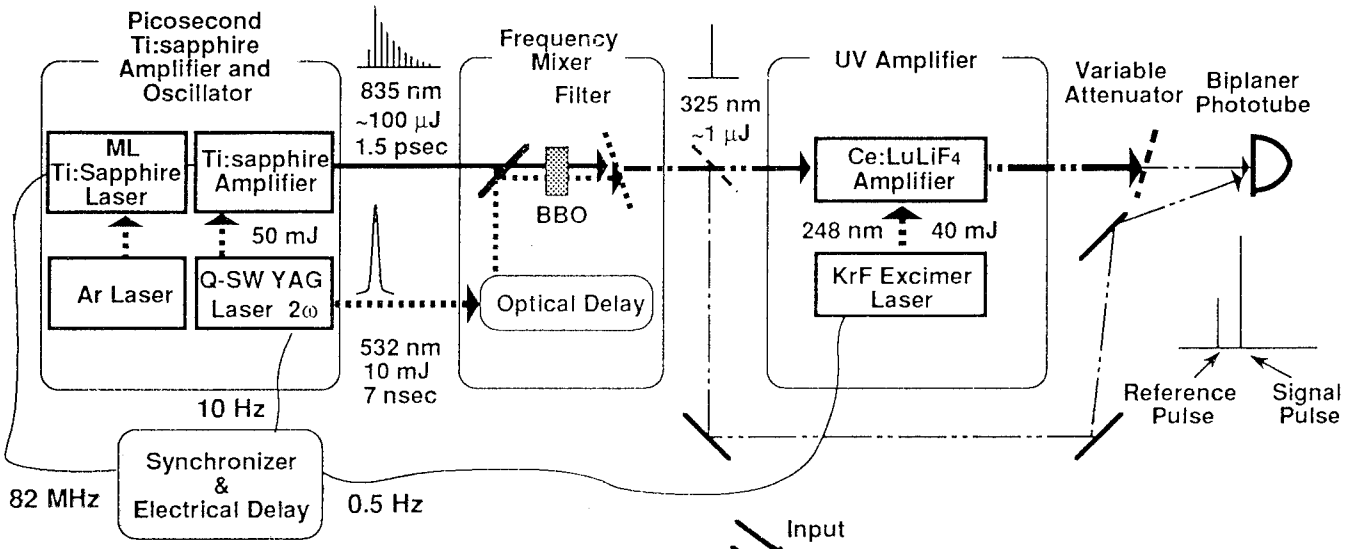


Fig. 2 The all-solid-state ultraviolet picosecond laser system. This system consisted of a Ce3+:LuLiF4 amplifier, a Ti:sapphire amplifier and oscillator, and a frequency mixer.

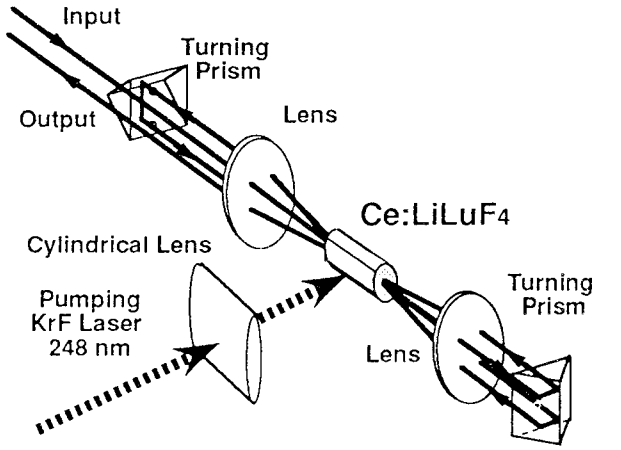


Fig. 3 The side-pumped confocal 4-pass Ce3+:LuLiF4 amplifier. The pumping area was 3 mm wide and 10 mm long. A confocal lens pair and prisms with the anti-reflection coating were used to reduce the loss.

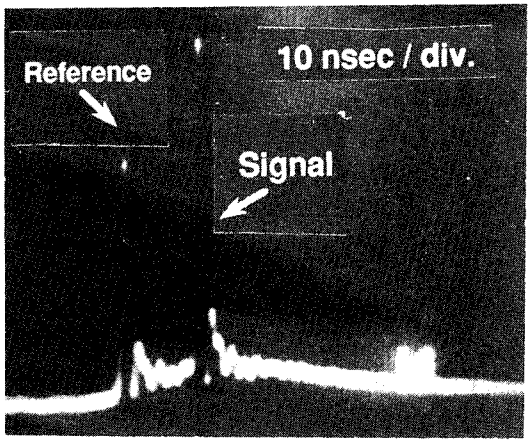


Fig. 4 The oscilloscope photograph showing 14-dB gain. To calibrate the gain factor, a reference pulse (separate from the input pulse) was detected together with the attenuated amplified pulse.

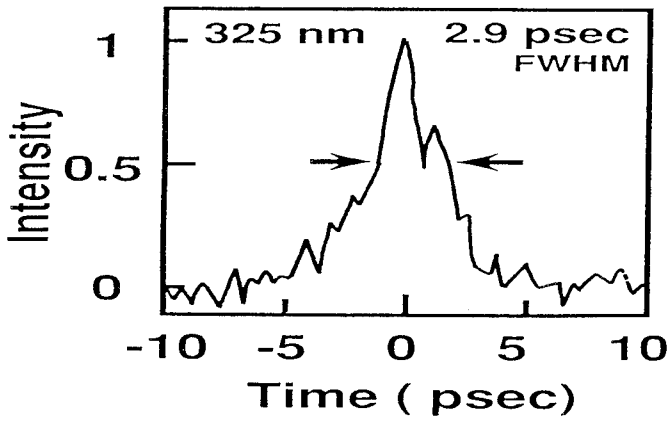


Fig. 5 The streak camera trace of the amplified ultraviolet pulse. The pulse duration was measured to be 2.9-psec (resolution limit).

Fluorescence of protonated and unprotonated Schiff base of retinal at room temperature.

S.M. Bachilo[1], S.L. Bondarev[2] and T. Gillbro[1]

[1]Dep. of Physical Chemistry, Univ. of Umeå, 901 87 Umeå, Sweden, tel. (+46)-90165368

[2]Dep. of Chemistry, Univ. of California, Riverside, California 92521-0403, USA, tel. (+1-909)-7873708

The Schiff base of retinal (SBR) is the only chromophore which is active in such important photobiological processes as vision and bacteriorhodopsin photosynthesis. The steady-state and time-resolved fluorescence techniques are the most sensitive to study properties of the lowest excited states of organic molecules. Unfortunately, emission studies of SBR and protonated SBR (PSBR) are complicated because of their very weak and fast fluorescence.

In the this work we present the first results of a systematic steady-state and time resolved fluorescence investigation of all-trans n-butylamine SBR and PSBR in different solvents at room temperature.

The PSBR was prepared from SBR solutions with excess trichloroacetic acid added directly before the measurements. Fluorescence kinetical measurements were performed by a single photon counting system. The samples were excited at 360-410 nm by about 10 ps pulses with a repetition rate of 800 kHz and an average excitation power of less than 1 mW. The full width at a half maximum of the instrumental response function (IRF) was in 45-55 ps range. The shortest lifetime limit of the direct decay reconvolution was found to be 3-5 ps.

RESULTS.

First it should be noted that small amounts of impurities might be a problem in the spectral and kinetical investigations of very weak emissions. Almost all emission traces of SBR contained additional slow components with lifetimes in the nanosecond range, which obviously originated from impurities in solvent or sample. The impurity fluorescence decreased with wavelength and was solvent depend. This dependence could also be observed in the steady-state spectra. The real part of the SBR and PSBR fluorescence showed a much faster decay. Fig.1 shows the SBR and PSBR kinetics in ethanol, measured at wavelengths that are close to the emission maxima. In this solvent the impurity fluorescence was almost absent. The SBR emission kinetics, detected in the 400-500 nm range (the short wavelength edge of fluorescence), were more complicated (Fig.2). Together with the 30-40 ps components we observed a very fast component, whose lifetime could not be resolved. The slow impurity fluorescence (1.5 ns in Fig.2) was more intensive in toluene and other nonpolar solvents.

We could calculate the radiative lifetimes for the absorption transition τ_a^0 from the absorption spectra and for the fluorescence transitions τ_f^0 from the emission lifetimes τ_f and quantum yields Φ (Table).

Table. The SBR and PSBR S_1 state fluorescence parameters in different solvents.

Compound	SBR				PSBR			
Solvent	τ_f, ps	$\Phi x10^4$	τ_f^0, ns	τ_a^0, ns	τ_f, ps	$\Phi x10^4$	τ_f^0, ns	τ_a^0, ns
hexane	38	0.85	450	1.25	19	1.8	105	2.5
hexadecane	37				19			
paraffin oil	34				15			
toluene	50	1.0	500	1.2	17	4.7	36	2.4
acetonitrile	36				17	6.5	26	2.5
methanol	36	1.5	240					
ethanol	60	2.4	250	1.2	16	3.5	45	2.4
propanol	80	3.2	250					

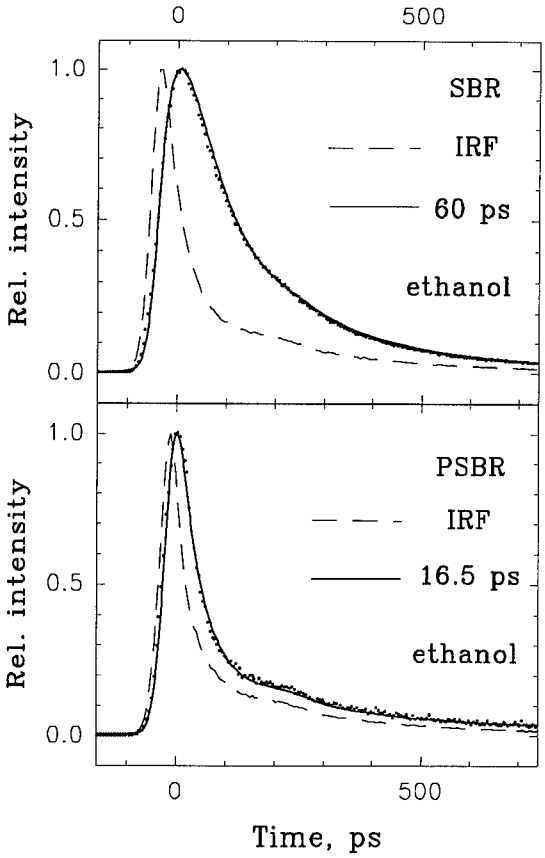


Figure 1

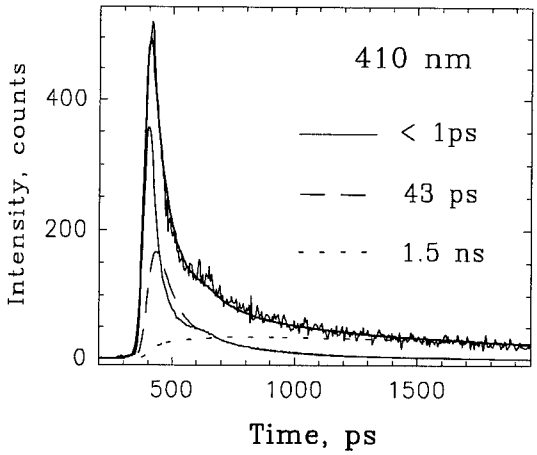


Figure 2

Both SBR and PSBR showed a bathochromic shift of the fluorescence maxima with solvent polarity. This dependence was stronger for SBR than for PSBR. The dependence of the SBR absorption position on polarity was almost absent, and the PSBR absorption maxima shifted to higher frequency with solvent polarity.

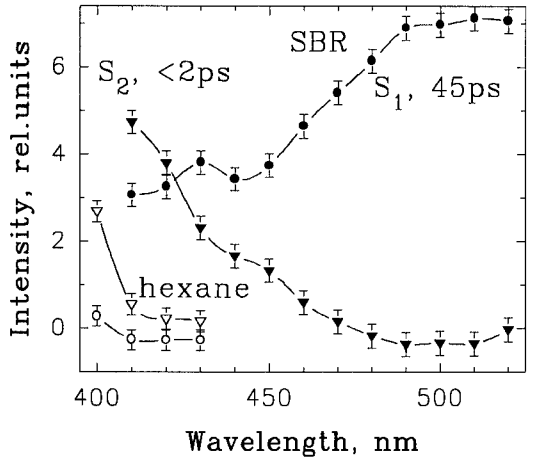


Figure 3

DISCUSSION.

As seen in the Table the radiative lifetime τ_a^0 are much shorter than τ_f^0. This difference obviously shows that for both SBR and PSBR a three-level model should be used. The absorption is the allowed $S_0 \rightarrow S_2$ transition and the fluorescence is due to the forbidden $S_1 \rightarrow S_0$ transition as has been observed for other polyenes [1].

This model helps to explain the kinetics of Fig.2. The short-wavelength ultrafast emission is due to the allowed $S_2 \rightarrow S_0$ transition. With global reconvolution of the SBR kinetic series at different wavelengths we were able to plot both the S_2 and S_1 state emission spectra (Fig.3). We could not measure the total spectrum of the $S_2 \rightarrow S_0$ fluorescence. However, we have estimated the S_2 state lifetime from the intensity of this SBR $S_2 \rightarrow S_0$ emission in hexane as 30±10 fs. We could not detect this emission in the case of PSBR, because the S_1 state emission is more intensive and faster than in the case of SBR. The lifetime of the PSBR excited state connected with the allowed absorption transition is, however, also less than 50-100 fs.

Accordingly, both SBR and PSBR have a lowest lying A_g-like excited state. Immediately after light absorption the molecules will appear in the S_2 (B_u-like) state which has a lifetime of less than 10^{-13}s. For SBR the S_1-S_0 transition is strongly forbidden (τ_f^0/τ_a^0 is about 400). It is also forbidden (τ_f^0/τ_a^0 = 10 ÷ 40) in the case of PSBR. The difference of the S_1 state emission rates for SBR and PSBR

should originate from the distortion caused by the proton and from the S_1–S_2 energy gap decrease, resulting in a stronger S_1–S_2 state mixing for PSBR. The last effect is obvious from the decrease of spectral distance between the $S_0 \rightarrow S_2$ absorption and $S_1 \rightarrow S_0$ emission spectra. Due to the large S_1–S_2 gap the SBR S_1 emission rate is less sensitive to solvent. Perhaps the S_1–S_2 gap decreases and the $S_1 \rightarrow S_0$ transition becomes more intensive in solvents with high polarizability (refractive index) and polarity (dielectric constant). The bathochromic shifts of the emission spectra in polar solvents (Table) showed that the SBR and PSBR S_1 states have rather large dipole moments.

The S_1 state lifetime was insensitive to solvent properties. Only for SBR with hydrogen bonding (in alcohol solvents) we have observed a lifetime change with solvent polarity. The SBR and PSBR have quiet fast channels of internal conversion which are not influenced by viscous or polar solvent.

It is interesting to compare our results with recent results on rhodopsin and bacteriorhodopsin [2-4]. It is known that the nuclear configuration of polyene molecules in the S_1 (A_g) state differs from the configurations in the S_0 and S_2 states, which are quite similar [5]. Moreover, the symmetrical 1,6-diphenylhexatriene (DPH) molecule, for instance, has a distorted structure in S_1 state with a dipole moment [6]. This indicates that the polyene S_1 state provides a more flexible nuclear structure and, consequently, a higher probability for isomerization. Normal long-chain polyenes like DPH, however, are not able to change the chain conformation enough for complete isomerization to occur. Only the PSBR undergoes an efficient trans-cis and cis-trans photoisomerization. This might be induced by the proton influence. Specific interactions in the protein can also increase the isomerization rates and thus decrease the S_1 state lifetime compared to PSBR in solvent. The first excited state in this model should thus be the B_u-like S_2 state with a lifetime of less that 100 fs. The subpicosecond nuclear relaxation in the S_1 state following the S_2-S_1 conversion is related to chain twisting, and the first stage of the isomerization in pigment-protein systems can take place in the A_g-like excited state of PSBR. The corresponding time can be about 400 fs [2] or 200 fs for rhodopsin [3] and about 500 fs for bacteriorhodopsin [4]. The S_1 state must no have an allowed emission. The PSBR molecule on the "bottom" of the S_1 state (which has possibly more than one potential surface minimum) can have a distorted chain conformation which is intermediate between the "trans" and "cis" isomers with a several picoseconds lifetime.

CONCLUSION.

We have carried out the first spectral and systematic kinetical investigation of the SBR and PSBR fluorescence at room temperature. It was shown that:

- both SBR and PSBR have the A_g-like S_1 excited states;
- the lifetime of the S_2 state which appears after light absorption is 30±10 fs for SBR in hexane solution and faster than 10^{-13}s for both SBR and PSBR;
- the S_1 state lifetime is about 38±5 ps for SBR and 18±3 ps for PSBR, and it is rather insensitive to solvent properties;
- not only the S_2 (B_u) state of SBR and PSBR, but also the S_1 state has a large dipole moment with the same direction and both states can be stabilized by specific electric fields in the protein.

References.

1. B.S.Hudson and B.E.Kohler, J.Chem.Phys., 59 (1973), 4984
2. T.Kabayashi, M.Taiji, K.Bryl, M.Nakagawa and M.Tsuda, Springer Ser.in Chem.Phys. 55 (1993) Ultrafast Phenomena VIII, 562.
3. R.W.Schoenlein, L.A.Peteanu, Q.W.Wang, R.A.Mathies and C.V.Shank, Springer Ser.in Chem.Phys. 55 (1993) Ultrafast Phenomena VIII, 53.
4.J.Dobler, W.Zinth, W.Kaiser and D.Oesterhelt, Chem.Phys.Lett., 144 (1988), 215.
5. B.E.Kohler, Synthetic metals, 41 (1991), 1215.
6. S.L. Bondarev and S.M. Bachilo, J.Photochem.Photobiol,A:Chem., 59 (1991), 27

Phase sensitive characterization of short scale-length plasmas.

J-P. Geindre, P. Audebert, F. Falliès, A. Rousse, J. C. Gauthier
LULI, école polytechnique, Palaiseau 91120 France

and

A. Antonetti, J. P. Chambaret, G. Grillon, A. Mysyrowicz
LOA, ENSTA, école polytechnique, Palaiseau 91120 France

By irradiation of solid targets with intense femtosecond pulses it is possible to create microplasmas of very small gradient scale length $l/\lambda<0.1$. Useful information on the early evolution of these plasmas on a picosecond or even subpicosecond time scale can be obtained via optical detection. For instance, subpicosecond time-resolved Schlieren measurements can determine the location of the critical density layer of the plasma.[1] However diffraction effects limit the accuracy to a value of the order of the incident wavelength. A method to detect plasma velocities relies on the spectral analysis of the reflected probe beam at different delays.[2] Expansion velocities can be inferred from Doppler shifts. However, the large Fourier spectrum $\Delta\omega\approx1/\Delta t$ of short pulses makes it difficult to estimate frequency shifts much less than $\Delta\omega$. Furthermore, this method is sensitive to the detrimental shot-to-shot frequency and spatial fluctuations of the lasers.

We have implemented a method to determine the plasma front and expansion velocity with greatly improved sensitivity. In the experiments, the moving plasma target is probed with two successive identical femtosecond probe pulses separated in time by an external Michelson interferometer. It is well known that the power spectrum of a double pulse sequence is modulated with a fringe period inversely proportional to the pulse separation. Any phase shift due the motion of the plasma critical layer occuring between the two pulses can be therefore detected directly in the reflected spectrum as a fringe displacement. The improvement of this method over single pulse spectrum analysis is manifold. First, the sharpness of fringes allows high precision measurements of small frequency shifts. Secondly, the inherent multiplexing of the information in all observed fringes for each laser shot further improves the signal to noise ratio. Finally, the method is largely insensitive to shot-to-shot frequency fluctuations. Indeed, besides phase shifts due to the signal, only phase fluctuations occuring inside the external interferometer during the time interval between both probe pulses affect the fringe position.

We have tested our method in two different regimes. In the first regime, the plasma-inducing strong pump pulse lies between both probe pulses. This type regime is well adapted to the absolute measurement of the location of the reflective plasma layer at a given delay. In the second regime the pump pulse precedes both probe pulses. This regime yields with high accuracy the relative location of the critical layer at two different times and is therefore well suited for the precise measurement of the plasma axial expansion velocity. An example of the first regime, obtained in a hot dense laser-induced plasma formed in SiO_2 is shown in figure 1. A fringe displacement to an accuracy of 0.016 rd (rms) is readily detected which corresponds to an accuracy Δx=0.78 nm in the location of the critical density surface of the plasma. An further improvement by one order of magnitude should be possible by implementation of better image recording and analysis techniques. The spatially-resolved expansion velocity of the laser-induced plasma in the same target was obtained by the described method set to the second regime. For instance we find a maximum radial expansion speed of 8.10^6 cm/s 4 ps after irradiation of the target with a pump beam of peak intensity $I \approx 10^{16}$ W/cm^2.

Our method is quite general and can be applied to other situations involving weak but fast phase shifts, such as in the characterization of laser-induced plasma waves in low density gases, or the study of conformational changes in solids occuring on a subpicosecond timescale.

references:
1) R. Benattar, J-P. Geindre, P. Audebert, J-C. Gauthier, A.Mysyrowicz, J-P.Chambaret, A.Antonetti Optics Comm. 88, 376 (1992)
2) Wm. M. Wood, C. W. Siders, M. C. Downer P. R. L. 67, 3523 (1991)

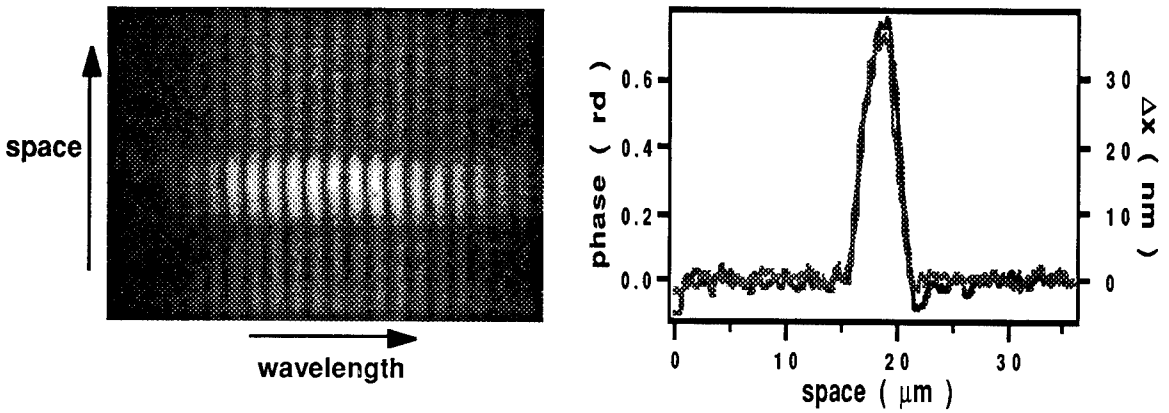


Figure 1) left : Spectrum of the double probe pulse sequence reflected from a SiO_2 target illuminated by an intense pump pulse. The pump pulse characteristics are: λ= 620 nm, pulse duration: 100 fs peak intensity on target $\approx 10^{15}$ W/cm^2. The two probe pulses have a duration of 100 fs and a wavelength at λ =560 nm. Interval between probe pulses is 500 fs . The pump pulse illuminates the target 200 fs after the first probe pulse. The induced phase shift is visible in the bright portion of the interference pattern (which corresponds to the highly reflecting plasma region of the target)

right: Measured phase shift and corresponding displacement of the critical density layer of the plasma as a function of position along the focal spot on target. The two curves are obtained from two different laser shots under same conditions. Each curve is recorded from a single pulse sequence.

Wave packet interference in the free induction decay from molecules

John N. Sweetser, Thomas J. Dunn and Ian A. Walmsley

The Institute of Optics, University of Rochester, Rochester, NY 14627

It is well known that the application of a pulse to a molecular electronic transition leaves the molecules vibrational modes in different electronic states in well-localized states, or wave packets[1]. One method of detecting the wave packets is via the time-dependent spectra of spontaneous emission from the excited molecule[2]. The emission consists in general of two parts, an incoherent part that depends only on the wave packet in the excited state, and a coherent part, that depends on the wave packets in both excited and ground electronic states (of a two-state molecule). This can be seen from the following simple calculation. The time-dependent spectrum of radiation from a collection of N molecules is related to the two-time dipole correlation functions[3]:

$$\left\langle \hat{E}^{(+)}(t)\hat{E}^{(-)}(t')\right\rangle = \sum_{i=1}^{N}\sum_{j=1}^{N}\left\langle \hat{d}_i^{\dagger}(t)\hat{d}_j(t')\right\rangle$$

$$= \sum_{i\neq j}\left\langle \hat{d}_i^{\dagger}(t)\right\rangle\left\langle \hat{d}_i(t')\right\rangle + \sum_{i=j}\left\langle \hat{d}_i^{\dagger}(t)\hat{d}_i(t')\right\rangle. \qquad (1)$$

The second term in equation (1) is the incoherent or spontaneous term, whereas the first is the coherent term. Coherent emission is clearly only possible when more than one molecule is excited. It arises because of a dipole moment that remains in the molecule after an excitation which leaves the molecule with incomplete inversion. The fields radiated by the polarizations of adjacent molecules may add in phase to generate a macrosopic field in the direction of the exciting pulse. The ratio of the energies in the coherent and incoherent components is proportional to the number of molecules excited. If there is complete inversion, however, there will be no coherent component initially.

In terms of the state vectors of the wave packets in the ground state ($\left|\Psi_g(t)\right\rangle$) and excited state ($\left|\Psi_e(t)\right\rangle$), the detected signal from the coherent emission takes the form:

$$\left\langle \hat{E}^{(+)}(t)\hat{E}^{(-)}(t')\right\rangle_{Coh} \propto \left\langle \Psi_e(t)\middle|\Psi_g(t)\right\rangle\left\langle \Psi_g(t')\middle|\Psi_e(t')\right\rangle, \qquad (2)$$

whereas the signal from the incoherent emission has the form:

$$\left\langle \hat{E}^{(+)}(t)\hat{E}^{(-)}(t')\right\rangle_{Inc} \propto \left\langle \Psi_e(t)\middle|\hat{W}(t-t')\middle|\Psi_e(t)\right\rangle. \qquad (3)$$

The window operator $\hat{W}(t-t')$ depends on the details of the molecular vibrational potentials.

In contrast to the incoherent emission, it is clear that the coherent signal will reflect the modulations arising from the interference of the ground and excited state wave packets, and will thus show modulations that are similar to the pump-probe measurements that are more commonly used in this experimental arena. The particular wave packet correlation function on which the coherent emission depends is slightly different from that found in the case of absorption, however. Note that if the ground state wave packet is time-stationary then the coherent emission will have the same temporal shape as that of the incoherent emission *provided* the spectrometer is tuned to a wavelength that matches a parametric transition. On the other hand, if the excited state wave packet is time-

stationary, then any signal modulation will be due solely to the motion of the ground state wave packet. It is this feature that leads to significant temporal modulation of the coherent emission even during periods when the excited state wave packet has "decayed" or become diffuse, due to Hamiltonian evolution on the anharmonic potential surface of the excited state.

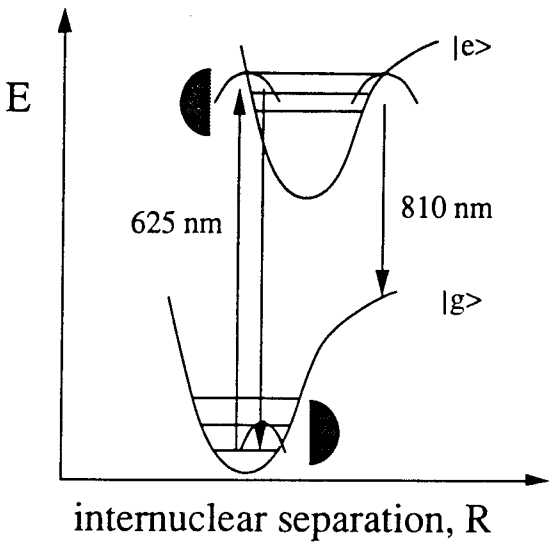


Fig. 1 Potential Energy diagram for diatomic molecule showing excited, |e>, and displaced ground, |g>, state wave packets. Shaded area denotes pulse bandwidth overlapping several vibrational levels.

The most important mechanisms for distributing population coherently among the vibrational levels of the ground electronic state is intrapulse Raman scattering, as shown in figure (1). If the exciting pulse is tuned close to an electronic resonance, and has sufficient bandwidth to overlap several of the ground state vibrational levels, then this mechanism can be quite efficient.

We have made measurements of the time-dependent spectrum of coherent emission from Na_2 when excited by a 50fs duration pulse of mean wavelength 625nm. The emitted radiation is upconverted by a short gate pulse to yield a temporal resolution of 70fs. The coherent emission is about 10^4 times as intense as the incoherent fluorescence, and is highly directional. Furthermore, it is polarized parallel to the exciting pulse field. Figs (2a) and (2b) show typical experimentally measured time signals for two different settings of the spectrometer. There are two interesting features of the temporal structure. First, the characteristic 310fs period of the wave packet in the excited ($A^1\Sigma_u^+$) state is absent, in complete contrast to the incoherent emission. Second, the radiation builds up slowly after a relatively long "dead time"shortly after excitation. Both of these phenomena may be explained if one considers the creation of ground state vibrational and rotational wave packets via intrapulse Raman scattering. In our experiments the exciting pulse can act as both pump and Stokes frequencies for the Raman process that generates a wave packet in the ground electronic state. The subsequent evolutiuon of the molecular dipole then reflects the dynamics of both wave packets. A theoretical calulation based on this idea is shown in Figs (2c) and (2d), and matches reasonably well the experimental result. The predominant 660fs temporal modulation at 625nm spectrometer tuning is approximately the commensurate period of the ground state vibrational period($X^1\Sigma_g^+$; 210fs) and the excited state ($A^1\Sigma_u^+$; 310fs). The slow modulation of the envelope of the temporal emission peaks is due both to the different vibrational frequencies in the excited and ground states and also to the anharmonicity of each of the corresponding vibrational potentials. The larger anharmonicity of the excited state potnetial causes the wave packet in that state to become spatially diffuse after roughly 40 vibrational periods - near τ=15ps. The coherent emission exhibits neither a decrease in peak intensity nor an increase in the duration of the individual peaks. This is becasue it reflects essentially the correlation function of the ground and excited state wave packets, and the ground state wave packet remains well-localized even for these long times after excitation.

The fast decay of the initial quantum beats arises, we believe, from the interference between the rotational wave packets that are formed within the two electronic states. From a full quantum mechanical model[4], we expect the turn-off time to be on the order of 1ps in Na_2. Following this fast decay there is a period of relatively little radiation. The coherent emission "turns on" agan suddenly after a delay of about 4ps. Qualitatively this phenomenon may also be explained via rotational wave packets. Since the molecules are initially at thermal equilibrium at a temperature of 750°K , their mean rotational quantum number is near j=40. In sodium this corresponds to a mean rotational period of 4ps, in rough agreement with our experimental result. This idea is further strengthened by similar

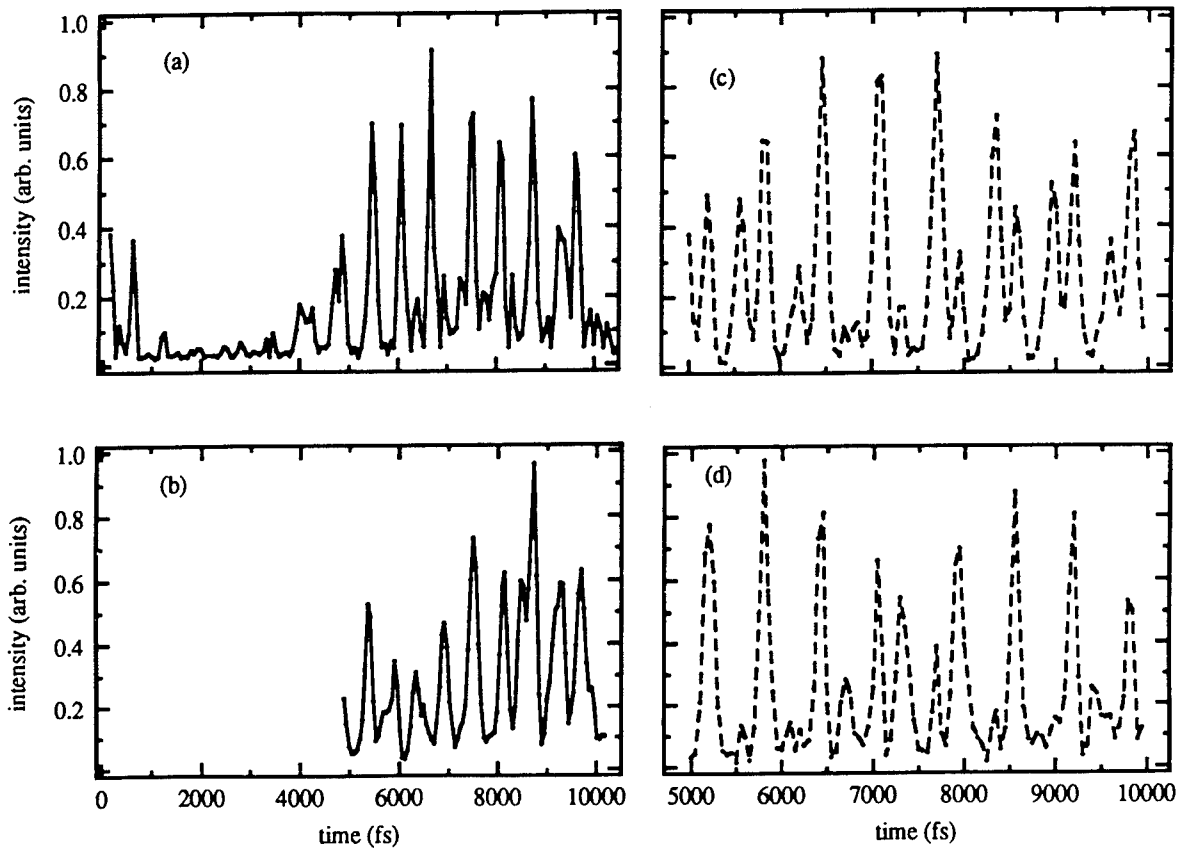


Fig 2. Experimental (a) and (b) and theoretical (c) and (d) plots of the coherent emission from a sodium molecule with wave packets in both the A and X states. The complicated temporal structure is in stark contrast to that exhibited by the incoherent emission, as illustrated in Fig 2 of Ref.[5].

measurements in I_2 at 300°K, where we find a turn-on time of about 18ps, or some 4 times longer than in sodium. The ratio of the moment of inertia in I_2 and Na_2 is also about 4. Quantitatively, however, we have found it difficult to match the experimental results . A full quantum-mechanical calculation of the rotational turn-on shows that the contrast between the period of suppression and revival of thecoherent emission is much smaller than observed experimentally, and furthermore the turn-on time is much shorter than measured.

In conclusion, we note that the fluorescence from an excited molecule reveals the effects of wave packet dynamics in different electronic states , through the coherent emission, and the wave packet dynamics in a single excited electronic state , through the incoherent emission. Thus the coherent emission is a sensitive probe of the quantum interference between vibrational wave packets in different electronic states - a feature that is not normally associated with fluorescent emission

References

[1] See, for example, A.H. Zewail, Science, 242, 1645 (1988), and innumerable works since then.
[2] P. Kowalczyk, C. Radzewicz, J. Mostowski and I. A. Walmsley, Phys. Rev. A, 42, 5622 (1990)
[3] C. Cohen-Tannoudji, G. Dupont-Roc and G. Grynberg, in *Atom-Photon Interactions* (Wiley, New York, 1992)
[4] A. Myers and R. Hochstrasser, J. Chem. Phys. 85, 6301 (1986); P. M. Felker and A. H. Zewail, J. Chem. Phys. 86, 2461 (1987).
[5] T. J. Dunn, J. N. Sweetser, I. A. Walmsley and C. Radzewicz, Phys. Rev. Lett. 70, 3388 (1993).

Ultrafast Electronic Processes in Porous Silicon

P.M. Fauchet,[1] Y. Kostoulas,[2] Ju.V. Vandyshev,[1]
L. Tsybeskov,[1] K.B. Ucer[1]
Laboratory for Laser Energetics, University of Rochester
Rochester NY 14623, USA; T: (716) 275-1487

L. Waxer, I.A. Walmsley
The Institute of Optics, University of Rochester
Rochester NY 14627, USA; T: (716) 275-0312

V. Petrova-Koch
Physics Department E16, Technical University of Munich
D-8046 Garching, Germany; T: (49) 89-32092342

The discovery in 1990 [1] that porous silicon is a strong light emitter in the visible at room temperature has changed our assessment of the usefulness of silicon as an optoelectronic material and raises the possibility of practical silicon light emitters [2]. The luminescence from light emitting porous silicon (LEPSi) usually occurs in the deep red to orange region with a quantum efficiency of a few percents at 300 K and >10% at low temperature. The luminescence decays with a lifetime that ranges from ~1-10 μsec at 300 K to >1 msec at low temperature. More than 15 different models have been proposed to explain the strong luminescence from LEPSi [3] but only two models have received strong experimental support. In the first model, light emission results from the recombination of a free electron-hole pair or exciton across the bandgap of silicon nanoparticles [1,4]. The emission is in the visible because the effective bandgap is increased by quantum confinement and the quantum efficiency is high because the bandgap of these silicon nanoparticles has become quasi-direct and because nonradiative recombination is suppressed thanks to the good passivation of the nanoparticle surface. In the second model, light emission results from radiative recombination involving carriers trapped in states localized on the nanoparticle surface [5]. These surface states are in the forbidden gap of the silicon nanocrystallites which is increased by quantumconfinement. The long lifetime of the luminescence is explained by the small overlap between the wavefunctions of carriers localized at physically separated states. To date, no experiment has been able to decide which model is correct.

(1) also with the Department of Electrical Engineering, Univ. of Rochester
(2) also with the Department of Physics & Astronomy, Univ. of Rochester

In this paper, we present the first results of femtosecond time-resolved spectroscopy of porous silicon. The experiments are pump and probe transmission measurements using tunable pulses performed on thin free-standing porous silicon films. We find that there is a strong, short-lived induced absorption signal which can be shorter than our pulse duration of ~100 fsec and is followed by a gradual recovery with a time constant greater than 10 psec. We interpret these results as evidence for trapping of free carriers into surface states.

The samples are free standing mesoporous silicon films oxidized at high temperature for periods of time ranging from several minutes to >100 hours. The typical cw luminescence spectrum peaks around 1.6-1.7 eV, a photon energy at which the films are transparent. The onset of absorption is near 1.75 eV and at 2 eV, the transmission of the film is ~50%. Fig. 1 shows typical transmission and cw luminescence data. The experiments are room-temperature pump-probe transmission spectroscopy measurements using different femtosecond laser systems. In the discussion below, we focus on results obtained with a 2-eV pump and a probe tunable from 2.2 eV to 1.4 eV.

As shown in Fig. 2, we observe induced absorption at all wavelengths, when the probe is tuned below and above the luminescence peak. This behavior is typical of free carrier absorption in an indirect gap material. The recovery of the induced absorption depends on the pump intensity. At low pump power, we observe a fast, pulsewidth-limited partial recovery which is then followed by a much slower transient with a time constant of ~40 psec. As the pump power is increased, the fast transient becomes slower and approaches 1 psec, whereas the slower transient becomes shorter. Fig. 3 illustrates these findings and demonstrates that the recovery law cannot be described by a simple exponential or a combination of exponentials. We attribute the initial recovery to trapping of the photoexcited carriers from extended states into surface states and the slower recovery to a combination of thermalization within the distribution of surface states and recombination, either with photon emission (luminescence) or without photon emission (Auger processes). The intensity dependence of the fast transient is consistent with trap saturation. These assignments can be checked by comparing the time evolutions of induced absorption and time-resolved photoluminescence measurements. We will report the results of femtosecond time resolved photoluminescence upconversion experiments which are in progress.

This work was supported in part by grants from Rochester Gas & Electric, the New York State Energy Research and Development Authority, and Xerox.

REFERENCES

[1] L.T. Canham, Appl. Phys. Lett. **57**, 1046 (1990)
[2] P.M. Fauchet et al, "Prospects for light-emitting diodes made of porous silicon from the blue to beyond 1.5 μm", to appear in *Advanced Photonics Materials for Information Technology*, S. Etemad editor [SPIE Proc. vol 2144, (1994)]
[3] *Microcrystalline Semiconductors: Materials Science and Devices*, edited by P.M. Fauchet et al, Mat. Res. Soc. Symp. Proc. **283** (MRS, Pittsburgh, 1993)
[4] P.D.J. Calcott et al, J. Luminesc. **57**, 257 (1993)
[5] F. Koch et al, in Ref. 3, p 197; J. Luminesc. **57**, 271 (1993)

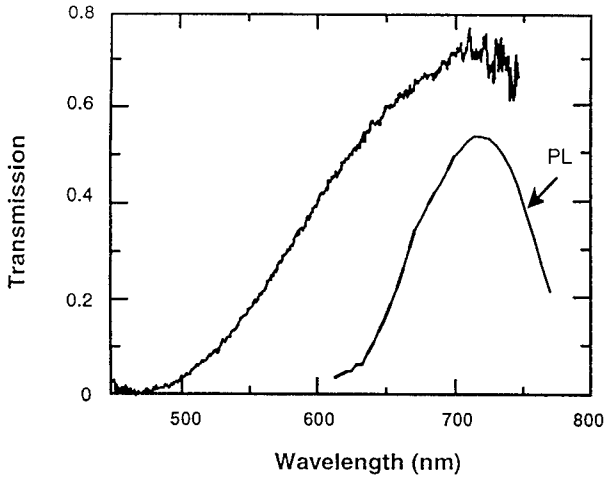


Figure 1:
Transmission and photoluminescence spectra of a free standing oxidized mesoporous silicon film measured at room temperature. The onset of weak absorption is near the PL peak.

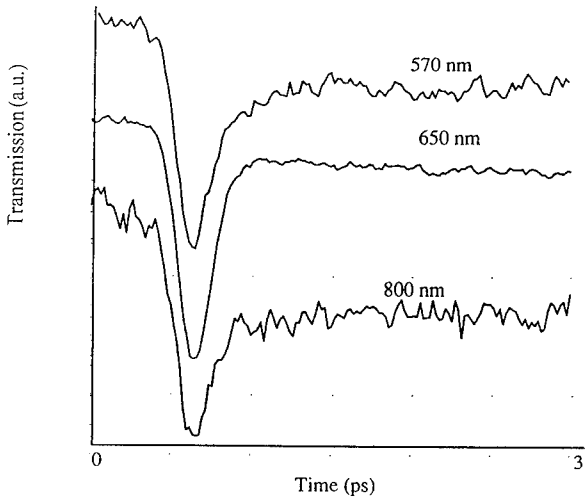
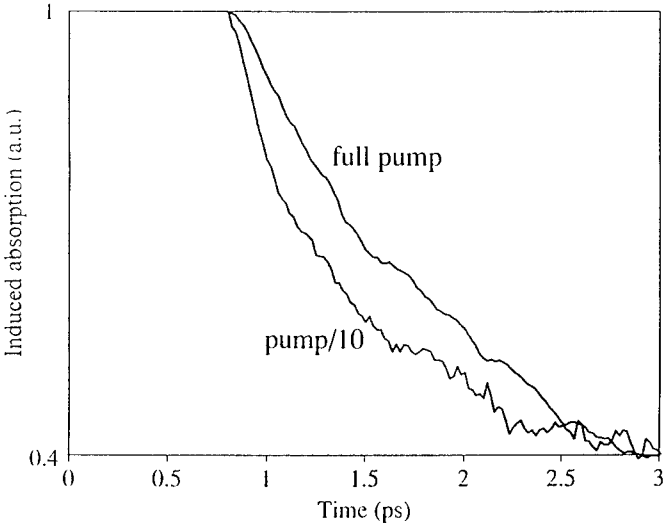


Figure 2:
Femtosecond induced absorption measured at different probe wavelengths for excitation with low-intensity 2-eV pump pulses. The curves are qualitatively similar.



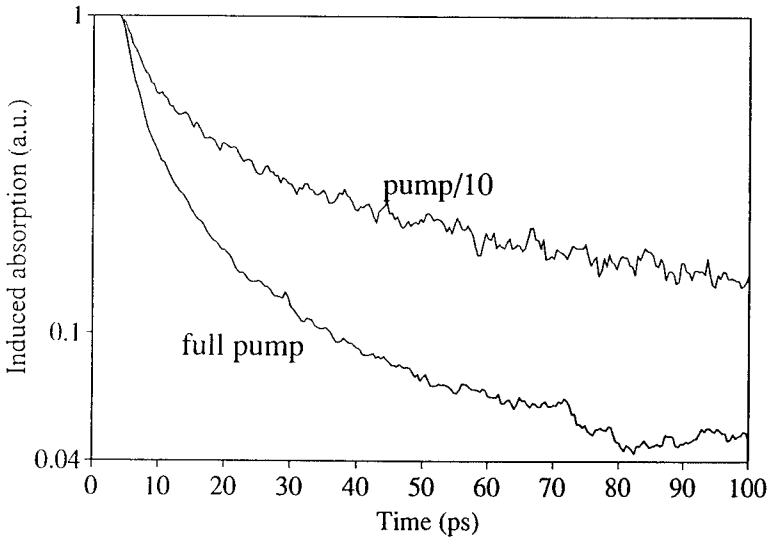


Figure 3:
Recovery of the induced absorption at intermediate pump intensity and high pump intensity. The initial recovery is faster at lower pump intensity while on a longer time scale, the recovery is faster at higher pump intensity. Note that the data are plotted on a semi-logarithmic scale.

Picosecond Laser Induced Electric Field Modulation of Carotenoid Absorption Bands

David Gosztola, Hiroko Yamada, and Michael R. Wasielewski
Chemistry Division
Argonne National Laboratory
Argonne, Illinois 60439
(708)252-6963

Observation of band shifts in the absorption spectra of *in vivo* carotenoids has been attributed to electric field effects generated by membrane potentials. This electrochromism is related to what is known as the Stark effect, a term which is used to describe the effect of an applied electric field on many physical processes. Previous *in vitro* studies of how electric fields effect the absorption spectra of molecules all have relied on applying the perturbing electric field by using external electrodes around a dielectric spacer containing the molecule to be studied. The maximum applied field in these examples has been between 0.5 MV/cm and 3 MV/cm. These electric field intensities are of the same magnitude as those thought to be present across the membranes studied in the *in vivo* experiments.

Here we present a new and unique way of forming an intense electric field near a molecule in order to induce electrochromism. We have done this by creating an electron-hole pair within close proximity to, but electronically isolated from, a polarizable molecule. The molecular system that we have utilized is shown in Figure 1. It consists of a zinc porphyrin - pyromellitic diimide light induced charge transfer complex held rigidly proximate to a β-carotene using a calix[4]arene linkage. The formation of the charge separated state of the porphyrin-diimide results in a dipole formed by the 8.4 Å separation of the electron-hole pair. The electric field from this dipole was found to induce electrochromism in the carotene.

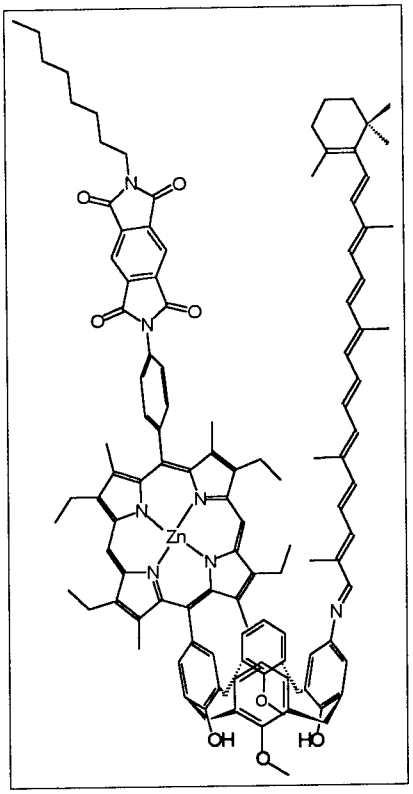


Figure 1. Molecule used to study electrochromism.

In order to detect the electrochromism we have synthesized three calix[4]arene based molecules. The complete molecule as shown in figure 1 as well as control molecules, one containing just the calix[4]arene and porphyrin-diimide and one containing just the calix[4]arene and carotene.

The lifetime of the charge separated state was found to be 3.7 ns in toluene. Transient absorption spectra of all of the molecules were recorded 150 ps after the formation of the charge separated state by a 200 fs pump pulse at 420 nm. To detect any change in the ground state absorption

spectrum of the carotene due to the presence of the electric field, a difference spectrum was calculated using transient spectra of the full molecule and the molecule containing only the porphyrin-diimide side chain. Absorption bands that were found to occur only in the charge transfer state of the porphyrin-diimide and which were well removed from the ground state absorption bands of the carotenoid were used to insure that the difference spectra did not contain artifacts due to differences in pump absorption between samples.

In order to change the electric field strength at the carotene, the dielectric constant of the solvent was changed over an order of magnitude by using mixtures of toluene and benzonitrile. Figure 2 shows the difference spectra between the full molecule and the porphyrin-diimide only molecule in toluene, 5% benzonitrile, 10% benzonitrile, and in neat benzonitrile. The Stark shift of the carotenoid absorption band resulted in a derivative shaped difference spectrum. Only part of the negative going ΔA band (below 450 nm) can be seen in figure 2 whereas the positive going lobe is clearly seen in the neat toluene through 20% benzonitrile spectra. As the dielectric constant of the solvent mixture increased the electrochromic shift decreased until it was virtually nonexistent in neat benzonitrile.

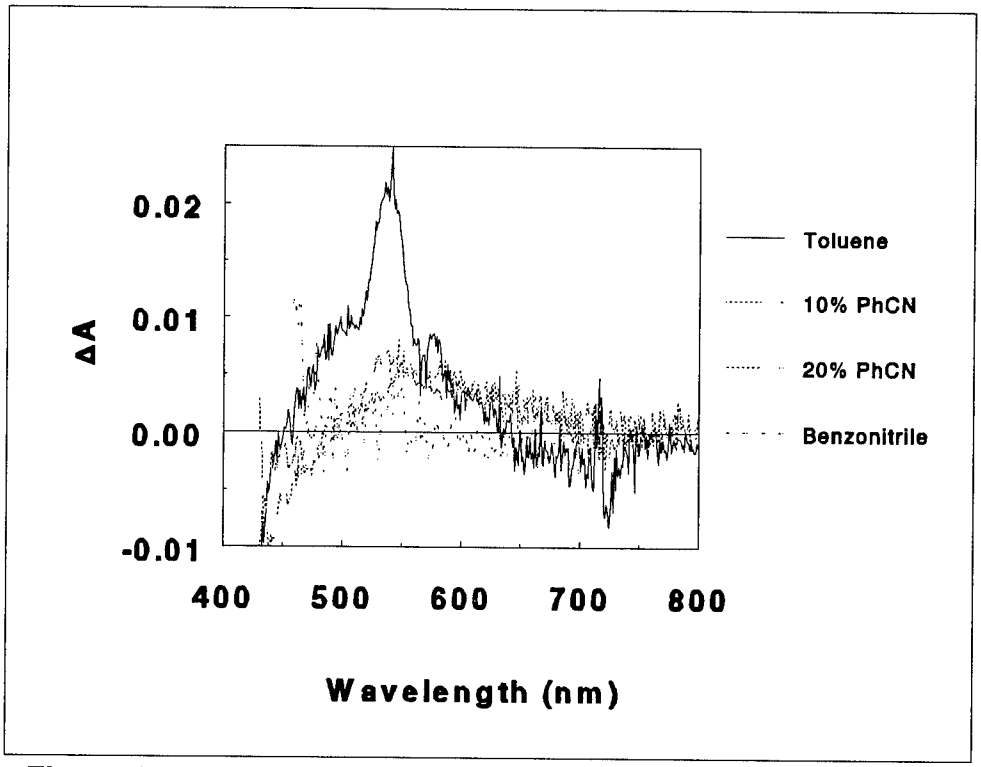


Figure 2: Absorption changes due to laser induced electric field.

This work was supported by the Division of Advanced Energy Projects, Office of Basic Energy Sciences of the United States Department of Energy under contract W-31-109-Eng-38.

Soliton compression in a Nonlinear Amplifying Loop Mirror

S. Gray, W. H. Loh, A. B. Grudinin,
V. V. Afanasjev* and D. N. Payne
Optoelectronics Research Centre, Southampton University
Southampton SO9 5NH, UK
* General Physics Institute. Russian Academy of Sciences
38 Vavilov Str. Moscow 117942, Russia

In many applications it is required to compress a soliton with as low a fraction of non-soliton component as possible. Proposed several years ago, the Nonlinear Amplifying Loop Mirror (NALM) [1] possesses both amplification and pulse shaping functions [2-4] and can be very attractive for soliton compression. In this paper we study soliton compression in a NALM and demonstrate the principle of operation of an all-fibre tunable source of femtosecond pulses.

As a source of solitons, we used a passive harmonic mode-locked fibre soliton laser based on Yb^{3+}/Er^{3+} codoped fibre which produced pulses with $\tau = 2.5$ps FWHM at a repetition rate of 50 MHz [5]. The laser output was connected to the NALM through an isolator to prevent feedback into the laser cavity. The NALM was formed between the output ports of a 50/50 coupler and comprised a 3 m long Yb^{3+}/Er^{3+} codoped fibre amplifier and a standard telecom fibre with group velocity dispersion of $D = 17\text{ps/nm} \cdot \text{km}$ and a length of 50m.

Compression ratio and switching efficiency of the NALM

To characterise the NALM transmission in the soliton regime we studied spectral and temporal characteristics of the output pulses and the switching efficiency for different gain levels. The switching efficiency is taken to be P_{out}/GP_{in} where P_{in} and P_{out} are the powers at the NALM input and output and G is the gain of the amplifier. Fig.1 shows the dependences of the compression ratio K and switching efficiency on gain.

Fig.1

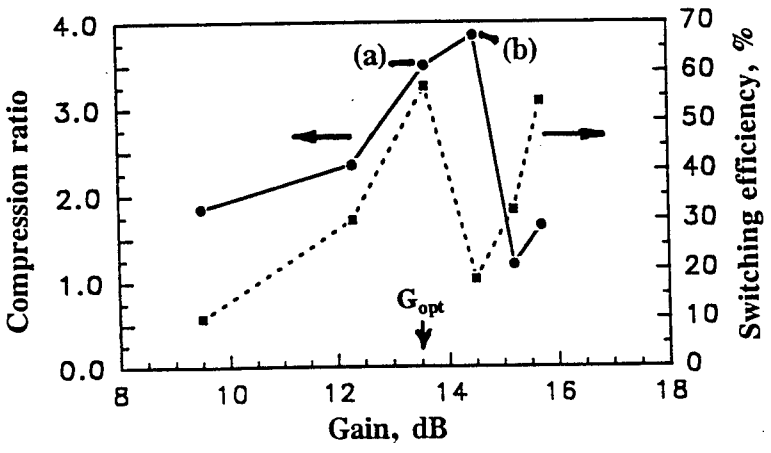


Fig.2(a) demonstrates the autocorrelation and spectrum of the transmitted pulse at a gain of 13.5 dB (point (a) in Fig.1) at which maximum swithing efficiency occurs. Fig.2(b) gives results at a gain of 15 dB (point (b) on Fig.1) where maximum compression ratio K is found.

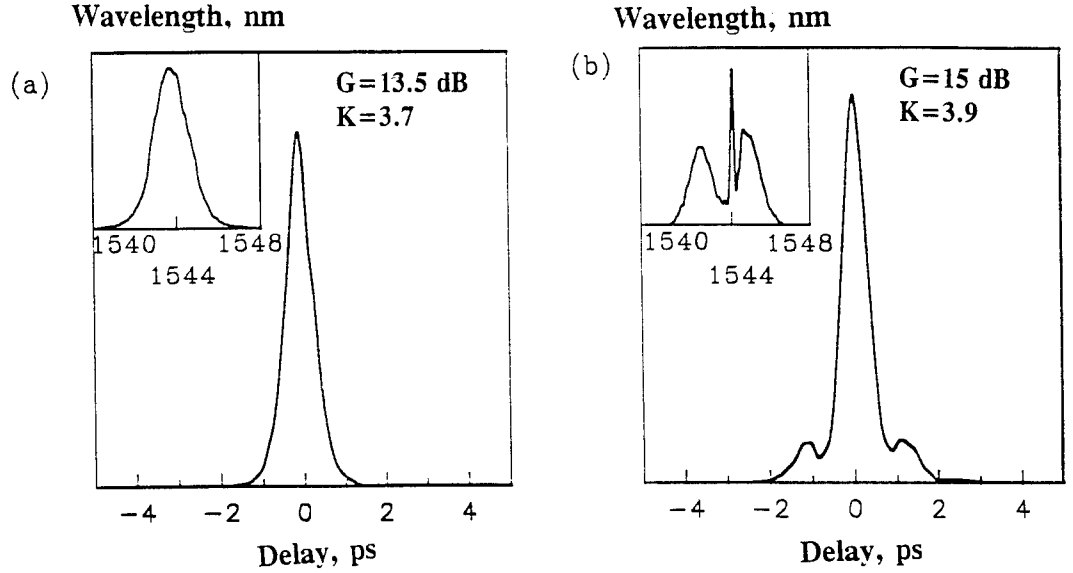


Fig.2

From the results of Fig.1 and 2 one can conclude that there is an optimal gain G_{opt}, corresponding to the maximum switching efficiency, where a clean compressed output pulse occurs. For gain exceeding G_{opt} at the NALM output we observed autocorrelations and spectra corresponding to multisoliton pulses (see Fig.2b). Note also that for $G < G_{opt}$ the time-bandwidth product of the output pulses was close to 0.31, while pulsewidths varied by over a factor of two (Fig.1).

Tunable all-fibre source of femtosecond pulses

The gain dependence of the pulsewidth gives rise to the possibility of developing a convenient tunable source of femtosecond pulses exploiting the effect of the soliton self-frequency shift. It is known that owing to Raman gain the soliton central wavelength λ_0 experiences a Stokes frequency shift, $d\lambda_0/dz(\mathrm{nm/m}) \simeq 2.3 \cdot 10^{-5} D/\tau^{-4}$ where τ is in picoseconds and D in ps/nm · km [6]. Thus using an auxiliary fibre at the NALM output one can translate the pulsewidth variation into a controllable wavelength shift.

To demonstrate such a source we decreased the pulsewidth of the fibre laser output to 1.3 ps by shortening the laser cavity length. The length of the undoped fibre in the NALM was also reduced to 3m. In this configuration by changing the NALM gain in the range of 13.5-15 dB we observed reduction of the pulsewidth from 660 fs to 250 fs, while

the time-bandwidth product change was from 0.32 to 0.28. For 250 fs solitons travelling in a lossless fibre with a dispersion of D=17 ps/nm ·km the soliton self-frequency shift is expected to be $\delta\lambda$ = 10nm/100m. Fig.3(a and b) shows the spectra of the pulses after 300 m of the auxiliary fibre and for NALM gains of 14.5 and 15 dB respectively. It can be seen that for small gain change the pulse central wavelength moves from original wavelength of 1544 nm to 1549 nm for 14.5 dB gain and to 1574 nm for 15 dB gain, giving tuning range of 30 nm.

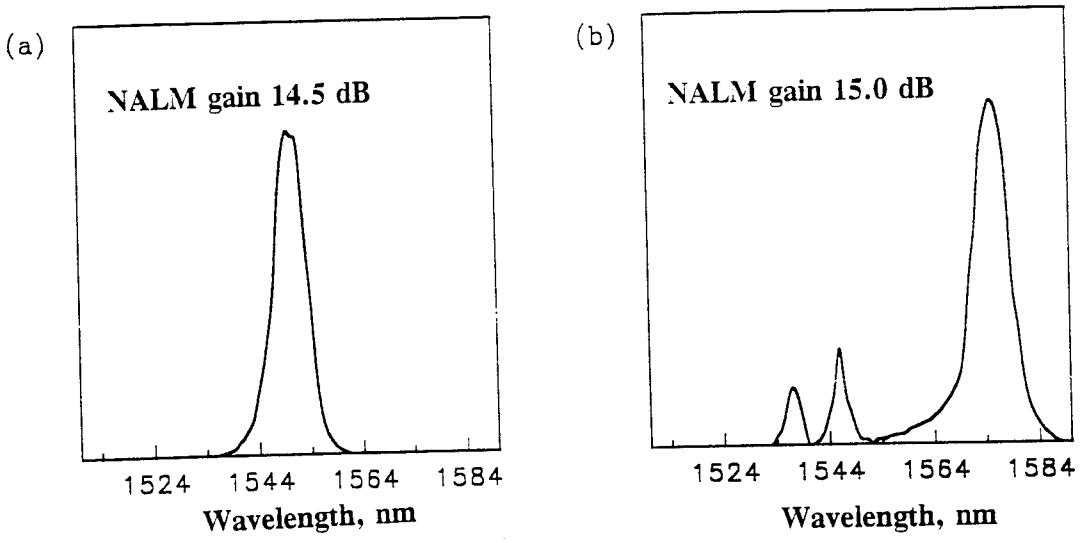


Fig.3

In conclusion, we have experimentally studied soliton propagation through a NALM and demonstrated the ability of the NALM to compress solitons with only an accompanying fraction of non-soliton component of about 10% and a switching efficiency of 60%. In this regime of NALM operation the pulsewidth dependence on gain allows the developmentof an all-fibre tunable source of femtosecond pulses and the principle of operation of such a source has been shown.

References

1. Fermann, M. N., Haberl, F., Hofer, M. and Hochreiter, H., Opt.Lett., 1990, **15**, pp.752-754

2. Blow, K., Doran, N. J. and Nayar, B. K., Opt.Lett., 1989, **14**, pp.754-756

3. Islam, M. N., Sunderman, E. R., Stolen, R. H., Pliebel, W., and Simpson, J. R., Opt. Lett. 1989, **14**, pp. 811 - 813

4. Smith, K., Greer, E. L., Doran, N. J., Bird, D. M. and Cameron, K. H., Opt.Lett., 1992, **17**, pp.408-410

5. Grudinin, A. B., Richardson, D. J. and Payne, D. N. Electron.Lett., 1993, **29**, pp.1860-1861

6. Gordon, J. P. Opt.Lett., 1986, **11**, pp.662-664

Dominant Effects of Two-Photon Coherence on Four Wave Mixing in GaAs Quantum Wells

Hailin Wang, Jagdeep Shah, and T.C. Damen
AT&T Bell Laboratories, Holmdel, NJ 07733
L.N. Pfeiffer
AT&T Bell Laboratories, Murray Hill, NJ 07974
908-949-5469

We present in this paper polarization dependent four-wave-mixing (FWM) measurements in homogeneously broadened GaAs quantum wells (QW). We have unambiguously demonstrated the important contribution of the two-photon coherence (TPC) between the ground and biexciton states to the nonlinear response. We show for the first time the dominant effects of the TPC on the polarization dependence of FWM. In particular, by including the TPC-induced contribution, we are able to account for the anomalous polarization dependence, a subject of considerable current interest [1].

Recent intense investigations of self-diffracted FWM of excitons in GaAs QW have revealed polarization dependence that challenges the validity of current understanding of coherent optical interactions in lower dimensional semiconductors. The observations include [1]:

(a) the signal intensity with $\mathbf{E}_1 \perp \mathbf{E}_2$ ($I_\perp$) can be much smaller than that with $\mathbf{E}_1 \| \mathbf{E}_2$ ($I_\|$),

(b) decay of $I_\perp$ as a function of the delay can be much faster than that of $I_\|$,

(c) $I_\perp$ behaves like a free polarization decay instead of a photon echo even in an inhomogeneously broadened system.

These results are very surprising since the heavy hole transition is characterized by independent $\sigma+$ and $\sigma-$ transitions. Various models have been proposed but none of them can consistently describe all three features of the polarization dependence.

Closely related to the above work, the biexcitonic contribution to coherent nonlinear responses has also attracted much attention although most of the measurements were deemed not conclusive. FWM due to the TPC has been suggested [2]. Biexcitonic quantum beats in FWM and differential absorption have also been reported, but the physical origin of these beats is still being debated [3].

Our measurements were carried out at 10 K with pulses of 400 fs duration and 4.5 meV spectral-width. The samples we used contain 15 periods of 175 Å GaAs well and 170 Å $Al_{0.3}Ga_{0.7}As$ barrier. The center frequency of the incident pulse is 2.5 meV below the hh exciton to avoid quantum beats between the heavy and light holes. Figure 1a shows self-diffracted FWM responses. It is evident that both $I_\|$ and $I_\perp$ feature significant contributions at *negative delay* ($t_2 < t_1$).

There are two different processes that can lead to a FWM signal. In the first process, two incident pulses produce in the sample a grating proportional to $\mathbf{E}_1^* \cdot \mathbf{E}_2$. Scattering of $\mathbf{E}_2$ (or the polarization induced by $\mathbf{E}_2$) from the grating generates a signal in the direction of $2\mathbf{k}_2$-$\mathbf{k}_1$. In the second process, $\mathbf{E}_2 \cdot \mathbf{E}_2$ creates a TPC proportional to $\exp(i2\mathbf{k}_2 \cdot \mathbf{r})$. Interactions of $\mathbf{E}_1^*$ (or the polarization induced by $\mathbf{E}_1^*$) with the TPC then give rise to the FWM signal. In a dilute medium, the grating-induced signal can be observed only for positive delay while the TPC-induced signal can be observed only for negative delay. However, the above requirement is relaxed in dense media such as semiconductors because of polarization scattering, complicating the interpretation of the measurement.

To distinguish the TPC-induced signal from the negative-delay signal due to polarization scattering, we show in Fig. 1b the FWM response where $\mathbf{E}_1$ and $\mathbf{E}_2$ have the same *circular* polarization. In this case the TPC does not contribute to FWM because the creation of the TPC requires both σ+ and σ- polarized fields as we will show later. Since the signal at negative delay decays much faster in the co-circular configuration than in the linearly polarized configuration, we conclude that *the negative-delay signal in both $I_{||}$ and $I_{\perp}$ results primarily from the TPC.* This signal remains nearly independent of the polarization change since creation of the TPC does not depend on the polarization direction as long as the applied field is linearly polarized.

In contrast, the grating-induced signal at large positive delay decreases by nearly a factor of 10 when we change the configuration from $\mathbf{E}_1 || \mathbf{E}_2$ to $\mathbf{E}_1 \perp \mathbf{E}_2$ as shown in Fig. 1a. As a result, $I_{\perp}$ *becomes dominated by the TPC-induced contribution.* Detailed measurements, however, show that decay rates of the grating-induced signal are the same for both the co- and cross-linear configurations in agreement with earlier measurements in high quality QW.

We further confirm the biexcitonic origin of the TPC using circularly-polarized three-pulse FWM. The solid line in Fig. 2a shows the FWM signal obtained with t_1=t_2 and all three beams σ+ polarized. The dashed line is obtained at the same condition except that $\mathbf{E}_2$ is σ- polarized. The signal at t_3>t_1 is due to the interaction of $\mathbf{E}_3^*$ with the TPC created by $\mathbf{E}_1 \cdot \mathbf{E}_2$ with $\mathbf{E}_1$ and $\mathbf{E}_2$ having opposite circular polarization. This signal *vanishes* when all three beams are co-circularly polarized as shown in Fig. 2a. The decay of this signal gives a TPC dephasing rate of 1.8 ps comparable to the exciton dephasing rate (1.9 ps) obtained from the solid curve, in contrast to the suggestion that biexciton dephasing is much faster than exciton dephasing. In addition, spectrally resolving the FWM emission gives a biexciton binding energy of 1.2 meV.

To show that the sample is homogeneously broadened, we delay t_2 by 5 ps with respect to t_1 to *eliminate* the contribution from the TPC. The resultant response shown in Fig. 2b is *symmetric*. The solid line is a fit with a single decay rate for both the positive and negative delay, showing that the sample is indeed homogeneously broadened. We emphasize that the use of *homogeneously* broadened samples is essential for obtaining results in Fig. 1a.

The origin of the drastic reduction of the grating-induced $I_{\perp}$ as well as effects of the TPC on self-diffracted FWM in inhomogeneously broadened systems can be understood by using the optical Bloch equations that include a biexciton resonance Our calculation shows that the grating-induced FWM emission at the exciton energy vanishes in the $\mathbf{E}_1 \perp \mathbf{E}_2$ configuration (the remaining emission is at the energy of the exciton to biexciton transition), leading to a decrease of the grating-induced $I_{\perp}$. We further show that in an inhomogeneously broadened system there is no rephasing for the TPC-induced self-diffracted signal, that is, *the TPC-induced FWM will behave like a free polarization decay instead of an echo.* Decay of this signal can be much faster than intrinsic biexciton dephasing.

Finally we note that the TPC model presented in this paper differs from previous biexcitonic proposals [4]. The earlier proposal is based on an incorrect selection rule and predicts vanishing TPC-induced contributions in $I_{\parallel}$. Furthermore, the models require biexciton dephasing being much faster than exciton dephasing and fail to explain the behavior of a free polarization decay in an inhomogeneously broadened system.

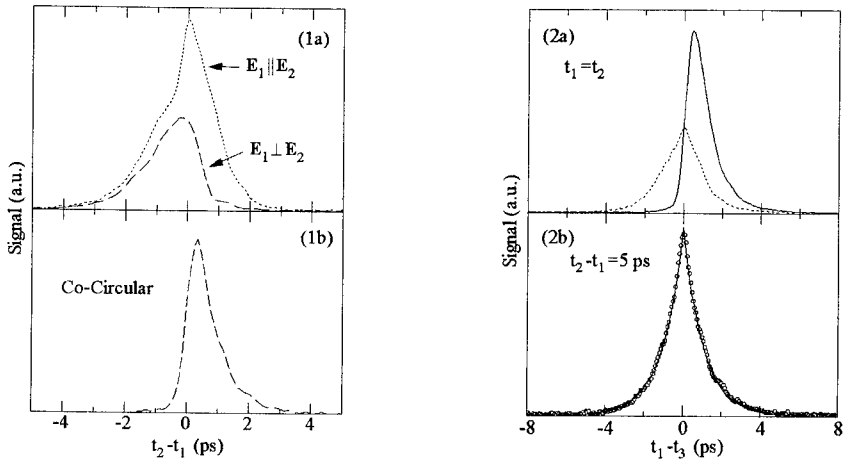


Fig. 1 Self-diffracted FWM responses in the direction of $2\mathbf{k}_2$-$\mathbf{k}_1$. (a) $\mathbf{E}_1$and $\mathbf{E}_2$ are linearly polarized. (b) $\mathbf{E}_1$and $\mathbf{E}_2$ are co-circularly polarized.

Fig. 2 Three pulse FWM responses in the direction of $\mathbf{k}_1$+$\mathbf{k}_2$-$\mathbf{k}_3$. (a) For the solid curve all three fields are co-circularly polarized. For the dashed curve $\mathbf{E}_2$ has the circular polarization opposite to $\mathbf{E}_1$ and $\mathbf{E}_3$. (b) The same as the dashed curve in (a) except that t_2 is delayed by 5 ps with respect to t_1.

References:

1) D. Bennhardt et al. Phys. Rev. B**47**, 13485 (1993) and extensive references cited there.
2) B.F. Feuerbacher, J. Kuhl, and K. Ploog, Phys. Rev. B**43**, 2439 (1991).
3) S. Bar-Ad and I. Bar-Joseph, Phys. Rev. Lett. **68**, 349 (1992); D.J. Lovering, et al., Phys. Rev. Lett. **68**, 1880 (1992); K.H. Pantke, et al., Phys. Rev. B**47**, 2413 (1993).
4) H. H. Yaffe et al., J. Opt. Soc. Am. **10**, 578 (1993); T. Saiki et al., to be published.

Femtosecond Measurements of Ballistic and Interactive Transport of Nonequilibrium Electrons in Thin Gold Films

T. Juhasz, C. Suárez and W. E. Bron
Department of Physics, University of California, Irvine, CA 92717
H. E. Elsayed-Ali
Department of Electrical and Computer Engineering, Old Dominion University, Norfolk VA 23529

The dynamics of nonequilibrium electrons in solids has attracted considerable recent attention. Nonequilibrium electrons in metals can be excited by laser pulses with durations less than, or comparable to the excited-electron energy-loss lifetime (τ_e), such that a transient inequality between the effective electron and lattice temperatures (T_e and T_l) occurs. The excited electron population can be probed through measurements of the transient differential reflectivity (or transmissivity) of the sample. Loss of electron energy in the excited volume is attributed to energy transfer to the lattice through electron-phonon interactions plus electron transport out of the excited region. It has been shown that the relaxation of the nonequilibrium electrons is influenced by the crystal structure of the films, and by the consequent enhanced electron-phonon scattering in the polycrystalline films [1]. It has been established on experimental and theoretical grounds that electron-grain boundary interactions impede electron transport in polycrystalline films [2]. Earlier experiments on this topic investigated electrons thermalized with the lattice. Unresolved, however, is the role of grain boundaries in the *transport* of nonequilibrium electrons in thin metal films. In the present experiment we investigate the transport of femtosecond laser generated nonequilibrium electrons in poly- and single-crystalline gold films, through measurements of the time-of-flight across the film thickness which is made possible through an application of a thermoreflectivity technique with femtosecond resolution [3].

A synchronously pumped femtosecond dye laser with output pulses of ~150 fs duration at 2 eV photon energy and 76 MHz repetition rate is used to excite the electrons with ~100 $\mu J/cm^2$ fluence per pulse on the front surface of the films. The skin depth $D \approx 15$ nm. Since an excitation gradient is generated between the skin depth and the rest of the sample, transport of the nonequilibrium electrons out of the excited volume occurs simultaneously with electron energy relaxation through electron-electron and electron-phonon interactions. Excited electrons which reach the back surface of the film introduce a change in the optical reflectivity which is probed with an appropriately delayed laser pulse. The intensity of the pump beam is modulated with an acousto-optic modulator and the differential reflectivity ($\Delta R/R(t)$) is detected with a lock-in amplifier tuned to the modulation frequency.

Polycrystalline gold films are evaporated on ~1 mm thick sapphire substrates. Examination of films evaporated on an electron microscope grid adjacent to the sapphire substrate reveals a wide distribution of grain sizes with an average of a_p=16 ±2 nm. Single-crystalline gold films are fabricated by epitaxial growth on a ~2 nm silver layer grown on a heated NaCl crystal. The film is floated on distilled water, washed in sulfuric acid to remove silver and silver-gold alloy, then washed in distilled water. Finally the film is caught on a sapphire substrate. Electron diffraction obtained from these films shows a single crystal pattern

in the (100) orientation. These films are known to posses high dislocation densities ($(10^{10}$-$10^{11})/cm^3$) and twins.

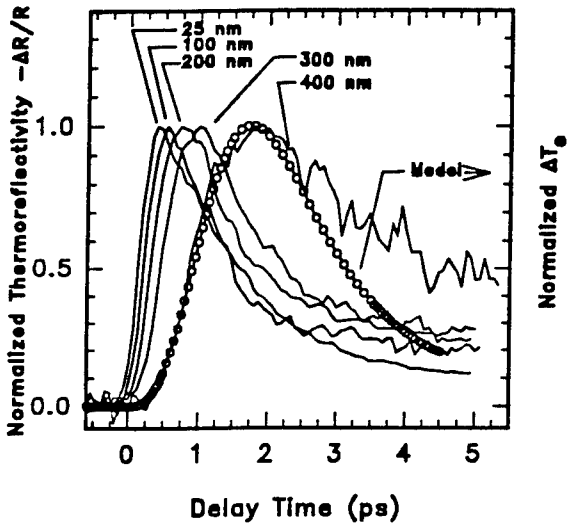


Fig. 1.

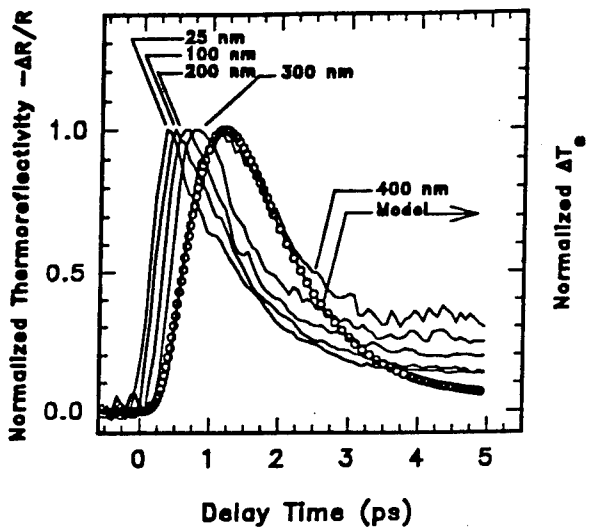


Fig. 2.

The transient thermoreflectivity, ($\Delta R/R(t)$), normalized to its maximum value, and as measured on the back surface of the polycrystalline gold film samples, with thicknesses of 25 nm, 100 nm, 200 nm, 300 nm, and 400 nm, are displayed in Fig.1. Similar results obtained on single-crystalline films are displayed in Fig.2. As the thickness of the films is increased the traversal time of the electrons to cross the film, and therefore the delay in the transient $\Delta R/R(t)$, is increased. It is also important to note, that the time to reach the maximum value of the transient $\Delta R/R(t)$, relative to its onset, also increases with increasing sample thickness of the polycrystalline samples. This effect is considerably smaller in the single-crystalline samples with thicknesses less than 400 nm. In order to measure the time required by the first wave of electrons to traverse the films, we measured the time to reach the signal onset of $\Delta R/R(t)$, relative to the excitation at t=0, for different sample thicknesses. For simplicity we assign the onset as 15% of the full signal level. The open symbols in Fig.3 display the results. The circles and triangles represent the poly- and single-crystalline samples, respectively. For each film thickness, the delay of the peak of $\Delta R/R(t)$ corresponds to the time required for the bulk of the excited electrons to reach the back surface. Measurements determining this delay (relative to t=0) in both, poly- and single-crystalline gold films are displayed by the filled symbols in Fig. 3.

As can be seen in Fig.3, the time for the first wave of electrons to traverse the films is linear with sample thickness for both polycrystalline and single-crystalline films if the thickness is less than or equal to 300 nm. The linear dependence of the traversal time on the sample thickness is characteristic of ballistic transport, when the transport of the excited electrons occurs without any interactions among the electrons or between the electrons and the lattice. The velocity of the ballistic component is measured to be $\cong 10^6$ m/s in agreement with previously published values [3]. In the case of the peak of $\Delta R/R(t)$ a linear dependence of the traversal times is observed for shorter thicknesses, namely up to 100 nm in both type of the

gold films. In the 400 nm thick samples deviations from the linear dependence are observed for the onsets as well as for the peaks in both types of the gold films.

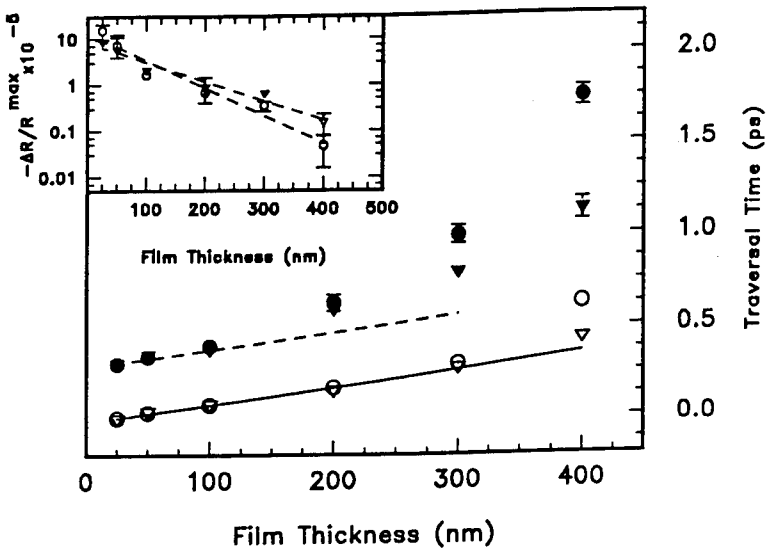


Fig. 3.

We interpret these results as follows. The transport of the excited electrons across the films with thicknesses less than, or equal to 100 nm is mostly ballistic in both single- and polycrystalline materials. As the thickness of the film increases the fraction of the ballistic component decreases, and the excess energy is carried by electrons interacting with other electrons or/and with the lattice. These electrons undergo one or more scattering events, and we refer to them as the interactive component of the transport. Interactive transport also includes the possibility of pure diffusion. Due to the scattering events the interactive electrons lose some of their excess energy during the transport. Since the interactive electrons arrive at the back surface of the sample later than the ballistic electrons, the appearance of the peak of the transient $\Delta R/R(t)$ signal is somewhat delayed. The effect is observed to be stronger in the polycrystalline samples, which indicates that the grain boundaries cause a slowing of the transport of the excited electrons. In samples with 400 nm thicknesses the ballistic component is diminished in both poly- and single-crystalline samples. The absence of the ballistic component could imply the presence of a thermal equilibrium among the electrons which reach the back surface, although no direct evidence of this is available from the present experiment. However, in order to move the analyses beyond this point we assume a thermal equilibrium among the electrons arriving at the back surface of the 400 nm thick films as well as a pure diffusive transport of these electrons and fit the so called two temperarue model [4] to the data obtained in the 400 nm thick samples. The best agreement with the experimental data provides diffusion coefficient κ_s=310 W/mK and κ_p=180 W/mK in the case of single-crystalline and polycrystalline films respectively. The results of the calculations, $\Delta T_e = T_e(t) - T_{ambient}$, are displayed with open circles in Figs. 1 and 2. The reflection coefficient of excited electrons at the grain boundaries is extracted from the experiment by analyzing the results in the terms of the Mayadas-Shatzkes model [2], and is estimated to be $r \cong 0.12$.

REFERENCES:

1. H. E. Elsayed-Ali, T. Juhasz, G. O. Smith, and W. E. Bron, Phys. Rev. B 43, 4488 (1991); H. E. Elsayed Ali, and T. Juhasz, Phys. Rev. B. 47, 13599 (1993).
2. A. F. Mayadas and M. Shatzkes, Phys. Rev. B 1, 1382 (1970);
3. S. D. Brorson, J. G. Fujimoto, and E. P. Ippen, Phys. Rev. Lett. 59, 1962 (1987).
4. S. I. Anisimov, B. L. Kapelovich, and T. L. Perelman, Z.h. Eksp. Theor. fiz. 66, 776 (1974) [Sov. Phys. - JETP 39, 375 (1974)].

Femtosecond Two-Dimensional Raman Spectroscopy of Liquid Water

S. Palese, J. T. Buontempo, Y. Tanimura, S. Mukamel, R. J. D. Miller
Department of Chemistry and Institute of Optics
University of Rochester
Rochester, NY 14627-0216, USA
(716)-275-4079

W. T. Lotshaw
General Electric Research and Development Center
P. O. Box 8
Schenectady, NY 12301, USA

Critical to the understanding of condensed phase reaction dynamics is the understanding of a solvent's response to and influence on the system dynamics. Although models of a solvent's vibrational and orientational dynamics can be tested against infrared and Raman studies of the neat solvent, thus far this has not proven fruitful because the influence of nuclear dynamics on infrared absorption, optical Kerr effect, spontaneous Raman and CARS spectra is usually masked by inhomogeneous broadening. However, valuable information about the solvent nuclear dynamics can be extracted from nonlinear spectroscopies such as infrared and Raman echoes. Using the formalism of Tanimura and Mukamel,[1] we have calculated the 3rd, 5th, and 7th order Raman spectra for liquid water employing a multimode Brownian oscillator model to represent the water modes. This model is expected to be appropriate for liquid water because it accounts for nuclear dynamics occurring on a finite time scale, extrapolating continuously between the limiting cases of homogeneous and inhomogeneous nuclear dephasing.

The $\chi^{(3)}$ response function of water was experimentally determined using femtosecond Optical Kerr Effect spectroscopy with pulses as short as 30 fs to provide the spectral density function between 1-800 cm^{-1}. The analytical fit to these results and calculated free induction decays are shown in Figure 1. Using the $\chi^{(3)}$ response function within homogeneous and inhomogeneous limits, the higher order Raman responses were calculated. These calculations are shown in Figure 2 for the 5th order ($\propto \chi^{(5)}$) response probed by a three-pulse sequence. The 7th order ($\propto \chi^{(7)}$) response is analogous to the Raman echo and is shown in Figure 3. It can be seen that in both 5th and 7th order there are clear distinctions between homogeneous and inhomogeneous contributions to the Raman line shape even for a multimode system as complex as the intermolecular modes of water. The most valuable diagnostic, in this regard, is the rephasing of the coherence in the nuclear polarization for the inhomogeneous limit. In addition to this feature, the differences in the temporal response for the 5th and 7th order highlight the importance in fully resolving the dynamics of higher order Raman processes. Preliminary experimental studies along these lines have also been conducted using amplified 60 fs pulses. These results will be discussed in the context of experimentally distinguishing inhomogeneous contributions to the structure of water on 100 fs time scales.

Reference

1. Y. Tanimura and S. Mukamel, *J. Chem. Phys.* **1994** (in press).

Figures

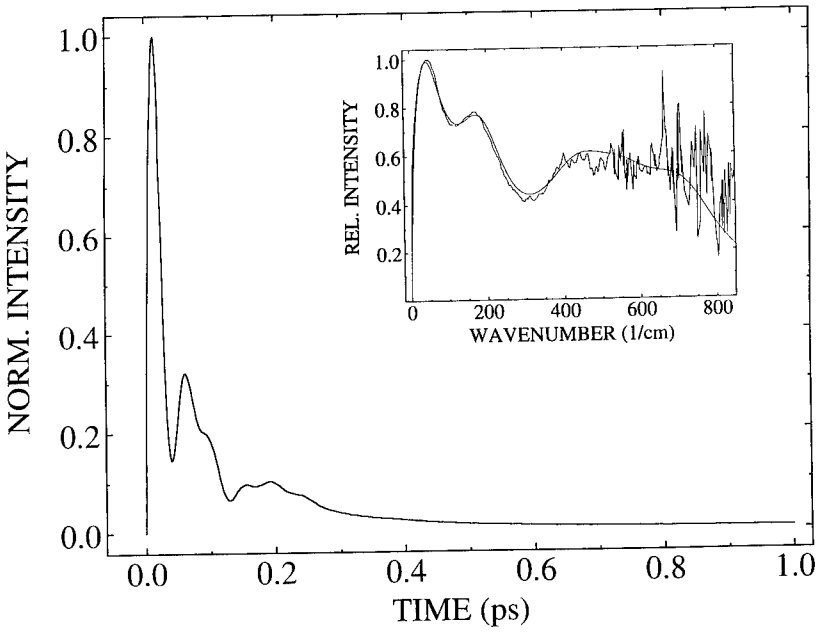


Figure 1. Calculated $\chi^{(3)}$ nuclear response for water. This response essentially reproduces the experimental OKE data. Inset: The noisy curve is the imaginary component of the FFT of the experimental OKE response for water determined using out-of-phase heterodyne detection. The smooth solid line shows the fit using a Brownian oscillator model to the experimental frequency distribution .

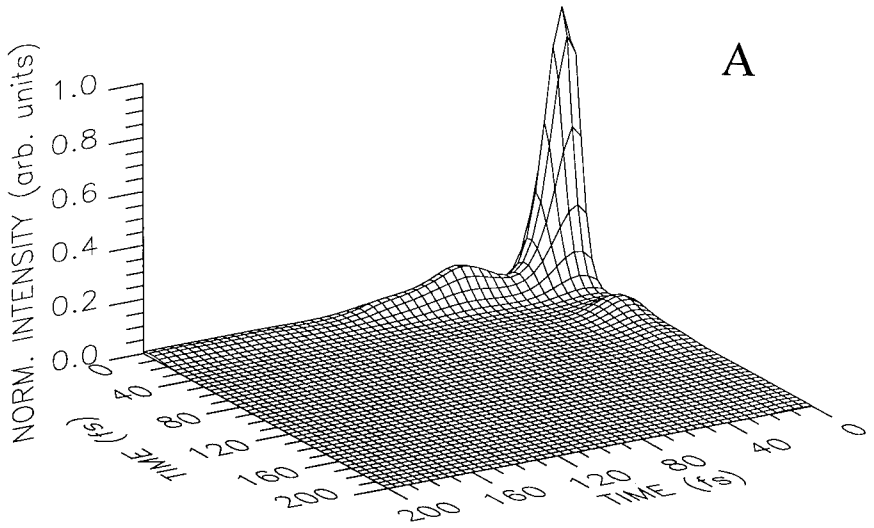


Figure 2A. Calculated $\chi^{(5)}$ response in the homogeneous limit based on the $\chi^{(3)}$ response of Figure 1.

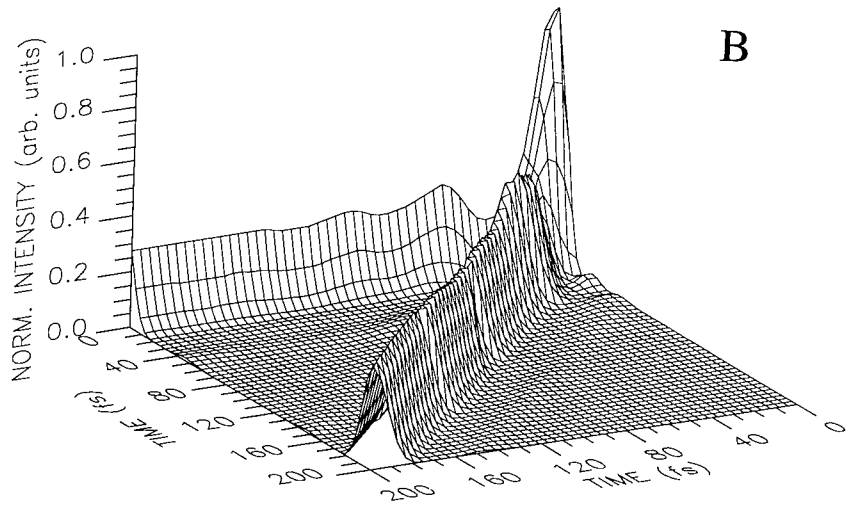


Figure 2B. Calculated $\chi^{(5)}$ response in the static inhomogeneous limit for the water spectrum.

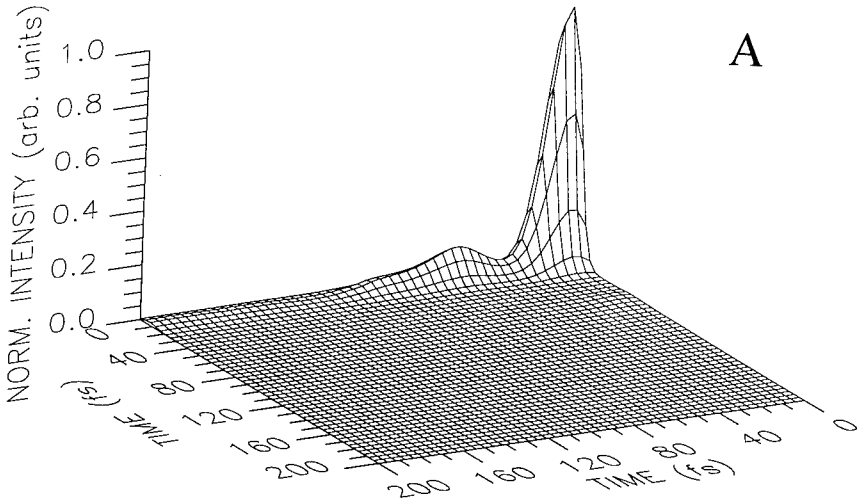


Figure 3A. Calculated $\chi^{(7)}$ response in the homogeneous limit based on the $\chi^{(3)}$ response of Figure 1.

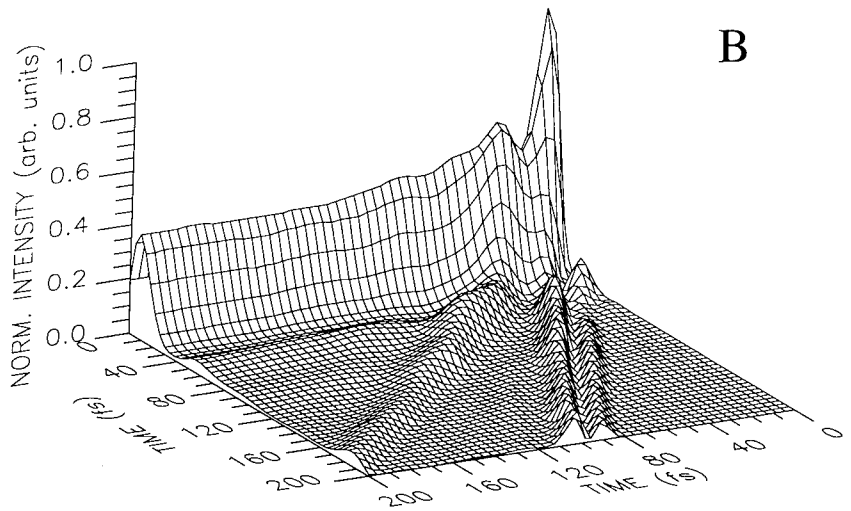


Figure 3B. Calculated $\chi^{(7)}$ response in the static inhomogeneous limit for the water spectrum.

Femtosecond, Cr^{4+}:YAG laser

Howard Nathel
Lawrence Livermore National Laboratory, P. O. Box 808, L-524, Livermore, CA 94551
(510)-423-3262

Alphan Sennaroglu and Clifford R. Pollock
School of Electrical Engineering, Cornell University, Ithaca, NY 14853
(607)-255-5032

Recent advances in mode-locked solid-state lasers have resulted in pulses as short as 8.5 fs in the 800 nm region from Ti:sapphire oscillators [1]. Using similar techniques, sub-50 fs pulses [2-4] have been generated in another solid-state laser system, Cr:forsterite, which operates in the 1.2 to 1.3 μm range. We report here results from both a regeneratively-initiated and self-initiated, mode-locked Cr:YAG laser [5] which is tunable from 1.51 to 1.53 μm. One hundred and twenty femtsosecond, nearly transform-limited pulses have been generated with peak output powers of 45 kW. The stable, high peak power pulses and room temperature operation of this laser make it a very suitable alternative to the cumbersome, cryogenic mode-locked NaCl laser [6] commonly used in both narrow bandgap semiconductor and optical communications research.

Lasing action in chromium-doped yttrium aluminum garnet (Cr^{4+}:YAG), first reported by Shestakov *et al.* [7], occurs over the wavelength range from 1.34 to 1.56 μm. Owing to this broad tunability, Cr:YAG is therefore a good candidate for femtosecond pulse generation. Active mode-locking of a Cr:YAG laser has resulted in 26 ps pulses at 1.44 μm [8]. However citing poor crystal quality resulting in low intracavity power, Kerr lens mode-locking was unachievable and consequently femtosecond pulse generation was not observed.

We have constructed a laser oscillator depicted in figure 1. A folded, astigmatically compensated z-cavity with approximately equal arm lengths and a total length corresponding to 81.27 MHz cavity repetition rate was used. The gain medium was placed slightly off-center between two curved high reflectors (M1 and M2) each having 10 cm radius of curvature and reflectivities exceeding 99.9% from 1.35 to 1.55 μm. A flat wedged output coupler (O.C.) having 1% transmission in the same wavelength range was used throughout the work. A 1 cm long Brewster-cut quartz acousto-optic cell (A.O.M.) was used for regenerative initiation and a pair of Brewster angled synthetic fused silica prisms (P1 and P2) separated by 39 cm tip-to-tip and placed at minimum deviation on the high reflector (H.R.) side of the cavity provided intracavity negative GVD compensation. The output beam of the Nd:YAG pump laser was focused into the Cr^{4+}:YAG crystal (20 mm long, 5 mm diameter, Brewster cut) using a 10 cm focal length, AR-coated lens (L1) that had 93% transmission at 1.064 μm. To facilitate mode matching between the pump beam and laser cavity a telescope comprised of two 5 cm focal length AR-coated lenses (L3 and L4) with adjustable separation length was employed in conjunction with L1. The laser crystal was temperature controlled at 20 °C. The differential absorption coefficient at this temperature was measured to be 1.33 cm^{-1} at 1.06 μm.

With no intracavity elements present, an absorbed pump power slope efficiency of 15% with threshold of 1.04 W was measured with the output of the laser centered at 1.45 μm. Continuous wave output powers of 840 mW was obtained. With the inclusion of

intracavity elements (A.O.M. and the prism pair), the slope efficiency dropped to 10%, and the output laser shifted to 1.49 μm, mainly due to wavelength dependent absorption and scattering from surface imperfections in the intracavity elements. The threshold absorbed pump power increased to 1.82 W.

To initiate mode-locking, 4% of the output beam was picked off via a beamsplitter (B.S.) and sent to an InGaAs photo diode which detected the cavity mode beating signal. The signal was frequency-divided and amplified with adjustable phase shift to drive the A.O.M. that had 0.4% modulation depth. Upon optimization of mirrors M1 and M2 to produce self focusing and induce Kerr nonlinearities, the femtosecond pulse train was initiated. Figures 2(a) and 2(b) show the background-free intensity autocorrelation and the spectrum, respectively, of the mode-locked pulses from the Cr^{4+}:YAG laser. Assuming a $sech^2$ intensity profile the pulse width was measured to be 120 fs. A simultaneous measurement of 20.8 nm spectral bandwidth yielded a time-bandwidth of 0.327 verifying that the pulses were nearly transform-limited. The onset of mode-locking resulted in the peak wavelength to shift to 1.52 nm and a reduction in output power from 460 mW to 440 mW. By placing an aperture between prism P2 and the high reflector (H.R.), the output wavelength could be tuned over a narrow range from 1.51 to 1.53 μm. Operation to longer wavelengths was inhibited by the optics coatings. At shorter wavelengths, tuning resulted in the collapse of the broad spectral bandwidth resulting in approximately 20 ps pulses. Losses introduced by the prism pair together with excited-state absorption (ESA) in the Cr^{4+}:YAG crystal are the dominant factors inhibiting femtosecond pulse formation on the shorter wavelength side. The role of ESA as a net negative saturable absorber quenching self-mode-locked operation has been studied and suggested previously [8,9].

With the A.O.M. turned off, self-sustained operation in excess of one hour was observed. The measured peak power and energy per pulse were 45 kW and 5.4 nJ, respectively. A threshold output power of approximately 100 mW was required to observe the onset of femtosecond pulse formation (self or Kerr lens mode-locking) corresponding to 1 MW intracavity peak power. In a separate experiment, the A.O.M. was removed from the laser and self-mode-locking was initiated without applying any periodic perturbation to the cavity round-trip gain. In this case, the mode beating signal detected by the InGaAs detector was maximized by adjusting the curved mirrors M1 and M2 and the cavity was slightly misaligned to initiate the femtosecond pulse train. Alternatively, one of the prisms could be slightly translated to initiate the pulse train. The output pulse characteristics were indistinguishable from the regeneratively-initiated case.

This work was supported by the U. S. Department of Energy under contract W-7405-Eng-48, the National Science Foundation under grant ECS-9111838, the Joint Services Electronics Program, and the Materials Science Center at Cornell University.

1. M. M. Murnane, H. C. Kapteyn, J. Zhou, C. P. Huang, D. Garvey, and M. T. Asaki, *Tech. Dig. Opt. Soc. Amer. Ann. Meet..*, Toronto, Canada, paper WD1, page 103.
2. A. Sennaroglu, C. R. Pollock, and H. Nathel, *Opt. Lett.. 18(10)*, 826 (1993).
3. A. Seas, V. Petricevic, and R. R. Alfano, *Opt. Lett.. 18(11)*, 891 (1993).
4. V. Yanovsky, Y. Pang, F. Wise, and B. I. Minkov, *Opt. Lett.. 18(18)*, 1541 (1993).
5. A. Sennaroglu, C. R. Pollock, and H. Nathel, accepted to *Opt. Lett..*
6. C. P. Yakymyshyn, J. F. Pinto, and C. R. Pollock, *Opt. Lett.. 14,* 621 (1989).
7. A. V. Shestakov, N. I. Borodin, V. A. Zhitnyuk, A. G. Ohrimtchyuk, and V. P. Gapontsev, *Digest of Conference on Lasers and Electro-Optics* (Optical Society of America, Washington D.C., (1993), paper CThS82.
8. P. M. W. French, N. H. Rizvi, J. R. Taylor, A. V. Shestakov, *Opt. Lett.. 18(1)*, 39 (1993).
9. A. Sennaroglu, C. R. Pollock, and H. Nathel, *Tech. Dig. Opt. Soc. Amer. Ann. Meet..*, Toronto, Canada, paper WZ3, page 138.

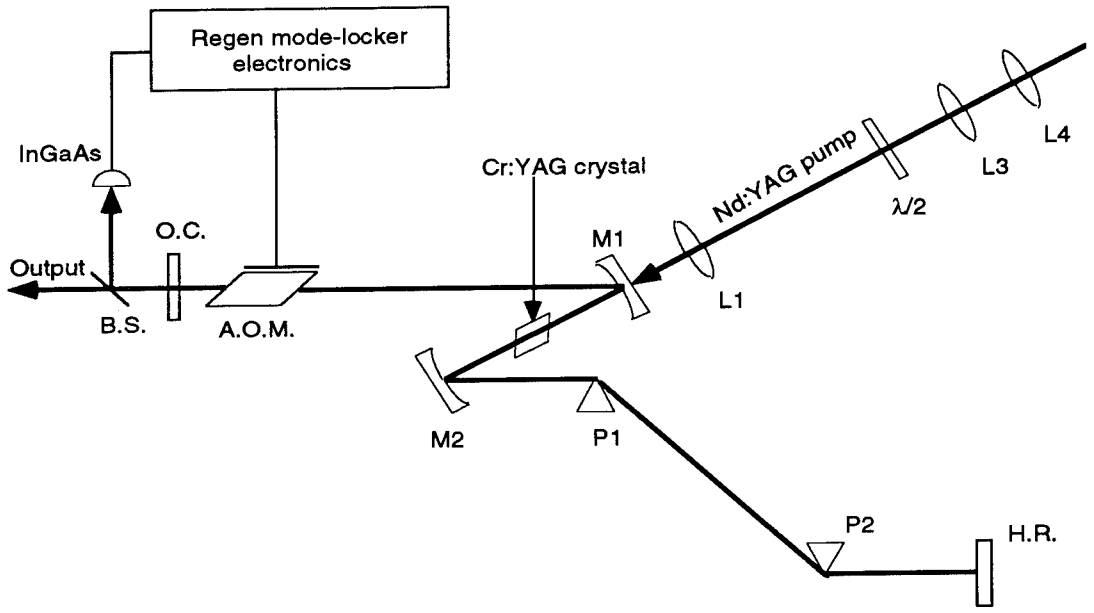


Figure 1. The schematic diagram of the femtosecond, mode-locked Cr^{4+}:YAG laser.

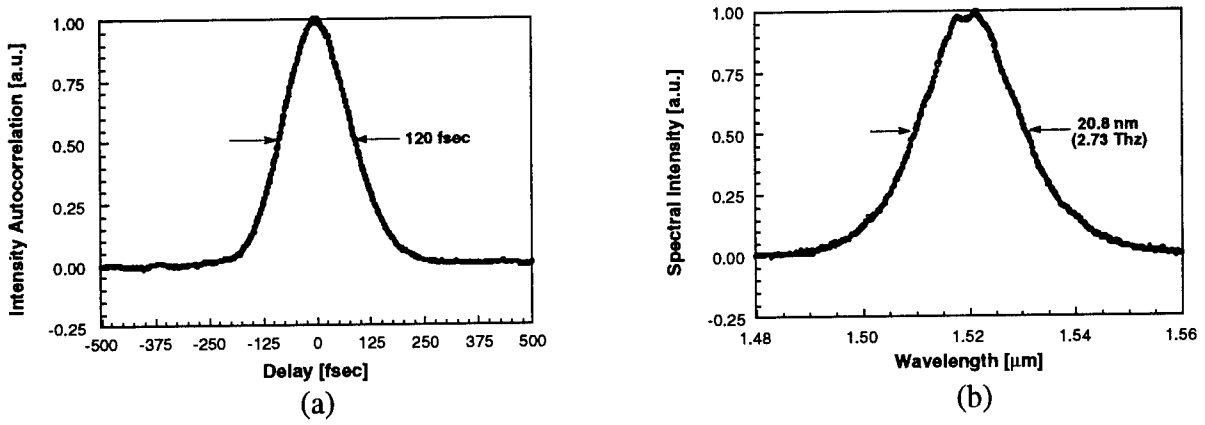


Figure 2. (a) The background-free autocorrelation of the mode-locked pulses; (b) The spectrum of the mode-locked pulses.

Enhancement of Coherent Charge Oscillations in Coupled Quantum Wells by Femtosecond Pulse Shaping

A.M. Weiner
Purdue University; School of Electrical Engineering; West Lafayette, IN 47907-1285
(317)494-5574

Considerable interest has arisen in the prospect of using specially crafted ultrashort laser pulses for coherent control of quantum mechanical motions in atomic and molecular systems. In this paper we analyze the possibility of applying coherent control concepts and femtosecond pulse shaping to a quantum well system, in particular to enhance coherent quantum mechanical charge oscillations in GaAs/GaAlAs coupled quantum wells.

Ultrashort pulse excitation of coherent charge oscillations has recently been observed in several elegant experiments performed in quantum well [1,2] and superlattice [3] samples. Here we concentrate on coupled quantum wells, in which one wide well and one narrow well are separated by a thin barrier region. An electric field is applied to tilt the energy bands until the lowest electron energy levels line up, leading to an energy level splitting and a delocalization of the wave functions across the two wells. When a short pulse excites from the valence band in one well into a superposition state in the conduction band, this results in an oscillation of the electron between the two wells, which has been observed, e.g., by terahertz [THz] emission.

Simple experiments aimed at controlling and possibly enhancing these oscillations have recently been performed . In one experiment an interferometer split an incident pulse into a pulse doublet, which was used to excite the coupled quantum well [4]. A second experiment used a pulse shaper to generate a pulse train in order to excite the sample at its natural oscillation frequency [5]. In both studies the peak THz emission for multiple-pulse excitation was roughly the same as that observed with the original [single] pulse. Thus, although these experiments did demonstrate control over the oscillation dynamics, they did not succeed in enhancing the peak oscillation amplitude. This raises the following question: can laser pulse shapes be designed that would significantly enhance the charge oscillation amplitude and hence the radiated THz signal?

Let us first explain why double and multiple pulse experiments produce roughly the same peak THz emission as single pulse experiments. In the absence of relaxation, the second order coherent polarization responsible for THz emission from a coupled quantum well is given by

$$P^{(2)}(t) \sim \mathrm{Re}\left\{ e^{i\omega_{21}t} \int^{t} dt' e_L(t') \exp(i\Delta_{13}t') \int^{t} dt' e_L^{*}(t') \exp(-i\Delta_{23}t') \right\}, \qquad (1)$$

$$\text{where } e_L(t) = \frac{1}{2\pi} \int d\omega E_{in}(\omega) H(\omega).$$

Here the Δs are the detunings of the laser center frequency from the interband transitions, and ω_{21} is the charge oscillation frequency. $e_L(t)$ is the shaped pulse either from a pulse shaper [6] or an interferometer and is given by the Fourier transform of the input spectrum $E_{in}(\omega)$ multiplied by a pulse shaping filter $H(\omega)$. *After the end of the shaped laser pulse*, the coherent polarization $P^{(2)}$ is proportional to $E_L(\Delta_{13})E_L^{*}(\Delta_{23})$, the product of the shaped laser spectral amplitudes at the two interband transitions. Note that pulse shapers (and interferometers) are passive linear filters which cannot increase the spectral amplitudes beyond those of the original input pulse. Thus, for a fixed

There is, however, the possibility of enhancing the oscillation amplitude and the THz emission *while the laser waveform is still on.* In this scenario the oscillation amplitude climbs during the excitation waveform, peaks significantly above the peak level corresponding to the original single laser pulse, and then decreases during the final portion of the pulse to reach a final value identical to single pulse case. In order to calculate laser pulse shapes (and pulse shaping filters) suitable to achieve such a peaking, we rewrite eq. (1) in the following simplified form:

$$P^{(2)}(t) \sim \mathrm{Re}\left\{ e^{i\omega_{21}t} \left(T_{\Delta_{13}} \cdot H\right) \left(T_{\Delta_{23}} \cdot H\right)^{*} \right\} \tag{2}$$

$$\text{where } T_{\omega} \cdot H = \int^{\tau_0} e_L(t') \exp(i\omega t') dt'$$

This formulation has the advantage that the operator T_ω can easily be calculated by performing a series of computer matrix multiplications. We can then solve for pulse shaping filters $H(\omega)$ which optimize the polarization at a target time τ_0.

An example of our computed results for $T_{\Delta_{13}}$ and $T_{\Delta_{23}}$ is shown in Fig. 1 for $\tau_0 = 2.5$ psec. The T_ω operators have a finite width as well as a very complicated phase profile. In this case of finite τ_0 one can enhance the peak polarization by picking a suitable pulse shaping filter in order to optimize the product $\left(T_{\Delta_{13}} H\right) \left(T_{\Delta_{23}} H\right)$. One useful choice for $H(\omega)$ is is a phase-only filter with a phase which is conjugate to $T_{\Delta_{13}}$ ($T_{\Delta_{23}}$) for $\omega < 0$ ($\omega \geq 0$), as follows:

$$H(\omega) = \begin{cases} T^{*}_{\Delta_{13}} / |T_{\Delta_{13}}|, & \omega < 0 \\ \\ T^{*}_{\Delta_{23}} / |T_{\Delta_{23}}|, & \omega \geq 0 \end{cases} \tag{3}$$

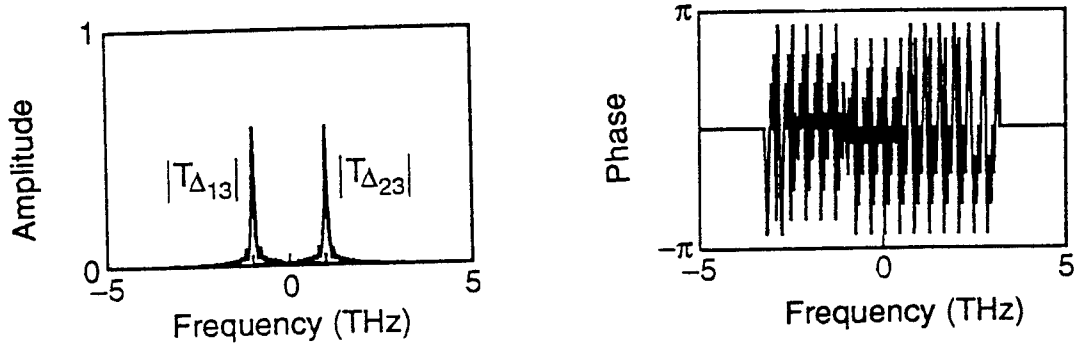


Fig. 1 Computed results for the operator T_ω for target time τ_0=2.5 psec. (**Left**) Amplitude of T_ω. (**Right**) Phase of $T_{\Delta_{13}}$.

Computed results for the coherent polarization are shown in Fig. 2. The top traces show the input (unshaped) laser pulse and the resultant induced polarization. As expected, the polarization turns on at t=0 and then oscillates with a constant amplitude at frequency ω_{21} (2 THz in these simulations). The lower trace shows one of our derived waveforms which causes the induced polarization to build up to a strong peak at $\tau_0 = 2.5$ psec, with an amplitude enhanced by a factor of three compared to the no pulse shaping case. Similar enhancements are seen for other values of the delay τ_0. The waveform shown, although complicated, can be created readily using a previously demonstrated 128-element phase modulator within a pulse shaping apparatus [6].

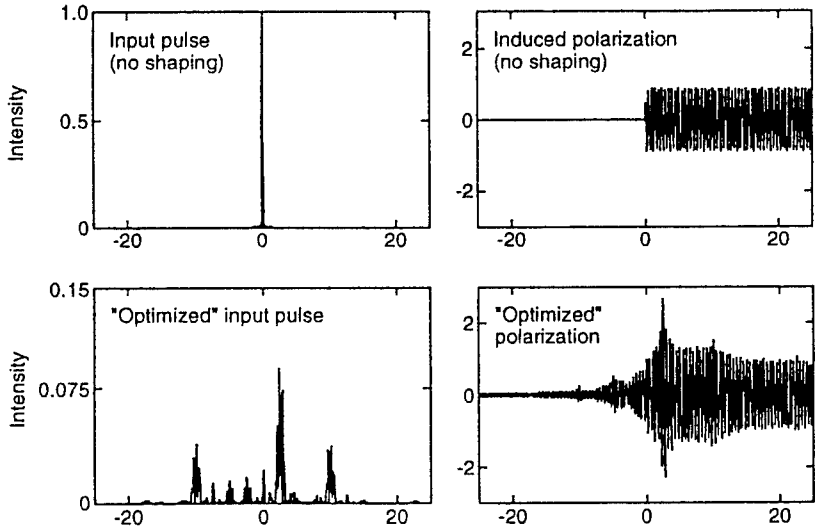


Fig. 2 Computed results for the coherent polarization. (**Top**) An input unshaped laser pulse (left) and the resultant induced polarization (right). (**Bottom**) Shaped input pulse (left) designed for τ_0=2.5 psec and resultant induced polarization (right) showing a strong enhancement in the peak polarization.

As part of our continuing research, we wish to investigate a number of further theoretical questions. Not the least of these is to study how dephasing, which typically occurs on a several picosecond time scale, impacts our results and to calculate shaped laser waveforms which are optimum in the presence of dephasing. Nevertheless, our initial theoretical results indicate the exciting possibility of applying ultrashort pulse coherent control techniques to strongly influence charge motions in semiconductor coupled quantum wells!

References

1. K. Leo, J. Shah, E.O. Gobel, T. Damen, S. Schmitt-Rink, W. Schafer, and K. Kohler, *Phys. Rev. Lett.* 66, 201 (1991).
2. H.G. Roskos, M.C. Nuss, J. Shah, K. Leo, D.A.B. Miller, A.M. Fox, S. Schmitt-Rink, and K. Kohler, *Phys. Rev. Lett.* 68, 2216 (1992).
3. C. Waschke, H. G. Roskos, R. Schwedler, K. Leo, H. Kurz, and K. Köhler, Phy. Rev. Lett. 70, 3319 (1993).
4. P.C.M. Planken, I. Brener, M.C. Nuss, M.S.C. Luo, and S.L. Chuang, *Phys. Rev.* B48, 4903 (1993).
5. I. Brener, P.C.M. Planken, M.C. Nuss, L. Pfeiffer, D.E. Leaird, and A.M. Weiner, *Appl. Phys. Lett.* 63, 2213 (1993).
6. A. M. Weiner, D. E. Leaird, J. S. Patel, and J. R. Wullert, *IEEE J. Quantum Electron.* 28, 908 (1992).

Sub-40 fs Pulse Generation in a KTP-based Optical Parametric Oscillator

D. T. Reid, J. M. Dudley, M. Ebrahimzadeh and W. Sibbett

J. F. Allen Research Laboratories, Department of Physics and Astronomy, University of St Andrews, Fife KY16 9SS, Scotland, UK

Tel. +44 334 76161 Fax +44 334 63104

The demand for femtosecond sources at new wavelengths in the near to mid-infrared together with the emergence of the self-mode-locked Ti:sapphire laser as a convenient pump source has led recently to the development of femtosecond optical parametric oscillators. We report here the operation of a synchronously pumped femtosecond optical parametric oscillator (OPO) based on a 1.5 mm thick crystal of KTP cut for non-critical phase-matching. Pumped by 85 fs pulses from a self-modelocked Ti:sapphire laser the OPO is tunable over the bandwidth of the mirrors from 1.1 - 1.3 μm and pump tuning over 100 nm is demonstrated. Our intracavity dispersion-compensated OPO has been operated in both three-mirror and four-mirror standing-wave geometries using single-pass pumping and exploiting a variety of mode-matching configurations. In addition, the observation of soliton generation in the femtosecond OPO is described. A typical spectrum and interferometric autocorrelation of the signal pulses produced in the three-mirror configuration are presented in Figure 1 and correspond to bandwidth-limited 39 fs pulses with intracavity peak powers approaching 1 MW [1]. The shortest pulses are observed when operating at near-zero intracavity GVD.

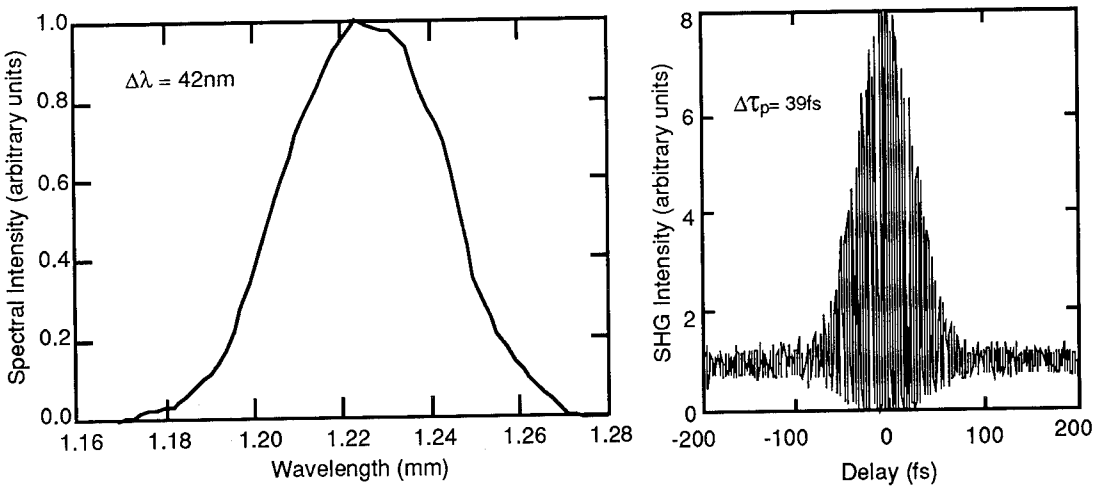


Figure 1 Spectrum and interferometric autocorrelation of signal pulse

A comparison of both three-mirror and four-mirror standing wave cavity configurations has been made. On optimising each configuration the oscillation thresholds were comparable. Thresholds of the non-dispersion-compensated oscillators were typically 230 mW whereas those of the dispersion-compensated cavities which included a pair of intracavity SF14 prisms were approximately 350 mW. Examination of amplitude stability when the devices are pumped at over twice threshold shows the 3-mirror cavity to be more stable, exhibiting intensity fluctuations of 4% and 10% for dispersion-compensated and uncompensated cavities respectively. By contrast, figures of <10% and 20% were measured for the four-mirror oscillator. Details of a more comprehensive comparison of spectral and temporal pulse characteristics will be presented.

Each of the OPO cavity configurations used provided extensive tuning achievable either by changing the crystal orientation or by altering the wavelength of the pump laser. Results of pump laser tuning are presented in Figure 2 together with the predicted tuning curve derived from Sellmeier data for KTP [2].

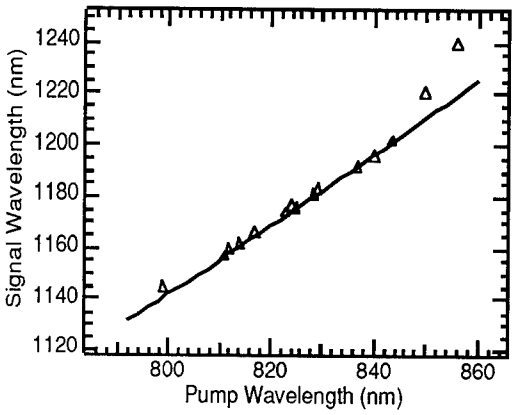


Figure 2 Experimental pump tuning data and theoretical curve derived from Sellmeier data.

Under appropriate conditions of net positive intracavity dispersion (~700 fs^2) the output of the OPO has characteristics of second or third order solitons. A deep periodic intensity modulation of frequency between 0.5 MHz and 2.2 MHz is observed and corresponding pulse duration measurements are consistent with the soliton theory reported by Salin *et al* [3].

This behaviour is accompanied by a shift in the signal spectrum towards longer wavelengths as depicted in Figure 3. Under appropriate circumstances strong components are produced at $\lambda > 1300$ nm without requiring to tune the pump laser to longer wavelengths.

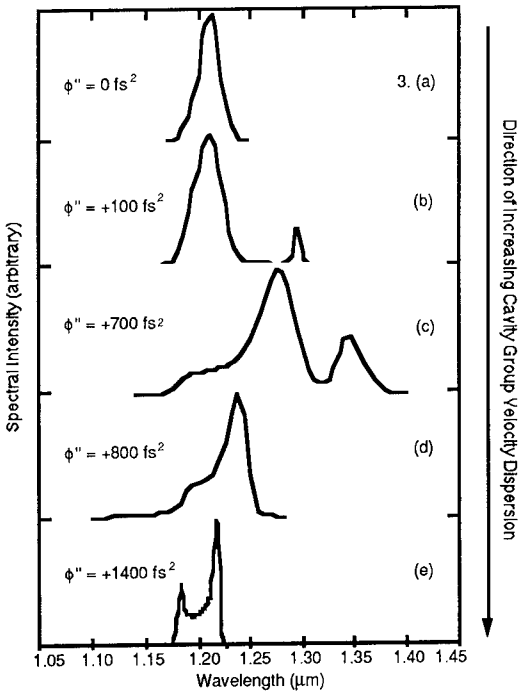


Figure 3 Spectral data for the signal pulse output of the OPO operated under positive dispersion.

The corresponding intensity autocorrelation profile of the output pulses presented in Figure 4 exhibits a triple-peaked structure characteristic of second or third order soliton propagation [4]. The noise present on the autocorrelation profile is typical of the OPO when operated in this configuration and the monitored real-time autocorrelation of the pulse showed rapid fluctuations.

The existence of soliton formation in femtosecond optical parametric oscillators may have consequences for the design of future devices. The large bandwidth exhibited by the OPO when operated in the region of positive dispersion may find applications but the associated increase in noise will limit the attractiveness of such an arrangement.

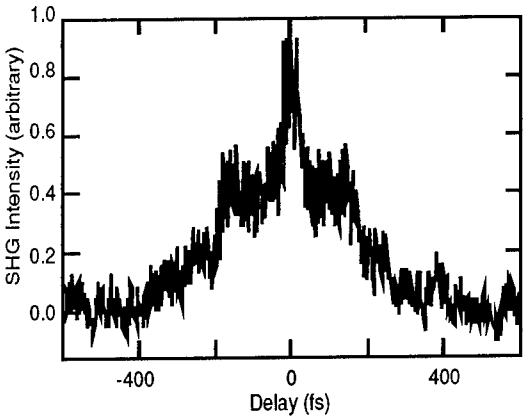


Figure 4 Intensity autocorrelation exhibiting three-fold splitting characteristic of second / third-order soliton propagation.

Investigations of other OPO standing-wave and travelling-wave cavity configurations are ongoing. Their respective performance characteristics will be discussed in the specific contexts of oscillation thresholds, stability and operational tolerances.

REFERENCES

1 J. M. Dudley, D. T. Reid, M. Ebrahimzadeh and W. Sibbett, Opt. Comm. **104**, 1994 (in press)

2 J. D. Bierlein and H. Vanherzeele, J. Opt. Soc. Am. B **6**, 622 (1989)

3 F. Salin, P.Grangier, G. Roger and A. Brun, Phys. Rev. Lett. **56**, 1132 (1986)

4 L. F. Mollenauer, R. H. Stolen and J. P. Gordon, Phys. Rev. Lett. **45**, 1095 (1980)

Time-Resolved Fluorescence Anisotropy in Chromophore Pairs

Alexander Matro and Jeffrey A. Cina
Department of Chemistry and the James Franck Institute,
The University of Chicago, Chicago, Illinois 60637
(312) 702-3166

Electronic excitation transfer has been the subject of numerous experimental and theoretical studies. Recent experimental measurements of time-resolved fluorescence and pump-probe anisotropy have revealed sub-picosecond excitation transfer processes, seen as decays in the anisotropy. The experiments of Xie et al.[1] on Allophycocyanin (APC) and C-Phycocyanin (C-PC) isolated from photosynthetic antenna systems in cyanobacteria, measuring time-resolved fluorescence anisotropy with $\sim$ 100 fs time resolution, found that the ultrafast decay component in the anisotropy showed a strong dependence on excitation/detection wavelength. The sub-picosecond decay anisotropy decay was seen in trimers of APC and C-PC and not in monomers, and, therefore, this fast decay has been attributed to pairwise excitation transfer among chromophores on different monomers of APC and C-PC.

We have developed a quantum mechanical model for the choromophore pairs which accurately represents the ultrafast electronic excitation, excitation transfer and detection. Each chromophore has two electronic states and a single vibrational mode. The singly excited states of the chromophore pair, in which only one of the chromophores is electronically excited, are coupled by an excitation transfer interaction. The detector consists of a collection of two-level systems with a Gaussian distribution of transition frequencies. Starting with the system (chromophore pair and detector) in the ground electronic state, the chromophore pair is excited with a laser pulse. The chromophore pair returns to its ground electronic state through an interaction with the detector. The emission rate is calculated from the change in excited state population of the detector over a time interval corresponding to the temporal resolution of the detection process. The dipole moment of the detector is set parallel or perpendicular to the polarization of the excitation pulse and the time-resolved fluorescence anisotropy R(t) is calculated from the parallel and perpendicular signals according to the expression $R(t) = \frac{S_{\|}(t) - S_{\perp}(t)}{S_{\|}(t) + 2S_{\perp}(t)}$, where $S_{\|}(t)$ and $S_{\perp}(t)$ are the parallel and perpendicular signals, respectively. This model allows us to include excitation and detection frequency dependence by choosing the center frequency of the excitation pulse and the center frequency (as well as bandwidth) of the detector.

A test calculation (not shown) neglecting all but the lowest singly excited states and the lowest three vibrational levels of the ground state of the chromophore pair illustrates the fact that the time-resolved fluorescence anisotropy is strongly dependent on the nature of the initial and final states of the chromophore pair. Exciting from the lowest ground state of the chromophore pair, the anisotropy resulting from emission back to that state can take values greater than 0.4 if the transition moments of the individual monomers are not parallel, while the maximum anisotropy resulting from emission to the higher-lying ground states is 0.4 and is independent of the angle between the two transition moments. This is in agreement with a theoretical study of pump/probe anisotropy by Wynne et al. [2] A chromophore pair with vibrational degrees of freedom will generally exhibit an anisotropy resulting from both types of contributions described above.

We have carried out numerical calculations of the time-resolved anisotropy including non-zero excitation pulse duration and non-zero time resolution of the detection process. Vibrational motion is assumed harmonic with 100 cm^{-1} frequency, and the two chromophores are identical except for differing by 150 cm^{-1} in their bare electronic transition frequency. The model parameters were chosen to correspond to the those of the strongly coupled chromophores in C-PC.[3] Two excitation/detection conditions examined are examined here: in the first case, the excitation is at the bare electronic transition frequency of the lower-energy chromophore, and in the second case, it is 150 cm^{-1} above the bare transition frequency of the higher-energy chromophore. In both cases, the detection frequency is 250 cm^{-1} below the excitation frequency.

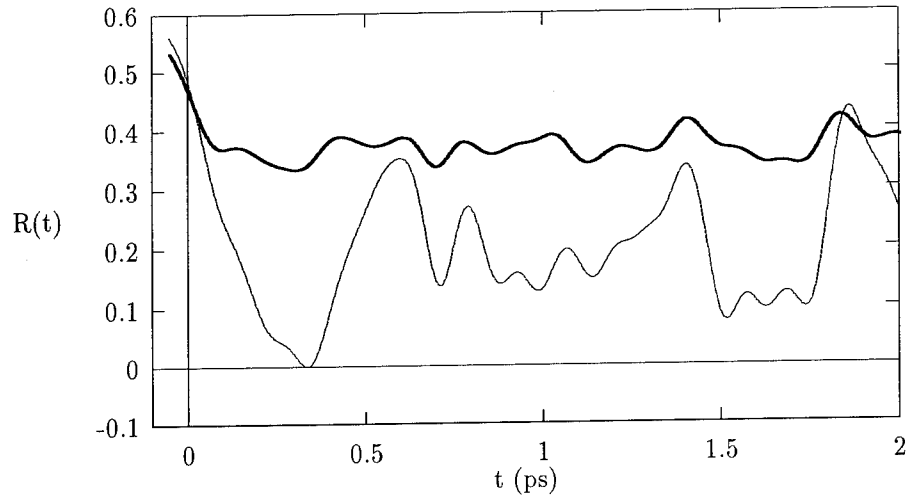


Figure 1. Time-resolved anisotropy calculated for model system described in text above. Upper (thick) curve corresponds to excitation at bare transition frequency of lower-energy chromophore, lower (thin) curve corresponds to excitation 100 cm^{-1} above the bare transition frequency of higher-energy chromophore.

As can be seen in Figure 1, the t = 0 anisotropy is greater than 0.4. The time dependence of the calculated anisotropies reflect both excitation transfer and nuclear dynamics. The anisotropy resulting from lower frequency excitation shows a relatively small amount of decay because the excitation pulse can only weakly populate the excited states of the higher energy chromophore. On the other hand, the anisotropy resulting from higher excitation frequency exhibits large oscillations and a lower overall value, due to efficient excitation of both chromophores. We also find that increasing the response time of the detector has the effect of lowering the initial anisotropy and smoothing out high frequency oscillations (see Figure 2).

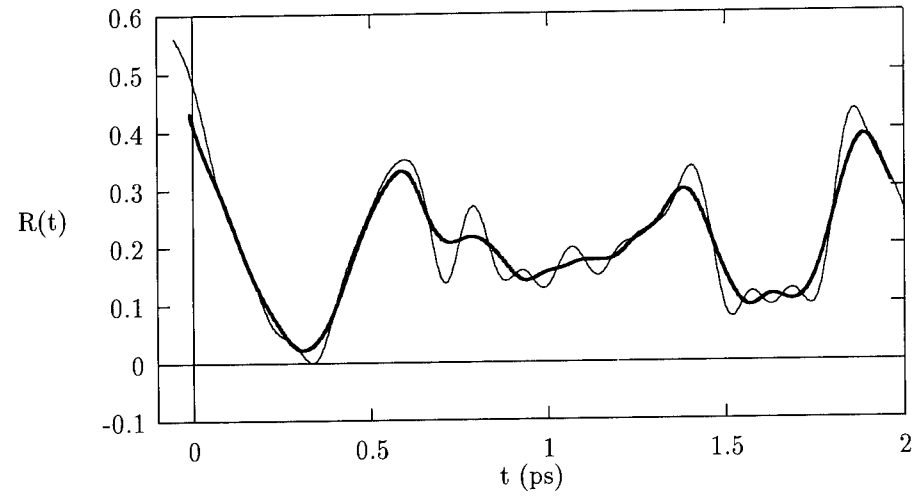


Figure 2. Time-resolved anisotropy corresponding to excitation at 100 cm^{-1} above bare transition frequency of higher-energy chromophore. Thin curve corresponds to time detection window of 70 fs (same as in Fig. 1), and thick curve corresponds to time detection window of 150 fs.

Finally, we examine the effect of vibrational energy relaxation on the time-resolved anisotropy. The intra-chromophore vibrations are coupled to a thermal bath using the Redfield theory of relaxation. It is assumed

that each chromophore is coupled to a statistically independent bath, and detailed balance is enforced in the ad-hoc manner of Jean et al.[4] The anisotropy in Figure 3 calculated with a vibrational relaxation rate of 1.5 ps^{-1}, roughly half of the vibrational period, shows the decay of the oscillations due to the coherences among the excitonic states. After the coherences have decayed, the anisotropy continues to decay due to the thermal equilibration of the populations in the excitonic states. Similar to the vibrationally unrelaxed calculations, excitation at higher frequency leads to a more rapidly decaying anisotropy than excitation at lower frequency.

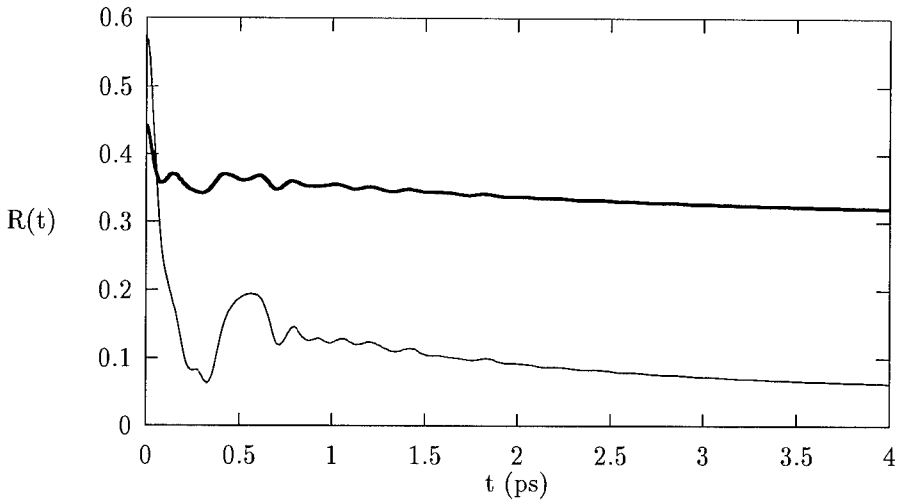


Figure 3. Time-resolved anisotropy calculated with 1.5 ps^{-1} vibrational relaxation rate. Upper (thick) curve corresponds to excitation at bare transition frequency of lower-energy chromophore, lower (thin) curve corresponds to excitation 100cm^{-1} above the bare transition frequency of higher-energy chromophore. This calculation is not valid for times less than 0.15 ps.

References

[1] X. Xie, M. Du, L. Mets and G.R. Fleming, SPIE Vol 1640, Time-Resolved Laser Spectroscopy in Biochemistry III (1992).

[2] K. Wynne and R.M. Hochstrasser, Chem. Phys. **171**, 179 (1993).

[3] K. Sauer and H. Sauer, Biochim. Biophys. Acta., **936**, 157 (1988).

[4] J.M. Jean, R.F. Friesner and G.R. Fleming, J. Chem. Phys. **96**, 5827 (1993).

Excited-State Processes and Photoinduced Antiviral Activity in Hypericin

F. Gai, M. J. Fehr, and J. W. Petrich

Department of Chemistry, Iowa State University; Ames, Iowa 50011, USA
voice: (515) 294-9422; FAX: (515) 294-0105; e-mail: jwp@iastate.edu

Hypericin (Figure 1) is a naturally occurring polycyclic quinone that has received recent notoriety for its antiviral capacity–in particular its ability to deactivate the human immunodeficiency virus (HIV) [1]. The antiviral activity of hypericin requires light [2]. Hypericin is also very closely related, both structurally and spectrally, to the chromophore of the photoreceptor complexes of the protozoan ciliates [3]. Optical excitation of hypericin produces both singlet oxygen [4] and a pH decrease [5] and gives rise to transient species of picosecond duration. The following observations indicate that excited-state, intramolecular proton transfer occurs in hypericin.

1. Immediately upon excitation a transient species is produced whose absorption lies between 620 and 650 nm, depending upon the solvent. In methanol measurement of the decay of this absorbance or of the rise time for the bleaching of the ground-state absorption, which overlaps the spectrum of the newly formed excited state, yields a lifetime of ~5-6 ps [6].

2. The hypericin analog with no hydroxyl groups and hence no intramolecular proton source, mesonaphthobianthrone (Figure 1), provides no absorption or emission in the visible region of the spectrum in aprotic solvents such as DMSO, unlike hypericin. In concentrated sulfuric acid, however, the absorption and emission spectra of the analog are very similar to those of hypericin. We thus interpreted these data in terms of the necessity of protonated carbonyl groups for the production of fluorescence at wavelengths longer than 580 nm. This result indicates that in the ground state, at least one of the carbonyls of hypericin is protonated. This result also suggests the likelihood of excited-state tautomerization in hypericin.

3. The occurrence of excited-state tautomerization in hypericin is verified by the rise time of the stimulated emission signal, which measures the excited-state population. In methanol, the rise time of the stimulated emission is within experimental error identical to the decay of the absorption transient produced upon optical excitation. Another confirmation of the excited-state proton transfer process is that in H_2SO_4 there is no transient with time constant > 1 ps. This indicates that in the ground state the entire population of hypericin is already protonated and does not require an excited-state reaction to produce the long-lived fluorescent species (Figure 2).

In a range of solvents, both hydrogen bonding and nonhydrogen bonding and protic and aprotic, over which the viscosity and the average solvation time change by factors of 60 and 100, respectively, the proton transfer time as measured by the rise time of the stimulated emission is found to be uncorrelated with these properties and to change by at most a factor of two. This result is very surprising when it is considered in the context of other examples of excited-state proton transfer.

For example, 3-hydroxyflavone in hydrogen-bonding solvents such as alcohols the ability of the solvent to weaken or to break the intramolecular hydrogen bond is a determining factor in the excited-state proton transfer reaction [7-10]. The proton transfer time in hypericin ranges from about 6 to 12 ps in the solvents we have investigated and hence is similar to the proton transfer time observed in 3-hydroxyflavone and attributed to solute-solvent structures in which two different alcohol molecules are coordinated to the carbonyl and alcohol groups of the solute [10]. Such a state of solvation cannot, however, explain the proton transfer rates in hypericin because the same results are obtained in both hydrogen-bonding and nonhydrogen-bonding solvents. This suggests that the intramolecular interactions between the O–H•••O group formed by the alcohol oxygen, the proton, and the carbonyl oxygen of hypericin are much stronger than any potential hydrogen bonding interactions with the solvent.

Hynes, Borgis, and coworkers [11] have presented a theory of proton transfer in both adiabatic and

nonadiabatic limits. For a large (> 2.7 Å) separation of the two oxygens between which the proton is transferred, the wavefunction for the proton is localized about one of the oxygens and a sufficiently large barrier exists such that proton transfer must be viewed as a nonadiabatic tunneling process. If, however, the separation is small (< 2.7 Å), the barrier to proton transfer is greatly decreased and the extent to which tunneling contributes to the rate of proton transfer can be greatly reduced. Finally, in reactions that involve the generation of charged or partially charged species, the solvent polarity is expected to accelerate the rate [12].

In the case of hypericin, the distances [13] between the keto and hydroxy oxygens between which the proton is transferred are all consistent with an adiabatic process: i.e., about 2.5 Å. The solvent dependence of the time constant for the excited-state process is also consistent with its assignment to proton transfer. The time constant decreases with increasing solvent polarity, as measured by $E_T(30)$, and suggests a process that involves the transfer of a charged particle, molecular rearrangement, and charge reorganization. Finally, temperature-dependent measurements in ethylene glycol indicate that there is a small barrier (~1.5 kcal/mol) between the "normal" and untautomerized forms. This small barrier is in agreement with the short distances between oxygens in hypericin.

In recent years, photodynamic therapy (PDT) has emerged as a promising tool in both antiviral and cancer chemotherapy. Photodynamic therapy is possible because some photoactive molecules have an affinity for tumor cells. In the presence of light of the appropriate wavelength, the photoactive molecules absorb the light and destroy the viral-infected cells or tumors. A major drawback is that PDT cannot be extended to the regions of the body where light does not penetrate. The development of new therapies for treatment of these tumors is one of the most exciting areas in medical research. Our approach is to combine a chemiluminescent light source with the antiviral agent, hypericin, so that photodynamic therapy can be extended to all regions of the body. We employ a chemical light source that has a broad emission spectrum in the region where the photoactive molecule absorbs. A natural light source is the luciferin molecule. The reaction of luciferin with the enzyme luciferase and molecular oxygen produces light in the 520-680 nm region. Hypericin, our photoactive molecule, absorbs light in the 540-660 nm range. We have demonstrated that hypericin reduces the infectivity of cell-free stocks of equine infectious anemia virus (EIAV), a lentivirus closely related to HIV, by 99.99%. The antiviral activity of hypericin is completely dependent on the presence of light.

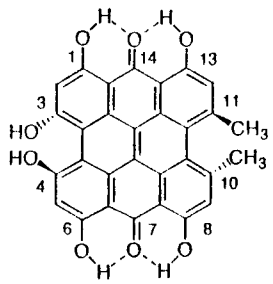
Figure 3 compares the spectrum of the chemiluminescent emission of the luciferase catalyzed oxidation of luciferin and the absorption spectrum of hypericin in the red region of the visible spectrum. The overlap between these spectra indicates (based on Förster theory) that the "critical distance" for energy transfer between these two species is about 100 Å.

Luciferase can be generated using the luciferase gene. We expect to be able to regulate specifically the activation of the light source in order that hypericin is photoactivated only in cells where it is needed. Regulation of luciferase activation will be achieved by regulating the expression of luciferase, which will be under the control of a viral promoter. In this way, replication of the virus will transactivate the viral promoter, resulting in increased expression of luciferase and consequently leading to activation of luciferin and the photoactivation of hypericin. A crucial aspect of this approach is that these events are localized to virus-infected cells, thereby targeting the antiviral activity of hypericin.

REFERENCES

1. Meruelo, D.; Lavie, G.; Lavie, D. *Proc. Natl. Acad. Sci. USA* 1988, **85**, 5230.
2. Carpenter, S.; Kraus, G. A. *Photochem. Photobiol.* 1991, **53**, 169.
3. Tao, N.; Song, P.-S.; Savikhin, S.; Struve, W. S. *J. Phys. Chem.* 1993, 97, 12379.
4. Racinet, H.; Jardon, P.; Gautron, R. *J. Chim. Phys.* 1988, **85**, 971.
5. Song, P.-S.; Walker, E. B.; Auerbach, R. A.; Robinson, G. W. *Biophys. J.* 1981, **35**, 551.
6. Gai, F.; Fehr, M. J.; Petrich, J. W. *J. Am. Chem. Soc.* 1993, **115**, 3384.
7. Strandjord, A. J. G.; Barbara, P. F. *J. Phys. Chem.* 1985, **89**, 2355.
8. McMorrow, D.; Kasha, M. *J. Phys. Chem.* 1984, **88**, 2235.
9. Brucker, G. A.; Kelley, D. F. *J. Phys. Chem.* 1987, **91**, 2856.

10. Schwartz, B. J.; Peteanu, L. A.; Harris, C. B. *J. Phys. Chem.* 1992, **96**, 3591.
11. Borgis, D.; Hynes, J. T. in The Enzyme Catalysis Process, eds. Cooper, A.; Houben, J; Chien, L. Plenum; New York, 1989; p. 293.
12. Keirstead, W. P.; Wilson, K. R.; Hynes, J. T. *J. Chem. Phys.* 1991, **95**, 5256.
13. Etzlstorfer, C.; Falk, H.; Müller, N.; Schmitzberger, W.; Wagner, U. G. *Monatsh. Chem.* 1993, **124**, 731; Falk, H. Personal communication.



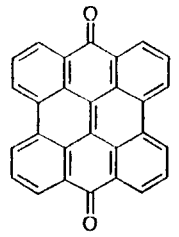


Figure 1. Structures of hypericin and mesonaphthobianthrone.

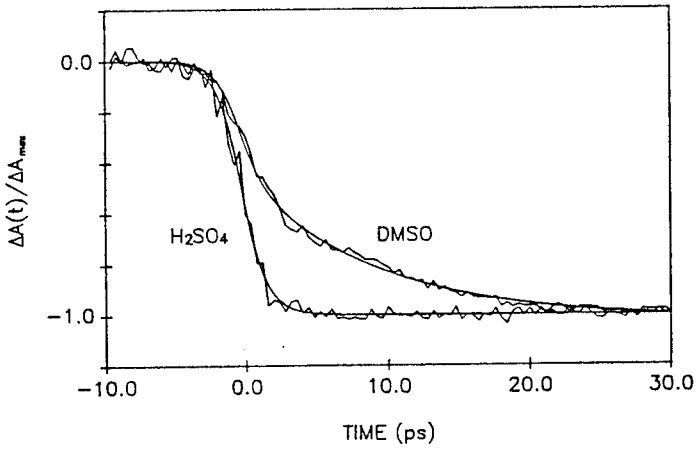


Figure 2. Comparison of the rise time for the formation of excited-state transients as measured by the delay time required to bleach maximally the ground-state absorption [6]. This rise time is finite for hypericin in an aprotic solvent where a portion of the ground-state population is not tautomerized (DMSO). But in a solvent where the entire ground-state population is protonated (H_2SO_4), the rise time is instantaneous. The fits to the data are as follows. DMSO, λ_{probe} = 610 nm: $\Delta A(t) = 0.23\exp(-t/9.6) - 0.41$; H_2SO_4, λ_{probe} = 630 nm: the bleaching of the ground-state absorption is complete within the time resolution afforded by the system and the excited state formed is long-lived on the time scale of the measurement.

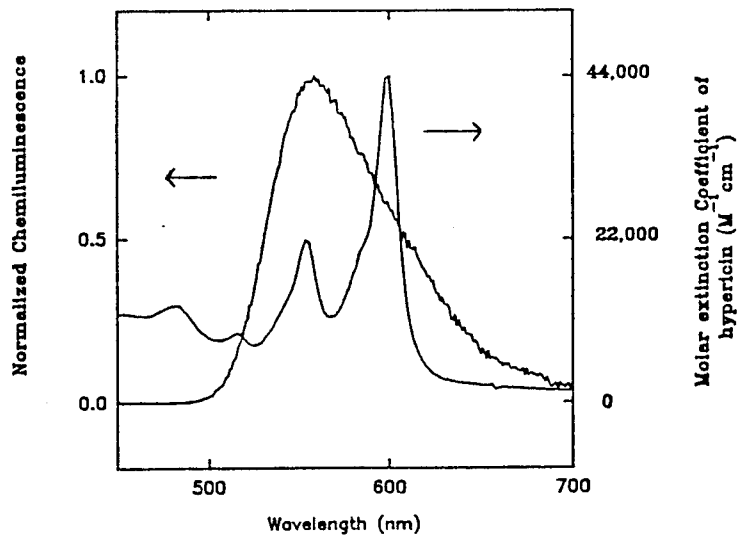


Figure 3. Spectral overlap between luciferin chemiluminescence and the visible absorption of hypericin.

An Efficient Kα X-ray Source from Femtosecond Laser-Produced Plasmas

A. Rousse, P. Audebert, J.P. Geindre, F. Falliès, J.C. Gauthier
Laboratoire pour l'Utilisation des Lasers Intenses, Ecole Polytechnique, 91128 Palaiseau, France
(33) 1 69334112

A. Mysyrowicz, G. Grillon, A. Antonetti
Laboratoire d'Optique Appliquée, Batterie de l'Yvette, ENSTA, 91120 Palaiseau, France
(33) 1 60100318

The generation of intense and ultrafast x-ray pulses is a challenge in the study of unexplored physics of high density and high temperature plasmas [1]. Such plasmas are produced when an intense ultra-short laser pulse (100 fs, $10^{16\text{-}17}$ W/cm^2) is focused on solid targets [2-6]. Laser energy absorbed within the laser skin depth gives rise to a thermal plasma of several hundred electron-volts temperature, close to solid density. Behind the thermal plasma, fast electrons resulting from the specific interaction of the incident laser light through a very steep density gradient [7] eject inner shell electrons of the target plasma. This produces fluorescence line radiation as the inner shell vacancy is filled from outer shells [4, 8].

It was found recently that the use of a corrugated or a rough target surface increases the total laser absorption [9]. In the present experiment, we control the roughness of the target surface by varying the amplified spontaneous emission (ASE) prepulse energy level [10]. A full width at half maximum (FWHM) 100 fs, 1.5 mJ laser pulse is provided by a 10 Hz colliding-pulse mode-locked oscillator followed by a series of dye amplifiers. The laser intensity is $3.x10^{16}$ W/cm^2 on target in a near diffraction-limited focal spot of 50 μm^2 (FWHM). Maximum x-ray conversion is reached in aluminum for an ASE fluence of 0.7 J/cm^2 [10]. This is close to the known damage threshold in this material. The bi-layered targets consist of different film thicknesses of aluminum deposited on SiO_2 and CaF_2 substrates. X-ray lines from the two layers of the target are collected at the same time by a double crystal VonHamos spectrograph built with two curved crystals positioned side by side. PET (2d=8.742Å) or LiF (2d=4.027Å) crystals, having both a 10 cm curvature radius, focused the x-ray lines on a film detector covered by a 25 μm Be filter. The film density is converted to intensity by using the known crystal reflectivity, the filter transmission and the spectrograph geometry.

We have measured the ratio of the Si to Al and Ca to Al Kα lines as a function of the aluminum film thickness. Results were analyzed with the help of a Monte Carlo (MC) simulation of Kα fluorescence emission and electron energy deposition [8]. An absolute calibration of the overall efficiency of our Kα x-ray diagnostic system, including the MC code predictions and the

VonHamos spectrograph and film detector, was obtained by using a monoenergetic electron beam as a Kα generator. A 20 keV electron beam has been focused in a 1 mm focal spot onto pure aluminum, Al/SiO_2 and Al/CaF_2 targets. Absolute X-ray PIN diode measurements of the resulting Kα x-ray emission were compared to the VonHamos spectrograph/film response and to the predicted MC Kα emission. Experiments and calculations were found to be in very good agreement with a systematic uncertainty of less than 50%.

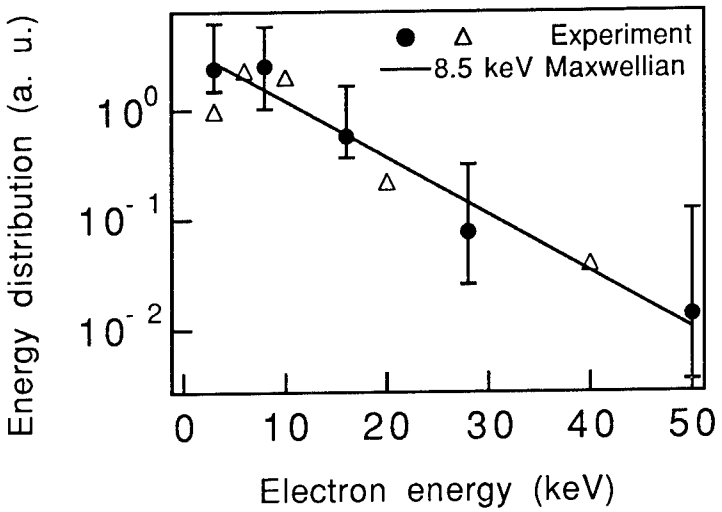


Figure 1. *Electron energy distribution function as a function of electron energy.*

Experimental data, with both CaF_2 and SiO_2 substrates, is well fitted by monoenergetic electron contributions at 3, 8, 16, 28 and 50 keV with corresponding weight factors in energy of 21%, 47%, 23%, 6.9%, and 2.1%. The corresponding energy distribution is shown in Fig.1 with filled circles. To cross-check the validity of our data analysis, we have changed the [3, 8, 16, 28, 50] keV electron energy groups to another set of energy groups, namely [3, 6, 10, 20, 40] keV. Results shown with triangles in Fig.1 agree very well with those obtained with the initial set of electron energies. The data points can be fitted with an exponential function having a slope corresponding to an electron "temperature" of 8.5 keV. The conversion efficiency of incident laser energy into hot electron energy was found to be 12±5 % by adjusting MC calculations of the Al Kα line intensity to our absolutely measured value.

To measure the Kα emission area, we have used a cooled (-40°C) x-ray sensitive CCD detector placed at 20° from target normal. Imaging of the Kα emission region was obtained by a knife edge technique. After deconvolution, we obtained an emitting surface of 95 μm^2, slightly larger than the visible laser focal spot. This gives an electron fluence of 220±50 J/cm^2. This electron beam heats the target bulk to a temperature of 20 eV. This temperature is in very good agreement with our measured intensity ratio of the Al Kα and O-like "shifted" Al Kα. Finally, Fig.2 gives a comparison of the CCD results and MC calculation of the number of photons

emitted per steradian for different target substrates and for an energy of 1 Joule of incident electrons having the energy distribution function shown in Fig.1.

The measured Kα x-ray intensity is about $5.x10^{12}$ W/cm^2. Being produced by highly non-linear effects, the fast electron pulse (and thus the Kα pulse) should not last longer than the duration of the laser pulse. Up to now, the time duration of the whole x-ray pulse has been measured [11] to be less than 2 ps, the ultimate resolution of ultra-fast streak cameras. This ultrafast incoherent x-ray flash can have interesting applications in the study of conformation change kinetics of biological molecules [12] or in photo-ionized x-ray laser schemes [13].

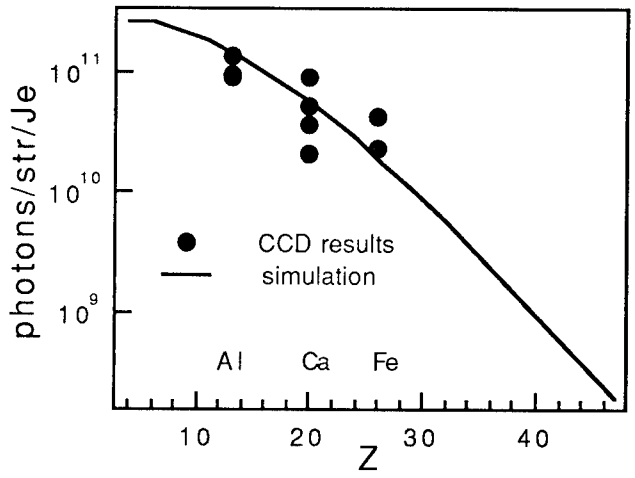


Figure2. *Number of Kα photons emitted per steradian (1J of incident electron energy) as a function of the target substrate material.*
The Kα photon energy is 1.49, 3.69, 6.40 keV for Al, Ca, Fe, respectively.

REFERENCES

1. Murnane, M.M., *et al.*, Science, 1991. **251**: p. 531.
2. Landen, O.L., M. Campbell, and M.D. Perry, Opt.Comm., 1987. **63**: p. 253.
3. Murnane, M.M., *et al.*,, Phys. Rev. Lett, 1989. **62**: p. 155.
4. Audebert, P., *et al.*, Europhys. Lett., 1992. **19**: p. 189.
5. Meyerhofer, D.D., *et al.*, Physics Fluids, 1993. **B5**: p. 2584.
6. Kieffer, J.C., *et al.*, Phys. Fluids, 1993. **B5**: p. 2330.
7. Brunel, Phys. Rev. Letters, 1987. **59**: p. 52.
8. Rousse, A., *et al. Short Wavelength V: Physics with Intense laser pulses Technical Digest.* (Optical Society of America, 1993),pp.40-43.
9. Gordon, S.P., *et al.*, same as Ref. 8, pp. 117-119.
10. Audebert, P., *et al.* . in *AIP Conf. Proc.* **257** (Portland,1991) p. 58.
11. Mens, A., *et al. Ultrafast Phenomena VIII.* **55** (Springer-Verlag,1992) p.147.
12. Eder, D.C., P. Amendt, and S.C. Wilks, Physical Review A, 1992. **45**: p. 6761.
13. Teng, T., H.W. Huang, and G.A. Olah, Biochemistry, 1987. **26**: p. 8066.

Einstein causality in time - resolved intra - atom transverse quantum correlations

A. Aiello, F. De Martini, P. Mataloni and D. Murra

Dipartimento di Fisica, Università "La Sapienza", Piazza A. Moro 2, Roma, 00185 Italy

phone: +39-6-49913525

FAX: +39-6-4463158

We report the first experimental investigation on the long standing, fundamental problem of QED intra-atom quantum correlations [1,2,3]. It is well known that the quantum analysis of the problem of the interacting atoms in free-space, based on a Dicke Hamiltonian, shows an unexpected non causal intra-atom correlation transfer. We show theoretically that the problem is fully resolved by the use of the *complete* hamiltonian, i.e.,including the anti-resonant contribution [4]. However, in spite of the existence of this satisfactory quantum-theoretical approach, the transfer of QED correlations within a single-mode, plane, Casimir microcavity still shows a somewhat puzzling noncausal behavior when the atoms are correlated by transverse interactions, i.e.,taking place in direction parallel to the plane of the cavity and then orthogonal to the **K** - vector of the allowed mode. The "spatial" conterpart of this problem, the establishment of the transverse "size" of the mode, was already investigated by us in an early paper [5]. In that work it was demonstrated that the transverse correlation between two atoms inside a microcavity takes place within the *coherence length* $l_c = 2\lambda(fm)^{1/2}$, where f and m represent the finesse and the order of the microcavity respectively. By the present work, the investigation is carried out to the theoretical, as said, and the experimental analysis of the complete correlation problem in space-time, then fully implying the Einstein causality within the process. The experimental layout is shown in Fig.1. Two equal, mutually delayed, 50 fs, 10 Mw laser pulses generated by an amplified CPM laser are injected and focussed in a region of 15 μm of diameter in an active microcavity with a molecular solution of oxazine - 725 as active medium: the two pulses are then the "pump" of two identical, virtually "thresholdless" microlasers placed at a transverse distance d in the cavity plane, with $d \ll l_c$.

The space-time properties of the quantum coupling taking place between the microlasers determines the shape and the mutual time - delay of the output microlaser sub-picosecond pulses. The generation of sub-picosecond pulses in the microlaser is guaranteed by the instantaneous pumping of the active medium and by the relatively small value of the cavity photon lifetime. As a matter of fact a high value of pumping with respect the threshold energy, which is possible because of the thresholdless behaviour of the microlaser, can reduce strongly the build-up time of the output pulse. This effect contributes to increase

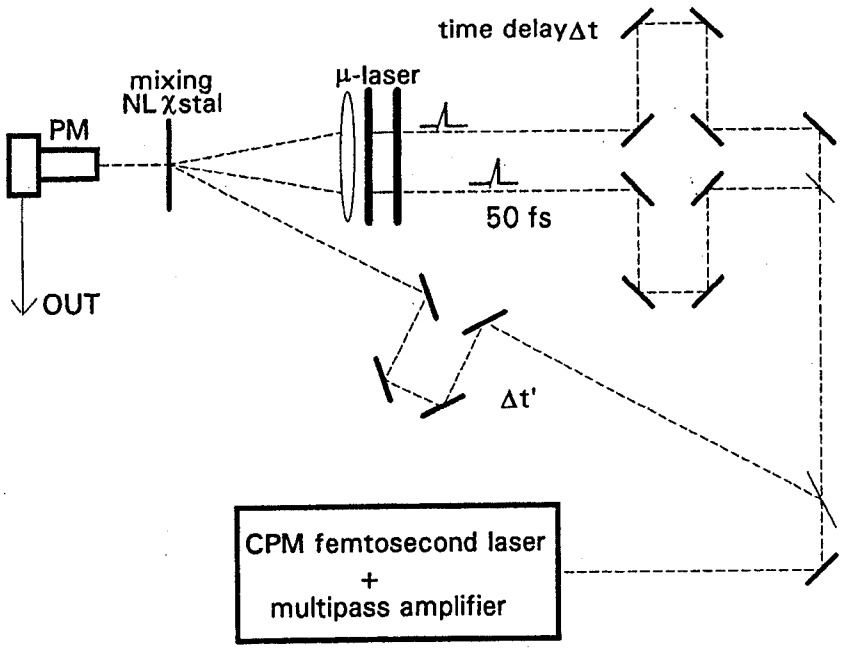


Figure 1: Experimental apparatus.

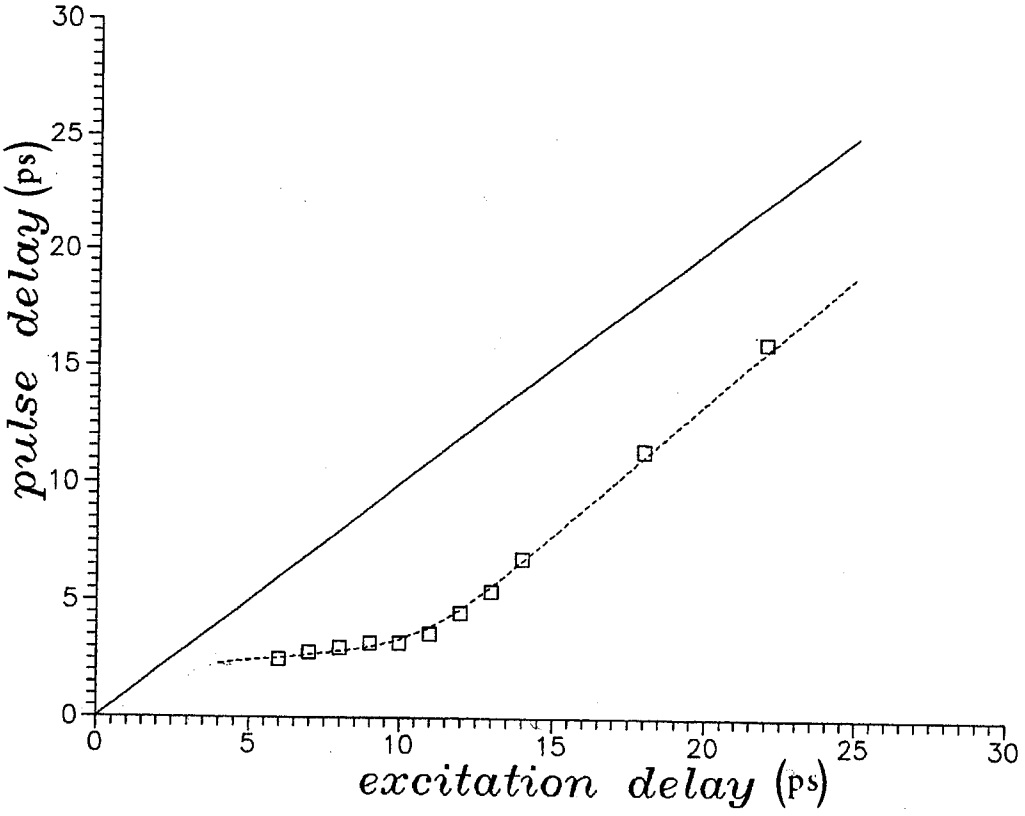


Figure 2: Time delay of the microlaser output pulses vs. delay of the excitation pulses.

the temporal resolution of the experiment. A simple analysis of this problem, based on a rate equation approach, gives a temporal uncertainty $\Delta\tau \simeq 20m(1+2m)/N\Gamma_o$, where N is the number of excited atoms and Γ_o represents the free - space spontaneous emission rate. It is evident that $\Delta\tau$ is independent on f and proportional to m(1+2m) and its value can be of the order of some hundred of femtoseconds. The experiment is performed by measuring the temporal shape of the output pulses of the two microlasers pumped by two delayed femtosecond pulses. These shapes are analyzed by a standard mixing up-conversion technique by beating in a thin KDP slab the microlaser output with an ultrashort pulse supplied by the pumping laser. This is shown in Fig.1. Fig.2 shows the time-delay measaured between the output pulses vs. the delay of the exciting ones for a plane microcavity with m = 26, for a mutual distance between the two microlasers of 50 μm. The linear dependence between the two delays, expressed by the straight in Fig.2, implies a full absence of space - time quantum correlations among the excited atoms. On the other hand the "plateau" of the curve, implying presence of transverse correlations, also gives the transverse "speed" of the intra - atom exchange of excitation.

We found, in agreement with the quantum theory, that the time of excitation-exchange is generally shorter than expected by the standard conception of relativistic causality which, since Einstein, has been nevertheless always related, within the domain of light-signals, to "longitudinal" interactions, i.e., travelling along the corresponding photon **K** - vector. The possible relations of the phenomenon we have discovered, with the superluminal, noncausal quantum correlations taking place in EPR - type experiments is presently under investigation. It is well known that these kinds of quantum correlations do not carry information.

References:

1) T.D. Newton, E.P. Wigner, *Rev. Mod. Phys.* 21, 400 (1949)
2) P.L. Knight, P.W. Milonni, *Phys.Lett. 56 A,* 275 (1976)
3) F.T. Arecchi, E. Courtens, *Phys. Rev. A2,* 1730 (1970)
4) A.K.Biswas, G. Compagno, G.M. Palma, R. Passante, F. Persico, *Phys.Rev. A,* 4291 (1990)
5) F.De Martini, M. Marrocco, D. Murra, *Phys. Rev. Lett.* 65, 1853 (1990)

Nonlinear Plasma Waves Resonantly Driven by Optimized Laser Pulse Trains

D. Umstadter, E. Esarey[1] and J. Kim
Center for Ultrafast Optical Science, University of Michigan, Ann Arbor, MI 48109 (313) 764-2284

The generation of large-amplitude, relativistic plasma waves is a subject of much current interest because of its potential use for ultrahigh gradient electron acceleration [2-5]. While conventional rf-driven accelerators are limited to fields $\leq$ 1 MV/cm, plasma accelerators have been shown experimentally to support gradients $\sim$ 10 MV/cm [5]. The maximum axial electric field of a relativistic plasma wave, as predicted by 1D cold fluid theory, is the "wave-breaking" field [6], $E_{WB} = (m_e c\omega_p/e)\sqrt{2(\gamma_p - 1)}$, which can exceed 1 GV/cm, where $\omega_p = (4\pi e^2 n_{e0}/m_e)^{1/2}$ is the electron plasma frequency, n_{e0} is the ambient electron density, $\gamma_p = (1 - v_p^2/c^2)^{-1/2}$, and v_p is the phase velocity.

Two major types of laser-driven, plasma-based accelerators have been proposed: the plasma beatwave accelerator (PBWA) [3] and the laser wakefield accelerator (LWFA) [4]. In the PBWA, two laser beams of frequencies ω and $\omega - \omega_p$ are optically mixed in a plasma to produce a laser beatwave, in effect a train of equally spaced pulses of equal pulsewidths. The temporal characteristics of the train are neither adjustable nor independent of each other; i.e., the pulse width is proportional to the interpulse spacing. In the LWFA, a single, ultrashort and intense laser pulse [7] drives a plasma wave "wakefield." In both cases, the maximum plasma-wave amplitude results when the pulse spacing and/or pulse width τ are "resonant" with the plasma, or $\tau \sim 2\pi/\omega_p$, where the initial unperturbed density n_{e0} and electron mass are used in ω_p. When a plasma wave grows to large amplitude, however, it becomes nonlinear and both its resonance width and period change. At this point, these schemes begin to loose their efficiency because the laser pulse widths and inter-pulse spacings do not change accordingly, known in the latter case as resonant detuning.

Recently, the self-modulated LWFA has been suggested [8], [9]. Here, a single laser pulse is incident on a plasma with a density that is higher than the "resonant density." Due to a self-modulation instability, the pulse breaks up into multiple pulses, each of which are "resonant." Although higher plasma densities and the high-intensity multiple-pulse structure lead to higher wakefield amplitudes, they are difficult to achieve simultaneously due to plasma defocusing [10].

Additionally, electron acceleration is limited at high n_{e0} by phase detuning, i.e., accelerated electrons (with $v \rightarrow c$) outrun the plasma wave (with $v_p \simeq v_g < c$). The maximum energy gain, ΔW_{max}, of an electron in a 1D sinusoidal plasma wave of amplitude $E_z = \epsilon E_{WB}$ is $\Delta W_{max} \simeq 4ec\epsilon E_{WB}\gamma_p^2/\omega_p$, where $\epsilon \leq 1$ is a constant. Since $\gamma_p \simeq \gamma_g \simeq \omega/\omega_p \gg 1$, $\Delta W_{max} \simeq \epsilon m_e c^2 (2\gamma_g)^{5/2}$. For example, $\Delta W_{max} \simeq 4.5$ GeV, assuming a laser wavelength of $\lambda \simeq 2\pi c/\omega = 1$ μm, $n_{e0} = 10^{18}$ cm^{-3} ($E_{WB} = 7.8$ GV/cm) and $\epsilon = 25\%$. Hence, at the high densities required either for self-modulation or for the use of an ultrashort pulse in the standard LWFA, γ_g is relatively low and acceleration is limited, $\Delta W \sim \epsilon n_{e0}^{-5/4}$.

We propose an alternative accelerator concept, which we call the resonant laser-plasma accelerator (RLPA), that combines the virtues of these other concepts, but has the following additional advantages: (i) by utilizing a train of laser pulses with independently adjustable pulse widths and interpulse spacings, which are varied in an optimized manner, resonance with both the changing plasma-wave period and resonance width can be maintained in the nonlinear regime, and the maximum plasma-wave amplitude is achieved; (ii) lower plasma densities can be used, thus avoiding electron phase detuning; and (iii) lower peak laser intensities can be used, thus allowing for a reduction of laser-plasma instabilities. Berezhiani and Murusidze [11] considered a secondary pulse to enhance or diminish the wakefield. Nakajima [12] considered using a ring resonator, in which the pulse width and interpulse spacing was fixed, to enhance the wakefield. Unlike our treatment, neither of these past studies considered the effects of variation of the plasma-wave resonance widths on the optimal widths of realistic, finite-risetime laser pulses, and the resulting efficiency of large-amplitude plasma wave generation and electron acceleration. Several techniques for producing the optimal train in practice are also suggested.

The maximum normalized electric field, x'_{max}/k_p, for a train of n square pulses of equal amplitudes, is plotted in Fig. 1 versus the quantity $a_T^2 = na_0^2$ [13]. The curves show the result for 1, 3, 5, 10, and 100 pulses.

Figure 2(a) shows an example of an optimized square pulse train ($n = 3$, $a_0 = 1$, $n_{e0} = 10^{15}$ cm^{-3}), in which the widths and spacing between pulses are varied in order to maximize x_{max}. The laser pulses are optimally located in the regions where $d\phi/d\zeta > 0$. When a train that is not optimum is used, for instance fixed interpulse spacings (as in the case of the PBWA), x_{max} reaches some saturated value before being driven down by destructive interference when the pulses become out of phase with the wave, i.e., when they are located in regions where $d\phi/d\zeta < 0$. The plasma wave is driven most effectively near $\phi = \phi_{min}$ and least effectively as $\phi \rightarrow \phi_{max}$.

The above results have assumed square pulses with an infinitesimally short rise time. In practice, the rise time

τ_{rise} of a pulse directly out of a laser is finite and determined by the bandwidth of the laser amplifiers, e.g., currently, the minimum amplified pulse width is $\tau_{min} \simeq 50$ fs. In the following, we will consider pulses with an envelope profile $a(\zeta)$ given by a half-period of a sine function. (Gaussian profiles give qualitatively similar results.)

Figure 2(b) shows an example of a sine pulse train ($n = 4$, $a_0 = 1.2$, $n_{e0} = 10^{16}$ cm^{-3}) that was optimized numerically. The first pulse in Fig. 2(b) has an optimum pulsewidth $\tau = \tau_{opt} = 940$ fs (resonant with $n_{e0} = 10^{16}$ cm^{-3} and $a_0 = 1.2$) and the final pulse has $\tau = \tau_{opt} = \tau_{min} \simeq 50$ fs, which gives $E_z = 0.34$ GV/cm ($\epsilon = 0.14$). As in the square wave case, λ_{N_n} and thus the spacing between pulses, increases with each succeeding pulse as x_{max} increases.

Just a few optimized sine pulses are far more efficient than a single pulse. Specifically, 19 times higher intensity ($a_0 = 5.2$, or $I = 7.3 \times 10^{19}$ W/cm^2 [14]), corresponding to 6 times more energy ($I\tau_{tot} = 32$ MJ/cm^2), is required of a single pulse ($\tau = \tau_{opt} = 450$ fs for $n_{e0} = 10^{16}$ cm^{-3}) to reach the same value of E_z (0.34 GV/cm) as the train of Fig. 2(b). A single pulse with the same intensity and pulse width as the first pulse in Fig. 2(b), corresponding to 2/3 the laser energy ($I\tau_{tot} = 3.6$ MJ/cm^2), results in a 7.7 times smaller E_z (44 MV/cm). Reducing the intensity required to reach large plasma-wave amplitudes also reduces strongly-driven instabilities, such as stimulated Raman scattering, self-focusing or filamentation, which disrupt either the plasma wave or the laser beam

There are several ways of producing the required pulse train in practice. The first is to use Fourier filtering. In this case, a mask is placed in the pulse stretcher of a chirped pulse amplification system [7] to modulate the beam in such a way that, when it is recompressed, a series of pulses with arbitrary spacings and widths will be produced [15]. The minimum rise time of each individual pulse is still governed by the gain bandwidth of the amplifiers. The second possibility is to use several separate compressors with adjustable lengths and delays.

Proof-of-Principle experiments are currently underway at our lab to test the RLPA concept, in which Thomson scattering of a synchronized probe beam is being used to diagnose the amplitude of the relativistic plasma wave.

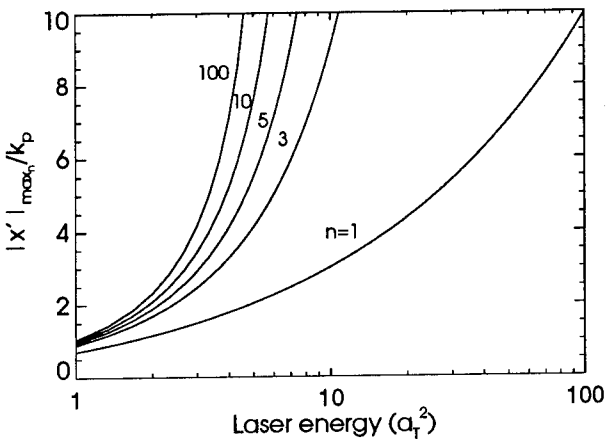


FIG. 1. The maximum electric field (x'_{max_n}/k_p) vs the quantity a_T^2 for n =1, 3, 5, 10 and 100.

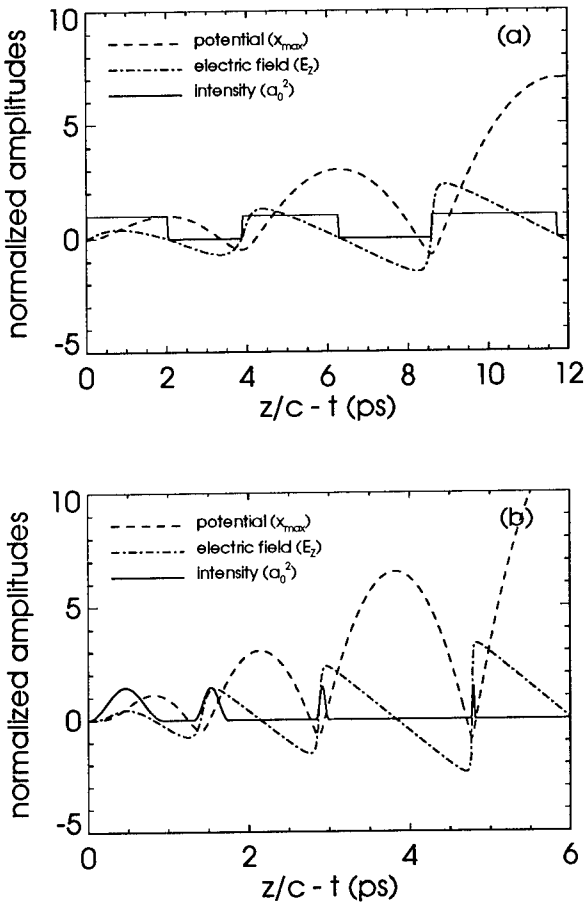


FIG. 2. Numerical solutions for optimized pulse trains: (a) square pulses at $n_e = 10^{15}$ cm^{-3} with $a_0^2 \simeq 1$, and (b) sine pulses at $n_e = 10^{16}$ cm^{-3} with $a_0 = 1.2$.

[1] The home institution of Eric Esarey is: Beam Physics Branch, Naval Research Laboratory, Washington, DC 20375 (202) 404-7720.

[2] See, *e.g., Advanced Accelerator Concepts*, ed. by J.S. Wurtele, AIP Conf. Proc. **279** (American Institute of Physics, New York, 1993).

[3] T. Tajima and J.M. Dawson, Phys. Rev. Lett. **43**, 267 (1979).

[4] L.M. Gorbunov and V.I. Kirsanov, Sov. Phys. JETP **66**, 290 (1987); P. Sprangle, et al., Appl. Phys. Lett. **53**, 2146 (1988).

[5] C. Clayton, et al., Phys. Rev. Lett. **54**, 2343 (1985); Y. Kitigawa, et al., Phys. Rev. Lett. **68**, 48 (1992); F. Amiranoff, et al., Phys. Rev. Lett. **68**, 3710 (1992).

[6] A.I. Akhiezer and R.V. Polovin, Sov. Phys. JETP **3**, 696 (1956).

[7] P. Maine, et al., IEEE J. Quant. Electron. **24**, 398 (1988); G. Mourou and D. Umstadter, Phys. Fluids B **4**, 2315 (1992).

[8] P. Sprangle, et al., Phys. Rev. Lett. **69**, 2200 (1992); J. Krall, et al., Phys. Rev. E **48**, 2157 (1993); E. Esarey, et al., Phys. Fluids B **5**, 2690 (1993).

[9] N.E. Andreev, et al., JETP Lett. **55**, 571 (1992); T. Antonsen, Jr. and P. Mora, Phys. Rev. Lett. **69**, 2204 (1992).

[10] W.P. Leemans, et al., Phys. Rev. A **46**, 1091 (1992); P. Monot, et al., J. Opt. Soc. Am. B, 1579 (1992).

[11] V.I. Berezhiani and I.G. Murusidze, Physica Scripta **45**, 87 (1992).

[12] K. Nakajima, Phys. Rev. A, **45**, 1149 (1992).

[13] In the limits $x^2 \ll x_{WB}^2$ and n small, $a_T^2 = na_0^2$ represents the total energy in the pulse train.

[14] This value, $I = 7.3 \times 10^{19}$ W/cm^2, exceeds by an order of magnitude what is the highest achievable with current laser technology, $I = 5.0 \times 10^{18}$ W/cm^2.

[15] A.M. Weiner, et al., IEEE J. Quant. Electron. **28**, 908 (1992).

Use of Monolithic Tunable Laser Diodes for Chirped Pulse Amplification in Fiber Amplifiers

A. Galvanauskas, M. E. Fermann and D. Harter

IMRA America, Inc.
1044 Woodridge Avenue
Ann Arbor, Michigan 48105
Phone: (313) 930-2560
Fax: (313) 930-9957

Here we study the use of tunable three-section distributed-Bragg-reflector (DBR) diode lasers as pulse sources for chirped pulse amplification (CPA) in a fiber amplifier. The broad continuous-tuning range of the laser allows the generation of nanosecond linearly chirped pulses, which are amplified in a fiber amplifier up to microjoule energies and then compressed to transform-limited subpicosecond duration. The energy of these ultrashort pulses is more than two orders of magnitude higher than any previously reported energies from a compact diode laser and fiber source.

The key of chirped pulse amplification is that long pulses with sufficiently low peak powers are amplified to avoid the distortions caused by nonlinear effects in the amplifying medium [1]. Long positively chirped pulses can be obtained by fast tuning of the emission wavelength of a DBR laser [2]. This structure contains a gain section, a phase-control section and a Bragg reflector section. The wavelength can be shifted continuously by introducing simultaneously changes in the refractive indices of the Bragg and the phase-control sections. An increase in free-carrier concentration lowers the refractive index and shortens the wavelength. By applying current pulses with sufficiently short rise times and properly chosen magnitudes to the tuning sections linear wavelength-shifts can be attained [3].

We studied the generation of linearly chirped pulses for CPA experimentally and theoretically. Numerical investigations of the carrier dynamics in the tuning sections were based on the carrier rate equation. We analyzed linearity, bandwidth and the duration of the linearly chirped pulses, which are critical for undistorted amplification and compression using CPA. Wavelength evolution of the fast-tuned DBR laser diodes was characterized experimentally using a monochromator and an ultrafast streak camera. In Fig. 1 two spectrally resolved streak-camera images of wavelength-tuned pulses from a DBR laser are shown. Mode jumps are present (Fig. 1(a)) when only the Bragg section was used for tuning. Smooth wavelength evolution was attained (Fig 1(b)) when both tuning sections were employed. The characteristic feature here is the linear wavelength decrease during the tuning pulse. The pulse bandwidth was 10 nm.

Numerical simulations show that after the current pulse was applied to a tuning section the carrier concentration increase is linear and starts to saturate after a few hundred picoseconds after the beginning of the tuning pulse. The spectral extent of the chirp increases with the magnitude of the tuning pulses. For low tuning currents this simple numerical model corresponds well to the experimental results. The saturation was clearly seen in the experimentally measured wavelength shift. However, at higher tuning

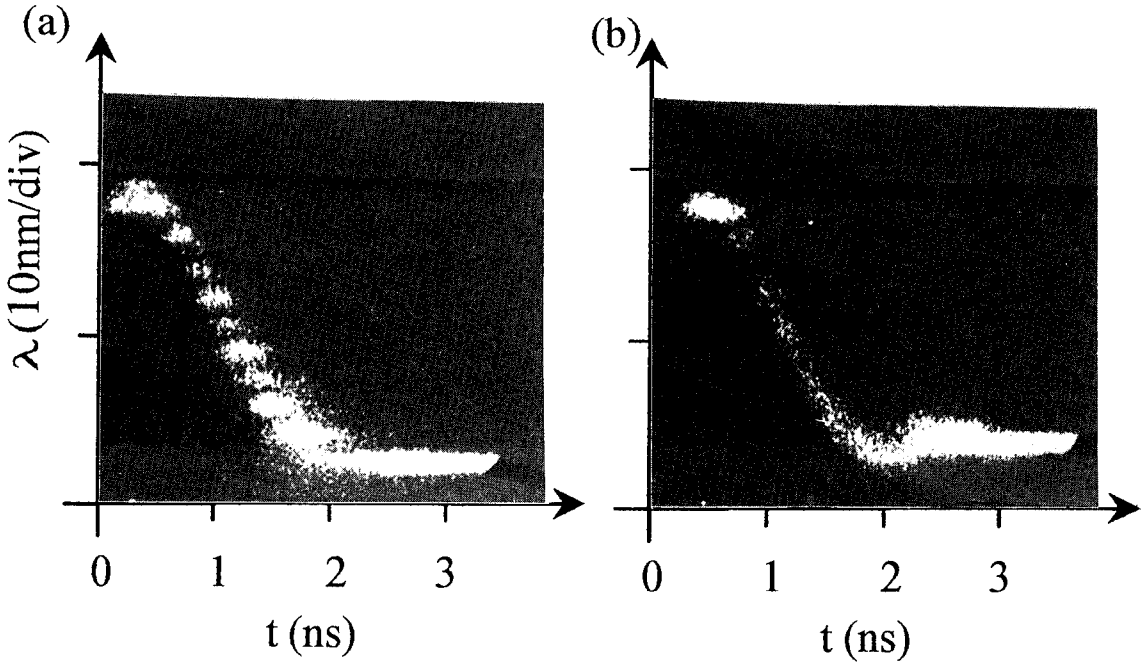


Fig. 1 Measured wavelength shift of a DBR diode laser when (a) only Bragg section is used for tuning and (b) both tuning sections are used. Wavelength shift ant time scales are shown. Tuning pulses were slightly delayed with respect to the gain pulse.

currents this sublinear wavelength shift disappears and emission wavelength becomes "clamped" after the maximum shift of about 10 nm (Fig. 1). This cannot be explained only by the effect of carrier recombination and this indicates the presence of some limiting processes in the diode structure (possibly in the blocking structure). The study of this phenomenon is under progress.

As a result of our studies we found that this fast-tuning technique has a number of properties that makes it uniquely attractive for attaining high-energy ultrashort pulses. The chirped pulses from a DBR diode laser have sufficient linearity and bandwidth for attaining femtosecond transform-limited compressed pulses [3]. The tuning range of these InGaAsP/InP devices is typically within the gain band of erbium-doped fiber amplifiers (EDFA). The duration (as well as the bandwidth) of the chirped pulses is electrically controllable from about 200 ps to 2 ns. Hence even at μJ energies in the amplifier, the peak power of the pulses remains sufficiently low.

The experimental set-up for chirped pulse amplification in a fiber amplifier is shown in Fig. 2. It consists of a DBR laser diode, cascaded EDFA with an optical gate between the two stages and a diffraction-grating compressor. The amplifier was pumped with two diode lasers with 1.48 μm and 980 nm pump wavelengths. Pump powers were respectively 70 mW and 900 mW. At the repetition rate of 10 kHz pulses from the tunable diode laser were amplified from 25 pJ up to 2 μJ (total gain of 49 dB). As an optical gate a fast digital acousto-optic modulator was used. The gate width was 150 ns and the diffraction efficiency of the modulator for this gate width was 70 %. Preliminary, the

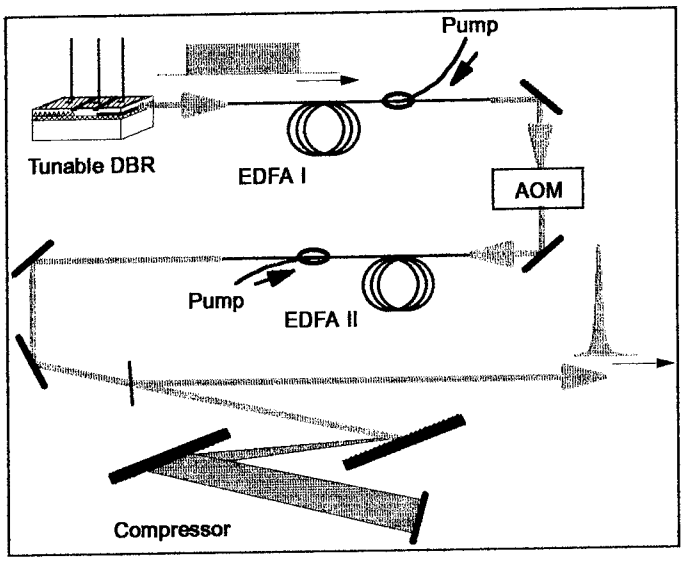


Fig. 2 Experimental set-up

compression of amplified pulses resulted in 1.8 ps pulses with 800 nJ of remaining energy. Considerable improvement in pulse duration and remaining energy is expected.

The important limitation on the energy of the amplified pulses is set by stimulated Raman scattering. At microjoule energies and nanosecond duration the amplified pulse peak powers reach the kW level. After propagating several meters in an optical fiber the spectrum of such pulses is considerably broadened to the Stokes side (up to 150 nm) and most of the pulse energy is removed from the linearly chirped part. To prevent this, in the final stage of the cascaded EDFA we used a short length (3.2 m) of a highly doped (5000 ppm) erbium-doped fiber. Less than 2 % of the total pulse energy was in the Raman component.

We believe that this technique will open the way for a new compact high-power ultrafast technology. The laser diode can be operated both in a single-pulse mode and with variable repetition rates up to tens of MHz. It is monolithic and does not exhibit the stability problems that are usual in modelocked sources. Therefore, such highly reliable semiconductor-lasers and fiber source can boost many practical applications of ultrafast techniques.

References

1. D. Strickland and G. Mourou, *Opt. Commun.* **56**, 219 (1985)

2. A. Galvanauskas, A. Krotkus, J. A. Tellefsen, M. Öberg, and B. Broberg, *Appl. Phys. Lett.* **60**, 145 (1992)

3. A. Galvanauskas, P. Blixt, and J. A. Tellefsen, *Appl. Phys. Lett.* **63**, 1742 (1993)

Femtosecond Spectroscopy of Nonadiabatic Photoisomerization Processes: Semiclassical Modelling

Gerhard Stock, Luis Seidner, and Wolfgang Domcke
Institut für Physikalische und Theoretische Chemie,
Technische Universität München, D-85748 Garching, Germany
phone: 089-3209-3450 e-mail: stock@pico.phys.chemie.tu-muenchen.de

The *cis-trans* isomerization in photo-excited polyenes represents a fundamental type of photoreaction which, despite of considerable experimental and theoretical efforts, is still not very well understood in many aspects [1]. Structureless absorption bands and the absence of detectable fluorescence have hampered standard spectroscopic investigations, so that even for the smallest systems as ethylene and butadiene the relaxation pathways (i.e. the involved electronic states and nuclear degrees of freedom) and corresponding timescales are not yet clear.

As an illustration, Fig. 1a shows *diabatic* model potential-energy surfaces (PESs) of the ground and first excited electronic states as a function of the torsional coordinate ϕ (of periodicity π) and a harmonic nontotally symmetric coordinate Q_c. It is seen that the two electronic states interchange upon torsion, i.e. the upper electronic state for $\phi = 0$ becomes the lower electronic state for $\phi = \pi/2$. The nontotally symmetric mode Q_c couples the two electronic states. As a result of this coupling, the corresponding *adiabatic* PESs (Fig. 1b) exhibit two conical intersections, representing a simple example of a "photochemical funnel" [1]. Preparing initially a wave packet in the Franck-Condon region of the excited PES (e.g. by by an ultrashort laser pulse), it is generally believed that the system relaxes through these conical intersections into the adiabatic electronic ground state on a femto- or picosecond timescale [1].

Fig. 1a diabatic potentials

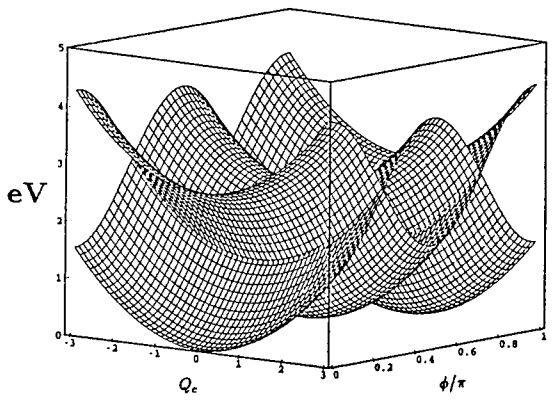
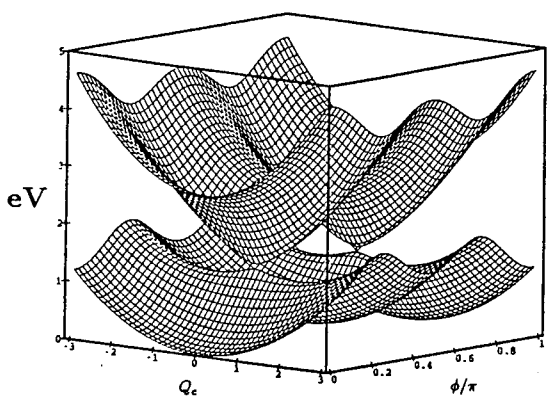


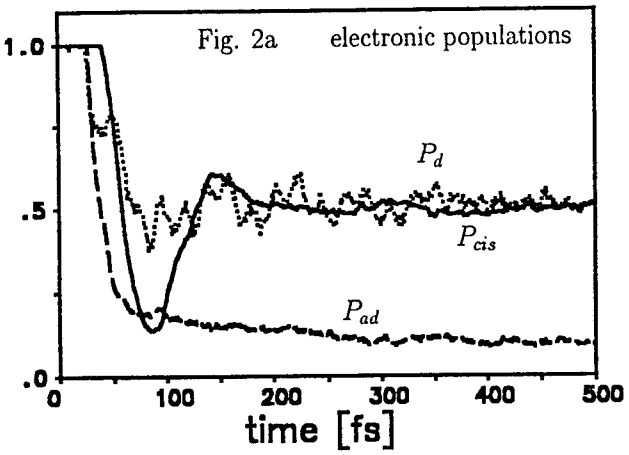
Fig. 1b adiabatic potentials

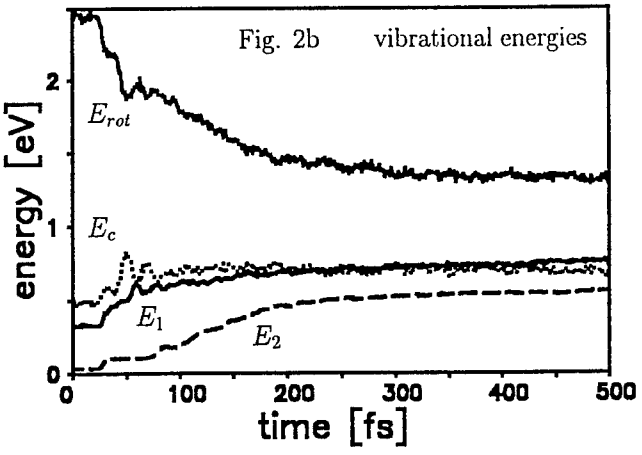


The goal of this work is to outline a semiclassical approach using the classical electron analog [2] to model the electronic and vibrational relaxation dynamics of photo-induced *cis-trans* isomerization in a truly microscopic manner. In particular, we want to explore the possibility of real-time monitoring of these femtosecond relaxation processes.

The classical electron analog model due to Meyer and Miller [2] is a classical path method that treats both electronic and nuclear degrees of fredom on an equal dynamical footing, and has been successfully applied to a variety of model problems [3]. In particular, it has been shown to describe surprisingly reliably the relaxation dynamics of strongly vibronically coupled systems [4, 5]. Recently, a general formulation of the spectroscopy of nonadiabatic excited-state dynamics has been developed in the framework of the classical electron analog formalism [6] and applied to the description of femtosecond pump-probe experiments. [5, 6] For the present example we have adopted an electronic two-state model and included the torsional mode ϕ, the nontotally symmetric coupling mode Q_c, and two totally symmetric Condon-active modes Q_1 and Q_2. (Other examples considered in our computational studies include up to 5 coupled electronic states and up to $\approx$ 20 vibrational degrees of fredom.)

Fig. 2a illustrates the electronic relaxation dynamics of the four-mode model during the first 500 femtoseconds after impulsive electronic excitation by an ultrashort laser pulse. The dotted line represents the *diabatic* electronic population probability $P_d(t)$ (i.e., the probability to be in the electronic state which is the upper state for $\phi = 0$, c.f. Fig. 1a). The dashed line corresponds to the *adiabatic* electronic population probability $P_{ad}(t)$ (i.e., the probability to be in the upper adiabatic electronic state, c.f. Fig. 1b), and the full line represents the probability $P_{cis}(t)$ that the wave packet is in the initially excited *cis* conformation. It is seen that the electronic relaxation is almost completed after $\approx$ 200 fs, leaving $P_d(t)$ and $P_{cis}(t)$ fluctuating around their long-time limit of ≈ 0.5, while the adiabatic population $P_{ad}(t)$ approaches a value of ≈ 0.2. To illustrate the vibrational relaxation dynamics, Fig. 2b shows the time-dependent energy content of the torsional mode (E_{rot}), the coupling mode (E_c), and the two Condon-active modes (E_1, E_2). It is seen that the vibrational energy of the torsional mode is redistributed into the the other vibrational degrees of freedom. It can be shown that the inclusion of further weakly-coupling modes slowly equilibrates the vibrational energies and eventually reduces the the adiabatic population $P_{ad}(t)$ to zero. The semiclassical method has been checked against quantum mechanical calculations and found to give only minor deviations from the exact results.

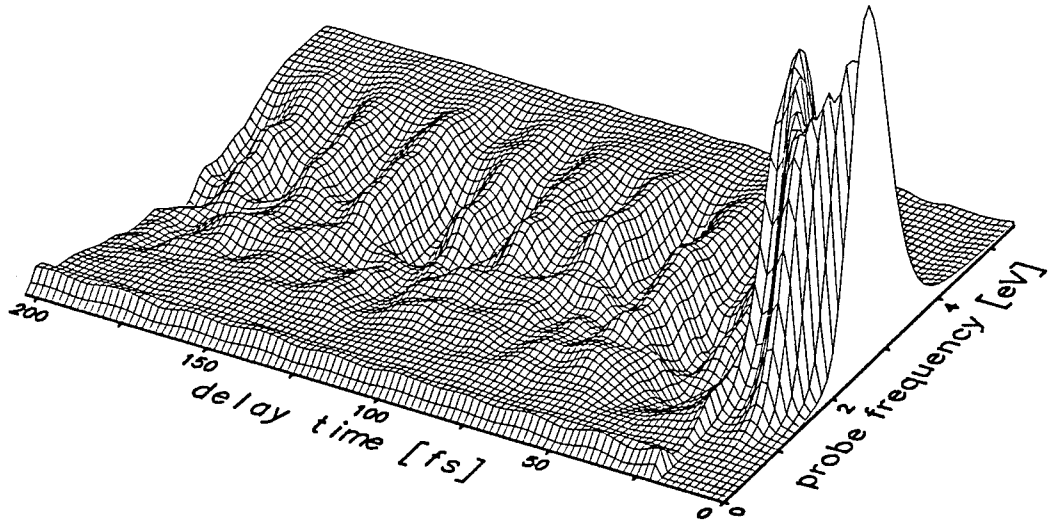




Femtosecond pump-probe spectrocopy of rhodopsin [7] and stilbene [8, 9] have shown that the *cis-trans* isomerization dynamics is reflected in complex transient spectra, which are difficult to relate to microscopic quantities. A major goal of our computational studies is therefore to investigate to what extent and under which experimental conditions (e.g.,

wavelength and duration of the pulses) the time-dependent intramolecular observables introduced above (cf. Fig. 2) may be measured in a realistic pump-probe experiment. Assuming impulsive excitation and a Gaussian probe pulse of 10 fs duration, Fig. 3 shows the time- and frequency-resolved pump-probe spectrum of the four-mode model. The pump-probe signal turns out to be rather complicated. It results from both emission from the upper diabatic electronic state and absorption from the lower diabatic electronic state as a consequence of the ultrafast interchange of the diabatic states upon torsion. An analysis of the pump-probe spectrum in terms of time-dependent intramolecular observables (as shown in Fig. 2) will be presented. The simulations clearly demonstrate that femtosecond time- and frequency-resolved pump-probe spectrocopy of small polyenes has the potential to provide novel information on the ultrafast nonadiabatic isomerization processes in these systems.

Fig. 3 pump-probe spectrum



References

[1] J. Michl and V. Bonačič-Koutecký, *Electronic Aspects of Organic Photochemistry*, (Wiley, New York, 1990).

[2] H.-D. Meyer and W. H. Miller, J. Chem. Phys. **70**, 3214 (1979).

[3] See references in [4-6].

[4] H.-D. Meyer, Chem. Phys. **82**, 199 (1983).

[5] G. Stock and W. H. Miller, Chem. Phys. Lett. **197**, 396 (1992).

[6] G. Stock and W. H. Miller, J. Chem. Phys. **99**, 1545 (1993).

[7] R. W. Schoenlein, R. A. Peteanu, R. A. Mathies, and C. V. Shank, Science **254**, 412 (1991).

[8] S. Petersen, L. Bañares, and A. H. Zewail, J. Chem. Phys. **97**, 8801 (1992).

[9] R. J. Sension, S. T. Repinec, A. Z. Szarka, and R. M. Hochstrasser, J. Chem. Phys. **98**, 6291 (1993).

Panel Discussion: Coherent Control?

WD 9:00pm–10:00pm
Dana Point Ballroom

Ahmed H. Zewail, *Presider*
California Institute of Technology

Coherent Control?

Panel Speakers

Kent Wilson, *University of California, San Diego*

Warren Warren, *Princeton University*

Keith Nelson, *Massachusetts Institute of Technology*

Panel Discussion: New Frontiers in Ultrafast

WE 10:00pm–11:00pm
Dana Point Ballroom

Gerard A. Mourou, *Presider*
University of Michigan

New Frontiers in Ultrafast

Panel Speakers

C.V. Shank, *Lawrence Berkeley Laboratories*

M. Campbell, *Lawrence Livermore National Laboratory*

P. Sprangle, *U.S. Naval Research Laboratory*

High Intensity

ThA 8:30am–10:00am
Dana Point Ballroom

M. C. Downer, *Presider*
University of Texas at Austin

Physics of solid density plasmas at 10^{18}-10^{19} W/cm^2

J.C. Kieffer, Z. Jiang, M. Chaker, C.Y. Côté, J.F. Pelletier

Y. Beaudoin, H. Pépin

INRS-Énergie et Matériaux, Varennes, Québec

G. Korn, C.Y. Chien, S. Coe

CUOS, Univ. of Michigan, U.S.A.

O. Peyrusse

CEA Limeil, Villeneuve St-Georges, France

Experiments were carried out with a table top terawatt laser system which employs the chirped pulse amplification technique [1]. The laser was delivering up to 2 J on targets in a 400 fs pulse at the wavelength of 1.053 μm. High contrast pulses have been obtained by frequency doubling (0.53 μm) the laser pulse using KDP crystals. Very high conversion efficiencies have been obtained [2] and the pulses have been focused with off axis parabola to intensities up to 4 x 10^{18} W/cm^2 ($I\lambda^2 = 10^{18}$ W μm^2/cm^2 for green irradiation). At these intensities relativistic effects and ponderomotive pressure [3] are important issues for the interaction.

Various target geometries have been irradiated with 1 μm (with prepulse) and 0.5 μm (prepulse free) pulses. We present also experiments with two 0.5 μm colinear pulses to study the interaction in a controled gradient scale length. Results obtained with various diagnostics [4] [5] (including high resolution spectroscopy, polarization spectroscopy) will be presented and discussed. A particular emphasis will be put on analysis of prepulse free experiments which are

the first of this kind at $I\lambda^2 = 10^{18}$ W $\mu m^2/cm^2$ and which indicate that solid density plasma are produced.

References

[1] P. Maine et al., IEEE J. Quantum Electr. 24, 398 (1988).

[2] G. Korn et al., this conference.

[3] X. Liu and D. Umstadter, Phys. Rev. Lett. 69, 1935 (1992).

[4] J.C. Kieffer et al., Phys. Fluids B5, 2676 (1993).

[5] J.C. Kieffer et al., Phys. Rev. E. 48, 4648 (1993).

Electron Energies In Plasmas Produced by High Intensity Optical Ionization

T. E. Glover, T. D. Donnelly, E. A. Lipman, A. Sullivan and R. W. Falcone

Department of Physics, University of California at Berkeley, Berkeley, California 94720 (510-642-8916)

J. C. Crane and M. D. Perry

Lawrence Livermore National Laboratory, University of California, Livermore, California 94550

Recently, several authors have proposed that x-ray lasers pumped by electron-ion recombination are feasible if cold electrons can be produced from the interaction of a high-intensity laser pulse with a gas sample [1]. Burnett and Corkum [2] have used a model based on tunneling ionization to predict that cold electrons can be produced from such an interaction. Initial experimental tests of such a prediction yielded conflicting results [2,3]. Measurements [4] have not previously been performed simultaneously at high density (where additional heating mechanisms can operate [5]) and on sub-picosecond time-scales relevant to transient recombination lasers [1].

In this work we use Thomson scattering and radiative recombination to measure electron energies at gas densities and time-scales relevant to transient recombination lasers. Our Thomson scattering experiments represent the first sub-picosecond temperature measurements of plasmas ionized by high-intensity optical ionization. While Thomson scattering is well suited to measuring temperature, it does not reveal the electron energy *distribution*. Recombination laser proposals [1] generally assume a Maxwellian distribution of electrons but this assumption has not been experimentally justified. Our recombination experiments constitute the first measurements of electron energy *distributions* in plasmas of interest to recent recombination x-ray laser schemes [1].

Thomson scattering experiments were performed in He using a two-pulse technique. An initial (125 fs, 2×10^{17} W/cm^2) laser pulse at 800 nm ionized the He gas and a second sub-picosecond pulse at 400 nm probed the preformed plasma.

Thomson spectra were taken at pressures ranging from 3 - 75 torr. A representative spectrum taken at 50 torr is shown in Fig. 1. The data has been fit to a theoretical Thomson spectrum (for He^{2+}) convolved with the response of the spectrometer and the probe laser spectrum. We obtain an electron temperature of 40 eV. While our fit to the short wavelength side of the data in Fig. 2 is good, an asymmetry results from stimulated Raman scattering (SRS) at long wavelengths. Our measured electron temperature (as given by the

short wavelength electron feature) is unaffected by the presence of SRS, in agreement with calculation [6].

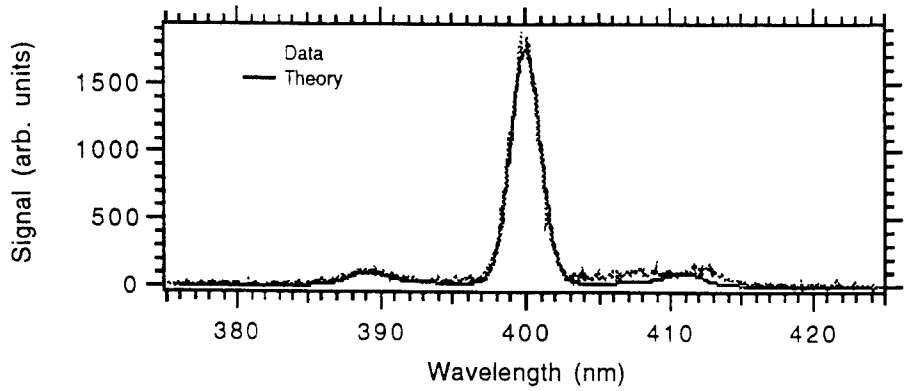


Figure 1. Thomson scattering spectrum from 50 Torr of doubly ionized He. The theoretical curve is for 50 torr of doubly ionized He at an electron temperature of 40 eV and an ion temperature of 3 eV.

We experimentally determined that plasma cooling was insignificant by varying the pump - probe delay. Additionally, the measured electron temperature did not change over a 3 to 75 torr pressure variation; this is consistent with calculations that show that electron heating is dominated by tunneling ionization. The predicted temperature is 40 eV, in good agreement with measurement. This agreement is in contrast to experiments at low density [3] which indicate that the tunneling model underestimates electron energies.

The central scattering feature, called the "ion feature," at 400 nm in Fig. 1 provides information on the ion temperature. Our data indicates that the ion temperature ranges from 0.5 eV at 3 torr, to 5 eV at 75 torr. These temperatures are consistent with heating expected from ion-ion inverse bremsstrahlung over the duration of our laser pulse.

We also measured radiative recombination spectra in He^{2+} and Ne^{8+} plasmas. Neon experiments were performed at 526 nm and 1.05 μm using 800 fs pulses focused to 5×10^{17} W/cm^2. The He experiments were performed using 616 nm, linearly and circularly polarized, 160 fs pulses focused to 2×10^{16} W/cm^2. XUV fluorescence was spectrally and temporally resolved on picosecond timescales.

The initial distribution of electron energies obtained from the He^{2+} plasma with linearly polarized pulses is shown in Fig. 2. The data has been best fit to a Maxwellian distribution of 20 eV. The average energy in the measured distribution is 30 eV. The average energy expected from the tunneling model is 32 eV, implying good agreement with the tunneling model. The measured distribution, however, exhibits a deficit of low energy electrons in comparison to both tunneling and Maxwellian distributions. This result is in contrast to earlier measurements in He [3] performed at low gas density which show good agreement between the measured distribution and a Maxwellian distribution. At late times

(Fig. 3), our measured distribution cools and thermalizes so that the agreement between the measured distribution and a Maxwellian distribution is good at late times .

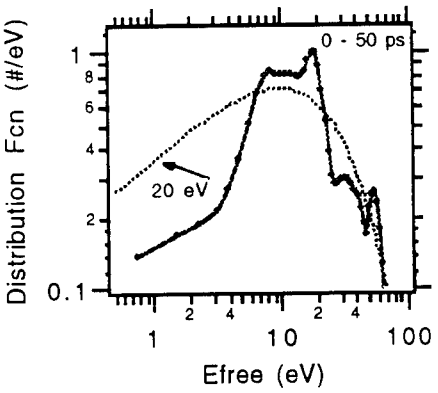


Figure 2. Measured initial distribution of electron energies from He^{2+}. Also shown is a Maxwellian of KT = 20 eV.

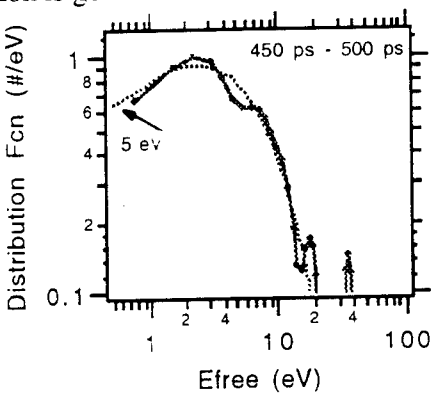


Figure 3. Late - time distribution of electron energies from He^{2+}. Also shown is a Maxwellian of KT = 5 eV.

The discrepancy between our initial He distribution measured at high density and the He distribution measured at low density [3] may be due to stimulated electron-ion recombination and re-ionization during the laser pulse. At high gas density, stimulated electron-ion recombination may modify the tunneling electron distribution; this process has not yet been investigated. Electrons which have been stimulated by a strong laser field to recombine to upper Rydberg states in an ion can be ionized before the peak of the optical cycle, resulting in heating which may explain our observed deficit of low energy electrons.

In summary, we used Thomson scattering and radiative recombination to measure electron energies in plasmas produced by high intensity optical ionization. The average electron energies are in good agreement with predictions based on the tunneling model of Corkum. The measured distribution functions, however, show a deficit of low energy electrons in comparison to present theory. The observed deficit of low energy electrons may be due to stimulated recombination and re-ionization during the laser pulse at high gas density.

References

1.Amendt,*et al.*,Phys.Rev.Lett.,**66**(1991);Burnett*et al.*, IEEE J.Q.E.,**26**(1990).
2.Burnett *et al.*, J. Opt. Soc. Am. B,**6**(1989);Corkum,*et al.*,Phys. Rev. Lett.,**62**(1989).
3.U. Mohideen, *et al.*,Phys. Rev. Lett.,**71**(1993).
4.Offenberger*et al.*, Phys. Rev. Lett.,**71**(1993); Leemans*et al.*, Phys.Rev. A, **46**(1992).
5.Penetrante and Bardsley, Phys. Rev. A,**43**(1991).
6.Eder, Amendt and Wilks, Phys. Rev.A,**45**(1992).

Mode Properties of a High Intensity Plasma Waveguide

C.G. Durfee, III and H.M. Milchberg
Institute for Physical Science and Technology
University of Maryland
College Park, MD 20742

New results are presented from the first experimental demonstration of the channeling of intense laser pulses over distances much greater than a Rayleigh length[1]. In this scheme, two laser pulses are used: The first pulse creates a column of hot plasma that forms a channel behind a radially expanding shock wave, and the second pulse is injected into the channel after an appropriate delay. Single-mode and multi-mode propagation of the channeled beam is observed, with the mode structure depending on the two-pulse delay, gas density, and input beam coupling. Pulses have been channeled for distances as long as 70 Rayleigh lengths at intensities of at least 10^{14} W/cm^2. As much as 75% of the energy in the focal spot of the injection lens is coupled into the guide.

A waveguide for high intensity laser pulses is generated when a plasma formed at the focus of a laser pulse is allowed to expand and create a channel into which a second pulse can be injected[1]. In the waveguide formation process, collisions at the interface between the radially expanding plasma and the neutral and weakly ionized gas on the outside lead to a shock wave. Behind the shock a depression in the plasma density forms, which gives rise to an index of refraction profile appropriate for guiding (Fig. 1). On-axis plasma density minima[2] had been produced in early studies of laser-gas interactions, but the resulting plasmas were much shorter than a Rayleigh length. Here, two sets of experiments were performed. In the first set of experiments, two pulses with variable delay were focused through the same lens, demonstrating the lensing effect in a channel of about two Rayleigh lengths in extent. In the second set of experiments, an axicon[3] was used to create a much longer plasma channel, in which optical guiding over distances up to 70 Rayleigh lengths was observed. This plasma waveguide should prove useful in experiments which require a long interaction length at high intensities, for example in recombination XUV/soft x-ray lasers[4], laser-plasma based electron accelerators[5] and high-harmonic generation[6].

The laser used in the experiments was a 10 Hz flashlamp-pumped Nd:YAG regenerative amplifier[7] (RGA) and power amplifier system seeded by a mode-locked oscillator (100 ps pulses at 1.064 μm), delivering pulse energies of up to 250 mJ. In the second set of experiments, the extended plasma waveguide was produced by an axicon[3], here a polished glass cone with a base angle of α=35°. When a collimated beam enters

the flat side, a line focus is formed along the optical axis from constructive interference of the resulting conical wavefront. An axial hole (diameter 3.2 mm) allows transmission of the oppositely directed coupling beam. Uniform sparks of length ≈1 cm with this axicon (and ≈2.5 cm with another axicon with α=20°) are produced in both the MPI and avalanche regimes.

A single pulse is split (see Fig. 2), with one pulse (P_1) directed to the axicon (energy 150 mJ, peak intensity $4x10^{13}$ W/cm^2) and the other (P_2), with variable delay, directed to a coupling lens L_1 (energy 5-40 mJ at f/10, w_0≈10μm, Rayleigh length = 290 μm) and focused onto the end of the axicon spark. Side-scattered laser light was observed through lens L_2 with a cooled CCD camera (CCD_1); CCD_2 monitored a magnified image of the beam profile at the channel exit. The data of Figure 3 was taken with a mix of gas (30 Torr Xe, 90 Torr N_2); electrons created through MPI from Xe promoted avalanche ionization of N_2. The (non-linear) scattering seen at the entrance and exit indicates the large throughput of the channel, 24 Rayleigh lengths in extent. A magnified image of the (weaker) Thomson scattered light from the center section of the channel (Fig. 4) shows that the guided light is restricted to a size consistent with channel exit mode images, described below.

Since the channel exit is axially located at least 24 Rayleigh lengths from the coupling lens focus (70 Rayleigh lengths with the 20° axicon), the image of the exit mode at CCD_2 is distinct from any unchanneled light (see Fig. 5). At low backfill pressures (30 Torr of Xe) the waveguide supports only a single Gaussian mode: the size changes only with delay (which controls the channel size and refractive index curvature). When the input coupling lens position is changed, only the degree of coupling is affected, while the shape and position of the mode remain fixed. Coupling efficiencies of up to 75% have been measured by comparison of an image of the focal spot with that of the exit mode. At higher densities, higher order modes are supported by the waveguide (Fig. 6).

References

1. C.G. Durfee III and H.M. Milchberg, Phys. Rev. Lett. **71**, 2409 [1993].
2. G.A. Askar'yan and N.M. Tarasova, JETP Lett. **20**, 123 (1974); L.C. Johnson and T.K. Chu, Phys. Rev. Lett. **32**, 517 (1974).
3. J.H. Mcleod, J. Opt. Soc. Am. **44**, 592 (1954).
4. *For example,* N.H. Burnett and P.B. Corkum, JOSA B **6**, 1195 (1989).
5. T. Tajima and J.M. Dawson, Phys. Rev. Lett **43**, 267 (1979).
6. A. McPherson, G. Gibson, H. Jara, U. Johann, T.S. Luk, I. McIntyre, K. Boyer, and C.K. Rhodes, JOSA B **4**, 595 (1987); X.F. Li, A. L'Huillier, M. Feray, L.A. Lompré, and G. Mainfray, Phys. Rev. A **39**, 5751 (1989).
7. C.G. Durfee, III, and H.M. Milchberg, Opt. Lett. **17**, 37 [1992].

Fig. 1

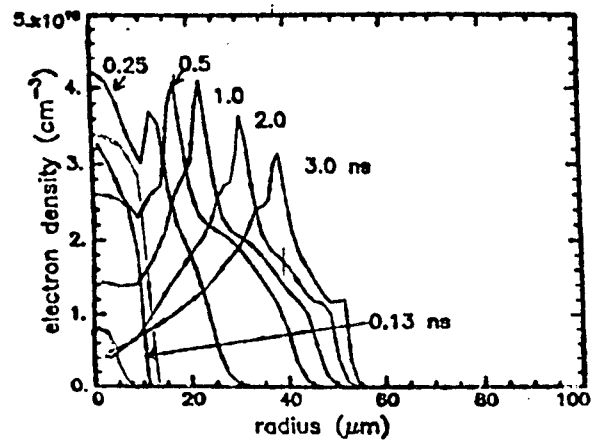


Fig. 2

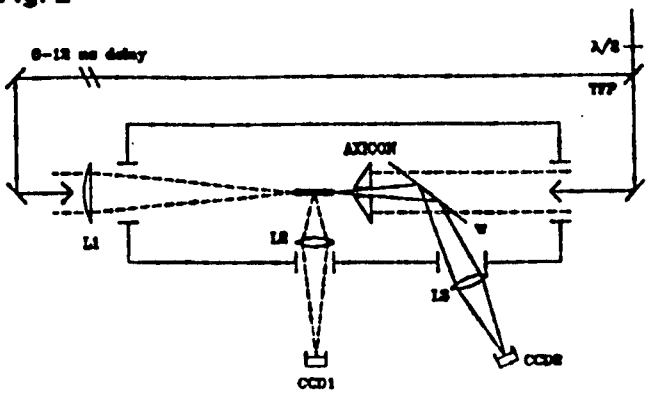


Fig. 3

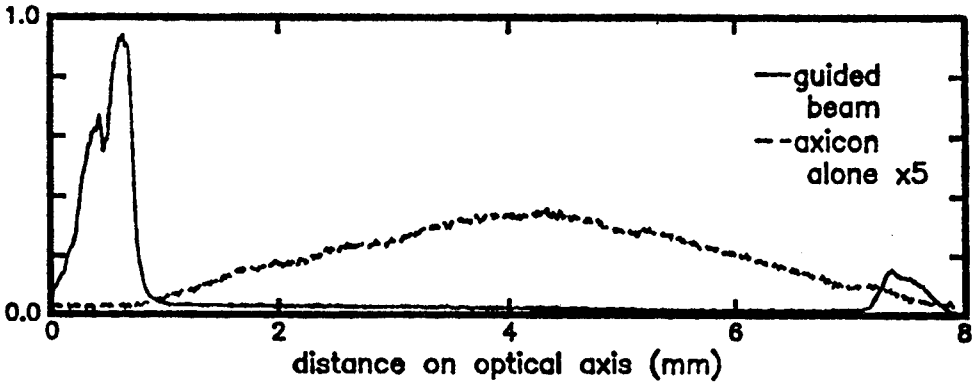


Fig. 4

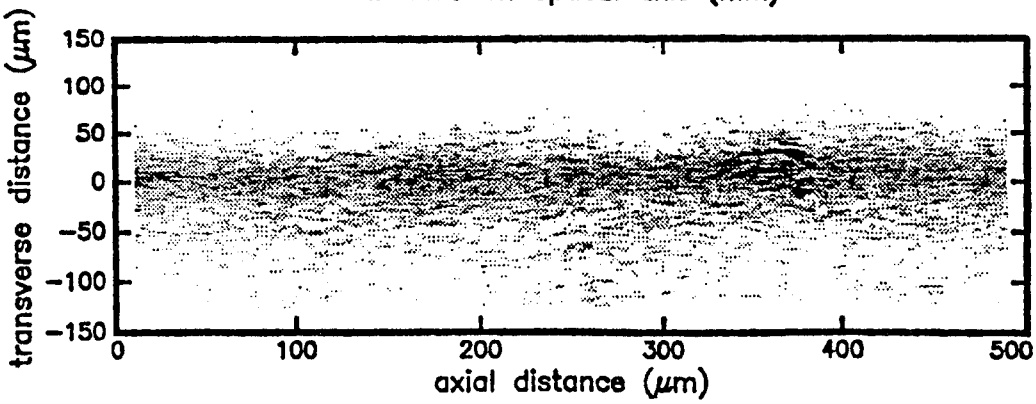


Fig. 5

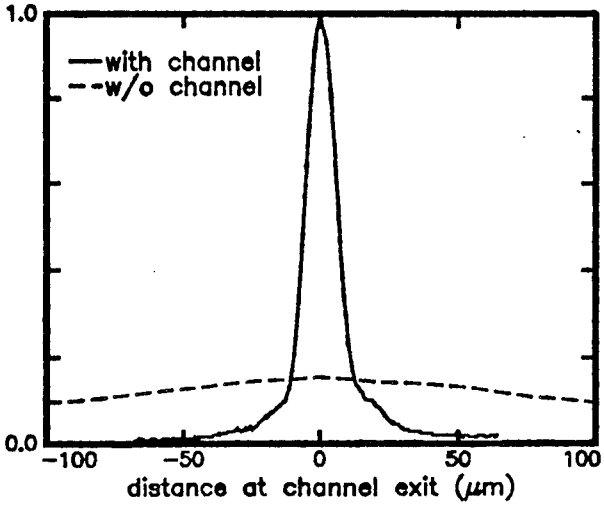
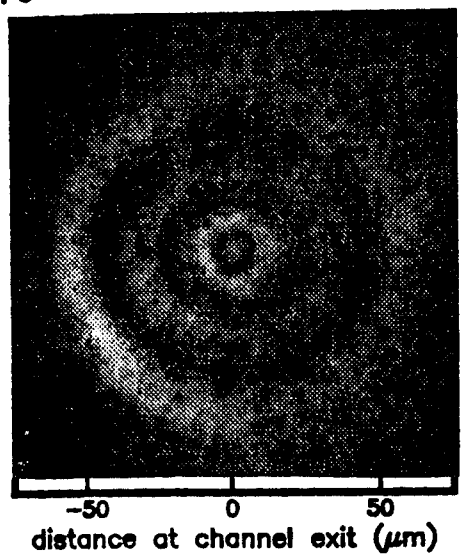


Fig. 6



Self-channeling of high peak-power femtosecond laser pulses in air

A. Braun, X. Liu, G. Korn, D. Du, J. Squier, and G. Mourou

Center for Ultrafast Optical Science, University of Michigan

2200 Bonisteel Blvd., Ann Arbor, MI 48109-2099

(313) 763-4875

The propagation properties of high peak-power ultrashort pulses through air are being studied. When the pulsewidths are as short as 100fs, laser pulses with less than 1 mJ of energy have peak powers exceeding the critical power for self-focusing. For the first time, it was observed that these pulses self-channel into a filament with a diameter of 50μm-100μm and propagate through distances greater than 30 meters. The propagation of these pulses have interesting applications such as laser induced lightning [1] and laser pumped x-ray sources [2].

We studied the beam propagation of femtosecond laser pulses from a Ti:sapphire based chirped pulse amplification laser system. The system delivered pulses with pulsewidths of 150 fs - 200 fs and energies up to 50 mJ/pulse at 10 Hz. The laser beam was collimated at low pulse energies, with a beam diameter of 3 mm (FWHM). As the pulse energy exceeded 0.5 mJ per pulse, the beam started to self-focus as the nonlinear phase delay increased with beam power. By imaging the beam's diameter at various distances from the output of the laser, we were able to determine the energy needed to start the whole beam self focusing process. As seen from Fig. 1, the energy needed to start the spatial collapse of the pulse is 2.7 mJ which gave a measured critical power of P_{cr} = 13.5 GW.

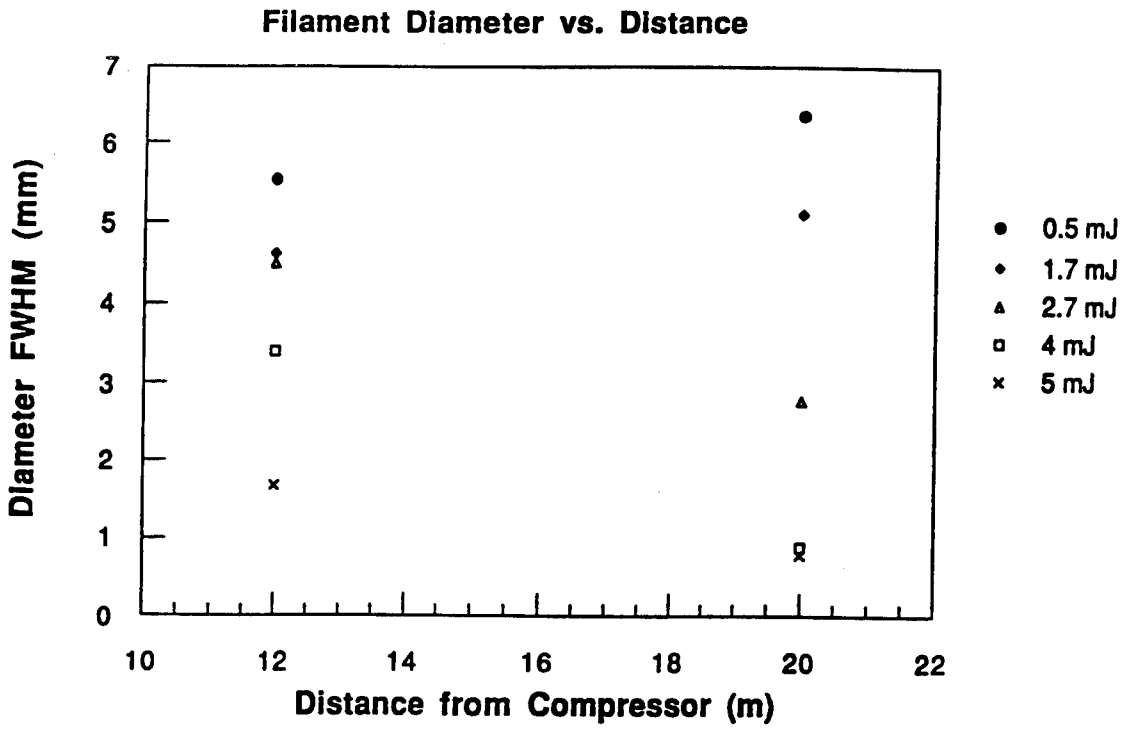


Figure 1: The beam diameter (FWHM) is measured at different distances from the compressor with varying energy per pulse. Whole beam self-focusing is seen to occur with a pulse energy of 2.7 mJ (peak power 13.5 GW).

When the energy per pulse exceeded 5 mJ, a small scale filament began to form. For energies greater than 5 mJ per pulse, the beam was up-collimated to a diameter of 1.2 cm prior to compression. By increasing the energy, the filament formation occurred earlier. The diameter of the filament was measured by imaging its spatial profile off a diffuser at grazing incidence at a distance of 28 meters from the laser. With an initial pulse energy of 27 mJ, a filament beam diameter of 68 μm was obtained.

The surprising result of our experiment was that the pulse stayed channeled over the 30 meters of available laboratory space. As is well-known, the trapped state of self-focusing is not stable if n_2 alone is the mechanism [3]. In our case, the negative lens effect of the plasma produced by the

intensity-dependent ionization can counter-balance the self-focusing. Using the value of n_2 of air to be 5×10^{-19} cm^2/W, at an intensity of 10^{13} W/cm^2, the index change due to n_2 is 5×10^{-6}. An ionization of 7.5×10^{15} cm^{-3}, or 2.8×10^{-4} of atmospheric air concentration, will balance out the self-focusing at λ=800 nm. As a significant portion of air starts to be ionized at this intensity, it is reasonable to believe that ionization can stabilize self-focusing, making filament channeling possible. The propagation of the trapped filament also resulted in white light generation and stimulated Raman scattering. These losses will attenuate self-focusing, and eventually cause the channeled filaments to disappear.

This work was supported by the National Science Foundation through the Center for Ultrafast Optical Science under STC PHY 8920108.

[1] X.M. Zhao, C.Y. Yeh, J.-C. Diels, and C.Y. Wang, *Ultrafast Phenomena VIII*, eds J.-L. Martin, A. Migus, G.A. Mourou, A.H. Zewail (Springer-Verlag, Berlin, 1993) p. 264.

[2] S.C. Rae and K. Burnett, Phys. Rev. A **46**, 2077 (1992).

[3] Y.R. Shen, *The Principles of Nonlinear Optics*, (Wiley-Interscience, 1984), pp. 303-324.

Observation of the Dynamics of Electron Plasma Oscillations in Femtosecond Laser-Produced Plasmas

D. von der Linde and H. Schüler
Universität Essen, Fachbereich Physik, Institut für Laser- und Plasmaphysik,
D- 45117 Essen, Germany, Phone: 49-201-183-2564, Fax: 49-201-183-2120

It is well known that one of the mechanisms of second harmonic generation (SH) in plasmas is coherent scattering of the fundamental electromagnetic wave from the electron density fluctuations associated with electron plasma waves [1]. By making use of the characteristic polarization selection rules of SH generation [2], it should be possible to directly observe electron plasma waves by measuring properly selected SH contributions.

Here we wish to report an experiment in which measurements of the SH were used to directly observe, for the first time, the ultrafast dynamics of electron plasma oscillations.

We used a pump-probe scheme in which an intense pump pulse produced a microplasma on the surface of a glass substrate, and a weak probe pulse was used to interrogate the plasma. The laser pulses were obtained from an amplified CPM dye laser system (λ=620 nm). The duration, the focal diameter and the peak intensity of the *pump* beam on the target surface were, respectively, 120 fs, 7 μm, and 6×10^{15} W/cm^2. The peak intensity of the *probe* pulse was down by more than a factor of ten, but otherwise pump and probe were the same.

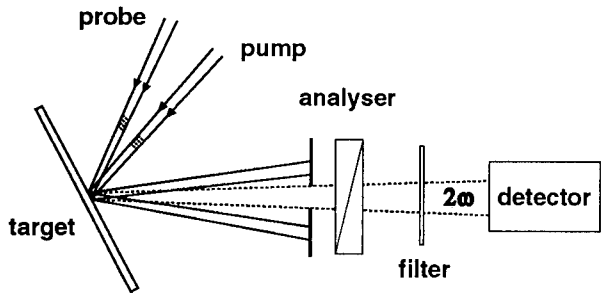


FIG. 1: Experimental setup of the SH pump-probe experiment

The experimental geometry is shown in Fig. 1. The p-polarized pump beam and the s-polarized probe beam were incident on the target surface at an angle of θ_{pump}=37° and θ_{probe} =50°, respectively. A diaphragm positioned approximately in the direction of the bisector of the reflected beams blocked the latter and passed the SH due to sum frequency mixing of pump and probe. A polarization analyser placed in the SH beam after the diaphragm suppressed scattered light from the strong pump beam and ensured that only s-polarized SH reached the detector.

The second order induced current density responsible for SH generation in a plasma can be written [2,3]:

$$\mathbf{J}_{2\omega}^{(2)} = \frac{ie}{4\pi m\omega}\left[\frac{\omega_p^2}{4\omega^2}\nabla \mathbf{E}_\omega^2 + \mathbf{E}_\omega \nabla\cdot\mathbf{E}_\omega\right] \qquad (1)$$

Here, $\mathbf{E}_\omega$ is the electric field vector of the fundamental wave at the frequency ω, and ω_p is the local

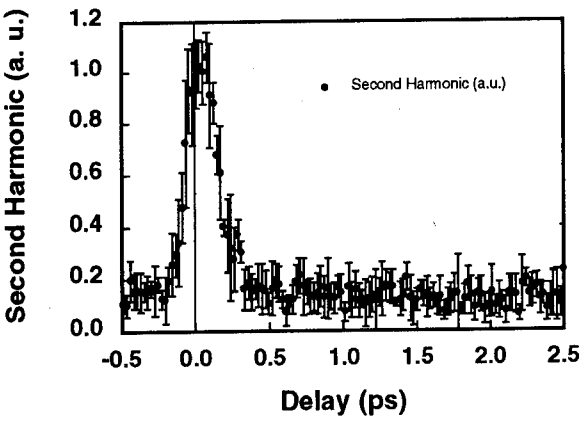


FIG. 1: Measured s-polarized second harmonic of the probe pulse as a function of delay time. The error bars correspond to the standard deviation of the individual measurements.

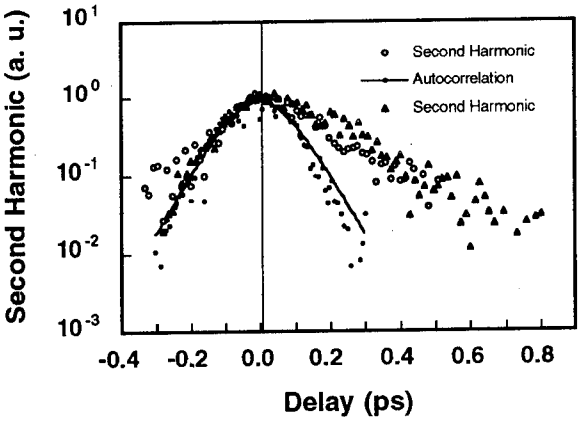


FIG. 2: Second harmonic as a function of delay time and autocorrelation function of the laser pulses. Two different experimental runs for the SH are shown.

plasma frequency. The other symbols have their usual meaning.

The second term in (1) is directly proportional to the first order electron density perturbation $n_{\omega}^{(1)}$ associated with the electron plasma wave driven by the fundamental field, $n_{\omega}^{(1)} \propto \nabla \cdot \mathbf{E}_{\omega}$. For a p-polarized pump field $\mathbf{E}_{pump}$ and a s-polarized probe field $\mathbf{E}_{probe}$ the component of the SH current density corresponding to s-polarization reduces to:

$$\mathbf{J}_{2\omega\perp}^{(2)} = \alpha \mathbf{E}_{probe} \nabla \cdot \mathbf{E}_{pump} \tag{2}$$

where α is some constant. It can be shown from the conservation of the wave vector components parallel to the target surface that the angle $\theta_{2\omega}$ of the SH generated by this current is given by:

$$\sin\theta_{2\omega} = \tfrac{1}{2}(\sin\theta_{pump} + \sin\theta_{probe}) \tag{3}$$

which is to a good approximation the direction of the bisector of the reflected beams. It follows that for the chosen experimental configuration the selected SH component should be proportional to the squared *amplitude of the electron plasma wave* generated by the pump pulse.

In the experiment we have observed a clear s-polarized SH signal. As expected the SH was critically dependent on the temporal and spatial overlap between pump and probe. The signal disappeared when either the temporal or spatial overlap was spoiled. By measuring the SH as a function of the position of the diaphragm it has been verified that the s-polarized SH was indeed centered between the reflected pump and probe beam near the bisector. Thus we conclude that the observed s-polarized SH provides direct evidence of the presence of density fluctuations associated with electron plasma waves.

A typical example of the observed time dependence is shown in Fig. 2, where the measured s-polarized SH is plotted as a function of the delay time. Figure 2 demonstrates that the s-SH is concentrated in a sharp peak of about 200 fs, which appears to be slightly asymmetric and shifted by approximately +100 fs with respect to zero delay time.

For a more detailed picture of the time dependence, the s-polarized SH is compared in Fig. 3 with the intensity autocorrelation of the laser pulses, which has been measured using a thin KDP crystal. The autocorrelation data can be represented, to a good approximation, by a squared hyper-

bolic secant function (solid line in Fig. 3). The comparison shows that the SH from the plasma deviates from the autocorrelation. In particular, it appears that the decrease of the SH for positive delay times is significantly slower than that of the autocorrelation. The decay of the SH signal can be fitted by an exponential function with a time constant of (160 ± 10) fs.

The observation of a distinct difference between the time dependence of the SH from the plasma and the autocorrelation of the laser pulses provides strong evidence that a two-step process is responsible for the SH and that the SH signal reveals the dynamics of the electron density oscillations. The two-step process can be described as follows. Firstly, a thin surface layer of the material is ionized and a rapidly expanding plasma is formed by the pump pulse. When the polarization of its electric field vector lies in the plane of incidence (p-polarization), the pump pulse couples with the longitudinal modes of the inhomogeneous plasma and drives coherent electron density oscillations at the frequency of the light. Secondly, the probe pulse is scattered from these charge density fluctuations. This process gives rise to anti-Stokes scattered light at the second harmonic frequency. Thus, in the pump-probe experiment measuring this SH signal, the rise and decay of the electron density oscillations is mapped out.

It is interesting to discuss decay of the electron density oscillations observed in our experiment. In a weakly excited, weakly inhomogeneous plasma the damping of long wavelength electron plasma waves is determined by the electron-ion collision frequency. For an electron temperature of several hundred eV the inverse collision frequency at the critical density is much less than the duration of the laser pulses in our experiment. However, the situation is probably quite different for a strongly inhomogeneous, short-scale-length plasma produced by a femtosecond laser pulse. For short times, when the intense pump pulse is still present, wave breaking phenomena might play a role, whereas for longer probe pulse delay times the expansion of the plasma should be taken into account. To our knowledge, a theoretical model describing electronic damping under these circumstances is still lacking.

In conclusion, it has been demonstrated that measurements of the SH can be used to detect electron density oscillations in femtosecond laser-produced plasmas. Pump-probe experiments using this method have revealed the femtosecond dynamics of electron plasma excitations.

References

1. N. G. Basov, Y. A. Zakharenkov, N. N. Zorev, A. A. Rupasov, G. V. Sklizkov, A. A. Rupasov, and A. S. Shikanov, *Heating and Compression of Thermonuclear Targets by Laser Beam,* Cambridge University Press (Cambridge, 1986).
2. D. von der Linde, in: *Laser Interaction with Atoms, Solids and Plasmas*, NATO Advanced Study Institute, Cargèse, Corsica, 1992.
3. K. Baumgärtel and K. Sauer, *Topics on Nonlinear Wave-Plasma Interaction*, Birkhäuser Verlag (Basel, 1987).

Gas Phase Clusters

ThB 10:30am–12:00m
Dana Point Ballroom

John Weiner, *Presider*
University of Maryland

TIME RESOLVED DYNAMICS IN LARGE MOLECULAR CLUSTER IONS

M. Nadal, V. Vorsa, J. M. Papanikolas, P. J. Campagnola
R. Parson and W. Carl Lineberger

Department of Chemistry and Biochemistry, University of Colorado
and Joint Institute for Laboratory Astrophysics, Boulder, Colorado, 80309-0440
(303) 492-7834

Photoabsorption in large mass-selected cluster ions is detected via evaporation of molecules from the cluster. The shape and size evolution of the absorption spectrum with cluster size provides a mechanism to identify the chromophore and to detect the extent of charge delocalization in the cluster ion. Photofragment mass spectra have been obtained for $Br_2^-(CO_2)_n$, $I_2^-(CO_2)_n$ and $ICl^-(CO_2)_n$cluster ions following photoexcitation of the $^1_{2g}(^2\Pi_{g,1/2}) \leftarrow ^1_{2u}(^2\Sigma_u^+)$ transition in I_2^- and Br_2^- and the analogous transition in ICl^-. Photodissociation of X_2^- within the cluster results in the production of both X^-- and X_2^--based ionic photofragments:

$$X_2^-(CO_2)_n + h\nu \xrightarrow{(1-F_n)} X^-(CO_2)_m + X + (n-m)CO_2 \quad \text{(uncaged products)}$$
$$\xrightarrow{F_n} X_2^-(CO_2)_k + (n-k)CO_2 \quad \text{(caged products)}$$

From these photofragment distributions the recombination probability can be determined. The homonuclear chromophores exhibit small caging fractions for the smaller cluster sizes, increasing to unity when the first solvation shell is completed at n=12 for Br_2^- and n=16 for I_2^-. In comparison, the recombination efficiency for I_2 in solution is only 10-70%, depending on the solvent.

Time-resolved reaction dynamics and the breakup of the solvent shell are

obtained using one-color ultrafast pump-probe techniques. The experimental data on $I_2^-(CO_2)_{16}$ show that the two photon photoproducts change substantially as the delay between the pump and probe pulses is varied from 0.2 - 3 psec. Time-resolved mass spectra show that the breakup of the solvent cage is essentially complete in 5 ps and that extensive relaxation has occurred in 10 ps for the larger clusters ($n \geq 16$). The absorption recovery of the larger cluster species exhibits a local maximum at 1.8 ps following dissociation. This structure is attributed to processes following the first "bounce" of the dissociating chromophore off of the solvent cage. The details of the recombination process are very strongly influenced by the electron localization on an atomic center during dissociation and by the electron delocalization during recombination. Both events are dominated by solvent dynamics. Simple models for the intracluster dynamics will also be presented.

Uses of Optical Phase-Controlled Pulse Sequences

Jeffrey A. Cina

Department of Chemistry and James Franck Institute
University of Chicago, Chicago, Illinois 60637 (312) 702-3166

There has been rapid experimental progress in the shaping of single ultrashort light pulses into sequences of pulses of specified separation, duration, and relative optical phase [1,2a]. Phase-controlled pulse sequences have found a number of applications to molecular systems [2b,c], and several more have been the subject of theoretical calculations. The salient feature of electronically resonant phase-controlled pulse trains is their ability to generate superpositions of multiple time-dependent contributions to the nuclear wave function in a given electronic state having well-defined relative *quantum* phases. Here we describe two uses to which that feature might fruitfully be put in preparing and probing time-dependent nuclear wave functions in the ground electronic state possessing chemically or spectroscopically useful properties.

Preparation and Degradation of Superpositions of Chiral Amplitudes. Cina and Harris [3] have recently shown how phase-locked ultrashort pulse-pairs can prepare nuclear wave functions in chiral molecules consisting of a sum of left- and right-handed amplitudes. The degradation of such left-right quantum coherence, by interaction with other rotational and vibrational modes of the molecule itself or by

molecular collisions, is believed to be the process that stabilizes handed states. [4] This stabilization process has not yet been observed in real time. In order to do so, one must probe the system with a second phase-locked pulse pair, variably delayed from the first, which probes the chiral coherence by exciting resonantly to an electronic state in which there is ready interconversion between left- and right-handed states. For an *intra*pulse-pair delay equal to the interconversion time (one half the excited state period) or an odd multiple thereof, the interference contribution to the excited state population depends on the retention of left-right phase coherence in the electronic ground state. Results will be presented for calculations on a chiral molecule embedded in a low temperature solid, showing how the interference signal depends on the bath density of states and the frequency dependence of the system-bath coupling.

Amplification of coherent vibrational motion and control of wave packet spreading in impulsive stimulated Raman excitation. Recent calculations have shown that sequences of electronically resonant vibrationally impulsive phase-related pulse-pairs can efficiently impart momentum to a selected low-frequency nuclear mode without transferring population to excited electronic states. [5] In the presence of vibrational anharmonicity or local curvature differences between the ground state potential curve and that of the pertinent electronic excited state, wave packet spreading is an inevitable (and limiting) concomitant of vibrational amplification. We will discuss a strategy for counteracting wave packet spreading during impulsive stimulated Raman excitation which is equally well applicable within a sequence of

single nonresonant ultrashort pulses. This strategy is based on the fact that, in addition to imparting a small moment change (proportional to the difference in slope between the excited- and ground-state potential curves) to all modes of frequency less than the inverse pulse duration, nonresonant pulses or pulse-pairs phased to prevent electronic absorption also induce a small change in the rms momentum width, $\delta\langle(\Delta p)^2\rangle^{1/2}$, whose value is proportional to the difference in curvature between the two potential curves.

Unlike the momentum itself, which oscillates with the full period of the molecular vibration, the momentum width increment oscillates with half the period (twice the frequency) of the vibration. Since the momentum width increment therefore changes sign after each quarter vibrational period, a light pulse or pulse pair at this time will cancel out the original momentum width increment and prevent wave packet spreading. Calculations detailing the efficacy of this approach are presented by Smith elsewhere in these proceedings.

This research was supported by NSF grant CHE-9121260.

1. (a) A. M. Weiner, D. E. Leaird, G. P. Wiederrecht and K. A. Nelson, Science **247**, 1317 (1990); (b) A. M. Weiner, IEEE J. Quantum Electron. **28**, 908 (1992).
2. (a) N. F. Scherer, A. J. Ruggiero, M. Du and G. R. Fleming, J. Chem. Phys. **93**, 856 (1990); (b) N. F. Scherer, R. J. Carlson, A. Matro, M. Du, A. J. Ruggiero, V. Romero-Rochin, J. A. Cina, G. R. Fleming and S. A. Rice, J. Chem. Phys. **95**, 1487 (1991); (c) N. F. Scherer, A. Matro, L. D. Ziegler, M. Du, R. J. Carlson, J. A. Cina and G. R. Fleming, J. Chem. Phys. **96**, 4180 (1992).
3. J. A. Cina and R. A. Harris, J. Chem. Phys. (15 Feb. 1994 issue).
4. R. Silbey and R. A. Harris, J. Phys. Chem. **93**, 7062 (1989).
5. (a) J. A. Cina and T. J. Smith J. Chem. Phys. **98**, 9211 (1993); (b) R. Kosloff, A. D. Hammerich and D. Tannor, Phys. Rev. Lett. **69**, 2172 (1992).

Deep Ultraviolet Femtosecond Multiphoton Ionization Studies of the Excited State Dynamics of Small Gas Phase Molecules

J.C. Owrutsky and A.P. Baronavski
Code 6111, Chemistry Division, Naval Research Laboratory, Washington, D.C. 20375, (202)767-0721

INTRODUCTION

Femtosecond studies using laser-induced fluorescence and multiphoton ionization (MPI)[1] have lead to considerable progress in understanding small molecule gas phase photodissociation dynamics. In this letter we describe experiments that extend these studies to shorter wavelengths. This makes it possible to investigate molecules that absorb weakly in the visible or near UV, which is often the case for many small molecules. We have generated femtosecond deep UV (near 205 nm) pulses, which have been used to directly measure the excited state lifetime for the predissociative S_3 state of CS_2 and to study the two-photon state of NO at 102 nm using time-resolved MPI. The lifetime measured for CS_2 is compared with several indirectly measured values, and the pressure dependence observed for the decay times for NO was measured and analyzed to obtain both the unimolecular lifetime and bimolecular rate constant.

EXPERIMENTAL

A femtosecond laser system produces pump and probes pulses, which are used for multiphoton ionization studies performed in a static gas cell containing parallel plates. Femtosecond pulses (80 fs, λ=618 nm) from a CPM laser are amplified to 150 μJ in a two stage amplifier pumped by a XeF excimer laser (351 nm, 300 Hz). Approximately 10% of the amplified CPM beam is used to generate pump pulses near 205 nm ($\sim$50 nJ) by frequency tripling with a pair of 0.2 mm thick BBO crystals. We estimate the 205 nm pulses are broadened to 200-300 fs because of group velocity mismatch, as indicated from the instrument function measured by observing MPI signals for several molecules exhibiting fast photodissociation (e.g., CH_3I). The pump beam wavelength is narrowly tunable (204.5-206.0 nm) by adjusting the phase matching angle of the second crystal. Probe pulses near 300 nm are generated by frequency doubling an amplified portion of continuum (in 0.5 mm BBO). The continuum is produced by focusing the amplified CPM beam into a water cell. A portion near 600 nm is spectrally filtered ($\Delta\lambda \approx$ 10 nm) and amplified to $\sim$30 μJ in two passes through a 2 cm long cell that is transversely pumped with the excimer laser. The amplified continuum is doubled to 300 nm with an energy of about 1 μJ.

The pump and probe pulses are focused (with a 50 cm focal length lens) colinearly into a gas cell with fused silica windows containing a static pressure of the sample (0.4-0.6 Torr of CS_2; 0.2-5. Torr NO) The photocurrent is collected on parallel plates that are separated by about 1 cm and biased to 200-400 V. The probe beam is synchronously chopped (*i.e.*, at 150 Hz) and the photocurrent is directed to a gated integrator and a lock-in amplifier.

LIFETIME OF THE S_3 STATE OF CS_2

The $S_3 \leftarrow S_0$ absorption band of CS_2 (220-190 nm) consists of $\sim$16 sequences separated by $\sim$410 cm^{-1}, which is due to excitation of ν_1 and ν_2 in the upper state and ν_2 hot bands. The dynamics of this predissociative band has been studied by various indirect methods. Hara and Phillips [2] found that the fluorescence quantum yield ($\Phi = 10^{-4}$-10^{-3}) increases with wavelength (200-216 nm) indicating that lifetimes are shorter at higher excitation energies, i.e., with more vibrational excitation. They estimated excited state lifetimes based on the yields and the radiative lifetime. In their photodissociation product state anisotropy distribution studies at 193 nm, Yang *et al.* [3] found an isotropic distribution of CS

fragments in their room temperature study and estimated the lifetime to be 1 ps and Waller and Hepburn [4] observed an anisotropic distribution of sulfur atoms in their low temperature study and estimated the lifetime to be 2 ps. The lifetimes measured by Li and Myers [5] using Raman depolarization ratios in several spectral regions of the S_3 state display a wavelength dependence consistent with that from the fluorescence quantum yield measurements. Liou *et al.* [6] reported the lifetime at 210 nm obtained by simulating a rotationally unresolved jet-cooled LIF spectrum. We present our directly measured results using time-resolved MPI with the signal observed for CS_2 as displayed in Fig. 1. The pump wavelength is 205.2 nm. An instrument-limited rise is followed by a clearly resolved decay that is well described by a single exponential decay with a lifetime of 600 ± 100 fs. The same decay time was measured over the pump pulse tuning range (204.8-206.0 nm.) The plot in Figure 2 summarizes lifetimes measured in different spectral regions (193-215 nm) of the $S_3\leftarrow S_0$ spectrum of CS_2. The lifetime we measure is consistent with those reported for CS_2 by Li and Myers [5] using resonance Raman depolarization ratios for the neighboring spectral regions assuming a smoothly varying wavelength dependence as indicated by the fluorescence quantum yield. The times from other indirect studies are too long. While resonance Raman depolarization ratios have be used successfully in this instance, direct measurements, such as the described here, are free from assumptions, constraints and the requirement of prior knowledge about the system, e.g., rotational constants, that often accompany indirect approaches to dynamical measurements.

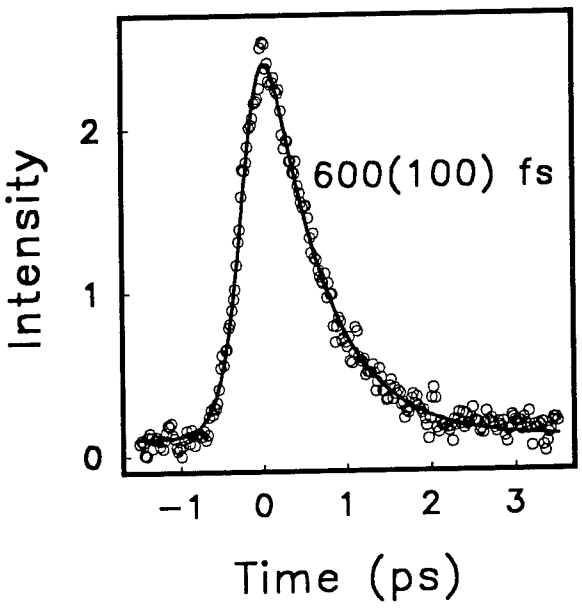


Figure 1. Femtosecond ultraviolet MPI signal observed with 205.2 nm pump and 300 nm probe pulses for CS_2. The circles are the data and the line is the result of a fit to a single exponential decay ($\tau=600\pm100$fs) convoluted with a 320 fs instrument response function.

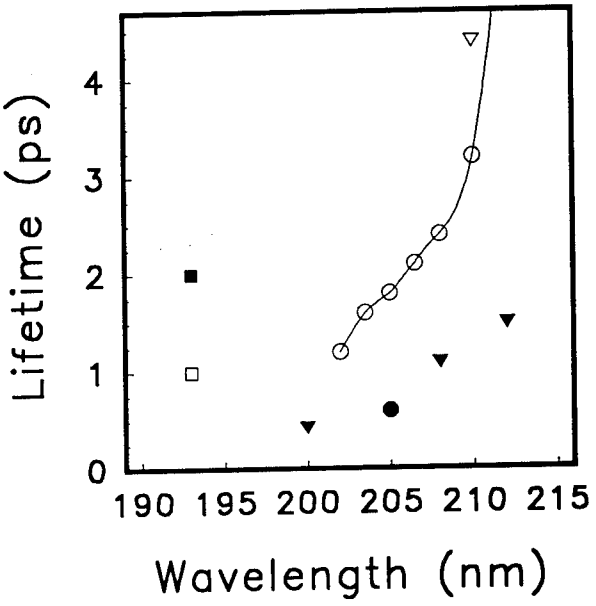


Figure 2. A plot of various measurements of the lifetime of the S_3 state as a function of wavelength in the region 190-215 nm: ● This work; ○ Hara and Phillips[2]; ▾ Li and Myers[5]; □ Yang *et al.*[3]; ■ Waller and Hepburn[4]; ▿ Liou *et al.*[6]

TIME-RESOLVED STUDY OF THE 102 NM STATE OF NO

We have used laser pulses near 205 nm for a time-resolved (2+1) multiphoton ionization study of the two-photon state of NO at 102 nm via a one-photon resonance with the $A^2\Sigma(3s\sigma)$ ($v=2$) state . The A state is relatively long-lived (> 10 ns) at pressures close to 1 Torr, but we have observed signals consisting of a picosecond decay in addition to one that persists for the length of the scan (100 ps). The transients (Fig. 3) are interpreted as a 2+1 MPI signal, which is consistent with our studies of the laser power, pump and probe wavelengths and isotope (^{15}NO). The lifetime measured for the 102

nm state exhibits a pressure dependence, which is very uncommon at these pressures on the picosecond time scale. By measuring and analyzing the pressure dependence, as shown in Fig. 3, we obtain both the collisionless lifetime (180±60 ps) and the very large bimolecular depopulation or quenching rate constant (0.05±.01 ps $^{-1}$ Torr^{-1}), where the latter corresponds to a cross section of 250,000 Å. The assignment of the 102 nm state is not obvious because it falls in a region of the NO spectrum that has not been clearly assigned. The large quenching rate constant is attributed to the state having a large spatial extent, indicating that it is a medium to high n Rydberg state rather than a valence or low n Rydberg state. A precedent exists for very large cross sections in studies of Rydberg atom-molecules collisions [7]. The most likely assignment is a highly excited vibrational level (v=11) of a medium (10-12) n Rydberg state in the series converging to the ground state of NO^+. The subnanosecond collisionless lifetime implies that the state is subject to nonradiative decay such predissociation and/or autoionization, which has been observed for other Rydberg states of NO.

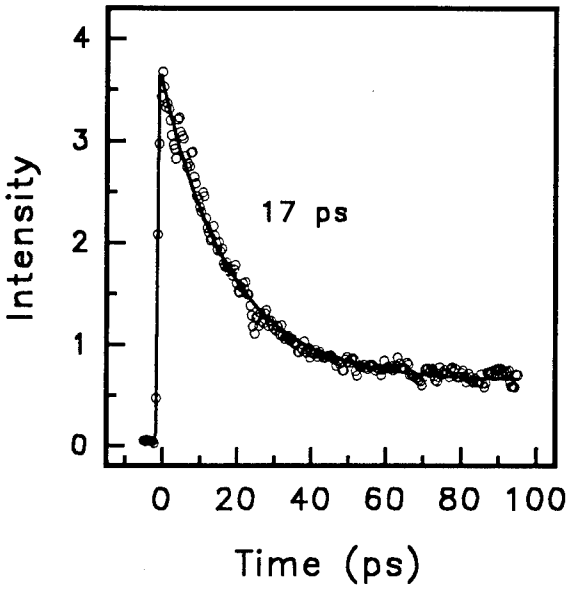


Figure 1. Time resolved MPI curve observed for 1 Torr of NO with 205 nm pump and 300 nm probe.

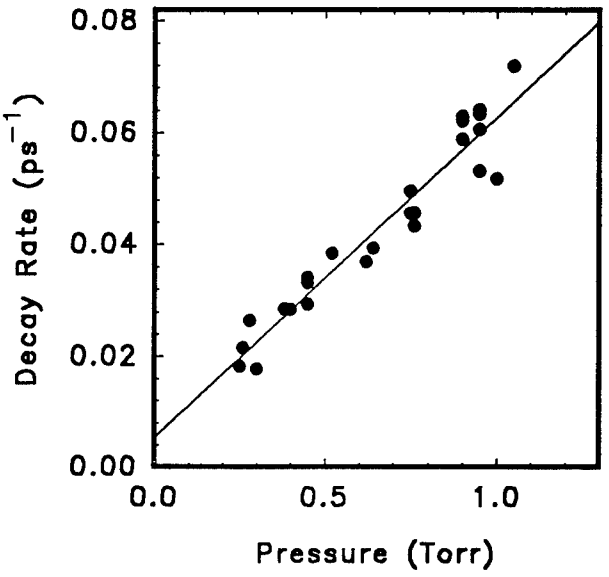


Figure 2. Pressure dependence of the decay rates observed for the 102 nm state of NO by 2+1 MPI.

References

1. A.H. Zewail, J. Phys. Chem. 97, 13532 (1993).
2. K. Hara and D. Phillips, Trans. Fara. Soc. 74, (1978) 1441.
3. S.C. Yang, A. Freedman, M. Kawasaki, and R. Bersohn, J. Chem. Phys. 72, (1980) 4058.
4. I.M. Waller and J.W. Hepburn, J. Chem. Phys. 87, (1987) 3261.
5. B. Li and A.B. Myers, J. Chem. Phys. 89, (1988) 6658; ibid, 94, (1991) 2458.
6. H.T. Liou, P. Dan, T.Y. Hsu, H. Yang and H.M. Lin, Chem. Phys. Lett. 192, (1992) 560.
7. R.F. Stebbings and F.B. Dunninng, "Rydberg states of atoms and molecules," Cambridge University, 1983).

Femtosecond Dynamics of Na_n and Hg_n Metal-Cluster

T. Baumert, R.Thalweiser, V. Weiss, E. Wiedenmann and G. Gerber
Fakultät für Physik, Universität Freiburg, D-79104 Freiburg, Germany
phone 011-49-761-2035727 ; fax 011-49-761-2035873

In recent years clusters and in particular metal clusters have been the fascinating subject of many experimental and theoretical studies. Cluster physics bridge the gap between molecular physics and solid state physics. Metal clusters exhibit distinct features ranging from molecular properties seen in small particles to solid state like behaviour of large aggregates. We report cluster size dependent studies of physical and chemical properties such as absorption resonances, lifetimes, decay channels and ionisation processes of the one- and two electron metal clusters Na_n and Hg_n . For these studies we introduced a new experimental technique consisting of the combination of a cluster beam, ion- and electron spectroscopy and tunable femtosecond laser pump-probe techniques.
A major result of our femtosecond experiments is that the conventional view of the optical response of metal cluster, e.g. absorption, ionisation and decay processes as well as the relevant time scale, had to be changed. Our results clearly show that for Na_n and cluster sizes $n \leq 21$ molecular structure, excitations and properties prevail over collective excitations and surface plasmon-like properties.
In the case of Hg_n prompt formation of singly and doubly charged cluster are observed up to $n \approx 60$. The transient multiphoton ionisation spectra show a "short" time wave packet dynamics, which is very similar for all singly and doubly charged cluster, whereas the "long" time fragmentation dynamics is different for each individual cluster. A preliminary analysis leads to a surprising result.. Very probably a Hg_2^*- chromophore imbedded within and common to all neutral Hg_n cluster carries the oscillator strength and determines the "short" time wave packet motion. The "long" time transient signals showing a decay and recovery are very similar to "cage-effect" signals seen in time-resolved condensed phase experiments. This indicates another unexpected physical process. Our real-time studies of metal clusters with femtosecond resolution open up new and exciting directions in cluster physics and yield results which in many cases are not accessible in ns- or ps laser experiments.

Ultrafast Spectroscopy of Alkali Clusters

E. Schreiber, K. Kobe, H. Kühling, S. Rohland, A. Ruff, S. Rutz, G. Sommerer, and L. Wöste

Freie Universität Berlin, Institut für Experimentalphysik
Arnimallee 14, 14195 Berlin, Germany

Abstract. The fragmentation and wavepacket propagation dynamics of small neutral potassium and sodium clusters in a supersonic cluster beam were investigated using pico- and femtosecond two photon ionization spectroscopy followed by mass-selective detection.

1. Introduction

To observe the dynamical behaviour like fragmentation or internal energy transfer processes of a cluster the application of ultrashort laser pulses and time-resolved spectroscopic techniques in the picosecond and femtosecond time domain are necessary. A first time-resolved experiment leading to the direct observation of the vibrational behaviour of the *ground state of the diatomic potassium* molecule on a femtosecond time-scale will be presented in Chap.3. Predissociated states as the higher vibrational levels of the sodium trimer's C-state or excited states of larger sodium clusters ($Na_{n=4...10}$) could never be detected by conventional two photon ionization (TPI) spectroscopy. However, applying *transient TPI spectroscopy on a ps or fs time-scale* a temporal window is opened to study the *fragmentation processes* of these clusters *with high temporal resolution* (Chap.4).

2. Experimental set-up

For all measurements modelocked titanium sapphire (Ti:Sa) lasers were used. Within the tuning-range the pulsewidth amounted —except for the C-state measurements— about $50fs$ with a bandwidth of about $400cm^{-1}$. Pulse energies of $20nJ$ were produced and used for frequency doubling. To observe the real time fragmentation of the Na_3 C-state *two Ti:Sa lasers both with a pulsewidth of* $1.4ps$ *had to be synchronized on a ps time-scale* [1]. To measure the real time dynamics, we applied transient multi photon ionisation using pump&probe technique [2]. The clusters were produced by coexpansion of potassium or sodium vapour [3]. The photoionized clusters were detected by a quadrupole mass spectrometer.

3. Wavepacket propagation in the ground state of K_2

To study wavepacket propagation phenomena the potassium dimer is an excellent candidate. Via coherent excitation wavepackets could simultaneously be produced in two of its electronic states (symmetry $1^1\Sigma_u^+$ and $4^1\Sigma_g^+$). By means of transient multi photon ionization a strong oscillation of the ion signal with a period of $380fs$ being superposed by a beat structure with a period of nearly $3ps$ could be detected (Fig.1). Against first expectations calculations by [4] on the basis of potential energy surface data determined by [5] demonstrate that the fast oscillation is neither mirroring the wavepacket propagation of the $1^1\Sigma_u^+$- nor of the

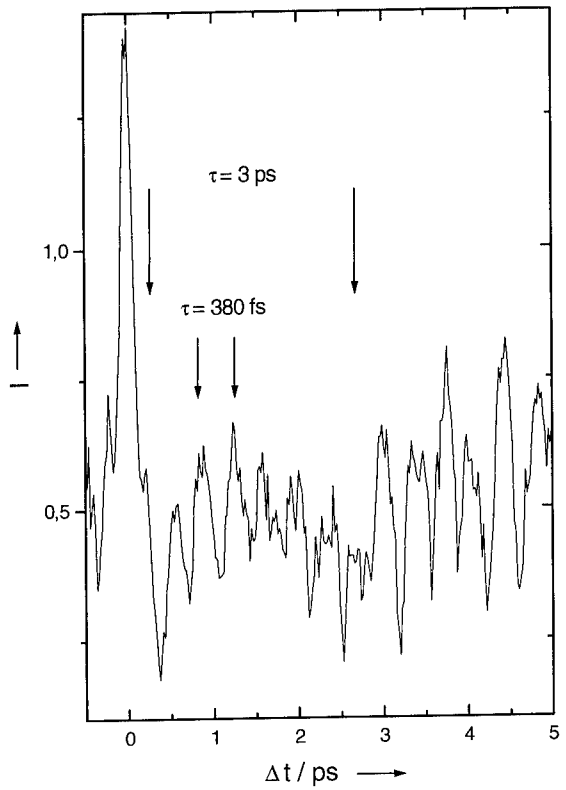


Fig.1: *Temporal evolution of the K_2 ion signal excited with $E = 1.48eV$.*

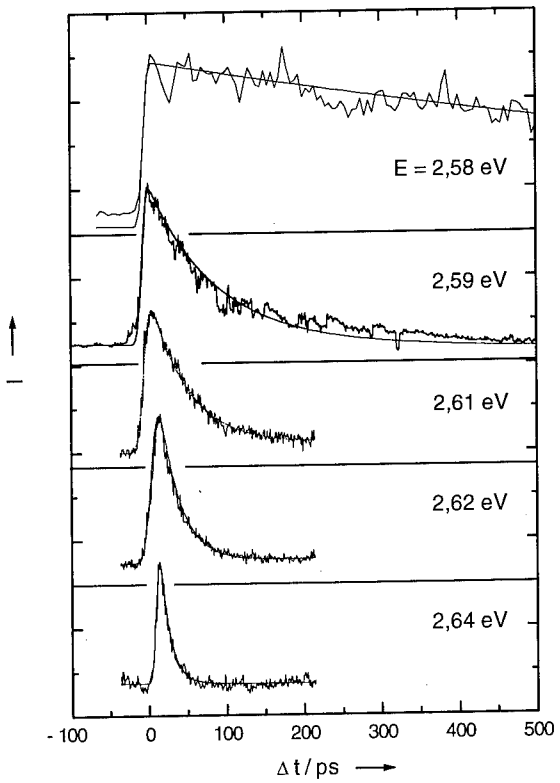


Fig.2: *Energy dependence of the Na_3 C-state transient TPI signal.*

$4^1\Sigma_g^+$-state. It rather represents the vibration of the K_2 ground state. Further results will be presented in [6].

4. Fragmentation dynamics of predissociated $Na_{3...10}$

Another exciting species is the sodium trimer being considered as the best-kwown metal cluster. Its excitation spectra exhibits several electronic states. For the B-state we recently were able to detect the temporal evolution of its fascinating pseudorotation features on a ps time-scale [7,8]. Since the higher vibrational states of the neighboured Na_3 C-state are predissociated quasi continuous-wave TPI spectroscopy never rendered a possible access to these excited states. However, the transition into these states is of high interest because it shows the onset of the dynamical behaviour at increasing cluster size. While depletion spectroscopy gave first energetic informations the application of ultrashort laser pulses allows directly to ionize these predissociated states. Fig.2 presents first results of the real time dynamics of the C-state for different excitation energies. To explain the measured dynamical behaviour a simple two-level energy scheme as used for transient TPI of the Na_3 D-state [9] is applied. Within this model a single exponential decay is expected for the temporal evolution of the transient TPI signal. To test the model the convolution of the over all system response to the laser pulses with a single exponential decay function is used to fit (—) the experimental data (...). The comparison is shown in Fig.2. The fragmentation time constants decrease from $1.1ns$ to $12ps$ with increasing excitation energy. Further results will be published soon [10]. In the case of larger sodium clusters the simple energy-level scheme as used just before

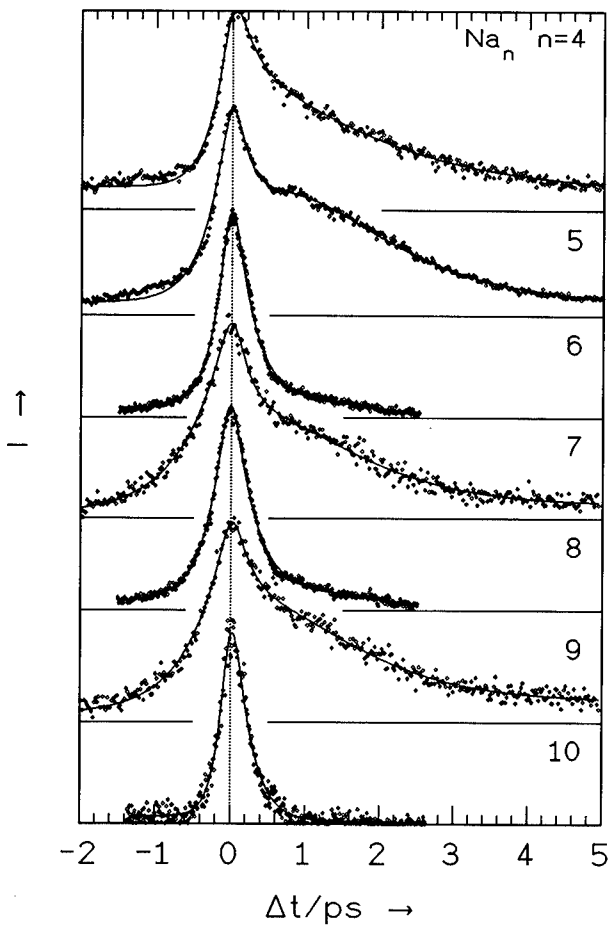


Fig.3: *Transient TPI signal of Na_n excited at $2.92eV$.*

is no more satisfactory. A more detailed "improved" model first sucessfully applied to the transients of the Na_3 D-state with fs temporal resolution [11] was applied. It assumes three decay times to be found in our observed ion signal. A decay time τ_0 represents the fragmentation time of the excited electronic state of those detected clusters being directly excited by the pump pulse. A decay time τ_{pop} arises from larger clusters being excited by the pump pulse and breaking into an excited state of the recorded cluster. Finally τ_1 is the fragmentation time of this excited state. For δ-shaped excitation the temporal evolution of the TPI signal can be calculated [11] to be $n(t) = N_0 e^{-\frac{t}{\tau_0}} + M_0(e^{-\frac{t}{\tau_{pop}}} - e^{-\frac{t}{\tau_1}})$. To analyze the measured decay curves of the Na_n the function $n(t)$ was convoluted with the overall time response employing a least-square fitting procedure. The least-square fit functions (—) well depicts the temporal dependence of the decay curves (...) for all excitation energies as can be seen in Fig.3. The fragmentation time τ_0 (about $900...240fs$ dependent on the excitation energy) is short compared to $\tau_1 = 0.5...2ps$ arising from the fragmentation of larger sodium clusters into a second different excited state of the observed cluster. It is remarkable that the fragmentation into clusters with an even number of atoms is neglectible while in the case of all odd clusters we observe a fairly strong "raining-in" of fragments. So we can state that in the fragmentation cascade of sodium clusters odd clusters split into a dimer and an odd fragment while even clusters prefer to break into an odd fragment and e.g. a monomer [12].

References:

1. K.Kobe, G.Sommerer, E.Schreiber, and L.Wöste : to be published
2. E.Schreiber, H.Kühling, K.Kobe, S.Rutz, and L.Wöste: Ber.Bunsenges.Phys.Chem.96, 1301 (1992)
3. J.P.Wolf, G.Delacrétaz, and L.Wöste : Phys.Rev.Lett. 63, 1946 (1989)
4. J.Manz and R.de Vivie-Riedle: private communications
5. W.Meyer: private communications
6. K.Kobe, S.Rohland, S.Rutz, E.Schreiber, and L.Wöste: to be published
7. J.Gaus, K.Kobe, V.Bonačić-Koutecký, H.Kühling, J.Manz, B.Reischl, S.Rutz, E.Schreiber, and L.Wöste : J.Phys.Chem. 97, 12509 (1993)
8. K.Kobe, H. Kühling, S.Rutz, E.Schreiber, J.P.Wolf, L.Wöste, M.Broyer, and P.Dugourd: Chem.Phys. Lett. 213, 554 (1993)
9. S.Rutz, K.Kobe, H.Kühling, E.Schreiber, and L.Wöste : Z.Phys.D 26, 276 (1993)
10. K.Kobe, G.Sommerer, S.Rutz, E.Schreiber, and L.Wöste : to be published
11. H.Kühling, S.Rutz, K.Kobe, E.Schreiber, and L.Wöste : J.Phys.Chem. 97, 12500 (1993)
12. H.Kühling, K.Kobe, S.Rutz, E.Schreiber, and L.Wöste : to be published

Thursday, May 5, 1994

High Field Atomic Physics

ThC 1:30pm–3:00pm
Dana Point Ballroom

P. Bucksbaum, *Presider*
University of Michigan

High-Harmonic Generation: The Route to Attosecond Pulses

P.B. Corkum, N.H. Burnett, P. Dietrich and M. Y. Ivanov

National Research Council of Canada

Ottawa, Ont. Canada

Ever since the development of the laser, obtaining shorter and shorter pulses has been a major emphasis of laser science. Now it is possible to produce pulses of only a few periods duration over much of the visible and infrared spectrum. Clearly future developments of short pulse coherent sources require that shorter wavelength radiation be used. Harmonic radiation, generated when atoms or molecules are illuminated by strong laser fields, is the most promising source of the next generation of ultrashort pulses.

We concentrate on the physics of high harmonic generation, showing that it can be easily understood within a semiclassical model as a three-step process. The steps are the following: (1) A portion of the electron wavefunction tunnels from the atom into the continuum. (2) Once free from the atom, the motion of the electron wave packet can be followed, to first order with classical physics. It moves in the strong electric field, first away from the atom, but as the field reverses, it moves back towards its origin. (3) Harmonic emission is due to the induced dipole $d=\langle g|r|c\rangle+cc$. In other words, it is due to the dynamic interference between that portion of the wavefunction remaining in the ground state, g, and that portion of the wavefunction, c, in the continuum.

This simple semiclassical model has many consequences, one being that it makes clear a simple route to sub-femtosecond pulse generation. In addition it can be easily generalized. For example, instead of emitting an harmonics in step three, the returning electron can collisionally ionize its parent ion, leading to double ionization. Indeed, such double ionization

has recently been observed [1].

The model suggests many means to control high harmonic generation and other strong field processes. One of the simplest is to use elliptically polarized light. In that case, step two leads to the electron moving in a spiral orbit. Consequently, the interference process in step 3 is greatly weakened because the electron can totally or partially miss the ion. That is, the strength of the harmonic emission (or the double ionization signal) will depend on ellipticity.

Experimentally, we studied the ellipticity dependence of both double ionization and harmonic generation and found that they are in quantitative agreement both between the experiments and with the model. Figure 1 shows the ellipticity dependence of the (a)41-st and (b) 21-th harmonic from neon illuminated by a 780 nm pulse with peak intensity of $8x10^{14}W/cm^2$. Figure 1c shows the ellipticity dependence of double ionization of neon when illuminated with 630 nm light with intensity $9x10^{14}$ W/cm^2. In all three cases the solid lines are upper and lower bound theoretical curves that result from a no free parameter model of the processes.

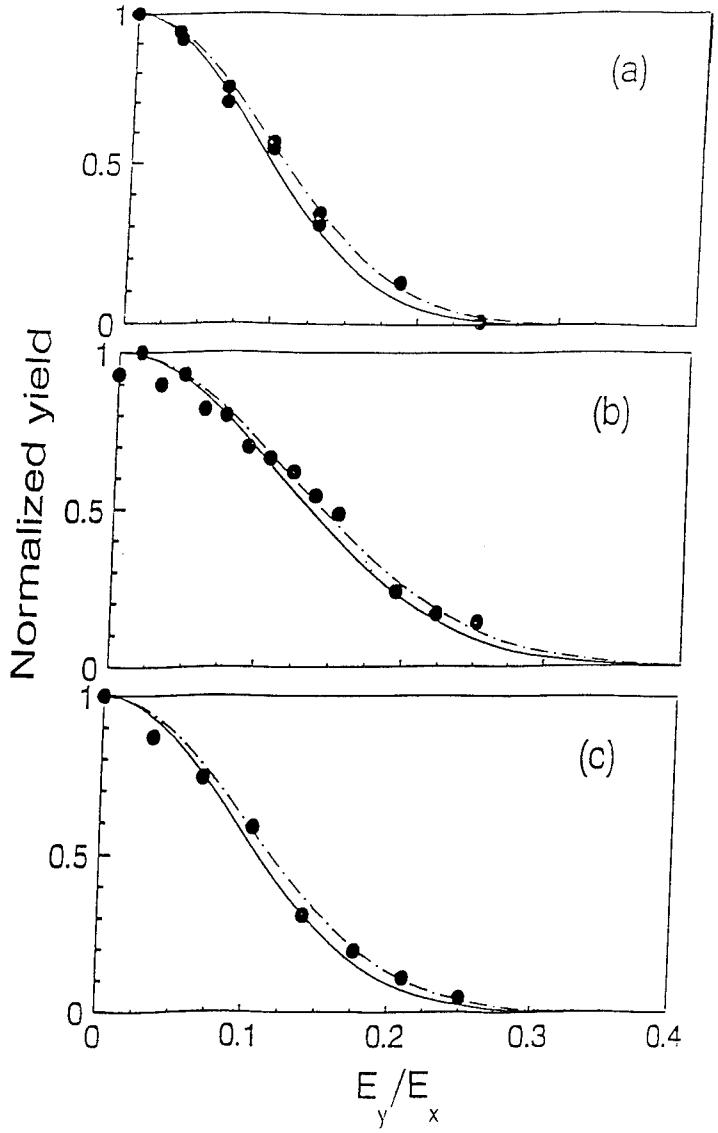
A corollary of these experiment is the possibility of sub-femtosecond emission of high harmonic radiation. A sub-femtosecond pulse obtained using a fundamental formed by combining two short, perpendicularly polarized pulses with frequencies centred at ω_1 and ω_2 where $\omega_1 - \omega_2 / \omega_1 << 1$ and ω_1 is 800 nm. Such a pulse has a dynamic polarization that sweeps from circular through linear back to circular.

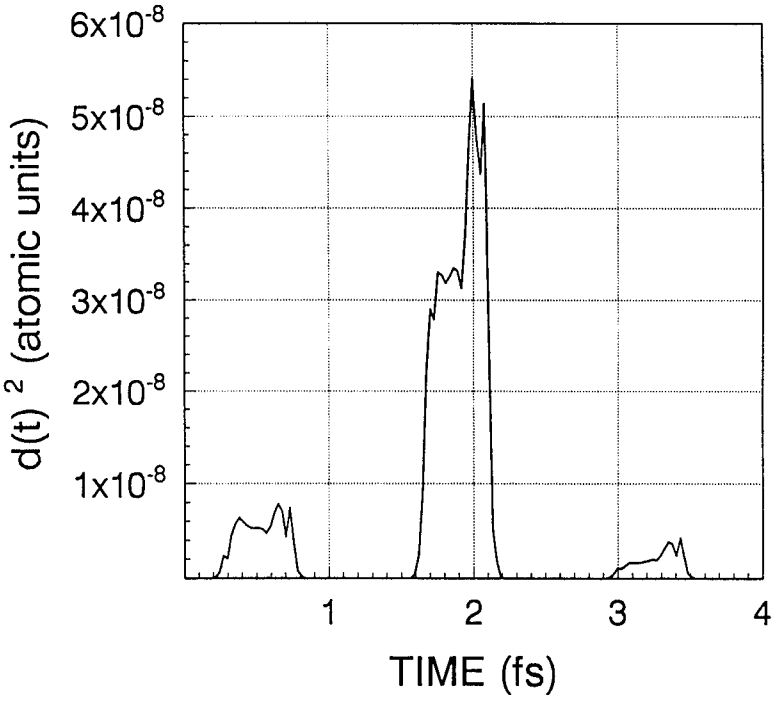
Figure 2 is a simulation of the square of the dipole moment as a function of time. For the simulation the peak intensity of each pulse that together make the fundamental was $3x10^{14}W/cm^2$, the phase difference was taken as zero at the time of peak intensity of each.

Although phase matching is often as important as the susceptibility for understanding the strength of the harmonic emission, under conditions required for phase matching, the harmonic emission will follow the second derivative of the time dependence of the dipole moment. To obtain Fig. 2 the harmonic emission was assumed to be observed through a 2000 Angstrom silver filter. The purpose of the filter was to eliminate the low harmonic emission which is not as sensitive to the ellipticity as are the high harmonics. Since the dispersion characteristics of silver are well known, we can include dispersive effects in the calculation. However, the filter will not modify pulse duration shown in Fig. 2 significantly.

In conclusion, we present a quantitative, but intuitively clear and physically transparent model of high harmonic generation. We test the model predictions by studying the harmonic conversion efficiency and the probability of double ionization as a function of the ellipticity of the fundamental. Finally, we show that the same physics allows the formation of attosecond pulses using fundamental laser pulses that can be constructed with current laser technology.

[1] D.N. Fittinghoff, et al., Phys. Rev. Lett., 69, 2642 (1992).


Normalized yield
(a)
(b)
(c)
1
0.5
0
0
0.1
0.2
0.3
0.4
E_y/E_x


d(t)^2 (atomic units)
6x10^-8
5x10^-8
4x10^-8
3x10^-8
2x10^-8
1x10^-8
1
2
3
4
TIME (fs)

Coherence Properties of High Order Harmonic Radiation

T. Ditmire, K. S. Budil, J. K. Crane, and M. D. Perry

Lawrence Livermore National Laboratory
P. O. Box 808, L-443
Livermore, California 94550

P. Salieres, and A. L' Huillier

Service des Photons, Atomes et Molecules
Centre d'Etudes de Saclay
C. E. A. 91191 Gif-sur-Yvette, France

The understanding of high order harmonic generation in gases exposed to strong laser fields has progressed significantly in recent years. Emphasis has shifted to the characterization and use of these harmonics as a coherent, high brightness source of XUV radiation. We have investigated some of the coherence properties of very high order harmonics in argon and neon by measuring the spectral distributions and the far-field spatial profiles of the harmonic radiation. We have conducted these studies at intensities both below and above the ionization saturation intensity.

The experiments were conducted by generating harmonics of a short pulse Cr:$LiSrAlF_6$ (LiSAF) laser[1] capable of producing pulse energies in excess of 200 mJ. This laser operates at a wavelength of 825 nm and has a pulse width of 140 fsec (FWHM). Special care has been taken to characterize the far-field focal profile of the laser which is approximately two-times diffraction limited with a 70 μm focal spot ($1/e^2$) using an f/17 focusing lens. For the spatial profile measurements the laser was focused with an f/17 optic into a gas plume provided by a pulsed gas jet. The divergence of the focused beam was 72 mrad ($1/e^2$). The harmonics produced were collected by a flat field spectrometer consisting of a flat, variable line spaced gold grating at grazing incidence and a single, flat carbon folding mirror. A CsI coated dual micro-channel plate (MCP) detector was located at the image plane of the spectrometer, 59 cm from the source of the harmonics. A phosphorus screen coupled to the MCP detector is read by an 8-bit CCD camera yielding simultaneous spectral and spatial information on each laser shot.

The results of harmonics produced in argon at roughly 4 $x10^{14}$ W/cm^2 are shown in figure 1. Spectral information is contained in the vertical direction with decreasing wavelength from top to bottom, and spatial information is contained in the horizontal direction. This image shows harmonics from the 21st in the plateau region out to the 33rd in the cutoff. We found that the harmonic profiles were extremely reproducible for a given intensity on a shot to shot basis. Averaged line-outs of harmonics 25, 29 and 33

produced in argon are shown in figure 2. These harmonics exhibit $1/e^2$ divergences that decrease from 12 mrad for the 25th down to 4 mrad for the 33rd harmonic.

Unlike the measurements of Tisch et al.[2] we find that the harmonic profiles are smooth and structureless both in the plateau and in the cutoff. Furthermore, the harmonics exhibit a divergence that is significantly less than the predictions of lowest order perturbation theory, (figure 2). It can be shown that in the limit the confocal parameter is much longer than the gas jet length that perturbation theory predicts that the qth harmonic divergence is $\frac{1}{\sqrt{q}}$ times the laser divergence while a harmonic that varies with effective order p will diverge with $\frac{\sqrt{p}}{q}$ times the laser divergence. The measured harmonic divergence is not unexpected in light of the non-perturbative behavior of these harmonics which typically exhibits nonlinear orders which are much lower than the actual process order.[3] Spatial profile measurements in neon yield results very similar to those in argon.

We have also investigated the harmonics spectral profiles with the use of a re-imaging monochrometer with an estimated resolution of .03 nm. The spectral width of the laser for these experiments was 8.5 nm. Profiles of the 27th harmonic in argon and neon produced at intensities near the ionization saturation intensities for each atom are shown in figures 3a and 3b respectively. Accounting for the resolution of the spectrometer we find that the fractional bandwidth of the harmonics was $\Delta\lambda/\lambda \approx 2 \times 10^{-3}$ in argon and was $\Delta\lambda/\lambda \approx 5 \times 10^{-3}$ in neon. This range of spectral linewidths is narrower than the linewidths predicted by perturbation theory and is roughly consistent with the predictions made by using a lower effective nonlinear order for the harmonic generation.

1 T. Ditmire, and M. D. Perry, Opt. Lett., **18,** 426 (1993).

2 J. W. G. Tisch, R. A. Smith, J. E. Muffett, M. Ciarrocca, J. P. Marangos, and M. H. R. Hutchinson, Phys. Rev. A., **49**, R28 (1994).

3 C. G. Wahlstrom, J. Larsson, A. Persson, T. Starczewski, S. Svanberg, P. Salieres, Ph. Balcou, A. L' Huillier, Phys. Rev. A., **48**, 4709 (1993).

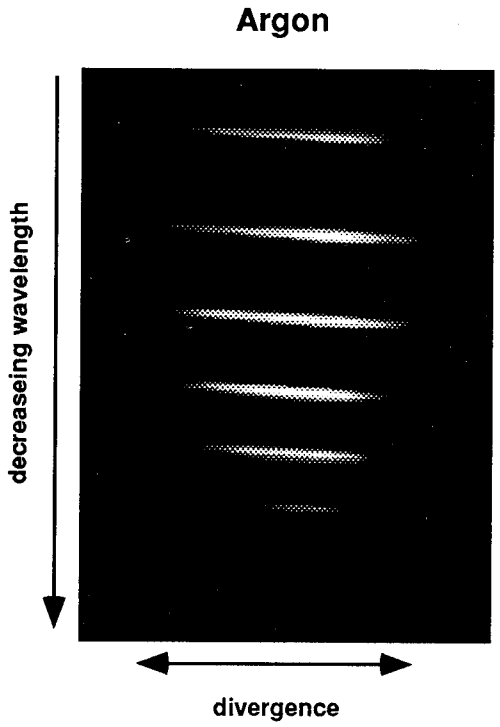


figure 1

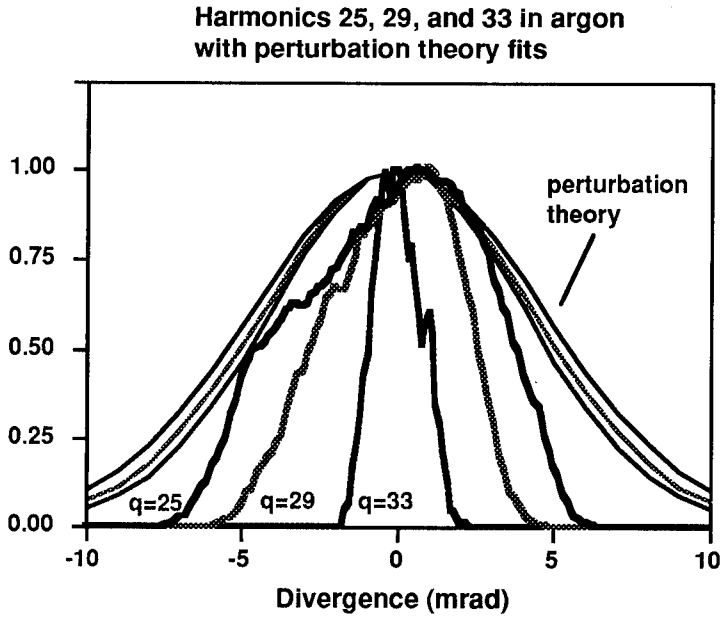


figure 2

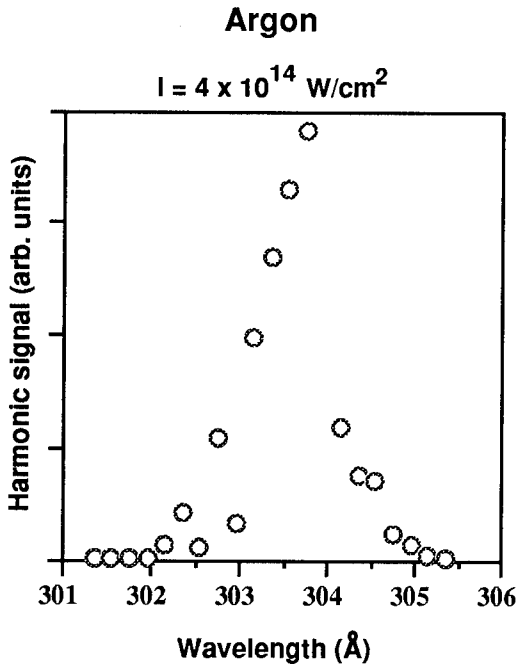


figure 3a

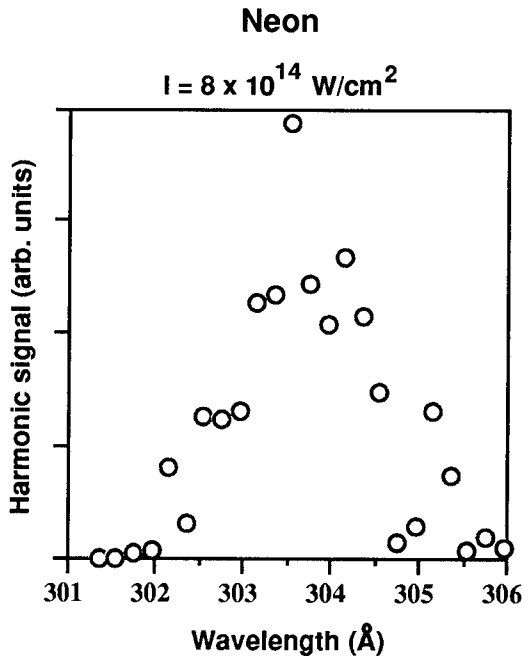


figure 3b

Climbing a Ladder System by Frequency Chirped Laser Pulses

L. D. Noordam, B. Broers, P. Balling, D. J. Maas, and H. B. van Linden van den Heuvell

FOM-Institute AMOLF, Kruislaan 407, 1098 SJ Amsterdam, The Netherlands,
phone: 31-20-6081234, fax: 31-20-6684106

Introduction

Excitation of vibrations of chemical bonds in molecules is of considerable interest for controlling chemical reactions. Ever since the advent of the laser, chemists have been dreaming about the possibility to use laser light to selectively excite molecular bonds all the way up to the dissociation limit. Direct single photon excitation to a highly excited vibrational state is forbidden due to the very small overlap between the initial and final state. This necessitates a step-wise excitation. So far two complications have frustrated this quest for bond-selective chemistry. Firstly, the anharmonicity of a chemical bond makes it difficult to attain a high level of vibrational excitation: although the ground state can be depleted in favour of the first excited state upon irradiation with a precisely tuned laser, further excitation steps will require slightly different frequencies. Secondly, the time scale on which the vibrational energy in a given bond delocalizes by redistributing itself through the molecule is very short (picosecond range).

Very short laser pulses present a solution to the problem. Intrinsically they have a large enough bandwidth to overcome the variation in spacing of the vibrational ladder due to anharmonicity. Furthermore, their pulse durations are smaller than the time scales for intra-molecular energy flow. Finally, it can be shown that 100% population can be transferred to a specific vibrational state, while in a multi-step approach this is in practice hindered by Rabi oscillations.

It has been suggested [1] that the vibrational excitation can be enhanced by applying short pulses whose frequency is swept ('chirped') in order to follow the change in size of the vibrational quanta. Calculations have indicated that in this way 100% of the population can be transferred from the ground vibrational state to a highly excited vibrational state, without leaving population in intermediate states. In principle the final state can be as high as the vibrational continuum, resulting in bond-selective dissociation into two fragments.

In this contribution we will present experimental evidence [2,3] of 100% population transfer in an atomic model system. In a three-step ladder in rubidium we achieved full population transfer from the electronic ground state (5s) to the final state 5d.

Experimental demonstration of population sweeping in a ladder system

Recently we have demonstrated [2] in an atomic model system with three levels that 100% population transfer can be obtained from the initial state to the final state by sweeping the frequency. Instead of *vibrational* levels in a molecule, in the atomic model system three *electronic* levels are studied. Rubidium atoms in the electronic ground state (5s) are excited via the intermediate state (5p) to the final electronic state (5d). Since the transition frequencies for these two steps are not identical (see figure 1) we have a quantum system that resembles three vibrations in an anharmonic molecular potential. With our laser system we produce sub-picosecond pulses with sufficient bandwidth to include both steps, and by means of a grating device we are able to vary the chirp the pulses continuously. In the experiment, after the short pulse we have probed the population of the upper state (5d) with another laser. As can be seen in fig. 1 indeed 100% population is transferred.

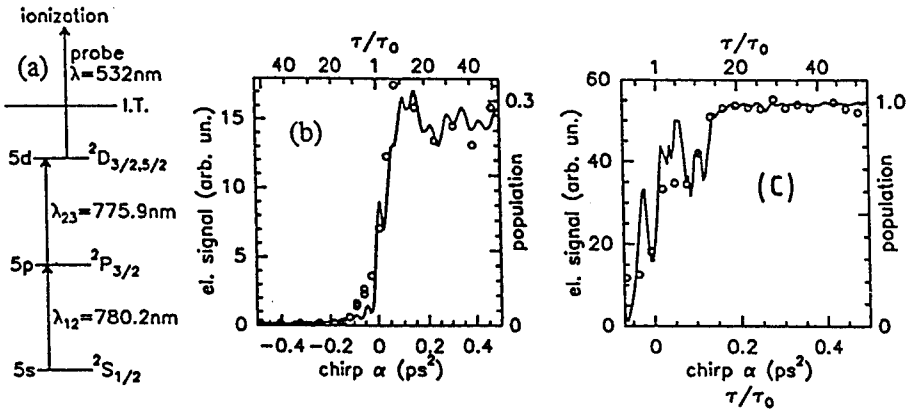


Fig. 1 (a) Energy levels of the three-state ladder in rubidium (5s,5p,5d). The population of the upper state is probed afterwards by photoionization by a second laser. (b) Measured enhancement of the upper state population for the chirped pulses; blue first (775.9 nm, $\alpha<0$) results in almost no population of the upper state; red first (780 nm, $\alpha>0$) enhances the population dramatically compared to no chirp ($\alpha=0$). [c] same as [b] but a higher intensity: all population is transferred to the final state.

A surprise

At somewhat higher laser intensities we found that the counterintuitive frequency sweep (applying the frequency for the second step first) gave 100% population transfer. The population transfer by this, at first glance, surprising frequency sweep is confirmed by solving the Schrödinger equation for this system numerically. In fact, in the counterintuitive sweep the population of the intermediate state is almost avoided and is thus well suited for systems with a short lived intermediate state.

Quantum interference

At intermediate intensities we observed [3] interference in the final state population as a function of chirp. Two routes are interfering: I) population of state |3> by sequential transfer; First the transition |1> to |2> is driven by the laser and subsequently the |2> to |3> transition. II) direct two-photon transition from state |1> to state |3> via a virtual intermediate state. The routes I) and II) require different frequencies within the pulse, and since the pulse is frequency chirped the transfer occurs at different times. The phase difference between the routes, causing the interference, is linearly proportional to chirp as is confirmed by the experimental results presented in figure 2.

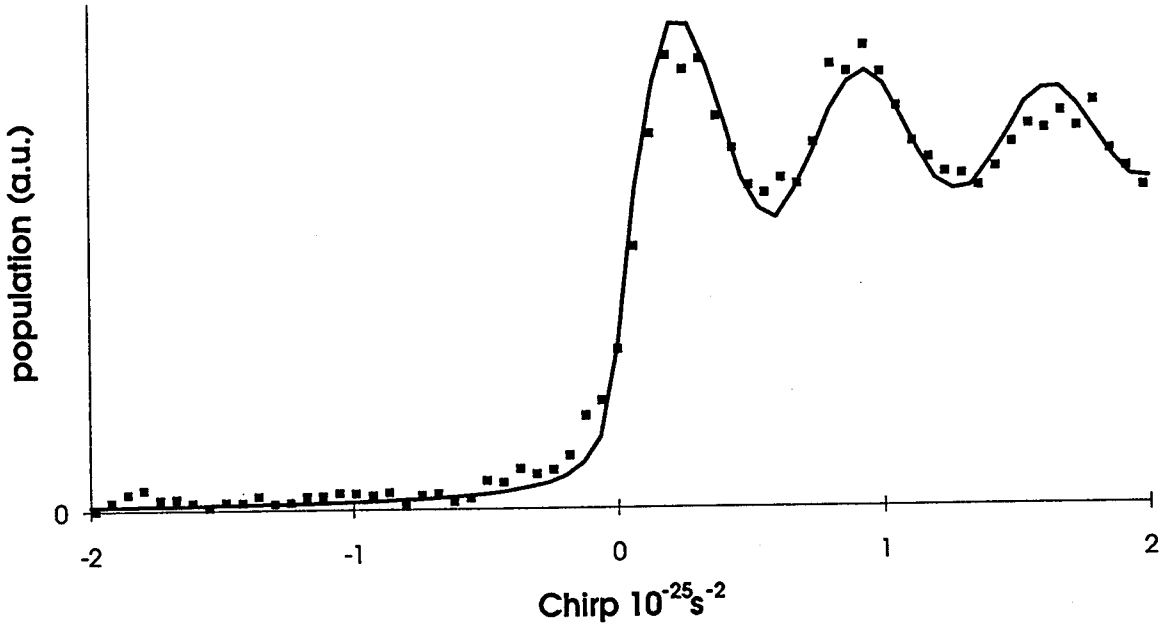


Fig. 2 Measured enhancement of the upper state population at moderate intensities. The wiggles are due to interference in the upperstate amplitude of direct 2-photon excitation and sequential 1+1-photon excitation.

Conclusion

The mechanism of adiabatic passage can be generalized to multi-level systems such as a vibrational ladder of a molecular bond. By sweeping the frequency of the light through the resonance all population is transferred from one participating level to the next. By sweeping through the sequence of vibrational lines (shifted with respect to each other because of anharmonicity of the interatomic potential) all molecules can be brought in the same highly excited vibrational state.

[1] S. Chelkowski, A. D. Bandrauk, and P. B. Corkum, Phys. Rev. Lett. **65**, 2355 (1990)
[2] B. Broers, H. B. van Linden van den Heuvell, and L. D. Noordam, Phys. Rev. Lett. **69**, 2062 (1992)
[3] P. Balling, D. J. Maas, and L. D. Noordam to be submitted to Phys. Rev. A

Poster Session 4

ThD 3:00pm–4:30pm
Dana Point Ballroom

Hybrid grating-prism compressor with cubic phase tunability and decreased alignment sensitivity

S. Kane, J.V. Rudd, A.-C. Tien, J. Squier, G. Korn, G. Mourou
Center for Ultrafast Optical Science
University of Michigan
2200 Bonisteel, IST Bldg., Rm. 1006
Ann Arbor, MI 48109-2099
Ph: (313) 763-4875 Fax: (313) 763-4876

P. Tournois
Thomson-CSF
Cedex 67
92045 Paris La Defense 10, France

Traditional pulse stretcher/compressor systems [1,2] have relied on high-groove-density gratings (~2000 l/mm) for systems operating in the 800-nm wavelength regime. These highly dispersive gratings provide significant stretching and compressing of >100-fs pulses in a relatively compact system. In addition, high-groove-density gratings are very efficient, typically yielding a 70% net throughput for a double-passed compressor. However, while these gratings work well for stretching and compressing >100-fs pulses, the alignment sensitivity of traditional high-groove systems makes them almost unusable for pulses shorter than 100 fs. Here we present a novel high-groove-density grating compressor which has relaxed alignment tolerances and can be used with ultrashort pulses.

In order to stretch a pulse and recompress it back to its transform limit, the stretcher and compressor must be matched to all orders of the phase. In the laboratory we have two alignment controls in the compressor: the grating separation G, and the incident angle θ_i. To null the quadratic phase we adjust G until the pulsewidth is a minimum, and then we adjust the incident angle to minimize the cubic phase. The incident angle is not an independent control of the cubic phase, however; the angle adjustment introduces an additional quadratic phase that scales with the square of the groove density.

If the quadratic chirp introduced by the angle adjustment is large, or if the pulse is short enough that it is catastrophically broadened by even a residual chirp, it will be nearly impossible to achieve perfect recompression of the pulse. Since the chirp introduced by angle-tuning goes as the square of the groove density, low-line/mm gratings will be much easier to align. A rule of thumb for stretcher/compressor systems is that the ratio of wavelength λ, to grating groove spacing d should be on the order of unity, as higher ratios will impose stricter alignment tolerances.

To illustrate the alignment sensitivity of high-groove-density gratings, consider a small mismatch between the angle of incidence in a stretcher and compressor. For a system using 1200 l/mm gratings (λ/d =.9) a misalignment of 20 arc minutes could be nearly compensated by slightly increasing the compressor grating separation. A residual cubic phase slightly distorts the pulse, but the pulsewidth remains essentially unchanged (FWHM≈90-fs.) For the case of 2380 l/mm gratings (λ/d=1.8) the same misalignment is uncompensatable, and the minimum pulsewidth that can be achieved is 144 fs. Thus, by using gratings with a ratio of $\lambda/d \sim 1$ we see that the alignment tolerances can be dramatically reduced. By using 1200 l/mm gratings we have recently demonstrated the stretching, amplification, and recompression of 55-fs pulses [3].

Nonetheless, there are several properties of higher line/mm gratings that make them desirable for CPA. As stated earlier, the net throughput of 2000 l/mm grating compressors is typically 70% (compared to only 50% for the 1200 l/mm grating compressors). In addition, the higher line/mm gratings generally posses higher efficiencies over a broader wavelength range. This is an especially important consideration for pulsewidths in the 10-20-fs range where reshaping of the spectrum

has occurred due to the wavelength-dependent diffraction efficiency of the gratings. Thus, a more broadly tunable system, as well as shorter pulses, is possible from this type of grating.

We have designed a novel series of stretcher/compressor systems which employ the higher groove density gratings, but which exhibit the dispersive characteristics of the 1200 l/mm gratings [4]. Thus, we can simultaneously take advantage of the properties of both systems to produce a more ideal stretcher/compressor system.

Figure 1 shows the design of the hybrid compressor. The use of an *intra-grating* prism pair allows for independent cubic-phase adjustments 100 times greater than an external prism sequence. In figure 2 we show the calculated group delay of a standard 2000 l/mm grating compressor and our hybrid compressor The measured group delay for both of these systems is illustrated in figure 3. Figure 4 shows the calculated quadratic phase delay for standard 2000 l/mm compressor and a hybrid compressor which uses 2000 l/mm gratings and SF-10 prisms. It is clear from figure (4) that this device yields a highly linear chirp. Finally, the additional advantage of this system is that fine cubic phase adjustments can be made without changing the angle of incidence into the grating pair, simply by changing the prism spacing. These cubic-phase adjustments are nearly independent; changing the separation of the prisms introduces minimal quadratic phase, making the system easy to align and useful for the stretching and compressing of ultrashort pulses.

This work was supported by the NSF through the Center for Ultrafast Optical Science under STC PHY 8920108.

1. E.B. Treacy, IEEE J. Quantum Electron. **QE-5**, 454 (1969).
2. O.E Martinez, IEEE J. Quantum Electron. **QE-23**, 59 (1987)
3. J.V. Rudd, G. Korn, S. Kane, J. Squier, G. Mourou, P. Bado, Opt. Lett. **18**, 23 (1993).
4. Other designs proposed by P. Tournois, to be published, and J. Squier, to be published. These devices use transmission gratings, which are not applicable to ultrashort pulses.

Figure Captions

1. Geometry for the hybrid compressor. A stretcher would be made simply by adding an imaging system (either lenses or mirrors) between the prisms.

2. Calculated group delay for 2000 l/mm Treacy and hybrid compressor (SF-10 prisms).

3. Measured group delay for a standard and hybrid compressor, both using 2000 l/mm gratings.

4. Calculated quadratic phase for standard 2000 l/mm compressor and a 2000 l/mm hybrid compressor.

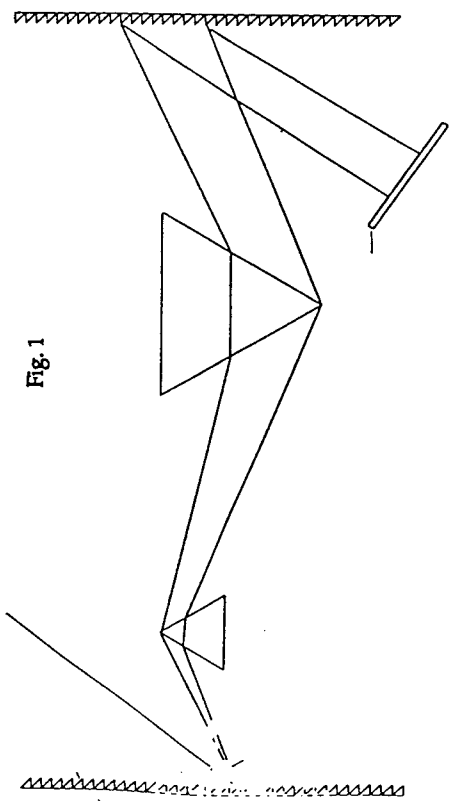


Fig. 1

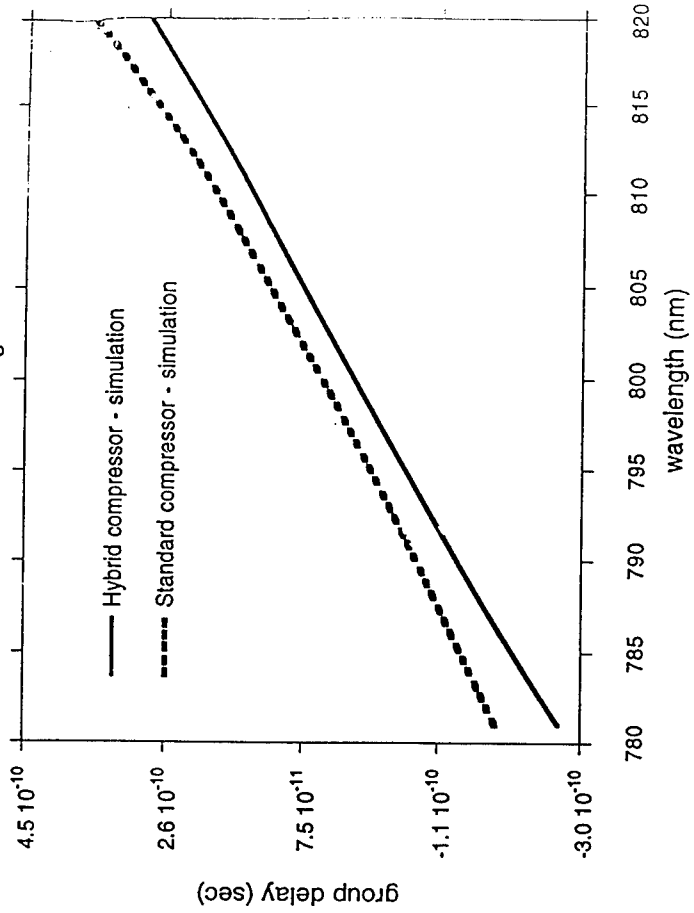


Fig. 2

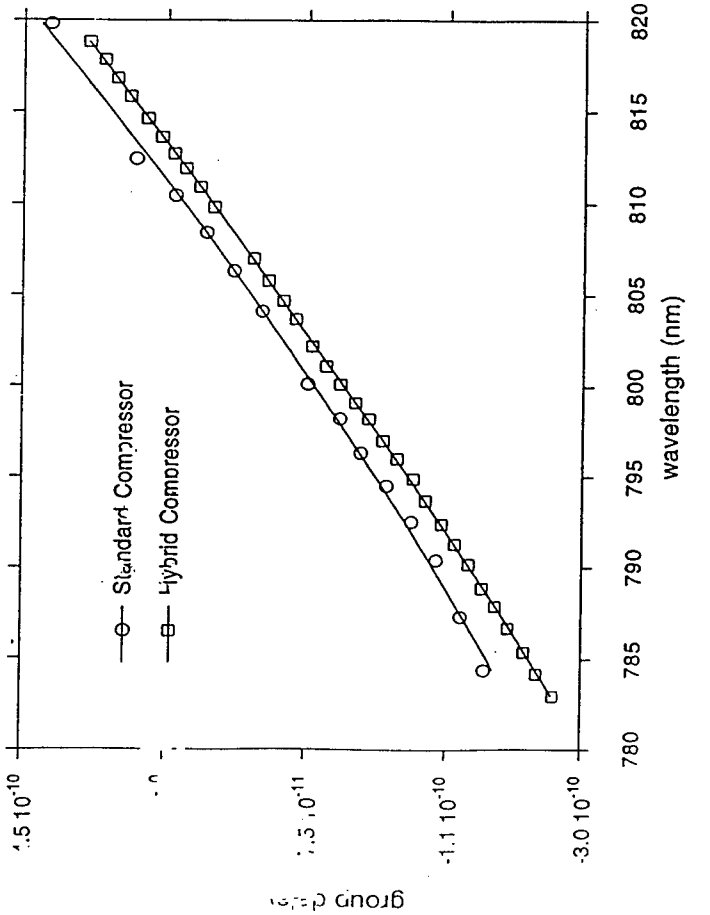


Fig. 3

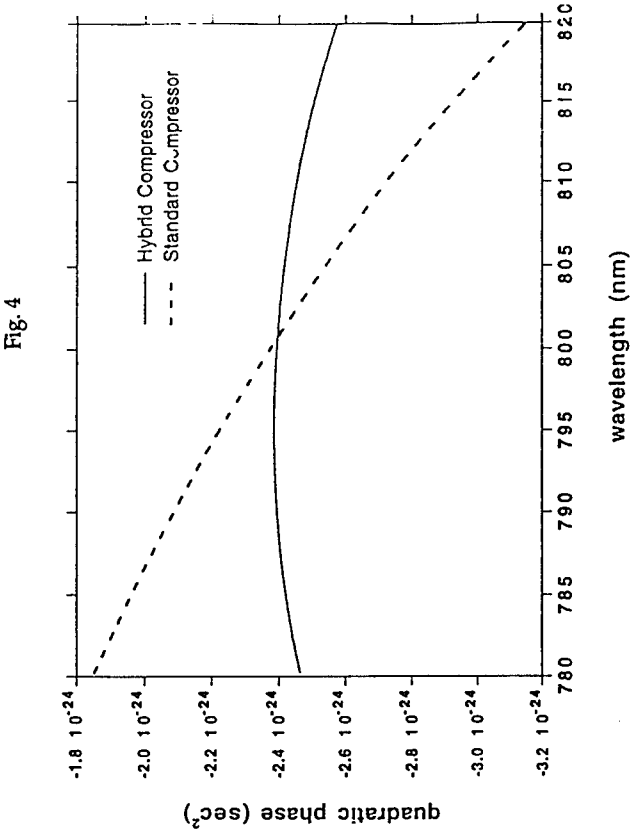


Fig. 4

Femtosecond Spectral Hole Burning in InGaAs/AlGaAs Strained-Layer Single-Quantum-Well Diode Lasers

C.-K. Sun[1,2], B. Golubovic[2], H. K. Choi[3], C. A. Wang[3], G. D. Sanders[4], C. J. Stanton[4], J. G. Fujimoto[2]

[1]Division of Applied Sciences, Harvard University, Cambridge, MA 02138; [2]Department of Electrical Engineering and Computer Science, Research Laboratory of Electronics, Massachusetts Institute of Technology, Cambridge, MA 02139; [3]Lincoln Laboratory, Massachusetts Institute of Technology, Lexington, MA 02173; [4]Department of Physics, University of Florida, Gainesville, FL 32611. (617) 253-8528

Studies of the high speed modulation response of semiconductor lasers, exhibited a strong damping of the relaxation oscillation resonance and suggested the presence of a nonlinear gain process with a characteristic time much shorter than the carrier lifetime[1]. Several possible mechanisms were proposed which might produce this nonlinear gain, including spectral hole burning, carrier heating, and four wave mixing related effects[2]. CW studies have been performed in an effort to indentify these nonlinear gain mechanisms[2,3]. However, time domain femtosecond measurements have the advantage that they can directly characterize the ultrafast gain dynamics. Several single-wavelength femtosecond pump-probe investigations were performed on various diode laser systems[4,5]. Carrier heating effects and spectral hole burning were reported, but to date, no direct femtosecond measurements of the wavelength dependence of spectral hole buring have been possible.

In this paper, we describe a novel heterodyne multiple wavelength femtosecond pump-probe technique for investigating gain dynamics in active devices. Studies in strained layer InGaAs SQW diode lasers have been performed and provide the first direct femtosecond measurements of the wavelength dependence of spectral hole burning. The femtosecond resolution and multiple wavelength measurement capability of this new experimental technique permits a more direct measurement of transient gain dynamics than is possible using conventional single-wavelength pump-probe techniques.

The schematic of the experimental setup is shown in Fig. 1. Studies were performed using a modelocked Ti:Al_2O_3 laser generating 100 fs pulses at 880-1060 nm. In order to perform multiple-wavelength measurements, the spectrum of the pulses was first broadened from 10 nm to 70 nm using self-phase-modulation in a single mode optical fiber. The wavelengths and the pulse durations of the pump and probe pulses were selected using spectral windowing[6]. In order to distinguish the pump and probe pulses in a waveguide device using a collinear geometry, we empoyed a novel heterodyne detection technique[7]. A portion of the probe pulse was split to provide a reference pulse and both probe and reference pulses were frequency shifted using acousto-optic modulators with 50 MHz and 51 MHz modulation frequencies respectively. The pump, probe, and reference pulses were coupled into the the diode laser with the reference pulse 1 ns ahead of the pump and the probe. A standard pump probe delay line was used to perform the femtosecond transient transmission measurements. An imbalanced Michelson interferometer was used after the device to delay the reference pulse and interfere it with the probe pulse at the detector. The reference pulse functioned analogously to a

local oscillator in heterodyne detection. An AM radio receiver was used to detect the probe signal by monitoring the 1 MHz beat frequency between the probe and reference pulses. A background-free measurement was performed by chopping the pump at a 1 kHz, and using lock-in detection.

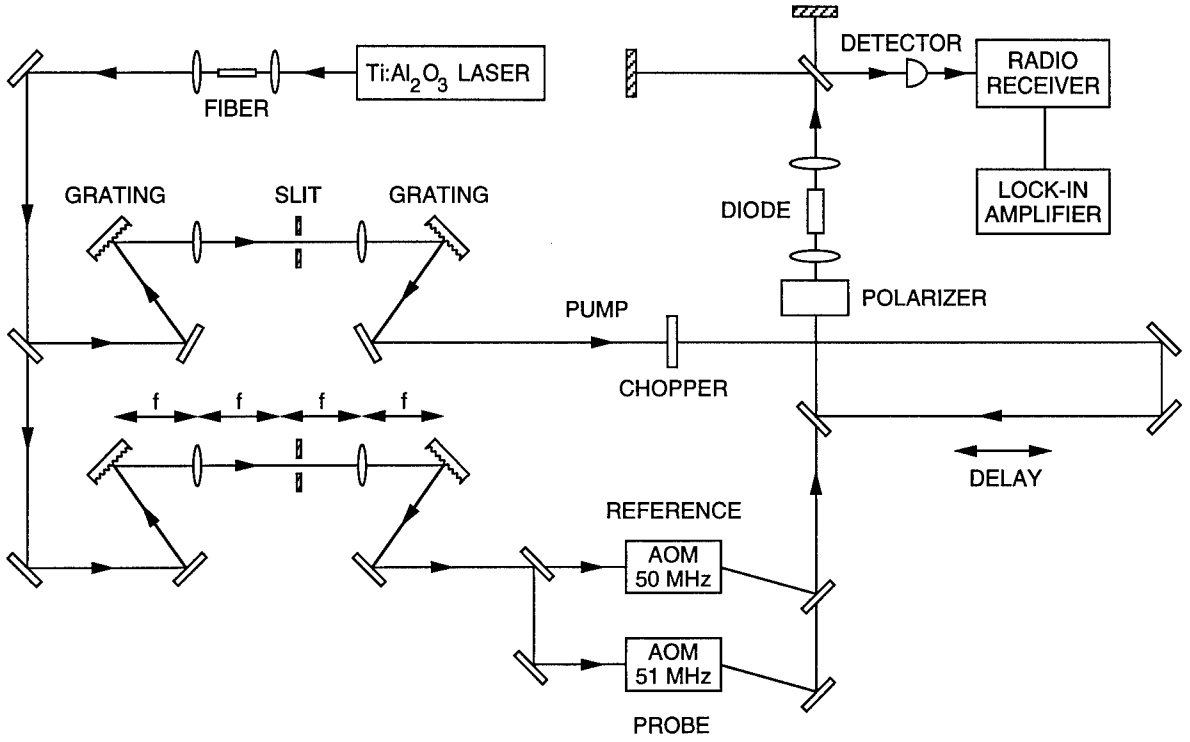


Fig. 1. Heterodyne multiple-wavelength pump probe measurement technique.

Studies were performed on InGaAs/AlGaAs graded-index seperate-confinement heterostructure SQW ridge-waveguide diode lasers[6]. The devices were 300 μm in length with a bandgap near 960 nm. The pulses had a 150 fs pulse duration with a 8 nm bandwidth. The pump wavelength was tuned in the gain region and the probe varied over a range of plus or minus 25 nm from the pump wavelength in order to investigate the gain dynamics across the gain bandwidth. Wavelengths were chosen so that only heavy-hole to conduction band transitions were allowed. By varying the bias current, the carrier density in the quantum well and quasi-chemical potential can be varied in order permit different regions of device operation to be characterized. The role of carrier heating from stimulated transitions, free carrier absorption, and two-photon absorption are functions of the operating conditions and their relative contributions to the gain dynamics can be separated using differnt measurement conditions.

Figure 2 shows differential transmission changes measured at different probe frequencies as a function of time delay. This measurement characterizes the evolution of the gain in both the spectral and the time domains. Around zero delay, a sharp transmission decrease was observed with time resolution limited recovery. This rapid transient may be attributed to spectral hole burning and two photon absorption. As the probe frequency is detuned from the pump, the transmission transient decreases. This wavelength dependent characterization provides direct evidence for spectral hole burning effects. At intermediate time delays, gain changes are mediated by changes

in the carrier temperature. At longer time delays on the picosecond scale, the carriers reach equilibrium with the lattice, and the observed gain changes are produced by changes in the carrier population.

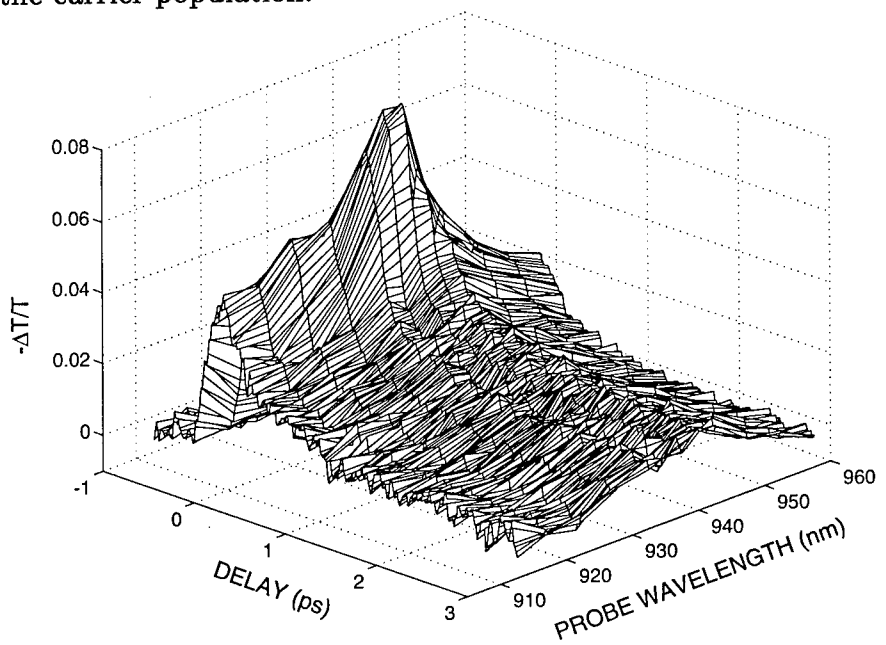


Fig. 2. Experimental data with pump at 935 nm and probe varied from 910 - 955 nm. The carrier density was $\sim 6 \times 10^{12}$ cm^{-2}.

Further investigations as a function of pump wavelength, bias current, and pump power will be presented to describe gain dynamics in different diode laser operating regimes. The effects of carrier dynamics on transient gain and implications for high speed device operation will be discussed.

We would like to acknowledge the scientific collaboration of Prof. E. P. Ippen and discussions with D. Dougherty, C. Hultgren, K. Hall, and G. Lenz. This research is supported in part by the ONR FEL program N00014-91-J-1956, the Joint Services Electronics Program contract DAAL03-92-C-0001, the Air Force Office of Scientific Research contract F49620-91-C-0091, and the Department of the Air Force.

References

[1] R. S. Tucker, J. Lightwave Technol. **3**, 1180 (1985).

[2] R. Frankenberger, and R. Schimpe, Appl. Phys. Lett. **57**, 2520 (1990).

[3] L. F. Tiemeijer, Appl. Phys. Lett. **59**, 499 (1991).

[4] M. P. Kesler and E. P. Ippen, Appl. Phys. Lett. **51**, 1765 (1987).

[5] K. L. Hall, J. Mark, E. P. Ippen, and G. Eisenstein, Appl. Phys. Lett. **56**, 1740 (1990).

[6] C.-K. Sun, H. K. Choi, C. A. Wang, and J. G. Fujimoto, Appl. Phys. Lett. **62**, 747 (1993).

[7] K. L. Hall, G. Lenz, E. P. Ippen, and G. Raybon, Opt. Lett. **17**, 876 (1992).

Femtosecond Spectroscopic Studies of Barrierless Reaction of Triphenylmethane Dye Molecules in Alcohol Solutions

Mei Du, Yiwei Jia, Graham R. Fleming*

Department of Chemistry, The University of Chicago, 5735 S. Ellis Ave. Chicago, IL 60637. Tel. 312-702-7517. Fax: 312-702-0805.

Many chemical and biological reactions proceed on a potential surface with a low barrier or lack of barrier from reactant to product along the reaction coordinate[1,2]. In a barrierless case, the interaction between the surrounding medium and reactants (or products) provide the only frictional force in affecting the chemical reactions. In general, the frictional force includes two parts: frictional force from the solvent and from non-reactive vibrational modes of reactants or products. Thus, from the perspective of chemical reactions in solution, a barrierless reaction is a prototype in studying both the interactions between reactants(or products) with the surrounding medium and the role of vibrational relaxation during the course of chemical reaction. In this work, we choose triphenylmethane dye molecules: malachite green and crystal violet in alcohol solutions as two model systems to investigate the nature of the barrierless process at initial time and the effect of both solvent and intramolecular vibrational modes during the reaction.

The femtosecond pulses used in this work were obtained from a 100KHz repetition rate laser system, originating from a cavity-dumped antiresonant ring dye laser that typically produces pulses of 60fs FWHM and ~3nJ pulse energy at 610nm. Three experimental apparatus were used in this work: fluorescence up-conversion apparatus, transient pump-probe spectrometer, and transient dichroism and birefringence apparatus. Fluorescence data and transient pump-probe data were taken with 60fs pulses while transient dichroism and birefringence data were taken with ~30fs pulses. Data analysis was performed by both nonlinear least square fitting and linear prediction single value decomposition(LPSVD). The fluorescence data can be well fitted as a sum of exponentials by non-linear least square fitting program. Attempt to fit transient absorption, transient dichroism and birefringence data to a sum of exponentials were unsuccessful. LPSVD was used to fit the data from t=0, which is determined by the corresponding cross correlation. The parameters for the exponentially damped cosinusoidal terms were determined for each data set. Also nonlinear fitting program including exponentially damped cosinusoidal terms was used to deconvolute the instrumental function and the fitting results agree with that of LPSVD.

Fig. 1 shows the fluorescence data and ground state recovery data for malachite green in water. The fluorescence decay is highly non-exponential, while the ground state recovery shows a unique feature: the signal rises then reaches a plateau before the signal decays. This lag in ground state recovery is similar to two other examples of barrierless reaction: (1) bacteriorhodopsin, where the ground state recovery shows ~200fs plateau[3] and all fluorescence data across the steady state fluorescence spectrum only give highly nonexponential decay[4]; (2) 1144-cyanine in decanol solution where the ground state recovery shows ~1ps plateau, but no such lag in the ground state recovery is observed in ethanol solution[5]. We note the difference in fluorescence measurement and ground state recovery: fluorescence measures the population change within a narrow window along the potential surface while ground state recovery monitors the total population change in the excited state. We have measured the transient absorption data with the probe polarization parallel and perpendicular to pump polarization respectively, no obvious difference was found. This result excludes the possibility that a transition dipole direction change is responsible for the "lag" observed. Also, both malachite green and crystal violet are good saturable absorber dyes thus the excited state absorption can be negligible in our

experimental wavelength region(which was also shown by wavelength dependent experiments). Thus the ground state recovery is expected to be the major contribution in our pump-probe signal.

In order to enhance and linearize the small amplitude signal and improve the signal-to-noise ratio, we have used transient dichroism and birefringence spectroscopy with hetrodyne detection. To understand the nature of the "lag" in ground state recovery, we measured a series of transient dichroism and birefringence signals of malachite green and crystal violet in alcohol solutions. Fig. 2 displays the transient dichroism data of malachite green in water, methanol, ethanol and propanol solution. It is obvious that the "lag" is strongly dependent on solvent environment. The data analysis with both non-linear least square fitting procedure and LPSVD reveals the low frequency components for malachite green in water, methanol and ethanol. No low frequency component is required to fit the data of malachite green in propanol (a rise time can fit the data well). Fig.3 displays the normalized low frequency components of malachite green in different solvents from transient dichroism and rise time of malachite green in propanol. The results here indicate two trends: One is that the "lag" is strongly dependent on solvent property, which has an inertial feature in low viscosity solvent and becomes diffusive when the solvent viscosity is increased. The other is that the frequency of the "lag" is a function of solvent where solvent molecules can adiabatically follow the phenyl ring rotation, the frequency is determined by the effective moment of inertia. The birefringence data of malachite green show similar phenomena. In crystal violet case, the data is different. Crystal violet in water and methanol gives the similar low frequency component but the other data does not require low frequency component to fit. It might be due to the electronic geometry of crystal violet. Frequency-resolved transient dichroism and birefringence were also measured to study vibrational relaxation in the barrierless reaction. Fig.4 shows the normalized oscillatory components of malachite green in water at 580nm$\pm$5nm spectral window. Pulse duration experiments have been done to study the "lag" and the analysis for the nature of the "lag" in pump-probe signals will be presented.

References

1. Sundstrom, V.; Aberg, U., *J. Mol. Liq.* (1993) in press.
2.Bagchi, B.; Fleming, G.R.; *J. Phys. Chem.* (1990) **94**, 9.
3. Dexheimer, S.L.; Wang, Q.; Peteanu, L.A.; Pollard, W.T.; Mathies, R.A.; Shank, C.V.; *Chem. Phys. Lett.* (1992) **188,** 61.
4.Du, M; Fleming, G.R.; Biophysical Chemistry **48**, 101(1993)
5. Aberg, U.; Sundstrom, V.; *Chem. Phys. Lett.* (1991) **185**, 461.

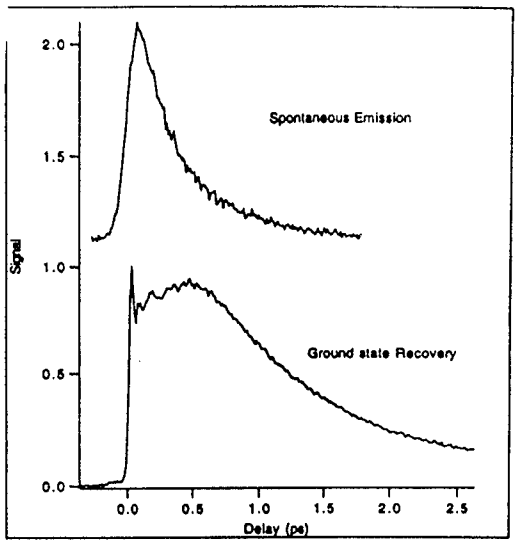


Fig.1 Comparison of fluorescence data and ground state recovery of MG in water.

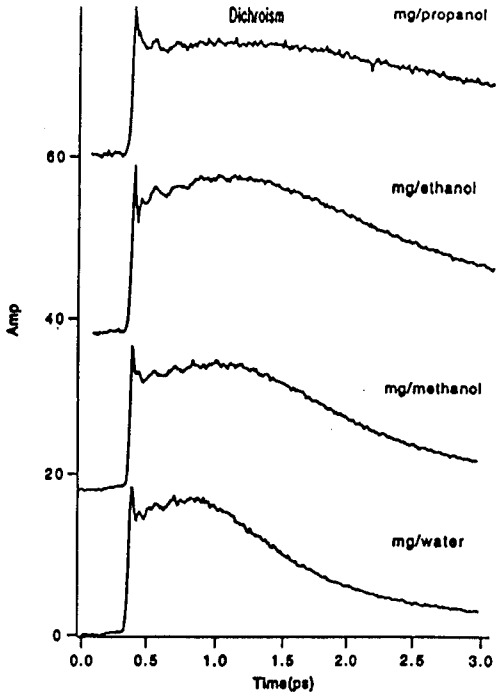


Fig.2 Transient dichroism data of MG in four different solvents.

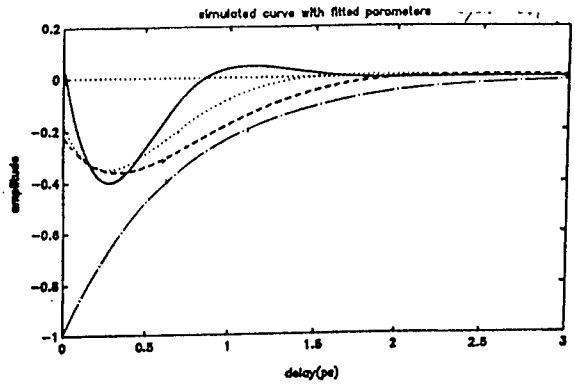


Fig.3 Comparison of low frequency components of MG in different solvents:Transient dichroism data(solid line-water; dot line-methanol; dashed line-ethanol; broken line-propanol).

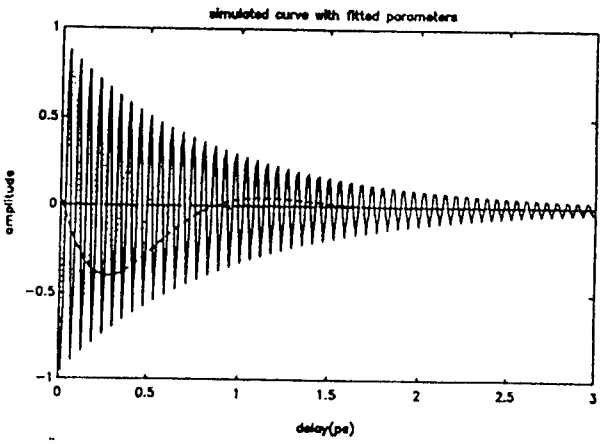


Fig.4 Oscillatory components in frequency resolved transient dichroism data of MG in water.

Coherent Pulse Shaping in a Self-Modelocked Ti:Sapphire Laser

J. D. Harvey [1], *J. M. Dudley* [1], *P. F. Curley* [2], *C. Spielmann* [2] and *F. Krausz* [2]

[1] Physics Department, University of Auckland, Private Bag 92019, Auckland, New Zealand. Ph +64-9-373-7599

[2] Abteilung Quantenelektronik und Lasertechnik, Technische Universität Wien, Gusshausstrasse 27, A-1040 Wien, Austria. Ph +43-1-58801-3879

The recent development of nonresonant passive modelocking techniques has stimulated considerable interest in the generation of ultrashort optical pulses from broadband solid state laser media. Self-modelocking [1] is now routinely exploited to generate sub-100 *fs* pulses from solid state lasers in the near infrared. Optimization of a solitonlike interplay between negative group delay dispersion (GDD) and self-phase modulation (SPM), and minimization of high-order dispersive perturbations [2] have resulted in sub-20 *fs* pulse generation from Ti:sapphire lasers [3 - 6]. In particular, the minimisation of the cubic phase distortion arising from intracavity prism pairs has resulted in the generation of exceptionally broad modelocked spectra with FWHM of up to 150 *nm* and pulse durations $\approx$ 10 *fs* [7].

A modelocked spectrum typical of this operating regime is shown as the solid line in Fig. 1(a) with the corresponding fringe-resolved autocorrelation trace shown in Fig. 1(b). The prominent double-peaked structure of the optical spectrum, the modulation in the envelopes of the autocorrelation, and the evaluated time-bandwidth product of > 0.6 [5] represent a striking deviation from the expected near *sech* ^{2} modelocked pulses.

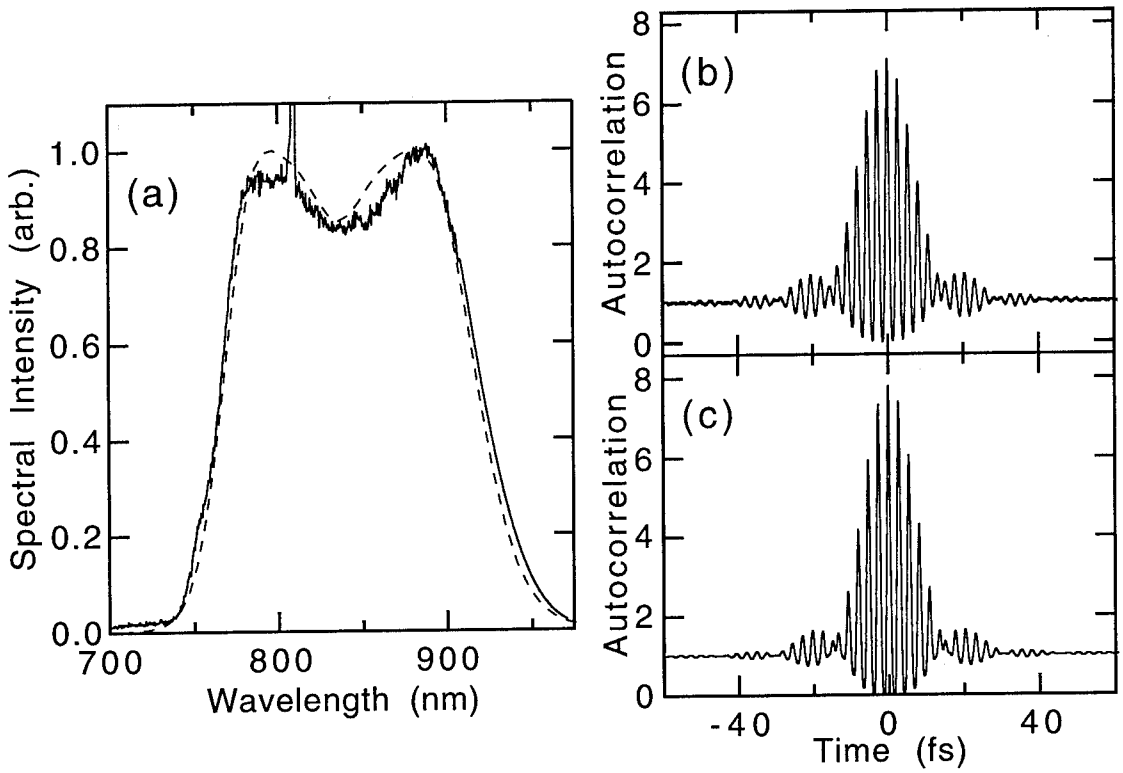


Figure 1 Mode-locked spectrum (a) and corresponding fringe-resolved autocorrelation (b) of a self-modelocked Ti:Sapphire laser operating in the 10 fs regime. The narrow spike in the spectrum relates to a low intensity background with negligible energy content. Plot (c) is the calculated fit to (b) assuming a pulse envelope with coherent ringing and the dashed line in Fig. 1(a) is the corresponding calculated spectrum.

Here we consider the possibility that the observed features occur because of a coherent interaction between the circulating pulse and the Ti:sapphire gain medium, and show that the experimental results can be understood with a simple qualitative model including coherent pulse propagation effects.

Existing models of pulse evolution in passively modelocked lasers [8, 9] use a rate-equation approach to describe the interaction between the circulating pulse and the laser gain medium which is justified if the pulse bandwidth is only a small fraction of the available transition bandwidth. As the pulse bandwidth approaches the transition bandwidth, however, the coherent interaction between the circulating pulse and the laser gain medium becomes important and can lead to effects that are not predicted by conventional mode locking theories. In particular, studies in the modelocked argon laser have shown that coherent pulse propagation gives rise to the pulse envelope taking on an oscillatory ringing structure as a result of the coherent Rabi oscillation of the atomic polarization in the gain medium [10, 11]. This coherent interaction is observed in a high-Q configuration where the interaction Rabi frequency Ω_R is comparable to the argon transition linewidth. In contrast, current modelocked solid state lasers do not meet this condition for strong coherent coupling because their broad bandwidth and small transition dipole moment imply that Ω_R is less than the homogeneous linewidth. For example, considering the 10-*fs* Ti:sapphire oscillator described in Ref. [5], the interaction Rabi frequency calculated at line centre is less than 10 *THz*, an order of magnitude less than the homogeneous linewidth of the gain medium. Consequently there is little dynamic gain saturation during the interaction between the modelocked pulse and the gain medium and strong-signal coherent coupling is not expected. Nonetheless, because the pulse duration is still comparable to the dephasing time T_2 , the atomic polarisation is not able to respond to the envelope of the electric field instantaneously, and the delayed polarisation response can still have a significant effect on the pulse shape.

In particular, if the modelocked laser is operated so that the centre wavelength of the modelocked pulse spectrum is detuned from the centre of the laser transition, then the induced coherent polarisation contains an oscillatory component at the detuning frequency Δ. In the weak-field regime such as is the case in the Ti:sapphire laser, the oscillation frequency of the coherent polarisation is dominated by the detuning, and coherent ringing can be generated at a sufficiently large frequency to modify the pulse shape significantly on the trailing edge. The results of numerical simulations based on the Maxwell-Bloch equations showing the effect of this coherent interaction are shown in Figure 2 where an initially smooth but detuned gaussian pulse is seen to develop weak coherent ringing on the trailing edge after making repeated passes through a gain medium.

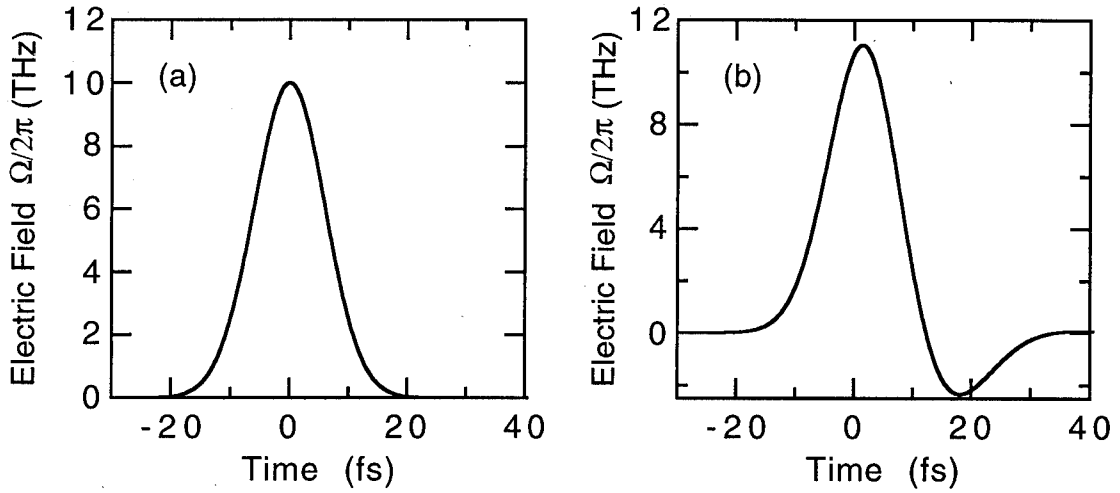


Figure 2 Results from numerical simulations of the Maxwell-Bloch equations for the Ti:sapphire laser showing how a weak nonresonant incident pulse (Fig 2a) with pulse duration (τ_0 ~ 10 fs) acquires coherent ringing on its trailing edge (Fig 2b) after 40 passes through a medium of small-signal gain g=10% and an approximately equal single pass distributed loss. The other parameters used in the simulations were T_2 = 3.2 fs, Ω_R = 10 THz, Δ = 27 THz.

Although this perturbation is small, in a modelocked laser configuration where there is wavelength selection to ensure that the pulse spectrum is always detuned from line-centre, these weak oscillations could accumulate over many roundtrips and result in a ringing on the

pulse envelope at the detuning frequency Δ. Note that this ringing is a weak-field ringing caused by the delayed coherent response of the atomic polarisation rather than a strong-field Rabi flopping behaviour as observed in the argon laser.

To investigate the effect of the ringing on the experimental pulse autocorrelation and spectrum shown in Figure 1, the pulse envelope was taken as a sequence of four gaussian pulses of identical pulse durations and temporal separations but decaying amplitudes of alternate signs.

$$E(t) = E_0 \left[e^{-\beta t^2} - \alpha_1 e^{-\beta(t-T)^2} + \alpha_2 e^{-\beta(t-2T)^2} - \alpha_3 e^{-\beta(t-3T)^2} + \alpha_4 e^{-\beta(t-4T)^2} \right]$$

Here $\beta = 2ln2/\tau_0^2$ where τ_0 is the pulse duration (intensity FWHM), α_1, α_2, α_3 refer to the relative amplitudes of the subsidiary pulses and T is the temporal delay between adjacent pulses With this model for the electric field we have carried out a fit to the autocorrelation function in Fig 1(b) which yielded optimum values for the pulse parameters of $\tau_0 = 11.2$ fs, $\alpha_1 = 0.32$, $\alpha_2 = 0.073$, $\alpha_3 = -0.018$ and $T = 16$ fs. The results of the fit are shown in Fig 1(c) and the corresponding spectrum is shown as the dashed line in Fig 1(a). The similarity between the experimental results and those obtained using this simple model is striking, with the double-peaked structure of the spectrum and the oscillatory nature of the autocorrelation both being well reproduced. Furthermore, according to this model, the ringing frequency should be determined primarily by the detuning of the pulse from the centre of the transition which in this case yields a temporal separation between afterpulses of $\pi/|\omega_0 - \omega_a| \approx 18$ fs, in good agreement with the experimental results.

To avoid the large time-bandwidth products associated with the coherent ringing, the modelocked spectrum must be centred near the peak of the laser transition, and the intracavity power must be low enough so that strong-field coherent ringing does not occur. While existing models of optimised femtosecond lasers include the effects of self-phase modulation as well as the effects of higher order dispersive perturbations, our preliminary investigations have indicated that coherent effects may also play an important role in the pulse formation process and will need to be included in any detailed quantitative analysis.

References

1 D. E. Spence, P. N. Kean, and W. Sibbett, Opt. Lett. **16**, 42 (1991)

2 See for example F. Krausz, M. E. Fermann, T. Brabec, P. F. Curley, M. Hofer, M. H. Ober, Ch. Spielmann, E. Wintner, and A. J. Schmidt, IEEE J. Quantum Electron. **QE-28**, 2097 (1992)

3 B. E. Lemoff and C. P. J. Barty, Opt. Lett. **17**, 1367 (1992).

4 P. F. Curley, Ch. Spielmann, T. Brabec, F. Krausz, E. Wintner and A. J. Schmidt, Opt. Lett **18**, 54 (1993)

5 B. Proctor and F. Wise, Appl. Phys. Lett. **62**, 470 (1993)

6 M. Asaki, C. Haung, D. Garvey., J. Zhou, H. C. Kapteyn and M. M. Murnane, Opt. Lett. 18, 977 (1993).

7 Ch. Spielmann, P. F. Curley, T. Brabec, and F. Krausz, "Ultrabroad-band femtosecond lasers," IEEE J. Quantum Electron. (in press)

8 O. E. Martinez, R. L. Fork, and J. P. Gordon, J. Opt. Soc. Am. B **2**, 753 (1985)

9 H. A. Haus, J. G. Fujimoto, and E. P. Ippen, IEEE J. Quantum Electron. **QE-28**, 2086 (1992)

10 J. D. Harvey, R. Leonhardt, P. D. Drummond, and S. J. Carter, Phys. Rev. A **40**, 4789 (1989)

11 J. M. Dudley, J. D.Harvey, and L. Leonhardt, J. Opt. Soc. Am. B **10**, 840 (1993)

Optical Enhancement of THz Emission from Bulk GaAs

B. B. Hu, P. C. M. Planken, M. C. Nuss, K. W. Goossen, and J. E. Cunningham
AT&T Bell Laboratories, 101 Crawfords Corner Rd., Holmdel NJ 07733-3030
Tel.: 908-949-4925, Fax: 908-949-2473

Recently, the technique of generation and detection of free-space THz radiation has been applied widely to study transient effects in different systems [1-3]. One applications is to use THz emission to probe the screening dynamics of the electric field in the picosecond time domain [2,3]. The usual setup for this application involves two femtosecond pulses. One pulse injects electron-hole pairs in the electric field region, which then screen the electric field. The second optical pulse, which comes later, produces THz emission. The change in the THz signal observed from the second pulse at different time delays reflects the screening dynamics of the electric field following the first optical pulse.

Usually, the THz signal generated by the second pulse is reduced because of the screening of the electric field by photocarriers generated by the pre-pulse. Here, we report the opposite case in semi-insulating bulk GaAs where the THz signal is actually *enhanced* by the prepulse. We believe the enhancement of the signal is due to traps in the bulk GaAs substrate.

In our experimental setup, two optical pulses (pulse 1 and pulse 2) of equal power colinearly strike the sample at 45 degree angle of incidence. The THz emission generated by each pulse is collected by a 50 μm photoconducting dipole antenna. With each pulse alone, the same amount of THz signal is detected. However, with two pulses present at the same time, the pulse which comes later in time is shown to produce *more* THz signal. Figure 1 shows the THz wave forms emitted from a semi-insulating GaAs substrate. In this measurement, we fix pulse 1 in time, and record the THz waveforms at different time delays of pulse 2. The THz signal generated by pulse 2 (shown in Fig. 1 as dashed curves) increases with the time delay. After 10 ps, roughly twice as much THz signal is observed. The signal eventually resumes its original value in about 2 ns, due to carrier recombination.

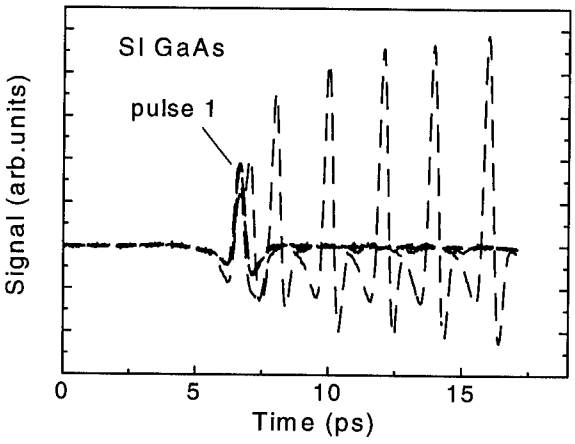


Fig.1. THz waveforms from an semi-insulating bulk GaAs sample. Dashed curves denote signal generated by the second pulse, while the solid curve is the signal from the pre-pulse.

Unlike in the case of optical excitation of excitons in MQW's, this is not due to the coherence between the carriers generated by two pulses [1], since in bulk semiconductors electronic dephasing times are shorter than 100 fs. This is also quite different from the experimental results on electric field screening reported by several other groups

previously [2-4]. To further investigate this point, we have repeated the measurement on a MBE-grown sample. The MBE sample consists of an intrinsic GaAs layer of 1 μm sandwiched by AlGaAs layers. The GaAs layer we used here has an impurity and defect density of less than $10^{10}\ cm^{-3}$, while for the semi-insulating bulk sample, the impurity density is as high as $10^{16}\ cm^{-3}$. To eliminate the substrate effect, the substrate is chemically removed. Figure 2 displays the experimental results from this sample. In this case, the THz signal produced by the second optical pulse is weaker than that the one from the first pulse. This is expected from the field screening due to the photocarriers generated by the pre-pulse. In this case we notice that the screening takes place very fast, within 1 ps after the pre-pulse [4].

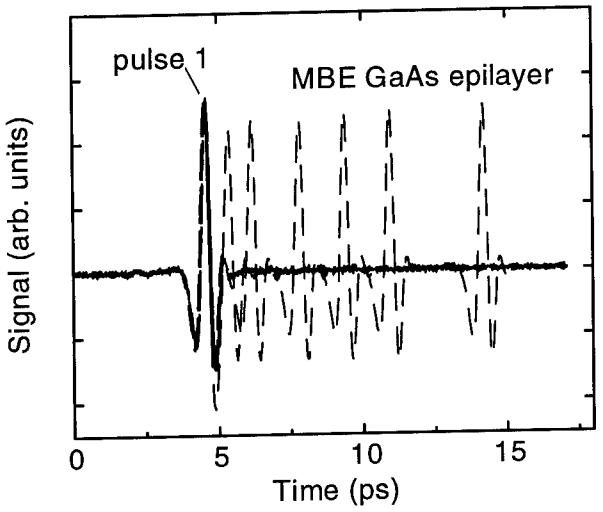


Fig.2. Results from the MBE grown sample. Dashed curves are THz signals generated by pulse 2, while the solid curve is the signal from the pre-pulse.

The same measurement has also been carried out at different temperatures. The field screening effect in the MBE-grown sample shows no temperature dependence. Interestingly, for the undoped semi-insulating bulk GaAs sample, however, we found that the enhancement of THz emission by the pre-pulse only occurs when the substrate temperature is above 130 K. Also, while the amplitude of the THz signal generated by the first optical pulse shows a temperature dependence similar to the dc mobility as previously reported [5], the THz signal generated by the second optical pulse, which comes later in time, is not very sensitive to the change of temperature.

All the above observations suggest that impurities and defects in the semi-insulating GaAs substrate are responsible for the enhancement. There are two possible ways in which defects and impurities can cause the enhancement observed here. First, they can trap the photocarriers generated by the pre-pulse, redistributing the space charges in the depletion region, therefore, causing a stronger depletion field [6]. Secondly, since the number of ionized impurity is reduced by capturing the photocarriers generated by the pre-pulse, the scattering centers for the photocarriers generated by the later pulse are reduced. This enhances photocarrier mobility experienced by the later pulse.

Both above pictures involve carrier capture by impurities or defects. The density of the

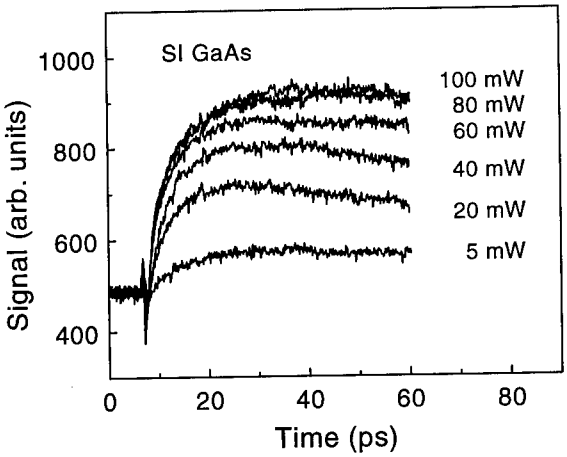


Fig.3. The amplitude of THz signal generated by pulse 2 vs. the time delay at different power levels of pulse 1.

impurities and defects in the sample should affect the amplitude and the rise time of the enhancement. It should eventually saturate at higher optical powers of the pre-pulse. This is verified in our measurement. We fix the optical power of pulse 2, and monitor the amplitude of the THz signal as a function of power from pulse 1. Figure 3 shows the results from a semi-insulating GaAs sample. The enhancement saturates when the average optical power of the pre-pulse is around 100 mW. This corresponds to a photocarrier density of 10^{16} cm^{-3}, which is close to the value of the impurity density in this type of material. The rise time of the enhancement shown in figure 3 should correspond to the photocarrier capture rate by impurities and defects. Using a capture cross section σ of 10^{-12} cm^2 [7], a carrier thermal velocity v of 10^7 cm/s, and a impurity density n of 10^{16} cm^3, the capture rate should be $1/\tau \cong \sigma n v \cong 10^{11} s^{-1}$. This gives a rise time of roughly 10 ps, which is close to what we deduce from figure 3.

To further investigate this mechanism, we have performed similar measurements on a large variety of samples. To find out the effects due to the surface potential, we have treated the same sample using H^+ ECR (Electron Cyclotron Resonance) method, as this treatment reduces the dangling bonds at the surface. In this case, the pre-pulse not only enhances the strength, but also flips the polarity of the THz signal generated by the later pulse. Also, compared with the untreated sample, the enhancement has a slightly shorter rise time. A similar behavior also occurs on the semi-insulating bulk GaAs samples with a thin metal film evaporated on the top surface. Figure 4 shows the comparison of the enhancement behavior of the three samples.

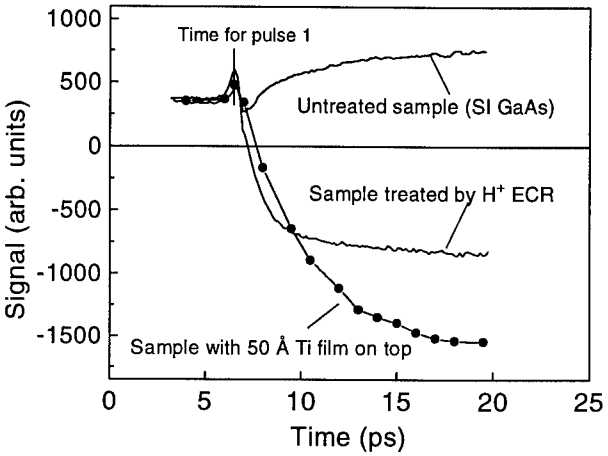


Fig.4. Comparison of the enhancement behavior for differently treated semi-insulating bulk GaAs samples.

In summary, we have observed an optical enhancement of the THz emission from a semi-insulating GaAs substrate by illuminating the sample with a pre-pulse. Our results suggest that extra caution should be exercised in interpreting THz data when studying field screening dynamics.

REFERENCES

[1] P. C. M. Planken, M. C. Nuss, I. Brener, M. S. C. Luo, and S. L. Chuang, Phys. Rev. B., vol. 48, 4903, (1993).

[2] W. Sha, J. K. Rhee, T. B. Norris, and W. J. Schaff, IEEE J. Quantum Electr. vol. 28, 2445, (1992).

[3] J. E. Pedersen, V. G. Lyssenko, J. M. Hvam, P. U. Jepsen, and S. R. Keiding, Appl. Phys. Lett., vol. 62, 1265, (1993).

[4] T. Dekorsy, T. Pfeifer, W. Kütt, and H. Kurz, Phys. Rev. B., vol. 47, 3842, (1993).

[5] B.B. Hu, X.C. Zhang, D. H. Auston, Appl. Phys. Lett. vol. 57, 2629, (1990).

[6] S. E. Ralph, and D. Grischkowsky, Appl. Phys. Lett. vol. 59, 1972, (1991).

[7] S. T. Pantelides, " Deep centers in semi-conductors", pg., 454, Gordon and Breach Science Publishers. (1986).

A dual beam sub-picosecond spectrometer in the 5-11μm spectral region.

P.Hamm, C.Lauterwasser, M.Zurek, W.Zinth

Institut für Medizinische Optik der Universität München, Barbarastraße 16, 80797 München, Germany

Tel: 49-89-185031
Fax: 49-89-183969

Time resolved pump and probe measurements with probing pulses in the mid-IR spectral region has proven to yield important information on fast reactional and relaxational processes in solid state physics, semiconductor physics, chemical physics, and biophysics. In order to make new experiments in those physical fields possible, one requires tunable subpicosecond mid-IR-pulses and a experimental setup, which allows the sensetive detection of absorption changes as small as 0.1 mOD. Our laser system is based on a femtosecond Ti-sapphire laser and regenerative amplifier which is the master light source used for a subsequent difference frequency mixing to obtain subpicosecond pulses in the mid IR-region. The amplifier operates at a repetition rate of 1 kHz, a wavelength of 815 nm, a pulse duration of 120 fs, and a pulse energy of 500 μJ [1].
A synchronized red shifted second light pulse needed for difference frequency generation is deduced from a small portion of the amplified Ti-sapphire pulse in a tunable traveling wave dye laser (TWDL). Approximately 250 μJ of the 815 nm pulses are now mixed with the output of the TWDL in a $AgGaS_2$ crystal using colinear type I phasematching [2]. By tuning the wavelength of the TWDL and rotating the phasematching angle of the nonlinear crystal we are able to obtain femtosecond pulses with between 5 and 11 μm. The pathlength inside the crystal is only 0.5 mm in order to minimize group velocity dispersion effects. By this means, mid-IR pulses as short as 300fs with a pulse energy of more than 10nJ can be obtained. The spectral bandwidth is independent on the absolute wavelength and was measured to be approximately $65cm^{-1}$.
For the exitation pulses in a standard pump and probe experiment, one can use the rest of the amplified Ti-sapphire pulses at 815 nm. But since there is enough energy left (>200μJ), a generation of other exitation wavelengths by nonlinear techniques such as frequency doubling, amplified white light continuum, optical parametrical generation or a TWDL is also possible. At present, a second TWDL is used to cover the spectral range between 860-1100nm (depending on the laser dye) with a pulse energy of several microjoules.
Since the bandwidth of the IR pulse is broader than the bandwidth of typical absorption bands of molecules parallel detection is possible: the probing pulses are dispersed by a grating spectrometer and are measured with a 10 element HgCdTe detector array with a spectral resolution between 5 and 10 cm^{-1} depending on the wavelength and on the grating in the spectrometer.
In order to archieve a high signal to noise ratio the experiment is performed as follows:

1.) The main part of the IR pulse is transmitted through the sample, is dispersed by a first grating spectrometer and measured by a HgCdTe detector array. A small part (15%) of the probing light which is split of in front of the sample is used as a (frequency resolved) reference signal. With this arrangement, statistical shot to shot fluctuation can be eliminated extensively.
2.) The exitation beam is chopped with half the repetition rate of the laser system exiting the sample only every second laserpulse. The transient spectrum is calculated from the transmission with the pump pulse on devided by the transmission with the pump pulse blocked. This allows to compensate long term drifts of the system.
The setup yields a single pulse standard derivation of the normalized signal of 20-30 mOD. This value may be improved by averaging over a sufficient number of laser pulses. In order to detect an absorbance change of 0.1mOD one requires a measurement time of less than 5 min.
As a first experiment to demonstrate the abilitity of the system the transient absorbance change of a laser dye was measured. The dye IR26 was dissolved in $C_2H_4Cl_2$ and held in a rotating cuvette. Exitation was performed at the short wavelength tail of the S_1 absorbance band at 870nm. The IR spectrum of the dye shows a intense band at 1530 cm^{-1} well seperated from the solvent bands. This band is probably due to the C-C stretching modes of the aromatic system of the molecule and should promise a significant change upon electronic exitation.
Transient difference spectra (resolution 6 cm^{-1}) are shown in Fig.1. At late delay times (>1ps) one observes a shift of the absorbance band from 1530 cm^{-1} towards 1508 cm^{-1} probably due to the decrease of the bonding strength by the electronical exitation. The shift decays with a time constant of approximately 18 ps going in parallel with the decay of the electronically exited S_1 state [3].
At early delay times the signal (at the center wavelength of the absorbance band) rises more slowly than the time resolution of the system (300 fs FHWM). Moreover, oscillations are observed at negative delay times are observed (-1ps trace in Fig 1). This coherent effect appears whenever the temporal resolution is shorter than the dephasing time T_2 of the probed absorbance band [4]. According to theory the signal at the center wavelength (1530 cm^{-1}) rises exponentially with T_2. A fit of the signal in Fig.2 yields a value of 550 fs in agreement with the spectral line width of the absorbance band (20 cm^{-1}). A detailed interpretation of the measurement will be given.
In summary, an experimental setup is presented which allows the measurement of small transient absorbance changes with high time resolution. The system covers a wide spectral range (900 cm^{-1} - 2000 cm^{-1}) where important absorbance bands of organic molecules are found.

References:
[1] F.Salin, J.Squier, G.Mourou, G.Vaillancourt, Opt. Lett. 16 (1991) 1964
[2] P.Hamm, C.Lauterwasser, W.Zinth, Opt. Lett 18 (1993) 1943
[3] A.Seilmeier, B.Kopainsky, W.Kranitzky, W.Kaiser, K.H.Drexhage, in Picosecond Phenomena III Editors: K.B.Eisenthal, R.M.Hochstrasser, W.Kaiser, A.Lauberau, Springer Verlag Berlin (1992) p.23
[4] M.Joffre, D.Hulin, A.Migus, A.Antonetti, C.Benoit a la Guillaume, N.Peyghambarian, M.Lindberg and S.W.Koch, Opt. Lett 13 (1988) 277

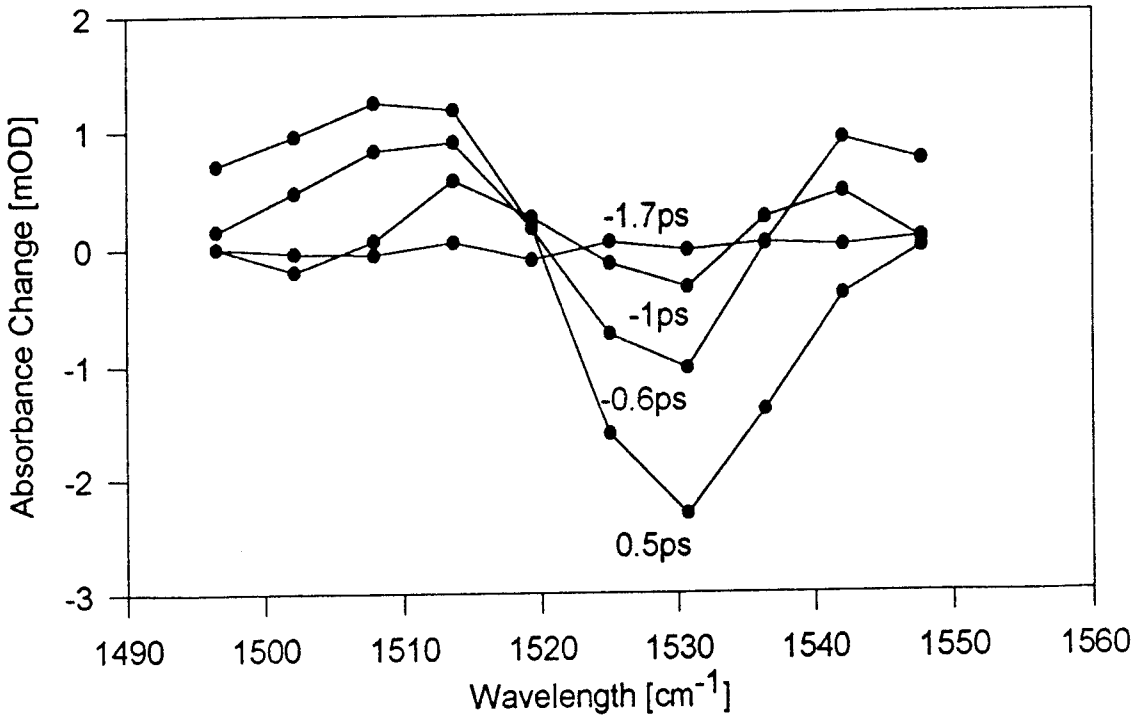


Fig 1. Transient difference spectra of the dye IR26 at several delay times.

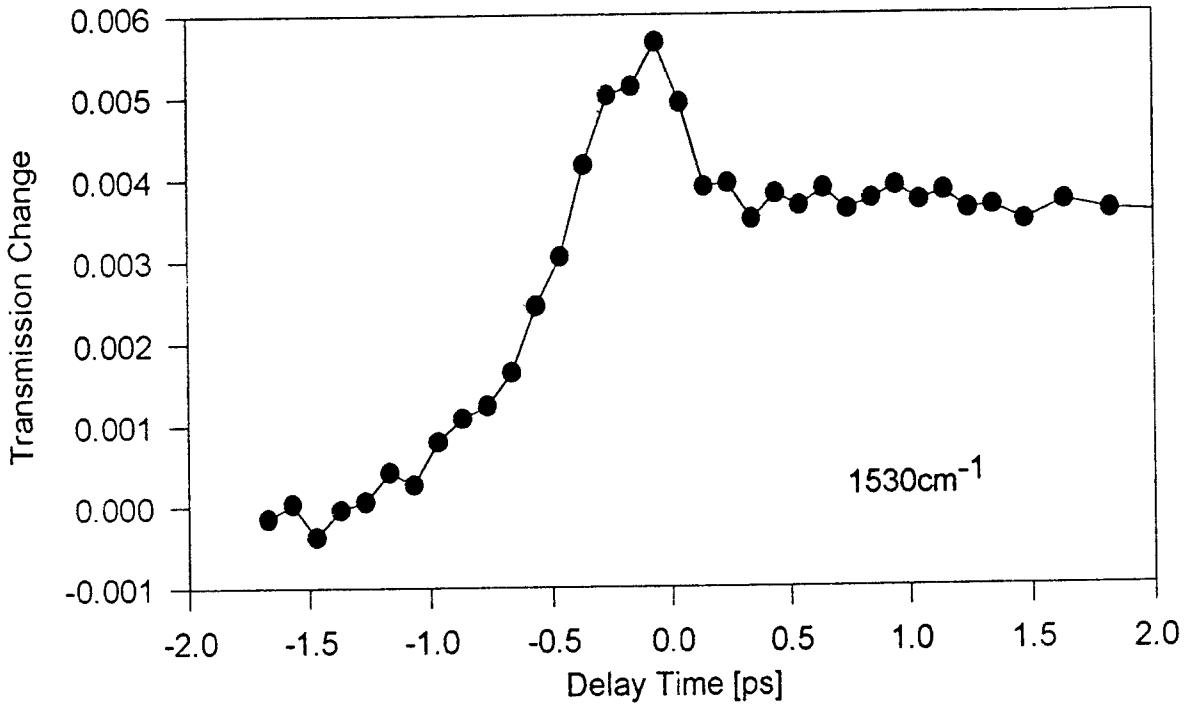


Fig 2. Time dependence of the transmission change at the center wavelength.

Pulse-Doped GaAs Nonlinear Transmission Lines for 630 fs, 1 V Shockwaves

Daniel van der Weide and Paul Brunemeier*

Max-Planck-Institute für Festkörperforschung

Heisenbergstraße 1, D-70569 Stuttgart, Germany

* Power Spectra Inc., Sunnyvale, CA (formerly with Watkins-Johnson Co., Inc., Palo Alto, CA)

Abstract

We have developed nonlinear transmission lines (NLTLs) having the fastest output transition times yet reported for electronic circuits: waveforms with 630 fs, 1 V edges, measured at T = 300 K. These circuits were realized on GaAs with a pulse-doped profile for maximum capacitance-voltage nonlinearity, and measured with on-chip integrated sampling circuits strobed by identical NLTLs. This epitaxial profile also allows high-cutoff-frequency sampling diodes by a simple etching process, enabling us to combine two essential requirements for an ultrafast electronic circuit onto one monolithic IC.

Introduction

Recently, increasingly faster nonlinear transmission lines have been reported in the literature with subpicosecond results now being observed for the first time from electronic circuits.[1,2,3] All-electronic pulse generation has lagged in speed behind that of electro-optic switching, although each method has been employed for producing ultrafast test signals which can be used both for advanced instrumentation and for probing the physics of carrier transport within the devices themselves.

The discrepancy arises from the fundamental differences in stimuli: the electo-optic switch is pulsed from a femtosecond laser with a pulse usually much shorter than the resulting electrical one; the nonlinear transmission line reaches its final output through successive compression of a waveform's edge. Thus, while the speed of an electro-optic switch is limited primarily by carrier lifetimes, the speed of a nonlinear transmission line is limited by the rate at which the depletion edge of a Schottky diode can move through the semiconductor. This edge speed involves both the electromagnetic environment of the diode and the carrier transport limitations of the semiconductor. We are investigating these limitations by designing and building nonlinear transmission lines on pulse-doped GaAs, combining the desirable properties of large capacitance-voltage nonlinearity and low doping for fast depletion and long mean-free paths. While the low doping level ultimately limits the amplitude of the output pulse, it does demonstrate that edge rates well below 1 volt per picosecond are achievable.

Nonlinear Transmission Lines

Nonlinear transmission lines are synthetic structures of series inductors (approximated by sections of high-impedance transmission line) with varactor diodes periodically placed as shunt elements. On this structure a voltage shock-wave develops from a sinusoidal input because the propagation velocity varies with the nonlinear capacitance-voltage relationship of the diodes, $v_p = 1/\sqrt{LC_{tot}(V)}$, where L is the inductance and $C_{tot}(V)$ the sum of the varactor and parasitic capacitance of the line, all per unit length. Limitations of the NLTL arise from its periodic cutoff frequency, $\omega_{per} = 2/\sqrt{LC_{tot}(V)}$, waveguide dispersion, interconnect metallization losses, and diode resistive losses.

Measurement of Subpicosecond Fall-Time

To make the measurements shown in Figures 1 and 2, we packaged the monolithic NLTL/sampler chip with suitable microwave connectors. The NLTL test port and sampler strobe inputs were offset by 0.5 Hz by splitting the output of a signal source and running the strobe arm through a rotating phase shifter to allow the sampled waveform to be traced out in equivalent time and viewed on a digital oscilloscope for accurate time-domain characterization. The harmonic distortion of the phase shifter was independently measured with a microwave mixer in place of the NLTL/sampler package, and it was found to be minimal, while the phase shifter itself offers < 20 fs RMS jitter in this scheme. A root-sum-squares deconvolution of the measured fall time with the sampler aperture time (assuming that the two times are equal) gives ~450 fs, which is reasonable in light of the epitaxial design

and periodic cutoff frequency $\omega_c = 2/\sqrt{LC_{tot}(V)}$ of these circuits.

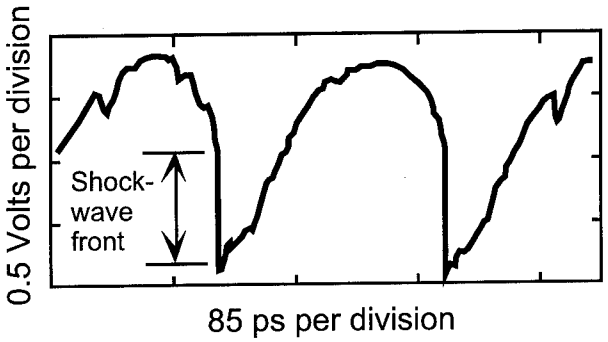


Figure 1. A 630 fs measured fall time shock-wave generated on a nonlinear transmission line and measured by an on-chip sampler at T=300 K.

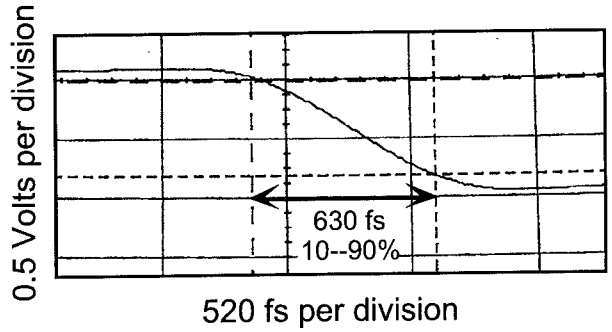


Figure 2. Detail of shock-wave front shown in Fig. 1. Markers are set at the 10% and 90% levels of the edge; their equivalent-time spacing is 630 fs.

Diode Profiles

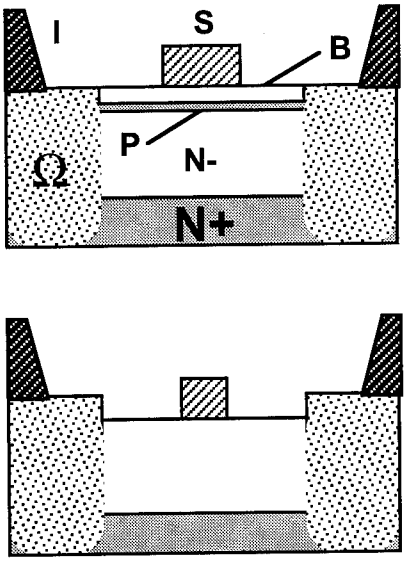


Figure 3. Diode profiles for pulse-doped (top) and etched abrupt-junction (bottom) devices used in the NLTLs. Symbols are described in the text below.

As shown in Fig. 3, the essential benefit in the pulse-doped profile we have employed is the ability to combine two distinct diode types in one circuit using a simple etch step. In the Figure, "B" stands for a buffer layer of 5E16 cm^{-3} Si-doped material, 500 Å thick to prevent surface breakdown. "P" is the pulse of carriers, 80 Å deep at 4E18 cm^{-3}. The N^- layer is 0.27 μm thick, followed by a N^+ layer 1 μm thick as a backside contact. "S" is the Schottky contact and "I" is the diode and transmission line interconnection to the ohmic (Ω) contacts. On the bottom of the Figure, the resultant abrupt-junction diode is shown after a simple etching step. The smallest of these diodes in the NLTL circuit are estimated to have RC_{j0} cutoff frequencies approaching 6 THz from auxiliary test structure measurements.

Conclusion

We have developed an electronic circuit capable of 630 fs, 1 V step generation using a pulse-doped epitaxial profile on GaAs. With further improvements to the epitaxial design and layout, we expect both higher voltages and shorter pulses—the circuits can also be tested cryogenically for even more improvement—with applications in free-space THz generation and MMIC characterization.

Acknowledgments

We gratefully acknowledge critical support from D. Bloom and J. Bostak (Stanford University), as well as useful discussions with D. Dobkin, W. Hitchens, W. Strifler, and R. Remba, and J. Martin of Watkins-Johnson Co. Thanks are due to T. Carver and C. Remen of Stanford for excellent technical support, and to D. Jäger and Watkins-Johnson Co. for loans of equipment.

References

1 D.W. Van Der Weide, J.S. Bostak, B.A. Auld, D.M. Bloom, "All-electronic generation of 880 fs, 3.5 V shockwaves and their application to a 3 THz free-space signal generation system", Appl. Phys. Lett. **62**, 22-24 (1993).

2 M. S. Shakouri , A. Black, B. A. Auld, D. M. Bloom, "500 GHz MMIC sampling wafer probe", Electron. Lett. **29**, 557-558 (1993).

3 S. T. Allen, U. Bhattacharya, M. J. W. Rodwell, "4 THz Sidewall-Etched Varactors for Sub-MM-Wave Sampling Circuits", IEEE GaAs IC Symp. Tech. Dig. **22**, 285-287 (1993).

Primary Electron Transfer Steps in Photosystem I Reaction Center with Reduced Number of Antenna Chlorophylls (12 - 30)

Shigeichi Kumazaki[1], Masayo Iwaki[2], Isamu Ikegami[3], Hideki Kandori[1], Shigeru Itoh[2], and Keitaro Yoshihara[1]

[1]Institute for Molecular Science, Myoudaiji, Okazaki 444, Japan

81 - 564 - 55 - 7350 (FAX 81 - 564 - 54 - 2254)

[2]National Institute for Basic Biology, Myoudaiji, Okazaki 444, Japan

[3]Laboratory of Chemistry, Faculty of Science, Teikyo University, Sagamiko, Kanagawa 199-01, Japan

The ultrafast dynamics of electron relays in the Photosystem I (PS I) reaction center (RC) is of particular interest because the amino acid sequences of the polypeptides show almost no homology to those of PS II-purple-bacterial type RC's. Electron carriers and energy levels of PS I RC are also different from those of the latter type of RC's. However, studies in Photosystem I have been scarce due to its large number of antenna chlorophylls (more than 100) per RC and to resultant spectral congestion. Even though the presence of the primary electron acceptor chlorophyll (A_0) has been suggested by a recent X-ray crystallographic work [1], spectroscopic detection of sequential reduction and reoxidation of A_0 has never been successful.

Procedures to reduce the number of antenna pigments of PS I RC complex while maintaining the photochemical activity in PS I RC particles have been developed [2]. Primary electron transfer can be separated from subsequent electron transfers by quinone-depletion and -reconstitution [3]. In this study, RC particles with antenna size of 12 - 30 were used and electron transfer from the chlorophyll dimer (P700) to the primary acceptor

chlorophyll (A_0) and to reconstituted secondary acceptor menaquinone-4 (Q_ϕ) were observed.

PS I RC particles with appropriate quinone conditions were prepared as was described previously [3]. Transient absorption spectra were measured in the range of 650 - 800 nm using white light continuum for probing. The amplified pulse at 638 nm with a pulse width (FWHM) of 200 fs was used at a repetition rate of 10 Hz both for excitation and for the continuum generation. The time dependent absorbance changes in the spectral region of 740 (±10) nm were plotted for both P700-preoxidized sample and -neutral one with antenna size of 12 under the phylloquinone-depleted conditions (Figure 1(a)). Appearance of the positive absorbance changes at this wavelength region due to the formation of A_0^- can be observed ($t_{1/e}$ = 6.5 ps). The difference between kinetics at 680 (±2) nm under the P700-neutral and -preoxidized conditions gives a similar time constant for the ground state depletion of A_0 ($t_{1/e}$ = 5.3 ps, open squares in Figure 1(b)).

Sequential electron transfer ($P700^*A_0Q_\phi \rightarrow P700^+A_0^-Q_\phi \rightarrow P700^+A_0Q_\phi^-$) was studied in the RC particles with antenna size of 30. The bleach of A_0 at 685 (±2) nm was monitored (Figure 2). In the phylloquinone-depleted particles, a bleach appears with a time constant of 7 ps and persists up to the maximum time studied (800 ps). In the menaquinone-4 reconstituted particles, a bleach appears and disappears with time constants of 7 and 38 ps, respectively. This corresponds to the sequential reduction and reoxidation of A_0.

In summary, an upper limit for the time constant of $P700^*A_0 \rightarrow P700^+A_0^-$ is given to be 6.5 ps, which is shorter than a previously reported time constant ($t_{1/e}$ = 13.7 ps) [4]. Reconstituted quinone accepts electron with a time constant of 38 ps, which is much shorter than the corresponding steps in PS II-purple-bacterial type RC's [5,6].

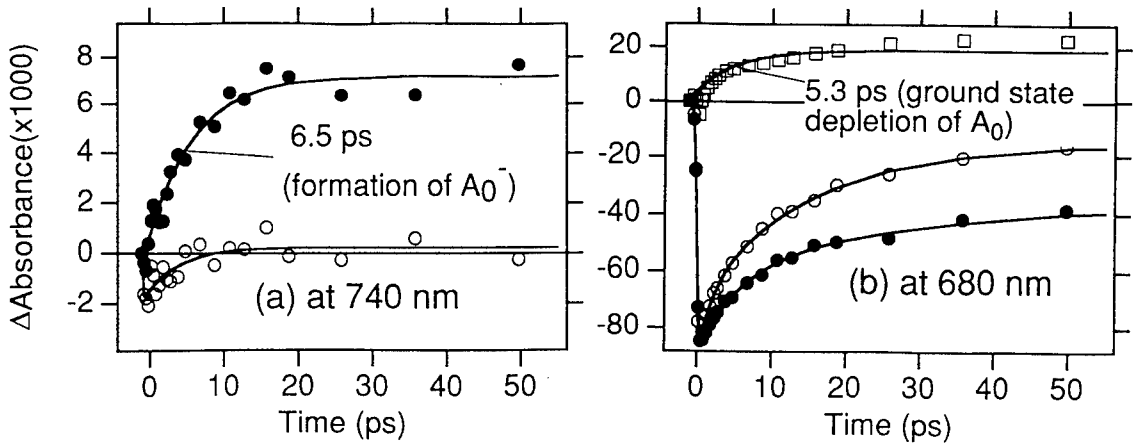


Figure 1. (a) Kinetics (closed circles) for the formation of A_0^- (b) Kinetics for the ground state depletion of A_0 (open squares) is estimated by the difference between the kinetics for P700-neutral and -preoxidized conditions.
Filled circles: under the P700-neutral conditions, Empty circles: under the P700-preoxidized conditions.

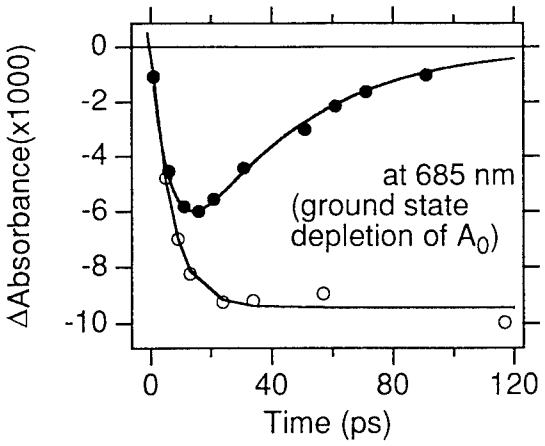


Figure 2. Effect of quinone-reconstitution to the kinetics of ground state depletion of A_0
(signals under the P700-preoxidized conditions were subtracted). Filled circles: menaquinone-4-reconstituted particles, Empty circles: phylloquinone -depleted particles.

References

[1] N. Krauss, W. Hinrichs, I. Witt, P. Fromme, W. Pritzkow, Z. Dauter, C. Betzel, K. S. Wilson, H. T. Witt and W. Saenger, Nature **361** (1993) 326
[2] I. Ikegami and S. Katoh, Biochim. Biophys. Acta **851** (1975) 75
[3] M. Iwaki and S. Itoh, FEBS Lett. **256** (1989) 11
[4] M. R. Wasielewski, J. M. Fenton and Govindjee, Photosynth. Res. **12** (1987) 181
[5] W. Holzapfel, U. Finkel, W. Kaiser, D. Oesterhelt, H. Scheer, H. U. Stilz and W. Zinth, Proc. Natl. Acad. Sci. USA **87** (1990) 5168
[6] H. -J. Eckert, N. Wiese, J. Bernarding, H. -J. Eichler, G. Renger, FEBS Lett. **240** (1988) 153

Polarized Ultrafast Transient Spectroscopy of the Hydrated Electron: Quantum Non-Adiabatic Molecular Dynamics Simulation

Benjamin J. Schwartz and Peter J. Rossky
Department of Chemistry, University of Texas at Austin
Austin, TX 78712 USA

The transient spectroscopy of the aqueous solvated electron has been the subject of intense experimental[1-3] and theoretical[4-8] interest recently. Hydrated electrons play an important role as intermediaries in the radiation chemistry of water, as well as in solution photochemistry and electron transfer reactions. Furthermore, the coupling of solvent fluctuations to the electronic absorption spectrum makes the hydrated electron an outstanding probe of electronic solvation dynamics in the aqueous environment. The optical absorption spectrum of the hydrated electron is comprised of three s–>p like transitions which are highly broadened and split by coupling to solvent fluctuations.[6]

Experiments by Migus *et al.*[1] and Long *et al.*[2] first studied the equilibration of solvated electrons injected into liquid water by multiphoton ionization. These experiments observed a broad infrared absorption which decayed into the known equilibrium spectrum of the hydrated electron on a subpicosecond time scale. This result was subsequently reproduced by quantum non-adiabatic molecular dynamics simulations,[4] which supported the assignment of the infrared absorption to an electronic excited state of the hydrated electron followed by non-adiabatic relaxation to the ground state. More recent experiments by Alfano *et al.*[3] have provided complementary information on the electronic solvation dynamics and non-adiabatic transition rate by probing the spectral dynamics of photoexcited equilibrium hydrated electrons. In addition to providing insights into nature of the optical spectrum by bleaching dynamics (hole-burning), these experiments also contain spectral contributions due to transient absorption from the excited state as well as stimulated emission from the excited state back to the ground state. All of the above experiments used effectively unpolarized light (relative pump and probe pulse polarizations set at the magic angle), and thus provided no information about the orientations of the spectroscopic states under investigation.

In this paper, we present the results of quantum non-adiabatic molecular dynamics calculations of polarized transient spectroscopy of the aqueous solvated electron. The results indicate distinct time scales for the relaxation of anisotropic and isotropic solvent fluctuations, allowing polarized spectral holes to be burned in the hydrated electron absorption spectrum. When combined with contributions from transient absorption and stimulated emission, this separation of time scales results in a distinct spectral signature, transient absorption in one set of polarizations and transient bleaching in the other, which can be directly probed by experiment. This work represents the first prediction of a polarized ultrafast spectroscopic signal using a molecular level Hamiltonian model.

The details of the non-adiabatic dynamics method used are essentially identical to those employed in previous studies of electron localization after injection,[5] and are also described elsewhere.[8] The model system consisted of 200 flexible classical water molecules and one quantum electron. Quantum dynamics were performed with the non-adiabatic algorithm of Webster *et al.*[4] using a 1 fs time step. Spectra were computed with the 40 lowest eigenstates of the electron, and were convoluted with a 300 fs Gaussian representing the experimental instrument response.[3] Twenty trajectories were launched from starting configurations in which the electronic absorption was resonant with the Ti:Sapphire laser (2.27±0.01 eV, corresponding, for the model Hamiltonian,[9] to an experimental pump wavelength of 780 nm with a 200 cm^{-1} bandwidth), and were used to

compute transient bleaching dynamics. Separate excited state trajectories were initiated from these same starting points to determine transient absorption and stimulated emission spectral contributions. Polarized spectra were computed from the appropriate transition dipole autocorrelation functions.[8] The calculated parallel and perpendicular transient spectra were then combined[10] to compute the "diagonal" (probing only to the initially prepared state) and "off-diagonal" (probing only the states with transition dipoles perpendicular to the initially prepared state) spectral transients.

The diagonal and off-diagonal transient bleach spectra (no excited absorption or emission contributions) for the hydrated electron excited at Ti:Sapphire wavelengths at various time delays are presented in Fig. 1 (solid curves). To emphasize the shape of the holes, the calculated equilibrium absorption spectrum, which would have been produced by uniform bleaching of the absorption band, is shown normalized to equal area at each time delay (dotted curves). The initial (t=0) diagonal hole is broadened by rapid solvent fluctuations, corresponding to essentially homogeneous bleaching of the lowest s–>p transition. This hole persists clearly past time delays of 0.5 ps before it begins to broaden and blue-shift. The off-diagonal spectra behave in a similar manner. The upper two s–>p transitions are bleached at early times, with absorption to the initial state growing in only at time delays past 500 fs. All of these spectra provide direct evidence that solvent fluctuations with different symmetries are relaxing on different time scales: The comparable widths of the diagonal and two off-diagonal holes indicate that the fast fluctuations causing the initial broadening are symmetric in nature, while the lack of uniform bleaching of the entire absorption band indicates that the anisotropic fluctuations which break the degeneracy relax much more slowly. In other words, the three excited p-like states do not interchange roles on a subpicosecond time scale.

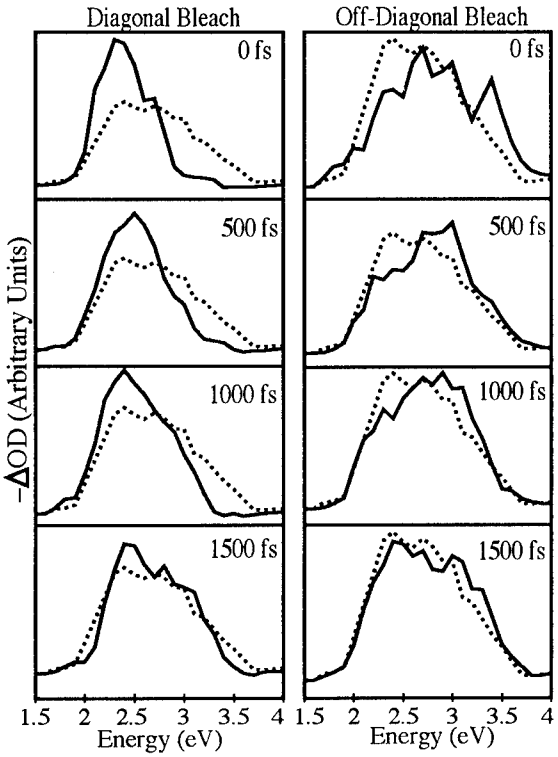


Fig. 1: Diagonal and Off-Diagonal Bleach Dynamics

Since the experimental spectral transients also probe contributions from transient absorption and stimulated emission, we have also computed the complete diagonal and off-diagonal transient spectra including these excited state components. These results are displayed on the experimentally accessible wavelength scale[9] in Fig. 2. The 300 fs instrumental resolution and non-adiabatic return to the ground state are reflected in the overall rise and decay of the spectral amplitudes. The slow, anisotropic bleaching dynamics result in the complex spectral shape and the lack of observed isosbestic point. In the 700-800 nm region, the diagonal spectra show an overall instrument-limited transient bleach while the off-diagonal spectra show a more slowly rising net transient absorption. This is an immediate consequence of the separation of time scales for the isotropic and anisotropic solvent fluctuations, and provides a direct experimental test of this phenomenon.

Additional dynamic information, not presented in Fig. 2, indicates that well to the red of the excitation wavelength (≥900 nm), both the diagonal and off-diagonal transient spectra show an instrument limited absorption rise followed by a roughly bi-exponential decay with a short time constant of a few hundred femtoseconds and a longer time constant of >1 ps. In the 800-900 nm region, the diagonal spectra show an initial bleach which rapidly recovers and overshoots into a transient absorption (a spectral signature which has also been observed in the magic angle experiments[3]) while the off-diagonal spectrum shows a more slowly rising transient absorption. To the blue of 650 nm, both sets of spectra show net transient bleaching, with the diagonal bleach appearing more quickly than the off-diagonal. Other details of the transient spectral dynamics will be discussed in a forthcoming publication.[8]

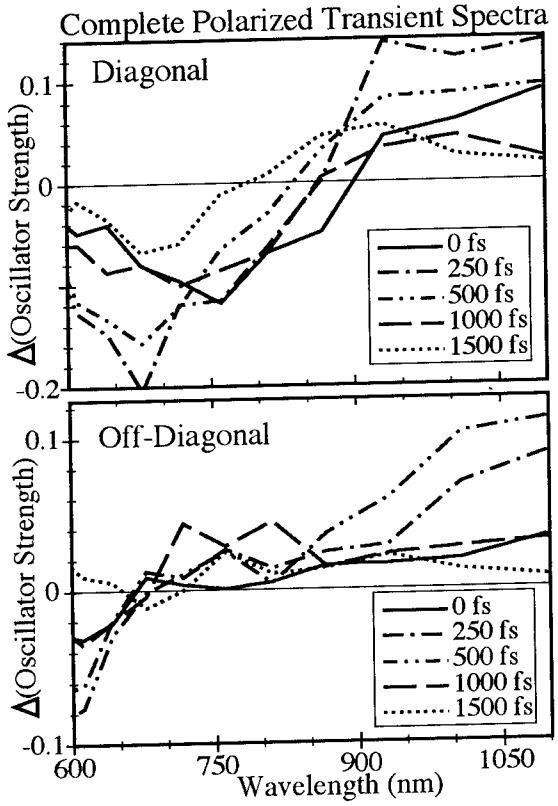


Fig. 2: Complete Diagonal and Off-Diagonal Spectra

In summary, we have provided the first directly testable prediction of ultrafast polarized spectroscopic transients using quantum non-adiabatic molecular dynamics simulation. Anisotropic contributions to electronic solute-solvent coupling are found to take place on a slower time scale than isotropic fluctuations. This result is manifest as a diagonal transient bleach and off-diagonal transient absorption at wavelengths near and just blue of the excitation in a polarized pump-probe experiment on the aqueous solvated electron. This separation of fluctuation time scales by symmetry and its impact on polarized transient spectroscopy has important ramifications for theories of solvation dynamics as well as for the general understanding of the properties of the hydrated electron.

References:

1. A. Migus, Y. Gauduel, J. L. Martin, and A. Antonetti, Phys. Rev. Lett. **58**, 1559 (1987).
2. F. H. Long, H. Lu, and K. B. Eisenthal, Phys. Rev. Lett. **64**, 1469 (1990).
3. J. C. Alfano, P. W. Walhout, Y. Kimura, and P. F. Barbara, J. Chem. Phys. **98**, 5996 (1993); Y. Kimura *et al.*, J. Phys. Chem (to be published).
4. F. A. Webster, J. Schnitker, M. S. Friedrichs, R. A. Friesner, and P. J. Rossky, Phys. Rev. Lett. **66**, 3172 (1991); F. A. Webster, P. J. Rossky, and R. A. Friesner, Comput. Phys. Commun. **63**, 494 (1991).
5. T. H. Murphrey and P. J. Rossky, J. Chem. Phys. **99**, 515 (1993).
6. J. Schnitker, K. Motakabbir, P. J. Rossky, and R. A. Friesner, Phys. Rev. Lett. **60**, 456 (1988).
7. K. A. Motakabbir, J. Schnitker, and P. J. Rossky, J. Chem. Phys. **90**, 6916 (1989).
8. B. J. Schwartz and P. J. Rossky, Phys. Rev. Lett., submitted.
9. Note that the calculated absorption spectrum is ~0.7 eV blue-shifted from experiment.[5,6] All figures presented in eV use the directly computed transition frequencies; wavelength figures were converted from eV taking this blue-shift into account.
10. J. Yu and M. Berg, J. Chem. Phys. **97**, 1758 (1993).

Generation of tunable narrowband free space THz radiation.

A. S. Weling, B. B. Hu*, N. M. Froberg* and D. H. Auston

Department of Electrical Engineering, Microelectronics Sciences Laboratories,

Columbia University, New York, NY 10027.

*Current address : AT & T Bell Laboratories, Crawfords Corner Rd.,

Holmdel, NJ 07733.

Recently, a variety of techniques have been developed to generate and detect ultrashort pulses of far-infrared radiation in free space using femtosecond optical excitation. The broadband nature of this THz radiation and the lack of frequency control limits the applicability of these devices to microwave communication systems. Previous efforts to optoelectronically generate narrowband microwave radiation with broad tunability include the use of cw laser heterodyne in photodetectors and HEMT's [1].

Our experimental scheme for producing quasi-sinusoidal optical radiation modulated at THz frequencies involves a Michelson interferometer arrangement (fig. 1), the input to which is a linearly chirped optical pulse whose instantaneous carrier frequency is linearly swept in time at a rate μ. At any instant the frequency content of the two split-off pulses in the arms of the interferometer differs by a constant beat frequency f_o, which is directly proportional to the time delay τ between them. The interference term in the interferometer output $I_{total}(t, \tau) = |E(t)+E(t+\tau)|^2 = I_1(t) + I_2(t+\tau) + I_{cross}(t, \tau)$ contains the sinusoidal modulation at the beat frequency $f_o \sim \tau\mu/2\pi$. Photoconducting antennas or non-linear crystals can be used as optical mixers which convert this optical modulation into THz radiation with a center frequency f_o which can be tuned by varying the delay τ. For a finite emitter bandwidth Δf_{max}, the bandwidth of the THz radiation is given by $\Delta f \sim \Delta f_{max}\sigma/\sigma_n$ where σ is the transform limited pulsewidth for the given optical bandwidth, and σ_n the FWHM of the chirped pulse.

We used a regenerative amplifier based on chirped pulse amplification in Ti:sapphire [2] to produce linearly chirped pulses at 800 nm with an FWHM of 22.5 ps and 400μJ pulse energy. A large aperture photoconducting antenna with 4 mm spaced Al electrodes on semi-insulating GaAs biased at 2.0 kV/cm was used as a THz emitter. The resultant free space THz radiation was characterized by a non-polarizing Michelson interferometer using a helium-cooled Si bolometer detector [3]. Fig. 2 shows the THz interferograms obtained for various time delays between the two chirped pulses. The results of our frequency tuning experiment along with a linear fit obtained by using a Gaussian σ of 80 fs are shown in fig. 3.

Optical difference frequency mixing in a non-linear crystal such as $LiNbO_3$ can be used to extend the tuning range to the optical bandwidth available (~ 3 THz). The above scheme of chirped pulse beating can be modified to spatially scan the narrowband THz radiation by having the two chirped pulses mix on the emitter surface in a non-collinear configuration and controlling the angle $\delta\theta$ between them. We gratefully acknowledge Harley Heinrich of IBM T.J.Watson Research Center, Yorktown Heights for suggesting the basic concept of chirped pulse beating. This research was supported by the Air Force Office of Scientific Research under grant no. F49620-92-J-0036.

References:-

1. G.J. Simmons and K.G. Purchase, IEEE Trans. Microwave Theory Tech., 38, 667 (1990); D.V. Plant, D.C. Scott, H.R. Fetterman, L.K. Shaw, W. Jones, and K.L. Tan, IEEE Photon. Technol. Lett., 4, 102 (1992).

2. P. Maine, D. Strickland, P. Bado, M. Pessot, and G. Mourou, IEEE J. Quantum Electron., 24, 398 (1988).

3. B.I. Greene, J.F. Federici, D.R. Dykaar, R.R. Jones, and P.H. Bucksbaum, Appl. Phys. Lett., 59, 893, (1991).

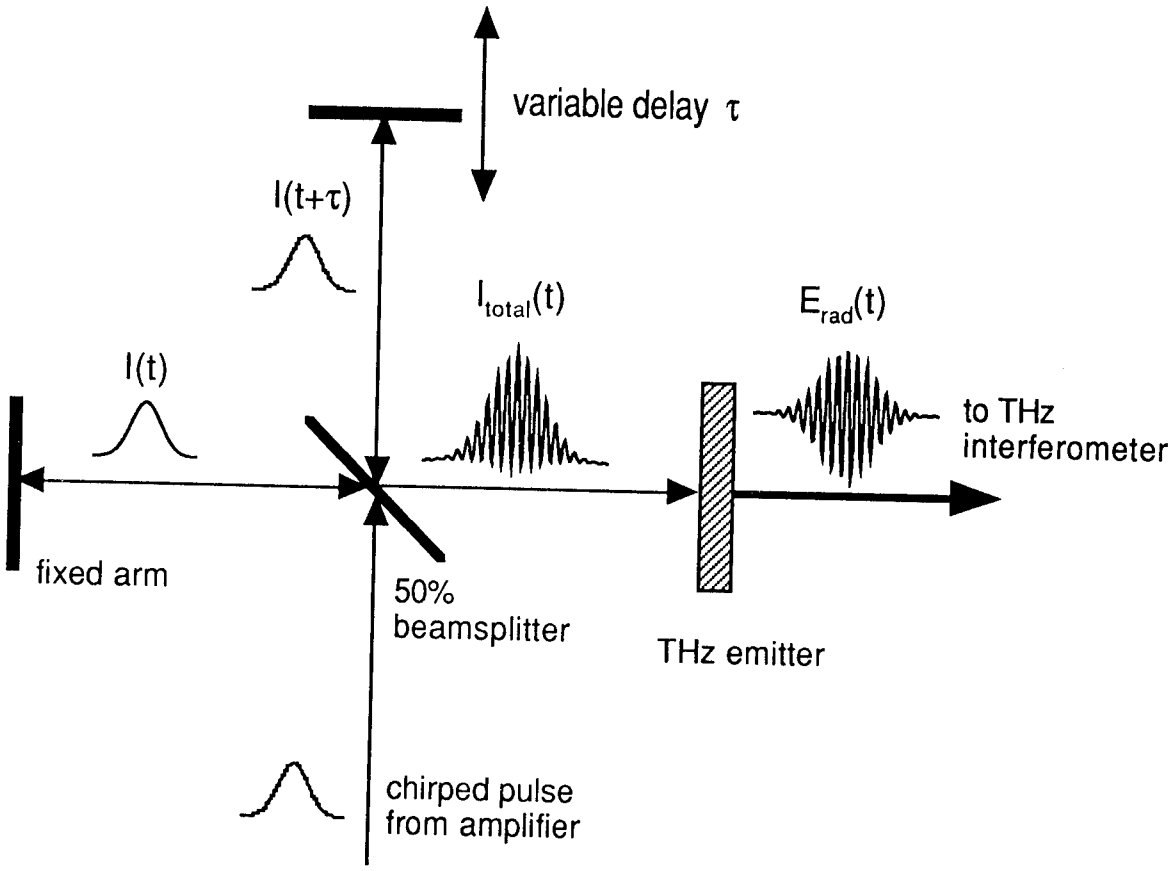


Figure 1. Schematic of experimental technique showing temporal overlap of the two chirped pulses in the optical interferometer.

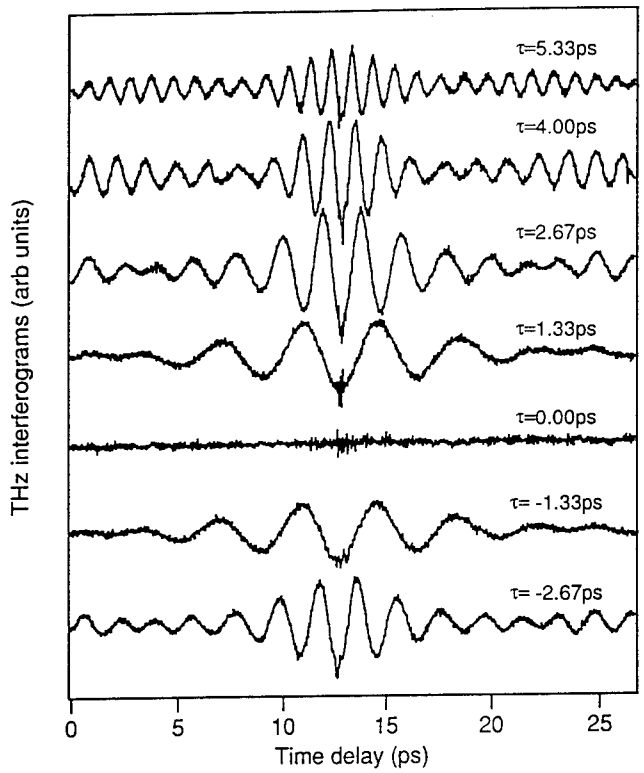


Figure 2. THz interferograms from beating of 22.5 ps chirped pulses at various delays τ; effects of satellite pulses at ± 12 ps due to multiple reflections in the emitter are visible.

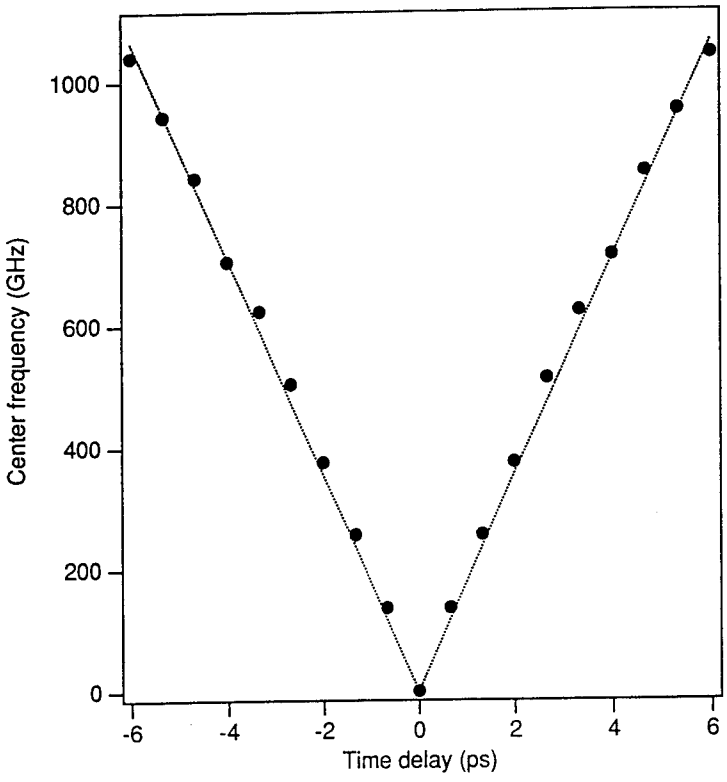


Figure 3. Tuning of THz frequency f_o with delay τ (dotted line shows linear fit using a Gaussian spectrum of 11.8 nm FWHM close to the measured value of 10.3 nm).

ULTRAFAST DYNAMICS OF THE EXCITED Br ATOM - MESITYLENE EDA COMPLEX

W. Jarzeba, A. Hörmann, K.A.M. Thakur, and P.F. Barbara

Department of Chemistry, University of Minnesota,
Minneapolis, MN 55455

We recently made the first measurements of the electron transfer (**et**) kinetics of a bromide/aromatic cation *contact ion pair* (Br^-/Ar^+). This type of contact ion pair (CIP) is prepared by ultrafast optical excitation of the charge transfer band of a Br atom/aromatic molecule charge transfer complex.[1] The simplest example is the benzene·Br complex:

$$Br/Bz \underset{et}{\overset{h\nu}{\rightleftharpoons}} Br^-/\ Bz^+$$

This class of reaction is a promising prototype for studying intermolecular **et** at the molecular level. It is relatively simple compared to other recently studied ultrafast intermolecular **et** systems, all of which involve donors and acceptors having more electronic, vibrational, and conformational degrees of freedom. Indeed, the Br^-/Bz^+ ion pair is an excellent candidate for detailed theoretical modeling of **et**, utilizing such techniques as state - of -the - art non adiabatic rate calculations.

This paper will describe femtosecond transient pump-probe spectroscopy on **et** and relaxation for various Br/benzene-derivative complexes, especially the Br atom - mesitylene charge transfer complex. Mesitylene is 1,3,5-trimethlybenzene. Br atom forms a charge transfer complex with mesitylene characterized by a charge transfer absorption band centered at 525 nm and of 165 nm bandwidth.[2] Mesitylene is a stronger electron donor than benzene and the formation constant of mesitylene·Br complex (K=59 dm^3/mol) is much higher than that of the benzene·Br complex (K=0.2 dm^3/mol).[3] At high mesitylene concentrations formation of 2:1 contact type complexes is observed with equilibrium constant K=0.1 dm^3/mol.

In our experiments Br radicals were prepared by photolysis of α-bromoacetophenone[4] (0.05M) with 355 nm, 7μJ, 100 ps pulses. After a 10 ns delay, sufficiently long to allow formation of mesitylene·Br complexes, the charge transfer band was studied by femtosecond pump-probe laser spectroscopy. Various pump and probe wavelengths were employed, using 80 - 100 fs pulses. The ultrafast laser system and spectrometer have been described in detail elsewhere.[5] The output of a synchronously - pumped dye laser (790 nm) was amplified in three dye cells pumped by the second harmonic output of a Nd:YAG regenerative amplifier (500 Hz). The amplified pulses were focused into a quartz cell containing water to generate white light continuum. Pump and probe pulses were independently tunable; they were derived by amplifying 10 nm portions of the continuum. Pump pulses were compressed before amplification in a double pass prism compressor. Third harmonic light from the regenerative amplifier was used to photolyze α-bromoacetophenone and produce the bromine atoms.

Fig. 1 shows transient absorption of the mesitylene·Br complex in 0.5 M mesitylene solution in methanol after 550 nm excitation at 395 nm, 550 nm, 600 m, and 790 nm probe wavelengths. After the excitation the ground state population is completely regenerated in a few hundred picoseconds and the observed bleach or absorption returns to the baseline. Transients at 550 nm probe wavelength show the recovery of the ground state charge transfer absorption band measured near the maximum of the CT band. The bleach recovery clearly shows three different relaxation times. The first two 1.1 ps and 10 ps are independent of mesitylene concentration, while the longest relaxation time increases as the donor concentration decreases. Transient at 395 nm corresponds to the absorption of the mesitylene cation (λ_{max} = 475 nm) formed after the charge transfer excitation. The kinetics of the decay of the mesitylene cation is similar to the relaxation of the two long

components in the bleach recovery observed at 550 nm. Therefore the two long components represent the kinetics of the back electron transfer of the mesitylene$^{+}Br^{-}$ ion pair. The long

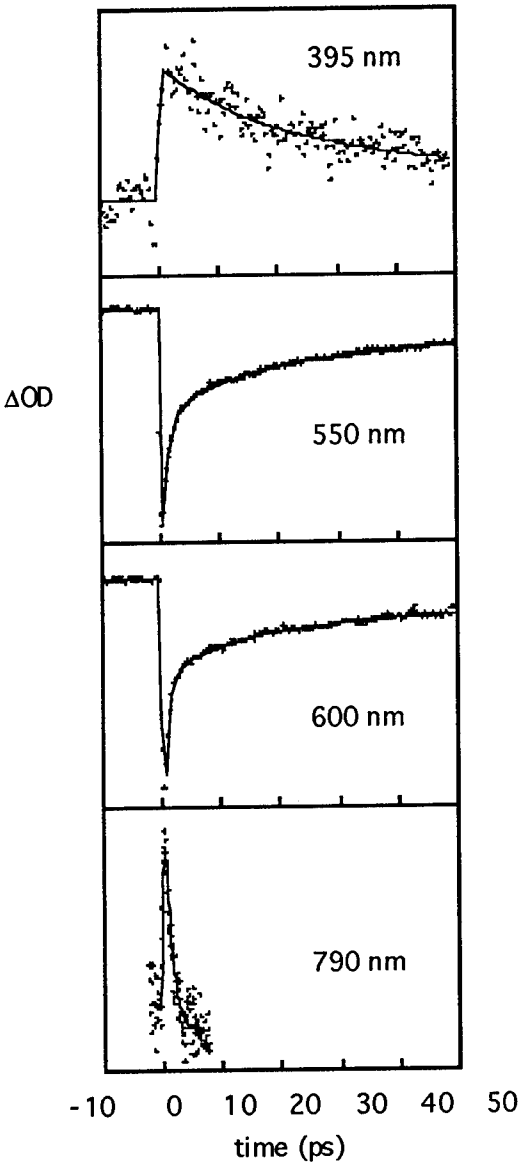
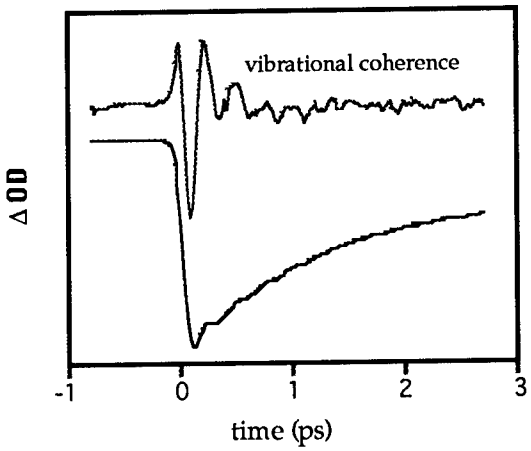


Fig. 1. Transient absorption of the mesitylene·Br complex in 0.5 M solution of mesitylene in methanol at 395 nm, 550 nm, 600 nm and 790 nm. Pump wavelength 550 nm.

Fig. 2. Bleach recovery for the mesitylene·Br complex in 1 M mesitylene solution in methanol. The inset shows the data with the multi-exponential part of the fit subtracted. 550 nm pump and probe wavelengths.



component is concentration dependent due to quenching of the ion pair by mesitylene molecules. Similar quenching was reported previously for the benzene·Br complex in nonpolar solvents.[6] The fast 1.1 ps component observed at 550 nm is not present in the transient absorption of the monomer cation. Instead a fast 1.1 ps absorption decay is observed in the 700 - 1000 nm spectral region.

At least three possible interpretations of these results have to be considered. The first is that the fast kinetics at early time may be due to transient absorption of vibrationally "hot" ground state molecules produced by a portion of the excited state population returning to the ground state on a much faster time scale than the remaining population. The distribution of ground state recovery rates may be due to a distribution of initial excited state geometries and/or a distribution of population of upper excited states. This interpretation requires very fast 200 - 300 fs relaxation of the excited CT state of the complex in order to rapidly produce the "hot" ground state molecules. We do not observe, however, the expected decay of absorption at 395 nm on 200 - 300 fs time scale. Such

behavior can be explained only if the early time absorption spectrum of the excited molecule is very broad and rather weak. We also do not observe an expected 200 - 300 fs bleach recovery at 550 nm. This latter result is consistent with the above model only if the "hot" molecule do not strongly absorb light at 550 nm.

The second possibility is that the fast dynamics are due to charge separation in the excited state, not ground state return. In this model, the transient absorption in the near infrared and the apparent bleach recovery at 550 nm would be due to excited state absorption of the complex. A good candidate for this absorption is the reverse charge transfer band between Br^- and mesitylene cation to yield an excited state of mesitylene.

An third interpretation, transient formation of the mesitylene dimer cation (λ_{max} = 1040 nm), has to be excluded since the ultrafast dynamics are observed even at very low mesitylene concentrations (0.05 M). Also, t-butylbenzene and tri-t-butylbenzene complexes with Br atom show presence of ~ 1 ps transient absorption in the 700 - 1000 nm region. Both donors are known not to form dimer cations in solution.

We also report in this communication observation of the low frequency D-A stretching mode in the mesitylene·Br complex. Fig. 2 presents pump - probe transient absorption experiments at 550 nm for the complex in 1 M mesitylene solution on methanol. Non-single-exponential bleach recovery is observed with an oscillation superimposed on this signal. The period of the oscillation is about 260 fs and it decays in ~ 700 fs. The inset in Fig. 2 presents the oscillation after the multi-exponential part of the signal was subtracted. Similar oscillation was observed at 620 nm probe wavelength. At both probe wavelengths the oscillation has the same zero phase shift if represented by a damped cos(ωt) function. The amplitude at t=0 corresponds to a bleach of the ground state absorption (increased transmission signal). The observed oscillation has a frequency of 120 cm^{-1}. We attribute oscillations to the coherent excitation of the ground state D-A stretching mode. The coherent excitation is likely to be due to impulsive stimulated Raman scattering (ISRS) process.

Acknowledgment

This research was supported by the Basic Energy Sciences program of the Department of Energy.

References

1. T. Kakitani, A. Yoshimori, and N. Mataga, in: Advances in Chemistry Series; *Electron Transfer in Inorganic, Organic and Biological Systems*; J.R. Bolton, N. Mataga, G. McLendon, Eds.; American Chemical Society: Washington 1991.
2. K.D. Raner, J. Lusztyk, and K.U. Ingold, *J. Phys. Chem.* **93**, 564 (1989).
3. W. Jarzeba, A. Hörmann, and P.F. Barbara, in preparation.
4. W.G. McGimpsey and J.C. Scaiano, *Can. J. Chem.* **66**,1474 (1988).
5. A.E. Johnson, N.E. Levinger, W. Jarzeba, R.E. Schlief, D.A.V. Kliner, and P.F. Barbara, *Chem. Phys.* **176**, 555 (1993).
6. R.E. Schlief, W. Jarzeba, K.A.M. Thakur, J.C. Alfano, A.E. Johnson, and P.F. Barbara, *J. Mol. Liquids*, in press.

Vibrationally Resolved Reaction Dynamics in the Condensed Phase: Excited Product States of DCN

D. Raftery, E. Gooding and R. M. Hochstrasser
Department of Chemistry, University of Pennsylvania
Philadelphia, PA 19104 - 6323

One of the goals of condensed phase reaction dynamics is to contrast results from experiments in the gas phase with observations of similar reactions in liquids so as to elucidate the effects of solvation on the kinetics and energy partitioning of simple reactions. To date, there have been few experimental studies having the requisite spectral and temporal resolution to test current theories. Transient infrared spectroscopy has been useful in the study of a variety of unimolecular reactions [1] and recently in a bimolecular reaction that is not diffusion controlled [2]. The present work shows that for products with large reaction exoergicity and sufficient anharmonic shifts in the vibrational coordinate of interest, it is possible to observe highly excited modes in a variety of different reaction schemes, and to measure the nascent vibrational distributions. Such dynamical detail should allow tests of model potential energy surfaces for the condensed phase analogous to Monte Carlo studies of gas phase potential energy surfaces.

Using the solvent as one of the reactants and a radical precursor to provide another reactant (via photolysis), we are studying a series of condensed phase hydrogen abstraction reactions which show unusual differences from similar reactions in the gas phase. In the present work, we produce CN radicals from the photolysis of ICN at 266 nm in chloroform solvent. The solvent has a profound caging effect on the precursor, favoring geminate recombination. However, a small portion (about 10%) of the CN radicals are able to escape recombination and go on to react with the solvent on a time scale (a few hundreds of ps) that is below the diffusion controlled regime.

In Figure 1 the kinetics for the formation of DCN from deuterated chloroform are shown at the peak of the absorption, 2606 cm^{-1}. A transient spectrum (not shown) that is in agreement with steady-state FTIR results taken much later confirms the production of DCN as a product in the reaction. A fit of the transient data to an exponential growth gives a formation time of 350 ± 50 ps. The corresponding reaction rate constant, 2.3 ± 0.3 x 10^8 M^{-1} s^{-1} is two orders of magnitude slower than for the same reaction in the gas phase [3].

In Figure 2 transient data are shown that correspond to the formation of the first vibrationally excited state of DCN around 2565 cm^{-1}. Again, a transient spectrum [4] positively identifies this transient with the v=1 to v=2 excited state transition. The peak of the absorption is approximately 40 cm^{-1} to lower frequency than the ground state absorption, as expected from the value of the anharmonicity of the C-D stretching coordinate. The transient data indicate the formation and decay of the excited state, with time constants of 145 ± 75 and 350 ± 150 ps. The constant signal observed at long times is ascribed to solvent heating. To the limit of our sensitivity, no transient signal was observed near 2525 cm^{-1}, which would have indicated the presence of v=2 population.

From the amplitudes of the ground and first excited states, we calculate the nascent vibrational population distribution to be P0 : P1 : P2 :: 0.85 : 0.13 : <0.02. This distribution is not in accordance with recent gas phase results of CN reactions with hydrocarbons, where inverted vibrational populations were observed, but do correspond roughly to an equipartitioning of the exoergicity of the reaction in solution. This result indicates that complex formation (followed by energy partitioning) is occurring in the liquid phase, perhaps due to the effects of solvent caging

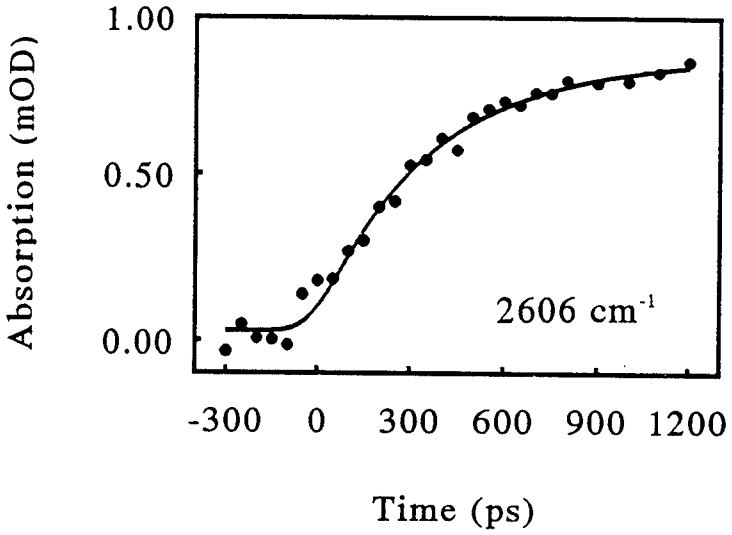


Figure 1. Ground state formation of DCN from ICN photolysis in deuterated chloroform.

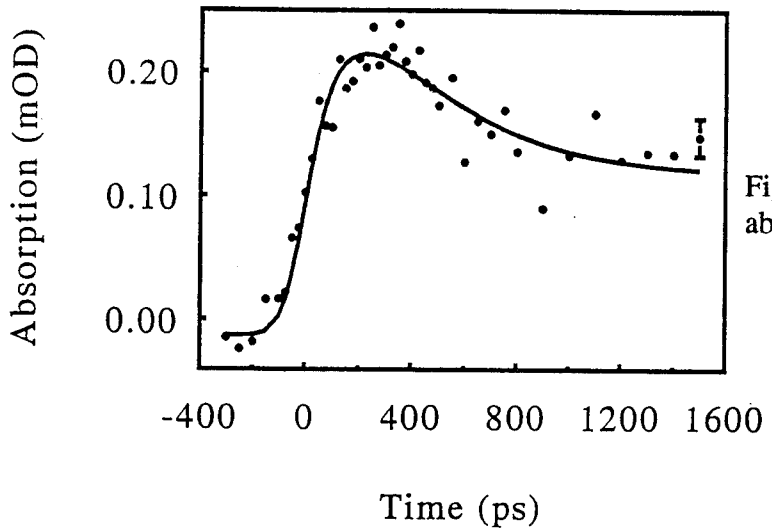


Figure 2. DCN excited state transient absorption data around 2565 cm^{-1}.

of the transition state. A very slight temperature dependence of the reaction rate was observed, indicating that friction (and not simply an activation barrier) plays an important role in reducing the reaction rate substantially upon solvation.

Transient infrared methods can also be used to follow the dynamics of unimolecular reactions. Recent studies of the photolysis of s-tetrazine-d_2 show that highly vibrationally excited products occur and can be individually monitored in the infrared. Figure 3 shows the transient data for the ground state absorption of the C-D stretch in DCN following 2 photon photolysis of s-tetrazine-d_2 at 532 nm. A fit to a single exponential (solid line) with an initially negative amplitude describes the dynamics much better than a simple exponential growth function (dashed line). The fitted growth time is 320 ± 20 ps, while the inverted population lasts for some tens of ps. The s-tetrazine system could form the basis for a tunable, liquid state infrared laser. We also observe excited state populations in the v=2 and v=3 states of the C-D stretch, as well as highly populated excited bending levels. This situation is quite different from that in the gas phase, where the reaction products are vibrationally cold.

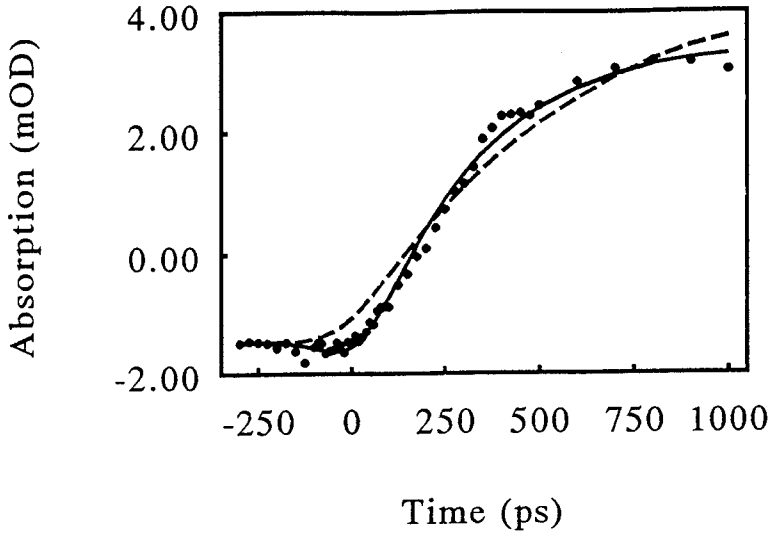


Figure 3. Transient signal for the ground state of DCN following photolysis of s-tetrazine-d_2. Fits to the data are shown with zero initial amplitude (dashed line) and with negative initial amplitude (solid line), corresponding to infrared gain.

These results point to the utility of transient infrared methods for the detailed study of condensed phase reactions. Experiments with higher time resolution are currently underway to investigate the first steps that occur in solution phase reaction dynamics.

References

[1] see, for example, P. A. Anfinrud, C.-L. Han, T. Lian and R. M. Hochstrasser, J. Phys. Chem. 95 (1991) 574.

[2] D. Raftery, M. Iannone, C. M. Phillips and R. M. Hochstrasser, Chem. Phys. Lett. 201 (1993) 513.

[3] V. Morris and W. M. Jackson, private communication.

[4] D. Raftery, E. Gooding and R. M. Hochstrasser, manuscript in preparation.

Ultrafast Vibrational Energy Relaxation in $[(NC)_5M^{II}CNM^{III}(NH_3)_5]^{1-}$ (M = Ru, Os) Studied by Picosecond Infrared Spectroscopy

Page O. Stoutland, Stephen K. Doorn, R. Brian Dyer, and William H. Woodruff

Division of Chemical and Science Technology (Mail Stop J-567, Tel. 505 665-4692), Los Alamos National Laboratory, Los Alamos, New Mexico 87545.

Mixed-valence transition metal complexes have long been used to study electron transfer reactions due to the availability of well-defined complexes with favorable spectroscopic properties.[1] These studies have resulted in a plethora of information concerning the fundamental aspects of electron transfer reactions. We have recently used complexes of this type to investigate ultrafast electron transfer and vibrational energy relaxation dynamics in cyanide-bridged mixed-valence transition metal dimers. These studies have allowed us to observe, for the first time in the solution phase, the vibrational excitation which accompanies electron transfer reactions. In previous publications[2] we have shown that (1) optical excitation into the metal to metal charge transfer (MMCT) transition of a series of mixed-valence transition metal complexes leads to formation of the excited state redox isomer, and that (2) subsequent ultrafast back electron transfer regenerates the original species, with much of the electronic excitation energy being converted into vibrational energy in the product. To date we have discussed the electron transfer and the coupled vibrational excitation. Here, we concentrate on the relaxation of the vibrationally excited molecules produced following the back electron transfer.

$$[(NC)_5M^{II}CNM^{III}(NH_3)_5]^{1-} \underset{ET}{\overset{h\nu}{\rightleftharpoons}} [(NC)_5M^{III}CNM^{II}(NH_3)_5]^{1-}$$

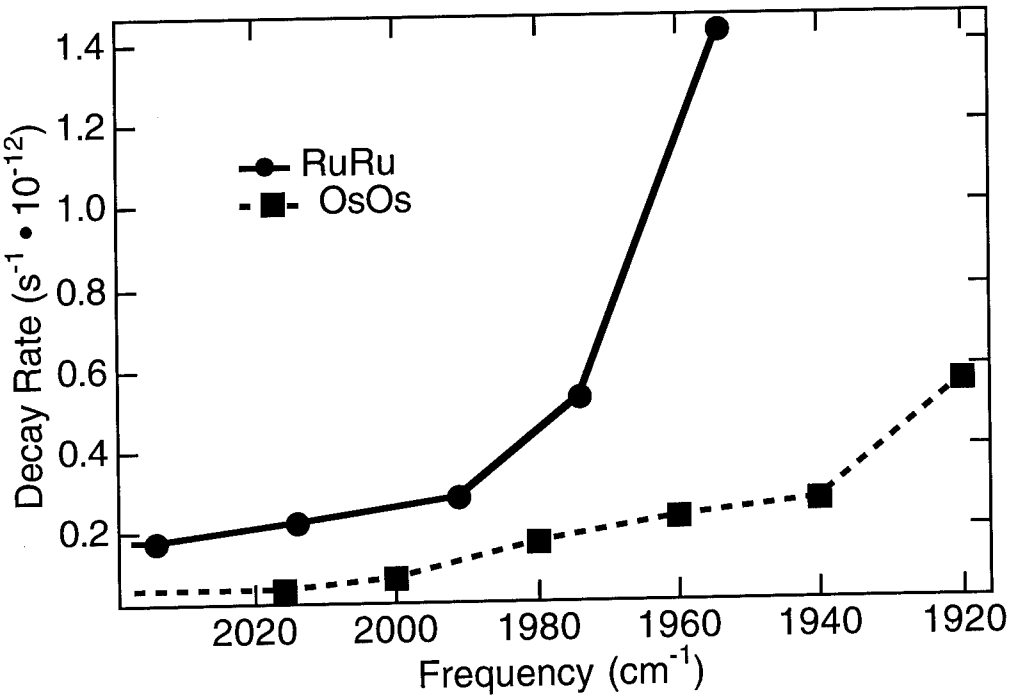
M = Ru, Os

We have studied the dynamics of $[(NC)_5M^{II}CNM^{III}(NH_3)_5]^{1-}$ (M = Ru, Os) following MMCT optical excitation with the use of picosecond infrared spectroscopy. We monitor the terminal MC≡N stretching vibrational frequency which is sensitive to the oxidation state of the ruthenium cyanide center and, because of anharmonicity, to the degree of vibrational excitation of this mode.

The production of highly vibrationally excited states in these dimers following electron transfer has provided us with a unique system for studying vibrational relaxation in inorganic

molecules. Little is known about vibrational relaxation in inorganic systems; what is known has typically been limited to studies of systems produced in low lying v states (v = 1 - 2). In the systems discussed here, relaxation of energy out of the MC≡N mode can occur either through an intramolecular mechanism (IVR) or through transfer of the excess energy to the surrounding solvent molecules. Thus at the heart of understanding condensed phase energy transfer dynamics is separating intramolecular energy redistribution (IVR), and transfer of energy from the solute to the surrounding solvent (ET2S). In the solution phase, however, separation of these two deactivation pathways is often difficult as it is usually possible to monitor only selected vibrational modes. We are fortunate in that we have data for both the ruthenium and osmium analogs in both H_2O and D_2O, and also have rate data for multiple vibrational states. This makes it possible to separate the contributions of IVR and intermolecular energy transfer in these systems.

For example, consideration of the decay rates of the v=1 -> v=0 transition in the osmium (OsOs) and ruthenium (RuRu) analogs in H_2O and D_2O allows us to separate the contributions of IVR and ET2S. We have been able to identify two limiting cases for the lowest lying v state: (1) for RuRu/D_2O we are observing "exclusively" IVR ($\tau \sim 7$ ps), and (2) for OsOs/H_2O we are observing "exclusively" energy transfer to the solvent ($\tau \sim 5$ ps). We can obtain information on the higher lying states by considering the v state dependence of the energy relaxation rates. For both dimers the vibrational relaxation rates show a steady increase as the degree of excitation in the cyanide stretch is increased (Fig. 1--The lowest frequency in each case corresponds to v ~ 7, with each vibrational state being separated by ca. 14 cm^{-1}.).



Wilson and Hynes[3, 4] have recently shown that vibrational relaxation of ions in polar solvents is typically dominated by long-range Coulombic interactions in which the relaxation can be understood as being caused by the force the solvent exerts along the vibrational coordinate of the oscillator, i.e. the frequency-dependent vibrational friction. Calculation of the frequency dependent friction for H_2O and D_2O shows that ET2S in D_2O should be ~ 8 times slower than in H_2O for a 2000 cm^{-1} oscillator. Our results for OsOs show that $\tau_{H2O} = 5$ ps while $\tau_{D2O} \geq 19$ ps, consistent with the prediction. In addition, this model predicts that there should be little difference in the ET2S rates (for either H_2O or D_2O) over the region 1900 - 2100 cm^{-1}. Thus in the case of OsOs/D_2O and RuRu/D_2O the observed steep increase in the phenomenological relaxation rates with decreasing frequency (increasing v state) is <u>not</u> due to ET2S, and must be due to IVR.

We have modeled the v state dependence of the IVR rates using simple models based on the Golden Rule, understanding that particularly at the lower v states there may be problems due to ET2S becoming significant.

$$k_{i\rightarrow j} = \left(\frac{2\pi}{\hbar}\right)\langle\, |\, V^{ij}\, |^2\, \rangle \rho_j(E_i)$$

While such models are not expected to be qualitatively correct, for large molecules we might expect the trends to be accurately represented. For example, it is not unreasonable to expect that high frequency vibrational states might lose their energy to a "continuum" of lower energy states, as the density of states for such molecules is very high.[5, 6] This model is successful in the present case at modeling the IVR, suggesting that it may be useful for estimating IVR rates in large molecules for which there is limited dynamical information. Finally, our results represent one of the first cases in which high-lying v states are produced in the solution phase, allowing experimental verification of energy relaxation models.

References.

[1] Brown, D.B. *Mixed-Valence Compounds* (D. Reidel, Dordrecht, The Netherlands, 1980).

[2] Doorn, S.D., Dyer, R.B., Stoutland, P.O., Woodruff, W.H. *J. Am. Chem. Soc.* **115**, 6398 (1993).

[3] Whitnell, R.M., Wilson, K.R., Hynes, J.T. *J. Phys. Chem* **94**, 8625-8628 (1990).

[4] Whitnell, R.M., Wilson, K.R., Hynes, J.T. *J. Chem. Phys.* **96**, 5354 (1992).

[5] Voth, G.A. *J. Chem. Phys.* **87**, 5272-5279 (1987).

[6] Voth, G.A. *J. Chem. Phys.* **88**, 5547-5552 (1988).

Frequency Doubling of Ultrashort Pulses from a Ti:sapphire Laser

M.T. Asaki, S. Backus, C. Shi, M.M. Murnane and H.C. Kapteyn
Department of Physics, Washington State University, Pullman, WA 99164-2814

Recent advances in mode-locked Ti:sapphire laser technology make possible the routine generation of pulses as short as 11 fs directly from a laser.[1] Frequency doubling the 800-850 nm fundamental of these lasers may make possible pulses of unprecedented short duration in the blue. Both intracavity and extracavity doubling of femtosecond pulses from Ti:Sapphire and CPM lasers have been demonstrated.[2-4] Intracavity doubling is simpler, and also has the advantage of much higher power in the doubling crystal, and therefore, much higher efficiency. Previously, the shortest pulses generated using intracavity doubling were 54 fs at 430 nm.

In order to choose the optimum crystal for this application, a number of parameters such as phase-matching angle, temporal walkoff, acceptance angle, bandwidth acceptance, and efficiency must be considered in detail. These parameters can be calculated using Sellemier equations available in the literature. Temporal walkoff and acceptance angle limit the thickness of the crystal which can be used. However, with proper selection of materials, walkoff can be kept below 10 fs for reasonable crystal thicknesses (~100μm). Our primary choice has been LBO, although BBO and KDP are also possible candidates for doubling ultrashort-pulse 830 nm light.

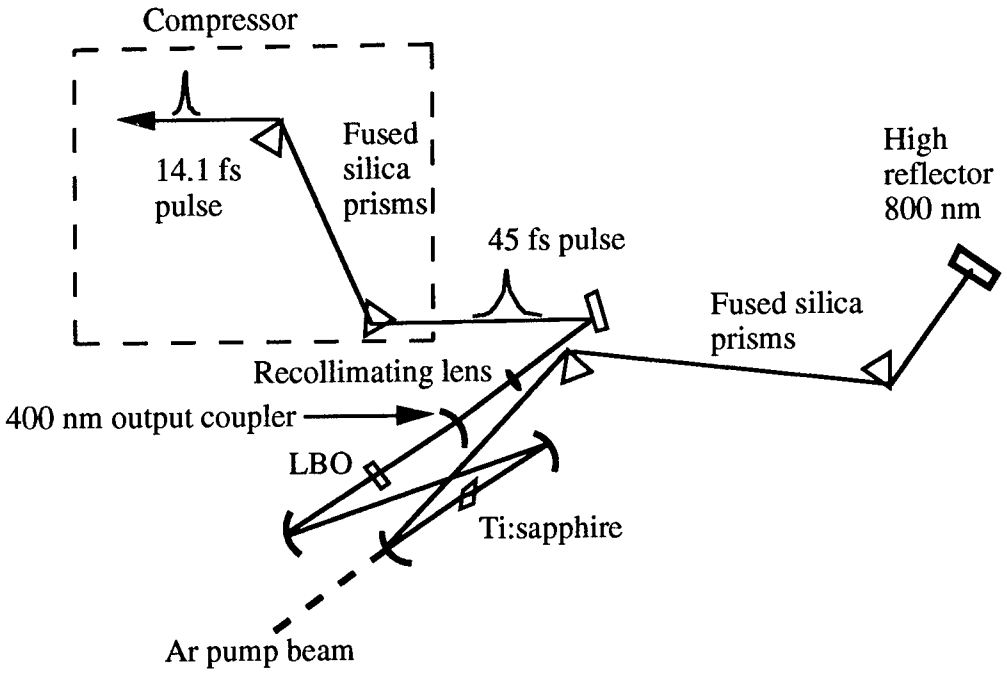


Figure 1: Configuration of the Ti:sapphire cavity for intracavity doubling, and the external compressor.

In our experimental setup, we use a Ti:Sapphire laser with a conventional linear cavity. The Ti:Sapphire crystal is 4.5 mm long, 0.15% doped material with FOM>150 (Union Carbide Corp.) , placed between two 10 cm curvature mirrors. The laser is pumped by 5 - 10 Watts of all-lines green from an argon-ion laser. On the prism side of the cavity, the end mirror is a flat 3% output coupler (Spectra-Physics) with a center wavelength of ~830 nm. The focus for the doubling crystal is created by a second set of 10 cm radius of curvature mirrors set on the side of the laser opposite the prisms. These mirrors (CSK Co.) are broadband high-reflectors in the red, and are partially transmitting (50%-75%) in the blue. The cavity setup is shown in Figure 1. The angle of incidence on the curved mirror is kept small ($\leq 5°$) to limit astigmatism. Mode-locking is readily achieved in this configuration by rotating the doubling crystal to adjust for no polarization rotation, observing the tunability of the laser when running CW, adjusting the curved mirror separation, and placing the crystal at the exact focus.

Only Type I doubling is acceptable for intracavity doubling, since Type II rotates the polarization of the fundamental. Initially, we used a Brewster cut KDP crystal, 400 μm in thickness. This crystal has a temporal walkoff of 30.6 fs, and an acceptance angle of 0.6 mrad, which limited the obtainable pulse width. We were, however, able to generate up to 50 milliwatts of blue in two beams. The blue bandwidth of ~80 Å corresponds to a 21 fs transform-limited pulse, and is consistent with the spectral acceptance of the KDP crystal.

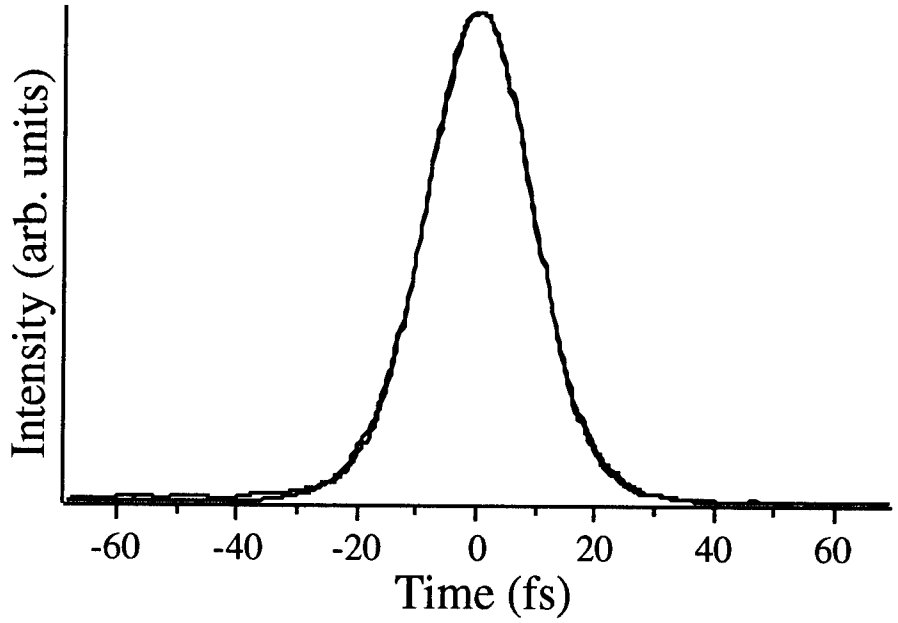


Figure 2: Autocorrelation measurement of intracavity frequency-doubled pulses at a center wavelength of 415 nm, with a pulse duration of 14 fs (assuming a $sech^2$ pulse shape).

Our latest work has been done with a 100 μm lithium triborate (LBO) crystal. This crystal has a temporal walkoff of about 10 fs, and an acceptance angle of 7.2 mrad. We were able to generate a total of more than 100 milliwatts of blue, with a bandwidth of ~20 nm at 4160 nm. This efficiency is consistent with our calculations. After compression, the measured pulse duration of the second harmonic is 14 femtoseconds, which is quite close to the

theoretical pulse duration based on the available bandwidth. Figure 2 shows the autocorrelation trace of the compressed blue output, and the $Sech^2(t)$ fit to the data.

The Ti:sapphire laser generates pulses of duration 12 - 14 fs at 800 nm. We note however that the pulse duration of the fundamental light at 800 nm is positively chirped to almost 40 fs within the LBO crystal.[5] Nevertheless, we can generate pulses as short as 14 fs in the blue. This indicates that at present we are not limited by temporal walkoff or finite acceptance angle, and further improvements in generating higher output powers will be possible.

References

1.M. T. Asaki, C. P. Huang, D. Garvey, J. Zhou, H. C. Kapteyn, M. M. Murnane, Opt. Lett. **18**, 977 (1993).
2.S. Backus, M. T. Asaki, C. Shi, H. C. Kapteyn, M. M. Murnane, Opt. Lett. To be published (1993).
3.R. A. Cheville, M. T. Reiten, N. J. Halas, Opt. Lett. **17**, 1343 (1992).
4.R. J. Ellingson, C. L. Tang, Opt. Lett. **17**, 343 (1992).
5.J. P. Zhou, G. Taft, C. P. Huang, H. C. Kapteyn, M. M. Murnane, Submitted to Optics Letters (1993).

AC- Stark effect of the Fermi Edge Singularity: Observation of "excitonic polarons" ?

I. E. Perakis[1,2], I. Brener[2], W.H. Knox[2] and D.S. Chemla[3]

1 - Physics Department, Rutgers University, Piscataway, NJ 08855
2 - AT&T Bell Laboratories, Holmdel, NJ 07733
3 - Physics Department, UC Berkeley, Berkeley, CA 94720

Ultrafast technology has created new opportunities for investigating the properties of many-body systems. For example, an intense pump optical pulse tuned in the transparency regime induces virtual charge fluctuations between the conduction and valence bands that renormalize all the semiconductor parameters. Augmented by correlation effects, such processes result in a "dressed" interacting system whose excitation spectrum can be measured by a weak probe pulse. The exciton absorption in undoped semiconductors was investigated with this technique in [1]. As the pump intensity increases, the bound state resonance shifts to the blue; this is called the AC (optical) Stark effect. Unlike atomic systems, in semiconductors the optically excited electrons and holes interact with each other; and many-body effects need to be addressed [2]. A narrow-band pump pulse blue-shifts the resonance and slightly enhances its oscillator strength [3,4]. The oscillator strength is significantly reduced if the pulse is ultrashort (100 fs or less) [5].

Modulation doping produces extremely high mobility two dimensional electron gases. In such systems, Coulomb many-body effects induce a resonant structure at the absorption edge called the Fermi Edge Singularity (FES). Even though the transition from low to high doping is continuous, the nature of the resonance changes. For low doping, a sharp excitonic bound state exists. This is no longer true above a critical density; bound states cannot lie inside the Fermi sea continuum. The FES results from correlations of a valence hole with the entire Fermi sea. As shown in Fig. (1), in these systems, excitation by ultrashort pulses in the transparency region

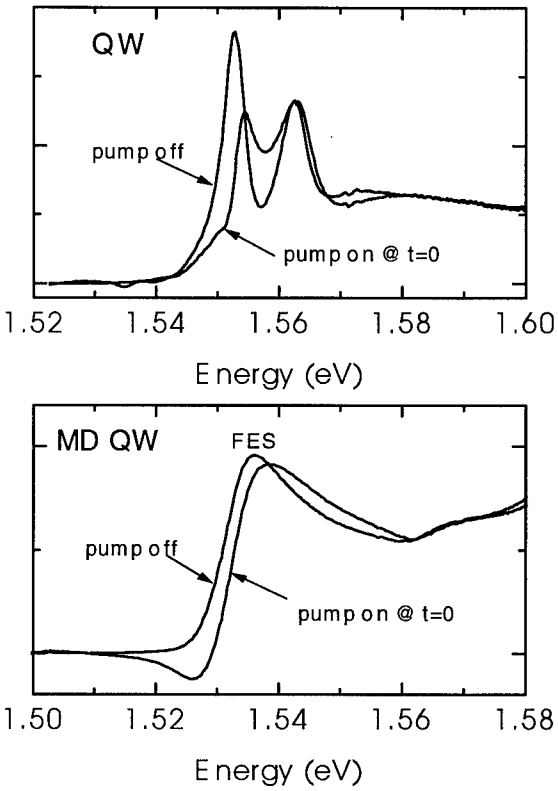


Figure 1. Nonlinear absorption specrta. Lower panel - effect of below gap pumping on FES, and upper panel - undoped QW.

results in a decrease of the oscillator strength much smaller than in undoped semiconductors, accompanied by a blue shift and a pronounced optical gain [6]. In modulation doped heterostructures, the photoexcited hole interacts, in addition to

the photoexcited electron, with the entire Fermi sea [7-9], and sharp excitonic bound states no longer exist. These many-body effects considerably complicate the extension of [2] especially, since the qualitative behavior also depends on the duration of the optical pulses.

To obtain a physical picture that clarifies the role of the time-dependent many-body processes, we introduced a new approach to the AC-Stark effect, which treats the doped system in a systematic way, but also recovers the features of undoped semiconductors and atomic systems. It is based on the separation of "fast" and "slow" semiconductor degrees of freedom. The former always adjust to the instantaneous pump amplitude and lead to time-dependent semiconductor parameters. The slow degrees of freedom adjust to the time-dependent changes only if the pump pulse is very smooth; the resonance is then enhanced by a polaronic effect. Intense ultrashort pump pulses, however, have a small effect on the slow Fermi sea excitations close to the Fermi surface. The oscillator strength of the resonance then decreases, primarily due to a pump-induced decrease in the effective transition matrix element, and blue-shifts, due to an increase in the effective gap.

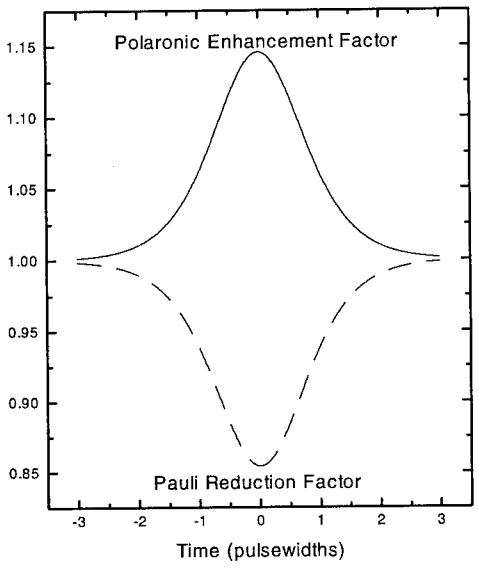


Figure 2. Polaronic enhancement factor, and Pauli reduction factor.

The semiconductor renormalizations arise from the interactions among the virtually excited interband e-h pairs, induced by the pump. By the Heisenberg uncertainty principle, these pairs last for time intervals determined by their inverse excitation energy, similar to the inverse pump pulsewidth. This is the shortest characteristic time in the rotating frame. We refer to these excitations as the "fast" degrees of freedom. The Fermi sea excitations however are much slower. This distinction leads to a factorization of the many-body wavefunction [10] that determines the probability amplitude for the emission or absorption of virtual interband e-h pairs. Such processes may be thought of as occuring independently and renormalize the entire Fermi sea; they are enhanced by correlation effects.

The optical excitation creates a virtual cloud of such fast interband e-h pairs, analogous to the optical phonons in the polaron problem [11]. These are typically faster than the changes in the pump amplitude. The size of the virtual cloud thus adiabatically adjusts to the instantaneous pump amplitude, or equivalently the nonresonant susceptibilities are essentially instantaneous. As in the polaron problem, the electrons and holes drag this virtual excitation cloud and become heavier "excitonic polarons". Their mass depends on the instantaneous pump amplitude and is enhanced by correlation effects. Fig. (2) displays the dynamics of the polaronic enhancement of the reduced e-h mass. Electron-hole pairs may also be created indirectly, assisted by the scattering of additional electrons or holes. Such virtual processes result in non-local screening of the interactions, weaker than the polaronic effect. Similar processes, mediated by optical phonons, lead to superconductivity.

The Pauli exclusion interactions among the virtual e-h pairs reduce the effective transition matrix element and increase the effective energy gap. The Pauli factor is shown in Fig. (2). It is important to note that all the manifestations of the virtual cloud

(effective mass, gap, and matrix element renormalizations) have similar magnitude.

The resonant structures considered here represent manifestations of e-h Coulomb correlations. The e-h Coulomb interaction easily excites large numbers of virtual pairs across the Fermi surface, at small energy cost. This was described in [8] and in [10] was generalized to include the effects of the time-dressing. The results of these calculations are shown in Figure (3).
This agrees qualitatively well with the experiment of Fig. (1). The optical gain below the FES, also found in a two-level system under similar excitation conditions, results from the finite duration of the dressing; this produces negative contributions to the absorption spectrum.

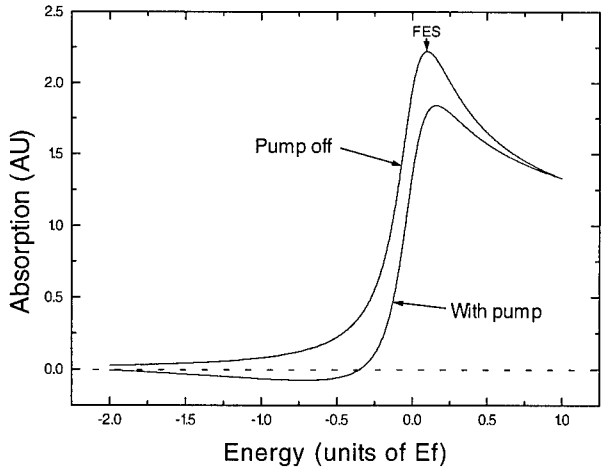


Figure 3. Calculated absorption spectrum of the FES with and without sub-bandgap pump beam

In an undoped semiconductor, we may view the effect of the pump on the bound state by using the semi-classical hydrogen atom picture. In the undressed system, the trajectory of a bound electron closes on itself after a full Bohr period due to the change in the effective mass. In the dressed semiconductor however, the Bohr radius changes over time intervals comparable to the Bohr period. The distortion in the trajectory is thus appreciable.

In conclusion, we discuss a new theoretical model which takes a new approach to the problem of virtual excitations. The results agree well with experiments, and may lead to a better understanding of the nature of the Fermi Edge Singularity.

[1] A. Mysyrowicz, D. Hulin, A. Antonetti, A. Migus, W. T. Masselink, and H. Morcoc, Phys. Rev. Lett. **56**, 2748 (1986); A. von Lehmen, D. S. Chemla, J. E. Zucker, and J. P. Heritage, Opt. Lett. **11**, 609 (1986); W. H. Knox, D. S. Chemla, D. A. B. Miller, J. B. Stark, and S. Schmitt-Rink, Phys. Rev. Lett. **62**, 1189 (1989).

[2] S. Schmitt-Rink and D. S. Chemla, Phys. Rev. Lett. 57, 2752 (1986); S. Schmitt-Rink, D. S. Chemla, and H. Haug, Phys. Rev. B **37**, 941 (1988).

[3] C. Ell, J. F. Muller, K. El Sayed, and H.Haug, Phys. Rev. Lett. **62**, 304 (1989).

[4] O. Betbeder-Matibet, M. Combescot, and C. Tanguy, Phys. Rev. **B44**, 3762 (1991).

[5] W. Schaefer, K. H. Schuldt, and R. Binder, Phys. Status Solidi **B150**, 407 (1988); I. Balslev, R. Zimmermann, and A. Stahl, Phys. Rev. **B40**, 4095 (1989); R. Binder, S. W. Koch, M. Lindberg, W. Schaefer and F. Jahnke, Phys. Rev. **B43**, 6520 (1991).

[6] I. Brener, W. H. Knox, G. E. Doran, J. E. Cunningham, and D. S. Chemla, International Conference on Quantum Electronics XVIII (1992).

[7] P. Nozieres and C. T. De Dominicis, Phys. Rev. **178**, 1097 (1969); K. Ohtaka and Y. Tanabe, Rev. Mod. Phys. **62**, 929 (1990).

[8] I. E. Perakis and Y.-C. Chang, Phys. Rev. **B44**, 5877 (1991); ibid **47**, 6573 (1993); ibid **43**, 12556 (1991).

[9]A. E. Ruckenstein and S. Schmitt-Rink, Phys. Rev. **B35**, 7551 (1987).

[10] I. E. Perakis and D. S. Chemla, Phys. Rev. Lett. (submitted).

[11] T. D. Lee, F. Low, and D. Pines, Phys. Rev. **90,** 297 (1953).

Solvent Dependence of the Femtosecond Three Pulse Photon Echo for LD690 in n-Alcohols.

C.J. Bardeen and C.V. Shank, Department of Chemistry, University of California, Berkeley, CA 94720 and Materials Sciences Division, MS 70-193A, Lawrence Berkeley Laboratory, Berkeley, CA 94720
phone : 510-486-6558, fax : 510-486-6720

The characteristic timescales of the solvent-solute interaction are of great interest to those studying the spectroscopy and reaction dynamics of molecules in condensed phases. These timescales influence a variety of linear and non-linear spectroscopic measurements, and together these different types of measurements should constrain the quantitative values of the interaction parameters. In this work we use both linear (absorption and fluorescence) and non-linear (resonance raman and femtosecond time-resolved 4-wave-mixing) spectroscopies to systematically investigate the spectral broadening of the dye molecule LD690 in a series of n-alcohols.

Steady-state absorption and fluorescence measurements were performed on standard instruments with a resolution of 1 nm. The resonance raman measurements were taken using the 514 nm line of an Ar laser and a standard raman detection setup. LD690's small Stokes shift and high fluorescence quantum yield prevented us from obtaining a full excitation profile. The time-resolved measurements were performed using a 10 fs compressed pulse, centered at about 620 nm and generated the standard way [1]. For most of these experiments, three pulses were used to generate scattered light in the $-k_1+k_2+k_3$ phase-matched direction, which was collected by a PMT. We find that there is substantial inhomogeneous broadening on the femtosecond timescale, and therefore refer to this type of experiment as a three pulse photon echo (3PPE).

Fig. 1 shows steady state absorption spectra of LD690 in methanol, 1-pentanol, and 1-decanol. Note that the absorption shifts red and narrows appreciably as the size of the alcohols increases. There are also shoulders visible in the spectra, indicative of vibronic structure. From the resonance raman measurements it was determined that at least 16 vibrational modes are significantly coupled to the electronic excitation. A knowledge of the frequencies and coupling constants of these modes is essential for the modeling the data. The fluorescence spectra in the various alcohols has a very small Stokes shift (from about 700 cm^{-1} in methanol to about 200 cm^{-1} in 1-decanol) and is slightly broadened with two discernible peaks, suggesting that the equilibrated excited state exists in two isomers, possibly differing by a hydrogen bond interaction [2]. We assume that the formation time for these isomers is long compared to the time resolved measurements. In Fig. 2 we see typical 3PPE data for LD690 in methanol, scanning t_{12} with the third pulse (arriving at t_{13}) fixed at 120 fs (to suppress the dominant 587 cm^{-1} mode oscillations) [1,3]. Fig. 3 shows the same measurement performed in 1-pentanol. In both figures the theoretical 3PPE response, calculated using a multimode offset harmonic oscillator model for the molecule [1] and a gaussian dephasing function, is indicated by the dashed lines.

The observed trend in the series of absorption spectra of LD690 indicates that one or several of the broadening mechanisms at work in solution is changing with alcohol size. The time-resolved data, which we have for the first half of the series (methanol through pentanol), bears this out. For methanol, using the set of modes and coupling parameters derived from the raman data, we can fit both the absorption spectrum and the 3PPE with a gaussian dephasing time of 45 fs ($\exp[(-t/T_{2g})^2]$) and a gaussian inhomogeneous distribution of 260 cm^{-1} HWHM. For 1-pentanol these values are 50 fs and 215 cm^{-1} respectively. The time-resolved data can also be fit fairly well with exponential T_2's of 40 fs and 50 fs, but then the calculated absorption spectrum is compromised, mainly by a large tail to the red which is not observed experimentally. Another approach is to use an exponentially

decaying frequency fluctuation correlation function [4,5] which interpolates between inhomogeneous and homogeneous broadening. If we use only a single non-Markovian function to fit the data, we find that for the case of methanol we can do a fair job of reproducing the absorption and 3PPE polarization decay (scanning t_{12}) using a correlation function with a rms deviation of 300 cm^{-1} and a correlation time of 300 fs. This model also predicts fairly rapid spectral diffusion, however, which is not apparent in 3PPE measurements with a fixed t_{12} and scanning t_{13}.

The variation of the fast polarization dephasing with solvent is worth special mention. The inhomogeneous broadening that we deduce from the 3PPE measurements is most likely due to slow solvent reorganization and its dependence on solvent can be estimated from steady state Stokes shift data [6]. The fast component of the dephasing, which determines the decays in Figs. 2 and 3, is thought to be due to inertial motions of the solvent molecules [7] and it is not clear that changing the length of the alcohol chain should have much effect on this short-time, small amplitude motion. Fig. 4, which is a plot of a "dephasing rate" defined to be the amount that the signal has decayed 40 fs from the peak, does show a clear trend of the fast dephasing rate as a function of alcohol chain length. Time constants (i.e. $1/T_2$ or $(1/T_{2g})^2$) extracted from the calculations that match the data also exhibit this roughly 20% change, which may reflect a difference in short-time solvation shell dynamics for the different sized alcohols.

No simple approach seems capable of modeling all the data, and a full treatment will probably require a hierarchy of timescales, all of which can vary with solvent [8]. We have shown that although vibronic congestion is not negligible in this case, there is a significant component of the spectral broadening due to the solvent, and that this broadening changes with solvent both on the femtosecond timescale and on much longer timescales.

1. C.J. Bardeen and C.V. Shank, Chem. Phys. Let. 203 535 (1993).
2. J. Yu and M. Berg, Chem. Phys. Let. 208 315 (1993).
3. R.W. Schoenlein, D.M. Mittleman, J.J. Shiang, A.P. Alivasatos, and C.V.Shank, Phys. Rev. Let. 70 1014 (1993).
4. J.Y. Bigot, M.T. Portella, R.W. Schoenlein, C.J. Bardeen, A. Migus, and C.V. Shank, Phys. Rev. Let. 66 1138 (1991)
5. E.T.J. Nibbering, D.A. Wiersma, and K. Doopen, Phys. Rev. Let. 66 2464 (1991).
6. R.A. Marcus, J. Chem. Phys. 43 1261 (1965)
7. N.E. Shemetulskis and R.F. Loring, J. Chem. Phys. 97 1217 (1992)
8. M. Sparpaglione and S. Mukamel, J. Chem. Phys. 88 3263 (1988), 88 4300 (1988).

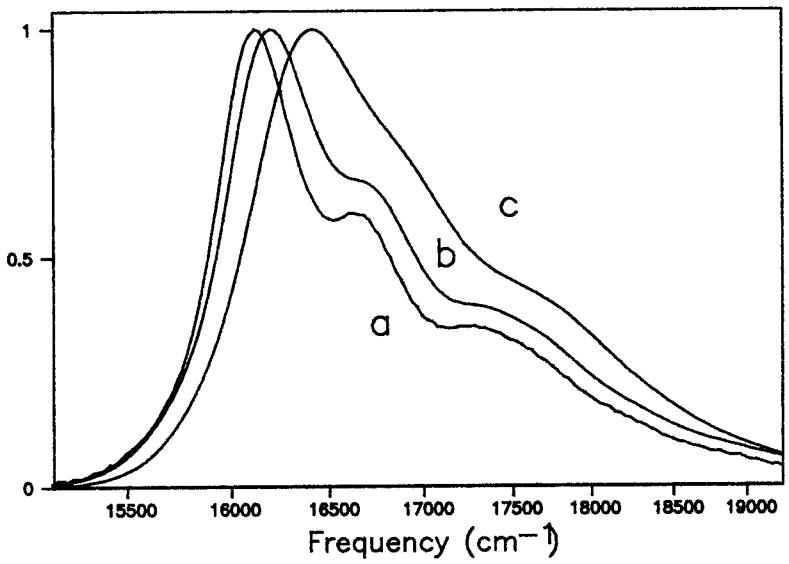


Fig. 1: Absorption spectra of LD690 in a) 1-decanol, b) 1-pentanol, and c) methanol.

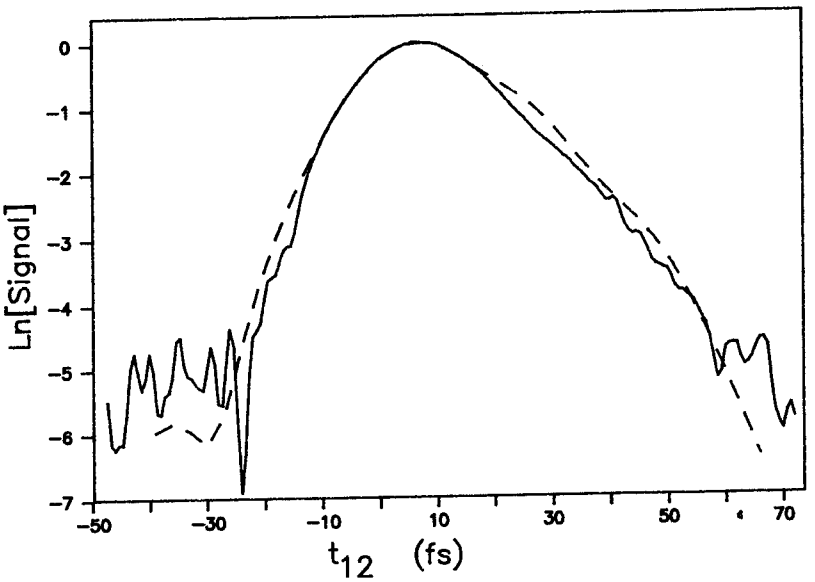


Fig. 2 : 3PPE for LD690 in methanol, t_{13}=120 fs. Dashed line is calculated response assuming a gaussian T_{2g}=45 fs and an inhomogeneous hwhm=260 cm^{-1}.

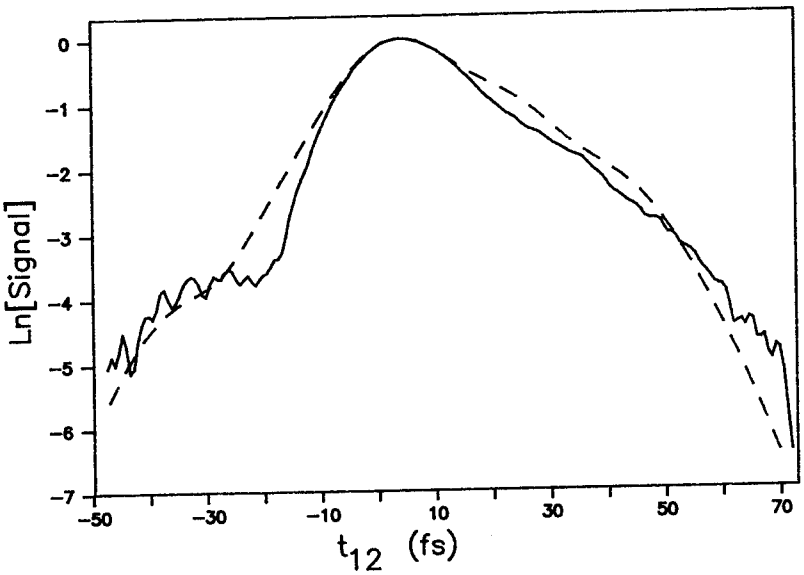


Fig. 3 : 3PPE for LD690 in 1-pentanol, t_{13}=120 fs. Dashed line is calculated response assuming T_{2g}= 50 fs and an inhomogeneous hwhm=215 cm^{-1}.

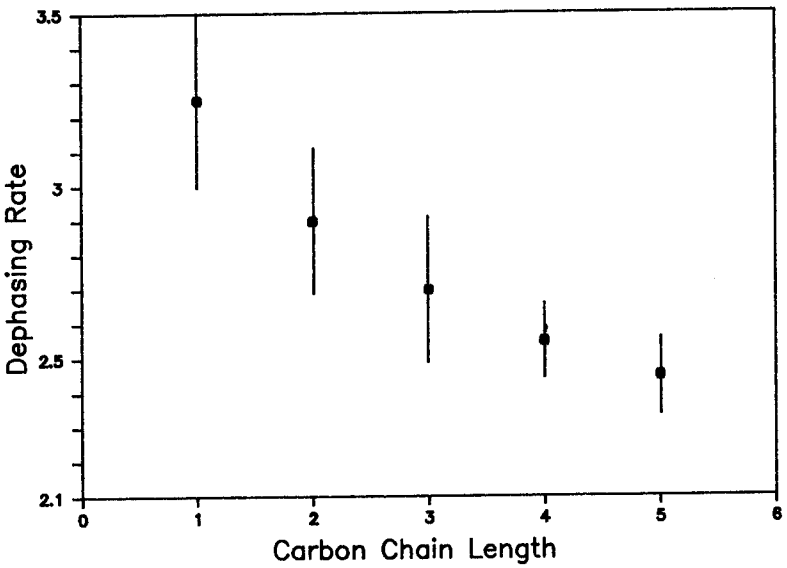


Fig. 4 : Dephasing rate (as defined in the text) vs number of carbons in alcohol solvent molecule.

FEMTOSECOND CARRIER DYNAMICS AT InP/LIQUID INTERFACES IN THE PRESENCE OF ELECTRIC FIELDS

Y. Rosenwaks, B.R. Thacker, A.J. Nozik, R.J. Ellingson*, K.C. Burr*, and C.L. Tang*

National Renewable Energy Laboratory, Golden, CO 80401
*Materials Science Center Cornell University, Ithaca, NY 14853

Recently there has been considerable interest in studying photogenerated carrier dynamics in semiconductors under the influence of electric fields[1]. This is a process of critical importance in recombination kinetics and electron transfer processes at semiconductor interfaces. At semiconductor-liquid interfaces, very large electric fields (typically 10^5 to 10^6 volts/cm) exist in the semiconductor close to its surface because of the formation of a space charge layer (SCL)[2]. Externally-applied potentials will drop across the SCL to increase or decrease the space charge fields (SCFs) and the surface band bending-V_B. Under bandgap illumination the SCFs are reduced because of screening by the photogenerated majority carriers, but strong residual SCFs are ubiquitous across any semiconductor liquid interface. It is expected that these SCFs may have a crucial role in electron transfer (ET) processes at semiconductor electrodes.

Photoluminescence (PL) experiments designed to measure the rate of surface recombination or ET from semiconductors to redox acceptors in an adjacent solution are usually done with very high intensity laser excitation in order to flatten the semiconductor bands and reduce the SCF to near zero[3]. This is because the presence of electric field terms greatly complicates the solution of the coupled continuity and Poisson equations that is needed to relate the observed rate of photogenerated carrier decay to the rate of surface recombination or ET. In this work we conduct fs time-resolved PL (TRPL) measurements in the presence of large SCFs that are controlled with an externally applied bias voltage. Using model calculations that allow us to separate the effects on PL quenching of field-enhanced ET from the effects of simple field-enhanced charge separation and surface recombination, we were able to observe and quantify the effect of the field on ET for the first time. The results show surprisingly high ET rates (ET velocities > 10^7 cm/s) as the applied potential is increased, and we present preliminary evidence that hot electron injection plays a role in these processes.

The photoelectrode is p-InP (Zn doped, $1.5\text{x}10^{17}$ cm^{-3}) single crystals with (100) surface orientation (from Nippon Mining). They were etched for 30 seconds in 2% Br_2/MeOH and then mounted in a sealed oxygen-free photoelectrochemical (PEC) cell. The electrolyte used was sodium sulfate and the redox couple was $Fe(CN)_6^{3-/4-}$; all the potentials were controlled with a potentiostat and were measured relative to a sodium saturated reference electrode (SSCE). Time-resolved PL (TRPL) spectra were obtained by the technique of sum frequency generation. Photoexcitation was with a Ti: sapphire laser that provided 80-fs pulses at a wavelength of 780 nm and 82 Mhz repetition rate. The laser spot size was $\approx$ 20 μ in diameter, and the temporal resolution of the system was 100 fs. The band-edge TRPL was measured at different potentials applied to the InP photoelectode.

Figure 1 shows the TRPL spectra of the InP electrode measured in air at two different laser intensities corresponding to excess carrier concentrations of $5\text{x}10^{18}$ and $2\text{x}10^{17}$ cm^{-3}. The solid

lines were calculated from our model described previously[4].
It is based on a numerical solution of the continuity equations for electrons and holes coupled through the electric field which is calculated via Poisson's equation in a self-consistent way. The model takes into account: (a) electron and hole surface recombination; (b) electron and hole transfer to the adjacent media i.e.,to the solution at the front surface, and to the ohmic contact at the back; and (c) radiative and non-radiative bulk recombination throughout the semiconductor.

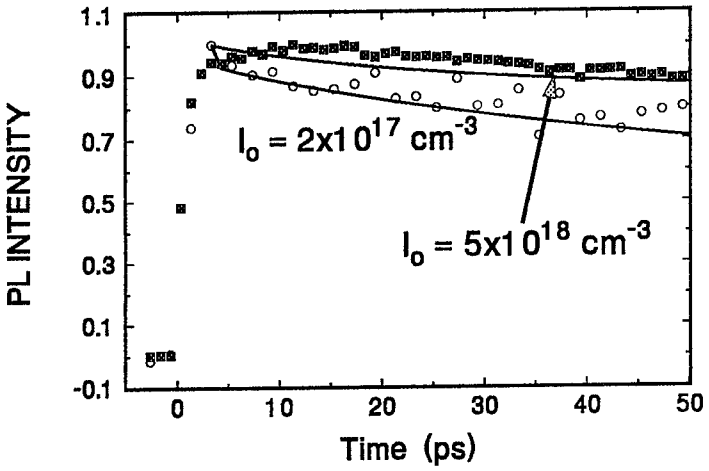


Figure 1. Experimental and calculated (solid lines) PL decay curves for p-InP in air under high and moderate injection conditions; I_o-photogenerated carrier density.

The calculations of the theoretical PL decay curves (solid lines) in Fig. 1 were done using parameters based on a recent study of InP[5]. A $\delta(t)$ laser pulse was assumed, and V_B (the surface band bending) was 0.5 V which is typical for air/p-InP. The injection level, I_{inj} (defined here as the ratio between the initial (at t = 0) excess carrier concentration and the semiconductor doping) was calculated to be 1 and 30, for the upper and lower curves respectively, based on the measured laser spot size and incident laser power. The values of the two adjustable parameters, S_{nf} and S_{pf} (defined as the SRV for electrons and holes at the front liquid interface, respectively) required for the best fit of the data were $S_{nf} = S_{pf} = 9 \times 10^3$ cm/s.

The very fast initial PL decay (t<5 ps) observed in the lower curve is due to charge separation in the SCR; this region is formed due to intrinsic surface states at the p-InP air interface. Calculations based on our model show[6] that under the injection levels used here (I_{inj}=1), it takes the holes about 1-5 ps to accumulate at the edge of the SCR; at this stage the carrier distributions reach a quasi-equilibrium, governed by the balance between the SCF and the built-in field created due to the charge separation. Following this, the band bending is reduced to about 0.1 eV[6], and the PL decay is controlled by carrier diffusion. When I_{inj} = 30 (the upper curve) the SCR field is instantaneously screened by the photogenerated carriers and the PL intensity starts to decrease only after about 10 ps; this is due both to the screening of the SCR field and to the slowed carrier cooling under such high injection conditions.

Figure 2 shows the TRPL decay of the InP electrode in 0.1 M $Fe(CN)_6^{3-/4-}$ measured at two different electrode potentials: 0.3 V, and -0.3 V; these potentials correspond to dark band bending (inferred from Mott-Schottky measurements, including band-movement effects) of 0.15 and 0.45 V, respectively. Using our model we were able to estimate the electron transfer velocity, S_{et}, which caused the PL quenching of the lower curve, to be above $1x10^7$ cm/s[7]. The possibility that the change in the TRPL spectra with this increased reverse bias potential is caused by field-

enhanced surface recombination was rejected for reasons discussed elsewhere[7].

This observation of a field dependent S_{et} that can reach values above 10^7 cm/sec is very interesting; these S_{et} values correspond to ET times faster than 3 ps ($\approx$ 0.7ps for S_{et} = 5 x 10^7 cm/s). It is interesting to note that this S_{et} value is about the same as the saturated drift velocity of electrons in InP. One factor that may explain these results is that the fields in the SCL easily create Type I hot carriers at the InP-liquid interface[8]. Since the transit time of hot electrons across the SCL is extremely fast ($\approx$ 100 fs), the hot electrons arrive at the surface with energies that are determined by the energy level of the field-free conduction band edge in the dark.

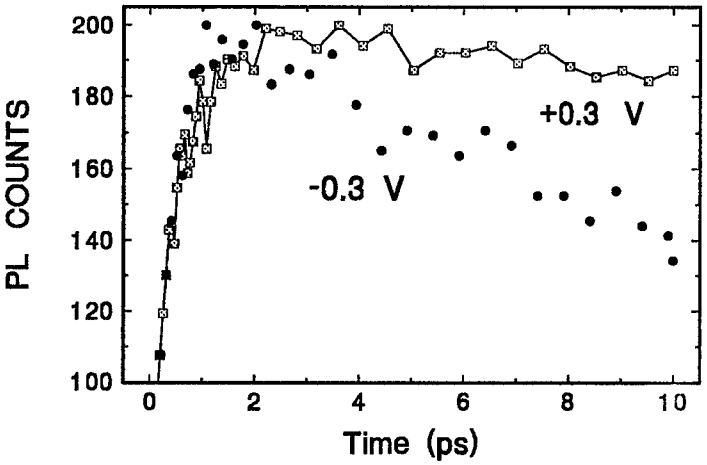


Figure 2. PL decay curves for p-InP in 0.1 M $Fe(CN)_6^{4-/3-}$ at two different electrode potentials.

The observed dependence of electron transfer kinetics on V_B appears to be correlated with the variation of hot electron energies with V_B. A close examination of the lower curve in Fig. 2 reveals that the PL intensity starts to decrease in about 1 ps following the laser pulse; since hot electron cooling times are about 5 ps at these injection levels, this indicates that the decrease in luminescence intensity in this time period is caused by hot electron transfer to the $Fe(CN)_6^{3-/4-}$ acceptor. The possibility that this PL decrease, (at -0.3 V), is caused by field-enhanced charge separation is rejected by comparing the results to Fig. 1; PL decay due to the latter is slower and different in shape. Further studies are in progress to understand the origin of the increase in S_{et} with electric field quantitatively, and to assess in detail the role of hot electron injection and carrier velocity in this process.

References

1. T. Dekorsy, T. Pfeifer, W. Kutt, and H. Kurz, Phys. Rev. B **47**, 3842 (1993).
2. A. J. Nozik, Annu. Rev. Phys. Chem. **29**, 189 (1978).
3. Y. Rosenwaks, Y. Shapira, and D. Huppert, Phys. Rev. B **45**, 9108 (1992).
4. Y. Rosenwaks, I. Yavneh, and A. J. Nozik, J. Appl. Phys. 15 April 1994.
5. Y. Rosenwaks, B. R. Thacker, A. J. Nozik, Y. Shapira, and D. Huppert, J. Phys. Chem. **97**, 10421, (1993).
6. Y. Rosenwaks, and A. J. Nozik, unpublished results.
7. Y. Rosenwaks, B.R. Thacker, A.J. Nozik, R.J. Ellingson, K.C. Burr, and C.L. Tang, submitted for publication.
8. G. Cooper, J. A. Turner, B. A. Parkinson, and A. J. Nozik, J. Appl. Phys. **54**, 6463 (1983); L. Min, and R. J. D. Miller, Appl. Phys. Lett. **56**, 524 (1990).

Optical Parametric Amplification of White-Light-Continuum Components at 250 kHz with a Ti:Sapphire Regenerative Amplifier

M. K. Reed, M. Steiner-Shepard and D. K. Negus

Coherent Laser Group, 5100 Patrick Henry Drive, Santa Clara, CA 95054
phone (408) 764-4305 fax (408) 764-4818

A ti:sapphire regenerative amplifier pumped by a cw-argon-ion laser was recently demonstrated by T. B. Norris [1]. We have developed a compact ti:sapphire mode-locked oscillator and regenerative amplifier system (Coherent *RegA-9000*) with a single argon-ion laser providing 8W to pump the oscillator and 14W to pump the amplifier. A 110fs duration, 820nm pulse from the *Mira-900* oscillator is injected into the *RegA-9000* amplifier using a TeO_2 acousto-optic cavity dumper. Chirped pulse amplification is accomplished over 25 roundtrips by allowing the dispersion in a TeO_2 Q-switch within the amplifier to expand these pulses to 30ps length. The cavity dumper then extracts a single pulse of more than 6μJ energy at a repetition rate of 250 kHz, corresponding to an average power of 1.5W.

The accumulated chirp acquired by the pulses in amplification is canceled with a simple single-grating compressor. At 70% efficiency the compressor produces 4μJ pulses with 220fs FWHM autocorrelation widths. For a Gaussian pulse shape assumption this corresponds to an overall broadening of approximately 1.5x. We have investigated the use of solid-state materials to generate broadband white-light from these pulses. For energies less than 2μJ, we find that focusing the beam into sapphire leads to a whole-beam self-focusing characterized by a collapse into an exceptionally stable single filament. The high intensities in this filament allow self-phase-modulation to create a white-light continuum extending across the entire visible spectrum, an example of which is displayed in Figure 1.

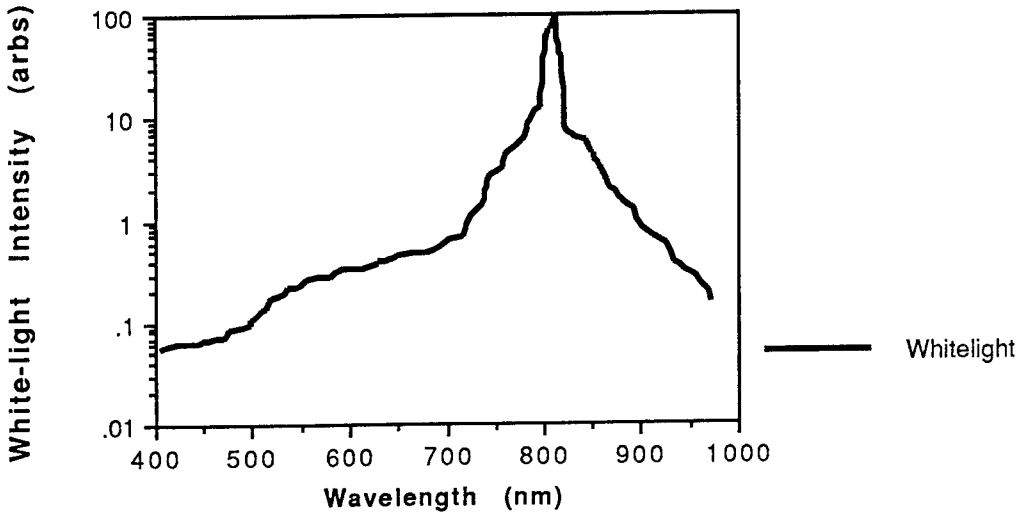


Figure 1: A typical white-light continuum spectra.

We observe the threshold for this single filament continuum generation to be less than 0.5μJ. For input energies >2μJ the collapse appears to involve multiple unstable filament formation attendant with much larger spatial and frequency fluctuations on the continuum beam. The single filament collapse leads to a gaussian output beam at all wavelengths.. The 1 to 2μJ regime therefore appears to be optimum for high beam quality continuum generation with this pulselength and wavelength in sapphire.

A stable white-light continuum is generated with a fraction of the available compressed 4μJ energy from the regenerative amplifier so the remaining energy can used to pump an optical parametric amplifier (OPA) to enhance a component in this spectrum. A similar system has recently been demonstrated with 30μJ of pump energy [2,3] but our high-repetition-rate ti:sapphire system requires significantly less energy to operate efficiently. The layout for the continuum generation and OPA is shown in Figure 2.

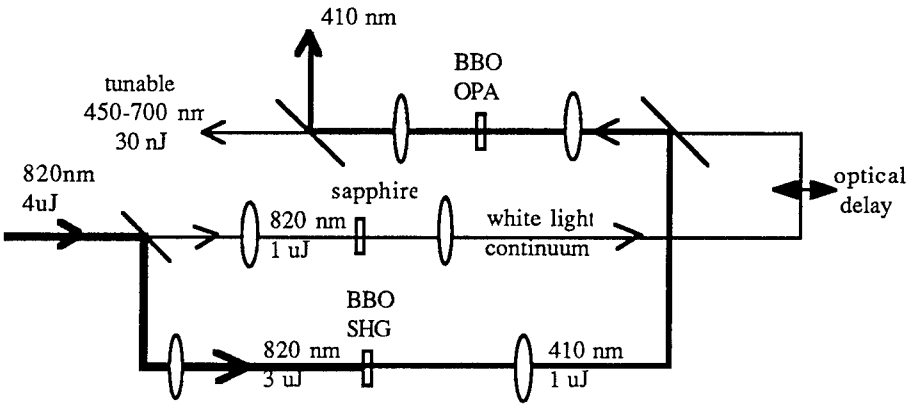


Figure 2: White-light generation and parametric amplification layout.

The input 820nm beam is split with a 75% reflector. The 1 μJ portion is focused into a sapphire crystal with a 35mm focal length lens to generate white-light and the output is collimated with a 20mm focal length achromat. The 3μJ portion of the 820nm beam is frequency-doubled in a 1mm thick BBO crystal, cut for Type I phasematching at $\theta = 29^{o}$ Placing the second harmonic generation (SHG) crystal slightly beyond the focus of a 200mm lens gives 35% SHG conversion, or 1μJ of energy at 410nm. This beam is recollimated with a 160mm lens and recombined on a dichroic 400nm reflector with the white-light beam after it has followed a path-length-matching optical delay line. The two colinear and cotemporal pulses are focused with an 80mm lens into a 2 mm thick BBO crystal of the same cut as the BBO SHG crystal. The phase matching curve for a BBO type I optical parametric amplifier (OPA) pumped at 410nm is shown in Figure 3. The experimental points agree well with the prediction derived from the Sellmeier coefficients given by Kato[4]. It is possible to significantly amplify the visible portion of the whitelight at wavelengths from 450nm to 700nm by rotating the BBO crystal and reoptimizing the optical delay to compensate for chirp in the continuum. As an example of the OPA performance Figure 4 shows the whitelight spectrum around 580nm out of the OPA with and without the pump. A 10nm FWHM bandwidth is amplified by over 80 times ($e^{4.4} = 80$). The whitelight output is recollimated and separated from the 410nm pump with a dichroic filter to allow measurement of the energy in the amplified component. For the OPA at 580nm the power gained in amplification is 8mW, or 32nJ per pulse. The autocorrelation width of the output was measured to be 200fs FWHM using a thin KDP crystal. Assuming a gaussian pulseshape this gives a pulsewidth of 142fs which with a 10nm bandwidth results in a time-bandwidth product of 1.2, about 3 times the minimum. The amplified beam has a symmetric Gaussian shape with a measured M^2 of less than 3. The output pulse shows 10% peak-to-peak high-frequency pulse-to-pulse noise which appeared to be highly correlated with the regen pulse output 2% peak-to-peak noise.

The quality of the output and the ease of tuning from 450nm to 700nm make this system an excellent source of visible ultrafast pulses. The results presented here are preliminary and the OPA has yet to be optimized for diffraction-limited as well as time-bandwidth-limited pulses. We anticipate that by using a preamplifier and power-amplifier OPA configuration pumped with the same SHG pulse it should be possible to achieve significantly higher conversion efficiency to the visible than demonstrated thus far.

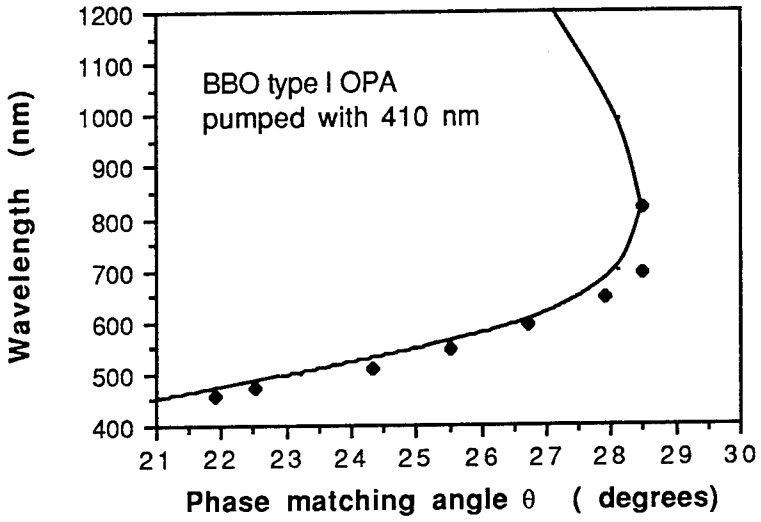


Figure 3: The phasematching curve for the BBO type I OPA. Experimental agreement with the Sellmeier prediction of reference 4 is excellent.

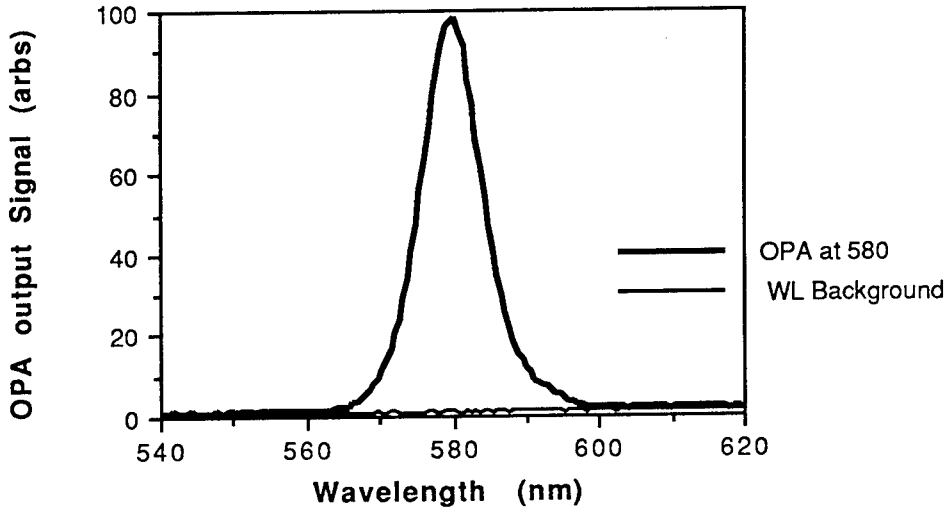


Figure 4: The white-light spectrum around 580 nm with and without optical parametric amplification. Single pass gain of more than 80 is shown.

References

1. T.B.Norris, Opt. Lett. 17, p 1009 July 15 1992.
2. G.P. Banfi et al., Opt. Lett. 19, p 1633, Oct. 1 1993.
3. R. Danielius et al., J. Opt. Soc. Am. B. Vol 10 p 2222, Nov. 1993.
4. K.Kato, IEEE JQE QE-27, p1138, May 1991.

Time gated x-ray imaging using an ultrashort pulse, laser produced plasma x-ray source

C. L. Gordon III, C. P. J. Barty, and S. E. Harris
Edward L. Ginzton Laboratory, Stanford University, Stanford, California 94305

The development of high peak power, ultrashort pulse duration Ti:sapphire laser systems[1,2] has led to the generation of hard, incoherent x-rays from laser-produced-plasmas (LPP).[3] In these experiments x-rays with energies as high as 1.5 MeV were produced. Also generated were copious amounts of diagnostic x-rays (20 keV to 150 keV). This fact suggests that ultrashort-pulse-pumped, LPP x-ray sources may have uses in medical imaging applications. In particular, there are two distinct differences between the LPP x-ray source and conventional x-ray sources, namely source duration and source size. The duration of the LPP source is believed to be <1 ps or nearly 6 orders of magnitude shorter than conventional x-ray sources. Because of this, it becomes possible to consider time gated imaging arrangements which require greatly reduced x-ray exposures to create the same quality image of a patient. The source size of the LPP x-ray source may be as much as 100 times smaller than conventional devices and thus may allow imaging of much smaller features than previously possible.

In LPP x-ray experiments, the total x-ray yield versus input laser energy has a 3/2 power law dependence. This fact suggests that the laser-driven x-ray source is similar to rotating anode x-ray tubes used in medical imaging applications. In the latter device, an electron beam is accelerated trough a potential, V, and impinges upon a high-Z target. The efficiency of such a device (i.e. yield/input) is roughly 10^{-9} ZV. The efficiency of the laser-driven source is proportional to the square root of the input laser intensity or proportional to the peak electric field of the input pulse. Thus, efficiency of both sources is proportional to the atomic number of the target material and electric field.

A comparison of the present laser-driven x-ray source and a conventional, state-of-the-art x-ray tube (Siemens Model # Meg 125/30/82C) is given in Table 1. The major deficiency of the laser-driven source is its low average power. However, it is not unreasonable to expect that future laser-driven sources may produce equivalent x-ray fluxes. As will be shown, it is possible with a short-duration (~ 1 ps) x-ray source to obtain the same quality image but with eight times less x-ray flux than a long duration (~ 5 ms) source. In addition, the laser system used in past studies was not optimized for x-ray production. Also included in Table 1 are the projected laser-driven source parameters for a higher repetition rate, shorter pulse, laser driver. Since x-ray yield is proportional to the peak electric field of the laser pulse, it should be possible to obtain an equivalent x-ray flux at a lower laser pulse energy if one reduces the laser pulse duration. A reduction in laser pulse duration of up to an order of magnitude is now possible and should allow efficient production of x-rays with ~ 8 mJ of laser energy. Infrared pulses of this energy may be produced at 1-kHz repetition rates.[4] Under these conditions, using time gating techniques and

Table 1. Comparison of conventional and laser-driven x-ray sources

	Rotating Anode X-ray Tube	Laser-Driven X-ray Source	Future Laser-Driven Source
Shots/Second	30	5	1000
Deposited Pump Energy	2.75 J	40 mJ	8 mJ
Efficiency	1%	0.3%	1%
Average X-ray Power	825 mW	0.6 mW	100 mW
X-ray pulse duration	5 ms	< 1 ps	~100 fs
X-ray Source Size	1 x 1 mm	<250 × 250 μm	~10 × 10 μm

assuming only slightly better conversion efficiency than previously measured, the effective x-ray flux of the laser-driven source is equivalent to that of a conventional x-ray tube. However, with time gating the patient would receive eight times less x-ray dosage. In addition, because of the much smaller x-ray source size, it should be possible to improve resolution by about an order of magnitude.

In traditional x-ray imaging, three things may happen to the x-ray photons as they pass through a sample: they may be absorbed by dense material, they may undergo a scattering event, or they may pass through the sample unaffected. It is the difference in flux between the unaffected or ballistic photons and those that are absorbed that is responsible for the formation of an image at the detector. Scattered photons that also reach the detector will decrease the contrast ratio and increase the noise of the image. In mammalian samples, this can be a significant problem. Typically, for every one ballistic photon passing through 20 cm of mammalian tissue with 2 cm of bone density material in the path, there will be ~ 0.1 absorption events and ~ 7 scattering events.[5]

To illustrate this problem, we consider the hypothetical case of a material that has only absorption and no scattering. In this case the contrast ratio, CR, of the image that is formed is

$$CR = \Delta N / N_B \tag{1}$$

where N_B is the total number of x-ray photons incident on the sample and ΔN is the number difference of the ballistic and absorbed photons. The image will have a signal-to-noise ratio that is determined by the statistics of the x-rays. At low photon numbers, the x-rays may be modeled by a Poisson distribution. Thus, the signal-to-noise ratio, SNR, is given by

$$SNR = \Delta N / \sqrt{N_B} = CR\sqrt{N_B} \tag{2}$$

Now if we consider the same material but add N_S scattered photons to the image then CR and SNR become

$$CR = \Delta N / (N_B + N_S) \tag{3}$$

$$SNR = \Delta N / \sqrt{N_B + N_S} \tag{4}$$

Clearly, CR and SNR are decreased by the presence of scattering. It is possible to increase CR and SNR in either case by increasing the x-ray flux. However, this is not desirable when working with live samples. In this situation, the minimum acceptable SNR of the image determines the flux that is used.

Because the x-rays from a laser-driven source have a duration that is short (< 1 ps) with respect to the transit time through the sample (~ 1 ns), it may be possible to eliminate the effects of scattered photons by time gating. When compared with ballistic photons, scattered photons travel a longer path and thus experience a longer delay in reaching the same location at the detector. If one uses a detector which may be turned off rapidly after the arrival of the ballistic photons, then the scattered photons may be removed from the image. For the same SNR, it is then possible to construct an image with much less flux. For mammalian objects, this can be seen by setting the right-hand sides of Eqs. (2) and (4) equal and making the substitution $N_S = 7N_B$. In this case, the number of photons needed to form the image is eight times less than that needed with time-integrated detection. An eight times reduction in dosage would greatly benefit many medical procedures. For instance, in x-ray coronary angiography, a patient may receive a full year's dose in a single 30-minute session.

The degree of image improvement or dose reduction will be limited by the speed with which the detector may be gated. Relatively simple microchannel plate detectors with gate times as short as 50 ps have been developed for time-resolved studies of x-ray emission in inertial

confinement fusion experiments.[6] To estimate the degree of x-ray reduction that may be possible with such detectors, a quasi-3D numerical simulation was performed. In this simulation, a temporal delta function of x-ray photons was input uniformly over one side of a 20 cm x 20 cm 2D area. Each x-ray was allowed to travel a random distance between zero and the mean scattering distance before scattering. Angular scattering was assumed to be isotropic which is characteristic of Compton scattering in the medical x-ray regime. A typical x-ray scatters seven times before it exits the square. To approximate a 3D model, the length between scattering events was modified by projecting the 3D length onto the 2D plane. This effectively shortened the scattering distance. When an x-ray exits the square on the opposite side of the input (the location of the detector), the path length of the scattered x-ray was computed and transformed into a traversal time. If an x-ray scatters out of the square through any other side, it was assumed lost and not counted as one of the x-rays reaching the detector. The traversal time of a ballistic (or straight through) x-ray was then subtracted from the traversal time of the scattered x-rays and a histogram of the photon number versus time was computed. The final output of the calculations is the temporal behavior of the scattered photons with time zero being the instant the ballistic photons exit the sample. The results of this model for a sample which is 4 times thicker than the mean scattering distance are shown in Fig. 1. In this case only 0.33% of the scattered photons arrive at the detector during the first 50 ps. This simulation indicates that a reduction in dosage of 7.99 times will be possible for a 50 ps gate width as compared to a factor of 8 times for ideal scatter reduction. Shown in Fig 2. is the result of the simulation with the detector plane moved 20 cm away from the output of the square. This situation is even more favorable for time gating.

This analysis shows that time gating with an ultrashort pulse, laser produced plasma x-ray source is possible. The availability of time fast time gated detector technology and the ideal characteristics of a laser-driven x-ray source make this arrangement experimentally realizable.

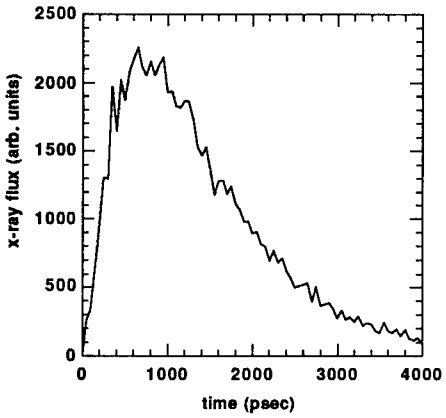


Fig. 1. X-ray output vs. time with detector plane at the output plane of the sample.

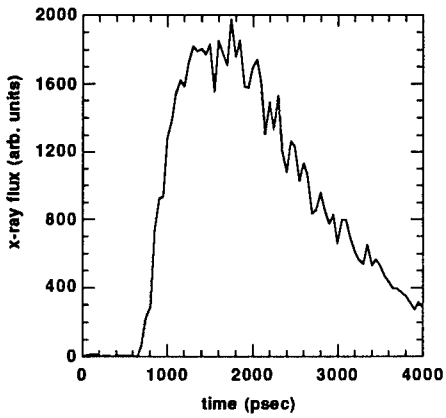


Fig 2. X-ray output vs. time with the detector moved 20 cm away from the output plane of the sample.

References

1. J. D. Kmetec, J. J. Macklin and J. F. Young, Opt. Lett., **16**, 13, 1001-1003, 1991.
2. A. Sullivan, H. Hamster, H. C. Kapteyn, S. Gordon, W. White, H. Nathel, R. J. Blair and R. W. Falcone, Opt. Lett., **16**, 18, 1406-1408, 1991.
3. J. D. Kmetec, C. L. Gordon III, J. J. Macklin, B. E. Lemoff, G. S. Brown and S. E. Harris, Phys. Rev. Lett., **68**, 10, 1527-1530, 1992.
4. F. Salin, J. Squier, G. Mourou and G. Vaillancourt, Opt. Lett., **16**, 24, 1964-1966, 1991.
5. A. Macovski, *Medical Imaging Systems*, Prentice-Hall, Inc., Englewood, NJ, 1983.
6. J. D. Kilkenny, P. Bell, G. Hanks, G. Power, R. E. Turner and J. Wiedwald, Rev. Sci. Instrum., **59**, 8, 1793-1796, 1988.

40 GHz soliton train generation through multi-soliton pulse propagation in a dispersion varying optical fiber circuit

D.J. Richardson and D.N. Payne
Optoelectronics Research Centre, Southampton University, Southampton, SO9 5NH, U.K.

A.V. Shipulin and E.M. Dianov
General Physics Institute, 38 Vavilova Street, Box 117333, Moscow, Russia.

Recent advances in telecommunications have led to a number of impressive high speed transmission results with data transmission at rates as high as 100 GBit/s recently demonstrated [1]. As data rates increase the source requirements on repetition rate and pulse quality become more and more stringent and the ultimate limits of conventional laser sources e.g. gain-switched DFBs, mode-locked fiber lasers are rapidly being approached. The development of alternative high-frequency pulse generation techniques that can extend from 20-40 GHz to far higher frequencies (> 200 GHz) is thus of great practical relevance.

One particular class of technique that has been the subject of considerable recent interest is based upon the transformation of a dual-frequency beat-signal into a train of solitons as a result of nonlinear propagation in a fiber circuit [2,5,7]. Generation of cw soliton trains at repetition rates in the range from 70-200 GHz have been obtained experimentally by propagation in Dispersion Decreasing Fiber (DDF) [3,4]. Unfortunately, impractically long lengths of DDF (> 10 km) are required to extend the techniques to repetition rates below ~60 GHz and the basic technique is therefore of little interest for current telecommunication applications. Spectral enrichment of the beat signal in Dispersion Shifted Fibre (DSF) prior to propagation in DDFs has been shown to lead to the generation of slightly lower repetition rates [5]. It has also been shown theoretically that an even greater length reduction can be obtained by compressing the initial beat signal through multi-soliton compression prior to propagation in a DDF enabling 40 GHz soliton train generation [6]. In this paper we demonstrate that a simple combination of spectral enrichment in DSF and multisoliton compression in standard fiber prior to propagation in a DDF can be used to generate a high quality 40 GHz soliton train. The technique should be capable of extension down to ≈30 GHz. Note that 32 GHz soliton trains have been generated from a beat signal by using multisoliton effects in a nonlinear loop mirror [7]. However, this particular technique suffers from acute environmental instability and requires additional (linear) chirp compensation at the system output- undesirable properties for any practical source.

The experimental configuration is illustrated in Fig.1. The outputs from two, pig-tailed, single frequency DFB lasers (DFB1 and DFB2) were combined using a 3dB coupler to create a beat-signal. The lasers emitted at wavelengths around 1550 nm. The temperature of the laser diodes could be independently tuned and the laser wavelength separation set between 0 and 2 nm. The beat-signal was amplified in a two stage 1064nm pumped, erbium-ytterbium doped fiber amplifier incorporating an in-line band pass filter. Upto 200 mW of amplified power was available at the isolated EDFA output. The amplified beat-signal was passed through 1km of DSF (D = 0.5 ps/nm.km) where four-wave mixing leads to sideband generation at -15 dB relative to the signal input level). The signal is then passed through 1km of standard fiber (D = 16 ps/nm.km) where it undergoes multisoliton compression by a factor of ≈2 before entering the DDF. The DDF had a length 3.5 km and a loss of ≈1 dB/km. The dispersion at 1550 nm varied along the fiber length from $D_{inp} = 11$ ps/nm/km to $D_{out} = 0.8$ ps/nm/km at the output. On its own the DDF was suitable for the

generation of 80-90 GHz pulse trains. The total system loss from DSF input to DDF output was 5.6 dB.

The behaviour of the system was investigated for a wide range of frequency separations and pump powers and the optimum performance determined. Due to the multisoliton compression stage high quality pulses could only be obtained around a relatively narrow repetition rate resonance 40 ± 3 GHz determined by the standard fiber length and beat-signal power. The source does not therefore exhibit the broadband repetition rate tunability of the basic adiabatic DDF technique [4]. Optimum system performance was obtained at a wavelength separation of 0.318 nm (R = 40 GHz) repetition rate and an input beat-signal power of 135mW. An autocorrelation trace and optical spectrum of the trains so obtained are shown in Fig.2 where we see that we have obtained a 40 GHz train of 3.4 ps pulses, corresponding to a mark-space ratio of 7.3:1. A $sech^2$ fit to the relative peak heights in the spectrum is shown plotted on a log scale in Fig.3- the fit is seen to be excellent. The best fit spectral halfwidth comes out as 0.75 nm yielding a best fit time.bandwidth product of 0.32 in excellent agreement with that expected for soliton pulses. The average output power of 37 mW yields an estimated pulse energy of 0.9 pJ in excellent agreement with the value 0.8pJ calculated for a fundamental order soliton calculated taking D = 0.8 ps/nm.km and assuming a mode area of 100 $(\mu m)^2$. In order to check the stability of the train the pulses were propagated over a 7.5km span of DSF (D = 0.4 (± 0.2) ps/nm.km), corresponding to approximately one soliton period for 3.4 ps pulses. Once the launched pump power into the DSF was adjusted to match the discrete dispersion change from DDF to DSF the pulses were found to propagate stably with little change in pulse parameters confirming the high quality of the train.

In conclusion, we have demonstrated for the first time a new technique for beat-signal to soliton train conversion based on multisoliton compression effects. This technique permits the use of considerably shorter fiber length than all previous DDF based conversion schemes and permits the generation of soliton trains with repetition rates in the range 30-40 GHz- a repetition rate of interest for future telecommunication applications. The method is also considerably simpler and less environmentally sensitive than other interferometric, NOLM based conversion schemes that can also operate in this repetition rate regime. The high quality of the solitons so generated is demonstrated by measurements of individual pulse parameter and by propagation of the pulses in an additional fiber span.

References.

1. S. Kawanashi, H. Takara, K. Uchiyama, M. Saruwatari, T. Kitoh: Proc. 19th European Conference on Optical Communication, Postdeadline Paper ThP12.1, 53 (Montreaux, 1993).
2. P.V. Mamyshev, S.V. Chernikov, E.M. Dianov: IEEE J. Quantum Electron. 27, 2347 (1991).
3. S. V. Chernikov, J. R. Taylor, P. V. Mamyshev, E. M. Dianov: Electron. Lett, 28, 931 (1992) and S.V. Chernikov, E.M. Dianov, D.G. Fursa, P.V. Mamyshev, A.M. Prokhorov: Tech. Digest second Intern. Conf. on Optical fibre Submarine Telecommunication Systems, 103 (Versailles 1993).
4 S. V. Chernikov, D. J. Richardson, R. I. Laming, E. M. Dianov, D. N. Payne: Appl. Phys. Lett., 63, 293, (1993).
5 S. V. Chernikov, D. J. Richardson, R. I. Laming, E. M. Dianov, D. N. Payne: Electron. Lett., 28, 1210, (1992).
6. A.V. Shipulin, D.G. Fursa, E.A. Golovchenko, E.M. Dianov: Electron. Lett, 29, 1401 (1993).
7 S. V. Chernikov, J. R. Taylor, P. V. Mamyshev, E. M. Dianov: Electron. Lett, 29, 658, (1993).

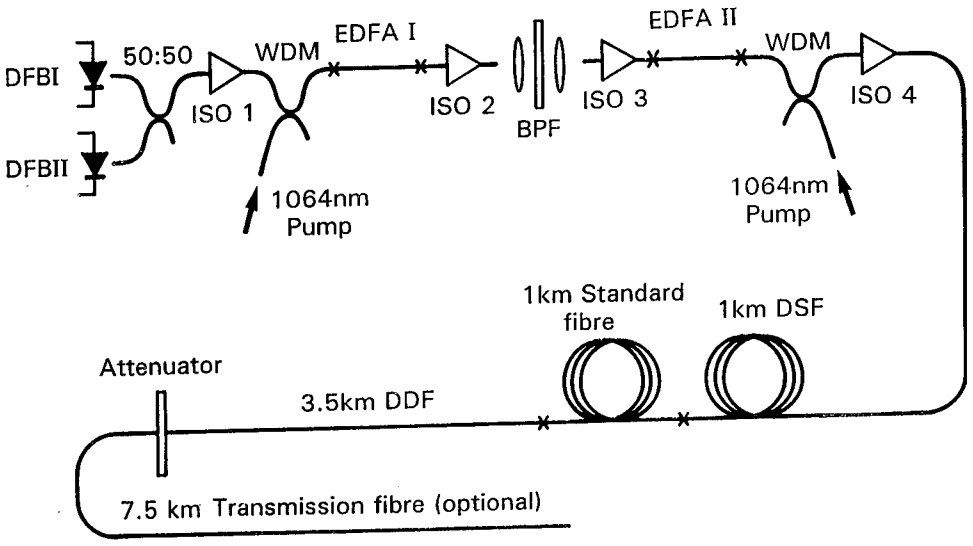


Fig.1 Experimental setup.

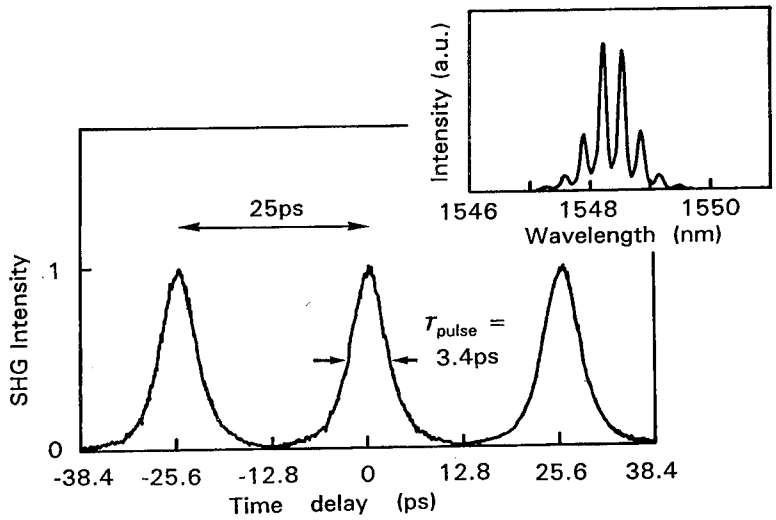


Fig.2 Experimental spectrum (a) and autocorrelation trace (b) of 40 GHz, 3.4 ps soliton train obtained at the end of the DDF fibre.

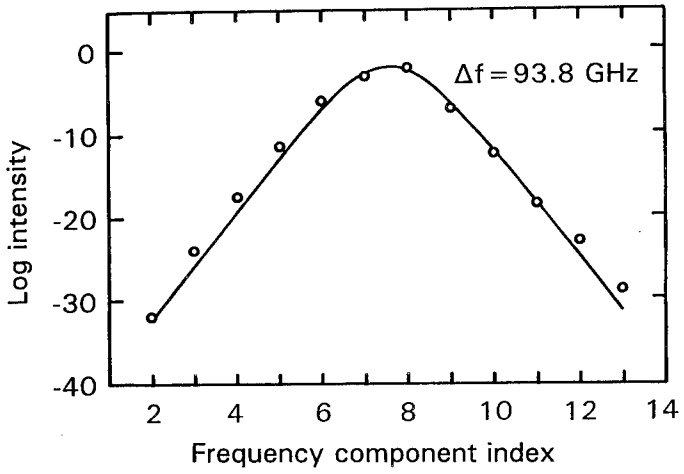


Fig.3 Sech^2 fit (solid line) to spectral peak amplitudes on logarithmic scale for 40 GHz pulse train shown in Fig.2. Best fit spectral halfwidth value of 93.8 GHz leads to an estimated time bandwith product of 0.32.

Attractive and repulsive forces in the decay of vibrational coherence

David Vanden Bout, Laura Muller, John Frietas and Mark Berg

Department of Chemistry and Biochemistry,
University of Texas, Austin, Texas 78712, USA
(512) 471-4999
(512) 471-8696 (FAX)

The decay of vibrational coherence is important because it affects the earliest stages of chemical reactions,[1-4] because it limits efforts at coherent control of reactions, and most generally, because it probes the solvent forces acting on the nuclear coordinates of chemical systems. A critical question in this area is the relative importance of attractive and repulsive solvent forces.[5] Each type of force is expected to have distinctly different properties, most especially different timescales. Raman spectroscopy of high-frequency vibrations and more recently time-resolved measurements of low-frequency vibrational motion[6] can measure the decay times of vibrational coherence. However, these techniques are relatively insensitive to the timescale of the forces driving the coherence decay.

We have previously demonstrated the Raman echo as an effective method for determining the timescale of the solvent forces leading to vibrational coherence decay.[7] The Raman echo compliments the recently demonstrated infrared echo.[8] In this paper, we examine the *sym*-methyl stretching motion in a 1:1 liquid mixture, CH_3I:$CDCl_3$.[9] In contrast to similar pure systems, the transition is inhomogeneously broadened. This result confirms earlier, indirect spectral evidence.[10] Spectral diffusion within the inhomogeneous band is also evident. The properties of the inhomogeneous broadening are characteristic of attractive forces acting on concentration fluctuations in the mixture.

The Raman echo is a multiple-pulse experiment. The first excitation creates a vibrational coherence. A second excitation initiates a rephasing process which can reverse the coherence loss induced by long-lived solvent forces. In contrast to many other echo techniques, the coherence decay following the second excitation is time resolved, and information is extracted from the decay shape.

Coherence decays for several separations of the two excitations (τ_1) are shown in Fig. 1. For comparison, the coherence decays observed without the rephasing excitation are also shown (solid). It is evident that a partial rephasing of the coherence is induced by the second excitation. As expected, the rephasing effect increases with increasing τ_1.

The Raman echo data have been modelled by assuming a static inhomogeneous broadening in addition to a homogeneous linewidth. The model is required to fit not only the Raman echo data, but also Raman line shape and time-resolved CARS data. The best results are shown as dashed lines in Fig. 1. Although qualitatively correct, this model cannot quantitatively account for the decay of the coherence, especially at long times.

This discrepancy is resolved by including spectral diffusion within the inhomogeneous linewidth (Fig. 2). A correlation time of 4-7 ps is found for the solvent force generating the inhomogeneity. This is exactly the time range for attractive force interactions predicted by Schweizer and Chandler.[5] The magnitude of the inhomogeneous broadening implies interaction with ~5-6 solvent molecules, i.e. the interaction range is approximately one molecular diameter. Again, this result is consistent with the predictions of Schweizer and Chandler.[5]

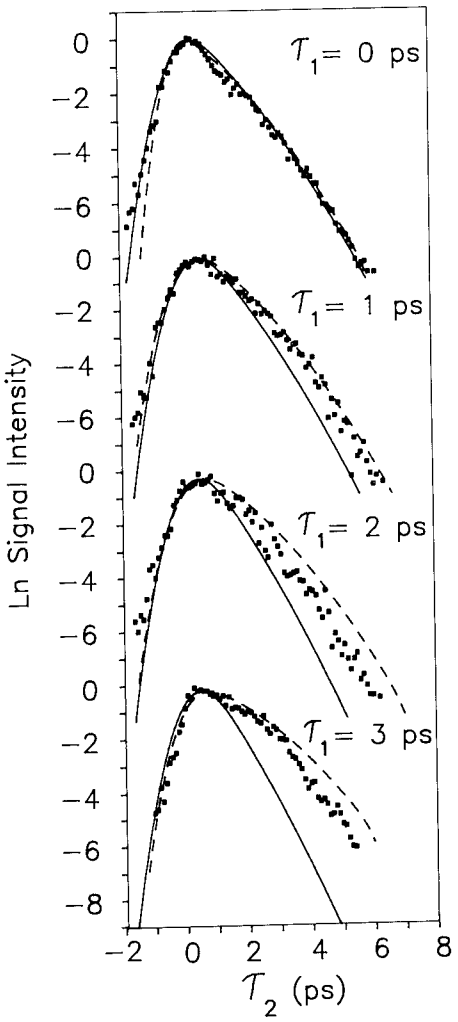


Fig. 1. Points: Raman echo data from 1:1 CH_3Cl:$CDCl_3$. Solid: Signal decay in the absence of a rephasing pulse. Dashed: Decay expected for static inhomogeneous broadening of the vibration.

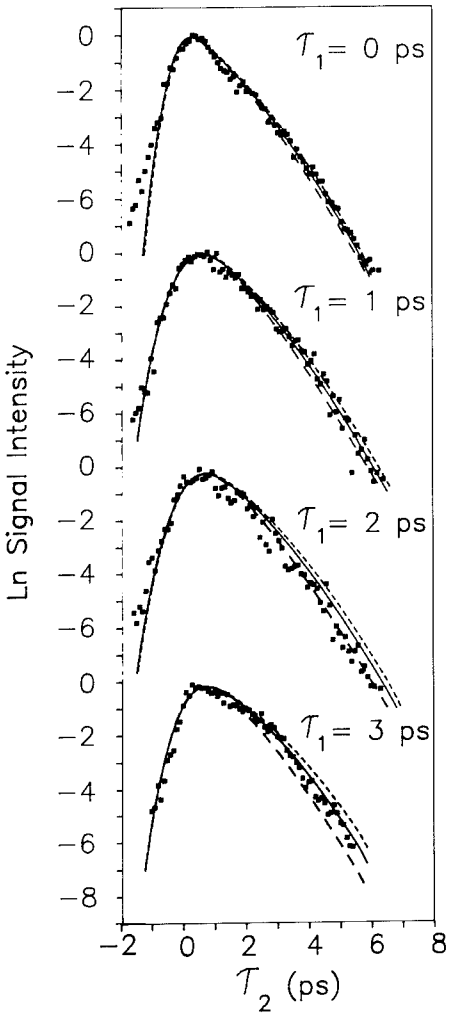


Fig. 2. Fits to the Raman echo data including spectral diffusion of various rates of 10 ps (short dashed), 5 ps (solid) and 2 ps (long dashed).

1. R.W. Schoenlein, L.A. Peteanu, R.A. Mathies and C.V. Shank, Science **254**, 412 (1991).
2. A.H. Zewail, M. Dantus, R.M. Bowman, and A. Moktari, J. Photochem. Photobiol. A: Chem. **62/3**, 301 (1992).
3. N.F. Scherer, L.D. Ziegler, and G.R. Fleming, J. Chem. Phys. **96**, 5544 (1992).
4. U. Banin and S. Ruhman, J. Chem. Phys. **98**, 4391 (1993).
5. K.S. Schweizer and D. Chandler, J. Chem. Phys. **76**, 2296 (1982).
6. Y.-X. Yan, L.T. Cheng, and K.A. Nelson, in *Advances in Nonlinear Spectroscopy*, edited by R.G.H. Clarke and R.E. Hester (Wiley, New York, 1987).
7. D. Vanden Bout, L. Muller and M. Berg, Phys. Rev. Lett. **67**, 3700 (1991).
8. D. Zimdars, A. Tokmakoff, S. Chen, S.R. Greenfield, M.D. Fayer, T.I. Smith and H.A. Schwettman, Phys. Rev. Lett. **70**, 2718 (1993).
9. L.J. Muller, D. Vanden Bout, and M. Berg, J. Chem. Phys. **99**, 810 (1993).
10. G. Doge, R. Arndt, H. Buhl and G. Bettermann, Z. Naturforsch. Teil A **35**, 468 (1980).

Observation of Biexcitons in Time-Resolved Degenerate-Four-Wave-Mixing on GaAs Quantum Wells

E.J. Mayer, G.O. Smith, and J. Kuhl
Max-Planck-Institut für Festkörperforschung,
Heisenbergstr. 1, D-70569 Stuttgart, Germany
Phone: (49) 711 689 1633, FAX: (49) 711 689 1010

D. Bennhardt, T. Meier, A. Schulze, and P. Thomas
Department of Physics, Philipps University
Renthof 5, 35032 Marburg, Germany

R. Hey and K. Ploog
Paul-Drude-Institut für Festkörperelektronik
10177 Berlin, Germany

Although the importance of exciton/exciton interactions for the nonlinear optical response of GaAs quantum wells (QW) is well established by many experimental observations, the role of biexciton states in these processes is still an open question, even at low excitation densities. Evidence for the formation of biexcitons has been independently derived from pump-probe studies [1], from the density dependence of the photoluminescence (PL) line shape [2] and from signal modulations observed in degenerate-four-wave-mixing (DFWM) with incoherent light pulses [3]. Here, we report on time-resolved DFWM with parallel (PP) and cross-polarized (CP) pulses. Depending on the polarization geometry, the signals reveal strong quantum beats which correspond to the splitting between either the heavy hole (hh) and light hole (lh) exciton or the hh exciton and the biexciton.

In the experiments, a single 20nm-GaAs/$Al_{0.3}Ga_{0.7}As$ QW kept at 10 K is excited by two 120 fs pulses from a mode-locked Ti:Sapphire laser using the backward reflection geometry for the signal detection. Time-resolution of the signal diffracted in the direction $2\vec{k}_2 - \vec{k}_1$ is accomplished via upconversion with a reference pulse in a 2 mm thick $LiIO_3$ crystal.

Figure 1 presents 3D plots of the time-resolved signal for parallel and perpendicular polarization of the exciting fields. Since the short laser pulse duration enables simultaneous excitation of the heavy and light hole exciton transition, the signal traces display a rich

quantum beat structure. Careful analysis of the beating phenomenon leads to the peculiar result that the beat frequencies appearing for PP and CP orientation differ and correspond to energy splittings of 3.7 meV and 1.2 meV, respectively. Whereas the beat frequency in case of the PP configuration agrees fairly well with the hh-lh splitting measured by PL excitation spectroscopy, the beating is distinctly slower for the CP geometry and the corresponding splitting agrees with the biexciton binding energy of 1.2 meV derived from the appearance of a second luminescence peak on the low energy side of the hh exciton transition. At higher excitation densities, the modulation can be attributed to quantum beats between bound and unbound two exciton states in our sample. The dependence of the beat structure on the polarization of the exciting fields is explained by a set of two five-level schemes, one for the hh and the other for the lh exciton states, each consisting of the ground state, two single exciton states representing excitons excited by x- and y- polarized light and two levels representing bound and unbound two-exciton states, which are separated by the biexciton binding energy. For the PP geometry and probe delay $\tau > 0$, identically polarized hh and lh single-exciton states yield the dominant contribution to the signal. In this case, we observe strong hh-lh-exciton beating. For the CP geometry, both transitions to the single-excitons with opposite spin are polarized; for this configuration the only possible mechanism involves bound and unbound two-exciton states. The de-excitation of the two-exciton states produce a beat frequency corresponding to the biexciton/unbound-two-exciton splitting. For the shorter dephasing time of the two-exciton states (T_2 = 3.6 ps) in comparison to that of the single-exciton state (T_2 = 5.3 ps), a smaller time-integrated DFWM signal is observed in the CP-configuration (inserts of Fig. 1). Close inspection of the signal traces for PP and $\tau < 0$, shows the superposition of two beating phenomena. This observation is in accordance with the polarization of the 5 level scheme since, under this condition, both single- and two-exciton transitions contribute to the 3rd order polarization.

[1] S. Bar-Ad and I. Bar-Joseph, Phys. Rev. Lett. **68**, 349(1992).

[2] R.T. Phillips, et al., Phys. Rev. B **45**, 4308(1992).

[3] K.-H. Pantke, et al., Phys. Rev. B **47**, 2413(1993).

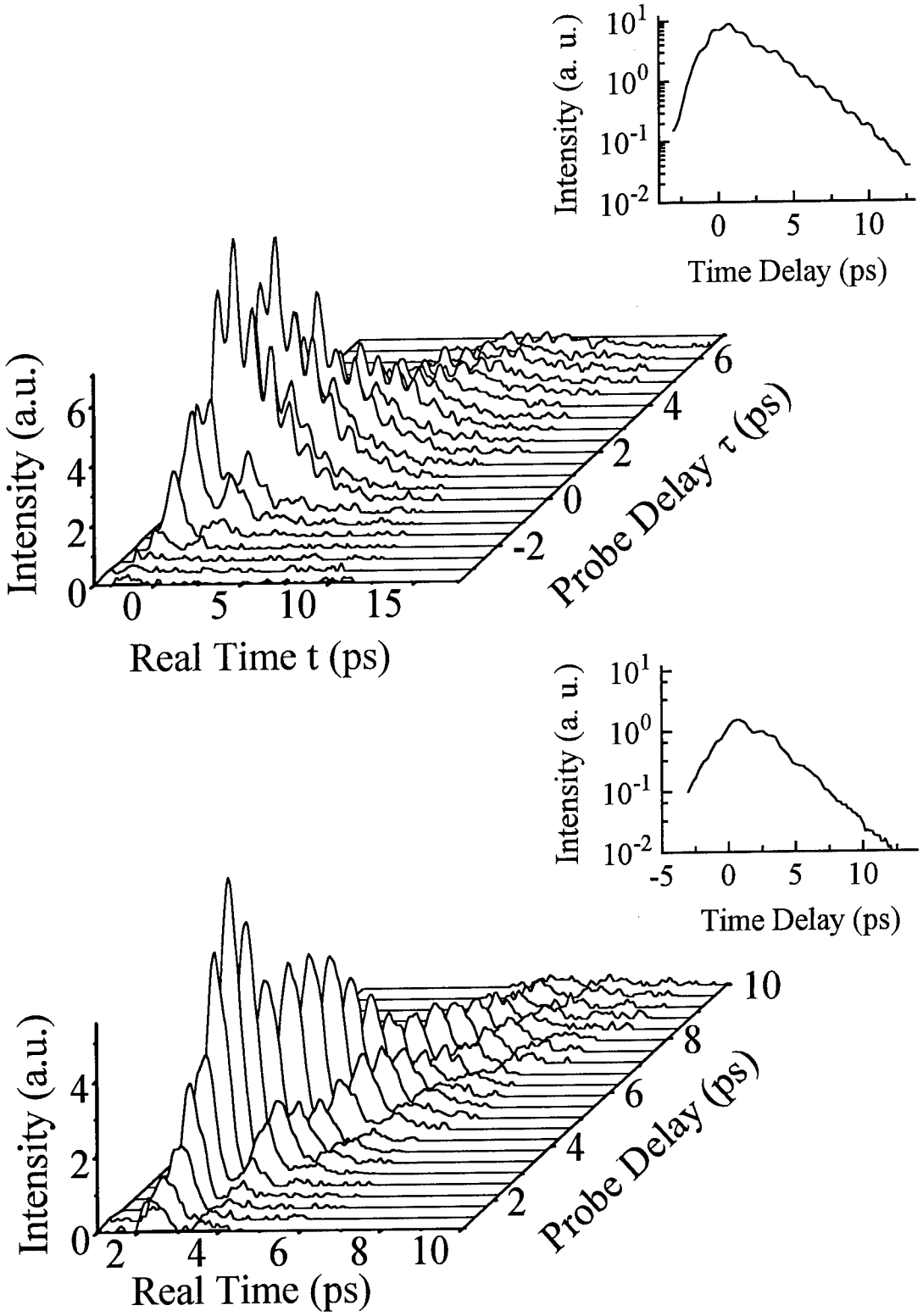


Fig. 1 The time-resolved and time-integrated (inserts) DFWM intensities for parallel (upper) and perpendicular (lower) polarization.

Direct Observation of Infrared Free Induction Decay of Liquid Water Molecules with a Femtosecond OPO at 3 Micron

Robert A. Crowell, Gary R. Holtom, Sunney X. Xie

Pacific Northwest Laboratory, Molecular Science Research Center
P.O. Box 999, Richland, WA 99352

Introduction

The importance of water as a universal and unique solvent for chemical and biological reactions has continued to stimulate theoretical, computational, and experimental efforts on understanding the structure and dynamics of liquid water. Liquid water has a broad absorption band in the 3μm region due to its fundamental stretching vibrations which are particularly sensitive to its hydrogen binding structure. Graener et al have originated picosecond hole burning experiments on liquid water in this spectral region and revealed the inhomogeneous nature of the hydrogen bonding structures (Ref. 1) Femtosecond coherent experiments would be particularly informative about the vibrational dephasing and other dynamical properties of the system. A 50fs pulse at 3μm is needed in order to coherently excite the entire inhomogeneously broadened band. However, this has been experimentally difficult due to the lack of femtosecond source in this spectral region.

We have demonstrated a stable femtosecond infrared source at 3μm using a sync pumed OPO(Ref. 2) which is suitable for performing femtosecond coherent spectroscopy in the OH stretching region. Here we demonstrate the observation of infrared optical free induction decay (FID) of water molecules dissolved in deuterated methylene chloride. The FID of CO stretching vibration have been observed on metal surfaces (Ref 3,4) and liquids at low temperate (Ref. 5). Our direct measurement of the vibrational FID of water molecules is made at room temperature with a 100fs resolution. This is an initial step toward femtosecond nonlinear infrared experiments on molecular liquids.

Experimental

An optical parametric oscillator synchronously pumped by a mode-locked Ti:sapphire is constructed to operate at a center frequency of 3660cm^{-1}, providing nearly transform limited 120fs pulses with 0.2 nanojoule pulse energy at a repetition rate of 76MHz. The detail of this OPO is described elsewhere (Ref. 2).

This femtosecond source is passed unfocused through a 2mm path length cell with CaF_2 windows which contains .2% water (H_2O) dissolved in 99.95% deuterated methylene chloride (CD_2Cl_2). This sample has an optical density of 1.3 at the absorption maximum. The up-conversion technique is used to time gate the FID following the excitation. A synchronous pulse train from the mode-locked Ti:sapphire (OPO pump residual, 816nm center frequency, 70fs pulse width and 300mW average power) is used as the gating beam. The coherent infrared radiation is focused onto the 1mm $LiIO_3$ mixing crystal (Type I phase matching) together with the gating beam in a noncollinear geometry. The bandwidth of the up-conversion is about 150cm^{-1}. The sum frequency light of 628nm is detected with a photomultiplier tube and lockin amplifier combination as a function of the time delay of the gating beam. The experiment was conducted in an environment vigorously purged with nitrogen to avoid the complication from water vapor.

Results and Discussion

The solid line in Figure 1 shows the FTIR absorption spectrum of H_2O dissolved in CD_2Cl_2. The 3600cm^{-1} peak is assigned to the symmetric stretching and the 3684cm^{-1} peak the asymmetric stretching of the water molecules. The IR spectrum indicates no water cluster formation at this concentration. Higher concentration results in a broad absorption at longer wavelength due to hydrogen bond formation. The dash line in Figure 1 shows the spectrum of the excitation pulses from the OPO, which clearly has enough bandwidth to coherently excite the two vibrational modes of the solute water molecules.

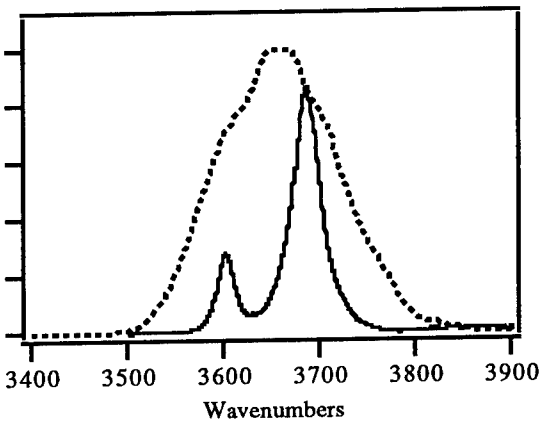


Figure 1. The infrared absoprtion spectrum of water dissolved in deuteriated methylene chloride (solid line) and the infrared spectrum of the pulses from femtosecond OPO(dashed line).

Figure 2a shows the up-converted infrared FID (solid line) and the instrumental response function response function (cross correlation of IR and 816 nm beam, dash line). The later has a FWHM of 180fs. The FID first follows the instrumental fuction and has the distinct first recurrence at 365 fs. The 365fs time delay coresponds to the 84cm^{-1} spliting in the IR spectrum in Figure 1. Figure 2b shows the logarithmic plot of the same data, which shows the subsequent beats. Such a FID is the result of the two interacting vibrational modes of water molecule radiating in a coherent manner. We have directly measured the ground state vibrational quantum beats of water molecules at room temperature.

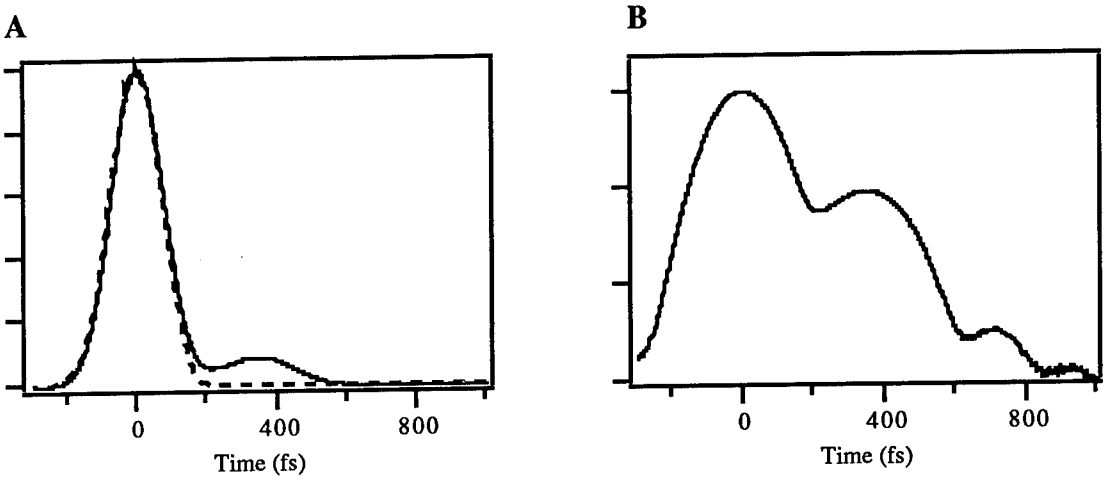


Figure 2. A. The up-converted infrared FID of water dissolved in CD_2Cl_2 (the solid line) and the instrumental response (the dashed line). B. The same data drawn with logarithmic scale.

The distinction between the concepts of local and normal modes at this fast time scale should be discussed. Short pulses (broad spectrum) prepare the system at a super position of local modes. The system then evolves when the dynamic coupling between the two local modes takes place. Our experiment is in this regime. On the other hand, longer pulses (narrow spectrum) prepare the system at the engeinstates (normal modes), and do not generate the oscillatory temporal behavior in the FID.

We are working on even shorter IR pulses as well as amplification of the IR source for nonlinear experiments. This initial experiment shows the promise for using multiple infrared pulse sequences to conduct femtosecond nonlinear vibrational spectroscopy in order to unscramble the complex molecular interactions and dynamics in molecular liquids (Ref 5).

This work was supported by the Chemical Sciences Division in the Office of Basic Energy Sciences of the U. S. Department of Energy at Pacific Northwest Laboratory under Contract No. DE-AC06-76RLO 1830.

References

1. H. Graener and G. Seifert, and A. Laubereau: *Phys. Rev. Lett.* **66**, 2092 (1991).

2. G. R. Holtom, R.A. Crowell, X.S. Xie: Ultrafast Phenomena IX.

2. J.D. Beckerle, R.R. Cavanagh, M.P. Cassassa, E.J. Heilweil, and J.C. Stephenson, *J. Chem. Phys.* **95**, 5403 (1991).

3. J. C. Owrutsky, J.P. Culver, M. Li, Y.R. Kim, M.J. Sarisky, M.S. Yeeganeh, A.G. Yodh, R.M. Hochstrasser: *J. Chem. Phys.* **97**, 4421 (1992).

4. D. Zimdars, A. Tokmakoff, S. Chen, S.R. Greenfield, and M.D. Fayer: *Phys. Rev. Lett.* **70**, 2718, (1993).

5. Yoshitaka Tanimura and Shaul Mukamel: *J. Chem. Phys.* **99**, 9496 (1993).

Use of self-trapped filaments in air to trigger lightning

Xin Miao Zhao, Jean-Claude Diels

Department of Physics and Astronomy

University of New Mexico, Albuquerque, NM 87131

(505) 277-4026

Alan Braun, Xinbing Liu, Detao Du, Georg Korn, Gerard Mourou

The Center for Ultrafast Optical Science

University of Michigan, Ann Arbor, MI 48109

(313) 763-4875

Juan M. Elizondo

Tetra Corporation

3701 Hawkings ST. NE, Albuquerque, NM 87109

(505) 345-8623

A study of the possibility of triggering lightning with optical pulses has been investigated. A theoretical analysis shows that a continuous ionized path of several tens of meters should be created. In recent experiments, long focal length lens were used to confine a low energy ($\approx$ 200 μJ) femtosecond ultra-violet laser pulse, resulting in a weak ionization ($< 10^{-6}$ of the air molecules) in a column between two electrodes spaced by 25 cm. A discharge was induced with this technique at half the self breakdown field of air [1]. The mechanism of laser induced guided discharge is a local field enhancement resulting from the migration of charges in the applied electric field. This mechanism is different from the standard laser induced spark gap, where the laser energy is sufficient to induce a plasma between the electrodes. Self-trapped filaments can create a continuously ionized path over very long distances, which is the main requirement for "seeding" and guiding a discharge over long distances with minimal laser energy.

A Ti:sapphire laser oscillator, combined with a Ti:sapphire amplifier (using the technique of chirped pulse amplification [2]) produces 200 fs pulses at 780 nm with an energy of up to 50 mJ. Self-channeling of such intense femtosecond laser pulses in air was reported [3]. When the peak power of a pulse exceeds a critial power, the laser beam starts self-focusing into a small scale filament. After propagating a distance of about 10 meters, a 1.2 cm diameter beam is self-focused into a filament of 50 to 100 micrometers. Such a filament was observed to propagate over a distance of 20 meters (the maximum free propagation space available in the laboratory). The continuous confinement of the energy inside the filament can be attributed to a balance between the self focusing action due to the n_2 of air, and the self-defocusing mechanism from the refractive index change due to the high density plasma generated inside the laser beam.

The index of refraction of any material can be written as: $n = n_0 + n_2 I + \ldots$, where n_2 is the second-order nonlinear refractive index. The n_2 of air is $5 \times 10^{-19}\text{cm}^2/\text{W}$ and the light intensity inside the filament, calculated from the measured critical power of 13.5 GW, is $1.8 \times 10^{14}\text{W}/\text{cm}^2$. The index change due to the second-order nonlinearity is $\Delta n^{(n_2)} = 9 \times 10^{-5}$. On the other hand, the high density electron plasma (N_e) created inside the laser field causes a negative index change which has an expression: $\Delta n^{(plasma)} = -1/2(\omega_p^2/\omega_\ell^2) = -1/2(e^2 N_e/\epsilon_0 m_e \omega_\ell^2)$, where ω_ℓ is the laser light frequency, ϵ_0 is the dielectric constant and m_e is the electron mass. The electron density being a high order nonlinear function of the laser power, a stable condition (self-channeling) will be reached when $\Delta n^{(plasma)} + \Delta n^{(n_2)} \approx 0$. The electron density required for a balance between self-defocusing and self-focusing is $N_e = 3.2 \times 10^{17}\text{e}^-/\text{cm}^3$.

Our previous theoretical and experimental observations indicate that the minimum electron density (in a high electric field) required to initiate a discharge is $5 \times 10^{11}\text{e}^-/\text{cm}^3$ [1, 4]. The estimated electron density inside a filament is several orders of magnitude higher than the minimum density required to initiate a lightning discharge. The most unique property of such a filament is that it propagates and creates a high density electron path over a long

distance, before absorption reduces its power below the critical power. This high density electron conducting path is ideal for triggering a lightning discharge.

The experiment is performed by applying a high voltage (up to 100 kV) to a pair of plane electrodes separated by 10 cm. The laser filament propagates through holes in the middle of the electrodes. The discharge could not be triggered by a laser induced high density plasma (air molecules totally ionized a the focus) created by tight focusing of a 20 mJ pulse at 780 nm between the electrodes (the standard configuration used for laser triggered spark gaps). However, a filament at 780 nm created with a 25 mJ pulse or with its second harmonic of 2.5 mJ did induce and guide the discharge (Fig. 1). The threshold for light triggered discharge indicated a local field enhancement by a factor of 4.5. The time delay between the passage of the laser pulse between the electrodes to the time of discharge is about 800 ns (Fig. 2), as opposed to the 3 μs measured for a 200 μJ ultra-violet pulse focused through the electrodes at 200 torr of air pressure [1]. The discharge process is accelerated in time at higher pressure and by higher initial density of electrons generated by the laser pulse, which is consistant with the results obtained by Guenther et. al [5].

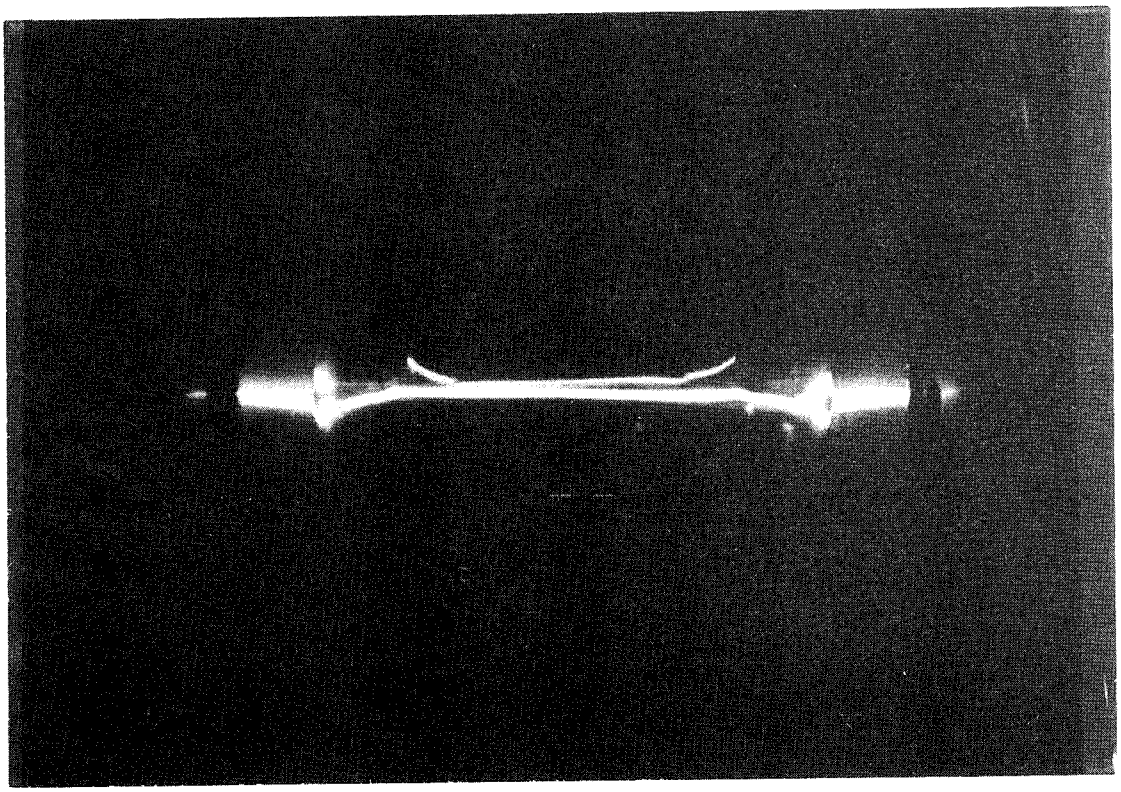


Figure 1: UV ultrashort pulses induced lightning discharge induced by self-filament in a high voltage testing cell.

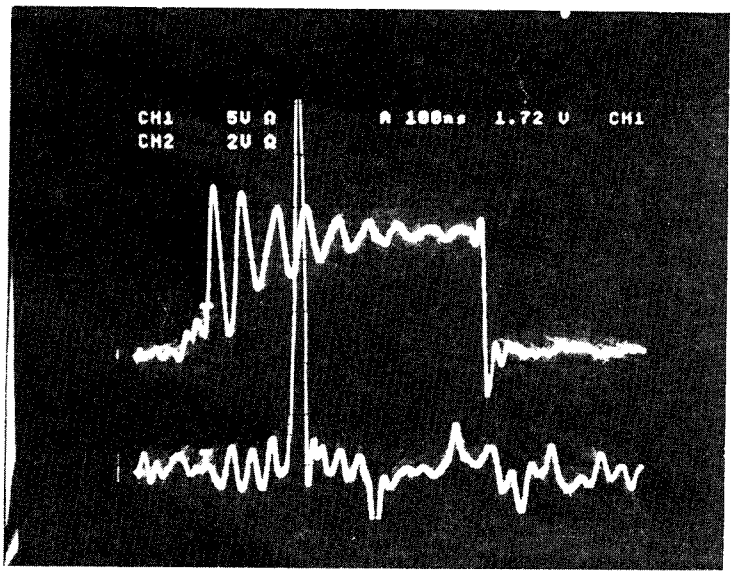


Figure 2: Electric field discharge (above curve) triggered by laser light (lower curve) vs. time.

References

[1] Xin Miao Zhao and Jean-Claude Diels. Femtosecond pulses to divert lightning. *Laser Focus World*, November:113–116, 1993.

[2] M. Pessot, P. Maine, and G. Mourou. 1000 times expansion/compression of optical pulses for chirped pulse amplification. *Optics Communications*, 62:419, 1987.

[3] A. Braun, X. Liu, D. Du, G. Korn, J. Squier, and G. Mourou. Self-channeling of intense fs laser pulses in air. *CLEO'94*, submitted, 1994.

[4] P. R. Krehbiel. *The Electrical Structure of Thunderstorms in The Earth's Electrical Environment*, pages 90–113. National Academy Press, Washington, D. C., 1986.

[5] A. H. Guenther and J. R. Bettis. 12.2 — laser-triggered megavolt switching. *IEEE J. Quantum Electronics*, QE-3(11):581–588, 1967.

Picosecond Dynamics of Carrier Cooling in CdSe : Reduced Energy Loss Rates Caused by Hot Phonon Effects

Arvind S. Vengurlekar, S.S. Prabhu, S.K. Roy and Jagdeep Shah†
Tata Institute of Fundamental Research, Bombay 400005, India
†AT & T Bell Laboratories, Holmdel, NJ 07733

We report the first picosecond luminescence measurements of hot carrier cooling rates in the II-VI semiconductor CdSe. We find that the carrier energy loss rates reduce with the excitation density n_o . The rates are much smaller than those expected in a simple theory of carrier energy transfer to the lattice via various phonon emission processes. At $n_o = 8 \times 10^{17}$ cm^{-3} for example, the rates are reduced by as much as factor of 75. We present a detailed comparison with the theory including the effects of hot phonons and all relevant energy loss mechanisms. We find that a large, density dependent value of 6 to 9 ps for the optical phonon lifetime (at 8 K) is required to explain the results.

Reduced hot carrier cooling rates in a variety of III-V semiconductors have been investigated extensively [1]. Increased current interest in II-VI semiconductors and their quantum wells make similar investigations in II-VI semiconductors of much relevance. Although the dynamics of high density electron-hole plasma in II-VI semiconductors like CdS and CdSe has attracted much attention in the past, mainly to study laser transitions, a detailed experimental study of hot carrier energy relaxation has not been reported previously. Earlier attempts to study hot carrier cooling in CdSe were made at a very high density ($n_o > 10^{19}$ cm^{-3}) in a pump-probe experiment [2] or using luminescence with an insufficient time resolution (> 20ps) [3].

Our results were obtained by using luminescence upconversion spectroscopy with 2.5 ps time resolution at a carrier excitation density n_o of 2×10^{17} cm^{-3}, 4×10^{17} cm^{-3} and 8×10^{17} cm^{-3}. For this, 1.8 psec wide pulses from a Nd-YAG pumped dye laser at a photon energy of 2.03 eV and standard photon counting detection were used. The energy resolution for the measurement was about 3 meV. The full time evolution of the interband luminescence following excitation at t = 0 ps at (8 K) is shown in Fig.1 for one of the excitation density used (= 8×10^{17} cm^{-3}). Under the conditions of our experiments, we expect the carriers to form a thermalized energy distribution during photoexcitation (centered at t = 0 ps) with a temperature T_c higher than the lattice temperature. That the carriers have a thermalized distribution at various delays after photoexcitation is confirmed by the $E^2 \exp(-E/kT_c)$ behavior of the luminescence energy distributions, as illustrated in Fig.2. The carrier cooling characteristics for the three excitation densities are seen in Fig.3. It may be noticed that the energy loss rate depends on the excitation density n_o, the rate decreasing as n_o increases. Also the measured temperatures of the carriers drop to 50K in approximately 30 ps, after which the cooling rate is slower.

To compare the results with theory, we first write the average energy per e-h pair as $\langle E \rangle = 3kT_c[\gamma_e(T_c) + \gamma_h(T_c)]/2$, where $\gamma_i(T_c) = F_{3/2}(\eta_i)/F_{1/2}(\eta_i)$, $\eta_i = \epsilon_{F_i}/kT_c$, ϵ_{F_i} = Fermi energy, i = e , h , 'F's are the Fermi integrals. We can then relate the cooling rate dT_c/dt to $d\langle E \rangle/dt$. Also, we expect $d\langle E \rangle/dt = -C_o \langle dE/dt \rangle$, with $C_o = 1$, $\langle dE/dt \rangle$ being the average energy loss rate per e-h pair

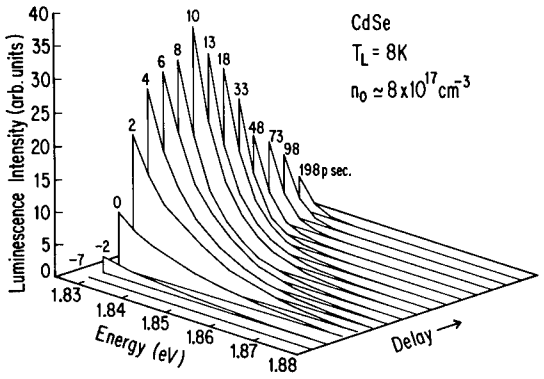


Fig.1 The time evolution of luminescence energy distribution for interband transitions.

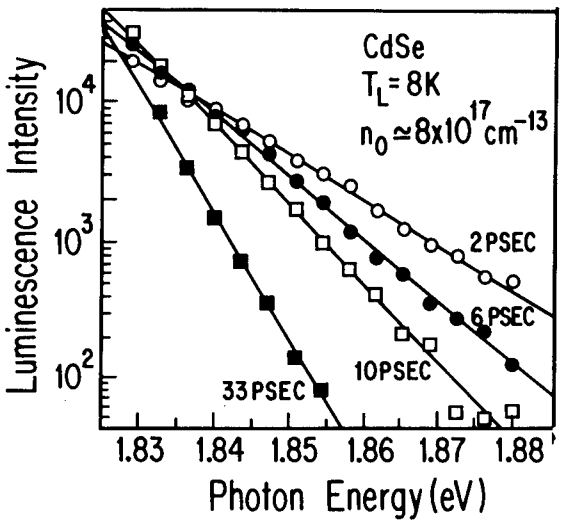


Fig.2 Luminescence intensity showing hot carrier thermalization.

due to phonon interactions. As a simplification, we assume that the carriers are thermalized with $T_c = T_o$ at generation at t=0. We include all the relevant electron and hole energy loss mechanisms, i.e. phonon interactions via the unscreened Fröhlich, nonpolar optical (NPO) and acoustic deformation potential and piezoelectric interactions [4] in our calculation of (dE/dt). A phenomenological factor of 0.5 is used to account for the reduced hole scattering due to the p-like valence band states.

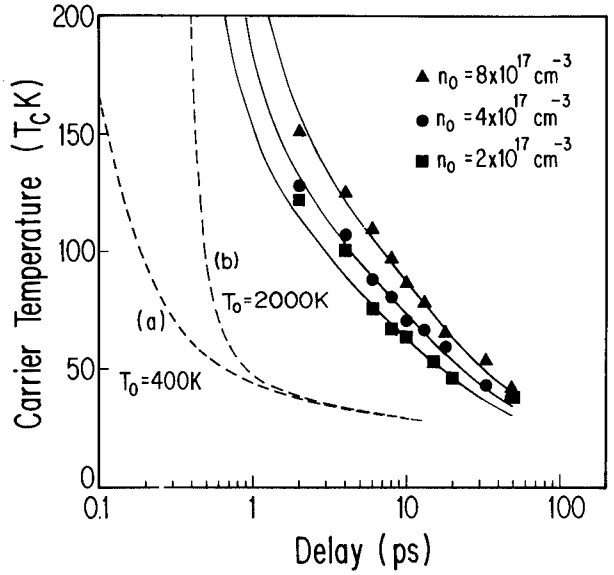


Fig.3 Experimental cooling behavior shown at three excitation densities (discrete points). Cooling rates calculated without the hot phonon effects (dashed curves) shown for T_o = 400 K (a) and T_o = 2000 K (b) are much faster. Calculations including the hot phonon effects (solid curves) however are seen to fit the data very well. T_o = 2050, 2100 and 2250 K for n_o of 2×10^{17} cm^{-3}, 4×10^{17} cm^{-3} and $8 \times 10^{17} cm^{-3}$ respectively. See text for details.

We write the NPO coupling D as $C_1 \times 10^8$ eV/cm, with $C_1 = 10$ for holes in CdSe, as given in Ref.5, and C_1=0 for electrons. We first consider the case in which reabsorption of the optical phonons emitted by the carriers is ignored ("no hot phonons"). Results of these calculations of the cooling behavior are shown in Fig.3 for $T_c = 400$ and 2000 K as illustration. It is clearly seen that the measured cooling rates are much slower. It turns out that a reduction factor $1/C_o$ of 30, 50 and 75 in the effective energy loss rate is required for the theory to satisfy the data for n_o of 2×10^{17} cm^{-3}, 4×10^{17} cm^{-3} and 8×10^{17} cm^{-3} respectively.

We next consider the so called hot phonon effects as a possible origin of the slow carrier cooling. Here, the amplification of nonequilibrium optical phonons via both the Fröhlich and NPO coupling leads to significant phonon reabsorption by the hot carriers if the lattice dynamical optical phonon lifetime $\tau_{LO} = \tau_{TO}$ is large enough [6]. We once again calculate the cooling behavior using the above phonon interactions, this time including the optical phonon reabsorption. For this, we solve the coupled time dependent equations for T_c and the LO and TO phonon occupancies, taking τ_{LO} as a parameter. It is seen in Fig.3 that the agreement of such a calculation with the experiments is quite good and this determines values of 6, 7.5 and 9 ps for the optical phonon lifetime for n_o of $2 \times 10^{17} cm^{-3}$, $4 \times 10^{17} cm^{-3}$ and $8 \times 10^{17} cm^{-3}$. respectively. Understanding this weak dependence of τ_{LO} on the excitation density requires further investigation, but this may be an apparent manifestation of effects like acoustic phonon bottleneck [7], screening and phonon renormalization [8], etc. which are not considered here.

In summary, we find significantly reduced hot carrier cooling rates in CdSe using picosecond upconversion luminescence spectroscopy. This can be explained to be due to the hot phonon effects provided the optical phonon lifetime τ_{LO} is 6 to 9 ps, depending upon the excitation density. This may be compared with the corresponding value of 7 ps for GaAs obtained using Raman measurements [9]. It would be interesting to have a direct experimental determination of τ_{LO} in CdSe.

References

1. K. Kash, J. Shah, D. Block, A.C. Gossard and W. Wiegmann, Physica 134B, 189 (1985).
2. Y. Masumoto and F. Sasaki, J. Lum. 48 / 49, 189 (1991).
3. H. Yoshida, H. Saito and S. Shionoya, Phys. Stat. Solidi B104, 331 (1981)
4. See for example, J. Shah and R.F. Leheny in 'Semiconductors Probed by Ultrafast Laser Spectroscopy', edited by R.R. Alfano (Academic Press, 1984) and references therein.
5. M. Pugnet, J. Collet and A. Cornet, Solid State Comm. 38, 531 (1981).
6. W. Potz and P. Kocevar, Phys. Rev. B28, 7040 (1983).
7. R. Baltramiejunas and A. Zukauskas, Phys. Stat. Solidi B149, 337 (1988).
8. S. DasSarma in 'Hot Carriers in Semiconductor Nanostructures' edited by J.Shah (Academic Press, 1992).
9. D. von der Linde, J. Kuhl and H. Klingenburg, Phys. Rev. Lett. 44, 1505 (1980).

Paper Withdrawn

Ultrafast Magnetoexciton Dynamics in GaAs

Mary-Ann Mycek, Uwe Siegner, Daniel S. Chemla
Department of Physics, University of California at Berkeley
and
Material Sciences Division, Lawrence Berkeley Laboratory
MS 2-300, 1 Cyclotron Rd., Berkeley CA 94720
Phone: (510)-486-5265 FAX: (510)-486-5530

A bulk semiconductor provides an excellent system for optically studying the ultrafast dynamics of Coulomb correlated magnetoexcitons. The application of a magnetic field to a 3-D system quantizes the energy levels of states with momentum perpendicular to B and, in contradistinction to experiments performed on 2-D quantum well systems, leaves a 1-D continuum of states with momentum parallel to B. The presence of the continuum states has a dramatic influence on both the linear and nonlinear optical properties. Thus, the experiments described below track the evolution of the semiconductor from a 3-D to a 1-D system and reveal surprising optical properties not observed in the previously reported studies in quantum wells.

In GaAs, under the application of a magnetic field, the discrete higher order magnetoexciton states are energetically degenerate with the 1-D continuum of states of the lowest order magnetoexciton. The configuration interaction between an isolated resonance superimposed energetically upon a continuum of states was described theoretically by Fano. [1] The resulting state is a superposition of the original discrete state and the continuum of states and the resulting resonance has a distinctive asymmetric lineshape due to quantum interference. Asymmetric Fano resonances have been observed in the linear absorption spectrum of GaAs under magnetic fields. [2] Our present experiments investigate both the absorption properties of these states and also the ultrafast coherent emission from these resonances.

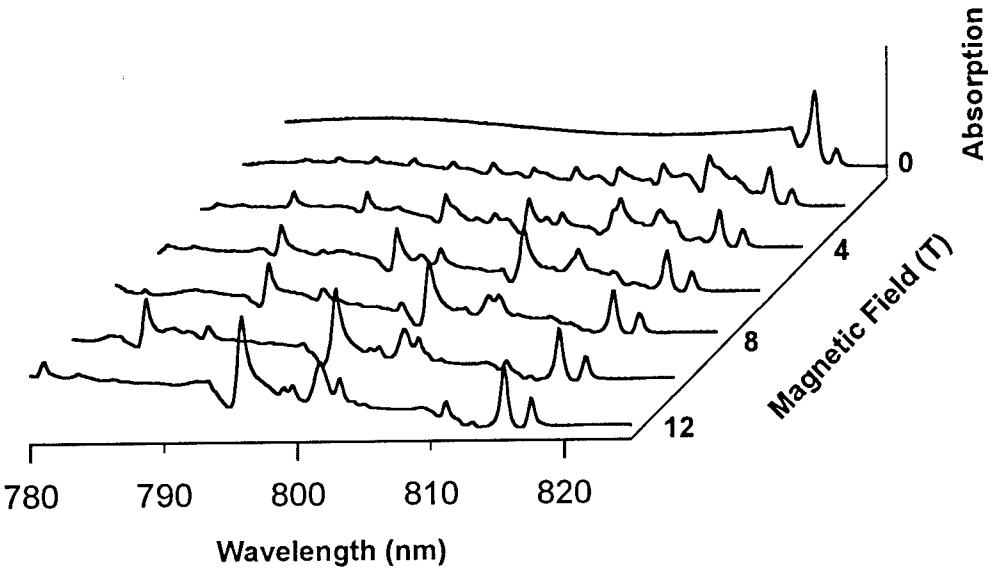


Figure 1: GaAs linear absorption at 1.6K for several magnetic field strengths.

Fig. 1 shows the linear absorption spectrum of our GaAs sample at 1.6K taken with circularly polarized light for several magnetic field strengths. At B=0T, we see that due to strain the light hole (LH) exciton and the heavy hole (HH) exciton are split, with the LH exciton at lower energy. [3] By increasing the field strength to 12T, we verified that the resonances observed in the spectrum form a fan chart pattern and do indeed correspond to two families of magnetoexcitons. The most interesting feature here is the asymmetric lineshape of the higher order magnetoexciton resonances. Immediately at 2T the resonances in the continuum show these features. As the field strength increases to 6T, say, the resonances become more pronounced. We attribute this change in profile to a field dependent coupling between the discrete state and the underlying continuum of states. Finally, at the highest field strengths, the magnetoexciton states are separated well enough to excite an isolated resonance with our 100fs laser pulse. In the nonlinear optical experiments described below, we concentrate on the ultrafast dephasing properties of the lowest lying magnetoexciton states.

Four wave mixing (FWM) experiments were performed using 100fs pulses from a Ti:Sapphire laser tuned to excite the lowest order HH and LH magnetoexcitons. The beam was split into two co-circularly polarized beams, propagating in directions k_1 and k_2, with pulses variably time delayed by Δt. The beams overlapped spatially on our sample, which was held at 1.6K inside of a split coil magnet-cryostat. The FWM signal emitted in direction $2k_1$-k_2 was then either time-integrated (TI), i.e. its intensity was measured vs. Δt, or for a fixed Δt the spectrum of the FWM emission was measured.

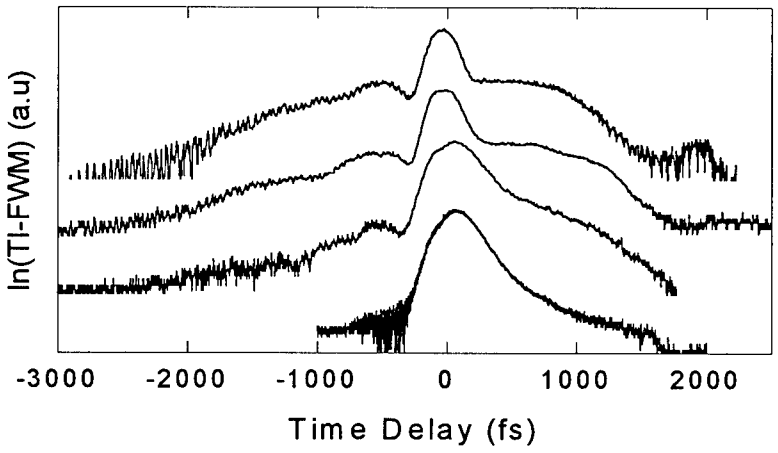


Figure 2: TI-FWM for B=10T (top), 6T, 2T, and 0T (bottom).

The TI FWM signal is shown in Fig. 2 for various field strengths and at excitation density $N_X \approx 10^{16} cm^{-3}$. At zero field, there is a nonexponential decay in approximately 1ps for positive time delays and otherwise the lineshape is featureless. With field, however, the temporal lineshape is completely different. There is an obvious beating modulation on the TI signal which changes significantly with increasing field strength. Importantly, this modulation is excitation density dependent and becomes much less pronounced at higher densities. Moreover, this non periodic beating is observed for both positive and negative Δt. These are indications of strong Coulomb interactions between magnetoexcitons. These interactions have been studied extensively for 2-D systems, where theoretical models [4] demonstrate that they are at the origin of these distinctive TI lineshapes. Fundamentally different from 2-D systems, where the interactions become

quenched at high fields, our measurements indicate that in 3-D these features persist for fields as high as 10T. This result is understood in terms of the 3-D linear data, which demonstrate a strong coupling between states for fields as high as 12T.

In order to better understand the TI beat modulation, we measured the spectrum of the FWM emission for each of several Δt for a 6T magnetic field and $N_X \approx 10^{16} cm^{-3}$. Fig. 3 shows the measured TI profile and the evolution in time of the FWM spectra around a beat node. It is clear that the competition between spectral components results in the beating observed temporally. From these data we also measure the dynamics of each component individually. We find that as these components evolve in time, they decay and/or beat asynchronously with distinct dephasing times. For example, the component at the HH exciton (λ=818nm) decays slowly (in at least 1.1ps) and exhibits a beating modulation, whereas a higher energy component decays very rapidly, in about 90fs. Thus, it is the complex interplay spectrally which manifests itself as non periodic beats in the time domain.

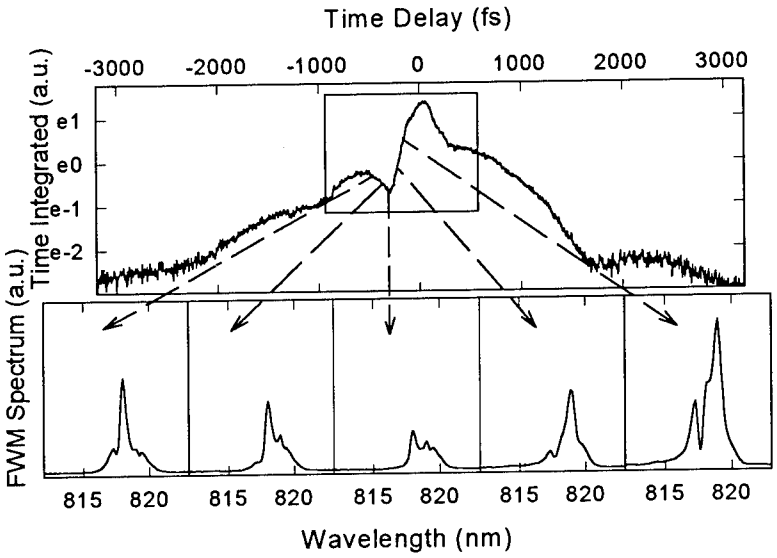


Figure 3: For B=6T, TI-FWM (top) and FWM Power Spectra (bottom) for Δt = -560fs, -400fs, -320fs, -240fs, and -160fs.

Experiments are in progress to investigate the microscopic origin of these various spectral components. From the magnetic field and excitation density dependent TI-FWM measurements, it is clear that Coulomb interactions between magnetoexcitons strongly affect the emission properties of the system. We attribute the observed spectral properties to these interactions and hope these results will stimulate the development of a model for ultrafast magnetoexciton dynamics in 3-D systems.

This work was supported by the US DOE under contract No. DE-AC03-76SF00098.

References:

[1] *U. Fano, Phys. Rev. 124, 1866 (1961)*

[2] *W. Becker, B. Gerlach, T. Hornung and R.G. Ulbrich, Proc.18th Int. Conf. Physics of Semiconductors, Stockholm, 1986 (World Scientific, Singapore, 1987), p.1713*

[3] *Fred H. Pollak and Manuel Cardona, Phys. Rev. 172, 816 (1968)*

[4] *M. Hartmann, W. Schafer, S. Schmitt-Rink, Int. Meeting on Optics of Excitons in Confined Systems, Inst. Phys. Conf. Ser. No.123, p.265*

Molecular Pulse Shaping

J. X. Tull, C. W. Hillegas, D. Goswami and W. S. Warren

Department of Chemistry and the Princeton Center for Photonics and Opto-Electronic Materials, Princeton University, Princeton, New Jersey 08544-1009

Interest in the uses of controlled radiation fields to alter molecular states or drive chemical reactions–originally called "laser selective chemistry," but now commonly called "quantum molecular control"[1]–has resurged in the last few years, largely because the technology for controlling optical fields has improved dramatically. Programmable pulse shaping has been demonstrated with temporal resolution of ≈30 fs and peak powers limited only by the amplifying lasers, and a tremendous range of applications can be readily envisioned. Nonetheless, pulse shaping has not become widely applied in the ultrafast optical community, for two basic reasons. *Robustness* is a fundamental issue–it is relatively easy to calculate waveforms which can break strong bonds or alter reaction dynamics, but in many cases, laboratory inhomogeneities or lack of knowledge of the exact Hamiltonian make practical implementation impossible. In addition, none of the demonstrated techniques for controllable fs pulse shaping is truly "easy." Arbitrary ps pulse shape generation was first demonstrated in 1985[2], but each new waveform required a new fabricated amplitude mask. Our electro-optic approach[3] was the first method which gave programmable pulse shapes, but in 1986 we used traveling wave EO modulators and microwave waveform generators which are past the commercial state-of-the-art even today. More recently, liquid crystal modulators (LCMs)[4]. or holographic patterns[5] have been used to tailor the optical waveform. Tremendous improvements have been demonstrated, particularly in the LCM-based approach; however, alignment, pixel isolation and calibration, and gaps between pixels become limiting factors when the desired waveform requires substantial frequency modulation.

We will present data from two new and easily implemented approaches to pulse shaping under development in our laboratory. One approach, acousto-optic modulation inside a zero-dispersion line[6,7] (Figure 1), can dramatically improve capabilities for generating complex optical waveforms, including phase and amplitude modulation. The other approach, which we call molecular pulse shaping (Figure 2), uses an interferometer and an absorption cell to create waveforms optimized for specific molecules. Together these techniques produce robust and highly controllable waveforms for chemical applications.

The acousto-optic shaper modulates fs laser pulses using **microsecond** rf pulses. The grating and lenses spatially disperse the different frequencies from the input laser pulse. A shaped radiofrequency pulse to the AOM's transducer creates a travelling acoustic wave in the crystal. The transit time of a fs pulse through the crystal is far too short for significant acoustic propagation, so the acoustic wave looks like a modulated diffraction grating. The diffraction efficiency and phase (and to some extent the beam direction) can

be different at different positions, limited only by the acoustic risetime. We then save the beam which is diffracted by the modulator. Experimental data to date are encouraging, and in principle the resolution should be absolutely stunning; our current (commercially available) waveform generator and TeO_2 AOM give spatial variations of the grating in 30 μm, so the 4 cm clear aperture of the modulators implies that a waveform with 1000 independently adjustable amplitudes and phases should be possible. In comparison with existing methods, this approach has the advantages of faster update times, no pixel gaps, high isolation and simple calibration. Issues associated with designing a system to take advantage of the full modulator bandwidth will be discussed.

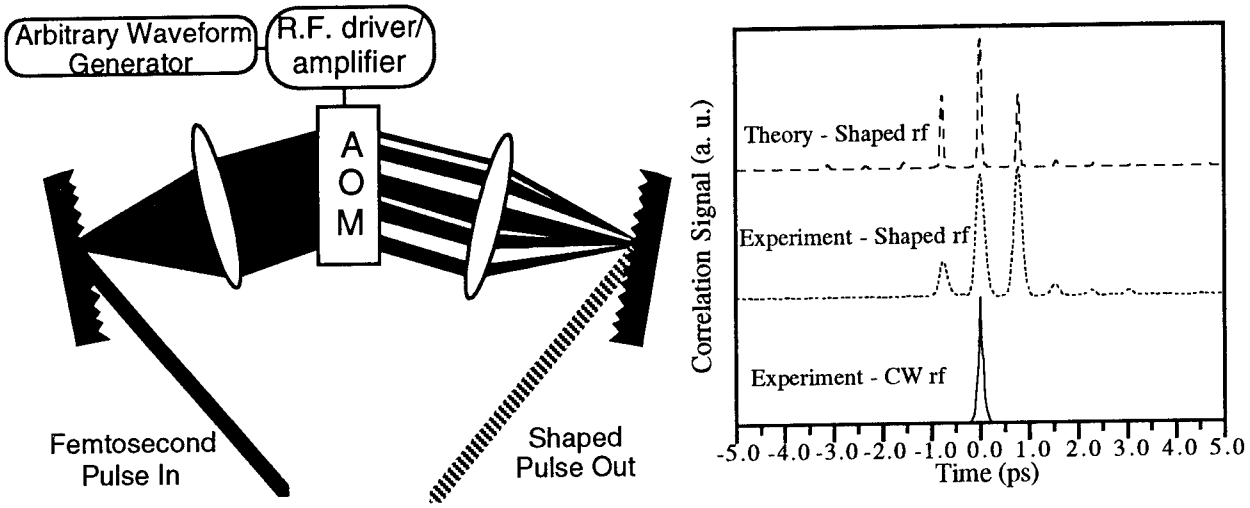


Figure 1. Left: an A-O modulator inside a zero-dispersion line provides a versatile new technique for crafting fs laser pulses with μs radiofrequency pulses. Right: one example of calculated and experimental crosscorrelations with a 100 fs CPM pulse, in this case from a train of 11 short r.f. pulses. Many other examples are given in reference [7].

In the weak-response limit, the optimum laser pulse for exciting any molecule with discrete spectral lines would be a pulse which contains only those frequency components. Such a pulse would also do the best possible job of selectively exciting a specific molecule in a background of competing absorbers. In the strong-response limit, pulses with such a frequency structure are a natural and logical starting point for generating efficient inversion, particularly if phase modulation or frequency sweeps can be imposed on this overall structure as well. These "modified wavepackets" in effect alter the energy level structure in the ground and excited electronic states by interaction with the radiation field. Such waveforms could look quite complex; no existing pulse shaping techniques have such frequency resolution or could generate waveforms with such complexity. However, the *molecule itself* knows how to generate such a waveform easily; the optical free induction decay after a short pulse has exactly the right frequency characteristics.

In our earliest work[6], we saved the free induction decay while deleting the intense original pulse with a Michaelson interferometer. When the arms of the interferometer are exactly equal, it produces constructive interference in one direction and destructive

interference in the other, independent of wavelength. Inserting a sample cell into one of the arms attenuates the resonant frequency components, and also introduces some phase shifts (depending on the optical density of the cell). This destroys the perfect cancellation in the destructive interference direction (counterpropagating with the entering laser pulse), leaving only the molecular free induction decay. We are currently using an intentionally misaligned Sagnac interferometer, which has dramatically improved stability because the two beams travel along nearly the same path (Figure 2). Even without active stabilization, we routinely get a contrast ratio of about 75:1 between fringes, and the fringes are stable for minutes to hours. We have also verified that the shaped pulse is absorbed much more efficiently in a second iodine cell than was the original ps pulse. For example, a 2 ps pulse centered at λ=605 nm is attenuated in a second iodine cell only one-sixth as rapidly as is the modulated pulse out of the Sagnac. Issues associated with path length equalization will be discussed, as will calculations of sensitivity enhancement for detection of dilute species and of strong-response effects.

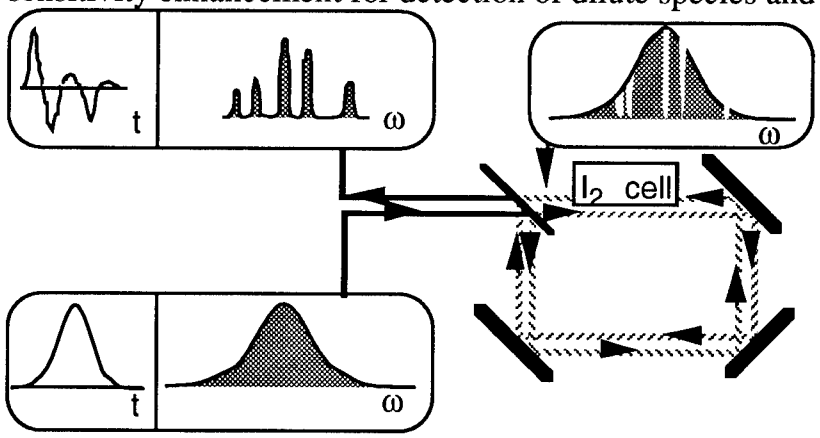


Figure 2. A sample cell in one arm of a Sagnac interferometer turns a ultrafast laser pulse into a highly modulated optical free induction decay. This pulse can be amplified if desired. The shape is ideally suited for a variety of applications on the molecule which shaped it.

This work is supported by the National Science Foundation.

References

[1]W. S. Warren, Science 262, 1008 (1993) (Perspective); W. S. Warren, H. Rabitz and M. Dahleh, Science 259, 1581 (1993); S. Rice, Science, 258, 412 (1992)

[2]A. M. Weiner, J. P. Heritage and R. N. Thurston, Opt. Lett. 10, 609(1985)

[3]M. Haner, F. Spano and W. S. Warren, Ultrafast Phenomena V (G. Fleming and A. Siegman, eds., Springer:New York, 1986), p. 514; M. Haner and W. S. Warren, Appl. Phys. Lett. 52, 1458 (1988).

[4] A. M. Weiner, R. N. Thurston, W. J. Tomlinson, J. P. Heritage, D. E. Leaird, and E. M. Kirschener, Opt.Lett. 14,868(1989) ; M. Wefers and K. Nelson, Opt. Lett. (in press)

[5] David Brady, Alan G.-S. Chen, and George Rodriguez, Opt. Lett. 17, 611(1991); K. B. Hill and D. J. Brady, Opt. Lett. (in press).

[6]D. Goswami, C. W. Hillegas, J. X. Tull and W. S. Warren, in "Femtosecond Reaction Dynamics" (D. A. Wiersma, editor; Royal Dutch Academy of Sciences, 1993).

[7]C. Hillegas, J. X. Tull, D. Goswami, D. Strickland and W. S. Warren, Optics Letters (submitted)

The Soliton-Self-Frequency Shift in Passively Modelocked Soliton Fiber Lasers

M. L. Stock† and M. E. Fermann

IMRA America, Inc.
1044 Woodridge Ave.
Ann Arbor, MI 48105
Tel. (313) 930-2560
Fax (313) 930-9957

†Center for Ultrafast Optical Science
University of Michigan
Ann Arbor, MI 48109-2099

Modelocked lasers are typically subject to a variety of instabilities that affect the quality of the output pulses. Particularly noticeable effects arise from the discreteness of the cavity elements[1] and third-order dispersion, which in turn lead to the formation of spectral side bands[2] and an asymmetric pulse spectrum[3]. However, any gain-pulling from these instabilities is minimal and therefore the spectrum of the modelocked pulses remains located close to the peak of the gain profile.

Here we show that in erbium soliton fiber lasers significant gain pulling can arise from higher-order nonlinear effects, such as the soliton self-frequency shift and cross-phase modulation. As a result a wavelength instability can arise and the location of the spectrum of the modelocked pulses can in fact be red-shifted by up to 14 nm, i.e. by nearly 30 % of the gain bandwidth of erbium. The red-shift is power dependent and can lead to a reduction in gain and the build-up of amplified spontaneous emission in subsequent fiber amplifier chains[4]. The wavelength instability may be suppressed by the selection of a suitable polarization state inside the fiber.

For experimental convenience we characterized the gain pulling effects in a Kerr-type modelocked environmentally stable erbium fiber soliton laser[5] (Fig. 1). In this, polarization maintaining fiber eliminates linear polarization mode-coupling and the Faraday rotator mirror (FRM) compensates for the group-velocity walk-off along the polarization eigenmodes of the fiber. The polarization controller (PCT), consisting of a $\lambda/4$ and a $\lambda/2$ waveplate, is characterized as a unique transformation from the intra-cavity polarizer to the fiber, which is defined on the Poincaré sphere as $(0,0) \rightarrow (2\psi, 2\alpha)$. Note that the cw loss of the cavity is given by $\sin^2 2\psi$ and α is the angle of the cw polarization ellipse with respect to the slow axis of the fiber. We used a 2.3 m length of fiber doped with $\approx 5\times10^{18}$ erbium ions/cm^3. The core diameter was 5 μm, the polarization beat length 10 cm and the group-velocity dispersion $\beta_2 = -13000$ fsec^2/m.

We measured the following stability range for the modelocked fiber laser

$$55^0 < \psi < 77^0 , \qquad 9^0 < \alpha < 32^0 .$$

Thus modelocking could be sustained for a cw intra-cavity loss between 20 and 90 % (modelocking could be started in only about 30% of the stability range). The pulse widths inside the stability range varied between 200 and 400 fsec and intra-cavity pulse

energies between 50 and 150 pJ could be sustained. When keeping the PCT fixed, stable modelocking without a cw background could be obtained for pump power variations of up to ±20%.

Typical pulse spectra measured for different values of intra-cavity pulse energy are shown in Fig. 2). In this the PCT is set at $\alpha \approx 10^{o}$, whereas $\psi \approx 75^{o}$ and 57^{o} for Figs. 2a) and 2b) respectively. The pulse widths for the two cases measured both parallel and orthogonal to the intra-cavity polarizer are shown in Fig. 3.

The pulse spectrum in Fig. 2a) exhibits a large power-dependent red-shift, which can extend up to 14 nm to the red side of the peak of the gain profile (as defined by the marked position of the cw emission). Note that for red-shifts larger than 10 nm, a cw instability arises at the spectral gain peak, as the amount of amplitude modulation in the cavity is not large enough to suppress it. On the other hand, in Fig. 2b) the position of the pulse spectrum is nearly power-independent and located close to the spectral gain peak. Clearly the most significant difference between the two cases is the intra-cavity loss, which is 25 % and 83 % in Figs. 2a) and 2b) respectively. As the intra-cavity loss is increased, the pulling force from the gain profile also increases and tends to center the pulse near the peak of the gain profile.

When keeping ψ (and the intra-cavity loss) constant and varying α, the largest spectral red-shifts were observed for large values of α, which also maximized the intra-cavity pulse energy and minimized the pulse width. Note that this control is quite unique, since it allows wavelength tuning by only changing the nonlinear polarization state in the cavity, leaving the linear polarization state unaffected.

These observations indicate that Raman self-scattering plays a very important role in the steady-state modelocking dynamics of the laser. Indeed, we were able to simulate numerically the correct magnitude of the expected red-shift and the onset of a cw instability for large red-shifts. However, the numerical simulations have shown further that the red-shift of the pulse spectrum is also influenced by cross-phase modulation. Cross-phase modulation can induce large spectral shifts, since solitons try to propagate as units, which is only possible when they develop a slight frequency difference along the two axes of the fiber, i.e. when vector solitons are formed. Net frequency shifts per round-trip then arise due to the non-reciprocal nature of nonlinear pulse propagation.

In contrast to Raman self-scattering, cross-phase modulation can also lead to spectral blue-shifts depending on the exact setting of ψ and α in the PCT. In fact a close inspection of Fig. 2b) reveals that the pulse spectrum exhibits a small blue shift with an increase in pulse power, which indicates that in this case the pulling force from cross-phase modulation opposes Raman self-scattering. In fact the PCT could be adjusted to give blue-shifts as large as 2 nm.

In summary we have observed and characterized the soliton self-frequency shift in soliton fiber lasers for the first time to our knowledge. The soliton self-frequency shift is minimized by large intra-cavity losses and can be compensated by cross-phase modulation. Finally the soliton self-frequency shift also allows a limited tunability of soliton fiber lasers.

Acknowledgements

We acknowledge stimulating conversations with H. Winful, T. Brabec and S.M.J. Kelly.

References

1. T. Brabec et al. Opt. Lett.,16, 1961 (1991)
2. S.M.J. Kelly, Electron. Lett., **28,** 806 (1992)
3. C. Spielmann et al., to be publ. in IEEE J. Quantum Electronics
4. M.E. Fermann et al., subm. to Appl. Phys. Lett.
5. M.E. Fermann et al., Opt. Lett., **19**, 1, (1994)

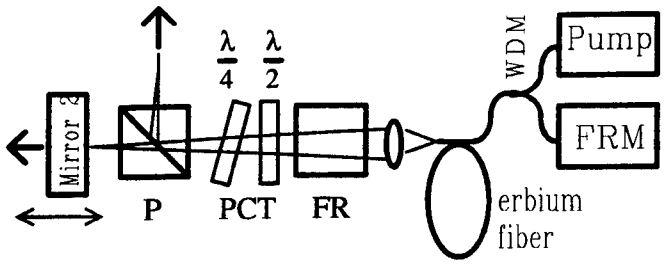
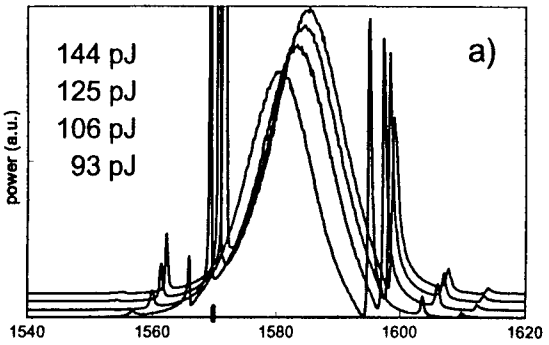


Fig. 1) Set-up of an environmentally stable erbium fiber laser.



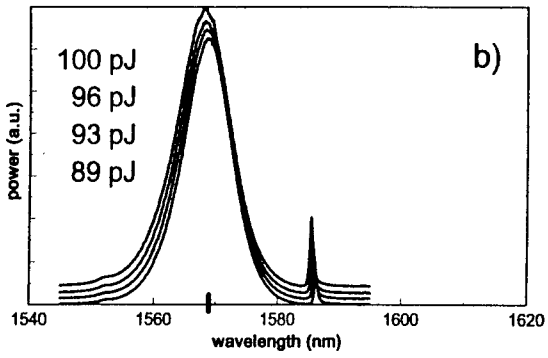


Fig. 2) Pulse spectra as a function of increasing intra-cavity pulse energy (bottom to top) in the presence of an a) uncompensated and a b) compensated soliton self-frequency shift. Note the mark near 1.57 μm denotes the cw emission wavelength.

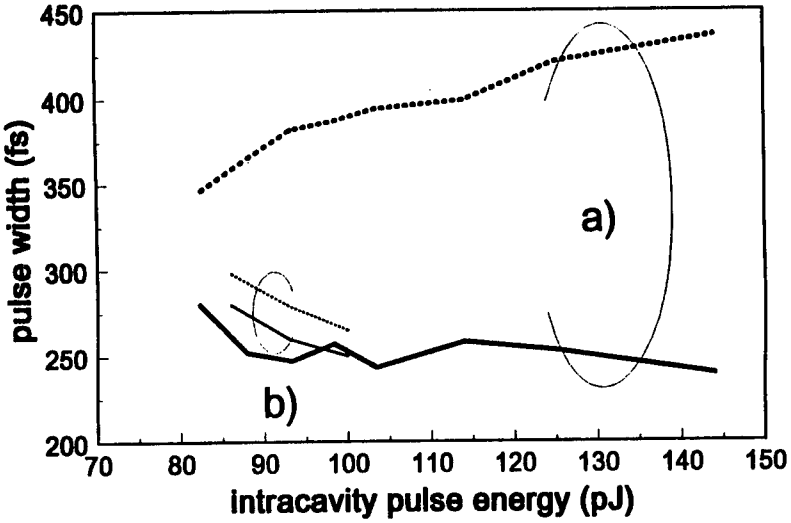


Fig. 3) Pulse widths as a function of intra-cavity pulse energy (corresponding to Fig. 2) measured parallel (solid line) and orthogonal (dotted line) to the intra-cavity polarizer.

Thursday, May 5, 1994

Reactions in Solution

ThE 4:30pm–6:00pm
Dana Point Ballroom

Kenneth Eisenthal, *Presider*
Columbia University

Femtosecond Dynamics in Polar Liquids

Graham R. Fleming, Taiha Joo, Minhaeng Cho, Yiwei Jia

Department of Chemistry
James Franck Institute
University of Chicago
5735 S. Ellis Avenue
Chicago, IL 60637

New non-linear spectroscopic methods for characterizing the interaction of solvents and solutes will be described. The nature of signals observed at 3rd and 5th order and their relationship to the underlying liquid dynamics will be discussed.

Femtosecond electronic dynamics by time-delayed four-wave mixing with incoherent light: iodine and azulene. Tzyy-Schiuan Yang, Ruihua Zhang and Anne B. Myers, Department of Chemistry, University of Rochester, Rochester, NY 14627-0216; (716) 275-2415.

Spectrally broadband, temporally "incoherent" light has been employed to obtain femtosecond time resolution in various nonlinear optical experiments by exploiting the fact that in many such processes it is the coherence time of the light source, not the duration of its pulse intensity envelope, that dictates the temporal resolution of the experiment.[1-4] One such process is the photon echo configuration of time-resolved four-wave mixing,[5-9] which can distinguish the contributions to molecular electronic spectral linewidths from "homogeneous" and "inhomogeneous" broadening if the latter is static on the time scale of the entire matter-radiation interaction sequence. In liquids, spectral diffusion--the interconversion of spectroscopically different local environments for different chromophores--is usually fast relative to the actual pulse durations of most incoherent light sources, complicating efforts to study electronic dephasing with such sources. When femtosecond pulses are used, the overall time scale of the experiment can be made subpicosecond if desired, or it can be made arbitrarily long by employing the three-pulse technique. No such tunability is possible when the light source has a temporally long intensity envelope, however short its correlation time.

We have explored the possibility of shortening the time scale on which spectral diffusion can act by making the first two fields orthogonally polarized such that they generate only an orientational grating.[10,11] Since this grating decays with the orientational relaxation time, any processes that cause spectral diffusion on longer time scales should appear as inhomogeneous broadening, and only processes faster than the rotational relaxation will appear as contributions to the homogeneous dephasing. We introduced this idea in two-pulse time-delayed four-wave mixing experiments with incoherent light on rhodamine B in polar solvents.[12] This work extends these measurements to I_2 in vapor and solution phases and azulene in solution.

The broadband excitation pulses (centered at 560-562 nm with a bandwidth of about 175 cm^{-1} for I_2 and 680-700 nm with a bandwidth of 400-1400 cm^{-1} for azulene) are generated from a cavityless Q-switched YAG-pumped dye "laser", containing no output coupler or tuning element, which generates spontaneous emission that is amplified by passage through a second dye cell. The pulse duration is about 8 ns. The probe pulse is obtained either by beamsplitting the dye output or from the 532 nm YAG pump, and is delayed by about 1 ns for the solution phase experiments and by more than 10 ns for the vapor phase studies. Signals are recorded as a function of time delay τ between the two pump pulses at constant probe delay. Care is taken to avoid the unequal spectral distortions of the two pump beams that can arise from unbalanced dispersive optics in the beam paths.[12]

Our theoretical description of time-delayed four-wave mixing with incoherent light in a multilevel system is presented in detail elsewhere.[13] The light source is modeled as a stochastic stationary Gaussian process. In our studies of I_2 vapor, parallel polarized pulses are used to form a long-lived population grating, allowing us to delay the probe by longer than its pulse envelope and insuring that the probe field interacts last. We assume exponential electronic dephasing and calculate the molecular response function as an explicit sum over rovibrational levels of the ground and B excited states, using literature values for the spectroscopic constants. Expressions for the signal as a function of pump pulse delay τ are derived both for the case in which no energy relaxation occurs during the "waiting time" for the probe pulse and in the limit where rotational relaxation is complete, but no vibrational relaxation occurs. For the solution phase experiments, perpendicularly polarized pump pulses are used to form an orientational grating. In order to probe this short-lived grating with our long pulses the probe pulse must temporally overlap the excitation pulses, and with degenerate pulses we must consider time orderings of the field interactions in which the "probe" is not the last to act. The theoretical signals for I_2 in solution are calculated by summation over the vibronic states assuming the vapor phase energies and Franck-Condon factors are transferrable to solution, with varying amounts of homogeneous and inhomogeneous broadening included. Experiments on azulene are also carried out

using a probe wavelength widely separated from that of the pump. In this case only time orderings in which the probe acts last will contribute. Then, if vibrational relaxation is complete during the waiting time between pump and probe interactions, the four-wave mixing signal for a homogeneously broadened system depends only on the Fourier transform of the linear absorption spectrum, a result that has been derived by others.[5]

Fig. 1 shows the experimental result for I_2 vapor. The signal exhibits beats with a separation corresponding to a vibrational energy spacing of 91 cm^{-1}, consistent with the known spacings in the B state at the energy of our 562 nm laser. Fig. 2 displays the curves calculated with no energy relaxation (top) and with complete rotational relaxation (bottom). In the first calculation the initial inhomogeneity due to the thermal distribution of J states is retained throughout, and an asymmetric signal about τ=0, the usual signature of an inhomogeneously broadened system, is observed; in the second, the rotational distribution is scrambled during the waiting time, and the resulting response is symmetric about τ=0. The experimental signals fall between these two limits, indicating that rotational relaxation is significant but not complete on the 10 ns time scale.

The points in Fig. 3 present the experimental trace from I_2 in hexadecane in the degenerate three-pulse configuration with orthogonal pump polarizations. The signal appears to be symmetric with delay time and no beats are observed to within the signal-to-noise ratio. The curves in Fig. 3 compare the experimental result with two very different calculations. The dashed curve assumes mostly inhomogeneous broadening with a homogeneous width of 30 cm^{-1} while the solid curve uses no inhomogeneous broadening and a homogeneous width of 415 cm^{-1}. Either set of parameters provides an acceptable fit to both the solution phase absorption and the photon echo decay, demonstrating the difficulty in distinguishing between models for the electronic spectral broadening. However, reducing the homogeneous width below about 25 cm^{-1} does lead to a definite beat at positive times which is inconsistent with experiment.

The points in Fig. 4 show the three-pulse nondegenerate signal for azulene in cyclohexane with orthogonally polarized pump pulses. The broadband pump pulses overlap both the electronic origin and the first strong vibronic band, generating clear beats in the signal. The curve compares the experimental signal with that calculated from the Fourier transform of the product of the absorption spectrum and the laser power spectrum. The agreement is reasonably good, suggesting that the electronic transition is essentially homogeneously broadened on the time scale of the orientational relaxation. The signal decay observed for azulene excited near the electronic origin (not shown) also agrees well with the calculation for pure homogeneous broadening.

In contrast with our previous study of rhodamine B in alcohols,[12] the present results in nonpolar solvents at room temperature provide no clear evidence for inhomogeneous broadening. Any inhomogeneity that may exist at short times is presumably washed out by spectral diffusion within the 4-8 ps reorientational time. The general utility of exploiting the short lifetime of an orientational grating to truncate the experimental waiting time is questionable, as rotation of the chromophore seems likely to randomize the solvent-solute interactions that lead to the instantaneous differences in electronic absorption frequency. Experiments employing temporally long, incoherent pulses can aid in separating homogeneous and inhomogeneous contributions to the electronic linewidth in solids where there is a quasi-static contribution to the width, but appear much less useful in the liquid state. The three-pulse stimulated photon echo with femtosecond pulses should be the cleanest way to use four-wave mixing to reveal time scales for spectral diffusion in liquids, although full interpretation of the data still requires a detailed multilevel model for the vibrational structure of the electronic transition.

1. N. Morita and T. Yajima, *Phys. Rev. A* **30**, 2525 (1984).
2. T. Kobayashi, A. Terasaki, T. Hattori and K. Kurokawa, *Appl. Phys. B* **47**, 107 (1988).
3. M.A. Dugan and A.C. Albrecht, *Phys. Rev. A* **43**, 3922 (1991).
4. F. Moshary, M. Arend, R. Friedberg and S.R. Hartmann, *Phys. Rev. A* **46**, R33 (1992).
5. A.M. Weiner, S. De Silvestri and E.P. Ippen, *J. Opt. Soc. Am. B* **2**, 654 (1985).
6. Y.S. Bai and M.D. Fayer, *Chem. Phys.* **128**, 135 (1988).

7. J.-Y. Bigot, M.T. Portella, R.W. Schoenlein, C.J. Bardeen, A. Migus and C.V. Shank, *Phys. Rev. Lett.* **66**, 1138 (1991).
8. E.T.J. Nibbering, D.A. Wiersma and K. Duppen, *Phys. Rev. Lett.* **66**, 2464 (1991).
9. T. Joo and A.C. Albrecht, *Chem. Phys.* **176**, 233 (1993).
10. B.S. Wherrett, A.L. Smirl and T.F. Boggess, *IEEE J. Quantum Electron.* **QE-19**, 680 (1983).
11. A.B. Myers and R.M. Hochstrasser, *IEEE J. Quantum Electron.* **QE-22**, 1482 (1986).
12. R. Zhang, T.-S. Yang and A.B. Myers, *Chem. Phys. Lett.* **211**, 541 (1993).
13. T.-S. Yang, R. Zhang and A.B. Myers, in preparation.

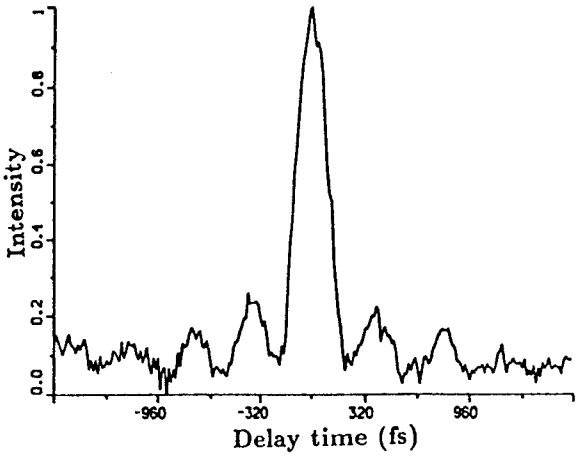


Figure 1. Experimental three-pulse degenerate four-wave mixing signal for I_2 vapor, parallel pump polarizations, 562 nm, pressure 14.8 Torr. The zero of time is arbitrary.

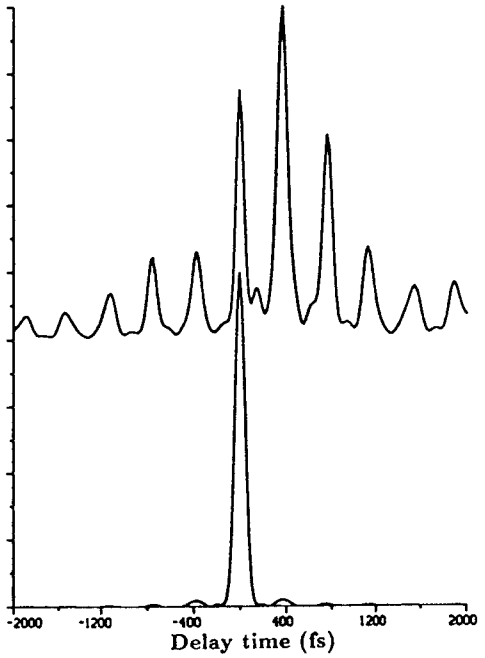


Figure 2. Theoretical signal for I_2 vapor calculated assuming no energy randomization during the waiting time (top) and complete rotational energy randomization (bottom).

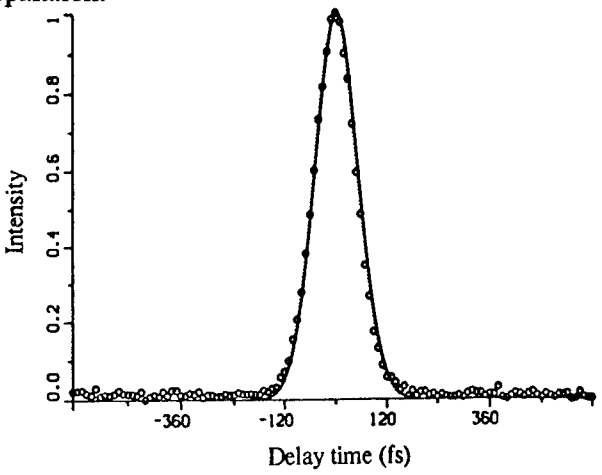


Figure 3. Experimental degenerate three-pulse four-wave mixing signal for 3 mM I_2 in hexadecane (open circles) with perpendicular pump polarizations, 560 nm, compared with calculated curves assuming homogeneous and inhomogeneous widths of 30 and 340 cm^{-1}, respectively (solid), and 415 and 0 cm^{-1}, respectively (dashed). The two calculated curves are nearly indistinguishable.

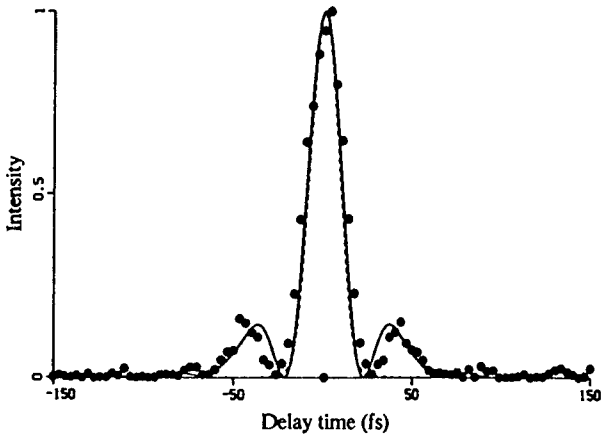


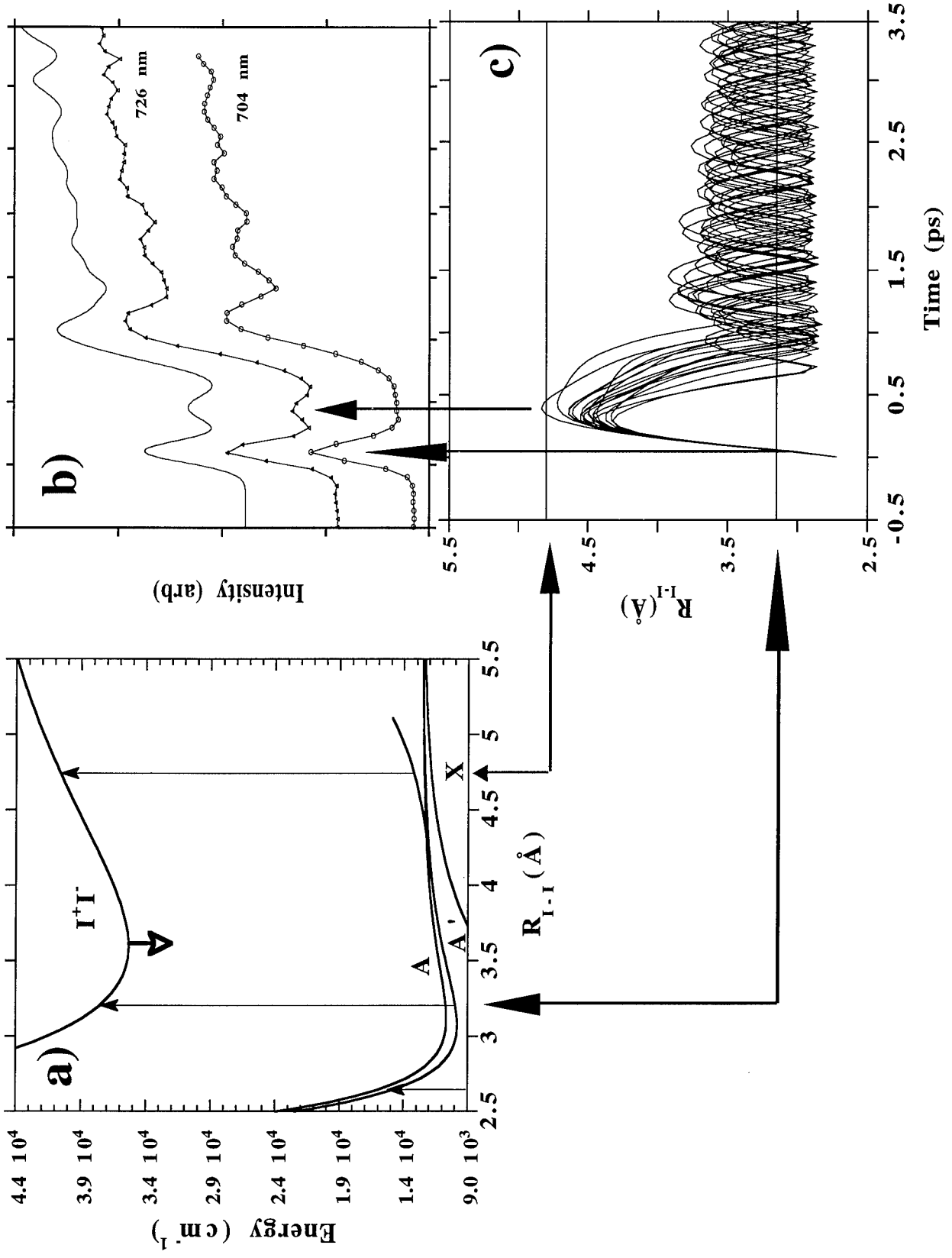
Figure 4. Experimental three-pulse nondegenerate four-wave mixing signal for 1 mM azulene in cyclohexane (points) using perpendicularly polarized pump pulses centered at 680 nm, probed at 532 nm. Curve: calculated signal for purely homogeneous broadening.

Coherence in photodissociation-recombination dynamics of I_2 isolated in rare gas solids

R. Zadoyan, Z. Li, C. C. Martens and V. A. Apkarian
Department of Chemistry
University of California
Irvine, CA 92717
phone: (714) 856-6851

I_2 doped rare gas solids are studied as prototypes of condensed phase reactive photodynamics. Moreover, given the large body of work on I_2 in different phases, detailed comparisons between solids, clusters, liquids and high pressure gas environments is possible; leading to a deeper understanding of the origin and fate of coherences in many-body dynamics. Of particular interest are photodissociative pumping experiments, in which the details of recoil and recombination are controlled by the details of solute-solvent interactions, which as will be described, can be probed by femtosecond pump-probe studies.

$I_2(A^3\Pi_{1u})$ excited above its dissociation limit in solid Ar or Kr, can be probed by laser induced fluorescence from the ion-pair states.[1] The relevant potential energy surfaces are shown in figure (a). Due to the double valued nature of the difference potential between A/A' and β/D' surfaces, for a given probe wavelength two molecular configurations are simultaneously interrogated, as shown in (a). The outer resonance occurs at large enough I-I distances to probe the cage wall directly. Transients obtained with a time resolution of 180 fs, and at pump wavelengths of 704 and 726 nm are shown in (b), along with the theoretical reproduction of the 726 nm data (top trace in (b)). The signal can be understood by making reference to the ensemble of trajectories shown in (c). Upon creation on the repulsive wall of the A state, the I-I bond stretches to ~ 4.6 Å, pushing the cage atoms away. The fragments then recoil, after losing energy to the lattice by creating shock waves. The caged fragments subsequently undergo vibrational relaxation in the bound part of the molecular potential. The initial stretch over the inner window, at 3.2 Å, is captured as the response limited first peak in the signal. The collision with the cage, which occurs at t~400 fs, is captured by the outer window in the 726 nm transient. This is the only contribution of the outer window to the signal. In the case of the 704 nm data, the trajectories do not reach the outer window. The first recursion to the inner window occurs at a delay of ~ 1ps, followed by oscillations with a period of 0.5 ps which last up to ~5 ps. The oscillations persist after complete loss of the excess energy, and significant loss of vibrational energy of the recombinant fragments. For such oscillations to be observable, the initially prepared wavepacket must remain localized, i.e. partially coherent. The extent of coherence is gauged by the depth of modulation of the signal. To reproduce the contrast, the zero-point motion of the lattice has to be incorporated in the simulations. This is accomplished by appropriately scaling temperatures in the classical simulations.[2] Details of the simulations, including the


a)
b)
c)
I+I-
A
A'
X
726 nm
704 nm
Energy (cm-1)
Intensity (arb)
RI-I (Å)
Time (ps)

method used in inverting trajectories to reproduce experimental observables, will be delineated.

Extensive measurements and simulations, as a function of temperature and energy, in Ar and Kr, have been conducted. These allow the conclusion that the nature of the initial molecule-cage collision controls the coherence in subsequent dynamics. The extent of coherence, at cryogenic temperatures of 7 K - 45 K, is found to be mainly determined by the zero-point fluctuations of the lattice; namely, the sampling of initial conditions in phase space. Due to the absence of structural order, and the larger phase space accessible in the liquid phase, the same dynamics cannot be sustained there.[3] These considerations are more delicate in the case of clusters, in which coherent dynamics can be sustained at low excess energies and in well defined, monodisperse cluster sizes and geometries.[4]

Although the caging of I_2 is complete in Ar and Kr, in Xe the ion-pair state is reactive and leads to dissociation of the molecule via ionic potentials. This reactive dynamics is akin to the condensed phase harpoon reactions, which show an inverse cage-effect, which has previously been characterized in both liquid[5] and solid rare gases.[6]

In contrast with the A state, excitation into the $B(^3\Pi_0)$ or $^1\Pi_{1u}$ states of I_2 doped rare gas solids, leads to fast vibronic relaxation, predissociation, and dephasing, precluding the observation of any coherent dynamics in real-time. Resonant Raman measurements reinforce the prior experiments[7] and theoretical treatments[8] of this system, which conclude that dephasing times range between 50 and 200 fs. Vibronic relaxation in the B state is complete in 6 ps, predissociation is complete in ~ 1ps. Nevertheless, caging of the predissociated molecule is complete in both Ar and Kr, even when the molecule is prepared at excess energies of ~1eV. Although recombination of the caged fragments on the A/A' surfaces is observed, all coherence is lost in this case. The vibrational relaxation times are well predicted by single surface, classical simulations. The dephasing and predissociation time scales are determined by electronic mixing among the dense manifold of states. The loss of coherence in recombination can be attributed to feedback from the strongly driven lattice.

References

1. R. Zadoyan, Z. Li, P. Ashjian, C. C. Martens, Chem. Phys. Lett. (in press).
2. J. P. Bergsma, P. B. Berens, K. R. Wilson, D. R. Fredkin, and E. Heller, J. Phys. Chem. **88**, 612 (1984).
3. A. H. Zewail, M. Dantus, R. M. Bowman and A. Mokhtari, J. Photochem. and Photobiol. A-Chemistry, **62**, 301 (1992).
4. Q. Liu, J. Wang and A. H. Zewail, Nature, **364**, 427 (1993).
5. R. Zadoyan and V. A. Apkarian Chem. Phys. Lett. **206**, 475 (1993).
6. M. E. Fajardo, R. Withnall, J. Feld, F. Okada, W. G. Lawrence, L. Wiedeman, and V. A. Apkarian, Laser Chem., **9**, 1(1988).
7. J. M. Grzybowski and L. Andrews, J. Raman Spectrosc. **4**, 99 (1975).
8. H. Kono and S. H. Lin, J. Chem. Phys. **84**, 1071 (1986).

Single-shot, pulse-length-limited ultrafast transient-absorption spectroscopy

John T. Fourkas, Lisa Dhar and Keith A. Nelson

Department of Chemistry, Massachusetts Institute of Technology, Cambridge, Massachusetts 02139. (617) 253-1562

In solids and viscous liquids, irreversible ultrafast dynamics, such as high-intensity processes and photo-induced chemical reactions, have to date proven difficult to study spectroscopically. In low-viscosity liquids, such processes can be monitored with conventional ultrafast techniques, so long as the liquid is flowed fast enough that each set of laser pulses interrogates a new portion of the sample. Such an approach is not practical in solids or viscous liquids, however.

One approach to applying ultrafast spectroscopic techniques to the study of irreversible processes in such samples is to develop a means of taking an entire data set in a single laser shot. Indeed, single-shot, time-resolved spectroscopic techniques were developed soon after the dawn of ultrafast lasers [1, 2]. The impetus for using these methods, which revolved around the spatial encoding of temporal information, arose from the generally low repetition rates of early picosecond lasers. However, as it became possible to produce shorter laser pulses at higher repetition rates, limited time resolution became an important constraint in single-shot techniques. At present, the prevalent practice in ultrafast spectroscopy is to delay variably the time between excitation and probe pulses, recording data on a point-by-point basis along the time axis and averaging the signal over thousands of laser shots. Nevertheless, even in low-viscosity liquids the advantages of single-shot time-resolved spectroscopy are undeniable, both for its insensitivity to shot-to-shot laser fluctuations and its fast data-collection rate.

We have recently demonstrated a new scheme for obtaining ultrafast transient-absorption

data sets in a single laser shot, using the spatial encoding of temporal information [3]. Pump and probe beams, which are separated by an angle that is generally much less than 90°, are cylindrically focussed such that their focal lines are spatially coincident within a sample. Because the pump and probe pulses reach different parts of the sample at different times, the inter-pulse delay is spatially encoded along the length of the sample. The transient-absorption information is then contained in the spatial intensity profile of the probe beam. This geometry is similar to ones used previously in single-shot autocorrelation schemes [4, 5]. As opposed to the geometries used in earlier single-shot transient-absorption techniques [1, 2], our geometry is capable of providing pulse-length-limited resolution with laser pulses as short as tens of femtoseconds in samples of readily attainable thicknesses [6].

The experimental setup is shown in Fig. 1. The pump and probe beams are both incident on a cylindrical lens that focusses the two beams onto a common focal line in a thin sample or a sample in which the pump beam is completely absorbed in a short distance. To normalize for shot-to-shot fluctuations in the intensity profile of the probe beam, a reference beam is incident on the sample before the pump beam. This reference beam is brought in to the first lens parallel to and directly below the probe beam, such that it interrogates the same part of the sample as the pump and probe beams (see Fig. 1). The probe and reference beams are then collimated and imaged onto a CCD, which records their spatial profiles every laser

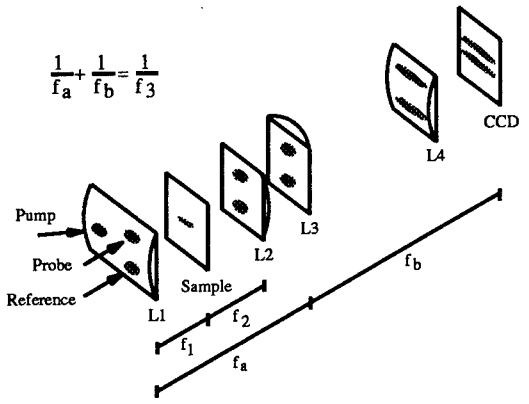


Figure 1. Experimental setup for single-shot transient-absorption experiment. The L's are lenses and the f's focal lengths.

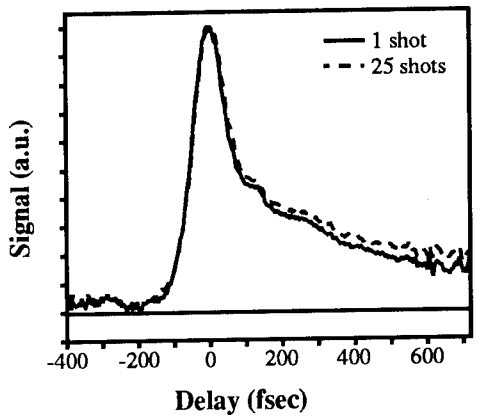


Figure 2. Single-shot data taken on ethyl violet in methanol with one and 25 laser shots. Note the 155-fs oscillations.

shot. To normalize for the intensity profile of the excitation beam, data are recorded in a sample that has an essentially constant response on the scale of the time encoded in the experiment, a few picoseconds.

Shown in Fig. 2 are two typical data sets, taken on a 100-μm-pathlength optical cell of ethyl violet in methanol, one set in a single shot and one set with 25 shots. The 620-nm laser pulses were 72 fs in duration and were separated by an angle of 25°. A normalization scan for the pump-beam profile was taken in a similar cell, using a solution of cresyl violet in methanol. The signal-to-noise ratio of the single-shot data set is comparable to that of the 25-shot data set. From standard transient-absorption data, ethyl violet is known to display a 155-fs molecular-vibrational oscillation [7] that is clearly evident in these data. To test the time resolution of our data, we have convolved the known response of ethyl violet with the instrument response function expected for 72-fs pulses in a standard, collinear pump/probe experiment. This curve provides an excellent fit to the data, showing that they are indeed pulse-length-limited.

These data demonstrate the great promise of single-shot ultrafast spectroscopy in studying irreversible phenomena on a femtosecond time scale. This and related techniques will open to investigation a wide range of samples that cannot be studied with conventional ultrafast techniques.

References

[1] M. Malley and P. M. Rentzepis, Chem. Phys. Lett. **3** , 534 (1969).

[2] M. R. Topp, P. M. Rentzepis, and R. P. Jones, Chem. Phys. Lett. **9,** 1 (1971).

[3] L. Dhar, J. T. Fourkas, and K. A. Nelson, Opt. Lett. (in press).

[4] A. Brun, P. Georges, G. Le Saux, and F. Salin, J. Phys. D **24,** 1225 (1991).

[5] D. J. Kane and R. Trebino, Opt. Lett. **18,** 823 (1993).

[6] J. T. Fourkas, L. Dhar, K. A. Nelson, and R. Trebino, submitted to JOSA B.

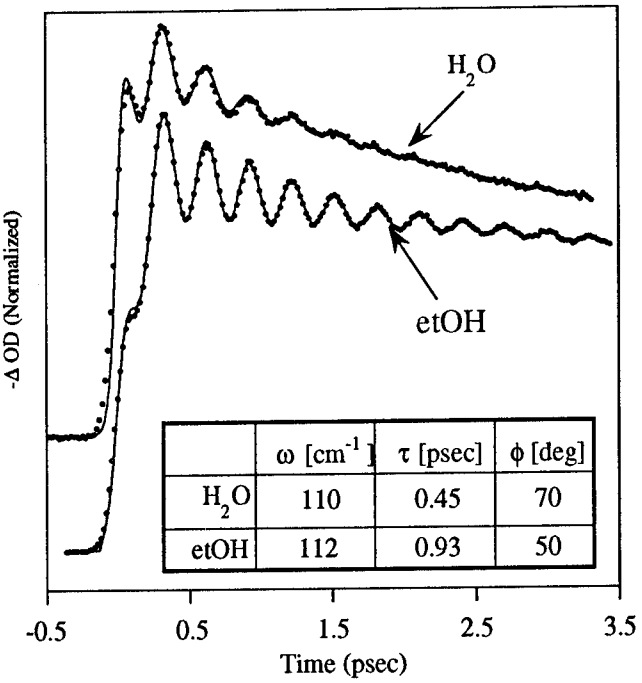
[7] F. W. Wise, M. J. Rosker, and C. L. Tang, J. Chem. Phys. **86,**2827 (1987).

THE "DYNAMICAL HOLE"; GROUND STATE VIBRATIONAL COHERENCE INDUCED BY RESONANT IMPULSIVE EXCITATION

Uri Banin, Allon Bartana, Sanford Ruhman and Ronnie Kosloff
Department of Physical Chemistry and the Fritz Haber and Farkas Research Centers, the Hebrew University, Jerusalem 91904, Israel, Tel. 972-2-585485

Resonant impulsive excitation creates vibrational coherence on the ground electronic surface, through the Resonant Impulsive Stimulated Raman Scattering process (RISRS)[1]. The ensuing vibrational motion has been detected in various schemes as periodical modulations in transient scattering or transmission of the delayed probe pulse[2]. An example for this process was observed by us in the photodissociation experiments of the I_3^- ion in different polar solvents[3]. The results for two solvents, water and ethanol, are presented in figure 1. Periodic modulations in the transient transmission of the 308 nm probe pulse are seen, the strong solvent dependence of the decay of the modulations is evident. The modulations are assigned to coherence in the ground state symmetric stretch vibration of triiodide. A general framework for interpreting these results is required. We chose to model the phenomena within a quantum mechanical model which takes into consideration strong field effects, solvent induced dissipation and thermal population.

The qualitative understanding of the experimental result can be obtained from a wavepacket calculation, solving the time dependent Schroedinger equation for two electronic surfaces coupled by the optical electric field. The impulsive excitation, by transferring part of the amplitude to the excited state, creates a *"dynamical hole"* on the ground electronic surface. The "dynamical hole" oscillates and modulates the transient transmission spectrum as observed in the experiment.



	ω [cm^{-1}]	τ [psec]	ϕ [deg]
H_2O	110	0.45	70
etOH	112	0.93	50

Figure 1: Transient absorption at 308 nm for triiodide in water and ethanol. The convoluted fit is shown along with the experimental data. The physically significant fit parameters are given in the table.

The impulsive light-matter interaction is approximated by a coordinate dependent two level formalism, enabling the analysis of this complicated process in terms of a well understood and illustrative model. For a short enough pulse the nuclear motion is frozen, this points out to the choice of the inverse mass 1/M as a perturbation paramater. The model results in a closed and simple formula for the ground and excited state wavepackets after the excitation. These equations serve as the main interpretive tool of the RISRS pump probe experiment. For short enough pulses, the picture obtained, is that the pump pulse carves out of the original ground

surface wavefunction a piece which is eliminated via the excited surface. The missing piece on the ground surface is the dynamical "hole". The maximum effect is obtained at the point of resonance, which can be controlled by tuning the carrier frequency of the pulse. Figure 2 compares the results of the two level approximation with the numerical solution for V=2 of the I_3^- symmetric stretch. The two level concepts of π and 2π cycling is also expected to occur for intense and short enough pulses.

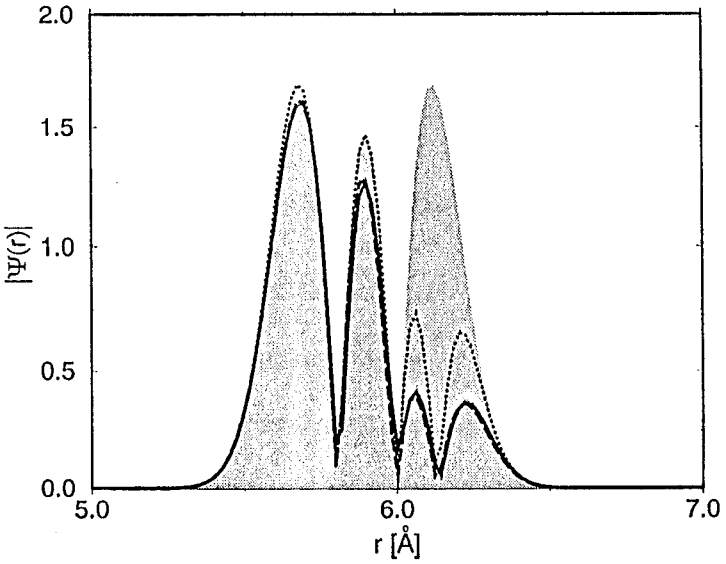


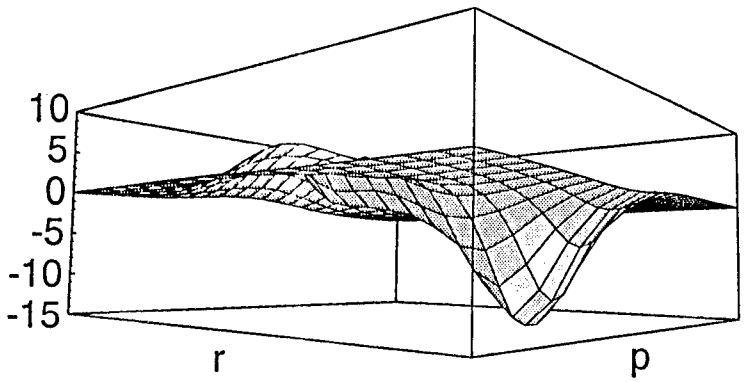
Figure 2: The ground surface wavefunction after the pump pulse (308 nm, 10 fsec). The initial state (shaded) is v=2. The impulsive approximation for a square pulse (dashed line), is compared to the numerical solution (solid line). Also shown, is the model result for a gaussian pulse (dotted line).

The "dynamical hole" missing on the ground state is not a pure state, the earlier concept of an "Anti-Wavepacket" on the ground state is thus wrong. Alternatively, a density matrix formalism must be incorporated in order to strictly define the "hole" as a dynamic density:

$$\rho_d = \rho_t - c_0^2\rho_0 - c_1^2\rho_1 \ldots - c_m^2\rho_m \qquad \text{----eq. 1}$$

Where $\rho_m = |\phi_m\rangle\langle\phi_m|$ and ϕ_m are the energy eigenfunctions. The density operator ρ_t describing the ground state after the pump interaction is decomposed into a static and dynamic part - ρ_d. In the energy representation, this reduces to separating ρ into its diagonal elements which are not effected by pure dephasing and will be identified as the static part, and the off diagonal elements which are the dynamical portion. The dynamical hole after a pump interaction is best visualized in phase space as shown in figure 3. An initial thermal density at 300 K was pumped by a 60 fsec pulse at 308 nm. By definition, the norm of the dynamical hole equals zero, the positive and negative portions cancel out. Solution of the Liouville von-Neumann equation including solvent induced vibrational and electronic dephasing, enables following the dynamics of the hole within a dissipative environment[4]. In one vibrational period, the hole is seen to complete a full cycle in phase space, and vibrational

Figure 3: The dynamical "hole" in phase space immediately after it was created. The initial density is a thermal distribution at 300 K.



dephasing gradually diminishes the amplitude of both the positive and negative parts. Within several vibrational periods, vibrational dephasing causes complete loss of coherence - the hole is "filled up".

A quantitative measure of the created coherence is an important tool in the analysis. The integrated square density of the dynamical hole serves as a natural definition of this measure:

$$C^2 = \mathrm{tr}\,\{\rho_d^{\,2}\} \qquad \text{----eq. 2}$$

Figure 4 shows the coherence measure as a function of time for the full simulation of the pump-probe experiment. It first shows a buildup of coherence during the pump pulse and then its disappearance due to vibrational dephasing. The simulated pump-probe signal is also shown, The modulations are fit to an exponentially decaying sine function. The decay time of 960 fsec, agrees well with the decay time of the coherence measure demonstrating it's quantitative significance.

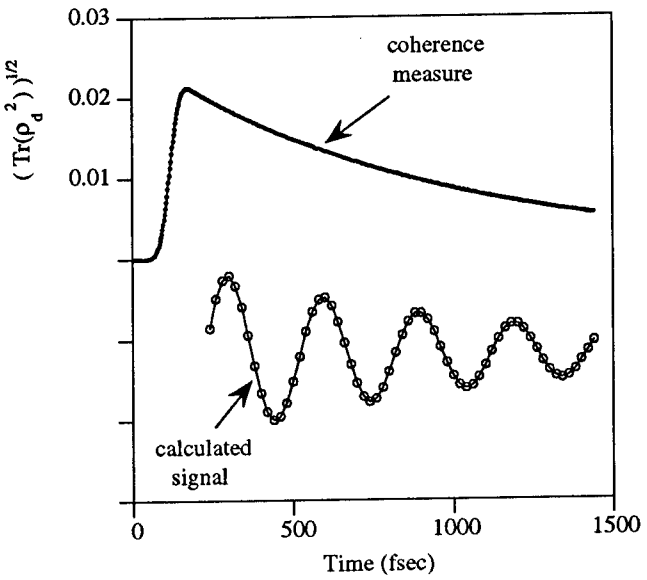


Figure 4: The coherence measure as a function of time (upper panel) for a full simulation of the pump probe experiment. An electronic dephasing time of 5 fsec, and vibrational dephasing time of 960 fsec have been used. The calculated signal is shown in the bottom panel.

The calculated signal can be directly compared to the experimental results of figure 1. The frequency of modulations, the phase and the decay times are all in good agreement. Another experimental observation is the amplitude to bleach ratio, which differs substantially between the calculation and experiment. Possible explanations for this discrepancy will be discussed.

The numerical tools developed can now be used for a comprehensive study of the effects of various pulse parameters and solvent induced processes on the signal. Effects of varying the pump and probe durations, frequencies and intensities are adressed. The intensity may be varied far beyond the weak pulse regime, into the domain of intense pump pulses common in many ultrafast studies. Electronic dephasing effects, specifically during the pump process, have been studied, and observably cause a degradation of the vibrational coherence induced by the excitation.

The complexity of the phenomena revealed by the experimental results, requires close partnership between the experiments, numerical simulations and illustrative theoretical models.

---

1) Y. X. Yan, L. T. Cheng, and K. A. Nelson, in *Advances in Nonlinear Spectroscopy*, Eds. R. G. H. Clarke, R. E. Hester, Wiley, New York (1987).

2) For numerous examples: See *Ultrafast Phenomena VIII*, Eds. J.-L. Martin, A. Migus, G. A. Mourou, and A. H. Zewail, Springer Verlag (1993).

3) U. Banin and S. Ruhman, J. Chem. Phys. **96**, 4391 (1993).

4) A. Bartana, R. Kosloff and D. Tannor, J. Chem. Phys. **99**, 196 (1993).

Friday, May 6, 1994

Dynamics in Solution

FA 8:30am–10:00am
Dana Point Ballroom

Benny Gerber, *Presider*
University of California, Irvine

Vibrational Dynamics in Liquids and Glasses Probed with Infrared Photon Echoes Using a Free Electron Laser

A. Tokmakoff, D. Zimdars, and M. D. Fayer
Department of Chemistry
Stanford University, Stanford, California 94305

Molecular vibrations are involved in a vast number of physical, chemical, and biological processes. Coupling between molecular vibrations and external mechanical degrees of freedom (heat bath) is responsible for the flow of energy into and out of molecules and for thermally activated processes. Fluctuations of vibrational energy levels of a molecule caused by interactions with a dynamic environment are important in fundamental chemical and biological processes, such as electron transfer and chemical reactions. In spite of the importance of the coupling of molecular vibrations to a heat bath, relatively little is known about the temperature dependent dynamics of molecular vibrations in liquids and glasses. Here we give an account of the first ps infrared (IR) vibrational photon echo experiments performed on molecular vibrations in liquids and glasses [1,2]. The photon echo experiment is an optical line narrowing experiment that has been applied extensively to the study of electronic excitation dynamics in condensed matter systems [3-6]. However, the study of vibrations in condensed phases using photon echoes has been limited because of the need to work with ps IR pulses. Very recently the first vibrational Raman echoes were performed [7] and a vibrational photon echo study of a group attached to a surface in high vacuum was conducted [8].

In general, coupling of vibrations to a bath is substantially weaker than the coupling of electronic states. This is demonstrated by the fact that vibrational transition energies have much smaller percentage gas to "crystal" shifts than electronic transitions. The weaker coupling makes it possible to perform vibrational photon echoes in liquids with relatively long pulses (~2 ps) that have narrow enough bandwidths that only a well defined pair of states is coherently coupled by the radiation field. Thus, the observed dephasing of the vibrational transition arises from coupling to the heat bath. By passing through the glass/liquid transition, it is possible to observe how the change of state influences the vibrational dynamics.

In principle, dynamic information can be obtained from vibrational lineshape analysis. However, in glasses and liquids a vibrational absorption line can have a contribution from inhomogeneous broadening caused by a variety of local solvent structures that surround the molecule of interest. In low temperature glasses, under most circumstances it is expected that inhomogeneous broadening will totally mask any contribution from the homogenous line. Therefore, the lineshape provides no information on dynamics. Even in liquids, a major contribution to a vibrational absorption line can come from inhomogeneous broadening. The functional form of a lineshape can not by itself distinguish between a homogeneously broadened and inhomogeneously broadened line. The shape of an inhomogeneously broadened line is determined by the coupling mechanism responsible for the inhomogeneous broadening. For example, static dipole-dipole coupling can give rise to a Lorentzian inhomogenous lineshape.

The photon echo experiment overcomes this problem by removing the inhomogeneous contribution from the line. In an vibrational photon echo experiment, two ps IR pulses tuned to the molecular vibration are crossed in the sample. One of the pulses is delayed. The echo is a third pulse that emerges form the sample in a unique direction. In the experiment, the intensity of the echo pulse is measured as a function of the delay between the two excitation pulses. As the separation between the pulses is increased, the echo decays. The echo decay is the Fourier transform of the homogeneous line. For a Lorentzian homogenous line, the echo signal decays as

$$I(\tau) = I_0 \exp\left(-4\tau/T_2\right) \tag{1}$$

where T_2 is the homogeneous dephasing time. The Fourier transform of the exponential decay is a Lorentzian, with homogeneous linewidth $1/\pi T_2$. There are two contributions to the homogenous linewidth, the vibrational lifetime (T_1) and the vibrational pure dephasing (T_2^*), i. e.,

$$1/\pi T_2 = 1/\pi T_2^* + 1/2\pi T_1 . \tag{2}$$

The vibrational pure dephasing is caused by fluctuations in the vibrational energy levels induced by coupling to the dynamic environment of the molecule. T_2^* is obtained by measuring T_2 with the vibrational echo experiment and T_1 with a pump-probe experiment.

Vibrational photon echo experiments were conducted on the CO asymmetric stretching mode of tungsten hexacarbonyl ($W(CO)_6$) in 2-methytetrahydrofuran (2-MTHF) [1] and in 2-methylpentane (2-MP) [2]. Additional IR pump-probe experiments [9] and IR pump/anti-Stokes Raman probe experiments [10] were conducted on $W(CO)_6$ and $Cr(CO)_6$ in CCl_4 and $CHCl_3$ as well as in 2-MTHF and 2-MP. The experiments were performed at a wavelength of 5.06 μm (~1980 cm^{-1}) These metal carbonyls were first studied by Heilweil and co-workers using pump-probe experiments at room temperature [11].

The photon echo experiments were conducted with the Stanford superconducting-linear-accelerator-pumped free electron laser (FEL). The FEL emits a 2 ms macropulse at a 10 Hz repetition rate. Each macropulse consists of ~0.5 μJ micropulses at a repetition rate of 11.8 MHz. The micropulses were measured to be Gaussian ~ 1.5 ps transform limited pulses by performing autocorrelations in $AgGaSe_2$. The micropulse repetition rate of 11.8 MHz was reduced to 50 kHz by a germanium AOM single pulse selector which provided 90% pulse selection efficiency. The effective experimental repetition rate is 1000 pulses/s. The signal and a reference were measured with two HgCdTe detectors sampled by a pair of gated integrators. The gated integrators were read out by a computer with a 16 bit A/D board. The computer also controlled a stepper motor delay line with a total travel corresponding to 330 ps.

The single IR pulse is beam split by a 10% (pump-probe) or 30% (photon-echo) coated zinc selenide (ZnSe) beam splitter. The reflected pulse (the probe pulse or first pulse in the echo sequence) was passed down a computer controlled stepper motor delay line. The transmitted pulse (the pump pulse or second pulse in the echo sequence) was chopped at half the single pulse rate by a second germanium AOM. The IR pulses were made parallel and then focused to 200 μm into the sample using an off axis parabolic reflector. For the pump-probe experiment the energy in the pump pulse was ~200 nJ and the energy in the probe was ~20 nJ. The maximum change in transmitted intensity was less than 1%. For the photon echo experiment the second pulse was ~150 nJ and the first pulse was ~60 nJ. The sample was sealed with a 100 μm Teflon gasket between two CaF_2 flats, and the temperature was controlled using a closed cycle refrigerator.

Figure 1 displays photon echo data taken $W(CO)_6$ in 2MTHF at 16 K, and the inset shows a semi-log plot of the data. The echo decay is a single exponential following a very fast feature around τ=0. In Fig. 1, the data decays in 15 ps yielding a T_2 of 60 ps. The homogeneous linewidth ($1/\pi T_2$) is 5.2 GHz. The pure dephasing time, T_2^*, can be found by removing the contribution to T_2 from the population decay of the excited vibrational state using eq. (3). At 16K, T_1 is 44 ps, yielding a pure dephasing time, T_2^*, contribution to the homogeneous linewidth of 1.6 GHz. This is in contrast to the absorption spectrum which is 15 cm^{-1} wide at 16 K. It is clear from these results that the vibrational spectrum in the glass is massively inhomogeneously broadened. Fig. 2 shows temperature dependent echo data plotted as linewidths. The open squares are the homogeneous linewidths, $1/\pi T_2^*$, and the filled squares are the pure dephasing linewidths $1/\pi T_2^*$ calculated using eq. 3. The T_1 values were obtained from pump-probe experiments conducted at each temperature. The vertical line at 88 K marks the glass to liquid transition temperature, T_g. Although the time resolution was insufficient to determine the echo decay time above 140K, it was possible to make photon echo decay measurements in the liquid state 50 K above T_g. In contrast to the experiments on $W(CO)_6$ in 2MTHF, it was possible to obtain photon echo data in the 2MP solvent from the room temperature liquid down to 10 K. This data is displayed in fig. 3. Tg = 88 K in 2MP. Like the data taken in 2MTHF, at low temperatures the change in the homogeneous linewidth with temperature is very gradual. In both

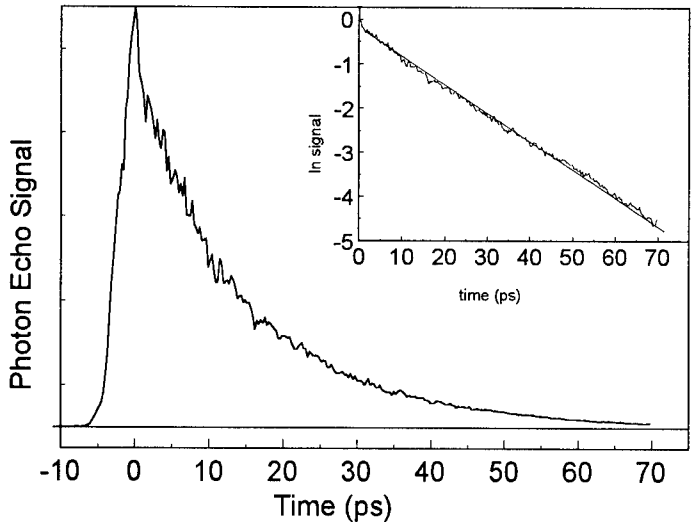


Figure 1 - Photon echo data for $W(CO)_6$ in 2-MTHF at 16 K.

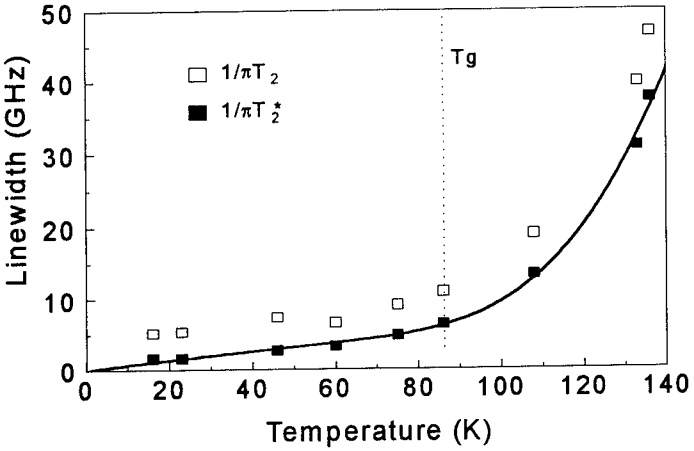


Figure 2 - Temperature dependence of the homogeneous linewidth of $W(CO)_6$ in 2-MTHF.

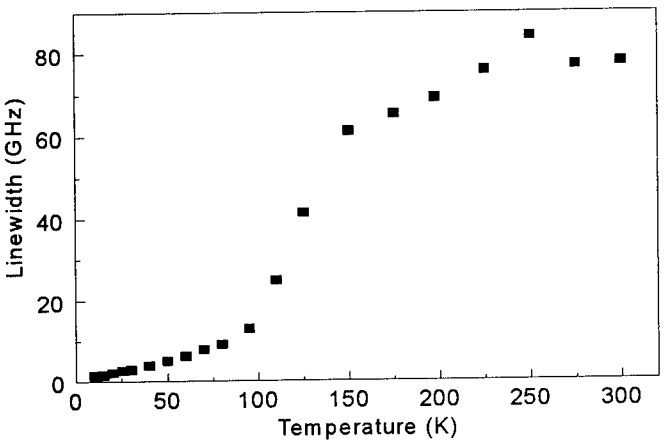


Figure 3 - Temperature dependence of the homogeneous linewidth of $W(CO)_6$ in 2-MP.

solvent systems there is an apparent change in the functional form of the temperature dependence at ~T_g. The low temperature portion of the data, below T_g, may arise from the dynamics of the tunneling two level systems in the glass [3, 12].

One thing that is clear even at this early stage of this type of experimental investigation: vibrational spectral lines in liquids can be inhomogeneously broadened even at room temperature. The experiments described briefly above are being continued and will be combined with investigations of vibrational population dynamics using ps IR pump-probe experiments [9] and IR pump-Raman probe experiments [10] to obtain a detailed understanding of vibrational dynamics in liquids and glasses.

Acknowledgments

The authors gratefully acknowledge the Professor Alan Schwettman and Professor Todd Smith and their groups at the Stanford FEL whose dedicated work made these experiments possible. This work was supported by the Medical Free Electron Laser Program (N00014-91-C-0170), the National Science Foundation (DMR90-22675), and the Office of Naval Research (N00014-92-J-1227-P02).

References

1. D. Zimdars, A. Tokmakoff, S. Chen, S. R. Greenfield and M. D. Fayer, Phys. Rev. Lett., **70**, 2718 (1993).
2. A. Tokmakoff, D. Zimdars, B. Sauter, R. Francis, and M. D. Fayer, submitted J. Chem. Phys.
3. L. R. Narasimhan, K. A. Littau, D. W. Pack, Y. S. Bai, A. Elschner, and M. D. Fayer, Chem. Rev., **90**, 439 (1990).
4. M. Berg, C. A. Walsh, L. R. Narasimhan, K. A. Littau, and M. D. Fayer, J. Chem. Phys., **88**, 1564 (1987).
5. P. C. Becker, H. L. Fragnito, J. Y. Bigot, C. H. Brito-Cruz, R. L. Fork, and C. V. Shank, Phys. Rev. Lett. **63**, 505 (1989).
6. E. T. J. Nibbering, D. A. Weirsma, and K. D. Duppen, Phys. Rev. Lett. **66**, 2464 (1991)
7. L. J. Muller, D. Vanden Bout and M. Berg, J. Chem. Phys., **99**, 810 (1993).
8. P. Guyot-Sionnest, Phys. Rev. Lett., **66**, 1489 (1991).
9. A. Tokmakoff, B. Sauter, and M. D. Fayer, Accepted J. Chem. Phys. (1994).
10. A. Tokmakoff, B. Sauter, A. S. Kwok, and M. D. Fayer, submitted to Chem. Phys. Lett. (1994).
11. E. J. Heilweil, R. R. Cavanagh and J. C. Stephenson, Chem. Phys. Lett., **134**, 181 (1987).
12. D. L. Huber, M. M. Broer, and B. Golding, Phys. Rev. Lett., **52**, 2281 (1984).

Broadband transient IR spectroscopy of metal carbonyl photochemistry

Thomas P. Dougherty
Edwin J. Heilweil

Molecular Physics Division,
Bldg. 221, Room B268
National Institute of Standards and Technology
Gaithersburg, MD 20899

(301) 975-2364 and (301) 975-2370

Introduction

A novel method for obtaining transient infrared molecular spectra with femtosecond time and high spectral resolution is described. New studies of metal-carbonyl photodissociation and solvation dynamics using this technique are described.

Femtosecond Broadband Double Beam Transient Infrared Spectrometer

The optical layout and performance of a multichannel dual-beam transient IR apparatus is published elsewhere.[1] Briefly, a 300 femtosecond, broadband (> 100 cm^{-1}) IR probe pulse is produced from two amplified dye laser pulses by difference frequency mixing in $LiIO_3$. The central wavelength of the IR pulse is approximately 5 μm (2000 cm^{-1}) and can be tuned by changing the dye laser frequencies. The IR pulse is split into a probe and reference pulse which are spatially separated at the sample, and only the probe pulse is spatially overlapped with the UV excitation pulse. After the sample, the IR pulses are independently sum-frequency mixed with visible dye laser pulses in a second $LiIO_3$ crystal to produce visible pulses which contain the frequency-dependant IR transmission information. The upconverted pulses are dispersed by a double grating spectrograph and detected by a CCD array which reports the intensity versus wavelength profile for both pulses on each laser shot. Figure 1 illustrates the optical arrangement of the probe and reference beams.

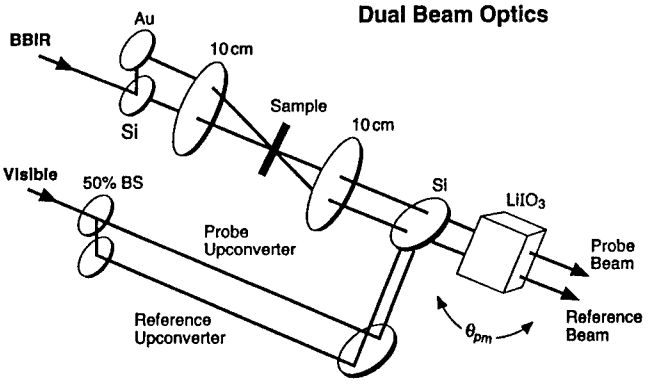


Figure 1: Optical layout of dual-beam femtosecond broadband infrared (BBIR) spectrometer illustrating the production of probe and reference IR pulses and sum-frequency mixing of the IR pulses with visible pulses for CCD detection.

A transient difference spectrum is obtained in the following manner. Normalized signal is produced by dividing the signal data by the reference data on each laser shot. The average normalized signal with the excitation pulse on is then divided by the average normalized signal with the excitation blocked to produce the transient spectrum. Generally 8000 laser shots with excitation on and blocked for alternate shots are used to collect a spectrum. With a 20 Hz laser system, a transient IR difference spectrum which is greater than 100 cm^{-1} wide and has 0.4 ps time resolution and 4 cm^{-1} spectral resolution is obtained in less than 10 minutes. The baseline noise in the resulting spectrum, $\Delta OD = 8 \times 10^{-4}$ ($\pm 1\sigma$), is approximately 6.5 times better than what is obtained without normalization under the same conditions.

Metal Carbonyl Photoreactions

The initial photochemical event for $M(CO)_6$ (M = Cr, Mo or W), $CpCo(CO)_2$ (Cp = η^5-C_5H_5) and $[CpFe(CO)_2]_2$ in room temperature solutions, involves a chemical change in the reacting species, usually the rapid loss of one CO ligand. As a result of UV excitation, absorptions at the CO-stretch frequencies of the parent species are observed to decrease (bleach) on an instrumentally limited time-scale and then remain constant at the decreased level for the remainder of the experiment (maximum Δt = 600 ps). In all cases, the observed photoproduct absorption bands are very broad near $\Delta t = 0$ and then sharpen and shift slightly to higher frequency with an approximately 10 ps time constant. While the time evolution of the product absorption bands is attributed to vibrational relaxation of lower frequency modes coupled to the CO-stretches, many of the observed photoproducts have a solvent molecule as a ligand in place of the lost CO, and the solvation process may contribute to changes in the absorption spectrum during the first few picoseconds.

A series of transient IR difference spectra for $W(CO)_6$ in n-hexane are shown in Figure 2. The characteristic features described above are readily seen. Removal of the parent species produces decreased absorption at its CO-stretch frequency, 1983 cm^{-1}. Absorption by the photoproduct is very broad initially, but well defined bands are observed by Δt = 40 ps. In addition to the expected absorption bands of the $W(CO)_5$-(n-hexane) at 1956 and 1928 cm^{-1}, two transient absorption bands are observed at 1942 and 1908 cm^{-1}. These additional bands, which are assigned to the $v = 1 \rightarrow 2$ overtones of the photoproduct CO-stretches, decay with an approximately 160 ps time constant. The results for $Cr(CO)_6$ and $Mo(CO)_6$ are qualitatively similar except for an additional unidentified photoproduct found in the $Mo(CO)_6$ experiment. CO-stretch overtone absorption has only been found in these $M(CO)_6$ species and in none of the other metal carbonyls we have studied to date.

UV photolysis of $CpCo(CO)_2$ in n-hexane found pulse duration limited kinetics for bleaches of the parent CO-stretches at 2031 and 1971 cm^{-1} and a 10 ps relaxation time for the narrowing and blue-shifting of the photoproduct (CpCo(CO)(n-hexane), **I**) absorption at 1990 cm^{-1}. When the experiment is repeated in 1-hexene, the results are similar except the photoproduct (CpCo(CO)(1-hexene), **II**) absorption is shifted to 1974 cm^{-1}. In mixed n-hexane/1-hexene solutions, photoproduct **I** is found to react rapidly with 1-hexene to form photoproduct **II**, as shown in Figure 3. The reaction of **I** with 1-hexene to form **II** was studied at six concentrations of 1-hexene (0.2 to 2.0 M), and the measured rate constant for the reaction, $1.4 \pm 0.2 \times 10^{10}$ $M^{-1}s^{-1}$, is approximately the diffusion controlled rate for this reaction (see reference 2 for more details on this experiment).

The photochemistry of $[CpFe(CO)_2]_2$ is more complex because formation of two

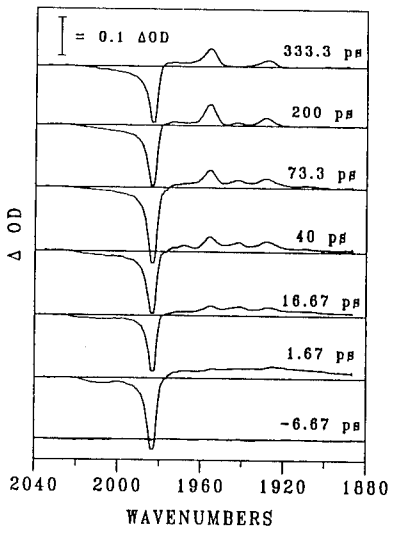


Figure 2: Time dependant IR transient difference spectra for $W(CO)_6$ in n-hexane (approx. $4x10^{-4}$ M) following UV excitation.

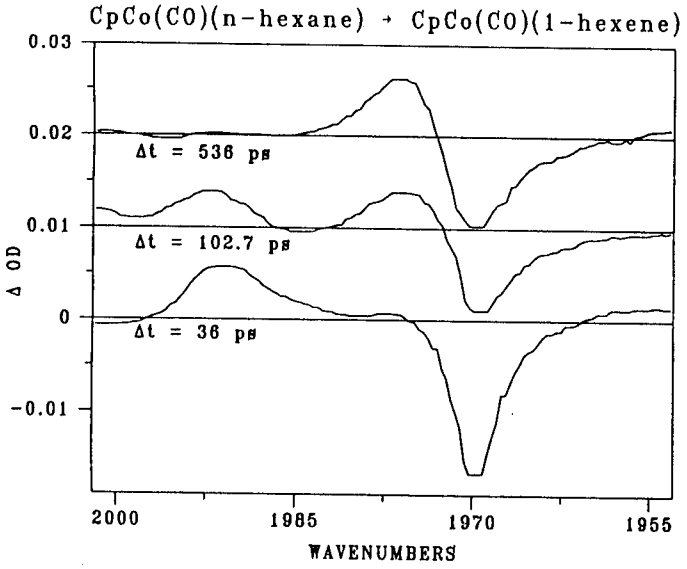


Figure 3: Transient IR spectra of $CpCo(CO)_2$ (1971 cm^{-1}) in 1-hexene/n-hexane solution ([1-hexene] = 0.6 M). 1-hexene reacts with CpCo(CO)(n-hexane) (1990 cm^{-1}) to form CpCo(CO)(1-hexene) (1974 cm^{-1}).

$CpFe(CO)_2$• radicals competes with loss of a terminal CO as the initial reaction. The CO loss product rapidly rearranges to form $CpFe(\mu\text{-}CO)_3FeCp$ or reacts with the solvent to form $Cp(CO)Fe(\mu\text{-}CO)_2FeCp$(n-hexane) (**III**). Product **III** is found to react with THF at nearly the diffusion rate to form $Cp(CO)Fe(\mu\text{-}CO)_2FeCp$(THF).

References:

1) T. P. Dougherty and E. J. Heilweil, Optics Letters 19, (Jan 15, 1994).
2) T. P. Dougherty and E. J. Heilweil, J. Phys. Chem. Communications (in press).

Chemical Substitution and Deuterium Isotope Effects on Ultrafast Intermolecular Electron Transfer: Possible Role of Molecular Vibrations

Yutaka Nagasawa†, Arkadiy P. Yartsev,‡ Keisuke Tominaga‡,
and Keitaro Yoshihara †‡

†. *The Graduate University for Advanced Studies, Myodaiji, Okazaki 444, Japan*
Tel 81-564-55-7352 Fax 81-564-54-2254

‡. *Institute for Molecular Science, Myodaiji, Okazaki 444, Japan*
Tel 81-564-55-7350

We have observed ultrafast non-exponential fluorescence quenching of 7-aminocoumarin dyes in electron donating solvents by means of femtosecond fluorescence up-conversion technique [1]. We regarded this fluorescence quenching as an ultrafast intermolecular electron transfer (ET) from the solvent to the excited dye. When the carbon chain on the amino group becomes longer, the rate of ET becomes slower, and when the amino group is fixed by hexagonal carbon ring, it becomes the slowest. Some of the fast reactions occur much faster than the diffusive solvent relaxation process. The fastest reaction with a time constant of ~200 fs was observed for coumarin 151 (C151) in N,N-dimethylaniline (DMA). In such a case, some dynamics faster than diffusive orientational polarization of the solvent is required to induce the reaction.

To examine the role of vibrations on such an ET, experiments on deuterium isotope effects were carried out. In Figure 1 (a), the fluorescence decay of coumarin 153 (C153) in AN-d7, aniline with all the hydrogens changed to deuterium (solid line), is compared with the one in normal AN-h7 (broken line), which show no difference. The lifetimes of C153 in AN-h7 are 17 ps (59 %) and 285 ps (41 %), which are somewhat longer than the solvent relaxation time of AN-h7, *i.e.*, 6.7 ps (81 %) and 13.3 ps (19 %) [2]. In Figure 1 (b), the fluorescence decay of C152 in AN-d7 (solid line) and in AN-h7 (broken line) are shown. The lifetimes of C152 in AN-h7 are 3.7 ps (41 %) and 12.4 ps (59 %), which is shorter than the solvent relaxation time. In AN-d7, it becomes slightly longer and the ratio between the reaction rate constants for AN-h7 and AN-d7 is $k_{h7}/k_{d7} = 1.1$. It can be seen that the effect of the deuteration is more effective for the reactions faster than solvation process. Therefore, the isotope effect should be related to the

processes faster than the diffusive solvent motions. The isotope effect of AN-d2, aniline with the two hydrogens on the amino group are deuterated, is shown in Figure 1 (c). This system also shows isotope effect and the ratio between the rate constants is k_{h7}/k_{d2} = 1.1. Therefore, the deuteration of the amino hydrogen seems to be much more important than that of the phenyl hydrogen.

In the present experiment, deuterium isotope effect of ultrafast intermolecular ET was observed for the first time. It was significant for the reaction faster than the diffusive solvation process, and the deuteration of the amino group was important. Therefore, it cannot be ascribed to the diffusive motion of the solvent, however, to a much faster motion such as the vibrational motion of the amino group. Solvent isotope effect of glycerol is known for intramolecular ET of metal-metal charge transfer complex [3]. In this case rotation of the hydroxyl group is treated as a librational motion which causes inertial component of the solvation process [4]. In the present intermolecular ET, AN is not only a solvent but also an electron donor. Therefore, such a motion can be treated not only as a librational mode of the solvent but also as an intra-molecular vibrational mode of the donor which induces nuclear reorganization for the reaction [5].

[1] Y. Nagasawa, A. P. Yartsev, K. Tominaga, A. E. Johnson, and K. Yoshihara, *J. Am. Chem. Soc.*, **115**, 7922, (1993).

[2] Y. Nagasawa, A. P. Yartsev, K. Tominaga, A. E. Johnson, and K. Yoshihara, to be published.

[3] K. Tominaga, D. A. V. Kliner, A. E. Johnson, N. E. Levinger, and P. F. Barbara, *J. Chem. Phys.*, **98**, 1228, (1993).

[4] S. J. Rosenthal, X. Xie, M. Du, and G. R. Fleming, *J. Chem. Phys.*, **95**, 4715, (1991).

[5] H. Sumi and R. A. Marcus, *J. Chem. Phys.*, **84**, 4894, (1986).

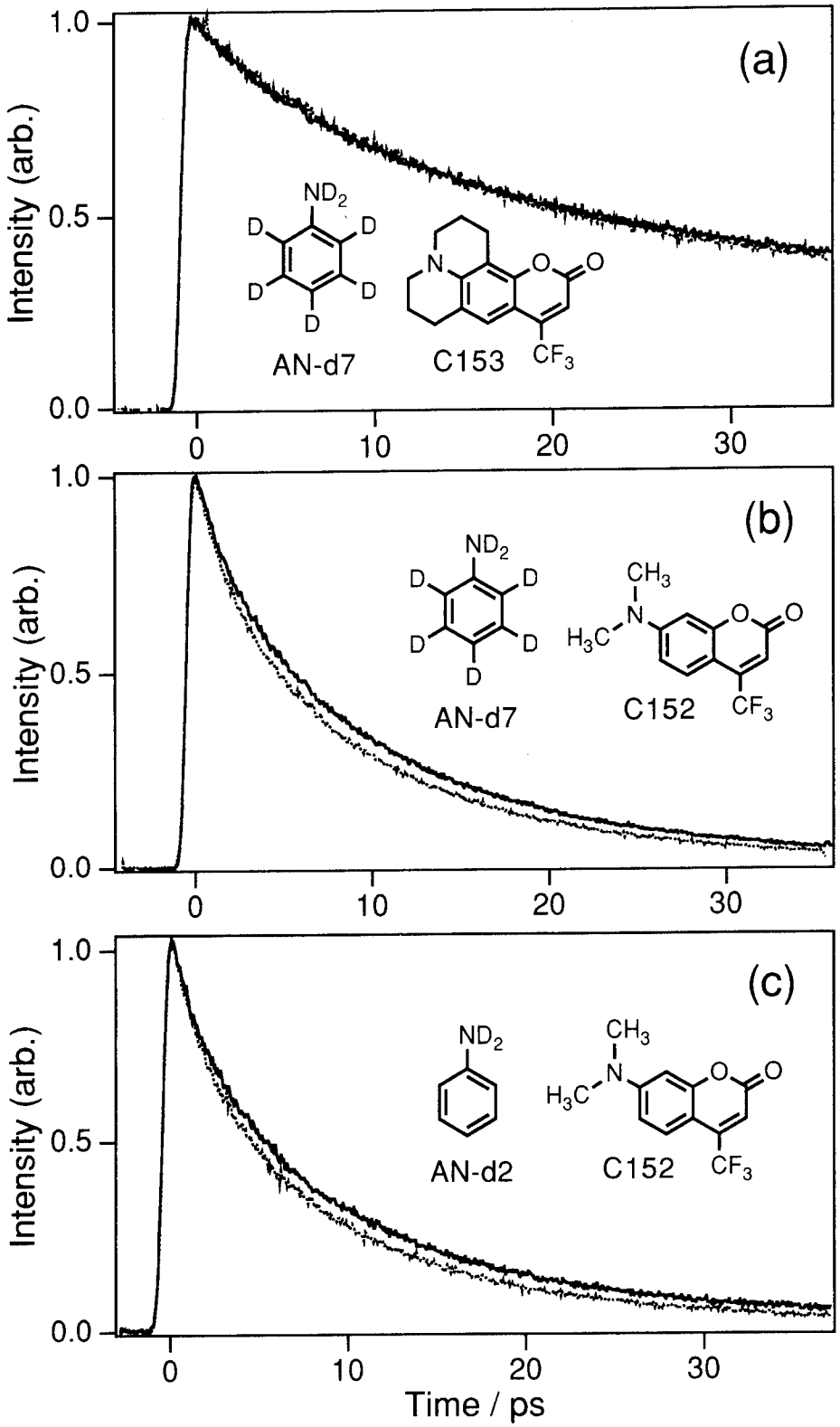


Figure 1. (a) Fluorescence decay of C153 in AN-h7 (broken line) and in AN-d7 (solid line).
(b) Fluorescence decay of C152 in AN-h7 (broken line) and in AN-d7 (solid line).
(c) Fluorescence decay of C152 in AN-h7 (broken line) and in AN-d2 (solid line).

Femtosecond Broadband Spectroscopy of the Styryl Dye DASPI in Solution: Interpretation in Terms of Dielectric Relaxation, Vibrational Energy Redistribution, and Isomerization

D. Bingemann[1], T. Bultmann[2], N.P. Ernsting[1] and A. Lochschmidt[1]

[1] Institut für Physikalische und Theoretische Chemie, Humboldt-Universität zu Berlin, Bunsenstr. 1, 10117 Berlin, Germany

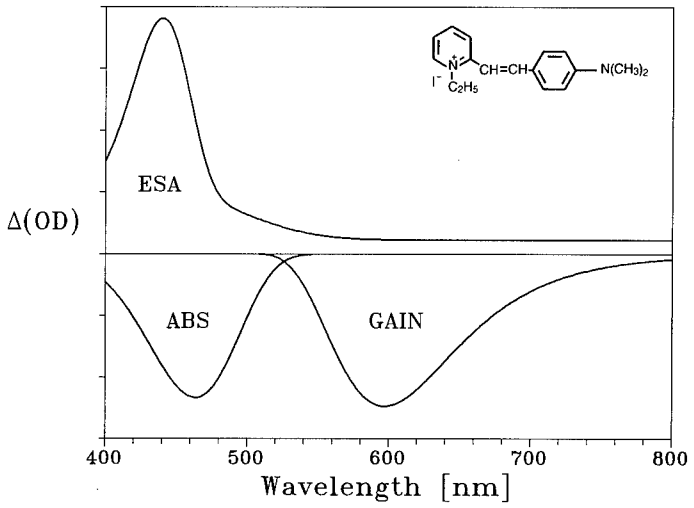
[2] Max-Planck Institut für Biophysikalische Chemie, Abteilung Laserphysik, Postfach 2841, 37018 Göttingen, Germany

1. Introduction

Dipolar styryl dyes have been used as molecular probes for the non-equilibrium dynamics of the surrounding solvent after ultrafast S_0 -> S_1 excitation [1,2]. Typically, the dynamic Stokes shift of fluorescence is measured by fluorescence upconversion at different wavelengths. The kinetic traces which are thus obtained must then be used for spectral reconstruction of the fluorescence band as function of time. This method is capable of highest time resolution, but the finer spectral details are likely to be lost in the reconstruction step.

Optical excitation of dipolar styryl dyes (like DASPI, *i.e.* 2-[p-Dimethylaminostyryl]-pyridylmethyl Iodide, see Fig. 1) will be followed by solvent reorganization, intramolecular vibrational energy redistribution, vibrational energy transfer to the first solvent shell, as well as - possibly - molecular isomerization. An elucidation of these processes requires an analysis of the fluorescence band shape. In a spectral approach to obtaining this band shape, we measured the transient absorption and gain spectrum of DASPI in various solvents (methanol, methanol-*d1*, ethanol, acetonitrile) at several temperatures.

Fig. 1



Decomposition of a transient absorption/gain spectrum of DASPI into ground-state bleaching ABS, excited-state absorption ESA, and GAIN.

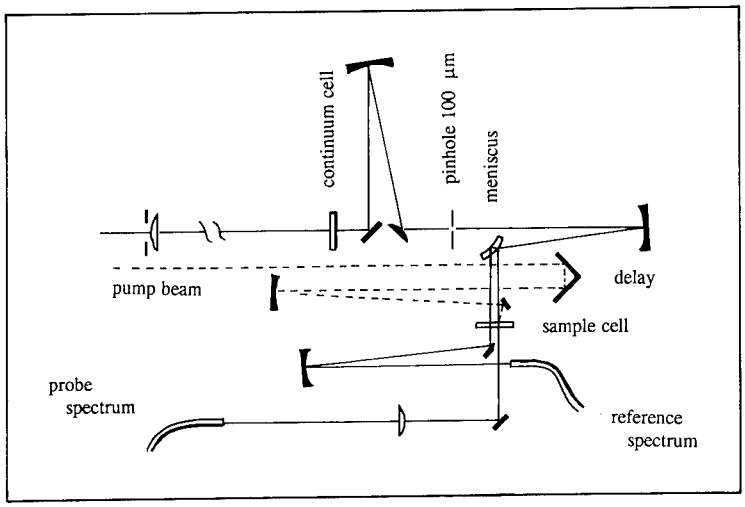


Fig. 2

Pump-Probe spectrometer with minimal dispersion and improved astigmatism.

Figure 1 shows, in principle, the three spectral components which contribute to a transient spectrum for a given delay time. Ground-state absorption is well represented by a "log-normal" distribution over photon energy [3]. It remains to separate excited-state absorption and gain. In analysing our data on DASPI, we represent ESA by a sum of three log-normal curves, the forms and positions of which are kept constant over time. The spectral evolution must then be due to a change of the gain band which is represented by a single log-normal curve. In this way, the band position, width, and assymmetry of the fluorescence band may be inferred.

2. Experimental

The dye solution is excited by a 70 fs pulse at 470 nm (20 µJ at 10 Hz). These pulses are obtained from a distributed-feedback dye laser system operating at 510 nm, which is followed by continuum generation and amplification at 470 nm. The probe consists of a supercontinuum generated at 470 nm in 2 mm of water. We employ an improved geometry for the pump-probe setup which is shown in Fig. 2.

Using only reflective optics, the astigmatism had to be controlled such that the spot of the continuum probe beam on the sample cell is circular with a diameter < 150 µm. This can be achieved by combining an imaging concave mirror, with small radius (224 mm) at low angle of incidence, and a convex mirror of large radius (typically 1000 mm) at a large angle of incidence. Within this concept, front and rear Fresnel reflections of the continuum beam from a quartz meniscus serve as probe and reference beam. Thick quartz fibers may be used to relay the probe and reference pulses to the spectrograph. Group velocity dispersion in sufficiently long fibers will stretch each spectral increment into the 30 ps range. In this way, saturation may be reduced for intensified cameras.

3. Results

Figure 3 shows transient spectra for DASPI in methanol (20°C) at various delay times. The measured spectra are distorted by residual group-velocity dispersion (GVD). A global fit to the measured data convolutes a spectro-temporal apparatus function, which was measured independently, with the spectral model mentioned above. In this way, the corrected gain

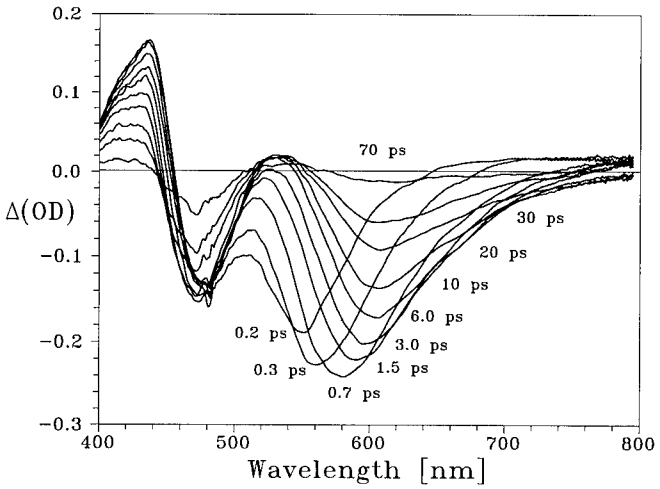


Fig. 3

Transient absorption and gain spectra of DASPI in methanol (at 20°C), as recorded at various nominal delay times (for 500 nm).

band is obtained as a log-normal distribution with time-dependent parameters.

The first moment of the gain band, as function of time, largely reflects *Dielectric relaxation.* Preliminary results on this are shown in fig. 4. We also observe a change of the asymmetry of the gain band: an ultrafast component up to 200 fs, and a slower process to10 ps. We attempt to assign this observation to intramolecular *vibrational energy redistribution* and *energy relaxation.* It is interesting to compare the amplitude of ground-state bleaching to that of the gain or excited-state bands. The corresponding kinetics are different. Tis observation may indicate an *excited-state isomerization* process. Comparison of spectra and kinetics in alcohols, to those in acetonitrile, suggests that a charge-transfer state may be involved.

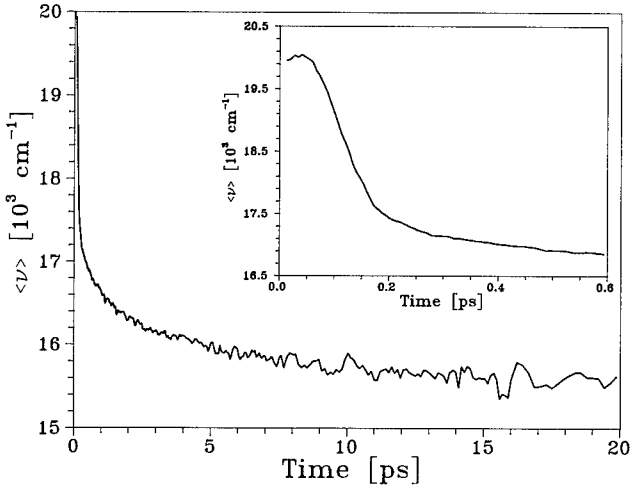


Fig. 4

Spectral position (first moment after spectro-temporal deconvolution) of the gain band of DASPI in methanol, as function of true delay time.

References

[1] S.J. Rosenthal, X. Xie, M. Du, G.R. Fleming, J. Chem. Phys. **95** (1991) 4715
[2] P. Hébert, G. Baldacchino, T. Gustavsson and. J.-C. Mialocq, Chem. Phys. Letters **213** (1993) 345
[3] D.B. Siano and D. E. Metzler, J. Chem. Phys. **51** (1969) 1856

Vibrational Relaxation of I_2^- in Polar and Non-Polar Solvents

P.K. Walhout, Joseph C. Alfano, Khalid A.M. Thakur, Paul F. Barbara
University of Minnesota, Chemistry Department
Minneapolis, MN 55455, USA

In this paper we present new results on the photodissociation, geminate recombination, and vibrational relaxation of I_2^- in various solvents. The photodissociation of I_2^- involves localization of the excess charge on a recoiling I• photofragment. This charge again delocalizes as the I• and I^- geminately recombine. The "charge flow" associated with recombination and subsequent large-amplitude vibrational motion is believed to greatly accelerate the vibrational relaxation of the nascent I_2^-. Coupling of the charge flow with accepting solvent modes leads to relaxation rates which are extremely fast and non-exponential, even near the bottom of the potential well. These results are in stark contrast to similar experiments performed on neutral I_2 which show nearly exponential vibrational relaxation rates that are an order of magnitude slower and are well-described by isolated binary interaction (IBC) theory. Specifically, our results on I_2^- show:

- the effects of charge and charge flow lead to a fast, non-linear form of vibrational relaxation in both polar and non-polar solvents
- new spectroscopic data supports the proposed claim [1] of trapped coherent motion in the $^2\Pi_{3/2,g}$ state immediately following recombination
- dephasing of ground state I_2^- vibrational coherence is complete in 300 fs.

Figure 1 shows pump-probe transient absorption spectra of I_2^- in dioxane and acetonitrile. The Ti:sapphire-based laser system used in these experiments has been described elsewhere [2]. In each case I_2^- is synthesized by photodissociation of I_3^- with a 390 nm pulse. After a 4 ns delay during which the I_2^- is allowed to equilibrate, a variably delayed 780 nm pump pulse excites the I_2^- to the dissociative $^2\Pi_{1/2,g}$ state. The probe pulse, either exciting the visible absorption band peak at 720-740 nm or the near-UV peak at 390 nm, interrogates the I_2^- as it geminately recombines and vibrationally relaxes.

The upper panel in Fig. 1 shows that the vibrational relaxation of I_2^- in dioxane is rapid despite the very non-polar environment. This data is complicated, however, by transient excited-state absorption of 720 nm photons, as proposed by Papanikolas et al. [1]. A more accurate determination of the vibrational relaxation rate is obtained by the second panel of Fig. 1. There is no competition for absorption of the 390 nm probe pulse, hence any bleach recovery is due to ground-state vibrational relaxation. Bleach recovery occurs on a ~7 ps timescale. For comparison, similar studies of neutral I_2 in non-polar solvents have yielded recovery times of 50 to several hundred picoseconds [3].

The fit to the two 390 nm probe transients of fig. 1 employ a modification to the linear spectral and kinetic model described in Kliner et al. which yielded an overall exponential decay of excess vibrational energy, consistent with IBC theory [2]. We have assumed the rate constant for vibrational relaxation, $k_{v\rightarrow v-1}$, increases with vibrational level v in an exponential rather than linear fashion. Hence $k_{v\rightarrow v-1}/k_{1\rightarrow 0} = v \cdot e^{v\cdot\alpha}$, where α is varied to provide the best fit. Note that a linear model results if α=0. Dioxane fits best to α=0.15, which indicates a highly non-linear mechanism of excess energy loss, especially at the top of the ground-state well.

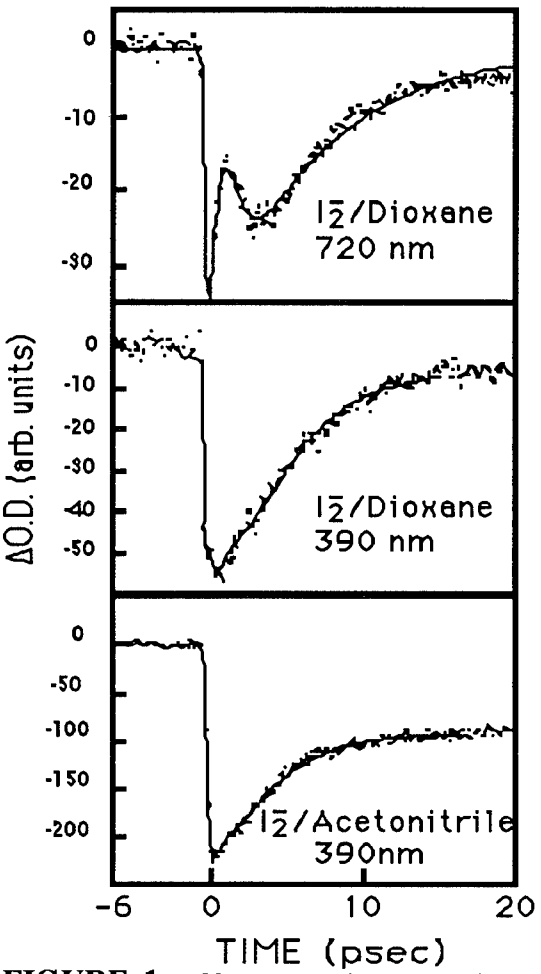


FIGURE 1. 780 nm pump/probe transient absorption spectra of I_2^- in dioxane and acetonitrile. The probe wavelength is indicated in each panel. Typical ΔO.D. values are 0.005. Pump and probe polarizations are oriented at magic angle. The top fiugre is fit with a four-exponential function.

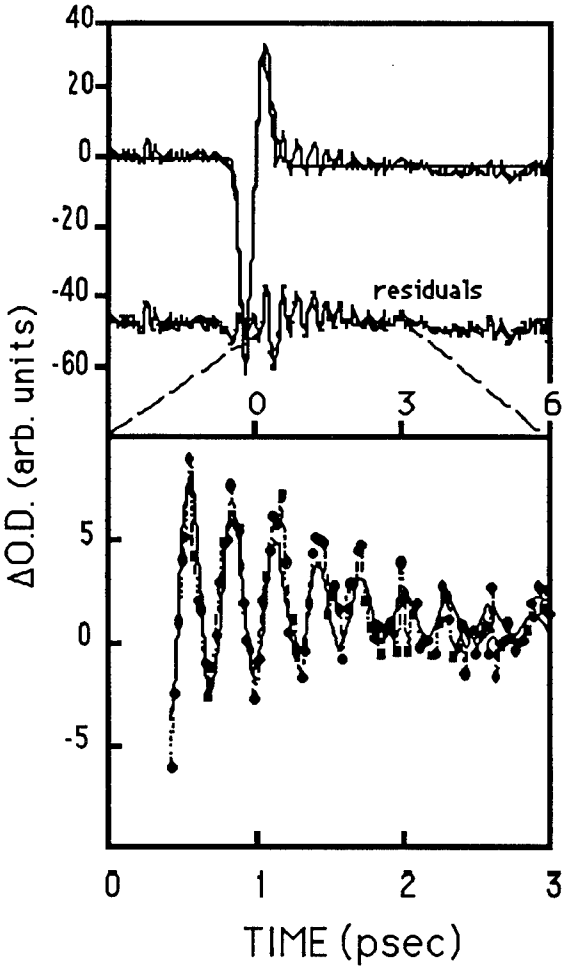


FIGURE 2. 780 nm pump/390 probe transient absorption spectrum of I_3^- in acetonitrile. The top panel shows the residuals to a multi-exponential fit. The oscillations are expanded in the bottom panel and fit to a damped sine wave.

The same non-linear kinetic and spectroscopic model shows that the acetonitrile data in the bottom panel of fig. 1 fits to α=0.30. This parameter thus doubles going from a low dielectric constant such as dioxane to a much more polar molecule. The average bleach recovery time for the acetonitrile is 4 ps, nearly twice as fast as dioxane. Moreover, the permanent bleach offset is much larger in acetonitrile, indicating the photodissociated I_2^- is more likely to be caged and geminately recombine in dioxane. It should be noted that the TBA^+ counter-ion used to prepare the sample in dioxane is likely ion-paired with the I_2^-, though the K^+ used in acetonitrile is probably not paired. These solvent and counter-ion effects will be explored in more detail in a future paper.

The fast relaxation times of I_2^- have prompted theoretical exploration into the role of charge flow on the relaxation dynamics of a charged species in solution. Studies have shown that two distinct reaction channels develop in the solvent coordinate following photodissociation of I_2^- due to solvent-induced localization of the excess electron on one of the two iodine photofragments [2],[4]. Large amounts of energy can be quickly lost through the "polarization force" which accompanies rapid charge flow in solution [4]. The influence of charge flow on ground-state energy relaxation is greatest at the top of the potential well where vibrating I_2^- samples a greater solvent volume and possesses more kinetic energy than at lower vibrational levels. This is reflected through our simple non-linear rate expression by the exponentially larger rates of vibrational relaxation at high levels of

v. The energy loss becomes more linear as the population reaches the bottom levels of the potential well.

The 720 nm dioxane data of fig. 1 shows a "bump" similar to that seen in studies of I_2^- photodissociation and recombination in CO_2 clusters. The absence of a bump in the 390 nm probe dioxane data supports the analysis of Papanikolas et al. [1]. It is reasoned that this bump reflects a transient increased absorption as some trapped fraction of the recombined molecules coherently move along the $^2\Pi_{3/2,g}$ state to a point where they can absorb a 720 nm probe photon. The Hund's case (c) coupling of excited states for I_2^- indicates that the $^2\Pi_{3/2,u} \leftarrow {}^2\Pi_{3/2,g}$ is an allowed transition, occurring at an internuclear distance of 3 Å. The rapid rise and decay of this transient increased absorption is evidence of coherent motion following recombination. The bump is seen in nearly all the data probing near 720, though the amplitude of the increased absorption is strongly solvent dependent. In each case, the bump disappears in the corresponding 390 nm probe data.

Figure 2 shows oscillations which are believed to be I_3^- vibrations excited by non-resonant impulsively-stimulated Raman scattering [5]. This is a two-pulse experiment, with the 780 nm pump and 390 nm probe focused on a sample of I_3^- in acetonitrile. The fast initial bleach and increased absorption signals are a coherence artifact due to interaction between the pump and probe pulses at t=0. The two-photon Raman process involving the 780 nm pump light impulsively places a wavepacket in an excited ground-state vibrational level. The 390 nm probe absorption is then modulated by motion of the excited wavepacket. The bottom panel expands the residuals of the multi-exponential fit. The residuals fit to a single, damped sine wave with a frequency of 110 cm^{-1}, corresponding to the I_3^- stretching frequency.

No oscillations are observed in the three-pulse, 390 nm probe experiments done on I_2^-. This provides some evidence that following geminate recombination, hot I_2^- in the ground state has lost all vibrational coherence within the 300 fs resolution of our instrument response. Our observation of I_3^- oscillations in many solvents suggests our time resolution is fast enough to see the 115 cm^{-1} I_2^- oscillations at 390 nm should they occur. 390 nm is near the equilibrium maximum of the near-UV I_2^- absorption band, however, which makes it less certain that oscillations would be observed if coherence were preserved.

The new data presented point towards a picture of extremely fast vibrational relaxation of I_2^- which proceeds via a non-linear coupling of charge and charge flow to the solvent. The molecules recombining on the ground state following photodissociation lose over half their energy and any vibrational coherence in less than one vibrational period. Strong solvent dependencies are observed for quantum yields of cage escape, rates of vibrational relaxation, and degree of coherence in the excited state. All solvents, polar and non-polar, exhibit fast, non-linear relaxation.

References

[1] J.M. Papanikolas, V. Vorsa, M.E. Nadal, P.J. Campagnola, W.C. Lineberger, *J. Chem. Phys.* **97**, 7002 (1992); J.M. Papanikolas, V. Vorsa, M.E. Nadal, P.J. Campagnola, H.K. Buchenau, W.C. Lineberger, *J. Chem. Phys.* **99**, 8733 (1993).

[2] D.A.V. Kliner, J.C. Alfano, P.F. Barbara, *J.Chem.Phys.* **98**, 5375 (1993); J.C. Alfano, Y. Kimura, P.K. Walhout, P.F. Barbara, *Chem. Phys.* **175**, 147 (1993).

[3] M.E. Paige, C.B. Harris, *Chem. Phys.* **149**, 37 (1990); A.L. Harris, J.K. Brown, C.B. Harris, *Annu. Rev. Phys. Chem.* **39**, 341 (1988); R. Lingle, X. Xu, S.-C. Yu, H. Zhu, J.B. Hopkins, *J. Phys. Chem.* **93**, 5667 (1990).

[4] B.J. Gertner, K. Ando, J.T. Hynes, *in press.*

[5] U. Banin, A. Waldman, S. Ruhman, *J. Chem. Phys.* **96**, 2416 (1992); U.Banin, S. Ruhman, *J. Chem. Phys.* **98**, 4391 (1993).

Friday, May 6, 1994

Biological Spectroscopy and Medical Applications

FB 10:30am–12:15pm
Dana Point Ballroom

J. G. Fujimoto, *Presider*
Massachusetts Institute of Technology

Time-Resolved Spectroscopic Techniques in Laser Medicine

S. Svanberg

Department of Physics, Lund Institute of Technology
P.O. Box 118, S-221 00 Lund, Sweden

Time-resolved spectroscopy observing fluorescence decay in biological chromophores provides improved molecular identification and allows studies of the dynamic behaviour of bio-molecules. Such spectroscopy enables atherosclerotic plaque to be distinguished from normal vessel wall, which can allow spectroscopic guidance in transluminal laser ablation of atherosclerotic plaque[1,2].

Time-resolved studies of optical photon propagation in tissue is a quickly evolving field with applications in brain oxygenation assessment and the development of optical mammography avoiding ionizing radiation[3]. Optical techniques have become even more attractive after the discovery of the *ataxia telangiectasia (AT)* gene in 1 per cent of the population, resulting in hypersensitization to X-rays. We have performed extensive studies of absorption and scattering in tissue[4-6] employing white light generated using high-power lasers[7], but also demonstrated tumour detection using simple diode lasers[8].

Laser-induced X-rays provide ultra-fast and ultra-sharp tissue imaging. We have used a chirped-pulse amplification terawatt laser to generate picosecond pulses of X-rays by focussing on a solid target[9]. Single-pulse X-ray image recording with an exposure time of about 10^{-12} s has been demonstrated[10]. Spectroscopic X-ray imaging might be developed using laser-produced X-rays.

1. S. Andersson-Engels, J. Johansson, U. Stenram K. Svanberg and S. Svanberg, J. Photochem. Photobiol. **B4**, 363 (1990).
2. S. Andersson-Engels, J. Johansson and S. Svanberg, Spectrochim. Acta **46A**, 1203 (1990).
3. G. Müller et al. (eds), *Medical Optical Tomography: Functional Imaging and Monitoring*, SPIE Institute Vol. IS11 (Bellingham, 1993).
4. S. Andersson-Engels, R. Berg, S. Svanberg and O. Jarlman, Opt. Lett. **15**, 1179 (1990).
5. S. Andersson-Engels, R. Berg and S. Svanberg, J. Photochem. Photobiol. **16**, 155 (1992).
6. R. Berg, S. Andersson-Engels and S. Svanberg, in Ref. 3, p. 397.
7. R. Berg, S. Andersson-Engels and S. Svanberg, Opt. Lett. **15**, 1697 (1993).
8. R. Berg, O. Jarlman and S. Svanberg, Appl. Opt. **32**, 574 (1993).
9. S. Svanberg, J. Larsson, A. Persson and C.-G. Wahlström, Phys. Scr. **49**, 187 (1994).
10. K. Herrlin, G. Svahn, G. Olsson, H. Petterson, C. Tillman, A. Persson, C.G. Wahlström and S. Svanberg, Radiology **189**, 65 (1993).

Femtosecond infrared spectroscopy of the photosynthetic reaction center

G. C. Walker[†], S. Maiti[‡], B. R. Cowen[‡], C. C. Moser[‡‡], R. S. Pippenger[‡], P. L. Dutton[‡‡], and R. M. Hochstrasser[‡]

[†]Department of Chemistry (412) 383-9650, University of Pittsburgh, Pittsburgh, PA 15260; [‡]Department of Chemistry (215) 898-8410 and [‡‡]Johnson Research Foundation (215) 898-8699, University of Pennsylvania, Philadelphia, PA 19104

The photosynthetic reaction center (RC) from the purple bacterium *Rb. sphaeroides* is a member of the closely related family of light harvesting membrane proteins that are responsible for carrying on photosynthesis in nature. The two C2 symmetry related subunits, L and M, consist of transmembrane alpha helixes and eight cofactors [4 Bacteriochlorophylls (Bchl), 2 Bacteriopheophytins (Bph) and 2 Ubiquinones (Q)]. The cofactors are arranged in a wishbone geometry, with a dimerized pair of bacteriochlorophylls at the center (also called the 'special pair', P), and one each of Bchl, Bph and Q (in that order) along each side of the wishbone. The primary events of photosynthesis consist of the formation of the excited singlet state P* of the dimer by the absorption of a near infrared (NIR) photon by P, and subsequent transfer of an electron to the Bph on the L side with a time constant of ca 3ps forming $P^{+}Bph^{-}$. The role of the L side Bchl in this process is uncertain.

Various visible/NIR spectroscopic techniques have been applied to characterize the electronic events in the RC. Much less is known about the participation of the protein in

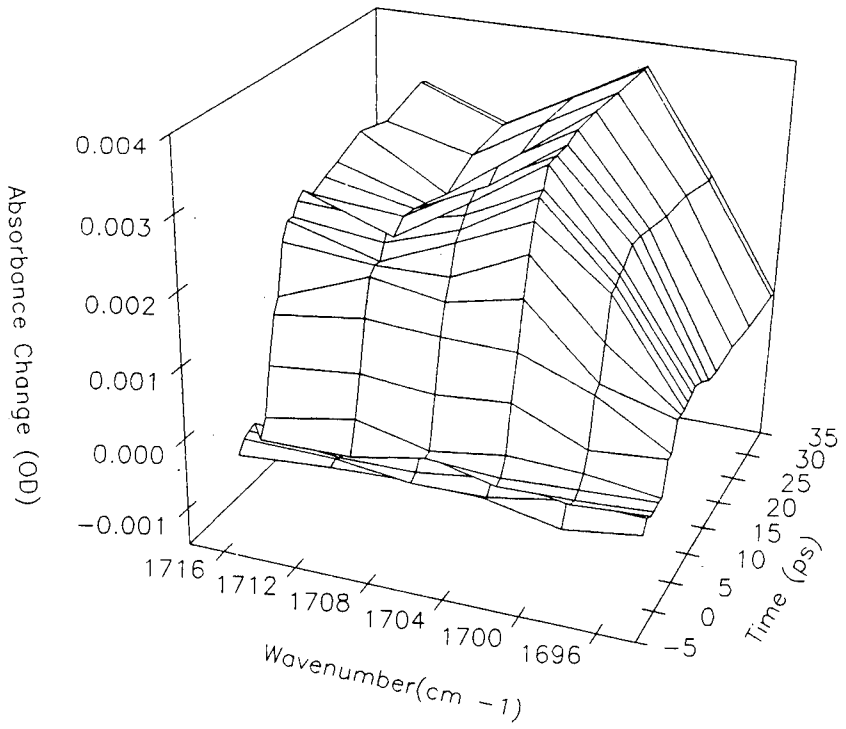


Fig. 1

such dynamics. We have developed a technique based on nonlinear gating of CW IR radiation that allows the measurement of infrared spectral changes with a few hundred femtosecond resolution and high enough sensitivity to record sub-milliOD changes in the spectrum.

In the present experiment, spectral kinetics measured in the region between 1590-1760 cm^{-1} access cofactor and side chain carbonyls and backbone amide adsorptions of the protein. Fig. 1 depicts the difference signal obtained from a representative vibrational band around 1702 cm^{-1}. The main contribution in this region comes from the 9-keto carbonyls of the special pair, which shift their resonance frequency from 1683 cm^{-1} to 1702 cm^{-1} when P becomes P^+. The evolution of the band at early times clearly manifests vibrational dephasing. The three dimensional data therefore affords a measurement of the bandwidths of the vibrational transitions in a protein for the first time.

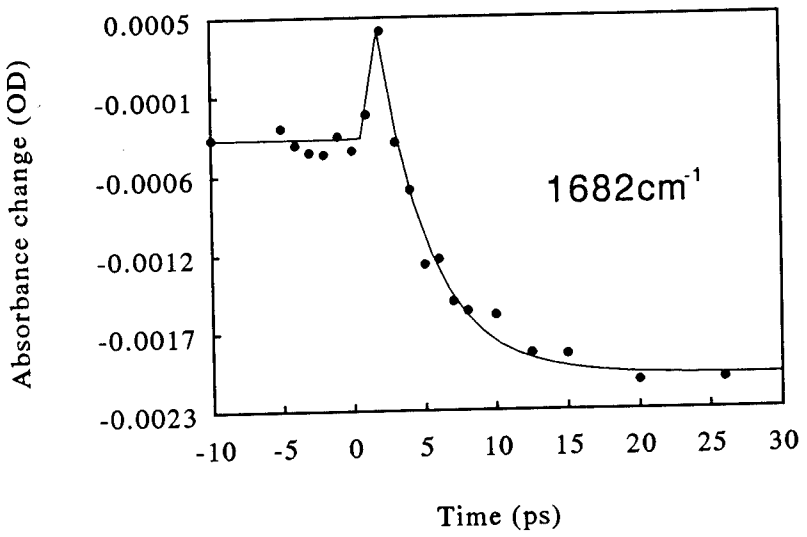


Fig. 2

Fig. 2 shows the evolution of the bleach of the special pair ground state (9-keto) occuring only on the time scale of electron transfer from P^*. This proves that the vibrations of P and P^* have essentially the same frequencies and dephasing times in this region. Data in other regions resolve the response of the Amide vibrations to the formation of P^* and P^+, and the evolution of most of the cofactor carbonyl can also be clearly identified. Existing steady state FTIR (1) and Raman (2) spectra and an analysis of the electrostatic fields inside the protein helps in assigning the dynamical signatures to specific vibrational groups. There is no evidence for any protein conformational relaxation that is slower than a few hundred femtoseconds. Also, no compelling vibrational signature of the $Bchl^-$ state (a proposed redox intermediate (3)) was yet found.

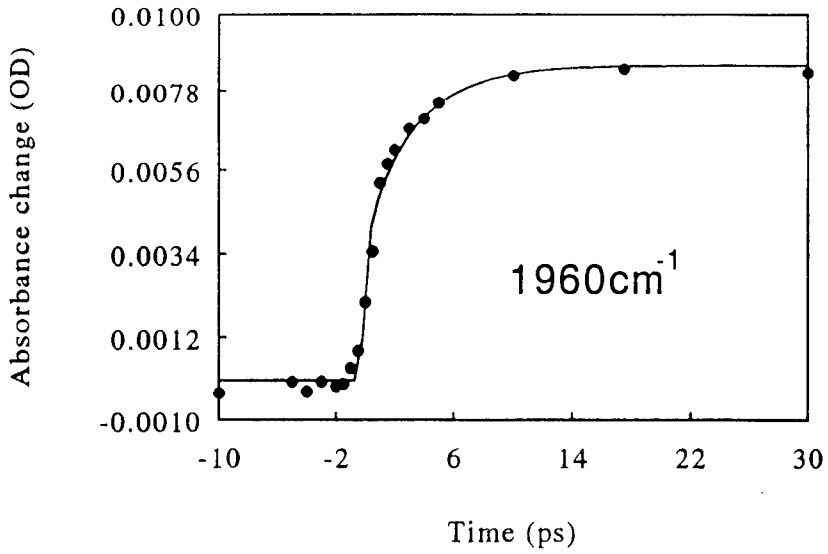


Fig. 3

The spectral region of 1700-1960 cm^{-1} resolves broad bands that we assign to low energy electronic transition of the P^* and P^+ states. Fig. 3 shows the kinetics obtained at a representative frequency, where the fit represents a 2:1 contribution from the P^+ and P^* components, respectively. The P^* electronic transition is identified with the interexcitonic transition of the special pair, based on earlier predictions made from theoretical calculations. The P^+ electronic band is assigned to a transition between hole transfer states of P, in accordance with steady state FTIR measurements at low temperatures (4). The measurement of anisotropy yields identical values for both transitions. This has been interpreted in terms of a simple model for the electronic nature of P^* involving excitonic and charge transfer states, and provides a constraint for the theoretical calculation of the electronic wave functions for the ground and excited states of P, including the amount of charge shifted.

Probing with nonlinearly generated IR pulses in our laboratory has recently provided even higher sensitivity for measuring absorption changes ($2x10^{-5}$ OD). Effort is underway to apply this technique to the RC so that kinetic assignments can be made in the frequency regions where recent assignments are not definitive.

References

1) Mantele, W., Wollenweber, A., Nabedryk, L., and Breton, J. *Proc. Nat. Acad. Sci. USA* **85** (1988) 8468-8472.

2) Mattioli, T. A., Hoffman, A., Robert, B., Schrader, B., and Lutz, M. *Biochemistry* **30** (1991) 4648-4654.

3) Zinth, W. and Kaiser, W., in *The Photosynthetic Reaction Center*, eds Deisenhofer, J. and Norris, J. (Academic, New York, 1993), vol II, 71-86

4) Parson, W. W., Nabedryk, L., and Breton, J., in *The Photosynthetic Bacterial Reaction Center II*, eds Breton, J. and Vermeglio, A. (Plenum, New York, 1992), 79.

Ultrafast energy transfer in the core light harvesting complex of photosynthetic bacterium *Rhodobacter sphaeroides* observed by fluorescence upconversion.

S. Bradforth,[a] R. Jimenez,[a] V. Fidler,[a] G. Fleming,[a] S. Nagarajan,[a,b] J. Norris,[a,b] F. van Mourik[c] and R. van Grondelle[c]

[a] Department of Chemistry, University of Chicago, Chicago, IL 60637
[b] Chemistry Division, Argonne National Laboratory, Argonne, IL 60439
[c] Department of Biophysics, Faculty of Physics and Astronomy, Vrije Universiteit, Amsterdam, The Netherlands.

Energy transfer in the core light harvesting complex (LHI) of the purple photosynthetic bacterium *Rb. sphaeroides* has been measured by the fluorescence upconversion technique[1]. LHI is thought to be constructed from aggregates of small building blocks containing transmembrane polypeptides and associated carotenoid and bacteriochlorophyll *a* (BChl*a*) pigment moieties.[2] There is evidence for a high degree of ordering of the pigments in the basic "minimal unit". The mechanism of energy transfer from carotenoid to BChl*a* and between BChl*a* pigments is not well understood. Although the two energy transfer processes proceed via different mechanisms, they are both highly efficient, and are both expected to occur on sub-picosecond timescales. LHI makes an excellent system for study of ultrafast energy transfer in a biological system because of the existence of only a single BChl spectral pool and one type of carotenoid. We have investigated energy transfer between B870 BChl*a* pigments in the complex as well as between carotenoid and BChl*a* pigments. A sub-picosecond decay observed in the fluorescence depolarization of LHI excited at 870 nm is assigned to energy transfer between BChl*a*'s in the minimal unit of the complex. In preliminary measurements where the carotenoid band is excited at 505 nm, a rise in the isotropic emission from BChl*a* is characterized by two time constants.

Two experimental arrangements were used in the work reported here. To monitor the fluorescence evolution of the Q_y BChl*a* band (B870) a single color experiment using the output of a CW mode locked Coherent Mira Ti:Sapphire oscillator operating at 870 nm was used. The IR beam is split, and 0.5 nJ per pulse used to excite the LHI B870 band. The remaining 1 nJ pulse traverses a variable delay, and is mixed with the focussed fluorescence from the sample in a 0.4 mm thick $LiIO_3$ crystal (Type I) which is angle tuned to upconvert 945 nm fluorescence.

For experiments where the carotenoid band is excited, the 505 nm excitation pulse is selected from the white light continuum output of a Coherent RegA 9000 Ti: Sapphire regenerative amplifier. The amplifier is seeded with selected pulses from the Mira oscillator operating at 820 nm and yields greater than 2000 nJ of compressed 820 nm light at 250 kHz repetition rate with autocorrelation of ~250 fs. 70% of this is used to generate a stable continuum in pure sapphire; the remainder is used as the gate pulse for the upconversion. A 25 nm bandpass interference filter is used to select the 505 nm excitation light from the continuum. The LHI sample is excited with ~0.5 nJ of this green light and the 400 nJ IR gate pulse upconverts emission from B870 at 910 nm in the $LiIO_3$ crystal. The excitation pulse overlaps the red edge of the $S_2 \leftarrow S_0$ carotenoid absorption band. In both experiments the upconverted fluorescence is detected with a 4 nm bandpass double monochromator and

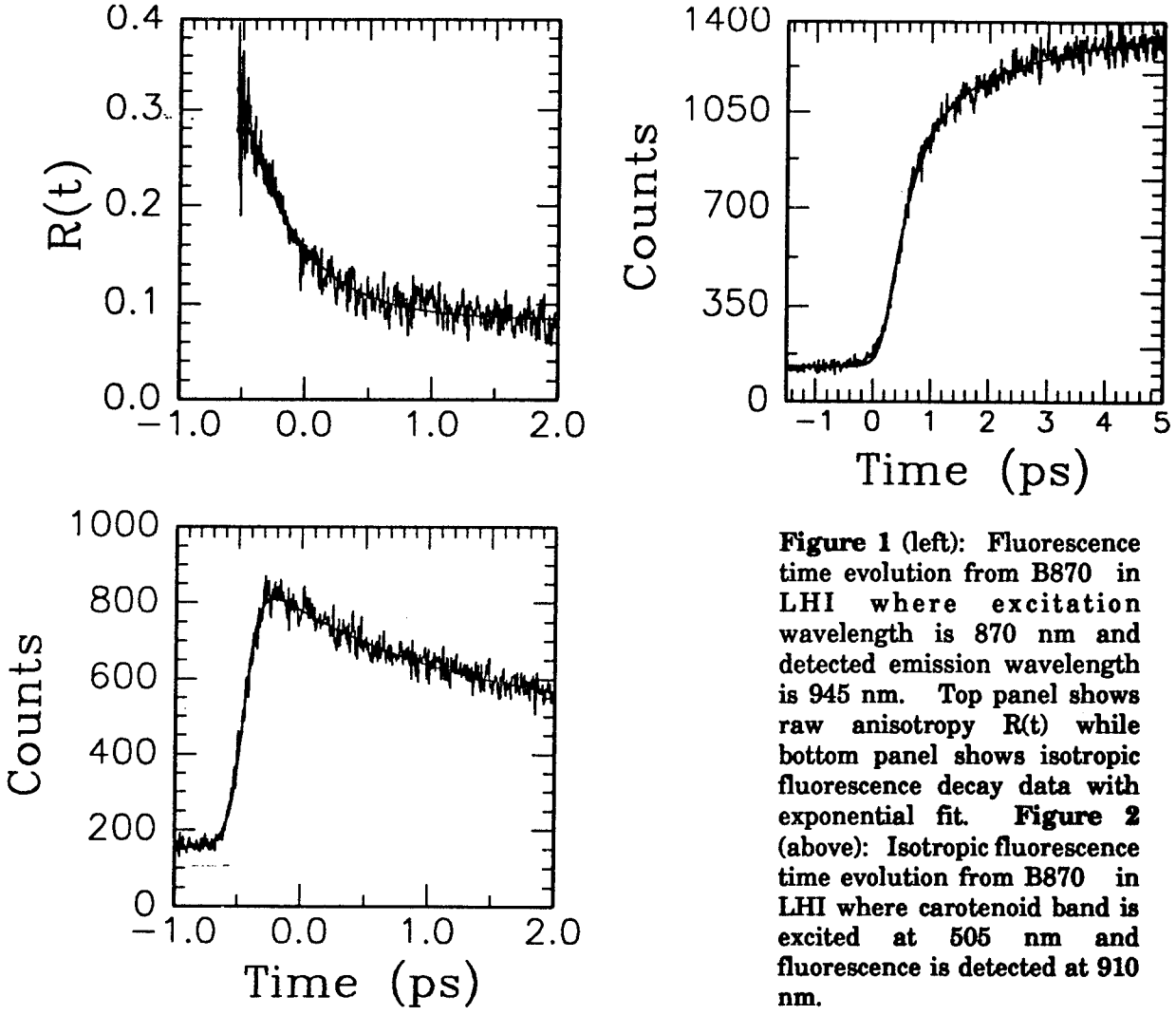


Figure 1 (left): Fluorescence time evolution from B870 in LHI where excitation wavelength is 870 nm and detected emission wavelength is 945 nm. Top panel shows raw anisotropy R(t) while bottom panel shows isotropic fluorescence decay data with exponential fit. **Figure 2** (above): Isotropic fluorescence time evolution from B870 in LHI where carotenoid band is excited at 505 nm and fluorescence is detected at 910 nm.

photomultiplier tube. The cross-correlation of the excitation pulse with the gate pulse is 190 fs FWHM for 870 nm / 870 nm and 285 fs for 505 nm / 820 nm. The latter cross correlation is measured in a 0.4 mm thick BBO crystal. Fluorescence curves were recorded with the polarization of the excitation pulse parallel, perpendicular or at the magic angle (54.7°) with respect to the gate pulse. The accuracy of depolarization measurements has been checked by verifying the initial fluorescence anisotropy of the dye IR132 in DMSO to be 0.39 +/- 0.02.

The LHI antenna complexes for both experiments were from *Rb. sphaeroides*. For the 870 nm excitation experiments a chromatophore preparation of the M2192 mutant[3] was used; for the 505 nm experiment complexes isolated from the strain PUC 705 BA using the detergent n-octyl-β-D-glucopyranoside were studied. Neither preparation contains LHII or reaction centers. The optical densities of the samples at the pump wavelength were 0.3 and 1.3 per mm for the one and two color experiment respectively. In both experiments the sample was continuously stirred by a platinum filament attached to an electric toothbrush. All measurements were made at room temperature.

The lower plot in Figure 1 shows a typical fluorescence decay when the BChl*a* band is excited at 870 nm and the pump polarization is at the magic angle with respect to the detected fluorescence. An exponential fit to this curve and ones recorded to longer delay times recovers 700 fs and 3.9 ps time constants. The upper plot shows the raw fluorescence anisotropy, $R(t) = [I_{par}(t) - I_{perp}(t)] / [I_{par}(t) + 2 I_{perp}(t)]$; the actual anisotropy decay must be recovered from deconvoluted $I_{par}(t)$ and $I_{perp}(t)$.[4] It shows a very fast decay from an initial value close to 0.4 to a value approaching the steady state anisotropy,[5] ~0.1, within 2 ps. The magnitude of the decay rate is similar to the kinetic component observed in a transient absorption study of the light harvesting antenna of *Rs. rubrum* and assigned to energy transfer between BChl*a* dimers.[6] In that study Visser found a 325 fs exponential rise in the red shift of the isosbestic point in the time resolved difference spectrum of *Rs. rubrum* but not in the disassembled form, B820, which is known to contain just a single BChl*a* dimer. The anisotropy decay observed here indicates that energy transfer beween BChl*a* dimers in *Rb. sphaeroides* also occurs on a very fast timescale.

Figure 2 shows the isotropic fluorescence at 910 nm when the carotenoid pigment in LHI is excited. There is a biphasic rise of the emission with time constants τ_1= 440 fs and τ_2 = 2.5 ps. In a study by Albrecht and coworkers on the related antenna system LHII, a 200 fs component was assigned to energy transfer between carotenoid and BChl850. These authors find evidence suggesting that carotenoid to BChl*a* energy transfer occurs from both carotenoid S_2 and S_1 states.[7] Furthermore, the energy transfer from the carotenoids may occur via coupling with either BChl Q_x or Q_y transition dipoles. Both of these factors may be used to explain the observation of multi-exponential rises in our data. Preliminary measurements of the fluorescence anisotropy indicate an instrumentally limited rise to close to the steady state anisotropy for energy transfer between these pigments in isolated LHI, ~ - 0.1.

We wish to thank Coherent Inc. for the loan of the regenerative amplifier used in this study.

1. M. Du, S. Rosenthal, X. Xie, T. DiMagno, M. Schmit, J. Norris and G. R. Fleming, *Proc. Natl. Acad. Sci. USA* **89**, 8517 (1992)

2. V. Sundstrom and R. van Grondelle in *Chlorophylls*, Hugo Scheer ed., p 1097, CRC Press, Bacon Rouge, FL, 1991

3. C. N. Hunter, R. van Grondelle and R.J. van Dorssen, Biochim. Biophys. Acta **973**, 383 (1989)

4. A. J. Cross and G. R. Fleming, *Biophys. J.* **46**, 45 (1984)

5. R. J. van Dorssen, C. N. Hunter, R. van Grondelle, A. H. Korenhof and J. Amesz, *Biochim. Biophys. Acta* **932**, 179 (1988); H. J. M. Kramer, J. D. Pennoyer, R. van Grondelle, W. H. J. Westerhuis, R. A. Niederman and J. Amesz, *ibid* **767**, 335 (1984)

6. H. M. Visser, manuscript in preparation

7. A. P. Shreve, J. K. Trautman, H. A. Frank, T. G. Owens and A. C. Albrecht, *Biochim. Biophys. Acta* **1058**, 280 (1991)

Ultrafast Mid-IR Spectroscopy of Carbonmonoxymyoglobin: The Dynamics of Ligand Motion

Manho Lim, Timothy A. Jackson, and Philip A. Anfinrud

Department of Chemistry, Harvard University, 12 Oxford Street, Cambridge, MA 02138, USA
Phone and Fax: (617) 495-5634

1. Introduction

Myoglobin (Mb) is an oxygen-binding protein found in muscle. The active binding site is an iron-II-containing porphyrin (heme) that is located within the hydrophobic interior of the protein. The X-ray structure of Mb reveals a distal cavity large enough to accommodate a ligand the size of O_2, but no channel large enough for the ligand to diffuse between the heme pocket and the surrounding solvent. Clearly, structural fluctuations of the protein are required to open channels for ligand transport to and from the binding site. What is the functional role of the heme pocket and the residues that circumscribe it? What pathways exist for ligand transport between the heme pocket and the solvent? On what time scale does the ligand escape into the surrounding solvent? We have sought to answer these questions by probing the time-resolved vibrational spectrum of CO, a ligand similar in size to O_2, following photodissociation of MbCO at physiological temperatures. We have developed a femtosecond time-resolved mid-IR spectrometer with the sensitivity required to measure the "free" CO absorbance. Ultrafast diffusion to a "docking" site has been observed, the orientation of the docked CO relative to the plane of the heme has been measured, and the rate of escape from the heme pocket has been determined. Additional studies with mutants of Mb are being conducted to probe the location of the docking site within the heme pocket and the pathways for ligand escape from the heme pocket.

2. Experimental Method

A time-resolved mid-IR absorption spectrometer was developed which provides spectral coverage of ≈ 3.3 - 5.5 μm, spectral resolution of 3 cm^{-1}, time resolution of < 250 fs, and a noise level of $\approx 5 \times 10^{-4}$ rms in absorbance units after 1 second of signal averaging. (For comparison, the noise level of a top-of-the-line Nicolet Model 800 FTIR spectrometer equipped with a liquid-N_2-cooled InSb detector was found to be $\approx 3 \times 10^{-4}$ rms after 1 second of signal averaging.) The fs mid-IR probe pulse is derived by difference-frequency mixing a fs optical pulse with an amplified continuum in a nonlinear crystal. The mid-IR probe is split into two portions: one portion passes through the photolyzed volume of the sample and the other portion, a reference, bypasses the sample. The sample and reference pulses are routed through an IR monochromator and detected with amplified InSb photodetectors. The two signals are digitized and their ratio is computed on a shot-by-shot basis in order to recover the transmission of the sample. Signal averaging at the 1.5 kHz repetition rate of the laser contributes to the very high signal-to-noise ratio. Time-resolved absorption measurements from fs to ns times are made by photolyzing the sample with an optically delayed portion of the amplified fs pulse; measurements from ns to ms times are made by photolyzing the sample with an electronically delayed optical pulse from a ns dye laser.

3. Orientation of Ligands

Figure 1 shows the polarized absorption spectra of photolyzed horse MbCO. The negative-going features near 1940 cm^{-1} correspond to loss of "bound" CO (A-states) while the features near 2130 cm^{-1} correspond to production of "free" CO (B-states). The relative amplitudes of the polarized spectra are related to the angle of the CO dipole relative to the heme normal [1,2]. For the A-state spectra, the orientation of CO is frequency dependent: the spectra can be modeled with three Gaussian features corresponding to CO oriented at 13, 16, and 21 degrees. The B-state spectra can be modeled with two Gaussian features having the same angle of approximately 62 degrees. Such structural details obtained at physiological temperatures provide useful constraints for MD simulations and for refinement of X-ray structures.

4. Ligand Diffusion within the Heme Pocket

The B-state features of Figure 1 are only modestly broader than those observed at 10K [3], but are much narrower than the features observed in CO-saturated cyclohexane (≈90cm^{-1}) or CO-saturated glycerol/water (≈20 cm^{-1}). This suggests that the "free" CO is strongly localized in some region of the heme pocket. Figure 2 shows the time-dependent B-state absorbance, which grows with a time constant of ≈1 ps. This suggests that the spectrum of dissociated CO is initially broad while it diffuses within the heme pocket and subsequently narrows after becoming localized in the heme pocket. The fact that the B-state features appear as early as 300 fs suggests that the CO becomes localized very near the heme iron.

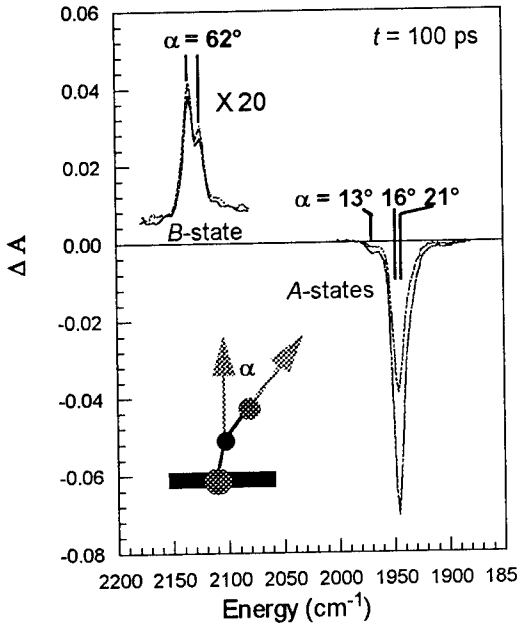


Figure 1. Parallel and perpendicular polarized transient absorbance spectra of photo-dissociated horse MbCO at 100 ps. The larger of the two A-state spectra was obtained with perpendicular polarization of pump and probe pulses. The larger of the two B-state spectra was obtained with parallel polarization of pump and probe pulses.

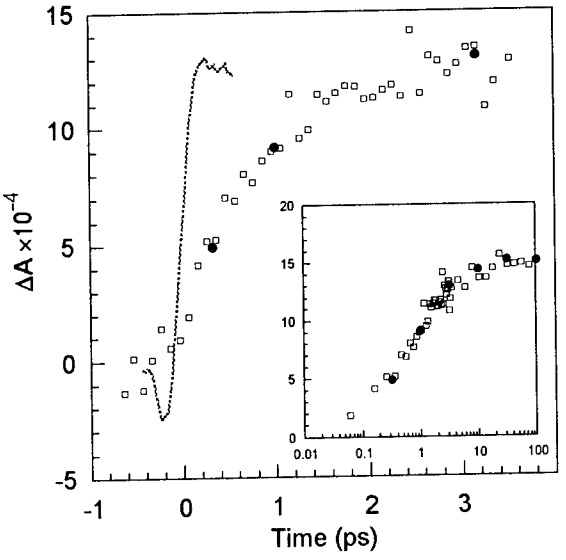


Figure 2. Time-resolved mid-IR absorbance. The open squares represent the time-dependent absorbance of the B-states; the filled circles are proportional to the integrated area of the B-state spectra; the steep curve is the onset of free carrier absorbance in GaAs, which illustrates the instrumental rise time.

One of the two observed B-states shifts and broadens nonexponentially in time (not shown), and becomes static at ~ 10 ns. This nonexponential evolution occurs on the same time scale as conformational relaxation of the protein [4,5]. Evidently, the site corresponding to one B-state is perturbed as the conformation of the protein relaxes, while that of the other B-state is unperturbed. This suggests that the two B-states correspond to different sites within the heme pocket, or the same site with the ligand oriented at a different azimuthal angle (polarization spectroscopy can be used to infer the orientation of the CO relative to the heme normal but not the azimuthal angle about that normal).

5. Rate of Escape from Heme Pocket

Figure 3 shows the ns evolution of the absorption spectra in the "free" CO region. The decay of the B-states corresponds to escape of the ligand from the heme pocket. The broad feature at long times corresponds to solvated CO. A small sharp feature located between the two B-states appears at intermediate times and evidently corresponds to ligands that have become trapped in another internal cavity (C-state) of the protein. A kinetic analysis of the of the A-, B-, and C-states suggests that the ligands escape from the heme pocket with a time constant of ~300 ns. Upon escape from the heme pocket, most ligands diffuse to the solvent very rapidly, i.e., the rate of diffusion to the surrounding solvent is faster than the rate of escape from the heme pocket. Only a small fraction of the escape trajectories lead to another internal cavity within the protein from which the ligand escape is slower. This suggests that the protein provides an efficient pathway for shuttling ligands between the solvent and the binding site.

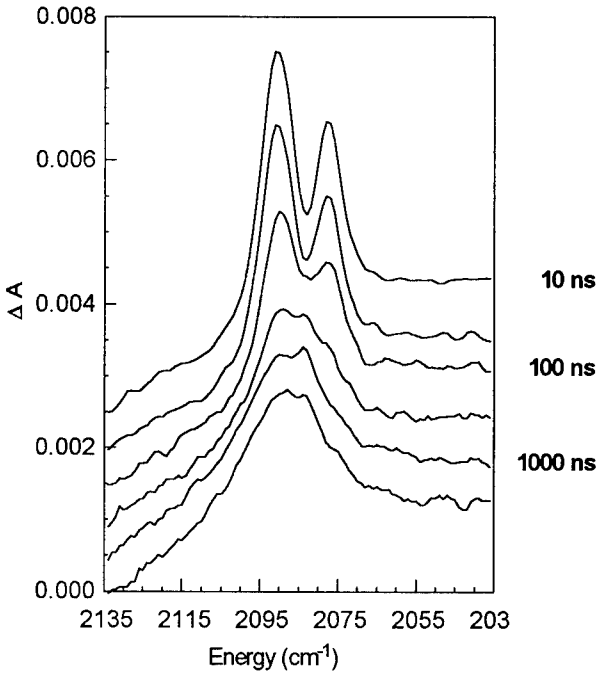


Figure 3. Time-resolved mid-IR absorption spectra.

References

1. J.N. Moore, P.A. Hansen, and R.M. Hochstrasser, *Proc. Natl. Acad. Sci. U.S.A.* **85**, 5062 (1988).
2. P. Ormos, D. Braunstein, H. Frauenfelder, M.K. Hong, S.L. Lin, T.B. Sauke, and R.D. Young, *Proc. Natl. Acad. Sci. U.S.A.* **85**, 8492 (1988).
3. J.O. Alben, D. Beece, S.F. Bowne, W. Doster, L. Eisenstein, H. Frauenfelder, D. Good, J.D. McDonald, M.C. Marden, P.P. Moh, L. Reinisch, A.H. Reynolds, E. Shyamsunder, and K.T. Yue, *Proc. Natl. Acad. Sci. U.S.A.* **79**, 3744 (1982).
4. M. Lim, T.A. Jackson, and P.A. Anfinrud, *Proc. Natl. Acad. Sci. U.S.A.* **90**, 5801 (1993).
5. M. Lim, T.A. Jackson, and P.A. Anfinrud, *Laser Spectroscopy of Biomolecules, Jouko E.I. Korppi-Tommola, Editor*, **Proc. SPIE 1921**, 221 (1993).

Intrastromal Corneal Reshaping Using Near Infrared Picosecond Laser Pulses

M. G. Speaker and M. S. Habib
Department of Ophthalmology, The New York Eye and Ear Infirmary

T. Juhasz
Department. of Physics, University of California, Irvine

Picosecond lasers working at wavelengths which are not absorbed in the refractive components of the eye have great potential for corneal intrastromal surgery due to their well localized surgical effect. The damage mechanism of the picosecond lasers begins with optical breakdown in the focus of the laser beam. The plasma creation is followed by the generation of the shock wave and cavitation bubble. As is suggested by previous results [1,2] tissue removal is due to the effect of the laser plasma. Using multiple picosecond pulses it is possible evaporate a disk-shaped volume inside the cornea by delivering the pulses along a spiral pattern. The collapse of the created intrastromal cavity results in a thinning of the central cornea and, therefore, a myopic refractive correction. The method is referred as intrastromal photorefractive keratectomy (IPRK). IPRK is attractive because it obviates the need for removal of the corneal epithelium, therefore it has the potential for avoiding wound healing responses which results in scarring and regression after surface ablation.

The efficiency of the intrastromal tissue removal, however, is strongly influenced by the development of the cavitation bubble. If the cavitation generated by the first laser pulse is greater than the actual plasma size, it may interact with the surgical effect of the next pulse. Moreover if the pulse hits inside an existing cavitation it does not remove tissue, but increases the size of the cavitation through heat transfer to the gas. In order to avoid re-heating the gas inside the cavitation, the next pulse must hit the tissue outside the bubble. Therefore, in the optimum case, the ratio of the cavitation diameter at the moment of the arrival of the next pulse, D_C, and the plasma diameter, D_p, should approach unity, when the most efficient tissue removal achieved by packing the plasma balls adjacent to each other. In order to find the best laser parameters for the most efficient intrastromal tissue removal, we have investigated the time and the energy dependence of the cavitation bubble diameter in bovine corneas with the method of time resolved photography. Fig. 1. displays the temporal development of the cavitation generated by 20 ps pulses with 270 μJ energy when the laser is focused to a 20 μm spot size. As is seen in the figure the cavitation undergoes a transient oscillation, then reaches a final size after approximately 500 μs. The bubble then slowly decreases and completely disappears after 5 to

30 minutes. Fig. 2. shows the dependence of the bubble diameter on the laser pulse energy. These experimental results and the above considerations indicate that intrastromal tissue removal should be performed with pulse energies close to the threshold of the optical breakdown when only small cavitation bubbles are generated. The results also indicate that the time between two surgical pulse should be longer than the period of the transient bubble oscillation, which limits the repetition rate of the laser to a few KHz.

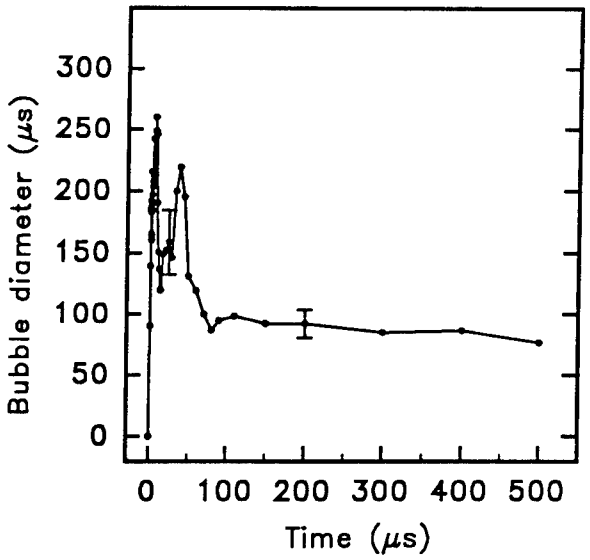


Fig.1.

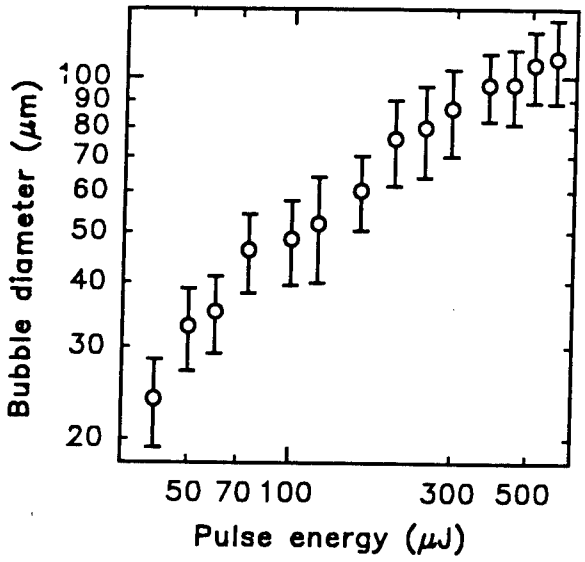


Fig. 2.

In the animal experiment output pulses from a regeneratively amplified Nd:YLF laser (ISL, Model 4000) were used to perform intrastromal tissue removal. The pulse duration is 40 ps and the focus spot diameter is 10 μm. Following the above considerations pulse energies between 20 and 40 μJ were chosen which are close to the threshold. D_c was measured to be approximately 15 μm under these circumstances. Spiral patterns were placed in the upper third of the central cornea of 12 cats with 6 mm in diameter. The spot separation in the pattern and the layer separation between patterns were chosen to be 15 μm according to the measurement of the cavitation bubble diameter D_c. The effects of 3 and 5 layer treatments were investigated. Post-operative corneal topography, ultrasonic biomicroscopy and ultrasonic pachymetry were performed at scheduled intervals. The follow up ranged from two weeks to 6 months. The pre-operative pachymetry ranged from 520-700 μm. Corneal thickness was increased an average of 50 μm at 24 hrs. The corneas were thinned over a period of 2 weeks and central flattening was apparent at 3 weeks. Central topographic flattening up to 13 diopters was achieved which was associated with a central thinning of 120 μm. After the surgery the average refractive power of the eyes at the center of the cornea as a function of time, as it is measured with corneal

topography, is displayed in Fig. 3. The central topographic change of the corneas was stable as far as 6 months and no evidence of regression was observed.

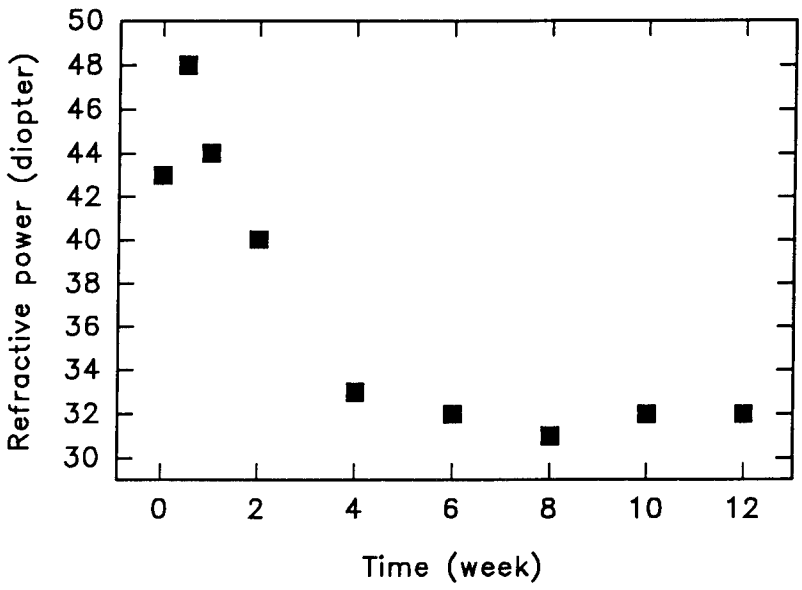


Fig. 3.

In summary, IPRK have been utilized for corneal refractive surgery. The efficiency of the procedure have been maximized using pulse energies which are close to the threshold and by optimizing the intrastromal patterns. Myopic corrections up to 13 diopters have been achieved in preliminary animal experiments.

1. M. H. Niemz, T. Hoppeler, T. Juhasz, and J. F. Bille, Lasers and Light in Ophthalmol., 5, 145, (1993).
2. A. Vogel, P. Schweiger, A. Freiser, M. N. Asyo, and R. Birngruber, IEEE J. of Quant. Electron. 26, 2240, (1990).

Damage Threshold as a Function of Pulse Duration in Biological Tissue

Detao Du, Jeff Squier, Xinbing Liu, Gerard Mourou
Center for Ultrafast Optical Science
University of Michigan.
2200 Bonisteel , IST Bldg. Rm. 1006
Ann Arbor, MI 48109-2099
Ph:(313) 763-4875 Fax: (313) 763-4876

Geoff Güttmann
Center for Ultrafast Optical Science
University of Michigan.
2200 Bonisteel , IST Bldg. Rm. 1006
Ann Arbor, MI 48109-2099
and
Department of Ophthalmology
Kellogg Eye Center
University of Michigan
1000 Wall Street
Ann, Arbor MI 48105

Ron Kurtz, Victor Elner
Department of Ophthalmology
Kellogg Eye Center
University of Michigan
1000 Wall Street
Ann, Arbor MI 48105

We measured damage thresholds for corneal tissue over a range of pulse durations (from 150 fs - 7 ns) that could not be examined previously with a single laser source, using a Ti:sapphire chirped-pulse amplification (CPA) laser [1]. Our results depart from previous findings [2,3], which had to use multiple laser sources to investigate a similar pulsewidth range.

For ultrashort pulse durations (<10 ps), the primary mechanisms for tissue damage have not been described. For certain applications, such as ophthalmic surgery, collateral damage must be minimized. By understanding the mechanisms and defining the breakdown thresholds for ultrashort pulse durations, we hope to reduce collateral damage for these precision applications.

Laser-induced optical breakdown consists of three general steps: free electron generation and multiplication, plasma heating and material deformation or breakdown. Avalanche ionization and multiphoton ionization are the two processes responsible for the breakdown. The laser-induced breakdown threshold in dielectric material depends on the pulsewidth of the laser pulses. An empirical scaling law of the fluence breakdown threshold as a function of the pulsewidth is given by $F_{th} \propto \sqrt{\tau_p}$, or alternatively, the intensity breakdown threshold, $I_{th} = F_{th}/\tau_p$. Although this scaling law applies in the pulsewidth regime from nanosecond to tens of picoseconds, recently, we found that the breakdown threshold does not follow the scaling law when laser pulses are shorter than ten picoseconds for SiO_2 [4]. Therefore, a systematic investigation of the breakdown threshold of cornea tissue as a function of the laser pulsewidth should enable us to identify the best operating parameters.

We performed a series of experiments to determine the breakdown threshold of cornea as a function of laser pulsewidth between 150 fs - 7 ns, using a CPA laser system . One advantage of this laser system is the laser pulsewidth can be varied while all other experimental parameters (spot size, wavelength, energy, etc.) remain unchanged. The laser was focused to a spot size (FWHM) of 26 μm. The plasma emission was recorded as a function of pulse energy in order to determine the tissue damage threshold. Histology was also performed to assess tissue damage.

Breakdown thresholds calculated from plasma emission data revealed deviations from the scaling law, $F_{th} \propto \sqrt{\tau_p}$. As shown in Figure 1, the scaling law of the fluence threshold is true to about 10 ps, and fails when the pulse shortens to less than a few picoseconds. The standard deviation of breakdown threshold measurements decreased with shorter pulses. Histological analysis reveals more localized ablation with pulses less than 10 ps.

The breakdown threshold for ultrashort pulses (< 10 ps) are less than longer pulses and have smaller standard deviations. The reduced collateral damage caused by ultrashort laser pulses show that these systems may have a future in ophthalmic and other precision surgical procedures.

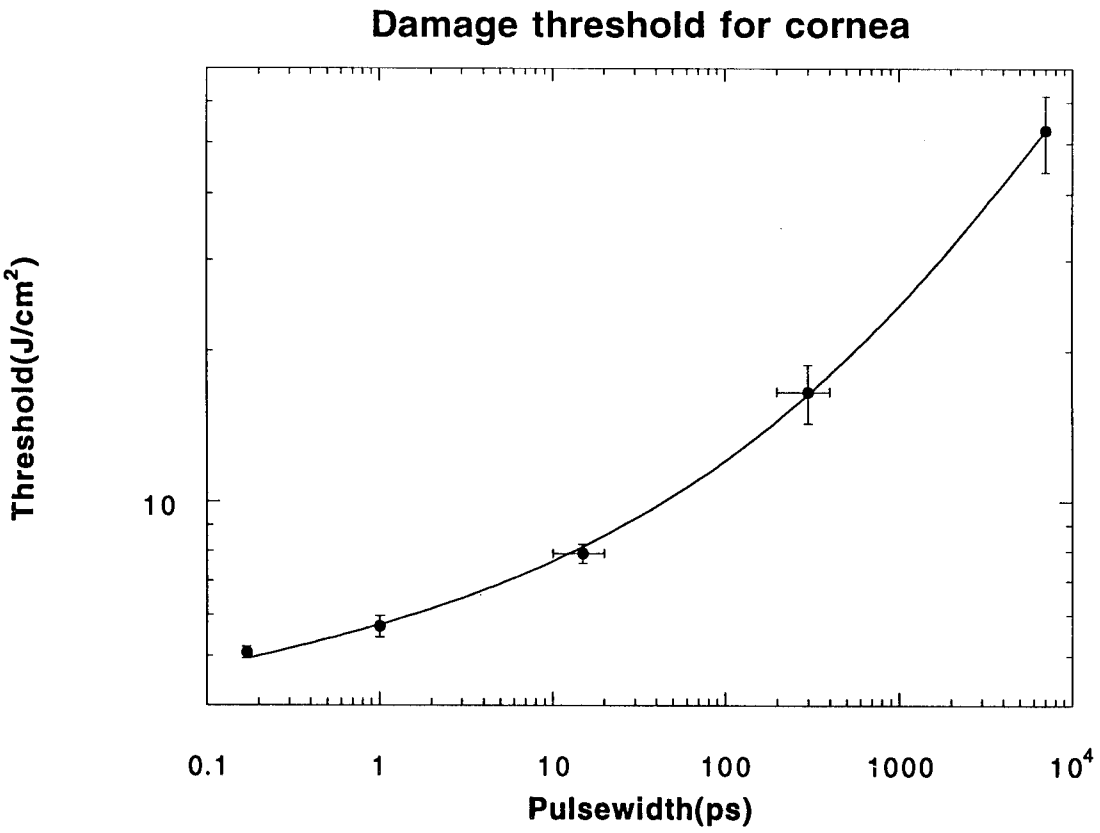


Figure 1. Damage threshold of cornea as a function of pulse duration.

This work was partially supported by the National Science Foundation under STC PHY 8920108 and the Midwest Eye Bank and Transplantation Centers.

[1] J. Squier, F. Salin, G. Mourou, Opt. Lett. **16**, 324

[2] D. Stern, R. Schoenkin, C. Puliafito, E. Dobi, R. Birngraber, J. Fujimoto, Arch. Opthalmol. **107**, 587 (1987)

[3] R. Birngruber, C. Puliafito, A. Gawande, W. Lin, R. Schoenlein, J. Fujimoto, IEEE J. Quantum Electron. **23**, 1836 (1987)

[4] D. Du, X. Liu, G. Korn, J. Squier, G. Mourou, submitted to App. Phys. Lett..

Abdulsabirov, Ravil Yu. — WC12
Aeschlimann, M. — TuC4
Afanasjev, V. V. — WC18
Aiello, A. — WC28
Alfano, Joseph C. — MB4, FA5
Alfano, Robert R. — MD29, MG
Alivisatos, A. P. — TuC5
Anfinrud, Philip A. — FB4
Antonetti, A. — WC14, WC27
Apkarian, V. A. — ThE3
Arakawa, Y. — TuE5
Arlt, T. — TuB7
Arnett, D. C. — ME4
Artemyev, M. V. — MD25
Asaki, M. T. — ThD14
Athey, Brian — WA3
Atkinson, G. H. — TuD10
Audebert, P. — WC14, WC27
Auer, H. — WC11
Auston, D. H. — ThD10
Azouz, A. — TuD4

Bachilo, S. M. — WC13
Backus, S. — ThD14
Bakker, H. J. — MD9, WC11
Balling, P. — ThC3
Banin, Uri — MB3, ThE5
Bar-Ad, S. — TuE4
Bar-Joseph, I. — TuE4
Barbara, Paul F. — MB4, TuD20, ThD11, FA5
Barber, James — TuD11
Bardeen, C. J. — ThD16
Baronavski, A. P. — ThB3
Bartana, Allon — ThE5
Barty, C. P. J. — WB3, ThD19
Baumert, T. — ThB4
Beaudoin, Y. — ThA1
Beaulieu, Y. — MD26
Beck, W. — TuE2
Becker, Michael F. — MD17
Benigno, Andrea — ME3
Bennhardt, D. — MD5, ThD22
Benzler, J. — WC2
Berg, Mark — ME3, ThD21
Betzig, E. — WA5
Bhargava, R. N. — WC4
Bingemann, D. — FA4
Birkedal, D. — WC5
Biswas, R. — TuD22
Blankenship, R. E. — TuB3
Bliton, Christyne — WA3
Bloom, D. M. — TuD22, WA1
Bondarev, S. L. — WC13
Bor, Z. — MD23
Borguet, E. — TuC3
Boskovic, A. — WC3
Bostak, J. — TuD22
Botkin, D. — WA2
Bouma, B. — MD24
Brabec, T. — MA1
Bradforth, S. — FB3
Brakenhoff, G. J. — WA3
Braun, Alan — ThA4, ThD24
Brener, I. — ThD15
Breton, J. — TuB1
Broers, B. — ThC3
Bron, W. E. — WC20
Brorson, S. D. — WC5
Brovelli, L. R. — MD8
Brun, Alain — MD17, TuD6
Brunemeier, Paul — ThD7
Buckman, A. Bruce — MD17
Bucksbaum, P. — TuD9, ThC
Budil, K. S. — ThC2
Bultmann, T. — FA4
Bungay, A. R. — WC6
Buontempo, J. T. — WC21
Burnett, N. H. — ThC1
Burr, K. C. — ThD17

Campagnola, P. J. — ThB1
Campbell, M. — WE
Cao, J. — TuC4
Castner, Edward W. Jr. — TuD17
Causgrove, Timothy P. — TuB4
Cavicchia, Michael A. — MD29
Chachisvilis, M. — TuB6
Chaker, M. — ThA1
Chambaret, J. P. — WC14
Champion, P. M. — TuB5
Chang, Yong Joon — TuD17
Chatenoud, F. — MD26
Chemla, Daniel S. — TuE1, WA2, ThD15, ThD27
Chen, Chun-Ying — WA4
Chen, Yaodong — MD12
Cheng, T. K. — TuA1
Chien, C. Y. — MD16, ThA1
Chiu, T. H. — MC3, MD8
Cho, Minhaeng — ThE1
Choi, H. K. — ThD2
Chronister, Eric L. — TuD28
Cina, Jeffrey A. — WC25, ThB2
Coe, J. S. — MD16
Coe, S. — ThA1
Colvin, V. L. — TuC5
Cong, Peijun — TuD18, WC7
Corkum, P. B. — ThC1
Côté, C. Y. — ThA1
Cowen, B. R. — FB2
Crane, J. C. — ThA2, ThC2
Craxton, R. S. — MD16
Crowell, Robert A. — ThD23
Cui, Yan — MD12
Culver, J. P. — TuC2
Cundiff, S. T. — TuD1, TuD2
Cunningham, J. E. — ThD5
Curley, P. F. — MA1, ThD4

Damen, T. C. — WC19
Darack, S. B. — WB2
de Boeij, Wim P. — ME2
De Martini, F. — WC28
de Vivie-Riedle, R. — WC8
Dekorsy, T. — TuE2, WC11
Delage, A. — MD26
Delfyett, P. J. — MA3, MF
DeLong, Kenneth W. — MC2, TuD5
Deuel, Hans P. — TuD18, WC7
Dhar, Lisa — ThE4
Dianov, E. M. — ThD20
Diels, Jean-Claude — ThD24
Dietrich, P. — ThC1
Ditmire, T. — ThC2
Domcke, Wolfgang — WC31
Dong, Y. — TuD20
Donnelly, T. D. — ThA2
Doorn, Stephen K. — ThD13
Dougherty, Thomas P. — FA2
Downer, M. C. — TuA4, WC9, ThA
Dresselhaus, M. S. — TuA1
Du, Detao — TuA2, ThA4, ThD24, FB6
Du, Mei — ThD3
Dubinskii, Mark A. — WC12
Dudley, J. M. — WC24, ThD4
Dunn, Robert C. — WA6
Dunn, Thomas J. — WC15
Duppen, Koos — ME2
Durfee, C. G., III — ThA3
Durrant, James R. — TuD11
Dutton, P. L. — FB2
Dyer, R. Brian — TuB4, ThD13
Dykaar, D. R. — WB2

Ebrahimzadeh, M. — WC24
Edamatsu, Keiichi — WC12
Eisenthal, Kenneth B. — TuC3, ThE
Elizondo, Juan M. — ThD24
Ellingson, R. J. — ThD17
Elner, Victor — FB6
Elsaesser, T. — MD6, TuD16
Elsayed-Ali, H. E. — WC20
Erland, J. — MD13
Ernsting, N. P. — FA4
Esarey, E. — WC29
Estable, Frederick — WC10

Fainberg, B. D. — TuD25
Falcone, R. W. — ThA2
Falliès, F. — WC14, WC27
Fauchet, P. M. — TuD7, WC16
Fayer, Michael D. — ME, TuD15, FA1
Fehr, M. J. — WC26
Feldmann, J. — TuD2, TuE3
Feldstein, M. J. — ME4
Fermann, M. E. — MF, TuD23, WC30, ThD29
Fidler, V. — FB3
Fleming, Graham R. — ThD3, ThE1, FB3
Florez, L. T. — MA3
Fourkas, John T. — ME3, ThE4
Franco, M. A. — MD28
French, P. M. W. — MA3, MF
Frenkel, A. — MD3
Frey, W. — TuD16
Frietas, John — ThD21
Froberg, N. M. — ThD10
Fröjdh, K. — MD10
Fujimoto, J. G. — MD24, ThD2, FB

Gai, F. — WC26
Gale, G. M. — WC1
Gallagher, D. — WC4
Galvanauskas, A. — TuD23, WC30
Gao, Y. — TuC4
Garside, B. K. — MD26
Gauthier, J. C. — WC14, WC27
Gavrilovic, P. — TuD4
Geindre, J-P. — WC14, WC27
Georges, Patrick — MD17, TuD6
Gerber, Benny — FA
Gerber, G. — TuD19, ThB4
Gillbro, T. — WC13
Glasbeek, M. — MD7
Glover, T. E. — ThA2
Göbel, E. O. — TuD1, TuD2, TuE3
Goldberg, S. Y. — TuD25
Goldman, J. R. — TuA3
Golubovic, B. — ThD2
Gong, Ke-Cheng — MD20

Gong, T. — TuD7
Gooding, E. — ThD12
Goossen, K. W. — ThD5
Gordon, C. L., III — WB3, ThD19
Goswami, D. — ThD28
Gosztola, David — WC17
Gouveia-Neto, A. — MD24
Grand, J. Y. — TuD19
Gray, S. — WC18
Grillon, G. — WC14, WC27
Grudinin, A. B. — WC18
Gurin, V. S. — MD25
Güttmann, Geoff. — FB6
Guy, M. J. — WC3

Habib, M. S. — FB5
Hache, F. — WC1
Hamm, P. — ThD6
Hansen, O. — WC5
Harris, Charles B. — MB
Harris, S. E. — ThD19
Harter, D. J. — TuD23, WC30
Harvey, J. D. — ThD4
Hattori, Toshiaki — MD14
Hattori, Yasuhiro — ME5
Haus, Hermann A. — WB
Heilweil, Edwin J. — FA2
Hey, R. — MD5, ThD22
Hillegas, C. W. — ThD28
Ho, F. — WA1
Ho, K. M. — TuD22
Hochstrasser, Robin M. — MB2, MD30, TuB, TuC2, ThD12, FB2
Hoheisel, W. — TuC5
Holtom, Gary R. — WA6, ThD23
Hong, J. — MA4
Hong, S. — MD15
Hörmann, A. — ThD11
Hou, A. S. — WA1
Hou, Jianmin — MD12
Hou, Xun — MD12
Hu, B. B. — ThD5, ThD10
Hu, X. F. — TuA4
Huang, Chung-Po — WB4
Huber, H. — TuB7
Hunsche, S. — MD9
Hunter, C. N. — TuB1, TuB6
Hunter, James — MC2
Hupp, J. T. — TuD20
Huppert, D. — TuD25
Hvam, J. M. — MD13

Ido, T. — MD21
Ikegami, Isamu — ThD8
Ippen, E. P. — TuA1
Itoh, Shigeru — ThD8
Itoh, Tadashi — WC12
Ivanov, M. Y. — ThC1
Iwaki, Masayo — ThD8
Izatt, J. A. — MD24

Jackson, Timothy A. — FB4
Jahn, L. G. — TuC2
Jahnke, F. — TuE3
Jarasiunas, K. — WC5
Jarzeba, W. — ThD11
Jia, Yiwei — ThD3, ThE1
Jiang, Z. — ThA1
Jimenez, R. — FB3
Jin, Y. — MD15
Jmako, S. P. — MD25
Johnsona, C. — TuC5
Jones, M. R. — TuB1, TuB6
Jonkman, A. M. — MD7
Joo, Taiha — ThE1
Joseph, D. Melissa — TuD11
Juhasz, T. — WC20, FB5

Kafka, J. D. — TuD21
Kaiser, W. — TuD16
Kandori, Hideki — TuD3, ThD8
Kane, Daniel J. — MC2
Kane, S. — ThD1
Kaplan, A. E. — MD19
Kapteyn, Henry C. — MA2, WB4, ThD14
Kartner, F. X. — MA5
Kawato, Sakae — MD14
Keiding, S. R. — WC5
Keller, U. — MA5, MD8, MD24, MF
Kelly, S. M. J. — MA1
Kieffer, J. C. — MD16, ThA1
Kim, B. — MD18
Kim, J. — WC29
Kimura, Y. — MB4
Kingsley, L. — MD15
Kittelmann, O. — TuD13
Klein, P. B. — WC4
Klug, David R. — TuD11
Knorr, A. — TuD2
Knox, Robert S. — TuD11
Knox, Wayne H. — MF, WA, WB2, ThD15
Ko'pev, P. S. — TuD1
Kobayashi, Shunsuke — MD11
Kobayashi, Takayoshi — ME5
Kobe, K. — ThB5
Koch, M. — TuE3
Koch, S. W. — TuD2, TuE3
Kochereshko, V. P. — TuD1
Kohler, Bern — TuD5, TuD9
Köhler, K. — TuE2
Kokta, Milan — MA2
Kopf, D. — MA5
Korableva, Stella L. — WC12
Korn, G. — MD16, TuA2, ThA1, ThA4, ThD1, ThD24
Kosloff, Ronnie — MB3, ThE5
Kostoulas, Y. — WC16
Kovács, A. P. — MD23
Krausz, F. — MA1, ThD4
Kuang, Tingyun — MD12
Kuhl, J. — MD5, ThD22
Kühling, H. — ThB5
Kuhn, T. — MD6
Kumazaki, Shigeichi — ThD8
Kurtz, Ron — FB6
Kurz, H. — MD9, TuE2, WC11

L'Huillier, A. — ThC2
Lago, A. — MD19
Lai, Tian-Shu — MD20
Lamb, K. — MA4
Lambry, C. — TuB1
Landgren, G. — MD10
Laubereau, A. — TuC1
Lauterwasser, C. — ThD6
Ledentsov, N. N. — TuD1
Lee, Y.-S. — WC9
Leiderer, P. — TuD19
Leisching, P. — MD6, TuE2
Leitenstorfer, A. — MD6
Lemoff, B. E. — WB3
Leo, K. — TuE2
Lepine, Thierry — MD17, TuD6
Levinson, Y. — TuE4
Li, M. — TuC2
Li, Melissa — MC3
Li, P. — TuB5
Li, Z. — ThE3
Lim, Manho — FB4
Lin, S. — TuB3
Lin, Wei-Zhu — MD20
Lineberger, W. Carl — ThB1
Linkersdörfer, S. — WC2
Lipman, E. A. — ThA2
Liu, Xinbing — TuA2, ThA4, ThD24, FB6
Liu, Y. — MD3
Liu, Zhenlin — WC12
Lochschmidt, A. — FA4
Loh, W. H. — WC18
Lohner, A. — MD6
Lotshaw, William T. — MD4, WC21
Lourtioz, J-M. — TuD4
Ludwig, C. — TuD16
Luther, K. — WC2
Lyssenko, V. G. — MD13

Ma, Jangseok — ME3
Maas, D. J. — ThC3
Maiti, S. — FB2
Mantell, D. — TuC4
Manz, J. — WC8
Marcinkevicius, S. — MD10
Martens, C. C. — ThE3
Martin, J. L. — TuB1
Mataloni, P. — WC28
Mathies, R. A. — TuB2
Matro, Alexander — WC25
Mayer, E. J. — MD5, ThD22
McGowen, J L. — MD1
McMorrow, Dale — MD4
Meier, T. — MD5, TuE3, ThD22
Melinger, Joseph S. — MD4
Mellish, R. — MA3
Merlin, R. — MD3
Mets, Laurens — WA6
Meyer, M. — TuB7
Michel, E. — TuD22
Mikhailov, V. P. — MD25
Milchberg, H. M. — ThA3
Miller, R. J. D. — TuC4, WC21
Mimuro, Mamoru — TuD3
Mittleman, D. M. — TuC5
Mizeikis, V. — MD13
Mo, Dong — MD20
Mohideen, U. — WA5
Mohrschladt, R. — MD22
Möller, R. — TuD19
Moser, C. C. — FB2
Moss, D. J. — MD21
Mourou, Gerard A. — MD16, TuA2, TuD23, WE, ThA4, ThD1, ThD24, FB6
Mukamel, S. — ME1, WC21
Muller, Laura — ThD21
Murnane, Margaret M. — MA2, WB4, ThD14
Murra, D. — WC28
Mycek, Mary Ann — ThD27
Myers, Anne B. — ThE2
Mysyrowicz, A. — MD28, WC14, WC27

Nadal, M. — ThB1
Naganuma, K. — WB1
Nagarajan, S. — FB3
Nagasawa , Yutaka — FA3
Nägele, T. — TuB7
Nakamura, Arao — MD2
Nakatsuka, Hiroki — MD14
Nathel, Howard — WC22
Naumov, Alexander K. — WC12
Nees, John A. — WA4
Negus, D. K. — ThD18
Nelson, Keith A. — MC4, WD, ThE4
Nickel, H. — TuE3
Nishioka, M. — TuE5
Noack, F. — TuD13
Noordman, L. D. — ThC3
Normandin, R. — MD26
Norris, J. — FB3
Norris, Ted B. — TuE5, WA3, WC4
Noske, D. U. — WC3
Nozik, A. J. — ThD17
Nuss, Martin C. — MC3, MG, ThD5

O'Neil, R. H. — MD1
Ogletree, D. F. — WA2
Olin, U. — MD10
Osvay, K. — MD23
Ou, Yang-Meng — MD20
Owrutsky, J. C. — ThB3
Özbay, E. — TuD22

Palese, S. — WC21
Palit, Dipak — MD30
Pantke, K.-H. — MD13
Papanikolas, J. M. — ThB1
Parson, R. — ThB1
Partovi, Afshin — MC3
Patkar, S. — TuD24
Paul, A. E. — TuD24
Pavlov, L. I. — WC1
Paye, J. — MC1
Payne, D. N. — WC18, ThD20
Pelletier, J. F. — ThA1
Pépin, H. — ThA1
Perakis, I. E. — ThD15
Perry, M. D. — ThA2, ThC2
Peteanu, L. A. — TuB2
Petrich, J. W. — WC26
Petrov, V. — TuD13
Petrova-Koch, V. — WC16
Peyrusse, O. — ThA1
Pfeiffer, L. N. — WC19
Pieterse, J. W. — TuD21
Pinkos, Dan — TuD9
Pippenger, R. S. — FB2
Planken, P. C. M. — ThD5
Ploog, K. — MD5, ThD22
Pollock, Clifford R. — WC22
Popov, S. V. — WC6
Popp, A. — TuD10
Portella, M. T. — TuD16
Porter, George — TuD11
Prabhu, S. S. — ThD25
Prade, B. S. — MD28
Prokoshin, P. V. — MD25
Prybyla, J. A. — TuA3
Pshenichnikov, Maxim S. — ME2
Pugliano, Nick — MD30
Pullerits, T. — TuB6

Raftery, D. — ThD12
Rech, Thomas — TuD11
Reed, M. K. — ThD18
Reid, D. T. — WC24
Reid, P. J. — TuD20
Reischl, B. — WC8
Rhee, J.-K. — TuE5
Richardson, D. J. — ThD20
Riffe, D. M. — WC9
Ringling, J. — TuD13
Roberti, T. W. — MD1
Rodwell, Mark — MG
Rohland, S. — ThB5
Rosenthal, S. J. — TuB2, TuC5
Rosenwaks, Y. — ThD17
Roskos, H. — TuE2, WC11
Rossi, F. — MD6
Rossky, Peter J. — MB1, ThD9
Rousse, A. — WC14, WC27
Roy, S. K. — ThD25
Rudd, J. V. — ThD1
Ruff, A. — ThB5
Ruhman, Sanford — MB3, TuD14, ThE5
Russell, J. — MD24
Rutz, S. — ThB5

Sage, J. T. — TuB5
Salieres, P. — ThC2
Salin, François — WC10
Salmeron, M. — WA2
Sanders, G. D. — ThD2
Sarukura, Nobuhiko — WC12
Sasabe, Hiroyuki — TuD3
Sasaki, Fumio — MD11
Sattler, F. — TuD19
Savikhin, S. — TuB3
Schafer, W. — TuE3
Scheer, H. — TuB7
Scherer, N. F. — ME4
Schmidt, A. J. — MA, MA1
Schmidt, S. — TuB7
Schmuttenmaer, C. A. — TuC4
Schoenlein, R. W. — TuB2, TuC5
Schreiber, E. — ThB5
Schroeder, J. — MD22
Schüler, H. — ThA5
Schulze, A. — MD5, ThD22
Schumacher, D. — TuD9
Schwartz, Benjamin J. — MB1, ThD9
Segawa, Yusaburo — WC12
Seidner, Luis — WC31
Seifert, F. — TuD13
Semashko, Vadim V. — WC12
Sengupta, Abhijit — TuD15
Sennaroglu, Alphan — WC22
Sha, W. — TuD24
Shah, Jagdeep — TuE, WC19, ThD25
Shank, C. V. — MC, TuB2, TuC5, WE, ThD16
Sheu, Wen Shyan — MB1
Shi, C. — MA2, ThD14
Shi, L. — TuD7
Shi, X. — TuC3
Shiang, J. J. — TuC5
Shipulin, A. V. — ThD20
Shkolnikov, P. L. — MD19
Shtrikman, H. — TuE4
Sibbett, W. — MA4, MF, WC24
Siegner, Uwe — ThD27
Sierra, R. — MD24
Silva, C. — TuD20
Simon, John D. — TuD18, WC7
Slusher, R. E. — WA5
Smirl, Arthur L. — TuD24
Smith, G. O. — MD5, ThD22
Smith, Kevin — MG
Sobolewski, Roman — TuD7
Sommerer, G. — ThB5
Sørensen, C. B. — WC5
Sosnowski, T. — WC4
Speaker, M. G. — FB5
Spence, D. E. — MA4
Spielmann, Ch. — MA1, ThD4
Spill, B. — TuD2
Sprangle, P. — WE
Squier, Jeff — MD16, TuA2, TuD5, TuD9, WA3, ThA4, ThD1, FB6
Stankov, K. A. — MD27
Stanton, C. J. — ThD2
Stark, J. B. — WA5
Staver, P. Randall — MD4
Steiner-Shepard, M. — ThD18
Stelmakh, N. — TuD4
Stingl, A. — MA1
Stock, Gerhard — WC31
Stock, M. L. — TuD23, ThD29
Stolz, W. — MD6, TuD2
Stoutland, Page O. — ThD13
Struve, W. S. — TuB3
Suárez, C. — WC20
Sullivan, A. — ThA2
Sun, C.-K. — ThD2
Sundstrom, V. — TuB6
Suzuki, Yoshiro — WC12
Svanberg, Sune R. — FB1
Svec, Walter A. — TuD8
Svirko, Yu. P. — WC6
Sweetser, John N. — WC15
Syage, Jack A. — TuD26
Szarka, Arpad Z. — MD30
Szipöcs, R. — MA1, MD23

Taft, G. — MA2
Tang, C. L. — ThD17
Tang, Chongqin — MD12
Tanimura, Y. — ME1, WC21
Taylor, J. R. — MA3, WC3
Thacker, B. R. — ThD17
Thakur, Khalid A. M. — ThD11, FA5
Thalweiser, R. — ThB4
Thantu, N. — MD18
Thomas, P. — MD5, TuE3, ThD22
Tien, A.-C. — ThD1
Tokizaki, Takashi — MD2
Tokmakoff, A. — FA1
Tom, Harry W. — TuC
Tominaga, Keisuke — FA3
Tournois, P. — ThD1
Trebino, Rick — MC2, TuD5
Troe, J. — MD22, WC2
Tsurumachi, Noriaki — MD14
Tsybeskov, L. — WC16
Tull, J. X. — ThD28
Tuttle, G. — TuD22

Ucer, K. B. — WC16
Uher, C. — MD3
Ujj, L. — TuD10
Umstadter, D. — WC29

van den Heuvell, H. B. van Linden — ThC3
van der Meer, P. — MD26
van der Meulen, P. — MD7
van der Weide, Daniel — ThD7
van Grondelle, R. — FB3
van Mourik, F. — FB3
Vanden Bout, David — ME3, ThD21
Vandyshev, Ju. V. — WC16
Vengurlekar, Arvind — ThD25
Vinet, J-Y. — MD28
Vogler, S. — TuD19
Vöhringer, P. — MD22, ME4
von der Linde, D. — ThA5
Vorsa, V. — ThB1
Vos, M. H. — TuB1
Votsmeier, M. — MD22

Wagoner, G. — MD15
Wakana, Shin ichi — WA4
Waldman, Amir — TuD14
Walhout, P. K. — MB4, FA5
Walker, G. C. — FB2
Wallin, J. — MD10
Walmsley, Ian A. — WC15, WC16
Walser, Rodger M. — MD17
Wang, C. A. — ThD2
Wang, Hailin — WC19
Wang, Hui — MD20
Wang, Q. — TuB2
Wang, Shuicai — MD12
Wang, X. Y. — WC9
Warren, W. S. — WD, ThD28
Waschke, C. — TuE2, WC11
Wasielewski, Michael R. — TuD8, WC17
Watson, J. — TuD6
Watts, M. L. — TuD21
Waxer, L. — WC16
Weber, P. M. — MD18
Weber, Willes H. — MG
Wefers, Marc M. — MC4
Weiner, Andrew M. — MG, WC23
Weiner, John — ThB
Weisbuch, C. — TuE5
Weiss, S. — WA2
Weiss, V. — ThB4
Weling, A. S. — ThD10
Weng, X. — TuD7
Westervelt, R. A. — ME4
Whitaker, J. F. — MD3
White, William E. — MC2
Wiedenmann, E. — ThB4
Wiederrecht, Gary P. — TuD8
Wiersma, Douwe A. — ME2
Wiesenfeld, Jay — MG
Williamson, Steve — MG
Wilson, Kent R. — TuD5, TuD9, WD
Wintner, E. — MA1
Woerner, M. — TuD16
Wolfrum, K. — TuC1
Woodruff, William H. — ThD13
Wöste, L. — ThB5

Xie, X. Sunney — WA6, ThD23
Xiong, W. — TuD7

Yakovlev, Vladislav V. — TuD5, TuD9
Yamada, Hiroko — WC17
Yan, Yi Jing — TuD18
Yang, Kunyun — MD12
Yang, L.-M. — TuD23
Yang, Tzyy-Schiuan — ThE2
Yartsev, Arkadiy P. — FA3
Ye, Tong — MD12
Yelland, C. — MA4
Yodh, A. G. — TuC2
Yoshihara, Keitaro — ThD8, FA3
Yoshizawa, Masayuki — ME5
Yu, Zhenbao — MD12
Yumashev, K. V. — MD25

Zadoyan, R. — ThE3
Zewail, Ahmed H. — WD
Zhang, H. — MD7
Zhang, J. Z. — MD1
Zhang, Ruihua — ThE2
Zhang, X.-C. — MD15
Zhao, Xin Miao — ThD24
Zheludev, N. I. — WC6
Zhou, Jianping — MA2, WB4
Zhu, L. — TuB5
Zhu, Y. — TuB3
Zimdars, D. — FA1
Zinth, W. — TuB7, ThD6
Zurek, M. — ThD6

ARO 32824.1-EL-CF

ULTRAFAST PHENOMENA

Sponsored by
Optical Society of America

ADDENDUM AND POSTDEADLINE PAPERS

MAY 2–6, 1994
DANA POINT, CALIFORNIA

1994 Ultrafast Phenomena Topical Meeting
May 2-6, 1994
Dana Point, California

POSTDEADLINE PAPER SESSION
8:00PM - 10:00PM

Thursday, May 5, 1994

8:00pm
PDP 1 Ultrafast observation of an electron gas in SiO2, P. Audebert, J.C. Gauthier, J.P. Geindre, LULI, France, P. Daguzan, S. Guizard, P. Martin, G. Petite, DRECAM/SRIM, France, A. Dos Santos, G. Hamoniaux, A. Antonetti, ENSTA, France.

8:08pm
PDP 2 Multielectron dissociative ionization of chlorine molecules in intense femto- and picosecond laser fields: a puzzling result, M. Schmidt, C. Cornaggia, P. D'Oliveira, P. Meynadier, D.Normand, CEA, France.

8:16pm
PDP3 Dephasing dynamics of epitaxial polydiacetylene films, T.A. Pham, A. Daunois, J-Y Bigot, J. Le Moigne, Institut de Physique et Chimie des Materiaux de Strasbourg, France.

8:24pm
PDP4 Vibrational dynamics at the active site of myoglobin: picosecond infrared free-electron laser experiments, K. Peterson, A. Tokmakoff, B. Sauter, D. Zimdars, M. Fayer, Stanford Univ., J. Hill, D. Dlott, Univ. of Illinois, Urbana Champaign.

8:32pm
PDP5 Ultrafast isomerization dynamics of 11-cis-locked 8-membered Rhodopsin, H. Kandori, H. Sasabe, RIKEN, Japan, T. Mizukami, Y. Shichida, Kyoto Univ., Japan, K. Nakanishi, Columbia Univ., T. Yoshizawa, Osaka Sangyo Univ., Japan.

8:40pm
PDP6 Observation of coherent surface optical phonons by time-resolved second-harmonic generation (SHG), L. Xu, Y. Chang, H. W.K. Tom, Univ. of California, Riverside.

8:48pm
PDP7 Observation of fifth order optical response of liquid CS2 by non-resonant six-wave mixing, K. Tominaga, Y. Naitoh, T. Kang, K. Yoshihara, Inst. for Molecuar Science, Japan.

8:56pm
PDP8 Femtosecond coherent generation of hot electrons monitored via band-to-acceptor luminescence in GaAs, A. Leitenstorfer, T. Elsaesser*, A. Lohner, Technische Universitat Munchen, Germany, T. Kuhn, Universitat Stuttgart, Germany, S. Haas, F. Rossi, Universitat Marburg, Germany.

9:04pm
PDP9 Vibrational relaxation of a charged species in nonpolar solvent, J. King, M. Asplund, C. Harris, Univ. of California, Berkeley.

9:12pm
PDP10 The femtosecond dynamics of aggregate excitons in liquids, M. v. Burgel, D.A. Wiersma, K. Duppen, Univ. of Groningen, The Netherlands.

9:20pm
PDP11 Programmable wavefunction engineering in Cs Rydberg states, P. Bucksbaum, D. Schumacher, D. Pinkos, Univ. of Michigan, J. Hoogenraad, FOM, The Netherlands, J. Krause, K. Wilson, Univ. of California, San Diego.

9:28pm
PDP12 THz study of field screening: 10 fs-100 fs regime, B. Hu, E. DeSouza, W. Knox, M. Nuss, J. Cunningham, AT&&T Bell Laboratories.

9:36pm
PDP13 The first determination of extremely fast biexcitonic radiative decay in GaAs quantum wells, H. Wang, J. Shah, T. Damen, L. Pfeiffer, AT&T Bell Laboratories.

*Max Born Institut

1994 Ultrafast Phenomena

ADDENDUM

ThD26 Impulsive excitation of LO phonons and induced transient refractive index charge measurement, D.P. Klein, O. Albert, J. Cl. Loulergue*, J. Etchepare, Ecole Polytechnique-ENSTA, France.

*Universite de Metz et Supelec is an additional affiliation

Ultrafast observation of an electron gas in SiO_2

P. Audebert,[1] P. Daguzan,[2] A. Dos Santos,[3] J.C. Gauthier,[1] J.P. Geindre,[1]
S. Guizard,[2] G. Hamoniaux,[3] K. Krastev,[2] P. Martin,[2] G. Petite,[2] A. Antonetti[3]

[1]*LULI, Ecole Polytechnique, 91128 Palaiseau, France.*

[2]*Commissariat à l'Energie Atomique, DRECAM/SRSIM,*
91191 Gif sur Yvette, France.

[3]*Laboratoire d'Optique Appliquée, ENSTA, Batterie de l'Yvette,*
91120 Palaiseau, France.

Abstract: Interferences in the frequency domain with sub-picosecond resolution are used to observe the ultra-fast excitation and relaxation of a photoexcited electron gas in SiO_2.

PD4-1

Ultrafast observation of an electron gas in SiO_2

P. Audebert,[1] P. Daguzan,[2] A. Dos Santos,[3] J.C. Gauthier,[1] J.P. Geindre,[1]
S. Guizard,[2] G. Hamoniaux,[3] K. Krastev,[2] P. Martin,[2] G. Petite,[2] A. Antonetti[3]

[1]*LULI, Ecole Polytechnique, 91128 Palaiseau, France.*

[2]*Commissariat à l'Energie Atomique, DRECAM/SRSIM,*
91191 Gif sur Yvette, France.

[3]*Laboratoire d'Optique Appliquée, ENSTA, Batterie de l'Yvette,*
91120 Palaiseau, France.

When an ultra-short and intense laser field propagates inside a dielectric medium, it induces a strong polarization field and, if the intensity is high enough, it produces a high density of electrons and holes. In this paper, we report on an experiment based on a new phase-sensitive technique [1,2] which allows the direct visualization of the polarization and the excitation density with a resolution of 120 femtosecond in time and 5 μm in space. To our knowledge, the very first relaxation events, concerning the *photogenerated carriers in the conduction band*, remain an unexplored domain in wide band-gap insulators.

The principle of this experiment is the following: the target is probed with two collinear femtosecond pulses separated by a fixed time delay (1 ps in this experiment). These two pulses are then analyzed in a spectrometer. The area of the sample of interest is imaged on a slit of variable aperture at the entrance of the spectrometer. The power spectrum of such a sequence is a fringe system with a period inversely proportional to the pulse separation. This interference pattern is visualized on a CCD camera: one axis represents the wavelength, while the radial spatial dimension is represented on the perpendicular axis. If a high intensity pump pulse (ranging from 10^{12} W/cm^2 to a few 10^{13} W/cm^2 in this experiment) is focused on the sample at some delay between the two probe pulses, the second probe pulse will experience a disturbed dielectric constant. This leads to a local distortion of the interference pattern. The induced phase shift can thus be recorded and analyzed as a function of delay and space. The absorption of the probe pulse is simultaneously

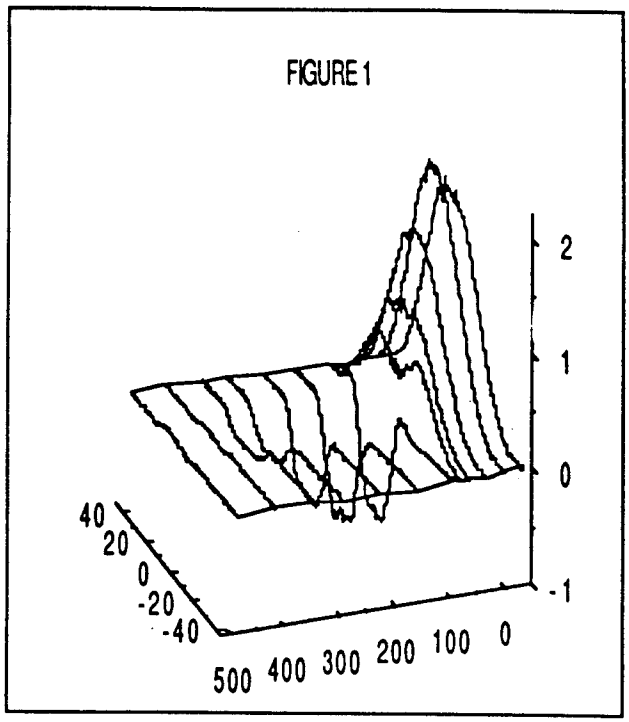
PD4-2

obtained by measuring the fringe contrast directly on the interference pattern. For this experiment we use as a pump a colliding-pulse mode-locked (CPM) dye laser which emits 70 fs pulses at 620 nm amplified to energies up to 3 mJ. Probe pulses are produced by continuum generation and frequencies around 560 nm are selected and amplified. Their time duration is 60 fs. The samples are 100 μm thick high purity amorphous (a-SiO_2) and crystalline (α-SiO_2) silicon-dioxyde.

In figure 1, the phase shift between probe pulses is shown as a function of space and time for a-SiO_2. The pump intensity is set at 2.7×10^{13} W/cm^2. The spot size is 25 μm (FWHM). We observe a very rapid evolution of the phase shift as a function of the time delay between the pump pulse and the second probe pulse. It is positive for time delay close to zero, becomes suddenly negative and finally goes back to a value close to zero. Concerning the space dependence, the positive phase shift occurs in a broader region, the half width of the signal is larger than in the case of negative phase shift. This result is interpreted as follows: the positive phase-shift is due to an induced phase-modulation and occurs as long as the pump pulse and the second probe pulse temporally overlap. Note that the temporal resolution (120 fs) can be directly observed in figure 1. On the other hand, a free-electron population, produced by multiphoton absorption, induces a negative phase shift which becomes visible even before the pump pulse has ended. Let us note that a decrease of the phase shift implies a decrease of the free-electron density. More precisely, electrons must be trapped into levels deeper than the photon energy, otherwise they would be seen as free by the laser field. The trapping of the gas is extremely fast and its time dependence is well fitted by an exponential law with a time decay of 150 fs. As a consequence, the gas has "disappeared" before expanding to a measurable extent. We find that this mean time does not depend on the pump intensities we consider. The similarity of the results between α-quartz and silica proves that these traps have an intrinsic character because the density of extrinsic defects in amorphous silica is known to be greater than in the crystallized form. We attribute the rapid variation of the excitation density to the formation of E' centers whose kinetic of formation has been recently measured [3].

In figure 2, we present the time-dependent absorption of the probe pulse. As in figure 1, the function is well fitted by an exponential time decay in both materials, which does not depend on the pump intensity.The absorption kinetic is however slightly slower: 200 fs instead of 150 fs. At short time delay, when the excitation density is of the order of 3×10^{19} cm^{-3}, the probe absorption is very high (25%). We attribute this absorption to free-carriers. This is supported by a Monte Carlo simulation, based on an approach similar to [4], in which we included electron-phonon collisions

PD4-3



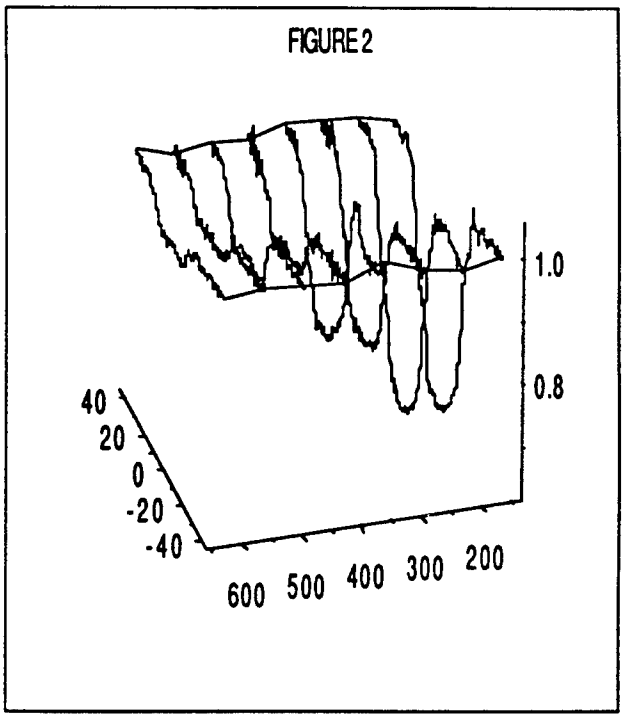


Figure 1 : phase shift (in radian) as a function of time (fs) and space (μm). The first five curves have been divided by 1.5. The pump intensity is 2.7×10^{13} W/cm^2.

Figure 2 : probe free-carrier absorption as a function of time (fs) and space (μm) for a-quartz

(optical and acoustical) and electron-photon-phonon collisions. Electrons are injected with a mean excess energy of 1 eV above the bottom of the conduction band. Although no traps have been included in the simulation, we found that free-carrier absorption is strongly dependent on the energy-relaxation due to electron-phonon collisions. This means that the observed decay-time in figure 2 is the result of two processes, namely the energy relaxation of the electron gas and the trapping of the free electrons. More accurate model for the trapping process will be needed to distinguish precisely the contribution of each mechanism.

[1] E. Tokunaga, A. Terasaki and T. Kobayashi, Opt.Lett. **18**, 370 (1992).

[2] J. P. Geindre, P. Audebert, F. Falliès, A. Rousse, J. C. Gauthier, A. Antonetti, J. P. Chambaret, G. Grillon, A. Mysyrowicz, to be published.

[3] P. N. Saeta, B. I. Greene, Phys. Rev. Lett. **70**, 3588 (1993).

[4] D. Arnold, E. Cartier, Phys. Rev. B **46**, 15102 (1992).

Multielectron Dissociative Ionization of Chlorine Molecules in Intense Femto- and Picosecond Laser Fields: a puzzling result.

M. Schmidt, C. Cornaggia, P. D'Oliveira, P. Meynadier and D. Normand

Service des Photons, des Atomes et des Molécules

CEA - Centre d'Etudes de Saclay

91191 Gif-sur-Yvette Cedex, France

Abstract

The multielectron dissociative ionization of the chlorine molecule shows identical near Coulomb explosion with femto- and picosecond pulses of same intensity.

PD11-1

Multielectron Dissociative Ionization of Cl_2 in Intense Femto- and Picosecond Laser Fields: a puzzling result.

M. Schmidt, C. Cornaggia, P. D'Oliveira, P. Meynadier and D. Normand
Service des Photons, des Atomes et des Molécules
CEA - Centre d'Etudes de Saclay
91191 Gif-sur-Yvette Cedex, France

I. Introduction

During the last few years the interaction of diatomic molecules with very intense pico- and femtosecond laser fields has become a field of intense research [1 - 5]. One essential issue of the multielectron dissociative ionization (MEDI) studies concerns the interaction dynamics, i.e., the competition between the removal of the electrons and the dissociation of the molecular ions [2]. The interaction of ultrashort laser pulses with heavy molecules has been suggested to avoid this competition since ionization would occur on a time scale where nuclear motion is essentially frozen and the Coulomb repulsion of such 'inertially confined' molecular ions would follow in field-free conditions. Indeed, the experiments performed on I_2 with 30 fs pulses [3] yield energy releases which are closer to those predicted by the Coulomb model (E_{Cb}) than it is the case for experiments with lighter molecules [1, 2, 4]. In order to determine the respective role of the molecular electronic structure and of the ultrashort pulse excitation, we have investigated the MEDI of Cl_2 with femto- and picosecond pulses. The results are somewhat puzzling, because the energy releases are found to approach the E_{Cb} values, although the Cl_2 molecule cannot be considered as frozen on the time scale of the interaction.

II. Experimental

Briefly, the femtosecond laser is a commercial Ti:sapphire (Ti:Sa) system (Continuum) of the DRECAM laser facility delivering pulses of 150 fs duration at 790 nm with an energy of 2 mJ and operating at 20 Hz. The picosecond synchro-pumped dye laser system, delivering 2.5 ps pulses at 616 nm at a rate of 10 Hz, has already been described in detail [4]. The dye laser beam is focused with a 50 mm parabolo-spheric lens yielding a peak intensity I_{max} of about 5×10^{15} W/cm^2, whereas the Ti:Sa beam is focused with a 60 mm achromatic lens ($I_{max} \approx 2\times10^{16}$ W/cm^2). By stopping down the Ti:Sa beam, equalization of the laser peak intensities is achieved. The fragment-energy measurement is based on the forward-backward splitting of the ion species in a time-of-flight mass-spectrometer (TOF-MS) [2, 4]. The extraction and acceleration fields of the TOF-MS are 100 V/cm and 400 V/cm, respectively.

III. Results and Discussion

A typical TOF mass-spectrum obtained from the MEDI of Cl_2 after interaction with Ti:Sa laser pulses at maximum intensity (see Section II) is presented in Figure 1. The spectrum is dominated by the three Cl_2^+ and Cl_2^{2+} molecular-ion signals corresponding to the different isotopic combinations ($^{35}Cl_2$, $^{35}Cl^{37}Cl$ and $^{37}Cl_2$) with the expected abundance ratio 9:6:1 (both Cl_2^{2+} and HCl^+ signals with m/q = 36, 38 are present). Identification of the different fragmentation channels has been achieved using high resolution TOF spectra and covariance mapping [1, 5].

PD11-2

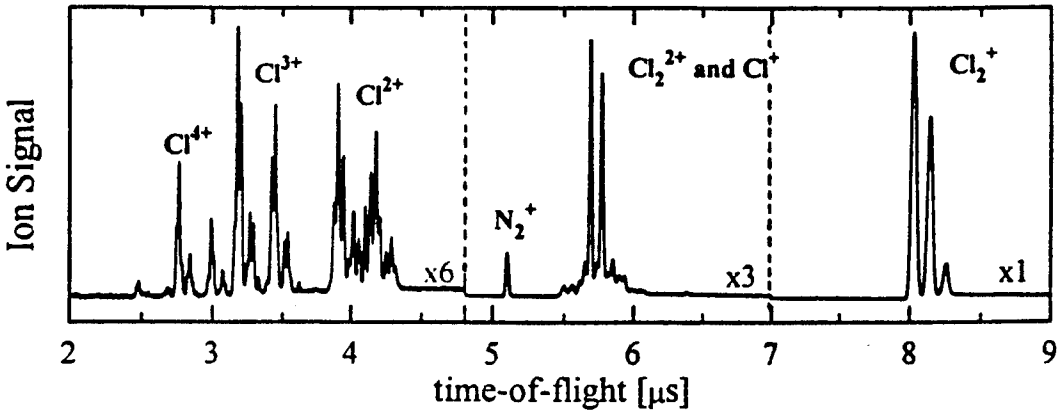


Figure 1: TOF ion mass-spectrum of Cl_2 recorded with 150 fs pulse duration, 790 nm wavelength and 2×10^{16} W/cm^2 laser intensity. The laser polarization is parallel to the detection axis. The extraction field in the interaction zone is 100 V/cm and the Cl_2 pressure is 2×10^{7} Torr. A global peak assignment is given in the figure. Note the different ion-signal scaling factors for Cl_2^+: (×1), Cl_2^{2+}, Cl^+ and N_2^+: (×3) and Cl^{2+}, Cl^{3+} and Cl^{4+}: (×6).

Table 1 shows the identified fragmentation channels for molecular ions up to Cl_2^{8+} and the measured respective kinetic energy releases E_{exp}. These energies have been compared to the values E_{Cb} expected from pure Coulomb repulsion and assuming the neutral ground-state internuclear distance ($R_0 = 2.0$ Å). Interestingly, a constant energy ratio E_{exp}/E_{Cb} of about 70 % is systematically found for all fragmentation channels.

Table 1: Measured kinetic energy releases E_{exp} from the MEDI of Cl_2 (same laser conditions as in Fig. 1) for different fragmentation channels $Cl_2^{(p+q)+} \rightarrow Cl^{p+} + Cl^{q+}$. The absolute error of the energy values is always better than 10 %. The ratio E_{exp}/E_{Cb} of the experimental and Coulomb energy releases is also given.

fragmentation channels (p, q)	E_{exp} [eV]	E_{exp}/E_{Cb} [%]
(1,1)	5	69
(1,2)	10	69
(2,2)	20	69
(2,3)	30	69
(3,3)	45	69
(3,4)	62	71
(4,4)	80	69

The constant energy ratios E_{exp}/E_{Cb} observed in our experiment suggest, that the multiphoton-ionization steps occur along a vertical path [2] with a constant equilibrium internuclear distance of $1.4 \times R_0$. However, the laser pulse duration is longer (150 fs) than the ground-state vibrational period of chlorine (60 fs), so that the molecular ions should start to dissociate during the interaction. In order to test this idea, the MEDI of Cl_2 has also been

PD11-3

performed with longer laser pulses. Figure 2 shows a comparison of the Cl^{2+} and Cl^{3+} ion spectra of chlorine, obtained with the 150 fs laser at 790 nm (Fig.2a) and the 2.5 ps laser at 616 nm (Fig.2b), for equal intensities ($I_{max} = 5\times10^{15}$ W/cm^2). As a matter of fact, the two spectra are almost identical, i.e., the kinetic energy releases are independent of the pulse duration.

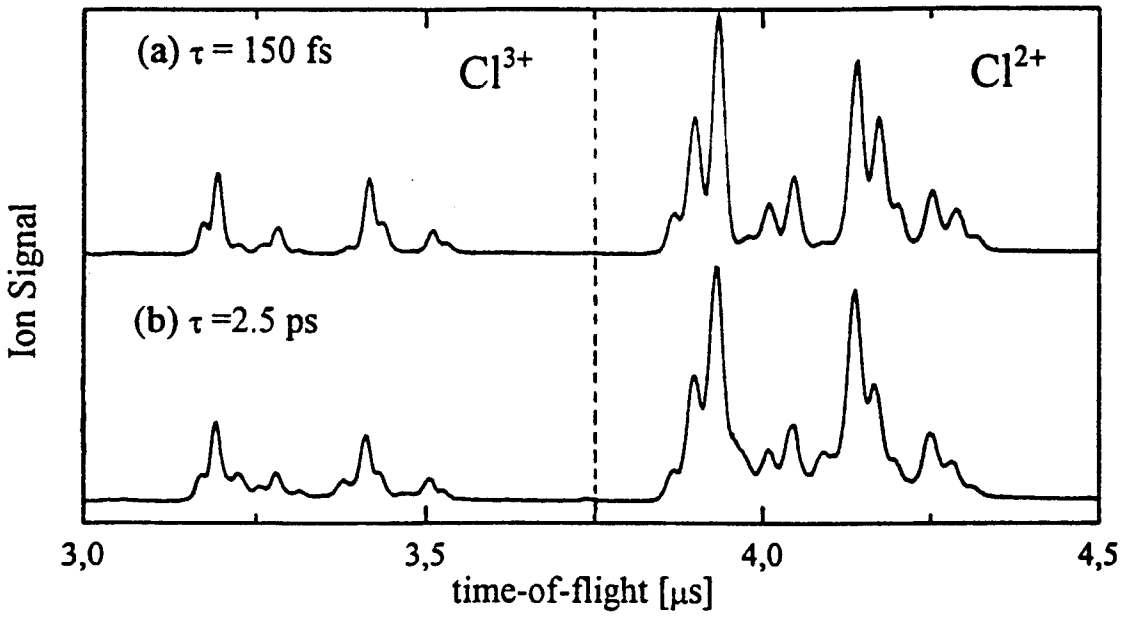


Figure 2: Part of the TOF ion mass-spectra of Cl_2 showing Cl^{2+} and Cl^{3+} fragment ions obtained with femtosecond or picosecond laser pulses at the same laser intensities (see text). The laser polarization is parallel to the detection axis.

In conclusion, the present result is the first example where near Coulomb energies are found in the long-pulse regime and raises the question of the interaction dynamics. Obviously, our experimental conditions are far from the laser field-free dissociation of inertially confined molecular ions [3], and yet the Cl_2^{n+} ions seems to follow a simple Coulomb explosion at $R = 1.4 \times R_0$. Surprisingly, the molecular ions would then remain frozen during the laser pulse duration, although the vibrational period of the molecule is much smaller. This result demonstrates that the electronic structure of the molecule certainly plays an important role in the MEDI processes [6], either through screening effects or through stabilization effects [7].

References

[1] D. Normand and C. Cornaggia 1993 *Laser Physics* **3, 3** 664 and references therein.
[2] C. Cornaggia, J. Lavancier, D. Normand, J. Morellec, P. Agostini, J.P. Chambaret and A. Antonetti 1991 *Phys. Rev. A* **44, 7** 4499.
[3] D.T. Strickland, Y. Beaudoin, P. Dietrich and P.B. Corkum 1992 *Phys. Rev. Lett.* **68, 18** 2755.
[4] C. Cornaggia, J. Lavancier, D. Normand, J. Morellec and H.X. Liu 1990 *Phys. Rev. A* **42, 9** 5464.
[5] L.J. Frasinski, K. Codling and P.A. Hatherly 1989a *Science* **246** 1029.
[6] C. Cornaggia, D. Normand and J. Morellec 1992 *J. Phys. B: At. Mol. Opt. Phys.* **25** 415
[7] A. Giusti-Suzor and F.H. Mies 1992 *Phys. Rev. Lett.* **68, 26** 3869.

Dephasing Dynamics of Epitaxial Polydiacetylene Films

T.A. Pham[1], A. Daunois[1], J. Le Moigne[2], J.-Y. Bigot[1]

[1]*Groupe d'Optique Non-Linéaire et d'Optoélectronique*

[2]*Groupe des Matériaux Organiques*

Institut de Physique et Chimie des Matériaux de Strasbourg

Unité Mixte 380046 CNRS–ULP–EHICS, 67037 Strasbourg Cedex, France

Tel. : (33)88.35.80.77 – FAX : (33)88.25.61.87

Abstract : The dephasing dynamics of epitaxial polydiacetylene films resonantly excited with 10fs optical pulses is investigated. A 52fs relaxation time and quantum beats with 23fs period are reported.

Dephasing Dynamics of Epitaxial Polydiacetylene Films

T.A. Pham[1], A. Daunois[1], J. Le Moigne[2], J.-Y. Bigot[1]

[1]*Groupe d'Optique Non-Linéaire et d'Optoélectronique*

[2]*Groupe des Matériaux Organiques*

Institut de Physique et Chimie des Matériaux de Strasbourg

Unité Mixte 380046 CNRS–ULP–EHICS, 67037 Strasbourg Cedex , France

Tel. : (33)88.35.80.77 – FAX : (33)88.25.61.87

The optical properties of conjugated polymers like polydiacetylenes (PDA) are influenced by the material characteristics such as the nature of the main chain and side groups or the degree of polymerization and the chain orientation [1]. It is therefore important to have high quality samples in order to investigate the intrinsic dynamical properties of PDA excited with ultrashort optical pulses. In this paper, we report measurements on the dephasing dynamics of highly oriented epitaxial PDA films using photon echoes produced by 10 fs pulses.

The samples are oriented poly[1,6 - di(N-carbazolyl) - 2,4 hexadiyne] films (pDCH) grown by epitaxy on a potassium acid phtalate crystalline substrate [2]. They are characterized by a large degree of polymerization ($> 98\%$) and present an uniaxial orientation of the polymer chains. The inset of figure 1 shows the absorption spectra of a 120 nm-thick sample for light polarization parallel and

perpendicular to the chain. The dichroic ration is $\sim$ 18 on the main excitonic resonance at 1.92 eV. The ultrafast relaxation dynamics of the PDA film was investigated with the pump-probe and photon echo techniques using 10 fs pulses produced by a compressed, copper vapor laser amplified CPM laser [3].

The pump-probe measurements (performed with 70 fs pump and 10 fs probe pulses) reveal a hole burning at the spectral position of the laser and a fast decay of the exciton with $\sim$ 800 fs time constant. This decay is followed by a longer relaxation ($\sim$ 3 ps) which we attribute to the decay of self-trapped excitons as already reported in partially oriented PDA-4BCMU samples [4]. The hole burning, which lasts during the pump pulse, suggests a fast polarization decay of the exciton within the inhomogeneous absorption linewidth. This was confirmed by observing self-diffracted photon echo signals as a function of the time delay between the two incident 10 fs pulses. In figure 1, we have plotted a typical signal obtained with an incident energy of 400 pJ/pulse (approximate power density : 5 GW/cm^2). In addition to the photon echo decay, periodic oscillations with 23 fs period show up, which we attribute to the double bond stretching modes (181 meV) of the PDA chain. The dashed curve is a fit using a simplified three-level system (ground state and two excited states $\mid 2 >$ and $\mid 3 >$), with a decaying behavior proportional to : $[1 + \alpha \cos\omega_{23} t]^2 \exp\left[-\frac{4t}{T_2}\right]$. The fitting parameters are $\omega_{23} = 0.273$Rd fs^{-1} corresponding to 180 meV for the energy splitting between levels $\mid 2 >$ and $\mid 3 >$, $T_2 = 52$ fs for the transverse excitonic relaxation, $\alpha = 0.11$ for the ratio of the dipole moments corresponding to the transitions to the two excited states. The main features are reproduced with this simple model, indicating that most of the dephasing is due to an energy tranfer to the system mode of the linear PDA chain. A detailed study of this energy transfer is being carried out under various excitation conditions and wave-mixing geometries.

REFERENCES

[1] see, for instance, *"Nonlinear Optical Properties of Organic Molecules and Crystals"*, Vol. 2, edited by D.S Chemla and J. Zyss (Academic Press Inc., Orlando, 1987)

[2] J. Le Moigne, F. Kajzar, and A. Thierry, Macromol., **24**, 2622 (1991)

[3] R.L. Fork, C.H. Brito Cruz, P.C. Becker, and C.V. Shank, Opt. Lett., **12**, 483 (1987)

[4] M. Yoshizawa, A. Yasuda , and T. Kobayashi, Appl. Phys. B, **53**, 296 (1991); M. Yoshizawa, Y. Hattori, and T. Kobayashi, Phys. Rev. B, **47**, 3882 (1993)

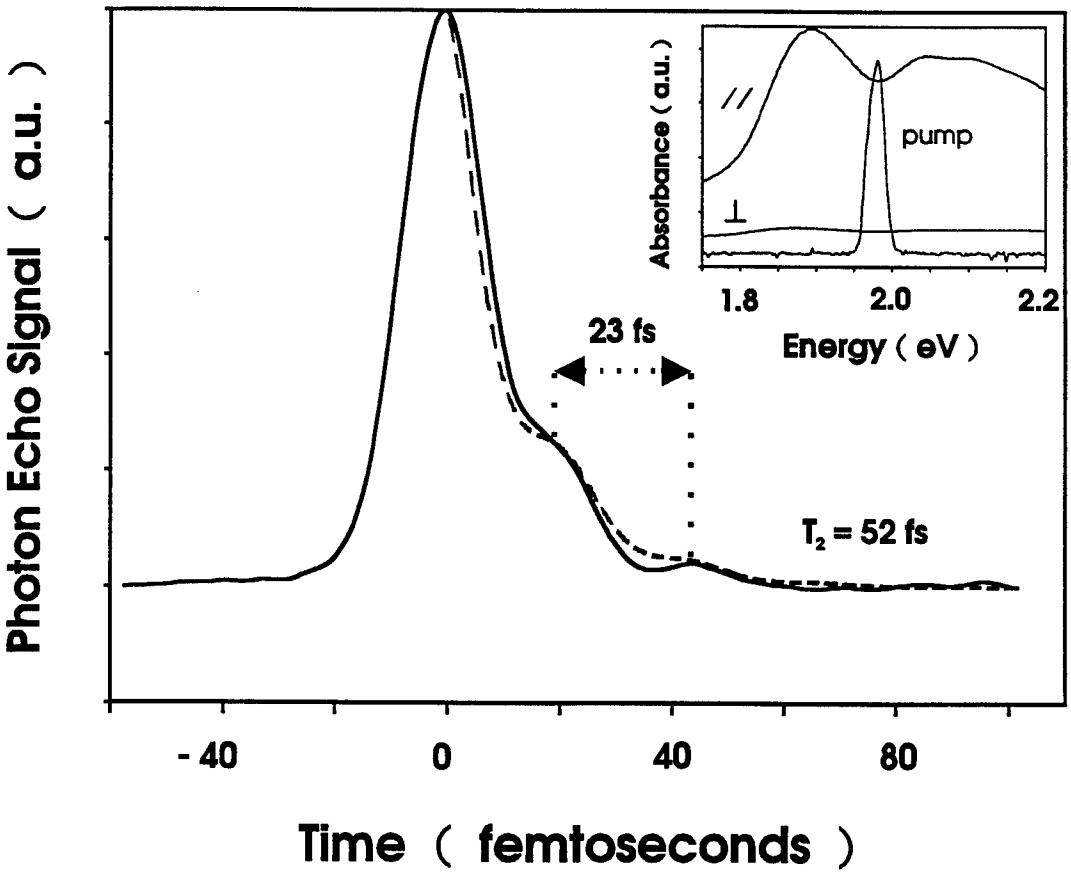


Figure 1 : Photon echo decay as a function of time delay between the 10 fs pulses. Inset : Transmission of the sample for excitation polarization parallel and perpendicular to the chain.

Vibrational Dynamics at the Active Site of Myoglobin: Picosecond Infrared Free-electron Laser Experiments.

K. A. Peterson[1], J. R. Hill[2], A. Tokmakoff[3], B. Sauter[3], D. Zimdars[3], D. D. Dlott[2], and M. D. Fayer[3]

[1]Hansen Experimental Physics Laboratory, Stanford University, Stanford, CA 94305
[2]School of Chemical Sciences, University of Illinois at Urbana Champaign, Urbana, IL 61801
[3]Department of Chemistry, Stanford University, Stanford, CA 94305

Abstract

Vibrational lifetimes of CO bound to myoglobin and to a water-soluble Fe:porphyrin were measured by ps infrared experiments. Vibrational relaxation rates are found to depend on protein conformational substate and porphyrin substitution.

Vibrational Dynamics at the Active Site of Myoglobin Picosecond Infrared Free-electron Laser Experiments.

Kristen A. Peterson[1], Jeffrey R. Hill[2], A. Tokmakoff[3], B. Sauter[3], D. Zimdars[3], Dana D. Dlott[2], and M. D. Fayer[3]

[1]Hansen Experimental Physics Laboratory, Stanford University, Stanford, CA 94305
[2]School of Chemical Sciences, University of Illinois at Urbana Champaign, Urbana, IL 61801
[3]Department of Chemistry, Stanford University, Stanford, CA 94305

Abstract: We have made direct measurements of molecular energy transfer at the active site of a protein using intense tunable mid-IR pulses from a free-electron laser to measure the loss of vibrational energy from CO bound to a bare water soluble heme and CO bound to the active sites of different conformational substates of myoglobin. Vibrational relaxation rates are found to depend on protein conformational substate and porphyrin substitution.

Experimental: Preparation of the Mb-CO samples follows the general procedure outlined previously [1]. Glycerol:water (60:40) samples were ~30 mM horse heart Mb (Sigma) buffered to pH = 7.0 with sodium phosphate, held in a 0.1 mm path cell with 1 mm thick sapphire windows. PVA samples [2] were prepared by dissolving Mb-CO in a solution of 10% by weight PVA in 1 mM phosphate buffer at pH = 7.0. The PVA solution was spread on a sapphire window and allowed to dry under 1 atm of CO. The concentration is estimated at 30 mM. Fe:TPPS was synthesized from tetraphenyl porphyrin by addition of H_2SO_4, followed by metallation. The Fe:TPPS-CO sample consisted of 30 mM Fe:TPPS in glycerol:water (75:25) adjusted to pH = 10.0 by addition of NaOH. Mid-IR spectra of Mb-CO in the region of the CO stretching frequency for the glycerol:water and PVA samples are shown in Fig. 1. Following Frauenfelder's nomenclature[3], we designate the bands as different A-states. The locations of the absorption maxima are identical within apparatus resolution (0.2 cm^{-1}) to those reported previously [3] despite minor differences in sample preparation. The substantial background is caused by window reflection and solvent and protein absorption. The IR spectrum of Fe:TPPS was also obtained. Only one band in the CO stretch region was observed and can be accurately fit to a gaussian lineshape centered at 1963.7 cm^{-1} with a FWHM of 27 cm^{-1}. The IR pump-probe apparatus using the Stanford free-electron laser (FEL) has been described in detail previously [4]. The IR pulse autocorrelation was ~2 ps transform limited gaussian. FEL pulse spectra are also shown inset in Fig. 1. Experimental details will be given in a future publication[5].

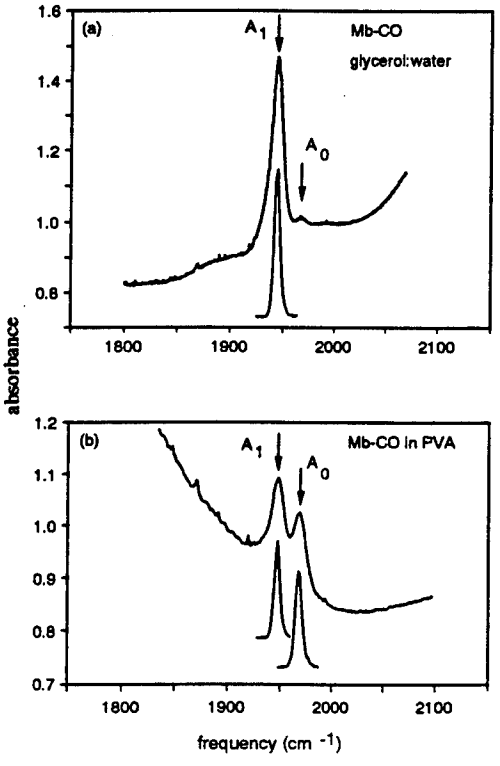


Figure 1. Infrared absorption spectra for Mb-CO in glycerol:water and PVA. Also shown are FEL pulse spectra.

Results: The lifetimes of bound CO stretching vibrations for Mb in glycerol:water and in PVA and for Fe:TPPS were obtained at ambient temperature. When the FEL was tuned off the absorption peaks, no transients were observed. This is because the background is caused by a large concentration of absorbers which cannot be optically saturated due to their smaller absorption cross-sections. The bound CO absorption can be appreciably saturated due to their far larger cross-sections, e.g., for the Mb-CO A_1 state in glycerol:water, $\sigma \approx 8 \times 10^{-17}$ cm^2. With the FEL tuned to either the A_0 or A_1 state absorption maxima of Mb-CO PVA samples, the absorption transients shown in Fig. 2 were measured. Also shown in the figure are single exponential fits and the FEL pulse

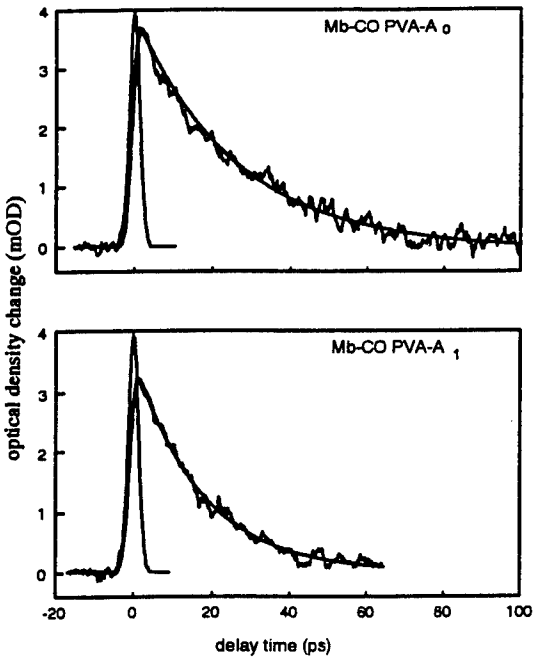


Figure 2. Vibrational relaxation of CO for the A_0 and A_1 states of Mb-CO in PVA at ambient temperature.

autocorrelation. The decays were determined by least-squares fitting to be exponential over at least 3 factors of e. The decay constants in PVA were τ = 18.2±1 ps for the A_1 state and τ = 26.6±1 ps for the A_0 state. For the A_1-state of Mb-CO in glycerol:water the decay was also exponential over at least 3 factors of e, and the time constant was τ = 17.4±1 ps. Here the error bounds denote one standard deviation from the best-fit exponential. For Fe:TPPS-CO the time constant is τ = 17±3 ps. In this case, the signal/noise was lower due to limited sample life. Pump-probe data were obtained at different temperatures in the 20-300K region. Within experimental error, no dependence on temperature was observed for the PVA samples. The A_1 state of Mb-CO in glycerol:water did evidence some temperature dependence in cooling the sample from 300K to ~200K. The decay time constant gradually increased from 17.4 ps to ~21 ps in this range, and this increase, although small, is clearly discernible with our apparatus. Below ~200K, the decay time constant is independent of temperature.

Discussion: Our observation that different A-states in Mb-CO can have different VR decay constants is significant. *It shows unambiguously that different conformational substates of the same protein can have different rates of vibrational energy transfer at the active site.* In order to explore possible contributions to vibrational relaxation and coupling in these heme/protein systems, we have plotted VR decay rate constants versus vibrational frequency in Fig. 3. using the results reported here and those obtained by Hochstrasser and coworkers for Mb-CO, Hb-CO (Hb is hemoglobin) and protoheme in D_2O [6]. All the compounds which contain protoheme (Ph) lie on a line also shown in the figure. The correlation coefficient of the least-squares fitted line is R = 0.982. Fe:TPPS which has a differently structured porphyrin, lies well off this line. Fig. 3 is highly suggestive of the following conclusions, although we caution that additional data are required to make a more compelling and statistically significant case:

1. The VR rate constant *increases linearly* with *decreasing* CO stretch frequency in proteins containing protoheme.
2. The VR rate constant shows no significant dependence on the nature or viscosity of the solvent.
3. The VR rate constant for Fe:TPPS is significantly different than that of protoheme containing compounds with similar CO stretching frequencies, suggesting that VR depends significantly on the structure of the porphyrin moiety.

We now consider some aspects of the influence of protein and heme structure on VR. In the A_1 state of Mb, the CO VR time constant is reduced by a factor of ~50% relative to the A_0 time constant or the Ph-CO time constant. There are two possible explanations for the lifetime reduction in the A_1 state: either the A_1-state conformation permits an additional energy transfer pathway from excited CO to the protein, possibly the proximal histidine residue, or the increased tilt of CO in the A_1 state enhances the coupling between excited CO and heme modes. We favor the latter interpretation because noncovalent interactions between CO and the protein are weaker than the covalently bonded interaction between CO and Fe.

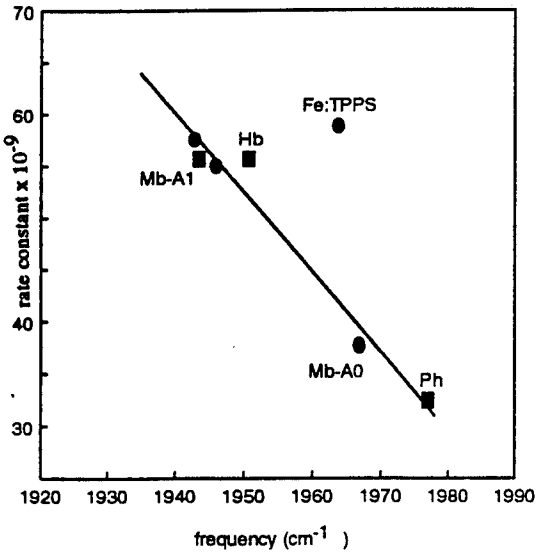


Figure 3. CO vibrational relaxation rate vs. frequency. ● = this study ■ = ref. 6

The two bare porphyrin compounds, protoheme and Fe:TPPS, have CO stretching frequencies which both lie in the higher frequency range of the compounds examined here. The different VR rates for these two compounds suggest the possibility that porphyrin structure can substantially influence VR. In comparing these two compounds, one should keep in mind that Fe:TPPS data were obtained in glycerol:water, whereas Ph data were obtained in D_2O which results in a different local solvent configuration and different proximal ligation. It does seem likely, however, that the effects of solvent are less than the effects of heme structure. For example, two protoheme-CO compounds with higher frequency CO stretching vibrations but very different solvent environments, Ph-CO in D_20 and the A_0-state of Ph-CO in Mb, are found to have similar VR rates. Effects of porphyrin structure on VR rates may be explained in two possible ways: either Fe:TPPS increases the rate of energy transfer from excited CO to heme modes, or Fe:TPPS increases the rate of energy flow from these modes into the bath. Both compounds have identical structures in the vicinity of the Fe-CO group, but differ at the molecular perimeter. Protoheme is a pyrrolic-substituted porphyrin, whereas Fe:TPPS is a meso-substituted porphyrin. The combined masses of the four sulfoxy phenyl groups on TPPS (MW = 624) is ~2.4 times greater than the combined masses of the protoheme substituent groups (MW = 260). The effects of these heavier substituents seem unlikely to exert significant influences on the vibrations which are strongly coupled to motions of the Fe-CO moiety, but very likely to increase the density of intramolecular states which provide a bath for irreversible decay of excited porphyrin vibrations.

Concluding Remarks: We have determined that different conformational substates of the same protein, Mb, have different energy transfer rates at the active site. By examining data obtained on a variety of systems containing protoheme, we have suggested the existence of a roughly linear correlation between increasing CO stretching frequency and decreasing VR rate, which indicates that VR of excited CO becomes more efficient as external influences cause the CO stretching frequency to be lowered from the ~1970 cm^{-1} value observed in compounds where CO lies nearly perpendicular to the heme plane. Continuing studies of this type on the effects of protein residue mutation, proximal ligand substitution and heme structure will further our understanding of structure and protein-ligand interactions at protein active sites.

The CO vibrational lifetime measurements should be of particular importance in investigating the accuracy of molecular dynamics simulations of heme proteins. Simulating the VR of the CO ligand does not require assumptions about transitions between different heme electronic states. The VR of excited CO occurs on the time scale readily accessible to molecular dynamics calculations (0-0.1 ns), and the entire process occurs on the ground electronic potential surface. Because the VR rate is sensitive to protein conformation, molecular dynamics studies of VR at the active site of different heme proteins, providing a range of heme pocket structures, could be an important method to understand the detailed relationships between protein structure and dynamical behavior.

Support was provided by the ONR Medical Free Electron Laser program and the National Science Foundation.

References

1. Alben, J. O.; Caughey, W. S. *Biochem.* **1968**, 7, 175. Caughey, W. S. ; Shimada, H.; Choc, M. C.; Tucker, M. P. *Proc. Natl. Acad. Sci. USA* **1981**, 78, 2903.

2. (a) Alben, J. O.; Beece, D.; Bowne, S. F.; Doster, W.; Eisenstein, L.; Frauenfelder,; Good, D.; McDonald, J. D.; Marden, M. C.; Moh, P. P.; Reinisch, L.; Reynolds, A. H.; Shyamsunder, E.; Yue, K. T. *Proc. Natl. Acad. Sci. USA* **1982**, 79, 3744; (b) Ormos, P.; Braunstein, D.; Frauenfelder, H.; Hong, M. K.; Lin, S.-L.; Sauke, T. B.; Young, R. D.; *Proc. Natl. Acad. Sci. USA* **1988**, 85, 8492.

3. Ansari, A.; Berendzen, J.; Braunstein, D.; Cowen, B. R.; Frauenfelder, H.; Hong, M. K.; Iben, I. E. T.; Johnson, J. B.; Ormos, P.; Sauke, T. B.; Scholl, R.; Schulte, A.; Steinbach, P. J.; Vittitow, J.; Young, R. D. *Biophys. Chem.* **1987**, 26, 337.

4. Zimdars, D.; Tokmakoff, A.; Chen, S.; Greenfield, S. R.; Fayer, M. D.; Smith,; T. I. Schwettman, H. A. *Phys. Rev. Lett.* **1993**, 70, 2718.

5. Hill, J.R.; Tokmakoff, A.; Peterson, K. A.; Sauter, B.; Zimdars, D.; Dlott, D. D.; Fayer, M. D., *Journal of Physical Chemistry,* **1993** submitted.

6. Owrutsky, J. C.; Li, M.; Culver, J. P.; Sarisky, M. J.; Yodh, A. G.; Hochstrasser, R. M., *Springer Proc. Physics* (Time-Resolved Vibrational Spectroscopy VI) **1993**

Ultrafast Isomerization Dynamics of 11-cis-locked 8-membered Rhodopsin

Hideki Kandori,*,# Hiroyuki Sasabe,* Koji Nakanishi,$ Toru Yoshizawa,+
Taku Mizukami,# and Yoshinori Shichida#

*Frontier Research Program, The Institute of Physical and Chemical Research (RIKEN), Wako, Saitama 351-01, Japan
$Department of Chemistry, Columbia University, New York, NY 10027, USA
+Department of Information System Engineering, Faculty of Engineering, Osaka Sangyo University, Daito-shi, Osaka 574, Japan
#Department of Biophysics, Faculty of Science, Kyoto University, Kyoto 606-01, Japan

Abstract

Femtosecond fluorescence spectroscopy of a rhodopsin analog revealed its extremely short lifetime (60 fs), suggesting coherent isomerization processes along C11-C12 rotation.

Ultrafast Isomerization Dynamics of 11-cis-locked 8-membered Rhodopsin

Hideki Kandori,*,# Hiroyuki Sasabe,* Koji Nakanishi,$ Tôru Yoshizawa,+ Taku Mizukami,# and Yoshinori Shichida#

*Frontier Research Program, The Institute of Physical and Chemical Research (RIKEN), Wako, Saitama 351-01, Japan

$Department of Chemistry, Columbia University, New York, NY 10027, USA

+Department of Information System Engineering, Faculty of Engineering, Osaka Sangyo University, Daito-shi, Osaka 574, Japan

#Department of Biophysics, Faculty of Science, Kyoto University, Kyoto 606-01, Japan

The primary isomerization dynamics of a rhodopsin analog having a flexible 8-membered ring retinal (Rh8) was studied by picosecond transient absorption and femtosecond fluorescence up-conversion spectroscopies. The former revealed the presence of a photorhodopsin-like product, suggesting that isomerization occurs in spite of fixation of 11-ene. The latter determined the fluorescence lifetime to be 60 fs, which was probing wavelength independent. Such ultrafast processes ($\phi_f \sim 10^{-6}$) meet well with the recent transient absorption results on the native rhodopsin, implying a coherent cis-trans isomerization along the barrierless potential surface of the excited state of rhodopsin.

Rhodopsin, a photoreceptor protein present in our eyes, is an excellent molecular switch to convert light signal to the electrical response of the photoreceptor cells. Elucidation of the primary photochemical event in rhodopsin has been one of the central issues in vision as well as ultrafast spectroscopy [1]. We have studied the primary isomerization mechanism by applying picosecond spectroscopies to rhodopsin analogs possessing 11-cis-locked chromophores. By observing the long-lived excited state (85 ps) and no product formation of a rhodopsin analog having an 11-cis-locked 5-membered retinal (Rh5), we have provided a direct evidence that cis-trans isomerization is a primary event in vision [2]. On the other hand, a ground-state product which resembles photorhodopsin (the first photointermediate of native rhodopsin [3]) was observed on excitation of a rhodopsin analog having an 11-cis-locked 7-membered retinal (Rh7) [2]. These results suggest that the flexibility along the 11-ene is closely related to the primary processes in vision. Thus, we extended the study by measuring the primary processes of a rhodopsin analog having an 11-cis-locked 8-membered retinal (Rh8), which has a more flexible ring structure including the 11-ene.

First, we applied picosecond transient absorption spectroscopy to the photochemical reactions of Rh8 [4]. The Rh8 sample was prepared from 11-cis-locked 8-membered retinal (Ret8) and bovine opsin. Upon excitation of Rh8 with a 532 nm, 21 ps pulse, we observed two products in picosecond regime, whose absorption spectra were similar to the primary intermediates of the native rhodopsin (i.e. photorhodopsin and bathorhodopsin) [3]. Thus, the transition from photorhodopsin

to bathorhodopsin seems to be coupled to the relaxation processes along the C_{11}-C_{12} rotation (Fig. 1).

Another interesting aspect of Rh8 was that the product formation yield was similar to that of the native rhodopsin, while that of Rh7 was about 5-times lower. This result suggested that the excited-state dynamics of Rh8 is not affected by the fixation of 11-ene through 8-membered ring and similar to that of the native rhodopsin. Therefore, we next measured the excited-state dynamics of Rh8 by means of femtosecond fluorescence spectroscopy. In order to measure the excited-state dynamics, we applied the femtosecond fluorescence spectrometer based upon the "up-conversion" technique [5]. In this apparatus, a combination of a sum-frequency generation and a single-photon counting enabled one to detect an extraordinary weak fluorescence with femtosecond resolution. The unbleached property of Rh8 is highly advantageous for the femtosecond experiments with high repetition rate (82 MHz), since the formed photoproducts revert to the original pigment within the repetition rate of the laser (< 10 ns).

Typical fluorescence decay kinetics of Rh8 probed at 578 nm is shown in Fig. 2. There present two components; a major one displays extraordinary rapid decay, which is comparable with the instrumental response (broken line in Fig. 2), and a minor one displays almost constant amplitude between 400–600 fs. The latter signal exists even at 20 ps (data not shown), indicating its lifetime to be longer than 20 ps. In comparison with the results of transient absorption spectroscopy [4], the slow component might not be coupled to the formation process of the photorhodopsin-like product, but due to the decay of the excited state of any impurity. The lifetime of the fast component was determined to be 60 ± 10 fs by the deconvolution procedure (Fig. 2). The rapid decay process is probably due to cis-trans isomerization of the chromophore. From the obtained lifetime, we estimated the fluorescence quantum yield of Rh8 to be in the order of 10^{-6} ($\phi_f \sim 6 \times 10^{-6}$) by using the lifetime (60 fs) and the natural radiative lifetime of Rh8 (~10 ns).

We next test the dependence of the probing wavelength on the fluorescence kinetics. In Fig. 3, we show the normalized fluorescence kinetics at 5 wavelengths. The obtained kinetic profile was essentially wavelength-independent in the region from 551 to 664 nm, possessing the similar kinetic features to that at 578 nm (Fig. 2). Thus, no dynamic Stokes shift was observed in this system, which is interpreted by either rapid relaxation within 60 fs, or faster reaction (60 fs) than the relaxation time. Since the lifetime (60 fs) corresponds to a few vibrations of C-C stretching, the C_{11}-C_{12} bond rotation probably occurs faster than the vibrational dephasing time, suggesting that the isomerization is a coherent process. Based upon the wavelength-independent nature, we can estimate the fluorescence spectrum of Rh8 by integrating the 60-fs component. The maximum of emission spectrum (~600 nm) is in good agreement with that observed in native rhodopsin [6].

Recent femtosecond transient absorption spectroscopy of the native rhodopsin revealed that the appearance of photorhodopsin completes within 200 fs [7]. The present femtosecond emission results on Rh8 meet well with those by transient absorption on the native rhodopsin. On the

assumption that the excited-state dynamics of Rh8 is similar to that of the native rhodopsin, we speculate the primary reaction dynamics of rhodopsin as follows;

"The excited wave-packet moves from fluorescent to non-fluorescent state in 60 fs along a barrierless potential surface of the C_{11}-C_{12} rotational coordinate. Visual cis-trans isomerization is a coherent process in its excited state and the isomerized photoproduct (photorhodopsin) is formed within 200 fs."

[1] (a) Y. Shichida, *Photochem. Photobiol.*, 52, 1179 (1990). (b) T. Yoshizawa and H. Kandori, *Progress in Retinal Research* 11, 33 (1992).

[2] H. Kandori et al., *Biochemistry* 28, 6460 (1989).

[3] Y. Shichida et al., *Photobiophys. Photobiochem.* 7, 221 (1984).

[4] T. Mizukami et al., *Proc. Natl. Acad. Sci. USA* 90, 4072 (1993).

[5] H. Kandori and H. Sasabe, *Chem. Phys. Lett.* 216, 126 (1993).

[6] A.G. Doukas et al., *Proc. Natl. Acad. Sci. USA* 81, 4790 (1984).

[7] (a) R.W. Schoenlein et al., *Science* 254, 412 (1991). (b) L.A. Peteanu et al., *Proc. Natl. Acad. Sci. USA* 90, 11762 (1993).

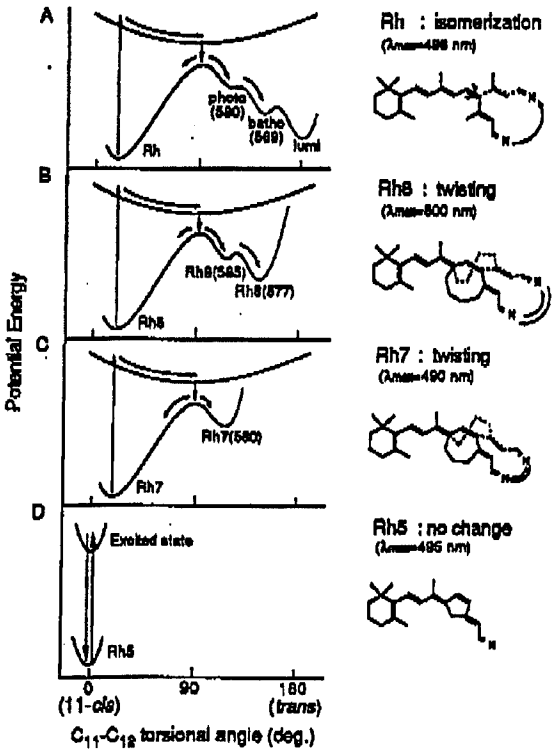


Fig. 1 Schematic drawing of potential surface of native and 11-cis-locked rhodopsins.

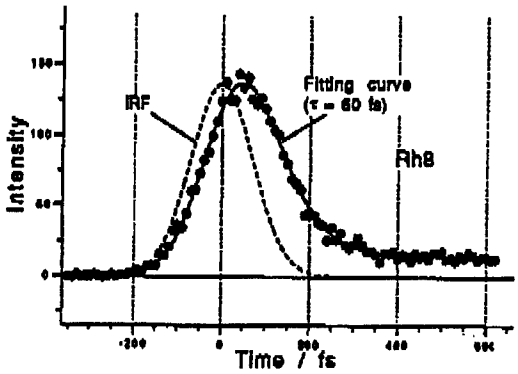


Fig. 2 Typical fluorescence decay of Rh8 measured at 578 nm.

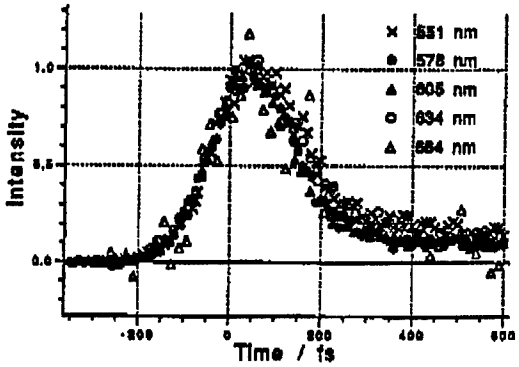


Fig. 3 Probing wavelength dependence of Rh8.

Observation of Coherent Surface Optical Phonons by Time-Resolved Second-Harmonic Generation (SHG)

Li Xu, Yuming Chang, and Harry W.K. Tom

Dept. of Physics, University of California, Riverside, CA 92521

Tel: 909-787-2818, Fax: 909-787-4529

Abstract

We report the first observation of coherent surface optical phonons. Time-resolved SHG from laser-excited GaAs (100) is modulated at 10.5 THz which is assigned to a surface phonon.

Observation of Coherent Surface Optical Phonons by Time-Resolved Second-Harmonic Generation

Li Xu, Yu-Ming Chang, and Harry W.K. Tom
Dept. of Physics, University of California, Riverside, CA 92521
Tel: 909-787-2818, Fax: 909-787-4529

Summary

We report the first observation of coherent surface phonons at optical phonon frequencies. We excite the surface phonon by impulsive stimulation and detect the surface phonon by time-resolving the second-harmonic generation (SHG) after the pump pulse. Several groups [1,2,3] have reported the observation of coherent bulk phonons in various media using short optical pulses to impulsively excite the vibrational mode. The coherent phonons are detected as modulations in the linear reflectivity after the excitation pulse. In contrast to linear reflectivity, SHG in reflection geometry is known to have decided surface sensitivity. SHG from surfaces is dipole-allowed but dipole-forbidden from the bulk of centrosymmetric media. Using the right excitation geometries, one can also measure SHG under conditions where the tensor elements are dipole-forbidden in the bulk of non-centrosymmetric media[4,5]. It should therefore be possible to observe coherent surface phonons using time-resolved surface SHG from almost any media. Indeed, we observe an oscillation in time-resolved SHG at 10.5 THz from a GaAs <001> excited with 50 fs, 850 nm pump pulses. The excitation conditions are similar to those under which bulk LO and TO coherent phonons are generated (as reported by Kurz and coworkers [2]). The bulk LO and TO phonon frequencies are 8.7 and 8.2 THz. Because SHG has a significant surface contribution and our observed oscillation at 10.5 THz is clearly higher than bulk phonon frequencies, we assign the 10.5 THz oscillation to a surface phonon.

The observation of surface optical phonons is significant for several reasons. First, this is the only technique for measuring surface phonons generally applicable to buried interfaces. Surface phonons are measured using He scattering and Electron Energy Loss Spectroscopy on clean surfaces in vacuum. SHG can be used on any interface where one side transmits the excitation and SH radiation. Second, the time-resolved technique allows measurement of the dephasing of surface phonons giving fundamental insight into surface phonon dynamics and possible technological information associated with carrier-surface phonon scattering. The latter may be especially important in devices. Third, the ability to excite coherent surface phonon oscillation and non-thermal "giant" amplitude motion opens the way to stimulating surface chemical reaction by non-thermal vibrational motion.

In Figure 1, we show the p-polarized SHG from GaAs <001> as the sample is rotated about its surface normal. The SHG is obtained at 50 degrees angle of incidence with s-polarized excitation. The data with closed circles is for n-doped GaAs with $7X10^{14}$ Si/cm^3 while the data in open circles is for n-doped GaAs with $3X10^{18}$ Si/cm^3. The built in DC fields for the 2 samples are about 6 kV/cm and 400 kV/cm, respectively. In general $E(2\omega)$ comes from both the surface and the bulk. The surface has mm2 symmetry. Bulk GaAs nominally has $\bar{4}3m$ symmetry but the symmetry near the surface is lowered to mm2 by the built-in DC field normal to the surface [6]. The SHG intensity should then be described by $I(2\omega)=|E(2\omega)|^2=|A+B\sin(2\varphi)|^2$, where A and B are linear combinations of bulk and surface susceptibilities and φ is the rotation angle. The SHG shows 4 relative maxima and overall 2-fold symmetry. B is very large and includes the dipole-allowed $\chi^{(2)}_{zxy}$ of the bulk GaAs. It is worth noting that in the absence of a DC field, the

bulk symmetry is $\bar{4}3m$ and A from the bulk is 0. The SHG from the low-doped sample shows A is small, consistent with a small DC field in the bulk. The surface contributes to both A and B.

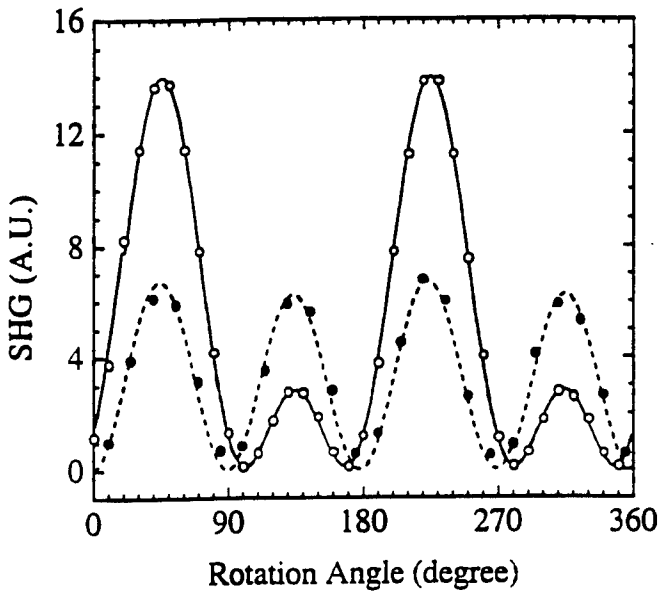


Figure 1: The orientation dependence of SHG (S_{in}-P_{out}) from n^- (dashed line) and n^+ (solid line) GaAs <001> samples. Rotation angle φ is the angle between the incident plane and <100> axis of GaAs.

In Figs. 2 and 3 we show data for the low and high doped samples, respectively. In Figs 2a and 3a, we show the time-resolved value of |B| after a pump pulse which is p-polarized and incident at 2 degrees from the surface normal. The pump spot is larger than the probe spot. The pump intensity injects 10^{19} carriers/cm^2. |B| is extracted from $2|B|^2 = |A+B|^2+|A-B|^2-2|A|^2$ which are obtained at φ=0, 45, and 90 degrees. In Fig. 2a, B increases roughly following the integral of the pump pulse (eg., maximum is after the pump pulse) and then decreases with a time constant of about 1 ps. There is a small oscillation on this signal. In Fig. 2b, the Fourier transform of |B(Δt)| shows the oscillation to be at 10.5 THz with a signal to noise ratio of 2.5. Significantly, the amplitudes at bulk LO and TO phonon frequencies at 8.7 and 8.2 THz are within the noise. In Fig. 3a, the transient response of the highly doped sample is similar to that for the low-doped sample except there is an initial transient downward which we believe is due to the initial screening of the DC field. This transient occurs during the optical pulse (eg., peak close to delay time =0) when there are enough injected carriers to completely screen the field. The DC field in the bulk will oscillate at the bulk phonon frequencies as observed in linear reflectivity [2]. The positive-going transient is similar to that in Fig 2a. In Fig. 3b, the Fourier transform of |B(Δt)| shows the signal is dominated by oscillation at 8.5 THz which is probably due to a bulk LO-phonon-plasmon coupled mode oscillation. The oscillation at 8.5 THz in the highly doped sample is 6X the oscillation at 10.5 THz in the low-doped sample. A surface phonon oscillation in the highly-doped sample may be hidden in the noise. Alternatively, a surface phonon in the highly-doped sample may not be as large or at 10.5 THz since the surfaces of the two samples are not the same. The low-doped sample was MOCVD-grown and the high-doped sample is a substrate wafer with no special surface preparation.

In conclusion, we have observed a coherent surface phonon at the GaAs <001>-native oxide interface with time-resolved surface second-harmonic generation. This technique may be applied to a variety of buried interfaces and to surfaces of interest in surface chemistry.

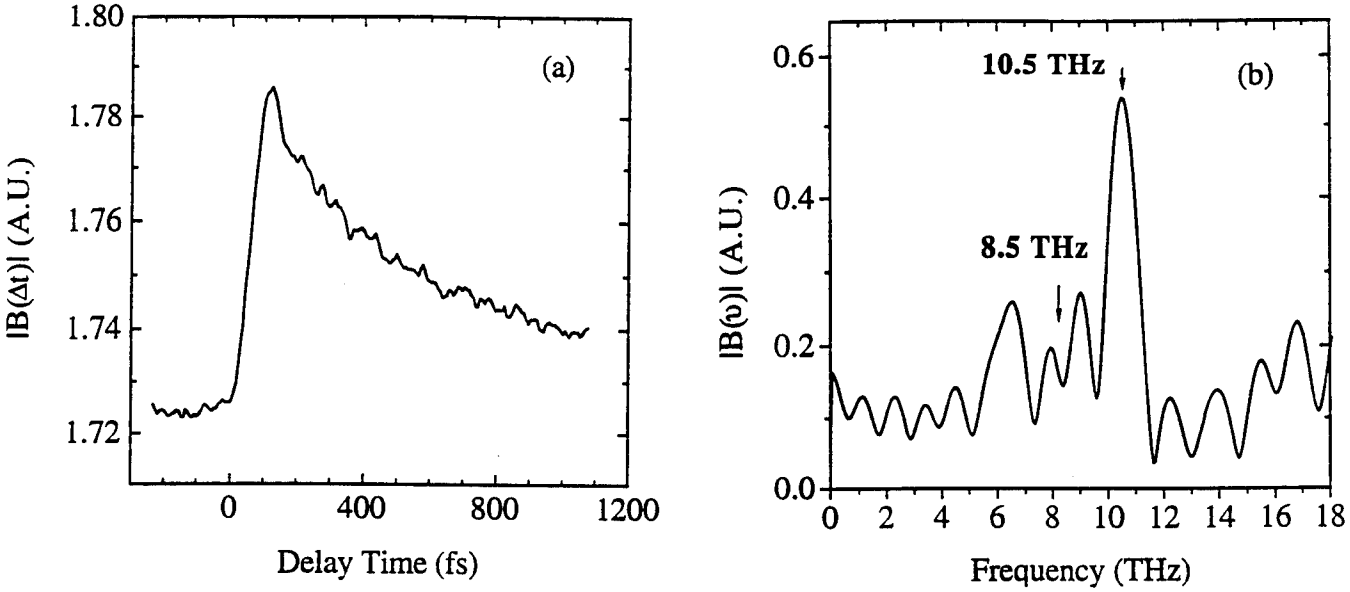


Figure 2 : (a) Time-resolved SH field IBI (see text) from n⁻ GaAs<001> sample; (b) The Fourier transform of IBI, where the peak at 10.5 THz is associated with the surface optical phonon, and the bulk LO phonon is within the noise.

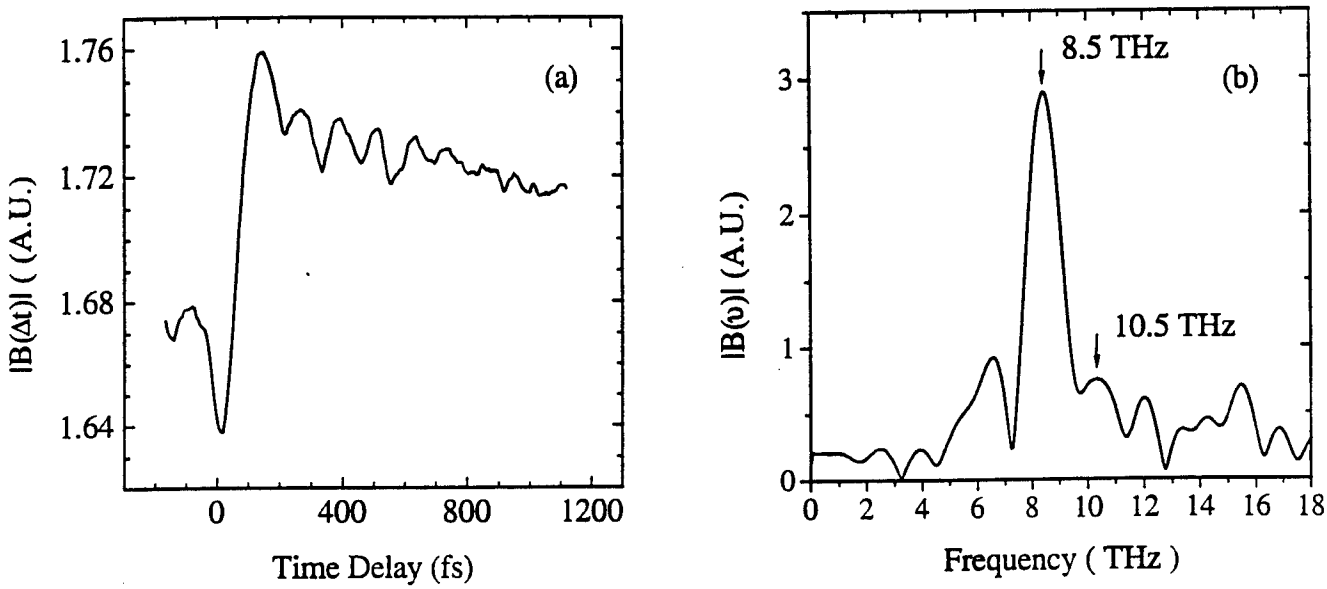


Figure 3 : (a) Time-resolved SH field IBI (see text) from n⁺ GaAs<001> sample; (b) The Fourier transform of IBI, where the peak at 8.5 THz corresponds to the bulk LO phonon, and the arrow at 10.5 THz indicates the surface optical phonon frequency.

References

1. W. Kutt, W. Albrecht, and H. Kurz, *IEEE J of QE* ***28***, 2434 (1992, and extensive refs therein).
2. G.C, Cho, W. Kutt, and H. Kurz, *Phys. Rev. Lett.* ***65***, 764 (1990).
3. T.K. Cheng, S.D. Brorson, A.S. Kazeroonian, et al, *Appl. Phys. Lett* ***57***, 1004 (1990).
4. T. Stehlin, M. Feller, P. Guyot-Sionnest, and Y.R. Shen, *Opt. Lett* ***13***, 389 (1988).
5. C. Yamada, and T. Kimura, *Phys. Rev. Lett.* ***70***, 2344 (1993).
6. J. Qi, M. S. Yeganeh, I Koltover, A. G. Yodh, and W. M. Theis, *Phys. Rev. Lett.* ***71***, 633 (1993).

Observation of Fifth Order Optical Response of Liquid CS_2 by Non-Resonant Six-Wave Mixing

Keisuke Tominaga, Yukito Naitoh, Tai Jong Kang, and Keitaro Yoshihara

Institute for Molecular Science, Myodaiji, Okazaki, 444 Japan. +81-564(55)7352

We repotrt the first observation of a fifth order optical response of liquid CS_2 by non-resonant six-wave mixing and discuss the vibrational dephasing of intermolecular modes.

Observation of Fifth Order Optical Response of Liquid CS_2 by Non-Resonant Six-Wave Mixing

Keisuke Tominaga, Yukito Naitoh, Tai Jong Kang[a], and Keitaro Yoshihara

Institute for Molecular Science, Myodaiji, Okazaki, 444 Japan. +81-564(55)7352

Vibrational dephasing in liquids has been a crucial probe of the interpretation of molecular dynamics in condensed phases. In these studies it is a key issue to investigate the relative importance of homogeneous and inhomogeneous contributions to the dephasing processes. Recent advances in nonlinear vibrational spectroscopies have allowed us to unambiguously determine these contributions to a vibrational linewidth, and the techniques have been demonstrated for high frequency intramolecular vibrational modes.[1-3] In this report we have performed time-resolved six-wave mixing spectroscopy in order to distinguish the homogeneous and inhomogeneous contributions to intermolecular vibrational modes in liquids.

Dephasing processes of low frequency modes have been observed by a femtosecond optical Kerr and impulsive stimulated light scattering (ISS) experiments using pulses whose durations are short compared to the vibrational oscillation period.[4] These experiments based on the third order susceptibility cannot distinguish the two contributions. Recently Tanimura and Mukamel have proposed a fifth order non-linear spectroscopy that is capable of distinguishing inhomogeneous contribution to low frequency vibrational modes.[5]

In the fifth order experiment a medium interacts with two pairs of short pulses at t=0 and Δt_1, and the vibrational coherence is probed by monitoring scattered light induced by a fifth pulse at $t=\Delta t_1+\Delta t_2$.[5] According to their calculations, an echo-like signal is observed at around $\Delta t_2=\Delta t_1$ in the inhomogeneous limit, while for the purely homogeneously broadened case the time-dependence of the fifth order signal is almost identical to that of the third order response when either Δt_1 or Δt_2 is scanned with the other time variable fixed.

We have performed a fifth order optical experiment on liquid CS_2 by non-resonant six-wave mixing at room temperature. A short pulse with a pulse duration of 90fs is split into five portions with almost equal intensities. The energy of each pulse is reduced down to 0.03μJ/pulse to avoid white light generation . The scattered light is identified as a fifth order signal $I^{(5)}$ by its disappearance when any of the five pulses is blocked and its appearance at the correct phase-matching angle expressed by

$$\mathbf{k}_S = \mathbf{k}_p + (\mathbf{k}_2 - \mathbf{k}_2') - (\mathbf{k}_1 - \mathbf{k}_1')$$

where $\mathbf{k}_S$ and $\mathbf{k}_p$ are the wave vectors of the fifth order response signal and probe pulse and $\mathbf{k}_i$ and $\mathbf{k}_i'$ are the wave vectors of the i-th pair of pulses. In order to separate $I^{(5)}$ from scattered light mainly arising from the third order response, the first and second pairs of pulses are mechanically chopped with different frequencies, and the signal is detected at the difference frequency. Although there are still a few third order signals which cannot be eliminated by this method, we can distinguish them from $I^{(5)}$ by their time-dependence since the probe pulse works as a "pump pulse" for these third order signals. The polarization condition is chosen so that $(\mathbf{k}_S \,//\, \mathbf{k}_p \,//\, \mathbf{k}_1' \,//\, \mathbf{k}_2') \perp (\mathbf{k}_1 \,//\, \mathbf{k}_2)$.

Figure 1(a) shows the ISS signal from CS_2 taken under the polarization condition of $(\mathbf{k}_p \,//\, \mathbf{k}_1') \perp (\mathbf{k}_1 \,//\, \mathbf{k}_S)$. The signal is almost the same as the one reported by Nelson and coworkers.[4,6] In Fig. 1(b) the fifth order signals are illustrated as a function of Δt_2 with

different fixed Δt_1. Scattered light at $\Delta t_2 = -\Delta t_1$ is mainly due to a third order response. The power dependence of the signal is shown in Fig. 2. The relative intensities at the peak of $I^{(5)}$ and the intensity change expected for the third and fifth order responses are shown in the figure. It can be seen that under the low power condition the signal varies as a function of the fifth power of the laser intensity. The ratio between $I^{(5)}$ and the scattered light at $\Delta t_2 = -\Delta t_1$ changes because of the cubic power dependence of the scattered light.

It is notable that the variation of $I^{(5)}$ as a function of Δt_2 is almost identical to that of the ISS signal. In Fig. 1(b) the relative intensity of $I^{(5)}$ at maximum is shown with that of the ISS signal. The change of $I^{(5)}$ as a function of Δt_1 is also quite similar to that of the ISS signal. All the experimental results are consistent with the prediction by Tanimura and Mukamel for the case where the inhomogeneous contribution to the broadening of the low frequency vibrational modes of CS_2 is minor.

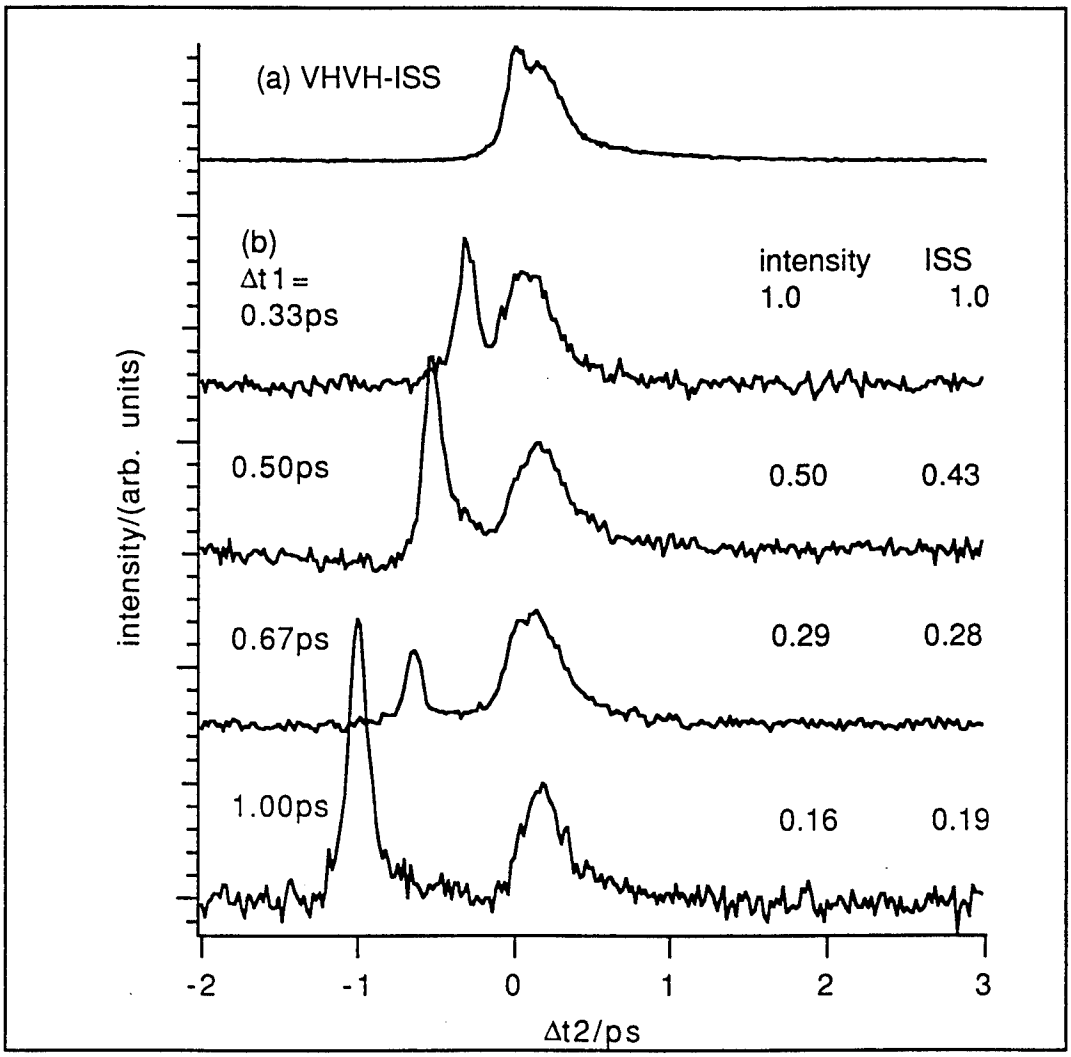


Fig. 1 (a) Impulsive stimulated light scattering (ISS) signal from CS_2 as a function of delay time of the probe pulse. (b) Fifth order response signal as a function of Δt_2 with different fixed Δt_1. The scattered light at $\Delta t_2 = -\Delta t_1$ is mainly due to a third order response. The relative intensities of the fifth order signal and ISS signal at different delay times are shown.

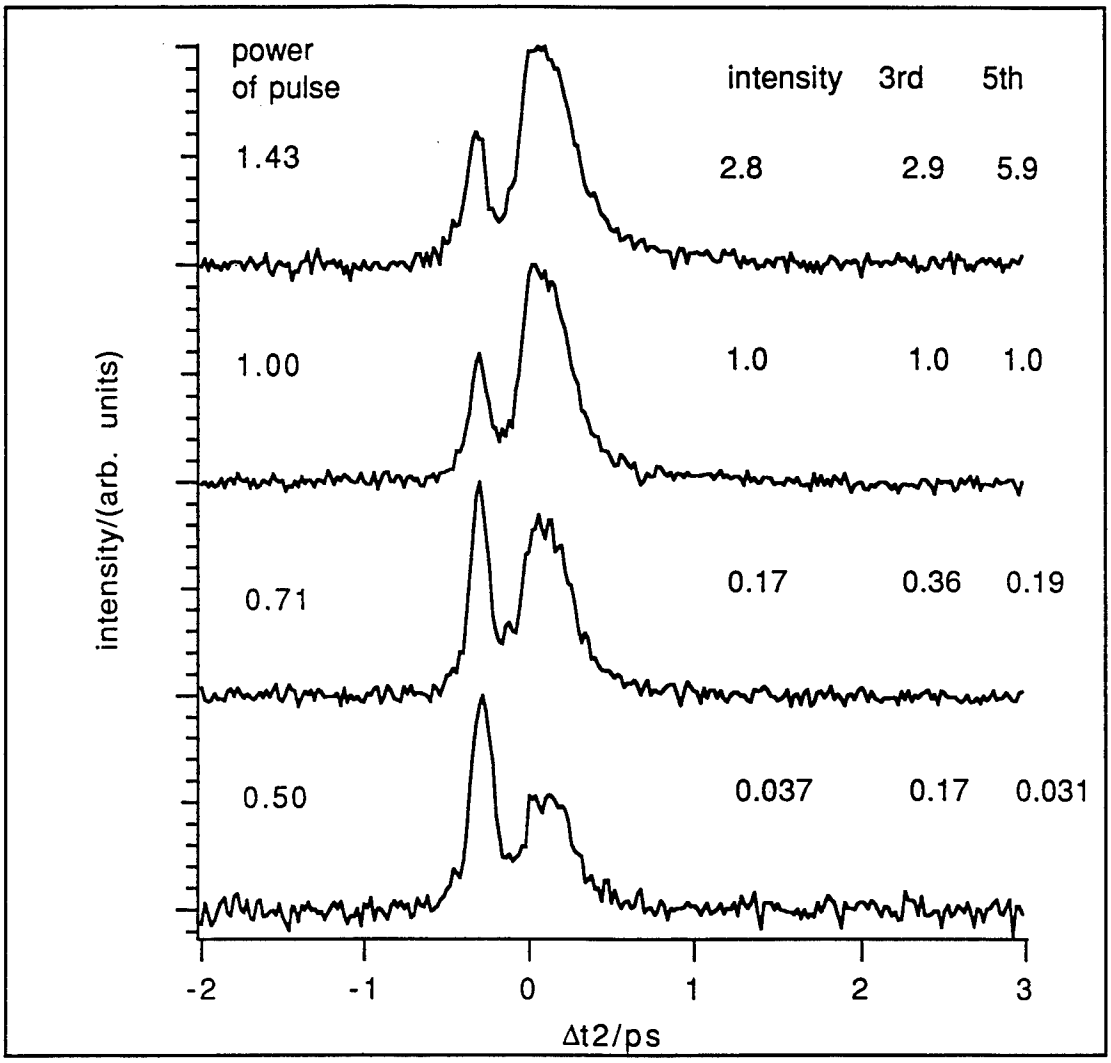


Fig. 2 Dependence of the signal intensity on the laser power. The signal is shown as a function of Δt_2 with Δt_1 fixed at 0.33ps. The relative intensities of the signal at different laser powers and the expected change for the third and fifth order responses are shown.

References;

[a]Permanent address, Department of Chemistry, Taegu University, Kyongsan 713-714, Korea.
1. D. Vanden Bout, L.J. Muller, and M. Berg, *Phys. Rev. Lett.* **67**, 3700 (1991). L.J. Muller, D. Vanden Bout, and M. Berg, *J. Chem. Phys.* **99**, 810 (1993).
2. R. Inaba, K. Tominaga, M. Tasumi, K.A. Nelson, and K. Yoshihara, *Chem. Phys. Lett.* **211**, 183 (1993).
3. D. Zimdars, A. Tokmakoff, S. Chen, S.R. Greenfield, M.D. Fayer, T.I. Smith, and H.A. Schwettman, *Phys. Rev. Lett.* **70**, 2718 (1993).
4. Y.X. Yan, L.T. Cheng, and K.A. Nelson, *Advances in Nonlinear Spectroscopy,* edited by R.J.H. Clark and R.E. Hester, Wiley, New York, 1988, p.299.
5. Y. Tanimura and S. Mukamel, *J. Chem. Phys.* **99**, 9496 (1993).
6. S. Ruhman and K.A. Nelson, *J. Chem. Phys.* **94**, 859 (1991). B. Kohler and K.A. Nelson, *J. Phys. Chem.* **96**, 6532 (1992).

Femtosecond Coherent Generation of Hot Electrons Monitored via Band-to-Acceptor Luminescence in GaAs

A. Leitenstorfer[1], T. Elsaesser[1,2], A. Lohner[1], T. Kuhn[3], S. Haas[4], and F. Rossi[4]

[1]Physik Department E 11, Technische Universität München, D-85748 Garching, Germany

[2]Max-Born-Institut für Nichtlineare Optik und Kurzzeitspektroskopie,
Rudower Chaussee 6, D-12489 Berlin, Germany, Phone +49 30 6392-1400,
Fax +49 30 6392-1409

[3]Institut für Theoretische Physik, Universität Stuttgart, D-70550 Stuttgart, Germany

[4]Fachbereich Physik, Universität Marburg, D-35032 Marburg, Germany

Luminescence spectra observed after femtosecond excitation demonstrate initial electron distributions strongly affected by the coherent coupling of the incident light field and the semiconductor.

Femtosecond Coherent Generation of Hot Electrons Monitored via Band-to-Acceptor Luminescence in GaAs

A. Leitenstorfer[1], T. Elsaesser[1,2], A. Lohner[1], T. Kuhn[3], S. Haas[4], and F. Rossi[4]

[1]Physik Department E 11, Technische Universität München,
D-85748 Garching, Germany
[2]Max-Born-Institut für Nichtlineare Optik und Kurzzeitspektroskopie,
D-12489 Berlin, Germany
[3]Institut für Theoretische Physik, Universität Stuttgart, D-70550 Stuttgart, Germany
[4]Fachbereich Physik, Universität Marburg, D-35032 Marburg, Germany

Optical interband excitation of semiconductors results in an ultrafast electron-hole dynamics which is influenced by both coherent and incoherent phenomena. Coherent polarizations have mainly been studied by femtosecond four-wave-mixing (see, e.g., [1]) whereas the redistribution of photoexcited carriers was investigated via transient absorption changes or time-resolved luminescence [2]. Until now, the influence of the coherent coupling between the femtosecond optical pulse and the semiconductor on the initial carrier distribution has not been clarified although the shape of this distribution is essential for the subsequent relaxation processes. In this contribution, we provide the first experimental evidence that nonequilibrium electron distributions created by femtosecond excitation are strongly affected by the coherent light-matter interaction. Non-equilibrium electron distributions in p-type GaAs are monitored via band-to-acceptor luminescence [3]. Our data are analyzed with the help of detailed theoretical simulations based on a generalized Monte-Carlo solution of the semiconductor Bloch equations.
In our experiments, a 3 μm thick layer of p-type GaAs (lattice temperature T_L=10 K) is excited by a transform-limited 150 fs pulse at E_{ex}=1.73 eV and time-integrated spectra of band-to-acceptor luminescence are measured with a spectral resolution of 1 meV.

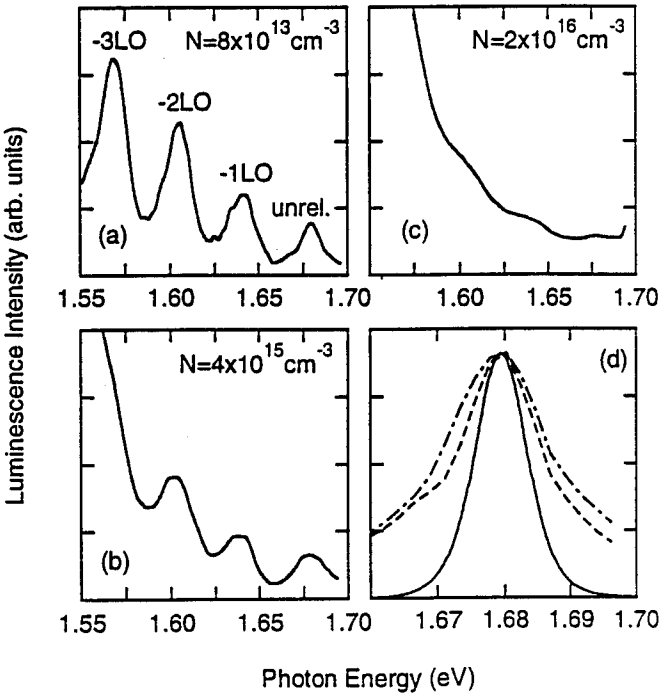


Figure 1 (a-c) Hot electron luminescence spectra of GaAs measured for different excitation densities N. The spectra show a first peak (unrel.) that originates from conduction band states optically coupled by the excitation pulse and a series of phonon replicas. The lines exhibit an identical spectral width and broaden with increasing carrier concentration.
(e) Spectral profile of the first luminescence peak for carrier densities of 8×10^{13} (dashed line) and 5×10^{14} cm^{-3} (dash-dotted line). The laser spectrum is given for comparison (solid line).

In Fig. 1 (a-c), we present hot luminescence spectra for excitation densities between 8×10^{13} and 2×10^{16} cm^{-3}. The spectra at low carrier density exhibit a first peak around 1.68 eV that originates from the recombination of electrons in conduction band states directly populated by laser excitation. In Fig. 1 (d), this part of the spectrum is plotted on an extended scale and compared to the laser spectrum. Even at low carrier concentration, this linewidth is substantially larger than the bandwidth of the laser pulses. At lower photon energies, a series of phonon replicas is observed which are due to electrons which have emitted one, two or three LO phonons and reflect the carrier dynamics at later times. With increasing carrier density, the luminescence maxima broaden due to the increasing strength of carrier-carrier (cc) scattering. At each density, the first ('unrelaxed') peak exhibits already the same spectral width as the phonon replicas occurring at later times. In Fig. 2, the spectral width of the unrelaxed peak is plotted as a function of excitation density (squares).

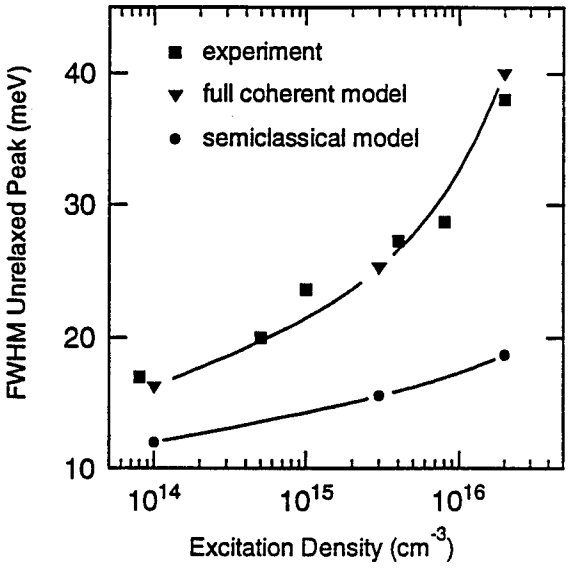


Figure 2 Spectral full width at half maximum (FWHM) of the first luminescence peak as a function of excitation density. The experimental results (squares) are compared to theoretical values calculated from a simulation including the coherent coupling of laser field and polarization in the sample (triangles) and from a semiclassical model of the incoherent carrier dynamics (circles).

In the standard semiclassical description of photoexcitation neglecting the coherent nature of this process, the laser pulse generates an electron distribution of a width essentially defined by the laser bandwidth. Results of such a simulation are presented in Fig. 2, where the spectral width of the first luminescence peak is plotted as a function of carrier density (circles). With increasing electron concentration, carrier-carrier scattering leads to a broadening of the luminescence line. This broadening increases with the time elapsed after excitation, i.e. phonon replicas at lower energy should show a larger bandwidth than the first peak. Those results are not in agreement with our data showing a significantly larger spectral width which is identical for all luminescence maxima, and a much stronger increase with density.

In contrast, our experimental results reveal the coherent nature of the excitation process. Phase breaking scattering events during excitation lead to a significant broadening of carrier generation in k-space, resulting in an energetic width larger than the laser bandwidth. The measured constant linewidth of the luminescence peaks is a clear consequence of the fact that the broadening is mainly introduced during carrier generation while the subsequent incoherent scattering processes are of minor importance.

This interpretation is supported by simulations of the coherent dynamics and of the car-

rier redistribution processes based on a Monte-Carlo solution of the semiconductor Bloch equations [4]. The linewidths calculated from this model are plotted in Fig. 2 (triangles) and reproduce the data very well. The calculation gives identical linewidths of the different luminescence peaks at a fixed density. These findings are related to the details of the carrier-carrier scattering processes : The efficiency of carrier-carrier interaction for dephasing is higher than that for electron redistribution. The decay of the interband polarization responsible for the linewidth is strongly enhanced by scattering among the holes created in the excitation process which is much faster than electron-electron scattering.

References

[1] A. Lohner, K. Rick, P. Leisching, A. Leitenstorfer, T. Elsaesser, T. Kuhn, F. Rossi, and W. Stolz, Phys. Rev. Lett. **71**, 77 (1993); Phys. Rev. **B 49**, in press (1994)
[2] T. Elsaesser, J. Shah, L. Rota, and P. Lugli, Phys. Rev. Lett. **66**, 1757 (1991)
[3] J.A. Kash, Phys. Rev. **B 40**, 3455 (1989)
[4] F. Rossi, S. Haas, and T. Kuhn, Phys. Rev. Lett. **72**, 152 (1994)

Vibrational Relaxation of a Charged Species in Nonpolar Solvent

J. C. King, M. C. Asplund and C. B. Harris
Department of Chemistry
University of California, Berkeley
Berkeley, CA 94720

We have performed the first study of the vibrational relaxation of an ionic species, I_2^-, in a nonpolar solvent, CCl_4. To determine the interaction of the charge with the solvent, results will be compared to a similar, but non-ionic species, I_2, in the same solvent.

Vibrational Relaxation of a Charged Species in Nonpolar Solvent

J. C. King, M. C. Asplund and C. B. Harris
Department of Chemistry
University of California, Berkeley
Berkeley, CA 94720

Vibrational energy relaxation is a fundamental process in solution phase chemical dynamics. In almost all chemical reactions, chemical bonds are broken and formed, and vibrational relaxation is usually the rate limiting step in forming new bonds. In addition, this process is completely dependent upon the interaction of the solute with the solvent environment.

Early studies of vibrational energy relaxation in solution focussed on relaxation of small, nonpolar, non-ionic molecules - the most thorough study being the dissociation and recombination of I_2.[1] This work showed that the rate of relaxation is primarily dependent upon the number of modes in the vibrationally excited species and the amplitude of the force autocorrelation function at the frequencies of those modes. The general trends being that larger molecules relax more quickly than smaller ones because of the increased number of modes and that solvents which can accept energy at the frequency of the excited modes facilitates cooling. With this body of work, a time scale of 10-100 ps for vibrational relaxation of *non-ionic species in polar solvents* has become accepted.

However one area that has not been studied until recently is the vibrational relaxation of ionic species in solution. Because of the additional terms in the interaction between solute and solvent in these systems, it is unclear how similar the process would be to the previous body of work on non-ionic species. In one of the first experiments on the vibrational relaxation of ions in solution, Hochstrasser and coworkers[2] found that vibrational relaxation of an ion, N_3^-, occurred in only 3 ps in polar solvents. This trend of extremely fast vibrational relaxation for an ionic species in polar solution has been further supported by studies of vibrational relaxation in I_2^-. Work by both Barbara and coworkers[3] and Banin and Ruhman[4] showed that vibrational relaxation occurs very quickly in this small molecule. In H_2O the relaxation takes 2.5 ps while in small chain alcohols it increases to 3-5 ps. These studies show that vibrational relaxation is an extremely rapid process for an ion in a polar solvent. However the reason for this increase in cooling rate and whether the same factors govern the rate of cooling as in neutral species is unclear. To more closely connect this work to the previous body of work on non-ionic species, *we have performed to our knowledge the first study of the vibrational relaxation of an ionic species (I_2^-) in a nonpolar solvent (CCl_4).* These results are directly comparable to the vibrational relaxation of I_2, the neutral, non-ionic equivalent, which has been previously studied in the same solvent.[5,6]

To study the vibrational relaxation of I_2^-, I_3^- is photolyzed to produce I and vibrationally excited I_2^- in the manner used by Banin and Ruhman. Their work showed that the I_2^- was excited to the v = 25 level and had ~2500 cm^{-1} of excess energy. We are probing the I_2^- near its absorption at 750 nm with a standard pump/probe scheme. One factor that has effected this study is the very low solubility of the I_3^- ion in the non-polar CCl_4. To make the anion more soluble we use a large non-polar counter ion -- the tetrapropyl ammonium cation. Even with this large

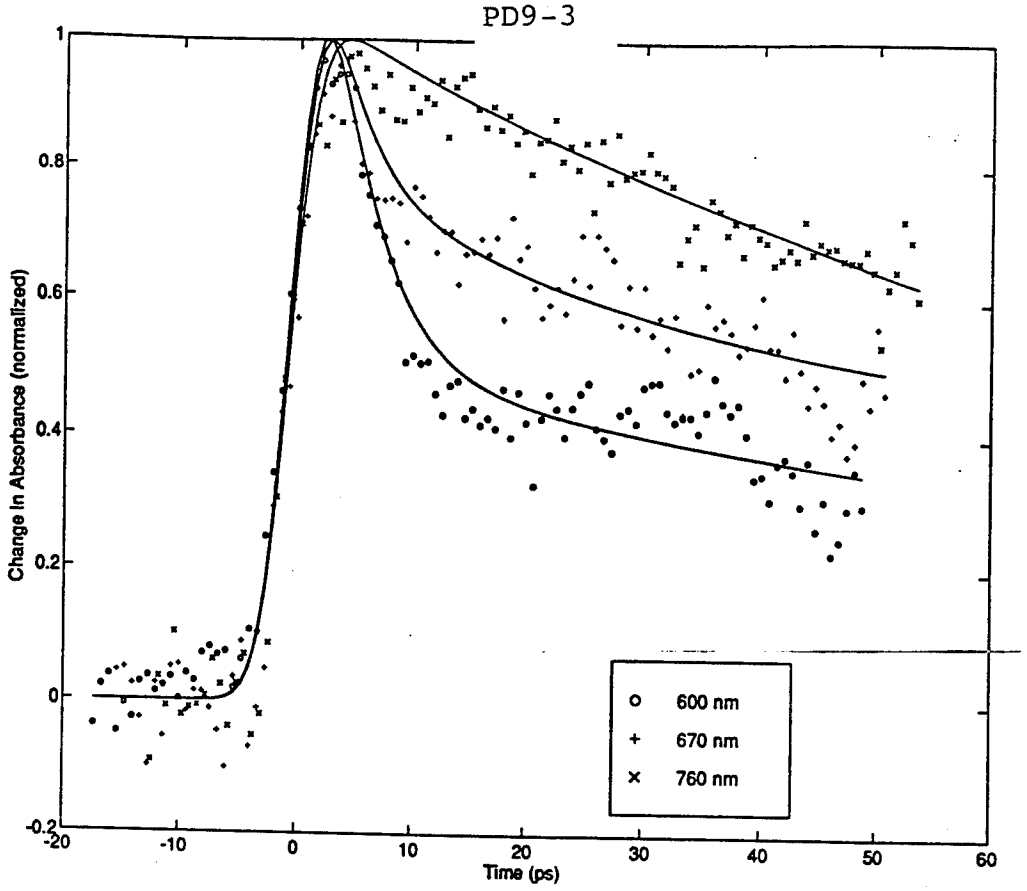


Figure 1 : Transient absorption curves at three wavelengths, showing red shifting of the absorption maximum due to vibrational cooling

counter ion the salt is sparingly soluble, forming a saturated solution with a concentration of about 0.1 mM. This low concentration of I_3^- precludes using a synthesis pulse to produce I_2^- and then dissociating it in the manner used by Barbara and co-workers. The low concentration also requires the use of a 1 cm sample cell to increase the optical density of the sample. This longer path length lowers our temporal resolution to ~ 4 ps because of the difference in the index of refraction of the sample at the UV pump wavelength and the visible of near IR probe wavelength. Even with the longer path length the optical density of the solvent is only 0.3 - 0.5. Because of this low optical density and the strong multiphoton absorptions of CCl_4 with the UV excitation pulse, the signals we are measuring are 0.1 % ΔOD or less.

In this preliminary work we have probed the dynamics of the cooling I_2^- at several wavelengths. In figure 1, the cooling at three wavelengths is shown. As shown in simulations in ethanol by Barbara and co-workers[3], the absorption at 600 nm represents a vibrationally excited I_2^-, at 670 nm an I_2^- with a lower amount of vibrational energy and at 760 nm, an I_2^- near (or at) the bottom of the well. What this data shows is faster cooling (~5 ps) near the top of the well at 600 nm, a mixture of cooling times (5 ps and 40 ps) at intermediate vibrational excitation and slower cooling (~55 ps) near the bottom of the well. Surprisingly, in this case the relaxation of the I_2^- is only a factor of 2 to 3 faster than for I_2 in the same solvent.

To find the reason for this change, or similarity as the case may be, in vibrational relaxation times, it is important to identify the differences between I_2 and I_2^-. The most obvious difference is of course the charged nature of the I_2^- and the subsequent charge/induced dipole interactions with the nonpolar solvent. These additional longer range forces may play an important role in reducing the relaxation time. Another important difference between I_2 and I_2^- is the intramolecular potentials. The I_2^- potential has a depth of ~1.1 eV and a frequency of ~ 115 cm^{-1} while iodine has a well depth of ~1.6 eV and a fundamental frequency of ~215 cm^{-1}. Previous

work has shown that the frequency of the oscillator and the amplitude of the force autocorrelation function (or equivalently the amplitude of the solvent's friction) at that frequency is an important indicator of how fast relaxation will occur and most solvents do have a larger amplitude at lower frequencies. This factor would also increase the rate of relaxation of I_2^- as compared to I_2. A priori it is not clear how much of the increase in relaxation rate is due to the charge/induced dipole interactions and how much is due to the change in oscillator frequency.

To understand the contributions from these two different factors, it is interesting to compare our results to what one would expect just considering the change in oscillator frequency. From a very simple perspective, theory predicts[7,8] that the relaxation rate is proportional to the amplitude of the friction of the solvent at the frequency of the oscillator. If we look at the friction or equivalently the I_2/CCl_4 force autocorrelation function of the solvent at the frequencies of the two oscillators (200 cm^{-1} for I_2 and 100 cm^{-1} for I_2^-) it should give an indication of what the increase in the rate of relaxation will be. Although we don't know the force autocorrelation function for CCl_4 in this low frequency region, if we neglect the internal degrees of freedom, it should be qualitatively similar to Xe, which has nearly the same mass as CCl_4 and polarizability. The force autocorrelation function of I_2 in Xe was previously determined[7,8] from molecular dynamics simulations and the difference at these two frequencies is of the same order as the observed change in relaxation rates. *Therefore the increase in relaxation rate is just what is expected for this change in oscillator frequencies.* The fact that the relaxation of I_2^- is well described by this simple theory indicates that the charge on the I_2^- does not couple well to any of the modes in the solvent. In addition, our work shows that the change in intramolecular potential from I_2 to I_2^- accounts for only about a factor of 3 increase in relaxation rates. This is similar to results of simulations by Whitnell and Benjamin[9] which showed that when the charge was removed from the I_2^-, it still relaxed 4-5 times faster than normal I_2 in water or ethanol.

In summary, our results show that relaxation of I_2^- in CCl_4 occurs in about 55 ps. This is a factor of ten slower than has been found for I_2^- in polar solvents. It is however a factor of three times faster than I_2 in the same solvent. This is approximately the change that would be expected for just the difference in oscillator frequency between the two species and indicates that the charge on the I_2^- does not couple well to modes in the solvent. We are currently working on extending the wavelength range for probing the I_2^- to get a more complete picture of the dynamics.

Acknowledgements

This work was supported by the National Science Foundation

1. A.L. Harris, J.K. Brown and C.B. Harris, Ann. Rev. Phys. Chem. 39, 341, (1988) and references therein.
2. J.C. Owrutsky, Y.R. Kim, M. Li, M.J. Sarisky, and R.M. Hochstrasser, Chem. Phys. Lett. 184
3. D.A.V. Kliner, J.C. Alfano and P.F. Barbara, J. Chem. Phys. 98, 5375 (1993).
4. U. Banin, A. Waldman and S. Ruhman, J. Chem. Phys. 96, 2416 (1992).
5. M. Berg, A.L. Harris and C.B. Harris, Phys. Rev. Lett. 54, 951 (1985).
6. A.L. Harris, M. Berg, and C.B. Harris, J. Chem. Phys. 84, 9788 (1986).
7. D. E. Smith and C.B. Harris, J. Chem. Phys. 92, 1304 (1990).
8. D.E. Smith and C.B. Harris, J. Chem. Phys. 92, 1320 (1990).
9. I. Benjamin and R.M. Whitnell, Chem. Phys. Lett. 204, 45 (1993).

The Femtosecond Dynamics of Aggregate Excitons in Liquids

M. v. Burgel, D.A. Wiersma and K. Duppen

Ultrafast Laser and Spectroscopy Laboratory,
Department of Chemistry, University of Groningen
Nijenborgh 4, 9747 AG, Groningen, The Netherlands

Abstract

Room temperature photon echo experiments show that optical dephasing in aggregates of dye molecules in solution is very slow ($T_2 > 100$ fs), due to motional narrowing over dynamic perturbations. By pump-probe experiments on multiple-exciton transitions the range of exciton delocalization was determined to be 18 molecules.

The Femtosecond Dynamics of Aggregate Excitons in Liquids

M. v. Burgel, D.A. Wiersma and K. Duppen

Ultrafast Laser and Spectroscopy Laboratory,
Department of Chemistry, University of Groningen
Nijenborgh 4, 9747 AG, Groningen, The Netherlands

Optical dephasing of electronic transitions of molecules in liquids is usually very fast. In recent years this was extensively studied by ultrafast two-pulse photon echo experiments [1,2], in which pulses with a duration of 10 fs or less were required to reach the necessary time-resolution. It became clear that a description of the dynamics in terms of homogeneous T_2-type phase relaxation and a (quasi-) static inhomogeneous distribution of transition frequencies is incorrect for liquids. The fundamental reason for the failure of the (in-) homogeneous broadening picture is that the optical dynamics in liquids is so fast, that it occurs on a similar time scale as the dynamics of the relevant heat bath. In these circumstances, a non-Markovian approach to the dynamics should be taken. Several models, based for instance on stochastic frequency fluctuations [2-4] or Brownian oscillator motion [5,6] were employed to take care of these non-Markovian effects.

It is well-known that aggregates of dye molecules in liquids exhibit optical properties that are distinctly different from those of single molecules [7]. The excited electronic states of these aggregates are best described as excitons, which are delocalized over several dye molecules. Hence, the optical properties of these systems are determined by "motionally averaging" over the corresponding single molecule properties. For a perfectly ordered aggregate, in which all molecules are identical, the excitonic states extent over the entire physical size of the aggreggate. However, when there is some energetic disorder among the molecules, the excited state wavefunctions localize on some finite section of the aggregate, and consequently the excitonic effects are less pronounced. This has been thoroughly studied for static disorder, a situation that applies to aggregates in solids near zero temperature [8].

In liquids at room temperature, the molecules of an aggregate are heavily perturbed by the rapidly moving solvent molecules. Hence, there is not static disorder, but instead a dynamic one. Again, localization of the exciton on a finite number of molecules will occur. It is conceivable that the optical dephasing of the aggregate is considerably slower than that of the single molecules, since the dynamic perturbations are more or less efficiently averaged out over the delocalization range of the exciton. It is even possible that the Markovian (homogeneous) limit of optical dephasing is reached in this way, since the optical dephasing occurs, due to the motional narrowing, on (much) longer time scales than the very rapid solvent movements that form the heat bath. To study these currently unknown aspects of aggregate excitons in room temperature liquids, we decided to perform photon echo experiments on these systems.

In Fig. (1) the absorption spectrum of a carbocyanine dye in water is shown, which is known as TDBC [9]. The chemical structure of this dye is shown in the inset. The formation of aggregates is characterized by the appearance of a new absorption band at high dye concentration, narrowed and red-shifted compared to the monomer absorption. Both these features are signatures of exciton behaviour, and are due to some degree of motional narrowing.

Results of photon echo experiments are shown in Fig. (2). The beam geometry is shown in the inset. At low pulse intensity, a decay is observed that can be fitted very well to a single exponent of 40 fs. At higher pulse intensities, the behaviour of the transient around

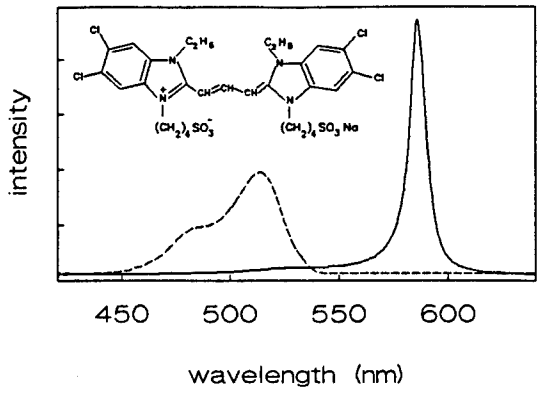


Figure 1 Absorption spectrum of TDBC in water. The dashed line is the monomer spectrum, the solid line the aggregate at high concentration ($c > 10^{-5}$M).

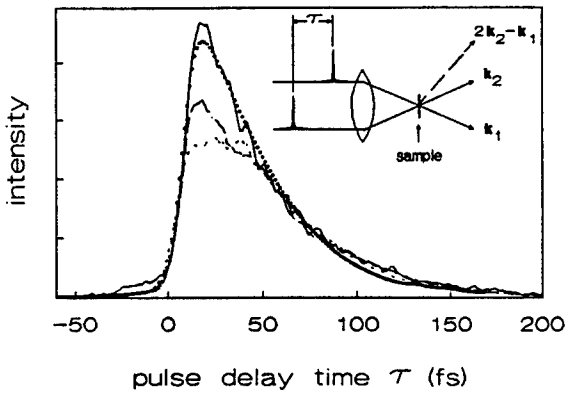


Figure 2 Two-pulse photon echo signals of TDBC. Solid line 0.01, dashed 0.03, dotted 0.05 nJ/pulse. The fit is shown as circles. Intensities are rescaled to overlap the tails.

zero delay is more complicated, probably due to the fact that coherences are generated on higher excitonic transitions as well (see Fig. (3) below). These are short lived, however, and the tail of the decay therefore always reflects the dephasing dynamics of the lowest exciton transition at 587 nm, which is also visible in the linear absorption spectrum. The mono-exponential decay suggests that the dynamics occurs in the Markov limit, which gives for the dephasing time: $T_2 = 160$ fs. *This is by far the longest coherence decay ever measured in a room temperature liquid.* Apparently, motional narrowing averages out the dynamic fluctuations of the single molecule energy levels.

Closer inspection of the absorption spectrum reveals that the Markovian T_2-concept is, just as for single molecules, too simple for these aggregate excitons in liquids. A pure exponential photon echo decay can only be expected when either the homogeneous width or the inhomogeneous width dominates the optical transition. For $T_2 = 160$ fs, the contribution from the inhomogeneous width should be comparable to that from the homogeneous width to obtain a reasonable fit to the absorption spectrum. But in those circumstances the echo decay will not be single exponential at all! We can reconcile the observed echo decay with the absorption spectrum, by assuming the presence of non-Markovian, stochastic fluctuations of the transition frequency which occur on two different time scales. These fluctuations are characterized by an amplitude Δ and a correlation time τ.

By fitting simultaneously the echo decay and the absorption line shape, we find for the parameters of the fast component of the fluctuations: $\Delta_f = 50$ THz and $\tau_f = 5$ fs, and for the slow components $\Delta_s = 10$ THz and $\tau_s = 10$ ps. This means that the fast modulation occurs close to, but not quite at the Markovian limit. This limit is reached when $\Delta_f \tau_f \ll 1$, with $T_2 \equiv (\Delta_f^2 \tau_f)^{-1}$. The slow modulation is not truly static, but occurs for the ultrafast photon echo experiment (almost) in the static limit. The echo trace, calculated with these parameters for the stochastic frequency fluctuations, is shown by the small circles in Fig. (2).

As stated above, the extremely long dephasing time is directly connected to the motional narrowing associated with the delocalization of the exciton. The delocalization length can be determined from pump-probe spectroscopy. In Fig. (3) the lowest two exciton bands are shown, that are relevant to a pump-probe experiment [10]. In the lowest exciton band, one single-molecule excitation is shared by a certain number of molecules, in the next highest exciton band two single-molecule excitations are present on these same molecules. In general, the transition frequency from the one- to two-exciton band has a higher energy than the transition from the ground state to the one-exciton band. The reason is that two excitations

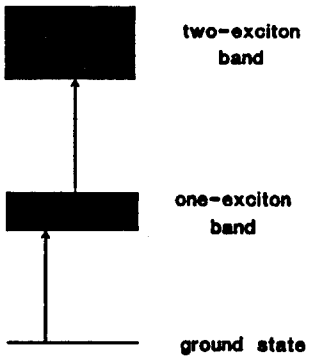


Figure 3 Level scheme for the two lowest exciton bands of TDBC. In a pump-probe experiment both transitions are observed.

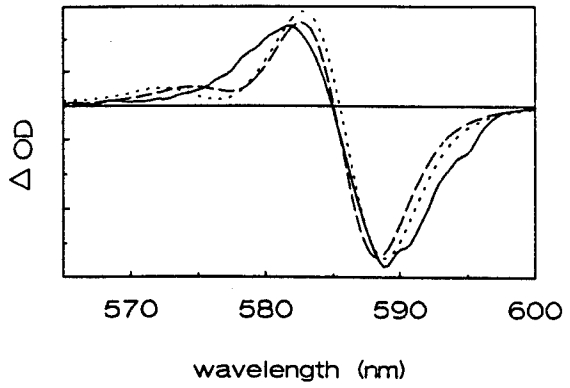


Figure 4 Pump-probe signal for TDBC in water. A bleach and induced absorption are observed. A fit to this lineshape gives the delocalization length of the exciton.

cannot be at the same time at the same single-molecule position, due to the Pauli exclusion principle. For small delocalization lengths this is much more likely to occur than for very large ones. Hence, the frequency difference between the two transitions depends directly on the delocalization length.

In a pump-probe experiment, a bleaching of the entire absorption lineshape is induced by an ultrashort pump pulse. This can be measured by a delayed probe pulse. In addition, absorption is induced on the one- to two-exciton transition [10-12]. Such an experiment is shown by the solid line in Fig. (4). When this line shape is fitted using conventional exciton band theory, a delocalization length in the order of 16 (dotted line) to 18 (dashed line) molecules is found. This is more than ever reported before, at room temperature. Hence, motional averaging over the solvent dynamic fluctuations is relatively efficient in this system.

In conclusion we can state that motional narrowing processes, associated with extended, delocalized exciton states of aggregates in liquids, considerably slow down optical dephasing processes compared to single molecules in the same liquid. Consequently, the dynamics tends to be much closer to the homogeneous (T_2) limit. However, for TDBC in water this limit is not quite reached, although the excitation is delocalized over about 18 molecules. The slow dephasing has important consequences for the nonlinear optical properties and for the physics of energy-transfer processes in these systems. A microscopic theory for motional narrowing of dynamic perturbations has not been formulated, yet.

References:

1. P.C. Becker, H.L. Fragnito, J.-Y. Bigot, C.H. Brito-Cruz, R.L. Fork and C.V. Shank, Phys. Rev. Lett. **63**, 505 (1989).
2. E.T.J. Nibbering, D.A. Wiersma and K. Duppen, Phys. Rev. Lett. **66**, 2464 (1991).
3. J.-Y. Bigot, M.T. Portella, R.W. Schoenlein, C.J. Bardeen, A. Migus and C.V. Shank, Phys. Rev. Lett. **66**, 1138 (1991).
4. K. Duppen, F. de Haan, E.T.J. Nibbering, and D.A. Wiersma, Phys. Rev. A **47**, 5120 (1993).
5. W.B. Bosma, Y.J. Yan and S. Mukamel, Phys. Rev. A **42**, 6920 (1990).
6. E.T.J. Nibbering, D.A. Wiersma and K. Duppen, Chem. Phys. **182**, 000 (1994).
7. A.H. Herz, Photogr. Sci. & Engin. **18**, 323 (1974).
8. H. Fidder, J. Knoester and D.A. Wiersma, J. Chem. Phys. **95**, 7880 (1991).
9. M. Lindrum, A, Glisman, J. Moll and S. Daehne, Chem. Phys. **178**, 423 (1993).
10. H. Fidder, J. Knoester and D.A. Wiersma, J. Chem. Phys. **98**, 6564 (1993).
11. A.E Johnson, S. Kumazaki and K. Yoshihara, Chem. Phys. Lett. **211**, 511 (1993)
12. K. Minoshima, M. Taiji, K. Misawa and T. Kobayashi, Chem. Phys. Lett. **218**, 67 (1994).

Programmable Wavefunction Engineering in Cs Rydberg States

P. H. Bucksbaum, D. W. Schumacher, Dan Pinkos

University of Michigan
Physics Department
Center for Ultrafast Optical Science.
Ann Arbor, MI 48109-1120

phone: (313) 764-4348
fax: (313) 763-9694

J. H. Hoogenraad

FOM-Institute for Atomic and Molecular Physics,
Kruislaan 407, 1098 SJ Amsterdam, The Netherlands

Jeffrey L. Krause, Kent R. Wilson

Department of Chemistry, University of California - San Diego,
La Jolla, CA 92093-0339

Abstract:

We used a computer controlled LCD to shape the spectrum of a short laser pulse which was then used to excite a shaped atomic wavepacket.

Programmable Wavefunction Engineering in Cs Rydberg States

P. H. Bucksbaum[a], D. W. Schumacher[a], Dan Pinkos[a], J. H. Hoogenraad[b], Jeffrey L. Krause[c], Kent R. Wilson[c]

[a]Physics Department and Center for Ultrafast Optical Science
University of Michigan Ann Arbor, MI 48109-1120
[b]FOM-Institute for Atomic and Molecular Physics
Kruislaan 407, 1098 SJ Amsterdam, The Netherlands
[c]Department of Chemistry, University of California - San Diego,
La Jolla, CA 92093-0339

Abstract.

We use amplified programmable shaped optical pulses to engineer Rydberg wavefunctions. The method employs a computer-controlled liquid crystal pulse shaper[1]. The wavefunctions, which are nonstationary states, are monitored by observing temporal interference via the optical Ramsey method[2,3].

Wavepacket generation, detection, and evolution has been the center of intense interest over the last decade ever since the lasers necessary to excite the appropriate assembly of states coherently became widely available. Most experiments have concentrated on excitation methods and solving the detection problem. Interest in the evolution of the wavepacket has centered on the correspondence that exists between a wavepacket's time dependent behavior and the classical trajectory of a particle. The current work takes advantage of insight gained from past research and uses an atomic wavepacket as the starting point for a control experiment. In principle, any arbitrary set of initial conditions for a wavepacket superposition can be obtained by manipulating the light that creates the excited state. We use this idea to control wavefunction formation by controlling the degree to which various states are excited.

The light for this experiment originates from 110fs pulses created by a Ti:Sapphire Kerr lens modelocked laser. This light contains about 10 nm of coherent bandwidth. Using a technique devised by Weiner[1], we send the light through a zero-dispersion grating-pulse expander. In the middle of the expander, where the light is focused, but dispersed in the horizontal plane, we insert a liquid crystal display (LCD). The dispersed light covers 128 LCD pixels, so that we have 128 independent phase delays, each set by computer control. The LCD may be oriented to produce either phase or polarization shifts; or, in conjunction with an external polarizer the LCD becomes an amplitude mask. In practice we use two displays, and thus we obtain both phase and amplitude control over each color in the pulse. When the LCD is turned off, the system produces nearly transform limited, 120 fs optical pulses at 10 Hz, and at a center wavelength of 785 nm. The pulses are characterized using a FROG[5] as well as other more traditional techniques.

A Cesium atomic beam is excited into an initial 7s state by a two-photon transition from the groundstate using a 7 ns pulsed dye laser. The shaped light is split into two identical pulses with a variable separation between them in time but spatially overlapped using a Michelson interferometer. Each pulse in the pair excites the Cesium to a sculpted wave

function or "wavepacket", i.e. a coherent superposition of np states centered around n=27. The two wavepackets are phase-coherent with respect to each other. Therefore they interfere, and the change in the interference with time delay provides information about the shape of the engineered wave function. We observe this interference by field ionizing the wavefunction in a slow (~4 μs) ramped electric field. The final populations of each excited Rydberg state can be measured after each laser pulse using this technique.

Figure 1 shows the results for a pulse with a "windowed" spectrum in which the Rydberg states excited have been limited to 26p through 31p. The interference between the two non-stationary states excited by the two optical pulse is evident and is indicative of a wavepacket as it oscillates between the classical inner and outer turning points in the atomic potential. As it oscillates, it breaks up because of dispersion in the atom. Also shown are the results of a model calculation where we numerically integrated Schrodinger's equation. In Figure 2 we "sliced" the spectrum used in Figure 1 to excite states 26p, 27p, 29p, and 31p. The Kepler time should now be halved because the effective energy spacing is larger. This can be clearly seen in the first peak to occur after the coherent spike that occurs for zero delay. The dispersive character of the atom is also now strongly reduced. Figure 3 plots the Fourier transforms of the above interferograms and peaks are clearly evident occurring at energies corresponding to the energy differences present in the system. The height of the peaks is a direct measure of the interaction strengths of the various transitions. A few of the various energy differences are labeled in the figure.

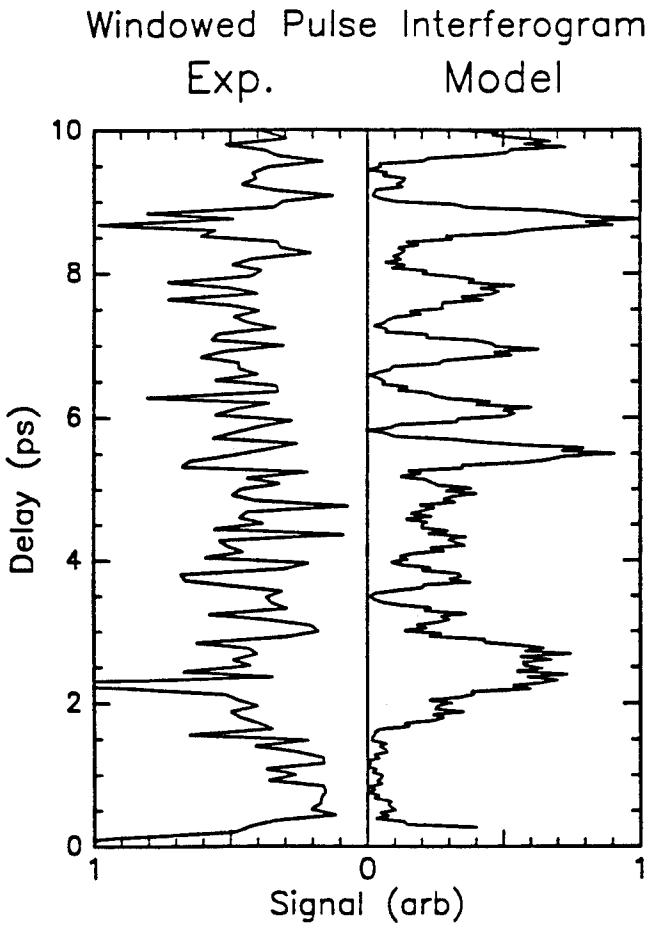


Figure 1

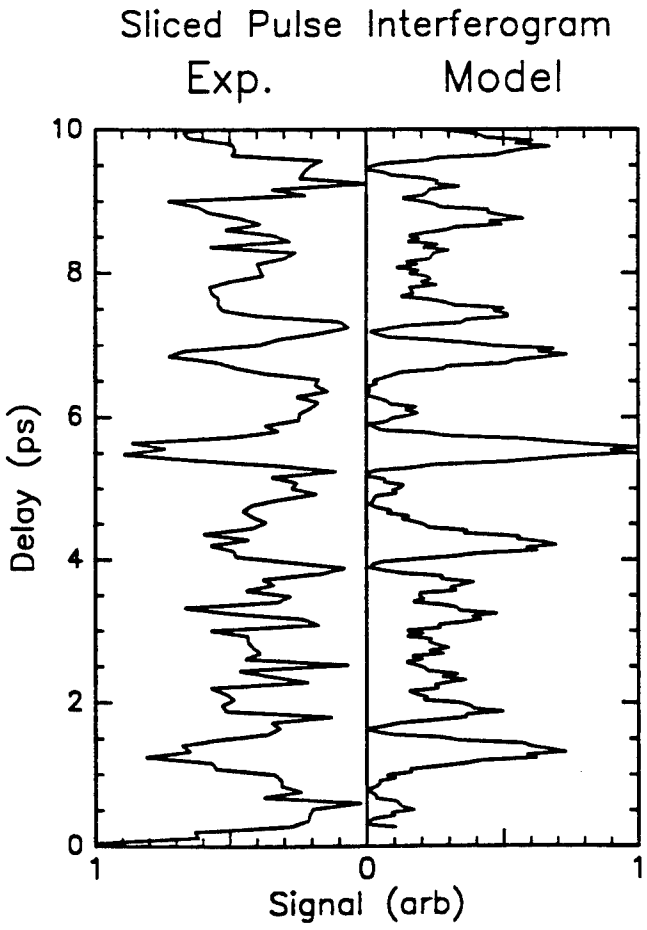


Figure 2

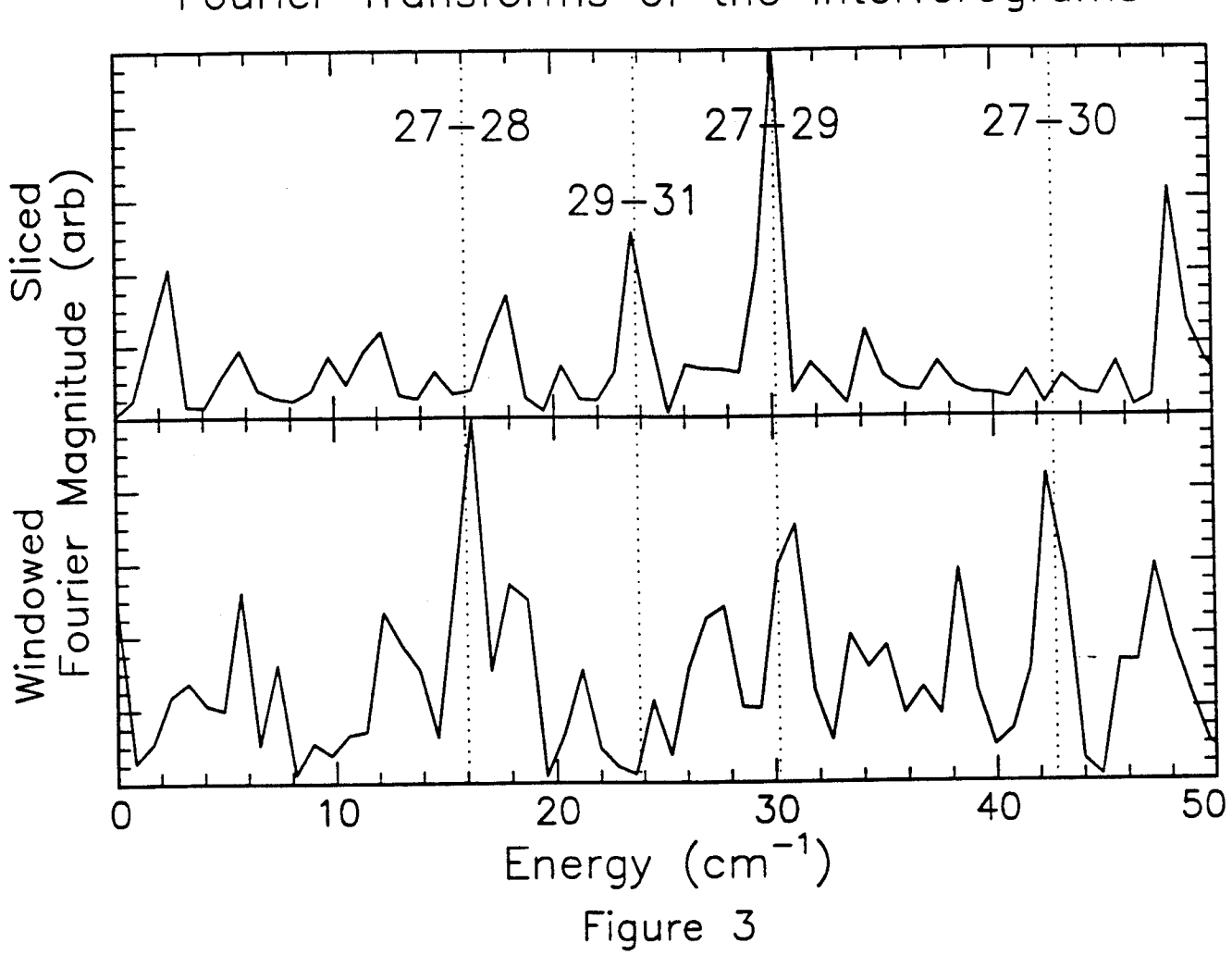


Figure 3

References:

[1] J. Parker and C.R. Stroud Jr., Phys. Rev. Lett. **56**, 716 (1986)

[2] R. R. Jones, C. S. Raman, D. W. Schumacher, and P. H. Bucksbaum, Phys. Rev. Lett, **71**, 2575 (1993).

[3] J.F. Christian, B. Broers, J.H. Hoogenraad, W.J. van der Zande, and L.D. Noordam, Opt. Comm. **103**, 79 (1993)

[4] Andrew M. Weiner, Daniel E. Leaird, J.S. Patel, and John R. Wullert II, IEEE JQE **28**, 908 (1992)

[5] Daniel J. Kane, Rick Trebino, Opt. Lett. **18** 823 (1993)

THz study of field screening: 10 fs - 100 fs regime

B. B. Hu, E.A. DeSouza, W. H. Knox, M. C. Nuss, and J. E. Cunningham
AT&T Bell Laboratories, 101 Crawfords Corner Rd., Holmdel NJ 07733-3030
Tel.: 908-949-4925, Fax: 908-949-2473

Abstract

We report the first THz study of field screening dynamics in the 10- 100 fs regime. The instantaneous polarization contribution and the transport contribution are clearly resolved in the time domain.

THz study of field screening: 10 fs- 100 fs regime

B. B. Hu, E.A. De Souza, W. H. Knox, M. C. Nuss, and J. E. Cunningham
AT&T Bell Laboratories, 101 Crawfords Corner Rd., Holmdel NJ 07733-3030
Tel.: 908-949-4925, Fax: 908-949-2473

One of the unsolved problems in studying THz emission from semiconductor surfaces is to distinguish between the contributions caused by acceleration of carriers and by instantaneous polarization of electron and hole pairs under an electric field. In a multiple-quantum-well structure where the carrier transport is prohibited by the quantum confinement, the instantaneous polarization is the only source for THz emission [1]. In a bulk sample, both effects contribute to the THz emission [2]. To unambiguously distinguish the two effects, we need to separate two effects in the time domain. Such a measurement requires a time resolution in the range of 10 fs, for the transport effect quickly increases due to the ballistic acceleration of photocarriers in the early time stage. Here, we report the first THz study on such a time scale. Our experimental results clearly distinguish the contributions of both effects in the different times.

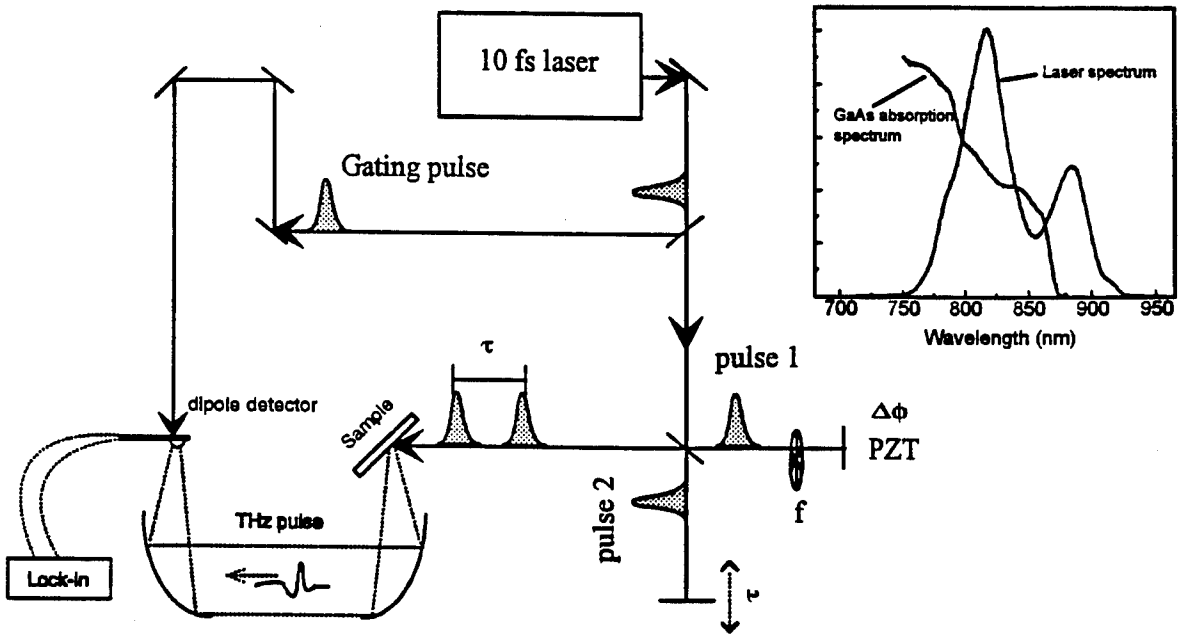


Fig.1 :The experimental setup. Inset: The laser spectrum for the 10 fs pulse, and the absorption spectrum for GaAs sample.

The experimental setup is shown in Fig. 1. The laser is identical in design to that by Margaret Murnane et al at Washington State University. The sample we use in the measurement has a 10 μm GaAs layer grown by MBE on an n^+ GaAs substrate. The built-in field is estimated to be 20 kV/cm. To achieve a time resolution of optical pulse duration, we use correlation techniques. We measure the total THz pulse energy by optical pulse 1 under the influence of the prepulse (pulse 2) at different time delays between the two pulses(pulse1 and pulse 2) since the change in THz pulse energy reflects the screening of the dc field by the prepulse. We record the THz temporal waveforms by pulse 1 for different time

delays relative to the prepulse (pulse 2). From each waveform, we calculate the THz pulse energy. In this case, the time resolution is limited only by the optical pulse duration, not the detector response. The experimental result is plotted in figure 2. The upper dots are the THz pulse energy by pulse 1 when the prepulse (pulse 2) is set at different relative time delays. For reference we have also measured the second harmonic autocorrelation of the optical pulse in the exactly same setup (the lower trace in Fig. 2). This measurement has been repeated at different crystal azimuthal angles. No crystal orientation dependence is observed within our experimental accuracy, indicating that the bulk $\chi^{(2)}$ effect in our measurements is not important.

The experimental results clearly demonstrate both the instantaneous polarization effect and the transport effect in different time domains. The sharp dip can only be attributed to the instantaneous polarization of photocarriers because during such a short time the carriers can hardly move any distance to screen the dc field. The polarization contribution detected here is proportional to the product of the two optical fields , and it has an opposite polarity to that caused by the transport effects, resulting in a reduction in total THz signal by pulse 1. This effect only occurs when the teime delay between two optical pulses is within the coherence of the electron and hole pairs. As time increases, photocarriers generated by the prepulse drift apart in opposite directions under the influence of the field, build up a space charge field which reduces the existing dc field. This is clearly reflected by the relatively slow decay in Fig. 2. In our measurement the photocarrier density is around $4\times10^{15}cm^{-3}$. Under such a low carrier density, in the initial 100 fs, the carrier transport motion does not suffer any scattering events,

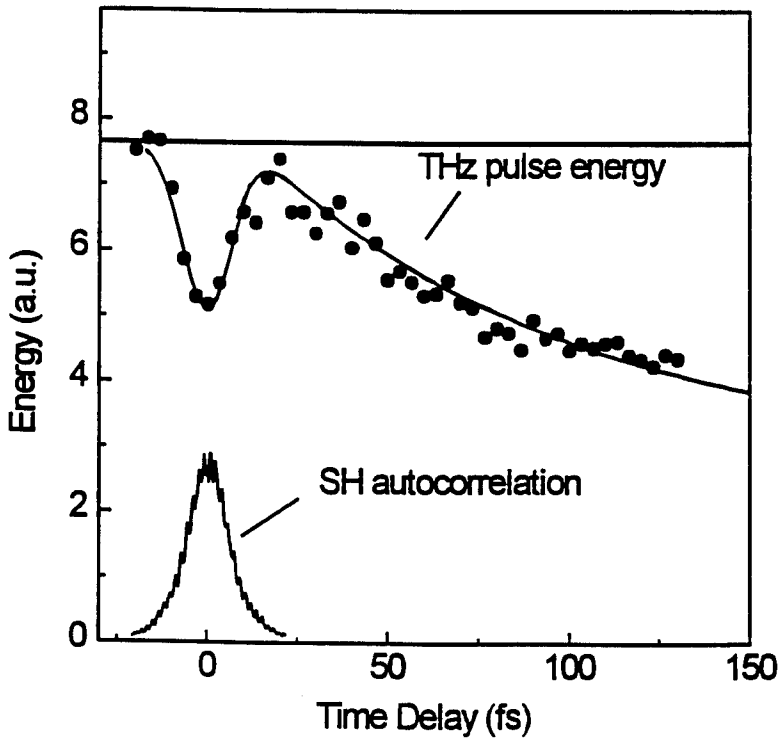


Fig.2: The upper dots are the THz pulse energy at different time delays relative to the prepulse (pulse 2). The lower solid curve is the SH autocorrelation of the optical pulse.

therefore is ballistic. The time dependence of the field can be approximated by: $E_{dc}(t)=E_{dc}(0)exp(-t/\tau)$, and τ is given by: $\tau=\sqrt{\varepsilon m_e / N e^2}$, where N the photocarrier density, e is the electron charge, ε is the dielectric constant, and m_e is the electron effective mass. The THz energy is proportional to the square of the dc field. Therefore, the THz energy decays with a time constant of $\tau/2$. We calculate from our experiment condition the decay time $\tau/2$ to be 120 fs, which is very close to that deduced form Fig. 2.

The instantaneous polarization occurs within the the time during which the electron and hole wavefunction are phase-correlated. We study this by measuring the change of THz field induced by varying the phase of the optical field. In the experiment, we modulate only the optical phase of pulse 1 with a PZT transducer and set the gating pulse of dipole detector at the maximum point of the THz waveform generated by pulse 1 alone (shown in fig. 3 as inset) . We record the change in THz while varying the time delay between pulse 1 and pulse 2. Figure 3 shows the experimental results. The coherent contribution detected seems to last as long as the optical pulse duration.

In summary, we have clearly demonstrated and separated the instantaneous polarization effect and transport effect in different time domains.

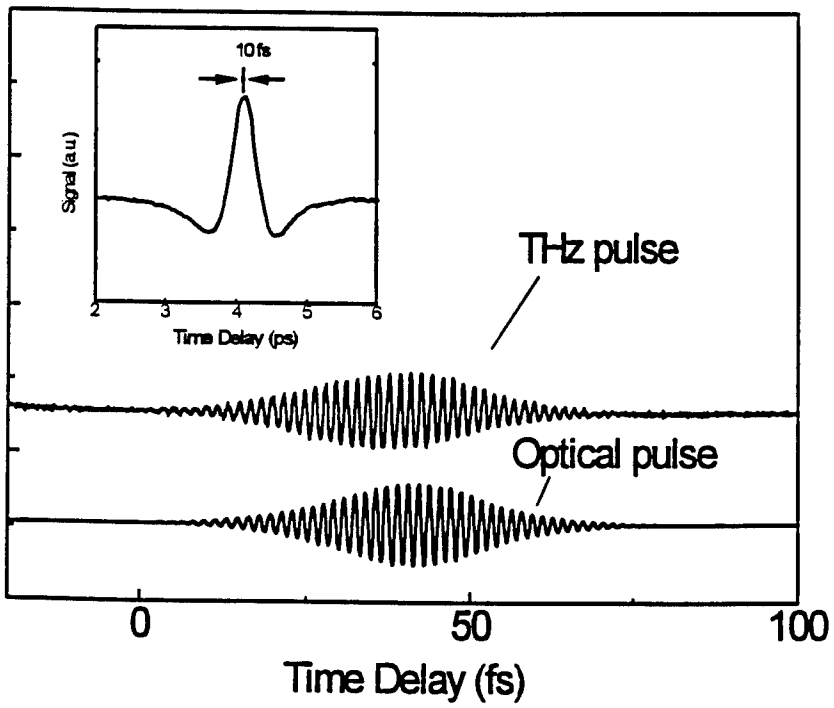


Fig. 3: The upper curve: is the Interference measurement for coherent contribution. The lower curve is a linear optical interferogram for ref. Inset: THz waveform by pulse 1 detected by dipole detector. The time scale we are interested is marked on the THz waveform.

Reference:

[1] P. C. Planken, M. C. Nuss, W. H. Knox, K. Goossen and D. A. B. Miller, Appl. Phys. Lett. vol., 61, 2009, 1992.

[2 B. B. Hu, A. W. Weling, D. H. Auston, A. V. Kuznetsov and C. J. Stanton, Phys. Rev. B. vol., 49, 2234, 1994.

The First Determination of Extremely Fast Biexcitonic Radiative Decay in GaAs Quantum Wells

Hailin Wang, Jagdeep Shah, T.C. Damen, and L.N. Pfeiffer

AT&T Bell Laboratories, Holmdel, NJ 07733

Abstract

Femtosecond time-resolved luminescence shows for the first time the surprisingly fast (2 ps) biexcitonic radiative decay in GaAs quantum wells. The decay is shown to be due to the giant biexciton oscillator strength.

The First Determination of Extremely Fast Biexcitonic Radiative Decay in GaAs Quantum Wells

Hailin Wang, Jagdeep Shah, T.C. Damen, and L.N. Pfeiffer
AT&T Bell Laboratories, Holmdel, NJ 07733

In this paper we present the first femtosecond study of resonantly-excited excitonic as well as biexcitonic luminescence in GaAs quantum wells. By directly creating biexcitons through two-photon absorption, we are able to measure for the first time the spontaneous emission rate of biexcitons in GaAs quantum wells. The extremely fast decay rate (nearly 2 ps) obtained is shown to be due to the giant oscillator strength for the biexciton to exciton transition. Differential transmission measurements further confirm the effect of the giant biexciton oscillator strength in absorption processes, which should impact interpretations of many previous nonlinear studies in GaAs quantum wells. The much improved time resolution also demonstrates for the first time the crucial role of momentum relaxation in initial spontaneous emission of excitons in quantum wells, reflecting the fundamental difference between the exciton-photon and the atom-photon interactions. Quantum beats in exciton luminescence have also been revealed

The femtosecond time resolution for resonantly-excited luminescence is achieved for the first time by upconverting the luminescence in a nonlinear crystal with output from a synchronously pumped optical parametric oscillator. Excitons are resonantly excited with 120 fs pulses centered at 6 meV below the heavy hole resonance. The samples were kept at 10 K and the exciton densities used are estimated to be between 10^9 to 10^{10} /cm^2.

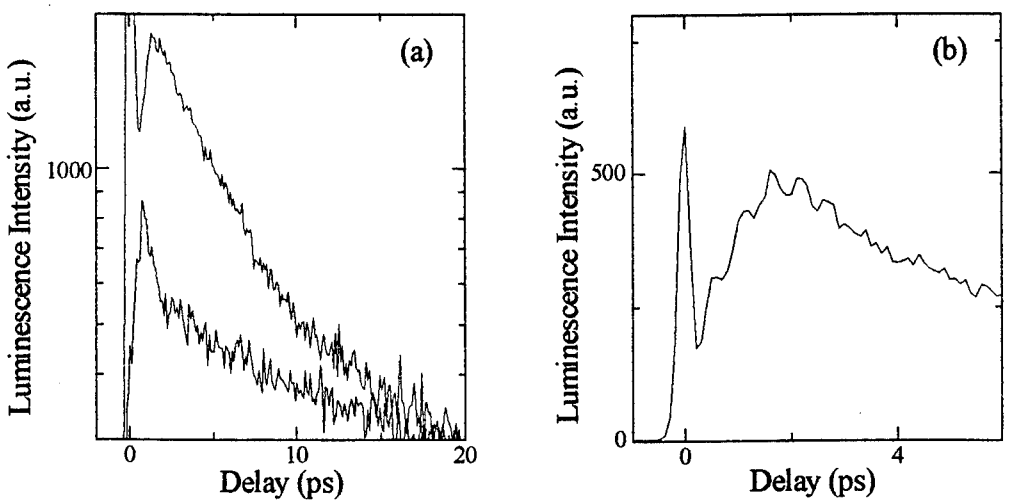


Fig. 1 Temporal evolution of resonantly-excited exciton and biexciton luminescence. The spike at t=0 is due to scattering of the laser pulse from the sample surface. (a) Excited with a linearly polarized field. Top curve: co-polarized luminescence. Bottom curve: cross-polarized luminescence showing extremely fast initial decay. (b) Excited with a circularly polarized field.

Although decay of the excitonic luminescence has been studied in detail in GaAs quantum wells [1,2], no information is available on decay of the biexcitonic luminescence. We investigate the biexcitonic spontaneous emission by using linearly polarized excitation pulse and detecting the decay of the cross-polarized luminescence. Because of the unique optical selection rule for the biexciton, in the absence of spin relaxation, the cross-polarized luminescence results from decay of the biexciton into a photon and an exciton. The biexcitons in this case are created resonantly through the biexcitonic two-photon absorption process. Figure 1a shows decay of both co-polarized and cross-polarized luminescence from a 135 Å quantum well. The ratio of the peak intensities of the cross-polarized over the co-polarized luminescence increases linearly with the input photon flux at low excitation levels, confirming the biexcitonic origin of the cross-polarized luminescence. The initial decay of the cross-polarized luminescence is extremely fast (2 ps), in sharp contrast to the exciton luminescence. The decay rate is much faster than both the exciton energy relaxation rate and the exciton recombination rate [1,2]. Below a temperature of 20 K and an exciton density of 10^{10} /cm^2, the initial decay is nearly independent of the excitation level and temperature. The extremely fast decay rate, however, is consistent with the giant oscillator strength for the decay of a biexciton into a photon and an exciton [3].

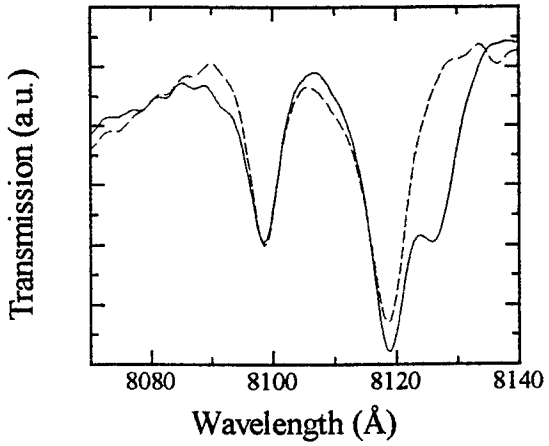


Fig. 2 Transmission of a circularly-polarized probe pulse in the presence of a co-circularly polarized pump (dash lines) and a cross-circularly polarized pump (solid line). A 170 Å GaAs quantum well is used.

The reverse process for the biexcitonic decay discussed above is the conversion of an exciton into a biexciton by absorbing an additional photon. This process is also expected to be greatly enhanced by the giant biexciton oscillator strength. Figure 2 shows the transmission spectra of a circularly polarized pulse. As expected, the giant biexciton-induced resonance appears when a cross-polarized pump is used. Effects of the giant biexciton oscillator strength

should also affect interpretations of many previous nonlinear optical studies in GaAs quantum wells.

The temporal evolution of the photoluminescence shown in Fig. 1b is obtained with a circularly polarized excitation field. The periods of the oscillation correspond to the heavy and light hole splitting of the sample. The observed quantum beats are the result of the excitation of a coherent superposition state of the heavy and light hole excitons. What is striking in Fig. 1b is that, unlike similar measurements in atomic vapors, the luminescence signal does not peak right after the excitation pulse but at 2 ps later. Conceptually, excitons created by the excitation pulse have a momentum $k_{||}$, the photon momentum along the plane of the quantum well. Because of momentum conservation., the exciton can not emit a photon in directions other than the transmitted or reflected direction of the excitation pulse before the exciton momentum is randomized through momentum scattering. Hence, the observed rise time of the exciton luminescence is determined by momentum relaxation. This is the first determination of the quasi-elastic momentum scattering of excitons in a semiconductor. It is interesting to point out that as shown in Fig. 1b, momentum relaxation is faster than exciton dephasing that determines the decay of the quantum beats. We also note that the rise time of the biexcitonic luminescence shown in Fig. 1a still remains to be explained.

We wish to thank Spectra-Physics Lasers, Inc. for the loan of an optical parametric oscillator.

1) B. Deveaud, F. Clerot, N. Roy, K. Satzke, B. Sermage, and D.S. Katzer, Phys. Rev. Lett. **67**, 2355 (1991).
2) A. Vinattieri, Jagdeep, Shah, T.C. Damen, D.S. Kim, L.N. Pfeiffer, and L.J. Sham, Solid State Comm. **88**, 189 (1993).
3) A.A. Golovin and E.I. Rashba, JETP Lett. **17**, 478 (1973).

Key To Author-Postdeadline
1994 Ultrafast Phenomena

Antonetti, A. - PD1
Asplund, M. - PD9
Audebert, P. - PD1

Bigot, Jean-Yves - PD3
Bucksbaum, Philip Howard - PD11
Burgel, M. V. - PD10

Chang, Yu-Ming - PD6
Cornaggia, C. - PD2
Cunningham, J. - PD12

D'Oliveira, P. - PD2
Daguzan, Ph. - PD1
Damen, T. - PD13
Daunois, A. - PD3
DeSouza, E. - PD12
Dlott, Dana - PD4
Dos Santos, A. - PD1
Duppen, Koos - PD10

Elsaesser, Thomas - PD8

Fayer, Michael - PD4

Gauthier, Jean-Claude - PD1
Geindre, J - PD1
Guizard, S. - PD1

Haas, Stephen - PD8
Hamoniaux, G. - PD1
Harris, Charles - PD9
Hill, J. - PD4
Hoogenraad, J. - PD11
Hu, BinBin - PD12

Kandori, Hideki - PD5
Kang, Tai Jong - PD7
King, J. - PD9
Knox, Wayne - PD12
Krastev, K. - PD1

Krause, Jeffrey - PD11
Kuhn, T. - PD8

Le Moigne, J. - PD3
Leitenstorfer, A. - PD8
Lohner, A. - PD8

Martin, P. - PD1
Meynadier, P. - PD2
Mizukami, Taku - PD5

Naitoh, Yukito - PD7
Nakanishi, Koji - PD5
Normand, D. - PD2
Nuss, Martin - PD12

Peterson, Kristin - PD4
Petite, Guillaume - PD1
Pfeiffer, L.N. - PD13
Pham, T. - PD3
Pinkos, Daniel - PD11

Rossi, F. - PD8

Sasabe, Hiroyuki - PD5
Sauter, B. - PD4
Schmidt, Martin - PD2
Schumacher, D. - PD11
Shah, Jagdeep - PD13
Shichida, Yoshinori - PD5

Tokmakoff, Andrei - PD4
Tom, Harry - PD6
Tominaga, Keisuke - PD7

Wang, Hailin - PD13
Wiersma, Douwe - PD10
Wilson, Kent - PD11

Xu, Li - PD6

Yoshihara, Keitaro - PD7
Yoshizawa, Toru - PD5

Zimdars, David - PD4

ThD26-1

Impulsive excitation of LO phonons and induced transient refractive index change measurement.

D. P. Kien[1], O. Albert[1], J. Cl. Loulergue[1,2] and J. Etchepare[1]

[1]Laboratoire d'Optique Appliquée CNRS URA 1406
Ecole Polytechnique-ENSTA 91120 Palaiseau, France
[2]Centre Lorrain d'Optique et Electronique du Solide
Université de Metz et Supelec 57078 Metz, France
tel: 33 1 60100318; fax: 33 1 60106085

Abstract.

We present a two-beam two-wavelength set-up which enables: (i) direct excitation of LO phonon(s), (ii) time resolved measurement of the resultant phase deformation by a far field analysis. This technique has been applied to the study of several ferroelectric crystals.

ThD26-2

Impulsive excitation of LO phonons and induced transient refractive index change measurement.

D. P. Kien[1], O. Albert[1], J. Cl. Loulergue[1,2] and J. Etchepare[1]

[1]Laboratoire d'Optique Appliquée CNRS URA 1406
Ecole Polytechnique-ENSTA 91120 Palaiseau, France
[2]Centre Lorrain d'Optique et Electronique du Solide
Université de Metz et Supelec 57078 Metz, France
tel: 33 1 60100318; fax: 33 1 60106085

LO and/or TO phonon study led to growing interest for these last few years due to a direct excitation by femtosecond pulses. Three beam techniques were connected mostly to CARS or transient grating arrangements whereas two beam experiments dealt with overall transmission or reflectivity change measurements.

M. Sheik-Bahae et al. developed recently1 a technique based on the phase modulation measurement which, apart from its seemingly easy implementation, lead to a linear dependency of the signal in the refractive index changes. This renewed interest in nonlinear property measurements of non-absorbing materials, for which current experiments correspond to the measurement of a signal quadratic with respect to refractive index changes.We present here an extension of this technique to a two-beam two-wavelength experiment which allows a temporal analysis of the various processes involved in the transient phase modulation.

Our experimental geometry uses a classical pump-probe scheme. Pump pulses at 620 nm and 80 fs FWHM are used with a typical intensity in the μJ level. Probe pulses, at 650 nm are picked up from a continuum of light. To obtain the kinetics of the phase change, the sample is set at the waist of the pump beam, which Rayleigh length is

higher than the sample thickness. We will first discuss on the sensitivity of the technique and the linearity of the transmittance as a function of the phase deformation amplitude in the case of different geometrical arrangements: location of the probe focal plane, shape of the aperture (hole and ring).

Figure 1 illustrates typical time-resolved phase changes in $KNbO_3$. Normalized transmittance is compared for a hole and a ring aperture. The large signal around zero time delay between pump and probe corresponds to (second and third order) nonresonant electronic susceptibilities. At positive time delays, two processes may be distinguished: an intricate shaped long lived signal with a non instantaneous rise time, and an oscillatory contribution. We will only focus hereafter on this sinusoidal part. Exact knowledge of the zero time delay allows to ascertain a sine-dependence of the signal, which is a signature of a ground state impulsive phonon excitation. Its period corresponds of the range of the spectral width of the pump pulses.

We will discuss on the polarization characteristics of the signal for $KNbO_3$ and several other ferroelectrics, with respect to crystal symmetries and second and third order susceptibility tensor elements relevant in the processes allowed for excitation and measurement procedures. We will finally focus on the differences between the processes involved in the case of polar and non polar modes.

References.

1. M. Sheik-Bahae, A. A. Said, T. Wei, D. J. Hagan and E. W. Van Stryland, J. of Quantum Electron., 26, 760, 1990.
2. T. Fukumoto, A. Okamoto, T. Hattori and A. Mitsuishi Solid State Commun., 17, 427, 1975.

ThD26-4

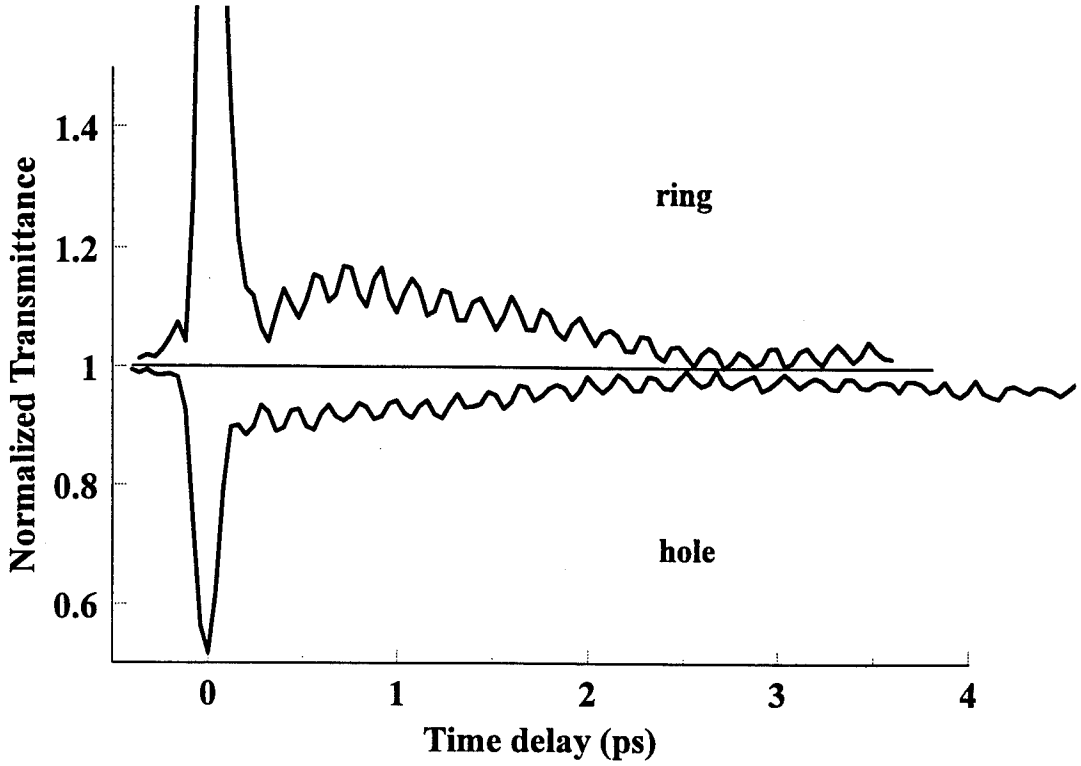


Fig.1: Variation of the normalized transmittance as a function of time delay for $KNbO_3$. Polarization of pump and probe pulses are parallel to c axis of the crystal.

TECHNICAL PROGRAM COMMITTEE

Gerard Mourou, *University of Michigan, Chair*
Ahmed H. Zewail, *California Institute of Technology, Chair*
Paul F. Barbara, *University of Minnesota, Program Chair*
Wayne H. Knox, *AT&T Bell Laboratories, Program Chair*
John E. Bowers, *University of California, Santa Barbara*
Philip H. Bucksbaum, *University of Michigan*
Paul B. Corkum, *National Research Council of Canada*
Irl N. Duling, *U.S. Naval Research Laboratory*
Roger N. Falcone, *University of California, Berkeley*
James G. Fujimoto, *Massachusetts Institute of Technology*
Edwin J. Heilweil, *National Institute of Standards and Technology*
Daniele Hulin, *Laboratoire d'Optique Appliquee, France*
Anthony M. Johnson, *AT&T Bell Laboratories*
James D. Kafka, *Spectra Physics, Inc.*
Takayoshi Kobayashi, *University of Tokyo, Japan*
Heinrich Kurz, *Institute of Semiconductor Electronics, Germany*
R. J. Dwayne Miller, *University of Rochester*
Margaret M. Murnane, *Washington State University*
Anne B. Myers, *University of Rochester*
Keith A. Nelson, *Massachusetts Institute of Technology*
Martin C. Nuss, *AT&T Bell Laboratories*
Sanford Ruhman, *Hebrew University, Israel*
Wilson Sibbett, *University of St. Andrews, U.K.*
John D. Simon, *University of California, San Diego*
Jurgen Troe, *Institut fur Physikalische Chemie de Universitat, Germany*
Douwe A. Wiersma, *University of Groningen, The Netherlands*
Keitaro Yoshihara, *Institute for Molecular Science, Japan*
Wolfgang Zinth, *University of Munich, Germany*

ADVISORY COMMITTEE

D. H. Auston, *Columbia University*
K. B. Eisenthal, *Columbia University*
Graham Fleming, *University of Chicago*
Charles B. Harris, *University of California, Berkeley*
Eric Ippen, *Massachusetts Institute of Technology*
Robin Hochstrasser, *University of Pennsylvania*
W. Kaiser, *Technical University of Munich, Germany*
J. L. Martin, *ENSTA, France*
Arnold Migus, *ENSTA, France*
Gerard Mourou, *University of Michigan*
C. V. Shank, *Lawrence Berkeley Laboratories*
Anthony Siegman, *Stanford University*
Tatsuo Yajima, *The University of Tokyo, Japan*
Keitaro Yoshihara, *Institute for Molecular Science, Japan*
Ahmed Zewail, *California Institute of Technology*